

Theodor Schneller · Rainer Waser
Marija Kosec · David Payne *Editors*

Chemical Solution Deposition of Functional Oxide Thin Films

 Springer

Chemical Solution Deposition of Functional Oxide Thin Films

Theodor Schneller • Rainer Waser • Marija Kosec •
David Payne
Editors

Chemical Solution Deposition of Functional Oxide Thin Films

 Springer

Editors

Theodor Schneller
Rainer Waser
RWTH Aachen University
Aachen
Germany

Marija Kosec
Jožef Stefan Institute
Ljubljana
Slovenia

David Payne
University of Illinois at Urbana-Champaign
Urbana
Illinois, USA

ISBN 978-3-211-99310-1 ISBN 978-3-211-99311-8 (eBook)
DOI 10.1007/978-3-211-99311-8
Springer Wien Heidelberg New York Dordrecht London

Library of Congress Control Number: 2013956214

© Springer-Verlag Wien 2013

This work is subject to copyright. All rights are reserved by the Publisher, whether the whole or part of the material is concerned, specifically the rights of translation, reprinting, reuse of illustrations, recitation, broadcasting, reproduction on microfilms or in any other physical way, and transmission or information storage and retrieval, electronic adaptation, computer software, or by similar or dissimilar methodology now known or hereafter developed. Exempted from this legal reservation are brief excerpts in connection with reviews or scholarly analysis or material supplied specifically for the purpose of being entered and executed on a computer system, for exclusive use by the purchaser of the work. Duplication of this publication or parts thereof is permitted only under the provisions of the Copyright Law of the Publisher's location, in its current version, and permission for use must always be obtained from Springer. Permissions for use may be obtained through RightsLink at the Copyright Clearance Center. Violations are liable to prosecution under the respective Copyright Law.

The use of general descriptive names, registered names, trademarks, service marks, etc. in this publication does not imply, even in the absence of a specific statement, that such names are exempt from the relevant protective laws and regulations and therefore free for general use.

While the advice and information in this book are believed to be true and accurate at the date of publication, neither the authors nor the editors nor the publisher can accept any legal responsibility for any errors or omissions that may be made. The publisher makes no warranty, express or implied, with respect to the material contained herein.

Printed on acid-free paper

Springer is part of Springer Science+Business Media (www.springer.com)

Preface

Chemical solution deposition (CSD) has emerged as a mature technique for the fabrication of functional oxide thin films due to a number of advantages. While the development of sol–gel type CSD processes for optical coatings of glass dates from the mid-twentieth century, the first chemical solution-deposited complex electronic oxide thin films were prepared only as recently as the 1980s. Since the initial studies, a wide variety of perovskite-related and other compounds on various types of substrates have been prepared as thin films with CSD techniques. Substantial progress in the understanding of the processes has been made which enables the fabrication of device quality films by CSD methods nowadays. Various symposia of the Materials Research Society on solution-based materials fabrication, workshops, and conferences have been held and a number of more or less comprehensive review articles and book chapters have been published on this topic. The whole diversification, however, is barely represented in the above-mentioned reviews and a comprehensive textbook on the CSD technology has not been available up to now.

The aim of the book is to comprise the experience of the last 25 years on CSD of mainly electroceramic thin films, with some extensions, as well as CSD-related application areas into a text and reference book. The content is written on a level that should be comprehensible for Material Science students in their third year. So, all the basic chemistry and physics knowledge for typical Material Science curricula should be present.

With the unexpected death of Prof. Fred Lange, author of Chap. 16, and Prof. Marija Kosec, coeditor and coauthor of several book chapters, during the work on this monograph, the community unfortunately lost two outstanding researcher personalities. While Lange was a pioneer in growing epitaxial films by CSD methods, Kosec's CSD-related work was dedicated to the understanding of complicated reactions during solution synthesis and how to control these reactions with regard to ferroelectric thin film preparation. She was always enthusiastically promoting the field of CSD processing in the materials science community. In this sense she was also an avid supporter of the European Union's program for Cooperation in Science and Technology (COST).

The editors would like to thank their 54 authors for their excellent contributions, for a wonderful communication over many years, for their willingness to adopt our ideas for modifications, and for their perseverance. Moreover the editors would like to thank Dagmar Leisten and Thomas Pössinger from IWE II, RWTH Aachen University, for their huge effort and expertly drawing, retracing, optimizing, and generation of most of the artwork of this book. They did an excellent job in creating printable figures from nonoptimal submissions and did their best to get the figures to a more uniform style. One of the editors, (TS), would also like to thank his wife and his children for their patience and understanding during the work on this book project.

Aachen, Germany
Aachen, Germany
Ljubljana, Slovenia
Urbana, IL
May 2013

Theodor Schneller
Rainer Waser
Marija Kosec[†]
David Payne

General Introduction

Chemical solution based preparation of inorganic solid state materials by sol–gel processing dates back to the mid of the nineteenth century, where Ebelmen discovered that silicon alkoxides react slowly with humidity (hydrolysis) to yield hydrated silica (gel) [1–3]. Almost 100 years later, first works to use sol–gel processes for modification of optical glasses was focused on SiO_2 layers [4] followed by further single oxide coatings, such as TiO_2 , ZrO_2 , Al_2O_3 etc., as well as multilayer coatings [5–7]. Since the 1950s optical coatings on large planes of glass have been produced in this way on an industrial scale [8, 9].

In the 1970s, optically transparent electrically conducting films were developed by the Philips research laboratory Aachen for heat-reflecting filters [10, 11]. In the 1980s, the pioneering works of Fukushima and coworkers [12] on metallo-organic decomposition (MOD) and of the Payne’s group [13, 14] on sol–gel processing of lead zirconate titanate (PZT) thin films have been the first steps into ternary and quaternary perovskites, demonstrating that complex electronic oxide thin films can be fabricated by chemical solution deposition (CSD) reaching desired properties similar to the corresponding bulk materials. Together with the excellent works of Klee [15–18], Sayer [19, 20], Kosec [21–24], Sporn [25], Milne [26, 27], Schwartz [28, 29], and others on wet chemical synthesis of materials [30], these studies gave the impetus for a rapid international growth of this field with investigations in the world on functional oxide thin film devices. This is reflected in a number of review articles and single book chapters [31–47]. The main drivers for the research progress were ferroelectric thin film materials for applications in different kinds of memory devices, in particular ferroelectric nonvolatile memories—FERAM, as well as piezoelectric sensors and actuators, pyroelectric detectors of infrared radiation, and integrated high-permittivity (high-k) capacitors. Thus most of the reviews focus on these materials. Meanwhile the CSD method was also successfully applied in other fields of functional oxides such as conducting thin films, i.e., electron conducting, ion conducting, and superconducting films, for applications in displays, solid oxide fuels cells, and coated conductors.

The present book summarizes the developments of the last 25–30 years in the field of CSD. It covers all relevant aspects starting from the precursor chemistry via the processing aspects up to examples for applications. A generalized flow chart of the CSD procedure, the main body of which is subdivided into parts according to the different processing steps, is shown in Fig. 1.

These “*Parts*” plus “*Analytical Methods*” represent the organization scheme of the book which will be shortly summarized below.

Film fabrication by CSD typically begins with the solution synthesis in the chemistry lab (Part I). The main precursors are salts, carboxylates, or other metallo-organic compounds such as metal alkoxides and metal β -diketonates, which can often be purchased commercially or synthesized in-house by common chemical synthesis strategies.

By simple dissolution or refluxing them at elevated temperatures in appropriate solvents, sometimes with intermediate distillation steps, and mixing in the correct stoichiometric ratio, precursor solutions are obtained, which usually contain the desired thin film stoichiometry. Often additives such as chemical stabilizers are included during synthesis to adjust the properties of the final coating solution. Under certain circumstances compositional corrections with respect to the exact metal oxide stoichiometry are required. These comprise:

- Losses due to the volatility of a component (e.g., PbO)
- Losses due to component diffusion into the substrate (e.g., Bi loss from strontium bismuth tantalate—SBT)
- Intentional off-stoichiometry for desired generation of secondary phases or native point defects

Next, the coating solution is deposited by a number of methods (Part III). Spin- and dip coating in various modifications are the by far most frequently applied techniques. Aerosol deposition (often denoted as spray coating) and, more recently, ink-jet printing are more sophisticated methods allowing for a more conformal coating or structured coating with reduced material consumption. Subsequently, the (wet) as-deposited film is dried, pyrolyzed,¹ crystallized, and (optionally) post-annealed for further densification or microstructure manipulation (Part IV). Often, individual processing steps such as gel formation and organic removal cannot be separated as implied in Fig. 1. The conversion of the wet, as-deposited film into the desired crystalline film is induced through controlled thermal processes in the temperature range from ~200 to 800 °C, which have to be adjusted to the character

¹ The term “pyrolysis” is normally defined as the conversion of solid organic materials into gases and liquids by indirect heat under exclusion of air, or oxygen, respectively. The material within the reaction chamber is heated to temperatures between 400 and 800 °C. The pyrolysis process is sometimes referred to as thermolysis. This is merely a preference in the choice of terminology. Although the process reaction volatilizes and decomposes solid organic materials by “heat,” the Greek translation of “pyro” is “fire,” whereas “thermo” is more correctly, “heat.” Thus—thermolysis. Hence in case of the CSD technology, the term pyrolysis is predominantly used to describe the decomposition of the organic matrix in air or oxygen [34].

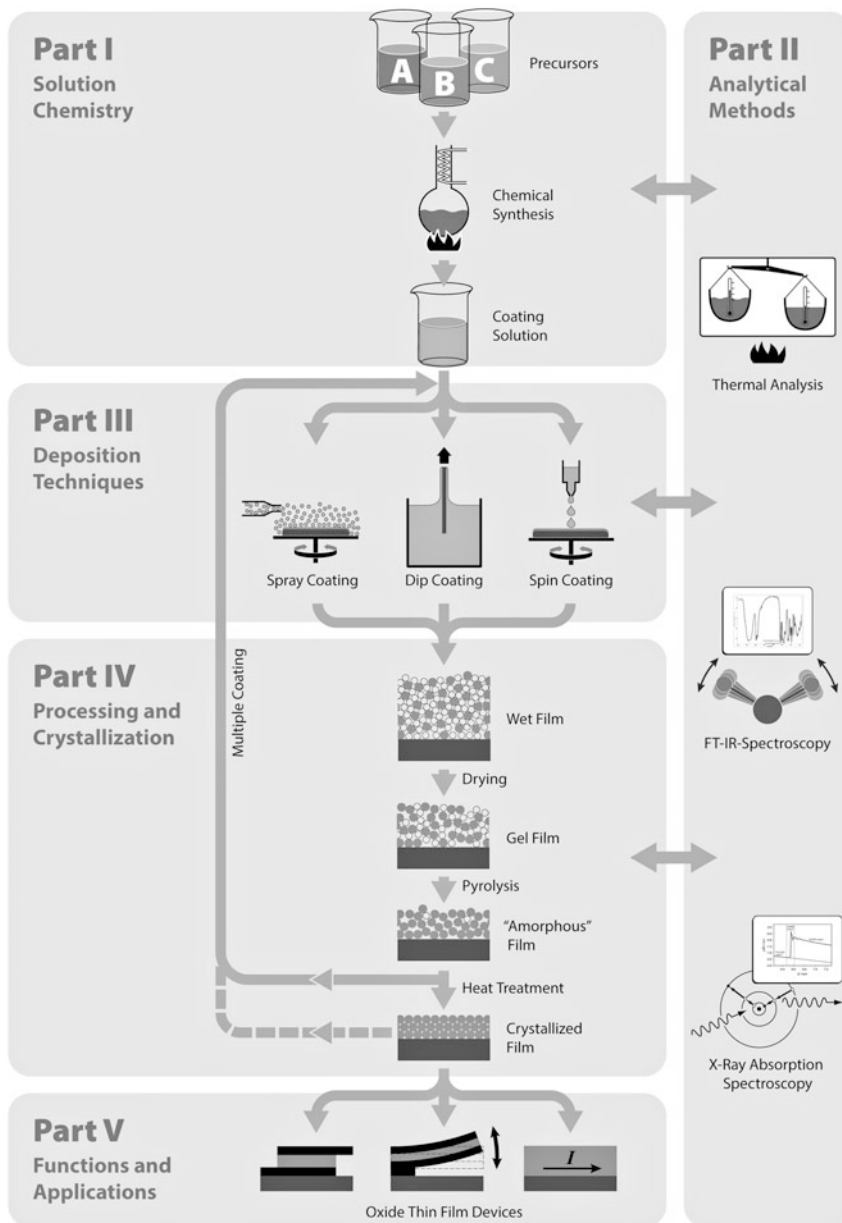


Fig. 1 Flow chart of a typical CSD process. It shows schematically the different processing steps starting with solution synthesis, followed by deposition and crystallization, and ending with functional oxide thin film devices. Frequently applied analytical methods are shown on the *right*

of the nucleation and growth behavior of the material under study. Typically hot plates in combination with a conventional furnace or a rapid thermal annealing (RTA) oven are employed for this transformation process. In specific cases, such as temperature-sensitive substrates, the use of lasers for the annealing may be indicated [48]. Depending on the specific CSD route and film deposition method, numerous variations in thermal processing conditions are utilized. For example, if the desired film thickness is not obtained in the first coating cycle, the deposition and thermal process sequence are repeated to prepare thicker films. When the desired film thickness is obtained, a final thermal treatment at a still higher temperature may be employed to initiate crystallization, to improve microstructure, or to increase film density.

As indicated by the double arrows in Fig. 1, the process can be monitored at various stages by a number of analytical methods (Part II). X-ray diffraction (XRD) and electron microscopy (scanning—SEM² and transmission—TEM), well established and often available in material science labs, are the standard methods to characterize phase and morphology of pyrolyzed and crystallized films. To study the solution chemistry and phase evolution, thermal analysis and Fourier transform infrared spectroscopy (FTIR) are the most frequently applied methods. Moreover X-ray absorption spectroscopy, although more sophisticated, is often employed since it yields structural information from the precursors independent of the physical state, i.e., also from solutions and amorphous solids.

Finally oxide thin film devices, such as capacitors, piezoelectric actuators, or conductors for various fields of applications can be fabricated from the crystallized films (Part V).

In order to implement the CSD method for a thin film material system, a number of general prerequisites for the precursor solutions, the substrates, and processing itself have to be fulfilled in order to yield the desired results:

- (a) Sufficient solubility of all educts in the solvent, i.e., formation of a stable 1-pot coating solution
- (b) Acceptable long-term stability of the precursor solution—reasonable minimum times are about 1 month
- (c) Selection of precursor systems that leaves solely the cations and oxygen present upon pyrolysis and crystallization
- (d) Adjusted solution rheology, i.e., modification of the solutions depending on the applied coating technique to avoid failures such as striations in spin coating, or sticking, and uncontrolled purging, respectively, of the precursor ink in the nozzles of an inkjet printer
- (e) Adequate wettability of the substrate.
- (f) Homogeneity, ideally at an “*atomic*” level, should be retained during the whole process, i.e., macroscopic phase separation of precursor components in the solution, during drying or pyrolysis must not occur

² Sometimes the term FESEM is used instead of SEM to indicate that the microscope works with a field emission cathode.

- (g) Crack and compositional nonuniformity formation during thermal processing have to be avoided
- (h) Marginal interdiffusion of film and substrate constituents
- (i) Minimal degradation of substrate properties during film processing.

If these requirements are fulfilled and if processing conditions are optimized, the CSD technique represents a rapid and cost-effective method of synthesizing high quality functional oxide thin films.

Organization of the Book

According to Fig. 1 the book is subdivided into the following five parts, which are further subdivided into individual chapters:

- Part I—Solution Chemistry
- Part II—Analytical Methods
- Part III—Deposition Techniques
- Part IV—Processing and Crystallization
- Part V—Functions and Applications

Each “*Part*” starts with a short survey on the corresponding content. A complementary “*Appendix*” chapter containing practical recipes for CSD processing concludes the book.

Aachen, Germany
Jülich, Germany

Theodor Schneller
Rainer Waser

References

1. Ebelmen M (1844) Sur les éthers siliciques. C R Hebd Seances Acad Sci 19:398–400
2. Ebelmen M (1846) Sur les combinaisons des acides borique et silicique avec les ethers. Ann Chim Phys 16:129–166
3. Ebelmen M (1847) Sur l’hyalite artificielle et l’hydrophane. C R Hebd Seances Acad Sci 25:854–856
4. Geffcken W, Berger E (1939) Verfahren zur Änderung des Reflexionsvermögens optischer Gläser. Deutsches Reichspatent, assigned to Jenaer Glaswerk Schott & Gen., Jena 736 411
5. Dislich H (1986) Sol-gel: science, processes and products. J Non-Cryst Sol 80:115–121
6. Schroeder H (1962) Properties and applications of oxide layers deposited on glass from organic solutions. Opt Acta 9:249–254
7. Geffcken W (1951) Dünne Schichten auf Glas. Glastechn Ber 24:143–151
8. Dislich H, Hussmann E (1981) Amorphous and crystalline dip coatings obtained from organometallic solutions. Procedures, chemical processes and products. Thin Solid Films 77:129–139
9. Aegerter MA, Mennig M (2004) Sol-gel technologies for glass producers and users, 1st edn. Springer, Heidelberg

10. Frank G, Kauer E, Köstlin H (1981) Transparent heat-reflecting coatings based on highly doped semiconductors. *Thin Solid Films* 77:107–117
11. Köstlin H, Jost R, Lems W (1975) Optical and electrical properties of doped In_2O_3 films. *Phys Status Solidi A* 29:87–93
12. Fukushima J, Kodaira K, Matsushita T (1984) Preparation of ferroelectric PZT films by thermal decomposition of organometallic compounds. *J Mater Sci* 19:595–598
13. Budd KD, Dey SK, Payne DA (1985) Sol-gel processing of PbTiO_3 , PbZrO_3 , PZT and PLZT thin films. *Brit Ceram Soc Proc* 36:107–121
14. Dey SK, Budd KD, Payne DA (1988) Thin-film ferroelectrics of PZT by sol-gel processing. *IEEE Trans UFFC* 35:80–81
15. Klee M (2001) Thin film capacitors for innovative microelectronic devices. *Ind Ceram* 21:31–33
16. Klee M, Mackens U (1996) Sol-gel and MOD processing of layered perovskite films. *Integr Ferroelectr* 12:11–22
17. Klee M, Mackens U, Pankert J, Brand W, Klee W (1995) Deposition of undoped and doped $\text{Pb}(\text{Mg},\text{Nb})\text{O}_3$ - PbTiO_3 , $\text{PbZr}_x\text{Ti}_{1-x}\text{O}_3$, alkaline earth titanate and layered perovskite thin films on Pt and conductive oxide electrodes by spin-on processing: correlation of growth and electrical properties. In: Auciello O, Waser R (eds) *Science and technology of electroceramic thin films. Proceedings of NATO advanced research workshop science and technology of electroceramic thin films*. Kluwer, Dordrecht, pp 99–115
18. Klee M, Brand W, de Vries JWC (1988) Superconducting films in the Y-Ba-Cu-O system made by thermal decomposition of metal carboxylates. *J Cryst Growth* 91:346–351
19. Yi G, Sayer M, Wu Z (1989) Piezoelectric lead zirconate titanate coatings on metallic wires. *Electron Lett* 25:907–908
20. Yi G, Wu Z, Sayer M (1988) Preparation of $\text{Pb}(\text{Zr},\text{Ti})\text{O}_3$ thin films by sol gel processing: electrical, optical, and electro-optic properties. *J Appl Phys* 64:2717–2724
21. Kosec M, Malic B, Mandeljc M (2002) Chemical solution deposition of PZT thin films for microelectronics. *Mater Sci Semicond Process* 5:97–103
22. Kosec M, Huang Y, Sato E, Bell A, Setter N, Drazic C, Bernik S, Beltram T (1995) Stoichiometry and phase structure of sol-gel-derived PZT-based thin films. In: Auciello O, Waser R (eds) *Science and technology of electroceramic thin films. Proceedings of NATO advanced research workshop science and technology of electroceramic thin films*. Kluwer, Dordrecht, pp 177–186
23. Drazic G, Beltram T, Kosec M (1994) Microstructural characterisation of sol-gel derived PLZT(9.5/65/35) thin films. *Ferroelectrics* 152:49–54
24. Beltram T, Kosec M, Stavber S (1993) Reactions taking place during the sol-gel processing of PLZT. *Mater Res Bull* 28:313–320
25. Merklein S, Sporn D, Schönecker A (1993) Crystallization behavior and electrical properties of wet-chemically deposited lead zirconate titanate thin films. *Mater Res Soc Proc* 310:263–268
26. Phillips NJ, Calzada ML, Milne SJ (1992) Sol-gel-derived lead titanate films. *J Non-Cryst Solids* 147–148:285–290
27. Phillips NJ, Milne SJ (1991) Diol-based sol-gel system for the production of thin films of PbTiO_3 . *J Mater Chem* 1:893–894
28. Schwartz RW, Xu Z, Payne DA, DeTemple TA, Bradley MA (1990) Preparation and characterization of sol-gel derived PbTiO_3 thin layers on GaAs. *Mater Res Soc Proc* 200:167–172
29. Tuttle BA, Schwartz RW, Doughty DH, Voigt JA, Carim AH (1990) Characterization of chemically prepared PZT thin films. *Mater Res Soc Proc* 200:159–165
30. Blum JB, Gurkovich SR (1985) Sol-gel-derived PbTiO_3 . *J Mater Sci* 20:4479–4483
31. Schwartz RW, Narayanan M (2009) Chemical solution deposition – basic principles. In: Mitzi D (ed) *Solution processing of inorganic materials*. Wiley, New York, pp 33–76

32. Schneller T, Majumder SB, Waser R (2008) Ceramic thin films. In: Riedel R, Chen IW (eds) *Ceramics science and technology*, 1st edn. Wiley VCH, Weinheim, pp 443–509
33. Schwartz R, Schneller T, Waser R, Dobberstein H (2005) Chemical solution deposition of ferroelectric thin films. In: Lee BI, Komarneni S (eds) *Chemical processing of ceramics*, 2nd edn. Taylor & Francis/CRC, Boca Roca, pp 713–742
34. Schwartz RW, Schneller T, Waser R (2004) Chemical solution deposition of electronic oxide films. *C R Chim* 7:433–461
35. Schneller T, Waser R (2002) Chemical solution deposition of ferroelectric thin films – state of the art and recent trends. *Ferroelectrics* 267:293–301
36. Waser R, Schneller T, Ehrhart P, Hoffmann-Eifert S (2001) Chemical deposition methods for ferroelectric thin films. *Ferroelectrics* 259:205–214
37. Waser R, Schneller T, Hoffmann-Eifert S, Ehrhart P (2001) Advanced chemical deposition techniques – from research to production. *Integr Ferroelectr* 36:3–20
38. Schwartz RW (1997) Chemical solution deposition of perovskite thin films. *Chem Mater* 9:2325–2340
39. Tuttle BA, Schwartz RW (1996) Solution deposition of ferroelectric thin films. *MRS Bull* 21:49–54
40. Schwartz RW, Boyle TJ, Lockwood SJ, Sinclair MB, Dimos D, Buchheit CD (1995) Sol-gel processing of PZT thin films a review of the state-of-the-art and process optimization strategies. *Integr Ferroelectr* 7:259–277
41. Lakeman CDE, Payne DA (1994) Sol-gel processing of electrical and magnetic ceramics. *Mater Chem Phys* 38:305–324
42. Chandler CD, Roger C, Hamden-Smith MJ (1993) Chemical aspects of solution routes to perovskite phase mixed metal oxides from metal-organic precursors. *Chem Rev* 93:1205–1241
43. Lee GR, Crayston JA (1993) Sol-gel processing of transition-metal alkoxides for electronics. *Adv Mater* 5:434–442
44. Yi G, Sayer M (1991) Sol-gel processing of complex oxide films. *Ceram Bull* 70:1173–1179
45. Haertling GH (1991) Ferroelectric thin films for electronic applications. *J Vac Sci Technol A* 9:414–420
46. Vest RW (1990) Metallo-organic decomposition (MOD) processing of ferroelectric and electro-optic films: a review. *Ferroelectrics* 102:53–68
47. Klein LC (ed) (1988) *Sol-gel technology for thin films, fibers, preforms, electronics, special shapes*. Noyes, Park Ridge, NJ
48. Baldus O, Waser R (2005) Experimental and numerical investigations of heat transport and crystallization kinetics in laser-induced modification of barium strontium titanate thin films. *Appl Phys A* 80:1553–1562

Contents

Part I Solution Chemistry

1 Simple Alkoxide Based Precursor Systems	3
Theodor Schneller	
2 Carboxylate Based Precursor Systems	29
Theodor Schneller and David Griesche	
3 Mixed Metallo-organic Precursor Systems	51
Barbara Malič, Sebastjan Glinšek, Theodor Schneller, and Marija Kosec	
4 Single Source Precursor Approach	71
Vadim G. Kessler	
5 Aqueous Precursor Systems	93
Marlies K. Van Bael, An Hardy, and Jules Mullens	
6 Polymer-Assisted Deposition	141
Anthony K. Burrell, Thomas M. McCleskey, and Quanxi Jia	

Part II Analytical Methods

7 Thermal Analysis	163
Barbara Malič, Alja Kupec, and Marija Kosec	
8 X-Ray Absorption Spectroscopy	181
Irene Schlipf, Matthias Bauer, and Helmut Bertagnolli	
9 Infrared Spectroscopy	213
Maria Zaharescu and Oana Cătălina Mocioiu	

Part III Deposition Techniques

10 Dip Coating	233
C. Jeffrey Brinker	
11 Spin Coating: Art and Science	263
Dunbar P. Birnie III	
12 Aerosol Deposition	275
Matt D. Brubaker	
13 Inkjet Printing and Other Direct Writing Methods	303
Paul G. Clem and Nelson S. Bell	
14 Chemical Bath Deposition	319
Mark R. De Guire, Luciana Pitta Bauermann, Harshil Parikh, and Joachim Bill	

Part IV Processing and Crystallization

15 Thermodynamics and Heating Processes	343
Robert W. Schwartz and Manoj Narayanan	
16 Epitaxial Films	383
Fred Lange	
17 Orientation and Microstructure Design	407
Susanne Hoffmann-Eifert and Theodor Schneller	
18 Low-Temperature Processing	431
Sebastjan Glinšek, Barbara Malič, and Marija Kosec	
19 Composite Film Processing	445
Robert Dorey, Subhasis Roy, A. Sharma, Chandan Ghanty, and Subhasish B. Majumder	
20 UV and E-Beam Direct Patterning of Photosensitive CSD Films . . .	483
Kiyoharu Tadanaga and Mohammad S.M. Saifullah	
21 Template Controlled Growth	517
Sven Clemens and Theodor Schneller	

Part V Functions and Applications

22 Thin Film Multilayer Capacitors	547
Hiroyuki Kambara, Theodor Schneller, and Rainer Waser	
23 Base Metal Bottom Electrodes	571
Jon F. Ihlefeld, Mark D. Losego, and Jon-Paul Maria	

24 Polar Oxide Thin Films for MEMS Applications	593
Paul Muralt	
25 Conducting Oxide Thin Films	621
Camilla Haavik and Per Martin Rørvik	
26 Transparent Conducting Oxides	655
Peer Löbmann	
27 Superconducting Films	673
Michael Bäcker, Martina Falter, Oliver Brunkahl, and Bernhard Holzapfel	
28 Antireflective Coatings and Optical Filters	707
Peer Löbmann	
29 Luminescent Thin Films: Fundamental Aspects and Practical Applications	725
Shinobu Fujihara	
Appendix A: Syntheses	747
Index	773

Part I

Solution Chemistry

In Part I the most important classes of educts, and precursor solutions respectively, used for CSD processing are discussed in detail. For solution synthesis from the different precursors various approaches ranging from simple dissolution of the starting material in a suitable solvent up to an initial conversion of the starting material into a more soluble or more stable derivative by refluxing and distillation are available. The simple rule “*similis similia solvuntur*” (like dissolves like), which was already known by the alchemists in ancient times, still helps to find a suitable solvent for the start of the syntheses. Certainly this rudimentary rule gives only the first hint for the starting point and optimization has to be performed later on. This means for example that highly polar educts like metal nitrates typically dissolve well in water, but not in cyclohexane but on the other hand long chain metal carboxylates such as 2-ethylhexanoates will not dissolve in water or methanol. In any case the preparation of a “*homogeneous*” solution including all the necessary cation species that may later be applied to a substrate according to the requirements enumerated in the corresponding chapters of this book is mandatory. But dissolution of the educts is not the only issue for the choice of synthesis strategy. One has also to consider other aspects like wettability, chemical stability and flowability of the resulting precursor solution. Furthermore the requirements of appropriate solubility combined with pyrolysis that leaves solely the cations (and oxygen) as a residue, represent an exceptionally significant limitation regarding the choice of educts. Typically, metallo-organic compounds are suitable due to the fact that their solubility in polar or non-polar solvents can be tuned by modifying the organic part of the molecule, and because the organic moiety pyrolyzes in oxidizing ambient atmosphere without residue. The synthesized precursor solution must also ensure that no macroscopic phase separation of precursor components during drying or pyrolysis occurs, i.e. the crystallization of the individual components upon solvent evaporation should be avoided and homogeneity at an “atomic” level should be retained.

The first two chapters will deal with the educts which are mainly employed for solution synthesis i.e. simple alkoxides and carboxylates. In Chap. 3 strategies to prepare stable coating solutions from mixtures of these two classes of compounds

as well as precursor solutions containing different metal alkoxides are explained. Then more specific precursor solution approaches, such as the single-source precursors, polymer assisted deposition, and water based precursor solution approaches will be described in Chaps. 4–6.

It has to be noted that also nitrates and sometimes chlorides (e.g. for indium tin oxide—ITO) have been used for the preparation of precursor solutions, but less frequently due to e.g. problems with “*micro-explosions*”, and the tendency of phase separation during drying, because of crystallization of one component. For the introduction of dopants however metal nitrates can be used due to the low absolute amount of some mole percent. Halides may cause problems, if they are not completely removed during processing and may change the defect chemistry of the final oxide.

As it becomes clear from this short review of solution synthesis aspects that exploring new or optimized compositions of (thin film) materials is often tedious work so that combinatorial synthesis approaches have been adopted from the biochemistry community. By means of PZT automated synthesis schemes have been used to create libraries of compositionally varied mixed oxide thin films from mixable precursor solutions of the end members lead titanate and lead zirconate with different lead excess. The complementary established automated setup for the measurement enabled a basic proof of concept [1, 2]. The influence of the kind of precursor chemistry on the nucleation and growth of the PZT, as it was found in conventional CSD has not been considered in this technique yet.

References

1. Rende D, Schwarz K, Rabe U, Maier WF, Arnold W (2008) Combinatorial fabrication of thin film-libraries and evaluation of their piezoelectricity by ultrasonic piezo-mode imaging. *Z Phys Chem* 222:587–600
2. Schroeter C, Wessler B, Schoenecker A, Keitel U, Eng LM (2006) High throughput screening of ferroelectric thin film libraries. *J Appl Phys* 100:114114-1–114114-7

Chapter 1

Simple Alkoxide Based Precursor Systems

Theodor Schneller

1.1 Introduction

Metal alkoxides, sometimes also called metal alcoholates, represent probably the most important class of compounds used in the synthesis of precursor solutions for CSD processing of metal oxide based thin film materials. Although they are typically more expensive than metal nitrates, oxides, hydroxides, carbonates or carboxylates, they offer a number of advantages such as purity and purification possibilities (crystallization or distillation), respectively, solubility in organic solvents, chemical reactivity and options for chemical modifications. Moreover these compounds have great potential as precursors in bulk for producing new or better ceramic materials which will not be part of this book but also shows the relevance of metal alkoxides for modern technology. This is consequently also reflected in a vast number of original research publications leading to an advanced knowledge of the structural, chemical and physical properties of these compounds. In 1978, Bradley and Mehrotra, and Gaur wrote the first in-depth book¹ which has become the reference book of choice for a large number of chemists and materials scientists for many years [2]. More recently Turova et al. [3] published a further valuable monograph on metal alkoxides which contains up-to-date findings and is devoted to the general questions on their chemistry, and is therefore extremely useful to chemists and technologists who apply metal alkoxides in practice.

It is not the aim of the present chapter to write a further detailed review on metal alkoxides but instead this set out to provide a general introduction into their chemistry, in particular in relation to the sol-gel reaction using commonly encountered homometallic alkoxides. The chemical principles which are important for using them as starting compounds for CSD precursor solution synthesis will be

¹The second, largely new edition of this popular book appeared in 2001 [1].

T. Schneller (✉)

Institut für Werkstoffe der Elektrotechnik II, RWTH Aachen University, Aachen, Germany
e-mail: schneller@iwe.rwth-aachen.de

given. Synthesis concepts for alkoxides are only briefly discussed since frequently used good quality alkoxides are commercially available. For comprehensive details on the manifold aspects of metal alkoxides, the reader is encouraged to refer to the textbooks mentioned above [1–3] and references therein. Details on the modification of titanium alkoxides, which represents the best investigated class of transition metal alkoxides, may be found in a more recent review of Schubert [4].

1.2 Fundamental Properties

Metal alkoxides possess the general chemical formula $[M(OR)_z]_n$ (where M can be a metal or metalloid of the valence z , R is a general organic residue (often simple alkyl, substituted alkyl, or alkenyl groups), and n represents the degree of molecular association). They are formally derived by replacing the proton of the hydroxyl group of an alcohol molecule (R-OH) with a metal cation and in some cases they are the result of a direct reaction between a metal, M, and an alcohol, ROH. The direct electrochemical preparation of metal alkoxides by anode dissolution of metals in absolute alcohols in the presence of a conductive admixture is another interesting method [5]. It represents a kind of extension of the simple dissolution to less reactive metals. Most of the metal alkoxides are synthesized from the corresponding metal chloride by reaction with an anhydrous alcohol. To remove the formed hydrochloric acid (HCl) and to drive the reaction to completion, ammonia is often added, leading to the formation of a precipitate of ammonia chloride, which can be filtered off [1, 3]. Detailed information on almost all alkoxides with regard to suitable preparation methods and physical properties may be found in the book of Turova et al. [3]. Since numerous different alcohols are available, a large variety of alkoxides can be produced for each metal. Table 1.1 gives an overview on the alkoxy ligands and alcohols [13] used for precursor preparation in CSD processing. A rating of the importance of certain alkoxides for the application in precursor solution synthesis is indicated in this table by “++” (most frequently), “+” (frequently).

Compared to silicon, metals possess a lower electronegativity and typically higher coordination numbers (N) than their oxidation state or rather valency, which results in more polar M-OR bonds (Fig. 1.1) and the tendency to the so-called coordination expansion. Thus metal alkoxides are typically regarded as Lewis acids, which means that they can interact with molecules having lone pairs of electrons, i.e. Lewis bases. The most obvious consequence of non-stabilized metal alkoxides is that they are very sensitive towards the nucleophilic attack of water molecules. On top of that, ligand exchange and molecular association may take place, depending on the type of central metal, organic residue (R) and nature of solvent (vide infra).

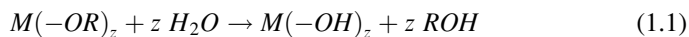
Hence in the presence of water, (often) hydrolysis is induced quickly and this leads to the formation of metal hydroxides (M-OH) with the concurrent release of alcohol molecules.

Table 1.1 Structural elements and nomenclature of alkoxy ligands, and alkoxides, respectively

Alcohol R(OH)	Skeletal structure of the metal-bound alkoxy ligand	Alkoxide R-O ⁻	Abbreviation OR residue
Methanol CH ₃ OH		Methoxide	OMe
Ethanol C ₂ H ₅ OH		Ethoxide ⁺	OEt
1-Propanol (n-propanol) C ₃ H ₇ OH		1-Propoxide ⁺⁺ (n-propoxide)	O ⁿ Pr
2-Propanol (iso-propanol) C ₃ H ₇ OH		2-Propoxide ⁺⁺ (iso-propoxide)	O ⁱ Pr
1-Butanol (n-butanol) C ₄ H ₉ OH		1-Butoxide ⁺⁺ (n-butoxide)	O ⁿ Bu
2-Butanol (sec-butanol) C ₄ H ₉ OH		2-Butoxide ⁺⁺ (sec-butoxide)	O ^s Bu
2-Methyl-1-propanol (iso-butanol) C ₄ H ₉ OH		2-Methyl-1- propoxide (iso-butoxide)	O ⁱ Bu
2-Methylpropan-2-ol (tertiary-butanol) C ₄ H ₉ (OH)		2-Methylpropan- 2-oxide (tert-butoxide)	O ^t Bu
1-Pentanol (n-amylalcohol) C ₅ H ₁₁ (OH)		1-Pentoxide n-amyloxide	O ⁿ Am
3-Methyl-1-butanol (iso-amyl alcohol) C ₅ H ₁₁ (OH)		3-Methyl-1-butan oxide iso-amyloxide	O ⁱ Am
2-Methyl-2-butanol (tert-amyl alcohol) C ₅ H ₁₁ (OH)		2-Methyl-2-butan oxide tert-amyloxide	O ^t Am
2,2-Dimethyl-1-propanol (neo-pentyl alcohol) C ₅ H ₁₁ (OH)		2,2-Dimethyl-1- propane oxide (neo-pentoxide)	ONep
2-Methoxyethanol CH ₃ OC ₂ H ₄ (OH)		Methoxyethoxide ⁺	- ^a
2-Aminoethanol NH ₂ C ₂ H ₄ (OH)		Aminoethoxide	- ^b

^aNo general abbreviation established, but sometimes “OMoe” may be found e.g. [6]. Usage of other glycolethers also described e.g. [7, 8]

^bNo general abbreviation established. Besides 2-aminoethanol (e.g. in [9]), also diethanolamines and triethanolamine were used e.g. [10–12]



In fact the situation is much more complex than what it seems from reaction equation (1.1) and finally leads to the well-known sol-gel transition which is

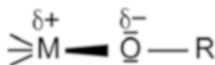


Fig. 1.1 Schematic of the polar metal-oxygen bond in metal alkoxides. This polarity is caused by the different electronegativities of the metal and the oxygen atoms leading to positive and negative partial charges on these atoms as indicated by $\delta+$ and $\delta-$, respectively

explained in more detail in Sect. 1.4.1. Moreover this reactivity towards water is a double-edged sword since on the one hand it helps to remove the organic material at very moderate temperatures by simple evaporation of the released alcohol molecules, but on the other hand several precautions, such as synthesis under inert gas atmosphere or addition of stabilizing agents (Sect. 1.5) in order to avoid premature particle or gel formation, have to be taken during solution synthesis (cp. Chap. 3).

1.3 Structural Aspects

The chemical structure of metal alkoxides, which is important for the reactivity and the usefulness in the synthesis of precursor solutions for CSD, usually does not simply resemble the elemental formula $M(OR)_z$ derived from the valence (z), of the metal M . In contrast to the silicon alkoxides, aggregation or coordination polymerization often takes place and the resultant real structural formula of metal alkoxides ($[M(OR)_z]_n$) is typically very hard to know. From the literature [1], the general electronic and sterical factors which influence the extent of aggregation or molecular complexity (n) can be summarized as follows:

- Higher electron deficiency of the metal atom increases the degree of aggregation, which depends on the electronegativity (e.g. according to the Pauling scale) of the metal
- Coordinatively unsaturated metal atoms try to reach their preferred coordination number (N), e.g. Ti^{+IV} with $N = 4$ tends to achieve an octahedral coordination ($N = 6$) (e.g. Fig. 1.2e)
- One or both of the lone pairs of the oxygen atom in the metal bound OR-group can basically act as an electron pair donor for another metal leading to the formation of alkoxo bridges (μ_2 or μ_3) (Fig. 1.2e, f)
- The larger the size of the metal atom, the greater is the tendency to increase the degree of association (n) by forming alkoxo bridged systems
- Steric hindrance due to bulky alkoxide groups, i.e. increasing size of the alkyl substituents R e.g. in the series $CHMe_2 < CMe_3 < CH^iPr_2 < CH^iBu_2 < C^iBu_3$, leads to a decrease in molecular complexity

These steric and electronic factors also influence the physical properties of the metal alkoxides to a large extent. According to Bradley et al. [1], the M-OR bonds (in alkoxides of metallic elements) would be expected to possess significant ionic

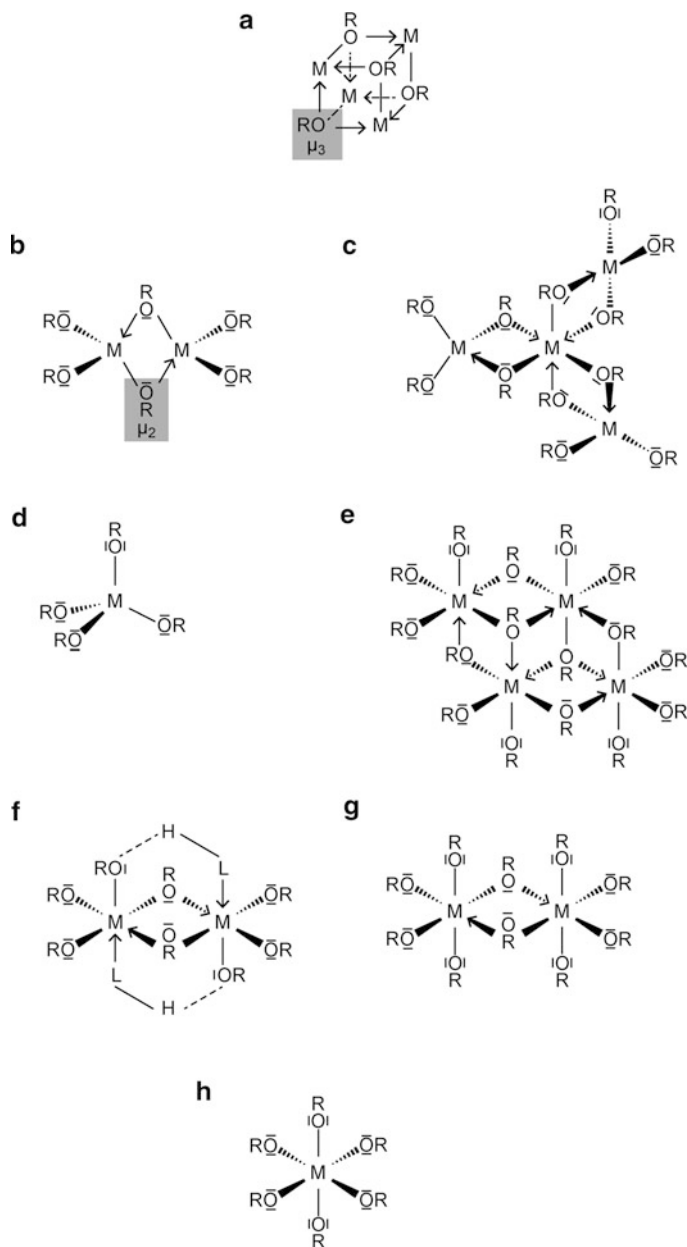


Fig. 1.2 Selection of structures, which have been found for different metal alkoxides. The *arrows* indicate the donor character of the free lone pairs of the oxygen atoms in the alkoxides enabling the coordinative bonding in the alkoxides and thus increased molecular complexity. The *grey boxes* in (a) and (b) indicate exemplarily the different bridging bonding modes μ_2 and μ_3 , where two and three, respectively, metals are bond through the oxygen of an alkoxide group by means of conventional two-electron covalent bonds. (a) cubane structure (e.g. $[\text{Ti}(\text{OMe})_4]$ [14], $[\text{M}(\text{O}^t\text{Bu})_4]$ with $\text{M} = \text{K}, \text{Rb}, \text{Cs}$ [15–18]); (b) dimer of bridged tetrahedral units, e.g. $[\text{Al}(\text{O}^t\text{Bu})_3]_2$ [19, 20]; (c) tetramer of mixed

character due to the high electronegativity of oxygen (3.5 on the Pauling scale). Thus the polar metal-oxygen bonds (Fig. 1.1) in metal alkoxides could be expected to possess around 65 % ionic character for metals with electronegativity values of the order of 1.5–1.3 (aluminium, titanium, and zirconium) to about 80 % ionic character for more electropositive metals with electronegativity values in the range of 1.2–0.9 (alkali, alkaline earth, and lanthanide metals). However, most of these alkoxides show a fair degree of volatility and solubility in common organic solvents, which can be considered as characteristic of covalent compounds. In order to explain the attenuation in the polarity of the metal-oxygen bond, three main factors have been suggested [1].

1. The inductive effect (electron releasing nature, i.e. +I) of the alkyl groups at the oxygen atom, which increases with the branching of the alkyl chain
2. The presence of *oxygen p to metal d* π -bonding for earlier transition metals, which increase the covalent character and hence metal-oxygen bond strength
3. The formation of oligomeric species (higher molecular complexity, n) through alkoxo bridges as shown for example in Fig. 1.2b

As an illustrative example, a comparison of the volatilities of the two isomeric zirconium butoxides $\text{Zr}(\text{O}^n\text{Bu})_4$ and $\text{Zr}(\text{O}^t\text{Bu})_4$ can be made. While the former butoxide had a high boiling temperature of 243 °C under 0.1 mmHg (1.33×10^{-4} bar) pressure [26] the latter could be distilled at 55 °C under practically the same pressure [39]. This surprisingly large difference led to an increased interest into these properties in the early 1950s [26, 30, 31, 39–41]. From the results of the extensive studies, it was concluded that the significant difference in the molecular complexity values of ~ 3.5 and 1.0 (in refluxing benzene) for the $\text{Zr}(\text{O}^n\text{Bu})_4$ and $\text{Zr}(\text{O}^t\text{Bu})_4$ isomers, respectively, causes this behavior. Hence, the more oligomeric $\text{Zr}(\text{O}^n\text{Bu})_4$ needs more energy to depolymerize the structure to liberate monomeric molecules in the gas phase, indicating that the alkoxide bridges are rather strong. Bradley states [42] that for most of the metal alkoxides, the strength of the alkoxide bridges is sufficiently great to preclude the alternative mechanism for coordination expansion, namely the addition of another ligand L containing a donor atom. This is typically observed in the case of non-polar solvents. On the other hand in polar solvents, the association of free solvent molecules is often preferred, leading to a lower degree of oligomerization (Sect. 1.2) [43]. It should be noted that this may have a large impact on the achievable precursor solution homogeneity in a given educt/solvent system.

Fig. 1.2 (continued) tetrahedral and octahedral units, e.g. $[\text{Al}(\text{O}^i\text{Pr})_3]_4$ [21, 22]; (d) tetrahedron, e.g. $\text{Ti}(\text{OR})_4$ ($\text{R} = {}^i\text{Pr}, {}^t\text{Am}$) [23]; (e) tetrameric octahedral units (e.g. $[\text{M}(\text{OEt})_4]_4$) $\text{M} = \text{Ti}, \text{W}$ [24, 25]; bridged (edge shared) octahedral units consisting of (f) $\text{M}_2(\text{OR})_8(\text{LH})_2$ with solvent adduct L-H ($\text{L} = \text{R}'$ or NHR'') which forms additional hydrogen bridges (e.g. $\text{M} = \text{Zr}, \text{Hf}, \text{Ce}$; $\text{R} = \text{O}^i\text{Pr}$; $\text{L} = \text{O}^i\text{Pr}$ [26–28], $\text{M} = \text{Ti}$; $\text{R} = \text{O}^i\text{Pr}$; $\text{L} = \text{NHPr}$ [29]) and (g), e.g. $[\text{M}(\text{OR})_5]_2$ ($\text{M} = \text{Nb}, \text{Ta}$; $\text{R} = \text{Me}, \text{Et}, {}^i\text{Bu}$) [30–34]; octahedron, e.g. $\text{W}(\text{OMe})_6$ [35–38]

Table 1.2 The effect of central atom electronegativity and atomic radius on some physical properties of tetravalent metal ethoxides, $M(OEt)_4$ after [2]

Central atom	M		$M(OEt)_4$	
	Electronegativity	Atomic radius (Å)	B.p. (°C/mmHg)	Degree of polymerization
C	2.50	0.77	158/760	1.0
Si	1.74	1.11	166/760	1.0
Ge	2.02	1.22	86/12.0	1.0
Sn	1.72	1.41	– ^a	4.0
Ti	1.32	1.32	103/0.1	2.4
Zr	1.22	1.45	190/0.1	3.6
Hf	1.23	1.44	178/0.1	3.6
Ce	1.06	1.65	– ^b	– ^b
Th	1.11	1.65	300/0.05	6.0

^aTin tetraethoxide could not be volatilized without decomposition even under reduced pressure [44]

^bCerium tetra ethoxide is an insoluble non-volatile solid (decomposition without melting above 200 °C under reduced pressure) pointing to high degree of polymerisation [45]

Looking at some of the simplest soluble representatives of some quadrivalent alkoxides (ethoxides²), the physical properties can be correlated to the size and electronegativity of their central metal atom (Table 1.2). A clear enhancement in molecular complexity and boiling points with reducing electronegativity and size of the central atom is revealed. It may be argued that for CSD processing, in contrast to metal organic chemical vapor deposition (MOCVD), the volatility of metal alkoxides is not directly relevant or even unwanted at least for the solution itself, but it should be considered as the volatility of various metal alkoxides is rather interesting from the structural point of view, as well as synthetical point of view. A reasonable volatility is quite useful for the purification of these precursor compounds by distillation prior to use in solution synthesis.

The simplest way to get a rough indication if a metal alkoxide is molecular, including oligomeric, or polymeric is through its solubility in organic solvents. However, it leaves the question of the exact degree of oligomerization, n , (e.g., monomer, dimer, trimer, ...) unanswered [46]. This molecular complexity is usually estimated from careful solution-phase molecular weight measurements by cryoscopy or ebulliometry [1], but one has to bear in mind that even under optimal conditions an accuracy of not more than 10 % for “real world” samples can be achieved [46]. When one addresses objectively the possible coexistence of two (or more) oligomers, this may cause certainly a problem. However in case of using alkoxides as educts for the synthesis of CSD precursor solutions, the data obtained from measurements of colligative properties still give good hints for the development of the understanding of homogeneity issues in precursor systems.

²The metal methoxides are typically polymeric and do not dissolve in organic solvents. They decompose without melting and cannot be evaporated [3].

With the advent of spectroscopic methods, such as infrared spectroscopy (FT-IR—see Chap. 9), nuclear magnetic resonance spectroscopy (NMR- ^1H and multinuclear), extended X-ray absorption spectroscopy (EXAFS—see Chap. 8) and mass spectrometry, higher accuracy and even details of chemical structures could be obtained. In some cases, single crystals could be prepared and the solid state structure could be determined by X-ray structure analysis. Summary of the results can be found in a number of text books and excellent articles [1, 4, 47–49].

Figure 1.2 shows some typical structures of metal alkoxides which are often found.

Gaining knowledge of the exact chemical structure of molecules is of substantial interest of every chemist, but in spite of the advanced spectroscopic methods available nowadays, it is often hard to obtain for the “genuine precursor molecules” in the real coating solutions. On the other hand, this lack of knowledge has not prohibited the community to prepare excellent functional oxide film materials from multi-source³ precursor solutions in most cases. However, some materials need special precautions in order to get crystallites with phase pure, dense, and/or in a specific orientation of the crystallites. The problem often happens if during thermal processing, intermediate phases are formed. In addition inhomogeneities or phase separation in the multicomponent precursor solutions prior or during the deposition process can additionally contribute to secondary phases. Such phases are either hard to decompose in the temperature range normally available for CSD, form gaseous products upon decomposition, or act as nucleation sites. Multiphase, fine-crystalline, nanoporous, and sometimes not well oriented ferroelectric (Ba,Sr)TiO₃ (BST), Pb(Zr,Ti)O₃ (PZT), and (K,Na)NbO₃ (KNN) films may serve as examples to illustrate these issues [50–57]. Therefore structural aspects are also relevant for the development of the microscopic understanding of the transformation process from the original solution to the finally crystalline film.

In addition to the more compound intrinsic factors mentioned above, extrinsic parameters, such as temperature, concentration, and nature of solvent (coordinating or non-coordinating), influence the degree of molecular complexity. This can give a starting point to tailor the metal alkoxide precursor for the use in solution synthesis for CSD because an increasing molecular complexity of a given metal alkoxide $\text{M}(\text{OR})_z$ leads to a decreasing reactivity [58]. On the other hand higher nuclearities may lead to inhomogeneities in precursor solutions, in particular for complex metal oxide thin films.

In the following sections, some general aspects of chemical reactivity including approaches to chemical modification are presented. The behavior of titanium, zirconium and aluminium alkoxides, representing the most frequently used and investigated types of alkoxides, may serve as illustrative examples.

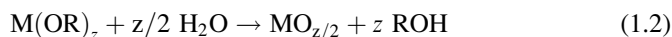
³ In contrast to single-source precursors (see Chap. 4), where well defined heterometallic precursor molecules are synthesized and used as precursors in the coating solution, multi-source means that individual educts, which could be alkoxides, carboxylates, nitrates are mixed together in such a way, that a chemically stable one-pot precursor solution results (see e.g. Chap. 3).

1.4 Chemical Reactivity

As already pointed out in Sect. 1.2 the Lewis acid properties⁴ of metal alkoxides govern the chemistry of metal alkoxides to a large extent [1, 3, 4, 60]. Water represents the most simple but also most critical Lewis base since it induces the sol-gel transition, which has to be controlled if stable precursor solutions and good coating properties are to be achieved. Due to the importance of metal alkoxides as precursor molecules, in the following section at first some details of the sol-gel transition are reviewed. Then in the further course of this section, typical possibilities to modify metal alkoxides in order to tailor their properties for CSD processing are presented.

1.4.1 The Sol-Gel Transition

Metal alkoxides undergo at first a hydrolysis reaction (often fast) which is typically not the final stage but an intermediate step followed by condensation reactions leading to metal-oxygen-metal bonds with an overall stoichiometric reaction equation given by:



This reaction will lead to oligomers, polymers or particle precipitates, i.e. a macromolecular three-dimensional oxide network. The generally accepted main steps of the key reactions of this so-called *sol-gel process* will be described in the following paragraphs [13, 60, 61].

1.4.1.1 Hydrolysis

During hydrolysis, the alkoxy groups are successively replaced either by hydroxoligands (-OH) or oxo-ligands (=O) by similar substitution reactions. The mechanism of the hydrolysis reaction is typically explained as a nucleophilic substitution [60, 61] where water acting as a Lewis base attacks the metal atom of the alkoxide (Lewis acid) in the first step (Fig. 1.3), followed by proton transfer from the entering water molecule to the leaving group in the transition state. Finally an alcohol molecule is released.

⁴ It should be noted that Kessler et al. [59] argued that metal alkoxides are rather Lewis bases and very weak Lewis acids and that ligand exchange and hydrolysis proceeds through a proton assisted S_N1 mechanism with a number of consequences. It is not the aim of this chapter to discuss this issue. In order to use and modify metal alkoxides for CSD precursor solution synthesis, as well as understanding the behavior at least on a qualitative level, the classical model description for the sol-gel behavior of alkoxides is very illustrative and will be therefore presented here.

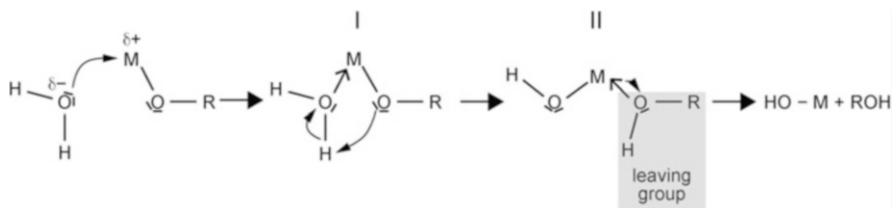


Fig. 1.3 Schematic of the hydrolysis mechanism after [60, 62]. The associative nucleophilic substitution is typically characterized by a three step process. In the first step one of the oxygen lone pairs of a water molecule attacks the partially positive charged metal atom M. This nucleophilic addition leads to the transition state (I) where the N of M has increased by one. In the second step a proton is transferred within this transition state from the entering water molecule to the partially negative charged oxygen of an adjacent alkoxy group leading to the intermediate state (II). The third step is the departure of the better leaving group (*grey box*) [In general a leaving group is an atom (or a group of atoms) that is displaced as stable species taking with it the bonding electrons. Typically the leaving group is an anion (e.g. Cl^-) or a neutral molecule (e.g. H_2O or ROH .)] which should be the most (partially) positive charged species within the transition state (II)

If the hydrolysis is extensive, precipitation of ill-defined metal hydroxide or oxide/hydroxide species may occur. However, the goal of using these alkoxide precursors for CSD processing is to control the hydrolysis and subsequent condensation reactions (shown below). If properly manipulated, these reactions lead to the formation of short chain polymeric species referred to as oligomers which are still soluble in the solvent of the precursor solution. The reaction is basically influenced by the following factors [13, 60]:

- Character of the alkyl group (long/short chain, branched etc.)
- Nature of solvent
- Concentration of each species in the solution
- Molar ratio of water to alkoxide $r_w = [\text{H}_2\text{O}]/[\text{alkoxide}]$
- Temperature [63, 64]

In principle, each metal alkoxide has to be considered separately. For a number of technically relevant alkoxides of titanium, zirconium, and aluminium, such hydrolysis studies have been performed, the details of which are beyond the scope of this chapter and may be found summarized elsewhere [3, 13]. Nevertheless the results from the different works lead to the generalized rule of thumb, that the sensitivity towards hydrolysis and condensation, depends mainly on the positive partial charge of the metal atom $\delta(\text{M})$ [60] and the ability to increase its coordination number (N). Table 1.3 lists the various factors that affect the sensitivity for some common cations.

A large positive partial charge corresponds to a rapid reaction rate for the transition metal alkoxides compared to the silicon alkoxides with similar organic residues. Thus the hydrolysis of the latter has to be typically accelerated by acid or base catalysts. The coordinative unsaturation, i.e. the difference between the usual coordination number and the valence z of the corresponding metal cation is a more simple reactivity criterion. Applied to the series of different metal tetra

Table 1.3 Data for coordinative unsaturation (N-z) of some tetravalent metal cations (z = +4) and positive partial charge $\delta(M)$ on the metal atom of their iso-propoxides

Cation	N	(N-z)	Alkoxide	$\delta(M)$
Si	4	0	Si(O ⁱ Pr) ₄	+0.32
Sn	6	2	Sn(O ⁱ Pr) ₄	–
Ti	6	2	Ti(O ⁱ Pr) ₄	+0.60
Zr	7 or 8	3 or 4	Zr(O ⁱ Pr) ₄	+0.64
Ce	8	4	Ce(O ⁱ Pr) ₄ ^a	+0.75

Data from [65]

^aCerium alkoxides are extremely sensitive to humidity. Even small amounts of water lead to precipitation

isopropoxies given in table above, the increasing values for N-z from Si to Ce are in accordance to the found order of increasing sensitivity-to-hydrolysis (Si << Sn < Ti < Zr < Ce) [1]. In addition to the positive partial charge and ability to achieve higher coordination numbers, differences in the molecular structure of metal alkoxide with the same central metal will also lead to a different behavior in hydrolysis and subsequent condensation reactions [66–68].

1.4.1.2 Condensation

Condensation, which is also a rather complex process, starts as soon as hydroxogroups have been formed. Different competitive pathways for the condensation reaction are typically described in literature. According to Livage et al. [60], condensation by (alkox)olation and by olation are defined as follows:

Condensation by (Alk)oxolation

Similar to the situation in aqueous metal salt solutions,⁵ in the condensation mechanism of alkoxides by oxolation, first an “ol” bridge has to be formed [13, 60]. Subsequently, a simple proton transfer to another hydroxy- or alkoxy group has to take place to form an “oxo” bridge and the “leaving group” (Fig. 1.4).

Finally, the metal-oxygen-metal bonds are formed by water- or alcohol elimination. To differentiate between proton transfer to a hydroxy- or an alkoxy ligand, the first condensation pathway (Fig. 1.4b) is denoted oxolation and the second one is called alkoxolation (Fig. 1.4a).

In some cases, the formation of metal-oxygen-metal bonds by oxolation can also result from a de-etheration as shown in Eq. (1.3) [13].

⁵ Metal salts are not subject of this chapter. However the hint to the similarity in the hydrolysis and condensation scheme is given, because metal salts in aqueous media are used in the chemical bath deposition technique, which is described in Chap. 14.

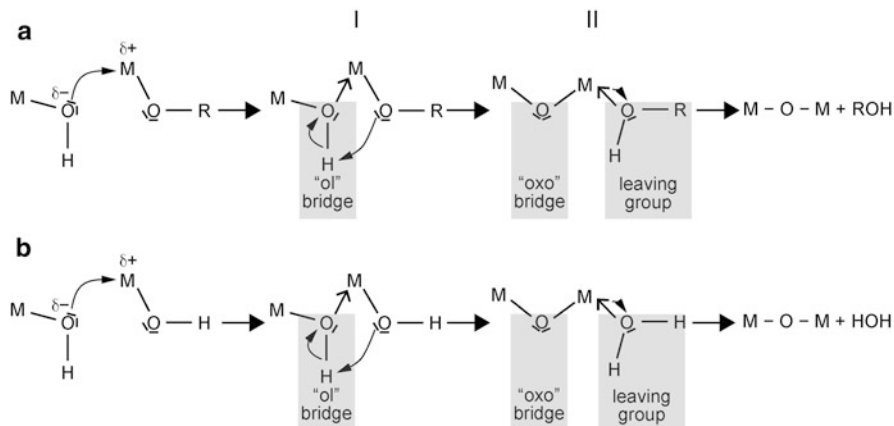
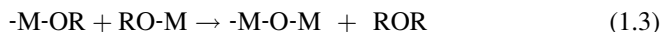


Fig. 1.4 Schematic of the condensation mechanism by (a) alkoxolation and (b) oxolation after [60]. In both reaction pathways the reaction sequence starts according to the same principle than in the hydrolysis, i.e. at first nucleophilic attack of an oxygen lone pair of a metal hydroxide species to the partially positive charged metal atom M takes place. This nucleophilic addition leads to the “ol” bridge containing transition state (I), followed by proton transfer yielding the “oxo” bridge containing intermediate state (II). The release of an alcohol molecule (a) or a water molecule (b) as leaving groups finalizes the sequence



Condensation by Olation

Depending on the experimental conditions and the nature of the metal alkoxide, olation, i.e., bridging two metals via an OH-group can occur. This so-called olation can occur if the metal alkoxide is coordinatively unsaturated ($N-z \neq 0$). As shown schematically in Fig. 1.5, it also follows a S_N2 nucleophilic substitution mechanism but without proton transfer in the transition state, which accelerates the whole reaction. The leaving group is either an alcohol (Fig. 1.5) or a water molecule, depending on the water and acid/base concentration in the medium [13, 60].

Water is released in case of solvated metal alkoxides and follows basically the same scheme as shown above by replacing the organic residue (R) with a hydrogen atom (H).

In summary, all of the four reaction types previously described may be involved in the ongoing hydrolysis-condensation processes, which gradually develop a three dimensional network. Depending on the degree and type of polycondensation in the early stages, a stable suspension of colloidal solid particles or polymers in a liquid (*sol*) and later a solid phase (*gel*) will form. By definition, gels consist of a porous, 3-D continuous network surrounded and supported by a continuous liquid phase (*wet gel*). These gels can be formed by agglomeration of dense colloidal particles (amorphous or crystalline), which are often denoted *particulate gels*, or the so called *polymeric gels* that is resulting from the entanglement of polymer chains or

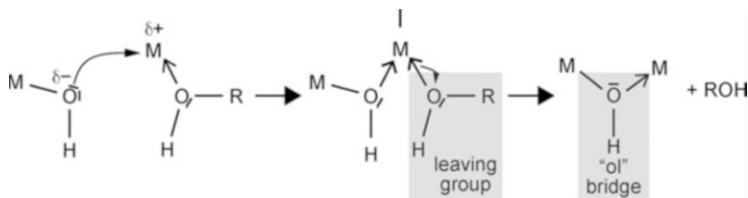


Fig. 1.5 Scheme of the condensation mechanism by formation of “ol”-bridges (olation) shown by means of alcohol as a leaving group. This is the case if the attacked metal alkoxide complex contains a protonated alkoxy ligand. Again the first step is a nucleophilic attack of the lone pair of an oxygen atom, but already in the second step the leaving group separates from the complex (I)

the aggregation of particles having a polymeric substructure [69]. Similar to any chemical reaction, this sol-gel process is accelerated by heat as the rate of both reactions increases together with the temperature [70]. In addition, the reaction mechanisms shown above directly suggest a significant influence of the pH on the kinetics and hence the type and shape of the inorganic polymers (linear or branched polymers, colloidal particles). If carefully controlled, these factors are useful for the tailoring of the sol-gel preparation of a large variety of bulk materials with different structures.

However in CSD processing, the gel formation has to be avoided under all circumstances until the as-deposited homogeneous film has been obtained. Thus during solution synthesis, and also during long term storage, gel formation has to be avoided or at least be significantly delayed by suitable measures. In the following section, common modifications of alkoxide precursors are described.

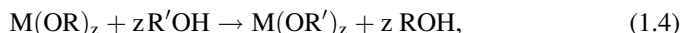
1.4.2 Chemical Modifications

The Lewis acid properties of metal alkoxides make them not only prone to fast hydrolysis-condensation reactions, but also give the researcher possibilities to chemically modify them. Thus substitution reactions lead to new molecular precursors displaying different behavior not only with respect to the sol-gel reaction but also display different volatilities and thermal stabilities. Nevertheless one has to bear in mind that with substitution, some metal alkoxides (e.g. $\text{Ti}(\text{OR})_4$), which are used in organic chemistry for a number of catalytic reactions due to their Lewis acid properties, may give rise to competing organic reactions. The simplest way to modify alkoxides is through the solvent itself, because it actually behaves as true chemical reagent. If a solvent possesses hetero atoms, e.g. oxygen or nitrogen, it is able to react with the metal alkoxides and change the precursor at a molecular level. Organic compounds containing only these atoms are of major interest for application in CSD of electronic oxides as they do not contain halide, sulfur, or phosphorous atoms, which, if they remain as impurities after decomposition, can have deteriorating influence on the electrical properties. Nabavi et al. illustrated this

role of the solvent using the sol-gel chemistry of titanium and vanadium alkoxides [71].

1.4.2.1 Alcohol Exchange

Alcohols, particularly their ether alcohol and polyol derivatives, represent the most frequently applied class of solvents, which simultaneously behaves as reagent in a metathesis reaction, named *transalcoholysis* or simply *alcoholysis* (Eq. 1.4).



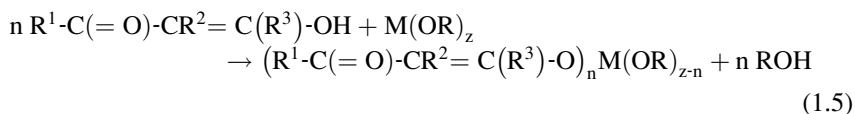
where OR is a reactive alkoxy group and OR' is another, often less reactive alkoxy group such as 2-methoxyethoxy. The latter is a key reaction that occurs in the standard procedures for PZT solution synthesis (Chap. 3) resulting in a decrease in the hydrolysis sensitivity of starting reagents such as zirconium tetra *n*-propoxide and titanium tetra *i*-propoxide.

A decreasing steric hindrance of the organic residue, R, of the attacking alcohol molecule leads to increasing facility of this interchange reaction [60], i.e. from tertiary to secondary to primary alcohols (e.g. MeOH \gg EtOH $>$ i PrOH $>$ t BuOH).

In general, transalcoholysis reactions are incomplete in case of bulky alcohols, while the lower solubility of methoxide derivatives normally promotes a complete substitution [46].

1.4.2.2 Reaction with β -Diketones and Related Compounds

β -diketones ($R^1-C(=O)-CR^2H-C(=O)-R^3$) are compounds which undergo a rapid keto-enol tautomerism. They possess a reactive hydroxyl group in the enolic form ($R^1-C(=O)-CR^2=C(R^3)-OH$), which may attack the alkoxide in a similar way as a simple alcohol, leading to the corresponding alcoholysis reaction with the release of the original alkoxy group as alcohol (Eq. 1.5).



The second oxygen atom of the β -diketonate ligand is able to form an additional bond to the central metal atom of the modified alkoxide, hence forming a chelate complex (Fig. 1.6). These chelate complexes have higher stability constants than the original metal alkoxide, which is the driving force for the reaction given in Eq. (1.5). Details on metal- β -diketonates can be found in [72]. As a further result, the bidentate ligand is less readily hydrolyzed than the remaining OR-groups upon exposure to water. This leads to a higher stability of the corresponding precursor

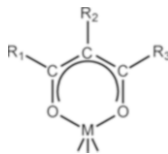


Fig. 1.6 Generalized schematic of the chelate bonding mode of β -diketonate (e.g. Acetylacetonate (*acac*): $R_1, R_3 = \text{CH}_3, R_2 = \text{H}$) and β -diketoester (e.g. ethyl acetoacetate (*eaac*): $R_1 = \text{OCH}_2\text{CH}_3, R_2 = \text{H}, R_3 = \text{CH}_3$) compounds

solutions (*vide infra*). Depending on the type of organic residues R^1, R^2 and R^3 , other properties such as volatility or UV-VIS absorption of the modified metal alkoxide complexes can be varied over a wide range. While volatility is an issue for the design of precursors for MOCVD processing (see e.g. [73]), changing the β -diketonate ligand can allow for adjusting the light absorption bands of CSD precursor solutions for photo-assisted techniques (see Chaps. 18 and 20). In addition the β -diketo-structure element can contain an organic component that is polymerizable (e.g. $R^1, R^3 = \text{Me}, R^2 = \text{allyl}$ in Eq. (1.5) and Fig. 1.6: 3-allyl-2,4-pentanedione, “*apd-H*”) or inorganic polymerizable (e.g. $R^1, R^3 = \text{Me}, R^2 = \text{trimethoxysilylpropyl}$ in Eq. (1.5) and Fig. 1.6: 3-acetyl-6-trimethoxysilylhexane-2-one, “*ats-H*”) groups and further modifications such as β -diketoesters (e.g. allyl acetoacetate, “*aaa-H*”). Such modifiers enable the incorporation of Ti complexes by chemical bonding into organic materials. Ethyl acetoacetate (*eaac-H*, i.e. $R^1 = \text{OCH}_2\text{CH}_3, R^2 = \text{H}, R^3 = \text{Me}$ in Eq. (1.5) and Fig. 1.6) may serve as an example for a non-polymerizable β -diketoester which attracted considerable attention [74–80].

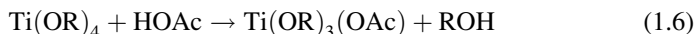
2,4-pentanedione ($R^1, R^3 = \text{Me}, R^2 = \text{H}$ in Eq. (1.5) and Fig. 1.6) or more often denoted acetylacetonate (*Hacac*) is the by far most frequently used stabilizer for metal alkoxides. In the classical sol-gel literature the reported examples comprise relevant metal alkoxides of W (e.g. $\text{W}(\text{OEt})_6$ [81]), Ti (e.g. $\text{Ti}(\text{O}^i\text{Pr})_4$ [82], or $\text{Ti}(\text{O}^n\text{Bu})_4$ [83]), Zr (e.g. $\text{Zr}(\text{O}^i\text{Pr})_4$ [84]) or Al ($\text{Al}(\text{O}^n\text{Bu})_3$ [85]). Consequently it is also well established in precursor solution synthesis for CSD. Though from a number of acetylacetonate modified compounds, the solid state structure could be determined, it turned out that the structure in solution is much more complex due to ligand exchange reactions and a series of equilibria encountered along the way [86, 87]. Any way in solution new complexes will form depending on the amount of added *Hacac*. Since the maximum N of Ti is 6 and a monodentate coordination mode of β -diketonate ligands is rather unfavorable, the OR group substitution is restricted to disubstitution [4]. For Zr alkoxides, the situation is more complex. In case of *Hacac* addition to $\text{Zr}(\text{O}^n\text{Pr})_4$, which is a frequently applied Zr educt for solution synthesis in CSD, a tri-substitution is possible but the complex is not stable and rearranges into the tetra substituted $\text{Zr}(\text{acac})_4$ and free zirconium alkoxide [86].

1.4.2.3 Reaction with Alkanolamines

Early works of Mehrotra [88] showed already that alkoxides can be modified with alkanolamines (monoethanol-, diethanol-, and triethanolamines). They are a further interesting group of modifiers which can substitute OR groups in metal alkoxides by alcoholysis, but nevertheless they are less frequently applied in CSD processing and their reaction products are typically not isolated [89–95]. Due to the lone pair of the nitrogen atom, chelate complexes are formed which could stabilize the compounds against premature hydrolysis and condensation for CSD processing. Corresponding heteroleptic titanium alkoxide aminoalkoxide complexes are summarized in [4].

1.4.2.4 Reactions with Carboxylic Acids

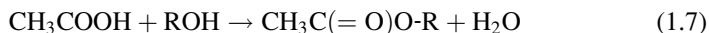
Carboxylic acids represent another class of common organic modifiers for metal alkoxides. Alkoxides from a number of metals (e.g. Ti, Zr, Al etc.) have been reacted with different carboxylic acids [8, 62, 96–106], but the mainly investigated examples stem from the reaction of Ti alkoxides with acetic acid (HOAc) [107–109]. Equation (1.6) describes the exothermic reaction which occurs initially in case of an equimolar addition of the acid to the titanium alkoxide:



A thorough spectroscopic study of this reaction using titania tetra butoxide showed that n-butanol was released and acetic acid was completely consumed. FTIR results point to a bidentate bridging mode of the carboxylate group and no esters were found in the initial state of the reaction [110]. The perception that the first step of this reaction is indeed the formation of carboxylato-coordinated titanium alkoxides is strongly supported by recent results of Czakler et al. [111]. Due to the preferred N of 6 for Ti the smallest structure is a dimer ($[\text{Ti(OR)}_3(\text{OOCR})]_2$), where two bridging alkoxide ligands and two bridging acetate ligands are present. This structure is similar to Fig. 1.2f and can be represented by a replacement of the “OR–H–L” group by the “O–CR–O” group of the carboxylate. However this simple exchange product normally cannot be isolated. Instead further reactions lead to the formation of carboxylato-coordinated oxido/alkoxido clusters of the generalized formula $\text{Ti}_a(\text{O})_b(\text{OR})_c(\text{OOCR}')_d$ [4]. If the very frequently used $\text{Ti}(\text{O}^i\text{Pr})_4$ and $\text{Ti}(\text{O}^n\text{Bu})_4$ compounds are reacted with HOAc, typically hexameric clusters ($a = 6, b = 4, c = 12 \text{ or } 8, d = 4 \text{ or } 8$) could be prepared as single crystals and structurally characterized by X-ray diffraction [104, 108]. A time dependent study of the reaction mixtures of the iso-propoxide derivative with different equivalents of HOAc (1 and 2) under inert atmosphere yielded in all investigated cases a hexameric cluster with slightly different ligand stoichiometry [99]. Iso-propylacetate formation was detected by ^1H NMR in all cases. Esters have

been also observed in the titanium tetrabutoxide based mixtures and two mechanisms for the ester formation have been proposed by Sanchez et al. [107].

1. Direct esterification within the initially formed substitution product via a template effect, known from homogeneous catalysis.
2. Esterification in the reaction solution according to the following equation:



The required free acid may stem from a certain dynamic exchange between acetic acid bound to the titanium atom and released to the solution in case of the equimolar reaction mixture. If acid to Ti alkoxide ratios are larger than 1, unreacted free acid may be directly available in the solution.

The in-situ produced water leads to homogeneous hydrolysis and condensation thus forming the oxo bridges of the clusters. For CSD processing such esterification reactions with the accompanied slow formation of water could account to the widely observed ageing of precursor solution in particular of ternary and quaternary compositions, e.g. in BST, where typically carboxylic acid based solutions of alkaline earth carboxylate and titanium alkoxides are employed (Chap. 3).

Overall there is a rich chemistry behind the apparently simple reaction of metal alkoxides with carboxylates. In spite of the considerable progress, this is still not completely understood and thus a field of further research. Depending on the type of metal alkoxide and carboxylic acid, a number of metal carboxylato-coordinated oxido/alkoxido clusters could be isolated as single crystals and fully characterized by spectroscopy and X-ray structure analysis. Most structurally characterized complexes were reported for titanium (for an excellent survey see [4]) and less frequently for other transition metals (e.g. Zr [97, 99, 102], Nb [101]). In the case of the reaction of relatively bulky trimethyl acetic acid (HOBc) with titanium tetra neopentoxide ($\text{Ti}(\text{ONep})_4$; cp. Table 1.1), even the simple substituted dimeric species (i.e. $[\text{Ti}(\mu\text{-OBc})(\text{ONep})_3]_2$) mentioned above could be isolated as single crystal and fully characterized [99]. Things get even more sophisticated if precursor solutions for multinary compositions such as perovskites have to be prepared. Nevertheless it can be safely concluded that the use of carboxylic acids also leads to a certain stabilization against hydrolysis. This might explain why mixed metallo organic precursor solutions (Chap. 3), which contain acetic acid or propionic acid are relatively stable. Care has to be taken with regard to the possible formation of larger clusters, e.g., the B-site cation in perovskites, due to the processes described above. As a consequence, inhomogeneities in the precursor solution can occur, which in turn can affect the nucleation and growth process.

1.5 Coating Solutions

This section will highlight some exemplary approaches and basic criteria for precursor solution synthesis for CSD. It will be predominantly restricted to solutions for binary metal oxides, which are interesting for electroceramic film

fabrication and have been studied as model systems for perovskites, e.g. $\text{Pb}(\text{Zr}_x, \text{Ti}_{1-x})\text{O}_3$ [103, 105]. Though it has to be pointed out that sol-gel derived titania and alumina layers for optical applications, such as antireflection filters (see Chap. 28) belong to the first examples where transition metal alkoxides were used for wet chemical film preparation [112].

The simplest option for the preparation of a coating solution is the dissolution of the alkoxide in the parent anhydrous alcohol. Depending on the central metal and the length of the hydrocarbon chain, such solutions are extremely prone to hydrolysis and often have to be deposited in a dry glove box [113]. For dense electroceramic thin films, these solutions are typically not suitable, but if porous films are required, the hydrolytic reactivity can be utilized. For example, by dissolution of highly reactive titanium ethoxide ($\text{Ti}(\text{OEt})_4$) in anhydrous ethanol, coating solutions have been prepared which were only stable under inert atmosphere. During the spin-coating process under different humidities, the in-situ build particles formed an amorphous porous layer. The subsequent thermal treatment crystallized these particulate layers into a porous anatase phase at ~ 400 °C. At ~ 850 °C, this layer began to transform to rutile [114]. If other alcohols such as 1-butanol or tert-butanol are used for the solution preparation, at first alcoholysis occurs and the particle growth kinetics of these solutions is altered. In case of $\text{Ti}(\text{OEt})_4$ in tert-BuOH, the particles formed upon exposure to water are smaller and have an irregular shape [115]. Studies on the consolidation behavior of titania films derived from such sols showed that the density increases with increasing heating rate [116, 117].

Nevertheless the high sensitivity of metal alkoxides towards water often requires the use of chemical additives which are mainly the various bidentate ligands mentioned in Sect. 1.4.2. This facilitates the handling of binary metal oxide precursor solutions during the coating process in ambient atmosphere and usually increases the lifetime of the coating solutions. The same applies for ternary and multinary metal oxide precursors and sometimes the preparation of a suitable mixed metallo organic precursor solution would even not be possible without stabilizing agents. In order to avoid a local over-concentration of the modifier, the synthesis commonly starts with diluting the initial metal alkoxide in a suitable anhydrous solvent, which is often the parent alcohol. Next the stabilizer (Hacac, HOAc etc.) is added in well-defined ratios such as 1:1 in case of $\text{Al}(\text{O}^t\text{Bu})_3$ [78], 0.5–2 in case of $\text{Zr}(\text{O}^n\text{Pr})_4$ [105], or 1:1⁶ in case of $(\text{TiO}^i\text{Pr})_4$ [93, 98]. Finally the solution concentration can be adjusted by further dilution with the solvent to the desired value and is then ready for deposition and thermal processing.

In order to elucidate the stabilizing effect of modifiers, a number of studies have been performed in which the amount of water, the type of metal alkoxide, the modifier and the ratio of modifier to metal alkoxide was varied [6, 7, 118–121]. Comparative spectroscopic studies on the hydrolysis behavior of solutions consisting of

⁶In case of multicomponent $\text{Ti}(\text{OR})_4$ based precursor solutions often 2 equivalents of Hacac are used.

Al-, Ti-, and Zr-butoxides complexes which have been reacted with saturated and unsaturated β -keto ligands in equimolar ratio showed that Hacac has the highest hydrolytic stability [7, 118]. Owing to this hydrolytic stability very small particles with mean hydrodynamic diameters in the range of 1.5–6 nm were found for Hacac modified Ti-, Zr-, and Ce-alkoxide colloidal solutions [7, 119–121]. If, however, for instance no stabilizer [122] or sub-stoichiometric amounts of Hacac are used for the solution preparation from $\text{Ti}(\text{OR})_4$ [123, 124], the addition of water leads to the formation of much larger particles (hydrodynamic diameters up to 40 nm) and less stable colloidal solutions. Similar results for the hydrodynamic diameters have been obtained for low-complexed cerium isopropoxides (45 nm) [121] and zirconium *n*-propoxides (50 nm) [120]. Such large particles destabilize the precursor sols and may lead to inhomogeneities in multicomponent precursor solutions for complex metal oxides, such as PZT. This in turn can lead to the local heterogeneities mentioned in Sect. 1.3.

Other strategies to stabilize metal alkoxide precursor solutions comprise the addition of different carboxylic acids to the metal alkoxides [98, 105, 125–127], aminoalkanols [92, 94], and combinations of different reagents such as carboxylic acids and glycoethers [8, 128] or polyalcohols (ethylenglycol, polyethylenglycol) [129]. To initiate a certain degree of hydrolysis and condensation, often various amounts of water (mainly diluted in an alcohol) are added. Precursor solutions prepared in such a way are useful for the preparation of rather porous binary metal oxide films due to a more polymeric or particulate nature of the precursor species in the sol and often high organic load.

To get dense films, small nuclearities or particles and an overall low organic content are required. This was also confirmed in a study in which titania films were prepared from spin coated solutions of well defined and fully characterized titanium carboxylate complexes dissolved in toluene [99]. It has to be also pointed out that multicomponent precursor solutions for complex oxide film processing should normally consist of rather monomeric species or very small oligomers in order to maintain a homogeneous distribution on a molecular scale. Therefore, either no hydrolysis or only partial hydrolysis by addition of sub-stoichiometric amounts of water is typically required. As already mentioned above, a certain degree of hydrolysis in the precursor solution enables the release of a larger portion of organic material by simple evaporation. This can be beneficial if in a given material system residual organic material is hard to remove by thermal decomposition in the accessible temperature range. In case of Nb_2O_5 films it has been shown that such a procedure improved the leakage current densities of the CSD prepared films considerably [125].

1.6 Concluding Remarks

The present chapter gives a survey on the fundamental properties of simple metal alkoxides, the knowledge of which is important and useful to understand the different approaches and issues of the CSD routes reported in various chapters of

this book. Metal alkoxides are a lively field of chemistry for different disciplines of material science as well as for pure chemists who are deeply interested in the manifold structural chemistry of these compounds. It was beyond the scope of this chapter to give a comprehensive overview but a condensed view through the eyes of a scientist, interested in finding ways of synthesizing stable and reproducible precursor solutions featuring a maximum degree of homogeneity and long term stability. The control of the hydrolysis behavior and the nuclearity of the metal alkoxide is the key to achieve this goal. Acetylacetone and acetic acid are often the reagents of choice to adjust the reactivity of the metal alkoxides in the precursor solutions. Further chelating reagents such as aminoalkanols, β -diketoesters or other carboxylic acids are available but less well explored for CSD processing.

References

1. Bradley DC, Mehrotra RC, Rothwell IP, Singh A (2001) Alkoxo and aryloxo derivatives of metals. Academic, London
2. Bradley DC, Mehrotra RC, Gaur DP (1978) Metal alkoxides. Academic, New York
3. Turova NY, Turevskaya EP, Kessler VG, Yanovskaya AI (2002) The chemistry of metal alkoxides. Kluwer AP, Boston
4. Schubert U (2005) Chemical modification of titanium alkoxides for sol-gel processing. *J Mater Chem* 15:3701–3715
5. Shreider VA, Turevskaya EP, Koslova NI, Turova NY (1981) Direct electrochemical synthesis of metal alkoxides. *Inorg Chim Acta* 53:L73–L76
6. Sedlar M, Sayer M (1995) Reactivity of titanium isopropoxide, zirconium propoxide and niobium ethoxide in the system of 2-methoxyethanol, 2,4-pentadione and water. *J Sol-Gel Sci Technol* 5:27–40
7. Hoebbel D, Reinert T, Schmidt H, Arpac E (1997) On the hydrolytic stability of organic ligands in Al-, Ti- and Zr-alkoxide complexes. *J Sol-Gel Sci Technol* 10:115–126
8. Glaubitt W, Sporn D, Jahn R (1994) A new way to spinnable sols derived from modified aluminumalkoxides. *J Sol-Gel Sci Technol* 2:525–528
9. Fric H, Kogler FR, Puchberger M, Schubert U (2004) Structural chemistry of titanium alkoxides substituted by the chelating bidentate ligands isoeugenolate or 2-aminoethanolate. *Z Naturforsch* 59b:1241–1245
10. Ban T, Ohya Y, Takahashi Y (2003) Reaction of titanium isopropoxide with alkanolamines and association of the resultant Ti species. *J Sol-Gel Sci Technol* 27:363–372
11. Harlow R (1983) Dimer of (2,2',2''-nitrilotriethanolato)(2-propanolato)titanium(IV), $[\text{Ti}_2(\text{C}_6\text{H}_{12}\text{NO}_3)_2(\text{C}_3\text{H}_7\text{O})_2]$. *Acta Crystallogr, Sect C: Cryst Struct Commun* 39:1344–1346
12. Menge WMPB, Verkade JG (1991) Monomeric and dimeric titanatranes. *Inorg Chem* 30:4628–4631
13. Pierre A (1998) Introduction to sol-gel processing. Kluwer, Dordrecht
14. Dahl LF, Davis GL, Wampler DL, West R (1962) The molecular and crystal structure of thallium (I) methoxide. *J Inorg Nucl Chem* 24:357–363
15. Chisholm MH, Drake SR, Naiini AA, Streib WE (1991) Synthesis and X-ray crystal structures of the one-dimensional ribbon chains $[\text{MOBu}^1\text{Bu}^1\text{OH}]_\infty$ and the cubane species $[\text{MOBu}^1]_4$ (M = K and Rb). *Polyhedron* 10:337–345
16. Weiss E, Alsdorf H, Kühn H, Grützmacher HF (1968) Röntgenographische, NMR- und massenspektrometrische Untersuchungen der tert.-Butylate des Kaliums, Rubidiums und Caesiums. *Chem Ber* 101:3777–3786

17. Weiss E, Alsdorf H, Kühr H (1967) Structure of alkali metal t-butoxides. *Angew Chem Int Ed Engl* 9:801–802
18. Mann S, Jansen M (1994) Crystal structure of cesium-tert-butanolate, CsOC₄H₉. *Cryst Mater* 209:852
19. Cayton RH, Chisholm MH, Davidson ER, DiStasi VF, Du P, Huffman JC (1991) Crystal and molecular structure of hexakis(tert-butoxo)dialuminum. Comments on the extent of M-O π bonding in Group 6 and Group 13 alkoxides. *Inorg Chem* 30:1020–1024
20. Shiner VJ, Whittaker D, Fernandez VP (1963) The structures of some aluminum alkoxides. *J Am Chem Soc* 85:2318–2322
21. Folting K, Streib WE, Caulton KG, Poncelet O, Hubert-Pfalzgraf LG (1991) Characterization of aluminum isopropoxide and aluminosiloxanes. *Polyhedron* 10:1639–1646
22. Turova NY, Kozunov VA, Yanovskii AI, Borkii NG, Struchkov YT, Tarnopolskii BL (1979) Physico-chemical and structural investigation of aluminium isopropoxide. *J Inorg Nucl Chem* 41:5–11
23. Babonneau F, Doeuff S, Leautic A, Sanchez C, Cartier C, Verdagner M (1988) XANES and EXAFS study of titanium alkoxides. *Inorg Chem* 27:3166–3172
24. Ibers JA (1963) Crystal and molecular Structure of titanium (IV) ethoxide. *Nature* 197:686–687
25. Chisholm MH, Huffman JC, Leonelli J (1981) Hexadecamethoxy- and hexadecaethoxy-tetratungsten: preparation and X-ray crystal and molecular structure of W₄(OEt)₁₆. *J Chem Soc Chem Commun* 1981:270
26. Bradley DC, Mehrotra RC, Swanwick JD, Wardlaw W (1953) Structural chemistry of the alkoxides. Part IV. Normal alkoxides of silicon, titanium, and zirconium. *J Chem Soc* 1953:2025–2030
27. Veith M, Mathur S, Mathur C, Huch V (1997) Synthesis, reactivity and structures of hafnium-containing homo- and hetero- (bi- and tri-) metallic alkoxides based on edge- and face-sharing bioctahedral alkoxometalate ligands. *J Chem Soc, Dalton Trans* 1997(12):2101–2108
28. Vaartstra BA, Huffman JC, Gradoff PS, Hubert-Pfalzgraf LG, Daran JC, Parraud S, Yunlu K, Caulton KG (1990) Alcohol adducts of alkoxides: intramolecular hydrogen bonding as a general structural feature. *Inorg Chem* 29:3126–3131
29. Fric H, Schubert U (2005) Amine adducts of titanium tetraalkoxides. *New J Chem* 29:232–236
30. Bradley DC, Wardlaw W, Whitley A (1955) Normal alkoxides of quinquevalent tantalum. *J Chem Soc* 1955:726–728
31. Bradley DC, Chakravarti BN, Wardlaw W (1956) Normal alkoxides of quinquevalent niobium. *J Chem Soc* 1956:2381–2384
32. Pinkerton AA, Schwarzenbach D, Hubert-Pfalzgraf LG, Riess JG (1976) Crystal and molecular structure of niobium pentamethoxide – a structure with two different conformers in the unit cell. *Inorg Chem* 15:1196–1199
33. Eichhorst DJ, Howard KE, Payne DA (1992) NMR investigations of lithium niobium alkoxide solutions. In: Uhlmann DR, Ulrich DR (eds) *Ultrastructure processing of advanced materials*. John Wiley, New York, pp 87–93, Chapter 8
34. Bradley DC, Holloway CE (1968) Nuclear magnetic resonance studies on niobium and tantalum penta-alkoxides. *J Chem Soc A* 1968:219–223
35. Haaland A, Rypdal K, Volden HV, Jacob E, Weidlein J (1989) The molecular structure of tungsten hexamethoxide, W(OCH₃)₆, by gas electron diffraction. *Acta Chem Scand* 43:911–913
36. Tatzel G, Greune M, Weidlein J, Jacob E (1986) Schwingungsspektren und Kraftkonstanten von W(OCH₃)₆, Mo(OCH₃)₆ und [Sb(CH₃)₄][Sb(OCH₃)₆]. *Z Anorg Allg Chem* 533:83–92
37. Jacob E (1982) Metallhexamethoxides. *Angew Chem Int Ed Engl* 21:142–143
38. Bradley DC, Chisholm MH, Extine MW, Stager ME (1977) Some reactions of hexakis(dimethylamido)tungsten(VI). *Inorg Chem* 16:1794–1801

39. Bradley DC, Mehrotra RC, Wardlaw W (1952) Structural chemistry of the alkoxides. Part II. Tertiary alkoxides of silicon, titanium, zirconium, and hafnium. *J Chem Soc* 1952:4204–4209
40. Bradley DC, Mehrotra RC, Wardlaw W (1952) Structural chemistry of the alkoxides. Part III. Secondary alkoxides of silicon, titanium, and zirconium. *J Chem Soc* 1952:5020–5023
41. Bradley DC, Mehrotra RC, Wardlaw W (1952) Structural chemistry of the alkoxides. Part I. Amyloxides of silicon, titanium, and zirconium. *J Chem Soc* 1952:2027–2032
42. Bradley DC (1989) Metal alkoxides as precursors for electronic and ceramic materials. *Chem Rev* 89:1317–1322
43. Peter D, Ertel TS, Bertagnolli H (1994) EXAFS study of zirconium alkoxides as precursor in the sol-gel process: I. Structure investigation of the pure alkoxides. *J Sol-Gel Sci Technol* 3:91–99
44. Bradley DC, Caldwell EV, Wardlaw W (1957) The preparation and properties of stannic alkoxides. *J Chem Soc* 1957:4775–4778
45. Bradley DC, Chatterjee AK, Wardlaw W (1956) Structural chemistry of the alkoxides. Part VI. Primary alkoxides of quadrivalent cerium and thorium. *J Chem Soc* 1956:2260–2264
46. Caulton KG, Hubert-Pfalzgraf LG (1990) Synthesis, structural principles, and reactivity of heterometallic alkoxides. *Chem Rev* 90:969–995
47. Mehrotra RC, Batwara JM, Kapoor PN (1980) Coordination chemistry of lanthanides with emphasis on derivatives with Ln-O-C bonds. *Coord Chem Rev* 31:67–91
48. Gugliemi M, Carturan G (1988) Precursors for sol-gel preparations. *J Non-Cryst Solids* 100:16–30
49. Hubert-Pfalzgraf LG (2004) To what extent can design of molecular precursors control the preparation of high tech oxides? *J Mater Chem* 14:3113–3123
50. Hasenkox U, Hoffmann S, Waser R (1998) Influence of precursor chemistry on the formation of MTiO_3 (M=Ba, Sr) ceramic thin films. *J Sol-Gel Sci Technol* 12:67–79
51. Gust MC, Evans ND, Momoda LA, Mecartney ML (1997) In-situ transmission electron microscopy crystallization studies of sol-gel-derived barium titanate thin films. *J Am Ceram Soc* 80:2828–2836
52. Malic B, Koscec M, Arcon I, Kodre A (2005) Homogeneity issues in chemical solution deposition of $\text{Pb}(\text{Zr,Ti})\text{O}_3$ thin films. *J Eur Ceram Soc* 25:2241–2246
53. Lakeman CDE, Xu Z, Payne DA (1995) On the evolution of structure and composition in sol-gel-derived lead-zirconate-titanate thin-layers. *J Mater Res* 10:2042–2051
54. Tuttle BA, Headley TJ, Bunker BC, Schwartz RW, Zender TJ, Hernandez CJ, Goodnow DC, Tissot RJ, Michael J, Carim AH (1992) Microstructural evolution of $\text{Pb}(\text{Zr,Ti})\text{O}_3$ thin-films prepared by hybrid metalloorganic decomposition. *J Mater Res* 7:1876–1882
55. Roescher M, Tappertzhofen S, Schneller T (2011) Precursor homogeneity and crystallization effects in chemical solution deposition-derived alkaline niobate thin films. *J Am Ceram Soc* 94:2193–2199
56. Chowdhury A, Bould J, Londesborough MGS, Milne SJ (2010) Fundamental issues in the synthesis of ferroelectric $\text{Na}_{0.5}\text{K}_{0.5}\text{NbO}_3$ thin films by sol-gel processing. *Chem Mater* 22:3862–3874
57. Derderian GJ, Barrie JD, Aitchison KA, Adams PM, Mecartney ML (1993) Microstructural changes due to process conditions in sol-gel derived KNbO_3 thin films. *Mater Res Soc Symp Proc* 310:339–343
58. Livage J, Ganguli D (2001) Sol-gel electrochromic coatings and devices: a review. *Sol Energy Mater Sol Cells* 68:365–381
59. Kessler VG, Spijksma GI, Seisenbaeva GA, Håkansson S, Blank DHA, Bouwmeester HJM (2006) New insight in the role of modifying ligands in the sol-gel processing of metal alkoxide precursor: a possibility to approach new classes of materials. *J Sol-Gel Sci Technol* 40:163–179
60. Livage J, Henry M, Sanchez C (1988) Sol-gel chemistry of transition metal oxides. *Prog Solid State Chem* 18:259–341

61. Brinker CJ, Scherer GW (1990) Sol-gel science. The physics and chemistry of sol-gel processing. Academic, San Diego
62. Sanchez C, Livage J, Babonneau F (1988) Chemical modification of alkoxide precursors. *J Non-Cryst Solids* 100:65–76
63. Bradley DC, Carter DG (1961) Metal oxide alkoxide polymers. *Canadian J Chem* 39:1434–1443
64. Yoldas BE (1986) Hydrolysis of titanium alkoxide and effects of hydrolytic polycondensation parameters. *J Mater Sci* 21:1087–1092
65. Livage J, Babonneau F, Sanchez C (1991) Some aspects of the chemistry of transition metal oxide gels. In: Harrod JF, Laine RM (eds) *Inorganic and organometallic oligomers and polymers*. Springer, Netherlands, pp 217–228
66. Livage J, Henry M, Jolivet JP, Sanchez C (1990) Chemical synthesis of fine powders. *Mater Res Soc Bull* 15:18–25
67. Aelion R, Loebel A, Elrich F (1950) Hydrolysis of ethyl silicate. *J Am Chem Soc* 72:5705–5712
68. Stockmayer WH (1943) Theory of molecular size distribution and gel formation in branched-chain polymers. *J Chem Phys* 11:45–55
69. Schubert U (2003) Sol-gel processing of metal compounds. In: McCleverty JA, Meyer TJ (eds) *Comprehensive coordination chemistry II*, vol 7. Pergamon, Oxford, pp 629–656
70. Kamiya K, Ohya M, Yoko T (1986) Nitrogen-containing SiO₂ glass fibers prepared by ammonolysis of gels made from silicon alkoxides. *J Non-Cryst Solids* 83:208–222
71. Nabavi M, Doeuff S, Sanchez C, Livage J (1990) Chemical modification of metal alkoxides by solvents: a way to control sol-gel chemistry. *J Non-Cryst Solids* 121:31–34
72. Mehrotra RC, Bohra R, Gaur DP (1978) *Metal β-diketonates and allied derivatives*. Academic, London
73. Hubert-Pfalzgraf LG, Guillon H (1998) Trends in precursor design for conventional and aerosol-assisted CVD of high-Tc superconductors. *Appl Organometal Chem* 12:221–236
74. Yamaguchi N, Tadanaga K, Matsuda A, Minami T, Tatsumisago M (2007) Antireflective properties of flowerlike alumina thin films on soda-lime silica glass substrates prepared by the sol-gel method with hot water treatment. *Thin Solid Films* 515:3914–3917
75. Saifullah MSM, Kang DJ, Subramanian KRV, Welland ME, Yamazaki K, Kurihara K (2004) Electron beam nanolithography of β-ketoester modified aluminium tri-sec-butoxide. *J Sol-Gel Sci Technol* 29:5–10
76. Bonhomme-Courty L, Babonneau F, Livage J (1994) Investigation of the sol-gel chemistry of ethylacetoacetate modified aluminum sec-butoxide. *J Sol-Gel Sci Technol* 3:157–168
77. Tadanaga K, Iwami T, Tohge N, Tsutomu M (1994) Precursor structure and hydrolysis-gelation process of Al(O-sec-Bu)₃ modified with ethylacetoacetate. *J Sol-Gel Sci Technol* 3:5–10
78. Uchihashi H, Tohge N, Minami T (1989) Preparation of amorphous Al₂O₃ thin films from stabilized Al-alkoxides by the sol-gel method. *J Ceram Soc Jpn* 97:396–399
79. Jain R, Rai A, Mehrotra R (1986) Synthesis and spectral studies of β-diketone and β-ketoester derivatives of aluminium zirconium isopropoxide. *Polyhedron* 5:1017–1021
80. Yamamoto A, Kambara S (1957) Structures of the reaction products of tetraalkoxytitanium with acetylacetone and ethyl acetoacetate. *J Am Chem Soc* 74:4344–4348
81. Unuma H, Tokoka T, Suzuki Y, Furusaki T, Kodaira K, Hatsushida T (1986) Preparation of transparent amorphous tungsten trioxide thin films by a dip-coating method. *J Mater Sci Lett* 5:1248–1250
82. Leautic A, Babonneau F, Livage J (1989) Structural investigation of the hydrolysis-condensation process of titanium alkoxides Ti(OR)₄ (OR = OP^r, OEt) modified by acetylacetone. 1. Study of the alkoxide modification. *Chem Mater* 1:240–247
83. Emeli M, Incoccia L, Mobilio S, Fagherazzi G, Guglielmi M (1985) Structural investigations of TiO₂/SiO₂ glassy and glass-ceramic materials prepared by the sol-gel method. *J Non-Cryst Solids* 74:129–146

84. Debsikdar JC (1986) Transparent zirconia gel-monolith from zirconium alkoxide. *J Non-Cryst Solids* 86:231–240
85. Debsikdar JC (1985) Preparation of transparent non-crystalline stoichiometric magnesium aluminate gel-monolith by the sol-gel process. *J Mater Sci* 20:4454–4458
86. Spijksma GI, Bouwmeester HJM, Blank DHA, Kessler VG (2004) Stabilization and destabilization of zirconium propoxide precursors by acetylacetone. *Chem Commun* 2004:1874–1875
87. Errington RJ, Ridland J, Clegg W, Coxall RA, Sherwood JM (1998) Beta-diketonate derivatives of titanium alkoxides: X-ray crystal structures and solution dynamics [$\{\text{Ti}(\text{OR})_3(\text{dik})\}_2$]. *Polyhedron* 17:659–674
88. Bharara PC, Gupta VD, Mehrotra RC (1974) Reactions of titanium alkoxides with N-methylaminoalcohols. *Z Anorg Allg Chem* 403:337–346
89. Losego MD, Ihlefeld JF, Maria J (2008) Importance of solution chemistry in preparing sol-gel PZT thin films directly on copper surfaces. *Chem Mater* 20:303–307
90. Halder S, Schneller T, Waser R (2005) Crystallization temperature limit of (Ba,Sr)TiO₃ thin films prepared by a nonoxocarbonate phase forming CSD route. *J Sol-Gel Sci Technol* 33:299–306
91. Kim SH, Kim DJ, Hong JG, Streiffer SK, Kingon AI (1999) Imprint and fatigue properties of chemical solution derived Pb_{1-x}La_x(Zr_yTi_{1-y})_{1-x/4}O₃ thin films. *J Mater Res* 14:1371–1377
92. Kato K, Tsuge A, Niihara K (1996) Microstructure and crystallographic orientation of anatase coatings produced from chemically modified titanium tetraisopropoxide. *J Am Ceram Soc* 79:1483–1488
93. Selvaraj U, Prasadarao AV, Komarneni S, Roy R (1992) Sol-gel fabrication of epitaxial and oriented TiO₂ thin films. *J Am Ceram Soc* 75:1167–1170
94. Takahashi Y, Matsuoka Y (1988) Dip-coating of TiO₂ films using a sol derived from Ti(O-i-Pr)₄-diethanolamine-H₂O-i-PrOH system. *J Mater Sci* 23:2259–2266
95. Tohge N, Takahashi S, Minami T (1991) Preparation of PbZrO₃-PbTiO₃ ferroelectric thin films by the sol-gel process. *J Am Ceram Soc* 74:67–71
96. Fric H, Jupa M, Schubert U (2006) The solid-state structures of a non-hydrated yttrium carboxylate and a yttrium carboxylate hemihydrate obtained by reaction of yttrium alkoxides with carboxylic acids. *Monatsh Chem* 137:1–6
97. Kogler FR, Jupa M, Puchberger M, Schubert U (2004) Control of the ratio of functional and non-functional ligands in clusters of the type Zr₆O₄(OH)₄(carboxylate)₁₂ for their use as building blocks for inorganic-organic hybrid polymers. *J Mater Chem* 14:3133–3138
98. Urlaub R, Posset U, Thull R (2000) FT-IR spectroscopic investigations on sol-gel-derived coatings from acid-modified titanium alkoxides. *J Non-Cryst Solids* 265:276–284
99. Boyle TJ, Tyner RP, Alam TM, Scott BL, Ziller JW, Potter BG (1999) Implications for the thin-film densification of TiO₂ from carboxylic acid-modified titanium alkoxides. Syntheses, characterizations, X-ray structures of Ti₃(μ₃-O)(O₂CH)₂(ONep)₈, Ti₃(μ₃-O)(O₂CMe)₂(ONep)₈, Ti₆(μ₃-O)₆(O₂CCHMe₂)₆(ONep)₆, [Ti(μ-O₂CMe₃)(ONep)₃]₂, and Ti₃(μ₃-O)(O₂CCH₂CMe₃)₂(ONep)₈ (ONep = OCH₂CMe₃). *J Am Chem Soc* 121:12104–12112
100. Kickelbick G, Schubert U (1999) Hydroxy carboxylate substituted oxozirconium clusters. *J Chem Soc, Dalton Trans* 1999(8):1301–1306
101. Stenou N, Bonhomme C, Sanchez C, Vaissermann J, Hubert-Pfalzgraf LG (1998) A tetranuclear niobium oxo acetate complex. Synthesis, X-ray crystal structure, and characterization by solid-state and liquid-state NMR spectroscopy. *Inorg Chem* 37:901–910
102. Kickelbick G, Schubert U (1997) Oxozirconium methacrylate clusters: Zr₆(OH)₄O₄(OMc)₁₂ and Zr₄O₂(OMc)₁₂ (OMc = methacrylate). *Chem Ber* 130:473–478
103. Boyle TJ, Schwartz RW (1994) An investigation of group(IV) alkoxides as property controlling reagents in the synthesis of ceramic materials. *Comments Inorg Chem* 16:243–278

104. Alam TM, Boyle TJ, Buchheit CD, Schwartz RW, Ziller JW (1994) Formation, structure, and material properties from the reaction product of $M(\text{OCHMe}_2)_4$ ($M = \text{Ti}, \text{Zr}$) and HOAc. *Mater Res Soc Symp Proc* 346:35–40
105. Schwartz RW, Boyle TJ, Voigt JA, Buchheit CD (1994) Densification and crystallization of zirconia thin films prepared by sol-gel processing. In: Bhalla AS, Nair KM, Lloyd IK, Yanagida H, Payne DA (eds) *Ferroic materials: design, preparation, and characteristics*, vol. 43. *Ceramic Transactions*, pp 145–163
106. Mehrotra R, Rai A (1991) Aluminium alkoxides, β -diketonates and carboxylates. *Polyhedron* 10:1967–1994
107. Sanchez C, Toledano P, Ribot F (1990) Molecular structure of metal alkoxide precursors. *Mater Res Soc Symp Proc* 180:47–59
108. Doeuff S, Dromzee Y, Taulelle F, Sanchez C (1989) Synthesis and solid- and liquid-state characterization of a hexameric cluster of titanium(IV): $\text{Ti}_6(\mu_2\text{-O})_2(\mu_3\text{-O})_2(\mu_2\text{-OC}_4\text{H}_9)_2(\text{OC}_4\text{H}_9)_6(\text{OCOCH}_3)_8$. *Inorg Chem* 28:4439–4445
109. Doeuff S, Henry M, Sanchez C, Livage J (1987) Hydrolysis of titanium alkoxides: modification of the molecular precursor by acetic acid. *J Non-Cryst Solids* 89:206–216
110. Barboux-Doeuff S, Sanchez C (1994) Synthesis and characterization of titanium oxide-based gels synthesized from acetate modified titanium butoxide precursors. *Mater Res Bull* 29:1–13
111. Czakler M, Artner C, Schubert U (2012) Preparation of carboxylato-coordinated titanium alkoxides from carboxylic anhydrides: alkoxido group transfer from metal atom to carbonyl group. *Eur J Inorg Chem* 21:3485–3489
112. Schroeder H (1969) Oxide layers deposited from organic solutions. In: Hass G, Thun RE (eds) *Physics of thin films: advances in research and development*, vol 5. Academic, New York, pp 87–141
113. Nagase K, Shimizu Y, Miura N, Yamazoe N (1992) Electrochromism of vanadium-titanium oxide thin films prepared by spin-coating method. *Appl Phys Lett* 61:243–245
114. Kim Y, Francis LF (1993) Processing and characterization of porous TiO_2 coatings. *J Am Ceram Soc* 76:737–742
115. Harris MT, Byers CH, Brunson RR (1988) A study of solvent effects on the synthesis of pure component and composite ceramic powders by metal alkoxide hydrolysis. *Mater Res Soc Symp Proc* 121:287–292
116. Keddie JL, Braun PV, Giannelis EP (1994) Interrelationship between densification, crystallization, and chemical evolution in sol-gel titania thin films. *J Am Ceram Soc* 77:1592–1596
117. Keddie JL, Giannelis EP (1991) Effect of heating rate on the sintering of titanium dioxide thin films: competition between densification and crystallization. *J Am Ceram Soc* 74:2669–2671
118. Hoebbel D, Reinert T, Schmidt H (1996) NMR and IR spectroscopic examination of the hydrolytic stability of organic ligands in metal alkoxide complexes and of oxygen bridged heterometal bonds. *Mater Res Soc Symp Proc* 435:461–467
119. Leautic A, Babonneau F, Livage J (1989) Structural investigation of the hydrolysis-condensation process of titanium alkoxides $\text{Ti}(\text{OR})_4$ ($\text{OR} = \text{OPr-iso}, \text{OEt}$) modified by acetylacetone. 2. From the modified precursor to the colloids. *Chem Mater* 1:248–252
120. Chatry M, Henry M, In M, Sanchez C, Livage J (1994) The role of complexing ligands in the formation of non-aggregated nanoparticles of zirconia. *J Sol-Gel Sci Technol* 1:233–240
121. Ribot FC, Toledano P, Sanchez C (1991) Hydrolysis-condensation process of β -diketonates-modified cerium(IV) isopropoxide. *Chem Mater* 1:759–765
122. Duonghong D, Borgarello E, Graetzel M (1981) Dynamics of light-induced water cleavage in colloidal systems. *J Am Chem Soc* 103:4685–4690
123. Toledano P, In M, Sanchez C (1991) Synthesis and structure of the compound $[\text{Ti}_{18}(\mu_5\text{-O})_2(\mu_4\text{-O})_2(\mu_3\text{-O})_{10}(\mu_2\text{-O})_8(\mu_2\text{-OBu}^n)_{12}(\text{acac})_2]$. *C R Acad Sci Ser II: Mec Phys Chim Sci Terre Univers* 313:1247–1253
124. Babonneau F, Leautic A, Livage J (1988) Structural investigation of the hydrolysis-condensation process of a modified titanium alkoxide. *Mater Res Soc Symp Proc* 121:317–322

125. Roescher M, Schneller T, Waser R (2010) Comments on the processing of the niobium component for chemical solution derived niobium oxide-based thin-films. *J Sol-Gel Sci Technol* 56:236–243
126. Dunuwila DD, Gagliardi CD, Berglund KA (1994) Application of controlled hydrolysis of titanium(IV) isopropoxide to produce sol-gel-derived thin films. *Chem Mater* 6:1556–1562
127. Ozer N, Tepehan F, Bozkurt N (1992) An “all-gel” electrochromic device. *Thin Solid Films* 219:193–198
128. Bahlawane N (2001) Novel sol-gel process depositing α -Al₂O₃ for the improvement of graphite oxidation-resistance. *Thin Solid Films* 396:126–130
129. Pascual R, Sayer M, Vasant Kumar CVR, Zou L (1991) Rapid thermal processing of zirconia thin films produced by the sol-gel method. *J Appl Phys* 70:2348–2352

Chapter 2

Carboxylate Based Precursor Systems

Theodor Schneller and David Griesche

2.1 Introduction

Besides the alkoxides described in the preceding chapter, metal carboxylates are the second most frequently employed class of educts which is used for the synthesis of precursor solutions. Chemically they are regarded as derivatives of carboxylic acids which are organic Brönstedt acids of the general formula $R-C(=O)OH$, usually written $R-COOH$ or $R-CO_2H$ where R is a general organic moiety. The length and chemical nature (single or double bonds, linear or branched shape, number and type of hetero atoms etc.) of this organic residue determines the polarity and the decomposition behavior of the acid and the corresponding carboxylate, respectively. Short chain carboxylic acids (1–4 carbons) are soluble in water, whereas longer carboxylic acids are less soluble in polar solvents due to the increasing hydrophobic nature of the longer alkyl chain. These longer chain acids tend to be rather soluble in less-polar solvents such as ethers, alcohols, toluene, xylene etc. Examples for commonly known, simple carboxylic acids are the formic acid $H-COOH$ ($R = H$), that occurs in ants, acetic acid $H_3C-COOH$ ($R = CH_3$), that gives vinegar its sour taste, and butyric acid ($R = CH_3-CH_2-CH_2$) that gives the odor of rancid butter. Acids with two or more carboxyl groups are called dicarboxylic, tricarboxylic, etc. Citric acid is an important example for a tricarboxylic acid and is used in the water based precursor systems described in Chap. 5. The release of the proton (Fig. 2.1) from the carboxylic acid corresponds to the formation of the carboxylate anion, which is stabilized by the negative charge shared (delocalized) between the two oxygen atoms (mesomerism). This means that each of the carbon-oxygen bonds in a carboxylate anion has a partial double-bond character, which is also reflected in the carbon-oxygen bond lengths (~ 136 pm). This value is between

T. Schneller (✉) • D. Griesche
Institut für Werkstoffe der Elektrotechnik II, RWTH Aachen University, Aachen, Germany
e-mail: schneller@iwe.rwth-aachen.de

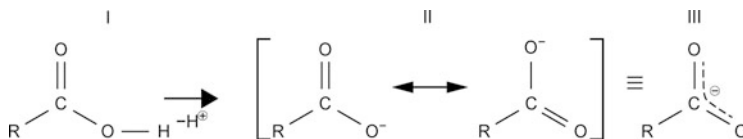


Fig. 2.1 Schematic of the acidity effect of the carboxylic acid (I) which leads to the carboxylate anion (III). This anion is stabilized by mesomerism (II), which is beside the polarity of the O-H bond a further reason for the acidity of carboxylic acids. The free electron pairs may form bondings to metal cations in different modes (see below)

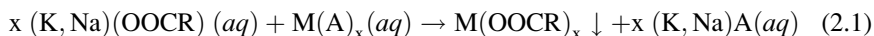
the bond length of a carbon-oxygen double-bond (~ 123 pm) and single-bond (~ 143 pm) [1].

By substituting the acid proton with a metal cation (M^{z+}), metal carboxylates are formed (Fig. 2.2). Thus according to their chemical structure, the carboxyl group can act as a bidentate ligand (Fig. 2.2a) either in a chelating or a bridging mode as shown in Fig. 2.2b [2, 3] and the binding mode can be determined via Fourier transform infrared (FT-IR) spectroscopy [4] (see Chap. 9) for example.

The main reason for the popularity of metal carboxylate precursors is that they are often commercially available, cheap, and insensitive to humidity. Moreover the parent carboxylic acids can be used as solvent and are often less toxic compared to other organic solvents such as 2-methoxyethanol. Although carboxylic acids are weak acids, which means that their negative logarithmic acidity constant pK_a is in the range of 4–6, there is a correlation between the chain length (number of carbon atoms) of the acids and the logarithmic acidity constants [5, 6]. It can be seen in Table 2.1 that the acid strength decreases with increasing chain length. For a more detailed discussion of the properties of metal carboxylates see also [7].

2.1.1 Synthesis Aspects

Several methods have been used to synthesize metal carboxylates [8–11]. One possible synthesis method is the aqueous metathesis. To provide the desired carboxylate ligands, an aqueous solution (*aq*) of the corresponding sodium or potassium carboxylate is prepared. Then another solution containing a salt of the desired metal is added. The metathesis reaction can be described by the following general reaction equation.



Here M represents the particular metal ion and A is the anionic leaving group of the metal salt $M(A)_x$. The metal carboxylate $M(OOCR)_x$ has low solubility in water, especially when its organic moiety R consist of more than six carbon atoms. Hence it can be removed by filtering, washed with an alcohol for example, and dried. Several salts $M(A)_x$ have been used, e.g. copper and lead dodecanoate

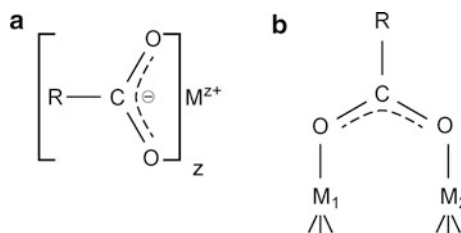


Fig. 2.2 Scheme of different bonding modes of metal carboxylates. In the chelating mode (a) the metal ion is centered between the two oxygen atoms of the carboxylate group and is attracted to both oxygen atoms, whereas in the bridging mode (b) each carboxylate-oxygen atom coordinates to one metal ion, which can be different (M_1 and M_2)

Table 2.1 Negative logarithmic acidity constants (pK_a) for different aliphatic carboxylic acids

Name of the acid	Number of carbon atoms	pK_a
Acetic	2	4.76
Propionic	3	4.87
Butyric	4	4.82
Isobutyric	4	4.86
Valeric	5	4.86
Hexanoic	6	4.88
Heptanoic	7	4.89
Octanoic	8	4.89
Nonanoic	9	4.96

In the mid column the number of carbon atoms is shown. Taken from [5, 6]

and octadecanoate prepared from the corresponding acetates [9]. Also the sulphates of zinc, magnesium, lead nitrate and calcium chloride were successfully transformed to the octadecenoates by metathesis reactions [10]. A second synthesis route is to treat the metal hydroxides with an alcoholic solution of the carboxylic acid [8]. This method had been used for the preparation of copper, silver, barium, mercury, lead iron cobalt, nickel and alkaline carboxylates [11]. The reaction formula can be given as follows.



The water which is formed in this reaction can be removed by distillation under reduced pressure or by washing with anhydrous solvents. However, this method has several disadvantages, e. g. the resulting carboxylates can be extremely viscous, and hence the filtration is sometimes difficult and non-reacted carboxylic acid can hardly be removed. In case of the carboxylates of lead, mercury, iron and the alkaline earths, a modification of this method leads to better results. The corresponding metal oxide was dissolved in the molten carboxylic acid and the product afterwards is cleaned with hot ethanol and petroleum ether [11]. One requirement of every synthesis is the accurate control of the product stoichiometry and this is related to a well-defined amount of water of constitution. The control of

this issue is not only quite important because the composition of the product directly relies on the used educts. The water of constitution can also change the solution behavior drastically. This is often strongly dependent on the chemical route which is used to prepare the desired metal carboxylate. The following example can serve as an illustration. The metathesis reaction of magnesium chloride with sodium octadecenoate in water yields a precipitate which could be identified as $\text{Mg}(\text{OOC}_{18}\text{H}_{33})_2 \cdot 2 \text{H}_2\text{O}$ [12]. It was only moderately soluble in benzene, but when it was refluxed in dry benzene and then recrystallized, the recrystallization product was found to be $\text{Mg}(\text{OOC}_{18}\text{H}_{33})_2$ and this had better solubility in benzene than the original precipitate [13].

In the following sections details on the use of metal carboxylates as an important class of chemical educts for the synthesis of CSD precursor solutions are described. Emphasis will be given to the carboxylates of alkaline and rare earth elements as well as selected metals from the groups 4 to 14 of the periodic table of elements, since they are relevant for the synthesis of precursor solutions for CSD of ferroelectric, dielectric and conducting perovskite thin films. The coating process for producing thin oxide films from pure carboxylate based precursor solutions is known as metallo-organic-decomposition (MOD),¹ which is an indication that the organic matrix which surrounds the metal ions in the as-deposited films has typically to be removed by thermal decomposition rather than simple in an evaporation process which takes place in case of classical sol-gel processes. The “o” in metallo_organic indicates that the bond formation of the organic ligands occurs via an oxygen atom and not via direct carbon-metal bond as in real metal organic compounds.

On top of syntheses based on only metal carboxylates, solution synthesis routes based on suitable mixtures of metal alkoxides (Chap. 1) and metal carboxylates are also frequently used. Such approaches are often called hybrid-routes and will be described in more detail in subsequent Chap. 3.

2.2 General Considerations of MOD-Processes

Metallo-organic-decomposition is well established and a huge number of inorganic thin films have been made by this technique [14, 15]. In many cases processing routes are based on a hybrid of sol-gel chemistry and MOD-chemistry. A strict separation between the pure sol-gel and the pure MOD chemistry is not always possible, but some important characteristics of “pure” MOD processes will be given in this section. Generally these types of CSD-processes can be divided into a few main steps, which are summarized as flow-chart in the general introduction of this book.

¹ In the literature the phrase “metal organic deposition” is also often used. It denotes the same kind of precursor chemistry.

In the first step, the M-carboxylates are dissolved in a suitable solvent such as the parent acid or xylene. The stoichiometry of the educts and therefore the composition of the resulting layer can be directly adjusted by mixing defined amounts of the prepared solutions or, in some cases, by direct weighting out the carboxylates and alkoxides in one pot followed by dissolution in the desired solvent. The properties of the resulting solutions such as viscosity can be influenced by further chemical or physical modification (distillation, etc.). The precursor solution can be deposited on the substrate by various techniques (e.g. spray coating, spin coating or dip coating, (see Chaps. 11–13) in the second step, where the so called wet film is generated. After this, a certain temperature treatment follows, in which the organic material is removed and a crystalline film is formed. The last two steps can be repeated until the desired layer thickness is achieved. Beside the mentioned often cheap and easy-manageable educts, the main advantage of the carboxylate-based-routines is the comparably low temperature which is needed in the crystallization step to form thermodynamically stable phases. This is because the educt molecules are mixed at the molecular level. Thus, the diffusion paths of the metal- and oxygen-ions are short compared to classical powder based syntheses of ceramic bulk materials. In addition the relatively low temperature often helps to prevent the evaporation of volatile decomposition products. A skillful temperature treatment leads to the possibility of precise control of the microstructure, e.g. grain size and orientation (see Chap. 17). The carboxylates used should fulfill a few requirements:

- The educts should be available as highly pure materials and should possess a defined molecular structure.
- If they are not commercially available, they should be easy to synthesize and purify.
- They should be stable in air in order to facilitate handling.
- The metal content should be high to prevent massive reduction in volume (which can lead to micro cracks in the layers) during pyrolysis and crystallization.
- They should show an adequate solubility in the desired solvent and they should be compatible with each other.
- The decomposition should not lead to the formation of volatile metal containing species, melts, carbon contamination, and toxic gases. This often restricts the choice of the carboxylate chain, because heteroatoms such as, nitrogen, sulphur, or in particular fluorine in the chain lead to highly toxic decomposition gases.

Next, a brief survey of the deposition and thermal treatment is given.

2.2.1 Thin-Film-Deposition and Thermal Treatment: Solvent Evaporation Behavior

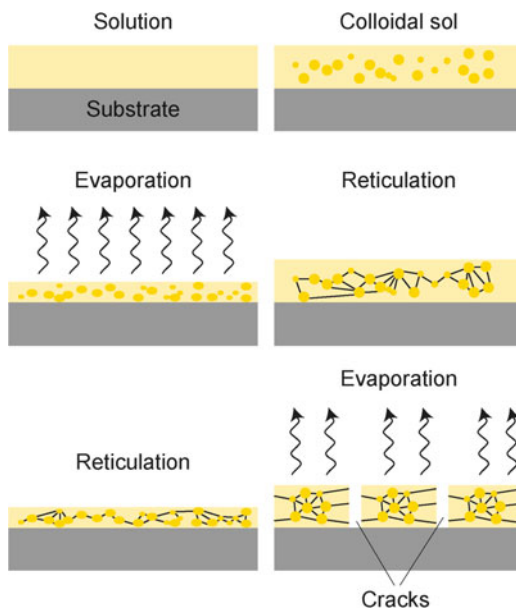
The deposition of a given MOD or hybrid solution is one of the most important steps [14, 15], since it determines the final uniformity of the resulting film to a large

extent, as can be seen in the later chapters (Chaps. 10–12). Spin coating is the most common deposition technique and was adopted from classical semiconductor fabrication technologies, i.e. deposition of photoresists for standard optical lithography. Naturally, the deposition should be carried out in a clean room environment to avoid the contamination of the film by dust particles. Such contaminations might lead to the appearance of dust streaks, which of course degrades the quality of the film. If the deposition process involves any solvent evaporation, the deposition should be very rapid, because the solubilities of the metallo-organic species may be different. Rapid processing might prevent the segregation of the species. In general, there is a direct dependence between the viscosity and the concentration of the metallo-organic species in the solution. With increasing concentration, the viscosity also increases. This effect is relatively strong in MOD-derived solutions in comparison to pure sol-gel processes. Less viscous solutions result in thinner films, i.e. more deposition steps are necessary to achieve thicker films. On the other hand, a lower thickness per coating step may enable the deposition of ultrathin films. A key feature of any deposition method is the ability to control the uniformity and film thickness which is related to the pyrolysis step. Pyrolysis here refers to the removal of the solvent followed by the decomposition of the organic residues through thermal treatment in oxygen containing atmospheres. The spin coating process of a simple MOD-system in a non-volatile Newtonian fluid, where no slip occurs at the liquid-solid interface, can be theoretically expressed using a modified Navier-Stokes equation [16]. Equation (2.3) describes the relation of the film thickness after pyrolysis (h_s) and the physical parameters of the precursor solution:

$$h_s = \frac{c}{2\omega\rho_s} \left(\frac{3\eta\rho_l}{t} \right)^{1/2} \quad (2.3)$$

Here ρ_s and ρ_l are the solid and liquid densities, ω respectively is the angular velocity, t refers to the spinning time, c is the mass concentration of the solution formulation (weight of solid film/weight of solution) and η is the viscosity of the liquid. This equation was verified experimentally with an MOD-derived lead titanate (PTO)-film with lead neodecanoate and titanium di-methoxy-di-neodecanoate as educts and xylene as solvent [15]. The agreement of the theoretically predicted film thickness and the experimentally derived values was notably good. When comparing the pyrolysis of sol-gel routines with MOD-derived films, there are also some significant differences. As described earlier, a MOD-solution can be considered as a system where the metal cations are solvated and complexed by the carboxylate functions. For this reason usually no or very little reticulation occurs between the molecules. Hence it can be said that the hydrocarbon chain of the carboxylate provides a kind of protection due to its hydrophobic nature. By contrast in pure sol-gel routines the precursor-solutions consist of more or less colloidal sols, and depend on the additives for chemical protection. Figure 2.3 shows the different events, which occur when the chemically different precursor solutions are deposited on the surface, and heating starts [17]. The

Fig. 2.3 Schematic comparison of the events which take place when a MOD-derived solution (*left side*) and a colloidal sol (*right side*) are deposited on a certain surface and pyrolysis starts. The main difference is that from a MOD-solution the evaporation starts earlier, followed by the reticulation, whereas in the case of colloidal sols these two events are switched, which may result in the formation of microcracks. Modified after [17]



evaporation of the solvent in MOD-processes occurs perpendicular to the substrate, which leads to a shrinkage in the perpendicular direction. Reticulation occurs later when the decomposition occurs. In the sol-gel process, reticulation starts earlier, e.g. before the evaporation of the solvent [17]. This early onset of reticulation is a consequence of the more reactive nature of the metal alkoxides (the details of which may be found in Chap. 1). Thus shrinkage parallel to the substrate takes place which might result in the formation of microcracks.

Further thermal treatment at higher temperatures results in the decomposition of the organic residues and leads to amorphous or crystalline ceramic thin films, which is explained in the next section.

2.2.2 Decomposition Behavior

If the as-deposited layer is treated at higher temperatures decomposition of organic residues takes place. This step usually results in a large decrease in volume, which may also lead to microcracks. As mentioned before and described in more detail in Chaps. 15 and 17, the thermal treatment determines the evolution of the microstructure and so the heat process has to be optimized for the desired film morphology (dense, porous, fine grained etc.). In particular the heating rates play an important role. In general, a low heating rate during solvent evaporation phase is desirable to prevent cracking. The heating rates in the decomposition and crystallization phase are specific for every given system. Thermogravimetric analysis can

be used to estimate the minimum temperature for decomposition and removal of the organic species. If it is coupled with a differential thermoanalysis, crystallization events are also distinguishable (for details see Chap. 7). The decomposition mechanisms of the carboxylate based precursor solutions are rather complex and not completely understood. A possible mechanism can be deduced from comparisons of thermoanalysis data obtained from decomposition studies of the individual PTO-precursors titanium-dimethoxy-dineodecanoate and lead-ethylhexanoate with a precursor mixture of both components in xylene. It was shown that the decomposition temperature of the individual components was significantly lower than the corresponding temperature for the mixture. This indicates a kind of domino effect in the decomposition process of the mixture. It was assumed that the decomposition of the mixture consists of three steps, in which radical reactions take place. First, free organic radicals are generated through thermal fission. This step is rate determining and followed by a second step that involves fast fragmentation of the organic radicals. The last step is a very fast oxidative chain reaction of the organic radicals to yield longer chains. If this mechanism is valid, the decomposition temperature should decrease with increasing chain length, branching and oxygen partial pressure. Indeed this behavior has been found in most but not all cases [14]. Thus the affirmation of this or other kinds of decomposition mechanism should be the interest of further research. Nevertheless, there are many reports about the decomposition of metal carboxylates as single components [18–34]. Care should be taken when single component decomposition behavior is directly compared with precursor solution decomposition mechanisms, but still the reaction pathways which have been determined for single components are a good starting point for continuative experiments.

In the following sub-sections the behavior of some important examples which concern the commonly used metal carboxylates (acetates, propionates and long-chain carboxylates) are reviewed, followed by selected studies on the decomposition of MOD-mixtures.

2.2.2.1 Metal Acetates and Propionates

Metal acetates can be considered as the most investigated carboxylates with respect to their decomposition behavior [18, 19]. One has to keep in mind the two important considerations in all the analyses of the decomposition processes which can be found in literature. First, metal carboxylates can contain a certain amount of water of constitution. The second point concerns the atmosphere in which the decomposition took place. In some cases the resulting decomposition products differ drastically in their nature according to the atmosphere under which the certain experiment was carried out. In an infrared-spectroscopic study of the decomposition of several metal acetates in air it was found that there are three temperature regions [18]: (a) the temperature of dehydration (80–130 °C), (b) the temperature where intermediates are formed (105–230 °C), and (c) the decomposition temperature (100–440 °C), where the intermediates are converted into the final product.

Based on the above discussion, the metal acetates can be classified by the intermediates and final products that occur. For the alkaline acetates (potassium and sodium), the intermediate is the corresponding oxalate, which decomposes and yields the metal carbonate. For barium acetate the corresponding carbonate occurs directly without an intermediate, whereas calcium acetate decomposes to the carbonate over a crystalline anhydrous modification. Magnesium, lead, nickel, and cadmium acetates form an intermediate basic salt. In case of cadmium, nickel, and lead acetate this intermediate decomposes at higher temperatures to give the metal, while magnesium acetate yields the corresponding metal oxide. The occurrence of the pure metal as final product was also observed for copper acetate, where the decomposition proceeds via a crystalline modification of the anhydrous acetate as the intermediate analogous to the calcium. Cobalt and silver acetate decompose to the pure metal without the formation of an intermediate. Under air all metals are immediately oxidized to form the oxides. The crystalline acetate modification as intermediate is also observed for zinc and manganese acetate, which decompose to the corresponding oxides. It should be noted that the generated carbonates can be transformed into the corresponding oxides at higher temperatures. This happened for example between 350 and 450 °C when anhydrous lead(IV) acetate ($\text{Pb}(\text{OOCCH}_3)_4$) was heat treated in air [20]. The decomposition of a number of rare earth acetates have also been investigated [19–24]. All the investigated rare earth acetates consisted of three acetate ions coordinated to the central metal cation complemented by 1–4 water molecules of constitution per metal ion. This leads to the general formula $\text{Ln}(\text{OOCCH}_3)_3 \cdot x\text{H}_2\text{O}$. Consequently the first reaction was always found to be dehydration at temperatures between 90 and 250 °C. It could elapse in one or more steps. For instance dysprosium acetate $\text{Dy}(\text{OOCCH}_3)_3 \cdot 4\text{H}_2\text{O}$ loses 3.5 molecules of water at 90 °C and the last 0.5 molecule is released at 150 °C [20]. The intermediate is a thermally unstable anhydrous acetate. This anhydrous form can undergo several phase transitions [21], where monodentate, bidentate or even polymeric species can occur. It could be shown that in the temperature range of 250–500 °C the anhydrous acetates were transformed into a broad range of secondary intermediates. These secondary intermediates can be the corresponding oxyacetates, carbonates, oxycarbonates, and even hydroxides [19]. In most cases these intermediates occur in succession. These in turn decomposed then to the oxides in the temperature range from 500 to 900 °C. The structure of the oxide is depending on the nature of the rare earth element. In most cases the sesquioxides (Ln_2O_3) can be found, but for praeosodymium e.g. the dioxide related structure $\text{PrO}_{1.833}$ was found [22].

Relatively less is known about the decomposition behavior of the metal propionates. The decomposition of the monohydrated alkaline earth propionates ($\text{M}(\text{OOCCH}_2\text{CH}_3)_2 \cdot \text{H}_2\text{O}$ with $\text{M} = \text{Ba}, \text{Sr},$ and Ca) proceeded over a single stage dehydration step for the strontium and calcium propionates and a two stage dehydration step for barium propionate, in which $\text{Ba}(\text{OOCCH}_2\text{CH}_3)_2 \cdot 0.5\text{H}_2\text{O}$ is formed at temperatures lower than 200 °C [25]. The anhydrous propionates crystallize at about 200 °C. Above 300 °C, the decomposition took place simultaneously with melting, resulting in the formation of carbonates at 350 °C.

In another study [26], the decomposition of the self-prepared propionates of nickel ($\text{Ni}(\text{OOCCH}_2\text{CH}_3)_2 \cdot \text{H}_2\text{O}$), cobalt ($\text{Co}(\text{OOCCH}_2\text{CH}_3)_2 \cdot 3\text{H}_2\text{O}$), copper ($\text{Cu}(\text{OOCCH}_2\text{CH}_3)_2 \cdot 0.5\text{H}_2\text{O}$) and zinc ($\text{Zn}(\text{OOCCH}_2\text{CH}_3)_2 \cdot \text{H}_2\text{O}$) was analyzed. It was found that the stepwise dehydration processes took place in the temperature range between 70 and 130 °C to form the anhydrous propionate, and the final decomposition give rise to a few unidentified intermediates in the range of 250–360 °C. In all cases the final products were the corresponding metal oxides. The decomposition behavior of iron propionate trihydrate ($\text{Fe}(\text{OOCCH}_2\text{CH}_3)_3 \cdot 3\text{H}_2\text{O}$) was also investigated [27]. Here it could be shown, that the decomposition of this carboxylate proceeds via the dehydration at 170 °C in one step, followed by the reduction of the Fe(III)-ions to form anhydrous iron(II) propionate at 230 °C. At 570 °C the resulting $\alpha\text{-Fe}_2\text{O}_3$ occurred. For in-situ-prepared nickel propionate and lanthanum propionate interesting differences in the thermospectroscopically detected decomposition behavior could be determined if one was varying the atmospheres in which the heat treatments were carried out [28]. For the nickel propionate it could be shown that by heating in air up to 150 °C, the dehydration process took place, which was followed by the endothermic transformation of the propionate ligands into acetate groups and the decomposition of these between 250 and 325 °C. The exothermic formation of nickel oxide was completed at 325 °C. In contrast, the decomposition to nickel oxide in nitrogen seems to be a complete endothermic process although the temperatures of the different decomposition were found to be only a few degrees lower than in air. In hydrogen atmosphere, a sharp exothermic signal was found due to the reduction of nickel oxide to elemental nickel around 325 °C. Contrary to these results the lanthanum propionate decomposes in air around 325 °C to give a mixture of the corresponding oxide and oxycarbonate. This mixture is transformed into the pure oxide at 720 °C. In nitrogen, only the oxycarbonate was found as intermediate in the temperature region between 250 and 575 °C. The characteristics in hydrogen atmosphere are in this case quite similar to that in nitrogen.

The combustion of rare earth precursors (Ln-propionates $\text{Ln}(\text{OOCCH}_2\text{CH}_3)_3 \cdot x\text{H}_2\text{O}$ with Ln = Ho, Er, Tm, and Yb) in an argon atmosphere revealed a similar decomposition behavior as discussed above [29]. Dehydration took place around 90 °C and the resulting anhydrous propionates decomposed to give the oxycarbonates ($\text{Ln}_2\text{O}_2\text{CO}_3$) between 300 and 400 °C. In the temperature region of 500–700 °C a mixture of the oxycarbonate and the corresponding sesquioxide (Ln_2O_3) could be detected. The transformation into the sesquioxide was found to be complete around 1,100 °C.

2.2.2.2 Long Chain Metal Carboxylates

The most remarkable difference between long-chain and short chain carboxylates is the onset state of thermal decomposition. While short chain carboxylates tend to decompose from the solid state, the long-chain analogs decompose from the melt [30]. The phase formation behavior and other characteristics of the melts are

discussed elsewhere [30]. The difference due to chain length can be clearly seen in a study involving eight saturated, non-branching sodium carboxylates [31]. The authors found that in air the decomposition temperature decreases from 330 °C for the formiate to 190 °C for the tetradecanoate. A similar behavior was found for heating the same carboxylates in nitrogen. However here the decomposition temperatures were slightly higher, which leads to the suggestion of an additional stabilization effect in inert gas atmosphere.

In case of the long-chain lead carboxylates (dodecanoate, tetradecanoate and octadecanoate) it revealed that the decomposition for the do- and tetradecanoate occurred in one step, whereas a two-step mechanism was found for the octadecanoate in all cases between 230 and 460 °C, resulting in lead oxide [32]. Furthermore, the thermal behavior of chromium, copper, nickel, and zinc dodecanoates was investigated [33]. The chromium dodecanoate decomposes via an oxydodecanoate intermediate, whereas the copper dodecanoate forms a temporary mixture of copper oxide and copper dodecanoate. The nickel containing molecule seemed to decompose to the oxide without any intermediate and in the case of zinc the zinc carbonate is transitionally formed. The temperature range for the occurrence of intermediates was found to be from room temperature up to 460 °C, depending on the corresponding metal dodecanoate.

The researchers also investigated the interaction of the described soaps when mixing them with different solvents such as the corresponding alcohol, ester, and amine. In case of the copper and chromium dodecanoate the DTA curves changed when the soaps were mixed with dodecanol. It was concluded that a form of complexation due to hydrogen bonding or electron lone pairs occurred. No comparable interaction was found for the other soaps. In a following study [34] the metal dodecanoate-solvent interaction was further investigated for the chromium, copper, nickel and zinc dodecanoates in combination with dodecanoic acid and octadecanoic acid. It was found that only the chromium salt formed a complex with the stoichiometry of soap/acid close to 2:1. The other soaps did not form such a complex. When heating the dodecanoic salts with octadecanoic acid a metathesis took place. Hence by heating the dodecanoic ligands were replaced by octadecanoic ligands. This behavior was confirmed for all of these metal salts.

In the next sections a general view over established MOD processes is given, with special emphasize on the precursor solution chemistry, the thermal treatment and the resulting thin films.

2.3 Long Chain Versus Short Chain Carboxylates: Solution Behavior and Established Processes

In general long chain carboxylates are popular for MOD type CSD routes since they are moisture insensitive and can be dissolved in relatively chemically inert solvents like toluene or xylene. In these solvents, often also alkoxides may be co-dissolved

which enables the relatively simple preparation of the hybrid solutions. Even if the long chain carboxylates are dissolved in alcohols like butanol, problems relating to hydrolysis are not expected, since the esterification reactions which release water are rather slow due to the lower acid constant of the long chain carboxylic acids (Table 2.1).

Due to the above mentioned advantage, relatively long chain lead(II) 2-ethylhexanoate was used in one of the first synthesis routes to lead zirconate titanate thin films in 1984 [35]. Using this route stable and moisture insensitive precursor solutions have been obtained and this principle has often been used in particular in the early days of PZT [36–38]. It was somewhat later transferred to other materials like yttrium barium copper oxide (YBCO) [39, 40], barium strontium titanate [41, 42], strontium bismuth tantalate [43] etc.

However sometimes problems may occur due to the relatively high content of carbon. This carbon is typically removed by combustion in air resulting in larger portions of carbon dioxide which in turn often leads to some porosity in the films and possibly also to residual carbon. The latter may be detrimental for the leakage properties of these MOD derived ferroelectric thin films [36, 38] or the current transport in superconducting YBCO films [39, 40]. In order to reduce the problematic parasitic carbon incorporation and crack formation short chain carboxylates like acetates or propionates were introduced. A pioneer work with such educts was carried out in 1984 by Heartling [44]. He used dip-coating to synthesize high quality, crack-free PLZT-films, with an average grain size of $\sim 1 \mu\text{m}$ in diameter. The educts lead, lanthanum, and zirconium as acetate and titanium-acetylacetonate were dissolved in a mixture of water and methanol. The use of water as solvent is often problematic if the used substrates have hydrophobic surfaces and therefore result in poor wetting. To overcome this issue, coating routines with short chain carboxylates were developed which use organic solvents instead of water. Later specific water based precursor systems (Chap. 5) and surface treatments were developed which also led to good coating results.

One good example of the use of short-chained carboxylates is the so called all-propionate-routine (APP), which was first published in 1997 [45, 46]. The authors prepared magnetoresistive alkaline earth metal doped lanthanum manganate thin films with perovskite structure on different substrates. Their precursor solution was made by dissolving the corresponding metal acetates in a mixture of propionic acid and propionic acid anhydride. The propionic acid anhydride was used in this case to remove the water of constitution from the educts. Because the acetate anion is the stronger base than the propionate anion, acetic acid was formed which could be easily distilled off, resulting in the in-situ formation of metal propionates. The authors point out that this routine fulfills the requirements listed in Sect. 2.2. In contrast to other commercially available educts, such as lanthanum acetate, the propionate showed significantly higher solubility. The precursor solution is moisture insensitive, can be easily prepared, and its substrate wetting behavior was found to be excellent. In addition, the stoichiometry of the resulting layer can be varied over a wide range. The decomposition was monitored by infrared spectroscopic analysis. It was found that $\text{La}_2\text{O}_2\text{CO}_3$ and CaCO_3 were the

intermediates formed by the thermal treatment. Dependent on the dopant concentration the crystallization occurred between 650 and 700 °C. The Curie temperature was determined to be -8.1 °C, with a resistivity of $1.6 \Omega \cdot \text{cm}$. This value was higher than for single-crystalline films grown by vapor phase techniques ($\sim 10^{-2} \Omega \cdot \text{cm}$) [47, 48]. The all-propionate route could be used for various other systems, such as LNO [49].

The issues of porosity, residual carbon, and poor leakage current properties are maybe also the reason why only a very few of researchers made use of the the MOD concept to prepare PZT. Most researchers use lead(II) acetate, which was introduced in the first pioneering work of Budd et al. [50] or the oxidized counterpart lead(IV) acetate [51] as the educt for the synthesis of PZT precursor solutions. Although their decomposition temperature is significantly higher than those of the long chain carboxylates (see Sect. 2.2.2.2), they have the benefit of having considerably lower amount of carbon. Another distinct advantage of this synthesis strategy is that Pb-O-M linkages are formed by release of an ester, reducing the amount of carbon in these kind of hybrid solutions (see Chap. 3).

Table 2.2 gives an overview on the most popular carboxylates used for various material systems and corresponding references. Certainly this list is not exhaustive and the reader may find in the literature further examples of less common carboxylates which might be useful for specific precursors.

Shaikh and Vest [70] characterized the PTO and the BTO system made through MOD-routines in a kinetic study. They used titanium(IV)-dimethoxy-dineodecanoate, barium(II)-neodecanoate, lead(II)-neodecanoate and commercially available lead(II)-acetate for the synthesis. For the BTO-system the barium- and titanium precursors were dissolved and mixed in xylene. XRD and DTA results revealed that the BTO-formation process occurs first by the formation of intermediate large BaCO_3 particles, small TiO_2 -particles and a certain amount of BTO up to a temperature of 600 °C. When the temperature was raised to 660 °C, only BTO was visible in the XRD. Comparing the MOD-route with classic powder syntheses of BTO, the reaction was shown to proceed 500 times faster in the MOD-route at constant temperatures. On the other hand, 900 °C were needed for completing the reaction in powder based synthesis at constant sintering time, while in MOD-syntheses, 660 °C were sufficient. It was concluded that this massive advantage was due to the smaller particle size and the greater homogeneity on the molecular level, as discussed in section 2.2 of this chapter. Because TiO_2 can typically occur in two modifications² (anatase and rutile), two different reaction pathways were possible. The reaction of the rutile phase with BaCO_3 is slower than the reaction of BaCO_3 with the anatase phase. In addition the BaCO_3 -rutile reaction proceeds via Ba_2TiO_4 as intermediate. This intermediate could not be found, which means that the BaCO_3 -anatase pathway was the more probable one.

² It has to be noted, that there is also brookite as third modification possible, which however occurs less frequently in CSD processes.

Table 2.2 Compilation of frequently used carboxyl groups and metal carboxylates, respectively as well as resulting thin film material

Carboxylate	Metal-cations	Resulting material	References	
Acetate	Pb ²⁺ , Pb ⁴⁺	PTO	[50, 51]	
		PZT		
	Ca ²⁺ , Sr ²⁺	LCMO, LSCO	[41, 42]	
		Ba ²⁺		BST
		Mn ²⁺		
	Trifluoroacetate	Co ²⁺		
		In ³⁺	ITO	[52]
Bi ³⁺		SrBi ₂ Ta ₂ O ₉	[43]	
Propionate	Y ³⁺ , Cu ²⁺	SrBi ₄ Ti ₄ O ₁₅	[53]	
		YBCO	[39, 40]	
	Ba ²⁺	BTO	[54]	
2-Ethylhexanoate	Pb ²⁺	PZT	[55]	
	Ba ²⁺ , Sr ²⁺	(Ba _x ,Sr _{1-x})(Ti _y ,Zr _{1-y})O ₃	[41, 42, 56]	
	La ³⁺ , Ni ²⁺	LNO	[49]	
	Ca ²⁺	LSCM		
	Co ²⁺	LSCO	[57]	
	Neodecanoate	Pb ²⁺		[35, 36]
La ³⁺			[58]	
Zr ⁴⁺		PLZT		
Ba ²⁺ , Sr ²⁺		BaTiO ₃ , SrTiO ₃	[59, 60]	
		Bi ³⁺	Bi(s)	[61]
Neodecanoate		Bi ³⁺	SrBi ₂ Ta ₂ O ₉	[62–65]
			SrBi ₂ Nb ₂ O ₉	
			SrBi ₄ Ti ₄ O ₁₅	
			ITO	[66]
		In ³⁺ , Sn ²⁺	CeO ₂	[67]
		Ce ³⁺	Y ₂ O ₃	[68]
		Y ³⁺	Fe ₂ O ₃	[69]
Neodecanoate		Fe ³⁺	PTO	[70, 71]
	Pb ²⁺	BTO	[72]	
	Ba ²⁺	YBa ₂ Cu ₃ O _{7-x}	[39, 40]	

In the PTO-system two Pb-educts were compared. Lead neodecanoate showed a slightly higher volatility than lead acetate. The addition of additives with a high boiling point such as ethyl- or methylstearate to the xylene based precursor solution could solve this problem. At firing temperatures below 625 °C, the two common PbO-modifications (litharge and massicot) and PTO were observed, whereas at temperatures over 625 °C only the PTO-phase was left. The decomposition of lead neodecanoate lead to spherical particles with a uniform size (diameter ~0.3 μm) developed. The decomposition of lead(II) acetate led to irregular shaped particles with diameters between 0.3 and 10 μm. In both cases, there is a TiO₂-shell on these particles. The larger diameter in the acetate-based system led to a slower long-term kinetics in the formation of BTO, because these larger particles dominate the process at longer firing times.

2.3.1 Another Well-Known Example: Trifluoroacetates

The first working precursor system for the preparation of superconducting YBCO thin films by MOD was found by Kumagai et al. [73]. They mixed yttrium stearate with barium- and copper naphthenate in an organic solvent. The DTA-TG analysis of the resulting precursor solution showed that pyrolytic decomposition took place between 200 and 500 °C followed by crystallization up to 800 °C. Hence the dip coated YSZ substrates were dried in air and fired at 800 °C. They found the quality of the films is directly related to the firing time. This could be evaluated by measuring the transition temperature, T_C (resistance (R) = 0 Ω), e.g. samples fired for 2 h have T_C that were significantly lower (23 K) than samples fired for 80 h (60 K). Although some improvements of the T_C ($R = 0 \Omega$) values could be achieved by the use of other carboxylates and heat treatment procedures [74, 75], the overall electrical properties remained poor owing to the formation of BaCO_3 , which is very stable, as an intermediate compound during the decomposition of the precursors [76], or the inadequate reactivity of the intermediate barium oxide [77].

Thus driven by the necessity to avoid intermediates such as carbonates, metal trifluoroacetates have been introduced in the CSD technology in particular for the preparation of superconducting thin films (see Chap. 27). Gupta et al. [77] therefore dissolved yttrium oxide, barium carbonate and solid copper in aqueous trifluoroacetic acid (TFA) and hydrogen peroxide. These solutions were dried and re-dissolved in methanol. The products of the pyrolysis of the single educts were found to be barium- and yttrium fluoride as well as a mixture of copper oxide and copper fluoride. The mixed educt solutions were spun on YSZ substrates and the annealing was done for 5–40 min in a humid or non-humid helium atmosphere at 850 or 920 °C. The resulting SEM images of the layers revealed large pellet-like, (111)-oriented grains of the superconducting phase with smaller, spheroidal grains lying on them when the samples were sintered without humidification. These small grains were found to be rich in barium. The authors concluded that these grains are barium fluoride, which was corroborated by XRD-measurements. Samples sintered in humid conditions did not show such barium-rich phases and the strict (111)-texture could not be found. Surprisingly, the specimen with barium fluoride-rich grains showed higher transition temperatures (92–94 K) and smaller transient regions. The group proposed that barium fluoride helps the superconducting phase to grow oriented and that maybe there is an additional fluoride substitution. After this study, further investigations of YBCO-layer syntheses were carried out. McIntyre et al. [78] used the described solution process to prepare epitaxial films on (001)-oriented LAO-substrates. They introduced a special kind of temperature treatment which consisted of three parts: a pyrolysis step up to 400 °C, followed by the crystallization at 700 °C, and the oxidation during the re-cooling. Pyrolysis and crystallization were carried out in a humid atmosphere. After the pyrolysis step, the layer consisted of the oxy-fluorides transformed into the tetragonal YBCO-phase during the crystallization. The oxidation led to the orthorhombic superconducting phase. There was a direct relationship between the partial pressure of the oxygen,

the texture development and the transition temperature during the oxidation step; as long as there were used low partial pressures, the XRD showed sharp (001)-reflexes. The transition temperature increases in these samples as well as the transient regions decreased. The described three-step temperature treatment with humid and non-humid atmospheres was more or less adopted by other authors [79–83] and is also relevant for industrial applications (Chap. 27). Yan et al. [81] found another modification of the trifluoroacetate routine by dissolving yttrium, barium, and copper-hydroxides in a mixture of water and TFA. After gelation, they were coated on different substrates and crystallization took place in humid argon at 752 °C. They found an adequate (001)-texture, but the layers were porous with a grain diameter of 1 µm. The transition of these layers was found to be at 91 K with a very small transient region. Obradors et al. systematically investigated the formation of the YBCO thin films on different substrates from TFA-based solutions with the metal acetates as educts [82]. The pyrolysis (up to 300 °C in humid oxygen) was pointed out to be an important step in morphology development. Slow heating rates were found to prevent morphological inhomogeneities. The humid oxygen helps to avoid the sublimation of the $\text{Cu}(\text{TFA})_2$. The crystallization at 700–800 °C in humid oxygen seemed to be a very complex process which needs further investigations. It was supposed that the crystallisation occurs through the formation of a liquid phase at the layer-substrate interface, where the nucleation process in c-direction took place. Also an exchange with the gas phase is important, because the water molecules of the humid atmosphere have to reach the interface. The water reacts there with the in situ formed hydrogen fluoride and removes it. Otherwise hydrogen fluoride would cause a kind of barrier for the further reaction. When temperatures during this process step are too low or the growth rate is too high caused by too high oxygen partial pressure, the crystal growth becomes faster in the a and b-direction, which would lead to porosity formation in the film. The oxidation was performed in dry oxygen at 450 °C. Finally the group could achieve high-quality films without pores and with strict c-orientation. No other phases could have been detected.

Another route was developed by Roma et al. [83]. Instead of TFA, they used the corresponding trifluoroacetic anhydride. In this so called anhydrous TFA route, the YBCO bulk material was directly dissolved in the anhydride, after drying and redissolving in anhydrous methanol a stable solution with a very small content of water was formed. The low water content had the advantage of shortening the pyrolysis step drastically. The slow pyrolysis in the other routes was due to the inhomogeneous distribution of the educt molecules in the solution, which often results in inhomogeneous layers. Water acts as a ligand especially for yttrium trifluoroacetate. This coordination may lead to the mentioned inhomogeneity. Nevertheless, high quality layers could be also made by this routine.

2.4 Summary

In this chapter, the basics of metal carboxylates which is a frequently used class of chemical educts for solution synthesis was first reported. Metal carboxylates offer several advantages in comparison to metal alkoxides, since they are insensitive against moisture and can be produced in a cheap and simple way, e.g. by metathesis reactions. In the second part, the concept of metallo-organic decomposition was introduced, which typically relies on these metal salts and represents a powerful technique for producing ceramic thin films. Concerning the deposition of a given precursor solution and its effect on the film thickness, proportionality to the solution concentration and to the root of the viscosity was found. Problems of substrate wetting can be overcome through the wide range of potential solvents for this routine. The thermal treatment of the as-deposited films leads to solvent evaporation and decomposition of the organic residues. A radical mechanism was proposed to explain the decomposition behavior. Shrinkage of the films parallel to the substrate surface may result in the formation of microcracks. A few examples for the decomposition of selected long-chain and short-chain metal carboxylates illustrated the possibilities. It was shown that the long-chain carboxylates in general decompose at lower temperatures, but the problem of carbon incorporation is reduced when the length of the carbon chain is decreased. Some impressive examples for established MOD processes are given, which resulted in thin films with comparable electrical performances to films which were produced by physical deposition techniques.

In this sense one remarkable research area is the solution based deposition of superconducting YBCO thin films, where fluorinated carboxylates are used to prevent the intermediate formation of carbonates and unreactive oxides. Decomposition and crystallization proceeds via intermediate fluorides and finally yields excellent film qualities. Thus this system is the precursor of choice for commercially CSD produced superconducting layers.

References

1. Clayden J, Greeves N, Warren S, Wothers P (2006) Organic chemistry, 1st edn. Oxford University Press, Oxford
2. Bala T, Prasad BLV, Sastry M, Kahaly MU, Waghmare UV (2007) Interaction of different metal ions with carboxylic acid group: a quantitative study. *J Phys Chem A* 111:6183–6190
3. Boyle TJ, Raymond R, Boye DM, Ottley LAM, Lu P (2011) Structurally characterized luminescent lanthanide zinc carboxylate precursors for Ln–Zn–O nanomaterials. *Dalton Trans* 39:8050–8063
4. Marques EF, Burrows HD, da Graca MM (1998) The structure and thermal behaviour of some long chain cerium(III)carboxylates. *J Chem Soc Faraday Trans* 94:1729–1736
5. Dippy JFJ (1938) Chemical constitution and the dissociation constants of monocarboxylic acids. Part X. Saturated aliphatic acids. *J Chem Soc* 1938:1222–1227

6. Davis MM, Pabo M (1966) Comparative strengths of aliphatic acids and some other carboxylic acids in benzene at 25°C. *J Org Chem* 31:1804–1810
7. Mehrotra RC, Bohra R (1983) *Metal carboxylates*, 1st edn. Academic, London
8. Pilpel N (1963) Properties of organic solutions of heavy metal soaps. *Chem Rev* 63:221–234
9. Piper JD, Fleiger AG, Smith CC, Kerstein NA (1939) Chemical, physical, electrical properties of systems containing lead or copper soaps in liquid paraffin. *Ind Eng Chem* 31:307–311
10. Nelson SM, Pink RC (1954) Solutions of metal soaps in organic solvents. Part IV. Direct-current conductivity in solutions of some metal oleates in toluene. *J Chem Soc* 1954:4412–4417
11. Lawrence ASC (1938) The metal soaps and the gelation of their paraffin solutions. *Trans Faraday Soc* 34:660–677
12. Parke JB (1934) The phase volume theory and the homogenisation of concentrated emulsions. Part II. *J Chem Soc* 1934:1112–1115
13. Pink RC (1938) 237. Studies in water-in-oil emulsions. Part I. Preparation of anhydrous magnesium oleate. *J Chem Soc* 1938:1252–1254
14. Vest RW (1990) Metallo-organic decomposition (MOD) processing of ferroelectric and electro-optic films: a review. *Ferroelectrics* 102:53–68
15. Vest RW, Vest GM (1989) Metallo-organic decomposition process for dielectric films. DTIC Annual Report for the period 4/1/88 – 3/31/89 on contract No. N00014-83-K-0321, pp 1–59
16. Yanagisawa M (1987) Slip effect for thin liquid film on a rotating disk. *J Appl Phys* 61:1034–1037
17. Gaucher P, Faure SP, Barboux P (1992) Ferroelectric thin film research in France. *Integr Ferroelectrics* 1:353–362
18. Baraldi P (1981) Thermal behavior of metal carboxylates: III-metal acetates. *Spectrochim Acta, Part A* 38:51–55
19. Hussein GAM (1996) Rare earth metal oxides: formation, characterization and catalytic activity. Thermoanalytical and applied pyrolysis review. *J Anal Appl Pyrolysis* 37:111–149
20. Hussein GAM, Kroenke WJ, Goda B, Miyaji K (1997) Formation of dysprosium oxide from the thermal decomposition of hydrated dysprosium acetate and oxalate. Thermoanalytical and microscopic studies. *J Anal Appl Pyrolysis* 39:35–51
21. Adachi G, Secco EA (1972) Thermal transformation in anhydrous rare earth acetates. *Can J Chem* 50:3100–3103
22. Hussein GAM (1994) Formation of praseodymium oxide from the thermal decomposition of hydrated praseodymium acetate and oxalate. *J Anal Appl Pyrolysis* 29:89–102
23. Patil KC, Chandrasekar GV, George MV, Rao CNR (1968) Infrared spectra and thermal decompositions of metal acetates and dicarboxylates. *Can J Chem* 46:257–265
24. Hussein GAM (1994) Spectrothermal investigation of the decomposition course of lanthanum acetate hydrate. *J Therm Anal* 42:1091–1102
25. Gobert-Ranchoux E, Charbonnier F (1977) Comportement thermique des propionates hydratés de calcium, strontium et baryum. *J Thermal Anal* 12:33–42
26. Bassi PS, Jamwal HS, Randhawa BS (1983) Comparative study of the thermal analyses of some transition metal (II) propionates. Part I. *Thermochim Acta* 71:15–24
27. Bassi PS, Randhawa BS, Jamwal HS (1983) Mössbauer study of the thermal decomposition of some iron (III) monocarboxylates. *Thermochim Acta* 62:209–216
28. Kaddouri A, Mazzocchia C (2002) Thermoanalytical study of some metal propionates synthesised by sol–gel route: a kinetic and thermodynamic study. *J Anal Appl Pyrolysis* 65:253–267
29. Grivel JC (2012) Thermal decomposition of $\text{Ln}(\text{C}_2\text{H}_5\text{CO}_2)_3 \cdot \text{H}_2\text{O}$ (Ln = Ho, Er, Tm, and Yb). *J Therm Anal Calorim* 109:81–88
30. Akanni MS, Okoh EK, Burrows HD, Ellis HA (1992) The thermal behavior of divalent and higher valent metal soaps: a review. *Thermochim Acta* 208:1–41
31. Roth J, Meisel T, Seybold K, Halmos Z (1976) Investigation of the thermal behavior of fatty acid sodium salts. *J Thermal Anal* 10:223–232

32. Ellis EA (1981) Kinetics and reaction mechanism for the thermal decomposition of some even chain lead(II) carboxylates. *Thermochim Acta* 47:261–270
33. Seddon AB, Wood JA (1986) Thermal studies of heavy-metal carboxylates. II. Thermal behavior of dodecanoates. *Thermochim Acta* 106:341–354
34. Seddon AB, Wood JA (1987) Thermal studies of heavy-metal carboxylates. III. Metal dodecanoate-carboxylic acid mixtures. *Thermochim Acta* 118:253–260
35. Fukushima J, Kodaira K, Matsushita T (1984) Preparation of ferroelectric PZT films by thermal decomposition of organometallic compounds. *J Mater Sci* 19:595–598
36. Klee M, Eusemann R, Waser R, Brand W, van Hal H (1992) Processing and electrical properties of $\text{Pb}(\text{Zr}_x\text{Ti}_{1-x})\text{O}_3$ ($x=0.2-0.75$) films: comparison of metallo-organic decomposition and sol-gel processes. *J Appl Phys* 72:1566–1576
37. Chen SY, Chen IW (1994) Temperature-time texture transition of $\text{Pb}(\text{Zr}_{1-x}\text{Ti}_x)\text{O}_3$ thin films: I. Role of Pb-rich intermediate phases. *J Am Ceram Soc* 77:2332–2336
38. Chen SY, Chen IW (1997) Comparative role of metal-organic decomposition-derived [100] and [111] in electrical properties of $\text{Pb}(\text{Zr}, \text{Ti})\text{O}_3$ thin films. *Jpn J Appl Phys* 36:4451–4458
39. Mantese JV, Hamdi AH, Micheli AL, Chen YL, Wong CA, Johnson JL, Karmarkar MM, Padmanabhan KR (1988) Rapid thermal annealing of high T_C superconducting thin films formed by metalorganic deposition. *Appl Phys Lett* 52:1631–1633
40. Hamdi AH, Mantese JV, Micheli AL, Laugal RCO, Dungan DF, Zhang ZH, Padmanabhan KR (1987) Formation of thin-film high T_C superconductors by metalorganic deposition. *Appl Phys Lett* 51:2152–2154
41. Hasenkox U, Hoffmann S, Waser R (1998) Influence of precursor chemistry on the formation of MTiO_3 ($M = \text{Ba}, \text{Sr}$) ceramic thin films. *J Sol-Gel Sci Technol* 12:67–79
42. Hoffmann S, Waser R (1999) Control of the morphology of CSD-prepared $(\text{Ba}, \text{Sr})\text{TiO}_3$ thin films. *J Eur Ceram Soc* 19:1339–1343
43. Boyle TL, Buchheit CD, Rodriguez MA, Al-Shareef HN, Hernandez BH, Scott B, Ziller JW (1996) Formation of $\text{SrBi}_2\text{Ta}_2\text{O}_9$: Part I. Synthesis and characterization of a novel “sol-gel” solution for production of ferroelectric $\text{SrBi}_2\text{Ta}_2\text{O}_9$ thin films. *J Mater Res* 11:2274–2281
44. Heartling GE (1991) PLZT thin films prepared from acetate precursors. *Ferroelectrics* 116:51–63
45. Hasenkox U, Mitze C, Waser R (1997) A novel propionate-based chemical solution deposition method of $\text{La}_{1-x}(\text{Ca}, \text{Sr})_x\text{MnO}_3$ thin films for microelectronics applications. *Integr Ferroelectr* 18:339–350
46. Hasenkox U, Mitze C, Waser R (1997) Metal propionate synthesis of magnetoresistive $\text{La}_{1-x}(\text{Ca}, \text{Sr})_x\text{MnO}_3$ thin films. *J Am Ceram Soc* 80:2709–2713
47. Gupta A, McGuire TR, Duncombe PR, Rupp M, Sun JZ, Gallagher WJ, Xiao G (1995) Growth and giant magnetoresistance properties of La-deficient $\text{La}_x\text{MnO}_{3-8}$ ($0.67 \leq x \leq 1$) films. *Appl Phys Lett* 67:3494–3496
48. Snyder GJ, Hiskes R, DiCarolis S, Beasley MR, Geballe TH (1996) Intrinsic electrical transport and magnetic properties of $\text{La}_{0.67}\text{Ca}_{0.33}\text{MnO}_3$ and $\text{La}_{0.67}\text{Sr}_{0.33}\text{MnO}_3$ MOCVD thin films and bulk material. *Phys Rev B* 53:14434–14444
49. Reichmann K, Schneller T, Hoffmann-Eifert S, Hasenkox U, Waser R (2001) Morphology and electrical properties of SrTiO_3 -films on conductive oxide films. *J Eur Ceram Soc* 21:1597–1600
50. Budd KD, Dey SK, Payne DA (1985) Sol-gel processing of PbTiO_3 , PbZrO_3 , PZT, and PLZT thin films. *Br Ceram Proc* 36:107–122
51. Schwartz RW, Bunker BC, Dimos DB, Assink RA, Tuttle BA, Tallant DR, Weinstock IA (1992) Solution chemistry effects in $\text{Pb}(\text{Zr}, \text{Ti})\text{O}_3$ thin film processing. *Integr Ferroelectrics* 2:243–254
52. Dippel AC, Schneller T, Gerber P, Waser R (2007) Morphology control of highly-transparent indium tin oxide thin films prepared by a chlorine-reduced metallo-organic decomposition technique. *Thin Solid Films* 515:3797–3801

53. Kambara H, Schneller T, Sakabe Y, Waser R (2009) Dielectric properties of highly c-axis oriented chemical solution deposition derived $\text{SrBi}_4\text{Ti}_4\text{O}_{15}$ thin films. *Phys Stat Sol (a)* 206:157–166
54. Fujihara S, Schneller T, Waser R (2004) Interfacial reactions and microstructure of BaTiO_3 films prepared using fluoride precursor method. *Appl Surf Sci* 221:178–183
55. Schneller T, Waser R (2007) Chemical modifications of $\text{Pb}(\text{Zr}_{0.3}\text{Ti}_{0.7})\text{O}_3$ precursor solutions and their influence on the morphological and electrical properties of the resulting thin films. *J Sol-Gel Sci Technol* 42:337–352
56. Halder S, Schneller T, Böttger U, Waser R (2005) Fabrication and electrical characterisation of Zr-substituted BaTiO_3 thin films. *Appl Phys A* 81:25–29
57. Hasenkox U, Waser R (1999) Microstructure and properties of highly oriented PZT thin films on epitaxial ceramic electrodes prepared by CSD. *Ferroelectrics* 225:107–115
58. Vest RW, Lu J (1989) Preparation and properties of PLZT films from metallo-organic precursors. *Ferroelectrics* 93:21–29
59. Braunstein G, Paz-Pujalt GR, Mason MG, Blanton T, Barnes CL, Margevich D (1993) The processes of formation and epitaxial alignment of SrTiO_3 thin films prepared by metallo-organic decomposition. *J Appl Phys* 73:961–970
60. Ousi-Benomar W, Xue SS, Lessard RA, Singh A, Wu ZL, Kuo PK (1994) Structural and optical characterization of BaTiO_3 thin films prepared by metal-organic deposition from barium 2-ethylhexanoate and titanium dimethoxy dineodecanoate. *J Mater Res* 9:970–979
61. Shen WN, Dunn B, Moore CD, Goorsky MS, Radetic T, Gronsky R (2000) Synthesis of nanoporous bismuth films by liquid-phase deposition. *J Mater Chem* 10:657–662
62. Chung CW, Chung I (1999) Effect of pre-annealing on physical and electrical properties of $\text{SrBi}_2\text{Ta}_2\text{O}_9$ thin films prepared by chemical solution deposition. *Thin Solid Films* 354:111–117
63. Desu SB, Joshi PC, Zhang X, Ryu SO (1997) Thin films of layered-structure $(1-x)\text{SrBi}_2\text{Ta}_2\text{O}_9-x\text{Bi}_3\text{Ti}(\text{Ta}_{1-y}\text{Nb}_y)\text{O}_9$ solid solution for ferroelectric random access memory devices. *Appl Phys Lett* 71:1041–1043
64. Amanuma K, Hase T, Miyasaka Y (1995) Preparation and ferroelectric properties of $\text{SrBi}_2\text{Ta}_2\text{O}_9$ thin films. *Appl Phys Lett* 66:221–223
65. Watanabe H, Mihara T, Yoshimori H, Paz de Araujo CA (1995) Preparation of ferroelectric thin films of bismuth layer structured compounds. *Jpn J Appl Phys* 34:5240–5244
66. Xu JJ, Shaikh AS, Vest RW (1988) Indium tin oxide films from metallo-organic precursors. *Thin Solid Films* 161:273–280
67. Morlens S, Ortega L, Rousseau B, Phok S, Deschanvre JL, Chaudouet P, Odier P (2003) Use of cerium ethylhexanoate solutions for preparation of CeO_2 buffer layers by spin coating. *Mater Sci Eng B* 104:185–191
68. Apblett AW, Long JC, Walker EH, Johnston MD, Schmidt KJ, Yarwood LN (1994) Metal organic precursors for Yttria, Phosphorus, Sulfur Silicon Relat Elem 93–94:481–482
69. Xue S, Ousi-Benomar W, Lessard RA (1994) $\alpha\text{-Fe}_2\text{O}_3$ thin films prepared by metalorganic deposition (MOD) from Fe(III) 2-ethylhexanoate. *Thin Solid Films* 250:194–201
70. Shaikh AS, Vest GM (1986) Kinetics of BaTiO_3 and PbTiO_3 formation from metallo-organic precursors. *J Am Ceram Soc* 69:682–688
71. Vest RW, Xu J (1988) PbTiO_3 films from metalloorganic precursors. *IEEE Trans Ultrason Ferroelec Freq Contr* 35:711–717
72. Xu J, Shaikh AS, Vest RW (1989) High k BaTiO_3 films from metalloorganic precursors. *IEEE Trans Ultrason Ferroelec Freq Contr* 36:307–312
73. Kumagai T, Yokota H, Kawaguchi K (1987) Preparation of superconducting $\text{YBa}_2\text{Cu}_3\text{O}_{7-\delta}$ thin films by the dipping-pyrolysis process using organic acid salts. *Chem Lett* 16:1645–1646
74. Klee M, Brand W, DeVries JWC (1988) Superconducting films in the Y-Ba-Cu-O system made by thermal decomposition of metal carboxylates. *J Cryst Growth* 91:346–351

75. Chen YL, Mantese JV, Hamdi AH, Micheli AL (1989) Microstructure and superconducting properties of Y-Ba-Cu-O and Yb-BaCu-O thin films formed by metalorganic deposition. *J Mater Res* 4:1065–1071
76. Parmigiani E, Chiarello G, Ripamonti N, Goretzki H, Roli U (1987) Observation of carboxylic groups in the lattice of sintered $\text{Ba}_2\text{YCu}_3\text{O}_{7-y}$ high- T_c superconductors. *Phys Rev B* 36:7148–7150
77. Gupta A, Jagannathan R, Cooper EI, Giess EA, Landman JI, Hussey BW (1988) Superconducting oxide films with high transition temperature prepared from metal trifluoroacetate precursors. *Appl Phys Lett* 52:2077–2079
78. McIntyre PC, Cima MJ, Smith JA, Hallock RB, Siegal MP, Phillips JM (1992) Effect of growth conditions on the preparation and morphology of chemically derived epitaxial thin films of $\text{YBa}_2\text{Cu}_3\text{O}_{7-x}$ on (001) LAO. *J Appl Phys* 71:1868–1877
79. Sathyamurthy S, Salama K (1999) Processing of Y123 coated conductors using metal organic decomposition. *IEEE Trans Appl Supercond* 9:1971–1974
80. Sathyamurthy S, Salama K (2000) Application of metal-organic decomposition techniques for the deposition of buffer layers and Y123 for coated-conductor fabrication. *Physica C* 329:58–68
81. Yan G, Liu CF, Feng Y, Zhang PX, Wu XZ, Zhou L (2003) New metal organic deposition method using trifluoroacetate for fabrication on YBCO thick film on metal tape. *Physica C* 913:3292–3296
82. Obrardors X, Puig T, Pomar A, Sandiumenge F, Piñol S, Mestres N, Castano O, Coll M, Cavallaro A, Palau A, Gazquez J, Gonzales JC, Gutierrez J, Roma N, Ricart S, Moreto JM, Rossel MD, van Tendeloo G (2004) Chemical solution deposition: a path towards low cost coated conductors. *Supercond Sci Technol* 17:1055–1064
83. Roma N, Morlens S, Ricart S, Zalamova K, Moreto JM, Pomar A, Puig T, Obrardors X (2006) Acid anhydrides: a simple route to highly pure organometallic solutions for superconducting films. *Supercond Sci Technol* 19:521–527

Chapter 3

Mixed Metallo-organic Precursor Systems

Barbara Malič, Sebastjan Glinšek, Theodor Schneller, and Marija Kosec[†]

3.1 Introduction

Chemical solution deposition (CSD) of complex-oxide thin films should ensure that homogeneity on the (sub)nanometer level is achieved already in the solution-synthesis step and then retained throughout the next processing steps, thus allowing to obtain good functional properties at a low thermal budget. In the present chapter strategies are presented where chemically different reagents such as metal alkoxides and metal carboxylates (also called “hybrid routes”) or metal alkoxides are dissolved and mixed and/or reacted in the solution-synthesis step to form a heterometallic complex or a compound in a suitable solvent system. After deposition on the substrate and in the subsequent heating steps, which may include further reactions, drying, pyrolysis (thermolysis) and crystallization, a crystalline film with the stoichiometry of the target material is obtained.

A huge amount of research has been dedicated to lead-based complex perovskites, with $\text{Pb}(\text{Zr},\text{Ti})\text{O}_3$ (PZT) as the leading representative, and to alkaline

[†] Author was deceased

B. Malič (✉)

Jožef Stefan Institute, Jamova 39, 1000 Ljubljana, Slovenia

Centre of Excellence on Nanoscience and Nanotechnology, Ljubljana, Slovenia

Centre of Excellence SPACE-SI, Ljubljana, Slovenia

e-mail: barbara.malic@ijs.si

S. Glinšek

Centre of Excellence SPACE-SI, Ljubljana, Slovenia

School of Engineering, Brown University, Providence, RI 02912, USA

T. Schneller

Institut für Werkstoffe der Elektrotechnik II, RWTH Aachen University, Aachen, Germany

earth titanates, such as (Ba,Sr)TiO₃ (BST). In recent years the environment awareness has initiated the research of lead-free materials, in bulk ceramic and also in thin film form. Complex alkali perovskites, niobates and tantalates, represent a group of materials which could replace the lead-based counterparts in some applications.

The aim of this chapter is to introduce and discuss mixed-metal precursor solutions containing metal alkoxides and/or other soluble compounds in organic solvents of these three exemplary systems. Simple alkoxides (Chap. 1) have been used as the reagents for B-site ions in the perovskite lattice, including transition metals (TM) Ti, Zr, Nb, and Ta. Due to the low electronegativity and unsaturated coordination number, the transition metal alkoxides are highly reactive and therefore require dry atmosphere for storing and manipulation. Large A-site cations, such as Pb, Bi, and Ba have been used as short-chain carboxylates, acetates or propionates (for details see Chap. 2). Alkalis have been introduced as alkoxides or acetates.

The widely used solution route for Pb(Zr,Ti)O₃ (PZT) or other Pb-containing complex perovskite thin films follows the procedures introduced by Gurkovich and Blum in 1984 for powders [1] and by Budd, Dey and Payne in 1985 for thin films [2] and it is usually referred to as the 2-methoxyethanol based route, as this ether alcohol was used as the solvent. Philips's group [3] introduced a polyfunctional alcohol 1,3-propanediol as the solvent, and this approach has been denoted as the diol route. In the inverse-mixing-order (IMO) route for PZT first the B-site cations were mixed and then the A-cation reagent in a methanol/acetic acid solvent system was added [4, 5]. A comprehensive review of processing technologies for high-permittivity thin films was written by G. Brennecke et al. [6].

The synthetic approaches for alkali perovskites have mainly included either all alkoxide-based precursors or acetate-alkoxide based ones.

In contrast, the barium and/or strontium titanate films have been mainly prepared from hybrid routes, i.e., mixtures of carboxylate precursors for the A-site component and stabilized titanium alkoxides, which have been thoroughly investigated by Waser's group [7–10].

3.2 PZT and Other Pb-Based Perovskites

Figure 3.1 shows the flow chart for the processing of La-modified PZT (PLZT, (Pb_{1-x}La_x)(Zr_{0.65}Ti_{0.35})_{1-x/4}O₃, x = 0.09), as described by Budd et al. [2]. The reagents are lead and lanthanum acetates hydrates and zirconium and titanium alkoxides, propoxides or butoxides. The first step was the dissolution of the acetate hydrate in 2-methoxyethanol (2-MOE) and removal of water by distillation. Then the transition metal alkoxides were added and the reaction mixture was distilled to remove volatile reaction by-products. Experimental details and reagents differed from one work to another, such as lead acetate was used either as hydrate or dehydrated in vacuum prior use, different alkoxides were compared, which strongly

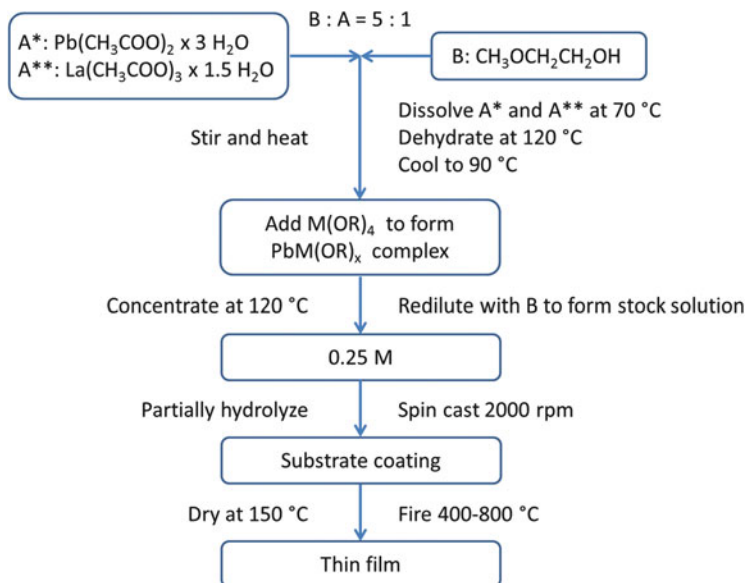
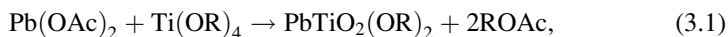


Fig. 3.1 Flow chart of the processing of PLZT gels and films (modified after [2]). M—Zr, Ti; R—alkyl group

influenced the course of reactions in solution, and consequently the structure of reaction products.

Early studies of the mechanism of the synthesis of PbTiO_3 gels and films from Pb-acetate hydrate, Ti-isopropoxide and 2-methoxyethanol included gas chromatography of distillates and distillation residues and Raman spectroscopy [11, 12]. The presence of iso-propylacetate could be explained by the reaction of ester-elimination between the Pb-acetate and Ti-isopropoxide:



where R is the isopropoxide group. The presence of isopropanol in the distillate indicated a reaction between the solvent 2-methoxyethanol and the Ti-alkoxide (Eq. 3.2). The transalcoholysis reaction, i.e., the exchange of alkoxide groups, resulted in a less reactive mixed alkoxide [13, 14].



Using a number of spectroscopic and chromatographic methods Dekleva et al. [15] confirmed the reaction between Pb-acetate and Ti-alkoxide and proposed the structure of the reaction product as $(\text{RO})_3\text{-Ti-O-Pb-OAc}$. A large fraction of propanol confirmed a strong transalcoholysis reaction of Ti-iso or n-propoxide with the solvent 2-methoxyethanol. Beltram et al. [16] studied the reactions upon the

synthesis of the $(\text{Pb},\text{La})(\text{Zr},\text{Ti})\text{O}_3$ sols for thin film deposition by nuclear magnetic resonance (NMR) and gas-liquid chromatography. They found that the Pb- and La-acetates partly reacted with the solvent 2-methoxyethanol and confirmed the reaction of the alkoxides with the acetates, similarly as in the case of PbTiO_3 .

Problems related to chemical heterogeneities in PZT thin films, evidenced by the presence of pyrochlore-like or zirconium-rich phases, have been reported [17–19]. Modification of TM alkoxides by substitution or addition of ligands less reactive towards hydrolysis, such as acetylacetone or acetic acid, has been used to decrease their reactivity [11, 20–22].

Extended X-ray absorption fine structure spectroscopy (EXAFS—see Chap. 8) has been proven successful in tracing chemical heterogeneity at sub-nanometre range both in coating solutions, in as-dried amorphous precursors and in amorphous thin films [23–25]. Malič et al. [26] found that selective modification of Zr-propoxide by acetic acid resulted in a more homogeneous distribution of constituent metal atoms in the PZT sol, prepared by the 2-methoxyethanol-based route as compared to the sol, synthesized from the as-received or acetylacetone-modified Zr-propoxide. A further EXAFS study of the as-pyrolyzed films, deposited on sapphire substrates revealed that in the case when the as-received Zr-alkoxide was used, segregation of Zr-species was confirmed both in the PZT sol as well as in the as-pyrolyzed film. In the case of acetic-acid-modified Zr-alkoxide, the dimeric structure of Zr-species present in the PZT sol was retained also in the film, contributing to a more homogeneous distribution of constituent metal atoms [27]. In Fig. 3.2, zirconium EXAFS spectra of the unmodified PZT and acetic-acid modified PZT sols, and as-pyrolyzed films on (0001) sapphire are collected, revealing a less-populated neighborhood of Zr-atoms in the latter case.

The 2-MOE solvent has been successfully replaced by other ether alcohols, especially 2-butoxyethanol as a less-toxic alternative [28–30]. Additionally other solvents, such as 1,3-propanediol, have been introduced [3].

In the so-called inverse-mixing-order (IMO) route, the Ti and Zr alkoxides are first reacted with acetic acid resulting in a more homogeneous distribution of B-site cations as obtained by the conventional 2-MOE route [4, 5].

In publications on solution-derived $(1-x)\text{Pb}(\text{Mg}_{1/3}\text{Nb}_{2/3})\text{O}_3-x\text{PbTiO}_3$ (PMN–PT) thin films the main difficulty has been related to the formation of non-ferroelectric pyrochlore phases and chemical inhomogeneity [31–33]. In bulk ceramic form the success in PMN preparation was achieved by developing the columbite method where the columbite MgNb_2O_6 and PbO react to form the perovskite phase [34]. The approach was implemented also in the synthesis of PMN and PMN-PT thin films. FT-IR spectroscopy revealed a large number of Mg–O–Nb bonds in the Mg–Nb precursor solution after a long reflux time [35].

A common problem related to the processing of lead-based perovskites is the expected PbO loss during heating. The vapor pressure of PbO above the PZT depends on the Zr/Ti ratio and is higher for the Zr-rich than for the Ti-rich solid solutions [36]. An excess of lead reagent in the amount of 10–20 mole % has been usually added already in the solution [37] or alternatively, introduced as an additional layer during the film processing [38, 39].

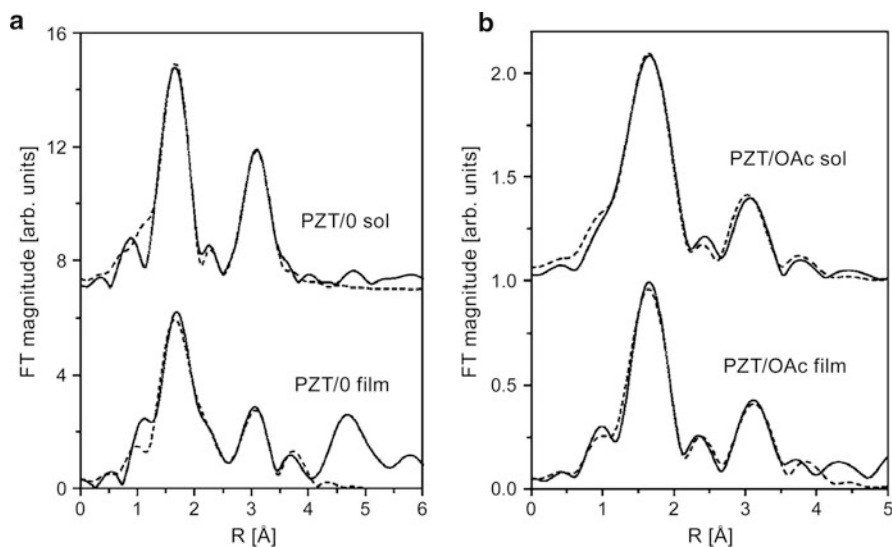


Fig. 3.2 The k^3 -weighted Fourier transforms of Zr EXAFS spectra of (a) the unmodified (PZT/0) and (b) acetic-acid modified (PZT/OAc) sols and as-pyrolyzed films on (0001) sapphire substrates. The films, pyrolyzed at 350 °C were XRD-amorphous (from [27]). k —wave vector. Reprinted with permission of AIP@2006

3.3 Alkali-Metals-Based Perovskites

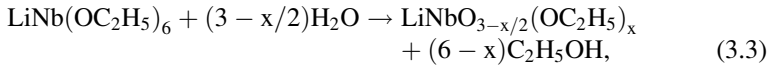
In recent years environmental issues evoked a large research interest in the field of lead-free piezoelectric and ferroelectric materials. Because of the cost efficiency and good composition control solution-derived thin films remain in focus. This sub-chapter is divided according to the A-site ions; first Li-based perovskites are reviewed, continuing with the K-based compounds. Special parts are devoted to $\text{Na}_{0.5}\text{K}_{0.5}\text{NbO}_3$ (KNN) and $\text{Na}_{0.5}\text{Bi}_{0.5}\text{TiO}_3$ (NBT), promising lead-free compounds.

3.3.1 LiNbO_3 and LiTaO_3

The research of these compounds was initiated by Hirano et al. [40], who refluxed Li- and Nb-ethoxides in ethanol up to 22 h. Using IR and ^1H NMR spectroscopies, the authors determined formation of heterometallic $\text{LiNb}(\text{OCH}_2\text{CH}_3)_6$, whose solid-state structure consists of alternating $\text{Nb}(\text{OC}_2\text{H}_5)_6$ octahedra linked by distorted tetrahedrally coordinated Li ions [41]. Its formation is strongly beneficial for the crystallization; films, prepared from the long-refluxed and partially hydrolyzed sols, start to crystallize as low as 250 °C [42].

Texture, grain size, porosity and roughness of the LiNbO_3 films strongly depend on R_w , defined as the ratio between moles of added water to the moles of metal

alkoxide in the sol. The effect was explained by the interplay between the hydrolysis,



and condensation reactions, the first leading to formation of different amorphous species (depending on x in Eq. 3.3), and the second to condensation of the molecules into an interconnected network. When larger amounts of water are used, high concentration of amorphous LiNbO_3 is formed. Ease of crystallization in this case promotes homogenous nucleation within the films and allows substantial grain growth. On the other hand, when lower amounts of water are used, the crystallization is shifted to higher temperature, favoring heterogeneous nucleation and grain growth in smaller extent [43].

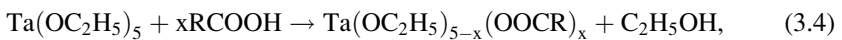
The Hirano's ethoxides-based synthesis of LiNbO_3 sols has been modified in terms of different starting compounds, i.e., Li-acetate [44, 45], Li-2,4-pentanedionate [46], or isopropoxides of both metals [47]. Different solvents were also used, such as methanol [47] and 2-methoxyethanol [44, 48], the latter being especially effective in enhancing the stability of the sols.

Hirano's group also developed an interesting water-based synthesis shown in Fig. 3.3 [49, 50]. The authors first prepared $\text{LiNb}(\text{OCH}_2\text{CH}_3)_6$ complex, performed complete hydrolysis, evaporated the residual solvent and dissolved the obtained gels in the excess of water. They proposed that the sols with $\text{pH} = 11$ consist of polynuclear oxo anions associated with the Li^+ ions, for instance $(\text{Li}_5\text{Nb}_6\text{O}_{19})^{3-}$. Acetic acid was used for the neutralization [50].

The water-based method was further modified by Takahashi et al. [51, 52], who added up to 0.6 mol/l (monomer unit concentration) of polyvinyl alcohol (PVA) in order to stabilize the sols and to increase the thickness of the individual dip-coated layers. Improvement of the surface roughness of the films on (0001) LiNbO_3 substrates was observed as well [51, 52].

Regarding LiTaO_3 , similar ethoxides-based synthesis with the optional refluxing step has been undertaken. Because of a difficult control of the hydrolysis rate for the Ta-ethoxide partial hydrolysis has been often avoided [53–55]. Several authors modified the synthesis by using Li-methoxide [55] or Li-acetate [56] as the starting compounds, as well as 2-methoxyethanol as the solvent [56, 57].

To control the hydrolysis rate Ta-ethoxide can be modified using a carboxylic acid, which also acts as a catalyst:



where R is H (hydrogen) or CH_3 , for formic or acetic acid, respectively. As an example, Ono and Hirano [54] used formic acid and successfully eliminated cracks and high porosity in LiTaO_3 films, which were present when non-modified Ta-source was used.

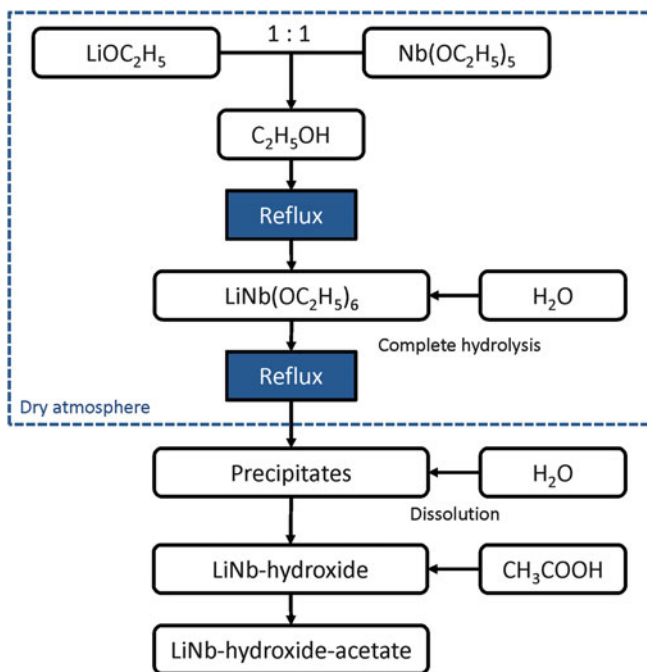


Fig. 3.3 Flow chart of the water-based LiNbO_3 sol preparation route (modified after [50])

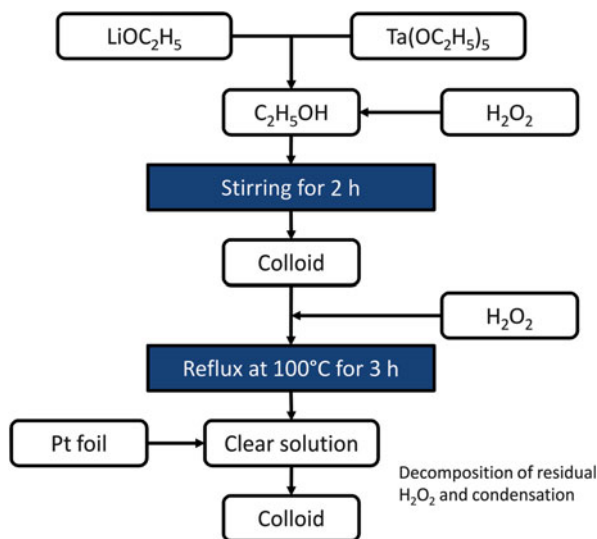
Kao and co-workers [58] used less sensitive starting compounds, i.e., Li-2,4-pentanedionate and Ta-isopropoxide. They first refluxed the Li-source in 1,3-propanediol solvent. Further refluxing was performed after the addition of B-site metal starting compound.

An alternative peroxide-based synthesis route is presented in Fig. 3.4. The starting Li- and Ta-ethoxides were mixed in ethanol, followed by the addition of 30 % aqueous hydrogen peroxide. The precipitated condensation product formed upon heating to the reflux temperature. During reflux the peroxo bridges (M-O-O-M, where M can be either Li or Ta) were formed and the precipitated product re-dissolved. However, the concentration limit was exceeded during the decomposition of the peroxide with Pt foil at 100 °C. Using these colloidal solutions, the LiTaO_3 films were successfully prepared on platinized silicon substrates [59].

3.3.2 $K(\text{Ta},\text{Nb})\text{O}_3$

The sol-gel synthesis of the $\text{K}(\text{Ta},\text{Nb})\text{O}_3$ (KTN) was studied in detail by the groups of Hirano [60–62] and Kahn [63, 64]. The TM-ethoxides and K-ethoxide or acetate were used as the starting compounds, while ethanol was used as the solvent. The alkali metal starting compound has an influence on the crystallization of the KTN

Fig. 3.4 Schematic presentation of the peroxide-based route for the preparation of LiTaO_3 sols (modified after [59])



powders. In the acetate case, the pyrolysis and crystallization processes are well separated, while the traces of the crystalline phases were observed in the air-gelled samples already at room-temperature, when the K-ethoxide was used [63].

Both groups were preparing the sols by refluxing the starting compounds in the solvent for at least 24 h. Recently, EXAFS was employed to follow the structural evolution of the K-acetate and TM-alkoxide-based $\text{KTa}_{0.6}\text{Nb}_{0.4}\text{O}_3$ sols in 2-methoxyethanol upon refluxing. While the monomeric Ta-species were found to be rather inert, the dimeric Nb-alkoxide started to form oligomers upon prolonged refluxing. The K-O-transition-metal correlations were detected in all the sols and the number of K neighbors around Nb increased upon refluxing, saturating at 24 h [65].

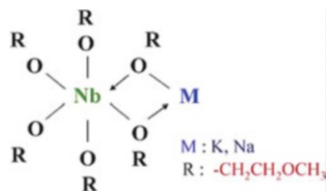
The formation of bimetallic species between K and both transition metals strongly affects the crystallization behavior of the films on polycrystalline alumina substrates. Single-phase perovskite films were obtained only from the 24-h-refluxed solutions, while the films prepared from the 1-h-refluxed solutions had a multi-phase composition and heterogeneous microstructures. The dielectric properties were strongly enhanced as well [66, 67].

Alternatively, Buršík et al. [68, 69] used metal isobutoxides, isobutanol solvent and diethanolamine as a modifier.

3.3.3 $\text{K}_{0.5}\text{Na}_{0.5}\text{NbO}_3$

Synthesis routes of the KNN-based sols can be divided according to the alkali metal starting compounds on acetates- [70–74] and alkoxides- (mainly ethoxides) [75–80]

Fig. 3.5 Molecular structure of the alkoxides-based KNN precursor after 18-h reflux (from [80]). Reprinted with permission of Elsevier©2011



based. Nb-ethoxide is usually employed as the transition metal source and 2-methoxyethanol is used as a solvent. Starting compounds are dissolved either simultaneously or alkali metal compounds are mixed and/or refluxed together prior to the addition of the Nb-ethoxide in order to enhance the A-site homogeneity.

According to the ¹H-, ¹³C- and ⁹³Nb-NMR analyses by Nakashima et al. [80], the ethoxides-based KNN sols refluxed for 18 h consist of KNb(OCH₂CH₂OCH₃)₆ and NaNb(OCH₂CH₂OCH₃)₆ species mixed at the molecular level. The proposed precursor structure is presented in Fig. 3.5. Both, acetates- and alkoxides-based route lead to perovskite films, still, the work of Čakare-Samardžija et al. [81] revealed that the crystallization of the single-phase films on platinumized silicon substrates at 670 °C is more favored in the case of the acetates sols.

Chowdhury et al. [82, 83] prepared the alkoxides-based KNN sols by simultaneously mixing the starting compounds. The gels were formed by stirring the sols at ambient environment at 60 °C and were analyzed using thermal analysis, IR spectroscopy and X-ray diffraction (XRD). The authors observed compositional segregation in terms of the crystallization of K- and Na-rich compositions. The heterogeneity was diminished by prolonged refluxing up to 70 h. However, in the high-temperature heated powders (above 900 °C) the authors always determined secondary alkali metal carbonate phases, residues of the intermediate products of the alkoxides thermal decomposition.

Stabilizers, such as acetylacetonone [70, 84] and acetic acid [77], are sometimes added to the sols, however, care should be taken since acetylacetonone may have a negative influence on the thermal decomposition of the Nb-complex [85]. Recently, Goh and co-workers [73] prepared acetates-based sols modified by the ethylenediaminetetraacetic acid (EDTA) and diethanolamine (DEA) in the ratio DTA:DEA:KNN = 0.25:2.1:1. The resulting films showed improved leakage current characteristics. The authors proposed that hydrogen and coordinate bonds were formed between both additives and alkali metal acetates in amorphous films, which effectively reduced the losses of K and Na upon heating.

A different approach for diminishing the alkali metal losses upon heating was proposed by Wang et al. [72, 86], who added polyvinylpyrrolidone (PVP) to the acetates-based sols in the ratio PVP:KNN = 1:1. In addition to the possible formation of the coordination complexes, the authors attributed the effect to large amount of the heat formed upon combustion of organics and corresponding decrease of the effective crystallization temperature. It should be noted that only PVP with the appropriate molecular weight, i.e. 3.6×10^5 , was effective.

For the recent review on solution-derived KNN thin films the reader is referred to [87].

3.3.4 $Na_{0.5}Bi_{0.5}TiO_3$

Notable amount of the research activities in the field of solution-derived thin films has been devoted to NBT. Either nitrates and/or acetates are used as the Na and Bi sources, while alkoxides, most often n-butoxide, are employed as the Ti-source. The synthesis begins with the dissolution of Na and Bi starting compounds in acetic acid at elevated temperatures. Ti-alkoxide, dissolved in alcohol like methanol or 2-methoxyethanol, and modified by the acetylacetone, is then added. Using these sols, single-phase perovskite NBT thin films were successfully prepared [88–90].

As mentioned above Ti-alkoxide is often stabilized by acetylacetone, forming more stable chelate complexes. However, it results also in an increased temperature of crystallization and/or even phase separation. Remondiere et al. [91] compared three different NBT sol synthesis routes. The first was the above described synthesis of the NBT sols, slightly modified by the 1-h reflux at 124 °C and subsequent distillation (see Fig. 3.6, route n°1). The second route was derived from the 2-methoxyethanol route for the PZT sols (Fig. 3.6, route n°2, see also Fig. 3.1), in which reactive dissolution of the starting acetates and alkoxide is performed by heating and 1-h reflux at 124 °C. The last route was similar to the route n°2, with the exception of vacuum distillation, which was used to decrease the reflux and distillation temperature down to 30 °C (Fig. 3.6, route n°3). Note that the use of Ti-alkoxide-modifier was avoided in the last two routes. The authors determined that only 21 % of the total acetate groups were removed from the sol by distillation in the route n°3, as compared to the 33 % of the acetate groups removed in the route n°2, meaning that the ester-elimination reaction (see Eq. 3.1) is promoted by the high-temperature reflux. The NBT xerogels, prepared by the route n°2, crystallized directly from the amorphous phase, in contrast to the other two routes, where some transient phases were observed. In addition, XRD-phase-pure perovskite films were prepared on platinized silicon substrates from the route n°2 sols already at $T = 460$ °C, while pyrochlore- or fluorite-type secondary phases were detected in the films prepared from the other routes. The enhanced perovskite crystallization in the NBT xerogels and thin films prepared from the route n°2 sols was attributed to three factors:

- a) absence of acetylacetone modifier, which retards the crystallization to higher temperatures and promotes phase separation,
- b) lower amount of organics in the sol due to enhanced ester-elimination reaction kinetics
- c) and enhanced homogeneity at the molecular level.

Kim and co-workers [92] used Na_2CO_3 and Bi_2O_3 , dissolved them in nitric acid (HNO_3) and mixed the solution with ethylene glycol (EG) in a ratio of metal ions:

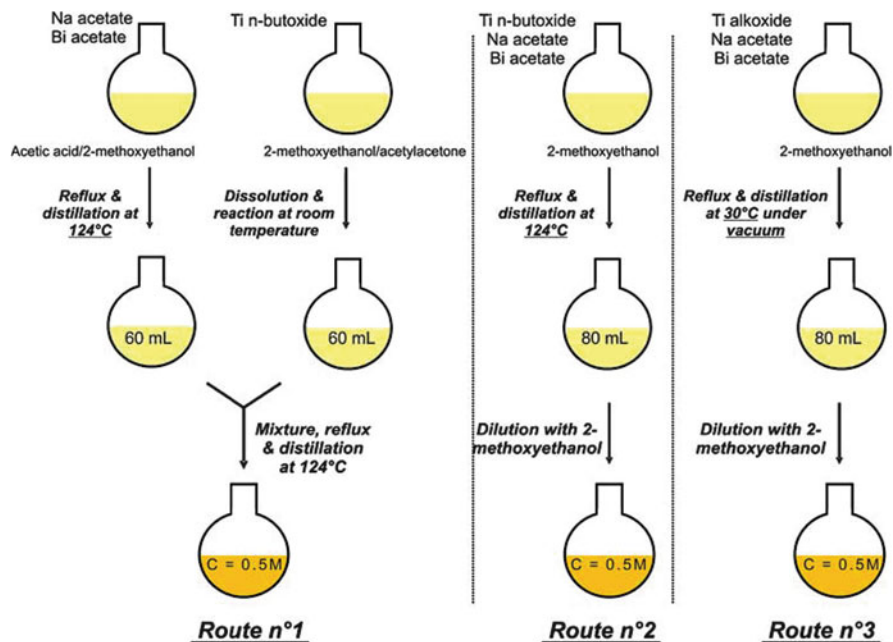


Fig. 3.6 Flowchart of three different synthesis routes of the NBT sols studied by Remondiere et al. [91]. Reprinted with permission of Springer©2008

EG = 1:10. Afterwards the Ti-isopropoxide was added. Based on the FT-IR and Raman investigations of the sols the authors proposed that the final solution consists of Ti alkoxide modified by coordinated glycolic and/or oxalic acid, which are formed upon oxidation of the EG by the nitric acid. The films were prepared on platinumized silicon substrates at 700 °C, however, secondary pyrochlore phase and remains of the amorphous NBT phase were determined by the XRD and transmission electron microscopy (TEM) analyses, respectively.

3.4 Barium Strontium Titanate (Ba,Sr)TiO₃ (BST) and Related Systems

The practically accessible chemical routes for typical CSD BST thin film growth are to some extent, limited by the availability of alkaline earth precursors with good solubility in chemical solutions with good wetting properties, such as alcohols or ether alcohols. Besides a few attempts to use single source precursors (Chap. 4), barium or strontium alkoxide compounds are rarely used because of their limited solubility in the parent alcohol and their high reactivity towards water which can lead to uncontrolled hydrolysis and condensation already during solution synthesis and deposition (cp. Chap. 1) [93]. Simple water based solutions often suffer from

solubility problems of some compounds and poor wettability properties. Thus although in recent years water based precursor systems have been developed (Chap. 5), well established synthesis routes for precursor solutions containing barium, strontium and titanium rely on alkaline earth carboxylates in combination with stabilized or non-stabilized titanium alkoxides, which are dissolved in a mixture of carboxylic acid and a suitable alcohol (simple alcohol, ether alcohol, or polyols) [7, 10, 94–101].

The flow chart in Fig. 3.7 shows the motif of this CSD route which can be found in the publications above in modified form. First, barium and strontium carboxylates are dissolved in their parent carboxylic acid and titanium tetra *n*-butoxide (TBT) is either stabilized by addition of acetylacetone forming $\text{Ti}(\text{O}^n\text{Bu})_2(\text{acac})_2$ or by addition of carboxylic acid. Second, the alkaline earth and the titanium solutions are mixed at room temperature. The final concentration of the CSD solution is adjusted by addition of a parent polar or less polar alcoholic solvent.

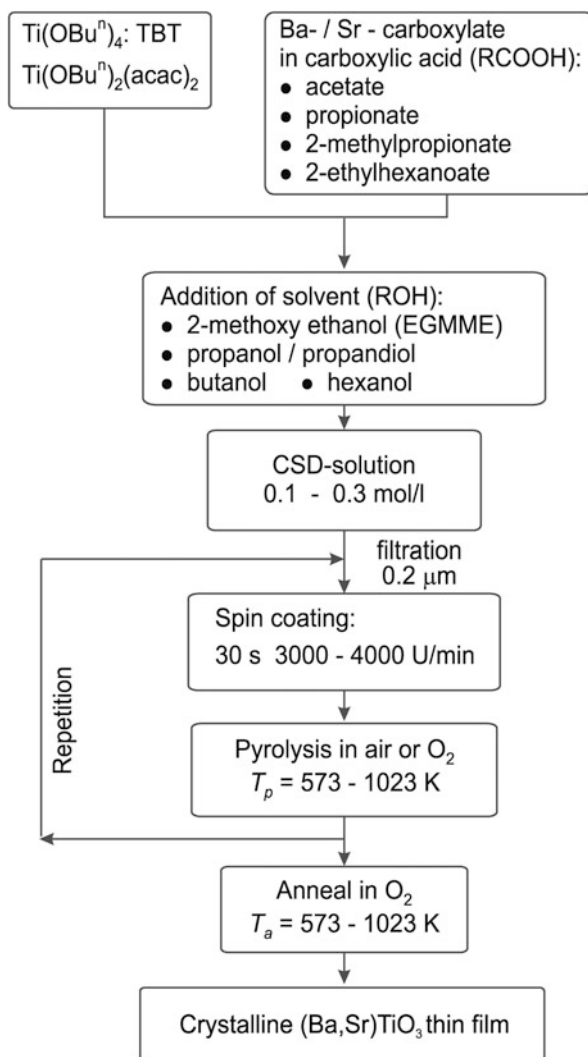
Often this hybrid approach is also classified in literature as “chelate process” due to the stabilization of the alkoxide by a chelating reagent such as acetylacetone [102]. Although the combination of metal carboxylate and metal alkoxide was already mentioned in the early 1990s [103] only Hasenkox et al. [7] investigated in detail the influence of different chain lengths of the metal carboxylates on the film properties and Hoffmann et al. [10] optimized the CSD routine in order to get high quality BST films with a columnar microstructure. For details how to control the morphology and consequently the properties the reader is referred to Chap. 17. With a very similar chemistry ($\text{Ba}(\text{OOCCH}_3)_2$, $\text{Sr}(\text{OOCCH}_3)_2$, TBT in acetic acid/methanol solvent the concept of morphology design was confirmed [98].

Alkaline earth acetates and propionates for the A-site, as well as TBT and titanium tetra isopropoxide for the B-site have proven to be the most popular chemical educts which are used to synthesize the solution. This general scheme offers high flexibility for modifications. Hence the related B-site substituted compounds barium titanate zirconate ($\text{Ba}(\text{Ti}_{1-y}\text{Zr}_y)\text{O}_3$, $y = 0-0.4$) [104–106] barium titanate hafnate ($\text{Ba}(\text{Ti}_{1-y}\text{Hf}_y)\text{O}_3$, $y = 0-0.4$) [107] have been prepared by a corresponding modification of the general scheme shown in Fig. 3.7. In addition dopants can easily be added [94, 108].

3.5 Summary

By means of a number of important perovskite material systems, solution synthesis principles for suitable mixed metallo-organic precursors have been reviewed. They are representative for other material systems with metal compounds, which have a chemically similar behavior. The precursor systems have been classified according to the A-site ions in the perovskite structure: Pb-based, alkali- and alkaline-earth-based systems. Acetates and alkoxides have been usually used as the A- and B-site ion sources in the $\text{Pb}(\text{Zr,Ti})\text{O}_3$ and related systems. Different solvents were used,

Fig. 3.7 Flow chart for the CSD growth of $(\text{Ba}_{1-x}\text{Sr}_x)\text{TiO}_3$ thin films utilizing a solution from (stabilized) titanium alkoxide and alkaline earth carboxylates. By modification of the thermal procedure including repetition of the coating step the overall morphology can be adjusted (thickness and microstructure). By courtesy of S. Hoffmann-Eifert



such as 2-methoxyethanol and other ether alcohols, methanol and 1,3-propanediol (diol-route). The starting compounds can be mixed in the solvent either together or separately, when the A-site precursor is added to the pre-reacted solution of the B-site alkoxides (inverse-mixing route).

An efficient all-ethoxide route was developed for the LiNbO_3 , in which the Li-Nb complex forms upon long-time refluxing. The same precursor system was used also in the course of the development of the water-based solutions. In the case of LiTaO_3 modifiers, usually carboxylic acid, must be used to stabilize the Ta-alkoxide.

Either acetates or alkoxides were used as the A-site-ion sources for the synthesis of K-based perovskites, such as $K(\text{Ta},\text{Nb})\text{O}_3$ and $\text{K}_{0.5}\text{Na}_{0.5}\text{O}_3$, and the complexes are formed upon prolonged refluxing. Several modifiers can be employed, such as acetic acid, acetylacetone, polyvinylpyrrolidone, diethanolamine and even ethylenediaminetetraacetic acid. In the case of $\text{Ti}[(\text{Na}_{0.5}\text{Bi}_{0.5})\text{TiO}_3]$ either nitrates or acetates were used as the Na- and Bi-sources and acetylacetone-modified Ti-alkoxide in 2-methoxyethanol solvent.

For alkaline earth titanates and zirconates a popular hybrid precursor system consisting of the alkaline earth carboxylate and the acetylacetone stabilized group IV metal alkoxide was presented. It offers a wide synthesis window for adjustments of the concentration, overall stoichiometry and dopant content.

References

1. Gurkovich S, Blum J (1984) Preparation of monolithic PbTiO_3 by a sol-gel process. In: Hench L, Ulrich D (eds) *Ultrastructure processing of ceramics, glasses and composites*. Wiley, New York 152–160
2. Budd K, Dey S, Payne D (1985) Sol-gel processing of PbTiO_3 , PbZrO_3 , PZT and PLZT thin films. *Proc Br Ceramic Soc* 36:107–121
3. Tu YL, Calzada ML, Phillips NJ, Milne SJ (1996) Synthesis and electrical characterization of thin films of PT and PZT made from a diol-based sol-gel route. *J Am Ceram Soc* 79:441–448
4. Yi G, Wu Z, Sayer M (1988) Preparation of $\text{Pb}(\text{Zr}, \text{Ti})\text{O}_3$ thin films by sol gel processing: electrical, optical, and electro-optic properties. *J Appl Phys* 64:2717–2724
5. Assink R, Schwartz R (1993) ^1H and ^{13}C NMR investigations of lead zirconate titanate $\text{Pb}(\text{Zr}, \text{Ti})\text{O}_3$ thin-film precursor solutions. *Chem Mater* 5:511–517
6. Brennecke GL, Ihlefeld JF, Maria JP, Tuttle BA, Clem PG (2010) Processing technologies for high-permittivity thin films in capacitor applications. *J Am Ceram Soc* 93:3935–3954
7. Hasenkox U, Hoffmann S, Waser R (1998) Influence of precursor chemistry on the formation of MTiO_3 ($\text{M} = \text{Ba}, \text{Sr}$) ceramic thin films. *J Sol-Gel Sci Technol* 12:67–79
8. Hoffmann S, Waser R (1999) Control of the morphology of CSD-prepared $(\text{Ba},\text{Sr})\text{TiO}_3$ thin films. *J Eur Ceram Soc* 19:1339–1343
9. Jia C, Urban K, Hoffmann S, Waser R (1998) Microstructure of columnar-grained SrTiO_3 and BaTiO_3 thin films prepared by chemical solution deposition. *J Mater Res* 13:2206–2217
10. Hoffmann S, Hasenkox U, Waser R, Jia C, Urban K (1997) Chemical solution deposited BaTiO_3 and SrTiO_3 thin films with columnar microstructure. *MRS Proc* 474:9–14
11. Hayashi Y, Blum J (1987) Sol-gel derived PbTiO_3 . *J Mater Sci* 22:2655–2660
12. Budd K, Dey S, Payne D (1986) The effect of hydrolysis conditions on the characteristics of PbTiO_3 gels and thin films. *MRS Proc* 73:711–716
13. Brinker CJ, Scherer GW (1990) *Sol-gel science: the physics and chemistry of sol-gel processing*. Academic, Boston
14. Turova NY, Turevskaya EP, Kessler VG, Yanovskaya MI (2002) *The chemistry of metal alkoxides*. Kluwer, Boston
15. Dekleva TW, Hayes JM, Cross LE, Geoffroy GL (1988) Sol-gel processing of lead titanate in 2-methoxyethanol: investigations into the nature of the prehydrolyzed solutions. *J Am Ceram Soc* 71:C.280–C.282
16. Beltram T, Kosec M, Stavber S (1993) Reactions taking place during the sol-gel processing of PLZT. *J Mater Res* 28:313–320

17. Carim AH, Tuttle BA, Doughty DH, Martinez SL (1991) Microstructure of solution-processed lead zirconate titanate (PZT) thin films. *J Am Ceram Soc* 74:1455–1458
18. Dražič G, Beltram T, Kosec M (1994) Microstructural characterisation of sol-gel derived PLZT (9.5/65/35) thin films. *Ferroelectrics* 152:49–54
19. Lakeman CDE, Xu Z, Payne DA (1995) On the evolution of structure and composition in sol-gel-derived lead zirconate titanate thin layers. *J Mater Res* 10:2042–2051
20. Milne SJ, Pyke SH (1991) Modified sol-gel process for the production of lead titanate films. *J Am Ceram Soc* 74:1407–1410
21. Tohge N, Takahashi S, Minami T (1991) Preparation of PbZrO_3 – PbTiO_3 ferroelectric thin films by the sol-gel process. *J Am Ceram Soc* 74:67–71
22. Sedlar M, Sayer M (1995) Reactivity of titanium isopropoxide, zirconium propoxide and niobium ethoxide in the system of 2-methoxyethanol, 2,4-pentanedione and water. *J Sol-Gel Sci Technol* 5:27–40
23. Malič B, Arčon I, Kodre A, Kosec M (1999) EXAFS study of amorphous precursors for $\text{Pb}(\text{Zr,Ti})\text{O}_3$ ceramics. *J Sol-Gel Sci Technol* 16:135–141
24. Sengupta SS, Ma L, Adler DL, Payne DA (1995) Extended X-ray absorption fine structure determination of local structure in sol-gel-derived lead titanate, lead zirconate, and lead zirconate titanate. *J Mater Res* 10:1345–1348
25. Feth M, Weber A, Merkle R, Reinöhl U, Bertagnolli H (2003) Investigation of the crystallisation behaviour of lead titanate (PT), lead zirconate (PZ) and lead zirconate titanate (PZT) by EXAFS-spectroscopy and X-ray diffraction. *J Sol-Gel Sci Technol* 27:193–204
26. Malič B, Kosec M, Arčon I, Kodre A, Hiboux S, Murali P (2000) PZT thin films prepared from modified zirconium alkoxide. *Integr Ferroelectr* 30:81–89
27. Malič B, Arčon I, Kodre A, Kosec M (2006) Homogeneity of $\text{Pb}(\text{Zr,Ti})\text{O}_3$ thin films by chemical solution deposition: extended X-ray absorption fine structure spectroscopy study of zirconium local environment. *J Appl Phys* 100:051612
28. Nouwen R, Mullens J, Franco D, Yperman J, Van Poucke L (1996) Use of thermogravimetric analysis-Fourier transform infrared spectroscopy in the study of the reaction mechanism of the preparation of $\text{Pb}(\text{Zr,Ti})\text{O}_3$ by the sol-gel method. *Vib Spectrosc* 10:291–299
29. Mandeljc M, Kosec M, Malič B, Samardžija Z (2000) Low temperature processing of lanthanum doped PZT thin films. *Integr Ferroelectr* 30:149–156
30. Schneller T, Waser R (2007) Chemical modifications of $\text{Pb}(\text{Zr}_{0.3}\text{Ti}_{0.7})\text{O}_3$ precursor solutions and their influence on the morphological and electrical properties of the resulting thin films. *J Sol-Gel Sci Technol* 42:337–352
31. Udayakumar KR, Chen J, Schuele PJ, Cross LE, Kumar V, Krupanidhi SB (1992) Polarization reversal and high dielectric permittivity in lead magnesium niobate titanate thin films. *Appl Phys Lett* 60:1187–1189
32. Shyu MJ, Hong TJ, Yang TJ, Wu TB (1995) Highly (100)-oriented thin films of sol-gel derived $\text{Pb}[(\text{Mg}_{1/3}\text{Nb}_{2/3})_{0.675}\text{Ti}_{0.325}]\text{O}_3$ prepared on textured LaNiO_3 electrode. *Jpn J Appl Phys* 34:3647
33. Fan H, Kim HE (2002) Microstructure and electrical properties of sol-gel derived $\text{Pb}(\text{Mg}_{1/3}\text{Nb}_{2/3})_{0.7}\text{Ti}_{0.3}\text{O}_3$ thin films with single perovskite phase. *Jpn J Appl Phys* 41:6768
34. Swartz SL, ShROUT TR (1982) Fabrication of perovskite lead magnesium niobate. *Mater Res Bull* 17:1245–1250
35. Nagakari S, Kamigaki K, Nambu S (1996) Dielectric properties of sol-gel derived $\text{Pb}(\text{Mg}_{1/3}\text{Nb}_{2/3})\text{O}_3$ – PbTiO_3 thin films. *Jpn J Appl Phys* 35:4933–4935
36. Härdtl KH, Rau H (1969) PbO vapour pressure in the $\text{Pb}(\text{Zr}_x\text{Ti}_{1-x})\text{O}_3$ system. *Solid State Commun* 7:41–45
37. Sato E, Huang Y, Kosec M, Bell A, Setter N (1994) Lead loss, preferred orientation, and the dielectric properties of sol-gel prepared lead titanate thin films. *Appl Phys Lett* 65:2678–2680
38. Tani T, Payne DA (1994) Lead oxide coatings on sol-gel-derived lead lanthanum zirconium titanate thin layers for enhanced crystallization into the perovskite structure. *J Am Ceram Soc* 77:1242–1248

39. Brennecka GL, Huebner W, Tuttle BA, Clem PG (2004) Use of stress to produce highly oriented tetragonal lead zirconate titanate (PZT 40/60) thin films and resulting electrical properties. *J Am Ceram Soc* 87:1459–1465
40. Hirano SI, Kato K (1987) Synthesis of LiNbO_3 by hydrolysis of metal alkoxides. *Adv Ceram Mater* 2:142–145
41. Eichorst DJ, Payne DA, Wilson SR, Howard KE (1990) Crystal structure of $\text{LiNb}(\text{OCH}_2\text{CH}_3)_6$. *Inorg Chem* 29:1458–1459
42. Hirano SI, Kato K (1988) Preparation of crystalline LiNbO_3 films with preferred orientation by hydrolysis of metal alkoxides. *Adv Ceram Mater* 3:503–506
43. Joshi V, Mecartney ML (1993) The influence of water hydrolysis on microstructural development in sol-gel derived LiNbO_3 thin film. *J Mater Res* 8:2668–2678
44. Eichorst DJ, Payne DA (1988) Sol-gel processing of lithium niobate thin-layers on silicon. *MRS Proc* 121:773–778
45. Derouin TA, Lakeman CDE, Wu XH, Speck JS, Lange FF (1997) Effect of lattice mismatch on the epitaxy of sol-gel LiNbO_3 thin films. *J Mater Res* 12:1391–1400
46. Prasada Rao AV, Paik DS, Komarneni S (1998) Sol-gel synthesis of lithium niobate powder and thin films using lithium 2,4-pentanedionate as lithium source. *J Electroceram* 2–3:157–162
47. Hur NH, Park YK, Won DH, No K (1994) Effect of substrates on the growth and properties of LiNbO_3 films by the sol-gel method. *J Mater Res* 9:980–985
48. Nashimoto K, Moriyama H, Osakabe E (1996) Control of crystallinity in sol-gel derived epitaxial LiNbO_3 thin films on sapphire. *J Appl Phys* 35:4936
49. Ono S, Takeo T, Hirano SI (1996) Processing of highly oriented LiNbO_3 films for waveguides from aqueous solution. *J Am Ceram Soc* 79:1343–1350
50. Ono S, Hirano SI (1997) Synthesis of highly oriented lithium niobate thin film from neutralized aqueous precursor solution. *J Am Ceram Soc* 80:2869–2875
51. Takahashi M, Yamauchi K, Yagi T, Nishiwaki A, Wakita K, Ohnishi N, Hotta K, Sahashi I (2004) Preparation and characterization of high-quality stoichiometric LiNbO_3 thick films prepared by the sol-gel method. *Thin Solid Films* 458:108–113
52. Takahashi M, Otowa R, Mori H, Sato S, Nishiwaki A, Wakita K, Ohnishi N, Yagi T, Uchida T (2004) Epitaxial growth and characterization of stoichiometric LiNbO_3 films prepared by the sol-gel method. *J Appl Phys* 96:6569–6573
53. Cheng SD, Zhou Y, Kam CH, Han XQ, Que WX, Lam YL, Chan YC, Oh JT, Gan WS (2000) LiTaO_3 films with c-axis preferred orientation prepared on Si(111) substrate by sol-gel method. *Mater Lett* 44:125–128
54. Ono S, Hirano SI (2002) Processing of highly oriented lithium tantalate films by chemical solution deposition. *J Mater Res* 17:2532–2538
55. Retuert PJ, Kneuer PG, Wittke O, Avila RE, Piderit GJ (1995) Synthesis and characterization of LiTaO_3 thin films deposited on Si by the sol-gel method. *J Mater Res* 20:2797–2800
56. Uchida H, Onofuji K, Funakubo H, Koda S (2007) Characterization of zinc-modified lithium tantalate thin films fabricated by chemical solution deposition method. *J Sol-Gel Sci Technol* 42:265–269
57. Tsuzuki A, Kani K, Watari K, Torii Y (1992) Preparation of magnesium-substituted LiTaO_3 films by the sol-gel method. *J Mater Sci Lett* 11:1157–1159
58. Kao MC, Lee MS, Wang CM, Chen HZ, Chen YC (2002) Properties of LiTaO_3 thin films derived by a diol-based sol-gel process. *Jpn J Appl Phys* 41:2982–2986
59. Cheng ZX, Kimura H, Ozawa K, Miyazaki A, Kanna CV (2005) Ferroelectric lithium tantalate thin film derived from peroxide. *J Alloy Compd* 402:208–212
60. Hirano S, Yogo T, Kikuta K, Morishita T, Ito Y (1992) Preparation of potassium tantalate niobate by sol-gel method. *J Am Ceram Soc* 75:1701–1704
61. Yogo T, Kikuta K, Ito Y, Hirano S (1995) Synthesis of highly oriented $\text{K}(\text{Ta,Nb})\text{O}_3$ (Ta:Nb = 65:35) film using metal alkoxides. *J Am Ceram Soc* 78:2175–2179

62. Suzuki K, Sakamoto W, Yogo T, Hirano S (1999) Processing of oriented $K(\text{Ta,Nb})\text{O}_3$ films using chemical solution deposition. *J Am Ceram Soc* 82:1463–1466
63. Nazeri A, Kahn M (1992) Preparation of KTaO_3 and KNbO_3 solid solutions through sol-gel processing. *J Am Ceram Soc* 75:2125–2133
64. Nazeri A, Kahn H, Bender B, Allen C (1994) Microstructure of $\text{KTa}_x\text{Nb}_{1-x}\text{O}_3$ thin films on MgO (100) single crystals. *J Am Ceram Soc* 77:2450–2454
65. Glinšek S, Arčon I, Malič B, Kodre A, Kosec M (2012) Structural evolution of the $\text{KTa}_{0.6}\text{Nb}_{0.4}\text{O}_3$ alkoxide-based solutions: probing the transition metals local environment by X-ray absorption spectroscopy. *J Sol-Gel Sci Technol* 62:1–6
66. Glinšek S, Malič B, Vukadinović M, Kužnik B, Kosec M (2009) Processing and electric field dependent dielectric properties of $\text{KTa}_{0.6}\text{Nb}_{0.4}\text{O}_3$ thin films on alumina. *Ferroelectrics* 387:112–117
67. Glinšek S, Malič B, Kutnjak Z, Wang H, Krupka J, Kosec M (2009) Dielectric properties of $\text{KTa}_{0.6}\text{Nb}_{0.4}\text{O}_3$ thin films on alumina substrates prepared by chemical solution deposition. *Appl Phys Lett* 94:172905
68. Buršič J, Drbohlav I, Vaněk P, Železný V (2004) Preparation of potassium tantalate thin films through chemical solution deposition. *J Eur Ceram Soc* 24:455–462
69. Buršič J, Železný V, Vaněk P (2005) Preparation of potassium tantalate niobate thin films by chemical solution deposition and their characterization. *J Eur Ceram Soc* 25:2151–2154
70. Ahn CW, Jeong ED, Lee SY, Lee HJ, Kang SH, Kim IW (2008) Enhanced ferroelectric properties of LiNbO_3 substituted $\text{Na}_{0.5}\text{K}_{0.5}\text{NbO}_3$ lead-free thin films grown by chemical solution deposition. *Appl Phys Lett* 93:212905
71. Wu X, Wang L, Ren W, Yan X, Shi P, Chen X, Yao X (2008) Preparation and properties of (110) oriented lead-free sodium potassium niobate thin films by MOD method. *Ferroelectrics* 367:61–66
72. Wang L, Yao K, Ren W (2008) Piezoelectric $\text{K}_{0.5}\text{Na}_{0.5}\text{NbO}_3$ thick films derived from polyvinylpyrrolidone-modified chemical solution deposition. *Appl Phys Lett* 93:092903
73. Goh PC, Yao K, Chen Z (2010) Lead-free piezoelectric $\text{K}_{0.5}\text{Na}_{0.5}\text{NbO}_3$ thin films derived from chemical solution modified with stabilizing agents. *Appl Phys Lett* 97:102901
74. Kupec A, Malič B, Tellier J, Tchernychova E, Glinšek S, Kosec M (2012) Lead-free ferroelectric potassium sodium niobate thin films from solution: composition and structure. *J Am Ceram Soc* 95:515–523
75. Söderlind F, Käll P-O, Helmersson U (2005) Sol-gel synthesis and characterization of $\text{Na}_{0.5}\text{K}_{0.5}\text{NbO}_3$ thin films. *J Cryst Growth* 281:468–474
76. Tanaka K, Kakimoto KI, Ohsato H (2006) Fabrication of highly oriented lead-free (Na, K) NbO_3 thin films at low temperature by sol-gel process. *J Cryst Growth* 294:209–213
77. Lai F, Li JF (2007) Sol-gel processing of lead-free (Na, K) NbO_3 ferroelectric films. *J Sol-Gel Sci Technol* 42:287–292
78. Goh PC, Yao K, Chen Z (2009) Titanium diffusion into $(\text{K}_{0.5}\text{Na}_{0.5})\text{NbO}_3$ thin films deposited on Pt/Ti/SiO₂/Si substrates and corresponding effects. *J Am Ceram Soc* 92:1322–1327
79. Chowdhury A, Bould J, Londesborough MGS, Večerníková E, Milne SJ (2010) Evidence of phase heterogeneity in sol-gel $\text{Na}_{0.5}\text{K}_{0.5}\text{NbO}_3$ system. *Mater Chem Phys* 124:159–162
80. Nakashima Y, Sakamoto W, Yogo T (2011) Processing of highly oriented (K,Na) NbO_3 thin films using a tailored metal-alkoxide precursor solution. *J Eur Ceram Soc* 31:2497–2503
81. Čakare-Samardžija L, Malič B, Kosec M (2008) $\text{K}_{0.5}\text{Na}_{0.5}\text{NbO}_3$ thin films prepared by chemical solution deposition. *Ferroelectrics* 370:113–118
82. Chowdhury A, Bould J, Londesborough MGS, Milne SJ (2010) Fundamental issues in the synthesis of ferroelectric $\text{Na}_{0.5}\text{K}_{0.5}\text{NbO}_3$ thin films by sol-gel processing. *Chem Mater* 22:3862–3874
83. Chowdhury A, Bould J, Londesborough MGS, Milne SJ (2011) The effect of refluxing on the alkoxide-based sodium potassium niobate sol-gel system: thermal and spectroscopic studies. *J Solid State Chem* 184:317–324

84. Röscher M, Tappertzhofen S, Schneller T (2011) Precursor homogeneity and crystallization effects in chemical solution deposition-derived alkaline niobate thin films. *J Am Ceram Soc* 94:2193–2199
85. Röscher M, Schneller T, Waser R (2010) Comments on the processing of the niobium component for chemical solution derived niobium oxide-based thin-films. *J Sol-Gel Sci Technol* 56:236–243
86. Wang L, Yao K, Goh PC, Ren W (2009) Volatilization of alkali ions and effects of molecular weight of polyvinylpyrrolidone introduced in solution-derived ferroelectric $K_{0.5}Na_{0.5}NbO_3$ films. *J Mater Res* 24:3516–3522
87. Chowdhury A (2012) Recent developments in the area of sodium potassium niobate (NKN) thin films by chemical solution deposition methods. In: Huang XL, Ma SL (eds) *Ferroelectrics: new research*. Nova, New York
88. Tang XG, Wang J, Wang XX, Chan HLW (2004) Preparation and electrical properties of highly (111)-oriented $(Na_{0.5}Bi_{0.5})TiO_3$ thin films by a sol-gel process. *Chem Mater* 16:5293–5294
89. Yang CH, Wang Z, Li QX, Wang JH, Yang YG, Gu SL, Yang DM, Han JR (2005) Properties of $Na_{0.5}Bi_{0.5}TiO_3$ ferroelectric films prepared by chemical solution decomposition. *J Cryst Growth* 284:136–141
90. Xu J, Liu Y, Withers RL, Brink F, Yang H, Wang M (2008) Ferroelectric and non-linear dielectric characteristics of $Bi_{0.5}Na_{0.5}TiO_3$ thin films deposited via a metallorganic decomposition process. *J Appl Phys* 104:116101
91. Remondiere F, Malič B, Kosce M, Mercurio JP (2008) Study of the crystallization pathway of $Na_{0.5}Bi_{0.5}TiO_3$ thin films obtained by chemical solution deposition. *J Sol-Gel Sci Technol* 46:117–125
92. Kim CY, Sekino T, Yamamoto Y, Niihara K (2005) The synthesis of lead-free ferroelectric $Bi_{1/2}Na_{1/2}TiO_3$ thin film by solution-sol-gel method. *J Sol-Gel Sci Technol* 33:307–308
93. Bradley D, Mehrotra RC, Rothwell I, Singh A (2001) *Alkoxo and aryloxo derivatives of metals*. Academic, London
94. Bretos I, Schneller T, Waser R, Hennings DF, Halder S, Thomas F (2010) Compositional substitutions and aliovalent doping of $BaTiO_3$ -based thin films on nickel foils prepared by chemical solution deposition. *J Am Ceram Soc* 93:506–515
95. Malič B, Boerasu I, Mandeljc M, Kosce M, Sherman V, Yamada T, Setter N, Vukadinović M (2007) Processing and dielectric characterization of $Ba_{0.3}Sr_{0.7}TiO_3$ thin films on alumina substrates. *J Eur Ceram Soc* 27:2945–2948
96. Ihlefeld J, Laughlin B, Hunt-Lowery A, Borland W, Kingon A, Maria JP (2005) Copper compatible barium titanate thin films for embedded passives. *J Electroceram* 14:95–102
97. Dawley J, Ong R, Clem P (2002) Chemical solution deposition of <100>-oriented $SrTiO_3$ buffer layers on Ni substrates. *J Mater Res* 17:1678–1685
98. Schwartz RW, Clem PG, Voigt JA, Byhoff ER, Stry M, Headley TJ, Missert NA (1999) Control of microstructure and orientation in solution-deposited $BaTiO_3$ and $SrTiO_3$ thin films. *J Am Ceram Soc* 82:2359–2367
99. Wang F, Uusimäki A, Leppavuori S, Karmanenko S, Dedyk A, Sakharov V, Serenkov I (1998) $Ba_{0.7}Sr_{0.3}TiO_3$ ferroelectric film prepared with the sol-gel process and its dielectric performance in planar capacitor structure. *J Mater Res* 13:1243–1248
100. Sedlar M, Sayer M, Weaver L (1995) Sol-gel processing and properties of cerium doped barium strontium titanate thin films. *J Sol-Gel Sci Technol* 5:201–210
101. Hoffmann S, Klee M, Waser R (1995) Structural and electrical properties of wet-chemically deposited $Sr(Ti_{1-y}Zr_y)O_3$ ($y = 0 \dots 1$) thin films. *Integr Ferroelectr* 10:155–164
102. Schwartz RW, Schneller T, Waser R (2004) Chemical solution deposition of electronic oxide films. *C R Chim* 7:433–461
103. Hennings D, Klee M, Waser R (1991) Advanced dielectrics: bulk ceramics and thin films. *Adv Mater* 3:334–340

104. Halder S, Schneller T, Böttger U, Waser R (2005) Fabrication and electrical characterisation of Zr-substituted BaTiO₃ thin films. *Appl Phys A* 81:25–29
105. Dixit A, Majumder S, Savvinov A, Katiyar R, Guo R, Bhalla A (2002) Investigations on the sol–gel-derived barium zirconium titanate thin films. *Mater Lett* 56:933–940
106. Hoffmann S, Waser RM (1997) Dielectric properties, leakage behaviour, and resistance degradation of thin films of the solid solution series Ba(Ti_{1-y}Zr_y)O₃. *Integr Ferroelectr* 17:141–152
107. Halder S, Schneller T, Waser R, Majumder S (2008) Electrical and optical properties of chemical solution deposited barium hafnate titanate thin films. *Thin Solid Films* 516:4970–4976
108. Schneller T, Schober T (2003) Chemical solution deposition prepared dense proton conducting Y-doped BaZrO₃ thin films for SOFC and sensor devices. *Solid State Ionics* 164:131–136

Chapter 4

Single Source Precursor Approach

Hydrolysis Mechanisms in Organic Media

Vadim G. Kessler

4.1 Introduction

The quest for single source precursors (SSP) in metal oxide sol-gel, more often referred to today as Chemical Solution Deposition (CSD), was set in the late 1980s in connection with the synthesis of complex ferroelectric oxide films, in the first hand, those of barium titanate, BaTiO_3 , and lead magno-niobate, $\text{Pb}(\text{Mg}_{1/3}\text{Nb}_{2/3})\text{O}_3$, and zinco-niobate, $\text{Pb}(\text{Zn}_{1/3}\text{Nb}_{2/3})\text{O}_3$. The difficulties in maintaining the stoichiometry of barium titanate using hydrolysis of metal alkoxides as approach have been underlined already in the pioneering works of Mazdiyasnı et al. [1, 2]. The idea of applying a single source precursor—a molecule already containing necessary atoms in a proper ratio, corresponding to the desired complex phase, comes originally from the Metal Organic Chemical Vapor Deposition (MOCVD) approach. It was urged by Boris Kozyrkin et al. (see [3] and refs therein) in the late 1970s, when the convincement that gallium arsenide, GaAs, was destined to replace silicon in electronic applications dominated the scientific community. It was practically impossible at that time to achieve the control over different sources down to the ppm scale, as required for the semiconductor applications, and the demand for a single molecular source was seen as the only option. The distinct focus on identification and purposeful construction of SSP for sol-gel applications was set in the beginning of 1990s by the groups of Turova [4] and Hubert-Pfalzgraf [5] respectively. The access to easy-to-handle and less hydrolysis sensitive derivatives of alkaline earth and late transition metals in combination with commercial availability of the alkoxides of early transition metals made heteroleptic (mixed-ligand) derivatives to natural candidates for the role of SSP. The interest to heteroligand SSP was additionally supported by the discovery of the fact that introduction of chelating organic ligands into alkoxide precursors was generally stabilizing the resulting colloid solutions applied then for film deposition [6].

V.G. Kessler (✉)

Department of Chemistry, SLU, Box 7015, 75007 Uppsala, Sweden

The evaluation of the need in and applicability of an SSP is determined by its fate in the hydrolytic transformations and in the subsequent deposition and thermal treatment procedures. Therefore, this chapter will commence with the description of the mechanisms of hydrolysis in organic media and subsequent particle growth and crystallization, and will continue with an overview of a large number of more and less successful examples in application of SSP. Its final part will provide some keys for understanding the design and synthesis of heterometallic alkoxide complexes—possible SSP.

4.2 Hydrolysis in Organic Media: What Happens with the Precursors?

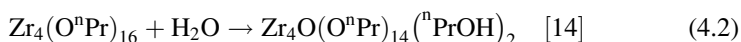
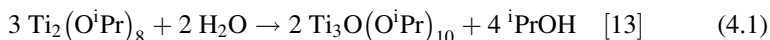
The apprehension of the sol-gel transformations of metal-organic precursors, e.g. metal alkoxides and chemically modified metal alkoxides, and even inorganic precursors was until very recently dominated by the hypothesis of kinetically controlled homogeneous hydrolysis-polycondensation supposed to result in the reaction mechanisms analogous to the growth of true inorganic polymers such as, for example, siloxanes [7–9]. Exploiting the knowledge about the alkoxides of silicon, which, however, as a non-metal is not a plausible analogue, it was supposed that the metal alkoxide “monomers” hydrolyze forming at the first step hydroxo-alkoxide species like “ $\text{Ti}(\text{OR})_3(\text{OH})$ ” or “ $\text{Zr}(\text{OR})_3(\text{OH})$ ”, which then can either be hydrolyzed further or undergo condensation with formation of oxo- (oxolation) or hydroxo (hydroxolation) bridges in independent kinetic regimes [7]. The sol-gel transition was attributed to the molecular percolation through polymeric condensation, i.e. it was supposed that the “polymeric oxo-hydroxo molecules” are growing so big that they come into contact with each other and built up a solid framework. The stabilization of the colloid solutions, obtained from precursors modified with chelating ligands, was explained through a supposition that introduction of chelating moieties leads to moderation of the kinetic hydrolysis sensitivity of precursors and is inhibiting the condensation reaction [10]. Possibility to form sols and gels of complex oxides was attributed to “harmonizing” of the speeds of hydrolysis and condensation between the species of different metals. Obtaining of heterometallic precursors seemed as an immediate remedy for this problem.

These hypotheses failed, however, to explain the reasons of two major failures experienced by the metal oxide sol-gel process: (1) in spite of numerous heterometallic precursors applied, it turned completely impossible to produce high temperature superconductor phases, as, for example, $\text{YBa}_2\text{Cu}_3\text{O}_{7-\delta}$, directly through sol-gel process (even lowering of the synthesis temperature for it could not be achieved) and (2) while modification of metal alkoxides with acetylacetone for zirconium precursors was supposed to produce randomly condensed polymers, the ZrO_2 films produced from them were dense and did not display any microporosity.

Supposition about kinetically controlled hydrolysis-polycondensation turned to be inconsistent.

4.2.1 *Molecular Mechanisms in Hydrolysis and Condensation*

Recent development in the studies of the structure and reactivity of metal alkoxide precursors revealed a completely different picture. The metal alkoxide complexes are in general not monomers, but oligomers. Even $\text{Ti}(\text{O}^i\text{Pr})_4$ generally considered earlier to be a monomer at least in solution [11] was recently shown to display dimeric structure in the solid state with possible monomer-dimer equilibrium in solution (see [12] and refs therein). It is especially important to keep in mind that the XANES/EXAFS data used in the early works on titanium precursors are for this element always strongly influenced by adsorption and are very difficult to use for structure elucidation. This trend is caused by the extreme Lewis basicity of the alkoxide anions $[\text{RO}]^-$, which are even strong Brønsted bases, being correspondent bases of the alcohols—common solvents in the synthesis of oxides. The addition of small amounts of water, microhydrolysis, does not proceed even for homometallic titanium or zirconium alkoxides via any hydroxide intermediates, but results directly in well-defined oligonuclear oxo-alkoxide species through one-step hydrolysis-condensation transformation associated with complete re-structuring of the precursor molecules, for example:



In the cases, when the hydroxide alkoxide complexes really can be isolated (for zirconium, but never for titanium species), they are not reactive intermediates, but fully thermodynamically stable complexes without any trend to further condensation under conditions for their isolation. For homometallic alkyl alcohol derivatives only a single example of hydroxo-species, $\text{Zr}_3\text{O}(\text{O}^i\text{Bu})_9(\text{OH})$ [15] with the molecular geometry practically identical to $\text{Ti}_3\text{O}(\text{O}^i\text{Pr})_{10}$ and the triangular core in $\text{Zr}_4\text{O}(\text{O}^n\text{Pr})_{14}(\text{}^n\text{PrOH})_2$ (see Fig. 4.1) has been reported so far.

The complex $\text{Zr}_3\text{O}(\text{O}^i\text{Bu})_9(\text{OH})$ was obtained with over 80 % yield on in situ microhydrolysis of monomeric $\text{Zr}(\text{O}^i\text{Bu})_4$ [16] with moist Li_2S and was found to be completely stable and well recrystallizable from a variety of solvents [15]. The majority of the described zirconium hydroxo-alkoxides are, however, heterometallic complexes. In this case, they also are thermodynamically stable and do not show any trend at all to condensation at room temperature. The structure of these oxo- or hydroxo-species is completely independent from the way of their preparation. Thus one and the same complex $\text{Ba}_2\text{Zr}_2(\text{OH})_2(\text{O}^i\text{Pr})_{10}(\text{}^i\text{PrOH})_6$ has

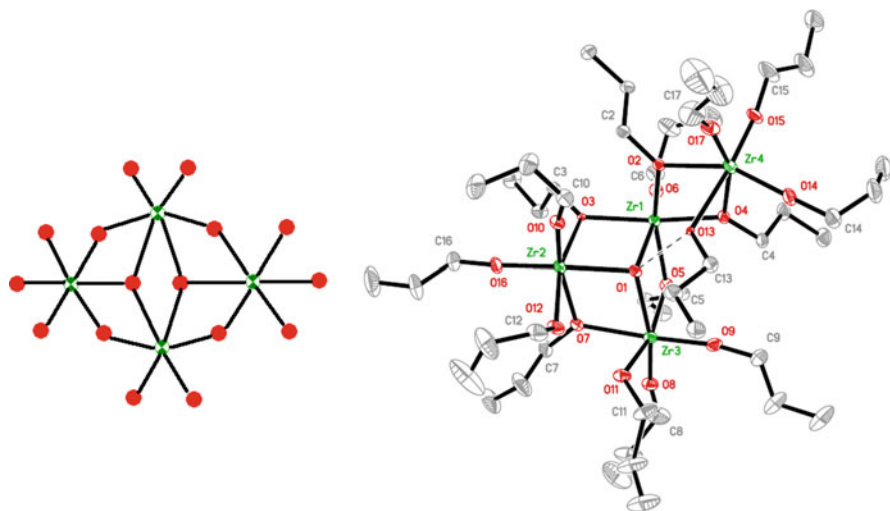


Fig. 4.1 The metal-oxygen core of $Zr_4(O^iPr)_{16}$ and the molecular structure of $Zr_4O(O^iPr)_{14}(O^iPrOH)_2$ [12]

been obtained with high yield both by alcohol interchange from a tert-butoxide complex $BaZr(O^tBu)_6(Thf)_2$ treated with excess of iPrOH and then hydrolyzed with 1 equivalent of water [17] and by adding directly 1 eq. of H_2O to a freshly prepared mixture of $Ba(O^iPr)_2(^iPrOH)_x$ and $[Zr(O^iPr)_4(^iPrOH)_2]$ [18]. The bimetallic barium-titanium oxoalkoxide $Ba_4Ti_4O_4(O^iPr)_{16}(^iPrOH)_4$, the first single-source precursor of $BaTiO_3$, was produced first via oxidation of a propoxide $Ba:Ti = 1:1$ solution by dry oxygen [19], but can be made quicker and with a higher yield just by addition of the equivalent amount of water to a diluted alcohol solution as in [18].

It is important to note that the molecular structures of the individual hydrolysis products of metal alkoxides follow the structure types well known for oligonuclear inorganic oxometallates, starting from trimolybdate type M_3O_{11} and continuing with, in particular, tetramolybdate type M_4O_{16} , Lindqvist type M_6O_{19} , Andersson type M_7O_{24} , Keggin type $M_{13}O_{40}$ etc. [20] (see Fig. 4.2). The degree of hydrolysis $h = [M(OR)_n]:[H_2O]$ is permitting to achieve the formation of a distinct structure, but is not itself determining the structure. The latter is resulting from dense packing of metal cations and oxygen atoms of the ligands and is a result of coordination equilibrium. This structural feature is in itself a strong confirmation of the principal conclusion that can be drawn from the theoretical studies of bonding in the structures of the alkoxide complexes [21, 22]: these species are not covalently bound molecules but ionic salts existing as close ion pairs and therefore often soluble in organic solvents. The ability of modern computer methods to provide molecular orbital structure and shape is often confusing the reader giving an impression that all bonding can be considered as covalent (at least to some extent). More thorough analysis of these results gives, however, a direct confirmation for

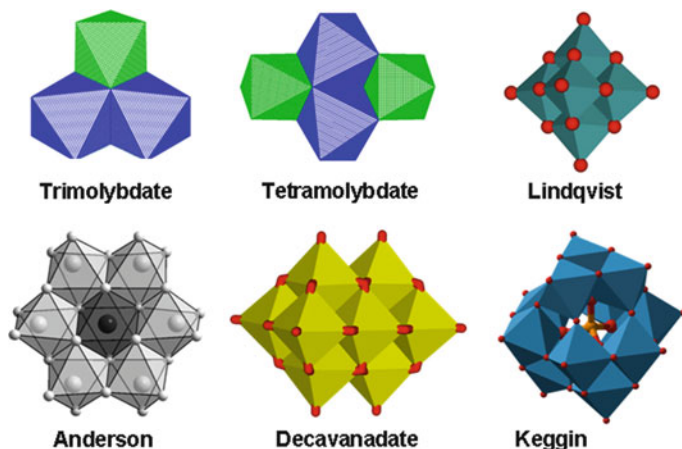
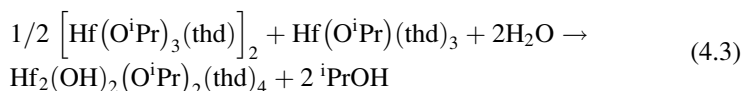


Fig. 4.2 Metal-oxygen cores in the structures of metal alkoxide complexes—analogs of the polyoxometallates [18] (the oxygen atoms are indicated by *red dots*)

the predominantly electrostatic character of bonding to oxygen for metal cations as the “bonding” orbitals do not contain any considerable contributions from the atomic orbitals of the metal atoms except for those of the platinum group ones.

The chelating heteroligands turned out also to play a role completely different from that put forward in the kinetic reactivity hypothesis. First and foremost, it has been clearly demonstrated that introduction of chelating ligands is strongly increasing the charge distribution in the molecules. The length of the bonds to oxygen atoms in the chelating ligands is appreciably higher than to the alkoxide oxygen atoms. This leads, in combination with the fact that the chelating ligands most often are appreciably smaller than the alkoxide groups they are replacing, to the easier accessibility of the metal centre for hydrolytic transformations. The introduction of chelating ligands can, of course, in exceptional cases give direct thermodynamic stabilization of an alkoxide complex over a hydroxide one (see [23] for such example). The heteroligands are even easily transferred both within one molecule and also between different molecules. The transfer of chelating β -diketonate ligands within an oligonuclear molecule of heteroleptic aluminium alkoxide has been first studied in detail by Wengrovius et al. already in 1986 [24]. The transfer of chelating ligands between different molecules has also been demonstrated recently [25]:



It has even been demonstrated recently that the complete blocking of the coordination sites does not have any effect towards decreased reactivity of metal alkoxide complexes in hydrolysis. Thus highly sterically hindered homoleptic

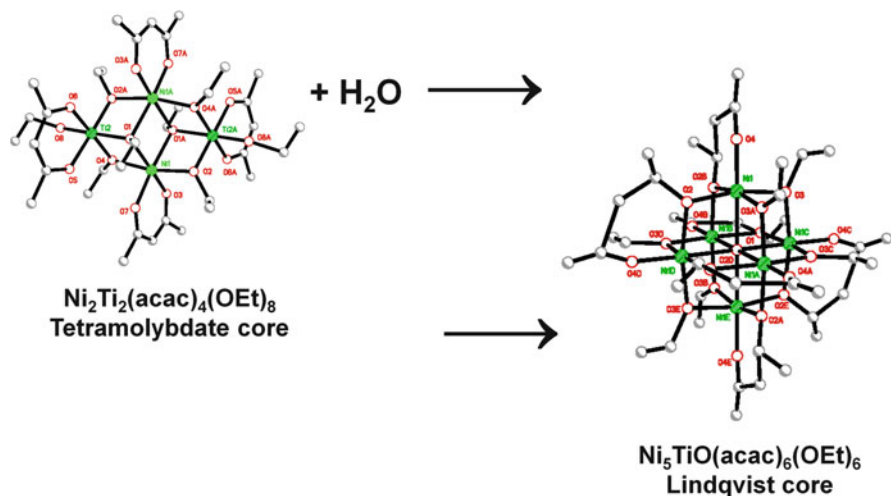


Fig. 4.3 Thermodynamically driven transformation from $\text{Ni}_2\text{Ti}_2(\text{acac})_4(\text{OEt})_8$ to $\text{Ni}_5\text{TiO}(\text{acac})_6(\text{OEt})_6$ on microhydrolysis [27]

pinacolates of niobium and tantalum $\text{HM}(\text{O}_2\text{C}_6\text{H}_{12})_3$ turned to be noticeably more hydrolysis-condensation sensitive than aliphatic alkoxides, $\text{M}_2(\text{OR})_{10}$, $\text{R} = \text{Me}, \text{Et}, \text{}^i\text{Pr}$ [26].

In total, the hydrolysis-polycondensation appears to be a single kinetic phenomenon, leading to products, corresponding to the local equilibrium conditions. A very illustrative demonstration of this fact is provided by the microhydrolysis of a bimetallic nickel-titanium precursor $\text{Ni}_2\text{Ti}_2(\text{acac})_4(\text{OEt})_8$, resulting on addition of 1 eq. of water in practically quantitative precipitation of a complex with completely different metal : metal and alkoxide : heteroligand ratios, $\text{Ni}_5\text{TiO}(\text{acac})_6(\text{OEt})_6$ [27] (see Fig. 4.3).

The hydrolysis of metal alkoxides is following normally the kinetically unhindered proton-assisted $\text{S}_{\text{N}}1$ mechanism [28] and introduction of chelating ligands, enhancing the charge distribution, is apparently facilitating it further and resulting in quicker and deeper condensation. Experimental confirmations of this fact have arrived quite early in the history of application for mixed ligand precursors. In particular, this observation was clearly stated in the comparison between alkoxide-only and carboxylate-alkoxide precursors made by Hubert-Pfalzgraf et al. [29].

4.2.2 *Supramolecular Sol-Gel Mechanisms, Formation and Fate of Colloid Particles*

The structures of the individual oxo-complexes resulting from microhydrolysis, the process, where the amount of the water added is less than required for complete removal of the organic ligands, are following the same structure types as the

structures of alkoxide derivatives in general and following those identified for the formation of polyoxometallate compounds from water solutions. This permits to conclude that the hydrolysis-condensation is a purely thermodynamically controlled process, driven by the electrostatic forces that stay for bonding in the metal alkoxide, hydroxide and oxide structures. The studies of formation of polyoxometallate complexes in water have revealed during the last decade that coordination equilibria for this type of particles can in fact result in well-defined individual species with the size exceeding 2 nm [30–34]. The sol-gel process, carried out in organic solvents, results normally at the first step in well-defined primary particles with the size in the range of 2–5 nm [35–37], originating apparently from the coordination equilibria in solutions. The growth of the particles is self-limited. In the organic solvents the size of the primary particles obtained does not normally exceed 5 nm. The reasons for this type of limitations can be thought both in thermodynamic, such as extremely low solubility and absence of transport for the oxide species, when they are formed, and kinetic factors. Among the latter can be named the interplay between kinetic dependence of the nucleation on concentration versus transport of non-hydrolyzed species to the already formed nuclei or even the increasing activation barrier for inclusion of one more oxide unit into the already formed particle. The theoretical estimations of the energies for surface interactions of the forming nanoparticles with the solvents can be considered to give favour to the latter mechanism [38, 39]. This gave rise to an idea that the growth of the particles can be limited by the growing force of the interaction between residual organic ligands on their surface with the solvent molecules, which lead to a term “Micelles Templated by Self-Assembly of Ligands” (MTSAL, see Fig. 4.4) for denoting the primary particles in sol-gel processes [27, 37].

These particles have a core structure of a polyoxometallate type, which means a crystalline or at least highly ordered one and an amorphous surface covered by residual ligands. Their future transformations depend on the nature of the surface ligands, degree of complexation, i.e. how densely it can be covered by them and the desorption equilibria. If the degree of complexation is low, the particles stick to each other and form bigger aggregates that even can develop a common surface and continue aggregation with each other until they arrive at macro-size formations of about 1 μm in size. If the degree of complexation is relatively high, the particles remain mainly individual or tend to form relatively small aggregates (see Fig. 4.5) [36, 37, 40, 41].

The MTSAL type particles are in reality NOT exclusively a product of application of alkoxide precursors. They have even been documented for hydrolysis of inorganic salts in alcohol and other organic media [42, 43]. The same type of behaviour is apparently the case even for non-hydrolytic sol-gel process as it has been recently demonstrated for the synthesis of TiO_2 by Bradley reaction, i.e. thermally enhanced ether elimination from a metal alkoxide in alcohol or carbonyl compound as solvent [44–47], carried out in benzyl alcohol [48].

An important question deals also with the fate of heterometallic species. In fact, the expectations set for them are very often not fulfilled. The oligonuclear complexes and even oxo-alkoxo species are not clusters and most often do not

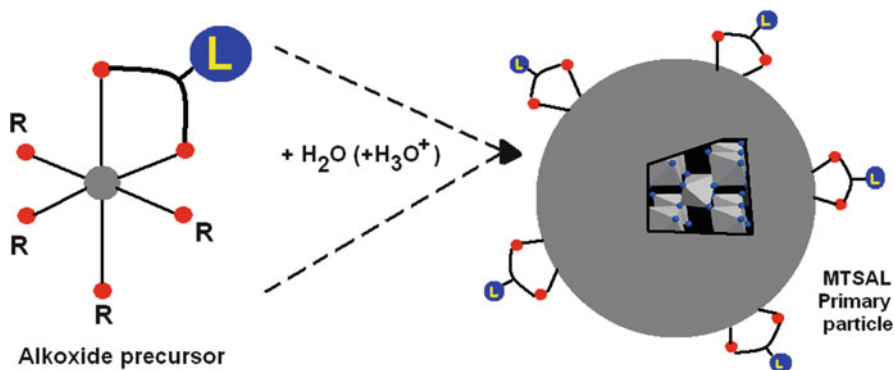


Fig. 4.4 Schematic presentation of the MTSAL concept (the *red dots* denote the oxygen atoms, while the *blue balls* stay for the rest of the ligand entities)

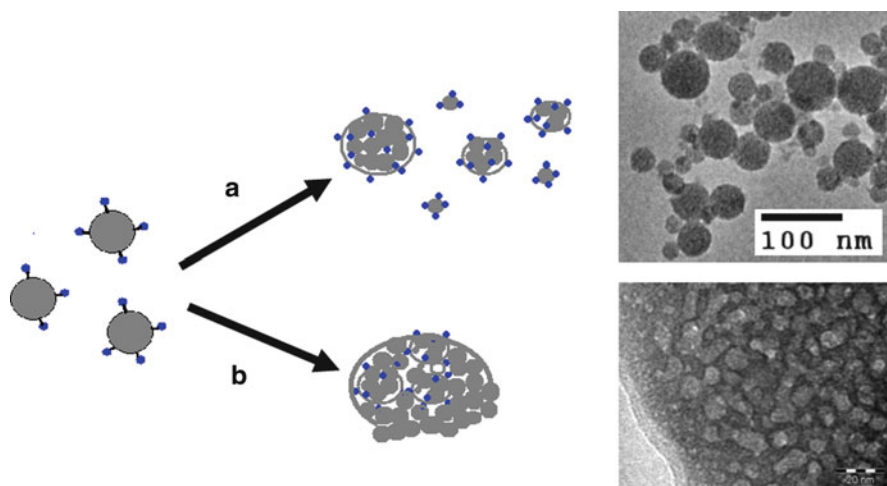


Fig. 4.5 Transformation of the MTSAL aggregates for higher complexation ratio, giving formation of a stable sol (a) and for lower complexation ratio leading to gelation (b). TEM image (b) reproduced with permission from [36]

guarantee any “cluster behaviour”, i.e. conservation of the metal-oxygen core in the course of hydrolytic transformation. Introduction of the oxo- or hydroxo-ligands, which is the primary result of (micro)hydrolysis, leads to complete redistribution of cations in at least relatively small aggregates. This phenomenon is demonstrated in Fig. 4.6 for the single source precursors of perovskite materials. All of them can be constructed following the tetramolybdate structure type, but addition of 1 eq. of water changes both the molecular geometry and the cation ratio. In contrast, addition of stoichiometric or superstoichiometric amounts of water is granting the unchanged composition as the thermodynamic conditions for complete phase separation for both oxide components is fulfilled [46].

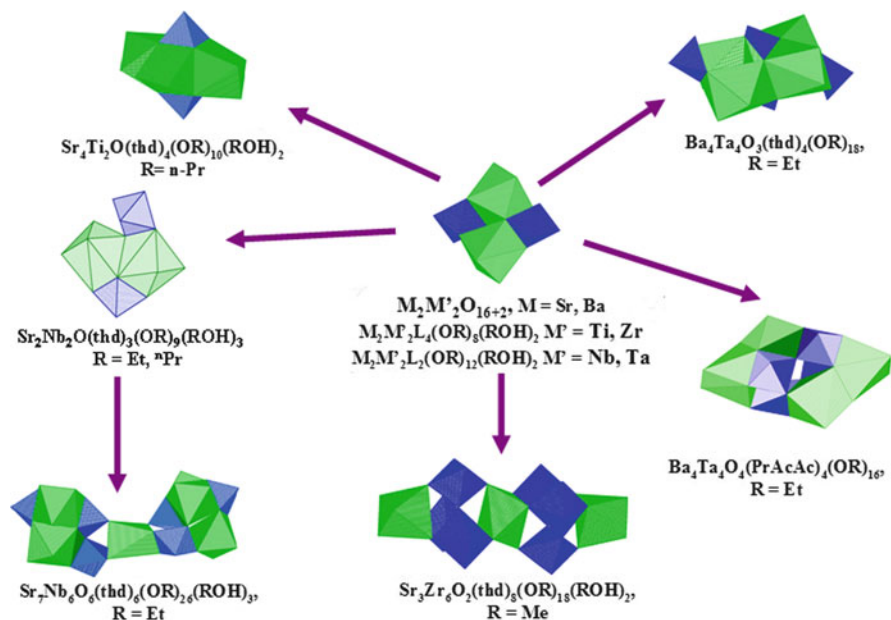


Fig. 4.6 Transformation of the single source precursors of perovskites on microhydrolysis

It should, however, be noticed that the heterometallic species introduce the proper stoichiometry on molecular level and in a few cases really do provide strong advantages over a mixture of homometallic ones. At least three well documented cases are reported in literature and will then be discussed in detail in the Sect. 4.3 below. First of them was the use of heterometallic oxoalkoxides for the synthesis of BaTiO_3 films [4], where the non-oxo homoleptic alkoxide precursors can lead otherwise to parasite phases deteriorating the electric properties. The second dealt with application of a heterometallic alkoxide $\text{ErAl}_3(\text{O}^i\text{Pr})_{12}$ in the preparation of laser waveguides, where the effect was achieved in separation of Er cations from each other and improved optical properties, while the use of homometallic $\text{Er}_5\text{O}(\text{O}^i\text{Pr})_{13}$ resulted in many Er-O-Er contacts and inferior characteristics [49]. The third case was the application of diethanolamine ligand for binding titanium and zirconium in a precursor for preparation of the homogeneous ZrTi_2O_6 phase for hydrothermally stable microporous membranes [50].

4.3 Application of Single Source Precursors for Preparation of Materials

In the described approaches to functional films, derived from SSP, it is possible to identify three principal groups: (1) spin-on deposition of dispersions, prepared from powders obtained by metallo-organic decomposition (MOD)—the powders were

first obtained in dry form and then re-dispersed, (2) spin-on or dip-coating deposition of the solutions of SSP on dense substrates for preparation of continuous coatings, and (3) dip-coating deposition of SSP solutions on porous substrates for the preparation of membrane or nanocomposite materials.

4.3.1 Deposition of Dispersions Obtained from Powders Produced from SSP by MOD

The historically first and actually rather complete demonstration of a single source precursor approach dealt with the synthesis of BaTiO₃ coating by spin-on approaches, applying powders, produced by metallo-organic decomposition (MOD) of such precursors. The challenge in identifying an approach to SSP for this system was caused by the problems in obtaining phase-pure BaTiO₃ from the initially applied ethoxide solutions. Analysis of the molecular composition of these solutions revealed simultaneous presence of two heterometallic complexes with “wrong” composition, BaTi₂(OEt)₁₀(EtOH)₅ and Ba₄Ti₂O(OEt)₁₄(EtOH)₂ [51]. A possibility to obtain an alkoxide with the required 1:1 composition was reported by Kirby, but the nature of this compound was not identified [52]. It was isolated in the form of poorly soluble crystals from solutions in isopropanol subjected to prolonged refluxing. The nature of these crystals was determined using the X-ray single crystal study that has shown them to be an oxo-alkoxide Ba₄Ti₄O₄(OⁱPr)₁₆(ⁱPrOH)₄ [17]. Thermal decomposition of this crystalline product in inert atmosphere and in carbon dioxide-free air offered phase-pure tetragonal (nano)powder of BaTiO₃ at 700 °C [51]. Further studies have demonstrated that an analogous oxo-complex with 1:1 composition is formed even in n-butanol solutions. The higher viscosity of n-butanol provided an attractive possibility to produce the (nano)powder of the desired oxide simply by hydrolysis from the precursor solutions subjected to prolonged thermal treatment [4]. The process has been commercialized by Symetrix Corporation in Colorado, USA for the production of capacitor materials [47] (see Figs. 4.7 and 4.8).

Application of more-or-less well defined individual molecular complexes for the hydrolytic or pyrolytic preparation of nanopowders for further use in film preparation, especially for perovskite materials for electronic applications, has become then the major SSP based route. Thus, synthesis of Ba(Mg_{1/3}Ta_{2/3})O₃ powder from a postulated trimetallic alkoxide SSP has been reported [54] in 1996, however, without any convincing characterisation of the latter. A thorough characterization of bimetallic precursors for barium magno-niobate has been reported in 1997, including such complexes as bimetallic alkoxides.

BaNb₂(OⁱPr)₁₂(ⁱPrOH)₂ and MgNb₂(OEt)₁₂(EtOH)₂ and acetate-alkoxides, MNb₂(OAc)₂(OⁱPr)₁₀, where M = Mg, Cd, Pb. The preparation of bimetallic powders by hydrolysis has been carried out aimed at comparison between the pure alkoxide and alkoxide-acetate routes [26]. The observations of the authors

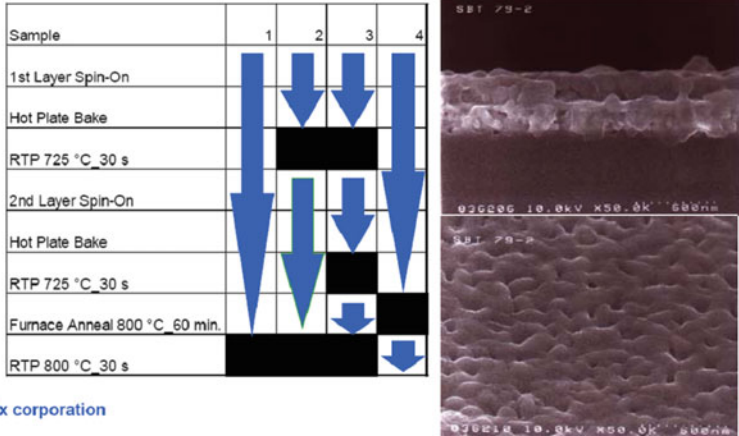


Fig. 4.7 Deposition methodology and the resulting morphology of single source precursor MOD derived film of barium strontium titanate. Copyright Symetrix Corp. [53]. The process is carried out stepwise with deposition, drying and then quick sintering for each layer

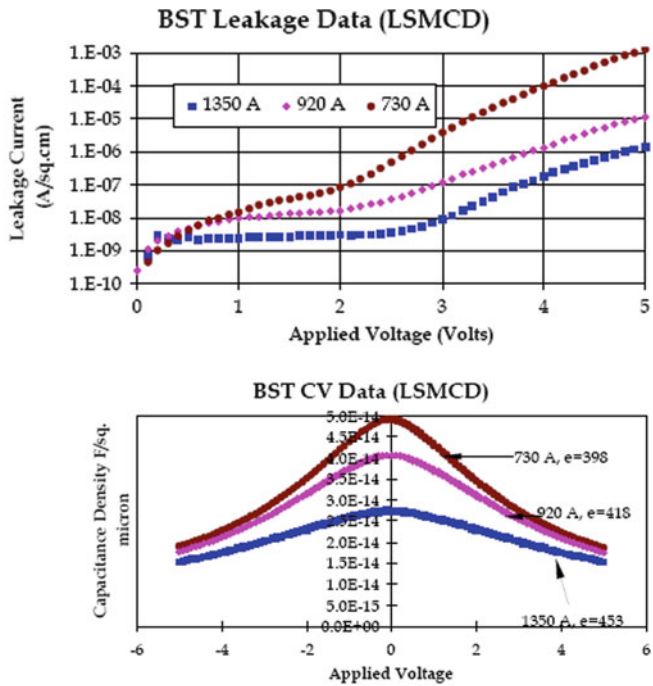


Fig. 4.8 Functional characteristics of the capacitor materials prepared by single source precursor MOD derived deposition procedure. Copyright Symetrix Corp. [53]

were in full agreement with the later proposed MTSAL concept and indicated lower crystallization temperature and higher crystallinity for the powders produced from acetate-alkoxides, and implied the ability of chelating ligands to facilitate hydrolysis and especially condensation of precursors. New SSP have then been identified and used for the preparation of powders of BaTiO_3 ($\text{Ba}_2\text{Ti}_2(\text{thd})_4(\text{OEt})_8(\text{EtOH})_2$ [5], $\text{Ba}_2\text{Ti}_2(\text{thd})_4(\text{O}^n\text{Pr})_8(\text{PrOH})_2$ [55]), BaZrO_3 ($\text{Ba}_2\text{Zr}_2(\text{OH})_2(\text{O}^i\text{Pr})_{10}(\text{PrOH})_6$ [15, 16], $\text{Ba}_2\text{Zr}_2(\text{thd})_4(\text{OPr})_8(\text{PrOH})_x$ [16]), SrZrO_3 ($\text{Sr}_2\text{Zr}_2(\text{OH})_2(\text{O}^i\text{Pr})_{10}(\text{PrOH})_4$ [16], $\text{Sr}_2\text{Zr}_2(\text{thd})_4(\text{O}^n\text{Pr})_8(\text{PrOH})_2$ [56]), and PbZrO_3 ($\text{Pb}_4\text{Zr}_4(\text{OCOR}')_8(\text{OR})_{16}(\text{ROH})_2$, where $\text{R}' = \text{C}_7\text{H}_{15}$, $\text{R} = \text{}^i\text{Pr}$, $\text{}^n\text{Bu}$ [57, 58]). An interesting approach to a powder of BaTiO_3 with application of octyl-beta-D-glucopyranoside along with postulated single source precursor barium titanium methoxyethoxide was also recently described [59]. It should, however, be mentioned that the identity of $\text{BaTi}(\text{OC}_2\text{H}_4\text{OMe})_6$ has never been proved. The only individual complex, obtained from the corresponding solutions in parent alcohol had the formula $\text{Ba}_4\text{Ti}_{13}\text{O}_{18}(\text{OR})_{24}$ [60]. Among other oxide powders produced from identified heterometallic alkoxide precursors one can also name GdFeO_3 (from $\text{Gd}_2\text{Fe}_2(\text{O}^i\text{Pr})_{13}(\text{PrOH})_2$ [61]), YAlO_3 (from $\text{Y}_2\text{Al}_2(\text{O}^i\text{Pr})_{13}(\text{PrOH})_2$ [62]) and ZnFe_2O_4 ($\text{ZnFe}_2(\text{OR})_8$, $\text{R} = \text{}^i\text{Pr}$, tBu [63]).

An attempt to prepare a series of MTi_2O_5 catalyst nanopowders for photochemical applications has been reported based on precursors with general formula $\text{MO}_2\text{Ti}_2(\text{O}^n\text{Pr})_6$, where $\text{M} = \text{Mg}$, Mn , Fe , Co , Zn , Sn [64]. The precursors were obtained via thermal condensation of metal acetates with titanium normal propoxide. The chemical individuality of these precursors is extremely doubtful. The only successfully obtained oxide with the desired composition was MgTi_2O_5 , while for the other metals the $\text{MTiO}_3/\text{TiO}_2$ composites were produced. This is extremely logical as even if the precursors are homogeneous on molecular level, the formation of the complex phases is controlled thermodynamically (*for details see Chap. 15 "Thermodynamics and Heating Processes"*). If the phase is not stable under provided conditions it cannot be obtained. That was exactly that reason that stood behind the inability of metal alkoxide sol-gel routes to produce high temperature superconductors under milder conditions: the stable phases at lower temperature in those systems were completely different and their crystallites had possibility to grow big enough to erase all the memory of the system about the molecular homogeneity in the starting point.

4.3.2 Deposition of SSP Solutions on Dense Substrates: Dense Films Through Self-Organization of MTSALs

High solubility of the solutions of mixed-ligand (heteroleptic) precursors and in many cases their essential viscosity in combination with the stabilization effect provided by the chelating ligands to the hydrolyzed solutions makes these systems attractive for direct applications in both spin-on and dip-coating deposition of films. The nature of the MTSAL particles that form in these solutions can in fact be

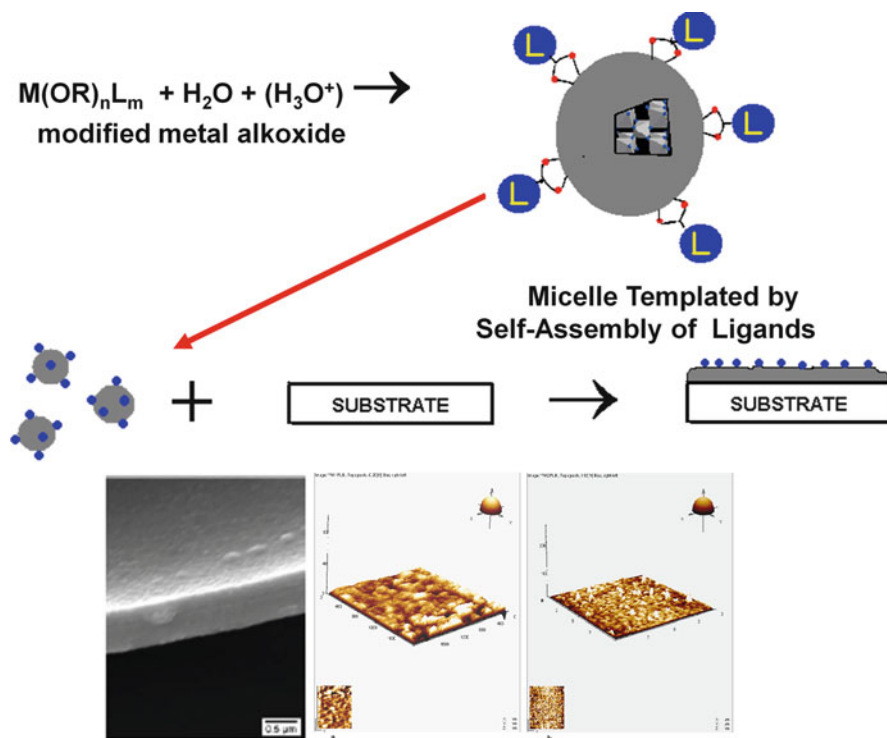


Fig. 4.9 Preparation of dense and smooth films from heteroligand SSP, exploiting the self-assembly approach. SEM and AFM images below are reproduced with permission from [36]

exploited to achieve formation of extremely dense, uniform and especially smooth films via self-assembly phenomenon. The aim of the synthesis should in this case be to facilitate the transfer of the residual ligands to the surface of the assembling layer. This can efficiently be achieved if the surface of the substrate and the molecules of the solvent have sufficiently different polarity and bonding preferences. Application of a polar surface in combination with non-polar solvent was demonstrated to be an effective tool in creation of dense and smooth coatings (see Fig. 4.9). Polar surface of aluminium oxide was successfully coated, for example, by a dense crack-free layer of $Co_3O_4/CoNb_2O_5$ oxide nanocomposite [33] and also by layers of different spinel phases [65, 66], applying alkoxide beta-diketonate precursors in toluene as solvent. Dense protective films of $NiTiO_3$ were produced also on smooth metallic surfaces, applying the solution of $Ni_2Ti_2(acac)_4(OEt)_8$ in toluene [24]. The mean square roughness of the obtained surface was in the order of magnitude of 2–4 nm. Compact multilayer films with indistinguishable single layers could be successfully produced.

An interesting example of a film for electronic applications deposited exploiting this type of approach was used for preparation of smooth and dense $LaCoO_3$ layers

on silica substrates, applying an SSP $\text{LaCo}(\text{ODiEt})_5$, where $\text{ODiEt} = \text{OC}(\text{Et})_2\text{CH}_2\text{OCH}_3$ [67]. The authors appreciated the functionality of this ligand, providing it with affinity for both more- and less polar media.

4.3.3 Deposition of SSP Solutions on Porous Substrates: Synthesis of Membrane and Nanocomposite Films

Control of porosity in application of organic precursors represents one of the major challenges in the deposition of coatings in general and especially in the solution deposition approaches, as the solvent has to be removed in this case from the forming gels of particles that are strongly interacting with it and in addition are often hydrated. The problems associated with cracking are treated separately in this book, but within the present chapter some general considerations concerning the chemically introduced porosity will be presented.

The MTSAL origin of the particles, interacting to form a coating, provides some general trends that could not really be anticipated in the earlier applied concepts of polymeric sol-gel processes. The absence of inherent porosity within the MTSAL, constructed as dense polyoxometallate cores, leads to formation in the films, deposited from sols, of either completely dense coatings, lacking porosity (such as those described in Sect. 4.3.2, see Fig. 4.9) through complete coalescence of the particles, or to areas with partly closed wormhole type mesoporosity (see Fig. 4.5b). Macroporosity is often introduced in parallel by cracking. The controlled formation of continuous microporous structure of metal oxides represents one of the major goals in creation of membrane materials.

Creation of reproducible microporosity requires application of precursors able to resist to the transfer of ligands at least partially, so that the residual ligands will be removed already after the formation of a dense layer through surface interactions between the particles. The solution to this problem was thought in introduction of ligands able to act as both chelating and bridging ones, so that their transfer to the surface of the particle will be associated with at least the activation energy connected with their bridging function. One of the structurally best studied examples is the modification of zirconium or zirconium and titanium alkoxides in combination with diethanolamine [68, 69]. The precursors demonstrate in this case a trend to transform into molecular species with the chelating-and-bridging ligands associated to a metal atom inside the precursor molecule, and not on its surface (see Fig. 4.10), which resulted in a reproducible synthesis of membrane materials with controlled microporosity [50].

Another, technically simpler but based on same idea approach has been realized via application of zirconium alkoxide sols modified by acetic acid (small carboxylate as chelating-and-bridging ligand) in n-hexanol (long chain alkoxide—good surface ligand for MTSAL-stabilization). The details of the permeability and the technical characteristics of industrially produced materials are reported in [70].

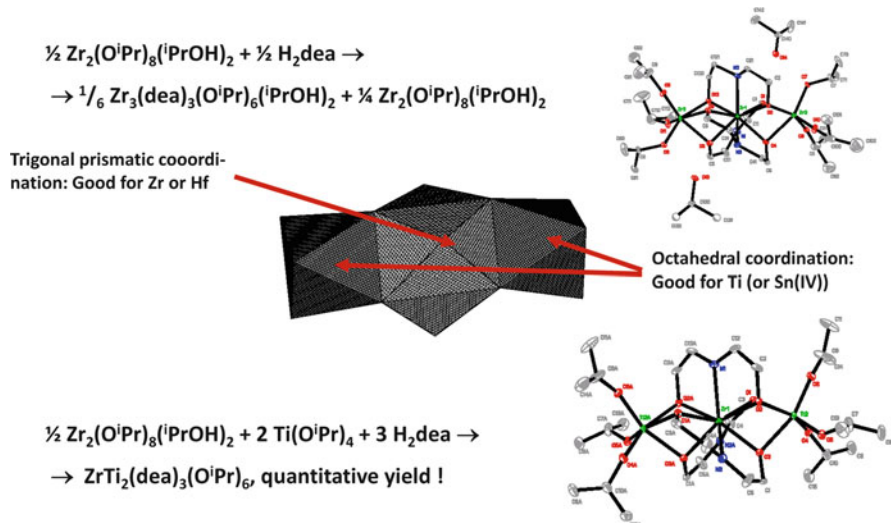


Fig. 4.10 Molecular design approach to precursors of microporous membrane materials: chelating-and-bridging ligand is locked within the precursor molecule

4.4 Molecular Design of Complex Alkoxide Precursors

Theoretical approaches to purposeful construction of heterometallic and/or heteroleptic alkoxides represent at present a relatively well established domain in crystallographic research [71, 72]. In the view of predominantly electrostatic interaction in the core of metal alkoxide complexes, the construction of a new complex has to follow in a modified form the general principles, proposed by V.M. Goldschmidt for the description and design of ionic inorganic solids [73]: the structures should follow for a chosen composition one of the possible structure types, which stability is provided by the size relationship between the cations and anions. For metal alkoxide complexes it means that for design of a new structure one has to choose a structure type possible for the desired cation stoichiometry and complete it by ligands, providing both the necessary number of donor atoms for the chosen structure and also the necessary sterical protection of the core. The proposed approach is illustrated by Fig. 4.11.

The application of the concept can be demonstrated on a number of examples already reported in literature. If, for instance, a precursor for a $\text{M}^{\text{II}}\text{M}^{\text{IV}}\text{O}_3$ phase is sought, the most logical is to choose the M_4O_{16} structure type (tetramolybdate one) as it is even the most wide-spread in the metal alkoxide structure chemistry and permits to incorporate two pairs of different metal atoms in the same molecule. The sum of formal positive charges, corresponding to the possible number of monodentate alkoxide ligands is in this case $2 \times 2 + 2 \times 4 = 12$, i.e. only 12 oxygen atoms of 16 are available. To be sure that this structure type is realised, we need actually four more donor oxygen atoms to be added. This can be achieved via use of

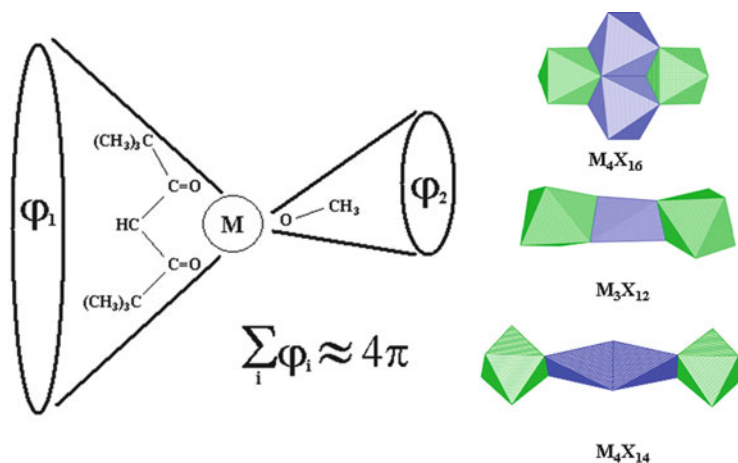


Fig. 4.11 Molecular structure design concept, the principle and the most widespread structure types. The requirement on the ligands is that they in combination have to cover all the space (4π radian) around each metal atom and fit at the same time an arrangement of coordination polyhedrons preset by the structure type

four single-charged chelating bi-dentate ligands, instead of the monodentate alkoxide ones. How these ligands are provided is not really important in the view of the electrostatic (ionic) bonding in the alkoxide molecules. In the first example, where this approach was implemented, 4 equivalents of a beta-diketone 2,2,6,6-tetramethyl-heptanedione, Hthd were added to a solution of 2 eq. of $Ba(OEt)_2$ and 2 eq. of $Ti(OEt)_4$ in toluene-ethanol mixture, resulting in quantitative formation of $Ba_2Ti_2(thd)_4(OEt)_8(EtOH)_2$ [5], belonging as expected to the M_4O_{16} structure type. For smaller cations than Ba or Sr, such as the late transition ones, e.g. Mn(II), Ni, Co, Zn, and even for Mg(II) much smaller beta-diketonate ligands such as acac-ones can be used. The advantage is that in this case the acac-derivatives of M(II) can be used as starting reagents. Thus $Ni_2Ti_2(acac)_4(OEt)_8$ has been produced for both sol-gel [24] and even MOCVD applications [74].

The complexes of 1:2 composition, derived from a late transition metal and an early transition metal can be produced starting with the M_3O_{12} structure type (see Figs. 4.11 and 4.12). For a combination of a M(II) with two M(IV) atoms the sum of the formal positive charges is $2 + 2 \times 4 = 10$, which means that two oxygen atoms are missing. The desired precursors can then be produced starting from a $M(acac)_2$ salt to be reacted with 2 eq. of $M(OR)_4$ alkoxide. If a complex of one M(II) and two M(V) atoms is desired, it can already be obtained without any chelating ligands as the sum of the formal positive charges, $2 + 2 \times 5 = 12$. An attractive simple synthetic approach in this case can be to add 2 additional eq. of $M(OR)_5$ to remove the excessive acac-ligands from the reaction mixture.

When an aluminate spinel precursor with this structure type has to be prepared, the sum of the formal positive charges is only $2 + 2 \times 3 = 8$, which means that

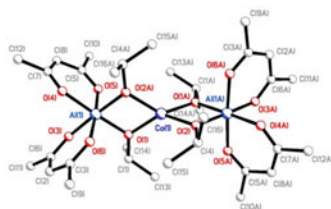
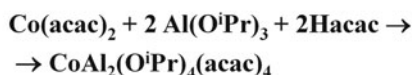
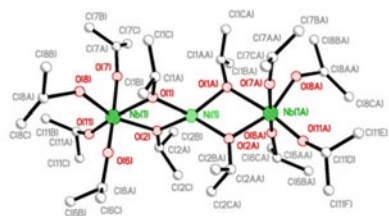
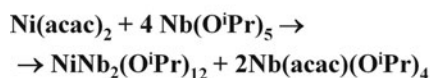
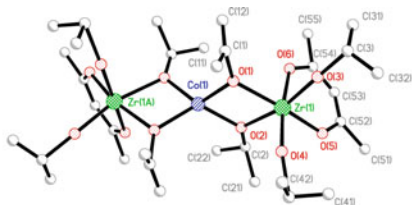
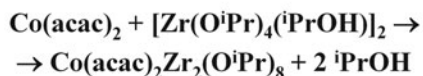


Fig. 4.12 Molecular structure design concept application for the synthesis of SSP with 1:2 composition derived from a late and an early transition metal

even the use of a $\text{M}(\text{acac})_2$ reagent will require then addition of 2 extra equivalent of Hacac. When the stoichiometry is followed, the formation of a precursor with desired structure, $\text{MAl}_2(\text{acac})_4(\text{OR})_4$, occurs again with quantitative yields [75].

4.5 Conclusions and Prospects

One can definitely put forward at this point a question in what circumstances the application of single-source precursors is distinctly justified, more favourable than simply the optimization of deposition conditions? It has been clearly demonstrated that the use of such complex precursors does not guarantee formation of a desired phase, because the precursor itself is destroyed in a coordination equilibrium producing primary colloid particles, MTSALs. The use of single-source compounds can be a mere simplification of otherwise challenging handling of homometallic precursor components and there is quite a library of such compounds available commercially.

The most attractive prospect in the use of complex heterometallic molecules emerges, however, with intensifying research in the fields of luminescent (and especially LED) materials and oxide matrices for dye-sensitized solar cells. These products are possessing rather complex compositions and set strong requirements on the uniformity of distribution of dopants in the volume of the corresponding (nano)powders and ceramics. It is also clear that the non-hydrolytic approach, the Bradley reaction, is winning terrain in the production of such materials. Setting together analogous heterometallic molecules with essentially the same thermodynamics and kinetics of solution transformations offers a superior approach to complex oxides with uniform distribution of the dopants. The first successful application of this principle has been demonstrated in the preparation of Eu-doped BaTiO₃ [55], produced hydrolytically from Ba₂Ti₂(thd)₄(OEt)₈(EtOH)₂ in combination with Eu₂Ti₂(thd)₄(OEt)₁₀, and in the non-hydrolytic synthesis of Nd-doped LaAlO₃ NIR nanophosphors from Ln₂Al₂(OⁱPr)₁₂(ⁱPrOH)₂, Ln = La, Nd [47].

References

1. Mazdiyasi KS, Dolloff RT, Smith JS II (1969) Preparation of high-purity submicron barium titanate powders. *J Am Ceram Soc* 52:523
2. Graham HC, Tallan NM, Mazdiyasi KS (1971) Electrical properties of high-purity polycrystalline barium titanate. *J Am Ceram Soc* 54:548
3. Schulz S (2002) In: Mingos DMP (ed) *Structure and bonding*, vol 103. Springer, Berlin, p 118
4. Turova NY, Turevskaya EP, Kessler VG, Yanovskaya MI (1994) Oxoalkoxides – true precursors of complex oxides. *J Sol-Gel Sci Technol* 2:17
5. Kessler VG, Hubert-Pfalzgraf LG, Daniele S, Gleizes A (1994) Single-source precursors for BaTiO₃: synthesis and characterization of β-diketonato alkoxides and molecular structure of Ba₂Ti₂(thd)₄(μ₃-OEt)₂(μ-OEt)₄(OEt)₂(EtOH)₂. *Chem Mater* 6:2336
6. Ribot F, Toledano P, Sanchez C (1991) Hydrolysis-condensation process of beta-diketonates-modified cerium(IV) isopropoxide. *Chem Mater* 3:759–765
7. Livage J, Henry M, Sanchez C (1988) Sol-gel chemistry of transition metal oxides. *Progr Solid State Chem* 18:259–341
8. Sanchez C, Livage J (1990) Sol-gel chemistry from metal alkoxide precursors. *New J Chem* 14:513
9. Livage J, Sanchez C (1992) Sol-gel chemistry. *J Non-Cryst Solids* 145:11
10. Sanchez C, Livage J, Henry M, Babonneau F (1988) Chemical modification of alkoxide precursors. *J Non-Cryst Solids* 100:65–76
11. Babonneau F, Doeff S, Leautic A, Sanchez C, Cartier C, Verdagner M (1988) XANES and EXAFS study of titanium alkoxides. *Inorg Chem* 27:3166–3172
12. Fric H, Puchberger M, Schubert U (2006) Coordination of mono- and diamines to titanium and zirconium alkoxides. *J Sol-Gel Sci Technol* 40:155–162
13. Senouci A, Yaakouyb M, Huguenard C, Henry M (2004) Molecular templating using titanium (IV) (oxo)alkoxides and titanium(IV) (oxo)aryloxides. *J Mater Chem* 14:3215–3230
14. Spijksma GI, Seisenbaeva GA, Kessler VG, Blank DHA, Bouwmeester HJM, Fischer A (2009) The molecular composition of non-modified and acac-modified propoxide and butoxide precursors of zirconium and hafnium dioxides. *J Sol-Gel Sci Technol* 51:10–22

15. Evans WJ, Ansari MA, Ziller JW (1998) Isolation and structural characterization of the polymetallic zirconium alkoxide complexes, $Zr_3O(OCH_2CMe_3)_9Cl$, $Zr_3O(OCMe_3)_9(OH)$, and $Na_4Zr_6O_2(OEt)_{24}$. *Polyhedron* 17:869–877
16. Turova NY, Turevskaya EP, Kessler VG, Yanovskaya AI (2002) The chemistry of metal alkoxides. Kluwer AP, Boston
17. Veith M, Mathur S, Huch V, Decker T (1998) Tuning metal stoichiometry in heterometal alkoxides: first structurally characterised molecular precursor to $BaZrO_3$. *Eur J Inorg Chem* 1998:1327
18. Seisenbaeva GA, Gohil S, Kessler VG (2004) Influence of heteroligands on the composition, structure and properties of homo- and heterometallic zirconium alkoxides. Decisive role of thermodynamic factors in their self-assembly. *J Mater Chem* 14:3177
19. Yanovsky AI, Yanovskaya MI, Limar VK, Kessler VG, Turova NY, Struchkov YT (1991) Synthesis and crystal structure of the double barium-titanium isopropoxide $[Ba_4Ti_4(\mu_4-O)_4(\mu_3-OR)_8(OR)_6(ROH)_4][Ba_4Ti_4(\mu_4-O)_4(\mu_3-OR)_2(\mu-OR)_9(OR)_5(ROH)_3]$. *J Chem Soc Chem Commun* 1991(22):1605
20. Pope MT (1983) Heteropoly and isopoly oxometalates, vol 8, Inorganic chemistry concepts. Springer, Hamburg
21. Seisenbaeva GA, Baranov AI, Shcheglov PA, Kessler VG (2004) Isolation, X-ray single crystal and theoretical study of quinquivalent metal oxoisopropoxides, $Nb_6O_8(^iPrO)_{14}(^iPrOH)_2$ and $Re_4O_6(O^iPr)_{10}$. *Inorg Chim Acta* 357:468
22. Gigant K, Rammal A, Henry M (2001) Synthesis and molecular structures of some new titanium(IV) aryloxides. *J Am Chem Soc* 123:11632
23. Seisenbaeva GA, Suslova EV, Kritikos M, Kessler VG, Rapenne L, Andrieux M, Chassagneux F, Parola S (2004) Purposeful construction versus self-assembly in approaches to single source precursors of spinel materials. Synthesis, structure and stability studies of $M^{II}A_{12}(acac)_3(O^iPr)_4(OAc)$, $M^{II} = Mn, Co, Zn$ – a new class of heterometallic heteroleptic alkoxide complexes. *J Mater Chem* 14:3150
24. Wengrovius JH, Garbaskas MF, Williams EA, Going RC, Donahue PE, Smith JF (1986) Aluminum alkoxide chemistry revisited: synthesis, structures, and characterization of several aluminum alkoxide and siloxide complexes. *J Am Chem Soc* 108:982
25. Spijksma GI, Bouwmeester HJM, Blank DHA, Fischer A, Henry M, Kessler VG (2006) Chemistry of 2,2,6,6-tetramethyl-3,5-heptanedione (Hthd) modification of zirconium and hafnium propoxide precursors. *Inorg Chem* 45:4938
26. Donat M, Seisenbaeva GA, Kessler VG (2008) Synthesis of highly sterically hindered niobium and tantalum alkoxides and their microhydrolysis in strongly basic medium. *J Sol-Gel Sci Technol* 48:61
27. Kessler VG, Spijksma GI, Seisenbaeva GA, Håkansson S, Blank DHA, Bouwmeester HJM (2006) New insight in the role of modifying ligands in the sol-gel processing of metal alkoxide precursor: a possibility to approach new classes of materials. *J Sol-Gel Sci Technol* 40:163
28. Fortner KC, Bigi JP, Brown SN (2005) Six-coordinate titanium complexes of a tripodal aminetris(phenoxide) ligand: synthesis, structure, and dynamics. *Inorg Chem* 44:2803
29. Boulmaâz S, Papiernik R, Hubert-Pfalzgraf LG, Septe B, Vaissermann J (1997) Chemical routes to oxides: alkoxide vs. alkoxide–acetate routes: synthesis, characterization, reactivity and polycondensation of $MNb_2(OAc)_2(OPr^i)_{10}$ ($M = Mg, Cd, Pb$) species. *J Mater Chem* 7:2053
30. Mueller A, Krickemeyer E, Boegge H, Schmidtman M, Peters F, Menke C, Meyer J (1997) An unusual polyoxomolybdate: giant wheels linked to chains. *Angew Chem Int Ed* 36:484
31. Mueller A, Krickemeyer E, Boegge H, Schmidtman M, Beugholt M, Das SK, Peters F (1999) Giant ring-shaped building blocks linked to form a layered cluster network with nanosized channels: $[Mo_{124}^{VI}Mo_{28}^V O_{429}(\mu_3-O)_{28}H_{14}(H_2O)_{66.5}]^{16-}$. *Chem Eur J* 5:1496
32. Mueller A, Shah SQN, Boegge H, Schmidtman M (1999) Molecular growth from a Mo_{176} to a Mo_{248} cluster. *Nature* 397:48

33. Mueller A, Das SK, Fedin VP, Krickemeyer E, Beugholt C, Boegge H, Schmidtman M, Hauptfleisch B (1999) Rapid and simple isolation of the crystalline molybdenum-blue compounds with discrete and linked nanosized ring-shaped anions: $\text{Na}_{15}[\text{Mo}^{\text{VI}}_{126}\text{Mo}^{\text{V}}_{28}\text{O}_{462}\text{H}_{14}(\text{H}_2\text{O})_{70}]_{0.5}$ $[\text{Mo}^{\text{VI}}_{124}\text{Mo}^{\text{V}}_{28}\text{O}_{457}\text{H}_{14}(\text{H}_2\text{O})_{68}]_{0.5}$ ca. 400 H_2O and $\text{Na}_{22}[\text{Mo}^{\text{VI}}_{118}\text{Mo}^{\text{V}}_{28}\text{O}_{442}\text{H}_{14}(\text{H}_2\text{O})_{58}]$ ca. 250 H_2O . *Z Anorg Allg Chem* 625:1187
34. Muller A, Todea AM, Boegge H, van Slageren J, Dressel M, Stammler A, Rusu M (2006) Formation of a “less stable” polyanion directed and protected by electrophilic internal surface functionalities of a capsule in growth: $[\{\text{Mo}_6\text{O}_{19}\}^{2-} \subset \{\text{Mo}^{\text{VI}}_{72}\text{Fe}^{\text{III}}_{30}\text{O}_{252}(\text{ac})_{20}(\text{H}_2\text{O})_{92}\}]^{4-}$. *Chem Commun* 29:3066
35. Goutailler G, Guillard C, Daniele S, Hubert-Pfalzgraf LG (2003) Low temperature and aqueous sol–gel deposit of photocatalytic active nanoparticulate TiO_2 . *J Mater Chem* 13:342
36. Werndrup P, Verdenelli M, Chassagneux F, Parola S, Kessler VG (2004) Powders and dense thin films of late transition metal oxide nanocomposites from structurally characterized single-source precursors. *J Mater Chem* 14:344
37. Kessler G, Seisenbaeva GA, Unell M, Håkansson S (2008) Chemically triggered biodelivery using metal-organic sol-gel synthesis. *Angew Chem* 47:8506
38. Lundqvist MJ, Nilsing M, Persson P, Lunell S (2006) DFT study of bare and dye-sensitized TiO_2 clusters and nanocrystals. *Int J Quantum Chem* 106:3214
39. Persson P, Gebhardt JCM, Lunell S (2003) The smallest possible nanocrystals of semiionic oxides. *J Phys Chem B* 107:3336
40. Uddin MJ, Cesano F, Bonino F, Bordiga S, Spoto G, Scarano D, Zecchina A (2007) Photoactive TiO_2 films on cellulose fibres: synthesis and characterization. *J Photochem Photobiol A* 189:286
41. Pati RK, Lee IC, Gaskell KJ, Ehrman SH (2009) Precipitation of nanocrystalline CeO_2 using triethanolamine. *Langmuir* 25:67
42. Epifani M, Andreu T, Magana CR, Arbiol J, Siciliano P, D’Arienzo M, Scotti R, Morazzoni F, Morante JR (2009) The chloroalkoxide route to transition metal oxides. Synthesis of V_2O_5 thin films and powders from a vanadium chloromethoxide. *Chem Mater* 21:1618
43. Epifani M, Pellicer E, Arbiol J, Morante JR (2009) Metal oxide nanocrystals from the injection of metal oxide sols in a coordinating environment: principles, applicability, and investigation of the synthesis variables in the case study of CeO_2 and SnO_2 . *Chem Mater* 21:862
44. Bradley DC, Chakravarti BN, Chatterjee AK (1958) Niobium and tantalum mixed alkoxides. *J Chem Soc* 1958:99
45. Kessler VG, Nikitin KV, Belokon’ AI (1998) A new argument in favor of the ether elimination mechanism: formation of acetals on action of molybdenum alkoxides on carbonyl compounds. *Polyhedron* 17:2309
46. Kessler VG, Seisenbaeva GA, Pazik R, Strek W (2008) Heteroleptic metal alkoxide “oxoclusters” as molecular models for the sol–gel synthesis of perovskite nanoparticles for bio-imaging applications. *Dalton Trans* 26:3412
47. Pazik R, Seisenbaeva GA, Gohil S, Wiglusz R, Kepinski L, Strek W, Kessler VG (2010) Simple and efficient synthesis of a Nd:LaAlO₃ NIR nanophosphor from rare earth alkoxo-monoaluminates $\text{Ln}_2\text{Al}_2(\text{O}^i\text{Pr})_{12}(\text{}^i\text{PrOH})_2$ single source precursors by Bradley reaction. *Inorg Chem* 49:2684
48. Jensen GV, Bremholm M, Lock N, Deen GR, Jensen TR, Iversen BB, Niederberger M, Pedersen JS, Birkedal H (2010) Anisotropic crystal growth kinetics of anatase TiO_2 nanoparticles synthesized in a nonaqueous medium. *Chem Mater* 22:6044
49. Westin G, Wijk M, Moustiakimov M, Kritikos M (1998) Alkoxide precursors for Er-containing glasses and ceramics. *J Sol-Gel Sci Technol* 13:125
50. Spijksma GI, Huiskes C, Benes NE, Kruidhof H, Blank DHA, Kessler VG, Bouwmeester HJM (2006) Microporous zirconia-titania composite membranes derived from diethanolamine-modified precursors. *Adv Mater* 18:2165
51. Yanovskaya MI, Turevskaya EP, Kessler VG, Obvintseva IE, Turova NY (1992) Application of metal alkoxides in the synthesis of oxides. *Integr Ferroelectrics* 1:343

52. Kirby KW (1988) Alkoxide synthesis techniques for BaTiO₃. *Mater Res Bull* 23:881
53. Solayappan N, Joshi V, DeVilbiss A, Bacon J, Cuchiario J, McMillan LD, Paz de Araujo CA (1998) Chemical solution deposition (CSD) and characterization of ferroelectric and dielectric thin films. ISIF Monterey. <http://www.symetrixcorp.com/Pub009.pdf>. Accessed 4 Mar 1998
54. Katayama S, Yoshinaga I, Yamada N, Nagai T (1996) Low-temperature synthesis of Ba(Mg_{1/3}Ta_{2/3})O₃ ceramics from Ba-Mg-Ta alkoxide precursor. *J Am Ceram Soc* 79:2059
55. Paźik R, Hreniak D, Stręk W, Kessler VG, Seisenbaeva GA (2008) Photoluminescence investigations of Eu³⁺ doped BaTiO₃ nanopowders fabricated using heterometallic tetranuclear alkoxide complexes. *J Alloys Comp* 451:557
56. Andrieux M, Gasquères C, Legros C, Gallet I, Herbst-Ghysel M, Condat M, Kessler VG, Seisenbaeva GA, Heintz O, Poissonnet S (2007) Perovskite thin films grown by direct liquid injection MOCVD. *Appl Surf Sci* 253:9091
57. Brethon A, Hubert-Pfalzgraf LG, Daran JC (2006) Interplay between lead carboxylate and Ti or Zr isopropoxides in solution routes to perovskites: synthesis, molecular structures and reactivity of single source non-oxo Pb–Zr and Pb–Ti carboxylatoalkoxides supported by 2-ethylhexanoate ligands. *Dalton Trans* 1:250
58. Brethon A, Hubert-Pfalzgraf LG (2006) Influence of the lead carboxylate on the molecular composition of its solutions with zirconium and titanium isopropoxides or *n*-butoxides: 2-ethylhexanoate vs acetate, a way to stabilize the first Pb–Zr carboxylatoalkoxides of 1:1 stoichiometry. *J Sol-Gel Sci Technol* 39:159
59. Chaudhary YS, Bhatta UM, Khushalani D (2008) Octyl-β-D-glucopyranoside mediated synthesis of nanocrystalline BaTiO₃ using a single-source precursor. *J Mater Res* 23:842
60. Campion JF, Payne DA, Chae HK, Mauria JK, Wilsoa SR (1991) Synthesis of bimetallic barium titanium alkoxides as precursors for electrical ceramics. Molecular structure of the new barium titanium oxide alkoxide Ba₄Ti₁₃(μ₃-O)₁₂(μ₅-O)₆(μ₁-η¹-OCH₂CH₂OCH₃)₁₂(μ₁, μ₃-η²-OCH₂CH₂OCH₃)₁₂. *Inorg Chem* 30:3244
61. Mathur S, Shen H, Lecerf N, Kjekshus A, Fjellvåg H, Goya GF (2002) Nanocrystalline orthoferrite GdFeO₃ from a novel heterobimetallic precursor. *Adv Mater* 14:1405
62. Mathur S, Shen H, Rapalaviciute R, Kareiva A, Donia N (2004) Kinetically controlled synthesis of metastable YAlO₃ through molecular level design. *J Mater Chem* 14:3259
63. Veith M, Haas M, Huch V (2005) Single source precursor approach for the sol – gel synthesis of nanocrystalline ZnFe₂O₄ and zinc – iron oxide composites. *Chem Mater* 17:95
64. Kapoor PN, Uma S, Rodriguez S, Klabunde K (2005) Aerogel processing of MTi₂O₅ (M = Mg, Mn, Fe, Co, Zn, Sn) compositions using single source precursors: synthesis, characterization and photocatalytic behavior. *J Mol Catal A* 229:145
65. Seisenbaeva GA, Suslova EV, Kritikos M, Rapenne L, Andrieux M, Chassagneux F, Parola S, Kessler VG (2004) Purposeful construction versus self-assembly in approaches to single source precursors of spinel materials. Synthesis, structure and stability studies of M^{II}A₁₂(acac)₃(OiPr)₄(OAc), M^{II} = Mn, Co, Zn – a new class of heterometallic heteroleptic alkoxide complexes. *J Mater Chem* 14:3150
66. Parola S, Seisenbaeva GA, Kessler VG (2004) Preparation of powders and films of NiAl₂O₄ spinel from a structurally characterized molecular precursor, NiAl₂(acac)₄(OiPr)₄. *J Sol-Gel Sci Technol* 31:63
67. Armelao L, Bottaro G, Crociani L, Seraglia R, Tondello E, Zanella P (2008) A versatile single-source precursor for the synthesis of LaCoO₃ films. *Mater Lett* 62:1179
68. Spijksma GI, Bouwmeester HJM, Blank DHA, Kessler VG (2004) Molecular design approach to a stable heterometallic zirconium-titanium alkoxide – potential precursor of mixed-oxide ceramics. *Inorg Chem Comm* 7:953
69. Spijksma GI, Kloof L, Bouwmeester HJM, Blank DHA, Kessler VG (2007) Nona-coordinated MO₆N₃ centers M = Zr, Hf as a stable building block for the construction of heterometallic alkoxide precursors. *Inorg Chim Acta* 360:2045
70. Kreiter R, Rietkerk MDA, Bonekamp BC, van Veen HM, Kessler VG, Vente JF (2008) Sol-gel routes for microporous zirconia and titania membranes. *J Sol-Gel Sci Technol* 48:203

71. Kessler VG (2003) Molecular structure design and synthetic approaches to the heterometallic alkoxide complexes (soft chemistry approach to inorganic materials by the eyes of a crystallographer). *Chem Commun* 1213
72. Kessler VG (2004) Geometrical molecular structure design concept in approach to homo- and heterometallic precursors of advanced materials in sol-gel technology. *J Sol-Gel Sci Technol* 32:11
73. Goldschmidt VM (1935) *Ind Eng Chem* 27:45
74. Tahir AA, Mazhar M, Hamid M, Wijayantha KGU, Molloy KC (2009) Photooxidation of water by NiTiO₃ deposited from single source precursor [Ni₂Ti₂(OEt)₂(μ-OEt)₆(acac)₄] by AACVD. *Dalton Trans* 19:3674
75. Kessler VG, Gohil S, Parola S (2003) Interaction of some divalent metal acetylacetonates with Al, Ti, Nb and Ta isopropoxides. Factors influencing the formation and stability of heterometallic alkoxide complexes. *Dalton* 4:544

Chapter 5

Aqueous Precursor Systems

Marlies K. Van Bael, An Hardy, and Jules Mullens

5.1 Introduction

One of the main advantages of chemical solution deposition of multimetal oxide films is the ability to preserve chemical homogeneity throughout the whole synthesis process. Maintaining a molecular scale mixing of the metal ions in the precursor solution and all further steps involved in the CSD process, is a scientific challenge requiring control over chemical reactions and physical phenomena during each of the different steps, being [1] selection of precursors, solution processes, coating, gel formation, removal of organic species and crystallisation. A relatively uncommon CSD method involves the deposition of water based solutions with carboxylate complexes as the metal ion precursors. While ceramic powder synthesis by means of aqueous metal carboxylate based sol-gel processes is being reported already more than two decades ago, e.g. in [2–10] the deposition of aqueous carboxylate solutions to form metal oxide films is only being fully explored since about 10 years, due to wetting issues. In the past decade, it has been demonstrated that aqueous chemical solution deposition of thin precursor films on top of an adequate substrate can produce functional electroceramic layers with a thickness between a few and a few hundreds of nanometers and with properties comparable to those obtained by more conventional deposition techniques. This chapter will discuss and review water based CSD of thin electronic oxide films from carboxylate based precursors. The economic and ecological advantages of water based deposition methods are very appealing. Water based deposition processes meet the current environmental awareness restricting the use of ecologically harmful substances and processes. Since water is used as a solvent, instead of the often used teratogenic

M.K. Van Bael (✉) • A. Hardy • J. Mullens
Inorganic and Physical Chemistry, Institute for Materials Research, Universiteit Hasselt,
Martelarenlaan 42, B-3500 Hasselt, Belgium

IMEC, Leuven, Belgium
e-mail: marlies.vanbael@uhasselt.be

etheralcohols (e.g. methoxy-ethanol), the aqueous solution-gel synthesis can be considered healthier, safer and environmentally friendlier. Besides the absence of hazardous solvents, the simple and inexpensive synthesis- and deposition equipment is an additional asset. Unlike several conventionally used metal alkoxide based precursors, the water based precursor solutions are insensitive to ambient moisture. Therefore, an inert atmosphere to store and handle precursor solutions, e.g. the use of a nitrogen flushed glove box or Schlenk apparatus, is not a necessity. However very attractive, this 'new' CSD method had to deal with typical scientific and technological obstacles. The strategy to mitigate these obstacles will constitute the main part of this chapter.

First of all, the selection or development of water soluble precursors, especially when high valent metal ions are involved, in a chemical environment suitable for gel formation, has been and still is a real chemical challenge. A second obstacle, namely the difficulty to deposit homogeneous thin layers of water based precursor solutions onto typically silicon wafer based substrates is related with wetting incompatibilities.

In spite of these challenges, in the past 10 years water based precursor chemistry, deposition and film formation have been thoroughly studied and our insight in the mechanisms and possibilities has steadily increased. Most recent literature examples report on the deposition of films of various materials with control over morphology and properties. Even ultrathin layers (below 10 nm) and nanostructured layers are now being deposited by means of water based chemical solution deposition [11–17].

Before going into the different aspects of aqueous CSD or sol-gel deposition with carboxylate precursors, we will take a deeper look into the chemistry of metal ions in water. In Sect. 5.2, a brief overview of the behavior of metal ions and precursor complexes will demonstrate that it is far from evident to synthesize stable water based solutions of metal ions suitable for gel formation and CSD. However, insight in the basics of the chemistry involved, together with a pragmatic experimental approach allows a successful synthesis of precursor solutions. These aspects are discussed in Sect. 5.3 where we will give further details about the gel formation mechanism and its chemical structure. From this knowledge we can then assess the most important aspects of suitable water based precursor systems.

In Sect. 5.4 the decomposition mechanism of gels formed by the most commonly applied citrato(peroxo) complexes will be discussed together with possible routes towards the so undesired phase segregation. The film deposition of water based carboxylate precursors is discussed in Sect. 5.5. Besides the difficulty of preparing stable water based solutions, the second most demanding challenge concerns indeed the problematic wetting of water based solutions. Various ways to tackle this problem are described. In the following paragraphs, the potential and the possibilities of the aqueous carboxylate based CSD method from the field of electroceramic thin films is demonstrated and exemplified by means of concrete examples from our own work and from related work reported in literature. Film properties can be drastically optimised by means of controlling all different

processing steps. Finally, although the conviction existed that it was practically impossible to deposit uniform metal oxide films with a thickness far below 100 nm using chemical solution deposition, insights built-up during a decade of aqueous CSD research have led to the realization of ultrathin metal oxide layers, from 30 to 3 nm in thickness as reported in Sect. 5.5.6.

Aqueous CSD can therefore be considered as a fairly mature technique enabling the deposition of oxide layers for state of the art applications and providing a means for the fast screening of highly advanced materials systems and processes [18–20].

5.2 Metal Ions in Water

The start, and also one of the most challenging steps in aqueous carboxylate-based sol-gel synthesis of either powders or films, is the preparation of a water based start solution in which all metal ions are stably dissolved. Especially in the case of highly valent metal ions, this can be a very tough task. In order to synthesize water based precursor solutions, it is therefore of high importance that aqueous chemistry of metal ions is understood. A brief summary of the behavior of metal ions in water, in the frame of synthesizing carboxylate precursors for CSD is presented here. Based on the insights of the behavior of metal ions in water, appropriate precursors for sol-gel synthesis, allowing gel formation can be synthesized.

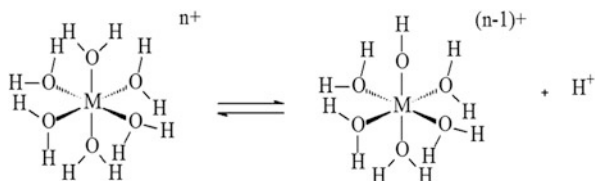
5.2.1 Solvation and Hydrolysis

Metal ions in water will undergo solvation (Fig. 5.1), followed by hydrolysis and condensation depending on the physicochemical circumstances of the solvent and the chemical properties of the metal ion. Whether a metal ion is ‘soluble’ in water or hydrolyses and precipitates, depends on the degree in which these reactions occur, which varies according to the metal ion.

In order to be able to discuss the carboxylate based aqueous chemical solution deposition method, and understand the chemistry behind this method, it is worthwhile to briefly overview the behavior of metal ions in water. For an elaborated discussion, we refer to some excellent instructive works presented in [21–23].

When a metal salt dissociates in water, the cation M^{n+} is initially solvated by water molecules. The number of solvating water molecules and the bond type depend basically on the polarizing strength (z/r^2) of the metal ion. Small-size, high-charge cations have strong electrostatic interactions with water, demonstrated by a high hydration energy and a well defined structural geometry. In the case of divalent and trivalent first row transition cations, these hydrated cations can be considered as true coordination complexes with six water molecules acting as σ -donating ligands.

Fig. 5.1 Schematic representation of a solvated cation and hydrolysis reaction

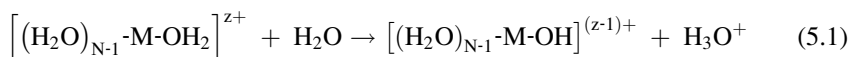


Reference works such as [24] and [21] comprehensively describe the thermochemistry of ion-solvent coordination interactions.

Small-size and small-charge cations, such as those of alkali metals, exhibit relatively weak electrostatic interactions with the surrounding solvating water molecules. As the charge of the cation increases, the electrostatic interaction with the water molecules becomes more strong. As a consequence of the high polarisability of high-charge and small-size cations, electron transfer from the molecular orbitals of the water molecules towards empty or partially filled (d-) orbitals of the metal ion will take place. The solvating water molecules can then be considered as true aqua ligands, due to the coordination type bonding with a strong covalent character.

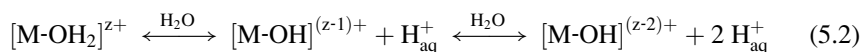
Metal ions with higher charges will exhibit a more complicated behavior in water, as the charge transfer from water molecules towards the metal ion will reduce the electron density in the bonding orbital of water, and therefore weaken the O-H bond. As a result, the solvated water molecules become more acidic than those of the surrounding solvent molecules and tend to release a proton (see Fig. 5.2).

This process, where a proton from a solvating water molecule is released, is called **hydrolysis** and can be represented by the following equation:



As a consequence of the hydrolysis reaction, aqua -OH₂ ligands become hydroxo -OH ligands, and the charge of the solvated complex is reduced, whereby also the positive charge on the metal ion decreases.

The higher the valency of the metal ion, the more charge is transferred from the water orbitals to the metal ion and the further the hydrolysis can proceed whereby even oxo -O ligands become possible. Hence, depending on the degree of hydrolysis, which is a consequence of the degree of charge transfer, three types of ligands can coordinate the metal ion, as is represented in the equation below:



Or, for metal ions with a coordination number of N (only the first equilibrium is presented):

Fig. 5.2 Protons of the aqua ligand become more acid as charge is transferred towards the metal ion

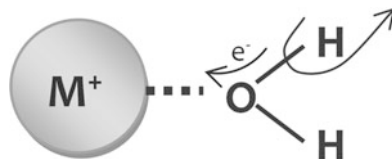
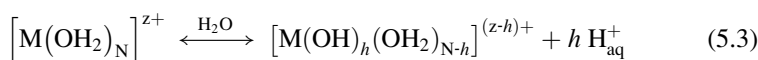
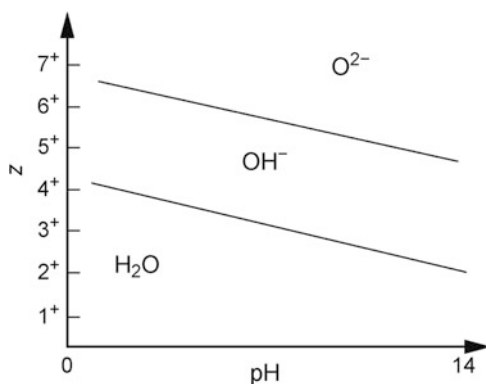


Fig. 5.3 Empirical charge (z) versus pH diagram after Jorgensen [25] from which domains for aqua-, hydroxo- and oxo- ligands can be distinguished



Whereby h is called the hydrolysis ratio.

Since these hydrolysis equilibria are essentially acid-base equilibria, they can be somehow displaced by changing the acidity of the surrounding medium. C. K. Jorgensen [25] has empirically determined the nature of the ligands coordinating a cation depending on its charge z and the pH of the medium (Fig. 5.3). This schematic can be used as a first guide to predict which species could be present in water at a certain pH. For example, it can be seen that high valent cations ($z > 4$) give rise to oxo-complexes in a basic environment. In less basic circumstances, oxo-hydroxo-anions are being formed. Tetravalent metal ions, such as Ti^{4+} can, at room temperature, not exist as purely aqua-complex. Lower valent cations ($z \leq 4$) tend to form aqua-complexes in acid environment. Upon increasing the pH, also aqua-hydroxo-complexes can be obtained. In general, one can derive that all coordinated water molecules keep their proton in the aqua domain, while in the oxo domain, oxygen cannot be protonated. In the hydroxo domain, at least one hydroxo ligand is present within the coordination sphere.

However, this scheme, though useful, is too simplified. For, not only the oxidation state of the cation (z), but also its size and the intrinsic nature of the element determines its polarizing strength, and acid base behavior, as mentioned before. E.g. this diagram does not explain for the difference in behavior between B^{3+} and Al^{3+} or between Si^{4+} and Ti^{4+} etc. . . . A more detailed discussion is given by Jolivet in [22]. Properties that come into play are for instance electronegativity and electron configuration.

A simple quantitative approach that does take into account electronegativity to assess the distribution of charges, and hence providing information on the polarity of bonds in a chemical entity is the Partial Charges Model, developed by Livage and Henry in the late 1980s [22, 23] and based on the electronegativity equalization principle, postulated by Sanderson [26]. When a chemical bond comes about between atoms, a charge transfer will occur: electron density is moved from the less electronegative towards the more electronegative atom. Or, in other words, the more electronegative atom acquires a negative partial charge $-\delta_i$, the less electronegative atom acquires a positive partial charge δ_i . As a result, electronegativities χ_i of each atom i in a structure change in a proportional manner to the acquired partial charge δ_i .

$$\chi_i = \chi_i^0 + k\sqrt{\chi_i^0}\delta_i \quad (5.4)$$

χ_i^0 is the electronegativity of the ‘neutral’ atom, and k a factor taking into account the used electronegativity scale (e.g. for Allred-Rochow electronegativities $k = 1,36$)

Charge transfer stops when the electronegativities of all atoms have become alike and similar to the average electronegativity $\bar{\chi}$ (Eq. 5.5) of all atoms involved.

$$\bar{\chi} = \frac{\sum_{i=1}^n \sqrt{\chi_i} + kz}{\sum_{i=1}^n (1/\sqrt{\chi_i})} \quad (5.5)$$

In this expression, n is the number of atoms in the structure and z the total charge of the compound.

Filling in this expression in the previous one, gives us the partial charge δ_i on each atom i in the compound:

$$\delta_i = \frac{\bar{\chi} - \chi_i^0}{k\sqrt{\chi_i^0}} \quad (5.6)$$

Based on this model, one can calculate the partial charge distribution in a compound. The model can be used in a fairly broad range of compounds going from organic molecules to complexes in aqueous solution. However, as always, it has its limitations because aspects such as the real structure of a compound, resonance and π -overlap effects are not being taken into account.

Jolivet et al. [22] explain in detail how the partial charges model can be used to predict the influence of the electronegativity of a metal ion and the pH on the degree of hydrolysis in an aqueous solution of solvated metal ions. In accordance with the principle of electronegativity equalization, proton exchange between a solvated metal complex and the solvent (water) takes place until their average electronegativities become equal.

$$\chi_{[M(OH)_h(OH_2)_{N-h}]^{(z-h)+}} = \chi_S \quad (5.7)$$

Using

$$\chi_S = 2.621 - 0.02pH \quad (5.8)$$

Speaking in terms of the partial charge model, the deprotonation reaction of an aqua complex occurs in order to equalize the electronegativities of the hydroxylated complex and the surrounding water.

It was found that the hydrolysis number, h , of a metal ion M with (Allred & Rochow) electronegativity χ_M^0 and coordination number N equals:

$$h = \left[\frac{1}{1 + 0.0138pH} \right] \left[(1.36z) + N(0.038pH - 0.25) - \frac{2.62 - 0.02pH - \chi_M^0}{\sqrt{\chi_M^0}} \right] \quad (5.9)$$

The value of h gives the number of protons spontaneously released by $M(OH_2)_N^{z+}$ in solution. Hence calculated hydrolysis ratios show reasonable agreement with experimentally observed species. For instance for Fe ($\chi_M^0 = 1.72$, $z = 3$ and $N = 6$), $h_{pH=0} = 1.9$ and $h_{pH=14} = 4$ are in fair accordance with the respective, experimentally observed, most acid and most basic forms $Fe(OH)(OH_2)_5^{2+}$ and $Fe(OH)_4^-$. Also the z -pH diagram from Fig. 5.3 can be reproduced quite satisfactory.

5.2.2 Condensation Reactions Can Lead to Precipitation

Most often, species resulting from partial hydrolysis of solvated metal ions, are not stable in their monomeric form. These hydrolyzed metal ions can undergo condensation reactions, via inorganic polymerization reactions, leading to the precipitation of hydroxides (e.g. upon the addition of a base to an aqua complex) or oxides (e.g. upon acidifying an oxo-hydroxo complex). However, depending on conditions of acidity, it is also possible that not a solid phase, but soluble entities such as polycations or polyanions are being formed. The condensation of metal ions is thus inherently associated with their acid-base behavior and these properties determine the course of the condensation reactions. Condensation can be limited to the formation of oligomers (polycations or polyanions) or can carry on until a gel forms or a solid phase precipitates. The solid phase can be a hydroxide $M(OH)_z$, oxyhydroxide $MO_x(OH)_{z-2x}$, or a hydrated oxide $MO_{z/2} \cdot x H_2O$.

Of course, when synthesizing precursor solutions for aqueous CSD, precipitation of a solid phase needs to be avoided. One must be able to achieve the synthesis of a stable solution of metal ions in water and then, upon evaporation of the water, form a homogeneous gel instead of a precipitate of one of the constituting metal ions. Gel formation instead of precipitation is a complicated process and depends on an

important number of parameters: a change of pH induced by the addition of a gelling agent (NaOH, NH₃, NaHCO₃, Na₂CO₃, etc.), the way it is added and even the stirring speed, the order by which the reagents are added, the geometry of the recipient, the temperature, . . . Gels are preferentially formed when both hydrolysis and condensation take place at a rather slow rate.

In order to obtain stable water based precursor solutions for aqueous CSD, it is therefore important that the hydrolysis rate of aqua and aqua-hydroxocomplexes is lowered. Moreover, in order to synthesize multimetal oxides, it is crucial that all metal ions constituting the precursor solution condensate indiscriminately and at the same time so as to form a homogeneous multi-metal precursor gel. A possibility to achieve this and obtain stable metal ion solutions which end up on homogeneous gels is by complexation with other ligands.

5.2.3 Complexation by Ligands Can Stabilize Metal Ions in Water

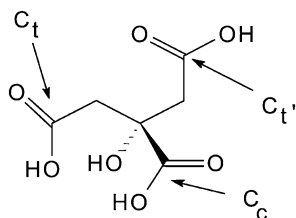
Anions or other molecules with electron donor atoms present in the aqueous solution, compete with aqua, hydroxo and oxo ligands in order to form coordination compounds with the metal ions. The occurrence of a complex is dependent on the relative nucleophilic character of the ligands (both from water and from external sources) under certain acid-base conditions and—of course—on their concentrations.

It is possible that certain ligands only temporarily form a complex with the metal ions, during specific stages of the hydrolysis or condensation, when the cation is in the monomeric or oligomeric form. The ligand anion is then not necessarily present in the finally formed solid phase, but plays a role in its formation out of the aqua-hydroxo or oxo-hydroxo complex and hence influences the properties of the formed solid (structure, morphology, . . .).

Also, it can be likely that only part of the coordination positions of the metal ion are occupied by mono- or polydentate ligands. In this case, hydrolysis and condensation are not completely inhibited. In the end, basic salts are being formed in which the complexing anions take part of the solid structure. Such anions can for instance be phosphates or sulfates.

Finally, polydentate molecules or anions (such as acid alcohols, polyamines, aminocarboxylates and hydroxocarboxylates) can be very strongly bound to the metal ion by means of multiple coordination bonds, which enables them to form very stable chelates, especially with transition metal ions. These kinds of ligands can elbow out all other ligands and shield the metal ion from any type of reactants. The complexed cation hence becomes almost insensitive for pH variances in a broad range and remains soluble as the monomer. The formation of such stable chelate complexes almost totally rules out hydrolysis and condensation reactions in the solution. E.g. the complexation of Fe³⁺ with

Fig. 5.4 Structure of citric acid. Ct, Ct' and Cc respectively represent terminal and central carboxylate functional groups



EDTA⁴⁻ (ethylenediaminetetraacetate) will result in a species of which the equilibrium constant for hydrolysis is a factor 10²² lower than that for the uncomplexed species [27, 28]. Other ligands used in water based sol-gel methods are anions from e.g. citric acid (HOOC-CH₂-C(OH)COOH-CH₂-COOH) (Fig. 5.4), lactic acid (CH₃-CH(OH)-COOH), tartaric acid (COOH-CH(OH)-CH(OH)-COOH), oxalic acid (COOH-COOH), propionic acid (CH₃-CH₂-COOH) or acetylacetonone (CH₃-CO-CH₂-CO-CH₃).

Citric acid (CitH₃) is, just like EDTA, a polybasic acid that, depending on the pH, can occur in different forms in an aqueous solution (CitH₃, CitH₂⁻, CitH²⁻, Cit³⁻). The respective pK_a values are 3.10, 4.80 and 6.39. The citric acid molecule contains an α-hydroxy functional group, which is of course much less acidic than the carboxylic acid functional groups. However, it can be deprotonated, e.g. when coordinated to a metal ion which is strongly polarizing. In that case the notation is Cit*, according to Cit⁴⁻.

The introduced (often polydentate) ligands protect the metal ion from reaction with other complexing groups (such as hydroxo-, aqua or oxo groups). Also these ligands are known to lower the partial positive charge on the metal ion, which causes it to be less prone to nucleophilic attack as well.

Interesting as a guide to predict the experimental conditions where precipitation can be avoided, are the so called pM'-pH diagrams [29]. pM' = -log[M'] whereby [M'] is related to the concentration of 'free' (not involved in a complex) metal ions [M^{z+}] by Ringbom's side reaction coefficient α_{M(X)}, X representing the ligands. The concepts of conditional equilibrium constants and side reaction coefficients have been developed in the 1950s and 1960s by Schwarzenbach and Ringbom [30, 31]. Ringbom's side reaction coefficient α_{M(X)} represents the ratio between the sum of the concentrations of all species containing the metal ion M and the free metal ion concentration.

These pM'-pH diagrams have been constructed, taking into account the stability constants for all complexation reactions that can occur, meaning with OH⁻ as well as with other ligands and the relevant solubility products.

As an example, we present here how such information can be used to synthesize stable precursor solutions of Pb-citrate. The influence of the citrate ligand on the solubility of Pb²⁺ in water is presented in the pM'-pH diagram of Fig. 5.5. The lines in this diagram tell us where, as a function of 'increasing Pb concentration' and 'increasing pH', precipitation occurs of hydroxylated lead compounds due to polycondensation reactions. In pM'-pH conditions above the curves, species are soluble,

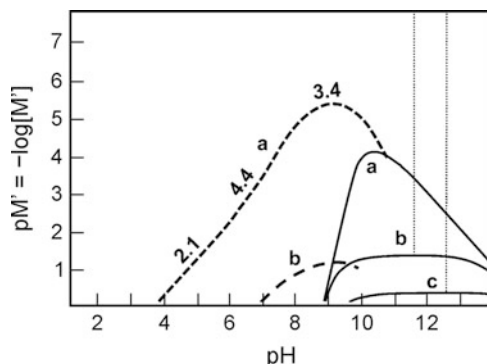


Fig. 5.5 pM' -pH diagram of Pb^{2+} -citrate complexation in water, after [29]. The *solid lines* a–c represent the borderlines of the precipitation regions in case of an excess of citric acid of (a) 0, (b) 10^{-4} M, (c) 10^{-3} M. (the *dotted lines* represent the pH limit above which more than 1 % of the metal-ligand complex has been hydrolyzed; the *dashed lines* with indication m.n are the 1 % borderlines for polyhydroxides $M_m(OH)_n$)

below the curves (each curve denotes different amounts of the ligand), precipitation occurs. Curve (a) indicates that hydrolyzed Pb^{2+} complexes are soluble in a large pH interval (between pH 1 and 9), although the dashed lines denote that there exist soluble polycations. In more alkalic conditions, hydrolysis of the Pb^{2+} ions can proceed and (initially) a Pb^{2+} hydroxide precipitate forms. This hydroxide easily undergoes oxolation leading to hydrated oxides. At even higher pH values, these precipitates are resolved again as soluble plumbites $PbO_2H_x^{(2-x)-}$ [22, 32].

When citric acid is added to the solution (curves b–c), it can be seen that the solubility of Pb^{2+} at higher pH's improves as the ligand concentration increases. However they do not become completely soluble. Therefore, it can be concluded that above pH 9 citric acid cannot prevent Pb^{2+} from hydrolyzing and precipitating. In order to keep the citrate ligands bound to the lead ions, it is needed to work below this pH. On the other hand, one should also take into account the solubility of the lead citrate complexes themselves. For, it is known that at pH values below 7.5 the lead citrate complexes have no charge and precipitate themselves [33–35]. This permits only a small window between pH 7.5 and 9 where (based on limited thermodynamic data) Pb^{2+} citrate can be expected to be soluble and stable.

The usefulness of pM' -pH diagrams is valuable, as they provide a first indication about the experimental conditions that could lead to stable solutions. Also when synthesizing multimetal oxides, it is possible to assess the experimental conditions based on a combination of the respective pM' -pH diagrams of each of the constituting metal ions. In practice, one can overlay the diagrams of different metal ions with the same ligand, or of one metal ion with different ligands. Very nice examples of this course of action are published in a study of the water based synthesis of high temperature superconductors $YBa_2Cu_3O_{7-\delta}$ [2–6, 8, 10] using EDTA as the complexant. For these systems, not only the precipitation of hydroxides but also that of carbonates of Ba^{2+} and Sr^{2+} is being taken into

consideration, as the solubility products of these carbonates are of the same order as the global formation constants of metal-EDTA complexes [36].

However, the practical use of these diagrams should not be overestimated. For, as mentioned above, one should bear in mind that these diagrams do not take into account precipitates other than hydroxides (or carbonates) and are based on thermodynamic data only valuable for diluted solutions, neither do they take into account kinetics. Furthermore, pM' -pH diagrams are only available for a limited set of metal ion—ligand systems.

5.2.4 Avoiding Precipitation During Water Evaporation

It is not at all straightforward to evaporate the water from stable solutions of metal ions without ending up with heterogeneous mixtures of precipitated condensation products or recrystallized salts, which were originally used as the source for the cations. As was explained in Sect. 5.2.5, the use of bulky chelating ligands can stabilize metal ions against hydrolysis and condensation, by protecting them within very stable complexes. However, also in this case, the crystallized metal ion complexes might precipitate.

During evaporation of the water from a stable solution of metal carboxylate complexes, condensation can occur between non hydrolyzed (because completely shielded by the ligands) and partially hydrolyzed species, leading to the formation of an inorganic polymer. Also here, the pM' -pH diagrams can be interesting first guides to predict where potentially precipitates can be formed as the concentration is increased during evaporation of the solvent.

However, the processes are so diverse and complex, that the calculations of the equilibrium concentrations of different species are difficult and burdened with uncertainties. This makes experimental observations during the evaporation of the solvent sometimes still unpredictable. According to Kakihana et al. [5] it is impossible to exactly describe the processes taking place during concentration of the solution. Anyhow, especially in multi-metallic solutions, it is of utmost importance that the homogeneity of the initial solution is preserved during evaporation of the solvent (water) and that precipitation due to condensation is being avoided.

5.3 Gel Formation Mechanism

Many solution-gel based CSD methods exist and differ according to the gel formation mechanism and whether or not the constituent metal ions are involved in the gel polymer network structure (see e.g. in [5] and [37]). The aqueous carboxylate based solution gel process can be categorized as a method in which molecular cross-links control the gel formation. The gel structure consists of metal carboxylate complexes, chemically connected one to another. This structure differs

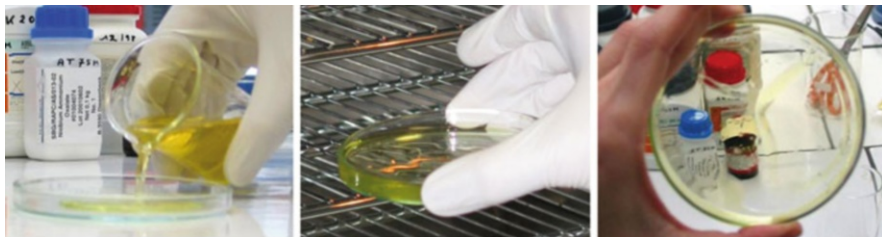


Fig. 5.6 Evaporation of the water from a stable aqueous carboxylate precursor solution in ambient conditions at 60 °C results in the formation of a clear and homogeneous solid gel phase

basically from the inorganic polymer controlled gelation routes such as the alkoxide sol-gel route, where inorganic polymerization reactions (hydrolysis and condensation) govern the gel formation. Also an important distinction with the polymer complex method can be noticed, where metal ion complexes are chemically fixed to a polymer network (see Chap. 6).

5.3.1 Basic Concept

The basic concept of the water based carboxylate sol-gel route can be summarized in the following ideas, which are illustrated in the photographs of Fig. 5.6.

- A water based start solution is prepared in which the metal ions are protected from hydrolysis by the formation of stable carboxylato complexes
- The chemistry of the solution is designed so as to form a highly viscous and amorphous metal carboxylate gel phase upon evaporation of the solvent (which spontaneously occurs during chemical solution deposition by spincoating or dipcoating)
- The gel structure ideally consists of metal carboxylate complexes linked to one another via metal-carboxylate, ammonium ($\text{NH}_4^+\text{-O}$) bridges (Fig. 5.7)
- During thermal treatment, the complexes decompose, leaving behind intimately mixed (multi)metal oxides and/or carbonates to form the final multimetal oxide phase by solid state reactions and in the case of thin films, possibly also by heterogeneous nucleation at the substrate.

The aqueous carboxylate based solution gel method has a number of specific advantages: Unlike the most commonly used alkoxide based precursors, aqueous carboxylate based precursors are insensitive to ambient moisture. As a consequence, these precursor solutions are very stable and aging behavior due to further hydrolysis and condensation reactions is excluded. Practical complications related with e.g. guaranteeing an inert atmosphere to store and handle precursor solutions can therefore be avoided. Also, most precursor materials—generally relatively

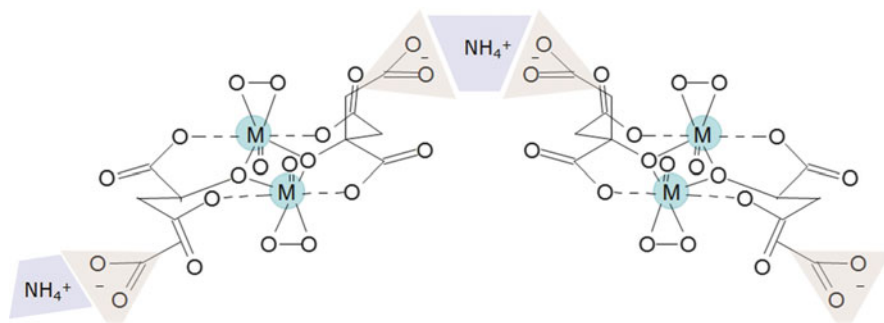


Fig. 5.7 Schematic of a possible network formation mechanism: ammonium ions bridging two carboxylate groups

simple carboxylate salts—are not expensive as compared to the majority of alkoxide start products. Obviously, since water is used as the solvent, instead of the often used teratogenic etheralcohols (such as methoxyethanol), the aqueous solution-gel methods can be considered healthier, safer and environmentally friendlier.

However, because of their high valency, specific electronegativity and small ionic radius, metal ions such as Ti(V), Zr(IV), Nb(V) or Ta(V) are extremely sensitive to hydrolysis and consequent condensation, leading to precipitation or undesired phase segregation of hydrated oxides and polyanions. Therefore, aqueous solution chemistry is very complicated and specific chemical strategies are needed to protect the cations from hydrolysis (see Sect. 5.2) while still allowing network formation.

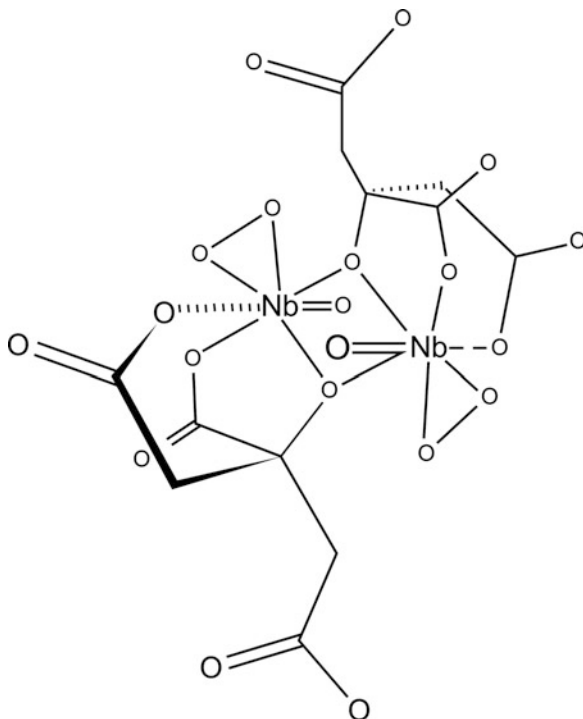
5.3.2 Carboxylates for Complexation and Gel Formation

5.3.2.1 Suitable Ligands

Citrato-ligands are very often the ligands of choice [certainly in CSD applications (see further, Sect. 5.5.1)], used in aqueous solution-gel routes besides other carboxylate based ligands such as EDTA [33, 38, 39], tartrates [40, 41], malonates [42, 43], nitrolotriacetic acid [44] or polyol compounds such as triethanolamine [45] or 1,2-ethanediol [41].

The reason why citrato ligands are so successful is not only that they (as well as other carboxylates) lower the partial positive charge on the metal ions (see Sect. 5.2.1), and hence stabilize the complex against hydrolysis. Moreover, and this is an important asset, citrate ligands are capable of ionically cross linking several complexes, thereby guaranteeing the formation of a three dimensional network and preventing segregation by precipitation.

Fig. 5.8 Model for the oxo-peroxo-citrato-Nb(V)-precursor complex obtained from EXAFS, FTIR and thermal decomposition investigations

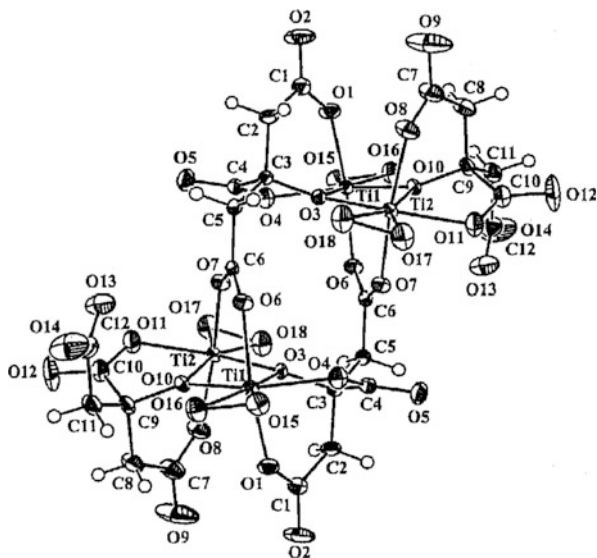


In several studies, besides citrate ligands, also peroxide was used as an electron donating ligand to form suitable water-soluble precursor complexes of highly valent metal ions [33, 44, 46–57].

Based on complementary structural analysis by EXAFS and FTIR [51, 58] as well as on systematic studies of the thermal decomposition behavior of the obtained gels [49, 50, 53, 59–61] it was determined in the case of e.g. Niobium(V) that the metal carboxylato-building blocks are made up of dimetallic oxo-peroxo-citrato metal complexes (as shown in Fig. 5.8).

EXAFS pointed out [59] that the citrato complex consists of a dimeric structure in which each Nb(V) ion is sp^3d^3 hybridized and surrounded by seven oxygen atoms: one from a niobyl group (Nb=O at 1.7 Å), two from a side-on bonded peroxo group (at about 2.0 Å) and four other oxygen atoms from the two coordinating citrato ligands (at 2.0 and 2.6 Å). It was presumed that the oxygen atoms at a relatively long distance of about 2.6 Å could be attributed to carboxylato groups for which a closer approach is hindered by increased strain within the citrato ligands. For the side-on metal-peroxo bonds, additional evidence was found in the UV spectrum of the solution, showing the characteristic ligand-metal charge-transfer band at 255–260 nm. The remaining four oxygens most probably originate from carboxylato and α -hydroxy groups of the citrato ion ($C(OH)(COO)(CH_2COO)_2^{3-}$).

Fig. 5.9 Structure of the tetranuclear ammonium-citratoperoxotitanate(IV) complex. Reprinted with permission from [63]. Copyright 2013 American Chemical Society



Specifically, the α -hydroxy coordination was expected because the complex synthesized with a substitute ligand (tricarballic acid) having the same structure as citric acid, however without the α -OH group, turns out to be unstable (and precipitates). Moreover, the FTIR spectrum of the gel displays a Nb-hydroxy coordination in the alkanol stretch region (ν_{C-O}). The presence of a single Nb neighbour at 3.30 Å indicates the formation of dimers via Nb-O-Nb links.

The results of this structural study appeared consistent with the structural model put forward by Narendar and Messing [46] and by Djordjevic et al. [62]. The inherent consequence of the above elucidated citrate peroxo complex structures is that two of the carboxylato groups can not coordinate to the central metal ions due to large distances, and must be directed away from the centre of the complex. These specific carboxylato groups in turn are free to form ionic bridges with other metal centers or ammonium groups in the direct neighbourhood of the complex, leading to the desired crosslinked gel structure (Fig. 5.9).

Experimental indications for these ammonium bridges can be provided by means of FTIR spectroscopy [57, 60]. The diffuse reflectance FTIR spectrum of a PZT gel at 25 °C indicates the interaction between NH_4^+ -ions and carboxylate groups by means of the typical $\nu_{as}(COO^-/NH_4^+)$ and $\nu_{sym}(COO^-/NH_4^+)$ stretches (around 1,595 and 1,400 cm^{-1} respectively) and the $\nu(OH)$ and $\nu(NH)$ stretches involved in hydrogen bonding (a broad band between 3,400 and 2,500 cm^{-1}).

An in depth study of a citratoperoxo-Ti(IV) precursor complex, its synthesis, gelation and thermo-oxidative decomposition and oxide formation was published by Hardy et al. [64] in which FT-Raman and XRD data confirmed the structure of the complex crystallized from the solution to be identical to that of $(NH_4)_8[Ti_4(C_6H_4O_7)_4(O_2)_4] \cdot 8H_2O$ synthesized by Kakihana et al. [63] (Fig. 5.9).

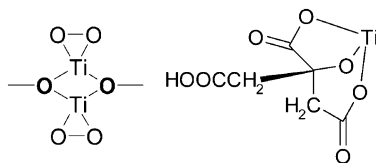


Fig. 5.10 Structural elements in the citratoperoxotitanate(IV) complex. (*left*) The α -O(H) groups of a citrate ligand are deprotonated and form a bridge between two Ti^{4+} ions within one binuclear fragment. (*right*) The citrate ligands form several five and six-membered chelate rings, however one carboxylate group for each binuclear fragment remains uncomplexed

This complex consists of a tetranuclear anion, connecting two binuclear fragments by means of bridging carboxylate groups of a citrate ligand. The Ti^{4+} ions have a coordination number of 7 in a pentagonal bipyramidal environment. A number of five and six-membered chelate rings (via carboxylate and α -O(H) groups of the citrate ligands, see Fig. 5.10) provide a stabilizing effect of the formed complex. The complexation of citrate-ligands together with the peroxo-ligands inhibit further polymerization of the tetrameric complex anion, because all active sites for nucleophilic attack are occupied. Since the complex in its whole has a negative charge, it is soluble in water [63] as the ammonium salt. An important feature of this complex structure is again that two non-coordinating carboxylate groups are present (Fig. 5.9), one for each binuclear fragment (Fig. 5.10), which are believed to play an important role in the formation of an amorphous gel, since they are available for crosslink formation (see further).

The behavior of different carboxylato complexes can definitely be significantly diverse and related to the possibility and the extent of cross linking between the carboxylato-metal complexes. Indeed, in their comprehensive review [33] Narendar and Messing explain the observation that precipitation is difficult to circumvent in EDTA gels compared to citrate gels to be connected with the structural differences between citrato-metal and EDTA-metal complexes. The EDTA ligand in the EDTA-metal complex is typically coordinating the metal ion in such a way that all functional groups are bonded to the metal ion, thereby excluding further cross linking.

5.3.2.2 Synthesis of a Precursor Solution

In order to synthesize a suitable precursor solution, first the appropriate start compounds that introduce the metal ions in the solution need to be selected. Requirements for this selection include the following:

- Start products should either be soluble in water themselves in a sufficiently high concentration, or should be able to be transformed into soluble species.
- The ligands or counter ions introduced by the start product of one metal, may not lead to the precipitation of other metal ions in the multimetal ion precursor, neither may they cause precipitation during gelation.

- All atoms from counter ions or ligands, apart from the metal ions themselves, should be decomposed during thermal decomposition. This is an important requirement, because it virtually excludes the use of simple salts such as chlorides, since the chlorine atoms cannot be easily removed as a volatile species during oxidative burning of the chemical precursor solution. Hence, foreign atoms are basically limited to oxygen, carbon and nitrogen. In this respect, one might consider the individual parent metal oxides as ideal candidates for the starting products. However, it appears that various commercial oxides have become kinetically inert towards dissolution, due to sintering effects during their preparation. On the other hand, a redundant amount of foreign atoms, even if they are removable, should be avoided as well, as they could induce unwanted porosity.
- In order to be able to deposit thin films, the counter ions or ligands that remain present in the precursor solution, may not deteriorate the wetting properties (see Sect. 5.5.1)

Taking all these considerations into account, carboxylate salts or complexes (if available) are effective candidates to be used as the start products in a precursor solution. In various cases indeed, simple carboxylate salts are dissolved in water and can serve as such as the start material, e.g. Pb-acetate or Pb-citrate are used in the water based synthesis of $\text{Pb}(\text{Zr}_{1-x}\text{Ti}_x)\text{O}_3$ and $(\text{Pb}_{1-x}\text{Ca}_x)\text{TiO}_3$ [57, 65] together with Ca^{2+} -citrate in the latter. Also Zn^{2+} -acetate has reacted with citric acid to form a precursor solution for ZnO [66]. For Bi^{3+} and Ln^{3+} , it was preferred to synthesize the citrate, starting from the oxide instead of the acetate [53] so as to introduce an as low as possible quantity of redundant atoms. Sr^{2+} and Bi^{3+} -acetate start salts have been used for the preparation of powders via citrate based gels [47] whereas for thin films it was attempted to avoid acetates (see Sect. 5.1). In the synthesis of $(\text{Bi},\text{La})_4\text{Ti}_3\text{O}_{12}$, $\text{SrBi}_2\text{Ta}_2\text{O}_9$ and $\text{SrBi}_2\text{Nb}_2\text{O}_9$ thin films, a Bi^{3+} -citrate solution was stabilized by means of ethanol amine [44, 48].

In the case of high valent metal ions, the high degree of hydrolysis and condensation causes simple salts to be insoluble. Here, water soluble start solutions need to be synthesized using the suitable start products, ligands and chemical conditions (pH, concentration, temperature, ...):

The complexation of the high valent metal ions and hence the formation of a soluble and suitable start solution, mostly occurs stepwise [64]. The more prone the metal ion is to hydrolysis, the more challenging the practical synthesis of the precursor solution.

In a first step, if present, undesired groups in the starting product are removed through chemical reaction. In the case of Ti and Zr (IV), the starting product can be an alkoxide, such as the isopropoxide or the propanolate [49, 50, 57]. The alkoxide ligands are removed by hydrolysis and partial condensation of the metal ion in water. In this way, a reactive oxy-hydroxide is obtained, which can be applied in further chemical reactions to obtain carboxylate complexes. Strong ageing, allowing progression of the oxolation reactions, however renders the precipitate insoluble. The commercial oxide was found to be kinetically inert and also allows

no more chemical transformation [64]. However containing chlorine, also zirconyl chloride has been used as such for Zr^{4+} in the synthesis of $ZrWO_8$ from EDTA or citrate gels [38, 67]. Its chemical formula being $ZrOCl_2$, this product actually consists of a cluster containing the tetrameric cation $[Zr_4(OH)_8(H_2O)_{16}]^{8+}$ [68]. Reports mentioning this $ZrOCl_2$ start product, do however not unambiguously demonstrate the absence of chlorine in the final product.

Alternatively, metallic Ti has also been used as a reactive starting product, but can only be applied for synthesis of peroxo containing carboxylate complexes [63]. For Nb and Ta(V) on the other hand, a water soluble ammonium oxalate can be applied as the starting product [47]. The oxalate counter ions, however, form insoluble oxalate salts with many metal ions such as alkaline earths, and therefore can be highly undesirable in a multimetal ion precursor, where precipitation should be avoided. The oxalate ions can be removed by oxidation with hydrogen peroxide in this case, where the product, CO_2 , evolves from the precursor solution. Accordingly, this is yet another advantage of the peroxide ion, besides its electron donating and complexing properties (see further).

Secondly, the (precipitated) pre-precursor has reacted with the ligands at low pH. The low pH serves different purposes: to dissolve the oxyhydroxide or analogous compounds, to ensure solubility of the metal ion prior to stabilization by complex formation, and to provide the right pH conditions for complete starting product counter ion decomposition in the case of oxalate. A low pH is accomplished by addition of strong acids [46], or of the carboxylic acid itself, which will act as the carboxylate ligand upon deprotonation. In the presence of hydrogen peroxide, at low pH already complexation with O_2^{2-} occurs, which is evidenced by UV or Vis absorption bands, with the wavelength depending on the metal ion involved. Simultaneously, complexation with citrate occurs as well, as can be shown by FTIR spectroscopy, e.g. in [64]. The stability of the low pH citratoperoxo complex is dependent on the metal ion: for Nb(V) instability of a low pH citratoperoxo complex towards condensation and precipitation of peroxoniobium hydrate $HNbO_4 \cdot H_2O$ is described, while, in contrast, for Ti(IV) no precipitation is observed in a wide pH range covering both acid and neutral, up to slightly basic regions.

Finally, the precursor solution's pH is increased, which shifts the deprotonation equilibria of the carboxylic acids, enables formation of new complexes with the deprotonated carboxylate functions, which can be characterized by higher stability constants and in this way prevents the hydrolysis and condensation reactions of the metal ions. The carboxylate groups play a central role in the stabilization of the highly valent metal ions, since merely peroxo ligands cannot prevent hydrolysis and condensation [69]. The gradual pH increase of the precursor solution, indicates that a number of buffer regions are being passed, due to deprotonation of citric acid, as well as hydrolysis and condensation of hydroxoperoxo metal complexes occurring simultaneously. Abrupt pH changes around 7.5 indicate there is a single species present. At lower pH, different species are present in the solution, with the different carboxylic acid functions protonated to a different degree. Increase of the pH to higher values generally leads to disintegration of the complex, hydrolysis and condensation ending in precipitation. Furthermore, in the case of application of

NH_3 to increase pH to the precursor solutions, a catalytic decomposition of H_2O_2 occurs which leads to effervescence caused by O_2 evolution [64].

This procedure has led to the successful synthesis of various other peroxocitrate complex precursor solutions by directly reacting a suitable salt with an excess of citrate and peroxide and subsequently raising the pH. E.g. the synthesis was reported of a citrate peroxo Ru precursor, starting from Ru-acetylacetonate [54] a citrate peroxo Mo^{6+} precursor was made from ammonium heptamolybdate tetrahydrate ($(\text{NH}_4)_6\text{Mo}_7\text{O}_{24}\cdot 4\text{H}_2\text{O}$), and a citratoperoxo- W^{6+} precursor from ammonium metatungstate hydrate ($(\text{NH}_4)_6\text{W}_{12}\text{O}_{39}$) [44]. It turned out that a citratoperoxo-V(V) complex is not stable, so that another complexing ligand, nitrilotriacetic acid, was used to form a nitrilotriacetatoperoxo- V^{5+} precursor complex [44] from the start product NH_4VO_3 . The synthesis of EDTA- and citrate-based gels as a precursor for ZrW_2O_8 have been described as well, by dissolving $(\text{NH}_4)_6\text{H}_2\text{W}_{12}\text{O}_{40}\cdot x\text{H}_2\text{O}$ without the use of peroxide [38, 67].

The formation of a stable solution of the citrate(oxoperoxo) complex, is strongly dependent of the molar ratio of ligand to metal ion, where an excess of ligand leads to improved stability and solubility. Furthermore, the reaction kinetics can be positively enhanced by carrying out reflux steps at increased temperature, below the decomposition temperature of the ligands. Besides merely improving the kinetics, furthermore, there is also a change of the precursor complexes with temperature, which can greatly affect the solubility. In the case of Zr^{4+} , the extensive polymerization degree of the hydrated amorphous ZrO_2 , that originates from the hydrolysis product of the alkoxide, a condensed tetranuclear $\text{Zr}_4(\text{OH})_8(\text{OH}_2)_{16}^{8+}$ -species, requires intense efforts to stabilize in solution [32]. A citrate to metal molar ratio of 1.2 as well as some high temperature reflux steps were necessary. Also it was believed that the addition of peroxide anions promotes the breaking of the ol-bonds in the tetranuclear $\text{Zr}_4(\text{OH})_8(\text{OH}_2)_{16}^{8+}$ - complexes [70] and allowed the complete depolymerization (and dissolving) of the hydrated oxide. In the case zirconyl chloride was used [67] no peroxide, but at least 6 equivalents of citrate ions were needed to avoid precipitation during gelation.

5.3.3 Related Polymer Complex Methods

In its most strict meaning, the water based carboxylate sol-gel route starts from a water based solution of metal carboxylate complexes, which upon evaporation of the water, will form chemical cross links by ionic or hydrogen bridges (see e.g. Fig. 5.7), with coordination bonds bridging several metal ions being possible as well. Although, the term aqueous carboxylate based sol-gel method is also used for a number of processes, where an amorphous solid is formed as well, but in which the crosslinks between carboxylates are not essentially formed. Not only different carboxylate ligands are used (e.g. citrates, EDTA, malonates, tartrates and acetates). Different counter- and bridging ions can be employed as well. Examples such as ethylenediamine ($\text{H}_2\text{N}-\text{CH}_2-\text{CH}_2-\text{NH}_2$) or ethanolamine ($\text{NH}_2-\text{CH}_2-\text{CH}_2-\text{OH}$) have chelating capacities themselves. Hence, a rich variety of similar routes

towards a carboxylato 'gel' can be grouped under the common title of water based carboxylate precursor route. However, as the chemical bonds responsible for the crosslinking are mainly ionic, this means the aqueous carboxylato gels redissolve in water. This is a main difference with other methods such as the Pechini route [71], also called polymer complex method, where covalent crosslinks are being formed.

The idea of organic polymerization methods is to entrap stable metal ion chelate complexes within a growing (or existing) polymer network in order to immobilize them and hence prevent metal ion segregation. The network is broken up during thermal treatment at a relatively low temperature ($>300\text{ }^{\circ}\text{C}$) which results in a fine mixture of oxides, together with residual organics and carbon. Further heating leads to the total decomposition of the organic components and the formation of the multimetal oxide in a stoichiometric homogeneous reaction.

The polymer network can be synthesized in different ways. One of them, and probably the best known, is the *Pechini route*. In the Pechini process not water but ethylene glycol is used as the solvent for a carboxylic acid (mostly citric acid) and metal carboxylate complexes (mostly citrate complexes) [1, 5, 71]. The ethylene glycol and molecular carboxylic acid, as well as the metal carboxylates present, react to form (covalent) ester bonds upon heating and consequently the degree of crosslinking between carboxylato-metal complexes is increased with ester polymerization (and to some degree metal carboxylate bridges in the gel). Carboxylic acids with at least three functional groups will give rise to the formation of branched polyester chains. This branching would suppress cation mobility during thermolysis so as to avoid segregation.

Other compounds used to form a polymer network are acrylic acid ($\text{CH}_2=\text{CH}-\text{COOH}$) and acrylic amide ($\text{CH}_2=\text{CH}-\text{CONH}_2$) which polymerize by means of a radical mechanism into linear chains which can get entangled. An advantage of the Pechini route is that the viscosity and polymer molecular weight can be adapted so as to control the thickness of deposited layers [72]. This in situ polymerization of a polybasic acid and a polyalkanol typically governs a gel structure in which the backbone is made up of an organic polymer *to which* cations are attached. The Pechini process therefore often is referred to as the *in situ polymerized complex method* [73–76].

A similar result is obtained by the *polymer complex solution method*, and *polymer assisted deposition*, respectively (see Chap. 6), in which a metal-coordinating polymer (e.g. Polyvinylalcohol, polyacrylic acid, polyethyleneimine as well as other polymers with appropriate functional groups) and metal salts are directly dissolved in an appropriate solvent (mostly water) [5, 77, 78].

In this case, yet cations are attached to the organic polymer, although in situ polymerisation does not take place. Depending on the type of polymer, and the abundance of functional groups, the metal ions can crosslink within the gel structure. The latter route is similar to the aqueous solution-gel route starting from carboxylate complexes, however, it differs since the metal ions are crosslinked by much larger organic polymeric molecules, instead of carboxylate ligands.

5.4 Gel Decomposition

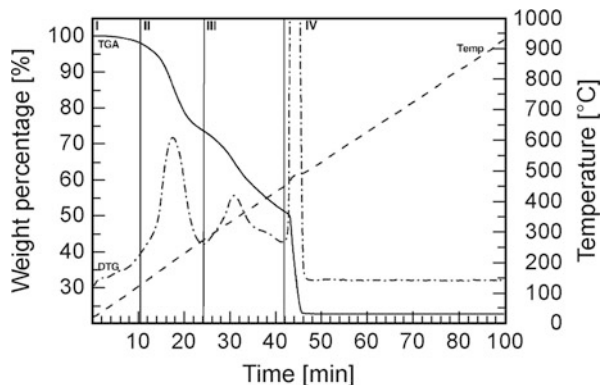
5.4.1 Mechanism

Once a homogeneous gel or gel film is formed, a thermal treatment in optimal conditions can transform the amorphous network into the desired crystalline oxide phase. During thermal treatment, either in one or in a sequence of different steps, a number of overlapping processes are taking place: Calcination refers to [19] the process of heating the gel polymer network, containing metal compounds, to convert it into an oxide network. Part of these decomposition reactions can take place without oxygen being used [1] (e.g. dehydration or dehydroxylation reactions), other reactions will be real combustion reactions of organics with oxygen so as to form carbon oxides and water. In addition, oxidation of the decomposition products and of the remaining metal compounds can take place, followed by crystallisation of metal oxide phases. In thin film processing, calcined gel films are mostly subjected to additional anneal steps in order to enhance crystallization and/or optimize morphology (see Chaps. 15 and 16).

Regularly published TGA and DTA profiles show that most carboxylate based gels exhibit a quite similar decomposition path (Fig. 5.11). However, only rarely the complete decomposition pathway is being unravelled. Moreover, variations may occur due to the presence of e.g. nitrates which can induce vigorous autocombustion reactions [45]. In various studies, reported in literature [33, 59–61, 64, 65, 79–81] the thermal decomposition of a bulk gel was studied by means of a variation of complementary experimental techniques such as thermogravimetric analysis (TGA) coupled with mass spectroscopy (MS) or FTIR spectroscopy to investigate mass loss as a function of temperature, and to identify the evolved gases during the various decomposition steps. Complementary in situ high temperature diffuse reflectance FTIR spectroscopy (HT-DRIFT) is applied to follow the functional groups remaining in the gel during heating, while in situ high temperature X-ray diffraction (HT-XRD) provides information on the crystallisation of oxide phases. Based on these extensive studies, a general pathway of the decomposition of carboxylate based gels, focusing on citratoperoxo metal ion gels can be described in a sequence of the following steps:

- I. Below 120 °C, remaining solvent (water) and some volatile molecules present evaporate as can be detected by evolved gas analysis by means of mass spectroscopy (MS).
- II. A following step (below ± 300 °C) involves decarboxylation and dehydroxylation reactions, particularly of carboxylate groups not bonded to the metal cations [82–84]. It may be noted that until this stage, no oxygen is consumed.
- III. Between 250 and 450 °C the metal ion complexes themselves become unstable and their direct coordination sphere decomposes. The residual products are metal oxide (or metal (oxy)carbonate) compounds together with an organic

Fig. 5.11 TGA profile of the thermal decomposition (in dry air, heating rate 10 °C/min) of an acetate-citratoperoxo precursor gel for SrBi₂Ta₂O₉. The four decomposition regions are indicated. Reprinted from [61] with permission from Elsevier



residual fraction. It may be noted that also in this decomposition region no oxygen is consumed.

- IV. Finally, during heating in air between 450 and 600 °C, all remaining and relatively stable (nitrogen containing) organic rest species are oxidatively decomposed. In the thermal decomposition of bulk gels (powders), the exothermic decomposition causes an extremely fast and considerable weight loss in a very small temperature interval of approximately 50 °C. The exothermic effect can be noticed by the temperature increase beyond the programmed temperature (see Fig. 5.11) and accompanied by the consumption of O₂ as confirmed by the decrease in the oxygen signal in MS ($M/z = 32$). In some cases, this consumption of oxygen for the combustion of organic species causes the local environment inside the decomposing gel to be much less ‘oxidative’ than expected and can lead to the formation of inhomogeneities (see Sect. 5.4.2)

In various cases, crystallisation of the oxide phase is possible as soon as the direct coordination of the metal ions has been removed. This implies that crystallisation can begin before the nitrogen containing matrix is completely removed.

5.4.2 From Homogeneous Gels to Phase Pure Products

In previous paragraphs, already the importance of starting with a completely homogeneous precursor solution as well as obtaining a homogeneous gel or gel film was emphasized. However, various studies have suggested that a homogeneous gel is no guarantee for obtaining the desired monophasic end product [33, 85, 86]. Chemical phase segregation is on the one hand governed by thermodynamics (minimisation of free energy) and on the other by the kinetics of ion diffusion. During the thermal decomposition of metal ion chelate complexes, present in the precursor gels, large amounts of gases are set free, such as H₂O, CO₂, CO, ... This

obviously is accompanied by the change in the coordination sphere of the metal ions, by a change in the nature of metal ion ligand bonds and possibly also by the formation of oligomeric M-O-M- species. The cation homogeneity is being controlled by the thermal stabilities of the different metal ion—ligand bonds and the decomposition behavior of the different metal ion complexes. Mostly, those thermal stabilities will differ and as a consequence different complexes decompose at different temperatures, resulting in sequential decomposition of carboxylates, which can explain phase segregation by the formation of individual metal oxides. Another cause for phase segregation is the reaction of electropositive metal ions, such as alkali metals, alkaline earth metals and lanthanides with evolving CO₂-gas. Contrary to alkoxide-based gels, evolving water does not influence phase segregation in the carboxylate based precursors.

However, even when a homogeneous cation distribution is present in the gel after all carboxylate complexes have been decomposed, phase segregation can still occur during oxide formation, as experimentally verified by TEM in e.g. [87]. In gel precursors, nucleation of oxide crystallites happens typically at heterogeneous sites such as interfaces or surface heterogeneities. Phase formation is being controlled by the phase which has the fastest nucleation kinetics. Therefore, not necessarily the thermodynamically most stable phase will be formed. The nucleation rate is determined by intrinsic factors, such as the free energy of formation, the crystal density, the compositional stability interval, and also by extrinsic influences, such as the stoichiometry of heterometallic complexes, heating rate and the presence of impurities. In e.g. Pb-containing perovskite phases, an intermediate pyrochlore phase can be formed first, as it is a disordered structure which is stable over a broad compositional range. In the perovskite phase, on the other hand, the stoichiometry is fixed and only deviations of less than 1 % are tolerated. However, by changing extrinsic factors, e.g. by heating at a high rate up till elevated temperatures, it becomes possible to form the perovskite phase directly [88]. Fast heating rates, realized in so-called RTP (rapid thermal processing) furnaces, allow to progress across the temperature regime where pyrochlore formation occurs and to arrive straight at those high temperatures where thermodynamic aspects dominate.

5.4.2.1 Strategies for Preserved Homogeneity During Thermal Decomposition

One of the first reports on this homogeneity issue was published by Narendar et al. [86] and involves a study on phase separation mechanisms during Pb(Mg_{1/3}Nb_{2/3})O₃ formation from both EDTA and citrate based precursor systems. A homogeneous cation distribution was obtained by carefully adjusting the composition of the precursor system (with respect to cation/ligand ratios and pH) and maintained during thermal treatment by avoiding stepwise decomposition of the individual carboxylate complexes. The strategies applied for this purpose consisted of either

using a high heating rate under oxidizing atmospheres (in the EDTA precursor) or the formation of a ternary Pb-Mg-Nb citrate complex (in the citrate system).

The formation of binary Pb-Nb citrate complexes has as well been observed during the synthesis of $\text{Pb}(\text{Zn}_{1/3}\text{Nb}_{2/3})\text{O}_3$ from citrate-based precursors [89]. When Pb and Nb citratoperoxo precursor solutions are mixed, an extra absorption band appeared in the UV absorption spectra. Substantiated by UV fluorescence spectra, Raman spectra and a Job's plot [90] these features were suggested to be due to the formation of a 1:1 heteronuclear Pb-Nb complex. In the same way, the difference between the decomposition profile of the mixed citrate based Pb-Zr precursor from a superposition of those of the individual Pb and Zr precursors, suggests that a heterometallic Pb-Zr complex is being formed in the PZT citrate based precursor as well [91]. Also in literature, examples are reported where the observed thermal decomposition profile of a multicomponent gel is different from a superposition of the decomposition of the individual carboxylato complexes e.g. in the case of $\text{NdBa}_2\text{Cu}_3\text{O}_{7-x}$ from an acetate precursor [45]. However, the straight conclusion that heterometallic complexes are formed should not be drawn in all these cases, as changing multimetallic gel decomposition profiles might as well be due to heat effects or to a catalytic effect of one of the constituent metal ions.

5.4.2.2 Powders Versus Films

Unquestionably, the thermal decomposition and phase formation in powders can differ substantially from that in thin films. The interactions with film substrates can have a huge impact on crystallisation pathways and on phase homogeneity as can be learned from the many literature reports on this topic. Furthermore, even without the substrate being involved, there is the effect of the sample 'shape' and its different surface to volume ratio, on the accessibility of reagent gases or the dissipation of energy and reaction products. As an example, specifically connected to the carboxylate based solution gel method Nelis et al. report [49, 61] that during the synthesis of $\text{SrBi}_2\text{Nb}_2\text{O}_9$ powder from acetate-citrato-peroxo gels, excess Bi used to improve the crystallization [92, 93] was found to be reduced and segregated as metallic Bi islands. A reason for the observation of metallic Bi in the decomposing gel can be found in the lack of oxygen arising during thermal decomposition. As a consequence, Bi^{3+} is reduced either by the organic material present in the gel, or by the CO gas that is set free during (incomplete) burning, to the metallic state, which melts (melting point around 271.4 °C) and therefore becomes very mobile. The in situ created reducing atmosphere in the powder samples, is however also correlated with the vigorousness of the decomposition step, which is in turn related to the oxygen partial pressure in the sample environment. During further heating, the metallic state is oxidized again into Bi^{3+} which is then incorporated in the $\text{SrBi}_2\text{Nb}_2\text{O}_9$ crystal structure. The cause of these inhomogeneities, observed in decomposing gel powders, is however attributed to a bulk effect.

Indeed, thin films prepared by the same precursor, using a Bi excess, and heated in the same conditions until and beyond 400 °C, did not show any inhomogeneity due to bismuth reduction.

Evidently, these observations reflect the much easier access of oxygen and dissipation of heat and reaction products in thin films compared to bulk samples.

5.5 Film Deposition and Control of Film Properties

5.5.1 *Wetting*

Essentially, chemical solution deposition (CSD) implies that a suitable precursor solution is being deposited on an appropriate substrate after which an appropriate thermal treatment decomposes the precursor structure and allows the desired oxide to crystallize [1, 72, 94]. The wet layer deposition is mostly performed by either spin coating (The basics and the physics of spin coating are discussed in Chap. 11 or dip coating (The basics of dip coating are described in Chap. 10). As far as it can be classified as a CSD method, liquid source misted chemical deposition (LSMCD—see Chap. 12) combines the advantages of chemical solution deposition with a remedy to the drawbacks with respect to conformal deposition and continuity for ultrathin layers. As far as we know however, the LSMCD technique has not been explored yet for the deposition of metal oxide films from water-based solutions. On the other hand, recently it has been demonstrated that the deposition of ultrathin and/or highly textured layers by spincoating or dipcoating is feasible [14, 39, 95, 96] (see also Sects. 5.5.5 and 5.5.6).

Although the use of entirely water-based precursor solutions is very attractive from an economical point of view and the potential for reduced environmental impact, the number of literature reports on the chemical solution deposition of metal oxide thin films from water based precursor is rather limited. Obviously, a major reason for this can be found in the (mostly chemical) challenges associated with aqueous chemical solution deposition methods among which the most imperative ones are:

- The lack of suitable readily commercially available water soluble and stable precursors;
- the chemical challenge to prepare a stable multi-metal precursor solution;
- the difficult wetting behavior of many substrates towards water-based solutions.

Indeed, several functional and especially electroceramic (multi)metal oxides contain high valent metal ions like those of Ti, Nb, Ta, Ru, Bi, Zr, Readily utilizable water soluble precursors of these metal ions are either scarce or are composed of salts containing undesired counter ions such as chlorine, which are difficult to eliminate from the system during thermal treatment. Moreover, it takes

some chemical insight to prepare stable water based precursor solutions of complex multimetal oxides (as was discussed in a previous section 5.2).

Besides the chemical issues, related to solubility, stability and ‘gellability’ of the precursor solution, a major issue, related to the chemical solution deposition of water-based solutions, concerns problems with film homogeneity, which arise due to insufficient ‘wetting’ of the substrate by the aqueous solution and drying issues. Indeed, one of the foremost challenges in water-based chemical solution deposition is the poor affinity of polar aqueous solutions to the substrate surface. Reasons can be found in the intrinsic hydrophobic surface properties or as a result of organic contamination. In most cases, if reported at all, this stumbling block is handled by the addition of a surface-wetting reagent to the precursor solution in order to adjust its viscosity and surface tension.

Additives that have been referred to are e.g. polyvinyl alcohol (PVA) [77, 97] Triton X [97] and methoxyethanol [98]. However, these additives can disturb the sometimes subtle complexation equilibria in the aqueous solution, as a result of which the precursors stability may be undermined/emasculated.

Instead of improving the surface adhesion by the addition of a surface wetting reagent, alternative strategies are put forward that do not exhibit the risk to disturb the precursor’s chemistry. They comprise a thorough cleaning and sometimes even a modification of the substrate (being glass, metal or an electroded silicon layer). Mild cleaning treatments with the predominant purpose to degrease the surface are those with (combinations of) e.g. detergent [99, 100] acetone [45, 100–103], trichloroethylene [45, 101], alcohol [45, 100–102, 104, 105], sometimes followed by a heat treatment [45].

Sometimes, in case of metallic surfaces, a mechanical polishing treatment is performed prior to these chemical cleanings [103, 106] or they are combined with an ultrasonic treatment [102, 103].

More severe chemical cleanings with chromic acid [99, 103, 105, 107, 108] or SPM-APM (Fig. 5.12) in e.g. [14, 48, 57, 65, 66, 109–112] have the ability to etch the surface to a certain extent.

SPM or piranha is a 4:1 mixture of concentrated sulfuric acid and hydrogen peroxide. When the substrate is immersed in this mixture, H_2SO_5 is generated, which has strong oxidizing properties and is capable of decomposing just about all heavy organic contamination. The APM mixture consists of water, H_2O_2 and NH_3 in a ratio of 5:1:1 and will remove all remaining lighter organic contamination as well as some transition metals such as Cu, Ag, Ni, Co and Cd, which dissolve after complexation. It is presumed when all the hydrophobic impurities have been removed from the substrate’s surface, wetting will improve drastically and homogeneous and continuous wet films can be deposited. In the case of oxide substrates, the ammonia/peroxide mix regenerates the surface layer whereby surface metal-oxide groups are hydroxylated rendering it more hydrophilic.

Also a physical UV/ozone technique has been reported (Fig. 5.12) [48]. For this cleaning procedure, the substrate is placed in a room where continuously ozone is produced and destroyed by the illumination of oxygen with UV radiation of two different wavelengths. During this process, atomic oxygen is formed as an

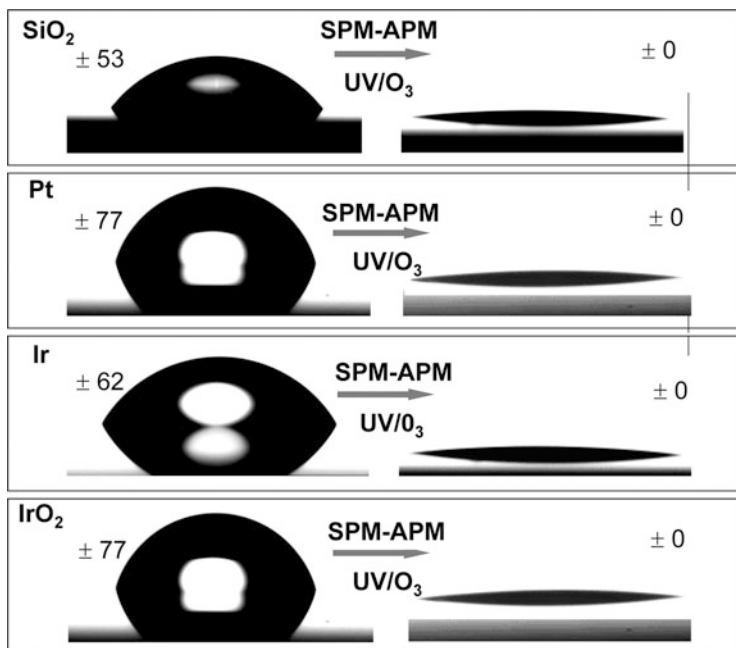


Fig. 5.12 Either SPM or UV/O₃ treatments reduce the contact angle of water to almost zero. These substrate treatments allow excellent wetting behavior of (most) water based precursor solutions on different types of substrates

intermediate product, which being a very strong oxidizer, is able to decompose all organic contaminants from the substrate by oxidation [113].

In a study of the deposition of a PZT water based precursor [91], it was found out however that a thorough cleaning alone is not always a guarantee for smooth and homogeneous wet films. Indeed, even after a thorough SPM/APM cleaning of the platinized silicon wafer, a PZT precursor solution using Pb-acetate as well as a PZT precursor solution using Pb(II)-citrate were deposited by spincoating using identical deposition conditions. It was observed that a uniform film formed after spin deposition of the citrate based precursor, while a radial pattern was observed in the wet films as deposited from the Pb(II) acetate based precursor solution. After possible causes related with the solutions' rheology and viscosity had been excluded, it was assumed that the difference in the wetting behavior might be found in the precursor chemistry. The presumed cause is directly linked to the used ligands and more precisely to the free (i.e. uncoordinated) ligands present in the precursor solution. Free acetate groups, if present in sufficient amounts, might arrange themselves with their single polar COO⁻ group pointed towards the hydrophilized surface. In this way, they form a monolayer onto the substrate with an apolar hydrophobic top surface. The citrate anions contain different polar groups which are not able to point all to the same direction, due to the sp³ hybridization of the central atom (Fig. 5.13). This could mean that, even if a molecular surface layer

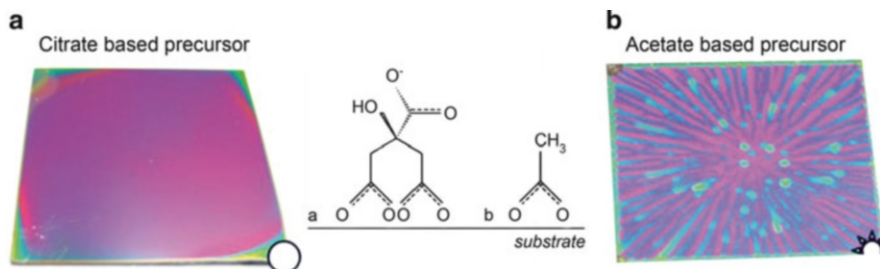


Fig. 5.13 Photographs showing the different wetting behavior of a spin coated PZT aqueous precursor solution based on (a) Pb(II) citrate and (b) Pb(II)-acetate on an SPM-APM cleaned platitized Silicon substrate

is formed, there will always be carboxylate groups pointing towards the deposited solution, enabling a satisfactory wetting behavior. Further experiments with lactato and tartrato complexes corroborated this hypothesis.

5.5.2 Control of Film Properties in Carboxylate Based Aqueous CSD

In order to achieve a crystalline oxide film with the desired morphological properties and, consequently, performance, CSD routes generally are carried out in a series of processing steps which all can be optimized (see e.g. Chaps. 15, 16, and 18).

Precursor composition, concentration, stoichiometry and viscosity can have an important influence on the (wet) film's thickness, on the thermal decomposition pathway, crystallization processes and for instance on the resulting porosity. Also, deposition parameters such as spin velocity or withdrawal speed determine the thickness of films deposited by means of spincoating or dipcoating. The thermal decomposition profile of precursor solutions or bulk gels, investigated by means of thermogravimetric analysis, generally provides a first guideline for the different thermal processing steps of the deposited layers, which are mostly carried out on a hot plate, in a conventional oven or an RTP (rapid thermal processing) oven. In order to remove all organics gradually and reduce the risk of forming cracks, typically each decomposition step observed in the TGA profile is performed as a separate hot plate step. Accordingly, in most reports where the heat treatment of carboxylate based gels is optimized, a series of different hot plate steps is generally applied, corresponding to the gel drying at low temperature between 100 and 200 °C, a first pyrolysis step below 300 °C to decompose the uncomplexed carboxylates constituting the gel matrix and another pyrolysis step at higher temperatures to decompose the metal ion complexes (Sect. 5.4.1).

Because the crosslinking reactions in carboxylate gels are mainly ionic by nature, a typical property, even if they are dried after deposition, is that these gels and gel films redissolve in aqueous solutions, which hampers multiple wet depositions without intermediate treatments impossible. However, after decomposing the carboxylate based gel films at elevated temperatures, the precursor material becomes insoluble, depending on the type of oxide and chemical nature of the precursor solution, so that the deposition of a next layer of precursor solution turns out to be possible. Complications, e.g. when the formed oxide is ZnO, which is amphoteric, are handled by adjusting the precursor's pH to a value at which the oxide doesn't dissolve [114].

After the commonly named 'pyrolysis' treatments (involving basically gel calcination) i.e. when all the organics have decomposed, the obtained oxide films are generally still amorphous. Therefore, each individual layer is subjected to a further crystallization step (intermediate crystallization), and mostly a final crystallization or anneal treatment is carried out after the complete stack of layers is deposited and thermally processed.

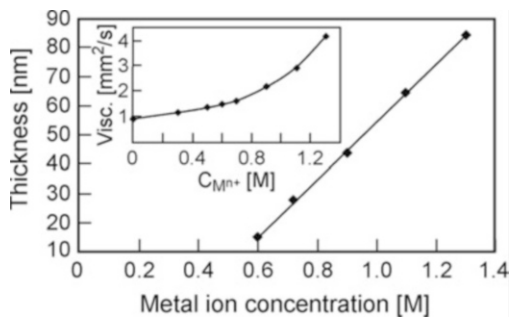
Schwartz et al. [115] have already shown that the precursor solution characteristics and the pyrolysis steps during thermal treatment affect the crystallization behavior of alkoxide sol-gel derived $\text{Pb}(\text{Zr},\text{Ti})\text{O}_3$ thin films, specifically studying orientation and surface morphology. Bhaskar et al. [116] demonstrated that the type of precursor solution and especially the degree, to which organics are removed from the precursor during heat treatment, has an effect on the ferroelectric properties of $\text{Pb}_{0.85}\text{La}_{0.15}\text{TiO}_3$. Likewise, it turns out that in carboxylate based aqueous CSD methods, each of the individual processing steps can be optimized in order to realize the best possible result with respect to morphology, composition and performance.

5.5.3 Film Thickness

Different applications require different film thicknesses to be deposited. And, also within a certain thickness range, control of the film thickness is important, as it is known to be of influence (in combination with the heat treatment) on the properties of the final film (e.g. for PZT [117–120]). Film thickness can be controlled by means of viscosity, precursor concentration and the number of deposited layers. The viscosity of a water based carboxylate precursor can be increased by adding bridging chelate ligands such as e.g. 1,2-diaminopropane or ethylene diamine [114] or using a non reacting polymer such as polyvinylalcohol (PVA) [121].

Alternatively, the metal ion concentration (and accordingly also the viscosity) can be increased by evaporating a certain volume of solvent from a stable precursor solution (and re-establishing the pH value). For various precursor solutions, it was found that film thickness increases linearly with increasing precursor concentration in a range between about 15 and 100 nm as can be seen for PZT in Fig. 5.14. Even for ultrathin layers, as will be shown later, this regime remains valid.

Fig. 5.14 Layer thickness (after crystallization) as a function of precursor metal ion concentration for spin coated PZT from a water based carboxylate based precursor. The inset shows that the kinematic viscosity also increases with increasing precursor concentration, though not linearly [91]



However, it should be noted that an increasing amount of additives generally only establishes a higher thickness of the deposited wet layer, and has—when dense layers are aimed at—the disadvantage of introducing extra organic material that needs to be decomposed. Moreover, adding these ligands, might disturb the complexation equilibria leading to destabilized precursor solutions.

Remarkably, however, is that the (kinematic) viscosity (measured however at low shear rates) of the solution doesn't show a linear increase with respect to precursor concentration. The linear increase of the film thickness in this broad range of metal ion concentrations, is ascribed to the non-Newtonian flow behavior of the precursor solution at higher concentrations (above 0.7 M). It is assumed that during spincoating relatively high shear rates are attained, at which the resistance to flow and as a consequence also the viscosity is lowered.

A third way of increasing film thickness is by depositing an increasing number of layers [114]. Also here, various examples demonstrate the linear increase of the final thickness as a function of the number of deposited layers (with intermediate heat treatments) with an equal concentration (Figs. 5.15 and 5.16).

Spin-coating of carboxylate based precursors generally produces continuous crystallized single layers with a thickness between 10 and 100 nm. Thicker layers of TiO₂ up to 800 nm were obtained by tape casting of a 0.8 M peroxocitrate Ti precursor solution to which 7.5 wt.% PVA was added in order to increase the viscosity [121]. On the other hand, applying very diluted precursor solutions has proved to be a successful strategy towards extremely thin layers (see Sect. 5.5). Besides spin coating, also dip coating permits a broad range of film thicknesses to be reached, going from a few tens of nanometers [122] to 1 micron per single dip [45].

5.5.4 Morphology Control Through Process Conditions

Various examples in literature demonstrate how the process conditions can be adjusted in order to change and optimize the films morphological and functional properties. A few illustrations are given below.

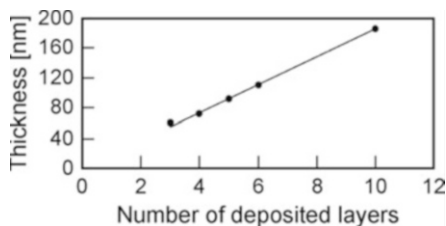


Fig. 5.15 Film thickness after crystallization of TiO_2 as a function of layers deposited by spin coating from a 0.4 M citratoperoxo Ti(IV) precursor. Reprinted from [100] with kind permission from Springer Science and Business Media

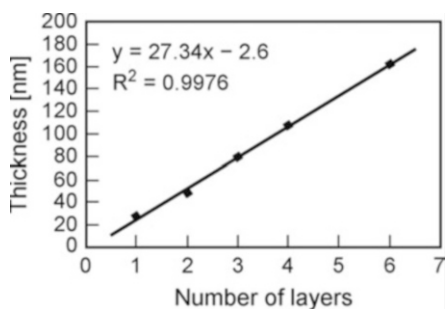
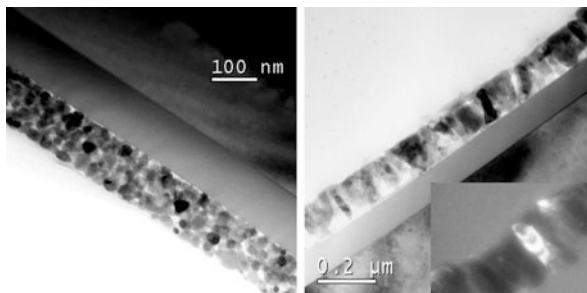


Fig. 5.16 Influence of the number of layers deposited by spin coating with a carboxylate based PZT precursor with a metal concentration of 0.72 M (on the thickness of the final crystalline film [91])

Mondelaers et al. [66] developed a procedure to deposit ZnO layers by means of spincoating an aqueous carboxylate solution. The morphology of these films could be changed by changing the process [114] (Fig. 5.17). When one single layer of a highly concentrated precursor solution is deposited and processed at once at 500 °C, a polycrystalline layer is formed. On the other hand, the deposition of many thin layers from a precursor solution with a concentration of 0.1 M with intermediate crystallization steps led to the formation of a polycrystalline film with a columnar grain structure and a pronounced c-axis orientation. Each subsequent layer is assumed to nucleate heterogeneously on the grains crystallized during the previous deposition.

Other examples illustrate the importance of the optimization of the thermal decomposition of the carboxylate based precursor by means of a series of hotplate steps before crystallization in an RTP oven. E.g. Nelis et al. studied the aqueous CSD of Strontium bismuth tantalate ($\text{SrBi}_2\text{Ta}_2\text{O}_9$) (SBT) [47, 61, 123], a promising ferroelectric compound [124–126]. A crystallization temperature of at least 650 °C, needed for alkoxide based sol-gel precursors [127], is also essential for aqueous precursors to be able to convert the intermediate fluorite phase into perovskite and to record an acceptable P_r value. Optimized P_r values could be obtained lowering the degree of (non-polar) c-axis orientation [128]. Nelis showed that both a change

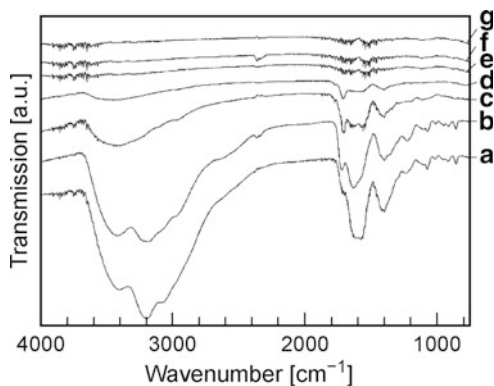
Fig. 5.17 BF TEM images of a ZnO film obtained by spincoating of (*left*) two layers with a highly concentrated precursor solution and (*right*) 21 layers with a low concentrated precursor solution



in the Bi vs. Sr stoichiometry [129, 130] and an optimization of the thermal decomposition of the carboxylate precursor led to a reduction of fluorite secondary phase and a fast crystallization of perovskite with reduced c-axis orientation. A crystallization ambient of pure oxygen proved to be beneficial over 20 % O₂ to reduce the c-axis preferential orientation and increase the P_r value to 6.8 $\mu\text{C cm}^{-2}$ which is in good accordance with other literature data for sol-gel SBT films [131]. Remarkable in this study was the effect of remaining organics in the layer before it was submitted to the crystallization in the RTP oven.

Also in the case of lanthanum substituted bismuth titanate (Bi,La)₄Ti₃O₁₂ (BLT) films, the remaining organics before crystallization turned out to be key in the optimization of the properties. Since BLT can be fabricated with a higher remanent polarization (P_r) than SrBi₂Ta₂O₉ ($P_r = 5\text{--}15 \mu\text{C cm}^{-2}$ compared to $4\text{--}10 \mu\text{C cm}^{-2}$) and at a lower crystallization temperature (600–700 °C compared to 700–850 °C), it received a lot of attention e.g. [132–134]. A new aqueous solution-gel route for the synthesis of BLT was developed, based on aqueous Bi³⁺- and La³⁺-citrate solutions and an aqueous citratoperoxo-Ti(IV) solution [53] whereby the molecular scale mixing and high degree of homogeneity throughout the entire process led to the direct crystallization of the Aurivillius phase from the amorphous phase at a crystallization temperature as low as 525 °C. The formation of cracks in the film was avoided by guaranteeing a gradual decomposition, applying a drying step and two pyrolysis steps. The crystallinity of the films improved and the P_r was observed to increase linearly with crystallization temperature between 600 and 700 °C do to an enlarged grain growth. Indeed, sufficiently large grains or crystallites seem to be a requisite requirement for obtaining a polarization hysteresis with a reasonable P_r [135]. Recognizing the importance of the Bi³⁺ stoichiometry during crystallization in SBT films, also in the case of BLT, the influence of the Bi³⁺ excess was investigated [111]. A too low nominal Bi concentration can lead to Bi loss by means of evaporation or diffusion in the bottom electrode [136]. A too high Bi³⁺ excess might result in segregation of the excess Bi atoms to the grain boundaries during crystallization, leading to the formation of leaking current paths [134]. Therefore, a slight excess is beneficial and the most favorable amount needs to be established experimentally for each synthesis method. For a CSD method with water based carboxylate precursors, the positive effect of the excess Bi³⁺ was ascribed to a decrease of the number of oxygen vacancies in the BLT

Fig. 5.18 AR-FTIR of BLT thin films after different thermal treatments: (a) as spun film; (b) 160 °C/1 min; (c) 160 °C/1 min, 260 °C/2 min; (d) 160 °C/1 min, 260 °C/2 min, 315 °C/2 min; (e) 160 °C/1 min, 260 °C/2 min, 370 °C/2 min; (f) 160 °C/1 min, 260 °C/2 min, 425 °C/2 min; (g) 160 °C/1 min, 260 °C/2 min, 480 °C/2 min



crystal structure, which are considered responsible for the domain-pinning of ferroelectric domains. An additional effect of the Bi³⁺ excess is an enhanced grain growth of the Aurivillius phase, due to the high ion mobility of Bi³⁺, which is favorable for the P_r . On the other hand an increased c-axis orientation was observed, which is in fact undesired, as the polarization of BLT along the c-axis is lower than that along the a-axis. Nevertheless, the most favorable P_r value was observed for a nominal excess of 10 % Bi³⁺.

Moreover, it was clearly shown [110] that a correlation exists between the ferroelectric properties of BLT thin films deposited by aqueous carboxylate based chemical solution deposition and the thermal treatment applied, more specifically, the temperature of the third hot plate step (HP3 concerns the final pyrolysis treatment before crystallization in an RTP oven). However, and in contrast to the findings of Fè et al. [137] and Schwartz et al. [115] who studied the relation between orientation selection and chemical structure evolution or precursor pyrolysis behavior for sol-gel prepared Pb(Zr,Ti)O₃, the variation of the temperature of the third hot-plate step had little influence on the crystallographic phase development and orientation of the aqueous BLT thin films. The reason for the differences in ferroelectric properties was found to be due to residual organic material in the layers. The presence of a residual fraction of organic material in the thin film prior to and during the crystallization step in the RTP furnace, was found to have a negative effect on film density and ferroelectric properties. The properties of the BLT films are improved when the amount of organic material is decreased prior to rapid thermal processing, i.e., when the third hot plate step is carried out at a higher temperature.

Absorption Reflection FTIR (AR-FTIR) measurements verified the presence or absence of remaining organics (Fig. 5.18). The minimal pyrolysis temperature of 370 °C that removed all organics before crystallization resulted after crystallisation in films with high P_r values (ca. 6 $\mu\text{C cm}^{-2}$), which are uniform over the entire film surface and all of the top electrode dots. The optimal final pyrolysis temperature for obtaining the maximum P_r value (6.6 $\mu\text{C cm}^{-2}$) was 425 °C at a crystallization temperature of 650 °C, compatible with CMOS (complementary metal oxides semiconductor) processing.

5.5.5 Highly Oriented Layers

5.5.5.1 Lattice Match with the Substrate in Superconducting and Buffer Layers

Especially in the synthesis of superconducting layers and associated buffer layers (see Chap. 27), the achievement of biaxial texture is very important as it turned out to be a decisive prerequisite for achieving sufficiently large critical currents. Whereas the realization of textured layers is mostly associated with vacuum based, layer by layer or sputter deposition, also epitaxial growth of highly textured layers were reported from water based chemical solution deposition demonstrating that the quality of the biaxial texture obtained in films deposited by an aqueous sol-gel method can be comparable to those obtained in e.g. atomic layer-by-layer growth.

Highly textured layers were obtained for CeO_2 [39] on the textured Ni-W (111) substrate by dip-coating a water based Ce-precursor. A combination of EDTA and acetic acid was used to establish complexation. Also nitrate containing Ce-citrate precursors dipcoated on metallic (001) Ni-alloy tape have led to the formation of highly (001) oriented CeO_2 films as long as their thickness did not exceed 50 nm and when the thermal treatment was performed in an Ar- H_2 atmosphere to avoid oxidation of the substrate [122].

Highly textured 1,000 nm thick films of $\text{NdBa}_2\text{Cu}_3\text{O}_{7-y}$ on monocrystalline (100) SrTiO_3 substrates with an in-plane mis-orientation angle of less than 4° were achieved by means of dip-coating [45, 138] of a mainly water-based precursor solution (a 1:4 mixture of acetic acid and water was used as the solvent) using metal acetates and triethanolamine as an additional complexing agent (Fig. 5.19). The synthesized $\text{NdBa}_2\text{Cu}_3\text{O}_{7-y}$ material showed a superconducting transition temperature of 94 K for bulk and 89 K for thin films. In addition, the importance of a good metal complex formation in the precursor solution and thus the necessity for stipulating the optimum complexation parameters using potentiometric titration curves was presented by XRD phase analysis.

A similar synthetic approach led to textured $\text{YBa}_2\text{Cu}_3\text{O}_{7-x}$ layers of 450 nm thickness [95]. HR-TEM images showed an excellent orientation match between the (100) SrTiO_3 single-crystal substrate and the $\text{YBa}_2\text{Cu}_3\text{O}_{7-x}$ layer which can only be caused by coherent heterogeneous nucleation. This coherent nucleation induces strong texture development in the layer as can be deduced from the small values of the FWHM in the pole figures. Critical current densities of these films are promising, though there is still room for improvement, as the obtained films suffer from porosity due to the relatively high amount of gases released during the applied thermal treatment.

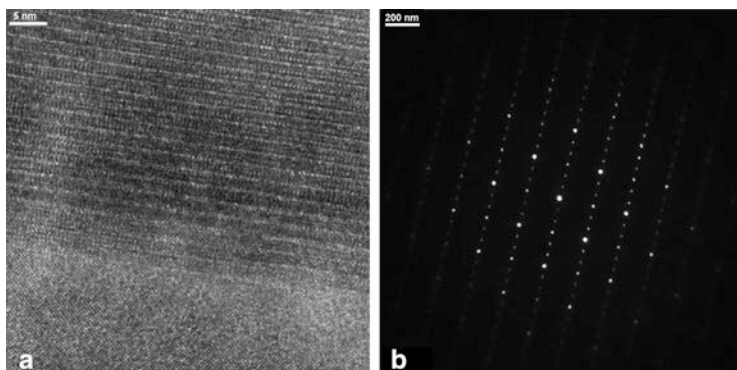


Fig. 5.19 HR-TEM image (*left*) and diffraction pattern (*right*) of the interface between a SrTiO₃ substrate and a NdBa₂Cu₃O_{7-y} film, obtained by dipcoating of an acetate-triethanolamine based aqueous precursor solution. Reproduced from [45] with kind permission from Springer Science and Business Media

5.5.5.2 Towards Ultrathin Layers

Ultrathin (Nb_{1-x}Ta_x)₂O₅ films, with x between 0 and 1 and thicknesses from ~3 to ~25 nm, have been deposited by chemical solution deposition starting from aqueous citratoperoxo-niobate(V) and -tantalate(V) precursor solutions [14] (see also Sect. 5.5.6). Clear dependence of the properties on film thickness was observed. First, crystallization temperatures increased when the film thickness was decreased (in accordance with other reports [12, 139, 140]).

For Nb₂O₅ it was shown that the (001) orientation seems to become more preferential with increasing film thickness, as compared to (100). In the ‘thicker’ films (~25 nm) interfaces and cross sections were studied by means of HR-TEM which showed crystal planes continuous throughout the entire film thickness (Fig. 5.20), although XRD patterns did show some presence of (100) oriented grains as well. It was concluded furthermore that besides the substrate and film thickness, the deposition route strongly affects the crystallization temperature. In aqueous CSD as compared to e.g. CVD, a minimum heat treatment limit is set by the thermal stability of the metal ion complexes, which have to be decomposed before oxide formation can start. In the following paragraph we will discuss this new area of ultrathin layers from carboxylate based aqueous precursors.

5.5.6 Ultrathin Film Deposition by Aqueous CSD

For a long time, in pertaining literature the conviction could be found that it was impossible to deposit uniform metal oxide films with a thickness far below 100 nm using chemical solution deposition. Reports were made of incomplete coverage of the substrate, leading to defective functional properties, or even none at all. In contrast, recently it was shown that ultrathin metal oxide films, from 30 to 3 nm in

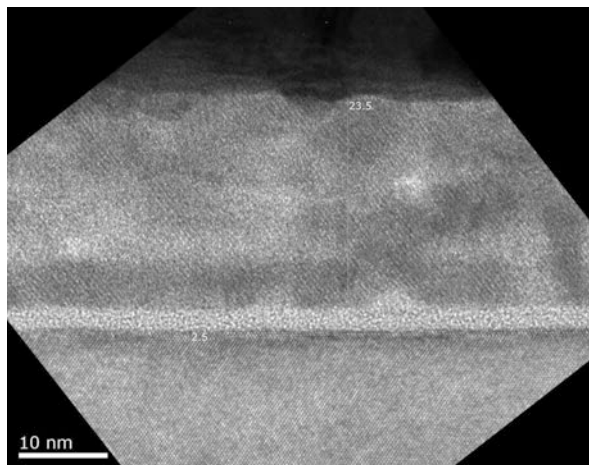


Fig. 5.20 High resolution X-TEM of Nb_2O_5 deposited from a 0.075 mol/l citrate-peroxo Nb(V) precursor. Reproduced from [14] by permission of ECS—the electrochemical society



Fig. 5.21 Ultrathin neodymium oxide film on SiO_2/Si substrate deposited by an aqueous CSD process. Reprinted from [11] with permission from Cambridge University Press

thickness, could be deposited by aqueous CSD (see Fig. 5.21), starting from aqueous solutions of carboxylate complexes [11, 20]. At the same time, reports using non-aqueous CSD routes have emerged as well [141–143], as well as a method consisting of layer-by-layer adsorption of metal alkoxide precursors in a surface sol-gel process followed by annealing [144, 145].

The strict definition of “ultrathin” differs between authors, ranging from 50 to 10 nm or beyond. Consistently the film thicknesses are always well below 100 nm, however. So far, the deposition of ultrathin films from aqueous CSD was mainly focused on the fabrication of high- k dielectric oxides ($k > 3.9$, the value for SiO_2) with applications as alternative gate dielectrics for CMOS (complementary metal oxides semiconductor) devices, DRAM (dynamic random access memory) or flash memory. Due to the dependence of materials’ properties on the film thickness, mediated by phase changes, interfacial reactions, grain boundary effects etc., it is important to study the materials in the thickness range of the final applications. Therefore, only film thicknesses well below 30 nm are relevant in view of the applications currently envisaged. Furthermore, an interesting opportunity exists

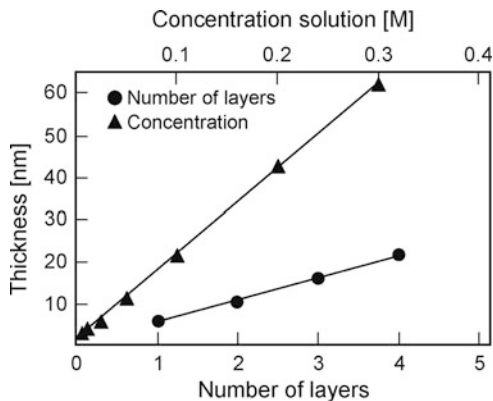
within the CSD approach to allow quick access to many different complex (substituted) multimetal oxide systems, since it allows strong compositional control and high compositional flexibility from an instrument point of view, as compared to vacuum deposition systems. This material screening objective was the original application driven motivation for studying the fundamental aspects in deposition of ultrathin high- k oxide films by aqueous CSD. Among the studied materials were binary oxides such as those of lanthanide, hafnium, zirconium, niobium and tantalum, while in a next stage multimetal oxides were prepared as well: mixed lanthanide oxides, lanthanide or strontium niobates, niobium tantalum oxides, barium and strontium zirconate or titanate and mixtures thereof, bismuth titanates, lanthanide aluminates etc. [11–14, 16, 19].

A specific advantage of ultrathin film deposition by aqueous routes compared to solvent based routes, on the level of the precursor solutions, is worth mentioning. The depositions of ultrathin films are carried out starting from precursor solutions with low concentrations. At lower concentration, solubility limits of the carboxylato complexes in water are no longer exceeded, enhancing the solution's stability. At the same time, the hydrolysis and condensation reactions, leading to precipitation of (hydroxo)oxocomplexes [29], are prevented at a lower ligand to metal ion ratio or even without excess ligands (see also Sect. 5.2). Due to the lower excess of carboxylate ligands for obtaining stable solutions in water, the organic content of the solution is lowered. As such, the lower concentration required for ultrathin film deposition is considered an advantage. In contrast, in solvent-based routes, a higher organic content is quoted by Brennecka et al. [143] when using low-molarity solutions, leading to stronger reducing environment during the pyrolysis step and possible negative effects on the oxidation state of the metal ions involved. For material systems such as lead zirconate titanate, this can subsequently be followed by certain material specific, adverse effects such as Pb loss through alloy formation with a Pt bottom electrode.

The aqueous CSD film thickness was simply controlled by variation of the number of deposited layers (1–4 layers) or by the concentration of the oxide precursor, typically in a range from 0.005 mol l^{-1} to 0.1 mol l^{-1} (Fig. 5.22). A linear trend of film thickness with increasing concentration was generally observed in this region for different kinds of binary or ternary oxides, at constant annealing temperature. In contrast, a quadratic relation showed a better agreement with the experimentally obtained thicknesses as a function of precursor concentration for aquo-diol deposited films [142, 146].

Theoretically it was predicted for spin-coating of polymers that the film thickness would vary according to the relationship $t = A c^n \omega^{-m}$ where t is the film thickness, c is the concentration of the solution and ω is the rotation velocity [142, 147]. Even though the model does not take into account effects such as densification by crystallization, which is occurring for oxide films, it appears to be applicable for the case of CSD deposited metal oxides with $n = 1$ down to very low thickness ranges and at a constant rotation speed, as well. The linear relation between the film thickness and the number of layers on the other hand, indicated there are no undesirable interactions of subsequent deposited layers occurring, such

Fig. 5.22 Film thickness as measured by X-ray reflectometry as a function of precursor concentration for zirconium oxide films calcined at 600 °C. A linear trend is observed as a function of concentration (four layers) and number of layers (0.1 mol/l) down to 3.3 nm



as dissolution etching, which of course also depends strongly on the chemical properties of the deposited oxide and the chemical properties of the precursor solution.

Due to the chemical similarity of the metal's precursors, all being based mainly on citrato-complexes, they generally showed similar decomposition profiles for the bulk gels, as explained earlier. It could be derived that similar thermal programs were applicable for all the different oxides, consisting of stepwise hot plate treatments followed by final calcination/anneal treatment in a furnace. Depending on the specific metal oxide, e.g. the constituent metal ion's tendency towards carbonate formation, the possibility for interfacial reaction with the substrate and the thickness dependent crystallization behavior, the thermal treatment requires optimization in order to reduce the carbon content in the films [19], optimize the film uniformity [148], induce crystallization [12] or avoid interfacial reactions [149]. Such detailed studies of specific metal oxide systems, have revealed that the effects of calcination and annealing conditions, such as temperature, time or layer-by-layer annealing on the film's characteristics are strongly dependent on the type of oxides but also on the ratio of their constituting metal ions, which is explained by the differences in crystalline phases, that may be obtained depending upon this ratio.

The film thickness uniformity and continuity was verified by common methods such as scanning electron microscopy (only for the thickest layers), by atomic force microscopy and by cross sectional TEM. Further indication for film uniformity was obtained from electrical characterization, mainly the magnitude of leakage currents obtained from I-V curves measured on circular Pt top electrodes. It was shown that amorphous films generally, have high uniformity and continuity over a wide thickness range, while the individual layers, resulting from the layer-by-layer deposition flow in case of stacking four layers on top of each other, could not be distinguished. Upon anneal treatment up to relatively high temperatures, several effects may occur:

Crystallization with or without conservation of the film uniformity: dependent on the nature of the metal oxide and the thermal budget applied.

Interactions with the substrate: silicate formation was observed for the case of SiO_2/Si substrates, to which attenuated total reflectance Fourier transform infrared spectroscopy was shown to be highly sensitive [150]. (Multi)metal oxide films containing rare earth or alkaline earth metal ions were prone to this interfacial interaction, at temperatures depending on the metal ions involved.

The high uniformity during spin-coating deposition of the precursor solutions can be explained by the low viscosity of the aqueous solutions applied and the relatively limited vapor pressure of this solvent at room temperature, which allows a good spread of the precursor over the substrate surface and a uniform evaporation. Of course, this is dependent on the substrate pretreatment (cleaning) as well, where the requirement of hydrophilicity is as important as in the case of thicker films (Sect. 5.5.1) and on the chemical properties of the precursor solution, including its pH. In contrast, it was found that a bulk gelation behavior of the precursor solution, without precipitation, is not a prerequisite for obtaining uniform ultrathin films in the case of monometal oxides, such as ZrO_2 [15].

As the drying kinetics are different in case of spin-coating highly diluted solutions, the film gelation behavior may differ from that in bulk. In any case, segregation of the metal ions on a nm scale may be of substantial effect in case of deposition of multimetal oxides, as it could lead to continuation of the segregation during thermal treatment and affect the phase formation.

However, the uniformity should be maintained throughout the subsequent thermal processing steps as well. By application of stepwise drying and pyrolysis treatment on hot plates with increasing temperatures, rupture of the films due to a too abrupt evolution of decomposition gases is avoided, as is traditional in CSD. Such a thermal treatment process can be based on thermal analysis of the bulk precursors, which allows assessment of the temperature range of the major decomposition steps, where a large volume of gases will be evolved. Certainly here, possible differences between the film's and bulk precursor's decomposition are kept in mind, which are related to volume effects such as the contact surface area with the reactive ambient (oxygen containing) required for oxidizing removal of the ligands, as well as the exothermic nature of the combustion reaction, resulting into full decomposition of the precursors. The thinner the layer, the stronger these volume effects may be by the enhanced contact with the reactive ambient gas and the reduced effect of self-heating during combustion. Also, the tendency for rupture of the films by evolving gases is reduced with reducing film thickness.

After careful consideration of the thermal processing to maintain film uniformity during precursor decomposition with increasing annealing temperatures, depending on the oxide, microstructural instability leading to island formation is often still observed. This phenomenon was described and explained in earlier literature considering the ratio of grain size and film thickness [151]. Once this ratio exceeds a critical value, the surface energy reduction due to formation of discontinuous or island-like films will lead to disruption of the film's uniformity. This is a general observation, also made for non-aqueous deposited films [152], which confirms that it can be related to the properties of the final oxide rather than solely to the precursor route followed [142]. Nonetheless, detailed comparative studies of this effect for

different precursor systems, including aqueous systems, were not carried out to the best of our knowledge.

The microstructural instability phenomenon can be avoided by reducing grain growth, by keeping the anneal temperature sufficiently low or decreasing the annealing times. On the other hand, in case of reaction with the substrate, the formation of an amorphous silicate phase at their interface may lead to stabilization of the uniform film morphology, and prevention of crystallization of the films. This was observed for both aqueous CSD deposited films and ALD deposited ultrathin films [153]. The strong impact the substrate has on the development of substrate-based nano-islands, by aqueous CSD processing, was shown recently [17], comparing Pt, SrTiO₃ as well as SiO₂/Si substrates for the case of PbTiO₃ films. This strong effect may not only be traced back to the possibility for interfacial interactions/reactions, but also be related to effects such as the contact angle of the crystallization nuclei on the substrate in question.

Finally, the functionality of aqueous CSD deposited ultrathin films towards high-*k* applications was confirmed by dielectric measurements, such as C-V and I-V characterization. For film thicknesses down to a minimum of 3 nm on SiO_x/Si, high-quality dielectric properties were obtained, as observed from the well-behaved C-V curves measured on MOS devices defined by circular Pt topelectrodes. The electrical properties, most importantly EOT values and leakage currents, were comparable after optimization to those obtained by atomic layer deposition, which is accepted widely as the designated deposition technique for ultrathin oxide layers [19]. On the other hand, functional capacitors characterized down to 6 nm [154], were obtained by aqueous CSD on 10-nm thick TiN bottom electrodes as well. This allowed to obtain CET values down to ~2 nm. Low temperature processing, required by the oxidation sensitive substrate, led to higher leakage currents due to higher carbon levels in these films.

The study of ultrathin oxide films from aqueous chemical solution deposition, has shown great potential for fundamental materials' research, which may find different applications beyond the main focus of high-*k* dielectrics and ferroelectrics that was cited here. Open research questions, currently worked on, are related to the behavior of ultrathin films by aqueous CSD on different substrates besides SiO₂/Si, prevention of interfacial reactions and peculiarities of specific material systems.

References

1. Schwartz RW, Schneller T, Waser R (2004) Chemical solution deposition of electronic oxide films. *CR Chimie* 7:433–461
2. Statt BW, Wang Z, Lee MGJ, Yakhmi JV, de Camargo PC, Major JF, Rutter JW (1988) Stabilizing the high-*T_c* superconductor Bi₂Sr₂Ca₂Cu₃O_{10+x} by Pb substitution. *Phys C* 156:251
3. Fransaeer J, Roos JR, Delaey L, van der Biest O, Arkens O, Celis JP (1989) Sol-gel preparation of the High *T_c* Bi-Ca-Sr-Cu-O and Y-Ba-Ca-O superconductors. *J Appl Phys* 65:3277

4. Fujisawa T, Tagaki A, Honjoh T, Okuyama K, Ohshima S, Matsuki K, Muraishi K (1989) Preparation of superconducting Y–Ba–Cu–O and Bi–Pb–Sr–Ca–Cu–O compounds by chelating method. *Jpn J Appl Phys* 8:1358
5. Kakihana M (1996) “Sol-Gel” preparation of high temperature superconducting oxides. *J Sol-Gel Sci Technol* 6:7
6. Fransaer J, Eggermont T, Arkens O, Van der Biest O, Roggen J, Boon W, Dhalle M, Vanacken J, Wuyts B, Bruynseraede Y (1989) A new method of synthesizing high-Tc superconducting materials. *Phys C* 162:881
7. Okada K, Otsuka N, Somyia N (1991) Review of mullite synthesis routes in Japan. *Am Ceram Soc Bull* 70:1633
8. Van der Biest O, Kwarciak J, Dierickx D, Dhalla M, Boon W, Bruynseraede Y (1991) Ceramic superconductors synthesized by sol-gel methods. *Phys C* 190:119
9. Lakeman CDE, Payne D (1992) Processing effects in the sol-gel preparation of PZT dried gels, powders and ferroelectric thin layers. *J Am Ceram Soc* 75:3091
10. Brylewski T, Przybylski K (1993) Physicochemical properties of high-TC (Bi, Pb)-Sr-Ca-Cu-O and Y-Ba-Cu-O superconductors prepared by sol-gel technique. *Appl Supercond* 1:737
11. Hardy A, Van Elshocht S, D’Haen J, Douheret O, De Gendt S, Adelman C, Caymax M, Conard T, Witters T, Bender H, Richard O, Heyns M, D’Olieslaeger M, Van Bael MK, Mullens J (2007) Aqueous chemical solution deposition of ultrathin lanthanide oxide dielectric films. *J Mater Res* 22(12):3484
12. Hardy A, Van Elshocht S, Knaepen W, D’Haen J, Conard T, Brijs B, Vandervorst W, Pourtois G, Kittl J, Detavernier C, Heyns M, Van Bael MK, Van den Rul H, Mullens J (2009) Crystallization resistance of barium titanate zirconate ultrathin films from aqueous CSD: a study of cause and effect. *J Mater Chem* 19:1115
13. Hardy A, Van Elshocht S, D’Haen J, De Gendt S, Van Bael MK, Heyns M, D’Olieslaeger M, Mullens J (2008) In pursuit of “super” high-k ternary oxides: aqueous CSD and material properties. In: Pantisano L, Gusev E, Green M, Niwa M (eds) *Materials science of high k dielectric stacks—from fundamentals to technology*, vol 1073E, Materials research society symposia proceedings. Materials Research Society, Warrendale, PA
14. Hardy A, Van Elshocht S, Dewulf D, Clima S, Peys N, Adelman C, Opsomer K, Favia P, Bender H, Hoflijk I, Conard T, Franquet A, Van den Rul H, Kittl JA, De Gendt S, Van Bael MK, Mullens J (2010) Properties of ultrathin high permittivity (Nb_{1-x}Ta_x)₂O₅ films from aqueous CSD. *J Electrochem Soc* 157:G13
15. Hardy A, Van Elshocht S, Adelman C, Conard T, Franquet A, Douheret O, Haeldermans I, D’Haen J, De Gendt S, Caymax M, Heyns M, D’Olieslaeger M, Van Bael MK, Mullens J (2008) Aqueous solution-gel preparation of ultrathin ZrO₂ films for gate dielectric application. *Thin Solid Films* 516:8343
16. Hardy A, D’Haen J, Van den Rul H, Van Bael MK, Mullens J (2009) Crystallization of alkaline earth zirconates and niobates from compositionally flexible aqueous solution-gel syntheses. *Mater Res Bull* 44:734
17. De Dobbelaere C, Hardy A, D’Haen J, Van den Rul H, Van Bael MK, Mullens J (2009) Morphology of water-based chemical solution deposition (CSD) lead titanate films on different substrates: towards island formation. *J Eur Ceram Soc* 29:1703
18. Daenen M, Zhang L, Erni R, Williams O, Hardy A, Van Bael MK, Wagner P, Haenen K, Nesladek M, Van Tendeloo G (2009) Diamond nucleation by carbon transport from buried nanodiamond TiO₂ sol-gel composites. *Adv Mater* 21:670
19. Van Elshocht S, Hardy A, Adelman C, Caymax M, Conard T, Franquet A, Richard O, Van Bael MK, Mullens J, De Gendt S (2008) Impact of process optimizations on the electrical performance of high-k layers deposited by aqueous chemical solution deposition. *J Electrochem Soc* 155:G91
20. Van Elshocht S, Hardy A, Witters T, Adelman C, Caymax M, Conard T, De Gendt S, Franquet A, Heyns M, Van Bael MK, Mullens J (2007) Aqueous chemical solution deposition – fast screening method for alternative high-k materials applied to Nd₂O₃. *Electrochem Solid State Lett* 10:G15

21. Baes CF, Mesmer RE (1976) The hydrolysis of cations. Wiley, New York
22. Jolivet JP, Henry M, Livage J (2000) Metal oxide chemistry and synthesis – from solution to solid state. Wiley, New York, NY
23. Livage J, Henry M, Sanchez C (1988) Sol-gel chemistry of transition metal oxides. *Prog Solid State Chem* 18:259
24. Burgess J (1988) Ions in solution: basic principles of chemical interactions. Halsted Press, Chichester
25. Jorgensen CK (1963) Inorganic complexes. Academic, London
26. Sanderson RT (1951) An interpretation of bond lengths and a classification of bonds. *Science* 114:670
27. Flynn CM (1984) Hydrolysis of inorganic Iron(III) salts. *Chem Rev* 84:31
28. Gustafson RL (1960) Polymerization of metal chelates in aqueous solution. *J Chem Educ* 37:603
29. Kragten J (1978) Atlas of metal ligand equilibrium in aqueous solution. Wiley, Chichester
30. Ringbom A (1963) Complexation in analytical chemistry. Interscience, New York
31. Schwarzenbach G (1957) Complexometric titrations. Interscience, New York
32. Richens DT (1997) The chemistry of aqua-ions. John Wiley, Chichester
33. Narendar Y, Messing GL (1997) Mechanisms of phase separation in gel-based synthesis of multicomponent metal oxides. *Catal Today* 35:247
34. Bobtelsky M, Graus B (1953) Lead citrates, complexes and salts, their composition, structure and behavior. *J Am Chem Soc* 75:4172
35. Ekstrom LG, Olin A (1979) Complex formation between Lead-(II) and citrate ions in acid, neutral and weakly alkaline-solution. *Chem Scripta* 13:10
36. Sillen LG, Martell AE (1964) Stability constants of metal-ion complexes. London Chemical Society, London
37. Van den Rul H, Van Bael MK, Hardy A, Van Werde A, Mullens J (2009) Aqueous solution based synthesis of nanostructured metal oxides. In: Tseng T, Nalwa HS (eds) Handbook of nanoceramics and their based nanodevices. American Scientific Publishers, Valencia, CA
38. De Buysser K, Van Driessche I, Schaubroeck J, Hoste S (2008) EDTA assisted sol-gel synthesis of ZrW_2O_8 . *J Sol-Gel Sci Technol* 46:133
39. Thuy TT, Hoste S, Herman GG, Van de Velde N, De Buysser K, Van Driessche I (2009) Novel water based cerium acetate precursor solution for the deposition of epitaxial cerium oxide films as HTSC buffers. *J Sol-Gel Sci Technol* 51:112
40. Kareiva A, Bryntse I, Karppinen M, Niinistö L (1996) Influence of complexing agents on properties of $YBa_2Cu_4O_8$ superconductors prepared by the sol-gel method. *J Solid State Chem* 121:356
41. Kareiva A, Barkauskas J, Mathur S (2000) Oxygen content and superconducting properties of Hg-based superconductors synthesized by sol-gel method. *J Phys Chem Solids* 61:789
42. Camargo ER, Kakihana M (2002) Low temperature synthesis of lithium niobate powders based on water-soluble niobium malato complexes. *Solid State Ion* 151:413
43. Camargo ER, Longo E, Leite ER, Kakihana M (2004) Qualitative measurement of residual carbon in wet-chemically synthesized powders. *Ceram Int* 30:2235
44. Hardy A, D'Haen J, Goux L, Wouters D, Van Bael MK, Van den Rul H, Mullens J (2007) Aqueous chemical solution deposition of ferroelectric Ti^{4+} cosubstituted $(Bi,L)_4Ti_3O_{12}$ thin films. *Chem Mater* 19:2994
45. Schoofs B, Mouganie T, Glowacki BA, Cloet V, Hoste S, Van Driessche I (2007) Synthesis of highly textured superconducting $NdBa_2Cu_3O_{7-y}$ thin films by two aqueous sol-gel dip coating techniques. *J Sol-Gel Sci Technol* 41:113
46. Narendar Y, Messing GL (1997) Synthesis, decomposition and crystallization characteristics of peroxo-citrato-niobium: an aqueous niobium precursor. *Chem Mater* 9:580
47. Nelis D, Van Werde K, Mondelaers D, Vanhoyland G, Van Bael MK, Mullens J, Van Poucke LC (2001) Synthesis of $SrBi_2Ta_2O_9$ (SBT) by means of a soluble Ta(V) precursor. *J Eur Ceram Soc* 21:2047

48. Nelis D, Van Bael MK, Van den Rul H, Mullens J, Van Poucke LC, Vanhoyland G, D'Haen J, Laureyn W, Wouters DJ (2002) Ferroelectric SrBi₂Nb₂O₉ thin films by aqueous chemical solution deposition. *Integr Ferroelectr* 45:205
49. Nelis D, Van Werde K, Mondelaers D, Vanhoyland G, Van den Rul H, Van Bael MK, Mullens J, Van Poucke LC (2003) Aqueous solution-gel synthesis of strontium bismuth niobate (SrBi₂Nb₂O₉). *J Sol-Gel Sci Technol* 26:1125
50. Hardy A, Mondelaers D, Vanhoyland G, Van Bael MK, Mullens J, Van Poucke LC (2003) The formation of ferroelectric bismuth titanate (Bi₄Ti₃O₁₂) from an aqueous metal-chelate gel. *J Sol-Gel Sci Technol* 26:1103
51. Van Werde K, Vanhoyland G, Nelis D, Mondelaers D, Van Bael MK, Mullens J, Van Poucke LC (2001) Phase formation of ferroelectric perovskite 0.75 Pb(Zn_{1/3},Nb_{2/3})O₃-0.25 BaTiO₃ prepared by aqueous solution-gel chemistry. *J Mater Chem* 11:1192
52. Storms A, Van Bael MK, Van den Rul H, Mullens J, Van Poucke LC (2004) Phase formation of perovskite lead magnesium niobate prepared by an aqueous solution-gel method. *Key Eng Mater* 264:347
53. Hardy A, Mondelaers D, Van Bael MK, Mullens J, Van Poucke LC, Vanhoyland G, D'Haen J (2004) Synthesis of (Bi, La)₄Ti₃O₁₂ by a new aqueous solution-gel route. *J Eur Ceram Soc* 24:905
54. Pagnier J, Mondelaers D, Vanhoyland G, Van Bael MK, Van den Rul H, Mullens J, Van Poucke LC (2004) Synthesis of RuO₂ and SrRuO₃ powders by means of aqueous solution-gel chemistry. *J Eur Ceram Soc* 24:919
55. Pagnier J, Hardy A, Mondelaers D, Vanhoyland G, D'Haen J, Van Bael MK, Van den Rul H, Mullens J, Van Poucke LC (2005) Preparation of La_{0.5}Sr_{0.5}CoO₃ powders and thin film from a new aqueous solution-gel precursor. *Mater Sci Eng B* 118:79
56. Bayot D, Devillers M (2006) Peroxo complexes of niobium(V) and tantalum(V). *Coord Chem Rev* 250:2610 and references therein
57. Van Werde K, Vanhoyland G, Mondelaers D, Van den Rul H, Van Bael MK, Mullens J, Van Poucke LC (2007) The aqueous solution-gel synthesis of perovskite Pb(Zr_{1-x},Ti_x)O₃ (PZT). *J Mater Sci* 42:624
58. Van Bael MK, Arcon I, Van Werde K, Nelis D, Mullens J, Van Poucke LC (2005) Structure determination via EXAFS of Niobium-peroxo-citrate complexes in liquid and amorphous precursors for aqueous solution-gel synthesis. *Phys Scripta* T115:415
59. Hardy A, Van Werde K, Vanhoyland G, Van Bael MK, Mullens J, Van Poucke LC (2003) Study of the decomposition of an aqueous metal-chelate gel precursor for (Bi,La)₄Ti₃O₁₂ by means of TGA-FTIR, TGA-MS and HT-DRIFT. *Thermochim Acta* 397:143
60. Van Werde K, Mondelaers D, Vanhoyland G, Nelis D, Van Bael MK, Mullens J, Van Poucke LC, Van der Veken B, Desseyn HO (2002) Thermal decomposition of the ammonium zinc acetate citrate precursor for aqueous chemical solution deposition of ZnO. *J Mater Sci* 37:81
61. Nelis D, Mondelaers D, Vanhoyland G, Hardy A, Van Werde K, Van den Rul H, Van Bael MK, Mullens J, Van Poucke LC, D'Haen J (2005) Synthesis of strontium bismuth niobate (SrBi₂Nb₂O₉) using an aqueous acetate-citrate precursor gel: thermal decomposition and phase formation. *Thermochim Acta* 426:39
62. Djordjevic C, Lee M, Sinn E (1989) Oxoperoxo(citrate)vanadates(V) and dioxo(citrate)vanadates(V) synthesis, spectra, and structure of a hydroxyl oxygen bridged dimer K₂[VO(O₂)(C₆H₆O₇)]₂·2H₂O. *Inorg Chem* 28:719
63. Kakihana M, Tada M, Shiro M, Petrykin V, Osada M, Nakamura Y (2001) Structure and stability of water soluble (NH₄)₈[Ti₄(C₆H₄O₇)₄(O₂)₄].8H₂O. *Inorg Chem* 40:891
64. Hardy A, D'Haen J, Van Bael MK, Mullens J (2007) An aqueous solution-gel citratoperoxo-Ti(IV) precursor: synthesis, gelation, thermo-oxidative decomposition and oxide crystallization. *J Sol-Gel Sci Technol* 44:65
65. Bretos I, Jiménez R, Calzada ML, Van Bael MK, Hardy A, Van Genechten D, Mullens J (2006) Entirely aqueous solution-gel route for the preparation of (Pb_{1-x}Ca_x)TiO₃ thin films. *Chem Mater* 18:6448

66. Mondelaers D, Vanhoyland G, Van den Rul H, D'Haen J, Van Bael MK, Mullens J, Van Poucke LC (2003) Chemical solution deposition of ZnO thin films by an aqueous solution gel precursor route. *J Sol-Gel Sci Technol* 26:523
67. De Buysser K, Smet PF, Schoofs B, Bruneel E, Poelman D, Hoste S, Van Driessche I (2007) Aqueous sol-gel processing of precursor oxides for ZrW₂O₈ synthesis. *J Sol-Gel Sci Technol* 43:347
68. Rajendran M, Rao MS (1994) Synthesis and characterization of Barium bis(citrate) oxozirconate(IV)tetrahydrate – a new molecular precursor for fine-particle BaZrO₃. *J Mater Res* 9:2277
69. Mühlebach J, Müller K, Schwarzenbach G (1970) The peroxo complexes of titanium. *Inorg Chem* 9(11):2381
70. Thompson RC (1985) Equilibrium studies and redox kinetics of the peroxo complex of Zirconium(IV) in acidic perchlorate solution. *Inorg Chem* 25:3542
71. Pechini MP (1967) US Patent No 3. 330, p 697
72. Schwartz RW (1997) Chemical solution deposition of perovskite thin films. *Chem Mater* 9:2325
73. Popa M, Frantti J, Kakihana M (2002) Lanthanum ferrite LaFeO_{3+d} nanopowders obtained by the polymerizable complex method. *Solid State Ion* 154:437
74. Popa M, Kakihana M (2003) Ultrafine niobate ceramic powders in the system RE_xLi_{1-x}NbO₃ (RE : La, Pr, Sm, Er) synthesized by polymerizable complex method. *Catal Today* 78:519
75. Kakihana M, Yoshimura M (1999) Synthesis and characteristics of complex multicomponent oxides prepared by polymer complex method. *Bull Chem Soc Jpn* 72:1427
76. Zanetti SM, Longo E, Leite ER, Varela JA (1999) SrBi₂Nb₂O₉ thin films deposited by dip coating using aqueous solution. *J Eur Ceram Soc* 19:1409
77. Javoric S, Kosec M, Malic B (2000) Water-based synthesis of La_{0.5}Sr_{0.5}CoO₃ (LSCO) electrodes for ferroelectric thin films. *Integr Ferroelectr* 30:309
78. Jia QX, McCleskey TM, Burrell AK, Lin Y, Collis G, Wang H, Li ADQ, Foltyn SR (2004) Polymer-assisted deposition of metal-oxide films. *Nat Mater* 3:529
79. Hardy A, Vanhoyland G, Geuzens E, Van Bael MK, Mullens J, Van Poucke JC, D'Haen J (2005) Gel structure, gel decomposition and phase formation mechanisms in the aqueous solution–gel route to lanthanum substituted bismuth titanate. *J Sol-Gel Sci Technol* 33:283
80. Truijen I, Hardy A, Van Bael MK, Van den Rul H, Mullens J (2007) Study of the decomposition of aqueous citratoperoxo-Ti(IV)-gel precursors for titania by means of TGA-MS and FTIR. *Thermochim Acta* 456:38
81. Mullens J, Van Werde K, Vanhoyland G, Nouwen R, Van Bael MK, Van Poucke LC (2002) The use of TGA-MS, TGA-FTIR, HT-XRD and HT-DRIFT for the preparation and characterization of PbTiO₃ and BaTiO₃. *Thermochim Acta* 392:29
82. Streitwieser A, Heathcock CH (1992) Introduction to organic chemistry, vol 4. MacMillan, New York
83. Fischer J, Merwin LH, Nissan RH (1995) NMR investigation of the thermolysis of citric acid. *Appl Spectrosc* 49:120
84. Sankaranarayanan VK, Gajbhiye NS (1989) Thermal decomposition of dysprosium iron citrate. *Thermochim Acta* 153:337
85. Narendar Y (1996) Regulating oxide crystallisation from Pb, Mg and Nb-carboxylate gels. Thesis in Materials Science Engineering, Pennsylvania State University
86. Narendar Y, Messing GL (1999) Effect of phase separation in metal carboxylate gels on perovskite lead magnesium niobate crystallization. *J Mater Res* 14:3921
87. Cloet V, Feys J, Hühne R, Hoste S, Van Driessche I (2009) Thin La₂Zr₂O₇ films made from a water-based solution. *J Solid State Chem* 182:37
88. Moursour SA, Liedl G, Vest RW (2005) Microstructural developments and dielectric properties of rapid thermally processed PZT films derived by metallo-organic decomposition. *J Am Ceram Soc* 7:1617

89. Van Werde K (2003) De realisatie en de optimalisering van de waterige sol-gel methode voor de bereiding van perovskiet PZN en gedopeerde PZN verbindingen. PhD Thesis, University of Hasselt
90. Job P (1928) Formation and stability of inorganic complexes in solution. *Ann Chim* 9:113
91. Van Genechten D (2005) Watergebaseerde bereiding van ferro-elektrische nano-structureerde $\text{Pb}(\text{Zr}_{0.3}\text{Ti}_{0.7})\text{O}_3$ films. PhD Thesis, University of Hasselt
92. Chen TC, Li TK, Zhang XB, Desu SB (1997) Structure development studies of $\text{SrBi}_2(\text{Ta}_{1-x}\text{Nb}_x)_2\text{O}_9$ thin films. *J Mater Res* 12:2165
93. Koiwa I, Okada Y, Mita J, Hashimoto A, Sawada Y (1997) Role of excess Bi in $\text{SrBi}_2(\text{NbTa})_2\text{O}_9$ thin film prepared using chemical liquid deposition and sol-gel method. *Jap J Appl Phys* 36:5904
94. Tuttle BA, Schwartz RW (1996) Solution deposition of ferroelectric thin films. *MRS Bull* 21:49
95. Vermeir P, Cardinael I, Bäcker M, Schaubroeck J, Schacht E, Hoste S, Van Driessche I (2009) Fluorine-free water-based sol-gel deposition of highly epitaxial $\text{YBa}_2\text{Cu}_3\text{O}_{7-\delta}$ films. *Supercond Sci Technol* 22:075009
96. Thuy TT, Hoste S, Herman GG, De Buysser K, Lommens P, Feys J, Vandeput D, Van Driessche I (2009) Sol-gel chemistry of an aqueous precursor solution for YBCO thin films. *J Sol-Gel Sci Technol* 52:124
97. Lin CT, Li L, Webb JS, Leung MS, Lipeles RA (1995) Deposition and characterization of photoconductive PZT thin-films. *J Electrochem Soc* 142:1957
98. Wu XM, Li XH, Xu MF, Zhang YH, He ZQ, Wang Z (2002) Preparation of LiMn_2O_4 thin films by aqueous solution deposition. *Mater Res Bull* 37:2345
99. Gujar TP, Shinde VR, Lokhande CD, Mane RS, Han SH (2005) Bismuth oxide thin films prepared by chemical bath deposition (CBD) method: annealing effect. *Appl Surf Sci* 250:161
100. Truijen I, Van Bael MK, Van den Rul H, D'Haen J, Mullens J (2007) Synthesis of thin dense titania films via an aqueous solution-gel method. *J Sol-Gel Sci Technol* 41:43
101. Andeen D, Loeffler L, Padture N, Lange FF (2003) Crystal chemistry of epitaxial ZnO on (111) MgAl_2O_4 produced by hydrothermal synthesis. *J Cryst Growth* 259:103
102. Berkat L, Cattin L, Reguig A, Regraguib M, Bernède JC (2005) Comparison of the physico-chemical properties of NiO thin films deposited by chemical bath deposition and by spray pyrolysis. *Mater Chem Phys* 89:11
103. Kajiyoshi K, Yanigasawa K, Feng Q, Yoshimura M (2006) Preparation of complex oxide thin films under hydrothermal and hydrothermal-electrochemical conditions. *J Mater Sci* 41:1535
104. Lee B, Zhang J (2001) Preparation, structure evolution and dielectric properties of BaTiO_3 thin films and powders by an aqueous sol-gel process. *Thin Solid Films* 388:107
105. Gao XD, Li XM, Yu WD (2004) Preparation, structure and ultraviolet photoluminescence of ZnO films by a novel chemical method. *J Solid State Chem* 177:3830
106. Dinesh R, Fujiwara T, Watanabe T, Byrappa K, Yoshimura M (2006) Solution synthesis of crystallized AMO(4) (A=Ba, Sr, Ca; M=W, Mo) film at room temperature. *J Mater Sci* 41:1541
107. Collins RJ, Chaim NS (1995) Sulfonate-functionalized, siloxane-anchored, self-assembled monolayers. *Langmuir* 11:2322
108. Liu JF, Nistorica C, Gory I, Skidmore G, Mantiziba FM, Gnade BE (2005) Layer-by-layer deposition of zirconium oxide films from aqueous solutions for friction reduction in silicon-based micro electromechanical system devices. *Thin Solid Films* 492:6
109. Van Bael MK, Nelis D, Hardy A, Mondelaers D, Van Werde K, D'Haen J, Vanhoyland G, Van den Rul H, Mullens J, Van Poucke LC, Frederix F, Wouters DJ (2002) Aqueous chemical solution deposition of ferroelectric thin films. *Integr Ferroelectr* 45:113
110. Hardy A, Nelis D, Vanhoyland G, Van Bael MK, Van den Rul H, Mullens J, Van Poucke LC, D'Haen J, Goux L, Wouters DJ (2005) Effect of pyrolysis temperature on the properties of

- $\text{Bi}_{3.5}\text{La}_{0.5}\text{Ti}_3\text{O}_{12}$ thin films deposited by aqueous chemical solution deposition. *Mater Chem Phys* 92:431
111. Hardy A, Nelis D, Vanhoyland G, Van Bael MK, Mullens J, Van Poucke LC, D'Haen J, Wouters DJ (2004) Aqueous CSD of ferroelectric $\text{Bi}_{3.5}\text{La}_{0.5}\text{Ti}_3\text{O}_{12}$ (BLT) thin films. *Integr Ferroelectr* 62:205
 112. Nelis D, Mondelaers D, Vanhoyland G, Van den Rul H, Van Bael MK, Mullens J, Van Poucke LC, D'Haen J, Wouters DJ (2004) Influence of heat treatment on $\text{Sr}_{0.9}\text{Bi}_{2.2}\text{Ta}_2\text{O}_9$ thin films prepared by aqueous CSD. *Integr Ferroelectr* 62:205
 113. Vig JR (1993) Handbook of semiconductor wafer cleaning technology. In: Kern W (ed) Science, technology and applications. Noyes, New Jersey
 114. Van den Rul H, Mondelaers D, Van Bael MK, Mullens J (2006) Water-based wet chemical synthesis of (doped) ZnO nanostructures. *J Sol-Gel Sci Technol* 39:41
 115. Schwartz RW, Voigt JA, Tuttle BA, Payne DA, Reichert TL, DaSalla RS (1997) Comments on the effects of solution precursor characteristics and thermal processing conditions on the crystallization behavior of sol-gel derived lead zirconate titanate thin films. *J Mater Res* 12:444
 116. Bhaskar S, Majumder SB, Fachini ER, Katiyar RS (2004) Influence of precursor solutions on the ferroelectric properties of sol-gel-derived lanthanum-modified lead titanate (PLT) thin films. *J Am Ceram Soc* 87:384
 117. Majumder SB, Agrawal DC, Mohapatra YN, Kulkarni VN (1995) Perovskite phase formation in sol-gel derived $\text{Pb}(\text{Zr}_x\text{Ti}_{1-x})\text{O}_3$ thin films. *Integr Ferroelectr* 9:271
 118. Wouters DJ, Norga GJ, Maes HE (2003) The role of precursor chemistry in the ferroelectric properties of donor doped $\text{Pb}(\text{Zr}, \text{Ti})\text{O}_3$ thin films. *Mat Res Soc Symp Proc* 541:381
 119. Maiwa H, Ichinose N (2003) Thickness dependence of the electrical and electromechanical properties of $\text{Pb}(\text{Zr}, \text{Ti})\text{O}_3$ thin films. *Jpn J Appl Phys* 42:4392
 120. Es-Souni M, Zhang N, Iakovlev S, Solterbeck CH, Piorra A (2003) Thickness and erbium doping effects on the electrical properties of lead zirconate titanate thin films. *Thin Solid Films* 440:26
 121. Truijen I, Haeldermans I, Van Bael MK, Van den Rul H, D'Haen J, Mullens J, Terryn H, Goossens V (2007) Influence of synthesis parameters on morphology and phase composition of porous titania layers prepared via water based chemical solution deposition. *J Eur Ceram Soc* 27:4537
 122. Penneman G, Van Driessche I, Bruneel E, Hoste S (2004) Deposition of CeO_2 buffer layers and $\text{YBa}_2\text{Cu}_3\text{O}_{7-8}$ superconducting layers using an aqueous sol-gel method. *Key Eng Mater* 264:501
 123. Nelis D (2004) Studie van de waterige oplossing-gel methode voor de bereiding van ferro-elektrische $\text{SrBi}_2\text{Ta}_2\text{O}_9$ en $\text{SrBi}_2\text{Nb}_2\text{O}_9$ poeders en dunne lagen. PhD Thesis, University of Hasselt
 124. Scott JF, Paz de Araujo CA (1989) Ferroelectric memories. *Science* 246:1400
 125. Paz de Araujo CA, Cuchiari JD, McMillan LD, Scott MC, Scott JF (1995) Fatigue-free ferroelectric capacitors with platinum electrodes. *Nature* 374:627
 126. Auciello O, Scott JF, Ramesh R (1998) The physics of ferroelectric memories. *Phys Today* July:22
 127. Koiwa I, Kanehara Y, Mita J, Iwabuchi T, Osaka T, Ono S, Maeda M (1996) Crystallization of $\text{Sr}_{0.7}\text{Bi}_{2.3}\text{Ta}_2\text{O}_{9+a}$ thin films by chemical liquid deposition. *Jap. J Appl Phys* 35:4946
 128. Subbarao EC (1962) A family of ferroelectric bismuth compounds. *J Phys Chem Sol* 23:665
 129. Yang CH, Yoon SG, Choi WY, Kim HG (1999) The correlation between composition and preferred orientation of ferroelectric $\text{SrBi}_2\text{Ta}_2\text{O}_9$ thin films. *Electrochem Solid State Lett* 2:39
 130. Park JD, Oh TS (2000) Effects of the Sr content on the ferroelectric characteristics of $\text{Sr}_x\text{Bi}_{2.4}\text{Ta}_2\text{O}_9$ films. *J Mater Sci Lett* 19:1693
 131. Uhlmann DR, Dawley JT, Poisl WH, Zelinski BJJ, Teowee G (2000) Ferroelectric films. *J Sol-Gel Sci Technol* 19:53

132. Lee HN, Hesse D, Zakharov N, Gösele U (2002) Ferroelectric $\text{Bi}_{3.25}\text{La}_{0.75}\text{Ti}_3\text{O}_{12}$ films of uniform a-axis orientation on silicon substrates. *Science* 296:2006
133. Lee HN, Hesse D (2002) Anisotropic ferroelectric properties of epitaxially twinned $\text{Bi}_{3.25}\text{La}_{0.75}\text{Ti}_3\text{O}_{12}$ thin films grown with three different orientations. *Appl Phys Lett* 80:1040
134. Sato T, Kuroiwa T, Sugahara K, Ishiwaru H (2002) Preparation of $\text{Bi}_{3.25+x}\text{La}_{0.75}\text{Ti}_3\text{O}_{12+y}$ films on ruthenium electrodes. *Jpn J Appl Phys Part 1* 41:2105
135. Tanaka K, Uno T, Shimada Y (2002) Ferroelectric characteristics of $\text{Bi}_{4-x}\text{La}_x\text{Ti}_3\text{O}_{12}$ thin films crystallized at low temperatures. *Integr Ferroelectr* 46:285
136. Kim JP, Yang YS, Lee SH, Joo HJ, Jang MS, Yi S, Kojima S (1999) Microstructure and dielectric properties of lanthanum bismuth titanate thin films. *J Korean Phys Soc* 35:S1202
137. Fè L, Norga GJ, Wouters DJ, Maes HE, Maes G (2001) Chemical structure evolution and orientation selection in sol-gel-prepared ferroelectric $\text{Pb}(\text{Zr,Ti})\text{O}_3$ thin films. *J Mater Res* 16:2499
138. Schoofs B, Van de Vyver D, Vermeir P, Schaubroeck J, Hoste S, Herman G, Van Driessche I (2007) Characterisation of the sol-gel process in the superconducting $\text{NdBa}_2\text{Cu}_3\text{O}_{7-y}$ system. *J Mater Chem* 17:1714
139. Lee JW, Ham MH, Maeng WJ, Kim H, Myoung JM (2007) Dependence of electrical properties on interfacial layer of Ta_2O_5 films. *Microelectron Eng* 84:2865
140. Kukli K, Ritala M, Leskelä M (2001) Development of dielectric properties of niobium oxide, tantalum oxide, and aluminum oxide based nanolayered materials. *J Electrochem Soc* 148: F35
141. Sigman J, Brennecke GL, Clem PG, Tuttle BA (2008) Fabrication of perovskite-based high-value integrated capacitors by chemical solution deposition. *J Am Ceram Soc* 91:1851
142. Ricote J, Holgado S, Ramos P, Calzada ML (2006) Piezoelectric ultrathin lead titanate films prepared by deposition of aquo-diol solutions. *IEEE T Ultrason Ferr* 53:2299
143. Brennecke GL, Parish CM, Tuttle BA, Brewer LN, Rodriguez MA (2008) Reversibility of the perovskite-to-fluorite phase transformation in lead-based thin and ultrathin films. *Adv Mater* 20:1407
144. Aoki Y, Kunitake T (2004) Solution-based fabrication of high-k gate dielectrics for next-generation metal-oxide semiconductor transistors. *Adv Mater* 16(2):11
145. Blanchin MG, Canut B, Lambert Y, Teodorescu VS, Barau A, Zaharescu M (2008) Structure and dielectric properties of HfO_2 films prepared by a sol-gel route. *J Sol-Gel Sci Technol* 47:165
146. Ricote J, Holgado S, Huang Z, Ramos P, Fernandez R, Calzada ML (2008) Fabrication of continuous ultrathin ferroelectric films by chemical solution deposition methods. *J Mater Res* 23:2787
147. Walsh CB, Franes EI (2003) Ultrathin PMMA films spin-coated from toluene solutions. *Thin Solid Films* 429:71
148. Hardy A, Van Elshocht S, Adelmann C, Kittl JA, De Gendt S, Heyns M, D'Haen J, D'Olieslaeger M, Van Bael MK, Van den Rul H, Mullens J (2009) Strontium niobate high-k dielectrics: film deposition and material properties. *Acta Mater* 58:216
149. Hardy A, Van Elshocht S, Adelmann C, Clima S, De Dobbelaere C, D'Haen J, Pourtois G, Kittl JA, Van den Rul H, Van Bael MK, D'Olieslaeger M, Heyns M, Mullens J (2009) Ultrathin partly substituted bismuth titanate films with high dielectric constant from aqueous CSD. E-MRS oral presentation, Strasbourg
150. Hardy A, Adelmann C, Van Elshocht S, Van den Rul H, Van Bael MK, De Gendt S, D'Olieslaeger M, Heyns M, Kittl JA, Mullens J (2009) Study of interfacial reactions and phase stabilization of mixed Sc, Dy, Hf high-k oxides by attenuated total reflectance infrared spectroscopy. *Appl Surf Sci* 255:781
151. Miller KT, Lange FF, Marshall DB (1990) The instability of polycrystalline thin-films – experiment and theory. *J Mater Res* 5:151
152. Szafraniak I, Harnagea C, Scholz R, Bhattacharyya S, Hesse D, Alexe M (2003) Ferroelectric epitaxial nanocrystals obtained by a self-patterning method. *Appl Phys Lett* 83:2211

153. Adelman C, Van Elshocht S, Franquet A, Conard T, Richard O, Bender H, Lehnen P, De Gendt S (2008) Thermal stability of dysprosium scandate thin films. *Appl Phys Lett* 92:112902
154. Van Elshocht S, Hardy A, Adelman C, Caymax M, Conard T, Franquet A, Richard O, Van Bael MK, Mullens J, De Gendt S (2007) Screening of high-k layers in MIS and MIM capacitors using aqueous chemical solution deposition. ECS2007, Washington

Chapter 6

Polymer-Assisted Deposition

Anthony K. Burrell, Thomas M. McCleskey, and Quanxi Jia

6.1 Introduction

Metal-oxides are emerging as important materials for their versatile properties such as high-temperature superconductivity, high conductivity, ferromagnetism, ferroelectricity, ferroelasticity, multiferroicity, piezoelectricity, pyroelectricity, thermoelectricity, semiconductivity, dielectricity, and so forth. Metal-oxide films can be grown by physical- and chemical-vapor depositions [1, 2]. Physical-vapor deposition generally has the features of (a) excellent thickness control and (b) smooth surface morphology. On the other hand, it requires large capital investment since a typical physical vapor deposition is often carried out under vacuum conditions. In a typical chemical-vapor deposition process, the substrate is exposed to one or more volatile precursors that react or decompose onto the substrate surface to form the desired film. One of the most important advantages of chemical-vapor deposition is that the coating can be conformal since the reactants are gases. However, chemical-vapor deposition generally involves complicated processes. Furthermore, it very often uses toxic and corrosive gases.

Chemical solution depositions (CSDs) [3] such as sol-gel [4] are more cost-effective since vacuum is not required. However, the formation of high density and electronic quality materials based on CSDs is generally considered challenge due to the use of solvents in the precursor solutions. In addition, many metal-oxides are difficult to deposit and the control of stoichiometry is not always straight forward due to differences in chemical reactivity among the metals. In this chapter, a new process, polymer-assisted deposition (PAD) [5–8], to grow metal-oxide films with

A.K. Burrell

Los Alamos National Laboratory, Los Alamos, NM 87545, USA

Argonne National Laboratory, Argonne, IL 60439, USA

T.M. McCleskey • Q. Jia (✉)

Los Alamos National Laboratory, Los Alamos, NM 87545, USA

e-mail: qxjia@lanl.gov

desired structural and physical properties is described. In the PAD process, the polymer controls the viscosity and binds metal-ions, resulting in a homogeneous distribution of metal precursors in the solution and the formation of uniform metal-organic precursor films. The latter feature makes it possible to grow simple and complex epitaxial metal-oxides with desired physical and structural properties.

6.2 Synopsis of Standard CSDs

To have a better understanding of the chemistry and processes of PAD, we will briefly discuss other CSDs at the beginning of this chapter. For more details to the other CSD methods the reader is referred to the corresponding chapters of the present book.

6.2.1 *Sol-Gel*

Sol-Gel is perhaps the most well-known and extensively studied method for chemical solution deposition of metal-oxide thin films [4]. In general, the sol-gel process involves the transition of a system from a liquid “sol” (mostly colloidal) into a solid “gel” phase. The starting materials used in the preparation of the “sol” are usually reactive inorganic metal salts or metal organic compounds typically as metal alkoxides. In a typical sol-gel process, the precursor is subjected to a series of hydrolysis and polymerization reactions to form a colloidal suspension, or a “sol”.

As far as alkoxides chemistry is concerned, it is useful to distinguish the case of silicon alkoxides (Si being a semimetal) and the case of metal alkoxides. The sol-gel process involving silicon alkoxide can be described in two steps, the hydrolysis of the alkoxide and its polycondensation (cp. Chap. 1). Since the silicon alkoxides are usually stable towards hydrolysis, the hydrolysis step often requires catalysis [9]. In comparison, metal alkoxides generally react very quickly with water even in the absence of catalysts. In particular, transition metal alkoxides are very reactive [10].

6.2.2 *Citrate Gel or Pechini Process*

There are a number of variations of the sol-gel method. One of the most popular methods is generally called the citrate gel [11] or Pechini process [12]. The citrate process can avoid complex steps such as refluxing of alkoxides, resulting in less time consumption compared to other techniques. The ability to utilize the bare metal cations eliminates much of the uncertainty involved in the hydrolysis of metal alkoxides typically observed in the sol-gel process. The citrate process involves complexation of metal ions by polyfunctional carboxyl acids such as citric acid or

tartaric acid having one hydroxyl group. On heating this mixture, the viscosity increases as soon as the water starts to evaporate. With full removal of water, the dried product is a polymeric glass where the constituents are mixed at atomic level. This resin, upon heating at higher temperature, produces the particular oxides. The citrate gel process offers a number of advantages for the preparation of fine powders of many complex oxides [13, 14]. The Pechini process can be considered as a modification of citrate process where a polyhydroxy alcohol or ethylene glycol is added to the mixture. In this process, the solution is heated to 150–250 °C to allow the chelates to polymerize. Upon sintering to a temperature in the range of 500–900 °C, the polymer and citrate decompose to yield the metal-oxides.

6.2.3 Chemical Bath Deposition

Chemical bath deposition (CBD) is perhaps the oldest known chemical solution method for the formation of thin films, dating back to 1884 when PbS was deposited using thiourea. This technique usually involves the simple immersion of a substrate into a solution containing both a metal salt and a chalcogenide precursor. This method has mostly been used to prepare sulfides and selenide films [15]. However, considerable work on the formation of metal-oxide films has been carried out in recent years [9] and details to CBD can be found in Chap. 14. CBD requires that the product of the metal ion concentrations and the chalcogenide must exceed the solubility of the desired product. The maximum obtainable thickness is, therefore, limited by the supply of the reactants in the solution. The control of film thickness, composition, and density requires complex management of the solution composition, pH, and temperature. Different variants of CBD such as SILAR or LPD are known.

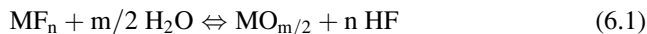
6.2.3.1 Successive Ion Layer Absorption and Reaction

Successive ion layer absorption and reaction (SILAR), as was developed in the early 1980s as an alternative method for the formation of metal-sulfide [16] and metal-oxide films [17]. SILAR employs emersion of the substrate in alternating aqueous solutions of metal cations and chalcogenide salts [18]. This results in layer-by-layer build-up of individual atomic layers of the material in the order of 1.3 Å per cycle on the substrate. This process is very laborious. However, it can be automated and high quality films can be obtained.

6.2.3.2 Liquid Phase Deposition

Liquid phase deposition (LPD) employs metal fluorides, which are hydrolyzed in water by boric acid, as precursors to prepare metal-oxide thin films. The boric acid acts as a fluoride scavenger. The use of the fluoride scavenger allows for the better

control of the hydrolysis reaction and of the solution's supersaturation. The general reactions can be described as



This process has been used to produce a wide range of metal-oxide materials. In particular, LPD silica has been used in semiconductor technologies and other applications such as solar cells [19].

6.2.4 Metal Organic Deposition

Metal organic deposition (MOD) is yet another variation of CSDs where the metal cations do not require hydrolysis. The basic process involves dissolving metal-organic compounds in a solvent such as xylene and combining different solutions to form the right stoichiometry if a complex compound is the target. Metal acetates (cp. Chap. 2) are generally served as the metal precursors in the MOD process. The metal acetates can be mixed and suspended in a suitable solvent, and then coated onto a substrate. Thermal decomposition of the mixed metal acetates results in the formation of the metal-oxide. In the last several years, MOD process has been accepted as a cost-effective approach to grow high temperature superconducting thick films for coated conductors (for details see Chap. 27). The most popular variant of this technique employs trifluoroacetic (TFA) acid as the acetate precursor [20]. The TFA-MOD system has proven to be one of the most reliable chemical routes to the formation of high performance $\text{YBa}_2\text{Cu}_3\text{O}_7$ (YBCO) thick films [21]. The impact of TFA-MOD to low cost processing of superconducting films has resulted in considerable work devoted to the production of YBCO thick films.

6.3 Polymer-Assisted Deposition

Overall, one of the greatest challenges in solution-based processes of metal-oxide films has been to produce high-quality films with desired structural and physical properties. In 2000, a new concept, polymer-assisted deposition (PAD), was developed to prepare metal-oxide films [5–8]. The PAD process is illustrated in Fig. 6.1.

As PAD itself is a chemical solution deposition method, it has the traditional advantages of CSD. Importantly, the precursors are stable, and they can be coated by spin, dip, or spray on to the substrate. Furthermore, it has the features such as binding metals directly to the polymer. The direct binding between the metal and polymer makes it possible to eliminate the pre-formation of metal-oxide in the solution before the polymer is decomposed. In the following, we discuss the

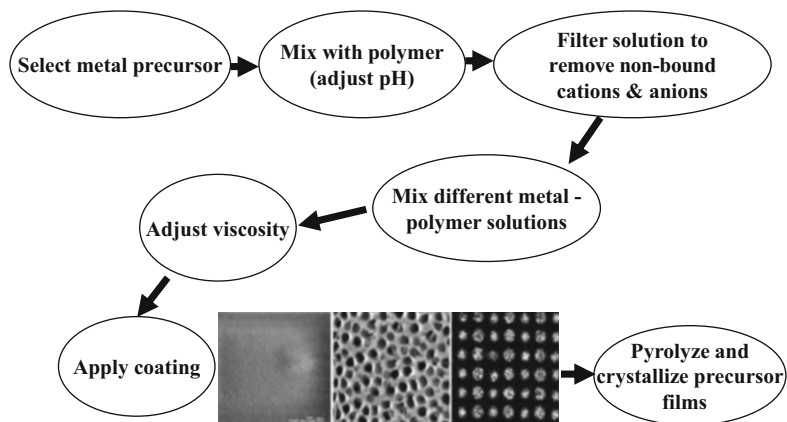


Fig. 6.1 Flow chart of a typical polymer-assisted deposition process to prepare film coatings. Different surface morphologies are illustrated in the inset SEM pictures (spin-coating for the flat surface (*left image*), dip-coating for the 3D structure (*middle image*), and ink-jetting for the patterns (*right image*))

detailed chemistry, the processing steps, and formation of both simple and complex metal-oxide coatings based on PAD technology.

6.3.1 Metal Polymer Solutions

The key to PAD is the inherent stability of the metal polymer solutions. The simplest view of the metal polymer interactions is the formation of covalent complexes between the lone pairs on the nitrogen atoms and the metal cation. This classic Werner-type chemistry is clearly the simplest method for the formation of first row transition metals using nitrates, acetates, or chlorides. One of the key features in the formation of the complexes is the use of Amicon® filtration to remove non-coordinated species. The Amicon® filtration uses semi-permeable membranes (or filter-like devices with convoluted paths) and pressure to separate molecular species on the basis of size. This is possible because of the large difference in molecular weight and size between the polymer and the cations.

The first row transition metals bind well to the polyethyleneimine (PEI), presumably in a fashion similar to that shown in Fig. 6.2a. It is also possible to chemically modify the PEI polymer so that hard metals, such as titanium, are provided a stable coordination environment as shown in Fig. 6.2b. Another method for binding metals utilises the ability of protonated PEI to coordinate anionic metal complexes as shown in Fig. 6.3b. While these options provide for the formation of a wide range of metal bound polymers, experimental results have shown that

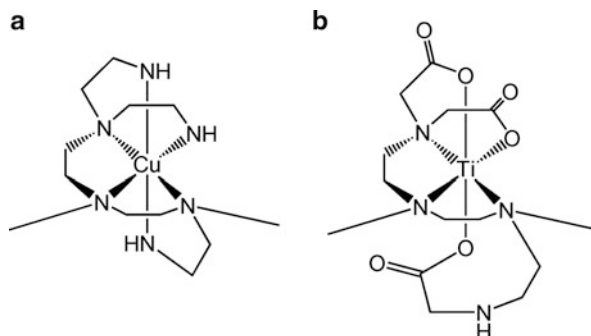


Fig. 6.2 Schematic drawings of putative structures of polyethyleneimine (PEI) and carboxylic acid functionalized PEI metal complexes: (a) first-row transition metals such as Cu bind to PEI, and (b) hard metals such as Ti bind with polymer through PEI functionalized with carboxylic acid (Reprinted with the permission from A. K. Burrell et al., *Chem. Commun.* 11, 1271 (2008). Copyright 2008, The Royal Society of Chemistry)

ethylenediaminetetraacetic acid (EDTA) complexes in combination with PEI work as well as functionalized PEI in most cases. The major advantage of the EDTA route is that EDTA forms stable complexes with almost all metals. The EDTA complexes bind to the PEI via a combination of hydrogen bonding and electrostatic attraction as seen in Fig. 6.3a. This hydrogen bonding is sufficiently stable that the Amicon® filtration can also be used to remove non-coordinated species.

In general, it is possible to mix polymers (such as PEI and EDTA) in desired ratio. These solutions can remain stable for months even when multiple metals are used. Once the metal polymers have been prepared, their viscosity can be adjusted by removal of water under vacuum or by dilution with deionised water. The solution can then be applied onto a substrate through either spin-coating or dip-coating.

6.3.2 Thermal Depolymerization

Perhaps the most important aspect of the PAD process is the thermal removal of the polymer. At temperatures below the thermal depolymerization of the polymer, the polymer protects metals from premature condensation. When the polymer is heated at temperatures $>350\text{ }^{\circ}\text{C}$ the polymer undergoes thermal depolymerization by forming $\text{NH}_2\text{CH}=\text{CH}_2$. The EDTA decomposes to acetic acid, formic acid, and/or ethylenediamine [22]. These non-combustion processes result in extremely clean metal-oxide films even in inert or reducing atmospheres. In fact, PEI can be completely depolymerized in a hydrogen atmosphere with no coke formation. During the thermal decomposition of the polymer, the film is effectively molten providing for a very effective mixing of the metal cations. The fact that the metals

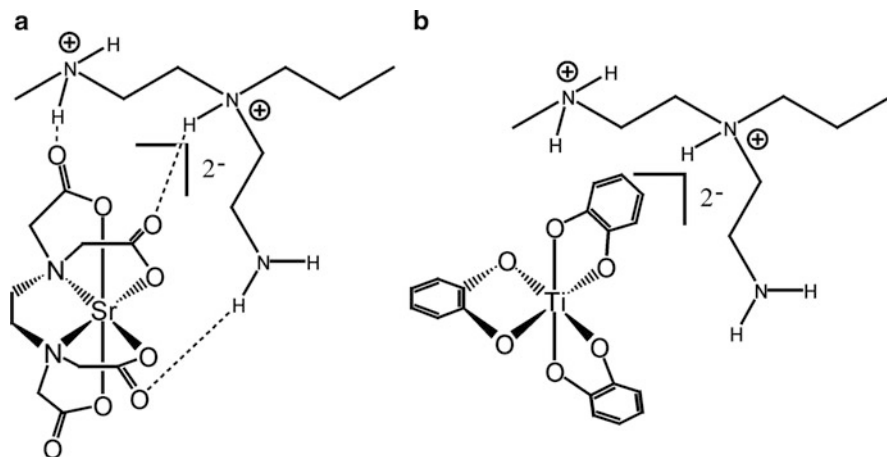


Fig. 6.3 Schematic drawings of putative structures of (a) ethylenediaminetetraacetic acid (EDTA) complex binds to PEI via a combination of hydrogen bonding and electrostatic attraction, and (b) protonated PEI coordinating with anionic metal complex acid (Reprinted with the permission from A. K. Burrell et al., *Chem. Commun.* 11, 1271 (2008). Copyright 2008, The Royal Society of Chemistry)

remain homogeneously mixed until the polymer is removed allows for the formation of high quality complex metal-oxide films without second phase inclusion.

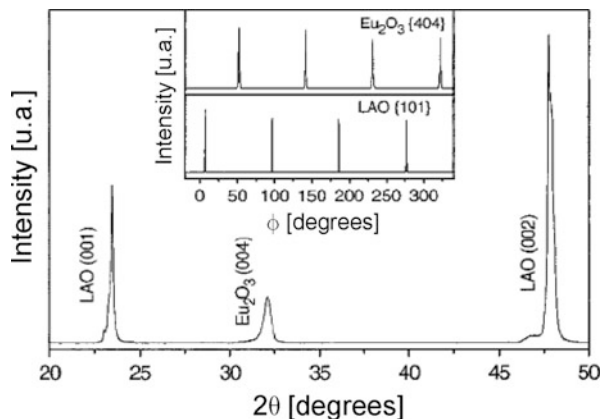
6.3.3 Simple Metal-Oxide Films

Growth of simple metal-oxide film by PAD is rather straight forward. Many simple oxides such as ZnO [23], HfO₂ [24], TiO₂ [6], UO₂ [25], ZrO₂ [26], Tm₂O₃ [27], U₃O₈ [25], and Eu₂O₃ [28] have been prepared by PAD. Here three examples are given to illustrate the PAD process in the preparation of high quality epitaxial films with desired structural properties.

6.3.3.1 Epitaxial Eu₂O₃ Films [28]

To grow epitaxial Eu₂O₃ films, a solution containing both europium and polymer is prepared. In this case, carboxylated-polyethylenimine (PEIC) is dissolved in water, Eu(NO₃)₃ was added and the pH value of this solution is adjusted to ~6.5. The mixture is placed in a bioseparations vessel, diluted with water, pressurized with nitrogen gas, washed by water, and concentrated to a suitable viscosity. The resulting solution can be spin-coated on different substrates such as LaAlO₃. The precursor film is then thermally annealed in oxygen. Figure 6.4 shows the typical x-ray diffraction (XRD) pattern from the θ - 2θ scan for a film annealed at 1,000 °C.

Fig. 6.4 XRD θ - 2θ scans of the Eu_2O_3 thin film on LaAlO_3 (LAO) substrate; the inset shows XRD ϕ scans from (404) Eu_2O_3 film and (101) LaAlO_3 substrate respectively (Reprinted with the permission from Y. Lin et al., Appl. Phys. Lett. 85, 3426 (2004). Copyright 2004, American Institute of Physics)



Only (001) peaks of Eu_2O_3 and LaAlO_3 are observed, indicating that the Eu_2O_3 film is single phase with a preferential c -axis orientation.

The inset of Fig. 6.4 shows the ϕ scans on Eu_2O_3 (404) and LaAlO_3 (101). Four peaks from Eu_2O_3 (404), with an average value of FWHM of 0.9° , shows the film to be of good epitaxial quality. The 45° shift between the film and the substrate indicates a rotation of 45° between these two lattices. This epitaxial relationship is not unreasonable considering the lattice parameter of bulk Eu_2O_3 ($\sim 10.86 \text{ \AA}$, cubic structure) and that of LaAlO_3 ($\sim 3.78 \text{ \AA}$, cubic structure).

Transmission electron microscopy (TEM) and selected area diffraction (SAD) further confirmed the high quality epitaxial growth of Eu_2O_3 on LaAlO_3 (LAO) substrate. Figure 6.5a shows a low magnification bright-field TEM image of Eu_2O_3 . It is clear that the interface is flat and without any visible secondary phases. The Eu_2O_3 film has a relatively uniform contrast with no columnar grain growth. Corresponding SAD pattern at the interface area is shown in Fig. 6.5b. Diffraction dots from Eu_2O_3 are sharp and distinguished, indicating the high quality of the film. Figure 6.5c is the high resolution TEM image from the interface of Eu_2O_3 and LaAlO_3 . The interface of Eu_2O_3 and LaAlO_3 is very sharp, and no other phases or precipitations are present at the interface or in the film.

6.3.3.2 Epitaxial TiO_2 Films [6]

There are two main polymorphous phases in TiO_2 : rutile and anatase. Rutile is a high-temperature stable phase and anatase, a low-temperature phase, both having tetragonal unit cells, but with their lattice parameters (rutile: $a = 4.593 \text{ \AA}$ and $c = 2.959 \text{ \AA}$; anatase: $a = 3.785 \text{ \AA}$ and $c = 9.514 \text{ \AA}$), space groups, and atomic positions in the unit cells different from one another.

To grow these oxide films, a solution containing titanium and peroxide and PEIC is prepared [6]. The x-ray diffraction 2θ -scan of the TiO_2 film on the R-plane sapphire ($a = 5.364 \text{ \AA}$ and $c = 13.11 \text{ \AA}$), annealed at $1,100^\circ\text{C}$, is shown in

Fig. 6.5 Cross-sectional transmission electron microscopy (TEM) images from Eu_2O_3 on LAO substrate, (a) low magnification image; (b) corresponding SAD pattern from Eu_2O_3 and LAO; (c) high resolution image showing the interface between Eu_2O_3 and LaAlO_3 (Reprinted with the permission from Y. Lin et al., Appl. Phys. Lett. 85, 3426 (2004). Copyright 2004, American Institute of Physics)

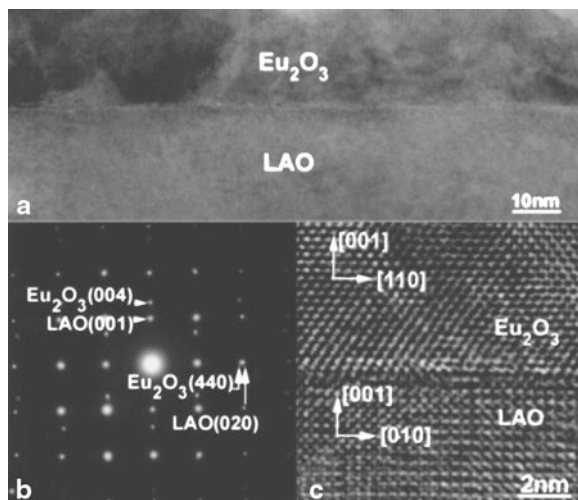


Fig. 6.6a. The film has a rutile structure and is preferentially oriented out of the plane. Epitaxial anatase TiO_2 is also achieved as a result of the lattice strain produced from the substrate where pseudocubic LaAlO_3 ($a = 3.793 \text{ \AA}$) is used as the substrate. Figure 6.6b is the XRD 2θ -scan of the film annealed at $980 \text{ }^\circ\text{C}$, showing the anatase structure and its preferentially out-of-the-plane orientation. The epitaxial nature of anatase TiO_2 on LaAlO_3 is evidenced by the ϕ -scans of (101) TiO_2 and (101) LaAlO_3 as shown in Fig. 6.6c.

6.3.3.3 Epitaxial UO_2 and U_3O_8 Films [25]

The precursor for the epitaxial growth of UO_2 and U_3O_8 films is a simple aqueous solution of $\text{UO}_2(\text{OAc})_2 \cdot 2\text{H}_2\text{O}$ added to PEI with an adjusted pH of 8.0. This solution is spun coated onto the desired substrates such as LaAlO_3 and c -plane $\alpha\text{-Al}_2\text{O}_3$, which are then annealed at $1,000 \text{ }^\circ\text{C}$ under the atmosphere of either O_2 or air.

Figure 6.7 shows the x-ray diffraction patterns of (a) θ - 2θ scans and (b) ϕ -scans from (220) UO_2 and (101) LaAlO_3 . As shown in Fig. 6.7a, only the ($h00$) peaks of UO_2 and LaAlO_3 are observed, indicating that the UO_2 film has a single phase with a preferential a -axis orientation. The calculated lattice parameter of the UO_2 film based on the diffraction pattern is 0.5472 nm , which is almost the same as the 0.5466 nm of the bulk cubic UO_2 .

The four peaks from the reflections of the (220) UO_2 , shifted 45° with respect to (101) LaAlO_3 (see Fig. 6.7b), show that the UO_2 is epitaxy when rotated 45° with respect to the LaAlO_3 lattice. A cross-sectional TEM analysis on the film further confirms the successful epitaxial growth of high quality UO_2 on the LaAlO_3 substrate. As shown in Fig. 6.8a, there is a sharp interface (marked with two

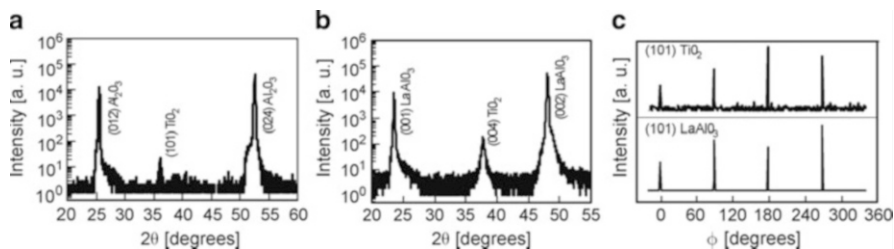


Fig. 6.6 X-ray diffraction pattern of (a) θ - 2θ scans of rutile TiO_2 films deposited by PAD on R-plane sapphire, (b) θ - 2θ scans of epitaxial anatase TiO_2 films deposited by PAD on LaAlO_3 , and (c) ϕ -scans from (101) LaAlO_3 and (101) anatase TiO_2 (Reprinted with the permission from Q. X. Jia et al., *Nat. Mater.* 3, 529 (2004). Copyright 2004, Nature Publishing Group)

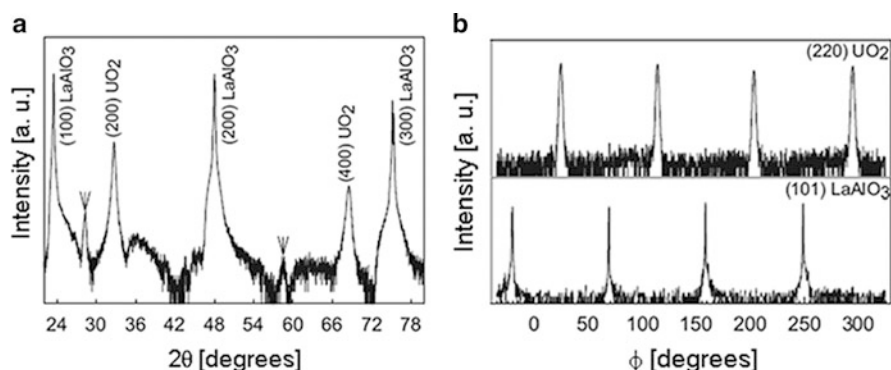


Fig. 6.7 X-ray diffraction pattern of (a) θ - 2θ scans of UO_2 films deposited on a single crystal (100) LaAlO_3 substrate. The arrows mark the (111) peak that is less than 2 % relative to (100) peak; (b) ϕ -scans of the (220) epitaxial UO_2 films and the (101) LaAlO_3 substrate (Reprinted with the permission from A. K. Burrell et al., *Adv. Mater.* 19, 3559 (2007). Copyright 2007, Wiley-VCH Verlag GmbH & Co.)

wedges) between the UO_2 and the LaAlO_3 without any indication of interfacial reactions. SAD patterns, shown in Fig. 6.8b, show the same epitaxial relationship with an x-ray analysis.

Polymorphic hexagonal and orthorhombic U_3O_8 films are grown as well using different substrates with appropriate in-plane lattice parameters. Figure 6.9 shows θ - 2θ scans for films on both the c -plane and the R -plane α - Al_2O_3 substrates. As can be seen from Fig. 6.9, films on α - Al_2O_3 substrates exhibit completely different x-ray diffraction patterns than films on LaAlO_3 do, even though they have been coated with the same solution and treated under the same conditions. Detailed structural analysis [25] of the U_3O_8 films on different substrates indicated that the epitaxial U_3O_8 on the c -plane α - Al_2O_3 has a hexagonal structure with lattice parameters of $a = 0.6815$ nm and $c = 0.4144$ nm. On the other hand, U_3O_8 on the R -plane α - Al_2O_3 substrate has an orthorhombic structure.

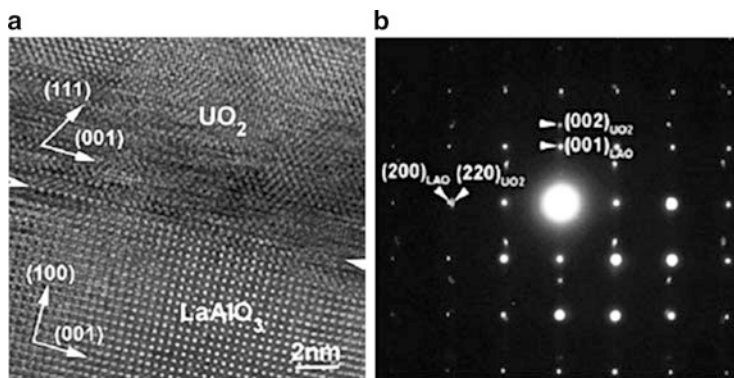


Fig. 6.8 Epitaxial (100) UO_2 films deposited on a single crystal (100) LaAlO_3 . (a) A cross-sectional high-resolution electron microscopy (HRTEM) image taken along the [100] LaAlO_3 zone axis; (b) the selected-area electron diffraction pattern. The HRTEM image shows a very sharp interface between the UO_2 film and the LaAlO_3 substrate. There are no detectable second phases and no voids in the film. The well-defined and sharp diffraction dots on the diffraction patterns further confirm that the UO_2 film is of high quality epitaxy (Reprinted with the permission from A. K. Burrell *et al.*, *Adv. Mater.* 19, 3559 (2007). Copyright 2007, Wiley-VCH Verlag GmbH & Co.)

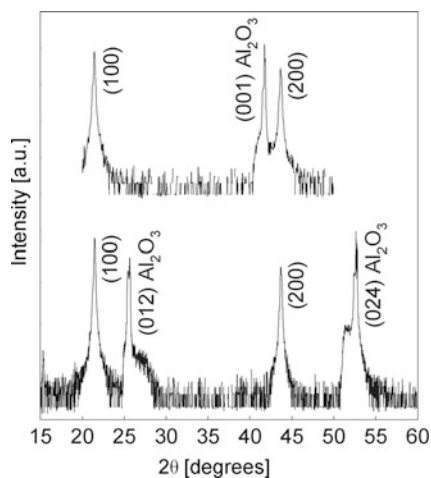


Fig. 6.9 X-ray diffraction pattern of (top) a θ - 2θ scan of the U_3O_8 film deposited on a single crystal (001) Al_2O_3 substrate; (bottom) a θ - 2θ scan of the U_3O_8 film deposited on a single crystal (012) Al_2O_3 substrate. The preferential orientation of U_3O_8 along (100) is obvious regardless of the orientation of the Al_2O_3 substrate (Reprinted with the permission from A. K. Burrell *et al.*, *Adv. Mater.* 19, 3559 (2007). Copyright 2007, Wiley-VCH Verlag GmbH & Co.)

6.3.4 Complex Metal-Oxide Films

The growth of complex metal-oxide films by PAD is very controllable and reproducible. Since PAD enables the use of stable metal complexes as the metal sources it can avoid the nonstoichiometry commonly observed in the other CSD processes caused by different hydrolysis rates of various alkoxides. Many complex metal-oxide films such as $\text{Ba}_{1-x}\text{Sr}_x\text{TiO}_3$ [29], $\text{La}_{0.67}\text{Ca}_{0.33}\text{MnO}_3$ and $\text{La}_{0.67}\text{Sr}_{0.33}\text{MnO}_3$ [30], SrRuO_3 [31], CuAlO_2 [32], nanocomposite BaTiO_3 : NiFe_2O_4 [33], YVO_4 [34], silica nanoparticles in SrTiO_3 [35], BiVO_4 [36], and YBCO [6, 37, 38] have been grown by PAD. Here three examples are given to illustrate the PAD process for the growth of high quality epitaxial films with desired structural and electrical properties.

6.3.4.1 Epitaxial Ferroelectric $\text{Ba}_{1-x}\text{Sr}_x\text{TiO}_3$ Films [29]

To grow epitaxial $\text{Ba}_{1-x}\text{Sr}_x\text{TiO}_3$ films, at first three separate solutions of Ba, Sr, and Ti bound to polymers were synthesized. Titanium is bound to PEIC. Barium is bound as an EDTA complex to PEI. Strontium is bound to PEI as an EDTA complex using a similar process. These separate solutions are then mixed accordingly to the final solution for $\text{Ba}_{1-x}\text{Sr}_x\text{TiO}_3$ with different Ba, Sr, and Ti ratios.

XRD and TEM analysis show that all the $\text{Ba}_{1-x}\text{Sr}_x\text{TiO}_3$ films are epitaxial. To study the structural and dielectric properties of $\text{Ba}_{1-x}\text{Sr}_x\text{TiO}_3$ films with different Ba/Sr ratio, a series of $\text{Ba}_{1-x}\text{Sr}_x\text{TiO}_3$ films with various x values but the same thickness of 150 nm is compared. Figure 6.10a, b show the typical sections of normal ($\chi = 90^\circ$) and tilted ($\chi = 45^\circ$) θ - 2θ scans of the $\text{Ba}_{1-x}\text{Sr}_x\text{TiO}_3$ films for $x = 0.3$ and $x = 0.7$. The out-of-plane and in-plane lattice parameters of the $\text{Ba}_{1-x}\text{Sr}_x\text{TiO}_3$ films can be calculated by fitting these peaks using the Lorentz function, as demonstrated in Figure 6.10c. For comparison, the a - and c -axis lattice constants of bulk $\text{Ba}_{1-x}\text{Sr}_x\text{TiO}_3$ [39] are also given. As can be seen from the figure, the lattice parameters of the films exactly follow the same trend of the bulk $\text{Ba}_{1-x}\text{Sr}_x\text{TiO}_3$.

Figure 6.11a, b show the zero-field dielectric constant (ϵ_0) and tunability [$(\epsilon_0 - \epsilon_E)/\epsilon_0$, where ϵ_E is the dielectric constant at an applied field E] versus x . The dielectric values of the films are comparable to the reported values of the films grown by PLD [40], demonstrating the good quality of the $\text{Ba}_{1-x}\text{Sr}_x\text{TiO}_3$ films grown by PAD. In addition, the change of the dielectric properties of the $\text{Ba}_{1-x}\text{Sr}_x\text{TiO}_3$ films with the variation in the x values is also very similar to the $\text{Ba}_{1-x}\text{Sr}_x\text{TiO}_3$ films grown by PLD [40].

6.3.4.2 Epitaxial Ferromagnetic $\text{La}_{1-x}(\text{Sr,Ca})_x\text{MnO}_3$ Films [30]

PAD technique has been also used to grow the epitaxial films of $\text{La}_{0.67}\text{Sr}_{0.33}\text{MnO}_3$ (LSMO) and $\text{La}_{0.67}\text{Ca}_{0.33}\text{MnO}_3$ (LCMO) with properties comparable to those

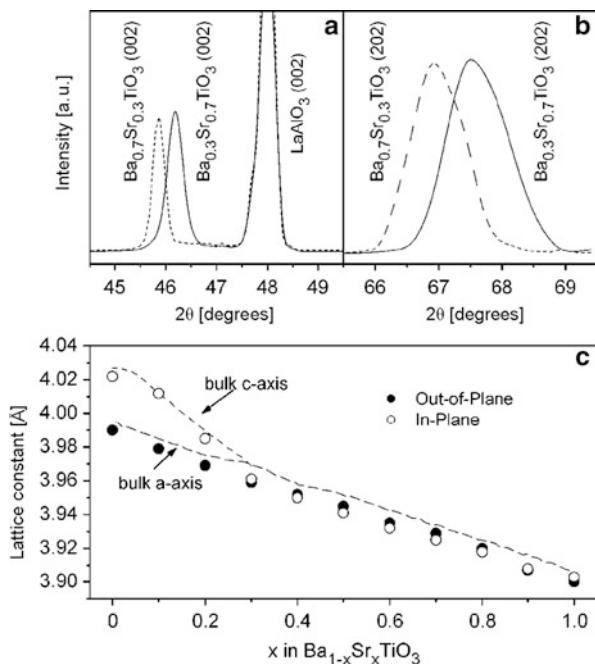


Fig. 6.10 XRD θ - 2θ scans of the $\text{Ba}_{0.3}\text{Sr}_{0.7}\text{TiO}_3$ and $\text{Ba}_{0.7}\text{Sr}_{0.3}\text{TiO}_3$ films (a) normal $\chi = 90^\circ$ and (b) tilted $\chi = 45^\circ$; (c) the in-plane and out-of-plane lattice constant vs x in $\text{Ba}_{1-x}\text{Sr}_x\text{TiO}_3$ for the film. Bulk data are from [39] (Reprinted with the permission from Y. Lin *et al.*, *Appl. Phys. Lett.* 85, 5007 (2004). Copyright 2004, American Institute of Physics)

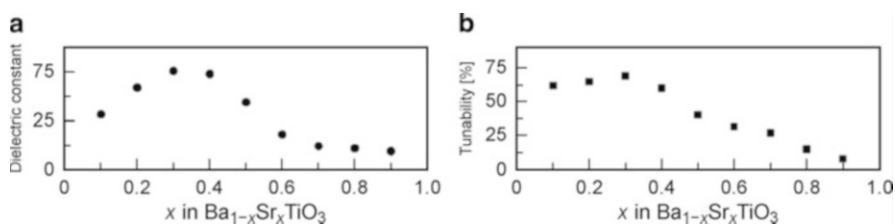
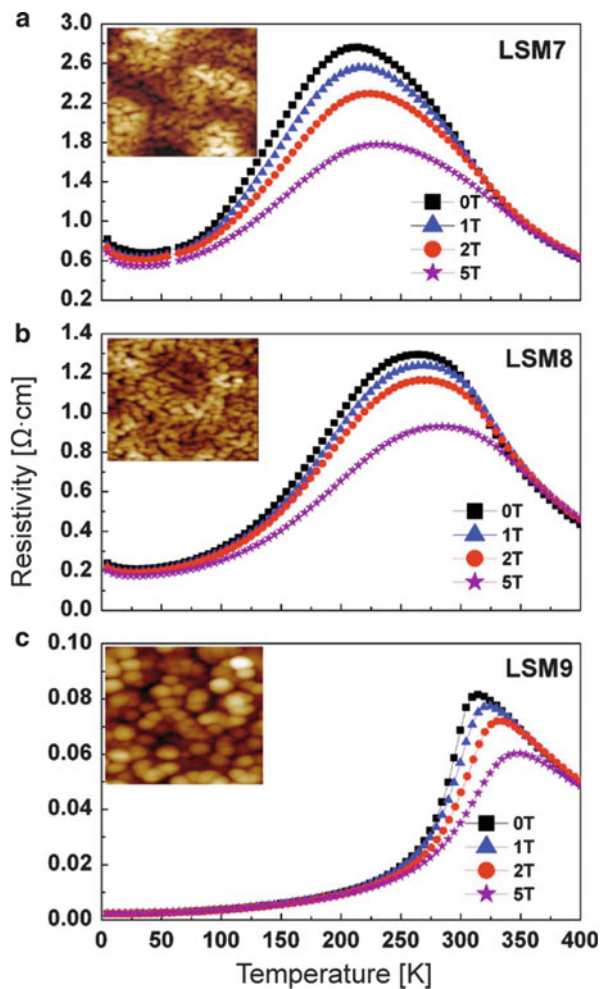


Fig. 6.11 (a) Dielectric constant and (b) tunability vs x in $\text{Ba}_{1-x}\text{Sr}_x\text{TiO}_3$ films at 1 MHz and room temperature, where the tunability is defined as $(\epsilon_0 - \epsilon_E)/\epsilon_0$; ϵ_0 is zero-field dielectric constant, and ϵ_E is the dielectric constant at an applied field E (Reprinted with the permission from Y. Lin *et al.*, *Appl. Phys. Lett.* 85, 5007 (2004). Copyright 2004, American Institute of Physics)

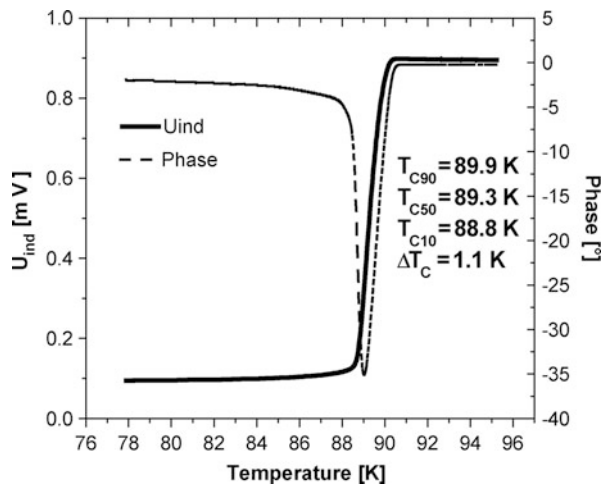
prepared by other physical vapor deposition techniques. The precursors for the LSMO and LCMO solutions are aqueous solutions of high purity (>99.99 %) metal salts [$\text{La}(\text{NO}_3)_3 \cdot 6\text{H}_2\text{O}$, $\text{Sr}(\text{NO}_3)_2$, $\text{MnCl}_2 \cdot \text{H}_2\text{O}$, and $\text{Ca}(\text{OH})_2$], prepared separately with a PEI and EDTA. These solutions are mixed in the appropriate stoichiometric ratios and spun coat onto single crystalline LaAlO_3 substrates. These films are then annealed at various temperatures (750, 850, and 950 $^\circ\text{C}$) in oxygen atmosphere.

Fig. 6.12 Temperature dependent resistivity (ρ) of the $\text{La}_{0.67}\text{Sr}_{0.33}\text{MnO}_3$ films annealed at (a) 750 °C, (b) 850 °C, and (c) 950 °C, with $\mu_0 H = 0, 1, 2,$ and 5 T. Insets show the respective AFM micrographs ($1 \times 1 \mu\text{m}$) (Reprinted with the permission from M. Jain *et al.*, *Appl. Phys. Lett.* 88, 232510 (2006). Copyright 2006, American Institute of Physics)



X-ray diffraction 2θ -scans for all LSMO and LCMO films show only $(00l)$ peaks, indicating that pure c -axis oriented films processed under these conditions. The epitaxial nature of the films is confirmed by the in-plane alignment with respect to the major axis of the substrate. Figure 6.12a–c show the resistivity, $\rho(T)$, at different applied magnetic fields for films annealed at different temperatures. For the film annealed at 750 °C, the transition peak is broad with the temperature of maximum resistivity, T_p , at 210 K (at 0 T). As the annealing temperature is increased, T_p is shifted to higher temperature and the transition peak sharpens. For film annealed at 950 °C, the transition peak is sharpest with $T_p \sim 330$ K. It is believed that as the annealing temperature is increased, the compositional inhomogeneity decreases and hence, the transition peak becomes sharper. Some of such improvements can be attributed to improved crystallinity, grain size, epitaxy, etc.

Fig. 6.13 Inductive measurement of the superconducting transition. The *solid* and *dashed lines* represent the diamagnetic and dissipative response of the YBCO film (Reprinted with the permission from C. Apetrii *et al.*, *IEEE Trans. Appl. Supercond.* 15, 2642 (2005). Copyright 2005, IEEE)



The resistivity of the films also decreased with the increase in the annealing temperature, which can be understood in terms of the grain growth with increase in annealing temperature, as observed in the AFM images of these films (presented in the insets of Fig. 6.12).

6.3.4.3 Epitaxial Superconducting $\text{YBa}_2\text{Cu}_3\text{O}_{7-x}$ Films

To prepare metal polymer precursor solution for high-temperature superconducting $\text{YBa}_2\text{Cu}_3\text{O}_{7-x}$ (YBCO) films [37], stoichiometric amounts (1:2:3) of Y-, Ba-, and Cu-nitrates are chosen as starting substances. Yttrium-, barium-, copper-nitrates, and polyacrylic acid (PAA) are dissolved in dimethylformamide (DMF) to obtain the precursor solution. Polymethacrylic acid (PMAA) can also be used instead of polyacrylic acid. A small additional amount of the solvent and water has been found to strongly increase the solubility of the starting substances in the polyacrylic acid.

The prepared solution is coated on SrTiO_3 substrates by spin coating at 3,000–4,000 rpm and then dried in air at 170 °C for 3 h to remove the solvent. This process can be repeated in order to increase the film thickness. The samples are transferred to a tube furnace and heated in oxygen under very carefully designed processing steps [37]. For example, it has been found that a mixture of oxygen (~100 ppm) and nitrogen during the first step of the heat treatment can lead to better performance of superconductors. Figure 6.13 shows the superconducting transition of a YBCO film prepared under such conditions. A transition temperature of 89.9 K and a transition width of 1.1 K have been obtained. The critical current density of the film is as high as 10^6 A/cm² at liquid nitrogen temperature.

Polymer-nitrate precursor solutions are also prepared for the growth of YBCO films [38]. In this case, the cations are derived from $\text{Ba}(\text{NO}_3)_2$, $\text{Y}(\text{NO}_3)_3 \cdot 6\text{H}_2\text{O}$, and $\text{Cu}(\text{NO}_3)_2 \cdot 3\text{H}_2\text{O}$ powders. Several polymers, including polyvinyl alcohol (PVOH,

average MW15,000, Sigma-Aldrich), methyl cellulose (MC, Alfa Aesar/Sigma-Aldrich), hydroxypropyl methyl cellulose (HPMC, Sigma-Aldrich), and hydroxyethyl cellulose (HEC, Sigma-Aldrich) are used as rheology modifiers. The highest critical current density achieved is 3.73 MA/cm^2 for a 42 nm YBCO film obtained from the PVOH-nitrate precursor solution, but much thicker films are achieved by the other rheology modifiers.

6.4 Conclusion Remarks

Both simple and complex metal-oxide films have been grown by polymer-assisted deposition. The desired structural and physical properties of these materials illustrate that PAD is an alternative approach to the growth of high-quality epitaxial metal-oxide films, even though such films are not necessarily better than those deposited by other physical and/or chemical vapor deposition. Compared to other chemical solution deposition techniques, the development of PAD technology is still in the early stage. It should be noted that small amount of polymers have been added into the solution as buffer media in the commonly used sol-gel process. In this case, the polymer is either used as a wetting agent to improve the surface wetting behavior [41] or as a modifier to enhance the critical film thickness without micro-cracks as well as to stabilize the chemical phase to be deposited [42–45]. It is clear that many issues related to materials science and chemistry need to be investigated, and further optimization of processes is necessary for the high quality materials.

As the discussion of this chapter is mostly concentrated on metal-oxide films based on PAD, it should be pointed out that PAD has emerged as a universal process for synthesizing a remarkably broad range of electronic materials such as semiconductor Ge [46], metal-nitrides [47], and metal-carbides [48].

References

1. Elshabini-Riad A, Barlow FD III (1998) Thin film technology handbook. McGraw-Hill, New York
2. Smith DL (1995) Thin film deposition. McGraw-Hill, New York
3. Lange FF (1996) Chemical solution routes to single-crystal thin films. *Science* 273:903
4. Brinker CJ, Scherer GW (1990) Sol-gel science: the physics and chemistry of sol-gel processing. Academic, Boston
5. Li DQ, Jia QX (2003) United States Patent No. 6,589,457
6. Jia QX, McCleskey TM, Burrell AK, Lin Y, Collis G, Wang H, Li ADQ, Foltyn SR (2004) Polymer-assisted deposition of metal-oxide films. *Nat Mater* 3:529
7. Burrell AK, McCleskey TM, Jia QX (2008) Polymer assisted deposition. *Chem Commun* 11:1271
8. McCleskey TM, Burrell AK, Jia QX, Lin Y (2008) United States Patent No. 7,365,118

9. Niesen TP, De Guire MR (2001) Review: deposition of ceramic thin films at low temperatures from aqueous solutions. *J Electroceram* 6:169
10. Livage J, Henry M, Sanchez C (1988) Sol-gel chemistry of transition-metal oxides. *Prog Solid State Chem* 18:259
11. Baythoun MSG, Sale FR (1982) Production of strontium-substituted lanthanum manganite perovskite powder by the amorphous citrate process. *J Mater Sci* 17:2757
12. Pechini M (1967) United States Patent No. 3,330,697
13. Xu Q, Chen S, Chen W, Wu S, Zhou J, Sun H, Li Y (2005) Synthesis and piezoelectric and ferroelectric properties of $(\text{Na}_{0.5}\text{Bi}_{0.5})_{1-x}\text{Ba}_x\text{TiO}_3$ ceramics. *Mat Chem Phys* 90:111
14. Dhage SR, Gaikwad SP, Muthukumar P, Ravi V (2004) Synthesis of $\text{Ce}_{0.75}\text{Zr}_{0.25}\text{O}_2$ by citrate gel method. *Mater Lett* 58:2704
15. Mane RS, Lokhande CD (2000) Chemical deposition method for metal chalcogenide thin films. *Mater Chem Phys* 65:1
16. Nicolau YF (1985) Solution deposition of thin solid compound films by a successive ionic-layer adsorption and reaction process. *Appl Surf Sci* 22:1061
17. Ristov M, Sinadinovski GJ, Grozdanov I (1985) Chemical-deposition of Cu_2O thin-films. *Thin Solid Films* 123:63
18. Pathan HM, Lokhande CD (2004) Deposition of metal chalcogenide thin films by successive ionic layer adsorption and reaction (SILAR) method. *Bull Mater Sci* 27:85
19. Lee KC, Hwu JG (1998) Efficiency improvement in low temperature metal-oxide-semiconductor solar cells by thin metal film deposition on photon receiving area. *J Vac Sci Technol A* 16:2641
20. McIntyre PC, Cima MJ, Ng MF (1990) Metalorganic deposition of high-Jc $\text{Ba}_2\text{YCu}_3\text{O}_{7-x}$ thin-films from trifluoroacetate precursors onto (100) SrTiO_3 . *J Appl Phys* 68:4183
21. Rupich MW, Verebelyi DT, Zhang W, Kodenkandath T, Li X (2004) Metalorganic deposition of YBCO films for second-generation high-temperature superconductor wires. *MRS Bull* 29:572
22. Kirillina IE, Voronov VN, Dolgonosov AM, Lazeikina MA (1988) The composition of gaseous products of decomposition of ethylenediaminetetra-acetate. *Thermal Eng* 35:538
23. Lin Y, Xie J, Wang H, Li Y, Chavez C, Lee SY, Foltyn SR, Crooker SA, Burrell AK, McCleskey TM, Jia QX (2005) Green luminescent zinc oxide films prepared by polymer-assisted deposition with rapid thermal process. *Thin Solid Films* 492:101
24. Garcia MA, Ali MN, Parsons-Moss T, Ashby PD, Nitsche H (2008) Metal oxide films produced by polymer-assisted deposition (PAD) for nuclear science applications, *Thin Solid Films* 516:6261
25. Burrell AK, McCleskey TM, Shukla P, Wang H, Minogue EM, Jia QX (2007) Controlling oxidation-states in uranium-oxide through epitaxial stabilization. *Adv Mater* 19:3559
26. Shukla P, Minogue EM, McCleskey TM, Jia QX, Lin Y, Lu P, Burrell AK (2006) Conformal coating of nanoscale features of microporous anodisc™ membranes with zirconium and titanium oxide. *Chem Commun* 8:847
27. Garcia MA, Ali MN, Chang NN, Parsons-Moss T, Ashby PD, Gates JM, Stavsetra L, Gregorich KE, Nitsche H (2008) Heavy-ion irradiation of thulium(III) oxide targets prepared by polymer-assisted deposition. *Nucl Instrum Methods Phys Res, Sect A* 592:483
28. Lin Y, Wang H, Hawley ME, Foltyn SR, Jia QX, Collis GE, Burrell AK, McCleskey TM (2004) Epitaxial growth of Eu_2O_3 thin films on LaAlO_3 substrates by polymer-assisted deposition. *Appl Phys Lett* 85:3426
29. Lin Y, Lee JS, Wang H, Li Y, Foltyn SR, Jia QX, Collis G, Burrell AK, McCleskey TM (2004) Structural and dielectric properties of epitaxial $\text{Ba}_{1-x}\text{Sr}_x\text{TiO}_3$ films grown on LaAlO_3 substrates by polymer-assisted deposition. *Appl Phys Lett* 85:5007
30. Jain M, Li Y, Hundley MF, Hawley M, Maiorov B, Campbell IH, Civale L, Jia QX, Shukla P, Burrell AK, McCleskey TM (2006) Magnetoresistance in polymer assisted deposited Sr- and Ca-doped lanthanum manganite films. *Appl Phys Lett* 88:232510

31. Luo HM, Jain M, Baily SA, DePaula RF, Dowden PC, Jia QX (2007) Structural and ferromagnetic properties of epitaxial SrRuO₃ films by a chemical solution deposition. *J Phys Chem B* 111:7497
32. Luo HM, Jain M, McCleskey TM, Bauer E, Burrell AK, Jia QX (2007) Optical and structural properties of single crystal epitaxial p-type transparent oxide thin films. *Adv Mater* 19:3604
33. Luo HM, Yang H, Baily SA, Ugurlu O, Jain M, Hawley M, McCleskey TM, Burrell AK, Bauer E, Civale L, Holesinger TG, Jia QX (2007) Self-assembled epitaxial nanocomposite BaTiO₃-NiFe₂O₄ films prepared by polymer-assisted deposition. *J Am Chem Soc* 129:14132
34. Luo HM, Mueller AH, McCleskey TM, Burrell AK, Bauer E, Jia QX (2008) Structural and photoelectrochemical properties of BiVO₄ thin films. *J Phys Chem C* 112:6099
35. Luo HM, Lin Y, Baily SA, Wang H, Hawley ME, McCleskey TM, Burrell AK, Bauer E, Civale L, Jia QX (2008) Silica nanoparticles-oxide composite epitaxial thin films. *Angew Chem Int Ed* 47:5768
36. Bauer E, Mueller AH, Usov I, Suvorova N, Janicke MT, Waterhouse GIN, Waterland MR, Jia QX, Burrell AK, McCleskey TM (2008) Chemical solution route to conformal phosphor coatings on nanostructures. *Adv Mater* 20:4704
37. Apetrii C, Schlorb H, Falter M, Lampe I, Schultz L, Holzapfel B (2005) YBCO thin films prepared by fluorine-free polymer-based chemical solution deposition. *IEEE Trans Appl Supercond* 15:2642
38. Patta YR, Wesolowski DE, Cima MJ (2009) Aqueous polymer-nitrate solution deposition of YBCO films. *Phys C* 469:129
39. McQuarrie M (1955) Structural behavior in system (Ba,Ca,Sr)TiO₃ and its relation to certain dielectric characteristics. *J Am Ceram Soc* 38:444
40. Gim Y, Hudson T, Fan Y, Kwon C, Findikoglu AT, Gibbons BJ, Park BH, Jia QX (2000) Microstructure and dielectric properties of Ba_{1-x}Sr_xTiO₃ films grown on LaAlO₃ substrates. *Appl Phys Lett* 77:1200
41. Kim BJ, Lee J, Yoo JB (1999) Sol-gel derived (La,Sr)CoO₃ thin films on silica glass. *Thin Solid Films* 341:13
42. Kozuka H, Kajimura M, Hirano T, Katayama K (2000) Crack-free, thick ceramic coating films via non-repetitive dip-coating using polyvinylpyrrolidone as stress-relaxing agent. *J Sol-Gel Sci Technol* 19:205
43. Kozuka H, Higuchi A (2001) Single-layer submicron-thick BaTiO₃ coatings from poly(vinylpyrrolidone)-containing sols: gel-to-ceramic film conversion, densification, and dielectric properties. *J Mater Res* 16:3116
44. Yao K, Yu S, Tay FEH (2006) Preparation of perovskite Pb(Zn_{1/3}Nb_{2/3})O₃-based thin films from polymer-modified solution precursors. *Appl Phys Lett* 88:052904
45. Du ZH, Ma J, Zhang TS (2007) Densification of the PLZT films derived from polymer-modified solution by tailoring annealing conditions. *J Am Ceram Soc* 90:815
46. Zou GF, Luo HM, Ronning F, Sun B, McCleskey TM, Burrell AK, Bauer E, Jia QX (2010) Facile chemical solution deposition of high-mobility epitaxial germanium films on silicon. *Angew Chem Int Ed* 49:1782
47. Luo HM, Wang H, Zou GF, Bauer E, McCleskey TM, Burrell AK, Jia QX (2010) A review of epitaxial metal-nitride films by polymer-assisted deposition. *Trans Electr Electron Mater* 11:54
48. Zou G, Wang H, Mara N, Luo HM, Li N, Di ZF, Bauer E, Wang YQ, McCleskey TM, Burrell AK, Zhang X, Nastasi M, Jia QX (2010) Chemical solution deposition of epitaxial carbide films. *J Am Chem Soc* 132:2516

Part II

Analytical Methods

Due to the limited space in this part only those methods are covered in separate chapters which are predominantly used for the characterization of the solutions and intermediate stages between solutions and crystalline films. Characterization methods for probing the physical properties of the final functional oxide thin films are beyond the scope of this book and will not normally be explained in detail, but brief information might be given in the corresponding chapters. Furthermore, standard methods will also not be covered since they are content of the typical curricula of any material scientist education. Although XRD, for example, is extremely useful for phase analysis, and it is most frequently applied, XRD is not covered in a separate chapter in the present book. Other very useful and typically applied methods for the phase evolution analysis are thermal analysis (Chap. 7), X-ray absorption spectroscopy (Chap. 8), and FTIR-spectroscopy (Chap. 9). In particular FTIR spectrometers and thermal analysis equipment are often available in material science laboratories and they provide quick and reasonable hints on useful temperature ranges for pyrolysis and crystallization. FTIR is highly sensitive and can thus also be applied on as-deposited and pyrolyzed thin films in order to check for characteristic groups such as carbonate, hydroxyl etc., which give hints for intermediate phases and helps to get a better understanding of what is going on during the transformation process.

Raman spectroscopy, as the complementary technique to FTIR, is a useful tool to sensitively detect local distortions in the crystal lattice of solid mater, which is of particular importance for functional oxides with anisotropic physical properties such as ferro- or piezoelectricity [1]. It has been also applied to CSD derived thins (see e.g. [2–6]).

X-ray absorption spectroscopy (Chap. 8) is powerful in detecting structural relationships in the solutions as well as in the solid state independent of any long range order. Even the deposited thin films can be investigated by using a dedicated setup. Examples for the study of amorphous and differently heat treated PZT thin films may be found in [7, 8].

Structural information on chemical compounds can also be obtained by multi nuclear (^1H , ^{13}C , ^{207}Pb , etc.) magnetic resonance spectroscopy (NMR), which

represents a standard method in chemistry labs. The complex “*chemical cocktails*”, which are often present and additionally complicated by hydrolysis-condensation processes in the precursor solutions for multinary compositions, makes the interpretation of the spectra extremely difficult and sometimes impossible. In addition due to limited amount of material and the lower sensitivity of the NMR method (compared to FTIR) it’s almost impossible to get information from as-deposited and/or pyrolyzed thin films. Nevertheless in a number of studies NMR was successfully applied to obtain information on the local structure of individual precursor molecules and the reaction chemistry including ageing of the precursor solutions [2, 9–20], and pyrolysis behavior. Most of these studies employed solution NMR, but also solid-state NMR of ^{13}C and ^{207}Pb nuclei in different modes (magic angle spinning and static) were applied to characterize the lead educts (hydrated and anhydrous lead carboxylates [9, 10]), dried precursor powders [14] and the bulk pyrolysis products of PZT precursor solutions prepared from these lead compounds [10]. In rare cases, i.e. if well-defined mixed metallo-organic compounds are formed during solution synthesis and other disturbing compounds are absent, it is possible to get real structural information by NMR spectroscopy. By probing the ^1H , ^{13}C , and ^{93}Nb nuclei of an all-alkoxide precursor approach for $\text{K}_{0.5}\text{Na}_{0.5}\text{NbO}_3$ (KNN), evidence for the formation of a single molecule (essentially a single-source precursor; cp. Chap. 4) could be found [2].

In many cases solution NMR was valuable to qualitatively trace continuing chemical reactions and by-product formation, which occur e.g. during the ageing of precursor solutions by following the ^1H NMR resonances of formed esters [12]. Thus indirect hints on the connectivity in the precursor molecules such as Pb-O-Ti links could be deduced by combination with other analysis methods, such as gas chromatography (GC; sometimes denoted GLC from “gas liquid chromatography”) of the volatile residues (e.g. [15, 17, 20]), which yields quantitative ratios of the different organic ingredients.

Further analytical methods which should at least be mentioned without claiming to be complete are (1) secondary ion mass spectrometry (SIMS) for proof of compositional film uniformity throughout the film thickness, (2) Rutherford back-scattering (RBS) for checking quality of epitaxial films, (3) ellipsometry and profilometry for refractive index and thickness measurements, (4) dynamic light scattering (DLS) and small angle X-ray scattering (SAXS) for particle size and shape.

In conclusion, it is the combined application of the plethora of analytical methods that yields the required information to gain a fundamental understanding of the *solution—phase transformation—property relationship* of a dedicated material system.

References

1. Pithan C, Schneller T, Shiratori Y, Majumder SB, Haegel FH, Dornseiffer J, Waser R (2006) Microemulsion mediated synthesis of nanocrystalline BaTiO₃: possibilities, potential and perspectives. *Int J Mater Res* 97:499–507
2. Nakashima Y, Sakamoto W, Yogo T (2011) Processing of highly oriented (K,Na)NbO₃ thin films using a tailored metal-alkoxide precursor solution. *J Eur Ceram Soc* 31:2497–2503
3. Schneller T, Halder S, Waser R, Pithan C, Dornseiffer J, Shiratori Y, Houben L, Vyshnavi N, Majumder SB (2011) Nanocomposite thin films for miniaturized multi-layer ceramic capacitors prepared from barium titanate nanoparticle based hybrid solutions. *J Mater Chem* 21:7953–7965
4. Dixit A, Majumder SB, Katiyar RS, Bhalla AS (2006) Studies on the relaxor behavior of sol-gel derived Ba(Zr_xTi_{1-x})O₃ (0.30 ≤ x ≤ 0.70) thin films. *J Mater Sci* 41:87–96
5. Dixit A, Majumder S, Savvinov A, Katiyar RS, Guo R, Bhalla AS (2002) Investigations on the sol-gel-derived barium zirconium titanate thin films. *Mater Lett* 56:933–940
6. Agrawal DC, Majumder SB, Mohapatra YN, Sathaiyah S, Bist HD, Katiyar RS, Ching-Prado E, Reynes A (1993) Micro-Raman spectroscopy of sol-gel-derived Pb(Zr_xTi_{1-x})O₃ thin films. *J Raman Spectrosc* 24:459–462
7. Schneller T, Kohlstedt H, Petraru A, Waser R, Guo J, Denlinger J, Learmonth T, Glans PA, Smith KE (2008) Investigation of the amorphous to crystalline phase transition of chemical solution deposited Pb(Zr_{0.3}Ti_{0.7})O₃ thin films by soft X-ray absorption and soft X-ray emission spectroscopy. *J Sol-Gel Sci Technol* 48:239–252
8. Arcon I, Malic B, Kosec M, Kodre A (2005) Zr k-edge EXAFS study of PZT thin film formation from sols. *Phys Scr T* 115:448–449
9. Schneller T, Waser R (2007) Chemical modifications of Pb(Zr_{0.3}Ti_{0.7})O₃ precursor solutions and their influence on the morphological and electrical properties of the resulting thin films. *J Sol-Gel Sci Technol* 42:337–352
10. Brieger J, Merkle R, Bertagnolli H, Müller K (1998) Investigation of the pyrolysis and crystallization of lead zirconate titanate ceramics prepared via the sol gel process. *Ber Bunsenges Phys Chem* 102:1376–1386
11. Spiccia L, West BO, Zhang Q (1998) Studies on the synthesis of Pb-Ti-oxo-alkoxo-carboxylato complexes. *Polyhedron* 17:1851–1861
12. Boyle TJ, Dimos D, Schwartz RW, Alam TM, Sinclair MB, Buchheit CD (1997) Aging characteristics of a hybrid sol-gel Pb(Zr,Ti)O₃ precursor solution. *J Mater Res* 12:1022–1030
13. Calzada ML, Sirera R, Carmona F, Jimenez B (1995) Investigations of a diol-based sol-gel process for the preparation of lead titanate materials. *J Am Ceram Soc* 78:1802–1808
14. Schwartz RW, Assink RA, Dimos D, Sinclair MB, Boyle TJ, Buchheit CD (1995) Effects of acetylacetone additions on PZT thin film processing. *Mater Res Soc Proc* 361:377–387
15. Coffman PR, Dey SK (1994) Structure evolution in the PbO-ZrO₂-TiO₂ sol-gel system: Part I—characterization of prehydrolyzed precursors. *J Sol-Gel Sci Technol* 1:251–265
16. Assink R, Schwartz R (1993) ¹H and ¹³C NMR investigations of lead zirconate titanate Pb(Zr, Ti)O₃ thin-film precursor solutions. *Chem Mater* 5:511–517
17. Beltram T, Kosec M, Stavber S (1993) Reactions taking place during the sol-gel processing of PLZT. *J Mater Res* 28:313–320
18. Schwartz RW, Assink RA, Headley TJ (1992) Spectroscopic and microstructural characterization of solution chemistry effects in PZT thin film processing. *Mater Res Soc Proc* 243:245–254
19. Ramamurthi SD, Payne DA (1990) Structural investigations of prehydrolyzed precursors used in the sol-gel processing of lead titanate. *J Am Ceram Soc* 73:2547–2551
20. Dekleva TW, Hayes JM, Cross LE, Geoffroy GL (1988) Sol-gel processing of lead titanate in 2-methoxyethanol: investigations into the nature of the prehydrolyzed solutions. *J Am Ceram Soc* 71:C280–C282

Chapter 7

Thermal Analysis

Barbara Malič, Alja Kupec, and Marija Kosec[†]

7.1 Introduction

The methods of thermal analysis: thermogravimetry and differential thermal analysis and/or differential scanning calorimetry, have been implemented in chemical solution deposition (CSD) of functional oxide thin films predominantly as tools to follow the thermal decomposition of thin-film precursors and crystallization of the oxide. The as-obtained data enabled insight into the chemical composition and structural characteristics of the as-dried amorphous precursors of thin film materials and to study their thermal behavior since the early work on CSD-derived $\text{Pb}(\text{Zr,Ti})\text{O}_3$ thin films [1].

Although the substrate obviously plays a significant role in the thermal decomposition and structural evolution of the thin film material, the majority of the studies have focused on the as-dried precursors and not on the as-deposited films as a consequence of the extremely low film/substrate mass ratio and therefore a low signal [2, 3].

The liquid precursors have been typically dried before the analysis in order to increase the sensitivity of the method; otherwise the largest weight loss and coincident enthalpy change were inevitably due to the evaporation of the solvent.

The main information which can be obtained by thermal analysis of the as-dried amorphous precursors includes the total mass loss, the temperature range of thermal decomposition and its constituent parts, i.e., evaporation of residual solvent, thermal decomposition of functional groups bonded to the inorganic network, and crystallization of the target material. It should be noted that the thermal analysis itself can not provide full information on the processes occurring in the CSD precursors upon heating; consequently, a number of other techniques of materials

[†] Author was deceased

B. Malič (✉) • A. Kupec
Jožef Stefan Institute, Ljubljana, Slovenia
e-mail: barbara.malic@ijs.si

characterization have been coupled to selected methods of thermal analysis, most often mass spectrometry or infra-red spectroscopy of volatile by-products of thermal decomposition.

The present chapter provides basic information on selected methods of thermal analysis, which have been most frequently implemented, and, in the second part, some examples of thermal analysis studies of CSD precursors and thin films.

7.2 Basics of Thermal Analysis

According to the IUPAC definition, thermal analysis (TA) comprises a group of techniques in which a physical property of a substance and/or its reaction product (s) is measured as a function of temperature while the substance is subjected to a controlled temperature program [4]. The analyses are performed in a controlled atmosphere: oxidizing, reducing, and inert or in vacuum. The materials are analysed in a broad temperature range under a selected dynamic or isothermal temperature program.

The measured physical properties include mass in thermogravimetry (TG) or mass change in derivative thermogravimetry (DTG), temperature difference between the sample and an inert reference material in differential thermal analysis (DTA), heat or enthalpy change between the sample and an inert reference material in differential scanning calorimetry (DSC), and measurements of selected physical (optical, electrical, mechanical, etc.) properties as a function of temperature and/or time.

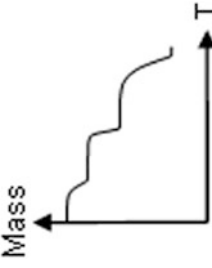
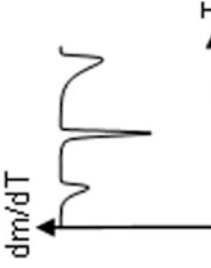
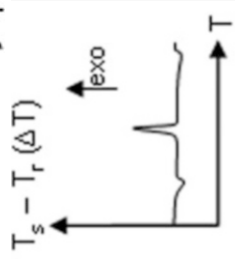
The TG and DTA are often measured simultaneously, i.e., in a single equipment. Coupled analysis of gaseous thermal decomposition products or evolved gas analysis (EGA) can be implemented in parallel to TG and/or DTA by means of measurement of gas volume, mass fragments by mass spectrometry (MS), functional groups by infra-red or Fourier transform infra-red spectroscopy (IR, FTIR), gas conductivity, or other selected property. Extensive information on the methods of TA can be found for example in [5, 6].

Brief descriptions of selected TA methods, most frequently used to characterize the CSD precursors, are collected in Table 7.1, and explained in more detail in further text.

The equipment for thermal analysis contains the furnace or temperature chamber, the sample holder, the sensor to measure the selected property, e.g., mass, and temperature, and the control unit to collect and process the data [6].

The results of thermal analyses are strongly influenced by both instrumental factors and by the properties of the samples; therefore they should be specified when reporting the TA results. The former include the atmosphere in the furnace, selected temperature program, the type of the furnace (size, shape), the choice of the crucibles (material, size, and shape), the type of the thermocouple and its position relative to the sample. While the first two parameters can be selected arbitrarily, the rest depend on specific equipment. The characteristics of the sample

Table 7.1 Basic methods of thermal analysis: a brief description of selected techniques (after [5, 6]) and characteristic curves of individual methods

Technique	Abbreviation	Measured property	Use	Characteristic curve ^a
Thermogravimetry	TG	Mass (m)	Decomposition, reaction	
Derivative thermogravimetry	DTG	Mass change, dm/dT or dm/dt	Decomposition, reaction	
Differential thermal analysis	DTA	Temperature change, $T_s - T_r (\Delta T)$	Phase changes, reaction	

(continued)

Table 7.1 (continued)

Technique	Abbreviation	Measured property	Use	Characteristic curve ^a
Differential scanning calorimetry	DSC	Heat flow, dH/dT	Phase change, reaction, heat capacity	
Evolved gas analysis	EGA	Selected property of the evolved gas: volume, conductivity, mass fragments, type of the functional groups, etc.	Decomposition	

^aThe TA curves demonstrate the thermal decomposition of calcium oxalate hydrate ($\text{CaC}_2\text{O}_4 \cdot \text{H}_2\text{O}$), a frequently used reference material: dehydration and the two-step decomposition of the oxalate groups with evolution of carbon dioxide. The TG/DTA/EGA-mass spectrometry (MS) curves were recorded between room temperature and 900 °C at 10 K/min in a dynamic air atmosphere (100 ml/min) in Pt/Rh crucibles (Netzsch STA 409, Thermostat 300). The DSC curve was recorded between room temperature and 700 °C at 10 K/min in a dynamic air atmosphere in a Pt pan. (Netzsch DSC 204 F1). The sample masses in the two experiments were about 50 and 9 mg, respectively (Courtesy of Electronic Ceramics Department, Jožef Stefan Institute)

include the mass, density, temperature conductivity, heat capacitance, dilution, in case of solid samples the particle size and size distribution, crystallinity [5, 6].

7.2.1 Thermogravimetry and Derivative Thermogravimetry

The TG is a technique in which the mass of a substance (and/or its reaction product(s)) is measured as a function of temperature whilst the substance is subjected to a controlled temperature programme [4]. The analyses are performed in a selected atmosphere or in vacuum. Obviously, the mass loss is detected only if volatile species are evolved. In reactions or processes without any mass change other TA techniques, such as DTA or DSC should be used.

In the DTG the derivative of the mass change is recorded as a function of temperature or time. The area under the curve is proportional to the mass loss. The DTG allows quantitative assessment of the rate of the mass change and is useful in determination of overlapping processes.

The basic equipment, denoted as thermobalance, includes an analytical balance inside a furnace. The maximum temperature may reach 1,700 °C; however, temperatures not exceeding 1,200 °C or 1,550 °C are more common. The temperature is controlled by a thermocouple, and its choice depends on the maximum temperature of the furnace. The important instrumental factors are the sensitivity and the precision of the balance. The sample is positioned inside an inert crucible, typically consisting of platinum or alumina. Up-to-date equipments use sample masses in the range of a few mg or a few 10 mg. Such low masses allow better heat transfer upon analysis.

Before the analysis the thermobalance should be calibrated for temperature and mass and the base-line of the balance should be recorded mainly to take into account the buoyancy effect as a consequence of the change in the density of the working gas upon heating and cooling [5, 6].

7.2.2 Differential Thermal Analysis and Differential Scanning Calorimetry

In DTA the temperature difference between a substance and a reference material is measured as a function of temperature, while the substance and reference material are subjected to a controlled temperature program [4]. The difference in the temperature of the sample and the reference material, generally Al_2O_3 , is measured as the voltage difference of the thermocouples, positioned in the walls of the sample and reference crucibles. The area of a DTA peak is proportional to the released heat (in the case of an exothermic reaction upon heating). The result of a DTA analysis is presented as the temperature difference expressed in $\mu\text{V}/\text{mg}$ versus temperature or

time. As an example, when a sample melts upon heating, its temperature is lower relative to the reference and in DTA a negative (endo) peak is detected.

The DSC is a technique in which the difference in energy inputs into a substance and/or its reaction product(s) and a reference material is measured as a function of temperature whilst the substance and reference material are subjected to a controlled temperature program [4]. The operating principle of DSC is either power compensation or heat flux. In the former case the instrument provides heat (thermal power) to the sample when its temperature is different from the programmed value. In the latter case the sample and the reference or an empty sample holder are heated in the same chamber and the measured temperature difference between them generates the DSC signal. The difference between the heat flux DSC and the DTA is therefore in the conversion of the measured temperature difference and it strongly depends on the design of a selected instrument and the software.

Physical and chemical changes detected by DTA or DSC include phase transitions/changes, adsorption, desorption, and oxidation, reduction, dehydration, decomposition, reactions within/with solids, liquids or with gases, and so on. It should be noted that reversible processes, such as phase transitions, have different signs of DTA or DSC signals upon heating and cooling.

The temperature range for the majority of DSC instruments spans from about $-150\text{ }^{\circ}\text{C}$ (cooling by liquid nitrogen) to $500\text{ }^{\circ}\text{C}$ or $700\text{ }^{\circ}\text{C}$, depending on the type of the chamber, thermocouples and crucibles. High-temperature heat-flux DSC reaches up to $1,500/1,600\text{ }^{\circ}\text{C}$.

The DTA analyses are often performed simultaneously with the TG. Similarly as for TG, the instruments need to be calibrated prior analysis both for temperature and temperature/heat change [5, 6].

The sensitivity of the DSC is strongly enhanced as compared to DTA, as shown in the case of the DTA and DSC curves of the as-dried $(\text{Pb}_{0.88}\text{La}_{0.08})(\text{Zr}_{0.65}\text{Ti}_{0.35})\text{O}_3$ precursor shown in Fig. 7.1. The precursor synthesis is described in [7]. Note that the sample mass in the DSC is in this case three times less than for the DTA analysis.

Both DTA and DSC measurements can be used for quantitative determination of thermodynamic and kinetic data, such as enthalpy and activation energy [5, 6].

The enthalpy of a reaction is directly proportional to the area of a DTA or DSC peak. The activation energy for a reaction may be determined from the shift of a DTA or DSC peak maximum with increasing heating rates [8].

7.2.3 Evolved Gas Analysis

In EGA the nature and/or amount of volatile products released by a substance are measured as a function of temperature as the substance is subjected to a controlled temperature programme [4]. The gasses may be analysed by any method that can determine their amount and/or composition, for example mass spectrometry or infrared spectroscopy, optical or electrical property measurement, etc. [5]. In

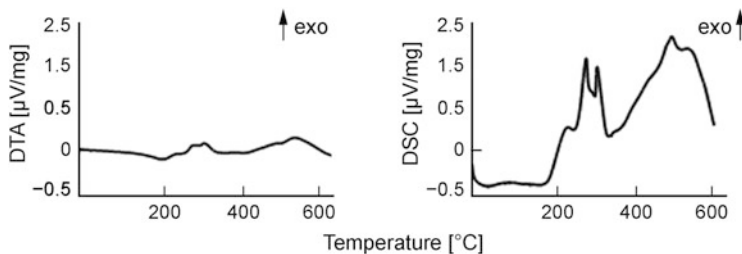


Fig. 7.1 Comparison of the DTA and DSC analyses of the acetate-alkoxide-derived ($\text{Pb}_{0.88}\text{La}_{0.08}$) ($\text{Zr}_{0.65}\text{Ti}_{0.35}$) O_3 precursor, dried at 100 °C (Netzsch STA 409 and DSC 204 F1). Both analyses were recorded in flowing air atmosphere between room temperature and 650 °C with the heating rate of 10 K/min. The samples were positioned in a PtRh crucible for DTA and in a Pt pan with a lid for DSC. The sample masses were 54 and 18 mg, respectively (Courtesy of Electronic Ceramics Department, Jožef Stefan Institute)

practice, an MS, FTIR or other instrument is coupled to the outlet of the thermobalance via a heated capillary to avoid any condensation of the volatiles. The results of a selected TA method and EGA are usually plotted together with temperature or time as the independent variable.

7.3 Thermal Decomposition of CSD Precursors

7.3.1 Alkoxide Derived (Organic) CSD Precursors

As a case study, the thermal decomposition of the as-dried $\text{Pb}(\text{Zr}_{0.3}\text{Ti}_{0.7})\text{O}_3$ precursor, followed by the simultaneous TG/DTG/EGA-MS/DTA analysis in air is shown in Fig. 7.2. The precursor was prepared by a modified 2-methoxyethanol synthesis [9]. It can be described by a general formula $\text{Pb}(\text{Zr}_{0.3}\text{Ti}_{0.7})(\text{OH})_v(\text{OAc})_w(\text{OBu})_x(\text{OR})_y\text{O}_z$ ($\text{Ac} = \text{CH}_3\text{CO}$, $\text{Bu} = \text{C}_4\text{H}_9$, $\text{R} = \text{C}_2\text{H}_4\text{OCH}_3$) and it probably contains some solvent and/or water. Note that 10 mole % PbO was added to compensate possible PbO loss upon heating. According to XRD the precursor is amorphous upon drying and crystallizes to perovskite with traces of pyrochlore upon heating to the final temperature of the TA, 700 °C.

The total mass loss between room temperature and 600 °C upon heating in air is 16.4 %. The thermal decomposition takes place stepwise and at least five predominantly overlapping steps of mass loss are distinguished from the minima of the DTG curve. The EGA-MS curves show temperature evolution of H_2O (mass fragment 18), CO_2 (mass fragment 44) and acetone, CH_3COCH_3 (mass fragment 58). The DTA curve exhibits first a broad endo peak to about 200 °C and then two groups of overlapping exo peaks between 260 and 440 °C and 440 and 600 °C.

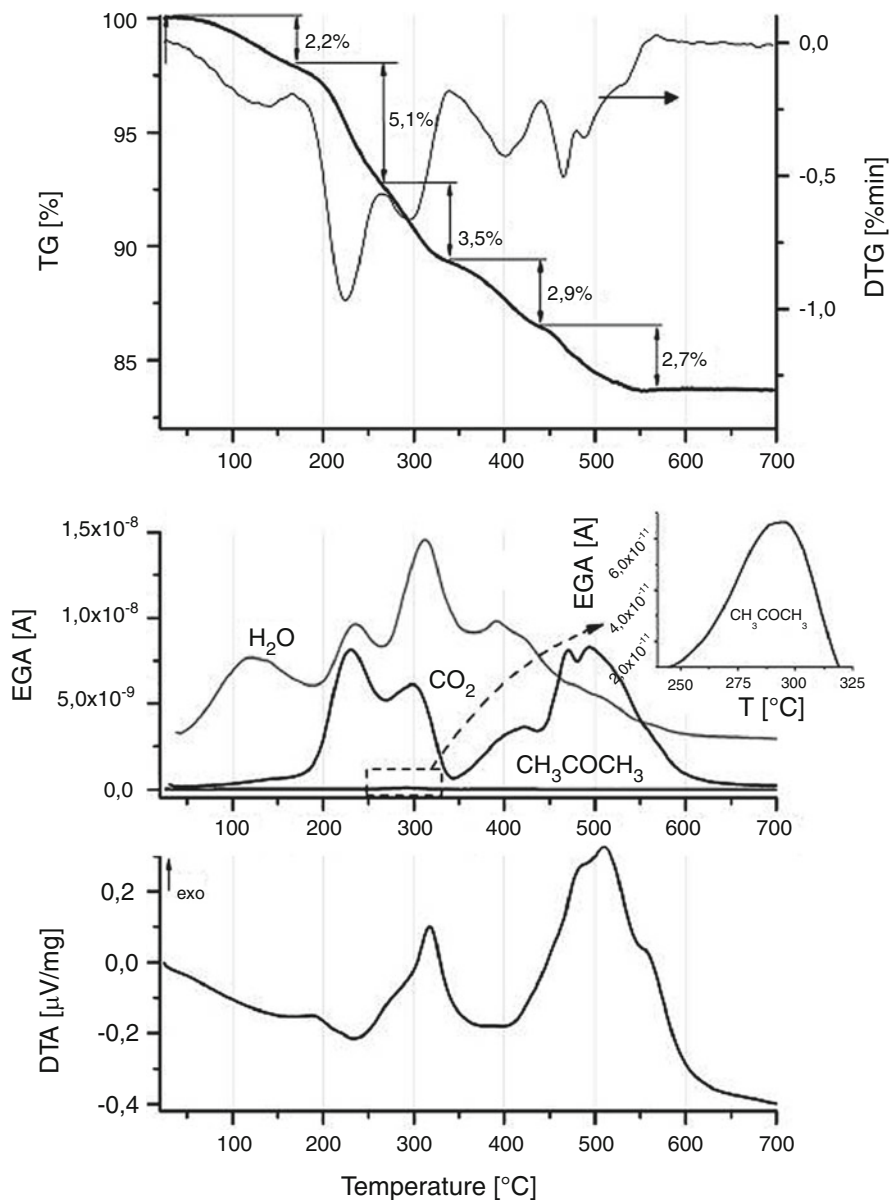
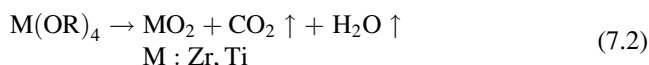


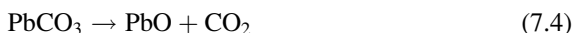
Fig. 7.2 Simultaneous TG/DTG/EGA/DTA analysis of $\text{Pb}(\text{Zr}_{0.3}\text{Ti}_{0.7})\text{O}_3$ precursor, dried at $60\text{ }^\circ\text{C}$ in air. The sol was obtained by reacting anhydrous lead acetate, Zr- and Ti- butoxides in 2-methoxyethanol as described in [9]. The analysis was performed between room temperature and $700\text{ }^\circ\text{C}$ at 10 K/min in a dynamic synthetic air atmosphere (50 ml/min) in Pt/Rh crucibles (Netzsch STA 409, ThermoStar 300). The sample mass was about 30 mg . From [10] with the permission of the author

The mass loss step upon heating to about 200 °C is due to evaporation of water and possibly of residual solvent, which is an endothermic event as evidenced by a broad endo DTA peak. Upon further heating, major mass loss-steps in two main temperature ranges are accompanied by the two groups of strong exo DTA peaks with maxima at about 300 and 520 °C. Note that the maxima of EGA peaks correspond to the minima of DTG peaks.

In the first step of organics decomposition, CO₂, H₂O, and traces of acetone are detected. According to literature, the thermal decomposition of metal alkoxide in inert atmosphere occurs via oxo-alkoxide to oxide with release of alkenes and alcohol (7.1). In oxidizing atmosphere, the alkoxide is completely oxidized to H₂O and CO₂ (7.2) [11].



The presence of a low amount of acetone in the EGA is due to a stepwise decomposition of the acetate groups which follow the same decomposition pathway as in Pb-acetate alone (Eqs. 7.3 and 7.4) [12–14].



Between 440 and 600 °C the main volatile species is CO₂, while the amount of H₂O is decreasing. The thermal processes are therefore the decomposition of carbonates and oxidation of carbon residues [14]. Note that oxidation of both C and CO is strongly exothermic.

The crystallization of perovskite phase, which is an exo effect in DTA, is obviously overlapped with the last step of organics decomposition.

Another example of a coupled TA analysis is a study of the thermal decomposition of Pb(Zr_{0.3}Ti_{0.7})O₃ precursor by TG/EGA FT-IR shown in Fig. 7.3. The thermal decomposition of the precursor occurred upon heating to about 500 °C. The in-situ IR analysis of evolved gases enabled monitoring of temperature ranges of hydroxyl groups (3,600–3,700 cm⁻¹), CO₂ (2,300–2,400 cm⁻¹) and different organic species: ester (1,750 cm⁻¹, 1,260 cm⁻¹), ether (1,130 cm⁻¹), and alcohol groups (1,060 cm⁻¹) and provided information on the temperature ranges of solvent evaporation, dehydroxylation and organic group thermal oxidation [15].

Activation energies (E_A) for individual steps of pyrolysis of Pb(Zr_xTi_{1-x})O₃ CSD precursors from Pb-acetate, Zr- and Ti-propoxides in 2-methoxyethanol have been evaluated by following the shift of the peak DTA and DTG temperatures with increasing heating rate. The precursors were dried at 90 °C and 20 mbar. The first pyrolysis step yielded acetone and CO₂, and was similar to decomposition of Pb-acetate, the second step included thermal oxidation of remaining organic groups and the last one oxidation of carbon residues. This last step could be avoided by

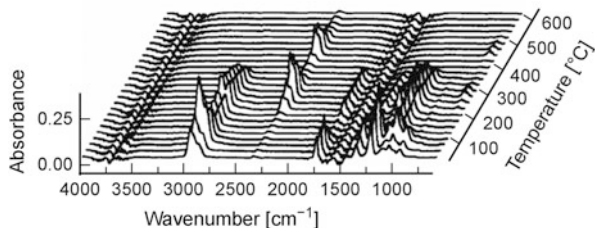


Fig. 7.3 FTIR reflection spectra of the volatile species evolved upon thermal decomposition of the alkoxide-derived $\text{Pb}(\text{Zr}_{0.3}\text{Ti}_{0.7})\text{O}_3$ precursor as a function of temperature. The spectra were obtained by coupling the FTIR spectrometer via a heated capillary. The analysis was performed with a heating rate of 10 K/min in air (50 ml/min). From [15]. Reproduced by permission of Elsevier

introducing steam treatment of the dried gels (6 h at 105 °C in humid atmosphere) with the exception of the precursors with a high Zr content ($x = 0.75, 1$), the reason for that being bonding of acetate groups to zirconium atoms. The activation energy for the first step of thermal decomposition of the steam-treated precursors was between 113 ± 5 kJ/mol for PbTiO_3 and 162 ± 8 kJ/mol for PbZrO_3 , for the second step around 130 kJ/mol notwithstanding the composition, and for oxidation of carbon residues about 399 ± 15 kJ/mol for $\text{Pb}(\text{Zr}_{0.75}\text{Ti}_{2.5})\text{O}_3$ and 263 ± 16 kJ/mol for PbZrO_3 as determined from DTGA peak shifts [14].

The atmosphere strongly influences the thermal decomposition of CSD precursors. Clearly, an oxidizing atmosphere (air or O_2) enables thermal oxidation of the functional groups, which is an exothermic process. In an inert atmosphere, such as argon, the organic groups pyrolyse without major DTA effects. Carbon or carbonaceous residues present in the precursor may hinder crystallization of the perovskite [1, 13–15].

Since the early work on CSD of thin films from alkoxide derived solutions it has been recognized that both the inorganic (metal) and the organic part of the precursor influence the course of the thermal decomposition [1].

As an example, the DTA curves of Ti, Zr isopropoxide, and Pb-Ti and Pb-Zr acetate-isopropoxide derived precursors are presented in Fig. 7.4 (left). The materials were synthesized by the 2-methoxyethanol route and hydrolyzed with 1 mole of H_2O per mole of alkoxide groups. The as-dried Pb-Zr-Ti precursors were amorphous and crystallized to perovskite phase between 450 and 600 °C as determined by XRD. In all four cases a broad endotherm below 200 °C was observed and attributed to volatilization of residual solvent and/or physically bonded volatile species, followed by one or more exothermic effects between 250 and 500 °C, due to thermal oxidation of organic groups. Clearly, the DTA patterns of the single-metal and bimetallic samples differ within and between the two groups.

In Fig. 7.4 (right) there is a further comparison of the effect of the type of the alkoxide group—iso- or n-propoxide—on the DTA patterns of the PZT precursors.

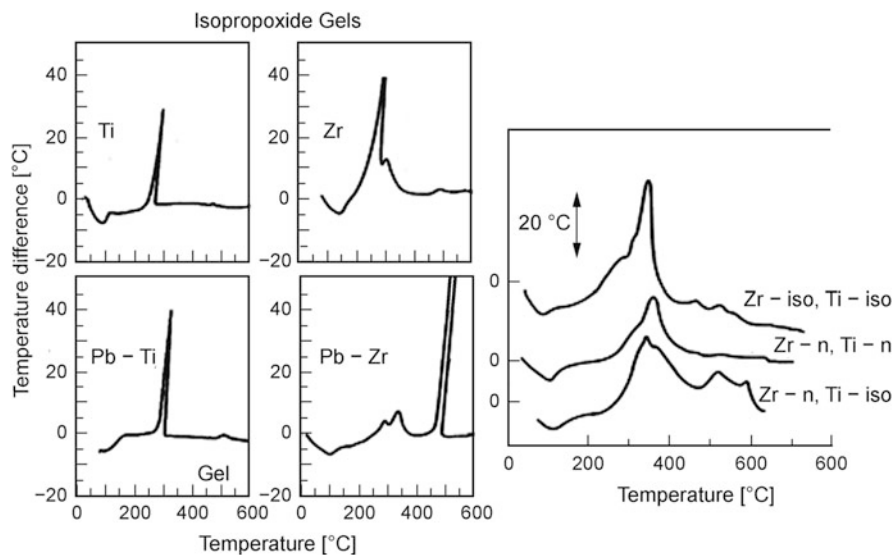


Fig. 7.4 The DTA curves of Ti, Zr, Pb-Ti and Pb-Zr isopropoxide precursors (*left*) and Pb-Zr-Ti precursors prepared from either iso- or n propoxides (*right*). The precursors were dried at 150 °C prior analysis. The analyses were performed in flowing oxygen with a 10 K/min heating rate. From [1]

The choice of the isomer influences the temperature range and the intensity of the exothermic effects between approximately 200 and 600 °C [1].

The thermal decompositions of CSD precursors prepared at different synthesis conditions (reagents, modifiers, catalysis, conditions of hydrolysis, etc.) has been studied in a number of works, e.g. in [1, 10, 12–21]. In addition to the studies of CSD precursors prepared in 2-methoxyethanol, thermal decompositions of the precursors based on other solvents were studied, including less toxic 2-butoxyethanol [15, 19, 22].

Within the study of diol-based CSD route of PbTiO_3 and $\text{Pb}(\text{Zr}_{0.53}\text{Ti}_{0.47})\text{O}_3$, thermal decompositions of the precursors prepared from propanediol, butanediol and pentanediol were compared. The reagents were lead-acetate-trihydrate, titanium diisopropoxide bis-acetylacetonate and acetylacetonate-stabilized zirconium n-propoxide. The thermal decompositions of the precursors, dried at 100 °C performed in air at 5 K/min were completed at 500 and 550 °C for PbTiO_3 and $\text{Pb}(\text{Zr}_{0.53}\text{Ti}_{0.47})\text{O}_3$, respectively. The DTA curves revealed two groups of exothermic peaks with maxima at about 320 and 525 °C, respectively. The last peak was assumed to be associated with the crystallization of the perovskite phase. The type of diol influenced the shape of the DTA [23].

The choice of the material system influences the patterns of thermal decompositions of respective CSD precursors. TA was implemented in the studies of the precursors of $\text{Pb}(\text{Zr,Ti})\text{O}_3$ solid solution with different Zr/Ti ratios, covering the whole compositional range from 100/0 to 0/100 [1, 10, 12–17, 21–25],

Table 7.2 Approximate temperature ranges of processes occurring upon thermal decomposition of alkoxide-based CSD precursors in air

Temp. range, T/°C	TG/DTA	Process
25 to ≈250	TG: mass loss DTA: endo	Evaporation of residual solvents, dehydration and dehydroxylation
≈250 to ≈400	TG: mass loss DTA: exo	Decomposition of alkoxide and acetate and/or other functional groups
≈450 to ≈600	TG: mass loss DTA: exo	Decomposition of residual organic groups and carbon residues, crystallization

Pb(Mg_{0.33}Nb_{0.67})O₃–PbTiO₃ [26, 27], (Ba,Sr)TiO₃ solid solution and its end-members [18, 19], or lead-free materials such as K_{0.5}Na_{0.5}NbO₃ [28], KTa_{0.65}Nb_{0.35}O₃ [29] or Na_{0.5}Bi_{0.5}TiO₃ [20, 30] to select only a few examples.

In summary, thermal decompositions of alkoxide derived CSD precursors in air follow a similar course, and may be divided into three main parts with temperature ranges depending upon the specific system: evaporation of residual solvents, dehydration and dehydroxylation, and two steps of organics decomposition. Crystallization often overlaps with the last step of functional group decomposition (Table 7.2).

As written above, crystallization of the target phase often coincides with the last step of thermal decomposition, however in the case of Na_{0.5}Bi_{0.5}TiO₃ prepared by alkoxide based sol-gel route the processes are almost separated as shown in Fig. 7.5. The major mass loss coinciding with a strong DTA exo peak at 380 °C is due to decomposition of organics and the exo DTA peak at 489 °C due to perovskite crystallization, as confirmed by XRD, together with evolution of a low amount of CO₂ determined by the coupled EGA-MS [20].

In the case of alkoxide-derived Pb(Zr_{0.3}Ti_{0.7})O₃ CSD precursor, the decomposition of organic residues overlapped with the crystallization. Therefore, the enthalpy of crystallization was determined so that prior the DTA analysis the organics were completely removed by heating at 400 °C, yet the material remained XRD-amorphous. Figure 7.6 shows the DTA curve and XRD patterns of the samples quenched at selected temperatures. The exo DTA peak at 473 °C corresponds to crystallization of amorphous PZT precursor to thermodynamically stable perovskite together with the transient pyrochlore-type phase. The enthalpy of crystallization calculated from the DTA peak area between 430 and 520 °C was 33 kJ/mol. The enthalpy calculated from the weak exo DTA peak at 551 °C equal to 1.6 kJ/mol was attributed to crystallite growth [24]. In the case of Pb(Zr_{0.3}Ti_{0.7})O₃ prepared from Pb-acetate and Zr- and Ti-propoxides, the enthalpy of crystallization was 12 kJ/mol [13].

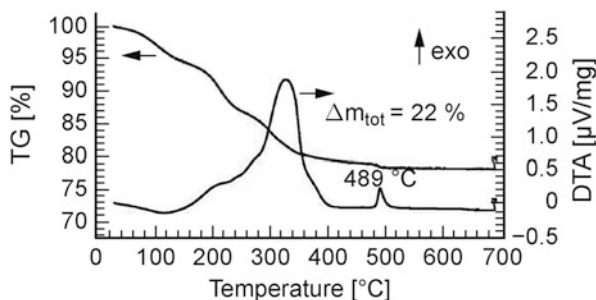


Fig. 7.5 The TG/DTA curves of $\text{Na}_{0.5}\text{Bi}_{0.5}\text{TiO}_3$ acetate-butoxide based precursor. The precursor was dried at 80°C prior analysis. The analyses were performed in flowing air atmosphere with a 10 K/min heating rate. From [20]. Reproduced with permission of the author

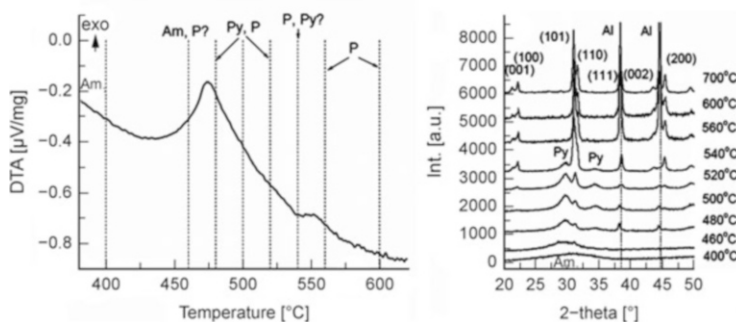


Fig. 7.6 DTA curve of the $\text{Pb}(\text{Zr}_{0.3}\text{Ti}_{0.7})\text{O}_3$ precursor, prepared via alkoxide based sol-gel route (left). Phase compositions of the same precursors, heated to the temperatures between 400 and 700°C (right). Al: sample holder, Am: amorphous phase, Py: pyrochlore phase. The reflections of the perovskite phase (P) are marked. From [24]. Reproduced with permission of Slovenian Chemical Society

7.3.2 Water-Based CSD Precursors

A detailed thermal analysis study of water-based $\text{Pb}(\text{Zr}_{0.53}\text{Ti}_{0.47})\text{O}_3$ CSD precursor (cp. Chap. 5) was performed by coupling TG/DTA with EGA-MS and FTIR. The precursor consisted of peroxy-citrato and citrato ligands cross-linked by ammonium carboxylate groups. The thermal decomposition occurred in three major steps: evaporation of residual solvent and decomposition of ammonium carboxylate upon heating to about 260°C , which is an endothermic effect and two steps of functional group decomposition, at about $270\text{--}420^\circ\text{C}$ and $420\text{--}520^\circ\text{C}$, both effects are exothermic [31].

In the case of LaCoO_3 synthesized from a nitrate-citrato based gel the TG/DTA coupled with EGA-MS was performed. In two steps of thermal decomposition, at about 200 and 350°C , the same gases: CO_2 , H_2O and NO_2 , were evolved.

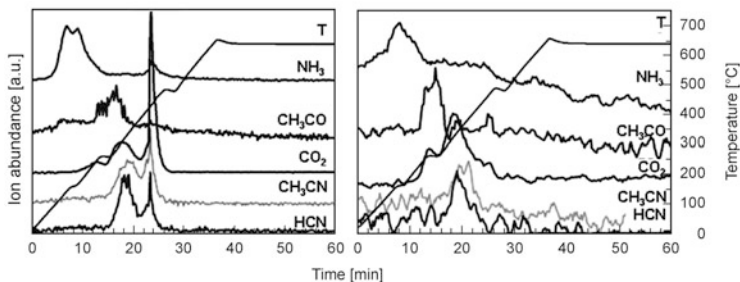


Fig. 7.7 EGA of the dried $(\text{Bi,Nd})_4\text{Ti}_3\text{O}_{12}$ precursor gel (*left*) and of the as-deposited film (*right*), showing the temperature profile and traces of $(m/e) = 17$ (NH_3), $(m/z) = 43$ (CH_3CO), $(m/e) = 44$ (CO_2), $(m/z) = 41$ (CH_3CN), and $(m/z) = 27$ (HCN) as a function of time (atmosphere: dry air 100 ml/min, heating rate: 20 K/min). From [40]. Reproduced with permission of the author

The authors concluded that the citrate and nitrate groups were bonded in two ways to the metal network, both as bound and as coordinated ligands and not as previously proposed that the metal atoms were coordinated only by citrate groups [32].

7.4 Thermal Analysis of Thin Films

There are not many TA studies of CSD thin films deposited on planar substrates. The reasons are related mainly to a too low mass of the film, so that the mass change upon thermal decomposition could not be detected in TG. In DSC, the enthalpy changes related to the film are again small, predominantly diluted by the substrate and consequently too low to be measurable. Some solutions for TA of thin films have been proposed or summarized in review papers [2, 3, 33, 34]. The options include removal of the film from the substrate, dissolution of the substrate, deposition of the film on a thin foil, use of larger samples to increase the sample mass, or development of more sensitive techniques. For example, thin-film Ag-Bi thermocouples were evaporated on the borosilicate glass substrate to enhance the sensitivity of the DTA analysis of physical vapor deposited selenium films [35]. Thin magnetic films could be analysed with the enhanced precision in a magnetic field gradient (thermomagnetometry) [36]. Emanation thermal analysis (ETA) based on the detection of radioactive inert gas atoms from a sample upon heating has been implemented in thermal analysis of CSD-derived titania thin films [37].

Mass spectrometry (EGA-MS) was sensitive enough to detect dehydration of sputtered iridium oxide films on gold foils [38] or crystallization of RF-sputtered indium-tin-oxide films accompanied by evolution of water [39].

Peroxo-citrate derived $(\text{Bi,Nd})_4\text{Ti}_3\text{O}_{12}$ as-dried precursor and as-deposited thin films were analysed by EGA-MS. The comparison of the analyses revealed that the decomposition of the film was completed at a lower temperature than that of the gel (Fig. 7.7) [40].

7.5 Conclusions

The chapter summarizes the basics of thermal analysis and the implementation of selected methods in characterization of CSD precursors and only in a limited amount of thin films. Thermogravimetry in combination with differential thermal analysis and coupled to evolved gas analysis has been employed to obtain insight into the processes occurring upon thermal decomposition and crystallization of CSD precursors.

Acknowledgments Ms. Jena Cilensek is acknowledged for performing the thermal analyses of CSD precursors shown as examples in this chapter. Dr. Romana Cerc Korosec is acknowledged for discussion on thermal analysis of thin films. The work was supported by the Slovenian Research Agency (P2-0105, PR-03099 and J2-1227).

References

1. Budd KD, Dey SK, Payne DA (1985) Sol-gel processing of PbTiO_3 , PbZrO_3 , PZT, and PLZT thin films. *Brit Cer Pr* 36:107–122
2. Gallagher PK (1992) Applications of thermoanalytical methods to the study of thin films. *J Therm Anal* 38:17–26
3. Leskela M, Leskela T, Niinisto L (1993) Thermoanalytical methods in the study of inorganic thin films. *J Therm Anal* 40:1077–1088
4. McNaught AD, Wilkinson A (1997) IUPAC compendium of chemical terminology, 2nd edn. Blackwell, Oxford
5. Wendlandt WWM (1986) Thermal analysis, 3rd edn. Wiley, New York
6. Haines PJ (ed) (2002) Principles of thermal analysis and calorimetry. Royal Society of Chemistry, Cambridge
7. Mandeljc M, Malic B, Kosec M, Drazic G (2002) Crystallization of zirconium-rich PLZT thin films below 500 °C. *Integr Ferroelectr* 46:329–338
8. Kissinger HE (1957) Reaction kinetics in differential thermal analysis. *Anal Chem* 29:1702–1706
9. Mandeljc M, Kosec M, Malic B, Samardzija Z (2001) Contribution to the low – temperature crystallization of PZT-based CSD thin films. *Integr Ferroelectr* 36:163–172
10. Mandeljc M (2006) Študij kristalizacije tankih plasti na osnovi $\text{Pb}(\text{Zr,Ti})\text{O}_3$ (Study of crystallization of $\text{Pb}(\text{Zr,Ti})\text{O}_3$ thin films). PhD Thesis, Uni Ljubljana, Ljubljana
11. Turova NYA, Turevskaya EP, Kessler VG, Yanovskaya MI (2002) The chemistry of metal alkoxides. Kluwer, Boston
12. Coffman PR, Barlingay CK, Gupta A, Dey SK (1996) Structure evolution in the $\text{PbO-ZrO}_2\text{-TiO}_2$ sol-gel system: Part II – pyrolysis of acid and base – catalyzed bulk and thin film gels. *J Sol-Gel Sci Technol* 6:83–106
13. Merkle R, Bertagnolli H (1998) Investigation of the crystallization of lead titanate and lead zirconate titanate with X-ray diffraction and differential thermal analysis. *Ber Bunsen Ges Phys Chem* 102:1023–1031
14. Merkle R, Bertagnolli H (1998) Investigation of the pyrolysis of lead zirconate titanate gels with coupled differential thermal analysis, thermogravimetry and infrared spectroscopy. *J Mater Sci* 33:4341–4348

15. Nouwen R, Mullens J, Franco D, Yperman J, Van Poucke LC (1996) Use of thermogravimetric analysis – Fourier transform infrared spectroscopy in the study of the reaction mechanism of the preparation of $\text{Pb}(\text{Zr},\text{Ti})\text{O}_3$ by the sol-gel method. *Vib Spectrosc* 10:291–299
16. Malic B, Kosec M, Arcon I, Kodre A (2005) Homogeneity issues in chemical solution deposition of $\text{Pb}(\text{Zr},\text{Ti})\text{O}_3$ thin films. *J Eur Ceram Soc* 25:2241–2246
17. Malic B, Kosec M, Smolej K, Stavber S (1999) Effect of precursor type on the microstructure of PbTiO_3 thin films. *J Eur Ceram Soc* 19:1345–1348
18. Hasenkox U, Hoffmann S, Waser R (1998) Influence of precursor chemistry on the formation of MTiO_3 ($M = \text{Ba}, \text{Sr}$) ceramic thin films. *J Sol-Gel Sci Technol* 12:67–79
19. Halder S, Schneller T, Waser R (2005) Crystallization temperature limit of $(\text{Ba},\text{Sr})\text{TiO}_3$ thin films prepared by a non oxocarbonate phase forming CSD route. *J Sol-Gel Sci Technol* 33:299–306
20. Remondiere F, Malic B, Kosec M, Mercurio JP (2008) Study of the crystallization pathway of $\text{Na}_{0.5}\text{Bi}_{0.5}\text{TiO}_3$ thin films obtained by chemical solution deposition. *J Sol-Gel Sci Technol* 46:117–125
21. Calzada ML, Malic B, Sirera R, Kosec M (2002) Thermal-decomposition chemistry of modified lead-titanate aquo-diol gels used for the preparation of thin films. *J Sol-Gel Sci Technol* 23:221–230
22. Fe L, Norga G, Wouters DJ (2000) Absorption-reflection infrared spectroscopy studies of sol-gel prepared ferroelectric $\text{Pb}(\text{Zr}, \text{Ti})\text{O}_3$ thin films on Pt electrodes. *J Sol-Gel Sci Technol* 19:149–152
23. Tu YL, Calzada ML, Phillips NJ, Milne SJ (1996) Synthesis and electrical characterization of thin films of PT and PZT made from a diol-based sol-gel route. *J Am Ceram Soc* 79:441–448
24. Malic B, Cilensek J, Mandeljc M, Kosec M (2005) Crystallization study of the alkoxide-based $\text{Pb}(\text{Zr}_{0.30}\text{Ti}_{0.70})\text{O}_3$ thin-film precursor. *Acta Chim Slov* 52:259–263
25. Malic B, Arcon I, Kosec M, Kodre A (1997) A structural study of amorphous alkoxide-derived lead titanium complexes. *J Mater Res* 12:2602–2611
26. Calzada ML, Alguero M, Ricote J, Santos A, Pardo L (2007) Preliminary results on sol-gel processing of $\langle 100 \rangle$ oriented $\text{Pb}(\text{Mg}_{1/3}\text{Nb}_{2/3})\text{O}_3$ - PbTiO_3 thin films using diol-based solutions. *J Sol-Gel Sci Technol* 42:331–336
27. Malic B, Calzada ML, Cilensek J, Pardo L, Kosec M (2010) Thermal analysis study of diol-based precursors for chemical solution deposition of $0.7 \text{Pb}(\text{Mg}_{1/3}\text{Nb}_{2/3})\text{O}_3$ - 0.3PbTiO_3 thin films. *Adv Appl Ceram* 109(3):147–151. doi:[10.1179/174367509X1250262](https://doi.org/10.1179/174367509X1250262)
28. Lai F, Li JF (2007) Sol-gel processing of lead-free $(\text{Na},\text{K})\text{NbO}_3$ ferroelectric films. *J Sol-Gel Sci Technol* 42:287–292
29. Lu CJ, Kuang AX (1997) Preparation of potassium tantalate niobate through sol-gel processing. *J Mater Sci* 32:4421–4427
30. Remondiere F, Malic B, Kosec M, Mercurio JP (2007) Synthesis and crystallization pathway of $\text{Na}_{0.5}\text{Bi}_{0.5}\text{TiO}_3$ thin film obtained by a modified sol-gel route. *J Eur Ceram Soc* 27:4363–4366
31. Van Werde K, Vanhoyland G, Mondelaers D, Den Rul H, Van Bael MK, Mullens J, Van Poucke LC (2007) The aqueous solution-gel synthesis of perovskite $\text{Pb}(\text{Zr}_{1-x}\text{Ti}_x)\text{O}_3$ (PZT). *J Mater Sci* 42:624–632
32. Predoana L, Malic B, Zaharescu M (2009) LaCoO_3 formation from precursors obtained by water-based sol-gel method with citric acid. *J Therm Anal Calorim* 98:361–366
33. Sawada Y, Mizutani N (1989) Thermal analyses of thin films. *Netsu Sokutei* 16:185–194 (in Japanese)
34. Cerc Korosec R, Bukovec P (2006) Sol-gel prepared NiO thin films for electrochromic applications. *Acta Chim Slov* 53:136–147
35. Przyluski J, Plocharski J, Bujwan W (1981) Application of thin-film DTA to amorphous selenium layers. *J Therm Anal* 21:955–960
36. Gallagher PK, Gyorgy EM, Schrey F, Hellman F (1987) The use of thermomagnetometry to follow reactions of thin-films. *Thermochim Acta* 121:231–239

37. Hirashima H, Imai H, Miah MY, Bountseva IM, Beckman IN, Balek V (2004) Preparation of mesoporous titania gel films and their characterization. *J Non-Cryst Solids* 350:266–270
38. Hackwood S, Beni G, Gallagher PK (1981) Phase transitions of iridium oxide films. *Solid State Ion* 2:297–299
39. Wang MH, Tokiwa S, Nishide T, Kasahara Y, Seki S, Uchida T, Ohtsuka M, Kondo T, Sawada Y (2008) Thermally induced changes in amorphous indium-tin-oxide thin films. Gas evolution and crystallization. *J Therm Anal Calorim* 91:249–254
40. Hardy A, Van den Rul H, Van Bael MK, Mullens J (2009) Hyphenated thermal analysis for in situ study of $(\text{Bi,Nd})_4\text{Ti}_3\text{O}_{12}$ formation from aqueous solution-gel synthesis. *J Therm Anal Calorim* 96:955–960

Chapter 8

X-Ray Absorption Spectroscopy

Irene Schlipf, Matthias Bauer, and Helmut Bertagnolli

8.1 Basic Principles of EXAFS

In the following chapters, a basic introduction into the theory of EXAFS, the data analysis and experimental procedure will be given to allow a better understanding of the application of this method in CSD.

8.1.1 Short Introduction to EXAFS Theory

The attenuation of a monochromatic beam of X-rays of the energy E , which passes through a homogeneous sample of the thickness d , obeys the Lambert-Beer law [1]:

$$I(E) = I_0(E)\exp(-\mu(E) \cdot d) \quad (8.1)$$

where $I(E)$ and $I_0(E)$ are the incident and transmitted X-ray intensities, and $\mu(E)$ is the linear absorption coefficient.

The absorption coefficient μ decreases with increasing energy of the incident photon, until a critical wavelength is achieved, where the absorption coefficient increases abruptly. This steep rise of the absorption coefficient indicates the ejection of a core electron of an atom and is called absorption edge. Beyond the absorption edge the absorption coefficient decreases monotonically with increasing energy, until the next absorption edge is reached (Fig. 8.1, left).

I. Schlipf • H. Bertagnolli (✉)
Institut für Physikalische Chemie, Pfaffenwaldring 55, 70569 Stuttgart, Germany
e-mail: h.bertagnolli@ipc.uni-stuttgart.de

M. Bauer (✉)
Fachbereich Chemie, Erwin-Schrödinger-Str. 54, 67663 Kaiserslautern, Germany
e-mail: bauer@chemie.uni-kl.de

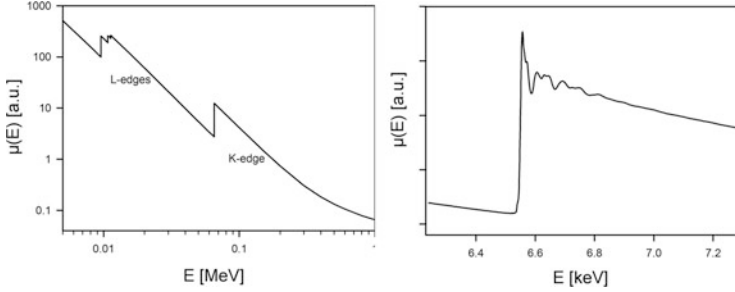


Fig. 8.1 *Left*: X-ray absorption coefficient $\mu(E)$ of a metallic hafnium sample in dependence of the energy of the incident radiation. The L- and K-edges indicate the shell, from which the electron is ejected. *Right*: X-ray absorption spectrum at the Mn K-edge of manganese oxide MnO_2 . The oscillatory structure after the edge jump is clearly visible [2]

This behaviour is only found for isolated atoms. For atoms in a molecule or in a condensed phase, the absorption coefficient above the absorption edge displays a fine structure (Fig. 8.1, right), termed EXAFS as acronym for Extended X-ray Absorption Fine Structure. This phenomenon was first detected in 1920 by Fricke [3] and Hertz [4], but the information contained therein was not fully recognized until the 1970s.

8.1.2 EXAFS Equation

The extended X-ray absorption fine structure refers to the oscillation of the X-ray absorption coefficient beyond the X-ray absorption edge. In order to obtain the EXAFS function

$$\chi(E) = \frac{\mu(E) - \mu_0(E)}{\mu_0(E)} \quad (8.2)$$

the atomic background $\mu_0(E)$ has to be removed from the experimental data and the resulting difference has to be normalized to $\mu_0(E)$. After the atomic background removal and normalization, the obtained energy dependent function $\chi(E)$ is converted into a k -dependent function $\chi(k)$ by application of the relation

$$k = \sqrt{\frac{2m}{\hbar^2} (E - E_0^{\text{exp}})} \quad (8.3)$$

E_0^{exp} is the “experimentally determined” threshold energy and the difference $(E - E_0^{\text{exp}})$ is the kinetic energy of the ejected electron, which can be expressed by the momentum p of the electron or by the change of the amount of the wave vector k of the electron

$$(E - E_0^{\text{exp}}) = \frac{p^2}{2m} = \frac{\hbar^2 k^2}{2m} \quad (8.4)$$

The theory of EXAFS is complicated, nevertheless a rather simple explanation, which follows the outline of Stern in [5], can be given. When an X-ray photon is completely absorbed, an electron is excited. The electron will be ejected, when the photon energy is larger than the binding energy of the electron. Its kinetic energy is given by the difference between the photon energy and the binding energy (see Eq. 8.3). For an isolated atom the photoelectron can be presented as an outgoing spherical wave. If the atom, whose electron is excited, is surrounded by other atoms, the outgoing spherical wave is scattered and the final state of the photoelectron is a superposition of the outgoing wave and the scattered wave. The resulting destructive and constructive interferences at the excited atom generate the oscillations in the absorption coefficient.

From this qualitative description it may be deduced that the oscillations in the absorption coefficient $\mu(k)$ depend on the position r_j of the neighbouring atoms, their numbers N_j , and the type of the backscattering atom j . The backscattering ability of the atom j is characterized by a backscattering amplitude $F_j(k)$ and a phase shift $\varphi_{ij}(k)$. Because not all the atoms are located at the same distance due to thermal vibrations or static disorder, a Debye-Waller-like factor σ_j is introduced. Finally, one has to bear in mind the lifetime of the state of the excited photoelectron. This lifetime effect is taken into account by introducing a mean free path term $\exp(-2r_j/\lambda)$, where the term λ is the mean free path length. The change of the effective potential of the absorbing atom of approximately one unit, felt by outer shell electrons, induces shake processes. As a result, one or more outer electrons can be *shaken up* to upper sub-shells or *shaken off* to continuum states. As these shake up/shake off processes reduce the amplitude of the EXAFS oscillations, the amplitude reduction factor S_0 is introduced. Putting all together we obtain the EXAFS formula [6]:

$$\chi(k) = \sum_j \frac{N_j}{kr_j^2} S_0 F_j(k) e^{-2\sigma_j^2 k^2} e^{-\frac{2r_j}{\lambda}} \cdot \sin [2kr_j + \varphi_{ij}(k)] \quad (8.5)$$

As it can be seen from this formula, the analysis of the EXAFS signal can provide information about the type (with amplitude $F_j(k)$), number of neighbouring atoms (which value of N_j) and their distances from the absorbing atom (which value of r_j). The values of the backscattering amplitudes and the phase shifts are tabulated or can be determined from reference substances with well defined coordination numbers and distances. The most commonly used method is to determine the structural parameters by fitting distances, coordination numbers and Debye-Waller-like factors and to vary the type of the backscattering atoms, when different atoms are likely.

The method is independent of the state of aggregation and is very sensitive up to a concentration of one atomic percentage, but synchrotron radiation is required. As the absorption spectrum is element specific, an individual element can be selected in samples that contain a complex chemical mixture of different elements, simply

by changing the X-ray wavelength. These features make EXAFS spectroscopy to a method of extremely wide applicability.

8.1.3 *Experimental Design*

EXAFS is based on the measurement of the energy dependence of the X-ray absorption coefficient or of a secondary process that is directly related to the absorption of X-rays. The experiment for a direct measurement of the absorption coefficient is described in Fig. 8.2 (top). In order to select a particular photon energy from the broad spectral range of synchrotron radiation Bragg diffraction from crystals is used. According to the Bragg equation a beam of the wavelength λ is reflected into the angle 2ϑ , when the following condition is valid [1]

$$n\lambda = 2d \sin(\vartheta) \quad (8.6)$$

where d is the interplanar spacing and n is an integer. The first crystal (Fig. 8.2, top) serves as primary monochromator and the second crystal suppresses higher harmonics like 2λ , 3λ etc. and unwanted reflection. The wavelength is changed by changing the angle 2ϑ . Two ionisation chambers, in front of and behind the sample, measure the incident and transmitted intensities. Additionally, the absorption spectrum of a reference system is recorded in order to calibrate the energy scale and to monitor any irregularities in course of the measurement.

In some cases it is advantageous to measure the absorption spectrum by recording processes that are proportional to the absorption cross section. As it can be seen from Fig. 8.2 (bottom), the absorption of an X-ray photon creates a core hole in an inner shell. Any process, by which the hole is annihilated, is proportional to the absorption of a photon, and can therefore be used as a measure of the absorption coefficient. The hole of the shell is filled by a radiative and non-radiative transition of an electron from an outer shell. The radiative transition produces X-ray fluorescence radiation with a wavelength that is characteristic of the energy difference between the two shells. Therefore it can be easily separated from the absorbed radiation, especially when the detector is perpendicularly orientated to the incident beam. The non-radiative transition corresponds to an internal photo-electric effect and generates Auger electrons or secondary electrons. The ratio of the both competitive processes increases with increasing atomic number of the excited atom. In a typical experiment for the measurement of fluorescence EXAFS (Fig. 8.2) the incident intensity is monitored by the front detector, whereas a detector, located perpendicular to the incident beam, measures the fluorescence radiation. EXAFS measurements in the fluorescence mode are applied, when the thickness of the sample is large or the concentration of the element of interest is very low.

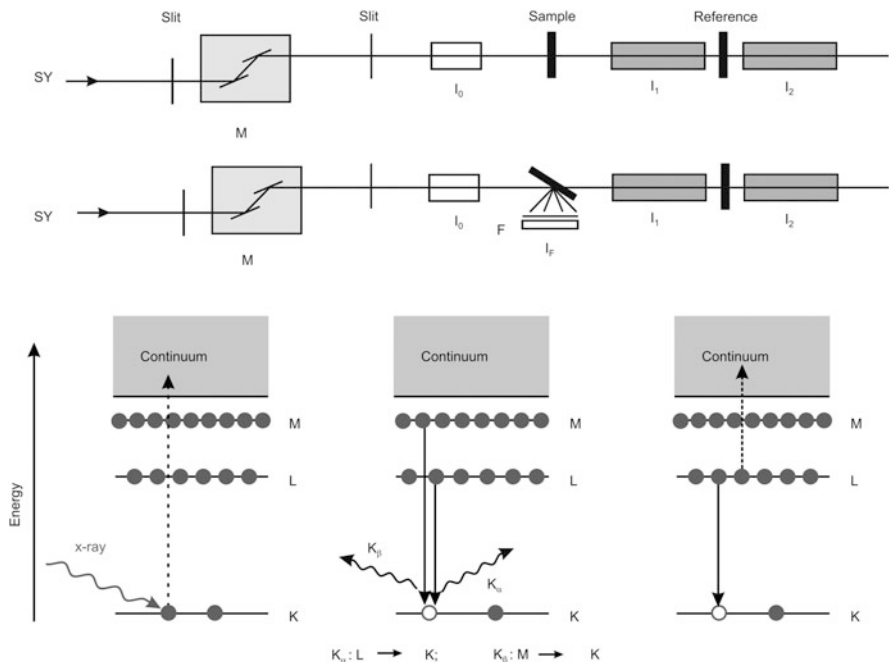


Fig. 8.2 *Top*: Experimental set-up for transmission (*top*) and fluorescence (second from *top*) mode measurements (SY = Synchrotron radiation, M = Monochromator, F = Fluorescence detector, I_0, I_1, I_2 = beam intensity recorded from the first, second and third ionization chamber, I_F = Intensity of the fluorescence radiation). *Bottom*: Schematic representation of the primary excitation process of X-ray absorption (*left*), the secondary processes fluorescence (*middle*), and Auger electron emission (*right*) [2]

8.1.4 Data Reduction and Evaluation

In general four steps of data reduction are necessary in order to extract the oscillatory part of the X-ray absorption coefficient. The individual steps are pre-edge background removal, atomic background removal and data normalization, conversion into k -space and Fourier transformation. As the results depend very sensitively on the correctness of each step, some details are given in the following section.

For EXAFS analysis only the region above the X-ray absorption edge step (shown as a solid line in Fig. 8.3, left) is of interest. In the first step the contribution of lower-energy edges and Compton-scattering to the absorption coefficient below the absorption edge has to be subtracted. Usually, a Victoreen-spline of the form

$$\mu_{\text{pre-edge}} = cE^{-3} - dE^{-4} \tag{8.7}$$

is used to approximate this pre-edge region. Also simple linear or quadratic polynomials can be used to model the shape of the pre-edge function. The fitted

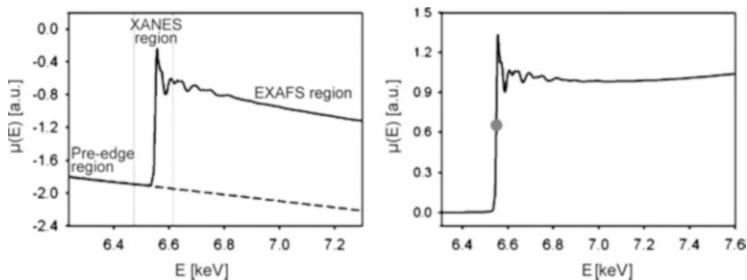


Fig. 8.3 *Left:* Experimental X-ray absorption coefficient $\mu(E)$ (solid line) and the adjusted pre-edge function (dashed line). *Right:* Isolated “elemental” absorption coefficient after subtraction of the pre-edge function. The threshold energy of the photoelectron is marked with a circle [2]

function (shown as dashed line in Fig. 8.3, left) is then extrapolated beyond the edge, and subtracted from the measured absorption coefficient. The result is the “elemental” absorption coefficient (Fig. 8.3, right) of the chemical element under investigation.

Then the resulting difference has to be normalized to $\mu_0(E)$ (cf. Eq. 8.2). It is crucial to know that in fact $\mu_0(E)$ is not the absorption coefficient of a physically isolated atom, but of an atom in its surrounding, where the effects of the neighbour atoms are “switched off”. Due to scattering of the ejected photoelectron from valence electrons, and also due to unspecific background factors (like spectrometer baseline, energy responses of detectors etc.), this atomic background contains low-frequency oscillations that cannot be measured independently or calculated from first principles. Its analytical form has to be determined by a least-square adjustment of a spline function to the experimental data. Whether the background is correctly determined, can be detected by inspecting the Fourier transform (cf. Sect. 8.1.5), since low frequency oscillations cause signals at unphysical low distances around 1 Å. In Fig. 8.4, the optimal spline to the absorption spectrum of Fig. 8.3 is shown as dashed line, in which an oscillation of low frequency is visible.

After the atomic background removal and normalization, the obtained energy dependent function $\chi(E)$ is converted into a k -dependent function $\chi(k)$ (cf. Eq. 8.3). The threshold energy is equivalent to the energy position of half of the edge jump marked with a circle in Fig. 8.3 (right) or the inflection of the absorption edge. Figure 8.5 shows $\chi(E)$ and $\chi(k)$, which differ only in the abscissa, the ordinate values are unaffected by the conversion procedure.

Although the EXAFS function $\chi(k)$ can be analyzed and is interpreted by fitting the function with theoretical models, usually a Fourier transformation of $\chi(k)$ into a pseudo radial distribution function is the last step of the data reduction. The Fourier transformed function can also be fitted with theoretical models or just be used as simple physical picture of the local structure around the absorber. The transformation is performed according to

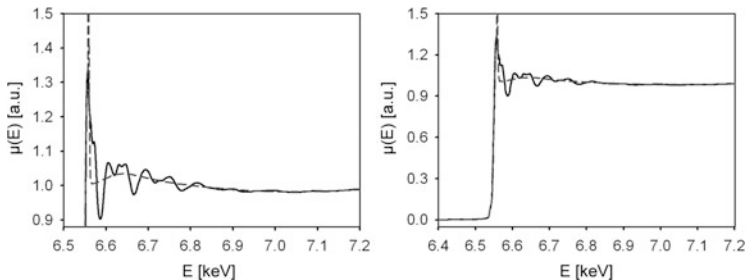


Fig. 8.4 *Left*: “Elemental” absorption coefficient (*solid line*) and the adjusted atomic background $\mu_0(E)$ (*dashed line*). *Right*: Enlarged view of the oscillatory part of the absorption coefficient. The low-frequency oscillation of the atomic background is clearly visible [2]

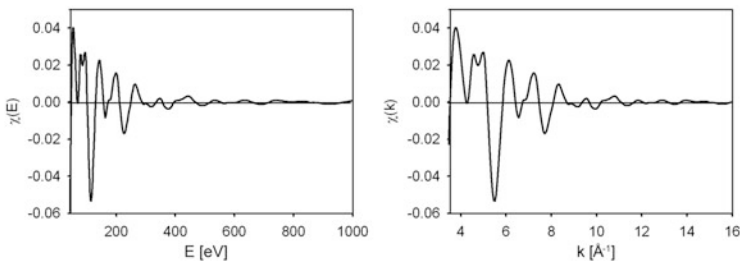


Fig. 8.5 *Left*: Isolated oscillatory part of the absorption coefficient in energy space after subtraction of the atomic background $\mu_0(E)$ and normalization. *Right*: The oscillatory function $\chi(k)$ after conversion into k -space [2]

$$\tilde{\chi}(r) = \frac{1}{\sqrt{2\pi}} \int_0^\infty k^n \chi(k) e^{2ikr} dk, \tag{8.8}$$

which yields a *complex* function that consists of an imaginary sine and a real cosine part, since even and odd functions contribute to the function $\chi(k)$. To obtain the most illustrative picture usually the modulus function of the Fourier transformation is used, which is defined as

$$|FT[\chi(k)]| \equiv Mod[\chi(r)] = \sqrt{\text{Re}^2[\tilde{\chi}(r)] + \text{Im}^2[\tilde{\chi}(r)]}. \tag{8.9}$$

In this representation the data can be physically interpreted in terms of a pseudo radial distribution function, which peaks at distances of the individual neighbouring shells. Figure 8.6 shows $\chi(k)$ and the corresponding modulus function of the Fourier transformed spectrum.

The experimental spectrum $\chi(k)$ can be weighted prior to Fourier transformation by different powers of k^n (with $n = 0, 1, 2, 3$) to account for the attenuation of the oscillations with increasing values of k and to obtain an approximately constant

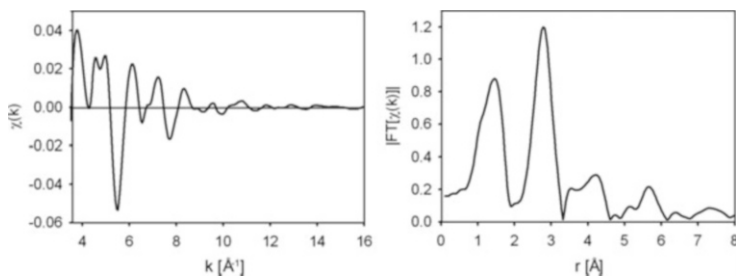


Fig. 8.6 Left: EXAFS function $\chi(k)$. Right: Fourier transformation of the $\chi(k)$ -function [2]

amplitude over the k -range, that is used for the Fourier transformation and the fit. Figure 8.7 shows the spectra of Fig. 8.6, but with k^3 -weighting. It is obvious that the signal of $\chi(k)$ at larger k -values is more pronounced with higher k -weighting, and the resolution is increased, as can be seen in the Fourier transformed function. But it should be kept in mind, that the noise of the EXAFS signal is also strengthened.

8.1.5 Data Analysis and Interpretation

To extract desired structural information from experimental spectra, it is necessary to fit the theoretical EXAFS formula to the experiment. While the number N_j of backscattering atoms in a shell of identical atoms, their average distance r_j to the X-ray absorbing atom and the degree of their disorder, reflected by the Debye-Waller-like factor σ_j^2 , are structural parameters, the backscattering amplitude $F_j(k)$ and the phase-shift $\varphi_{ij}(k)$ are element specific. Therefore, a rough estimation of the chemical constitution of the system under investigation is necessary to select the appropriate amplitudes and phase shifts.

In order to understand the data interpretation, theoretically calculated functions will be presented and discussed in the following section. Figure 8.8 shows the $k^3 \cdot \chi(k)$ -function with Mn as excited atom and oxygen (red line) and bromine (blue line) as backscatterer. The corresponding distances are 2 Å with identical Debye-Waller factors of 0.01 Å². The backscattering amplitude is the envelope of the $\chi(k)$ -function, which can be easily distinguished for O- and Br-backscatterers. In the Fourier transformation, the shape of the envelope itself is not visible. Only in case of bromine its larger maximum value is reflected in the more intense signal of this backscatterer.

If two types of backscatterers are present in one system, their signals add up. In Fig. 8.9 this case is shown for the combination of a Mn-O shell with one O-Atom at 2 Å and a Mn-Br shell with one Br-Atom at 3.5 Å.

The interference of both signals is clearly visible in the $\chi(k)$ -function and also the Fourier transformation shows two well-separated peaks. In such a case, the two shells can be analyzed separately by filtering each with a window function and

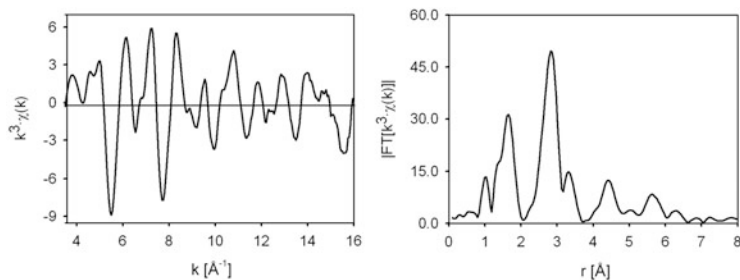


Fig. 8.7 *Left*: k^3 -weighted EXAFS function $k^3\chi(k)$. The amplitude of the function is approximately constant over the considered k -range. *Right*: Fourier transformation of the EXAFS functions $k^3\chi(k)$. Not only the intensity of the peaks is increased, but also the resolution is enhanced [2]

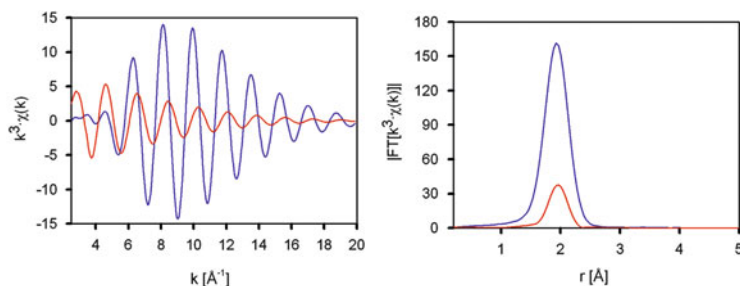


Fig. 8.8 *Left*: Theoretical EXAFS functions $k^3\chi(k)$ for Mn-O (red line) and Mn-Br (blue line) absorber-backscatterer pair. The following structural parameters were used: $r(\text{Mn-O/Br}) = 2 \text{ \AA}$, $N(\text{O/Br}) = 1$, $\sigma^2(\text{O/Br}) = 0.01 \text{ \AA}^2$. *Right*: The corresponding Fourier transforms [2]

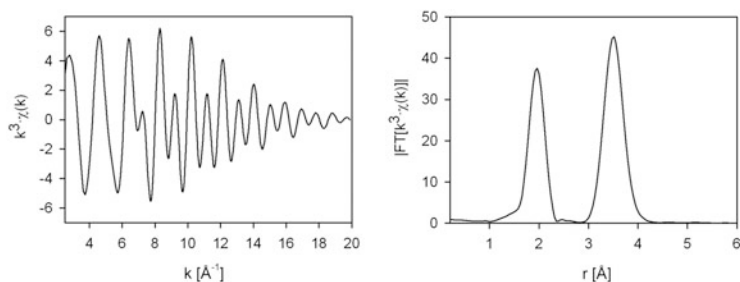


Fig. 8.9 *Left*: Theoretical EXAFS function $k^3\chi(k)$ for the superposed Mn-O and Mn-Br absorber-backscatterer pair. The following structural parameters were used: $r(\text{Mn-O}) = 2 \text{ \AA}$, $r(\text{Mn-Br}) = 3.5 \text{ \AA}$, $N(\text{O/Br}) = 1$, $\sigma^2(\text{O/Br}) = 0.01 \text{ \AA}^2$. *Right*: The corresponding Fourier transform [2]

backtransforming it into k -space, where the least-square fit is usually performed. On the other hand, if the shells are not well separated, such a procedure is not possible.

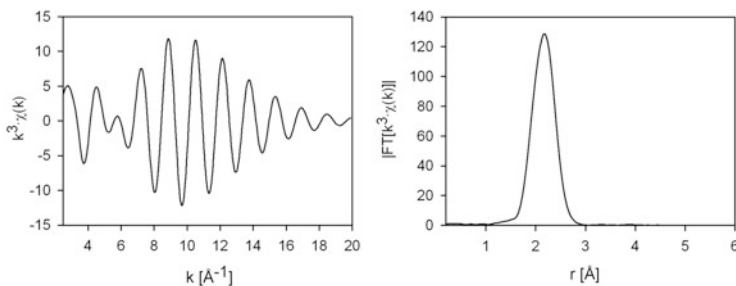


Fig. 8.10 *Left*: Theoretical EXAFS function $k^3\chi(k)$ for the superposed Mn-O and Mn-Br absorber-backscatterer pair. The following structural parameters were used: $r(\text{Mn-O}) = 2 \text{ \AA}$, $r(\text{Mn-Br}) = 2.2 \text{ \AA}$, $N(\text{O/Br}) = 1$, $\sigma^2(\text{O/Br}) = 0.01 \text{ \AA}^2$. Now the contribution of the Mn-Br pair is clearly dominating the signal. *Right*: The corresponding Fourier transform [2]

In Fig. 8.10 the same type of neighbour shells like in Fig. 8.9 are shown, but now with a Mn-Br distance of only 2.2 \AA instead of 3.5 \AA .

The signal of oxygen in the $\chi(k)$ -function is only significant up to 6 \AA^{-1} , and bromine is dominating the spectrum. Also, only one signal is found in the Fourier transform. In this case, two shells need to be fitted simultaneously, since no Fourier filtering is possible. It should be mentioned that elements of similar atomic number exhibit similar amplitude and phase functions. As a rule of thumb, two different types of backscatterers can be distinguished, if their atomic numbers differ by a factor of 2.

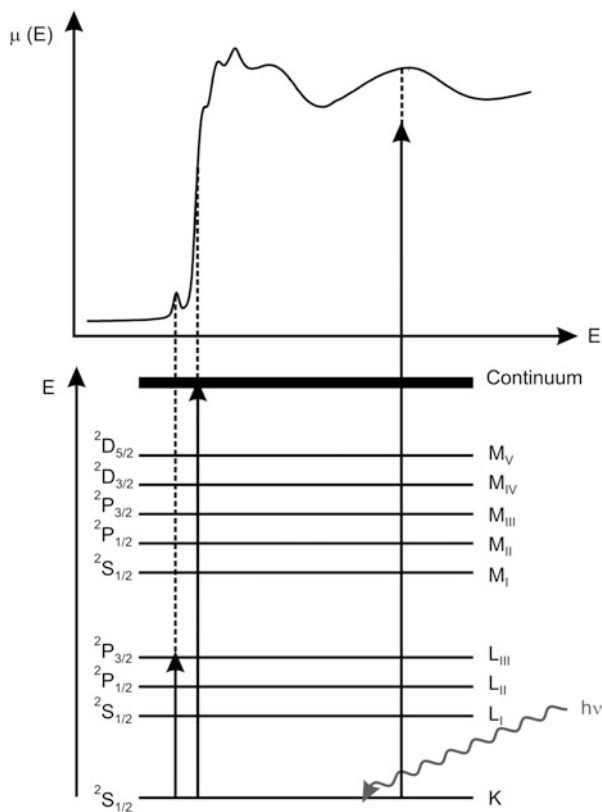
The theoretical calculation of backscattering amplitudes and phases as well as the photoelectron mean free path $\lambda(k)$ can be carried out with program packages, which are all based on an exact curved-wave formalism, for example EXCURV98 [7], FEFF [8] and GNXAS [9].

Although a certain amount of knowledge about the system is necessary to evaluate EXAFS data in a sound manner, and considerable accurateness is required for systems, in which more than one type of backscatterers exist, distances can be reliably determined with an accuracy up to 1 %, and coordination numbers depending on the distance of the shells within 10–20 % uncertainty. Moreover, these values can be significantly improved, if model compounds and high resolution measurements are applied.

In addition to the structural parameters contained in the EXAFS signal, information about the oxidation state and the coordination geometry around a central atom can be found in the so-called pre-edge and XANES (X-ray absorption near edge structure) region of an X-ray absorption spectrum. The pre-edge region consists of one or more signals at around 15–20 eV before the edge step. These pre-edge signals are caused by bound-to-bound state transitions of the excited photoelectron, whereas the edge-jump itself represents the photoionisation, where the photoelectron is excited to the continuum (Fig. 8.11).

In Fig. 8.12 different manganese compounds in the oxidation states +II, +III, +IV and +VII are shown. One can see that the edge step is shifted to higher energies

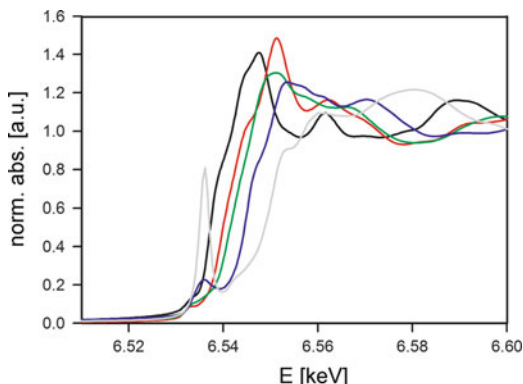
Fig. 8.11 Three different transitions within the XAS region of a K-edge spectrum: the pre-edge signal is caused by a bound-to-bound state transition $s \rightarrow p$, while the edge jump can be found at the energy of transition $s \rightarrow \text{continuum}$. After the edge jump, the photoelectron is excited to energy states above the continuum level



with increasing oxidation number, since the core electrons are more strongly attracted to the nucleus and their photoionization requires higher photon energies.

For unknown samples, the oxidation state can thus be determined by comparison with appropriate, structurally related references [10]. Additionally, the position of the prepeak can be used as a more structurally independent probe for the determination of the oxidation state. Its intensity reflects the geometry around the central atom. Since the prepeak of metal K-edge spectra is caused by $1s \rightarrow 3d$ transitions, which are dipole-forbidden, only $3d-4p$ hybridization enables parity allowed transitions. The extent of such a hybridization is strongly correlated to the coordination geometry. While for tetrahedral coordination sites the prepeak is usually of maximal intensity (which can be seen for KMnO_4 in Fig. 8.12, which contains MnO_4 tetrahedra), the existence of an inversion centre causes a reduction of the

Fig. 8.12 Influence of the oxidation state of the X-ray absorbing atom on the edge position for the example of different manganese oxides: Mn(II)O (*black line*), Mn(III)₂Mn(II)O₄ (*red line*), Mn(III)₂O₃ (*green line*), Mn(IV)O₂ (*blue line*), KMn(VII)O₄ (*grey line*) [2]



prepeak intensities. Therefore ideal octahedral coordination sites, such as found in MnO, show very low prepeak intensities. With current program codes, prepeaks can also be calculated for hypothetical structures and compared with experimental data, thus such calculations can be used to verify or complete structural models obtained by EXAFS analysis (*tt*-multiplett, FEFF8.02 [8]). Through the combination of EXAFS, prepeak and XANES analysis, an analytical method is available that can provide valuable information.

8.2 EXAFS Application on CSD Systems

At the present stage there are only a few CSD systems to which the XAS spectroscopy has been applied. But the authors are convinced that the use of the XAS spectroscopy for the investigations of thin films prepared by the CSD techniques will be increased in the future.

8.2.1 Binary Systems

Since the properties of materials obtained by the sol-gel processing depend very sensitively on the used alkoxide and solvent, it is essential to know the structure of the precursors in solution and their structural modifications in course of the sol-gel process. In 1994 Peter et al. [11] performed an EXAFS study of the structure and the molecular complexity of zirconium-*n*-propoxide and zirconium-*n*-butoxide, dissolved in their parent alcohol. The fitted spectra and the corresponding Fourier transforms of the EXAFS functions are shown in Fig. 8.13.

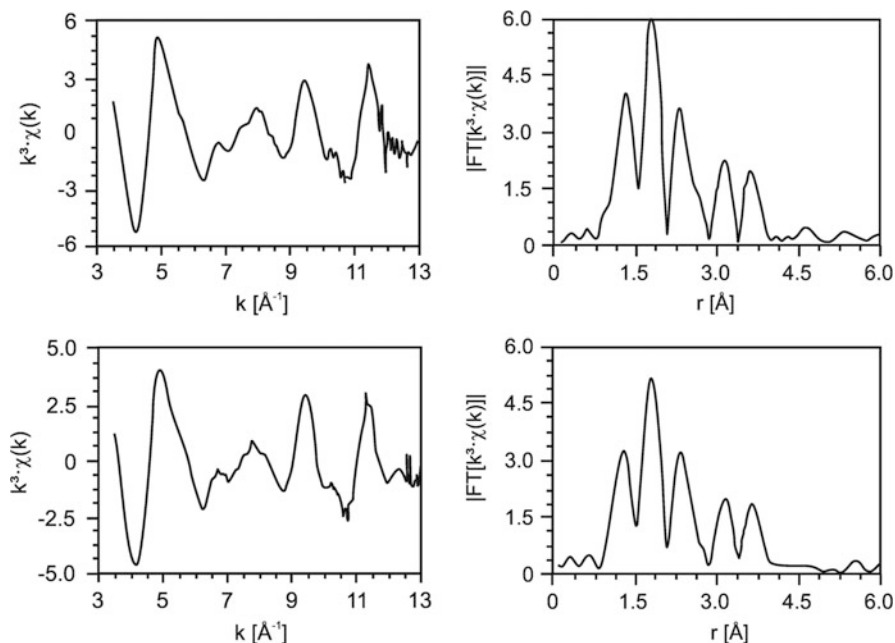


Fig. 8.13 *Left:* Experimental EXAFS functions $k^3 \cdot \chi(k)$ at the Zr K-edge for zirconium-*n*-propoxide (*top*) and zirconium-*n*-butoxide (*bottom*), both dissolved in its parent alcohol. *Right:* The corresponding Fourier transforms [11]

As it can be seen from Table 8.1, the local structure of both systems is nearly the same. In order to deduce structural information from the determined parameters, six structure models of zirconium complexes, given in Fig. 8.14, were examined [11]. Zr-O distances derived from the crystal structure of zirconium alkoxides increase in the sequence terminal or axial, bridging and coordinating O-atoms. This fact is used for the deduction of the structure models (Tables 8.2 and 8.3) and is later applied to the interpretation of the determined Zr-O distances in zirconium-*n*-propoxide and zirconium-*n*-butoxide.

The existence of a Zr-Zr distance at 3.52 Å for both the alkoxides propoxide and the butoxide, indicates oligomeric species in the parent alcoholic solution and rules out structure I. Among the oligomers, structure IV is most unlikely due to the high Zr-coordination number of the cyclic trimer. The most probable structures that agree best with the EXFAS data are dimer II or trimer III in accordance with molecular weight measurements of Bradley and Carter [12], who proposed a mixture of di- and trimeric species in case of the propoxide and predominantly dimers for the butoxide system.

In the deepening part of the study mainly the chemical modification of zirconium-*n*-propoxide and zirconium-*n*-butoxide was investigated [13]. The alkoxides were dissolved in their parent alcohols and in case of $\text{Zr}(\text{O}^i\text{Bu})_4$ modified with acetylacetonate (Hacac) in the molar ratios $\text{Zr}:\text{Hacac} = 1:1, 1:2, 1:3, 1:4$, whereas

Table 8.1 Parameters of the nearest coordination shells around zirconium atoms in zirconium-*n*-propoxide and zirconium-*n*-butoxide dissolved in their parent alcohol: type of neighbour atoms, average number *N*, distance *r*, and Debye-Waller factor σ

Zr neighb.	Zirconium- <i>n</i> -propoxide			Zirconium- <i>n</i> -butoxide		
	N	<i>r</i> [Å]	σ [Å]	N	<i>r</i> [Å]	σ [Å]
O	2.29	1.95	0.050	1.71	1.96	0.032
O	2.23	2.12	0.045	1.86	2.12	0.022
O	2.04	2.26	0.059	1.86	2.27	0.045
(C)	0.86	2.80	0.081	–	–	–
(C)	2.03	3.05	0.067	1.47	3.09	0.059
Zr	0.69	3.52	0.059	0.98	3.52	0.074
(C)	2.72	3.56	0.050	2.97	3.53	0.074

The distances for atoms in brackets are of low significance because of interfering effects [11]

Fig. 8.14 Proposed models for the structure of zirconium alkoxides with linear alkyl chains [11]

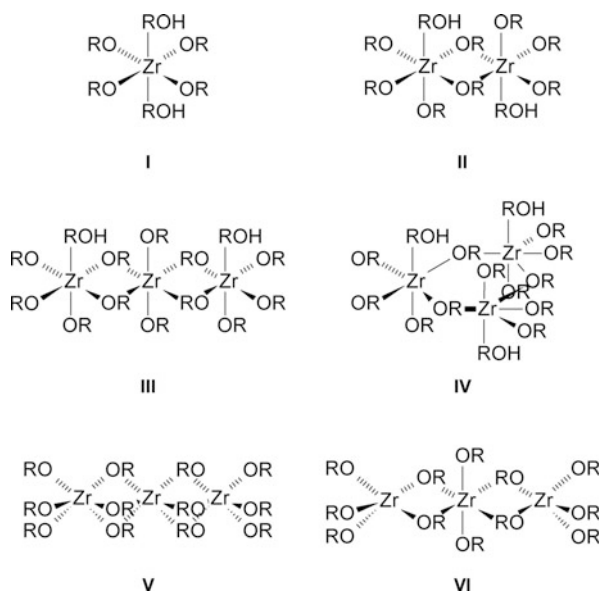


Table 8.2 Range of Zr-O distances in crystals and the type of coordination of oxygen ligands in zirconium complexes [11]

Coordination form of the ligand	Corresponding Zr-O distance ranges [Å]
Zr-O (RO-, terminal, axial, sixfold)	1.90–2.10
Zr-O (RO-, terminal, axial, eightfold)	1.90–2.10
Zr-O (RO-, bridging)	2.10–2.20
Zr-O (Hacac, mono- or bidentate)	2.10–2.20
Zr-O (HOAc, mono- or bidentate)	2.10–2.20
Zr-O (ROH, coordinated)	2.20–2.40

acetic acid (HOAc) was added to $Zr(O^iPr)_4$ in the molar ratio $Zr:HOAc = 1:2$. In comparison with the unmodified alkoxide spectra, already the shape of the XANES

Table 8.3 Zirconium and oxygen coordination numbers, characterizing the proposed structure models for zirconium alkoxides with linear alkyl chains shown in Fig. 8.14 [11]

		N(Zr)	N(O _{term})	N(O _{bridg.})	N(O _{ax})	N(O _{coord.})
I	Monomer	–	4.0	–	–	2.0
II	Dimer	1.0	2.0	2.0	1.0	1.0
III	Trimer	1.3	1.3	2.6	0.6	1.0
IV	Trimer, cyclic	2.0	2.0	2.0	1.0	1.0
V	Trimer, triple bridged	1.3	2.0	4.0	–	–

spectra of the Hacac-modified samples indicates a change of the coordination geometry of the Zr-atom from a sixfold to an eightfold coordination.

The evaluation of the EXAFS spectra reveals a degradation of the oligomeric species with increasing amount of the modifier Hacac. Moreover, the two peaks of the Fourier transform of pure $Zr(O^iBu)_4$ in the range between 1.5 and 3 Å, which are assigned to Zr-O distances, collapse to one symmetric peak. The authors conclude that the dimeric alkoxide degrades to the monomeric $Zr(acac)_4$ complex, according to the reaction scheme (Fig. 8.15), given below.

In contrast to the Hacac modification, the addition of acetic acid does not change the degree of oligomerisation, as it can be seen from the Zr-Zr coordination number (Table 8.4).

The absence of an oxygen shell shorter than 2.0 Å indicates that the terminal alkoxy groups are replaced by acetyl groups. The Zr-Zr distances of systems are shorter than in the pure alkoxide (–0.17 Å for $Zr(O^iPr)_4$ and –0.13 Å for $Zr(O^iBu)_4$), maybe due to alkoxide bridging ligands.

In order to check this explanation FTIR measurements were performed (Fig. 8.16).

According to these measurements an equilibrium between two species exists, which is shifted to the left side in case of modified zirconium-*n*-propoxide, whereas it is located on the right side in case of modified zirconium-*n*-butoxide. This equilibrium explains, why the first Zr-O shell of modified $Zr(O^iBu)_4$ splits into three sub-shells, whereas the signal collapses to one Zr-O distance for the modified $Zr(O^iPr)_4$ system.

The group of Sanchez [15] performed a similar study on the titanium alkoxides $Ti(O^iAm)_4$, $Ti(O^iPr)_4$, $Ti(OEt)_4$ and $Ti(O^iBu)_4$. The intensity of the most significant features of the titanium K-edge spectra, namely the prepeak, is too large for a symmetric sixfold environment and gives strong evidence for a fourfold coordination for $Ti(O^iPr)_4$ and for $Ti(O^iAm)_4$, whereas the similarity of the prepeaks of $Ti(OEt)_4$ and $Ti(O^iBu)_4$ spectra with the prepeak of the fivefold coordinated reference substance, namely titanyl phthalocyanine, indicates a square pyramidal environment.

The two titanium alkoxides with bulky ligands, $Ti(O^iAm)_4$ and $Ti(O^iPr)_4$, coordinate four oxygen atoms at a distance of 1.76 and 1.81 Å, respectively, and the absence of a titanium backscatterer indicates a monomeric species. In contrast, for the systems $Ti(OEt)_4$ and $Ti(O^iBu)_4$ the authors deduce an oligomeric species

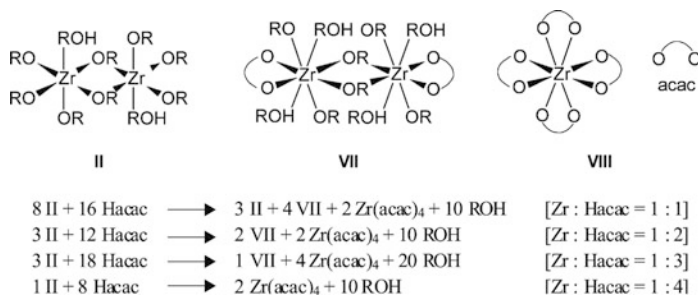


Fig. 8.15 Structure models of **II**, **VII** and Zr(acac)_4 (**VIII**) with $\text{OR} = n$ -propoxide or n -butoxide as well as the proposed reaction equations [13, 14]

Table 8.4 Parameters of the nearest coordination shells around zirconium atoms in zirconium- n -propoxide and zirconium- n -butoxide dissolved in their parent alcohols and modified with acetic acid in molar ratios ($\text{Zr}:\text{HOAc}$ of 1:2): type of neighbour atoms, average number N , distance r , and Debye-Waller factor σ [13]

Zr neighb.	Zirconium- n -propoxide + 2 mol HOAc			Zirconium- n -butoxide + 2 mol HOAc		
	N	r [Å]	σ [Å]	N	r [Å]	σ [Å]
O	–	–	–	0.72	1.94	0.074
O	5.66	2.16	0.092	4.05	2.19	0.071
O	–	–	–	0.70	2.36	0.022
Zr	0.79	3.35	0.071	0.76	3.39	0.067
C	3.17	3.56	0.067	2.16	3.61	0.063
C	1.25	4.23	0.050	1.30	4.24	0.045
C	2.63	4.61	0.067	2.20	4.68	0.077

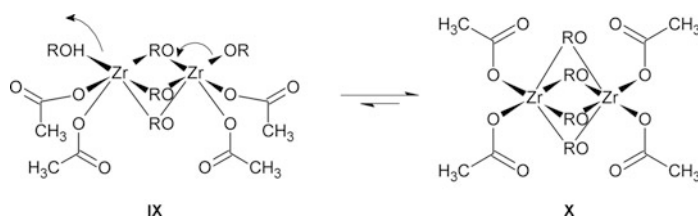


Fig. 8.16 Proposed equilibrium between the two complexes **IX** and **X** with $\text{OR} = n$ -propoxide or n -butoxide [13]

with trigonal bipyramidal oxygen environment made up of three shorter and two longer Ti-O distances and one Ti-Ti distance (Table 8.5).

The third precursor material that is commonly used in PT and PZ thin film syntheses via sol-gel route is lead(II)acetate trihydrate. Until 1997 the species, that is formed when lead(II)acetate is dissolved in alcohol, was unknown. Kolb et al. [16] performed EXAFS studies of lead(II)acetate trihydrate, in solid state as

Table 8.5 Parameters of the nearest coordination shells around titanium atoms in various titanium alkoxides: type of neighbour atoms, average number N , distance r , and Debye-Waller factor σ [13, 14]

	Ti neighb.	N	r [Å]	σ [Å]
Ti(O ⁱ Am) ₄	O	4.3	1.81	0.070
	O	3.0	1.76	0.077
	C	6.0	2.95	0.059
Ti(O ⁱ Pr) ₄	C	3.8	3.24	0.059
	O	3.4	1.82	0.072
	O	1.8	2.05	0.072
Ti(OEt) ₄	Ti	1.2	3.12	0.056
	O	4.2	1.83	0.087
	O	2.7	2.07	0.087
Ti(O ⁱ Bu) ₄	Ti	0.7	3.08	0.031

well as dissolved in methanol and 2-methoxyethanol. The results of this investigation are given in Table 8.6.

The EXAFS spectra exhibit a change in the structure of lead acetate, when it is dissolved in methanol. A simulation of the EXAFS spectra yield two oxygen backscatterers at the distance of 2.3 and 2.5 Å, one at 2.8 Å and two at 4.0 Å. Nearly the same results are obtained for the system Pb(OAc)₂·3H₂O, dissolved in 2-methoxyethanol. The discrepancies of the fitting results presented in the Table 8.6 are assigned to differences in the quality of the spectra.

By combination with IR-spectroscopy, the short Pb-O distance of 2.3 Å could be explained by hydrolyzation of lead(II)acetate. The formed Pb-OH group reacts with another Pb-OH group, forming a Pb-O-Pb bond. The Pb-O distances of 2.5 and 2.8 Å are assigned to an acetate ligand. This result is corroborated by the fact, that 1 h after dissolving lead(II)acetate trihydrate in methanol a white substance precipitates, which is identified by powder X-ray diffraction and chemical analysis as lead subacetate hydrate of the composition 3 Pb(OAc)₂ · PbO · H₂O. The same compound was also isolated after refluxing a solution of lead(II)acetate in 2-methoxyethanol. A possible structure of the formed species is shown in Fig. 8.17.

In 1997 Malic et al. published a study of the lead titanate system (PT) as a representative for perovskite-type ferroelectric materials [17]. Alkoxide-based PTs are generally produced by reaction of lead acetate with titanium metal alkoxides. Starting from lead(II)acetate and titanium- n -propoxide or titanium- n -butoxide dissolved in their parent alcohol, the authors performed EXAFS measurements at the Ti K-edge and the Pb L_{III}-edge in order to study how the different alkoxides influence the local environment around the metal centres in the products. Additionally to the heterometallic lead titanium precursors (denoted as PbTi-p and PbTi-b, respectively), the corresponding amorphous titanium gels, prepared by hydrolyzing Ti(O^{*i*}Pr)₄ in n -propanol or Ti(O^{*n*}Bu)₄ in n -butanol and dried at 150 °C (denoted as Ti-p and Ti-b, respectively), have also been measured as homometallic reference. The EXAFS functions at the Ti K-edge and the corresponding Fourier transforms are given in Fig. 8.18.

At a first glance there are no significant differences between the PT-intermediates, processed from titanium- n -propoxide (PbTi-p) or titanium- n -butoxide (PbTi-b). The signal-to-noise ratio in the Ti K-edge shown in the spectra

Table 8.6 Results of curve fitting procedures for lead(II)acetate trihydrate: type of neighbour atoms, and distance r

Pb(OOCCH ₃) ₂ ·3H ₂ O solid		Pb(OOCCH ₃) ₂ ·3H ₂ O dissolved in methanol		Pb(OOCCH ₃) ₂ ·3H ₂ O dissolved in methoxyethanol	
Pb neighb.	r [Å]	Pb neighb.	r [Å]	Pb neighb.	r [Å]
O	2.34 (1)	O	2.30 (1)	O	2.31 (1)
O	2.94 (1)	O	2.49 (1)	O	2.49 (1)
O	3.28 (2)	O	2.77 (1)	O	2.76 (1)
Pb	4.13 (2)	O	4.01 (2)	C	2.95 (2)
O	4.26 (2)			O	3.95 (2)
O	4.56 (2)			Pb	4.12 (2)

Uncertainty of the last digit is given in parentheses [16]

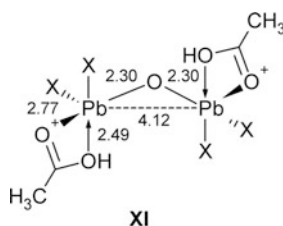


Fig. 8.17 Structure model of the lead compound, formed by dissolution of lead(II)acetate trihydrate, **XI**, in methanol and 2-methoxyethanol with X = H₂O, CH₃OH, CH₃OCH₂CH₂OH. The distances that were determined by EXAFS spectroscopy, are assigned and given in Å [16]

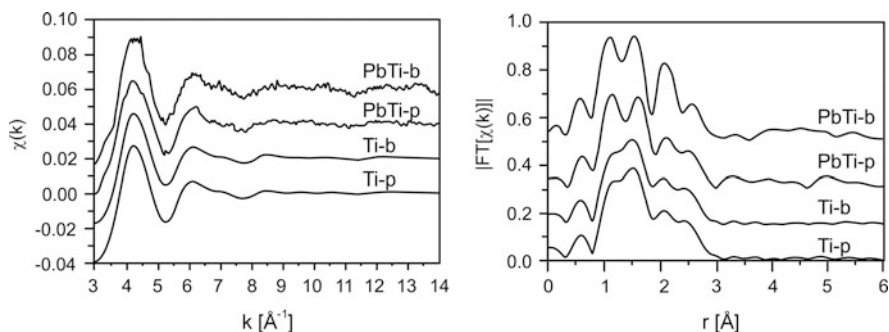


Fig. 8.18 *Left:* EXAFS functions $\chi(k)$ at the Ti K-edge of PbTi-p and PbTi-b and reference Ti-p and Ti-b. *Right:* The corresponding Fourier transforms [17]

of the lead titania samples PbTi-p and PbTi-b (Fig. 8.18, left) is inferior to that of the titania samples Ti-p and Ti-b, due to the presence of lead. According to the Ti K-edge EXAFS analysis given in Table 8.7, the local environment of the titanium centres is the same in pure (Ti-p, Ti-b) and mixed metal gels (PbTi-p, PbTi-b), independent of the alkoxide that is used.

Table 8.7 Parameters of the nearest coordination shells around titanium atoms in reference Ti-p and Ti-b and PbTi-p and PbTi-b: type of neighbour atoms, average number N , distance r , and Debye-Waller factor σ^2

Ti neighb.	N	r [Å]	σ^2 [Å ²]	N	r [Å]	σ^2 [Å ²]
	Ti-p			Ti-b		
O	2.0 (2)	1.79 (1)	0.007 (1)	2.0 (2)	1.79 (1)	0.010 (1)
O	3.0 (1)	1.94 (1)	0.007 (1)	3.0 (1)	1.93 (1)	0.008 (1)
Ti	1.3 (1)	2.89 (2)	0.005 (1)	1.3 (1)	2.89 (2)	0.006 (1)
Ti	0.7 (1)	3.05 (1)	0.005 (1)	0.7 (1)	3.05 (1)	0.006 (1)
	PbTi-p			PbTi-b		
O	2.0 (2)	1.79 (2)	0.003 (1)	2.0 (3)	1.77 (2)	0.004 (2)
O	3.0 (2)	1.96 (1)	0.004 (1)	3.0 (3)	1.94 (2)	0.003 (2)
Ti	1.3 (1)	2.87 (2)	0.004 (1)	1.2 (1)	2.91 (4)	0.002 (1)
Ti	0.7 (1)	3.04 (2)	0.004 (1)	0.8 (1)	3.08 (4)	0.002 (1)

Uncertainty of the last digit is given in parentheses [17]

The similarity of the Ti K-edge XANES spectra presented in Fig. 8.19 indicates the same local symmetry of titanium atoms in all samples. A very significant feature is the intensity of the prepeak. Typically, it has an intensity of more than half of the edge jump, if the central atom is coordinated by four neighbours, and less intensity, if a five- or sixfold coordination sphere surrounds the titanium centre [18].

The comparison of the investigated samples with the reference spectra of the octahedrally coordinated titanium dioxide modifications rutile and anatase gives a strong indication of more than four backscatterers, which is in good agreement with the EXAFS data of five oxygen backscatterers.

The question whether homo- or heterogeneous M-O-M bond exist, is more difficult to answer. EXAFS experiments at the titanium K-edge reveal homogeneous Ti-O-Ti-bonds, whereas titanium backscatterers are detected by fitting the Pb L_{III} EXAFS functions of the as-dried gels PbTi-p and PbTi-b, which is shown in Table 8.8.

Summarizing all the experimental data, the authors postulate a distorted hexagonal ring, formed by Ti-O-units, with terminal Ti-O-Pb linkages as structure of the gels dried at 150 °C. In another work, thermal treatment of such gels at 375 °C yielded a homonuclear network consisting of Ti-O-Ti linkages, where no Ti-O-Pb contributions could be detected [19].

Malic et al. [20] performed a similar study of zirconium-based ceramic materials of the perovskite type (PZs) and detected that, in contrast to titanium, the coordination sphere of the zirconium atoms is influenced by different alkoxide groups of the precursors, but the local environment of the lead atoms in the PZ system shows no difference within the analysed range. The Fourier transforms of Zr EXAFS data, shown in Fig. 8.20, exhibit for zirconium-*n*-propoxide or zirconium-*n*-butoxide based precursors an oxygen shell at a distance of 2.12–2.17 Å and a shell of Zr-atoms at 3.41 Å. In the zirconium-*n*-propoxide based precursor, however, an additional Zr-Zr contribution is detected at 2.91 Å, but not interpreted. The structural parameters are summarized in Table 8.9.

Fig. 8.19 Ti K-edge XANES spectra in PbTi-p and PbTi-b and reference Ti-p and Ti-b. Spectra of TiO₂ anatase and rutile are added for comparison [17]

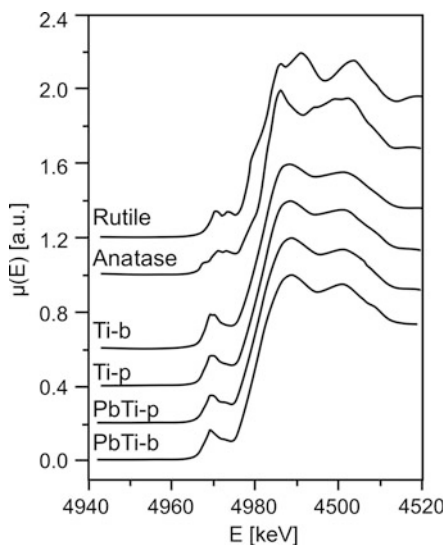
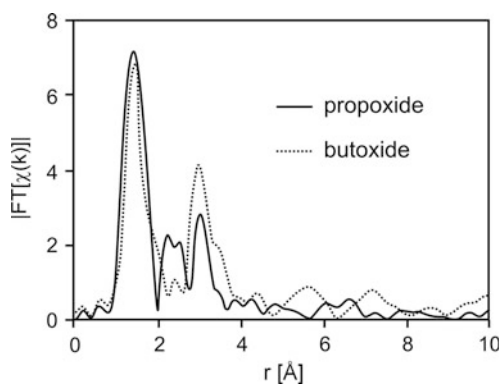


Table 8.8 Parameters of the nearest coordination shells around lead atoms in PbTi-p and PbTi-b: type of neighbour atoms, average number N , distance r , and Debye-Waller factor σ^2

Pb neighb.	PbTi-p			PbTi-b		
	N	r [Å]	σ^2 [Å ²]	N	r [Å]	σ^2 [Å ²]
O	1.0 (1)	2.23 (3)	0.008 (1)	1.0 (1)	2.26 (3)	0.015 (2)
O	1.0 (1)	2.38 (4)	0.008 (1)	1.0 (1)	2.30 (4)	0.015 (2)
Ti	1.0 (2)	3.37 (2)	0.020 (2)	1.0 (2)	3.40 (4)	0.024 (3)

Uncertainty of the last digit is given in parentheses [17]

Fig. 8.20 Fourier transforms of the Zr K-edge EXAFS spectra of n -propoxide (solid line) and n -butoxide (dotted line) based precursors, respectively [20]



The EXAFS evaluation and FTIR measurements of the hydrolysed and dried complexes, synthesized from lead acetate and zirconium- n -propoxide or zirconium- n -butoxide, reveal that the amorphous sol of the n -propoxide based precursor

Table 8.9 Results of curve fitting procedures for the zirconium-*n*-propoxide and the zirconium-*n*-butoxide based precursors: type of neighbour atoms, and distance r [20]

	Zirconium- <i>n</i> -propoxide, r [Å]	Zirconium- <i>n</i> -butoxide, r [Å]
Zr neighb.		
O	2.12	2.17
Zr	2.91	–
Zr	3.41	3.41
Pb neighb.		
O	2.39	2.39

contains a larger amount of acetate bridging groups than the *n*-butoxide one and the crystallisation paths of both systems depend on the alkoxides used for the syntheses.

In a subsequent study, the group of Malic also measured EXAFS spectra at the lead L_{III}- and zirconium K-edge of concentrated fresh solutions of transition metal alkoxides and lead acetate in 2-methoxyethanol [21]. In all sols, the local environment was the same and Pb-O-M (M = Zr or Ti) linkages were found (Tables 8.10 and 8.11). Two oxygen backscatterers are coordinated to the lead atom while the zirconium is surrounded by six oxygen atoms. Additionally PbO was tested as an alternative lead source. As it can be seen from the analysis of the EXAFS data in Table 8.10, the lead source does not seem to influence the environment of the lead atom itself, but it has a significant effect on the Zr-Zr correlation.

Comparing both sols, only about two third of Zr-O-Zr linkages found in Pb(OAc)₂ based precursors exist in sols based on PbO. In course of the drying process, the lead EXAFS spectra of both PZ and PT species show a weakly reduced lead-metal correlation.

The role of the starting material in the crystallization process of the lead titanate thin film intermediates, produced by the sol-gel process, and their parent sols, prepared with different lead sources, were also studied intensively [22]. Following the classical 2-methoxyethanol route, a titanium 2-methoxyethoxide solution was added to either lead oxide, lead acetate or *in-situ* prepared lead 2-methoxyethoxide. For the EXAFS analysis, the sols were dried at 150 °C and measured at the Ti K and Pb L_{III}-edge. In all three cases the titanium atoms are fivefold coordinated, but in different positions. In the lead oxide-based as-dried sol (lead-PT) and in the methoxy-PT three oxygen atoms at 1.92 Å and two at 2.09 Å surround the central titanium, while in acetate-PT all five backscatterers are located at 2.00 Å. The second coordination shell of the oxide-PT and the methoxy-PT consists of two titanium atoms at different distances. The titanium centre of acetate-PT is surrounded by 4–5 titanium atoms in the second shell with one to two backscatterers at 2.92 Å and three at 3.12 Å.

The data for oxide-PT and methoxy-PT are interpreted that three Ti-O-units form a distorted hexagonal ring with additionally three oxygen atoms attached terminally to each titanium atom, whereas in the acetate-PT the existence of trimers has to be excluded due to the five equidistant oxygen atoms in the first shell and more than two titanium atoms in the second shell.

Table 8.10 Parameters of the nearest coordination shells around lead and zirconium atoms in PZ precursors: type of neighbour atoms, average number N , and distance r

	Sol (Pb(OAc) ₂)		Sol (PbO)		As-dried (PbO)	
	N	r [Å]	N	r [Å]	N	r [Å]
Pb neighb.						
O	1.8 (1)	2.28 (1)	2.2 (4)	2.27 (2)	2.2 (2)	2.25 (1)
Zr	2.4 (4)	3.91 (2)	1.4 (2)	3.80 (2)	1.1 (2)	3.82 (2)
Zr	–	–	1.0 (2)	3.95 (2)	0.7 (1)	3.98 (2)
Zr neighb.						
O	2.0 (2)	2.09 (2)	1.8 (2)	2.09 (2)	2.0 (1)	2.08 (2)
O	2.0 (4)	2.16 (2)	2.0 (2)	2.16 (2)	2.0 (3)	2.16 (2)
O	2.1 (3)	2.26 (1)	1.9 (2)	2.27 (1)	2.0 (3)	2.26 (1)
Zr	5.4 (8)	3.48 (1)	3.4 (7)	3.50 (1)	3.7 (7)	3.45 (1)

Uncertainty of the last digit is given in parentheses [21]

Table 8.11 Parameters of the nearest coordination shells around lead atoms in PT precursors: type of neighbour atoms, average number N , and distance r

Pb neighb.	Sol (Pb(OAc) ₂)		Sol (PbO)		As-dried (PbO)	
	N	r [Å]	N	r [Å]	N	r [Å]
O	0.5 (3)	2.21 (2)	1.0 (3)	2.21 (2)	0.9 (3)	2.20 (2)
O	0.9 (3)	2.31 (2)	0.9 (2)	2.35 (2)	1.0 (3)	2.33 (2)
Ti	0.6 (2)	3.34 (1)	0.5 (2)	3.29 (1)	0.8 (3)	3.33 (1)
Ti	0.6 (2)	3.51 (1)	0.5 (2)	3.45 (1)	–	–

Uncertainty of the last digit is given in parentheses [21]

Analysis of the Pb L_{III} EXAFS spectra of the PT samples yields the same results for the nearest coordination shells around lead atoms in all three cases: Two oxygens, located around 2.29 and 2.38 Å, and one titanium at 3.43 Å. This outcome confirms the existence of heterometallic Pb-O-Ti links and proves the results of a former study, that the lead source does not influence the lead environment. Additional XRD measurements of the calcined thin films indicate a different annealing behaviour of acetate-PT in comparison with the oxide-PT and methoxy-PT [22].

8.2.2 Ternary Systems: Formation of Lead Zirconate-Lead Titanate-Solid Solutions

As already pointed out, an important factor that determines the kinetics of the hydrolysis and condensation reactions in preparing PZT materials via the sol-gel process is the degree of oligomerisation of the alkoxide precursor. In order to obtain information about the molecular structure of mixtures of titanium and zirconium precursors, and especially to answer the question, whether structural motifs of PZT are already preformed in solution, Reinöhl et al. [23] performed Zr K-edge experiments on a mixture of titanium- and zirconium-*n*-propoxide as well as titanium- and zirconium-*n*-butoxide dissolved in their parent alcohol. In all

investigated systems, the Zr-atom is surrounded by six O-atoms. A Zr-Zr distance found in the pure zirconium alkoxides indicates the existence of dimers or oligomers. In the mixture of zirconium- and titanium alkoxides, the hetero-association is preferred, since Zr-Ti distances could be detected.

In the year 1995, Sangupta et al. [19] presented an EXAFS study of sol-gel processed PZTs from butoxide educts and performed EXAFS measurement on hydrolyzed amorphous gels, as-dried precursor gels (heated to 375, 425 and 500 °C) at the Zr and Ti K-edge as well as the Pb L_{III}-edge. The EXAFS analysis of the sols reveals a sixfold coordination of oxygen atoms, forming a distorted octahedron, around the Ti-atoms and the Zr-atoms of the PZT gels. The second shell, both in case of Zr or Ti, shows a strong preference for homo-condensation, i.e. the formation of Ti-O-Ti and Zr-O-Zr bonds. Hetero-metallic Ti-O-Zr bonds contribute only to a small fraction. The Pb cations do not participate in the Ti and Zr polymeric M-O-M framework and occupy random positions in the amorphous gels. Its local structure is highly disordered.

In order to find out the reason for the heterogeneity in amorphous PZT based materials, Malic et al. [24] prepared solid solutions of Pb(Zr,Ti)O₃ with Zr/Ti ratios 75/25, 50/50 and 25/75, using standard synthesis routes. From the EXAFS spectra at the Ti and Zr K-edge and at the Pb L_{III}-edge, it follows that the environment of titanium and lead are nearly unaffected by the Zr/Ti ratio, but the surrounding of Zr is sensitive to the zirconium concentration. In systems with high concentration of Zr the local environment consists of distorted octahedra of oxygen with Zr-O-Zr bonds, whereas in systems with low zirconium concentration Zr-O-Ti bonds are observed and the distortion of the oxygen octahedra is reduced. The observed large number of Zr-O-Zr bonds of the investigated systems indicates a high degree of homo-condensation and therefore of heterogeneity. This strong tendency of zirconium to build up networks is, in contrast to titanium, caused by its more electro-positive character and its higher coordination number [25]. It might be speculated that this predominance of Zr-O-Zr links is the reason of the persistence of the transient pyrochlore-type phase in course of thermal treatment and homogeneity can be improved by lowering the Zr : Ti ratio.

In this paper, Malic et al. already suggested that a homogeneous contribution of the transition metals in the sols and in the final products might be generated by use of modifiers. Consequently, they studied zirconium alkoxides modified by acetic acid or acetylacetone and their sols [26]. The results are given in Table 8.12.

As it can be seen from this table, the number of oxygen in the first coordination sphere of Zr is smaller in the PZT-OAc sample than in PZT or PZT-Acac. Bearing in mind that a large amount of Zr-O-Zr links is typical of a final product with a high content of ZrO₂, the application of modifiers, especially acetic acid, turns out to be advantageous, since the coordination number of Zr is reduced to 0.8 in the PZT-OAc system in comparison to 2.9 in the unmodified sample and 2.5 in PZT-Acac. An additional indication of a homogeneous distribution of the metal components is the formation of the perovskite phase at lower temperatures and an improvement of the electric properties [27, 28]. Due to their lower electronegativity and a higher coordination number, zirconium alkoxides are more reactive than

Table 8.12 Parameters of the nearest coordination shells around zirconium atoms in PZT sols: type of neighbour atoms, average number N , and distance r

Zr neighb.	PZT		PZT-Acac		PZT-OAc	
	N	r [Å]	N	r [Å]	N	r [Å]
O	4.2 (5)	2.10 (4)	5.8 (9)	2.13 (4)	4.0 (4)	2.14 (1)
O	3.6 (5)	2.20 (4)	3.2 (9)	2.25 (4)	2.2 (4)	2.28 (2)
C	2.2 (4)	3.25 (1)	2.7 (9)	3.29 (4)	3.8 (7)	3.30 (4)
Zr	2.9 (5)	3.49 (2)	2.5 (9)	3.47 (2)	0.8 (4)	3.44 (4)
C	4.2 (7)	3.62 (5)	4.8 (9)	3.65 (5)	6.5 (8)	3.68 (4)

Uncertainty of the last digit is given in parentheses [26]

titanium alkoxides. Therefore a reduction of the reactivity of zirconium alkoxides by selective modification can improve the homogeneity of the PZT sol.

Ahlfänger et al. [29] performed EXAFS measurements at the Zr K-edge for lead zirconate titanate precursors of the composition $\text{PbZr}_{0.45}\text{Ti}_{0.55}$ in the sol and in the gel state. The analysis reveals for both, sol and gel, that the zirconium is surrounded by an oxygen sphere consisting of six backscatterers at 2.29 Å (sol) and 2.23 Å (gel). The shorter Zr-O distance in the gel indicates its higher density compared to the sol. In course of the fitting procedure, both titanium and zirconium have been tested as a second shell. Titanium showed the best agreement, therefore it is concluded that the Zr-O-Ti links already exist in the sol. Apparently the composition on a microscopic scale is uniform and structural motifs similar to structure of crystalline PZT are preformed in the sol and gel.

This conclusion was confirmed by a detailed study of the formation of PZT films. Sols for a $\text{PbZr}_{0.53}\text{Ti}_{0.47}\text{O}_3$ -PZT thin film were prepared by 2-methoxyethanol route from lead acetate, titanium-*n*-propoxide, and zirconium-*n*-propoxide, the latter either unmodified or modified with acetylacetone (Hacac) or acetic acid (HOAc) in the molar ratio 2:1 [30]. But one has to take into account that zirconium-*n*-propoxide reacts with the solvent 2-methoxyethanol by a transalcoholysis [31]. The structural changes of the Zr local environment were followed from the preparation of the sol to the amorphous film by Zr K-edge EXAFS spectroscopy. The PZT films were prepared from the sol on sapphire (001) by spin coating and pyrolysed at 350 °C (Table 8.13).

EXAFS analysis reveals that zirconium-*n*-propoxide, dissolved in 2-methoxyethanol, forms dimeric species. The modifying agent acetic acid does not change the degree of oligomerisation, whereas the addition of acetylacetone degraded the dimeric species to monomers. In the unmodified as well as acetylacetone-modified PZT sol, the Zr-Zr coordination number of 2.9 and 2.5, respectively (Table 8.12), is interpreted as an indication of phase segregation or clustering of Zr species.

The local environment changes significantly after pyrolysis of the sol at 350 °C. The local structure of the amorphous film, produced from the unmodified sol, is similar to that found in tetragonal zirconia. In PZT films with acetic acid as modifier, the local Zr environment remains nearly unaltered in comparison with the corresponding sol. In PZT films with acetylacetone as modifying agent, Zr-Zr

Table 8.13 Parameters of the nearest coordination shells around zirconium atoms in different Zr sols: type of neighbour atoms, average number N , distance r , and Debye-Waller factor σ^2

Zr neighb.	Zr/O			Zr/Acac			Zr/OAc		
	N	r [Å]	σ^2 [Å ²]	N	r [Å]	σ^2 [Å ²]	N	r [Å]	σ^2 [Å ²]
O	1.7 (5)	1.96 (1)	0.003 (1)	1.0 (3)	2.01 (1)	0.002 (1)	1.2 (4)	1.96 (1)	0.002 (1)
O	4.5 (5)	2.17 (1)	0.007 (1)	3.1 (5)	2.14 (1)	0.002 (1)	5.7 (4)	2.16 (1)	0.006 (1)
O	–	–	–	3.9 (5)	2.23 (1)	0.005 (1)	–	–	–
C	2.1 (6)	2.96 (2)	0.002 (1)	–	–	–	2.4 (6)	2.97 (2)	0.003 (1)
C	3.5 (8)	3.09 (3)	0.002 (1)	0.8 (5)	3.19 (3)	0.002 (1)	3.4 (8)	3.11 (3)	0.003 (1)
Zr	0.9 (2)	3.53 (2)	0.004 (1)	–	–	–	1.0 (2)	3.54 (2)	0.004 (1)
C	4.2 (9)	3.69 (5)	0.002 (1)	4.5 (9)	3.67 (1)	0.003 (1)	6.0 (2)	3.69 (5)	0.002 (1)

Uncertainty of the last digit is given in parentheses [30]

distances are found as in the sol, but the number of coordinated Zr-atoms is higher and the Zr-Zr distances are shorter than in the PZT film modified with acetic acid. In both cases, the films contain carbon. Apparently, the pyrolysis is not yet completed (Table 8.14).

The essential result is that after the modification with acetic acid, the original dimeric structure of the zirconium precursor is retained in the PZT sol and it should be noted that the type of coordination remains unchanged in the amorphous film. Hence, selective modification of zirconium- n -propoxide with acetic acid generates a more homogeneous distribution of zirconium atoms in the PZT sol and amorphous film than in both as-received and acetylaceton-modified zirconium propoxides and improves the functional response even after low annealing temperatures.

Figure 8.21 illustrates the modifying effect on the local environment of zirconium in course of the transition from sol to film.

8.2.3 Quaternary Systems: Lanthanum Doped Lead Zirconium Titanate

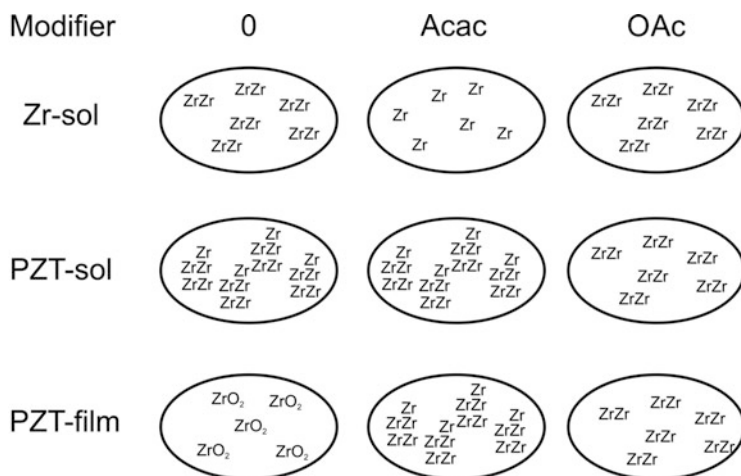
Materials of composition $\text{Pb}_{1-x/100}\text{La}_{x/100}(\text{Zr}_{y/100}\text{Ti}_{1-y/100})_{1-x/400}\text{O}_3$, denoted lanthanum doped lead zirconium titanate (PLZT) $x/y/(100-y)$, exhibit excellent optical, dielectric, electrooptical and piezoelectric properties. Greegor et al. [33, 34] investigated the structure of PLZT films and performed Ti K-edge XANES measurements for highly oriented PLZT films on differing substrates and bulk ceramic materials. The (100) orientation of the films was perpendicular to the substrate surface. For the XANES analysis, four systems were selected: highly oriented PLZT 28/0/100 film deposited on Al_2O_3 (1 $\bar{1}$ 02), highly oriented PLZT 28/0/100 film deposited on SiO_2 buffer layer over a Si(100), highly oriented PLZT 28/0/100 film deposited only on SiO_2 , and a commercial hot-pressed, optically polished PLZT 9/65/35 ceramic wafer. All the surface and bulk films are similar

Table 8.14 Parameters of the nearest coordination shells around zirconium atoms in PZT thin films: type of neighbour atoms, average number N , distance r , and Debye-Waller factor σ^2

Zr neighb.	PZT/O film ^a			PZT/Acac film			PZT/OAc film		
	N	r [Å]	σ^2 [Å ²]	N	r [Å]	σ^2 [Å ²]	N	r [Å]	σ^2 [Å ²]
O	4.0 (7)	2.14 (4)	0.003 (1)	5.0 (8)	2.14 (2)	0.004 (2)	4.4 (4)	2.14 (1)	0.001 (1)
O	2.8 (7)	2.67 (4)	0.002 (1)	2.0 (4)	2.29 (2)	0.004 (2)	2.0 (4)	2.32 (2)	0.007 (5)
C	–	–	–	–	–	–	1.5 (7)	2.83 (4)	0.001 (1)
C	–	–	–	3.3 (5)	3.36 (3)	0.003 (1)	2.0 (7)	3.32 (4)	0.001 (1)
Zr	3.0 (1)	3.43 (2)	0.006 (2)	1.6 (4)	3.39 (2)	0.004 (2)	1.0 (4)	3.44 (4)	0.004 (2)
C	–	–	–	7.0 (9)	3.71 (3)	0.003 (1)	6.5 (8)	3.68 (4)	0.001 (1)
O	6.0 (1)	4.19 (5)	0.007 (3)	–	–	–	–	–	–

Uncertainty of the last digit is given in parentheses [30]

^aThe data for PZT/O film are taken from [32]

**Fig. 8.21** Reproduced from [30], the scheme illustrates the changes in zirconium local environment in the process of PZT thin film formation depending on the choice of the modifier [30]

and all the PLZT 28/0/100 films resemble the spectra of PLZT 9/65/35, indicating cubic perovskite structures for these materials (Fig. 8.22).

The signature from approximately 0 to 12 eV in Figs. 8.18 and 8.19 are $1s \rightarrow 3d$ bound state transitions, which are dipole-forbidden, but very weakly quadrupole allowed [35]. For PLZT with perovskite structure, a cubic closest packing of oxygen, in which the oxygen anions occupy the octahedral interstices, is expected. If the centre of inversion at the octahedral Ti site is distorted, the dipole transition becomes allowed and its intensity increases with increasing distortion from centrosymmetry. As the $1s \rightarrow 3d$ transition of PLZT 9/65/35 is more intense than in the thin film PLZT 28/0/100, the higher intensity indicates a higher degree of disorder in the Ti-O octahedral cage in the bulk material and can be explained with a slightly distorted rhombohedral perovskite structure for PLZT 9/65/35 (Fig. 8.23).

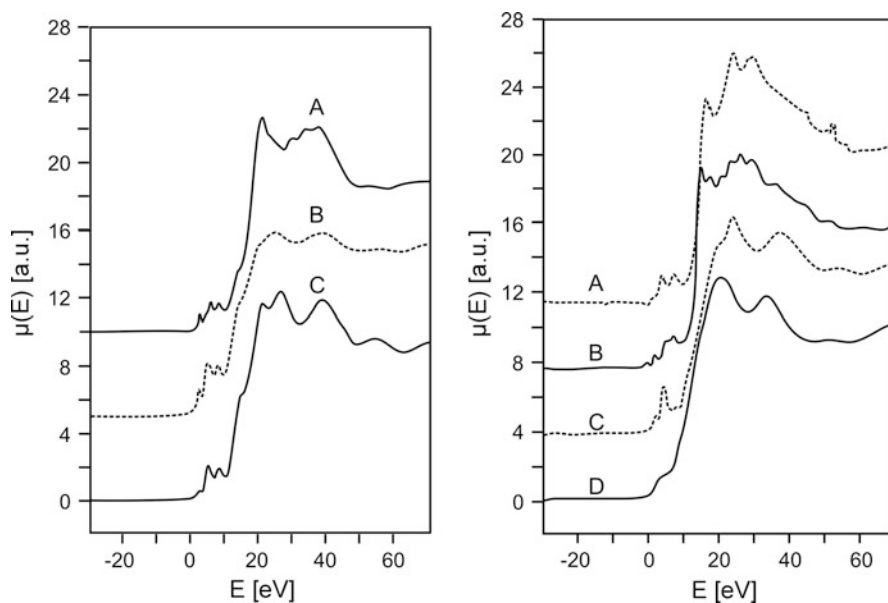


Fig. 8.22 *Left:* Ti K-edge XANES spectra of the TiO₂ modifications anatase (A), brookite (B) and rutile (C) *Right:* The comparison with Ti K-edge XANES of thin film PLZT 28/0/100 on SiO₂/Si (A), SrTiO₃ (B), BiTiO₃ (C) and Ti₂O₃ (D). The zero of energy is taken at the Ti metal K-edge (4,966 eV) [34]

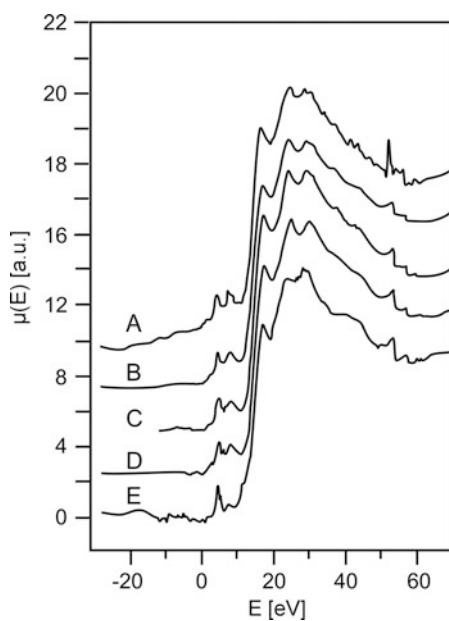


Fig. 8.23 Ti K-edge XANES spectra of PLZT materials (measured in fluorescent mode, except A which was measured in transmission mode): 28/0/100 PLZT on SiO₂ (A), 28/0/100 PLZT on SiO₂ (B), 28/0/100 PLZT on Al₂O₃ (C), 28/0/100 PLZT on SiO₂/Si (D), 9/65/35 commercial wafer (E) [34]

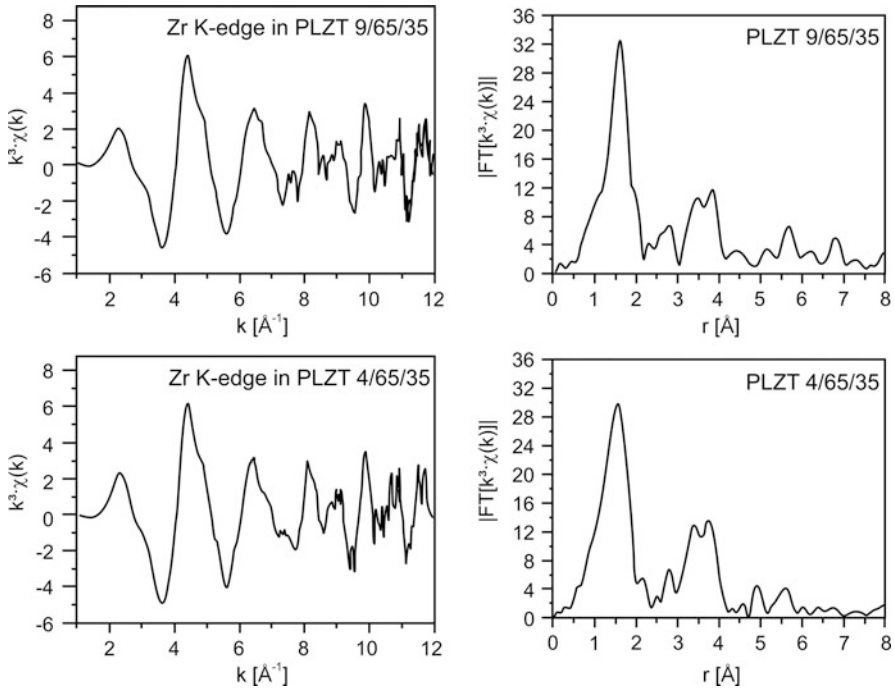


Fig. 8.24 *Left:* Experimental EXAFS functions $k^3 \cdot \chi(k)$ at the Zr K-edge of PLZT 9/65/35 powder (top) and PLZT 4/65/35 powder (bottom). *Right:* The corresponding Fourier transforms [36]

In a combined study by EXAFS, Raman and X-ray diffraction, Efimov et al. [36] analyzed PLZT materials prepared by a two-stage hot-pressing from chemical coprecipitation. The Zr K-edge EXAFS spectra of the two ferroelectric ceramics 4/65/38 and 9/65/35 are dominated by the low-frequency signal of the six oxygen atoms of the first coordination shell. The shoulders of the main oscillations, e.g. at 3.2 and 5 \AA^{-1} are contributions of outer shells. Observable dissimilarities between the two systems become obvious in the range of $7\text{--}9 \text{ \AA}^{-1}$ (Fig. 8.24).

The associated Fourier transforms (not phase corrected) can be separated into three regions. The first strong peak at $\sim 1.5 \text{ \AA}$ arises from the first coordination shell build up by six oxygen atoms. This part is followed by the region between 2.4 and 4.3 \AA . Four contributions generate this signal pattern: multiple scattering from the first coordination shell, Pb/La backscatterers from a second shell, the third shell consisting of the transition metal atoms Ti and Zr, and the 24 O-atoms from the farthest detectable fourth shell. But because of a high signal-to-noise ratio, a quantitative data evaluation for backscatterers above 2.4 \AA is rather difficult. Therefore it was not possible to reconstruct differences of the two samples, which presumably are beyond the first shell. The results from the evaluation of the first shell are identical. Altogether, the results of these EXAFS experiments support

perovskite-type compounds, in agreement with the results of the other applied methods.

8.3 Related Applications of EXAFS Techniques on Innovative Materials and Outlook

The development of high-temperature Superconductor (HTS—see Chap. 27) materials [37] in 1986 was a great scientific and technical innovation. The relatively high superconducting transition temperature offers a great application spectrum for these materials, and therefore the interest in both, a quick and cheap large-scale production and understanding of the phenomenon of superconductivity, has been and still is great. It was the EXAFS method that provided first fundamental and reliable insights into the phenomenon of superconductivity.

It turned out that a strong coupling between the lattice vibration and the electrons is prerequisite for the appearance of superconductivity. This strong electron-phonon interaction originates from changes in the local crystalline structure, but it is not in a scale that it can be probed by conventional diffraction methods. But also techniques like optical spectroscopy [38], pair distribution function analysis of neutron scattering [39] and Mössbauer spectroscopy [40] reached their limits. XAFS [41], however, is a method probing selectively the local environment and it has been applied to elucidate the phenomenon of superconductivity [42]. Additionally, in order to detect dynamical distortions, the characteristic time scale of the measurement must be shorter than the characteristic time scale in which the system changes. Since the time scale of a typical vibrational motion is roughly 10^{-13} s, while it takes only around 10^{-17} s for the photoelectron to travel the distance $2r_j$ between the absorbing and backscattering atom, EXAFS is well suited to study dynamical distortions [43].

Already in 1989 Conradson et al. [44, 45] reported on Copper K-edge XAS data that indicate an axial oxygen-centred lattice instability, which accompanies the superconducting transition in $\text{YBa}_2\text{Cu}_3\text{O}_7$ at 92 K. This conclusion was drawn by comparison of the EXAFS functions and their Fourier transforms at different temperatures given in Fig. 8.25, as the contribution of a Cu-O distance at 2.3 Å changes when the temperature is lowered from 105 K to the transition temperature $T_C = 92$ K [44].

The contribution of a Cu-O pair around $r = 2$ Å is relatively large at low temperature, but undetectably small relative to the contribution of the other neighbouring atoms above T_C . The increased contribution of this atom pair to the EXAFS function just below T_C is interpreted as an increase of the harmonic oscillation of the Cu-O mean square displacement, or a decrease of its amplitude. This increase, however, should lower the electron-phonon coupling and explains the superconductivity transition.

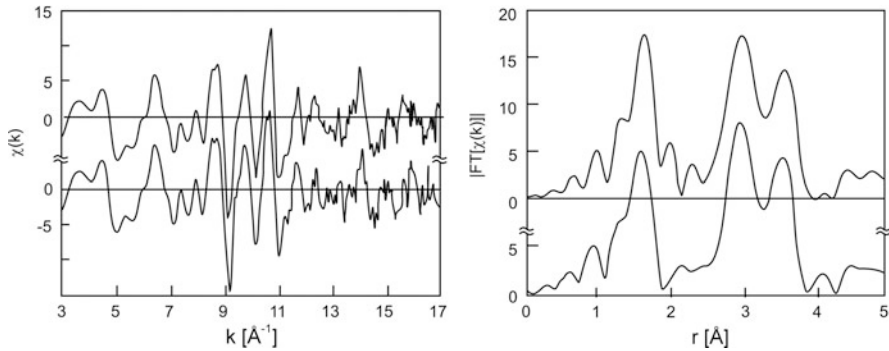


Fig. 8.25 *Left:* Experimental EXAFS functions $\chi(k)$ at the Cu K-edge at T_C (lower curve) and 105 K (upper curve). *Right:* The corresponding Fourier transforms. The feature near $r = 2.0$ Å in the 105 K spectrum is actually a side lobe, which is cancelled out when the contribution of Cu-O shell at 2.3 Å gets significant as the temperature is lowered [44]

In a later paper [45] the same group studied once more Yttrium barium copper oxide of the composition $\text{YBa}_2\text{Cu}_3\text{O}_7$ by XAS spectroscopy and they detected that the already mentioned axial oxygen-centred lattice instability accompanying the superconducting transition is of pseudo-(anti)ferroelectric type. The structure consistent with the EXAFS data is an anharmonic double well potential with two distinct Cu-O positions that are approximately equally populated above T_C . A similar experiment was performed on $\text{La}_2\text{CuO}_{4.1}$ by Mustre de Leon et al. [46]. The determined and isolated Cu-O XAFS signal could only be reproduced by a double parabolic potential. Apparently, a two-site radial distribution function seems to be an evident feature of the HTS materials.

As these examples on compact materials demonstrate, XAS spectroscopy is a very suitable method in order to investigate the temperature dependence of local potentials, as well as the extent of disorder and the microscopic mechanisms of physical phenomena and it should be noted that the studies of HTS materials by means of XAS spectroscopy, mainly done in the late 1990s, provided the breakthrough in theoretical interpretation of superconductivity. Simultaneously, the recognition of the EXAFS technique has been increased significantly.

Bearing in mind that the progress not only in the theoretical description, but also in the experimental technique is very rapid, one can expect that the XAFS spectroscopy will be applied in an increasing amount to the investigation of films and other low-dimensional systems. There is no doubt that it will provide a lot of very important and essential information in the future.

Acknowledgments Diana Zauser is acknowledged for her great help with reproducing the figures.

References

1. Wedler G (1997) Lehrbuch der Physikalischen Chemie, 4th edn. VCH, Weinheim
2. Bauer M, Bertagnolli H (2007) X-ray absorption spectroscopy – the method and its applications. *Bunsenmagazin* 9:216
3. Fricke H (1920) The K-characteristic absorption frequencies for the chemical elements magnesium to chromium. *Phys Rev* 16:202
4. Hertz G (1920) Über die Absorptionsgrenzen in der L-Serie. *Z Phys* 3:19–25
5. Stern EA (1988) In: Koningsberger DC, Prins R (eds) X-ray absorption. John Wiley, New York, p 26
6. Teo BK (1986) EXAFS: basic principles and data analysis. Springer, Berlin
7. Gurman SJ, Binsted N, Ross I (1984) A rapid, exact curved-wave theory for EXAFS calculations. *J Phys C: Solid State Phys* 17:143
8. Rehr JJ, Mustre de Leon J, Zabinsky SI, Albers RC (1991) Theoretical x-ray absorption fine structure standards. *J Am Chem Soc* 113:5135
9. Filipponi A, Di Cicco A, Tyson TA, Natoli CR (1991) “Ab-initio” modelling of x-ray absorption spectra. *Solid State Commun* 78:265
10. Farges F (2005) Ab initio and experimental pre-edge investigations of the Mn K-edge XANES in oxide-type materials. *Phys Rev B* 71:155103
11. Peter D, Ertel TS, Bertagnolli H (1994) EXAFS study of zirconium alkoxides as precursor in the sol-gel process: I. Structure investigation of the pure alkoxides. *J Sol-Gel Sci Technol* 3:91
12. Bradley DC, Carter DG (1961) Metal oxide alkoxide polymers part I. The hydrolysis of some primary alkoxides of zirconium. *Can J Chem* 39:1434
13. Peter D, Ertel TS, Bertagnolli H (1995) EXAFS study of zirconium alkoxides as precursors in the sol-gel process: II. The influence of the chemical modification. *J Sol-Gel Sci Technol* 5:5
14. Bauer M, Gastl C, Köppl C, Kickelbick G, Bertagnolli H (2006) EXAFS spectroscopy of the alkoxide precursor $Zr(O^iBu)_4$ and its modification in solution. *Monatsh Chem* 137:567
15. Babonneau F, Doeuff S, Leautic A, Sanchez C, Cartier C, Verdageur M (1988) XANES and EXAFS study of titanium alkoxides. *Inorg Chem* 27:3166
16. Kolb U, Gutwerk D, Beudert R, Bertagnolli H (1997) An IR- and EXAFS-study of the precursor system lead(II) acetate trihydrate, dissolved in methanol and 2-methoxyethanol. *J Non-Cryst Solids* 217:162
17. Malic B, Arcon I, Kosec M, Kodre A (1997) A structural study of amorphous alkoxide-derived lead titanium complexes. *J Mater Res* 12:2602
18. Farges F, Brown GE, Rehr JJ (1996) Coordination chemistry of Ti(IV) in silicate glasses and melts: I. XAFS study of titanium coordination in oxide model compounds. *Geochim Cosmochim Acta* 60:3023
19. Sengupta SS, Ma L, Adler DL, Payne DA (1995) Extended X-ray absorption fine structure determination of local structure in sol-gel-derived lead titanate, lead zirconate, and lead zirconate titanate. *J Mater Res Commun* 10:1345
20. Malic B, Arcon I, Kosec M, Kodre A (1997) A study of amorphous precursors for $PbZrO_3$ - $PbTiO_3$ based ceramic materials. *J Sol-Gel Sci Technol* 8:343
21. Arcon I, Malic B, Kosec M, Kodre A (1998) Study of the lead environment in liquid and as-dried precursor of PZ, PT and PZT thin films. *J Sol-Gel Sci Technol* 13:861
22. Malic B, Kosec M, Arcon I, Kodre A (2000) Influence of the structure of precursors on the crystallization of $PbTiO_3$ thin films. *J Sol-Gel Sci Technol* 19:153
23. Reinöhl U, Ertl TS, Hörner W, Weber A, Bertagnolli H (1998) EXAFS investigation of mixed zirconium-titanium alkoxides. *Ber Bunsenges Phys Chem* 102:144
24. Malic B, Arcon I, Kosec M, Kodre A (1999) EXAFS study of amorphous precursors for $Pb(Zr, Ti)O_3$ ceramics. *J Sol-Gel Sci Technol* 16:135
25. Livage J, Henry M, Sanchez C (1988) Sol-gel chemistry of transition metal oxides. *Prog Solid State Chem* 18:259

26. Malic B, Kosec M, Arcon I, Kodre A, Hiboux S, Murali P (2000) PZT thin films prepared from modified zirconium alkoxide. *Integr Ferroelectr* 30:81
27. Arcon I, Malic B, Kosec M, Kodre A (2003) EXAFS study of PZT sols. *Mater Res Bull* 38:1901
28. Malic B, Kosec M, Arcon I, Kodre A (2005) Homogeneity issues in chemical solution deposition of $\text{Pb}(\text{Zr}, \text{Ti})\text{O}_3$ thin films. *J Eur Ceram Soc* 25:2241
29. Ahlfänger R, Bertagnolli H, Ertel T, Kolb U, Naß R, Schmidt H (1991) 1st evidence of the preformation of an inorganic network in sol-gel processing of lead zirconate titanate, obtained by EXAFS spectroscopy. *Ber Bunsenges Phys Chem* 95:1286
30. Malic B, Arcon I, Kodre A, Kosec M (2006) Homogeneity of $\text{Pb}(\text{Zr}, \text{Ti})\text{O}_3$ thin films by chemical solution deposition: extended x-ray absorption fine structure spectroscopy study of zirconium local environment. *J Appl Phys* 100:51612
31. Brinker CJ, Scherer GW (1990) Sol-gel science: the physics and chemistry of sol-gel processing. Academic, San Diego
32. Arcon I, Malic B, Kosec M, Kodre A (2005) Zr k-edge EXAFS study of PZT thin film formation from sols. *Phys Scr T* 115:448
33. Gregor RB, Lytle FW, Wu AY (1992) Structural investigation of thin film PLZT using X-ray absorption spectroscopy. In: ISAF '92: proceedings of the eighth IEEE international symposium on applications of ferroelectrics, p 436
34. Gregor RB, Lytle FW, Wu AY (1994) Structural investigation of bulk and thin film PLZT using X-ray absorption spectroscopy. *Thin Solid Films* 240:22
35. Grunes LA (1983) Study of the K edges of 3d transition metals in pure and oxide form by x-ray-absorption spectroscopy. *Phys Rev B* 27:2111
36. Efimova VV, Efimova EA, Iakoubovskii K, Khasanov S, Kochubeyd DI, Kriventsov VV, Kuzmina A, Mavrinf BN, Sakharov M, Sikolenko V, Shmakov AN, Tiutiunnikova SI (2006) EXAFS, X-ray diffraction and Raman studies of $(\text{Pb}_{1-x}\text{La}_x)(\text{Zr}_{0.65}\text{Ti}_{0.35})\text{O}_3$ ($x = 0.04$ and 0.09) ceramics irradiated by high-current pulsed electron beam. *J Phys Chem Solids* 67:2007
37. Leggett AJ (2006) What DO we know about high T_c . *Nat Phys* 2:134
38. Friedl B, Thompson C, Cardona M (1990) Determination of the superconducting gap in $\text{RBa}_2\text{Cu}_3\text{O}_{7-\delta}$. *Phys Rev Lett* 65:915
39. Toby HB, Egami TE, Jorgenson JD, Subramanian MA (1990) Observation of a local structural change at T_c for $\text{Ti}_2\text{Ba}_2\text{CaCu}_2\text{O}_8$ by pulsed neutron diffraction. *Phys Rev Lett* 64:2414
40. Wu Y, Pradhan S, Boolchand P (1991) Motional broadening of ^{57}Fe Mössbauer-effect resonance in cuprate superconductors. *Phys Rev Lett* 67:3184
41. Mustre de Leon J, Conradson SD, Batistić I, Bishop AR (1990) Evidence for an axial oxygen-centered lattice fluctuation associated with the superconducting transition in $\text{YBa}_2\text{Cu}_3\text{O}_7$. *Phys Rev Lett* 65:1675
42. Mustre de Leon J, Conradson SD, Bishop AR, Raistrick ID (1993) The local structure of high-temperature superconductors. *Jpn J Appl Phys Suppl* 32–2:573
43. Stern EA, Yacoby Y (1996) Structural disorder in perovskite ferroelectric crystals as revealed by XAFS. *J Phys Chem Solid* 57:1449
44. Conradson SD, Raistrick ID (1989) The axial oxygen atom and superconductivity in $\text{YBa}_2\text{Cu}_3\text{O}_7$. *Science* 243:1340
45. Conradson SD, Raistrick ID, Bishop AR (1990) Axial oxygen-centered lattice instabilities and high-temperature superconductivity. *Science* 248:1394
46. Mustre de Leon J, Acosta-Alejandro M, Conradson SD, Bishop AR (2005) Local structure fluctuations as a signature of an inhomogeneous ground state in high- T_c superconductors. *J Synchrotron Rad* 12:193

Chapter 9

Infrared Spectroscopy

Maria Zaharescu and Oana Cătălina Mocioiu

9.1 Introduction

One of the most frequently-used methods for the investigation of precursors, solutions and the resulting films (and powders) of chemical solution deposition is infrared spectroscopy. Infrared refers to that part of the electromagnetic spectrum between the visible and microwave regions. Figure 9.1 presents the spectral domains of infrared, visible and microwave of the electromagnetic field. The infrared domain of electromagnetic radiation is between $12,820$ and 50 cm^{-1} (800 – $200,000\text{ nm}$), and it comprises three subdomains or divisions [1–6]:

- Near-infrared: approximately $12,820$ – $4,000\text{ cm}^{-1}$ (780 – $2,500\text{ nm}$), can excite overtone or harmonic vibrations
- Mid-infrared: approximately $4,000$ – 400 cm^{-1} ($2,500$ – $25,000\text{ nm}$), may be used to study the fundamental vibrations and associated rotational-vibrational structure
- Far-infrared: approximately 400 – 50 cm^{-1} ($25,000$ – $200,000\text{ nm}$), adjacent to the microwave region, has low energy and may be used for rotational spectroscopy

Infrared spectroscopy analyzes the interaction of infrared radiation with a sample (solid, liquid or gas). The samples can be organic compounds, inorganic compounds, or mixed organic–inorganic compounds. Infrared spectroscopy measures the frequencies at which the sample absorbs radiation, as well as the intensities of absorption [1–5]. Chemical functional groups are known to absorb radiation at specific frequencies. The intensity of the absorption is related to the concentration of a compound.

M. Zaharescu (✉) • O.C. Mocioiu
Institute of Physical Chemistry of the Romanian Academy, 202, Splaiul Independentei,
Bucharest 060021, Romania
e-mail: mzaharescu@icf.ro; mzaharescu2004@yahoo.com

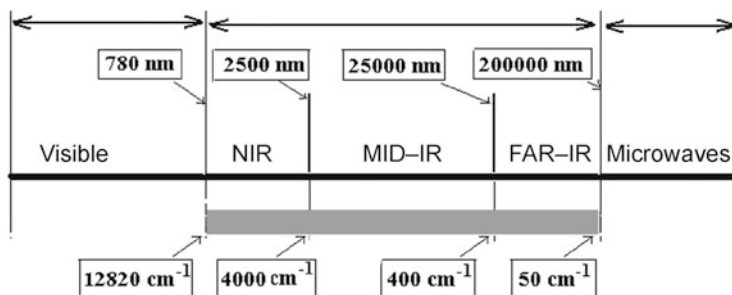


Fig. 9.1 Infrared domain in the electromagnetic field

The intensity and frequency of sample absorption are depicted in a two-dimensional plot called a spectrum [1–5]. These spectra are produced by the motion of molecules such as vibration and rotation.

The abscissa of a spectrum can be expressed in wavelength λ [nm] or in frequencies ν [cm^{-1}] [2] (see relation 9.1). The relation of conversion between wavelengths and wavenumbers is:

$$\nu[\text{cm}^{-1}] = 10000/\lambda[\mu\text{m}] = 10000000/\lambda[\text{nm}] \quad (9.1)$$

Usually, the Y-axis is expressed in transmittance [%]. Zero transmittance means 100 % absorption of light at that wavelength [1–5]. Band intensities can also be expressed as absorbance (A). Relation 9.2 between two such band intensities shows that the absorbance is the logarithm to the base 10 of the reciprocal of the transmittance:

$$A = \log_{10}(1/T) \quad (9.2)$$

In a spectrum with the Y-axis in transmittance, the bands point downwards, and in a spectrum with the Y-axis in absorbance, the bands point straight up (Fig. 9.2). The sum of absorption and transmittance must be 100, as shown in relation 9.3.

$$A + T = 100 \quad (9.3)$$

The spectra in the infrared domain are used to obtain information about the structure of a compound. In some cases, the purity of a compound can also be detected. Infrared spectroscopy works almost exclusively on samples with covalent bonds and is based on the fact that molecules have specific frequencies at which they rotate or vibrate depending on discrete energy levels (vibrational modes). These frequencies are determined by the structure of molecules, the mass of the atoms, and the changes in the dipole.

A diatomic molecule has only one bond, and it can be approximated by a harmonic oscillator with two atoms in the margins within the plane. When the atoms move from one plane to another, the stretching is symmetric; when they

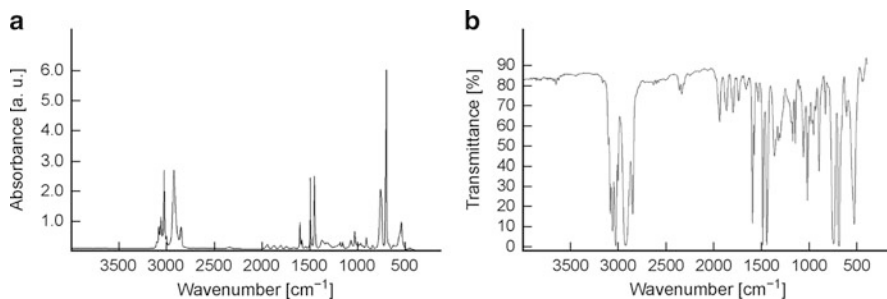


Fig. 9.2 FTIR spectra of polystyrene recorded on Nicolet 6700 FTIR: (a) absorbance and (b) transmittance (*Note*: polystyrene is the etalon sample for IR spectroscopy)

move on opposite sides, the stretching is asymmetric; and when they move out of plane, the motion is termed rocking. If diatomic molecules are symmetric molecules, they have no active vibrations in the infrared spectrum [2].

The resonant frequencies appear to depend on the neighboring equilibrium molecular geometry at electronic ground-state potential energy, which can be correlated to the strength of the bond and the mass of the atoms. This means a bond type presents a particular vibration frequency.

Complex molecules have many bonds, and vibrations can be conjugated, leading to infrared absorptions at characteristic frequencies that may be related to chemical groups.

For example, the atoms in a CH_2 group, commonly found in organic compounds, can vibrate in six different ways: symmetric and asymmetric stretching (ν_s and ν_{as}), scissoring (δ), rocking (ρ), wagging (w), and twisting (see Fig. 9.3) [2, 4].

The advantages of infrared spectroscopy are:

- It is a non-destructive technique. The spectra can be recorded directly on the samples.
- The method has a high selectivity. Substances absorb in a wavelength depending on the shape of the molecular potential energy surfaces, the mass of the atoms, and the dipole.
- Infrared spectroscopy is a good analytical tool for identifying compounds
- It allows the identification of amorphous compounds

The disadvantages of the method are:

- The vibrations of the symmetric molecules are inactive in infrared
- The method does not verify most of the ionic bonds
- Sometimes the characteristic bands overlap and their identification can be difficult if not impossible. There are solutions, such as deconvolution of bands, but only if there is sufficient information about the number and exact position of independent bands. If exact data are not known, complementary methods of analysis are needed.

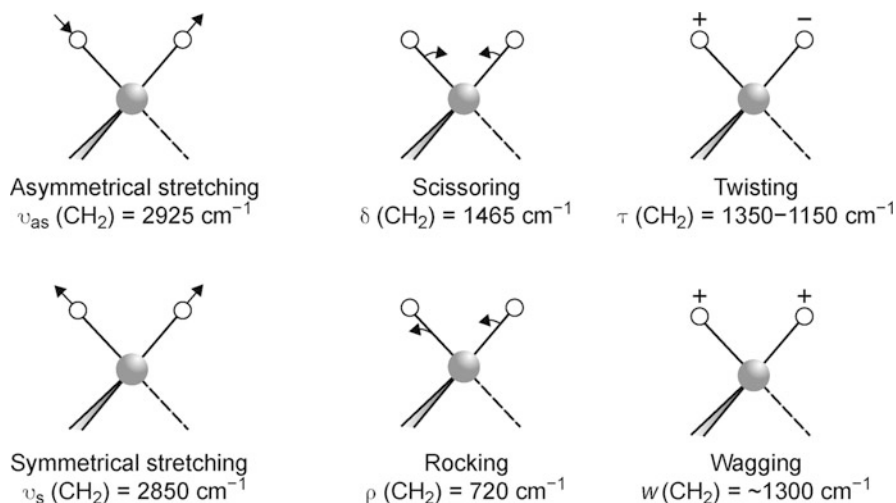


Fig. 9.3 Vibrational modes of CH_2 groups in the infrared region [2, 4]

- Infrared spectroscopy is a qualitative method. Semi-quantitative analysis can be done by using an attenuated total reflectance (ATR) device (see next section). In some cases, quantitative data can be obtained based on the calibration curve.

9.2 Principle of Apparatus

Infrared spectra can be recorded using the transmission or attenuated total reflectance method. Each of these methods requires specific devices. Transmission is a more commonly used technique and has already been described before. Infrared light passes through the sample and the spectrum is recorded. The method can be applied for solid, liquid and gaseous samples. IR spectra are acquired using special instruments known as spectrometers. Spectrometers have two models: dispersive and FTIR.

The dispersive spectrometer has double fascicules and it uses the network or prism. It uses a monochromatic beam, which changes in wavelength over time. Figure 9.4 shows the schematic of a dispersive spectrometer. Source 1 emits the infrared fascicules that pass through reference 2 and sample 3. The fascicules are reflected by mirrors 4, and then pass through slots 5 and network 6 before arriving at detector 7.

The modern type of spectrometer is a single-beam spectrometer known as FT-IR and it uses a modulator (interferometer). The energy that passes through the sample is examined using a Fourier transform instrument. Figure 9.5 shows the schematic of a FTIR spectrometer.

Fourier transform infrared (FTIR) spectroscopy is a measurement technique for collecting infrared spectra. Instead of recording the amount of energy absorbed when the frequency of the infrared light is varied, the IR light is guided through an

Fig. 9.4 Schematic of the dispersive spectrometer:
1—source, 2—reference substance, 3—sample, 4—mirror, 5—slots, 6—network, 7—detector [2, 4]

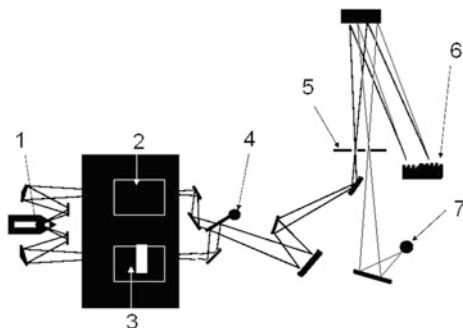
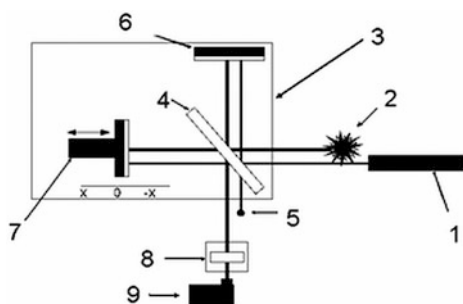


Fig. 9.5 Schematic of the FTIR spectrometer:
1—laser, 2—source, 3—modulator, 4—beam splitter, 5—diode laser, 6, 7—mirrors, 8—sample, 9—detector [Nicolet 6700]



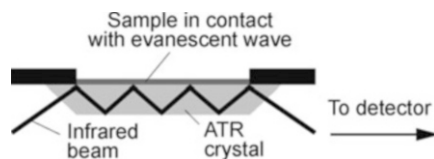
interferometer. After passing through the sample, the measured signal produces the interferogram. When a Fourier transformation is performed on this signal data, a spectrum that is identical to that from conventional (dispersive) infrared spectroscopy is produced.

The advantages of the FTIR technique are the following:

- The measurement of a single spectrum is faster using the FTIR technique because the information at all frequencies is collected simultaneously.
- The errors are spread throughout the spectrum because all regions of the spectrum are observed simultaneously.
- FTIR gives accurate frequencies and this make subtraction between spectra possible.

Attenuated total reflectance (ATR) uses the property of total internal reflection resulting in an evanescent wave. ATR uses multiple reflections of light through a crystal (diamond, Ge, Sapphire, ZnSe, Si, KRS-5) (see Fig. 9.6). A beam of infrared light is passed through the ATR crystal in such way that is reflected a few times off the internal surface which is in contact with the sample. This reflection forms the evanescent wave which extends into the sample. The penetration depth into the sample is typically between 0.5 and 4 μm , with the exact value being determined by the wavelength of light, the angle of incidence, and the indices of refraction for the ATR crystal and the medium being probed [1–4]. This method is applicable to solid and liquid samples.

Fig. 9.6 ATR principle. The infrared beam is reflected by a crystal with a high reflection index. [Perkin Elmer—Technical Info]



Well-known substances can be identified automatically in the instruments' library of spectra.

9.3 Sample Preparation

Gaseous samples require a sample cell with a long path length (typically 5–10 cm) because gases show relatively weak absorbance [1–4]. Liquid samples can be added between two plates of a high-purity salt (sodium chloride, potassium bromide or calcium fluoride) [1–4]. The plates are transparent to the infrared light and will not introduce any lines into the spectra. Some salt plates (potassium bromide, sodium chloride) are highly soluble in water, so the sample and washing reagents must be anhydrous [1–4].

Solid samples are usually prepared by homogenizing a quantity of sample (approx. 1 mg), finely ground, with 200 mg of pure salt (usually potassium bromide or cesium chloride) [1–4]. This powder mixture is then pressed in a mechanical press under vacuum to form a translucent pellet. Another method is to crush the sample with a mulling agent (Nujol) in an agate mortar. A thin film of the mull is then applied onto salt plates (KRS-5) [1–4].

It is important to note that spectra obtained from different sample preparation methods will appear slightly different from each other due to differences in the physical states of the samples.

9.4 Infrared Spectra of CSD Precursors

In the chemical solution deposition, the starting materials are organic or inorganic compounds. Infrared spectra are useful for identifying chemical groups in precursors and for determining the purity of these precursors. Table 9.1 lists the most common inorganic group frequencies, while Table 9.2 shows the most common organic groups and the characteristic frequencies.

Table 9.1 Example of group frequencies for inorganic ions [5, 6]

Inorganic group	Group frequencies in the spectra (cm^{-1})	Intensity	Assignment	Compounds
CO_3^{2-}	1,410–1,490	i	ν_{as} (CO)	Carbonates
	850–880	m–w	ν_{s} (CO)	
NO_3^-	1,350–1,380	i	ν_{as} (NO)	Nitrates
	810–840	m–w	ν_{s} (NO)	
SO_4^{2-}	1,080–1,130	i	ν_{as} (SO)	Sulfates
	610–680	m–w	ν_{s} (SO)	
PO_4^{3-}	1,000–1,100	m	ν_{s} (PO)	Phosphates
NH_4^+	3,030–3,300	i	ν_{as} (NH)	Ammonium salts
	1,390–1,430	m–w	ν_{s} (NH)	

i intensive, *m* medium, *w* weak

Table 9.2 Examples of group frequencies in infrared for organics [2, 4, 6]

Organic group	Group frequencies in the spectra (cm^{-1})	Intensity	Assignment	Compounds
-CH ₃	2,962	i	ν_{as} (CH ₃)	Alkane, alkenes, alkynes, primary alcohols, acetates, etc.
	2,872	m	ν_{s} (CH ₃)	
	1,460	m	δ_{as} (CH ₃)	
	1,380	m	δ_{s} (CH ₃)	
	1,045	m	ρ (CH ₃)	
-CH ₂ -	2,925	i	ν_{as} (CH ₂)	
	2,853	m	ν_{s} (CH ₂)	
	1,430–1,470	m	δ_{as} (CH ₂)	
	1,300	w	w_{s} (CH ₂)	
	720–780	w	ρ (CH ₂)	
>CH-	2,890	m	ν_{s} (CH)	chain vibrations
	1,170	m		
>C<	1,255, 1,210	w		
-CH=O	2,800–2,900	m	ν_{as} (CH)	Aldehyde
	2,680–2,780	m	ν_{s} (CH)	
	1,675–1,725	i	ν (C=O)	
>C=O	1,715–1,720	i	ν (C=O)	Ketones
	1,100–1,300	i	ν (C=C)	
-C-O-H	3,500–3,640	i	ν (OH)	Alcohols
	1,010–1,230	i	ν (OH)	
N-H	3,325–3,510	i	ν (NH)	Amine
	1,590–1,660	m	δ (NH)	
COOH	2,300–2,500	m	ν (OH)	Organic acids
	1,710–1,760	i	ν (C=O)	
	1,420	w	ν (C=O)	
	1,210–1,320	i	δ (OH)	
	920	m	γ (OH)	
COO ⁻	1,550–1,610	i	ν_{as} (C=O)	Organic salts or dissociated acids
	1,300–1,420	m–i	ν_{s} (C=O)	

i intensive, *m* medium, *w* weak

9.4.1 Alkoxide-Derived (Organic) Precursors

Infrared spectroscopy is useful for following the processes that occur with precursors during synthesis. In this section, examples will be discussed of infrared spectra of alkoxide precursors in different systems.

Alkoxides react in two ways in a CSD process: (a) self-condensation, and/or (b) reaction with a solvent. It is well known that due to their high reactivity, transition metals alkoxides coordinate in solution during storage. Coordination expansion of the metal atom occurs via alkoxy bridging, leading to the formation of more or less condensed oligomers when the metal alkoxides $M(OR)$, ($M = Ti, Zr, V, Ta, Ce$) are used in a pure form or in non-polar solvents [7].

Another aspect of interest is the dilution of pure metal alkoxides in a solvent. The literature shows that the resulting material depends on the solvent in which hydrolysis and condensation reactions are performed [8–11]. Solvents are able to react with metal alkoxides and change them at a molecular level [12].

Titanium alkoxides modified with carboxylic acids have been frequently studied as molecular precursors to ceramic materials [13, 14]. Thus, in the case of reaction with a solvent, such as carboxylic acid, three coordination modes of carboxylic acids to a metal atom are known: monodentate via one oxygen atom, bidentate bridging between two metal atoms, and bidentate chelating via both oxygen atoms, as shown in Fig. 9.7 [13, 14]. In the infrared spectra, each kind of coordination mode appears at a different frequency.

In order to obtain a $Bi_{1/2}Na_{1/2}TiO_3$ (BNT) thin film with ferroelectric properties, a BNT sol was synthesized by mixing bismuth oxide and sodium carbonate dissolved in nitric acid and titanium tetraisopropoxide in ethylene glycol [15]. Figure 9.8 shows the FTIR spectra of the individual reagents used and of their corresponding mixtures [15].

When titanium tetraisopropoxide was added to ethylene glycol, bands around $1,130\text{ cm}^{-1}$ and 915 cm^{-1} (solid squares) were observed and attributed to Ti-O-C stretching vibration [15]. The bands at $1,399\text{ cm}^{-1}$ and 826 cm^{-1} that appear in the spectra of the precursor solutions were attributed to $Bi(NO_3)_3$ and $NaNO_3$. In the $Bi_{1/2}Na_{1/2}TiO_3$ precursor sol, two bands appear at $1,709\text{ cm}^{-1}$ and $1,554\text{ cm}^{-1}$, which were attributed to $\nu(COO^-)$ vibrational modes [15]. According to previous data, Ti was present in two coordination modes as a monodentate acetate ligand and bidentate chelating ligand. Infrared spectra indicated the modification of titanium tetraisopropoxide by oxidation products of ethylene glycol. In the precursor sol of $Bi_{1/2}Na_{1/2}TiO_3$, the corresponding bonds were identified.

Figure 9.9 shows titanium tetraisopropoxide modified by glycolic acid in the bidentate form and oxalic acid in the monodentate form.

Other examples of infrared spectra are shown in Fig. 9.10 for the mixture of phosphoesters and Ti isopropoxide [16]. The intense and broad band in the $3,500\text{--}3,100\text{ cm}^{-1}$ region is attributed to the stretching vibrations of OH from alcohols. The disappearance from the spectra of phosphoester of bands located at $2,700\text{ cm}^{-1}$, $2,300\text{ cm}^{-1}$ and $1,650\text{ cm}^{-1}$ characteristic of *n* OH and *d* OH can be

Fig. 9.7 Different coordination modes occurring in metal carboxylates [14] (Reproduced by permission of Elsevier)

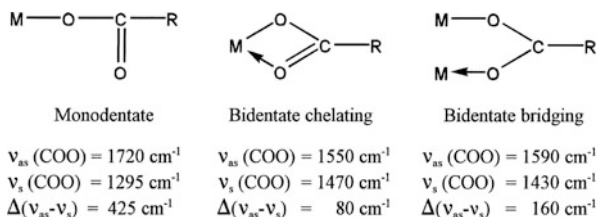


Fig. 9.8 FTIR spectra of the precursors: (a) ethylene glycol (EG), (b) titanium tetraisopropoxide (TTIP), (c) titanium tetraisopropoxide in ethylene glycol, (d) Bi_2O_3 and Na_2CO_3 solution in ethylene glycol, (e) $\text{Bi}_{1/2}\text{Na}_{1/2}\text{TiO}_3$ sol precursor [15] (Reproduced by permission of Springer)

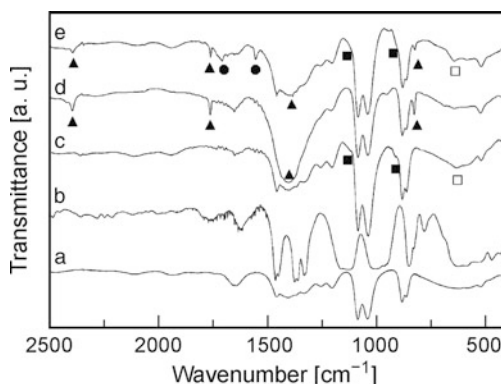
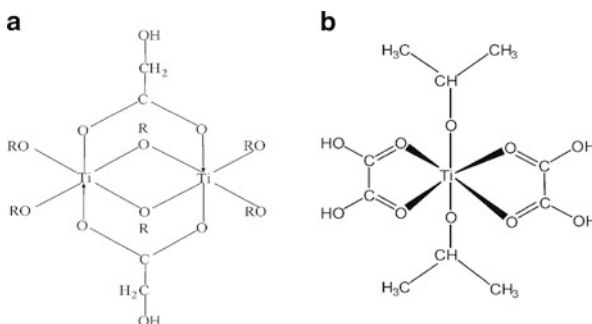


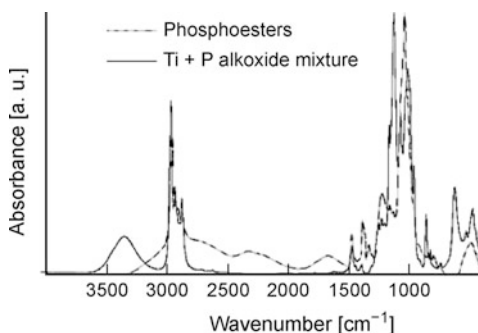
Fig. 9.9 Titanium tetraisopropoxide modified by (a) glycolic acid and (b) oxalic acid [15] (Reproduced by permission of Elsevier)



explained by the condensation of the hydroxyl groups with isopropoxy groups of the titanium alkoxide [16].

The P-O and the P-O-C stretching vibrations were located at $1,230 \text{ cm}^{-1}$ and $1,050 \text{ cm}^{-1}$. Major transformations were present when the titanium alkoxide was added to the phosphoester mixture. The two vibrations characteristic of the P=O bond of the separate compounds $\text{OP}(\text{OH})(\text{O}i\text{Pr})_2$ and $\text{OP}(\text{OH})_2(\text{O}i\text{Pr})$ are located at $1,235 \text{ cm}^{-1}$ and $1,225 \text{ cm}^{-1}$, respectively, and they are combined into one broad peak in the phosphoester mixture [16]. The decoupling of the peak and the shift in the wavenumber can be explained by the condensation of OH^- with titanium alkoxide, which leads to an accentuated difference in the phosphorous environment and an increase in the frequency interval between the two stretching vibrations [16].

Fig. 9.10 FTIR spectra of the phosphoesters and the Ti + P alkoxide mixture (titanium isopropoxide and phosphoester) [16] (Reproduced by permission of Springer)



The same effect is responsible for splitting the P-O-C band located at $1,050\text{ cm}^{-1}$ into two bands located at $1,080\text{ cm}^{-1}$ and $1,020\text{ cm}^{-1}$.

9.4.2 Inorganic (Water-Based) Precursors

FTIR spectra can be also used to investigate inorganic (water-based) precursors. In the case of inorganic precursors, chelating agents must usually be added to the reaction mixture.

Among the inorganic precursors, nitrates are mostly used. The gelling process in the aqueous lanthanum-cobalt-citric acid system was studied by Predoana et al. [17]. Lanthanum and cobalt nitrates were used as starting reagents in the presence of citric acid as a chelating agent. Figure 9.11 shows the evolution of the IR spectra of the reaction mixture at $80\text{ }^{\circ}\text{C}$.

In the initial solution, in addition to the characteristic band assigned to NO_3^- vibration at $1,330\text{ cm}^{-1}$, bands indicating the presence of citric acid ($\sim 1,397\text{ cm}^{-1}$) and water ($1,636\text{ cm}^{-1}$) were observed. During storage at $80\text{ }^{\circ}\text{C}$, the intensity of all vibrational bands increased and new bonds were identified as a result of the precursor reaction in solution. The studied solution was used for LaCoO_3 film deposition or powder preparation.

The FTIR spectra of the pyro-P and tripoly-P aqueous solutions at different pH levels are illustrated in Fig. 9.12a, b, respectively [18].

The peak assignments for the infrared spectra of the pyro-P and tripoly-P solutions are mainly based on the distribution of the species of aqueous phosphates at different pHs, and the available peak assignment data for pure solids [19–21] and for solutions [21, 22].

The peak assignment for a condensed phosphate solution usually indicates that (1) bands in the region $1,200\text{--}1,270\text{ cm}^{-1}$ can be assigned to the asymmetric stretching vibrations of the bridging $\text{PO}_2^-(\text{O}=\text{P}-\text{O}^-)$ ($\nu_{\text{as}}\text{ PO}_2^-$) [19–21, 23]; (2) bands near 900 cm^{-1} belong to the asymmetric stretching vibration of P–O–P

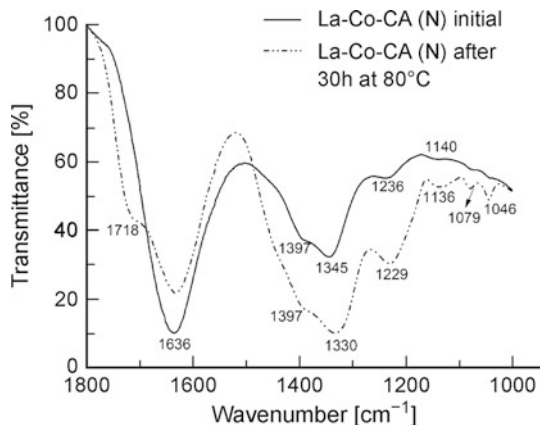


Fig. 9.11 FTIR spectra of the solution in the La-Co-CA system starting from nitrates after synthesis (*solid line*) and after 30 h at 80 °C (*dash-dotted line*) [17]

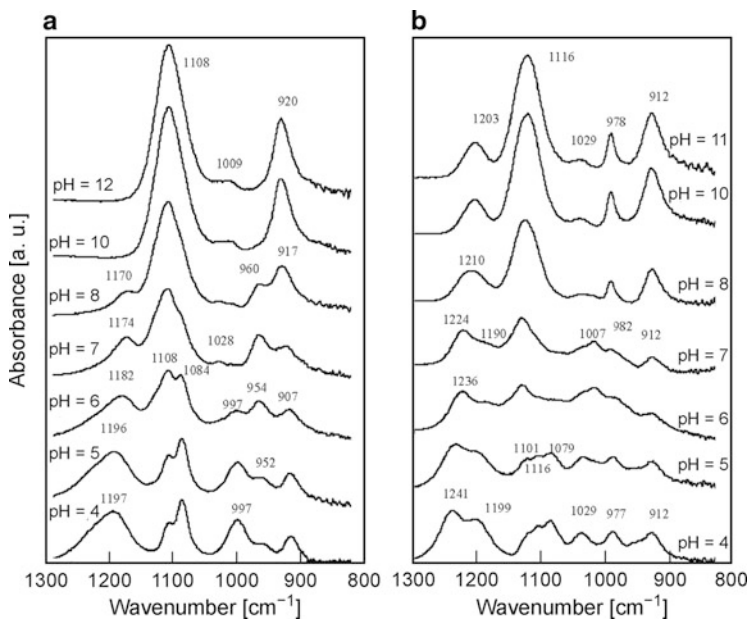


Fig. 9.12 ATR-FTIR spectra of aqueous condensed phosphate solutions at different pH levels: (a) pyro-P solution, (b) tripoly-P solution [18] (Reproduced by permission of Elsevier)

(ν_{as} P–O–P) [22, 24]; (3) bands in the regions 1,080–1,120 cm⁻¹ and 1,000–1,030 cm⁻¹ correspond to the asymmetric and symmetric stretching vibrations of the PO₃²⁻ (ν_{as} PO₃²⁻ and ν_{s} PO₃²⁻), respectively [22].

9.5 Evolution of CSD Processes Recorded by Infrared Spectroscopy

The evolution of the CSD process leads to the formation of the M-O-M bonds which were also identified in the infrared spectra. Infrared spectroscopy can describe the formation of new bonds by modification of the metallic coordination, after reaction with the initial solution, by identifying new vibrations. The final compounds after chemical solution deposition are amorphous, vitreous or crystalline films. In the amorphous films, infrared spectroscopy detects the bonds in the sample such as Me-O, Me-O-H, etc.

In vitreous materials (such as glasses and solid polymers), molecular groups have a number of characteristic vibrational modes determined by the masses of atoms, interatomic forces and geometric arrangements, i.e. the structure [25]. The infrared spectra can be good detectors of medium- and short-distance arrangements.

In the case of crystals, the direct determination of the structure from vibrational spectra is not possible [25]. The structure must be known from other methods, such as X-ray diffraction. In crystals, the groups interact with their neighbors, which means that if the crystals are almost perfect, infrared spectroscopy is very useful, but in the case of crystals with defects, this approach is more difficult due to the increase in the complex approximations used, which in turn can increase the errors [26].

The groups in glasses and crystals are the same. In crystals, the groups interact with their neighbors. In glasses, the groups can be isolated polyhedral units, or units arranged as chains (part of the network). Group frequencies for some of the most-studied inorganic groups present in glasses or in crystals are presented in Table 9.3.

In the case of films prepared by CSD, the process was monitored from precursor to amorphous deposited films and their crystallization process. Some examples are given below.

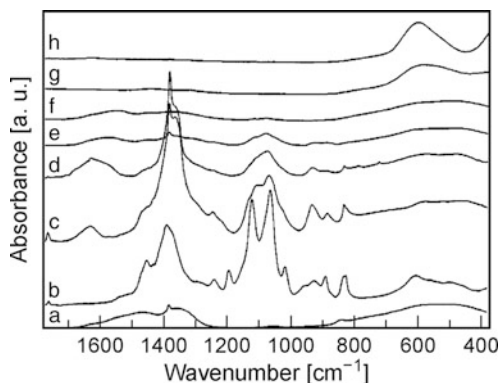
Lashgari and Westin [26] reported on the preparation of a lead zirconium titanate (PZT) film and powder by the sol-gel technique using Ti- and Zr-alkoxides and a novel Pb precursor, and they described the whole process using the FTIR technique. As shown in Fig. 9.13, they recorded the evolution of the process from precursor solution to treated powder. Their aim was to study the phase evolution when decomposing the hydroxyls and organic groups to form PZT. The precursor solution was deposited on glass substrates, and the films formed were removed after drying [26].

The IR spectrum of the gel film showed peaks from polyether groups ($1,250\text{--}800\text{ cm}^{-1}$), H_2O ($1,630\text{ cm}^{-1}$) and nitrate groups ($1,384\text{ cm}^{-1}$) [26]. The absence of a peak at $1,194\text{ cm}^{-1}$ showed that the gel was free of MOE(H) [26]. The band at $1,384\text{ cm}^{-1}$ due to the NO_3^- group was quite broad in the precursor solution as well as in the gel.

Ion et al. published a study of the crystalline lanthanum zirconate [27]. In Fig. 9.14, the spectra of 2-methoxyethanol, lanthanum nitrate (LN), LN-sol, lanthanum zirconate (LZ)-sol, dried LZ and crystalline LZ are presented [27].

Table 9.3 Examples of group frequencies of inorganic units that appear in the spectra of glasses and crystals (taken from Zarzycki and Nakamoto) [5, 25]

Inorganic group	Group frequencies in the spectra (cm^{-1})	Assignment	Observations
SiO_4^{4-}	800–1,050	ν (Si-O)	In isolated groups
SiO_4^{4-}	800–1,050	ν (Si-O)	In condensed groups
SiO_6^{6-}	800–1,050	ν (Si-O)	In condensed groups
TiO_4^{4-}	690–800	ν (Ti-O)	In isolated groups
TiO_6^{6-}	Below 500	ν (Ti-O)	In isolated groups
TiO_4^{4-}	~900	ν (Ti-O)	In condensed groups
TiO_6^{6-}	~700	ν (Ti-O)	In condensed groups
AlO_4^{4-}	650–800	ν (Al-O)	In isolated groups
AlO_6^{6-}	400–500	ν (Al-O)	In isolated groups
AlO_4^{4-}	700–870	ν (Al-O)	In condensed groups
AlO_6^{6-}	400–650	ν (Al-O)	In condensed groups
ZnO_4	400–600	ν (Zn-O)	Condensed and isolated group frequencies overlap
$\text{Al}(\text{OH})_4^{4-}$	615–720	ν (Al-O)	
$\text{Zn}(\text{OH})_4$	470–570	ν (Zn-O)	

Fig. 9.13 FTIR spectra of (a) PZT powder, (b) PZT precursor solution, (c) PZT gel, (d) gel heated to 185 °C, (e) gel heated to 285 °C, (f) gel heated to 355 °C, (g) gel heated to 550 °C, and (h) gel heated to 700 °C [26] (Reproduced by permission of Springer)

The organic bands from 2-methoxyethanol can be observed in sols while they disappear in spectra of dried LZ and crystalline LZ.

Hardy et al. [28] used FTIR spectroscopy to study the crystallization of strontium niobate films processed by water-based chemical solution deposition (cf. Chap. 5), which is shown in Fig. 9.15. A special device known as a grazing angle attenuated total reflectance—Fourier transform infrared spectroscope (GATR-FTIR, Harrick, Ge hemispherical crystal) was used [28].

The authors [28] reported that GATR-FTIR spectra for the thickest $\text{Sr}_2\text{Nb}_2\text{O}_7$ (SNO 1:1) calcined at 600 °C show M–O bond vibration below $1,000 \text{ cm}^{-1}$ (875 cm^{-1} , 810 cm^{-1} , 780 cm^{-1} and 710 cm^{-1}) and the presence of a peak around $2,340 \text{ cm}^{-1}$, which may be ascribed to nitrogen in organics or trapped CO_2 .

Fig. 9.14 IR spectra of 2-methoxyethanol (MOE), $\text{La}(\text{NO}_3)_3 \cdot x\text{H}_2\text{O}$, LN-sol, LZ-sol, dried LZ and crystalline LZ [27] (Reproduced by permission of Elsevier)

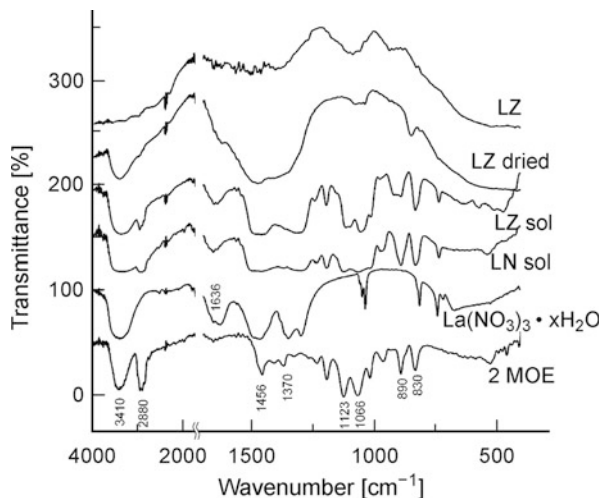
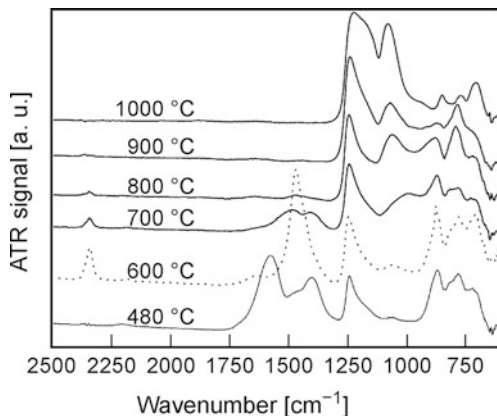


Fig. 9.15 GATR-FTIR spectra of SNO films as a function of annealing conditions 0.075 M SNO 1:1 ($\text{Sr}_2\text{Nb}_2\text{O}_7$) [28] (Reproduced by permission of Elsevier)

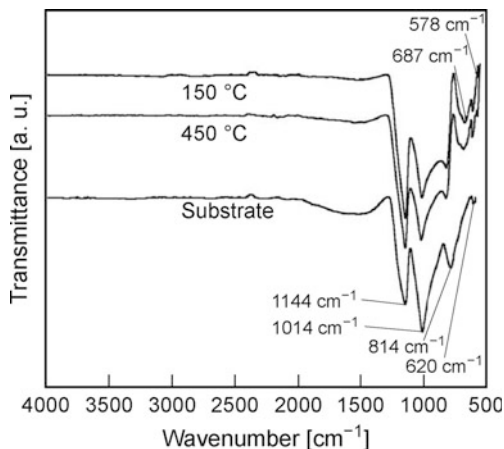


Niobium silicate formation can be identified according to the bands around 850 cm^{-1} assigned to the $\text{Nb-O}(\text{Si})$ vibrations [29] or $\text{Si-O}(\text{Nb})$ vibrations that are reported to occur at 960 cm^{-1} [30, 31]. Niobium oxide vibrations below $1,000\text{ cm}^{-1}$ (885 cm^{-1} , 810 cm^{-1} , 780 cm^{-1} , 730 cm^{-1}) [30, 32, 33] can also be observed in Fig. 9.15. In this case, the band of Nb-O appears in all films.

Tellier and Colab. [34] obtained a pure and transparent ZnO film on a SiO_2/Si substrate. The infrared spectra are shown in Fig. 9.16. The FTIR spectra of the ZnO film have similar bands at 687 cm^{-1} and 578 cm^{-1} , which correspond to Zn-O bonds [34]. The infrared spectra of the SiO_x/Si substrate is characterized by four bands at 620 cm^{-1} , 814 cm^{-1} , $1,014\text{ cm}^{-1}$ and $1,144\text{ cm}^{-1}$, which are assigned to the stretching of Si-Si bonds and Si-O-Si bending and stretching modes [34, 35].

Jitaru et al. [36] studied the doped lanthanum chromites. Figure 9.17 shows the FTIR spectra of acetate precursors in aqueous solution (spectrum a), the thermal

Fig. 9.16 FTIR spectra of the SiO₂/Si substrate and ZnO films deposited on a SiO₂/Si substrate and heated at 150 °C and 450 °C in air. The samples consisted of ten deposited layers [34] (Reproduced by permission of Elsevier)



decomposition in steps of La-Cr-acetate precursors (spectrum b), and precursors calcined at 800 °C (spectrum c).

Spectrum (a) presents bands of stretching of bidentate bridging CH₃COO⁻ ion at 1,456 cm⁻¹, 1,559 cm⁻¹, 1,620 cm⁻¹, the bands of coordinated H₂O at 3,390 cm⁻¹, 1,620 cm⁻¹, 650–670 cm⁻¹, and OH⁻ groups at 940 cm⁻¹ and 1,030 cm⁻¹. In spectrum (b), the frequencies of bidentate CH₃COO⁻ ion and coordinated H₂O disappear, and only δM-OH and νOCO (monodentate CH₃COO⁻ ion) frequencies remain. Spectrum (c) presents just the strong bands around 600 cm⁻¹ and 425 cm⁻¹ corresponding to the stretching vibration of the Cr-O and O-Cr-O bonds.

Impurity traces and compound formation were identified by using FTIR spectroscopy by Stanulis [37], as can be seen in Fig. 9.18.

The absence of a very strong signal at 790 cm⁻¹ in Fig. 9.18b confirms that stannic acid does not contain any traces of oxalate ions (bands in Fig. 9.18a). The band around 600 cm⁻¹ shows the formation of the Sn-O bond (Fig. 9.18b). Thermal treatment at 800 °C caused changes in the FTIR spectrum of stannic acid, verifying the dehydroxylation (Fig. 9.18c) and formation of SnO₂.

Based on these insights, the precursor can be regarded as a reliable source for tin-oxide film deposition [37].

As a general feature, in all investigated systems the as-deposited films presented infrared vibration bands characteristic of the components of the solution used for film deposition. Thermal treatment decreased the intensity of these vibrational bands before they vanished due to the evolution of the volatile species and the formation of new chemical bonds of the M-O-M type.

Fig. 9.17 FTIR spectra of $[\text{LaCr}(\text{CH}_3\text{COO})_3(\text{OH})_3(\text{H}_2\text{O})_3] \times 4\text{H}_2\text{O}$: (a) 25 °C; (b) 370 °C; (c) 800 °C [36] (Reproduced by permission of Elsevier)

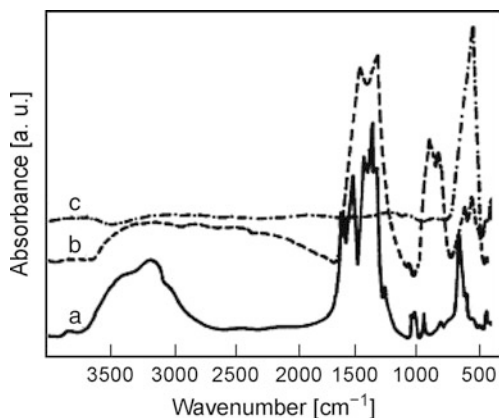
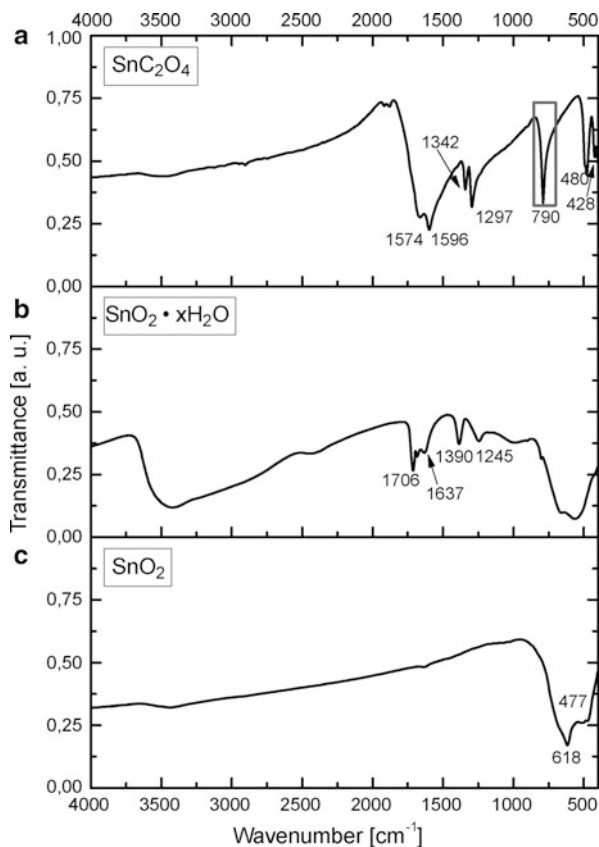


Fig. 9.18 FTIR spectra of (a) tin (II) oxalate, (b) hydrated tin (IV) oxide, and (c) tin (IV) oxide [37] (Reproduced by permission of Springer)



9.6 Conclusions

This section presents some general considerations on IR spectroscopy and its application to study the chemical solution deposition of thin films. Data concerning the IR characteristics of organic and inorganic precursors were presented together with information on the influence of the type of solutions (alcoholic or aqueous) on the characteristics of the deposited films. Crystallization by thermal treatment of the films that are usually amorphous as deposited was also discussed. It should be mentioned that IR spectroscopy is one of the most powerful methods for characterizing solutions and amorphous materials. In the case of crystalline materials, other methods could provide more detailed information on structure.

References

1. Harwood LM, Moody CJ (1989) *Experimental organic chemistry: principles and practice*. Wiley-Blackwell, Oxford, 292 p
2. Pogany I, Banciu M (1972) *Metode fizice in chimia organica*. Stiintifica, Bucuresti, 106 p
3. Lau WS (2001) *Infrared characterization for microelectronics*. World Scientific, Singapore
4. Balaban AT, Banciu M, Pogany I (1983) *Aplicatii ale metodelor fizice in chimia organica*. Stiintifica si Enciclopedica, Bucuresti, pp 13–38 (in romanian)
5. Nakamoto K (2009) *Infrared and Raman spectra of inorganic and coordination compounds, part A, theory and application in inorganic chemistry*. Wiley
6. Coates J (2000) Interpretation of infrared spectra, a practical approach. In: Meyers RA (ed) *Encyclopedia of analytical chemistry*, vol 12. Wiley, Chichester, p 10817
7. Pouxviel JC, Boilot JP, Beloeil JC, Lallemand JY (1987) NMR study of the sol/gel polymerization. *J Non-Cryst Solids* 89:345
8. Harris MT, Byers CH (1988) Effect of solvent on the homogeneous precipitation of titania by titanium ethoxide hydrolysis. *J Non-Cryst Solids* 103:49
9. Kundu D, Ganguli D (1986) Monolithic zirconia gels from metal-organic solutions. *J Mater Sci Lett* 5:293
10. Barringer EA, Bowen HK (1985) High-purity, monodisperse TiO_2 powders by hydrolysis of titanium tetraethoxide. 1. Synthesis and physical properties. *Langmuir* 1:414
11. Harris MT, Byers CH, Brunson RR (1988) A study of solvent effects on the synthesis of pure component and composite ceramic powders by metal alkoxide hydrolysis. *Mater Res Soc Symp Proc* 121:287
12. Nabavi M, Doeuff S, Sanchez C, Livage J (1990) Chemical modification of metal alkoxides by solvents: a way to control sol–gel chemistry. *J Non-Cryst Solids* 121:31
13. Doeuff S, Henry M, Sanchez C, Livage J (1987) Hydrolysis of titanium alkoxides: modification of the molecular precursor by acetic acid. *J Non-Cryst Solids* 89:206
14. Urlaub R, Posset U, Thull R (2000) FT-IR spectroscopic investigations on sol–gel-derived coatings from acid-modified titanium alkoxides. *J Non-Cryst Solids* 265:276
15. Kim CY, Sekino T, Yamamoto Y, Niihara K (2005) The synthesis of lead-free ferroelectric $\text{Bi}_{1/2}\text{Na}_{1/2}\text{TiO}_3$ thin film by solution-sol–gel method. *J Sol–Gel Sci Technol* 33:307
16. Barbe CJ, Harmer MA, Scherer GW (1997) Sol–gel synthesis of potassium titanyl phosphate: solution chemistry and gelation. *J Sol–Gel Sci Technol* 9:183
17. Predoana L, Jitianu A, Malic B, Zaharescu M (2012) Study of the gelling process in the La-Co-citric acid system. *J Am Ceram Soc* 95:1068

18. Guan XH, Liu Q, Chen GH, Shang C (2005) Surface complexation of condensed phosphate to aluminum hydroxide: an ATR-FTIR spectroscopic investigation. *J Colloid Interf Sci* 289:319
19. Abbas MH, Davidson G (1994) Vibrational spectra of $X_2O_7^{2-}$ anions. *Spectrochim Acta Part A* 50:1153
20. Ivashkevich LS, Lyutsko VA, Nikanovich MV (1988) Calculation of the vibrational spectrum of the triphosphate anion. *J Appl Spectrosc* 2:180
21. Rulmont A, Winand JM, Tarte P (1991) Nouvelles solutions solides $L^I(M^{IV})_{2-x}(N^{IV})_x(PO_4)_3$ (L = Li, Na, M, N = Ge, Sn, Ti, Zr, Hf) synthèse et étude par diffraction x et conductivité ionique. *J Solid State Chem* 93:341
22. Scorates G (2001) Infrared and Raman characteristic group frequencies: tables and charts. Wiley, New York
23. Gong W (2001) A real time in situ ATR-FTIR spectroscopic study of linear phosphate adsorption on titania surfaces. *Int J Miner Process* 63:147
24. Michelmoré A, Gong W, Jenkins P, Ralston JJ (2000) The interaction of linear polyphosphates with titanium dioxide surfaces. *Phys Chem Chem Phys* 2:2985
25. Zarzycki J (1991) Glasses and the vitreous state. Cambridge University Press, Cambridge, p 114
26. Lashgari K, Westin GK (1999) Preparation of PZT film and powder by sol-gel technique using Ti- and Zr-alkoxides and a novel Pb-precursor; $Pb(NO_3)_2 \cdot 1.5EO_3$. *J Sol-Gel Sci Technol* 13(1-3):865
27. Ion ED, Malič B, Arčon I, Padežnik Gomilšek J, Kodre A, Kosec M (2010) Characterization of lanthanum zirconate prepared by a nitrate-modified alkoxide synthesis route: from sol to crystalline powder. *J Eur Ceram Soc* 30:569
28. Hardy A, Van Elshocht S, Adelman C, Kittl JA, De Gendt S, Heyns M, D'Haen J, D'Olieslaeger M, Van Bael MK, Van den Rul H, Mullens J (2010) Strontium niobate high-k dielectrics: film deposition and material properties. *Acta Mater* 58:216
29. Aronne A, Sigae V, Champagnon B, Fanelli E, Califano V, Usmanova LZ (2005) The origin of nanostructuring in potassium niobosilicate glasses by Raman and FTIR spectroscopy. *J Non-Cryst Solids* 351:3610
30. Ziolk M, Nowak I (2003) Characterization techniques employed in the study of niobium and tantalum-containing materials. *Catal Today* 78:543
31. Ko YS, Jang HT, Ahn WS (2007) Hydrothermal synthesis and characterization of niobium-containing silicalite-I molecular sieves with MFI structure. *J Ind Eng Chem* 13:764
32. Nyquist RA, Putzig CL, Leugers MA (1997) Handbook of infrared and Raman spectra of inorganic compounds and organic salts. Academic, San Diego, CA
33. Prasetyoko D, Ramli Z, Endud S, Nur H (2005) Preparation and characterization of bifunctional oxidative and acidic catalysts $Nb_2O_5/TS-I$ for synthesis of diols. *Mater Chem Phys* 93:443
34. Tellier J, Kuščer D, Malič B, Cilenšek J, Škarabot M, Kovač J, Gonçalves G, Mušević I, Kosec M (2010) Transparent, amorphous and organics-free ZnO thin films produced by chemical solution deposition at 150 °C. *Thin Solid Films* 518:5134
35. Tolstoy VP, Chernychova IV, Skryshevsky VA (2003) Handbook of infrared spectroscopy of ultrathin films. John Wiley, New York
36. Jitaru I, Berger D, Fruth V, Novac A, Stanica N, Rusu F (2000) Lanthanum chromites doped with divalent transition metals. *Ceram Int* 26:193
37. Stanulis A, Hardy A, Dobbelaere C, D'Haen J, Van Bael M, Kareiva A (2012) SnO_2 thin films from an aqueous citrate peroxy $Sn(IV)$ precursor. *J Sol-Gel Sci Technol* 62:57

Part III

Deposition Techniques

General routes and prerequisites of deposition techniques are described in various chapters of Part III. At first the three main techniques (dip coating, spin coating and aerosol deposition) will be described in Chaps. 10–12. It should be noted that “*aerosol deposition*” is the more precise generic term for all deposition methods which spray a precursor solution onto a cold or more often preheated substrate (spray coating or spray pyrolysis [1]). In literature the names MAD technology (from “*metalorganic aerosol deposition*” [2]) or aerosol MOCVD may also be found [3], which is rather a question of the wording than a real physical difference to other kinds of spray pyrolysis techniques.

In Chap. 13 advanced methods of deposition which simultaneously enable the patterning of the deposited films are reviewed. The focus is laid on inkjet printing of precursor solutions which works with directed deposition of a jet of fine droplets (~15–200 μm) onto a substrate. Since it is an additive process with strongly reduced chemical waste and applicable in industry, it represents an emerging technique in CSD technology for various materials ranging from metals to functional oxides. Other direct writing methods such as micro-contact printing are also briefly mentioned. For a comprehensive survey on direct-writing technologies the reader is referred to the book of Piqué and Chrisey [4].

Chemical bath deposition (CBD) is a further deposition method, which typically leads to a laminar coating and relies on once or repeated immersion of the substrate into a suitable, often water based precursor solution. The solid thin film is produced by exsolvation from the solution. By controlling temperature (typically below 100 $^{\circ}\text{C}$), pH , and concentration of the coating solution, the film formation can be tailored. Chapter 14 is dedicated to all aspects of this special method.

References

1. Perednis D, Gauckler L (2005) Thin film deposition using spray pyrolysis. *J Electroceram* 14:103–111

2. Moshnyaga V, Khoroshun I, Sidorenko A, Petrenko P, Weidinger A, Zeitler M, Rauschenbach B, Tidecks R, Samwer K (1999) Preparation of rare-earth manganite-oxide thin films by metalorganic aerosol deposition technique. *Appl Phys Lett* 74:2842–2844
3. Khoroshun IV, Karyayev EV, Moshnyaga VT, Kiosse GA, Krachun MA, Zakosarenko VM, Davydov VY (1990) Characteristics of epitaxial Y-Ba-Cu-O thin films grown by aerosol MOCVD technique. *Supercond Sci Technol* 3:493–496
4. Piqué A, Chrisey DB (2002) Direct-write technologies for rapid prototyping applications: sensors, electronics, and integrated power sources. Academic, San Diego

Chapter 10

Dip Coating

C. Jeffrey Brinker

10.1 Introduction

Among the various wet chemical thin film deposition methods dip coating represents the oldest commercially applied coating process. The first patent based on this process was issued to Jenaer Glaswerk Schott & Gen. in 1939 for sol-gel derived silica films [1]. Nowadays sol-gel [2] or more general CSD derived coatings are being studied for a manifold range of applications such as ferroelectrics, dielectrics, sensors and actuators, membranes, superconducting layers, protective coatings, passivation layers, etc. (see Part V of this book). Basically the process may be separated into three important technical stages:

1. Immersion & dwell time: The substrate is immersed into the precursor solution at a constant speed followed by a certain dwell time in order to leave sufficient interaction time of the substrate with the coating solution for complete wetting.
2. Deposition & Drainage: By pulling the substrate upward at a constant speed a thin layer of precursor solution is entrained, i.e. film deposition. Excess liquid will drain from the surface.
3. Evaporation: The solvent evaporates from the fluid, forming the as-deposited thin film, which can be promoted by heated drying. Subsequently the coating may be subjected to further heat treatment in order to burn out residual organics and induce crystallization of the functional oxides.

At first glance this coating method is rather simple, however a more detailed understanding of the microscopic processes during dip coating enables tailoring of the final films since it is the coating process that serves as one important link between the structure of the solution or sol, respectively, and the microstructure of the deposited film. Hence this chapter addresses the fundamentals of the underlying

C.J. Brinker (✉)

Sandia National Laboratories, Albuquerque, NM 87185, USA

e-mail: cjbrink@sandia.gov

physics and chemistry of the thin film formation by dip coating including recent findings. Although the dip coating process can be applied to all types of precursor solutions (sol-gel, MOD and hybrid, compare Chap. 3 the use of sol-gel type solutions offers the most possibilities to influence the film properties by modifying the size and structure of the inorganic species in the sol together with the solvent(s). Thus though already mentioned in other chapters of this book briefly the corresponding aspects of sol-gel chemistry are reviewed at first. Then the features of the classical dip coating process are discussed by means of sol-gel derived coatings. This comprises the deposition of inorganic sols with regard to time scales and the effects of sol structure and capillary pressure on such properties as refractive index, surface area, and pore size of the deposited film. Finally advanced dip coating approaches like angular dependent dip coating and the evaporation-induced self-assembly (EISA-process), which enable the rapid production of patterned porous or nanocomposite thin film materials, are presented.

10.2 Precursor Solution Chemistry

At first some general comments to the requirements of precursor solutions with regard to successful dip coating are presented in this section. A trivial but probably most important precondition is that the condensed phase remain dispersed in the fluid medium, that macroscopic gelation be avoided, and that the sol be sufficiently dilute so that upon deposition the critical cracking thickness not be exceeded (see discussion in Sect. 10.3.3). Thus in principle all different kinds of sols or solutions described in Part I of this book can be used for dip coating, although as will be shown in the following sections, the differences in the structures of the condensed phase lead to differences in the structures of the deposited films. Since sol-gel type precursor solutions offer the most obvious opportunities to influence these structures of the condensed phase during the coating process, some basics of sol-gel chemistry are briefly reviewed at this point.

In general the sol-gel process uses inorganic or metallo-organic precursors [2]. In aqueous or organic solvents, the precursors are hydrolyzed and condensed to form inorganic polymers composed of M-O-M bonds. For inorganic precursors (salts), hydrolysis proceeds by the removal of a proton from an aquo ion $[M(OH_2)_n]^{z+}$ to form a hydroxo (-OH) or oxo (=O) ligands. Condensation reactions involving hydroxo ligands result in the formation of bridging hydroxyl (M- μ (OH)-M) or oxo (M-O-M) bonds. Normally, monomeric aqueous ions are the only stable species at low pH and various monomeric or oligomeric anions the only species observed at high pH. At intermediate pH, well-defined polynuclear ions are often the stable solution species, but the metal solubility is normally limited there and, when exceeded, results in the precipitation of oxyhydroxides or oxides [3]. The most commonly used molecules are metal alkoxides which are described in more detail in Chap. 1 in this book. Often the alkoxide is dissolved in its parent alcohol and hydrolyzed by the addition of water plus, in the case of more electronegative metals

or metalloids, acid or base catalyst. Hydrolysis replaces alkoxide ligands with hydroxyl ligands. Subsequent condensation reactions involving the hydroxyl ligands produce oligomers or polymers composed of M-O-M or M- μ (OH)-M bonds.

For both inorganic and metallo-organic precursors, the structure of the evolving oligomers or polymers depends on the extent of hydrolysis and the preferred coordination number or functionality of the metal [2, 4].

In the case of inorganic precursors, the extent of hydrolysis is generally controlled by the pH (cp. also Chap. 14), while the effective functionality may be controlled (reduced) through complexation with mono- or multidentate anionic species. The extent of hydrolysis of metallo-organic precursors is controlled through the molar ratio (r) H_2O/M and the catalyst concentration. Since many of the metals of interest for functional oxide thin films (e.g. Al, Ti, Zr, Nb, Ta etc.) have coordination numbers (CN) ≥ 4 , complete condensation would lead to compact, particulate metal oxides. In order to avoid this, chemical modification of the metal alkoxide with chelating or bridging multidentate ligands is generally used to reduce both the effective functionality and the overall extent of condensation [4]. NMR, SAXS, and diffraction studies have documented that the above strategies allow the structure of the condensed species to be varied over a wide range spanning monomers, oligomers, polymers, and nanocrystals [2]. Often so-called “polymeric sols” are characterized by a mass or surface fractal dimension (see discussion in Sect. 10.3.4).

By using humidity insensitive MOD-type precursor solutions unintended hydrolysis&condensation reactions can be avoided. However in this case the microstructure directing influence of the classical sol-gel reaction is lost.

10.3 Classical Dip Coating

In the standard approach, the substrate is withdrawn vertically from the solution reservoir at a constant speed U_0 (Fig. 10.1) [5]. According to the streamlines in Fig. 10.1 the moving substrate entrains the liquid in a fluid mechanical boundary layer that splits in two above the liquid bath surface, returning the outer layer to the bath [6].

Above the stagnation point S (Fig. 10.1), when the upward moving flux is balanced due to evaporation, the film position and shape of the film profile remain steady with respect to the coating bath surface. Since the solvent is evaporating and draining, the entrained film acquires an approximate wedge-like shape that terminates in a well-defined drying line ($x = 0$ in Fig. 10.2). Above this vapor-liquid-solid three-phase boundary (drying line) the non-volatile species form the as-deposited layer which may be subjected to further curing. Figure 10.2 shows schematically the microscopic processes which occur within the thinning film. The

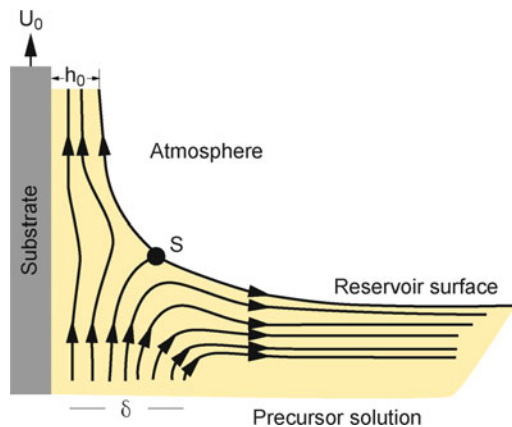


Fig. 10.1 Detail of the flow patterns (streamlines) during the dip-coating process. U_0 is the withdrawal speed, S is the stagnation point, δ the boundary layer, and h_0 is the thickness of the entrained fluid film on the substrate

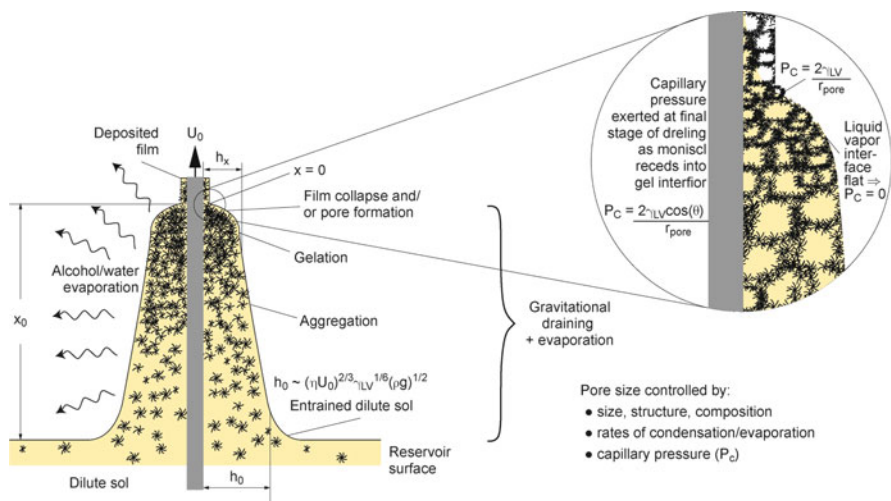


Fig. 10.2 Schematic of the steady-state dip-coating process, showing the sequential stages of structural development that result from draining accompanied by solvent evaporation and continued condensation reactions. U_0 is the withdrawal speed; $h(x)$ is the film thickness at position x measured from the drying line $x = 0$; h_0 is the entrained film thickness just above the stagnation point S, i.e. before evaporation; η is the liquid viscosity; ρ is the liquid density; P_C is the capillary pressure; γ_{LV} is the liquid-vapor surface tension; r_{pore} is the pore size and θ is the wetting angle

inorganic species are progressively concentrated by evaporation, leading to aggregation, gelation, and final drying to form a type of dry gel or *xerogel layer*.

In order to model the thickness evolution during dip-coating several regimes have been taken into account. According to Scriven [6] the entrained thickness h_0

(see Fig. 10.2) of the deposited film is related to the streamline dividing the upward and downward moving layers (Fig. 10.1). In principle a competition between various forces in the film deposition region governs the film thickness and the position of the stream line [6].

- When the liquid viscosity η and withdrawal speed U_0 are high enough to lower the curvature of the gravitational meniscus, the deposited film thickness h_0 is that which balances the viscous drag (ηU_0) and gravity force (ρg) [6, 7] according to:

$$h_0 = c_1(\eta U_0/\rho g)^{1/2} \quad (10.1)$$

where ρ is the liquid density, g is the acceleration of gravity and the constant c_1 is about 0.8 for newtonian liquids.

- When the substrate speed (typical range of $\sim 1\text{--}10$ mm/s) and liquid viscosity η are low, as is often the case for sol-gel film deposition, this balance (Eq. 10.1) is modulated by the ratio of viscous drag to liquid-vapor surface tension γ_{LV} , according to the relationship derived by Landau and Levich for a newtonian and non-evaporating fluid [7]:

$$h_0 = 0.94 \frac{(\eta U_0)^{2/3}}{\gamma_{LV}^{1/6} (\rho g)^{1/2}} \quad (10.2)$$

At usually applied withdrawal speeds in the range of $\sim 1\text{--}10$ mm/s this draining approach often describes the thickness evolution of dip-coating derived films relatively well, however recently the group of Grosso [8, 9] showed by means of various silicon-/titanium oxide precursor solutions, that in case of ultra-slow withdrawal speeds, i.e. below 0.1 mm/s or other extreme conditions such as high evaporation rate, highly reactive species in the precursor solution etc., this model cannot describe the coating results. In order to explain the finding that the (final) thickness vs. withdrawal speed curve (Fig. 10.3a) shows a minimum, the ‘‘capillarity regime’’ was introduced and modeled by semiexperimental equations.

- In case of very low withdrawal speeds, i.e. in the capillarity regime, the solvent evaporation becomes faster than the movement of the drying line leading to a continuous feeding of the upper part of the meniscus by the precursor solution through capillary rise (Fig. 10.3b).

By assuming that the evaporation rate E is constant and applying the mass conservation law the following relation for the final film thickness h_f (i.e. after stabilization by thermal treatment) could be derived for the capillarity regime [9]:

$$h_f = \frac{c_i M_i E}{\alpha_i \rho_i L U_0} = k_i \left(\frac{E}{L U_0} \right) \quad (10.3)$$

where c_i is the inorganic precursor solution concentration, M_i is the molar weight of inorganic material, α_i is the fraction of inorganic material in the film [9], ρ_i is the density of the inorganic material, and L is the width of the film. Since α_i does not vary significantly with U_0 a new solution dependent material proportion constant k_i

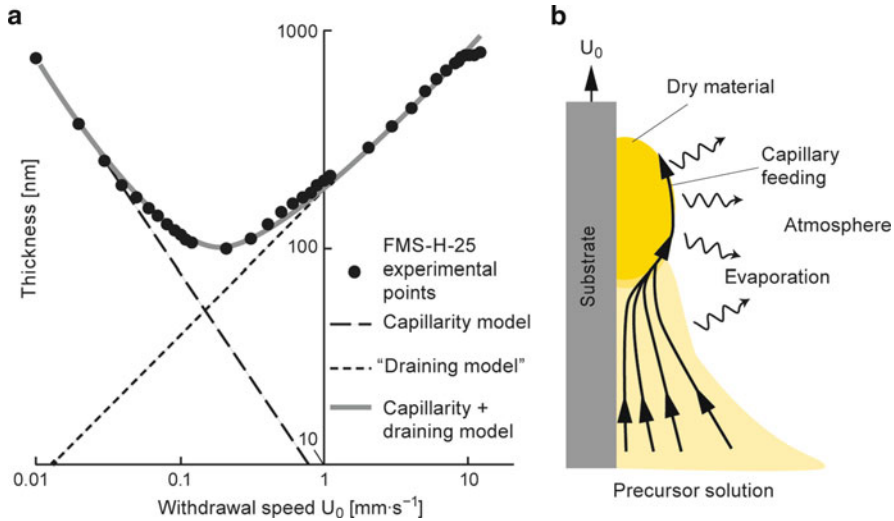


Fig. 10.3 (a) Plot of the final thickness (h_f) versus withdrawal speed (log-log scale) for a precursor solution system consisting of tetraethylorthosilicate, methyltriethylorthosilicate and the block copolymer Pluronic® F 127 in ethanol (FMSi-H-25)—experimental points and corresponding models for both independent (*dashed line*) and combined (*solid line*) capillarity and draining regimes of film formation (modified after [9]). (b) Schematic illustration of the dip coating process in case of the capillarity regime

is introduced. Equation (10.3) describes relatively well the (final) thickness in case of withdrawal speeds of 0.01 mm/s to ~ 0.1 mm/s are applied.

- In order to model the intermediate U_0 values (~ 0.1 and 1 mm/s), where the $h_f(U_0)$ curve exhibits a minimum (Fig. 10.3a), it was taken into account that both regimes (“draining” and “capillarity”) are overlapping. Before summing up both contributions at first a relation for the final thickness h_f in case of the draining regime (Landau-Levich model) was derived from Eq. (10.2) considering the evaporation by introducing the material proportion constant k_i into the equation. The physicochemical constants of the precursor solution are combined to a global constant D leading to Eq. (10.4) which now describes the final film thickness, disregarding any evaporation-dependent parameters, such as viscosity, surface tension and possible condensation in sol-gel type precursors.

$$hf = k_i D U_0^{2/3} \quad (10.4)$$

Since k_i and h_0 were known for each speed U_0 , D was calculated from experimental data and found to be roughly constant if U_0 was in the typical range of 1 to ~ 10 mm/s, which is a requirement for the Landau-Levich based model. Only a slight decrease of D is found for the highest values of U_0 [9] which was attributed to the fact that under these conditions the thickness of the deposited solution is too high for the gravity-induced viscous drag to be

counterbalanced by the adhesion of the layer to the surface [10]. Hence summing up Eqs. (10.3) and (10.4) yields Eq. (10.5) which describes the experimentally measured thickness evolution of a number of dip coated sol-gel type precursor solutions quite well (Fig. 10.3) [9].

$$hf = k_i \left(\frac{E}{LU_0} + DU_0^{2/3} \right) \quad (10.5)$$

From setting the derivative (dh_f/dU_0) of Eq. (10.5) to zero the intermediate critical speed $U_{0,C}$ at the minimum thickness $h_{f,min}$ can be calculated by Eq. (10.6).

$$U_{0,C} = \left(\frac{2DL}{3E} \right)^{-3/5} \quad (10.6)$$

Although this semiexperimental approach cannot describe time dependent parameters like viscosity variation, evaporation cooling, thermal Marangoni flow etc., the calculated values for the critical speed and minimum thickness for a number of precursor systems was in good agreement with experimental data [9]. The observed tendency to two opposite film thickness evolution regimes enables a good control of the thickness (from very thin to ultrathick) by using the same precursor solution. Thereby the speed of deposition in the capillary regime can be considerably increased by using warm air because it is governed by the evaporation rate E .

10.3.1 Pure and Binary Fluids

Although the classical expression (10.2) was developed for pure fluids (i.e. those with no condensed phase), several studies of sol-gel dip coating have verified the $h_0 \sim U_0^{2/3}$ relationship predicted by Eq. (10.2) (e.g., [11]), suggesting that the entrainment of inorganic species has little effect on the hydrodynamics of dip coating, at least at the early stages of deposition where the entrained sol is quite dilute. Some insight into the sol-gel film deposition was revealed by “imaging ellipsometry” [12] and “fluorescence imaging” [13, 14] of the steady state film profile (Fig. 10.2). Thereby imaging ellipsometry allowed the in situ determination of film thickness h and film refractive index n over the complete film profile, while embedded organic dyes acted as molecular sensors of the progressively changing physical and chemical environments created within the thinning film.

Whereas the entrained film thickness immediately above the stagnation point depends on hydrodynamic factors, the shape of the film profile $h(x)$ in the vicinity of the drying line is established by the evaporation rate. Hurd showed that for a planar substrate geometry, the evaporation rate E of a pure fluid was not constant but diverged at the drying line ($x = 0$ in Fig. 10.2) according to expression (10.7) [15]:

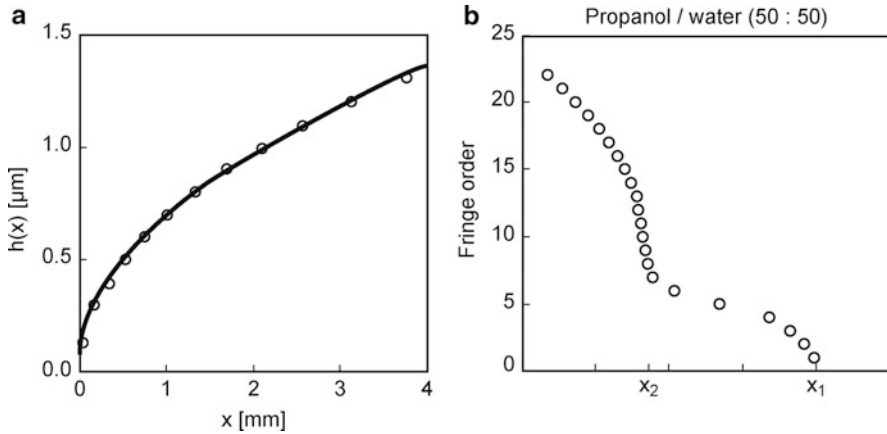


Fig. 10.4 Thickness profiles two of dip coated films from different solutions. (a) Ethanol film (circles) where the profile can be fitted quite well by Eq. (10.8) (solid line). (b) Double parabolic profile of a 50:50 propanol:water film (volume ratio) caused by differential volatilities and surface tension gradient driven flows. x_1 is the position of the drying line; x_2 is the position of the “false” drying line created by the depletion of the propanol-rich phase. The film thickness equals approximately the fringe order times 240 nm. Modified after [15, 16]

$$E(x) = D_v a x^{-1/2} \quad (10.7)$$

where D_v is the diffusion coefficient of the vapor, and a is a constant.

The divergence of the evaporation rate causes the film to thin more quickly in the vicinity of the drying line, so instead of exhibiting a wedge-shape (the expectation for uniform evaporation) the film profile acquires a parabolic shape (Fig. 10.4a):

$$h(x) \sim \int E(x) dx \sim x^{1/2} \quad (10.8)$$

For multicomponent fluids (e.g., alcohol/water mixtures often used in alkoxide-based sols) differences in the evaporation rate’s and surface tensions of the individual fluid components alter the shape of the film profile and create convective flows within the depositing film. For example, for binary alcohol/water mixtures, the film profile shows two roughly parabolic regions (see Fig. 10.4b). The first corresponds to the preferential evaporation of alcohol to leave a water-rich fluid. The difference in surface tensions between the water-rich and alcohol-rich regions induces liquid flow into the water-rich “foot” with velocity u the so-called “Marangoni effect” [5, 11]:

$$u = \frac{1}{\eta} \left[\frac{d\gamma}{dx} \right] z - U_0 \quad (10.9)$$

where z is the direction normal to the substrate surface (i.e. $z = h$). The foot slowly grows until this flux is balanced by that of evaporation from the expanding free

surface. There are several consequences of preferential evaporation and surface tension gradient driven flows with respect to sol-gel film deposition:

- It is the composition of the fluid that persists to the drying line that establishes the surface tension and hence the magnitude of the capillary pressure exerted on the condensed phase (Fig. 10.2). Fluorescence imaging performed by Nishida and co-workers [13] has shown that for ethanol/water/silica sols, the composition of the fluid at $x = 0$ is greater than 80 % water, when the initial sol contains only 12.5 volume % water.
- The surface tension gradient-driven flow of liquid through a thin “neck” can create quite high shear rates during dip-coating. For the toluene:methanol (50:50) system, the shear rate resulting from surface tension gradient driven flow is estimated to be 10^4 s^{-1} [15]. Such shears could be sufficiently strong to align or order the entrained inorganic species.

10.3.2 Effect of Condensed Phases

The previous sub-sections have largely ignored the effects of the entrained inorganic species, viz., polymers or particles. These species are initially concentrated by evaporation of solvent(s) as they are transported from the coating reservoir toward the drying line within the thinning fluid film during withdrawal. They are further concentrated (compacted) at the final stage of the deposition process by the capillary pressure P_C (Fig. 10.2). In the following paragraphs the various factors are discussed.

10.3.2.1 Solids Concentration and Time Scale

Above the stagnation point (see Fig.10.1) all fluid elements are moving upward, which means that all the entrained inorganic species that survive past the stagnation point are incorporated in the final deposited film. Steady state conditions in this region require conservation of non-volatile mass, thus the solids mass in any horizontal slice (dm_i in Fig. 10.5a) of the thinning film must be constant [16]:

$$h(x)\phi(x) = \text{constant} \quad (10.10)$$

where $\phi(x)$ is the concentration, or volume fraction solids, respectively. From Eq. (10.10) it can be seen that ϕ varies inversely with h , if $h \ll h_0$ (the normal case for sol-gel dip-coating). In case of planar substrates which have a parabolic thickness profile ($h(x) \approx x^{1/2}$) [6], ϕ should vary as $1/h \approx x^{-1/2}$ in the thinning film [15].

The rapid concentration of the entrained inorganic species is more evident from consideration of the mean particle (polymer) separation distance $\langle r \rangle$, which varies

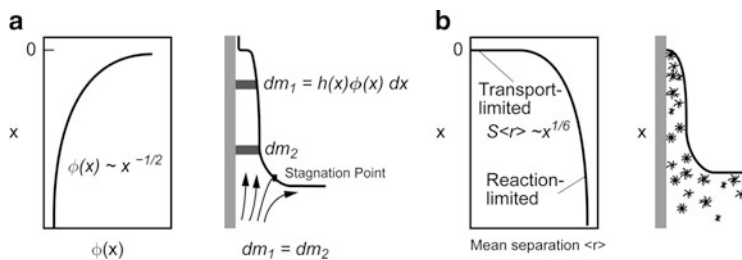


Fig. 10.5 (a) Fluid profile-concentration relationship for dip-coating. The conservation of non-volatile mass provides a relation between thickness profile $h(x)$ and the concentration $\phi(x)$ according to $h(x)\phi(x) = \text{constant}$. (b) Fluid profile mean separation relationship during dip-coating. From [15]

as the inverse cube root of ϕ , $\langle r \rangle \sim x^{1/6}$ (Fig. 10.5b). This precipitous function implies that half the distance between particle (polymer) neighbors is traveled in the last 2% of the deposition process, establishing a time scale of about 100 ms during which the condensed species are in close proximity. Several consequences of the short time scale of the film deposition processes may be anticipated:

- There is little time available for reacting species to “find” low energy configurations. Thus (for reactive systems) the dominant aggregative process responsible for network formation may change from reaction-limited (near the bath surface) to transport-limited near the drying line (Fig. 10.5b).
- For sols composed of repulsive particles, there is little time available for the particles to order as they are concentrated in the thinning film.
- There is little time available for condensation reactions to occur. Thus gelation may actually occur by a physical process, through the concentration dependence of the viscosity rather than a chemical process (In some systems this is evident by the fact that the deposited film is quickly re-solubilized when immersed in a solvent [17]).
- Since the thin physical or chemical gels are likely more weakly condensed, and hence, more compliant than bulk gels, they are more easily compacted first by evaporation and then by the capillary pressure exerted at the final stage of the deposition process (see Fig. 10.2). In such compliant materials the effects of capillary forces are enhanced, because greater shrinkage precedes the critical point, where the liquid-vapor interface first recedes into the gel (Fig. 10.2 inset), causing the pore size to be smaller and the maximum capillary pressure to be greater (see following discussion of drying).

10.3.2.2 Stages of Drying

Scherer [18] divides the drying of gels into two stages a constant rate period (CRP) and a falling rate period. During the constant rate period, mass transfer is limited by convection away from the gel surface, whereas during the falling rate period, mass

transfer is limited by the permeability of the gel. Extending these ideas to dip coating, it might be expected that a CRP would obtain throughout most of the deposition process, since the liquid-vapor interface remains located at the exterior surface of the thinning film except at the final stage of drying (see Fig. 10.2). As already mentioned above a constant evaporation rate implies a wedge-shaped film profile. This is not observed for pure fluids, nor is it observed for inorganic sols. For example, the film profile of a titanate sol prepared from titanium ethoxide hydrolyzed under acidic conditions in ethanol is described by $h(x) \sim x^{0.62}$ [5], which indicates that the evaporation rate increases as $x \rightarrow 0$, although not quite as rapidly as for pure ethanol ($h(x) \sim x^{0.5}$). Thus even for the deposition of inorganic sols, the film profile, and hence the concentration profile, are largely established by the dependence of the evaporation rate on the geometry of the depositing film. Experiments performed on a variety of substrates, including metals, ceramics, and plastics all showed similar thickness profiles emphasizing that the evaporation rate, not the wetting characteristics are responsible for determining the profile shape [15]. For sols containing fluid mixtures of differing volatilities, the fluid composition changes with distance x , contributing to further changes in the evaporation rate. The critical point, where the liquid first recedes into the gel (see Fig. 10.2 inset) should mark the beginning of the falling rate period. Depending on the distribution of liquid in the pores, the drying rate is limited by flow or diffusion. For compliant molecular networks that are collapsed prior to the critical point, drying occurs by Fickian diffusion, if the temperature is above the glass transition temperature of the mixture [18]. The onset of a falling rate period near the drying line may account for the differences in the exponents that describe the shape of the pure fluid and the titanate sol film profiles.

10.3.2.3 Rheology

As the film becomes more concentrated in the condensed phase through evaporation, the rheological response of the liquid changes from Newtonian to shear thinning (aggregated systems) or thixotropic (ordered systems) and then to viscoelastic. Eventually gelation extends throughout the film and the material no longer yields, i.e. the film behaves as an elastic solid. It is at this final stage of the deposition process that the capillary pressure P_C created by tiny menisci as they recede into the gel, is maximized (see inset Fig. 10.2). The curvature of the menisci causes the liquid to be in tension and the network in compression. Generally the magnitude of the capillary pressure is estimated by the Laplace equation:

$$P_C = \frac{2\gamma_{LV} \cos(\theta)}{r_P} \quad (10.11)$$

where θ is the wetting angle and r_P is the pore size. For wetting pore fluids ($\cos\theta \rightarrow 1$), P_C could approach or possibly exceed 1,000 bar, because the pore size may be very small (less than 1.0 nm), i.e. approach molecular dimensions.

The capillary pressure thus represents a very strong driving force to densify the depositing film.

It is balance between this capillary pressure, which compresses the network, and the modulus of the network, which enables it to resist collapse, that establishes the final density and pore size of the film. Initially as the solvent evaporates, the gel is able to shrink. The volume fraction solids ϕ increases, causing the bulk modulus K to increase as a power law. In case of silica as an example, the following relationship is observed, valid for both wet and dry silica gels [18]:

$$K \sim \phi^{3.8} \quad (10.12)$$

At the same time the spacing between polymers (effective pore size) is decreasing, causing the maximum possible capillary pressure to increase approximately as:

$$\frac{1}{\langle r \rangle} \sim \phi^{1/3} \quad (10.13)$$

Thus for silica films, the modulus is expected to increase more rapidly than the capillary pressure. When the modulus rises sufficiently to balance the capillary pressure, shrinkage stops, thereby establishing the pore size and density. Beyond this so-called critical point any further solvent loss creates porosity within the film. For precursor systems in which K exhibits a much weaker dependence on ϕ , for example as a consequence of organic modification or complexation of the metal centers with multidentate, non-hydrolyzable ligands, we might expect the network to be completely collapsed by the rising capillary pressure. However the rising viscosity accompanying solvent loss combined with the short time scale of the deposition process may represent a kinetic limitation to achieving a non-porous state. (It should also be pointed out that subsequent thermolysis and pyrolysis, respectively, of organic ligands will normally create porosity, even though the as-deposited film could be considered non-porous).

10.3.3 Drying Stress and Cracking

As the film dries, it shrinks in volume. Once the film is attached to the substrate and unable to shrink in that direction, the reduction in volume is accommodated completely by a reduction in thickness. When the film has solidified and stresses can no longer be relieved by flow, tensile stresses develop in the plane of the substrate. Croll [19] estimated the stress (σ) as:

$$\sigma = \left[\frac{E}{(1-\nu)} \right] \left[\frac{(f_S - f_r)}{3} \right] \quad (10.14)$$

where E is Young's modulus (Pa), ν is Poisson's ratio, f_S is the volume fraction solvent at the solidification point, and f_r is the volume fraction of residual solvent in the "dry" film.

The solidification point was defined for a polymer film as the concentration where the glass transition temperature has risen to the experimental temperature. Thus stress is proportional to Young's modulus and the difference between the solvent fraction at the solidification point and that of the dried coating. Scherer [2, 18] states that the stress in the film is very nearly equal to the tension in the liquid ($\sigma \approx P_C$). Despite such a large stress, it is commonly observed that cracking of films does not occur if the film thickness is below a certain critical thickness $h_c \approx 0.5\text{--}1\ \mu\text{m}$ [18]. For films that adhere well to the substrate, the critical thickness for crack propagation or the growth of pinholes is given by [20, 21]:

$$h_c = \left(\frac{K_{Ic}}{\sigma\Omega} \right)^2 \quad (10.15)$$

where K_{Ic} is the critical stress intensity or "fracture toughness" and Ω is a function that depends on the ratio of the elastic modulus of the film and substrate (for gel films $\Omega \approx 1$). For films thinner than h_c , the energy required to extend the crack is greater than the energy gained from relief of stresses near the crack, so cracking is not observed [18]. When the film thickness exceeds h_c , cracking occurs, and the crack patterns observed experimentally are qualitatively consistent with fractal patterns predicted by computer simulation [22]: Atkinson and Guppy [23] observed that the crack spacing increased with film thickness and attributed this behavior to a mechanism in which partial delamination accompanies crack propagation. Such delamination was observed directly by Garino [24] during the cracking of sol-gel silicate films. Based on Eqs. (10.14) and (10.15) above, strategies to avoid cracking include (a) increasing the fracture toughness (K_{Ic}) of the film, (b) reducing the modulus of the film, (c) reducing the volume fraction of solvent at the solidification point, and (d) reducing the film thickness. In organic polymer films, plasticizers are often added to reduce the stiffness of the film and thus avoid cracking [25]. For sol-gel systems, analogous results are obtained by organic modification of alkoxide precursors [26], chelation by multidentate ligands such as β -diketonates [27] or a reduction in the extent of hydrolysis of alkoxide precursors [24].

It should be noted that for particulate films Garino [28] observed that the maximum film thickness obtainable without cracks decreased linearly with a reduction in particle size. Since for unaggregated particulate films, the pore size scales with the particle size, this effect may be due to an increase in the stress caused by the capillary pressure ($\sigma \approx P_C$) and/or an increase in the volume fraction solvent at the solidification point resulting from the manner that the electrostatic double layer thickness (estimated by the Debye-Hückel screening length) varies with particle size [29].

10.3.4 Control of Microstructure

Basically the final film microstructure (of the as-deposited film) depends on a number of factors:

- the structure of the entrained inorganic species in the original sol (for example, size and fractal dimension)
- the reactivity of these species (for example, condensation or aggregation rates)
- the time scale of the deposition process (related to evaporation rate and film thickness)
- the magnitude of shear forces and capillary forces that accompany film deposition (related to surface tension of the solvent or carrier and surface tension gradients)

The most common means of controlling the film microstructure is through particle size. For unaggregated, monosized particulate sols, the pore size decreases and the surface area increases with decreasing particle size. Asymmetric, supported membranes have been prepared successfully from particulate sols for use in ultra-filtration [30]. As noted above difficulties arise when trying to prepare microporous membranes due to an increased tendency for cracking. Particulate sols may be intentionally aggregated prior to film formation to create very porous films [31] (e.g., volume porosity > 65 %). For electrostatically stabilized silica sols, a transition from random-close packing to ordered packing is observed with increasing substrate withdrawal rates (U_0) [31]. This may be due to a longer time scale of the deposition process (providing more time for ordering) or an increase in the shear rate accompanying deposition for higher U_0 [31]. A second strategy [2] for controlling porosity is based on the scaling of mass M_f and size r_f of a mass fractal object:

$$M_f \sim r_f^D \quad (10.16)$$

where D is the mass fractal dimension (in three dimensional space, $0 < D < 3$). Since density equals mass/volume, the density ρ_f of a mass fractal object varies in three dimensional space as $\rho_f \sim r_f^D/r_f^3$, and the porosity varies as $1/\rho_f \sim r_f^{(3-D)}$. Thus the porosity of a mass fractal object increases with its size. Providing that such fractals do not completely interpenetrate during film formation (i.e., they are mutually opaque, requiring $D < 1.5$ [2]), the porosity may be controlled by the size of the entrained fractal species prior to film formation. The efficacy of this approach is illustrated in ref. [31] where the refractive index, volume fraction porosity, pore size, and surface area of a multicomponent silicate film were shown to vary monotonically with aging time employed to grow the fractal species prior to film deposition. The extent of interpenetration of colliding fractals depends on their respective mass fractal dimensions and the condensation rate or “sticking probability” at points of intersection. A reduction of either D or the condensation rate increases the interpenetration and decreases the porosity [2, 31]. From

Eq. (10.16) and surrounding discussion, it follows that to generate porosity using this fractal scheme, r_f should be rather large, $1.5 \ll D \ll 3$, and the condensation rate should be high. Conversely dense films should be formed from small, unreactive precursors consistent with observations made on a variety of films prepared from chelated single and multicomponent alkoxide precursors [17]. The magnitude of the capillary pressure P_c should also be quite influential in determining microstructure. For bulk gels, elimination of surface tension by removal of the pore fluid above its critical point [32] results in highly porous aerogels. Deshpande and co-workers have recently shown that, for aprotic pore fluids, the surface area, pore volume, and pore size of bulk silica xerogels are all reduced monotonically by an increase in surface tension of the pore fluid [33]. Such studies are more difficult for films, since it is not possible to wash the coating sol, and distillation of solvents often leads to premature gelation. The most revealing studies are those comparing the effects of different hydrolysis ratios, $H_2O/M(OR)_n$, on film properties. Since the theoretical ratio for complete hydrolysis and condensation is $n/2$, greater ratios must produce “excess” water. As described above in mixed solvent systems, the least volatile component survives to the drying line and therefore dictates the magnitude of the capillary pressure. Fluorescence imaging experiments have shown that for alcohol/water mixtures containing more than about 10 volume % water, the composition of the fluid at the drying line is 100 % water [13]. It has been shown that as the “excess” water is increased from 0.5 to 6.0 volume %, the refractive index of silica films deposited by dipping increases from 1.342 to 1.431, corresponding to a reduction in porosity from 22 % to 7 % [34]. Further increases in the excess water content cause a reduction in refractive index (increase in porosity). Since water increases both the surface tension and the extent of condensation of the silicate matrix, this behavior reflects the competition between capillary pressure, which compacts the film, and aging, which stiffens the film increasing its resistance to compaction. In a similar dip-coating study, Warren and coworkers [35] observed that, for silica films annealed at 800 °C, the dielectric strength increased and the HF etch rate decreased as the hydrolysis ratio of the coating sol increased from 1 to 7.5. Further increases caused the reverse behavior. This implies that the effects of capillarity and aging also strongly influence the subsequent consolidation process. Finally it is anticipated that shear forces accompanying film formation could influence the microstructure. Although the withdrawal rates U_0 are often very low in dip-coating, it has been shown that surface tension gradient driven flows can cause high shear rates (10^4 s^{-1}) near the drying line [34]. Such shear rates might be partially responsible for the ordering of monosized particulate films [34].

10.3.5 Special Technical Approaches

In order to adjust the dip coating process to different substrates and substrate shapes the standard method has been technologically modified according to the specific

needs [36]. The major variations, which also found industrial interest, are presented briefly in the following paragraphs.

10.3.5.1 Drain Coating

The most self-evident modification is obtained, if not the sample is withdrawn from the coating solution, but the solution itself is removed by a constant draining rate. Although the simplest way of performing the draining can be achieved by gravity, in order to get a better control of the flow pulsation free liquid pumping is strongly recommended. This procedure called drain-coating leads physically to the same result as standard dip coating however requires less technical effort. On the other hand the substrate is in the more or less saturated solvent atmosphere of the vessel above the solution level for longer times compared to standard dip coating, which might lead to delayed drying and less hydrolysis/condensation reactions, i.e. film formation is hampered. In particular in case of sol-gel type precursor solutions the film formation is difficult to control and inhomogeneous coatings can result.

10.3.5.2 Angle-Dependent Dip Coating

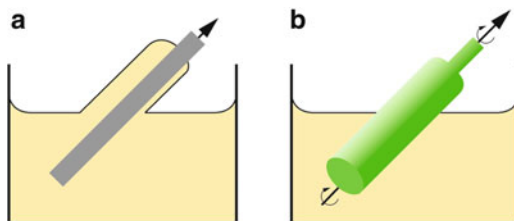
In another modification the substrate withdrawal from the precursor solution is performed under a variable angle of inclination [37–39].

Different film thicknesses on both sides of the substrate with the thicker-coating on the upper side (Fig. 10.6a) are the outcome of this technique [40], whereupon the coating thickness is dependent on the angle between the substrate and the liquid surface. Thus a large number of thickness combinations on both sides can be realized by simple variation of the angle of inclination, the withdrawal speed and the solution concentration. Due to increasing border effects on the upper side, however, the operational range is limited to angles of inclination $<60^\circ$ and withdrawal speeds <10 mm/s [36]. A main field of interest of such unsymmetric coating systems is the preparation of optical interference filters [38, 39] because the number of coating steps can be reduced in most cases compared to other techniques.

10.3.5.3 Other Modifications

Further adaption may be applied to tailor the dip-coating technique to the corresponding applications [36]. Since naturally both sides of the substrate are coated but sometimes only coating on one side is tolerable the other side has to be protected from being coated. In order to accomplish this either two substrates e.g. in case of flat glass, could be joined at the borders with a chemically inert glue so that the interior is sealed or alternatively the side which should not be coated is protected by an adhesive foil. After coating the glue is removed by thermal processing resulting in two single side coated substrates, or the protective foil is

Fig. 10.6 Schematic of the technical setup for ADDC; (a) planar substrates and (b) rotationally symmetric bodies like bottles which are revolved during the withdrawal process



peeled of before high temperature curing of the as-deposited or dried film. Variations of the classical technique are also required for substrates with complex shapes such as bottles, threads or flange tubes, due to problems with thickness variations. In particular if deepened or leveled regions are coated the liquid film is too thick and thus may flake off. By revolving such rotationally symmetric substrates during the withdrawal process eventually combined with an angle like in angle-dependent dip coating (ADDC), a sufficient film leveling even on horizontal areas can be achieved due to the superposed centrifugal forces (Fig. 10.6b).

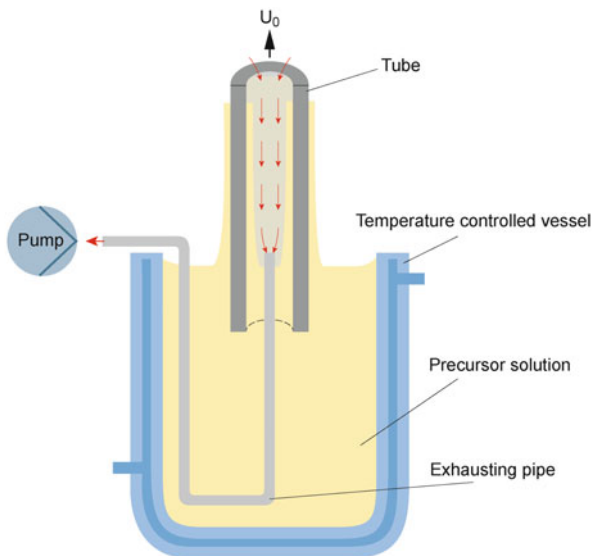
Even tubes and other cylindrical cavities can be coated from inside by special adaptations [41], which have to guarantee a forced laminar flow inside the tube in order to enable a complete solvent evaporation and hydrolysis of the film. Otherwise the drying of the liquid film is restricted in closed volumes due to saturation of evaporated solvents from the precursor solution and less hydrolysis. Puetz et al. [41] accomplished a suitable dip coating apparatus by an additional exhausting glass pipe (5 mm outer diameter) that was placed in the solution vessel and introduced from below into the tube with the internal end rising 5 mm above the solution (Fig. 10.7). After optimization optical ATO (antimony doped tin oxide) coatings were deposited inside tubes with inner diameters down to 11 mm exhibiting excellent thickness uniformity and an average roughness of less than 1 nm with a high reproducibility.

Beside these variations for batch conditions, continuous dip coating processes for endless flexible substrates like fibers and tapes are basically possible.

10.4 Evaporation Induced Self-Assembly

Among the modified dip coating methods the EISA process plays a prominent role since it allows not only for film formation but also for nanostructuring by using self-assembly principles of the nature. EISA is based on the fact that in dip coating film formation occurs through evaporation of solvents concentrating the system in non-volatile species (cp. Fig. 10.2), which leads to aggregation and gelation and hence can be also used to induce the formation of functional nanoscopic materials [42–46]. Thus precursor solutions containing amphiphilic molecules are utilized which become progressively concentrated through solvent evaporation thereby passing through structural and connectivity transitions taking place over seconds

Fig. 10.7 Experimental set-up for the dip coating of tubes under forced flow conditions consisting of an internal exhausting pipe and a temperature controlled vessel. The external end of the exhausting pipe was connected to a diaphragm vacuum pump with an adjustable, constant flow of air of up to 210 l/h. The flow of air that is necessary to obtain homogeneous films depends on the withdrawal speed, on the inner diameter of the tube and also on the coating solution so that an optimisation is necessary. Modified after [41]



or fractions of a second. Figure 10.8 shows the several stages which can be stated [47].

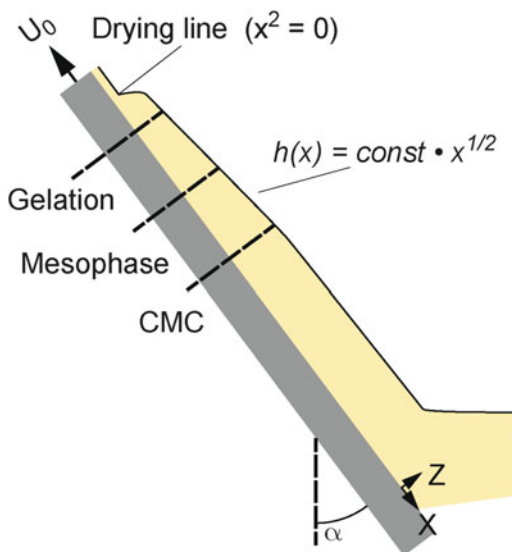
As the solution becomes concentrated, the first transition that is important is the critical micelle concentration (CMC), in which the amphiphiles aggregate together into micellar or lamellar structures in a self-assembly process (Sect. 10.4.1). Upon further evaporation-induced crowding, these aggregates interact to form mesophases whose structures are determined—assuming there is time for equilibrium—by the phase behavior of the solvent(s) and surfactant. Finally, there is gelation of the sol-gel species, effectively locking into place the mesophase structure as evinced by its presence after complete evaporation of the solvents. It should be mentioned that during this drying environmental conditions, such as relative humidity, temperature and air flow have large impact on the microstructure development and hence have to be carefully controlled since sol-gel chemistry is highly sensitive to the water content and temperature.

In the following subsections some basic aspects of the EISA process and examples are described by means of silica in more detail.

10.4.1 Some Basics of Self-Assembly

A general definition of self-assembly is the spontaneous organization of materials through non-covalent interactions (hydrogen bonding, Van der Waals forces, electrostatic forces, π - π interactions, etc.) with no external intervention. Self-assembly typically employs asymmetric molecules that are pre-programmed to organize into well-defined supramolecular assemblies. Most common are amphiphilic surfactant

Fig. 10.8 Schematic representation of the different stages occurring during the drying of a liquid precursor film in dip coating. For generality withdrawal (U_0) is depicted at an angle α with respect to the vertical. The sequential transitions leading to the ordered porosity in thin films by the EISA process include the critical micelle concentration (CMC), in which surfactants aggregate into micelles, a transition from isotropic to a mesophase, and gelation of the sol to lock the mesophase structure in place. Adapted from [47]

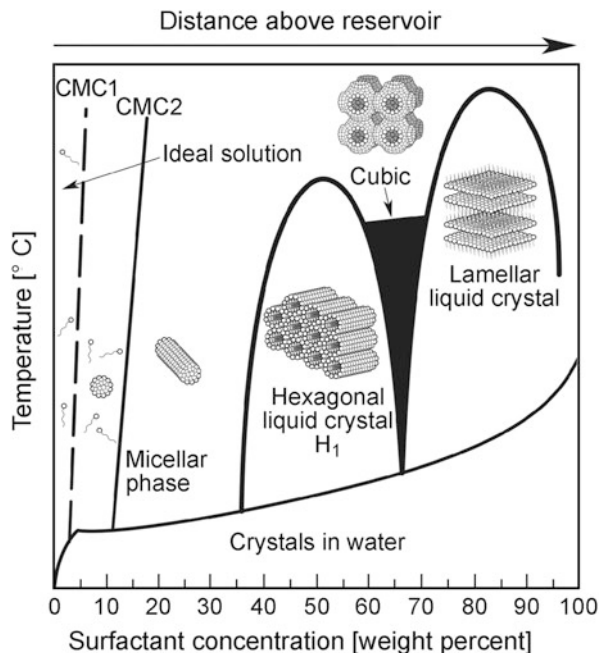


molecules or polymers composed of hydrophobic and hydrophilic parts. In aqueous solution above the CMC, surfactants assemble into micelles, spherical or cylindrical structures that maintain the hydrophilic parts of the surfactant in contact with water while shielding the hydrophobic parts within the micellar interior (see Fig. 10.9).

Further increases in surfactant concentration result in the self-organization of micelles into periodic hexagonal, cubic, or lamellar mesophases (see insets in Fig. 10.9). Obviously such detergent mesophases do not themselves represent robust engineering materials suitable for nanotechnologies. However in 1992 Mobil researchers [48] discovered that surfactant self-assembly conducted in aqueous solutions of soluble silica species results in spontaneous coassembly of silica-surfactant mesophases. Surfactant removal creates periodic mesoporous solids, essentially silica fossils of the liquid-crystalline assembly. Over the last years, this pioneering work has been extended to produce a wide compositional range of mesoporous solids, and, using a variety of surfactants, the pore sizes have been varied in the approximate range, 1 nm to over 10 nm [49–53].

Despite excellent control of pore size, early mesoporous materials were made in the form of powders, precluding their use in thin film applications like membranes, low dielectric constant interlayers, and optical sensors. Stable, supported, mesoporous silica films were reported in 1996 [54–56]. Typically, substrates were introduced into silica/surfactant/solvent systems used to prepare bulk hexagonal mesophases (initial surfactant concentrations $c_0 > \text{CMC}$). Under these conditions, hexagonal silica-surfactant mesophases are nucleated on the substrate with pores oriented parallel to the substrate surface. Growth and coalescence over a period of hours to weeks resulted in continuous but macroscopically inhomogeneous films

Fig. 10.9 Schematic phase diagram for cetyltrimethylammonium bromide (CTAB) in water. *Arrow* denotes evaporation-driven pathway during dip-coating, aerosol processing, etc. (Figure from [43] Brinker CJ, Lu YF, Sellinger A, Fan HY (1999) Evaporation-induced self-assembly: Nanostructures made easy. *Adv Mater* 11:579–585)

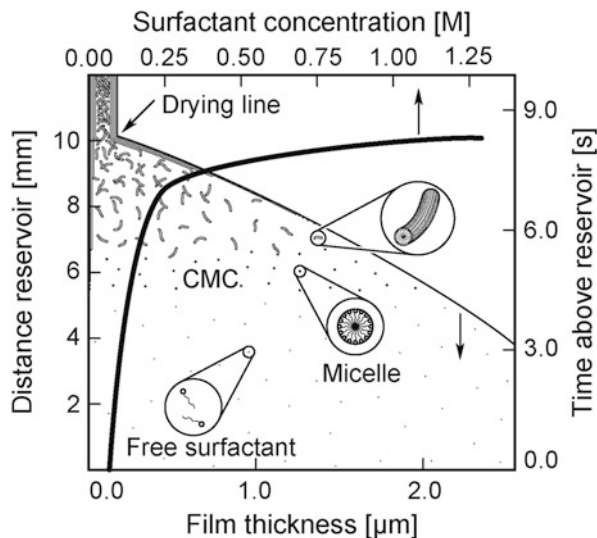


characterized by granular textures on micrometer-length scales. Göltner and Antonietti reviewed the advantages of direct templating by using liquid crystalline phases in the generalized preparation of mesoporous materials [57].

10.4.2 Details of the EISA Process

Consideration of Fig. 10.9 in the context of sol-gel dip coating suggests an alternative route to the formation of thin film mesophases. Beginning with a homogeneous solution of soluble silica and surfactant prepared in ethanol/water solvent with $c_0 \ll \text{CMC}$, preferential evaporation of ethanol concentrates the depositing film in water and nonvolatile surfactant and silica species (Fig. 10.10). The progressively increasing surfactant concentration drives self-assembly of silica-surfactant micelles and their further organization into various liquid crystalline mesophases [46, 58, 59]. Pre-existing, incipient silica-surfactant mesostructures (which exist at solid-liquid and liquid-vapor interfaces at $c < \text{CMC}$) serve to nucleate and orient the mesophase development [54, 59]. The result is rapid formation of thin film mesophases that are highly oriented with respect to the substrate surface. Through variation of the initial alcohol/water/surfactant molar ratio it is possible to follow different trajectories in composition space and to arrive at different final mesostructures. For example, using cetyltrimethylammonium bromide (CTAB), the formation of 1-D hexagonal, cubic, 3-D hexagonal and lamellar silica-surfactant

Fig. 10.10 Steady-state film thinning profile established during dip-coating of a complex fluid comprising soluble silica, surfactant, alcohol, and water. Initial surfactant concentration $c_0 \ll \text{CMC}$. Surfactant concentration increases with distance above the reservoir surface. Figure from [43]



mesophases was demonstrated [46, 56, 60]. Cubic thin film mesophases e.g. are essential for applications like membranes and sensors because they guarantee pore accessibility and through-film pore connectivity.

The dip coating scheme depicted in Fig. 10.10 represents a rapid (~ 10 s), dynamic self-assembly process conducted in a rather steep concentration gradient. Its steady, continuous nature promotes continuous accretion of micellar or perhaps liquid-crystalline species onto interfacially organized mesostructures. Large, liquid-crystalline domains grow progressively inward from the solid-liquid and liquid-vapor interfaces (with increasing distance above the reservoir surface, Fig. 10.10). Deposited films are optically transparent and completely featureless on the micrometer-length scale.

Essential to the ability to rapidly organize thin film mesophases is suppression of inorganic polymerization during the coating operation. For silicates this is achieved under acidic conditions at a hydronium ion concentration corresponding closely to the isoelectric point of colloidal silica ($[\text{H}_3\text{O}^+] \sim 0.01$) [2]. By first turning off siloxane condensation, an unimpeded proceeding of a cooperative silica-surfactant self-assembly is enabled, and the resulting as-deposited films exhibit liquid-crystalline (semi-solid) behavior. Thus the depositing film maintains a fluid state, even beyond the point where ethanol and water are largely evaporated. Subsequent aging, exposure to acid or base catalysts, or thermal treatment can solidify the silica skeleton, thereby locking in the desired mesostructure. Evidence for the liquid-crystalline nature of as-deposited films is several-fold:

1. There is dramatically less tensile stress developed during mesophase thin film deposition (5–10 MPa) compared to deposition of the same silica sol prepared without surfactants (~ 200 MPa). This virtual absence of drying stress suggests

that the film completely dries prior to solidification (i.e., as-deposited films are not solidified) [43].

2. Completely different mesophases (e.g., lamellar \rightarrow cubic) can be obtained by transformation from the as-deposited mesophase films [46].
3. The as-deposited films exhibit self-healing tendencies, which enables the use of virtually any evaporation-driven process (spin-/dip coating, inkjet printing [61], or aerosol processing [44, 62] to create ordered nanostructures films, patterns [63], or particles. Even on complex shapes of (curved and flat) substrates (silicon wafers, glass slides, polymeric transparencies) self-assembled mesostructured silica can be prepared by a robot-directed aerosol printing process [62].

These combined liquid-crystalline characteristics make the EISA process robust and versatile. Due to this potential several other material systems have been successfully prepared meanwhile. For more details the reader is referred to some corresponding original works and references therein [64–68].

10.4.3 Extensions of EISA

In order to develop specific processes for different application purposes the EISA conditions have been modified and extended, respectively. Since an exhaustive description of all extensions leading to a bunch of periodically organized materials is beyond the scope of this chapter, two examples presented briefly in the following may serve to illustrate the possibilities.

10.4.3.1 Organic-Inorganic Nanocomposites

In standard EISA processing a calcination or solvent extraction step to remove the solvent follows in order to create inorganic mesoporous materials. Alternatively, EISA was used to create nanocomposite materials in which organic polymers or other organic components are uniformly incorporated within a periodic inorganic nanostructure [69]. The nanoscale organization of hard and soft materials is of interest for the development of optimized mechanical properties similar to those that occur in natural materials such as seashells, which are composed of alternating layers of crystalline calcium carbonate and biopolymers.

By using alcohol or tetrahydrofuran (THF) as a cosolvent, homogeneous, complex, multicomponent solutions can be prepared containing (in addition to the silicic acid precursors), organic monomers, cross-linkers, initiators, and coupling agents. During EISA, preferential evaporation of alcohol or THF concentrates the system in water. Rather than undergoing macroscopic phase separation, the hydro-phobic components are incorporated into micelles and mesophases. This allows hundreds of alternating silica/organic layers to be organized in a single step [69]. Subsequent in situ organic/inorganic polymerization results in a poly

(alkyl methacrylate)/silica nanocomposite with a covalently bonded polymer/silica interface. Such structures bear some relationship to seashells and other natural materials that are simultaneously hard, tough, and strong, i.e. mimicking biology.

An advancement of this nanocomposite self-assembly strategy is the use of polymerizable surfactants as structure-directing agents and monomers [70, 71]. The surfactant organizes the silicate nanostructure, as described earlier; subsequently, light, heat, or another treatment is used to polymerize the surfactant monomers, uniformly confined within a nanometer-scale “reaction vessel.” As an advantage of this approach it is expected that the monomers to be uniformly organized within the surfactant mesophase, allowing potentially facile topochemical polymerization, where the topography of the monomeric diacetylenic (DA) assembly is preserved in the polymerized product, polydiacetylene (PDA). Using this approach Lu et al. [70] got blue PDA/silica nanocomposites after UV exposure, that exhibited thermo-, solvato- and mechanochromism, which are coloration effects occurring in response to thermal, mechanical, and chemical stimuli, respectively, to form the red fluorescent form. It should be noted that these properties are normally not observed in bulk PDA.

10.4.3.2 Nanocrystal Self-Assembly

The nanocomposite self-assembly strategy described above was expanded by employing other hydrophobic components in addition to hydrophobic organic monomers/molecules. Fan et al. investigated the self-assembly of hydrophobic nanocrystal (NC) mesophases within hydrophilic silica mesophases [72].

Typical NC synthesis procedures use hydrophobic ligands (alkane thiols, trioctylphosphine oxide, etc.) to stabilize them from aggregation. Monosized NCs can be considered as moderate-sized hydrophobic molecules. It has been postulated that their incorporation as individual NCs in surfactant micelles would allow further self-assembly into ordered nanocrystalline mesophases, as anticipated from generic detergent phase diagrams. Rather than add hydrophobic NCs directly to isotropic surfactant/solvent/silica systems, as in polymer/silica self-assembly, a generic microemulsion procedure was developed to create water-soluble nanocrystal micelles. As represented schematically in Fig. 10.11a, a concentrated nanocrystal solution prepared in organic solvent (chloroform, hexane, etc.), is added to an aqueous solution of surfactant under vigorous stirring to create an oil-in-water microemulsion. Organic solvent evaporation then transfers the NCs into the aqueous phase by an interfacial process driven by the hydrophobic van der Waals interactions between the primary alkanes of the NC stabilizing ligands and the secondary alkane of the surfactant. This results in thermodynamically defined interdigitated bilayer structures (Fig. 10.11b). Cationic, anionic, and non-ionic surfactants and phospholipids can all form NC micelles, allowing facile control of micelle surface charge and functionality. In addition, fluorescent semiconducting CdSe NCs (stabilized by trioctylphosphine oxide) have been formed into NC

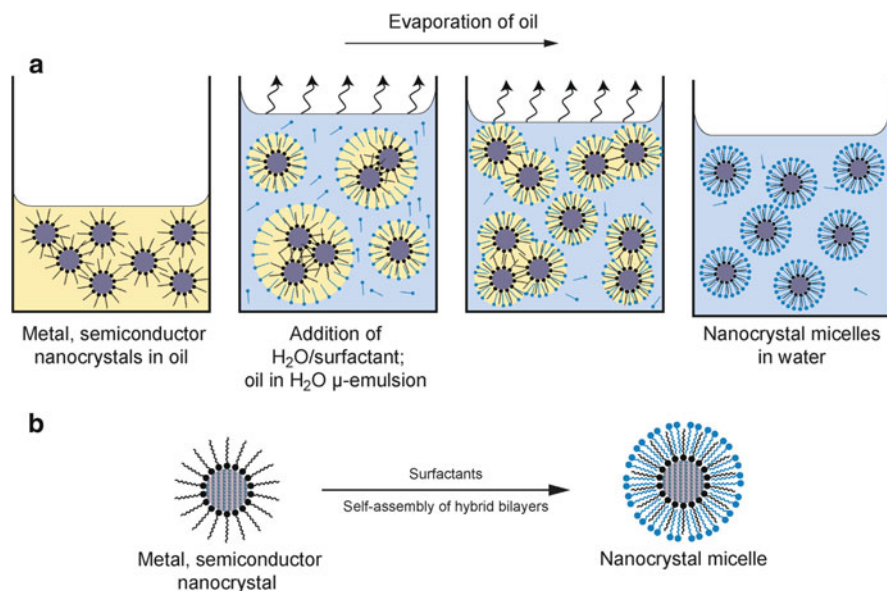


Fig. 10.11 Process scheme for the synthesis of water-soluble nanocrystal micelles. (a) The addition of oil containing nanocrystals (NCs) to a surfactant containing aqueous solution during vigorous stirring leads to the formation of an oil in H_2O microemulsion. Subsequent evaporation of oil transfers the NCs into the aqueous phase by an interfacial process driven by the hydrophobic van der Waals interactions between the primary alkane of the stabilizing ligand and the secondary alkane of the surfactant, resulting in thermodynamically defined interdigitated bilayer structures that encapsulate the NCs and make them water-soluble (b). Figure modified after [42]

micelles with maintenance of optical properties. This demonstrates the general nature and flexibility of this approach.

It has been discovered that in aqueous media, NC micelles organize hydrophilic components or precursors at the surfactant/water interface. This occurs through electrostatic and hydrogen-bonding interactions in a mechanism analogous to that of surfactant-directed self-assembly of silica/surfactant mesophases [73].

For example, addition of tetraethyl orthosilicate under **basic conditions** results in the formation of hydrophilic oligo-silicic acid species that organize with NC micelles to form a new type of ordered gold NC/silica mesophase. This nanocrystal mesophase has fcc symmetry (space group $\text{Fm}\bar{3}\text{m}$) [72]. From a TEM investigation a fcc unit cell with a $\cong 10.2$ nm and uniform spacing between NCs of $\cong 6$ nm was deduced. This work [72] appears to be the first example of an ordered fcc nanocrystal array formed spontaneously by self-assembly in aqueous media rather than by solvent evaporation [74, 75]. Compared with other ordered NC arrays, the embedding silica matrix provides for greater chemical, mechanical, and thermal robustness. Furthermore, thermodynamically controlled self-assembly provides greater order and control of NC spacing, as compared with other connected nanocrystal systems such as those prepared by DNA hybridization [76, 77].

Thin film formation by means of typical deposition techniques like spin coating, etc. is allowed if **acidic conditions** designed to minimize the siloxane condensation rate are used. By suppressing siloxane condensation, and thereby gel formation, solvent evaporation accompanying coating induces self-assembly of NC micelles into fcc nano-crystal thin-film mesophases. This occurs in a manner similar to the evaporation-induced self-assembly of cubic or hexagonal silica/surfactant thin-film mesophases discussed earlier [46].

The formed ordered 3D NC arrays have been the subject of considerable interest, as they serve as model “artificial solids” with tunable electronic, magnetic, and optical properties stemming from single-electron charging and quantum confinement energies of individual NCs mediated by coupling interactions with neighboring NCs. Initial investigations of the charge transport properties of an ordered 3D nanocrystal array have been performed by means of planar metal–insulator–metal (MIM) devices, incorporating a Au NC/silica array as the insulator layer [72].

10.5 Summary

Although one of the oldest and apparently simplest film deposition methods, it is the dip coating process that serves as the link between the structure and properties of the liquid precursor sol and the microstructure of the corresponding deposited film. In spite of the fact that no universally valid model for the dip coating process has been obtained yet, the increasingly gained knowledge enables the controlled fabrication of various thin film microstructures from dense to ordered porous, nanocrystalline. Thereby film thickness is determined by the competition between surface tension (capillary force), gravity and viscosity. In many systems as a rule of thumb the faster the substrate is withdrawn, the thicker the film deposited. On the other hand however, thicker films may also be obtained if the “capillarity regime” is applied, where very low withdrawal speeds are used. Here solvent evaporation becomes faster than the movement of the drying line leading to a continuous feeding of the upper part of the meniscus and finally also to thicker films.

Since evaporation plays an important role in dip coating, the combination with suitable surfactants enables self-assembly of sol-gel precursor species leading to ordered nanoscopic thin films. Numerous variations of the generalized EISA process leading to ordered porous thin-film nanostructures have been carried out. Such porous materials are of interest for membranes, low-dielectric-constant (low-k) insulators, and dye sensitized solar cells. EISA can also be used to simultaneously organize hydrophilic and hydrophobic precursors into hybrid nanocomposites that are optically or chemically polymerizable, patternable, or adjustable. In some cases, even a pathway to materials is provided, that have no bulk nanostructured counter-parts (e.g., organic/inorganic nanocomposites). It is expected that further modifications of the theme of EISA processing will provide a convenient pathway to the formation of functional hierarchical devices, also in order to better emulate biology.

References

1. Geffcken W, Berger E (1939) Verfahren zur Änderung des Reflexionsvermögens optischer Gläser. Deutsches Reichspatent, assigned to Jenaer Glaswerk Schott & Gen., Jena 736 411
2. Brinker CJ, Scherer GW (1990) Sol-gel science. The physics and chemistry of sol-gel processing. Academic, San Diego
3. Baes CF, Mesmer RE (1976) The hydrolysis of cations. Wiley, New York
4. Livage J, Henry M, Sanchez C (1988) Sol-gel chemistry of transition metal oxides. *Prog Solid State Chem* 18:259–342
5. Brinker CJ, Hurd AJ, Frye GC, Schunk PR, Ashley CS (1991) Sol-gel thin film formation. *J Ceram Soc Jpn* 99:862–877
6. Scriven LE (1988) Physics and application of dip-coating and spin-coating. In: Brinker CJ, Clark DE, Ulrich DR (eds) Better ceramics through chemistry III, vol 121, Materials Research Society symposium proceedings. Materials Research Society, Pittsburgh, PA, pp 717–729
7. Landau LD, Levich VG (1942) Dragging of a liquid by a moving plate. *Acta Phys Chim URSS* 17:42–54
8. Grosso D (2011) How to exploit the full potential of the dip-coating process to better control film formation. *J Mater Chem* 21:17033–17038
9. Faustini M, Louis B, Albouy PA, Kuemmel M, Grosso D (2010) Preparation of sol-gel films by dip-coating in extreme conditions. *J Phys Chem C* 114:7637–7645
10. Lee CH, Lu YF, Shen AQ (2006) Evaporation induced self-assembly and rheology change during sol-gel coating. *Phys Fluids* 18:052105–052111
11. Brinker CJ, Hurd AJ, Schunk PR, Ashley CS (1992) Review of sol-gel thin film formation. *J Non Cryst Solids* 147–148:424–436
12. Hurd AJ, Brinker CJ (1988) Optical sol-gel coatings ellipsometry of film formation. *J Phys France* 49:1017–1025
13. Nishida F, Dunn B, Mckiernan JM, Zink JJ, Brinker CJ, Hurd AJ (1994) In situ fluorescence imaging of sol-gel thin film deposition. *J Sol-Gel Sci Technol* 2:477–481
14. Nishida F, Mckiernan JM, Dunn B, Zink JJ, Brinker CJ, Hurd AJ (1995) In situ fluorescence probing of the chemical changes during sol-gel thin film formation. *J Am Ceram Soc* 78:1640–1648
15. Hurd AJ (1994) Evaporation and surface tension effects in dip coating. In: Bergna HE (ed) The colloid chemistry of silica, vol 234, Advances in chemistry series. American Chemical Society, Washington, DC, pp 433–450, Chapter 21
16. Hurd AJ, Brinker CJ (1990) Sol-gel film formation by dip coating. In: Zelinski BJJ, Brinker CJ, Clark DE, Ulrich DR (eds) Better ceramics through chemistry IV, vol 180, Materials Research Society symposium proceedings. Materials Research Society, Pittsburgh, PA, pp 575–581
17. Schwartz RW, Voigt JA, Buchheit CD, Boyle TJ (1994) Densification and crystallization of zirconia thin films prepared by sol-gel processing. *Ceram Trans* 43:145–163
18. Scherer GW (1992) Recent progress in drying of gels. *J Non-Cryst Solids* 147–148:363–374
19. Croll SG (1979) The origin of residual internal stress in solvent-cast thermoplastic coatings. *J Appl Polymer Sci* 23:847–853
20. Evans AJ, Dory MD, Hu MS (1988) The cracking and decohesion of thin films. *J Mater Res* 3:1043–1054
21. Thouless MD (1988) Decohesion of films with axisymmetric geometrics. *Acta Metall* 36:3131–3139
22. Meakin P (1991) Models for materials failure and deformation. *Science* 252:226–229
23. Atkinson A, Guppy RM (1991) Mechanical stability of sol-gel films. *J Mater Sci* 26:3869–3875
24. Garino TJ (1990) The cracking of sol-gel thin films during drying. In: Zelinski BJJ, Brinker CJ, Clark DE, Ulrich DR (eds) Better ceramics through chemistry IV, vol 180, Materials Research Society symposium proceedings. Materials Research Society, Pittsburgh, PA, pp 497–502

25. Cohen ED, Guttoff EB, Lightfoot EJ (1990) A primer on forming coatings. *Chem Eng Prog* 86:30–36
26. Takahashi Y, Matsuoka Y, Yamaguchi K, Matsuki M, Kobayashi K (1990) Dip coating of PT, PZ, and PZT films using an alkoxide-diethanolamine method. *J Mater Sci* 25:3960–3964
27. Schmidt H, Rinn G, Nass R, Sporn D (1988) Film formation by inorganic-organic sol-gel synthesis. In: Brinker CJ, Clark DE, Ulrich DR (eds) *Better ceramics through chemistry III*, vol 121, Materials Research Society symposium proceedings. Materials Research Society, Pittsburgh, PA, pp 743–752
28. Garino TJ (1988) PhD Thesis, MIT
29. Brinker CJ, Scherer GW (1990) Sol-gel science. The physics and chemistry of sol-gel processing. Academic, San Diego, pp 235–301, Chapter 4
30. Bhavé RR (ed) (1991) *Inorganic membranes*. Van Nostrand Reinhold, New York (many examples are provided)
31. Brinker CJ, Hurd AJ, Frye GC, Ward KJ, Ashley CS (1990) Sol-gel thin film formation. *J Non-Cryst Solids* 121:294–308
32. Brinker CJ, Scherer GW (1990) Sol-gel science. The physics and chemistry of sol-gel processing. Academic, San Diego, pp 493–505, Chapter 8
33. Deshpande R, Hua D-W, Smith DM, Brinker CJ (1992) Pore structure evolution in silica gels during aging and drying: 3. Effects of surface tension. *J Non-Cryst Solids* 144:32–43
34. Brinker CJ, Frye GC, Hurd AJ, Ashley CS (1991) Fundamentals of sol-gel dip coating. *Thin Solid Films* 201:97–108
35. Warren WL, Lenahan PM, Brinker CJ, Shaffer GR, Ashley CS, Reed ST (1990) Sol-gel thin film electronic properties. In: Zelinski BJJ, Brinker CJ, Clark DE, Ulrich DR (eds) *Better ceramics through chemistry IV*, vol 180, Materials Research Society symposium proceedings. Materials Research Society, Pittsburgh, PA, pp 413–419
36. Puetz J, Aegerter MA (2004) Dip coating technique. In: Aegerter MA, Mennig M (eds) *Sol-gel technologies for glass producers and users*, 1st edn. Kluwer, Boston
37. Schröder H (1969) Oxide layers deposited from organic solutions. In: Hass G, Thun RE (eds) *Physics of thin films*, vol 5. Academic, London, pp 87–141
38. Arfsten NI, Eberle A, Otto J, Reich A (1997) Investigations on the angle-dependent dip coating technique (ADDC) for the production of optical filters. *J Sol-Gel Sci Technol* 8:1099–1104
39. Mennig M, Oliveira PW, Frantzen A, Schmidt H (1999) Multilayer NIR reflective coatings on transparent plastic substrates from photopolymerizable nanoparticulate sols. *Thin Solid Films* 351:225–229
40. Tallmadge IA (1971) A theory of entrainment for angular withdrawal of flat supports. *AIChE J* 17:243–246
41. Puetz J, Chalvet FN, Aegerter MA (2003) Wet chemical deposition of transparent conducting coatings in glass tubes. *Thin Solid Films* 442:53–59
42. Brinker CJ (2004) Evaporation-induced self-assembly: functional nanostructures made easy. *MRS Bull* 29:631–639
43. Brinker CJ, Lu YF, Sellinger A, Fan HY (1999) Evaporation-induced self-assembly: nanostructures made easy. *Adv Mater* 11:579–585
44. Lu YF, Fan HY, Stump A, Ward TL, Rieker T, Brinker CJ (1999) Aerosol-assisted self-assembly of mesostructured spherical nanoparticles. *Nature* 398:223–226
45. Lu YF, Cao GZ, Kale RP, Prabakar S, Lopez GP, Brinker CJ (1999) Microporous silica prepared by organic templating: relationship between the molecular template and pore structure. *Chem Mater* 11:1223–1229
46. Lu Y, Ganguli R, Drewien CA, Anderson MT, Brinker CJ, Gong W, Guo Y, Soyoz H, Dunn B, Huang MH, Zink JI (1997) Continuous formation of supported cubic and hexagonal mesoporous films by sol-gel dip-coating. *Nature* 389:364–368
47. Hurd AJ, Steinberg L (2001) The physics of evaporation-induced assembly of sol-gel materials. *Granul Matter* 3:19–21

48. Kresge C, Leonowicz M, Roth W, Vartuli C, Beck J (1992) Ordered mesoporous molecular sieves synthesized by a liquid-crystal template mechanism. *Nature* 359:710–712
49. Huo Q, Margolese D, Ciesla U, Feng P, Gier TG, Sieger P, Leon R, Petroff PM, Schuth F, Stucky G (1994) Generalized synthesis of periodic surfactant/inorganic composite materials. *Nature* 368:317–321
50. Firouzi A, Kumar D, Bull LM, Besier T, Sieger P, Huo Q, Walker SA, Zasadzinski JA, Glinka C, Nicol J, Margolese D, Stucky GD, Chmelka BF (1995) Cooperative organization of inorganic-surfactant and biomimetic assemblies. *Science* 267:1138–1143
51. Tanev PT, Pinnavaia TJ (1995) A neutral templating route to mesoporous molecular sieves. *Science* 267:865–867
52. Antonelli DM, Ying JY (1995) Synthesis of hexagonally packed mesoporous TiO₂ by a modified sol–gel method. *Angew Chem Int Ed Engl* 34:2014–2017
53. Zhao D, Feng J, Huo Q, Nelosh N, Fredrickson G, Chmelka B, Stucky GD (1998) Triblock copolymer syntheses of mesoporous silica with periodic 50 to 300 angstrom pores. *Science* 279:548–552
54. Aksay I, Trau M, Manne S, Honma I, Yao N, Zhou L, Fenter P, Eisenberger P, Gruner S (1996) Biomimetic pathways for assembling inorganic thin films. *Science* 273:892–898
55. Yang H, Kuperman A, Coombs N, Mamiche-Afara S, Ozin GA (1996) Synthesis of oriented films of mesoporous silica on mica. *Nature* 379:703–705
56. Ogawa M (1996) A simple sol–gel route for the preparation of silica–surfactant mesostructured materials. *Chem Commun* 1996:1149–1150
57. Göltner CG, Antonietti M (1997) Mesoporous materials by templating of liquid crystalline phases. *Adv Mater* 9:431–436
58. Bruinsma PJ, Kim AY, Liu J, Baskaran S (1997) Mesoporous silica synthesized by solvent evaporation: spun fibers and spray-dried hollow spheres. *Chem Mater* 9:2507–2512
59. Ogawa M (1994) Formation of novel oriented transparent films of layered silica–surfactant nanocomposites. *J Am Chem Soc* 116:7941–7942
60. Yang H, Coombs N, Sokolov I, Ozin GA (1996) Free-standing and oriented mesoporous silica films grown at the air–water interface. *Nature* 381:589–592
61. Fan H, Lu Y, Stump A, Reed ST, Baer T, Schunk R, Perez-Luna V, López GP, Brinker CJ (2000) Rapid prototyping of patterned functional nanostructures. *Nature* 405:56–60
62. Pang J, Stuecker JN, Jiang Y, Bhakta AJ, Branson ED, Li P, Cesarano J III, Sutton D, Calvert P, Brinker CJ (2008) Directed aerosol writing of ordered silica nanostructures on arbitrary surfaces with self-assembling inks. *Small* 4:982–989
63. Doshi DA, Huesing NK, Lu M, Fan H, Lu Y, Simmons-Potter K, Potter BG Jr, Hurd AJ, Brinker CJ (2000) Optically defined multifunctional patterning of photosensitive thin-film silica mesophases. *Science* 290:107–111
64. Brezesinski K, Haetge J, Wang J, Mascotto S, Reitz C, Rein A, Tolbert SH, Perlich J, Dunn B, Brezesinski T (2011) Ordered mesoporous α -Fe₂O₃ (Hematite) thin-film electrodes for application in high rate rechargeable lithium batteries. *Small* 7:407–414
65. Kuemmel M, Grosso D, Boissière C, Smarsly B, Brezesinski T, Albouy PA, Amenitsch H, Sanchez C (2005) Thermally stable nanocrystalline γ -alumina layers with highly ordered 3D mesoporosity. *Angew Chem Int Ed* 44:4589–4592
66. Smarsly B, Grosso D, Brezesinski T, Pinna N, Boissière C, Antonietti M, Sanchez C (2004) Highly crystalline cubic mesoporous TiO₂ with 10-nm pore diameter made with a new block copolymer template. *Chem Mater* 16:2948–2952
67. Grosso D, Boissière C, Smarsly B, Brezesinski T, Pinna N, Albouy PA, Amenitsch H, Antonietti M, Sanchez C (2004) Periodically ordered nanoscale islands and mesoporous films composed of nanocrystalline multimetallic oxides. *Nat Mater* 3:787–792
68. Grosso D, Cagnol F, Soler-Illia GJAA, Crepaldi EL, Amenitsch H, Brunet-Bruneau A, Bourgeois A, Sanchez C (2004) Fundamentals of mesostructuring through evaporation-induced self-assembly. *Adv Funct Mater* 14:309–322

69. Sellinger A, Weiss PM, Nguyen A, Lu Y, Assink RA, Gong W, Brinker CJ (1998) Continuous self-assembly of organic–inorganic nanocomposite coatings that mimic nacre. *Nature* 394:256–260
70. Lu Y, Yang Y, Sellinger A, Lu M, Huang J, Fan H, Haddad R, Lopez G, Burns Alan R, Sasaki DY, Shelnutt J, Brinker CJ (2001) Self-assembly of mesoscopically ordered chromatic polydiacetylene/silica nanocomposites. *Nature* 410:913–917
71. Yang Y, Lu Y, Lu M, Huang J, Haddad R, Xomeritakis G, Liu N, Malanoski AP, Sturmayer D, Fan H, Sasaki DJ, Assink RA, Shelnutt JA, van Swol F, Lopez GP, Burns AR, Brinker CJ (2003) Functional nanocomposites prepared by self-assembly and polymerization of diacetylene surfactants and silicic acid. *J Am Chem Soc* 125:1269–1277
72. Fan H, Yang K, Boye DM, Sigmon T, Malloy KJ, Xu H, Brinker CJ (2004) Self-assembly of ordered, robust, three-dimensional gold/silica nanocrystal arrays. *Science* 304:567–571
73. Beck JS, Vartuli JC, Roth WJ, Leonowicz ME, Kresge CT, Schmitt KD, Chu CTW, Olson DH, Sheppard EW, McCullen SB, Higgins JB, Schlenker JL (1992) A new family of mesoporous molecular sieves prepared with liquid crystal templates. *J Am Chem Soc* 114:10834–10843
74. Murray CB, Kagan CR, Bawendi MG (1995) Self-organization of CdSe nanocrystallites into three-dimensional quantum dot superlattices. *Science* 270:1335–1338
75. Sun SH, Murray CB, Weller D, Folks L, Moser A (2000) Nanocrystal superlattices monodisperse FePt nanoparticles and ferromagnetic FePt. *Science* 287:1989–1992
76. Mirkin CA, Letsinger RL, Mucic RC, Storhoff JJ (1996) A DNA-based method for rationally assembling nanoparticles into macroscopic materials. *Nature* 382:607–609
77. Alivisatos AP, Johnsson KP, Peng XG, Wilson TE, Loweth CJ, Bruchez MP, Schultz PG (1996) Organization of ‘nanocrystal molecules’ using DNA. *Nature* 382:609–611

Chapter 11

Spin Coating: Art and Science

Dunbar P. Birnie III

11.1 Introduction and Outline

Spin coating can be thought of as having three important stages: (1) dispense of the coating solution, (2) fluid flow dominated thinning, and (3) solvent evaporation and coating “set”. These three aspects will be described in sequence, though the stages are not always very distinctly separated in time. During the first stage, a quantity of the desired coating solution (usually the coating material is well dissolved in an appropriate solvent) is dispensed onto a smooth substrate. For single wafers or small numbers of samples then this may be done manually with a pipette or syringe. It is usually important during the dispense stage to ensure that the full extent of the substrate will be covered with coating solution. Therefore in some cases the spin coater is set to rotate at a very low speed to help facilitate a slow outflow of solution and full wetting of the surface. For automated systems and mass production then the dispense nozzles may even have programmed motion over the slowly spinning substrate to help ensure full wetting and coverage. Since good coverage of the spinning wafer by the solution is important to help ensure good coating quality then it may be important to consider making modifications to the coating solution (or substrate) to ensure good wetting. For example, the substrate surface may need a pretreatment to change it from hydrophobic to hydrophilic (or vice versa) depending on the nature of the coating solution. Or it may be advantageous to add a surfactant into the formulation to help facilitate complete substrate coverage during dispense.

Next, the spin coater is accelerated to a faster spinning speed (often in the range of a couple thousand rotations per minute, RPM's). For some spin coater controllers the speed may be reached nearly instantly, in other cases this is done by ramping up to that speed over a specified number of seconds. More gradual ramping is better for

D.P. Birnie III (✉)

Department of Materials Science and Engineering, Rutgers, The State University
of New Jersey, New Brunswick, NJ, USA

e-mail: dunbar.birnie@rutgers.edu

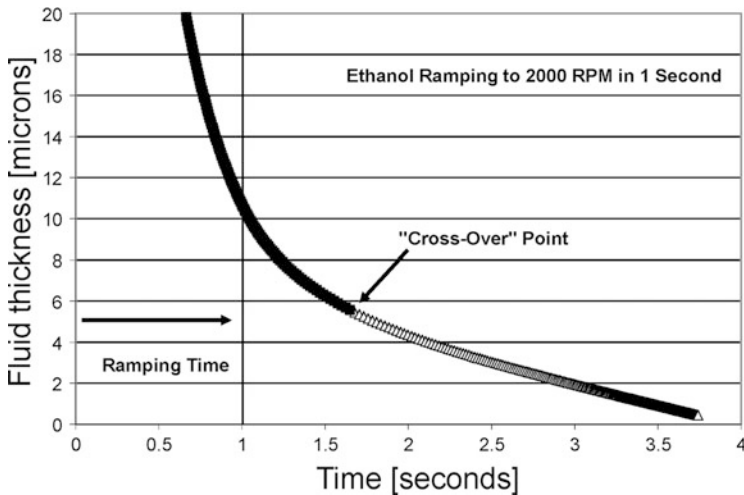


Fig. 11.1 Fluid thickness evolution with time for ethanol ramping up with constant acceleration to a spin speed of 2,000 RPM in a period of 1 s and then holding. The fluid started at 100 microns thick at time zero. The *filled black squares* are thickness values where flow is dominating the process (stage 2). The *open triangles* denote fluid thickness values where evaporation is controlling the thinning (stage 3). “Cross-over” refers to the time when the process evolves from stage 2 to stage 3

spinner longevity, but the details of ramping rate and final spin speed *do* impact the final coating thickness and may influence coating uniformity as well. Finally, this peak spin speed is held constant for a set time period (often 30–60 s) allowing the combined effects of fluid flow and solvent evaporation to leave a very thin layer of coating material on the substrate. The coated wafer may then be subjected to further processing (heating, photo-polymerization, washing, etc.).

Figure 11.1 shows the results of a simple fluid dynamic calculation for a flow of ethanol as an example (based on the governing equations described further below [1]). This helps to illustrate the progress of these stages and the effect it might have on the final coating development. It is noteworthy that for solvents with a moderate volatility (like ethanol, shown here) then the evolution of the process to the last stage and evaporative drying happens very early, here less than 2 s into the process, even considering a slow ramp up to speed. Also, the fluid thickness values help to explain the final coating thicknesses that might be accessible; the coating materials would normally be dissolved in the solvent and seldom more concentrated than 5 % or 10 % of the volume of the solution. So, for example an ethanolic solution at 5 % concentration would dry to a gel layer that might be only a quarter micron in thickness. Further thickness reduction might also happen during annealing if the coating constituents decomposed or were pyrolyzed to make the final microstructure.

Thus, the “art” of spin coating requires the formulation of a stable coating solution and testing that solution under a variety of spinning protocols and mapping out the resultant final thickness values—and further characterization of the coating properties to ensure the right properties are achieved and that adequate uniformity has resulted. Often, since final coating thickness is usually a key device parameter, then master plots might be constructed that map the thickness that results (after annealing) for different values of final (stage 3) spin speed that were used (that being the primary process variable). As long as the coating solution is not aging when stored (often this *cannot* be assumed, though), then this master plot can be used to select a spin speed to achieve a specific desired final coating thickness. The ability to rely on the process reproducibility is important, but since changes in key solution properties are critical (e.g. viscosity), then in some cases it is valuable to delve further into the physics of fluid flow and solvent evaporation during the spin coating process. This is the topic for the next section of this chapter.

11.2 Fundamentals of Fluid Flow and Evaporation

The basic physics of fluid flow on a spinning substrate has been rigorously described in the seminal work of Emslie, Bonner, and Peck [2] (hereafter referred to as “EBP”). The fluid layer is assumed to be thin enough that the radial rotational forces are exactly offset by the viscous drag imposed within the fluid. Mathematically, this force balance is expressed by this differential equation (Eq. 11.1):

$$-\eta \frac{\partial^2 v}{\partial z^2} = \rho \omega^2 r \quad (11.1)$$

where: η is the fluid’s viscosity, v measures the radial velocity component, z is a vertical height dimension, ρ is the fluid density, ω is the rotation rate, and r is the radius being considered.

Note, that the left hand side calculates the gradient in the shear developed by the velocity vs. depth profile and that this must exactly balance the rotational forces felt by the same volume element. When this equation was solved with the appropriate boundary conditions, EBP found the following expression for the fluid velocity profile with depth:

$$v = \frac{1}{\eta} \rho \omega^2 r \left[hz - \frac{z^2}{2} \right] \quad (11.2)$$

where, h is the instantaneous fluid thickness and z is the internal height coordinate ranging from 0 to h . By integrating over z they were able to determine the total fluid thinning rate and derive a function for the fluid depth versus time. Their thinning rate was found to be:

$$\frac{dh}{dt} = -2Kh^3 \quad (11.3)$$

where K is a flow constant defined by:

$$K = \frac{\rho\omega^2}{3\eta} \quad (11.4)$$

Interestingly, this thinning rate and flow constant are both independent of radius, even though the viscous forces (in Eq. 11.2) do include a radius factor. This is one of the key advantages of spin coating: that basic flow physics favors general coating uniformity, a key attribute when trying to make consistent devices over the entire area of a wafer being coated.

EBP's treatment neglected the fact that most coating solutions have volatile solvents in the recipe, and that the evaporation of these solvents also contributes to fluid thinning. Meyerhofer [3] added this important factor into the equation. He recognized that the evaporation rate was not dependent on the physical thickness of the fluid, but rather depended on vapor diffusion through the aerodynamic boundary layer above the wafer surface. This evaporation contribution to thinning was therefore:

$$\frac{dh}{dt} = -e \quad (11.5)$$

where e is a function of spin speed because the vapor boundary layer changes thickness as the rotation rate changes [3–5]. Thus, e is found to conform to:

$$e = C\sqrt{\omega} \quad (11.6)$$

where C is a proportionality constant that depends on whether airflow above the surface is laminar or turbulent, and on the diffusivity of solvent molecules in air.

Now, in most real spin coating conditions, the action of *both* processes will be contributing simultaneously—and throughout the entire process. This results in the thinning rate differential equation shown here:

$$\frac{dh}{dt} = -2Kh^3 - e \quad (11.7)$$

This equation was the basis for fitting interferometry data to extract the e and K constants for particular coating solutions in earlier studies [6–12]. This combination of processes (flow and evaporation) then also corresponds back to the stages of the process in an operational sense. “Stage 2” is in force when the *first* term on the RHS of Eq. (11.7) dominates. Since this term depends on the *cube* of the instantaneous thickness, it can be seen that it gets smaller quite rapidly with time. “Stage 3” is in force when the *second* term on the RHS of Eq. (11.7) dominates. This term does not depend on thickness because evaporation happens geometrically out of the top of

the coating solution exposed on the wafer surface. The “cross-over” point that was mentioned above is mathematically defined by the point when these two terms are equal to one another. This point was identified earlier in Fig. 11.1 for the specific case of ethanol rotating at 2,000 RPM. While the cross-over is defined by equating the two terms, it should be emphasized that flow and evaporation are both happening throughout the full process, but the relative contributions of each may be quite imbalanced. This is quite true near the end of spinning because with each small bit of evaporative drying then the $2Kh^3$ flow term gets smaller and smaller and the fluid becomes essentially static on the surface of the substrate.

Meyerhofer used this fact to combine the flow and evaporation contributions to provide an estimate of final coating thickness based on the physical characteristics of the solution [3]. He essentially solved for the “cross-over” point (equating the two terms discussed above) and then assuming that the fluid thickness that exists at the cross-over point will dry in place. With this approach he was able to predict the final coating thickness, h_f , in terms of the key solution parameters described above, according to:

$$h_f = x \left(\frac{e}{2(1-x)K} \right)^{1/3} \quad (11.8)$$

where e and K are the evaporation and flow constants, defined above, and x is the effective volumetric solids content of the solution.

Once the rotation dependencies for the viscous flow rate (Eq. 11.4) and the evaporation rate (Eq. 11.6) are included, then it is expected that the final coating thickness should vary with the spin speed, ω , according to the $-1/2$ power and this is supported by many experimental tests, though exponents can deviate from $-1/2$, especially with less volatile solvents where the flow/evaporation cross-over assumed by Meyerhofer may not have been reached [1]. Still, since deviations can occur, then real plots of the thickness vs. spin speed must usually be constructed to be able to tune the final device structures. Typical coating thickness values are usually below 1 micron when sol-gel films are deposited by spin coating. This is partly due to the relatively low solids loading that sol-gel solute ions usually provide and the large amount of physical shrinkage that must accompany drying and film solidification. Attempts to make thicker coatings can result in profusely cracked coatings.

The EBP and Meyerhofer treatments are relatively simple in their execution. However many more complicated computational modeling studies have been published that include a variety of refinements [13–20], however the basic principles and behavior are not dramatically different than the EBP seminal work.

11.3 Coating Uniformity and Defect Diagnosis

As noted above, spin coating often makes very uniform thin coatings on flat substrates, yet there are times when the coatings have thickness variations or flaws that cannot be tolerated in the final application. Some important defects and possible solutions are presented below.

11.3.1 *Comets*

Any contaminant particles that make their way into the coating solution—either during synthesis or during the coating run—can cause flow defects called comets. The particle sticks to the substrate surface and the fluid flow around each impediment causes a streak that points radially outward. The airflow conditions found near the spinning wafer can influence this problem directly: the spinning wafer pushes a boundary layer of air radially outward, which requires a net downward pull of ambient air toward the center of the wafer. This air circulation essentially exposes the coating to all the particles present in the ambient. Using a lid during coating is one way to reduce airborne particle sources, but it substantially modifies the solvent evaporation occurring during coating. Some coaters are built with active air circulation and venting; care should be taken that only clean, filtered, air is admitted to the spin bowl region. Particles that come from the coating solution may be reduced by using sub-micron syringe filters during the fluid dispense stage.

11.3.2 *Striations*

Striations are probably the most commonly appearing coating thickness defect that appears during spin coating. These defects are radial ridges and thickness undulations that point nearly directly along the fluid flow direction during the spin coating process. Near the center of the wafer they are more localized, whereas at larger radius values they are drawn out into long linear features. If we consider a coating thickness cross-section then we usually find a nearly sinusoidal thickness variation with a wavelength ranging from 10s to 100s of microns. Interestingly, this spacing is in marked contrast to the fluid thickness values when these defects are forming (just a few microns [21]). These defects are now known to result from capillary forces that become unbalanced during spin coating as a result of the solvent evaporation process [22, 23]. Figure 11.2 shows a schematic representation of how the surface tension changes during spinning and how tiny surface tension differences cause lateral fluid movements before the viscosity rises too much during coating formation. Eventually solvent evaporation progresses enough to freeze in these thickness undulations to form the striation defects. The patterns

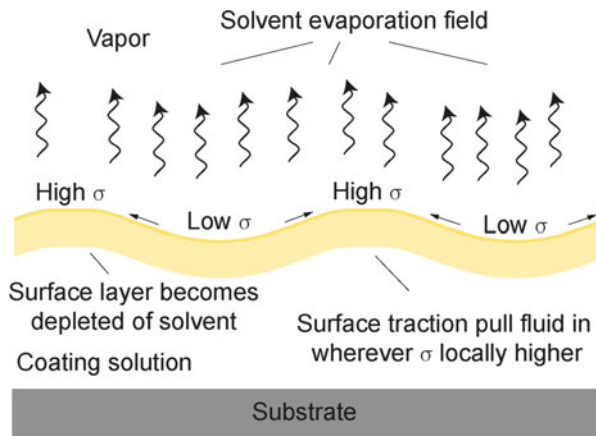


Fig. 11.2 Solvent evaporation from the surface of the coating solution can lead to an instability where neighboring local surface tension values are imbalanced: areas with slightly higher surface tension pull in, which develops into the peak regions; areas with slightly lower surface tension are stretched thinner with time (and become the troughs). If the average surface tension rises with solvent evaporation then this lateral tug-of-war can become imbalanced

formed at the center of the wafer are reminiscent of the fluid thickness perturbations called Bénard cells. Bénard cells are regular surface dimples or undulations that arise because of convection rolls that are established when a temperature gradient is applied across a fluid layer. Either buoyant or thermocapillary effects are known to drive this kind of convection effect [24, 25]. The potential link between Bénard cells and the development of striations during the spin coating process is suggested by the similarity between the cellular pattern sometimes seen near the wafer center and the regular surface ripples found in Bénard cells. The lateral gradient-driven capillary effects are collectively known as “the Marangoni effect” [24], and could easily be instigated by solvent evaporation occurring during spin coating. One important difference between stable cellular convection driven by surface tension gradients and the conditions found in spin coating is that the fluid solution is also experiencing extensive shear flow radially outward (causing simultaneous dramatic continual thickness reduction), therefore a stable cellular pattern will not be able to develop across a spinning and thinning film. Nonetheless the gradients in surface tension which develop as a result of evaporation and solvent depletion can drive a similar process within the spin coated film as higher surface tension regions draw fluid away from lower surface tension neighboring regions.

The easiest way to prevent striation formation is to completely prevent evaporation during spinning [22, 23], but this results in much thinner coatings and ones that may also require a hot-plate drying step or furnace bake after spinning to remove the solvent. Since many spin coaters operate under conditions where evaporation cannot be fully prevented, it is useful to also develop methods for modifying the solution formulation in ways to combat the surface tension instability. In our earlier work, we have advocated the addition of sacrificial solvents that make important

surface tension adjustments [26]. An advantageous co-solvent will be one that is fully miscible with the starting coating formulation—and might have a somewhat higher volatility than the other solution constituents. Another key characteristic is that the co-solvent should also have a relatively higher surface tension than the other next-most-volatile constituent. This leads to a situation when the coating is being deposited where the co-solvent is removed by evaporation more intensively than the other components—and because its specific surface tension is relatively high then it drives the average surface tension down, a condition which is thought to be stable against surface tension variations of the Bénard type. We have demonstrated this strategy for an Al-Ti containing sol-gel coating, where ethyl acetate was effective at preventing striations in the final coating [27]. More recently we have published work showing that the surface tension values are *indeed* changing as we had thought [28], which further substantiates the solvent mixing strategy for reducing striation defect formation.

It should be noted that there is a recent body of literature, mostly involving composite polymer coatings, where these striations are investigated as a source for interesting aligned microstructure creation [29–32]. Usually when these effects are noticed or enhanced, then there is different phase development in the *thicker* parts of the striation compared to the *thinner* parts. This is fully consistent with the above discussion. Thicker coating regions may dry more slowly and develop larger scale microstructure features, while the thinner regions experience faster drying and have less time to nucleate and grow the phase separation or other structures that are found.

11.3.3 Chuck Marks

Sometimes solution-derived coatings are made that have obvious coating thickness patterns that match the under-side gripping by the vacuum chuck or other fixture that was used for spin coating. A dramatic example of this is shown in Fig. 11.3. The coating shown here was an ethanolic silica-titania sol-gel deposited onto a glass substrate. Two distinct features are evident in the coating thickness pattern. First, the cross in the center corresponds to the locations where the grooves in the metal vacuum chuck were located. And, the circular feature is where the o-ring in the vacuum chuck was located. The o-ring sealed the vacuum and caused the substrate to flex slightly into contact with the metal parts of the vacuum chuck. The variation in physical contact on the back side of the substrate then caused variations in thickness in the coating that was forming on the top.

The mechanism for creating coating thickness variation related to back-side physical contact is through thermal effects [33, 34]. Solvent evaporation is caused by the wafer spinning rapidly in ambient air. The solvent evaporation causes evaporative cooling—and this happens uniformly over the entire top surface of the wafer. Heat within the nearby materials is then able to flow upward at different rates, depending on how close the physical contact is and what the thermal

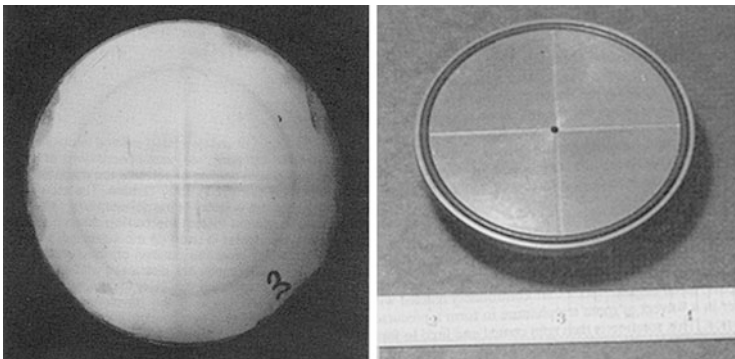


Fig. 11.3 Coating thickness variations associated with differences in physical contact with the *backside* contact to the vacuum chuck used for spin coating. These marks arise because of temperature variations imposed by solvent evaporative cooling—which then influences the evaporation coefficient and finally results in a different coating thickness [33]

conductivity values are. Areas with good back-side contact to metal are able to compensate for the evaporative cooling better than areas that have no contact. Changes in thermal contact then translate into top-side temperature differences. And, since solvent vapor pressure rises exponentially with temperature, we will have different evaporation rates from the top depending on the back side contact. And, referring to Eq. (11.8) above, we see that faster evaporation rate will result in a slightly thicker coating under otherwise identical coating conditions. This was consistent with the thickness variations shown in Fig. 11.3—thicker areas were directly over the parts in direct contact with metal on the back-side.

As mentioned above for striation defects, since the chuck marks are inherently driven by evaporation of the solvent, then reducing solvent volatility (by re-formulating the coating solution) or spinning in a solvent-rich environment can help reduce this problem. It is also advisable to redesign vacuum chucks so that they have uniform physical contact on the back-side of the substrate.

11.3.4 Gradual Radial Thickness Variation

The aim of most coating depositions is to achieve complete 2D uniformity in film thickness over the whole substrate; however there are occasional coating solutions and circumstances that result in gradual radial thickness variations from center to edge. These can be either concave or convex, and usually depend on specific non-Newtonian viscosity variations within the solution during spinning. As noted above, the normal flow condition is a balance between the rotational accelerations and the viscous drag. The EBP derivation showed that the local shear rate will be proportional to radius, as well as varying with depth within the flowing solution, as recounted in Eqs. (11.1) and (11.2) [2]. So, if a coating solution experiences

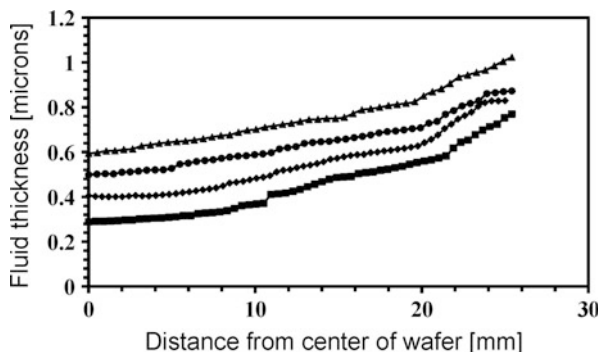


Fig. 11.4 Fluid thickness profiles determined using a combination of color video and laser interferometry for propanol spinning on a silicon wafer at 2,000 RPM. The triangles, circles, diamonds and squares are taken at 3.87, 3.93, 4.00, and 4.07 s into the spinning run, respectively. Slight discontinuities are from the fitting algorithm and not the true fluid profiles. The average evaporation rate was calculated by subtracting the lowest line from the highest line

shear-thinning (as might be typical for a nanoparticle sol) then the flow will be more rapid at larger radius, resulting in gradually thinner coating at larger radius. Britten and Thomas did the first quantitative match between the shear-thinning behavior and this gradual thickness variation with radius [35]. More recently, another possible contribution to radial thickness variations was observed in our labs [36]. Using real-time video observation of the interference colors present near the end of the coating run, we determined that for propanol the evaporation was slightly slower near the edge of the wafer compared to the center (about 20 % slower). Figure 11.4 shows our measured fluid thickness profiles for specific video frames showing the basic dished shape of the solvent. The importance of a local difference in evaporation rate is through Meyerhofer's treatment as described above in Eq. (11.8). With a slightly lower evaporation rate then we will expect that the coating fluid will "set" at a slightly later point in time resulting in a thickness profile that is slightly thinner for locations further from the wafer center. A full fluid dynamic air-flow and mass-transport model that accurately incorporates the solvent evaporation will need to be tackled in order to fully tease apart these possible and important contributions. It can be seen that thickness variations and defect modes can often be attributed to evaporation rate differences. So, it is also possible to intentionally manipulate evaporation rate to achieve thickness control as was recently demonstrated using IR lamp heating [37], which raised the temperature (and evaporation rate) and gave significantly thicker final films.

One final radial thickness variation of note is "edge bead". This is a result of the surface tension effects that make it difficult for the coating fluid to detach itself at the perimeter of the wafer. This usually doesn't cause a large problem, but will create substantial thickness differences right around the whole perimeter of the wafer—probably a width of a couple mm's wide, depending on the spin speed, surface tension, and volatility of the solvent. In automated spin coating systems

then there are a number of strategies for removing these edge beads, including solvent jets directed at the perimeter and flat adjacent surfaces to allow fluid flow to continue at the edge without hindrance.

11.4 Conclusions

Spin coating remains a rapid and useful technique for depositing thin and uniform coatings from solution precursors. Usually these coatings have best quality when the solvent in the coating solution is not evaporating too quickly. Efforts to optimize coating solutions should include careful consideration of chemical reactivity, surface tension, and evaporation rate when trying to make uniform coatings.

References

1. Birnie DP III, Hau S, Kamber DS, Kaz DM (2005) Effect of ramping-up rate on film thickness for spin-on processing. *J Mater Sci Mater Electron* 16:715–720
2. Emslie AG, Bonner FT, Peck CG (1958) Flow of a viscous liquid on a rotating disk. *J Appl Phys* 29:858–862
3. Meyerhofer D (1978) Characteristics of resist films produced by spinning. *J Appl Phys* 49:3993–3997
4. Cobb EC, Saunders OA (1956) Heat transfer from a rotating disk. *Proc R Soc* 236:343–351
5. Kreith F, Taylor JH, Chong JP (1959) Heat and mass transfer from a rotating disk. *ASME J Heat Transfer* 81:95–105
6. Horowitz F, Yeatman E, Dawnay E, Fardad A (1993) Real-time optical monitoring of spin coating. *J Phys III France* 3:2059–2063
7. Horowitz F, Yeatman E, Dawnay E, Fardad A (1994) Optical monitoring of the sol to gel transition in spinning silica films. In: Mackenzie JD (ed) *Sol-gel optics III*, Proc SPIE 2288. pp 67–70
8. Gu J, Bullwinkel MD, Campbell GA (1995) Solvent concentration measurement for spin coating. *J Appl Polym Sci* 57:717–725
9. Gu J, Bullwinkel MD, Campbell GA (1996) Measurement and modeling of solvent removal for spin coating. *Polym Eng Sci* 36:1019–1026
10. Birnie DP III, Manley M (1997) Combined flow and evaporation of fluid on a spinning disk. *Phys Fluids* 9:870–875
11. Birnie DP III (1997) Combined flow and evaporation during spin coating of complex solutions. *J Non-Cryst Solids* 218:174–178
12. Haas DE, Quijada JN, Picone SJ, Birnie III DP (2000) Effect of solvent evaporation rate on skin formation during spin coating of complex solutions. In: Dunn BS, Pope EJA, Schmidt HK, Yamane M (eds) *Sol-gel optics V*, Proc SPIE 3943. pp 280–284
13. Bornside DE, Macosko CW, Scriven LE (1987) On the modeling of spin coating. *J Imaging Technol* 13:122–130
14. Flack WW, Soong DS, Bell AT, Hess DW (1984) A mathematical model for spin coating of polymer resists. *J Appl Phys* 56:1199–1206
15. Lawrence CJ (1988) The mechanics of spin coating of polymer films. *Phys Fluids* 31:2786–2795
16. Lawrence CJ (1990) Spin coating with slow evaporation. *Phys Fluids A* 2:453–456

17. Lawrence CJ, Zhou W (1991) Spin coating of non-Newtonian fluids. *J Non-Newtonian Fluid Mech* 39:137–187
18. Ohara T, Matsumoto Y, Ohashi H (1989) The film formation dynamics in spin coating. *Phys Fluids A* 1:1949–1959
19. Shimoji S (1987) A new analytical model for spin coating process with solvent evaporation. *Jpn J Appl Phys* 26:L905–L907
20. Jenekhe SA (1984) Effects of solvent mass transfer on flow of polymer solutions on a flat rotating disk. *Ind Eng Chem Fundam* 23:425–432
21. Haas DE, Birnie DP III (2001) Real-time monitoring of striation development during spin-on-glass deposition. In: Feng X, Klein LC, Pope EJA, Komarneni S (eds) *Sol-gel commercialization and applications*, vol 123, Ceramic transactions. American Ceramic Society, Westerville, OH, pp 133–138
22. Daniels BK, Szmanda CR, Templeton MK, Trefonas III P (1986) Surface tension effects in microlithography – striations. In: Willson CG (ed) *Advances in resist technology and processing III*, Proc SPIE 631. pp 192–201
23. Du XM, Orignac X, Almeida RM (1995) Striation-free, spin coated sol-gel optical films. *J Am Ceram Soc* 78:2254–2256
24. Scriven LE, Sterling CV (1960) The Marangoni effects. *Nature* 187:186–188
25. Thomson J (1855) On certain curious motions observable at the surfaces of wine and other alcoholic liquors. *Phil Mag* 10:330–333
26. Birnie DP III (2001) Rational solvent selection strategies to combat striation formation during spin coating of thin films. *J Mater Res* 16:1145–1154
27. Taylor DJ, Birnie DP III (2002) Striation prevention by targeted formulation adjustment: aluminum titanate sol-gel coatings. *Chem Mater* 14:1488–1492
28. Birnie DP III, Kaz DM, Taylor DJ (2009) Surface tension evolution during early stages of drying of sol-gel coatings. *J Sol-Gel Sci Technol* 49:233–237
29. Kim J-K, Taki K, Nagamine S, Ohshima M (2008) Periodic porous stripe patterning in a polymer blend film induced by phase separation during spin-casting. *Langmuir* 24:8898–8903
30. Liu T, Ozisik R, Siegel RW (2007) Phase separation and surface morphology of spin coated films of polyetherimide/polycaprolactone immiscible polymer blends. *Thin Solid Films* 515:2965–2973
31. Lu S-Y, Chen H-L, Wu K-H, Chen Y-Y (2007) Formation of nanowire striations driven by Marangoni instability in spin cast polymer thin films. *Langmuir* 23:10069–10073
32. Lua Y-Y, Cao X, Rohrs BR, Aldrich DS (2007) Surface characterizations of spin coated films of ethylcellulose and hydroxypropyl methylcellulose blends. *Langmuir* 23:4286–4292
33. Birnie DP III, Zelinski BJJ, Marvel SP, Melpolder SM, Roncone R (1992) Film/substrate/vacuum-chuck interactions during spin coating. *Opt Eng* 31:2012–2020
34. Birnie DP III, Zelinski BJJ, Perry DL (1995) Infrared observation of evaporative cooling during spin coating processes. *Opt Eng* 34:1782–1788
35. Britten JA, Thomas IM (1992) Non-Newtonian flow effects during spin coating large-area optical coatings with colloidal suspensions. *J Appl Phys* 71:972–979
36. Birnie DP III, Haas DE, Hernandez CM (2010) Laser interferometric calibration for real-time video color interpretation of thin fluid layers during spin coating. *Opt Laser Eng* 48:533–537
37. Dellert A, Schindler K, Roosen A (2009) Spin coating of hybrid suspensions using infrared-irradiation to increase layer thickness. *Thin Solid Films* 517:4571–4575

Chapter 12

Aerosol Deposition

Matt D. Brubaker

12.1 Comparison of Aerosol Deposition to Other CSD Techniques

Thin films can be deposited from chemical solutions via a number of established techniques. Chemical solution deposition typically refers to the deposition of a thin film of liquid precursor and subsequent thermal processing to form the solid thin oxide film. Spin coating (Chap. 11) and dip coating (Chap. 10) are well-known CSD techniques that have found widespread use. For the sake of comparison, it is also useful to consider methods that are not typically grouped within the CSD domain, but still use liquid solutions as precursors to the final film. Metal organic chemical vapor deposition (MOCVD) is an example of such a technique in which the deposition and thermal processing take place simultaneously as opposed to subsequently. Aerosol deposition processes and films typically have characteristics that will be intermediate of spin coating and MOCVD processes and films. Hence, it is useful to review these techniques in order to clarify the unique characteristics of aerosol deposition.

Spin coating (Chap. 11) is perhaps the simplest CSD method in which the precursor solution is dispensed onto the substrate and the substrate is then rotated at several thousand revolutions per minute to yield a thin liquid film as shown in Fig. 12.1. The primary process controls for the spin coating process are the spin speed and the molarity of the precursor solution, with rotation speed being inversely proportional and molarity being proportional to final film thickness. Spin coating is a fast and reproducible process that can yield good film uniformities on small to large diameter silicon wafers. However, spin coating is not particularly well suited for non-circular substrates, particularly larger flat panel displays or windows. Spin

M.D. Brubaker (✉)

Symetrix Corporation, 5055 Mark Dabling Boulevard, Colorado Springs, CO 80918

National Institute of Standards and Technology, 325 Broadway, Boulder, CO 80305

e-mail: matthew.brubaker@nist.gov

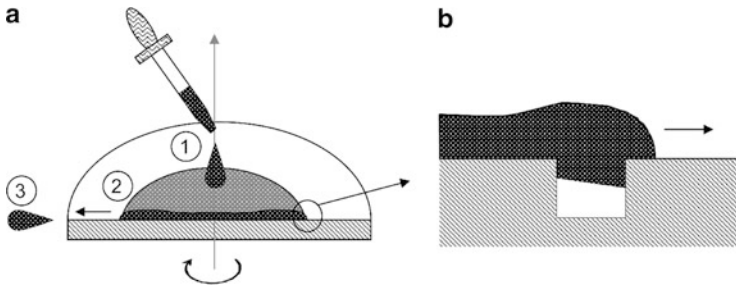


Fig. 12.1 Schematic illustration of (a) the spin coating process and (b) conformality-related film defect associated with topographical features

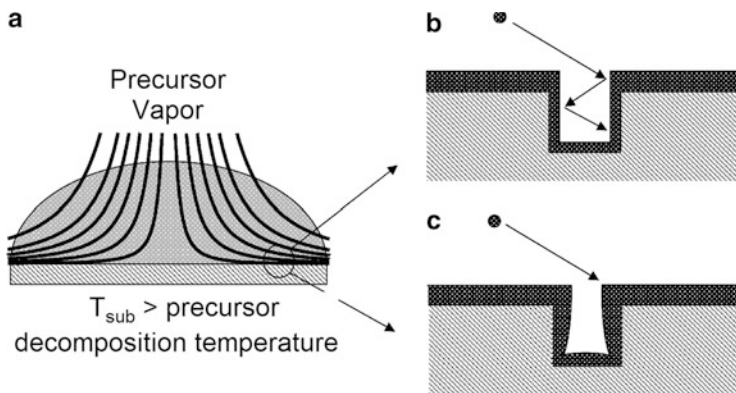


Fig. 12.2 Schematic illustration of (a) the MOCVD process and resulting film thickness conformality for (b) low sticking coefficient and (c) high sticking coefficient process conditions

coating is also not suitable for depositing films on substrates that have non-planar surface topography. For example, a spin coated film on a trenched structure can exhibit a snow-drift like profile and will in general possess a larger defect density (Fig. 12.1). One further shortcoming of spin coating is that a large fraction of the excess precursor solution is spun off of the wafer and lost to waste.

In contrast to spin coating, MOCVD is a technique that can yield high performance oxide films, but at the cost of a high level of sophistication and sensitivity in the processes and hardware. MOCVD usually is performed under vacuum conditions to minimize reactions between chemical precursors and reactants in the gas phase. MOCVD utilizes similar metallo-organic precursors to CSD, but the precursors must satisfy additional criteria including thermal stability above their evaporation temperature. The precursors are vaporized and transported to a heated substrate (Fig. 12.2), upon which they are reacted to form a solid oxide film and carbonaceous byproducts.

The byproducts are transported from the substrate surface and allow for a low carbon, high density oxide film to be fabricated in the as-deposited condition.

The process conditions for MOCVD are typically established to allow for multiple precursor molecule-substrate collisions prior to incorporation into the growing film. This permits transport of precursor molecules into deep trenches and results in deposited films with good thickness and stoichiometric conformality. There are numerous process controls utilized in MOCVD processing including deposition time, precursor flow rate, substrate temperature, ambient pressure, and ambient composition. While these controls give greater flexibility in tailoring the resulting film properties, the inherent complexity in the process can significantly increase the duration of the development cycle.

Aerosol deposition leverages several of the strengths from both the spin coating and MOCVD techniques. As such it allows for thickness control by a wider variety of process control parameters similar to the MOCVD technique while utilizing the fast materials development cycle associated with spin coating and CSD techniques. It can be used on substrates that do not lend themselves to spin coating including flat panel displays and windows. For sufficiently small aerosol droplets, aerosol deposition can yield thickness conformality over surface topography that resembles liquid films and their characteristic surface tensions. The defect density of aerosol deposited features will be lower than spin coated features [1] as spin coating allows for air to become entrapped in the features under the advancing liquid wavefront (Fig. 12.1). However, aerosol deposition techniques can sometimes require more sophisticated equipment than spin-coats and can have reduced throughput. The film quality of certain types of aerosol deposited films, particularly those deposited on heated substrates, can be more porous than for spin or MOCVD techniques.

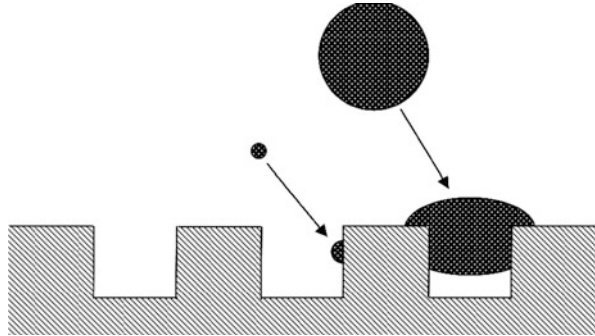
12.2 Mechanics of Aerosol Deposition

The aerosol deposition process can be broken down into several sub-processes that consist of generation of the aerosol, transport of the aerosol droplets to the substrate, nucleation and aggregation of the aerosol droplets in the thin film, and thermal processing of the film to produce the final composition and structure. These steps will be presented in the context of a particular type of aerosol deposition called Liquid Source Misted Chemical Deposition (LSMCD). The purpose for this approach is that in LSMCD these sub-processes will occur sequentially and hence provide the reader with a chronological layout for learning the aerosol deposition process. Once these sub-processes have been introduced, other variants of the aerosol deposition process will be introduced based on these sub-processes taking place simultaneously.

12.2.1 Aerosol Generation

Generation of aerosols from CSD precursor solutions involves the dispersion of a bulk liquid to form an ensemble of small spherical liquid droplets. This ensemble

Fig. 12.3 Diagram showing aerosol deposition inside topographical features illustrating the effect of aerosol particle size on internal surface coating



will have a characteristic distribution of droplet sizes and charge states that depend largely on the process and solution from which the aerosol is generated. The droplet size governs aerosol transport and deposition sub-processes, hence it is of paramount importance to establish the distribution and its statistical metrics for proper analysis and application.

The droplet size can also be a key parameter for particular applications. Consider a substrate as shown in Fig. 12.3 with an array of $1\ \mu\text{m}$ diameter holes that are to be deposited with a thin film inside the holes. If an aerosol with droplet diameter less than $1\ \mu\text{m}$ impinges on a $1\ \mu\text{m}$ hole, the droplet can adsorb onto the internal surface of the hole without plugging it. Alternatively, if an aerosol droplet that is greater than $1\ \mu\text{m}$ in diameter impinges a hole the droplet can plug the hole and entrap a bubble that can introduce a defect in the film structure. In general, when attempting to coat internal surfaces the droplet size distribution should not contain sizes that exceed the minimum topographical feature size on the substrate.

There are several techniques by which aerosols are generated for thin film deposition processes. These techniques are based on the transfer of pneumatic [2], ultrasonic [3], or electrostatic [4] energy to the bulk liquid in sufficient magnitude to break liquid tension forces. The LSMCD process typically employs pneumatic atomization as this technique is particularly effective in creating small aerosol particle diameters that extend into the submicron range. Figure 12.4 shows a schematic diagram of pneumatic atomization in which a liquid stream is sheared into aerosol particles by flow of compressed gas. The pressure of the input gas will affect the resulting aerosol particle size characteristics. The input pressure will also determine the overall gas flow rate and velocity, which are important to the process by which the aerosol is transported to the substrate. The shearing of bulk liquid surfaces during atomization causes buildup of electric charges on the aerosol particles, which again is important to transport processes. In the following pages the aerosol particle size and charge distributions will be presented in the context of pneumatically atomized aerosols, however, the methods of description can be applied to aerosols generated by other techniques.

In this section we will discuss the statistical methods by which the particle size distributions of an aerosol are described. Particle size distributions are plotted either as histograms or as continuous frequency functions that show the frequency of

Fig. 12.4 Schematic diagram of (a) precursor aerosol generation by atomization and (b) corresponding pressure vs. flow characteristics. Atomizer flow rate data courtesy of Primaxx Corporation

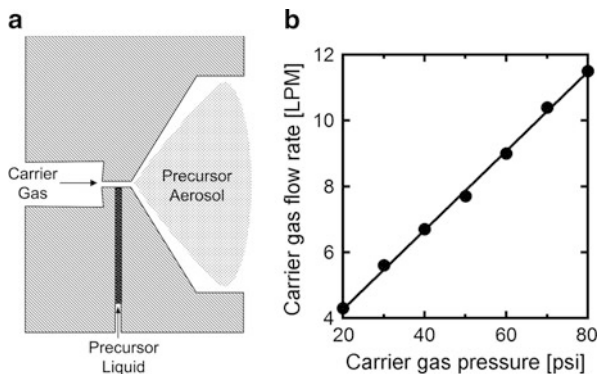
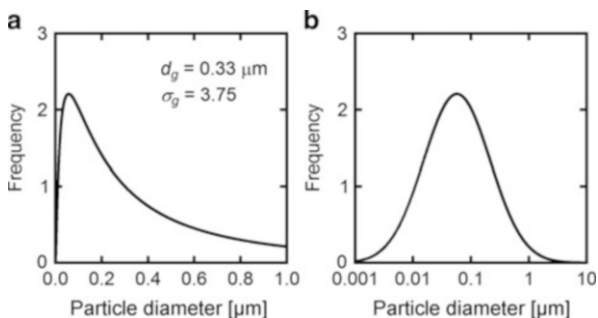


Fig. 12.5 Aerosol particle size distribution by count frequency for indicated geometric mean average and standard deviation. Aerosol particle diameter shown in (a) normal and (b) log scale



occurrence of a particular metric (count, mass, surface area, etc.) versus the particle diameter. Figure 12.5 shows the particle size distribution of an aerosol generated by atomization of a liquid solution. The shape of this distribution is representative of many aerosol distributions that will be encountered and is characterized by a skewed profile and long tail extending towards the larger particle diameters. The vertical axis in the plot shows the fraction of total particles in a given diameter interval, which is mathematically described via the frequency function

$$f(d_p) = \frac{df}{dd_p} \tag{12.1}$$

where $f(d_p)$ is the value of the frequency function at particle diameter d_p , and df is the fraction of particles in the incremental particle diameter range dd_p . In this way the fraction of particles in a given size range can be determined by integrating the frequency function over the limits of the range

$$f = \int_{d_a}^{d_b} f(d_p) dd_p. \tag{12.2}$$

Integrating the frequency function over the whole distribution will yield the entire fraction of particles and will give a value of 1 for normalized frequency functions

$$f = \int_0^{\infty} f(d_p) dd_p = 1. \quad (12.3)$$

Discrete histogram data is frequently used to estimate the shape of the continuous frequency function. In order to plot discrete data in an analogous manner to the frequency function the discrete data must be plotted as the fraction of particles in the interval divided by the width of the interval.

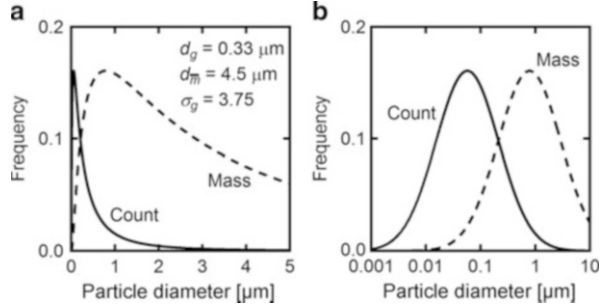
For many aerosols, including liquid aerosols generated by atomization, the frequency function can usually be fit to a lognormal distribution. For the present purposes it is sufficient to consider the lognormal distribution as an empirical model for fitting aerosol particle size distributions. The lognormal distribution has the familiar appearance of the normal (or Gaussian) distribution when the horizontal particle diameter axis is plotted in log scale (Fig. 12.5b). The mathematical form of the lognormal distribution is

$$f(d_p) = \frac{1}{\sqrt{2\pi} \ln \sigma_g \cdot d_p} \cdot \exp \left[\frac{-(\ln d_p - \ln d_g)^2}{2(\ln \sigma_g)^2} \right] \quad (12.4)$$

where d_g and σ_g are the geometric mean diameter and the geometric standard deviation, respectively. Much of the information for describing the aerosol distribution can be condensed into these two statistical parameters. The lognormal distribution also has several other characteristics that make it convenient for describing aerosols. Many aerosols span several decades in particle diameter. The lognormal distribution allows for the full range of diameters to be resolved, in contrast to normal distributions which tend to compress the distribution at smaller diameters. The lognormal distribution also allows for easy conversion between the various particle properties of the distribution (count, mass, surface area, etc.) by calculating the relevant d_g for that particular property, but retaining the same overall shape and σ_g . We will explore this feature of the lognormal distribution in the following paragraphs.

The particle size distributions discussed above are often manipulated to statistically describe other properties including aerosol mass and volume distributions. We have already considered that the diameter of the particles is important when depositing thin films over topographical microstructures. For the distribution shown in Fig. 12.5 about 90 % of the particles are less than 1.8 μm in diameter, hence this 90 % would be suitable for deposition on the interior surfaces of features greater than 1.8 μm . However, the amount of film deposited for a given diameter particle will be proportionate to the volume instead of the diameter itself. This causes the larger particles to contribute more material to the overall film thickness or to be weighted with respect to the smaller diameter particles. In this regard the volume distribution, or the more commonly used and proportional mass distribution, will be more relevant to the kinetics of the transport and film growth processes. Moreover, the mass distribution is typically measured when sampling aerosols as

Fig. 12.6 Aerosol particle size distribution comparing count frequency and average mass frequency for indicated geometric mean average, standard deviation, and mass average. Aerosol particle diameter shown in (a) normal and (b) log scale



these measurements are commonly performed by weighing particles that are differentially collected on the stages of a cascade impactor.

The lognormal distribution can be modified between the particle count distribution and the mass distribution by using the appropriate value of the geometric mean diameter (d_g). The median diameter can be used interchangeably with the geometric mean diameter as both of these values are equal for the lognormal distribution. The Count Median Diameter (*CMD*) is typically used for the particle count distribution, while the diameter of the average mass ($d_{\bar{m}}$) is used for the mass distribution. The equation for converting between these two average values is given by Eq. (12.5)

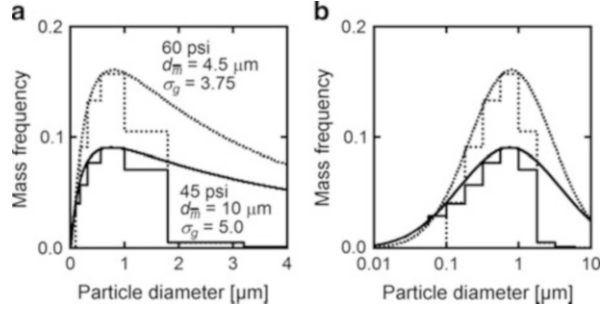
$$d_{\bar{m}} = CMD \cdot \exp(1.5 \ln^2 \sigma_g). \quad (12.5)$$

The geometric standard deviation (σ_g) will retain the same value for both the count and mass distributions as well as any moment of the lognormal distribution. The $d_{\bar{m}}$ and σ_g values are frequently extracted from cascade impactor data that has been plotted as cumulative mass fraction on a log-probability plot. Additional details of this approach, as well as a more comprehensive treatment of aerosol science, can be found in the referenced texts [5–7]. Figure 12.6 shows the particle count distribution from Fig. 12.5 plotted in addition to its mass distribution.

The overall shape of the particle mass distribution (log d_p plot) can be seen to be the same as the particle count, but shifted towards higher diameters. The particle mass distribution shown in the plot is normalized in a similar manner to the particle distribution plot in Fig. 12.5. It is worth noting that the particle count distribution in Fig. 12.6 has been adjusted by a factor of $CMD/d_{\bar{m}}$ for the sake of comparison, hence it is no longer normalized.

For a given particle size distribution it is possible to further tailor the distribution via a stage of downstream impactors. The mechanics of impaction will be discussed in the next section on transport, but will be introduced here as a technique for removing unwanted large diameter particles from the distribution. The particle size distribution introduced in Figs. 12.5 and 12.6 show that even though 90 % of the particle count is suitable for depositing in 1.8 μm diameter holes, the mass distribution shows that only 25 % of the particles by mass will be suitable for 1.8 μm geometries. A solution to the problem is to clip the distribution by capturing any particles that are larger than 1.8 μm . Figure 12.7 shows experimental measured

Fig. 12.7 Aerosol particle size distribution comparing mass frequency for atomizer pressure of 45 and 60 psi (310 and 414 kPa, respectively). Aerosol particle diameter shown in (a) normal and (b) log scale. Data courtesy of Primaxx Corporation



histogram data of an atomized liquid that has been clipped above 1.8 μm . The resulting distribution is now suitable for deposition in 1.8 μm geometries. While this approach allows customization of distributions for ever smaller geometries it is at the expense of the utilization efficiency of the precursor solutions, which can be a significant fraction of the operational costs in chemical solution deposition. In this case the volume of solution available for deposition has already been attenuated to 25 % prior to transport to the substrate, and will be referred to as the generation efficiency (ν_g). However, the 75 % removed from the original distribution can be easily reclaimed from the impaction chambers and recycled.

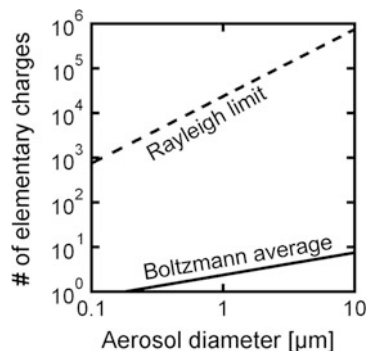
Figure 12.7 also shows the particle size distributions for two different input gas pressures. Increasing the input gas pressure has the effect of shifting d_m to smaller diameters and decreasing the geometric standard deviation of the distribution. The mass fraction of particles with diameter less than 1.8 μm is larger for higher input gas pressure, with values of 25 % for 60 psi (414 kPa) and 14 % for 45 psi (310 kPa). There is an engineering tradeoff to be considered when increasing input pressure, however, as this will also increase gas velocities and the associated loss of aerosol during the transport process.

Aerosol particles will take on a bipolar distribution of electric charge states during the atomization process. Charge neutrality will be preserved in the overall aerosol; hence the total positive charge will be balanced by the total negative charge. The average magnitude of the electric charge on the aerosol particles will fall within a given range that depends on the particle diameter. This range is defined by a maximum charge for which the aerosol particle will be stable and a minimum range from which the average charge will be statistically probable. The maximum charge is referred to as the Rayleigh limit and is expressed as

$$n_L = \left(\frac{4\pi\epsilon_0}{1} \cdot \frac{2\pi\gamma d_p^3}{e^2} \right)^{\frac{1}{2}}. \quad (12.6)$$

Particles with charge in excess of the Rayleigh limit will have repulsive electrical forces that exceed surface tension forces and result in fragmentation of the particle. The minimum charge is determined by the capture of ions by the aerosol particles in

Fig. 12.8 Aerosol charge distribution range as defined by Rayleigh limit (maximum) and Boltzmann average (minimum)



the gaseous medium. This interaction follows a Boltzmann distribution with the average particle charge being approximated as

$$\bar{n} = 2.37\sqrt{d_p} \quad (12.7)$$

with d_p in μm . The range of these maximum and minimum charges is shown as a function of aerosol particle diameter in Fig. 12.8.

The upper limit can be considered as an excited state of the aerosol particle that is induced during generation or by an external process such as corona charging. With time the excited charge states of the aerosol will relax to the equilibrium value. The LSMCD process utilizes the particle charge to increase deposition efficiency through the use of electrostatic forces. Hence, the LSMCD atomization process is typically optimized to maximize the aerosol charge. One approach to this end is the addition of a small concentration of polar solvent to the precursor solution, thereby promoting charge exchange during the shearing of the liquid stream. This has the advantage of enhancing charging efficiency without increasing the complexity of required equipment. An alternative approach involves the use of high electric fields (corona charging) to create a flux of ions that impart their charge onto the aerosol. This approach can significantly increase deposition efficiency during the transport stage due the large and more importantly unipolar aerosol charges; however it can be difficult to maintain process reproducibility.

12.2.2 Aerosol Transport

In this section we will describe the processes by which aerosol droplets are transported within the fluid medium to the substrate surface. We will examine the primary forces responsible for motion of the aerosol particles and determine their trajectories in a model that is representative of the LSMCD process. The significance of key process parameters will be presented within this model in regard to aerosol transport, film deposition and collection efficiency. The mechanics

elucidated from the model will be extended to larger aerosol diameters to describe spray deposition and inertial separation techniques.

Aerosol particles will be subject to various forces during transport processes and are generally categorized as internal or external forces [7]. Internal forces correspond to the forces exerted on the aerosol particle by the surrounding fluid medium. External forces correspond to forces that act independently of the fluid medium and include gravitational and electrical forces. Each of these forces will vary in relative magnitude depending on the size and inertia of the aerosol particle and on the ambient environment of the aerosol. It should be noted that these forces are vector quantities with direction and magnitude and will be represented with a bar above the quantity.

The force imposed by the fluid medium is referred to as the Stokes force. As described in the previous section, an aerosol generated by pneumatic atomization will be entrained within a gas flow created by the compressed gas input. The pressure of aerosol deposition processes is typically in the neighborhood of atmospheric pressure; hence the fluid flow will be characteristic of the viscous flow regime. The force exerted by this viscous flow will be proportional to the velocity of the gas flow relative to the aerosol particle and takes the form

$$\overline{F}_m = -6\pi\eta r_p(\overline{V} - \overline{U}) \quad (12.8)$$

where η is the dynamic viscosity of the fluid, r_p is the particle radius, \overline{V} is the velocity vector of the aerosol particle, and \overline{U} is the velocity vector of the fluid flow. This representation is accurate for small particle diameters and low relative velocities which are characteristic of the LSMCD process. At higher particle diameters and relative velocities the Stokes formula requires additional correction factors as described in [7]. Very small aerosol particles will require an additional slip correction factor if the particle diameter is on the order of the mean free path of gas molecules in the fluid [5].

The external force (\overline{F}_{ext}) experienced by an aerosol particle includes the combined effects of gravitational forces, electrical forces, and thermophoretic forces. The gravitational force on an aerosol particle takes the form of

$$\overline{F}_{ext} = m_p \overline{g} = \left(\frac{4}{3}\pi\rho r_p^3\right)\overline{g} \quad (12.9)$$

where ρ is density of the aerosol particle and g is the acceleration due to gravity. The electric force on an aerosol particle is given by

$$\overline{F}_e = q\overline{E} = n_e e \overline{E} \quad (12.10)$$

where the charge on the aerosol particle consists of the number of elementary charges (which will fall somewhere between the values given by \overline{n} and n_L) times the elementary charge constant. Thermophoretic forces occur when an aerosol particle is heated non-uniformly and the resulting fluid density gradient induces a buoyant force on the particle. These forces occur when an aerosol particle comes into close proximity to a heated substrate and are often taken into account in spray pyrolysis

techniques. LSMCD processes take place at ambient temperatures and subsequently will not be considered in the following quantitative model.

The equations of motion for the aerosol particles can be determined by considering the dynamics according to Eq. (12.11)

$$m_p \frac{d\bar{V}}{dt} = \bar{F}_m + \bar{F}_{ext} = -6\pi\eta r_p (\bar{V} - \bar{U}) + \bar{F}_{ext} \quad (12.11)$$

where $\frac{d\bar{V}}{dt}$ represents the acceleration of the aerosol particle. This equation can be manipulated to the following form which is more convenient for integration

$$\frac{d\bar{V}}{dt} = \frac{-6\pi\eta r_p}{m_p} (\bar{V} - \bar{U}) + \frac{\bar{F}_{ext}}{m_p} = \frac{-1}{\tau} (\bar{V} - \bar{U}) + \frac{\bar{F}_{ext}}{m_p} \quad (12.12)$$

where τ has units of time and is called the relaxation time. The relaxation time is a characteristic time response for an aerosol particle to come to dynamic equilibrium with its environment (i.e. settling of aerosol particles due to gravity) and is represented by

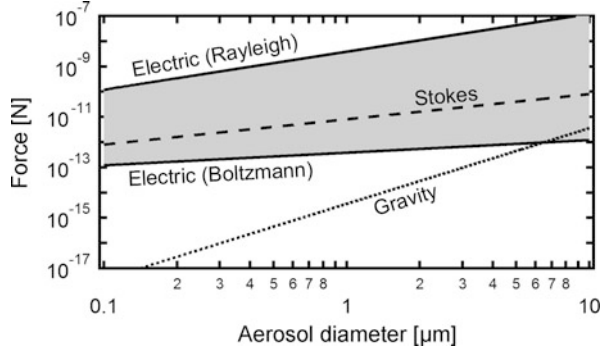
$$\tau = \frac{2\rho_p r_p^2}{9\eta}. \quad (12.13)$$

We will need to incorporate the appropriate external forces \bar{F}_{ext} by considering the relative magnitudes of the forces the aerosol particles will experience as a function of size. Figure 12.9 shows the electrical, gravitational, and stokes force under typical LSMCD process conditions. The electrical force will cover a range defined by the minimum and maximum aerosol charges. This range can be seen to bracket the stokes force, hence these forces are comparable and need to be accounted for in the external forces. On the other hand the gravitational force is at least an order of magnitude weaker than the electrical and stokes forces and falls off more quickly at smaller particle diameters. Resultantly, the electrical forces will be included and gravitational forces can be neglected among the external forces.

The velocity field \bar{U} can be represented by stagnation flow in which the carrier gas impinges the substrate surface at normal incidence [8]. This gas flow corresponds not only to the case of internal flow within the LSMCD reactor, but can also yield some insight into the operation of impactors for inertial separation of large diameter particles and external flow created by spray nozzles. We will employ three-dimensional stagnation flow represented in cylindrical coordinates. The velocity field will be axis-symmetric with respect to the z -axis, hence it is sufficient to consider only the radial and z -axis components. The velocity field is separable and represented via

$$U_r = a \cdot r \quad (12.14)$$

Fig. 12.9 Comparison of external and Stokes forces acting on aerosol particles, illustrating the negligible effect of gravity on sub-micron sized aerosol particles



$$U_z = -2a \cdot z \tag{12.15}$$

where a is gas velocity constant that can be determined from the input gas velocity ($z \gg r$). It should be noted that this model does not account for the boundary layer in which the velocity diminishes quickly with proximity to the substrate due to the no-slip condition. For the model presented in the following text the gas velocity will be overestimated within a few millimeters of the substrate.

We now apply Eq. (12.12) to determine trajectories of aerosol particles by of the LSMCD process. We can rewrite Eq. (12.12) by separation of variables using the same coordinate system as the gas velocity field

$$\frac{dV_r}{dt} = \frac{-1}{\tau} (V_r - U_r) \tag{12.16}$$

$$\frac{dV_z}{dt} = \frac{-1}{\tau} (V_z - U_z) + \frac{qE_z}{m_p} \tag{12.17}$$

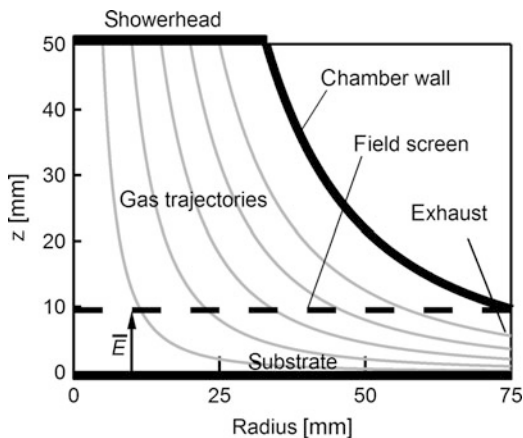
where V_r and V_z are the radial and z -components of the velocity, respectively, and E_z is the applied electric field. These equations can be integrated to solve for the aerosol velocities with applied boundary condition of $V_r = V_{r0}$ and $V_z = V_{z0}$ at $t = 0$ to yield

$$V_r = V_{r0} + (U_r - V_{r0}) \left(1 - e^{-\frac{t}{\tau}}\right) \approx V_{r0} + (U_r - V_{r0}) \cdot \frac{t}{\tau} \tag{12.18}$$

$$V_z = V_{z0} + \left(U_z - V_{z0} + \frac{qE_z \tau}{m_p} \right) \left(1 - e^{-\frac{t}{\tau}}\right) \approx V_{z0} + (U_z - V_{z0}) \frac{t}{\tau} + \frac{qE_z t}{m_p}. \tag{12.19}$$

Here we are approximating the exponential term by substituting its Taylor series and keeping only the first order terms ($e^{-\frac{t}{\tau}} \approx 1 - \frac{t}{\tau}$). We will ultimately be using an iterative computation to perform a stepwise calculation of the velocities and positions of the aerosol particles. By choosing a time step such that $t \ll \tau$, this approximation will be valid. We can integrate these expressions one more time to

Fig. 12.10 Axis-symmetric diagram of LSMCD chamber used for aerosol transport model simulations. Carrier gasses enter through the showerhead at the top of the figure and are transported to the exhaust according to the gas trajectories calculated by Eqs. (12.14) and (12.15). An electric field is generated between the substrate and ground-potential field screen through an applied substrate bias



arrive at the equations for the radial and z position of the aerosol particles with the applied initial conditions of $r = r_0$ and $z = z_0$ at $t = 0$ (Eqs. 12.20 and 12.21)

$$r = r_0 + V_{r0} \cdot t + \frac{t^2}{2\tau} (U_r - V_{r0}) \tag{12.20}$$

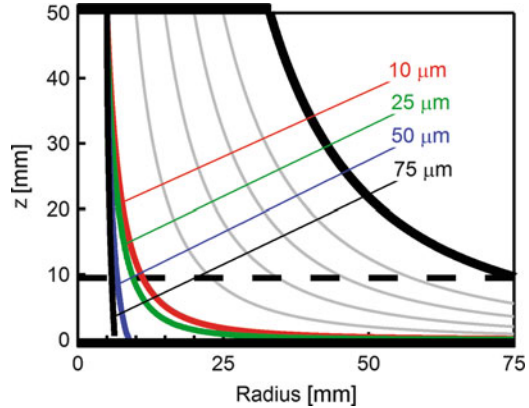
$$z = z_0 + V_{z0} \cdot t + \frac{t^2}{2\tau} (U_z - V_{z0}) + \frac{qE_z t^2}{2m_p} \tag{12.21}$$

These equations for velocity and position are parametric with time and can be easily incremented to generate a trajectory curve given the initial conditions of the aerosol particle.

The parameters of the model have been chosen to simulate a typical LSMCD process with an octane aerosol ($\rho = 0.7 \text{ g/mL}$) in a nitrogen carrier gas ($\eta = 1.77 \times 10^{-4}$ poise). Figure 12.10 shows a schematic diagram of the LSMCD deposition chamber in which the gas flow enters via a showerhead at the $z = 50 \text{ mm}$ plane and transits in the $-z$ direction. The aerosol will be fully entrained in the carrier gas flow at the showerhead; hence the initial aerosol velocity at a given radius will be equal to the carrier gas velocity at that radius. The substrate is a 150 mm diameter wafer placed so that the center of its surface is located at $r = z = 0 \text{ mm}$. A field screen is located 10 mm above and in the plane of the wafer surface. The chamber walls are delineated by the gas trajectory that intersects the field screen at the same radius as the wafer ($r = 75 \text{ mm}$). The field screen is held at ground potential and the bias is applied to the substrate such that the electric field is dropped entirely and uniformly over $10 \text{ mm} > z > 0 \text{ mm}$ as in a parallel plate capacitor. Field edge effects will not be considered in this model, but in practice tend to cause higher deposition rates. The carrier gas exits through an exhaust port delineated by the edges of the wafer and field screen.

Now that a basis for the mechanics of aerosol motion has been established, we can proceed to explore the variation in transport characteristics as a function of

Fig. 12.11 Aerosol particle trajectories calculated for input gas velocity of 1 m/s and no applied electric field, illustrating the effect of aerosol particle radius on deposition pattern. Larger aerosol particles possess sufficient inertia to diverge from the gas flow trajectories and deposit onto the substrate, while smaller aerosol particles remain entrained in the gas flow and are not deposited

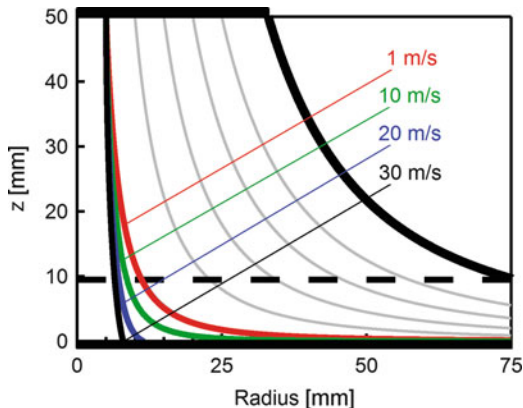


process conditions. First we will consider the effect of particle size on the aerosol transport as shown in Fig. 12.11. Carrier gas trajectories are shown for several radial entry points into the chamber and aerosol trajectories are shown for an entry point at $r = 5$ mm for particle radius of 10–75 μm . In this example the input velocity is 1 m/s and there is zero applied bias on the substrate. The larger particles have greater inertia and follow a path determined primarily by the direction of input velocity. As they approach the substrate their trajectory tends to diverge from the carrier gas trajectory and eventually they impact the substrate. Aerosol particles that impact the substrate will be incorporated into the thin film. Conversely, smaller aerosol particles with a radius less than 10 μm will tend to follow the carrier gas streamlines and be lost to the chamber exhaust without contributing any material to the thin film. Clearly an additional external force is necessary to induce deposition for smaller aerosol particles and will be discussed shortly when an electrostatic bias is applied to the substrate. The particle size significantly affects the overall deposition efficiency and defines two different transport regimes. The inertial deposition of aerosols greater than 10 μm radius is typically referred to as Spray Deposition in the literature, while deposition of particles less than 10 μm is typically referred to as Misted Deposition.

Refinement of the particle size distribution via impaction can also be understood within the context of Fig. 12.11. Let us consider the deposition chamber in this figure as an upstream impaction chamber with the substrate being replaced by a fixed diameter flow obstacle and the showerhead being replaced by a small diameter inlet orifice. Large radius aerosol particles will impact the flow obstacle and be deposited within the impaction chamber, while small radius aerosol particles will flow around the obstacle. In this way the particle size distribution can be clipped to the desired particle size based on the diameter of the flow obstacle and the geometry of the impaction chamber.

The input gas velocity can be used to shift the transition point between the Spray and Misted Deposition regimes as seen in Fig. 12.12. By increasing the input gas velocity a 10 μm radius aerosol particle can be made to deposit based on its inertial trajectory. This approach can be employed to increase the collection efficiency of smaller particles, but at the expense of causing most material to be deposited at the

Fig. 12.12 Aerosol particle trajectories calculated for $10\ \mu\text{m}$ radius aerosol particles and no applied electric field, illustrating the effect of input gas velocity on deposition pattern. Increased carrier gas velocity produces aerosol trajectories directed towards the center of the substrate, and can produce an image of the showerhead in the deposition pattern



center of the substrate. On the other hand, mist transport allows for sufficient material to be transported to the outer perimeter of the substrate.

We have learned that the transport of small aerosol particles by carrier gas alone will bring the particle within close proximity of the substrate surface, but will not cause the particles to deposit without an external force. The LSMCD process overcomes this effect by applying a DC voltage bias to the substrate which creates an electrostatic field between the substrate and field screen. Figure 12.13 shows the effect of this electrostatic field on the aerosol trajectories. For the following examples the particle radius has been chosen as $1\ \mu\text{m}$ as this corresponds to the cutoff particle size given by Fig. 12.7. The particles have a negative total charge equal to 100 elementary charges and the input carrier gas velocity is 1 m/s. By applying an electrostatic field in the positive z direction the aerosol particles are made to impinge the substrate and contribute to film growth. The trajectories diverge farther from the carrier gas trajectories for increasing electric field. The maximum field of $10\ \text{kV/cm}$ shown in the plot is determined based on the electrical breakdown of the fluid medium, which is about $1/3$ of the breakdown strength of air.

The charge polarity of the aerosol particles will determine whether their trajectories diverge toward or away from the substrate as shown in Fig. 12.14. In this example the direction of the electric field is the same as in Fig. 12.13, but now both positively and negatively charged aerosol particles with 100 elementary charges are shown. This is an illustrative example of the transport of a bipolar mist of atomized precursors by the LSMCD process. The trajectories of the negatively charged mist show good separation to the substrate edge, indicating that the aerosol is being deposited uniformly across the entire substrate. In practice film uniformities of less than 5% are achievable calculated as the range of thickness divided by twice the mean thickness [9].

We can also make some comments on the precursor utilization efficiency as affected by transport processes. To this end we will assume a monodisperse aerosol with $2\ \mu\text{m}$ diameter and 100 elementary charges of both polarities. As shown in Fig. 12.14, the positively charged aerosol particles are deflected away from the

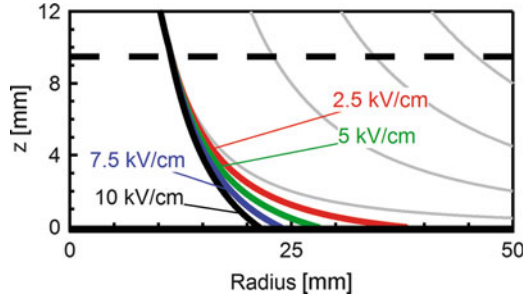


Fig. 12.13 Aerosol particle trajectories calculated for 1 μm radius aerosol particles with negative 100 elementary charges at an input velocity of 1 m/s, illustrating the effect of applied electric field on deposition pattern. Increasing electric field allows for smaller mist-sized aerosol particles to become deposited

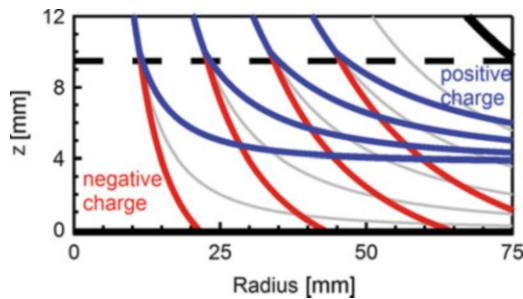


Fig. 12.14 Aerosol particle trajectories calculated for 1 μm radius aerosol particles with 100 elementary charges at an input velocity of 1 m/s, illustrating the effect of aerosol charge polarity on deposition pattern. Negatively charged aerosol particles are deposited onto the substrate, while positively charged particles are lost to the exhaust

substrate and transported to the exhaust, hence half of the mist is lost to exhaust. This effect of charge polarity on precursor utilization efficiency will be referred to as the ionization efficiency (ν_i) and will have a value of 50 % for the LSMCD process. Even some of the negatively charged mist that follows the trajectories close to the chamber walls will be lost to exhaust. We can estimate this fraction of material by determining the initial radius ($r_{0,c}$) of trajectories that intersect the substrate perimeter. All trajectories less than $r_{0,c}$ will be deposited on the wafer, while trajectories greater than $r_{0,c}$ will be transported to the exhaust. The collection efficiency (ν_c) can be calculated as the fraction of mist collected by the substrate divided by the total mist supplied by the showerhead as

$$\nu_c = \frac{\pi r_{0,c}^2}{\pi r_s^2} \tag{12.22}$$

where the r_s is the radius of the showerhead. The trajectories showing $r_{0,c}$ and collection efficiency as a function of applied electric field is shown in Fig. 12.15.

Fig. 12.15 Aerosol particle trajectories terminating at the substrate perimeter calculated for 1 μm radius aerosol particles with negative 100 elementary charges at an input velocity of 1 m/s. A greater fraction of aerosol is collected by the substrate for increasing electric field

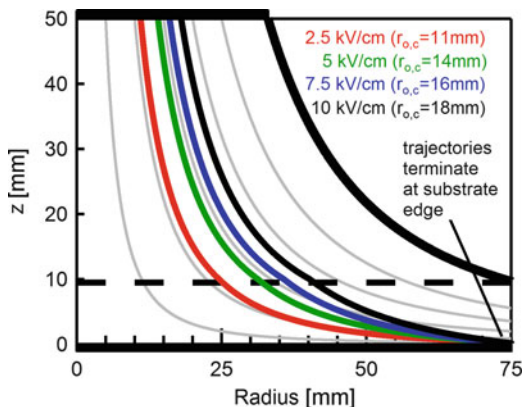
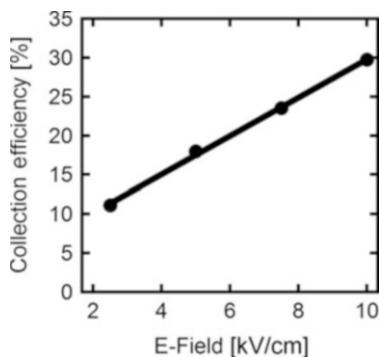


Fig. 12.16 Calculated collection efficiency for trajectories shown in Fig. 12.15 (1 μm radius, 100 elementary charges, 1 m/s inlet velocity). The collection efficiency and deposition rate are approximately linear with respect to applied electric field



The collection efficiency calculated from these trajectories is plotted in Fig. 12.16, and as expected the collection efficiency increases with applied electric field to a maximum value of about 30 % at 10 kV/cm. The overall precursor utilization efficiency can now be calculated as

$$\nu = \nu_g \cdot \nu_i \cdot \nu_c \tag{12.23}$$

The overall precursor utilization by this model predicts about 4 % utilization efficiency, which is comparable to spin coating. This value can be increased for some applications by optimizing the cutoff point for aerosol generation (for applications that do not require small aerosol particles) or increasing the ionization efficiency by unipolar charging [10].

The film deposition rate can be calculated using the precursor utilization efficiency, the quantity of precursor supplied, and the shrinkage factor associated with converting the precursor liquid to its final solid structure. The shrinkage factor (S) is defined as the ratio of the film volume (V_{film}) to the solution volume (V_{soln}) and can be estimated from the molar volumes of each as

$$S = \frac{V_{film}}{V_{soln}} = \frac{\frac{M_m}{d}}{\frac{1}{M_s}} = \frac{M_m M_s}{d} \quad (12.24)$$

where M_s is the molarity of the solution, M_m is the molar mass of the film, and d is the film density. The film volume can then be calculated by using the flow rate of precursor into the system (Q_{soln}) and the deposition time (t_{dep}) as

$$V_{film} = Q_{soln} \cdot t_{dep} \cdot S \cdot \nu. \quad (12.25)$$

The film volume is simply the film thickness multiplied by the substrate area (A_{sub}) which yields the following equation for film thickness

$$t_{film} = \frac{Q_{soln} \cdot t_{dep} \cdot S \cdot \nu}{A_{sub}} \quad (12.26)$$

from which the deposition rate (R_{dep}) is calculated finally as

$$R_{dep} = \frac{Q_{soln} \cdot S \cdot \nu}{A_{sub}}. \quad (12.27)$$

These equations show that the deposition rate is linear with respect to a number of process parameters including precursor solution flow rate, precursor solution molarity, substrate bias, and deposition time. Linearity of deposition rate in these process variables has been demonstrated for a number of material systems [2, 11] and provides flexibility in thickness control that is not otherwise available for other CSD coating techniques. Moreover, the LSMCD process provides a convenient way of controlling film thickness independent of precursor molarity, which is often convoluted with residual carbon in CSD films. An example deposition rate can be calculated as 100 Å/min using 0.75 M La_2O_3 precursor at 0.15 mL/min flow rate and 8 kV/cm substrate bias. This calculation agrees well with actual measured deposition rates and also represents a typical deposition rate achievable by the LSMCD process.

12.2.3 Aerosol Aggregation and Film Growth

Thin film growth from aerosols takes place via nucleation by adsorption of individual droplets, accumulation of a sufficient number of nuclei for the droplets to coalesce into a continuous film, and finally incorporation of additional aerosol flux into the thin liquid film. The droplets and liquid film will reflow throughout these steps in such a way as to minimize surface free energy. This particular aspect of aerosol deposition can yield planar thin films with significantly different characteristics than spin-coated films including incomplete-wetting and migration effects. As we have seen in previous sections aerosol deposition can enable

deposition of internal surfaces of microstructures. The resulting profiles of thin liquid films in these structures will be determined largely by liquid tension and meniscus effects.

The initial nucleation phase of film growth can be understood via contact angle theory and is illustrated in Fig. 12.17. A droplet adsorbs onto the substrate to form a spherical cap with the internal angle between the substrate and droplet surface being designated the contact angle. The spherical cap will have the same volume as the initial droplet and dimensions established by the volume and contact angle. In the absence of external potentials the contact angle can be determined by the surface energies of the liquid vapor interface (γ_{lv}), the solid vapor interface (γ_{sv}), and the solid liquid interface (γ_{sl}) via Young's equation [12]

$$\gamma_{sv} = \gamma_{sl} + \gamma_{lv} \cos(\theta). \quad (12.28)$$

Droplets that spread out to cover a large surface area for a given volume are said to “wet” the surface and exhibit a contact angle of zero degrees. In this case the surface energy of the solid vapor interface is greater than or equal to the sum of the solid liquid and liquid vapor interfaces ($\gamma_{sv} \geq \gamma_{sl} + \gamma_{lv}$) and the total energy is minimized when the droplet geometry reduces the exposed substrate area. Conversely, no-wetting corresponds to a contact angle of 180 degrees and occurs when the surface energy of the solid liquid interface is greater than or equal to the sum of the solid vapor and liquid vapor interfaces ($\gamma_{sl} \geq \gamma_{sv} + \gamma_{lv}$). For this case liquid droplets will retain their spherical shape and maintain only a point contact to the substrate surface. It should be noted that the actual contact angle can be significantly affected by the electric potential the droplet is subjected to and the quantity of charge that is induced in or retained by the droplet [13]. Hence the initial aerosol charge and bias used to assist deposition during transport will in general exert electrostatic forces in addition to liquid tension forces. Further complications exist when depositing on surfaces with conductive and insulating regions. This mixed character can cause an incongruent accumulation of charge on the droplets and create localized non-uniformities in the electrostatic field.

When two discrete liquid droplets make physical contact during deposition they will coalesce to form a single droplet with a smaller overall surface area. Towards the end of the nucleation stage the frequency of coalescence will increase until all droplets have combined to form a continuous thin liquid film [14]. The film thickness at the point of complete coalescence will be termed the critical thickness and represents a lower bound in the fabrication of continuous films. We can make an estimate of the minimum critical thickness based on the dimensions and geometry of the incoming aerosol flux, spherical cap droplets, and continuous thin film as shown in Fig. 12.18. Consider a scenario in which a monodisperse aerosol arrives at the substrate in a close packed hexagonal array. The adsorbing aerosol spreads out to form spherical caps that just touch their nearest neighbors at which point they coalesce to form a continuous film. The volume of the initial spherical aerosol particle becomes incorporated into a hexagonal slab with equivalent volume. Using the numbering scheme from the sequence in Fig. 12.18 we can state this

Fig. 12.17 Diagram of liquid spherical cap illustrating contact angle with respect to substrate surface

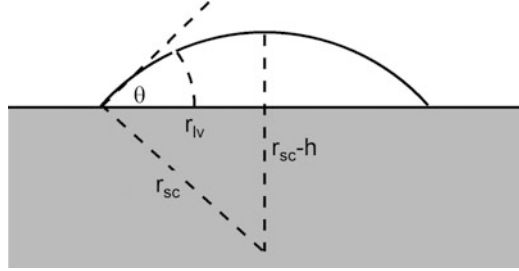
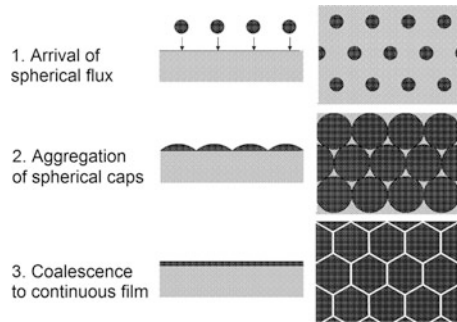


Fig. 12.18 Diagram of idealized nucleation behavior showing incidence, aggregation, and coalescence of aerosol particles



mathematically as $V_1 = V_2 = V_3$. By determining the interfacial area of the hexagon the critical thickness (t_{crit}) can be calculated as

$$t_{crit} = \frac{V_3}{A_3} = \frac{V_1}{A_3} = \frac{\frac{4}{3}\pi r_p^3}{2r_{ls}^2\sqrt{3}} \tag{12.29}$$

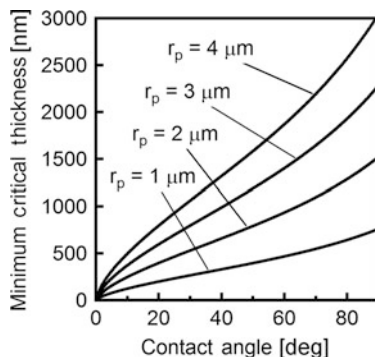
where r_{ls} is the radius of the liquid solid interface for the spherical caps. By equating $V_1 = V_2$ and solving for the radius of the spherical cap (r_{sc}), the radius of the liquid solid interface is found as

$$r_{ls} = \frac{r_p \sin \theta}{\left[\sin^4 \frac{\theta}{2} \cdot (3 - 2 \sin^2 \frac{\theta}{2}) \right]^{\frac{1}{3}}} \tag{12.30}$$

From Eqs. (12.29) and (12.30) it can be seen that the critical thickness for coalescence is determined by the contact angle (which is a function of surface energies and applied bias) and the aerosol particle radius. Figure 12.19 shows the minimum critical thickness as a function of these two parameters.

Note that these results are for liquid films, the final solid film thickness would need to be multiplied by the shrinkage factor S . Liquid films with below minimum critical thickness will exhibit discontinuity, while above critical thickness films have the potential for monolithic films depending on the actual sequence of nucleation events. The dependence of the critical thickness on aerosol particle

Fig. 12.19 Minimum critical thickness for thin liquid films calculated using Eq. (12.30). Uniform layers are obtained for thicknesses in excess of the critical thickness, while discontinuous films are obtained below the critical thickness



radius demonstrates another aspect in which the aerosol size can be a key parameter in applications requiring very thin continuous films.

Liquid films that have been deposited over trenches or surface topology will tend to exhibit a meniscus-like profile. This effect is again due to the minimization of surface free energy and results in an accumulation of excess material at the bottom of sidewall structures. This excess material can lead to unwanted parasitic effects in applications that require conformal thin films and film thicknesses that are significantly less than the width of the trench. In these cases a common approach has been to reduce the angle of the sidewalls so that there is less bridging of the liquid between the trench bottom and sidewalls. For other applications it is desirable to fill trenches evenly in a process called planarization. Here the deposited film thickness is usually equivalent to the dimensions of the trench and liquid tension forces assist the liquid in migrating to internal surfaces.

12.2.4 Thermal Processing

The final step in fabrication of thin films by aerosol deposition and by any type of chemical solution deposition is converting the thin liquid film into a thin solid film. Thermal processing has been presented in previous chapters, but will be reviewed here for contextual relevance. As the ambient temperature of the film is increased there are compositional and structural changes that take place during the phase change from liquid to solid. First organic solvents are evaporated from the film at a temperature above the solvent boiling point. Next the remaining metallo-organic precursors are pyrolyzed above the precursor decomposition temperature to create a solid amorphous metal oxide film. These processes are accompanied by a net reduction in the film volume as the organic components of the precursors are removed or converted to gaseous byproducts. Depending on the desired form of the solid film a final crystallization anneal can be applied to convert the oxide to the crystalline phase.

12.3 Aerosol Deposition Techniques

In the previous sections the generation, transport, and deposition of liquid aerosols was presented sequentially as it occurs in the LSMCD process. Thermal processing of the films was applied subsequent to the completion of the all deposition processes. In contrast to LSMCD, many aerosol deposition techniques involve the deposition of aerosols on heated substrates. In these processes the aerosol undergoes evaporation and pyrolysis during the transport and film growth steps of the aerosol deposition process and is termed “spray pyrolysis”. Spray pyrolysis processes usually take place across large temperature gradients that incur a significant dynamic response in the physical and chemical properties of the precursor aerosols. Consequently, analysis of transport processes becomes complex enough that the task will merit a qualitative rather than quantitative discussion here. Moreover, the arriving flux of material at the substrate surface will frequently consist of partially dried aerosol particles, precursor vapors, and reacted precursor powders. The resulting film structure will generally consist of an aggregate of these depositing species.

Aerosol particles will experience a thermal cycle en route to the substrate that depends largely on the precursor chemistry and substrate temperature. Figure 12.20 shows a schematic illustration of this cycle with key thermal processes delineating different regimes of the spray pyrolysis process. The precursor aerosol is initially generated as a liquid droplet in a similar manner to the processes previously described. As the aerosol approaches the solvent evaporation temperature during transit to the substrate it will begin to lose volume due to solvent evaporation. Physically this effects the particle inertia and the magnitude of the Stokes force and can reduce deposition efficiency. Chemically a situation is created in which dissolved solids can precipitate if enough solvent evaporates in the aerosol particle to increase the concentration above the precursor solubility limit. As temperature is increased above the precursor vaporization point the aerosol particles will dissociate to form a vapor of precursor molecules. The precursor molecules will pyrolyze during transport to form powder if the decomposition temperature of the precursor is exceeded. For precursors with a decomposition temperature less than their vaporization temperature, a larger solid particle will form directly from the aerosol particle.

The substrate temperature will determine the extent of reaction in the thermal cycle, however the rate at which these reactions proceed has a kinetic dependence that depends on the aerosol size. During solvent evaporation and pyrolysis mass transfer of solvent and gaseous byproducts will take place through the particle surface area. Smaller aerosol particles have greater surface area to volume ratio and will in general proceed through the thermal cycle at a faster rate than larger particles. Hence, for a given temperature and aerosol particle size distribution there may be particles present at various stages of the thermal cycle. Larger particles can also develop a thermal gradient across their diameter and induce a skin effect in which the outer surface begins to decompose prior to evaporation of the solvent. This is sometimes observed as hollow particles deposited on the substrate [15].

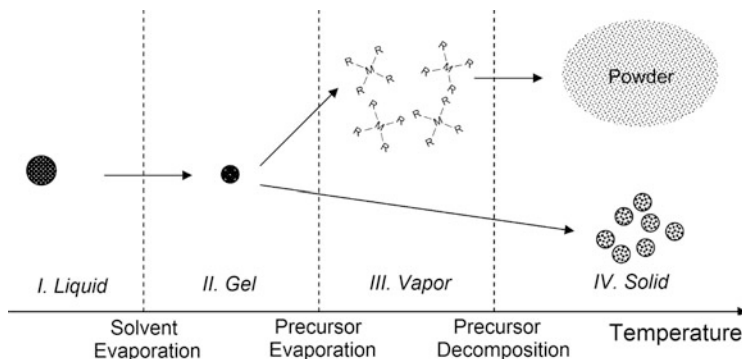


Fig. 12.20 Spray pyrolysis thermal cycle

The thermal cycle illustrated in Fig. 12.20 also delineates several spray pyrolysis operational regimes as determined by the substrate temperature. Regime I corresponds to low temperature liquid film deposition in which the precursor composition and aerosol particle size do not evolve with transport. This situation describes the LSMCD process presented in the previous section. Regime II corresponds to deposition of precursors that have lost enough solvent to increase the precursor viscosity whereby the droplets will not coalesce upon incorporation into the film. In actuality aerosol particles in both regimes will evaporate some of their solvent if the carrier gas is not at the equilibrium vapor pressure for the solvent. The distinction between regimes I and II is somewhat amorphous and they are consequently lumped together and termed “aerosol-gel processes” [14]. Regime III represents a type of spray pyrolysis in which the precursors are vaporized prior to adsorption onto the substrate. This process is very similar to the MOCVD process discussed earlier and is usually referred to as aerosol-MOCVD [16]. The aerosol-MOCVD process takes place at atmospheric pressure, while traditional MOCVD processes occur at vacuum pressures. As the substrate temperature reaches the precursor decomposition temperature the aerosol particles can be made to decompose at or within a proximal distance of the substrate in a region called the reaction zone [17]. Beyond this temperature the aerosol will form non-coherent powder and solid particles (regime IV). While these processes are not useful for growth of adherent films, they are of interest in the fabrication of powders and nanoparticles [18].

12.4 Structure-Processing-Property Relationships of Aerosol Deposited Films

The properties of thin films are intimately related to the microstructure of the films, which in turn are determined by the fabrication process. These correlations are generally referred to as structure-processing-property relationships. In the previous sections we outlined some of the key differences between spin coating and aerosol

deposition and noted how the macroscopic structure with respect to surface topology is related to the fabrication process. In this section we will explore how the fabrication process affects the microscopic structure of the films. A key point of differentiation between spin coating and aerosol deposition lies in the principle that substrate heating can be applied during aerosol deposition. In this way the carbonaceous byproducts can be removed during growth, which will increase the density of as-grown films. A greater degree of control over film crystallinity can also be achieved by substrate heating during spray pyrolysis. Finally, the depositing flux on heated substrates consists of partially reacted aerosol particles that will tend to aggregate as semi-solid particles in contrast to coalescing as a liquid.

As described in previous sections, thermal processing includes conversion of the metallo-organic precursor to a solid metal oxide. During conversion the organic components are evaporated or reacted to form volatile compounds and discharged from the film. In the case of liquid films (regime I from Fig. 12.20) with thermal processing applied as a post-process the reaction byproducts must be transported through the full film thickness. The amorphous network of metal oxide bonds will begin to form prior to the emission of all organic components and can result in porous structure and residual carbon in the film. In the case of higher substrate temperatures (regimes II and III from Fig. 12.20) the reaction byproducts need only desorb from the growth surface as opposed to through the full film thickness and will result in higher density films. In some cases microcracks can form as a result of film shrinkage during thermal processing, which imposes an upper bound on the thickness that can be deposited per layer. The simultaneous growth and densification inherent in the spray pyrolysis process will in many cases eliminate this constraint [19].

Crystallization of CSD deposited films will depend to a large extent on the growth temperature and whether crystallization takes place during growth or as a post-growth process. These relationships can be described using the structure zone model (SZM) published in reference [20], which is reproduced in Fig. 12.21. The axes in the SZM are the material-independent homologous temperature (sintering temperature/melting temperature) versus the ratio of intrinsic crystallite size to single layer film thickness. In regard to aerosol deposition the thermal axis corresponds to the substrate temperature. The intrinsic crystallite size/single layer thickness is presented here as a fabrication parameter that spans deposition of individual layers with subsequent thermal processing to simultaneous deposition and thermal processing (as in spray pyrolysis where the single layer thickness approaches zero). From the SZM it is apparent that the crystalline structure can take on significantly different characteristics depending on these two parameters. For single layer thicknesses greater than the crystallite size, the crystals will nucleate randomly in the bulk of the film and give rise to a granular structure, which has been observed in transparent conductive oxide thin films [20, 21]. As the single layer thickness approaches the crystallite size the film thickness constrains nucleation to a planar array of crystallites, causing a layer by layer growth of individual crystallites. As the single layer thickness falls below the crystallite size, nucleation of new crystallites will be seeded by the crystallites from the previous layer. Consequently, the morphology of the films will take on a columnar

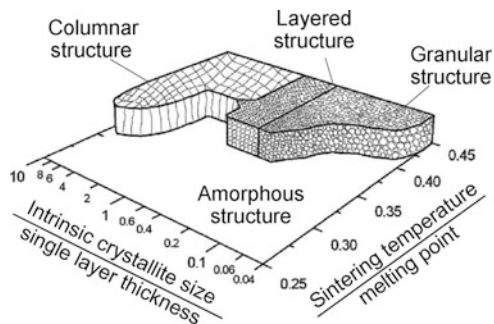


Fig. 12.21 Structure zone model (SZM) for CSD-derived thin films [20]. With kind permission from Springer Science and Business Media: *Journal of Sol-Gel Science and Technology, A microstructural zone model for the morphology of sol-gel coatings*, v. 31, 2004, pg. 235-239, T. Schuler, T. Krajewski, I. Grobelsek, M. Aegerter, Fig. 5

characteristic in which the crystal structure of the initial layer is templated through the entire film thickness. This film growth mode has been demonstrated by the aerosol-MOCVD process [22] and yields epitaxial thin films in which the crystallographic orientation of the substrate is transferred to the film during growth. It is also worth noting the phase transition temperature from amorphous phase to crystalline phase as a function of crystallite size to single layer thickness. In the granular growth region the film density will be low in comparison to the layer and columnar growth regions, as explained in the previous paragraph. Crystallization takes place by diffusion of atoms into their respective lattice sites at elevated temperature. Low density films will incur a longer diffusion length than high density films and require a higher crystallization temperature. This effect is illustrated in the SZM as a lower phase transition temperature for the layered and columnar modes of film growth. These various forms of crystalline structure are important as the grain boundaries often play a key role in defining film properties (i.e. grain boundary scattering of charge carriers in polycrystalline semiconductors).

12.5 Applications of Aerosol Deposited Films

The unique characteristics of aerosol deposition have enabled the utilization of chemical solution deposition in several commercial applications. Spray pyrolysis was developed to provide a large scale and low cost film growth technique that could yield similar film properties to vacuum based techniques. The spray pyrolysis technique has been in existence since the 1950s and has facilitated the fabrication of a vast number of materials. A significant share of spray pyrolysis development has focused the deposition of transparent conductive oxides and compound semiconductors. These particular materials have been pursued as transparent electrodes and active layers for solar cells [23] and for heat reflective coating for architectural windows [24]. These applications require inexpensive film deposition

over large substrate areas, both of which can be achieved by the spray pyrolysis technique.

More recently misted deposition techniques have found applications in microelectronics and nanotechnology as an alternative to spin coating. The LSMCD technique was originally developed as a means of depositing ferroelectric thin films as part of Metal-Insulator-Metal (MIM) capacitors for non-volatile memories [25]. Spin coating of these materials was already employed in the fabrication of planar capacitors, however device scaling rules required that the capacitor area be increased by implementing a three dimensional topology for future device generations. MOCVD techniques were not expected to be production worthy within the time frame in which 3D ferroelectric capacitors would become necessary. Hence, the LSMCD technique was developed to bridge the gap between obsolescence of spin coating processes and the realization of MOCVD processes.

During the course of development the LSMCD technique demonstrated that it was capable of fabricating a variety of microelectronic quality films. Thus, LSMCD was investigated for a number of other applications including high k capacitors for DRAMs [26] and high k gate dielectrics in Metal-Insulator-Semiconductor (MIS) structures [27]. These particular applications leverage the ability of LSMCD in depositing very thin films of multi-component metal oxides independent of precursor dilution. LSMCD has been used to deposit photoresist films [28] for patterning as well as pigmented photoresist and organic light emitting films [29] for use in flat panel displays. Here LSMCD has been demonstrated effective in depositing large and non-circular substrates. The unique wetting characteristics of LSMCD deposited films have been explored as a means of selective film deposition. By controlling the contact angle of precursor solutions on a heterogeneous deposition surface the deposited droplets could be made to migrate to desired locations [30–32]. This process is being explored as a means for fabrication of patterned metal oxide structures that do not require expensive ion based etch post processing.

Emerging applications in nanotechnology represent several current research thrusts for LSMCD applications. Conformal coating of carbon nanotubes with ferroelectric material has been demonstrated [33] as well as fabrication of nanotubes consisting entirely of ferroelectric material [34]. LSMCD has been used to deposit colloidal solutions of nanocrystal quantum dots (NQDs) consisting of CdSe/ZnS core shell structures for LED applications [35]. It was necessary to control the thickness of the NQD layer down to several monolayers, hence the LSMCD was well suited for fabrication of such thin layers.

References

1. Brubaker M, Mumbauer PD, Grant R (2001) Deposition and thermal processing of ferroelectric thin films with the Primaxx 2F platform. *Integr Ferroelectr* 36:305–312
2. Solayappan N, Joshi V, DeVilbiss A, Bacon J, Cuchiaro J, McMillan L, Paz de Araujo C (1998) Chemical solution deposition (CSD) and characterization of ferroelectric and dielectric thin films. *Integr Ferroelectr* 22:1–11

3. Kawasaki S, Motoyama SI, Tatsuta T, Tsuji O, Shiosaki T (2003) Fabrication of $\text{Pb}(\text{Zr,Ti})\text{O}_3$ thin films by liquid source misted chemical deposition method equipped with a mist-droplet size controller. *Integr Ferroelectr* 53:287–297
4. Grace JM, Marijnissen JCM (1994) Review of liquid atomization by electrical means. *J Aerosol Sci* 25:1005–1019
5. Hinds WC (1999) *Aerosol technology: properties, behavior, and measurement of airborne particles*, 2nd edn. Wiley, New York
6. Reist PC (1984) *Introduction to aerosol science*. Macmillan/Collier Macmillan, New York/London
7. Fuchs NA (1964) In: Davies CN (ed transl) *The mechanics of aerosols*. Pergamon, Oxford, pp 378–394 (revised and enlarged edn)
8. Schlichting H, Oertel H (2000) *Grenzschicht-Theorie*. English: *Boundary-layer theory*, 8th rev. and enl. edn. Springer, Berlin
9. Primaxx Technical literature. Primaxx, Inc, Allentown, PA <http://www.primaxxinc.com>
10. Siefert W (1984) Corona spray pyrolysis – a new coating technique with an extremely enhanced deposition efficiency. *Thin Solid Films* 120:267–274
11. Mumbauer P, Chang K, Mahoney W, Lee DO, Shanmugasundaram PK, Roman P, Brubaker M, Grant R, Ruzyllo J (2004) Mist deposition in semiconductor device manufacturing. *Semicond Int* 27:75–80
12. Adamson AW, Gast AP (1997) *Physical chemistry of surfaces*, 6th edn. Wiley, New York
13. Blake TD, Clarke A, Stattersfield EH (2000) Investigation of electrostatic assist in dynamic wetting. *Langmuir* 16(6):2928–2935
14. Langlet M, Vautey C, Mazeas N (1997) Some aspects of the aerosol-gel process. *Thin Solid Films* 299(1–2):25–32
15. Ortega J, Kodas TT (1992) Control of particle morphology during multicomponent metal oxide powder generation by spray pyrolysis. *J Aerosol Sci* 23(SUPPL 1):253–256
16. Khoroshun IV, Karyaev EV, Moshnyaga VT, Kiosse GA, Krachun MA, Zakosarenko VM, Davydov VY (1990) Characteristics of epitaxial Y-Ba-Cu-O thin-films grown by aerosol MOCVD technique. *Supercond Sci Technol* 3:493–496
17. Grigoriev D, Choy KL (2004) Aerosol deposition of films in an electrical field: modelling and experiment. *Scr Mater* 51:857–861
18. Kuang-Che H, Shih-Chieh L, Yi-Jia C (2007) Synthesis, characterization and photocatalytic property of nanostructured Al-doped ZnO powders prepared by spray pyrolysis. *Mater Sci Eng A* 447:71–76
19. Losego MD, Trolrier-McKinstry S (2003) *Mist deposition of micron-thick lead zirconate titanate films*. Materials Research Society, Boston, MA
20. Schuler T, Krajewski T, Grobelsek I, Aegerter M (2004) A microstructural zone model for the morphology of sol-gel coatings. *J Sol-Gel Sci Technol* 31:235–239
21. Takahashi Y, Okada S, Tahar RBH, Nakano K, Ban T, Ohya Y (1997) Dip-coating of ITO films. *J Non-Cryst Solids* 218:129–134
22. Moshnyaga V, Khoroshun I, Sidorenko A, Petrenko P, Weidinger A, Zeitler M, Rauschenbach B, Tidecks R, Samwer K (1999) Preparation of rare-earth manganite-oxide thin films by metalorganic aerosol deposition technique. *Appl Phys Lett* 74:2842–2844
23. Mooney JB, Radding SB (1982) Spray pyrolysis processing. *Annu Rev Mater Sci* 12:81–101
24. Aukkaravittayapun S, Wongtida N, Kasewatin T, Charojrochkul S, Unnanon K, Chindaudom P (2006) Large scale F-doped SnO_2 coating on glass by spray pyrolysis. *Thin Solid Films* 496:117–120
25. Solayappan N, McMillan LD, Paz de Araujo CA, Grant B (1997) Second generation liquid source misted chemical deposition (LSMCD) technology for ferroelectric thin films. *Integr Ferroelectr* 18:127–136
26. Chung HJ, Choi JH, Lee JY, Woo SI (2001) Preparation and electrical properties of $(\text{Ba,Sr})\text{TiO}_3$ thin films deposited by liquid source misted chemical deposition. *Thin Solid Films* 382:106–112

27. Lee DO, Roman P, Wu CT, Mumbauer P, Brubaker M, Grant R, Ruzylo J (2002) Mist deposited high-k dielectrics for next generation MOS gates. *Solid-State Electron* 46 (11):1671–1677
28. Mahoney WJ III, Roman P, Mumbauer P, Ruzylo J (2004) Mist deposition of thin photoresist films. In: Sturtevant JL (ed) *Advances in resist technology and processing XXI*, vol 5376. Proceedings of SPIE, Bellingham, WA, pp 861–866. doi:[10.1117/12.534149](https://doi.org/10.1117/12.534149)
29. Shanmugasundaram K, Price S, Chang K, Lee D, Ruzylo J (2006) Mist deposition for TFT technology. *ECS Trans* 3:255–259
30. Shanmugasundaram K, Brubaker M, Chang K, Mumbauer P, Roman P, Ruzylo J (2007) Studies of solution processed metal oxides on silicon. *Microelectron Eng* 84:2294–2297
31. Takakuwa A, Ishida M, Shimoda T (2005) Micropatterning of SrBi₂Ta₂O₉ ferroelectric thin films using a selective deposition technique combined with patterned self-assembled monolayers and liquid-source misted chemical deposition. *Jap J Appl Phys, Part 1* 44:1897–1900
32. Takakuwa A, Mitani T, Shimoda T (2007) Micropatterning of indium tin oxide thin films by selective deposition and improvement in selectivity by combination with substrate vibration. *Jap J Appl Phys, Part 1* 46:3016–3019
33. Kawasaki S, Catalan G, Fan HJ, Saad MM, Gregg JM, Correa-Duarte MA, Rybczynski J, Morrison FD, Tatsuta T, Tsuji O, Scott JF (2008) Conformal oxide coating of carbon nanotubes. *Appl Phys Lett* 92:053109
34. Morrison FD, Ramsay L, Scott JF (2003) High aspect ratio piezoelectric strontium-bismuth-tantalate nanotubes. *J Phys Condens Matter* 15:527–532
35. Zhu T, Shanmugasundaram K, Price SC, Ruzylo J, Zhang F, Xu J, Mohny SE, Zhang Q, Wang AY (2008) Mist fabrication of light emitting diodes with colloidal nanocrystal quantum dots. *Appl Phys Lett* 92:023111

Chapter 13

Inkjet Printing and Other Direct Writing Methods

Paul G. Clem and Nelson S. Bell

13.1 Introduction

In recent years, a large effort has been focused on the deposition of metallic systems via advanced printing techniques, e.g. direct write, inkjet and μ -contact printing. Such printing techniques are attractive alternatives to conventional photolithography and electroless routes, which are time-consuming, complicated, and expensive. With the emergence of flexible electronics, the ability to integrate dissimilar materials, i.e., ceramics, metals, semiconductors, and polymers, onto a single, temperature-sensitive substrate enables the fabrication of volumetrically-concise, multi-functional packages. In the past, the technical advances in low temperature co-fired ceramic (LTCC) packages allowed for integration of screen-printed metal traces at temperatures of approximately 800–900 °C. Coupling “drop-on-demand” deposition technologies with ink formulations based on nanoparticle, chemical solution precursors, and/or UV-curable chemistries provide lower-temperature, <200 °C, routes for deposition of highly conductive traces on polymeric commercial substrates. This presents an alternative maskless, cost-effective route to that of electrodeposited cladded substrates.

13.2 Development of Printable, Low Process Temperature Metal Inks

A major challenge in applying advanced printing techniques for the deposition of functional materials is the formulation of suitable inks. Ink chemistry and formulation determine not only the as-deposited characteristics, but also ink stability. The ability to deposit well-defined, uniform, and high quality print patterns without

P.G. Clem (✉) • N.S. Bell
Sandia National Laboratories, Albuquerque, NM, USA
e-mail: pgclem@sandia.gov

clogging the print head requires a fundamental understanding of the ink chemistry and the corresponding processing-property relationships. While the ability to deposit a suite of metallic compositions (Ag, Cu, Au, Al, Pt, Pd, etc. . .) is desirable, the following section details several routes for the deposition of low-temperature curing silver-based ink designs.

13.2.1 Nanoparticle Synthesis

Conventional low-temperature co-fired ceramic (LTCC) technology involves the production of multilayer circuits from ceramic substrates. Conductive and insulating thick films are screen-printed onto each LTCC as needed, facilitating monolithic structures of embedded resistors, capacitors, and interconnects. Often, thick film conductor formulations consist of (1) silver flake, a highly anisotropic, micron-sized particulate, (2) organic binder, and (3) a glass frit to reduce sintering temperatures (bulk Ag $T_m = 963$ °C). Sintering of LTCC at “low” temperatures, e.g. 850–900 °C, allows for the integration of low resistivity conductors, i.e., Ag, with LTCC packages.

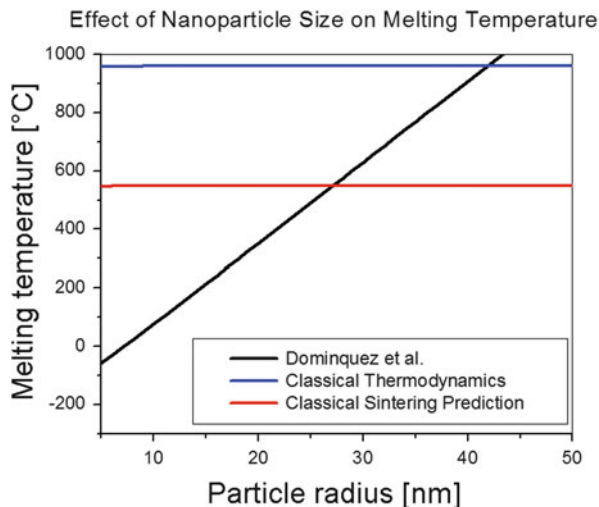
It is now well-established that by shrinking the size of a solid particle to the nanometer scale, one can alter its chemical, thermal, electrical, mechanical, and optical properties. With respect to melting temperatures, the presence of high curvature nanoparticles has been proposed to either generate a low-temperature sintering reaction, or else a high curvature-driven driving force for low temperature necking and conductivity development. Nanoparticle reactivity has been characterized experimentally to be much higher than classical thermodynamic predictions. Dominguez et al. [1] proposed the size dependence of surface melting on the basis of a Debye model with the Lindemann law and incorporated a phonon softening process according to the following equation:

$$T_m = \frac{Mk\Theta_b^2\delta^2a^2}{36\hbar^2\left[1 - (1 - na/R)^3\right]} + \frac{1}{8}\Theta_b \quad (13.1)$$

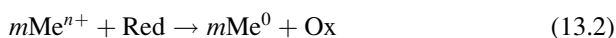
where M is the atomic mass, k is Boltzmann’s constant, \hbar is Plank’s constant, δ is the Lindemann law parameter for liquifaction ($\delta = 0.5$), a is the lattice parameter, Θ_b is the bulk Debye temperature, r is the nanoparticle radius, and na is the surface thickness where melting occurs, ($n = 3.5$). Equation (13.1) provides a good estimate of the temperature where sintering initiates and the relationship for silver is illustrated in Fig. 13.1. This predicts sintering to occur at room temperature for particles smaller than 25 nm due to increased nanoparticle reactivity.

Of the many various existing preparation schemes for Ag nanoparticle synthesis, the simplest and most commonly used synthesis route is the chemical reduction of a silver salt by a reducing agent, e.g., sodium borohydride, citrate, or ascorbate. The reduction of metallic ions leading to neutral atoms, the building blocks of metal

Fig. 13.1 Theoretical predictions of size-sintering relationship for silver nanoparticles



particles, is the result of a redox reaction in which electrons from a reducing agent are transferred to the metal according to:



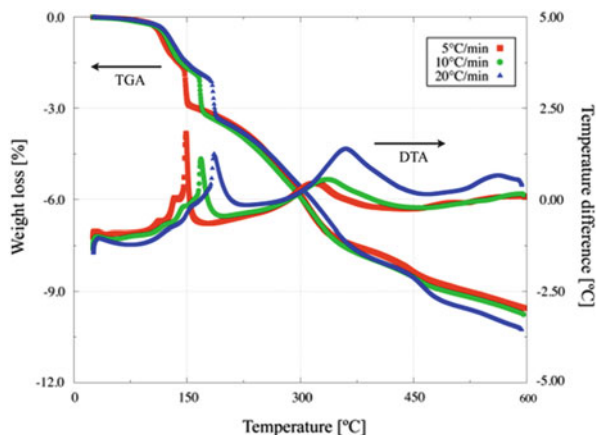
The driving force of the reaction is the difference between redox potentials of the two half cell reactions, ΔE . The magnitude of ΔE determines the value of the equilibrium constant of the reaction, K_e , according to the Nernst equation:

$$\ln K_e = nF\Delta E/RT \quad (13.3)$$

where n is the number of electrons transferred, F is the Faraday constant, R is the universal gas constant, and T is the absolute temperature. The reduction reaction is thermodynamically possible only if ΔE is positive, which implies that the redox potential of the reducing agent must have a more negative value than that of the metallic species. Thus, strongly electropositive metals, like Ag, will react even with mild reducing agents under ordinary conditions. Through reducing agent selection and tuning of experimental parameters (i.e., solvent selection, temperature, and time) the resulting particle size, distribution and morphology can be tailored.

To prevent particle agglomeration, many studies have assessed the role of stabilizers and complexing agents (e.g. reverse micelles, surfactants, dendrimers, alkanethiols, and carboxylic acids) on suspension stability, particle size/distribution, and morphology. The ability to prepare high volume fraction, monodisperse, and spherical nanoparticle (<100 nm) inks would both minimize clogging during deposition and enable high density, as-deposited metal traces. A common complication in low-temperature reaction to a pure, highly conductive metallic state is slow thermal decomposition of organic stabilizers, as illustrated in Fig. 13.2. Often, silver nanoparticle suspensions use high molecular weight polymers as dispersants,

Fig. 13.2 Thermal analysis of silver nanoparticles (<10 nm) stabilized with a long chain carboxylic acid



requiring slow ramp rates and high temperatures to ensure complete conversion. Figure 13.3 shows the time/temperature dependence of DC resistivity of a silver nanoparticle ink stabilized with a long chain carboxylic acid at two different annealing temperatures, 100 °C and 170 °C, on either side of the dispersant decomposition temperature. The corresponding *in-situ* high resolution TEM analysis illustrates the necking processes that initiate around 100 °C. Perelaer et al. demonstrated high conductivity values (56 % of bulk silver) at 80 °C by using very small amounts of organic additives, using weakly adsorbing species such as amines, amides, and mercapto groups [2].

Wakuda and co-workers reported a room temperature sintering route for Ag nanoparticles using a chemical dip treatment utilizing an alkylamine dispersant—dodecylamine [3]. During particle synthesis, the nanoparticles are coated and stabilized with dodecylamine, and the resulting sterically-stabilized suspensions are patterned on glass substrates or copper plates. For dispersant removal, the sample patterns are washed in methanol, resulting in pure metallic particles which sinter upon removal of the solvent at room temperature [3]. Upon completion of a 2 h methanol submersion, microstructural observations revealed that the Ag nanoparticles had agglomerated and coarsened, with a measured DC resistivity of $7.3 \times 10^{-5} \Omega \cdot \text{cm}$; this is often normalized to the bulk conductivity of silver, $1.6 \times 10^{-6} \text{ W-cm}$, or $45 \times$ bulk Ag ρ , in this case. Metal nitrate precursors, nanoparticle silver inks, and laser sintering enable low-temperature or even room temperature cure inks. Table 13.1 provides a summary of achieved conductivity values via different thermal treatment methods.

The use of strong reducing agents, i.e., borohydride, results in small particles that are somewhat monodisperse, but controlling particle growth is difficult. Additionally, such reducing agents may be associated with environmental toxicity or biological hazards. It has been, therefore, of increasing interest to develop “green” synthesis of colloidal silver nanoparticles. Research on chemical production routes utilizing green principles has increased in the past decade, where the most commonly used protecting agent is starch. The initial reference to “green” chemical

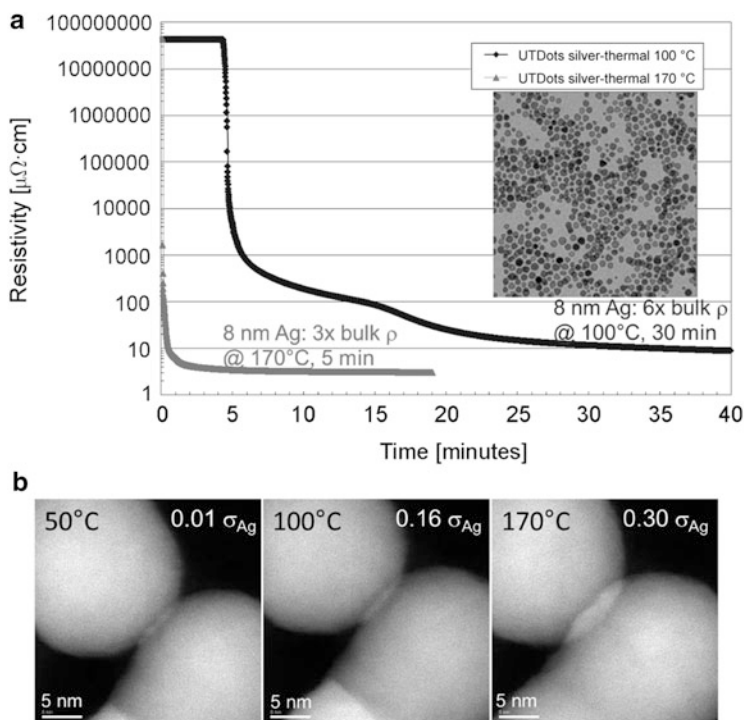


Fig. 13.3 (a) Time dependence of DC resistivity for direct written Ag traces. (b) HR-TEM demonstrating the necking and growth mechanisms of silver nanoparticles. HR-TEM images courtesy Prof. D. Kovar and P. Ferreira at University of Texas-Austin

Table 13.1 Summary of print method properties, and metal resistivities vs. thermal treatment

Topic	Method	Details
<i>Printable area</i>		
Area: 1 m ² area, 60 cm Δz	Syringe or aerosol jet	
Resolution: ≥16 μm	Syringe or aerosol jet	Working toward 5 μm
<i>Conductors (traces and via-fills)</i>		
Silver precursor (nitrate)	5× bulk Ag ρ	400 °C
25 nm silver nanoparticle inks	3× bulk Ag ρ	300 °C
5 nm silver nanoparticle inks	3× bulk Ag ρ	170 °C
Laser sintering	4× bulk Ag ρ	25 °C

routes to Ag nanoparticles was by Raveendran et al., who used β-D-glucose as a reductant and starch as a protecting agent [4]. Silver nanoparticles were formed at 40 °C over the course of 20 h. Alternatively, maltodextrins are polysaccharides derived from starch by either acid or enzymatic preparation routes, leading to partial hydrolyzation. As starch and glucose are applied to silver nanoparticle synthesis, the product is expected to serve as a copolymer that would provide

both the reduction and stabilization properties for nanoparticle silver synthesis. Bell and Lu [5] have recently utilized the maltodextrin route for room temperature synthesis of silver nanoparticles. The reactant molecule is a partially converted carbohydrate containing reducing sugar groups and having low molecular weight. To date, most “green” chemistries of silver derived nanoparticles focus on commercial anti-bacterial activity application such as catheters, dental materials, and textile fabrics, but efforts are carrying over into conductor applications.

13.2.2 Metallo-organic Precursor Routes to Silver Inks

For over a century, metallo-organic solutions have been used for the deposition of metal films, e.g., decoration on ceramics and silvered-glass mirrors. Only recently, however, have metallo-organic decomposition (MOD) designed inks been seriously investigated for use in electronics applications. As an alternative route to a particle based formulation, this is a true solution route. The silver molecular complex is very stable, even at concentrations up to saturation; neither requiring additional stabilizers nor reducing agents. The critical factor in development of MOD conductive inks is the selection of precursor chemical compounds. The precursor chemical structures should be designed to convert to conductive metals at relatively low temperatures and at high purity levels. Finally, the selected chemical precursors must be soluble in general organic solvents, produce uniform films, have a long shelf life, and adhere well to a wide range of substrates. Due to ease of preparation and high yield, silver carboxylate precursors are commonly used. Figure 13.4 illustrates thermal decomposition characteristics of several silver carboxylates.

One of the origin examples of ink design for an advanced printing application was reported by Teng and Vest [6]. To pattern collector grids on silicon wafers for photovoltaic solar cells applications, ink solution formulations were prepared with silver neodecanoate dissolved in xylenes (which is stable up to 20 wt% Ag). Through inkjet printing and thermal treatment at 300 °C of the MOD derived inks, the authors were able to avoid degradation of the p-n junctions, produce uniform line traces on the surface of the solar cells, and increase the overall efficiency of the solar cells. Dearden et al. used a similar experimental approach to evaluate conductivities of printed Ag neodecanoate lines from 125 to 200 °C [7]. Resistivity values were reported to approach 2–3 times the bulk resistivity values for thermal treatment conditions greater than 150 °C. Recently, it has been reported that β -ketocarboxylate derived silver inks can be cured as low as 95 °C on paper based substrates. It is interesting to note that one of the lowest reported decomposition temperatures is that of silver oxalate, ~100 °C. Unfortunately, the salt decomposes so exothermically that maintaining dense printed features proves to be difficult.

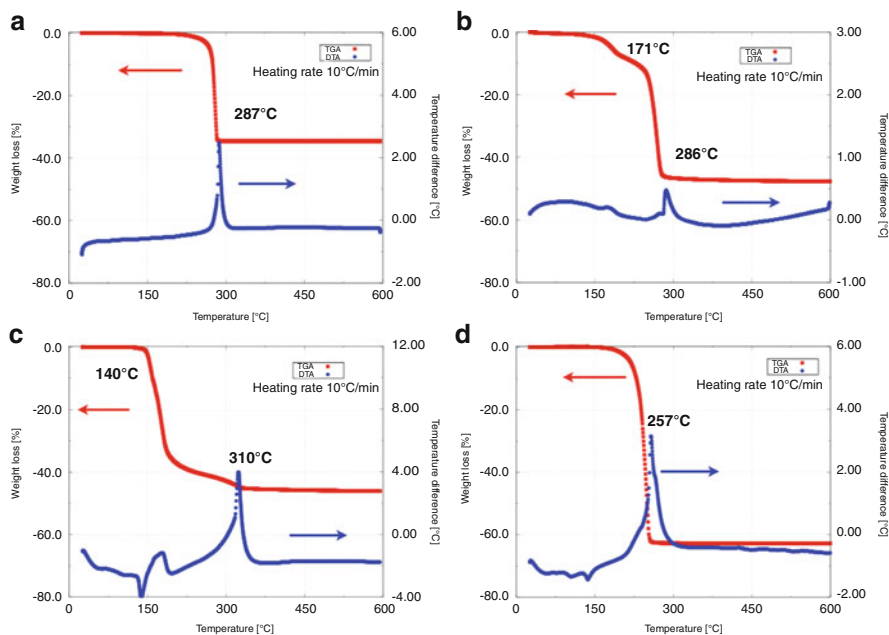


Fig. 13.4 TGA-DTA analysis of the decomposition characteristics for (a) silver acetate, (b) silver 2-methoxy[2-ethoxy(2-ethoxy)] acetate, (c) silver lactate and (d) silver neodecanoate

13.3 Inkjet, Microcontact and Nanocontact Printing of Solution Precursors for Oxides and Metals

Inkjet printing of functional oxide materials is relatively recent in development, and places difficult demands on ink formulation, surface tension, vapor pressure and chemistry [8]. These issues have recently been overcome by leading groups, utilizing novel ink chemistries and processing. Inkjet printing generally utilizes low viscosity inks, of viscosity 1–10 mPa·s, or 1–10 cP (centipoise). These may be dispensed by piezoelectric, pneumatic, or thermal (bubble jet) methods, in which ink is forced from a chamber, forms a droplet due to Rayleigh instability, and is ejected toward a substrate. Due to the low viscosity required, as well as need to avoid ink drying and clogging of the print head, low volume fraction inks with surface tension and humectant (low vapor pressure) additives are often used. A wide variety of materials have been printed using these methods, initially for graphic, and more recently for high performance electronics printing and even superconductor printing. Van Driessche and Glowacki have demonstrated printing of both high quality buffer layers and superconducting YBCO layers using ink jet printing of chloride and trifluoroacetate precursors [9, 10]. The ability to print precursors which may subsequently be converted to epitaxial or biaxially oriented films is a significant advance for inkjet printed electronics, and is potentially

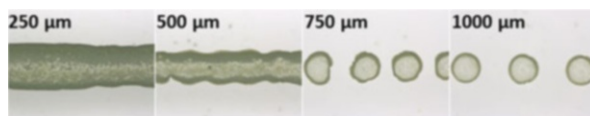


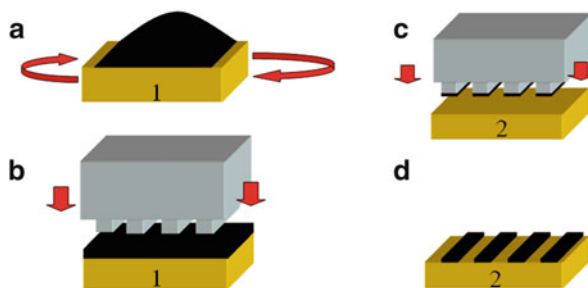
Fig. 13.5 Inkjet printed Al-doped ZnO (AZO) as a function of drop-to-drop spacing, illustrating transition from continuous lines to disconnected droplets

scalable to long lengths by utilizing commercial high rate inkjet printing systems originally designed for graphics printing. Printed electronics for display applications, utilizing complex oxides such as aluminum oxide, indium tin oxide (ITO), aluminum doped zinc oxide (AZO), indium gallium zinc oxide (IGZO), and alloys of these have also been printed from chloride and carboxylate precursors, which enables high mobility transparent conducting oxides for printed inorganic thin film transistors (TFTs), photovoltaic, and other printed electronics applications [11–13]. Use of chloride precursors in water or alternative solvents may simplify complications of using traditional metal alkoxide or metal carboxylate precursors, which often utilize highly volatile solvents, and may display condensation reactions in ambient humidity, which can complicate inkjet printing. Inkjet printing typically deposits small droplets, which can be overlapped to form continuous traces and uniform lines. Precursor drying, surface tension, and ink stability must be engineered carefully to enable uniform printed electronics with predictable material properties (Fig. 13.5).

Alternative methods to inkjet printing, with the potential for high throughput manufacturing, and possibly higher volume fraction inks, include roll to roll printing methods such as gravure and contact printing. Gravure printing of solution precursors is particularly attractive for printing transparent conductive oxides as transparent thin film transistors (TFT) for liquid crystal displays, and for solar cell manufacturing. In these printed electronics methods, the viscosity and surface tension are critical for high precision and reliability printing, while solution chemistry and materials science likely controls printed materials performance. As three examples of printed electronics, our group used copper, yttrium, and barium acetate precursors to print $\text{YBa}_2\text{Cu}_3\text{O}_{7-8}$ superconducting films (cp. Chap. 27), crystallized in an oxygen-containing atmosphere, Cu metal conductive traces, reduced from CuO using a reducing atmosphere of 4 % $\text{H}_2/96$ % N_2 , and Al:ZnO transparent conductive oxides [14].

In this method of solution stamping nano-lithography an elastomeric stamp containing relief patterns is first coated with a sol-gel precursor solution of inorganic (functional oxide or ceramic) materials, and then placed on a surface to transfer the precursor from the stamp to the substrate, as shown in Fig. 13.6. Polydimethylsiloxane (PDMS) is widely used as the stamping material, although vinyl or other polymers may also be used, if alternate physical or chemical properties are desired. Due to the flexible mechanical properties of the PDMS elastomeric material, the stamp forms a conformal contact with the surface. Ink transfer only occurs at locations where the stamp contacts the surface because of the

Fig. 13.6 Schematic of transfer printing of a solution precursor from a substrate or platen (1) to a patterned stamp and onto a substrate (2)



stamp morphology. Hence, the resulting patterns on the substrate mirror the stamp relief structures. For effective transfer from an initial coated substrate or platen, an effective method is for a coated precursor to evaporate some solvent, but remain a liquid with a high viscosity; an effective means of accomplishing this is to use a low volatility solvent such as an ethanolamine, glycol or glycerine additive to a traditional alkoxide solution precursor. The stamped patterns of this viscous, low vapor pressure organic precursor are then processed following standard thermal procedures, such as heating to 300–600 °C, to convert them to the final composition of the desired inorganic material. Resolution may be decreased to very fine, submicron feature sizes. Figure 13.7 (top) shows stamped precursors of copper acetate and ethanolamines, demonstrating features as fine as 200 nm. Figure 13.7 (bottom) displays images of three micron lines of the transparent printed copper precursor, and the resulting metallic copper traces produced following oxidation of the precursor to CuO at 500 °C, followed by a reducing atmosphere anneal at 250 °C to form Cu metal. The printed traces displayed resistivity of 2.1 mΩ-cm, around 80 % of the bulk conductivity of copper [14].

For applications in which crystalline alignment is required, such as superconducting and electrooptic applications, the ability to deposit epitaxial films is of interest. Using conventional methods for processing oxide thin films via non-hydrolyzed precursors on a lattice-matched substrate, the patterned thin films may be epitaxially registered to the substrate. Epitaxial deposition of 100 nm thick superconducting YBCO films on LaAlO₃ has been demonstrated with this method, using a variant of the trifluoroacetic acid precursor system, to which low volatility diethanolamine and triethanolamine were added. This precursor was solution transfer printed as 50 micron wide stripes onto LaAlO₃, pyrolyzed by rapid thermal annealing at 325 °C, and crystallized at 780 °C. The resulting YBCO film displayed epitaxial registry with the LaAlO₃ substrate, as shown in Fig. 13.8, an onset critical temperature T_c of 85 K, and a critical current density of 600 kA/cm², measured assuming perfect continuity within the 50 μm printed lines across the 1 cm substrate [15]. The ability to print patterned YBCO lines is of interest for reducing alternating current (AC) losses for AC superconducting magnet and motor applications, and may be a much less costly process than subsequent photolithography.

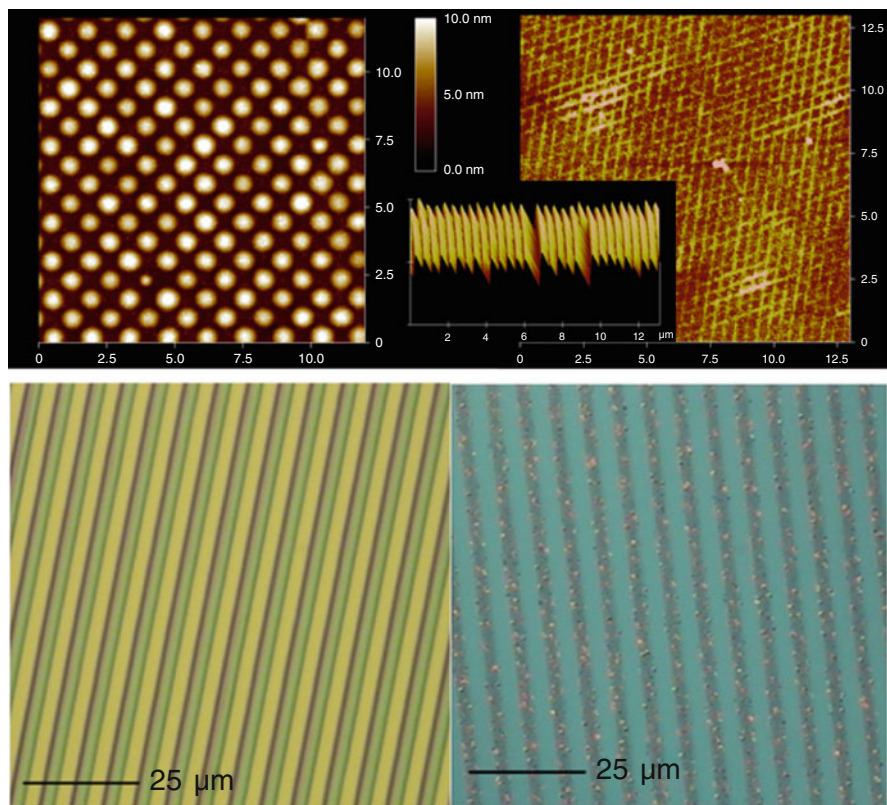
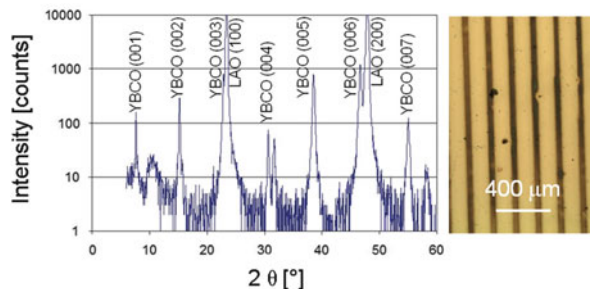


Fig. 13.7 *Top left*, 650 nm printed copper nanodots imaged by a $12 \times 12 \mu\text{m}$ AFM scan. *Top right*, 12.5×12.5 micron AFM scan image of 200 nm lines of Cu printed using a PDMS stamp cured atop a standard diffraction grating. The inset shows the topology of the dry PDMS stamp. *Bottom left*, printed copper acetate/diethanolamine precursors on silicon, and *bottom right*, the printed copper pattern after oxidation to 500 °C in air, and post-anneal at 250 °C in 4 % H_2/N_2

13.4 Application Examples: Printed Strain Gages and Load-Frame Testing

Printable electronics may find application in green energy for increasing the reliability and performance of photovoltaics and wind turbine systems. Development of these technologies is of interest since rising energy prices and carbon emission standards are driving development of alternative energy sources including biofuel, solar, wind, and clean coal. A decrease of 20–50 % in wind energy cost for renewable resources is an aggressive goal, motivating interest in new technologies to decrease system manufacturing cost, optimize power generation efficiency, improve reliability, and decrease operation and maintenance costs [15–17]. A promising technology to improve wind turbine efficiency is smart rotor blades

Fig. 13.8 X-ray diffraction and optical image of printed 50 μm width, 100 nm thick YBCO stripes on LaAlO_3 single crystal substrates, demonstrating epitaxial growth and continuous superconducting filaments



that monitor the physical loads being produced by the wind and adapt the airfoil for optimized energy capture. For extreme wind speeds and gust events, the airfoil could be changed to reduce the loads to prevent excessive fatigue or catastrophic failure. Prior Sandia work has developed an understanding of sensor placement sensitivity and methods for integrating internal strain and temperature sensors via fiber optic Bragg gratings [15]. However, sensor optimization in more complex blade models would require larger numbers of sensors [16], which is complicated by poor adhesion of surface mounted sensors, wiring of long (9–45 m) blades, altered aerodynamics, and high anemometer cost [17]. These opportunities for instrumenting generation systems to improve monitoring and reliability require placement of robust sensor networks into complex environments to provide diagnostic state of health information. Utilizing nanoparticle silver inks and an Optomec Aerosol Jet M³D print system, high resolution strain gages were produced by printing silver inks directly on commercial wind turbine blade test sections provided by Sandia's Wind and Water Power Technologies department. The wind turbine blade composites consist of 50 volume % E-glass fiberglass in an epoxy resin such as Hexion Infusion resin MGS® RIM 135 and hardeners MGS® RIMH 134—RIMH 137. The fiberglass-epoxy composite is coated with a UV-stable urethane epoxy coating, providing a flat, impermeable external surface, on which the silver nanoparticle inks and copper 55 %/nickel 45 % solution precursors were printed and annealed. Images of printed silver and constantan inks on Kapton and wind turbine sections are shown in Fig. 13.9.

Commercial foil-based strain gages utilize a Wheatstone bridge configuration to measure both transverse and longitudinal strain, and typically use values of 120 Ω , 400 Ω or 1,000 Ω . Designs compatible with 120 and 1,000 Ω bridge operation were developed and printed as shown in Table 13.2. The 1,000 Ω samples were accurate to within 0.24 % of design resistance:

Blade sections with these highly accurate printed resistance bridges were loaded to 5,000 lbs., which was the limit of the wedge-loaded grips in the load frame tester. The resulting strains were in the area of 4,000 microstrain, as measured by a 1" calibrated MTS extensometer. Using the 1,000 Ω resistors, which matched the internal resistors of the strain gage measurement electronics, the strain on the turbine blade section was cycled from -50 microstrain to $+4,300$ microstrain to measure the longitudinal and transverse strain response of the printed gages. In each

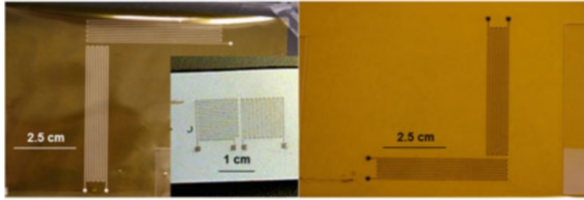


Fig. 13.9 Optical images of longitudinal and transverse strain gages: (*left*) printed silver on Kapton film and on a composite fiberglass-epoxy wind turbine blade section, and (*right*) printed constantan (Cu 55 %, Ni 45 %) on Kapton

Table 13.2 Summary of 4-element and 2-element printed strain gage values

Sample ID	Bridge elements	Design value	Measured resistance values
6A	1–4	1,000 Ω	1,000.4 Ω , 1,001.2 Ω , 1,001.5 Ω , 1,000.3 Ω
6B	1–4	1,000 Ω	1,001.4 Ω , 1,001.7 Ω , 1,002.4 Ω , 1,001.8 Ω
6C	1–2	120 Ω	122.4 Ω , 115.7 Ω

case, a 3.5 V excitation was used, with a bridge gain of 100. The resulting loading curves for the first cycle and second through fourth cycles are shown in Figs. 13.10 and 13.11.

For these samples, both high precision resistor values and highly linear strain sensing was demonstrated. Hysteresis, indicated by a small jump in voltage/resistance at a strain level of 0.0004 in Fig. 13.10, is observed in the first extension cycle, during which it is possible the printed silver undergoes some loss of network connectivity. Further fatigue testing would be of interest to evaluate long-term reliability of these printed strain gages.

An important consideration for such strain gages is the ability to both measure strain on an actual, in-operation 13–60 m rotating turbine blade, and to transmit this data remotely to an acquisition node. In addition, the ability to measure dense arrays of strain gages with a single transmitter would be of interest to accurately map blade “shape” to generate the real-time three dimensional deformation and determine true, real-time blade deflection.

A method to achieve these objectives was identified and briefly evaluated under this program. Recently, both wireless strain gage monitors, and energy-harvesting, self-powered wireless strain gage monitors have been developed by several companies for remote monitoring of industrial and structural products. Commercial off the shelf (COTS) systems exist for high-rate, real-time monitoring and data streaming of 120 Ω , 350 Ω , and 1 k Ω gauges, including integrated systems available from Microstrain, EnOcean, and Perpetuum. One of these systems, a Microstrain SG-Link, which can monitor up to eight strain gages simultaneously, and transmit data at a 4 kHz rate via 2.4 GHz to a universal serial bus (USB) receiver plugged into any personal computer, laptop, or other digital computing device. A methodology to retrieve this data from a printed network of strain gages down the length of a wind turbine blade is shown in Fig. 13.12.

Fig. 13.10 First cycle of transverse and longitudinal strain measured by printed silver 1,000 Ω strain gage Wheatstone bridge

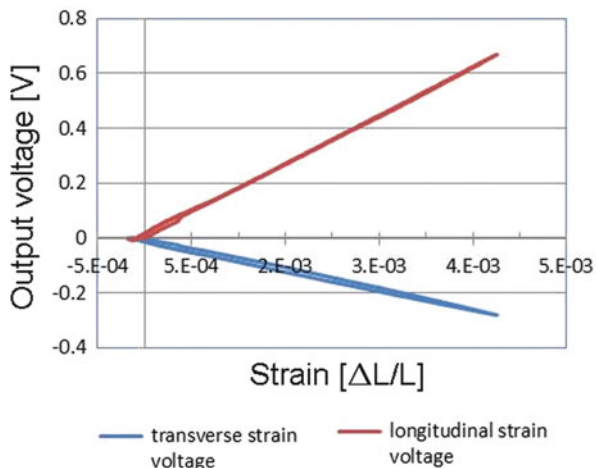
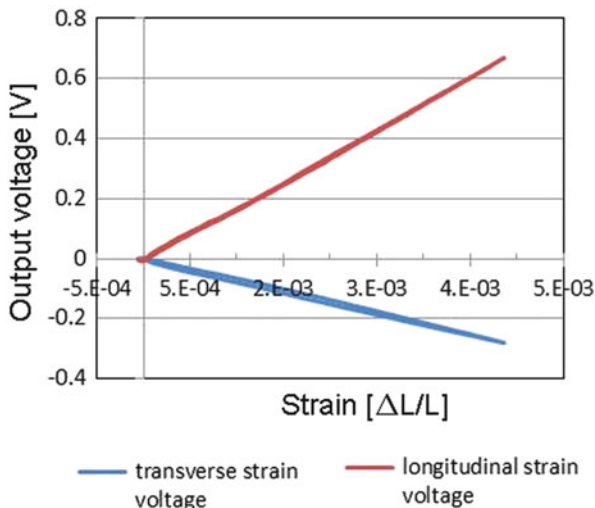


Fig. 13.11 Second, third and fourth cycles of transverse and longitudinal strain measured by printed silver 1,000 Ω strain gage Wheatstone bridge



For these SG-Link devices, an internal 600 mA-h AA Li cell is used, which provides 2–5 years of battery life for a 2.4 GHz transmission range of 70–500 m, at a 4 kHz transmission rate. For eight gages, transmission rate would be reduced to 500 Hz, but battery life would be decreased roughly twofold, requiring battery replacement consistent with normal quarterly to annual wind turbine maintenance schedules.

An attractive alternative option may be the use of new, energy-harvesting transmission nodes, such as the Microstrain EH-Link™, which may accept energy generated by vibrational (piezoelectric or inductive) generation on each rotation of the turbine, or by photovoltaic panels. As a thought experiment, a design using an integrated, 1 square foot, amorphous silicon photovoltaic panel, such as that

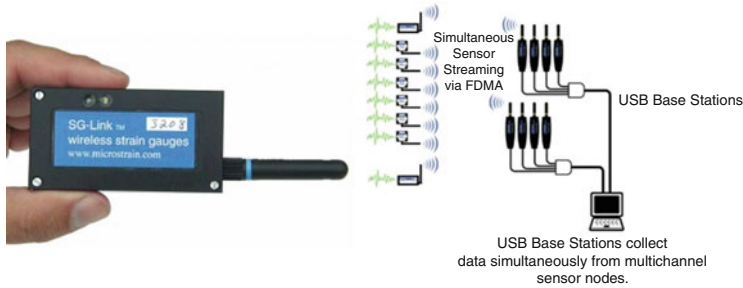


Fig. 13.12 *Left*, image of Microstrain SG-Link wireless strain gage transmitter, and, *Right*, methodology of monitoring up to 64 strain gages simultaneously: 8 gages per monitoring SG-Link uplink, and 8 receiving antennas per computer on two USB connections

manufactured by Powerfilm, was developed. An EH-LinkTM 8 strain gage system (Fig. 13.13) requires a 5 V power supply, with 25 mA for data streaming and 3 mA for each of eight channels, which equates to $5\text{ V} [25\text{ mA} + 8(3\text{ mA})] = 245\text{ mW}$ or 0.6 W-h/day. Powerfilm produces a 5 V output, 10 W, $60 \times 12.5\text{ cm}$ module which would produce this level of power in only 33 min of sunlight per day, appropriate even for cloudy climates. Alternatively, in full sunlight, sufficient power may be available from the same system to power 20 nodes, with eight nodes each, or a 160 strain gage array. Energy harvesting appears feasible at a cost of only around \$5–100 per 8-sensor node, plus the \$100–500 cost of each node.

It appears printed strain gages may hit the required $120\ \Omega$ or $1,000\ \Omega$ values needed for this implementation, and the that the transmission distance (70–500 m) is compatible with transmission from any point on a 9–60 m turbine blade to a USB receiver in the nacelle of a wind turbine. This capability for wireless, dense strain gage, high fidelity (0.5–4 kHz sampling) remote monitoring of wind turbine blades is hoped to enable calculation of real-time blade shape, deflection, vibration states, and damage levels, which would be additional inputs into smart turbine blade diagnostics and performance optimization systems. With further development, temperature and air speed wireless monitoring could also be developed as printed sensors.

13.5 Summary of Research Progress

Printing of solution precursors via inkjet, gravure printing, offset printing, microcontact printing and nanotransfer printing enables integration of many functional oxide and metal components without need for lithography or screen printing. Printing of solution precursors has recently been successfully applied to RFID tags/antennas, solar cells, thermocouples, conductive interconnects, superconductors, displays, transistors, and waveguides. Development of low vapor pressure precursors with low surface tension enables reliable printing via aerosol and contact



Fig. 13.13 *Left*, an energy harvesting-compatible, 8-strain gage wireless transmission node, and at *right*, a flexible, conformal 5 V output amorphous silicon photovoltaic system with sufficient power to power a single node from 40 min of sunlight per day

printing methods. Modifying precursor chemistry to enable low-temperature decomposition of nanoparticle surfactants and solution precursors enables integration of metallic components with low T_g polymeric substrates. While the traditional thermal route for metal conversion has been discussed, alternative conversation routes are emerging including microwave sintering, electrical conversion, and laser-sintering. These low-temperature, low thermal budget routes enable advanced integration capabilities on semiconductor, polymer, and composite materials.

By combining solution chemistry, metal nanoparticle solutions, and robotic direct printing technologies, the capability to directly print functional metal and metal oxide thin films to produce thermocouples, strain gages, and crack sensors on polymers, semiconductors, oxides, and composite materials has been demonstrated. This capability may have widespread impact on printable electronics for displays, flexible electronics, integrated microelectronics, and sensors. As an example of potential novel applications, printed nanomaterial ink traces have been highly engineered to enable achievement of precision resistors with less than 1 % variation from specification, which enabled printing of strain gage Wheatstone bridges directly on wind turbine blade composite sections. The printed gages were analyzed by traditional load-frame testing at 5,000 pound loads, and, after a first strain cycle, demonstrated reliable, linear sensing of longitudinal and transverse strain levels at all strain levels up the maximum, 0.44 % strain level tested, consistent with maximum strain tolerance required in real wind turbine blades.

For these conductive samples, both high precision resistor values and highly linear strain sensing were demonstrated. Additional work is necessary to continue development of this method, including measurements over thousands of cycles, detailed characterization of expected failure modes including printed gage delamination, and development of suitable encapsulation to avoid surface damage from debris/wind storms which real turbine blades must withstand. In addition, it is of interest to further explore the use of printed gages as binary (short circuit to open circuit) or analog (subsequent resistors which are opened as cracks extend) printed crack sensors. Conductor applications including continuous nondestructive evaluation and monitoring of wind turbine blades, industrial/utility equipment and piping may be enabled by this technology.

The potential power of this method is widespread, large area printing of functional materials on nontraditional substrates, including polymers, metals, papers, fabrics and composites. Careful use of chemical precursors, high surface area nanoparticle inks, reactive inks, and low temperature or non-thermal processing of inks (IR, UV, and microwave heating) enables processing of high performance materials on low temperature substrate materials. Extension of these methods to transparent conductors and dielectrics is currently underway by several groups, with implications for low cost electronics using lithography-free electronic materials patterning for sensor, display and logic applications.

References

1. Dominguez O, Champion Y, Bigot S (1999) Surface effects on the sintering behavior of nanometric metallic particles. *Rev Mex Fis* 45:74–77
2. Perelaer J, de Laat AWM, Hendriks CE, Schubert US (2008) Inkjet-printed silver tracks: low temperature curing and thermal stability investigation. *J Mater Chem* 18:3209–3215
3. Wakuda D, Kim KS, Suganuma K (2010) Ag nanoparticle paste synthesis for room temperature bonding. *IEEE Trans Compon Packag Technol* 33(2):437–442
4. Raveendran P, Fu J, Wallen SL (2003) Completely ‘green’ synthesis and stabilization of metal nanoparticles. *J Am Chem Soc* 125:13940–13941
5. Bell N, Lu P (2013) Green chemical synthesis of silver nanoparticles via maltodextrin reduction (manuscript in preparation)
6. Teng KF, Vest RW (1988) Metallization of solar-cells with ink jet printing and silver metallo-organic inks. *IEEE Trans Compon Hybrids Manuf Technol* 11:291–297
7. Dearden AL, Smith PJ, Shin DY (2005) A low curing temperature silver ink for use in ink-jet printing and subsequent production of conductive tracks. *Macromol Rapid Commun* 26(4):315–318
8. Derby B (2011) Inkjet printing ceramics: from drops to solid. *J Eur Ceram Soc* 31:2543–2550
9. Vandaele K, Mosiadz M, Hopkins SC, Patel A, Van Driessche I, Glowacki BA (2012) The influence of heat treatment parameters on pyrolysed TFA-derived YBCO films deposited by inkjet printing. *Mater Res Bull* 47:2032–2039
10. Mosiadz M, Tomov RI, Hopkins SC, Martin G, Hardeman D, Holzapfel B, Glowacki BA (2010) Inkjet printing of $\text{Ce}_{0.8}\text{Gd}_{0.2}\text{O}_2$ thin films on Ni-5%W flexible substrates. *J Sol-Gel Sci Technol* 54:154–164
11. Avis C, Jang J (2011) High-performance solution processed oxide TFT with aluminum oxide gate dielectric fabricated by a sol-gel method. *J Mater Chem* 21:10649–10652
12. Hoffmann RC, Dilfer S, Schneider JJ (2011) Transparent indium tin oxide as inkjet-printed thin film electrodes for organic field-effect transistors. *Phys Status Solidi A* 208:2920–2925
13. Han SY, Lee DH, Herman GS, Chang CH (2009) Inkjet-printed high mobility transparent-oxide semiconductors. *J Displ Technol* 5:520–524
14. Chang NA, Richardson J, Clem PG, Hsu JWP (2005) Additive patterning of conductors and superconductors by solution stamping nanolithography. *Small* 2:75–79
15. Rumsey MA, Paquette JA (2008) Structural health monitoring of wind turbine blades. *Proc SPIE* 6933:69330E
16. White JR, Adams DE, Rumsey MA (2009) Operational load estimation of a smart wind turbine rotor blade. *Proc SPIE* 7295:72952D
17. Moor GD, Beukes HJ (2004) Maximum power point trackers for wind turbines. 2004 IEEE 35th annual power electronics specialists conference (IEEE Catalog. No. 04CH37551), vol 3. pp 2044–2049

Chapter 14

Chemical Bath Deposition

Mark R. De Guire, Luciana Pitta Bauermann, Harshil Parikh,
and Joachim Bill

14.1 Introduction

Chemical bath deposition (CBD) is the name given to a variety of techniques that produce films of solid inorganic, non-metallic compounds on substrates by immersing the substrate (once, or repeatedly) in a precursor solution (often aqueous). Control of the temperature (usually below 100 °C), pH, and concentration of the solution induces a solid phase to exsolve and form a film on the substrate, often without any subsequent heat treatment. While such approaches have been used for many years to produce sulfide, selenide, and other non-oxide films [1], relatively little work had been done on oxide films until the early 1980s, when interest began increasing rapidly [2].

There are several motivations for this interest. The functional properties of oxides make them attractive in thin-film form in a variety of applications, such as sensors, transparent conductive oxide coatings, catalysts, thermal barrier coatings, and “superhydrophobic” layers. Producing such coatings at temperatures below 100 °C allows materials that cannot tolerate high temperatures, such as polymers, to be coated. Immersing a substrate in a liquid overcomes line-of-sight limitations of vapor-phase deposition or spraying techniques, and allows complex surfaces such as powders, tubes, and porous structures to be coated. Lastly, the equipment needed for CBD is much simpler than that used for vapor-phase film deposition techniques and readily lends itself to manufacturing scale-up and to continuous (as opposed to batch) processing.

M.R. De Guire (✉) • H. Parikh
Department of Materials Science and Engineering, Case Western Reserve University,
Cleveland, OH 44106, USA
e-mail: mark.deguire@case.edu

L.P. Bauermann • J. Bill
Institute for Materials Science, University of Stuttgart, 70569 Stuttgart, Germany
Max Planck Institute for Metals Research, 70569 Stuttgart, Germany

As a technique for depositing thin nonmetallic inorganic films from aqueous solutions, chemical bath deposition is at least 140 years old: Hodes [3] cites a report from 1869 by Puscher of sulfide layers deposited from thiosulfate solutions of copper, lead and antimony salts. The approach was not studied extensively or exploited commercially until the last quarter of the twentieth century, when CBD films of sulfides and selenides began to play crucial roles in the electrodes of photovoltaic solar cells.

During the same period, aqueous chemical routes for the synthesis of oxide *powders* received considerable attention, with a focus on producing fine particles with uniform shape and narrow size distributions. Although application of these routes for the synthesis of oxide films is not as widespread as for oxide powders or for sulfide and selenide films, their shared underlying chemical principles provide a foundation for understanding oxide film deposition.

To understand chemical bath deposition processes, and thereby to be able to exert control over aspects such as the growth rates, structures, and properties of the deposited films, it is helpful to divide the topic into three general areas:

- *Solution chemistry*—controlling solution parameters such as *pH*, temperature, and composition to yield desired phases and control deposition rate;
- *Substrate effects*—tailoring the surface energy, magnitude and sign of surface charge density, and hydrophilicity or -phobicity of a substrate so as to localize and promote the formation of films;
- *Process control*—designing a deposition process, based on an understanding of the mode of film formation, to control the growth rate and microstructure of the deposited film.

The next sections will address each of these topics. The chapter concludes with a discussion of the limitations and advantages of CBD and its most attractive areas for future research and potential applications.

14.2 Solution Chemistry

14.2.1 General Framework

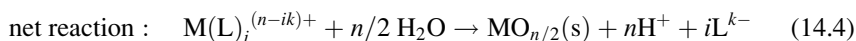
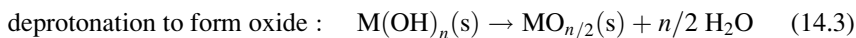
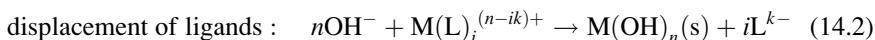
To deposit a compound $\text{MX}_{n/2}$ via CBD, the deposition medium will consist of one or more salts of metal M^{n+} and a source for the chalcogenide X ($\text{X} = \text{O}, \text{S}, \text{Se}$) in aqueous solution. Typically, these salts are chosen for their moderate to high solubility in water, low cost, or ready availability, *e.g.*, chlorides, nitrates, sulfates, or acetates. (Metal-fluoride precursors are usually used for the so-called “liquid phase deposition” approach, described in Sect. 14.2.2.)

Products containing multiple metals are relatively easily obtained when a specific cation stoichiometry is not required (doped materials or solid solutions) and the metals have similar precipitation behavior at a given temperature and *pH*.

A complexing agent (also called a complexant) may be added, as a means (in addition to adjustment of concentration, temperature, and pH , as discussed below) of controlling the rate of formation of the solid. Typically, complexants supply ligands for the metal, and the greater their affinity for the metal relative to that of the chalcogenide, the more the complexant helps slow down the hydrolysis reactions that lead to formation of the solid phase. When the desired compound contains multiple metals whose hydrolysis rates differ widely under a chosen set of deposition conditions, a complexant can be particularly useful for slowing the deposition kinetics of the more readily hydrolyzed species. The concentration of the complexant is usually chosen to be a predetermined ratio of the concentration of the metal precursor.

For non-oxide films, the chalcogenide source is present in a dilute concentration (typically 0.01–0.1 M). This concentration constitutes an additional parameter that permits control to be exerted over the rate of film deposition. When the desired solid is a sulfide, thiourea ($(NH_2)_2CS$), thioacetamide (CH_3CSNH_2) or soluble salts of thiosulfate ($S_2O_3^{2-}$) commonly serve as sources of S^{2-} ions, while selenourea ($SeC(NH_2)_2$) or selenosulfate ($SSeO_3^{2-}$) are examples of sources for Se^{2-} ions.

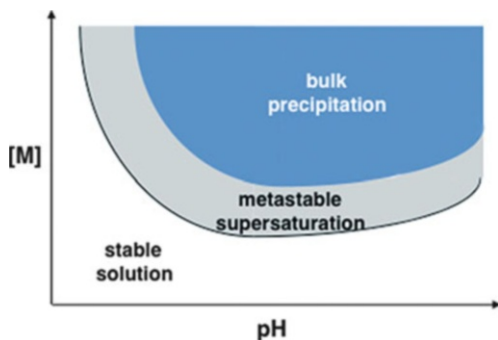
For oxide products, water provides oxygen in the form of OH^- ions. For a metal cation M^{n+} complexed by i ligands L^{k-} , the steps to forming the oxide $MO_{n/2}$ can be formulated as the following reactions:



The process depicted by reactions (14.2) and (14.3) is sometimes called “forced hydrolysis” [4]. Note an important contrast: for non-oxides, the amount of chalcogenide precursor added to the solution will primarily determine the concentration $[X^{2-}(aq)]$ of the free chalcogenide ion, one of the key parameters determining the degree of supersaturation of the solution (and therefore its tendency to produce the desired solid). Although pH and temperature allow some modulation of the free chalcogenide concentration, one of the easiest ways to slow down the rate of solid production is simply to reduce the starting concentration of the chalcogenide source. For oxides, on the other hand, the chalcogenide source is OH^- , of which its “precursor”—the water itself—provides a virtually unlimited supply. In CBD of oxide films from aqueous solutions, the chalcogenide source is essentially never exhausted. The remaining variables— pH and temperature—must therefore be closely controlled, as they directly influence the thermodynamics and kinetics of the deposition process.

Reactions (14.1), (14.2), (14.3), and (14.4) illustrate the roles that pH , temperature, and concentration play in controlling the rate of deposition:

Fig. 14.1 Schematic illustration of the effect of solution pH (*horizontal axis*) and metal concentration [M] (*vertical axis*) on the tendency of a solution to exsolve a solid phase (adapted from [6])



- The effect of pH ($\equiv -\log_{10}[H^+]$) is explicit in reactions (14.1) and (14.2). Note however that forced hydrolysis does not require addition of base; hydrolysis can occur even in acidic solutions when the metal cation is easily hydrolyzable, as with Al^{3+} , Ti^{4+} , Fe^{3+} , Zr^{4+} , Sn^{4+} , and Ce^{4+} .
- Increasing the concentration of the metal salt increases the rate of reaction by shifting reaction (14.2) to the right, and increases the amount of material able to be deposited from the solution according to the degree to which the solubility limit of $M(OH)_n$ is exceeded.
- The role of temperature is less obvious: with increasing temperature, the dissociation of water (reaction 14.1) shifts to the right, increasing the supply of hydroxyl ions needed to displace the ligands from the metal (reaction 14.2). Raising the temperature also induces deprotonation of the hydrated metal species (reaction 14.3). Both of these effects typically accelerate the formation of the solid. In fact, a common strategy in CBD of oxides is to use a precursor solution that is relatively stable against precipitation at room temperature, but which produces films in practical time frames when the temperature is raised.

The degree of supersaturation—a measure of the degree to which the concentrations of the free ions in solution exceed their solubility limits—plays a central role in film formation. Supersaturation is most often controlled by the concentration, pH , and temperature of the solution. When film growth occurs by particle attachment (see Sect. 14.3.1), the degree of supersaturation dictates the size, population and rate of formation of the particles making up the film.

Figure 14.1 schematically illustrates the interplay between metal ion concentration $[M^{n+}]$ and pH in the supersaturation of an aqueous solution. For acidic oxides such as TiO_2 , ZrO_2 , and SnO_2 , the tendency for solid to precipitate increases as pH increases from strongly acidic toward less acidic and basic values. Quantitative versions of Fig. 14.1 for specific oxides can be found in collections such as Baes and Mesmer [5].

If the pH and concentration place the solution deep in the field labeled “bulk precipitation” in Fig. 14.1 (adapted from [6]), solid forms rapidly in the solution. In the field labeled “metastable supersaturation,” solid may form on any solid surface that lowers the thermodynamic barrier to nucleation. Ideally, the only such surface

would be the substrate, but in practice it can be difficult to avoid nucleation on other surfaces (including container walls and adventitious particles in the solution) and to maintain the solution conditions continuously (and with spatial uniformity) in the metastable condition.

Because these solution parameters govern the rate of formation of solid, they have a major influence on the film deposition process, and they will be taken up again in the sections on substrate effects and process design. As discussed in [2] and references cited therein, films from less heavily supersaturated solutions typically grow more slowly but may ultimately reach higher thickness—a “tortoise and hare” effect. Overall, the growth rate is determined by supersaturation (temperature, concentration, and pH), while thickness is limited by the supply of reactants (starting concentrations and avoidance of bulk precipitation).

14.2.2 Variants of CBD

Within the scope of this general description of CBD, considerable latitude exists in the solution chemistry. Several specific approaches have been utilized for forming oxide films:

- **Liquid phase deposition (LPD)** utilizes an aqueous solution of a metal-fluoro complex $(MF_m)^{(n-m)}$, and slowly hydrolyzes this complex by adding water, boric acid (H_3BO_3) or aluminum metal. The great variety of oxides to which this technique has been applied, notably by Deki and co-workers [7–11], and the unique strategy of pitting fluoride complexes against fluorine scavengers to control the rate of hydrolysis, warrant listing it as a distinct technique. Also in contrast to CBD in general, LPD from its inception has been used predominantly for producing oxide films: the technique was first described in a patent [12] for producing titania films on glass in 1984.
- **Successive ion layer adsorption and reaction (SILAR)**, uniquely among CBD techniques, builds up a film through repeated immersions of the substrate alternately into a metal salt solution, then a hydrolyzing solution. SILAR is even able to promote epitaxial growth at room temperature, a fact that was related to the high surface diffusion coefficients of the adsorbed ions and the long surface diffusion time available to reach the lattice kinks. The sequential character of the SILAR technique avoids some of the incompatibilities in the deposition conditions that might exist between two components of a desired multicomponent film. The deposits usually need heat treatment to yield the desired crystalline phase. SILAR was first reported in the mid-1980s independently for sulfides [13] and for Cu(I) [14] and Zn(II) [15] oxides. Tolstoy [16] reviewed the potential applications of SILAR in gas sensing, photovoltaics, electronics, and lighting applications.
- **Electroless deposition (ED)** entails a change in the oxidation state of the dissolved metal cation to an insoluble state in the deposition medium, followed

by catalyzed deposition of the solid at a “sensitized” substrate without use of externally imposed sources of electrical energy [17]. This technique is an adaptation of electroless plating techniques that are widely used for depositing metal films. In a recent example [17], films of β -FeOOH or Fe_3O_4 were deposited from iron (III) nitrate solutions, and Fe from iron (III) sulfate solution, on amine-functionalized Si that had been immersed in a Pd salt solution for sensitization; dimethylamine borane complex (DMAB, $(\text{CH}_3)_2\text{NHBH}_3$) in the deposition medium served as the reducing agent.

Table 14.1 summarizes the oxide materials (and a few sulfides) that have been deposited in the form of thin films via these techniques or with the use of organic self-assembled monolayer surfaces (*vide infra*). Recent reviews [2, 18, 19] provide further details about these films and give citations to the original reports.

Some variations on CBD have been extensively developed for a specific category of materials. An example is ferrite plating [20, 21], which was developed by Abe and co-workers to deposit films of iron-containing magnetic oxides (ferrites). They reported depositing a wide variety of spinel ferrites (such as $(\text{Fe}_3\text{O}_4)_{1-x}(\gamma\text{-Fe}_2\text{O}_3)_x$, $\text{Mn}_x\text{Fe}_{3-x}\text{O}_4$, $\text{Co}_x\text{Fe}_{3-x}\text{O}_4$, $\text{Ni}_x\text{Fe}_{3-x}\text{O}_4$, $\text{Ni}_x\text{Zn}_y\text{Fe}_{3-x-y}\text{O}_4$, $\text{Fe}_{3-x}\text{Zn}_x\text{O}_4$), Ba-Fe oxides, and Y-Fe oxides. The route includes an aspect of electroless deposition in that it requires increasing the oxidation state of iron from (II) in solution to (III) in the films, although unlike ED this oxidation takes place in the bulk solution and is not believed to be catalyzed at the substrate. Many of the variations in technique discussed below, such as the use of flowing precursor solutions, photo-stimulated deposition, and application of electrical current to induce deposition, have been used in ferrite plating.

14.2.3 Use of Organic Additives

The presence of organic additives in the deposition liquid plays an important role in the control of the morphology of the formed particle and consequently the film. The variety of the obtained morphologies is large: sponges, honeycombs, ribbons, spheres, sheets, cubes and hexagonal platelets. The additives adsorb preferentially on specific faces of the inorganic crystal, inhibiting the growth of those faces. The uncoated faces then grow further, conferring unusual morphologies [22–31]. On the other hand, crystallographically non-selective adsorption of the additives leads to “miniaturization” of the formed crystallite by slowing the growth rate in all directions.

Many of the additives that adsorb onto crystal surfaces have functional groups similar to those found in effective complexants, especially carboxylic acid, alcohol, amide, and ether groups.

In some cases the role of the organic additive is not exclusively to control the growth rate of certain crystal faces, but also to promote formation of an intermediate amorphous phase during the crystal growth. The presence of these amorphous

Table 14.1 Listing of oxides (and three sulfides) that have been deposited as thin films via chemical bath deposition (CBD) and related techniques: liquid phase deposition (LPD), successive ion layer adsorption and reaction (SILAR), electroless deposition (ED), and use of organic self-assembled monolayers (SAM)

	CBD	LPD	SILAR	ED	SAM
Ag ₂ O	X				
AgO	X				
Cd ₂ SnO ₄	X				
CdO	X				
CdS	X				X
CeO ₂	X		X		
(Ce,Gd)O _{2-x}			X		
CoO	X				
Co ₃ O ₄	X				
Cu ₂ O	X		X		
CuO			X		
(Cu,Fe) ₃ O ₄		X			
Eu ₂ O _{3-x}			X		
Fe ₃ O ₄					X
FeOOH/Fe ₂ O ₃			X		
α-Fe ₂ O ₃		X			X
α-FeOOH					X
β-FeOOH		X			X
γ-FeOOH					X
In ₂ O ₃	X			X	X
In ₂ O ₃ :Sn	X				
La ₂ O _{3-x}			X		
LaCoO ₃		X			
LaCrO ₃		X			
LaFeO ₃		X			
La _{1-x} MnO ₃		X		X	
LaNbO _x			X		
MnO ₂	X		X	X	
NdCoO ₃		X			
NdCrO ₃		X			
NdFeO ₃		X			
NdMnO ₃		X			
NiO			X		
NiOOH	X				
NiFe ₂ O ₄		X			
α-PbO ₂				X	
PbS	X				X
SiO ₂		X			
SnO ₂	X	X			
SnO ₂ :Sb	X				
Sn ₁₆ (OH) _x PW ₁₉ O _y			X		
Ti ₂ O ₃			X	X	
TiO ₂	X	X			X

(continued)

Table 14.1 (continued)

	CBD	LPD	SILAR	ED	SAM
TiO ₂ -dopamine		X			
TiO ₂ -methylene blue		X			
TiO ₂ -SiO ₂		X			
TiO ₂ -V ₂ O ₅					X
V ₂ O ₅		X			X
Y ₂ O ₃ , Y ₂ O _{3-x}			X		X
Y ₂ O ₃ :Eu					X
Y ₂ O ₃ -ZrO ₂			X		X
ZnO	X	X	X	X	X
ZnO:Al	X				
ZnO:Cd		X			
ZnO:Cu		X			
ZnO:Ni		X			
ZnO:Sn		X	X		
ZnS	X				X
ZnAl ₂ O ₄		X			
ZrO ₂		X	X		X
ZrO ₂ :Eu		X			
ZrO ₂ :Tb		X			

particles can reduce the degree of supersaturation of the solution, suppressing the rapid formation of the initial crystals. The amorphous phase then dissolves, and nanocrystals are formed. The amorphous particles contain metal ions that are gradually released, promoting a more controlled crystallization process.

14.3 Substrate Effects

14.3.1 Mechanisms of Film Formation

The preceding discussion does not directly address the circumstances that would cause the forming solid phase to adhere to a substrate as a film. Expressed in broad terms: the solution chemistry primarily dictates *whether* a solid can form, while the substrate largely determines *where* the solid will deposit. The chemical nature of the substrate surface and its interactions with the depositing solid and the liquid deposition medium together influence the film's growth rate and morphology.

Two basic mechanisms (Fig. 14.2) have to be considered:

- Dissolved ionic species may attach to the substrate according to an ion-by-ion growth mechanism. In this case heterogeneous nucleation leads to directed growth of nuclei of the inorganic phase on the substrate.

Fig. 14.2 Mechanisms for the formation of inorganic films from aqueous inorganic solutions (after [32])

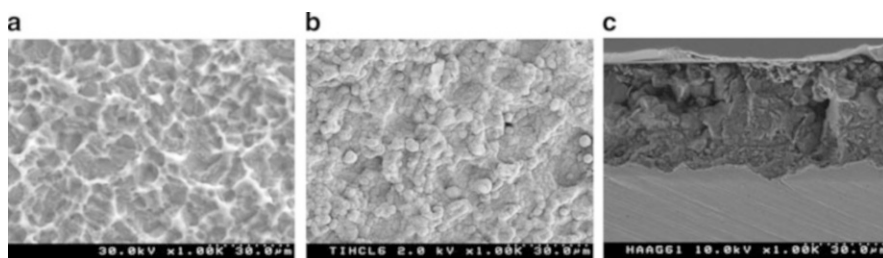
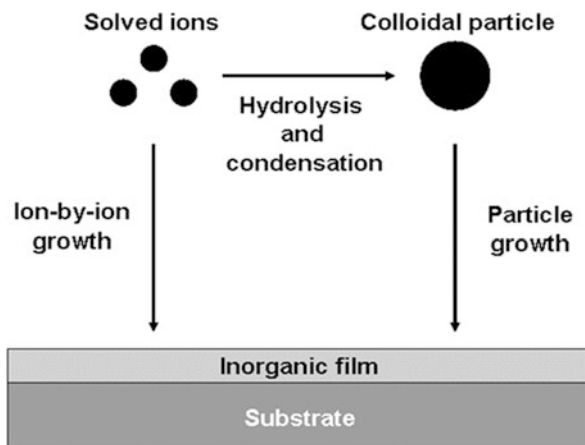


Fig. 14.3 Scanning electron microscope images of (a) etched titanium surface (plan view); (b) etched titanium surface with hydroxyapatite coating deposited from simulated body fluid (plan view); (c) cross-section of hydroxyapatite coating (*middle* of image) on etched titanium (*bottom* of image), showing coating “keyed-in” to the substrate surface. (Figure 14.3a and b reprinted from [33], © WILEY-VCH Verlag GmbH & Co. KGaA, Weinheim. Used with permission. Figure 14.3c reprinted from [34], © Carl Hanser Verlag, München. Used with permission)

- Colloidal particles may form in the solution by hydrolysis and condensation reactions of the dissolved species and subsequently be attracted to the substrate by electrostatic or van der Waals interactions. Here nucleation in solution is involved, and usually results in a polycrystalline film with random crystal orientation.

Both mechanisms can occur simultaneously, or ion-by-ion growth can be followed by particle attachment. Transparency of the solution does not rule out the possibility of film growth by particle attachment. Nor does the presence of particles in the solution rule out the possibility of film formation via heterogeneous nucleation and growth on the substrate. As discussed in Sect. 14.2.3, the ultimate oxide phase may be preceded by one or more intermediate phases. In practice, it is usually not possible to determine unambiguously which process dominated the formation of a specific film from the nature of the deposition medium alone, or by examining the film’s microstructure *ex situ*.

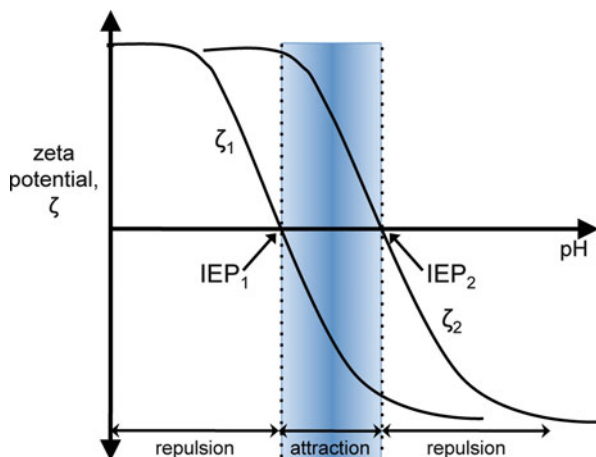


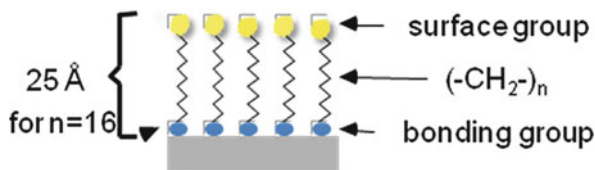
Fig. 14.4 Schematic illustration of the effect of the zeta potentials (ζ_1 and ζ_2) of two adjacent surfaces on the nature of the electrostatic interaction between them. When the pH of the solution between the two surfaces is between the isoelectric points (IEP_1 and IEP_2) of the two surfaces, the electrostatic interaction is expected to be attractive

When a supersaturated solution remains stable against precipitation for very long times unless a specifically prepared substrate is present to promote film formation, nucleation and growth is probably the dominant mechanism of deposition. One example is the deposition of hydroxyapatite coatings on titanium from supersaturated simulated body fluid (SBF) for orthopedic implant applications (Fig. 14.3) [33, 34]. Under deposition conditions, the supersaturated SBF remains solid-free for months unless a substrate that has first been treated with a silicate “nucleating layer” is placed in the solution.

In contrast, when particles are known to be present in the solution, and the occurrence or absence of film formation correlates with the nature of the electrostatic interaction between the substrate and the depositing solid, particle attachment is strongly implicated as a primary mechanism of film deposition. These electrostatic interactions are primarily governed by the zeta potentials of the substrate and the solid phase, which in turn depend on the pH of the surrounding liquid phase.

When the pH of the solution is such that the zeta potentials of two solid surfaces are opposite in sign, an electrostatic attraction is expected between the surfaces, and repulsion when the zeta potentials have the same sign (Fig. 14.4). The condition for electrostatic attraction is met when the pH of the solution is between the isoelectric points, IEP_1 and IEP_2 , of the two surfaces (Fig. 14.4). For example, films of vanadia (which has negative zeta potential [35, 36] in moderately acidic solutions) deposit on amine- and alkyl ammonium-treated surfaces, which are positively charged [37] in acidic and neutral solutions, but not on sulfonate-treated surfaces (which are negatively charged [37] at pH down to about 2) under otherwise identical conditions. (The functionalization of surfaces is discussed in Sect. 14.3.2.)

Fig. 14.5 Schematic illustration of an organic self-assembled monolayer (SAM)



Other interactions occur between solid surfaces in liquid media that can affect their mutual attraction or repulsion. These include:

- Induced-dipole effects, such as van der Waals interactions, are shorter-range, usually attractive,¹ and smaller in magnitude than the electrostatic interactions discussed above. Nevertheless such interactions are ubiquitous and may become significant when electrostatic interactions diminish or are weak to start with. When a substrate has been completely covered with electrostatically attracted particles, the attractive van der Waals interactions between the deposited layer and adjacent unattached particles in the solution may play a role in subsequent growth of the film.
- Interactions between species surrounding or adsorbed onto one or both solids, such as ionic double layers or polymer additives from the solution (Sects. 14.2.3 and 14.3.2).
- Very short-range interactions, when the separation between surfaces approaches the size of a water molecule (so-called hydrophobic interactions) [38].

14.3.2 Functionalization of Substrates

A significant recent trend in research on low-temperature deposition of thin films from liquid media has been the use of organic modifications of substrate surfaces to promote the formation of films. This can be achieved for example with surfactants, polyelectrolyte bilayers, and organic self-assembled monolayers (SAMs). The last of these will be discussed in more detail to illustrate the options that SAMs afford for engineering a substrate to promote film deposition.

SAMs are ultra-thin layers (typically 2.5 nm or less) formed via the spontaneous attachment of hydrocarbon-based surfactant molecules onto a substrate, comprising structurally ordered, two-dimensional arrays [39, 40]. One end of each surfactant molecule bonds to the substrate. Thiol groups (-SH) bond to clean unoxidized metal surfaces. Trichlorosilyl groups (-SiCl₃), after hydrolysis to silanol (-Si(OH)₃), bond via a condensation reaction to surfaces such as glass, sapphire, and the native oxides on Si, Ge, and Ti (Fig. 14.5).

¹ This presumes that the Hamaker coefficient for the two solid surfaces and the interposing liquid medium is positive. This is usually the case for aqueous solutions, oxide precipitates, and the substrates discussed here and in the literature cited.

The functional group at the opposite end of the molecule (or a group that replaces it in a post-deposition displacement or transformation) determines the surface chemistry of the SAM, whether acidic or basic, hydrophilic or hydrophobic, polar or non-polar. Thus SAMs from alkane thiols and trichlorosilanes, with terminal methyl groups or other saturated hydrocarbon groups, are hydrophobic surfaces. SAMs with surface sulfonic acid ($-\text{SO}_3\text{H}$), carboxylic acid ($-\text{COOH}$), and phosphonic acid groups ($-\text{PO}(\text{OH})_2$) deprotonate in aqueous solutions whose pH is above that of the pK_a of the SAM surface, giving hydrophilic, negatively charged surfaces. Other surface groups are hydrophilic but tend to acquire positive surface charge through protonation, as with amine ($-\text{NH}_2$) groups, or are cationic in character, such as alkyl ammonium ($-\text{NR}_3^+$) groups. (Amine- and alkyl ammonium-terminated SAMs were used in the deposition of the vanadia films that were cited in Sect. 14.3.1 as examples of film growth by particle attachment.)

Oxides that have been deposited as films on SAM-treated surfaces via CBD methods are listed in Table 14.1.

14.3.3 *Patterned Deposition*

When the surface treatment used to promote film growth is selectively applied to specific regions of the substrate, the subsequent film deposition can be made to conform to that spatially predetermined arrangement, leading to what is called patterned deposition. Patterned functionalization of a substrate can be achieved in the way the functionalization is first applied to the surface, through microcontact printing of a surfactant with what amounts to a “rubber stamp” [41]. Another approach is to shine UV light through a photomask onto a uniformly functionalized surface, either to alter the functional group photochemically or to cleave the adsorbed species from the surface. In contrast to standard photolithography, either approach permits patterning of the oxide to be achieved without use of photoresists and without a subtractive step such as etching to remove oxide material that has already been deposited. Such approaches offer the potential of creating patterned oxide films with fewer fabrication steps and fewer processing byproducts.

The resolution that can be achieved in the functionalized pattern (i.e., prior to deposition of the oxide film) can be well into the nanometer scale, depending on the technique used (electron-beam etching, photolithography, etc.). In a recent example of nanoscale patterning of an organic functional layer, Schimmel and co-workers achieved lateral resolution of 40 nm in photodimerized thiol layers 12 nm thick by using the tip of an atomic force microscope [42]. It remains to be seen whether this level of resolution in the organic layer will allow higher resolutions to be achieved in inorganic films subsequently deposited on the patterned surface.

The resolution of the deposited film itself is usually less fine than that of the patterned functional layer. An extensive review by Gao and Koumoto [18] surveyed this topic. Typical spatial resolutions in the range of 1–20 μm have been achieved for various oxide films (TiO_2 , ZrO_2 , SnO_2 , ZnO , iron oxides, Ta_2O_5). With the size

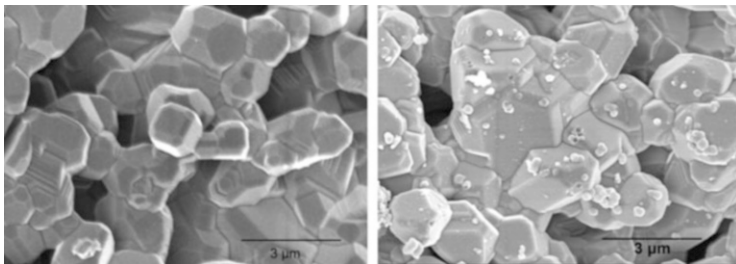


Fig. 14.6 *Left:* Porous nickel oxide layer in the anode of a solid oxide fuel cell. *Right:* Nanocrystalline cerium oxide film, ~100 nm thick, deposited via chemical bath deposition on the porous nickel oxide layer shown at left after treatment with a sulfonate-functionalized self-assembled monolayer. The ceria film was uniform, adherent, and conformal, and it penetrated throughout the 40- μm depth of the porous anode [43]

of the primary deposited particles typically 15 nm or smaller in such films, and with nanoscale resolution of the pattern itself having been demonstrated, the potential would seem to exist for sub-micron resolutions to be achieved. This would require overcoming at least two factors commonly observed in the deposited films. First, when films grow via particle attachment, the primary particles are often agglomerated into clusters 50–100 nm in size; this agglomeration may occur before the particles deposit on the substrate, limiting the fineness of the patterned deposit. Second, once the initial layer of particles or agglomerates is complete, subsequent deposition is likely to be governed more by the interactions between the clusters and the already-deposited film than by substrate-film interactions, so that the controlling influence of the patterned substrate on film deposition in lateral directions diminishes as the film grows thicker. This effect may be seen even if the films form initially by heterogeneous nucleation and growth on the substrate, for heterogeneous nucleation may later occur on the growing film. The review by Gao and Koumoto [18] shows that the same solution parameters that control growth rate (Sect. 14.2.1) also strongly affect the resolution of patterned films.

14.3.4 *New Morphologies*

An interplay of solution chemistry, film morphology, and application distinguishes several recent advances in functional oxide film deposition from aqueous solutions. For example, while most of the early literature on CBD of oxide films described deposition on flat planar substrates, the ability of a liquid to permeate porous structures and to coat fibers, particles, and other shapes with relatively concentrated precursors for solid films is a powerful advantage of CBD approaches. Figure 14.6 illustrates this capability, showing a porous nickel oxide layer on the anode of a solid oxide fuel cell before and after CBD of a 100-nm-thick nanocrystalline cerium oxide film [43]. The ceria film was deposited after the porous nickel oxide was

treated with a sulfonate-functionalized SAM. The high degree of conformity of the ceria film and its lack of cracks and voids are evident. The coating penetrated throughout the 40- μm -thick porous anode.

Infiltration of surfaces with complex topographies is also of interest for photonic crystals, data storage, and field emission devices [10]. Thus not only the chemical nature of the substrate surface, but also its topography plays a role in the utility of CBD as technique for depositing oxide films.

As the understanding of the deposition methods has increased, the forms of the synthesized materials have expanded beyond thin films. For example, nanorods of *c*-oriented wurzite structure ZnO [44] and nanoporous films of TiO₂ [45] were prepared by CBD routes after first depositing a dense “seed” layer of the respective oxides.

In a unique adaption of the LPD technique, Deki and coworkers [9] formed films of TiO₂, SnO₂ or β -FeOOH at a *liquid-liquid* interface, rather than on a solid substrate. This approach should work on a variety of CBD systems and suggests a way to produce free-standing films of virtually any oxides that are obtainable via CBD (Table 16.1).

In another example of material deposition at a non-solid interface [46], micelles of surfactants were used as “substrates” to control the morphology of TiO₂-V₂O₅ mesoporous powders. Surface area could be controlled by the choice of surfactant and the solution composition, illustrating how the deposition process could be engineered to achieve a desired level of performance in a functional oxide material synthesized via low-temperature deposition. Whereas these mesoporous materials were formed on the outside of the surfactant micelles, another approach [47] used a reverse micelle, synthesizing nanoparticles of monoclinic VO₂, orthorhombic Ta₂O₅, and Sn and Nb oxides of unidentified structures on the inside of micelles via LPD at 30 °C.

Using polymer (usually latex or polystyrene) spheres of uniform size as substrates for deposition of oxide films takes advantage of the low temperature of these deposition processes [22, 48]. Nanocrystalline ZnO was produced on sulfonate-functionalized polystyrene spheres. The polymer could be dissolved or pyrolyzed away, leaving intact hollow ZnO shells. The effects of a wide variety of surfactant and polyelectrolyte surface treatments of such spheres were investigated using LPD of TiO₂ (anatase) [49]. While the deposition was very sensitive to the surface functionalization of the films, electrostatic interactions between the substrate and the particles did not appear to play a decisive role in the film deposition. An LPD route yielded films of β -FeOOH on polystyrene spheres [50]. Pyrolysis of the spheres in vacuum at 400 °C for 2 h produced hollow spheres of magnetic Fe₃O₄. In a variant of this approach, polystyrene spheres were assembled to form a template for deposition of a “reverse opal” of SnO₂ via LPD [51]. After burnout of the spheres, the resulting voids in the SnO₂ were then infiltrated with Eu-doped ZrO₂.

The deposition of laminated multilayer films made of alternating oxide and organic layers was investigated. This approach aims to replicate to some extent the remarkable strength of biominerals such as nacre, whose structure consists of

crystalline layers of CaCO_3 (aragonite) between thin protein-based layers comprising approximately 5 vol% of the material. Laminated composites, consisting of alternating layers of TiO_2 120 nm thick and polyelectrolyte 25 nm thick were produced [52]. In nanoindentation measurements, films with three pairs of such layers on silicon showed hardness values 15 % higher than a liquid-deposited TiO_2 film of the same thickness.

In similar work on ZnO /polyelectrolyte laminate films [53], the laminated films were approximately 25 % harder. These polyelectrolyte layers consisted of poly(styrene sulfonate), poly-L-glutamic acid and poly-L-lysine hydrobromide.

14.4 Process Control

In its simplest form, a CBD process involves a single isothermal immersion of a substrate into a non-flowing liquid precursor of the desired film. Even if no external changes are imposed on the system—e.g. no more reagents are added to the deposition medium, the solution is not stirred or agitated, the temperature is not changed—the important solution parameters that affect the deposition process are far from static. In particular, once solid has begun to form, the supersaturation of the solution begins to decrease, and eventually reaches a level at which nucleation of new particles stops (although growth of existing particles may continue). The $p\text{H}$ may significantly change from the initial value, usually in a direction that slows particle nucleation and growth. As solid nucleates and grows (on the substrate, in the solution, or both), solid-solid interactions become more important: e.g. adjacent particles may agglomerate via van der Waals or other interactions, causing continuous changes in the number, size, and spatial distribution of solid particles. Overall, for a single-immersion deposition, there is usually an “incubation” period during which no film growth occurs, followed by a period of growth (which may exhibit a rising growth rate followed by a declining growth rate), then cessation of growth once supersaturation has dropped below a critical level.

Niesen and De Guire reviewed the growth rates and film thicknesses achieved by aqueous liquid deposition processes such as CBD, SILAR, LPD and their variations [2]. Typical growth rates for such processes are 200–1,500 nm/h with maximum film thickness up to 1,000 nm. For SILAR, typical growth rates are less than 1 nm/cycle, and ultimate film thicknesses are often lower than for other chemical bath processes.

Sequential deposition, a concept integral to SILAR, has also been adapted to other CBD techniques. It provides a simple way to overcome the “exhaustion” of the deposition process when the supersaturation of the original solution drops to a level too low to sustain further film growth. The substrate is simply removed from its solution and inserted in a fresh aliquot of the same precursor. In principle, this approach can lead to thicker films than single depositions and can be repeated indefinitely to build up thick films.

Another approach for avoiding the continuous change in solution concentration and pH is to monitor and adjust these parameters periodically or continuously to maintain desired values. Automated electronic systems for maintaining constant pH (“ pH -stats”) are readily available for small- and large-scale depositions. Sensors are commercially available for continuous measurement of the concentrations of some metal ions in the deposition medium. Complete systems for monitoring and maintaining solution parameters have been developed for the commercial deposition of CdS films for the photovoltaics industry, and these approaches could undoubtedly be adapted to the deposition of oxide films.

When a reactant is added to a solution, spatial gradients in supersaturation will occur. This can lead to inadvertent local precipitation and other inhomogeneities at the site of the addition until the added substance is uniformly mixed into the solution. One way of avoiding this situation, in solutions where a rise in pH can be used to trigger the formation of the solid, is to add urea ($(NH_2)_2CO$) to the solution before heating. In aqueous solutions at temperatures between ~ 40 and ~ 80 °C, urea will decompose to form ammonia and carbon dioxide. The net effect is a steady rise in pH , occurring uniformly throughout the solution.

A variant of CBD known as liquid flow deposition (LFD) is designed to reduce both spatial nonuniformities and temporal changes in supersaturation. In LFD, the reactant solution is flowed past the substrate at a controlled rate. It was first developed in the late 1980s [54, 55] as a variation of ferrite plating. In LFD, the reactants are replenished continuously, allowing more constant composition of solution and more constant degree of supersaturation to be maintained. The used precursor may be collected, reconstituted, and reused. The rate of flow of the deposition medium past the substrate becomes an additional and easily controlled variable for adjusting the deposition process. With appropriate adjustment of solution parameters, LFD can be applied to any CBD technique (except perhaps SILAR). Ferrites [54, 55], CdS, ZnO [2], SnO₂ [56] and TiO₂ [57] have been deposited using LFD at constant and high growth rates. In contrast, ZrO₂ films did not grow significantly faster or thicker via LFD than via conventional CBD [58]. Alternatively, by varying the flow rate and solution makeup during a deposition, LFD can be designed to vary the composition, growth rate, and microstructure within a single film, as reported by Deki et al. [59].

Using a simple LFD apparatus to deposit SnO₂ films (Fig. 14.7), Supothina et al. [56, 60] explored the interplay of solution parameters ($[Sn^{4+}]$ and pH) with chamber design and flow rate. Intermediate flow rates ($2\text{--}3\text{ mL min}^{-1}$) gave the thickest films, while thinner or no films were obtained at higher and lower flow rates. Their results indicate that, when film growth occurs by particle attachment, maximum growth rates can be obtained by coupling the residence time of the solution in the vicinity of the substrate to the incubation time for nucleation of particles in the solution. The maximum growth rate (85 nm h^{-1}) and the maximum film thickness ($1\text{ }\mu\text{m}$) were obtained when the deposition chamber was configured to decrease the distance that particles would have to travel to reach the substrate after being nucleated in the solution.

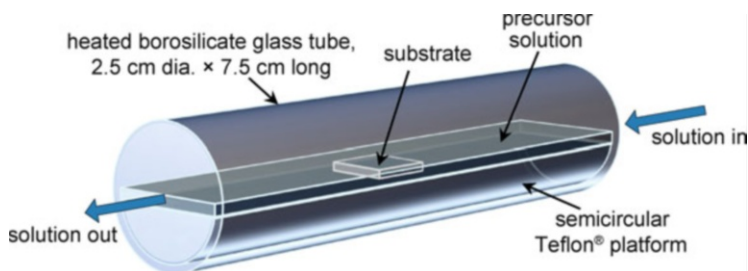


Fig. 14.7 Schematic illustration of an apparatus used for liquid flow deposition. A pump delivers the precursor solution (which may be preheated or which may be heated in the deposition chamber) to the substrate. After residing in the chamber for a time that depends on the flow rate, the volume of the chamber, and configuration of the flow field, the precursor flows out of the tube and may be collected, reconstituted, and reused [56, 60]

Boyle et al. [61, 62] reported a closed-loop LFD process for CdS films that filters, recirculates, and replenishes the used solution, significantly reducing the amount of (cadmium) waste.

Other variants of CBD use different strategies for initiating solid formation and inducing film formation. These include photochemical deposition (in which light is used to trigger formation of the solid phase) and deposition assisted by applied electric or magnetic fields or by ultrasonic agitation. The review by Niesen and De Guire [2] surveyed some of these techniques.

It is not always desirable to immerse an entire substrate in a CBD medium or to expose both sides of a substrate to a surface functionalization procedure such as those described in Sect. 14.3.2. In the deposition of SAMs on the electrodes of solid oxide fuel cells by Tang et al. [43, 63] it was found that one step in the sulfonate functionalization procedure had adverse effects on the cathode side of the cell. The problem was overcome by placing a cotton pad on the anode side of the cell, cut to the size and shape of the anode, and then carefully saturating the pad with the reagent in question so that none seeped out onto the rest of the cell. It is likely that a similar strategy could be implemented in general with CBD solutions if other parts of the substrate must be protected from contact with the deposition medium.

14.5 Conclusions and Prospects

While CBD approaches offer great versatility with regard to deposition of oxide films as discussed above, some of the limitations of these films should be kept in mind. For example, it remains challenging to synthesize multicomponent materials whose individual components precipitate at widely differing pH or temperature, or when the choice of complexants for the metals is limited. In such cases, non-aqueous solutions, e.g. using alcohols or other polar solvents for the metal and chalcogenide precursors, may offer more precise control over the supersaturation of the solution and therefore of the deposition rate. An extensive base of

experience can be tapped in developing such approaches. Much of the research on sol-gel synthesis of oxide materials over the last few decades [64] has utilized non-aqueous solvents to produce a wide range of technologically important oxide materials. Such approaches would increase the cost, and could increase adverse environmental impacts, of the process; no solvent is cheaper, nor more readily available, biocompatible, and environmentally benign than water. Nevertheless, there are many technologically important oxide materials, such as tin-doped indium oxide or ferroelectric oxides such as barium titanate, that do not lend themselves to purely aqueous CBD. For such materials, non-aqueous approaches represent a promising strategy for CBD processing.

In the as-deposited state, the films may contain residual water and other components from the precursor solution. They are often not completely crystallized. As a result, the films often do not exhibit the same physical properties as fully crystalline sintered materials. For example, the as-deposited films are mechanically much softer than fired polycrystalline ceramics, with little abrasion resistance. Dopants added to the film may not be in solid solution in the as-deposited host oxide, so that the as-deposited films may not show the intended optical properties or electrical conductivity. Many of these effects can be alleviated by a subsequent heat treatment to fully crystallize the film, to incorporate the dopants into solid solution, to form the desired compound (if necessary), and to develop physical properties more typical of a polycrystalline oxide. Such a heat treatment is likely to decompose any organic components, such as SAMs (which have been shown to pyrolyze from under the overlying oxide CBD film at temperatures between 200 and 400 °C [65]) or polymer additives in the precursor solution. If loss of the organic component is not deleterious to the film properties, and if the substrate can withstand somewhat elevated temperatures, such a heat treatment would not be a severe drawback, especially in light of the control over film formation, low costs, and other advantages associated with CBD.

In light of these limitations, the most likely first applications of CBD oxide films will not expose them to significant mechanical loads or wear. Examples include single or multilayer optical coatings or catalytic or sensing layers that are protected by harder materials such as glass or some other rigid support. The cerium oxide coatings applied to solid oxide fuel cell anodes by Tang et al. [43, 63] survived up to hundreds of hours of operation in the absence of direct mechanical impact or abrasion. Significantly, however, microstructural changes occurring in the anodes during operation, and which were implicated in cell failure, led also to disruption of the coatings.

The interactions of organic molecules with inorganic surfaces promise some of the most exciting new prospects for CBD films and broad opportunities for further research. These include control over film growth and morphology as discussed in Sects. 14.2.3 and 14.3.4, but also applications involving the adsorption, sensing, patterning, or other manipulations of biological molecules and assemblies, from various proteins, to pharmaceuticals, to DNA and entire cells. Organic-inorganic surface interactions lie at the heart of many potential applications in biochemical sensing, biomimetic materials synthesis, drug delivery, and biomedical devices.

References

1. Hodes G (2003) Chemical solution deposition of semiconductor films. Marcel Dekker, New York
2. Niesen TP, De Guire MR (2001) Review: deposition of ceramic thin films at low temperatures from aqueous solutions. *J Electroceram* 6:169
3. Hodes G (2007) Semiconductor and ceramic nanoparticle films deposited by chemical bath deposition. *Phys Chem Chem Phys* 9:2181
4. Matijevic E (1985) Production of monodispersed colloidal particles. *Ann Rev Mater Sci* 15:483
5. Baes CF, Mesmer RE Jr (1986) The hydrolysis of cations. Krieger, New York
6. Bunker BC, Rieke PC, Tarasevich BJ, Campbell AA, Fryxell GE, Graff GL, Song L, Liu J, Virden JW, McVay GL (1994) Ceramic thin-film formation on functionalized interfaces through biomimetic processing. *Science* 264:48
7. Deki S, Miki H, Sakamoto MA, Mizuhata M (2007) Fabrication of copper ferrite thin films from aqueous solution by the liquid-phase deposition method. *Chem Lett* 36:518
8. Saito Y, Sekiguchi Y, Mizuhata M, Deki S (2007) Continuous deposition system of SnO₂ thin film by the liquid phase deposition (LPD) method. *J Ceram Soc Jap* 115:856
9. Deki S, Nakata A, Sakakibara Y, Mizuhata M (2008) Deposition of metal oxide films at liquid-liquid interface by the liquid phase deposition method. *J Phys Chem C* 112:13535
10. Mizuhata M, Miyake T, Nomoto Y, Deki S (2008) Deep reactive ion etching (Deep-RIE) process for fabrication of ordered structural metal oxide thin films by the liquid phase infiltration method. *Microelectron Eng* 85:355
11. Deki S, Aoi Y, Hiroi O, Kajinami A (1996) Titanium (IV) oxide thin films prepared from aqueous solution. *Chem Lett* 25:433
12. Kawahara H, Honda H (1984) Method for producing glass coated with titanium oxide film. Japan Patent 59141441A
13. Nicolau YF (1985) Solution deposition of thin solid compound films by a successive ionic-layer absorption and reaction process. *Appl Surf Sci* 22–23:1061
14. Ristov M, Sinadinovski GJ, Grozdanov I (1985) Chemical deposition of Cu₂O thin films. *Thin Solid Films* 123:63
15. Ristov M, Sinadinovski GJ, Grozdanov I, Mitreski M (1987) Chemical deposition of ZnO films. *Thin Solid Films* 149:65
16. Tolstoy VP (2006) Successive ionic layer deposition. The use in nanotechnology. *Uspekhi Khimii* 75:183
17. Nakanishi T, Masuda Y, Koumoto K (2005) Deposition of γ -FeOOH, Fe₃O₄ and Fe on Pd-catalyzed substrates. *J Cryst Growth* 284:176
18. Gao Y, Koumoto K (2005) Bio-inspired ceramic thin film processing: present status and future perspective. *J Cryst Growth Des* 5:1983
19. Parikh H, De Guire MR (2009) Recent progress in the synthesis of oxide materials from liquid solutions. *J Ceram Soc Japan* 117:228
20. Abe M (2000) Ferrite plating: a chemical method preparing oxide magnetic films at 24–100°C, and its applications. *Electrochim Acta* 45:3337
21. Abe M (2000) A soft solution processing technique for preparing ferrite films and their applications. *MRS Bull* 25:51
22. Lipowsky P, Jia S, Hoffmann RC, Jin-Phillipp NY, Bill J, Ruhle M (2006) Thin film formation by oriented attachment of polymer-capped nanocrystalline ZnO. *Int J Mater Res* 97:607
23. Tian ZR, Voigt JA, Liu J, McKenzie B, Mcdermott MJ (2002) Biomimetic arrays of oriented helical ZnO nanorods and columns. *J Am Chem Soc* 124:12954
24. Tian ZR, Voigt JA, Liu J, McKenzie B, Mcdermott MJ, Rodriguez MA, Konishi H, Xu H (2003) Complex and oriented ZnO nanostructures. *Nat Mater* 2:821
25. Yahiro J, Kawano T, Imai H (2007) Nanometric morphological variation of zinc oxide crystals using organic molecules with carboxy and sulfonic groups. *J Colloid Interface Sci* 310:302

26. Hoffmann RC, Jia SJ, Bartolomé JC, Fuchs TM, Bill J, Graat PCJ, Aldinger F (2003) Growth of thin ZnO films from aqueous solutions in the presence of PMMA-graft-PEO copolymers. *J Eur Ceram Soc* 23:2119
27. Hoffmann RC, Jia S, Bill J, De Guire MR, Aldinger F (2004) Influences of additives on the formation of ZnO thin films by forced hydrolysis. *J Ceram Soc Jap* 112:1089
28. Hoffmann RC, Jia SJ, Jeurgens LPH, Bill J, Aldinger F (2006) Influence of polyvinylpyrrolidone on the formation and properties of ZnO thin films in chemical bath deposition. *Mater Sci Eng C Biomim Supramol Syst* 26:41
29. Lipowsky P, Hedin N, Bill J, Hoffmann LC, Ahniyaz A, Aldinger F, Bergstrom L (2008) Controlling the assembly of nanocrystalline ZnO films by a transient amorphous phase in solution. *J Phys Chem C* 112:5373
30. Gerstel P, Lipowsky P, Durupthy O, Hoffmann RC, Bellina P, Bill J, Aldinger F (2006) Deposition of zinc oxide and layered basic zinc salts from aqueous solutions containing amino acids and dipeptides. *J Ceram Soc Jap* 114:911
31. Gerstel P, Hoffmann RC, Lipowsky P, Jeurgens LPH, Bill J, Aldinger F (2006) Mineralization of zinc salts from aqueous solutions directed by amino acids and peptides. *Chem Mater* 18:179
32. Bill J, Hoffmann RC, Fuchs TM, Aldinger F (2002) Deposition of ceramic materials from aqueous solution induced by organic templates. *Zeitschrift Für Metallkunde* 93:478
33. Sampathkumaran U, De Guire MR, Wang RR (2001) Hydroxyapatite coatings on titanium. *Adv Eng Mater* 3:401
34. Zou L, De Guire M, Wang R (2006) Effect of organic self-assembled monolayers on the deposition and adhesion of hydroxyapatite coatings on titanium. *Int J Mater Res* 97:760
35. Kittaka S, Uchida N, Katayama M, Doi A, Fukuhara M (1991) Effect of intercalation of metal ions on the colloidal and solid properties of vanadium pentoxide hydrate, $V_2O_5 \cdot nH_2O$. *Colloid Polym Sci* 269:835
36. Hoffmann RC, Jeurgens LPH, Wildhack S, Bill J, Aldinger F (2004) Deposition of composite titania/vanadia thin films by chemical bath deposition. *Chem Mater* 16:4199
37. Shyue JJ, De Guire MR, Nakanishi T, Masuda Y, Koumoto K, Sukenik CN (2004) Acid-base properties and zeta potentials of self-assembled monolayers obtained via in situ transformations. *Langmuir* 20:8693
38. Attard P (2003) Nanobubbles and the hydrophobic interaction. *Adv Colloid Interface Sci* 104:75
39. Sagiv J (1980) Organized monolayers by adsorption. 1. Formation and structure of oleophobic mixed monolayers on solid surfaces. *J Am Chem Soc* 102:92
40. Ulman A (1996) Formation and structure of self-assembled monolayers. *Chem Rev* 96:1533
41. Whitesides GM (1995) Self-assembling materials. *Sci Am* 9:114
42. Barczewski M, Walheim S, Heiler T, Blaszczyk A, Mayor M, Schimmel T (2010) High aspect ratio constructive nanolithography with a photo-dimerizable molecule. *Langmuir* 26:3623
43. Tang L, Salamon M, De Guire MR (2010) Cerium oxide thin films on solid oxide fuel cell anodes. *Sci Adv Mater* 2:79
44. Gao Y, Nagai M (2006) Morphology evolution of ZnO thin films from aqueous solutions and their application to solar cells. *Langmuir* 22:3936
45. Gao Y, Nagai M, Seo WS, Koumoto K (2007) Template-free self-assembly of a nanoporous TiO_2 thin film. *J Am Ceram Soc* 90:831
46. Shyue JJ, De Guire MR (2005) Single-step preparation of mesoporous, anatase-based titanium-vanadium oxide and its application. *J Am Chem Soc* 127:12736
47. Nakata A, Mizuhata M, Deki S (2007) Novel fabrication of highly crystallized nanoparticles in the confined system by the liquid phase deposition (LPD) method. *Electrochim Acta* 53:179
48. Lipowsky P, Hoffmann RC, Welzel U, Bill J, Aldinger F (2007) Site-selective deposition of nanostructured ZnO thin films from solutions containing polyvinylpyrrolidone. *Adv Funct Mater* 17:2151
49. Strohm H, Löbmann P (2005) Liquid-phase deposition of TiO_2 on polystyrene latex particles functionalized by the adsorption of polyelectrolytes. *Chem Mater* 17:6772

50. Aoi Y, Kambayashi H, Deguchi T, Yato K, Deki S (2007) Synthesis of nanostructured metal oxide by liquid-phase deposition. *Electrochim Acta* 53:175
51. Mizuhata M, Kida Y, Deki S (2007) Enhancement of photoluminescence from Eu^{3+} doped ZrO_2 in SnO_2 inverse opal structure prepared by the liquid phase infiltration method. *J Ceram Soc Jap* 115:724
52. Burghard Z, Tucic A, Jeurgens LRH, Hoffmann RC, Bill J, Aldinger F (2007) Nanomechanical properties of bioinspired organic-inorganic composite films. *Adv Mater* 19:970
53. Lipowsky P, Burghard Z, Jeurgens LPH, Bill J, Aldinger F (2007) Laminates of zinc oxide and poly(amino acid) layers with enhanced mechanical performance. *Nanotechnology* 18:345707
54. Goto Y, Tamaura Y, Abe M, Gomi M (1988) Improvement in deposition rate and quality of films prepared by thin liquid-film ferrite plating method. *IEEE Transl J Magn Jpn* 3:159
55. Goto Y, Tamaura Y, Gomi M, Abe M (1987) Ferrite plating by means of thin film of reaction solution; 'thin liquid-film method'. *IEEE Transl J Magn Jpn* 2:235
56. Supothina S, De Guire MR, Heuer AH (2003) Nanocrystalline SnO_2 thin films via liquid flow deposition. *J Am Ceram Soc* 86:2074
57. Fuchs TM, Hoffmann RC, Niesen TP, Tew H, Bill J, Aldinger F (2002) Deposition of titania thin films from aqueous solution by a continuous flow technique. *J Mater Chem* 12:1597
58. Niesen TP, Sampathkumaran U, Fuchs T, De Guire MR, Bill J, Aldinger F (2000) Deposition of nanocrystalline zirconia thin films on organic self-assembled monolayers by a continuous flow technique. In: Proceedings of MATERIALS WEEK 2000—symposium L4 on synthesis and technological applications of nanocrystallites and materials assembled from nanometer-sized clusters, session – synthesis and processing, Werkstoffwoche-Partnerschaft GbR. <http://www.materialsweek.org/proceedings>
59. Deki S, Iizuka S, Akamatsu K, Mizuhata M, Kajinami A (2001) Novel fabrication method for $\text{Si}_{1-x}\text{Ti}_x\text{O}_2$ thin films with graded composition profiles by liquid phase deposition. *J Mater Chem* 11:984
60. Supothina S, De Guire MR, Heuer AH, Niesen TP, Bill J, Aldinger F (1999) Deposition of tin (IV) oxide ceramic films on organic self-assembled monolayers. In: Klein LC, Francis LF, De Guire MR, Mark JE (eds) *Organic-inorganic hybrid materials II*, vol 576. Materials Research Society, Warrendale, PA, p 203
61. Bayer A, Boyle DS, Heinrich MR, O'Brien P, Otway DJ, Robbe O (2000) Developing environmentally benign routes for semiconductor synthesis: improved approaches to the solution deposition of cadmium sulfide for solar cell applications. *Green Chem* 2:79
62. Boyle DS, Bayer A, Heinrich MR, Robbe O, O'Brien P (2000) Novel approach to the chemical bath deposition of chalcogenide semiconductors. *Thin Solid Films* 150:361–362
63. De Guire MR, Bayless D (2010) Sulfur tolerance and improved performance in SOFCs for aerospace applications. Final Technical Report for NASA Contract NNC06CA46C
64. Brinker CJ, Scherer GW (1990) *Sol-gel science: the physics and chemistry of sol-gel processing*. Academic, San Diego
65. Shin H, Wang Y, Sampathkumaran U, De Guire MR, Heuer AH, Sukenik CN (1999) Pyrolysis of self-assembled monolayers on inorganic substrates. *J Mater Res* 14:2116

Part IV

Processing and Crystallization

This part will cover all aspects which are necessary to transform the as-deposited films (cp. Fig. 1 in the general introduction) to the desired crystalline metal oxide thin films with well-defined phase, microstructure, texture, and pattern. This transformation typically takes place by a nucleation and growth determined process from an initially amorphous phase, which in turn is governed by thermodynamic and kinetic factors. Hence, in Chap. 15 these basics are discussed in detail. By controlling these factors it is even possible to grow epitaxial films on single crystalline substrates, which is described in Chap. 16. Next in Chap. 17, by means of alkaline earth titanate and lead titanate based thin film materials, it is demonstrated that these perovskites deposited on platinized silicon substrates can be tuned from fine grained to columnar microstructure and highly textured. These are only achieved if the thermodynamic and kinetic aspects are considered properly. The impact of the different morphologies and textures on the electrical properties impressively shows the importance of this control over film growth.

In the case of CSD on semiconductor substrates with integrated functionalities such as transistors or the deposition on temperature sensitive substrates, as for example plastics or glass the conventional crystallization temperatures ($\sim 600\text{--}800\text{ }^{\circ}\text{C}$) are often too high. Chapter 18 reviews approaches to minimize the thermal load of the substrates during crystallization.

For some applications thicker films (e.g. piezoelectric devices) or (nano) composites consisting of a distribution of one material in a matrix of another material are beneficial. Chapter 19 deals with methods to prepare such (nano) composite films either from precursor solutions containing particles with different sizes, i.e. $>100\text{ nm}$ to grow thicker films, or $<100\text{ nm}$ to create nanocomposite films. Included are also methods of infiltration of a porous network consisting of larger particles in order to increase the film density, and molecular mixing of precursors for two different materials, which do not form mixed phases (e.g. perovskite and spinel), but segregate into two separate, well distributed nanoscale phases.

The last two chapters of this part review the fabrication of patterned films and individual registered nanograins on different lateral scales (from 0.5 to $1.0\text{ }\mu\text{m}$

down to sub-10 nm). Usually patterning is performed in subtractive modes by fabricating films on the whole substrate area followed by lithographic and etching steps. By applying UV-beam and electron beam direct patterning of photosensitive CSD precursor films, which are described in detail in Chap. 20, not only the number of working steps can be reduced, but also deteriorating influences of the etching step on the functional oxides can be avoided. Using lead titanate based ferroelectrics as an example, Chap. 21 reviews a way of fabricating registered assemblies of individual sub-100 nm grains by using suitable templates, which can be generated by various methods. By bottom-up CSD-processing these templates can be transferred into fully functional ferroelectric nanograins, again without deteriorating influences of the patterning technique itself.

Chapter 15

Thermodynamics and Heating Processes

Robert W. Schwartz and Manoj Narayanan

15.1 Overview of Pyrolysis and Transformation to the Crystalline State

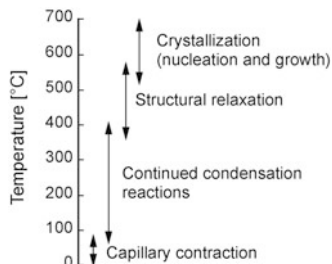
Following deposition by spin casting or dip coating, in the most commonly used solution deposition processes, the film may be described as a viscoelastic solid consisting of an inorganic network with bound organic moieties (the skeleton) and solvent entrapped within the pore structure of the film. Both the organic groups associated with the structural backbone and the solvent must be removed from the film prior to conversion to the crystalline state. This requires significant structural rearrangement, which occurs through a variety of chemical and physical processes at a variety of length scales over a range of temperatures.

The processes involved in the transformation from the as-deposited into the crystalline state, as well as typical temperature ranges in which they occur, are illustrated in Fig. 15.1 [1]. It is important to recognize that the temperatures at which specific reactions and structural rearrangement processes occur are highly dependent on solution synthesis and thin film processing parameters. Following the removal of organic species, as heat treatment temperature is increased, kinetic limitations to further atomic rearrangement are overcome and thermodynamic factors (e.g., the relative thermodynamic stability of the crystalline state vs. the amorphous state that is developed following organic removal) lead to the development of a crystallized film possessing the desired ferroelectric properties. Various other factors, such as substrate, ramp rate, heat treatment atmosphere, film thickness, and film composition may each impact the temperature regime in which the processes noted in Fig. 15.1 will occur. The extent of overlap of these processes,

R.W. Schwartz (✉)
University of Missouri System, Columbia, MO, USA
e-mail: rschwartz@umsystem.edu

M. Narayanan
Argonne National Laboratory, Lemont, IL, USA

Fig. 15.1 Approximate temperature ranges for processes contributing to densification and crystallization of solution derived thin films processed at moderate ramp rates ($\sim 5\text{--}50\text{ }^\circ\text{C}/\text{min}$). After [1]



film crystallization behavior, microstructure, orientation and epitaxial growth are all influenced by these parameters. Extensive investigations of such factors have been carried out and the results of some of these studies are reviewed below.

15.2 Thermolysis and Pyrolysis

15.2.1 *Thermolysis and Pyrolysis: Definitions and General Characteristics*

For films deposited by solution methods, the term “pyrolysis” is typically used to describe the removal of the organic constituents under an oxidizing environment (either air or oxygen) through conversion to volatile organic molecules, such as CO, CO₂, by combustion [2]. Organic species may also be removed in the absence of oxygen through the formation of volatile organics by “thermolysis” [2]. These processes typically involve different chemical reactions and decomposition pathways that may affect the specific nature of the oxide backbone, which may subsequently affect densification characteristics and crystallization behavior. As would be expected, time and temperature parameters for thermolysis and pyrolysis also impact the specific reactions that occur during heat treatment and nature of the species that are evolved.

Few studies have focused on the specific reaction pathways and differences between pyrolysis and thermolysis are typically not differentiated. It is much more common for individuals preparing solution-derived thin films to simply study transformation behavior from the perspective of the temperatures at which organic removal has been completed by using methods such as thermal gravimetric analysis (TGA, see Chap. 7). Weight loss between a few and a few 10’s weight percent is typical [2], though it should be noted that if solvent loss from within the pore structure of the film is considered, the total weight loss is significantly greater, approaching even 90 % or more. As solution methods for film fabrication were developed, particularly in the mid-1980s through the 1990s, the most common approach to study pyrolysis behavior was to study the pyrolysis characteristics of solution-derived powders prepared from the same solution chemistry and assume

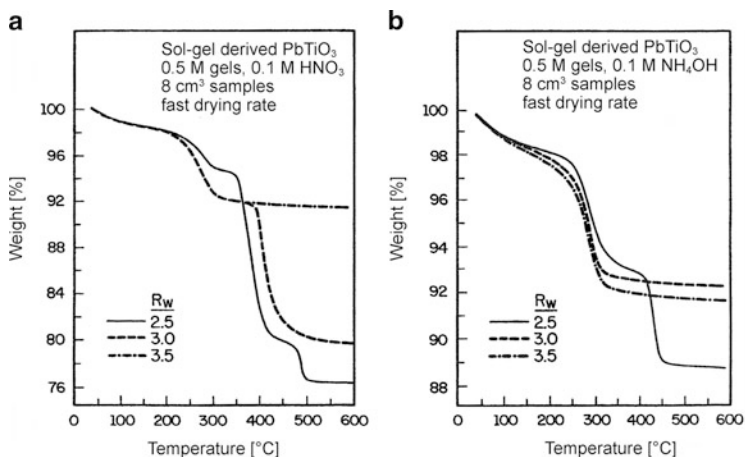


Fig. 15.2 Effects of hydrolysis conditions on the decomposition behavior of (a) acidic and (b) basic catalyzed PbTiO_3 gels (air atmosphere). After [3]

that the pyrolysis characteristics of the films would be similar to the powders. Though this is likely not a fully valid assumption, it is not unreasonable and has been used effectively in thin film preparation to identify a temperature for “removal of organics” prior to the use of higher heat treatment temperatures to induce crystallization. Quotations are used above because few studies have focused on residual carbon content (<0.5–1.0 %) and its possible influence on crystallization temperature.

Typical TGA results for solution-derived lead titanate (PbTiO_3 ; PT) powders prepared under different synthesis conditions are presented in Fig. 15.2 [3]. The results highlighted here are for the 2-methoxyethanol (2-MOE) solution chemistry pioneered by Budd, Dey and Payne for lead titanate and lead zirconate titanate (PbZrO_3 – PbTiO_3 ; PZT) film preparation [4–6]. Different hydrolysis and catalysis conditions have been used for the preparation of these samples and the figure is included simply to demonstrate the general nature of the variations in decomposition behavior that may result from different synthesis conditions. It should be noted that prior to thermogravimetric analysis (TGA), after gelation, the gel samples were aged for 0.5 h and then dried at 140 °C for 72 h.

The general effects of synthetic conditions that may be noticed are a decrease in the pyrolysis temperature and weight loss with increased hydrolysis ratio (R_w = moles H_2O /mole of alkoxide). Other changes in pyrolysis behavior, such as the number of decomposition steps and specific temperatures at which the decomposition reactions occur may also be noticed. Acidic versus basic catalysis conditions during hydrolysis also impact both pyrolysis temperature and behavior. Knowledge of decomposition characteristics and temperature may be subsequently used to select a temperature for crystallization of the powder or film.

15.2.2 *Decomposition Behavior and Pathway*

15.2.2.1 *Solution Precursor Effects*

Many studies have focused on the role of precursor chemistry and thermal treatment on structural evolution and resultant thin film microstructure [7–17]. The general nature of the solution synthesis route utilized can impact decomposition behavior, pathway and temperature, as well as crystallization behavior. The most commonly employed routes include: (1) metallo-organic decomposition or MOD, typically based on long-chain hexanoate or di-neodecanoate precursors; (2) hybrid, otherwise known as chelate or acetate-modified approaches, based on alkoxide precursors and chelation, typically by the acetate group of acetic acid; and (3) sol-gel approaches based on alkoxide precursors and hydrolysis and condensation reactions. Various reaction byproducts and intermediate phases serve to define the decomposition behavior, which depends upon precursor chemistry and thin film composition. The intermediate phases may be metallic, single component oxide, carbonate, or oxocarbonate in nature, or may represent another intermediate phase, such as pyrochlore or fluorite, which can have a significant impact on the thermodynamic driving force for crystallization.

Two of the more detailed studies that report on precursor effects on decomposition pathway are those of Polli and Lange [9] and Neumayer et al. [10]. Polli and Lange [9] report on the PZT (50/50) material system, while Neumayer et al. [10] report on the BaTiO_3 — SrTiO_3 (BST) system. These studies discuss the effects of solution chemistry (MOD, chelate and sol-gel) on decomposition behavior (temperatures and weight loss), as well as other effects, such as local reducing environments associated with high retained organic content within specific heat treatment temperatures. Both studies also report on pyrolysis conditions leading to homogeneous amorphous phases, which are critical to the production of high quality crystalline films.

Polli and Lange used X-ray diffraction (XRD) analysis of solution-derived powders to carry out their investigation [9]. Briefly, these authors noted that irrespective of solution chemistry, elemental Pb and PbO were the first phases formed during rapid pyrolysis to 400 °C. Longer times at reduced pyrolysis temperatures (e.g., 300 °C for 1 h) were effective at suppressing the formation of these phases for the sol-gel based process, but not for the MOD or chelate based processes. This led the authors to conclude that precursors with high carbonaceous content and the rate of hydrocarbon release during pyrolysis were key to avoid formation of elemental Pb during heat treatment.

Neumayer et al. used Fourier Transform Infrared (FTIR) spectroscopy (cp. Chap. 9) in their analysis of solution chemistry effects on BST formation [10]. Their MOD process utilized barium and strontium acetate precursors together with titanium diisopropoxide bis(acetylacetonate). The sol-gel chemistry studied was a relatively standard 2-MOE route, while the hybrid route utilized isopropoxide precursors for Ba, Sr and Ti, followed by chelation with acetic acid. The authors

note that the MOD route resulted in the least facile decomposition pathway and a larger thermal budget for organic removal than the other two processes. They also report that the hybrid route produced films with better crystallinity and lower carbonate content [10].

In general, shorter chain organic species and lower boiling point solvents produce materials that undergo decomposition at lower temperatures, however, the formation of specific intermediate phases, such as barium or strontium carbonate, which are relatively stable intermediate phases, can delay pyrolysis to higher temperatures. Variations in precursor selection, as well as solution synthesis and pyrolysis conditions, demand the use of thermal analysis techniques to determine the temperature at which organic removal is complete.

15.2.2.2 Additional Effects on Decomposition Behavior

There are certainly many more papers than those cited in [7–17] that describe a variety of effects observed during pyrolysis. Beyond solution chemistry, ambient atmosphere utilized during pyrolysis (and crystallization) can impact not only residual carbon content in the film, but also the nature of the intermediate phases formed [18, 19]. Other parameters, such as heating rate and pyrolysis temperature can also have a significant impact [20, 21]. One contributing factor to such observations is related to Fig. 15.1. Because these processes (in particular, capillary contraction, continued condensation reactions and structural relaxation) occur over a range of temperatures and each have their own governing kinetics and thermodynamics, the resulting processing behavior leading to removal of residual organic material, evolved amorphous structure, and even the formation of intermediate crystalline phases may be impacted. Examples of such effects are highlighted below.

15.2.3 Reactions and Byproducts

Relatively few studies have focused on the reaction chemistry associated with pyrolysis and thermolysis of organic constituents from as-deposited films. However, one detailed investigation that illustrates the nature of the reactions and byproducts associated with these processes is that of Coffman et al. [22]. These authors studied the thermal decomposition of methoxyethanol gel-derived PZT powders and films using a variety of analytical techniques, including FTIR and dynamic mass spectrometric analysis (DMSA) coupled with TGA and differential thermal analysis (DTA). As with other studies [3–5], effects of acid versus base catalysis were evaluated.

Figure 15.3 illustrates the capabilities of using combined methods to analyze thermolysis reactions and by-products through the study of evolved species [22]. At lower decomposition temperatures (100–200 °C), water and alcohol

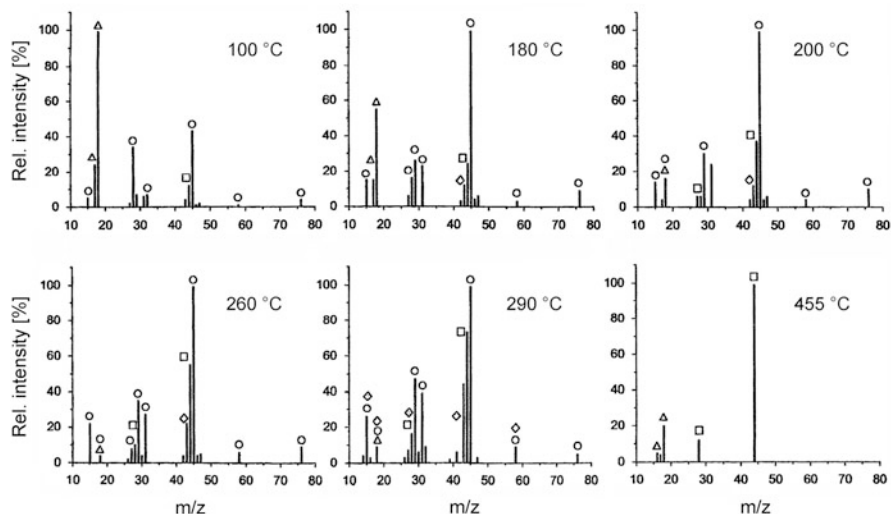


Fig. 15.3 Dynamic mass spectrometric analysis (DMSA) for 2-MOE derived PZT gels at different pyrolysis temperatures (He atmosphere). *Open triangle* = water; *open circle* = 2-methoxyethanol; *open diamond* = acetone; *open square* = carbon dioxide. After [22]

(2-methoxyethanol) are the principal volatile by-products. At temperatures between 290 and 455 °C, acetone and carbon dioxide become the principal by-products. The authors link the evolution of these species with thermal events noted in the DTA analysis. For acid-catalyzed gels, specific processes cited include: endothermic desorption of H₂O and ROH, where R is the 2-methoxyethyl group at temperatures between 20 and 220 °C; and exothermic condensation reactions evolving 2-methoxyethanol (220–290 °C). Acetone, carbon dioxide and 2-methoxyethanol are further evolved at temperatures between 290 and 380 °C, and with further increase in pyrolysis temperature to 600 °C, the principal evolved species is CO₂.

The observed behavior was further investigated by the authors through similar studies of simpler systems, notably, lead titanate gels and the lead acetate precursor used in solution and gel synthesis. Reactions that DTA/TGA and DMSA data supported include the decomposition of the lead acetate tri-hydrate precursor [Pb(OOCCH₃)₂·3H₂O] to lead carbonate and acetone, followed by the decomposition of lead carbonate to lead oxide and carbon dioxide. After dehydration at lower temperatures, these reactions may be written:



and



The endothermic nature of these reactions as observed in TGA/DTA were computed to be 47.7 and 88.6 kJ/mol, respectively, for reaction (15.1) and (15.2) [22]. The authors proceed to relate their studies of such reactions and structural evolution to synthesis conditions and identify conditions that are optimized for the preparation of films with desirable microstructural properties [22].

Other investigators have coupled FTIR with TGA to study reactions during pyrolysis. One such study is that of Nouwen et al. [23]. These authors, who utilized a modified 2-methoxyethanol-based process (substituting 2-butoxyethanol as the solvent and reactant) to prepare lead zirconate titanate gels, studied the evolution of gaseous species as a function of pyrolysis temperature. The results of their study, which together with spectral (see Fig. 7.3) analysis allowed for conclusions regarding changes in evolved species during gel decomposition. Key spectral ranges discussed by these authors include the 2,300–2,400/cm and 670/cm ranges (associated with CO₂); 1,750, 1,260, and 1,130/cm (C=O, C–C–O, and C–O–C stretching vibrations, respectively, associated with the presence of a gaseous ester product); and 1,060/cm associated with primary alcohols. The time evolution of different vibrational bands can thus be used to study reactions during pyrolysis. The authors suggest various reactions that may lead to the formation of the volatile alcohol, ester, ether and water byproducts that are formed in various temperature regimes, providing insight into the chemical reactions occurring during pyrolysis.

15.2.4 Atmosphere Effects

Global and local atmosphere (oxidizing, inert or reducing) effects can impact decomposition behavior and pathway, intermediate and/or transitory phase formation, and depending on the substrate, interfacial phase formation. Through their role on the thermodynamics associated with crystallization, the formation of transitory phases can also impact final thin film microstructure. Below, we briefly illustrate and discuss representative effects of atmosphere on pyrolysis behavior.

15.2.4.1 Global

Figure 15.4 shows representative results (TGA/DTA analyses) for the effects of inert (He atm., Fig. 15.4a) vs. oxidizing (O₂ atm., Fig. 15.4b) atmosphere on the pyrolysis behavior of base-catalyzed 2-MOE derived PZT gels [22]. The thermal behavior (DTA) for organic removal under inert conditions (thermolysis) is characterized by a well-defined strong endotherm at approximately 70 °C, a less intense but broader endotherm between 220 and 320 °C and a sharp exothermic peak at 328 °C. Studies of various precursor systems suggest that the exothermic peak at 328 °C is associated with the formation of elemental lead. The reactions associated with the endothermic peaks have been discussed above.

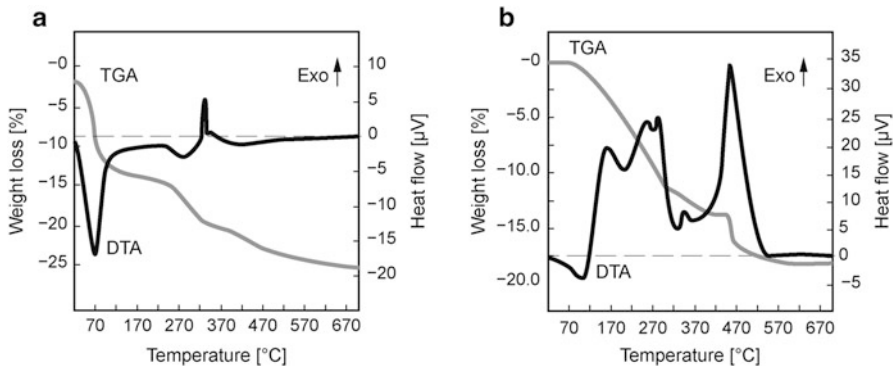


Fig. 15.4 Thermal gravimetric analysis (TGA) and differential thermal analysis (DTA) diagrams for base-catalyzed sol-gel derived PZT bulk material under (a) helium and (b) oxygen atmosphere. Figure modified after [22]

With regard to weight loss characteristics, three well-defined thermal events are evident in the TGA diagram with a gradual weight loss continuing throughout the remainder of the temperature range studied (to 670 °C). Weight loss was approximately 25 % although residual organic level within material heat treated to this temperature was not reported.

In contrast, under O₂ (Fig. 15.4b), both weight loss and reaction characteristics (endo/exothermic) demonstrate different behavior [22]; pyrolysis (organic removal under an oxidizing atmosphere) is thus different than thermolysis. The lowest temperature endothermic event is less well defined than under He and reaction characteristics are generally exothermic in nature, as organic constituents are removed through various reactions involving oxygen. Pronounced exothermic peaks at 170, 250, 280, and 345 °C are observed, as well as a dominant exotherm at 470 °C. The exothermic peak at 470 °C is also attributed to organic removal, which corresponds to the approximate 3 % weight loss observed in the TGA curve. The small peak at 635 °C is attributed to crystallization into the perovskite structure. Though not discussed here, these authors also report on the effects of acid vs. base catalysis on the pyrolysis and thermolysis behavior of their sol-gel derived PZT materials [22].

Though only one study has been highlighted to show the effects of heat treatment atmosphere, the general observations reported with regard to the nature of the thermal and weight loss behavior are representative of those noted by other investigators [24, 25].

15.2.4.2 Local/In-Situ Atmosphere Effects

Pyrolysis and crystallization of thin films is most often carried out by heating the film under either an air or oxygen atmosphere. Despite the use of such oxidizing conditions, local reducing conditions, which may lead to the formation of elemental

metals, may exist for some solution chemistries. Whether such local reducing conditions exist depends on the nature of the organic species, organic volume or amount, and nature of the decomposition reactions. Material composition, for example the zirconium to titanium ratio in PZT can also impact the nature of the local atmosphere since different chemical compounds, with different decomposition characteristics are used as sources for zirconium and titanium. In addition, varying the Zr/Ti ratio can also affect the nature of the chemical species in solution, and subsequently, the physical (pore size, pore volume, and surface area) and structural (metal-oxygen-metal; M-O-M network) characteristics of the film.

A review of the literature reveals several examples of locally reducing atmosphere for materials being processed under global oxidizing conditions [9, 26, 27]. Polli and Lange [9] note that PZT materials prepared from sol-gel, hybrid and MOD routes all produce elemental lead when heat treatment is carried out in air at 300 and 400 °C. In contrast, when an oxygen atmosphere is used during pyrolysis at these temperatures, the alkoxide-derived materials demonstrated no elemental lead formation, while the hybrid and MOD routes still exhibited the formation of Pb as evidenced by XRD. The differences in pyrolysis behavior were attributed to organic content and locally low oxygen partial pressure (pO_2).

Organic content and locally reducing atmosphere have also been reported to contribute to the formation of intermediate phases between PZT films and Pt electrodes, which can also contribute to thin film orientation [26–28]. For example, Chen and Chen [26] note the formation of $Pt_{5-7}Pb$ at the interface of PZT films and [111] oriented Pt and attribute the formation of this phase to a moderately reducing atmosphere associated with the depletion of oxygen within the film during the initial stages of pyrolysis, when atmospheric oxygen has not had the opportunity to diffuse from the film surface to the substrate interface. Other investigators have reported similar effects [27, 28].

Atmosphere effects (global and local) during pyrolysis and crystallization have been studied in detail for processing ferroelectric films on base metal and copper substrates [29–31]. These authors have studied the effects of solution chemistry, heat treatment atmosphere, and film thickness on dielectric and ferroelectric properties of the resulting films.¹ Choice of global atmospheric conditions is important to prepare high quality films (in this case, proper oxygen stoichiometry that reduces leakage current and enhances dielectric and ferroelectric properties) without substrate oxidation, which would degrade substrate electrical conductivity. In addition to degraded conductivity, the formation of a Cu_2O interfacial layer would degrade film electrical properties. These authors report on the effects of air, N_2 , H_2/N_2 ($pO_2 \sim 10^{-17}$ atm) and N_2/H_2O atmosphere on film properties [30, 31].

¹ While copper oxidation is more prevalent at the higher temperatures associated with crystallization (due to the more rapid oxidation kinetics), we discuss such atmosphere effects here since copper oxidation has been noted to begin at temperatures as low as 250 °C [28] or in the temperature range used for pyrolysis.

Narayanan et al. [32] used a kinetic-based approach to fabricate high quality PLZT films on copper without the formation of Cu_2O in nitrogen atmosphere. While the $p\text{O}_2$ level of 10^{-7} – 10^{-8} atm. in the furnace during crystallization was thermodynamically conducive to the formation of Cu_2O , a single layer (115 nm) of PLZT was sufficient to avoid its formation. This finding suggests the existence of a much lower $p\text{O}_2$ level locally at the film/substrate interface, similar to that reported by Yang et al. for the Ni–BaTiO₃ (BT) system [33], although it is also plausible that a single layer may physically act as a barrier layer, limiting the diffusion of oxygen to the interface.

In addition to global atmosphere effects, it was noted above that film organic content can also impact local oxidizing or reducing conditions. Local hydroxyl content may have a similar impact. Therefore, either of the following equilibrium reactions, where all species are gaseous and which define $p\text{O}_2$, may also dictate whether the conditions are oxidizing or reducing:



and



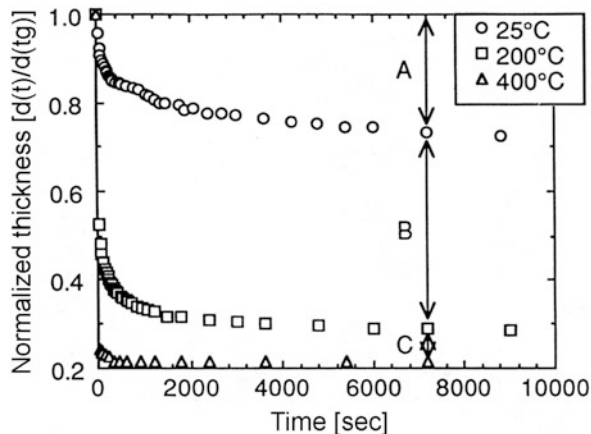
A thermodynamic strategy for successful processing of films on substrates such as copper is to work in a $p\text{O}_2$ window that can oxidize the ferroelectric phase (PZT or BST) while preserving the nature of the metal [30, 34]. Such an approach for the processing of BST films is illustrated in [31] and described in more detail in Chap. 23.²

Briefly, the approach is based upon classical Ellingham diagrams [35] to establish a “processing window” in which it is theoretically possible to obtain an oxidized ferroelectric film while retaining the metallic character of the substrate. A common assumption that is used in the establishment of the processing window is that the $p\text{O}_2$ under which the least reducible metal species in the film (e.g., Ti) is oxidized defines the lower $p\text{O}_2$ boundary of the processing window. Precursor selection (and associated organic content and decomposition behavior) may also be used to widen the effective processing window for film fabrication on metallic substrates [29].

A final atmosphere effect that has been reported is the use of a wet vs. dry O_2 for film crystallization. It has been found that film orientation may be influenced though control of this aspect of the heat treatment atmosphere [36].

² Although [31] deals with the preparation of films by sputtering, the basic arguments regarding atmosphere effects are still pertinent.

Fig. 15.5 Effects of heat treatment temperature and time on the consolidation behavior of solution derived ZrO_2 thin films. A, B and C denote relative shrinkages associated with heat treatment at 25, 200, and 400 °C. After [37]



15.3 Densification Processes

As shown in Fig. 15.1, the four main processes that contribute to densification are:

1. *Capillary contraction*, as the solvent and any reaction byproducts are removed from the pore spaces within the film, creating pressures that drive the collapse of the amorphous network;
2. *Continued condensation reactions*, as residual alkoxy (OR) and hydroxyl (OH) groups are removed from the M-O-M backbone;
3. *Skeletal densification and structural relaxation* as the structure approaches the state that would be characteristic of the metastable liquid (with concomitant decrease in the free energy of the material); and
4. *Viscous flow*, as further structural rearrangements occur at higher temperature.

For crystalline ferroelectric materials prepared by chemical solution deposition (CSD), viscous flow is less important than in materials such as chemically-derived SiO_2 . However, even without significant viscous flow, the first three processes can result in significant densification of the as-deposited film during processing.

As an example of the contributions of these processes to film consolidation/densification, Fig. 15.5 illustrates the behavior of solution-deposited ZrO_2 [37]. This material was studied as a model system for PZT and representative results are shown for ZrO_2 prepared from zirconium n-propoxide and acetic acid in n-propanol. Films were deposited onto Si by spin casting (3,000 rpm) from a 0.25 M solution. Gelation, as evidenced by stabilization of interference color during spin casting occurred in approximately 5–6 s, though casting time was fixed at 30 s. Thickness and refractive index of the deposited film were measured by ellipsometry, and for the results presented, a hot plate set at the specified temperature was used for heat treatment. Initial film thickness was 250–300 nm and normalized thickness as a function of time is reported, with $d(t_g)$ defined as the thickness of the film at gelation.

For this example, it would be expected that each of the first three processes above would be active and would contribute to film densification. As noted in [1, 38] and elsewhere, the specific processes that contribute to densification are highly dependent on precursor nature and heating rate utilized during processing. At 25 °C, the dominant processes are expected to be capillary contraction, associated with volatilization of the solvent at room temperature, and continued condensation reactions, which based on the solution chemistry, would evolve n-propanol, ester compounds, and water. Over the 2.5 h study, film shrinkage is approximately 30 %. At 200 °C, condensation reactions are further promoted and structural relaxation occurs. Consolidation is seen to be both more rapid and more extensive, with shrinkage in excess of 70 % being noted. Finally, at 400 °C, capillary contraction becomes nearly instantaneous, as do the continued condensation reactions. Structural rearrangement associated with a reduction in the free volume of the amorphous phases (e.g., increasing skeletal density) and likely porosity elimination contribute to the observed response. Consolidation is completed within approximately 8 min, with shrinkage approaching 80 %.

In the remainder of this section, we discuss driving forces for densification and structural evolution during heat-treatment up to the crystallization temperature.

15.3.1 Capillary Contraction

15.3.1.1 Driving Forces

Removal of the organic constituents during pyrolysis is necessary for subsequent crystallization. However, solvent removal also leads to a significant rearrangement of the solid phase due to forces that are generated through vaporization. In the as-deposited state, for films prepared by the processes described herein, solution derived thin films may be described as porous viscoelastic solids containing solvents entrapped within the pore structure of the viscoelastic solid [1, 2, 38]. During thermolysis or pyrolysis, as the solvent is removed from the pore structure as a gas, a gas-liquid interface develops within the pore [38]. The pressure across this interface depends on the nature of the liquid, pore size, and factors such as the specific energies (J/m^2) of the solid-liquid (γ_{sl}), solid-vapor (γ_{sv}) and liquid-vapor (γ_{lv}) interfaces. The solid-liquid-vapor system is defined by a contact angle, θ , which describes the wetting or non-wetting character of the liquid according to:

$$\gamma_{sv} = \gamma_{sl} + \gamma_{lv} \cos \theta \quad (15.5)$$

Extending this analysis to behavior of a liquid in a capillary tube, and by analogy to a pore within the film during drying, the following equation describes the capillary pressure, P_c :

$$P_c = -\frac{2\gamma_{lv} \cos \Theta}{a} \quad (15.6)$$

where a is the radius of the capillary tube and the negative sign indicates that the liquid is in tension [38]. This equation can be further extended to porous bodies through consideration of the surface-to-volume ratio of the empty pores [38]:

$$P_c = -\frac{\gamma_{lv} \cos(\Theta) S_p}{V_p} \quad (15.7)$$

where S_p/V_p is the surface-to-volume ratio of the empty pores. Assuming a uniform pore size distribution and defining the interfacial area per gram of solid phase, S , and the relative density of the body, ρ , we may express S_p/V_p as [38, 39]:

$$\frac{S_p}{V_p} = \frac{S\rho_S\rho}{1-\rho} \quad (15.8)$$

where relative density, ρ , is defined in terms of the bulk density, ρ_B , of the solid network (no liquid) and the skeletal density (the M-O-M backbone), ρ_S , as:

$$\rho = \frac{\rho_B}{\rho_S} \quad (15.9)$$

Drying stresses due to capillary contraction and network consolidation have been reported to be well in excess of 100 MPa [40]. Such stress levels may lead to cracking during drying if deposition and pyrolysis conditions are not properly controlled.

15.3.1.2 Relationship to Processing Conditions and Film Properties

Given the above background on the material properties that influence capillary contraction, films with smaller pores will experience greater capillary pressures for analogous solid-liquid systems. Thus, such films are prone to greater consolidation due to capillary pressure effects. For glass preparation, the role of porosity on the gel to glass transformation and sintering kinetics has been reported by Zarzycki [41]. One of the more thorough investigations on solution chemistry effects on material physical characteristics is that of Schwartz, who studied the effects of acid vs. base catalysis and hydrolysis ratio on surface area, pore diameter and pore volume for sol-gel derived PbTiO_3 powders (desiccated gels heated to 140 °C for 72 h) [3]. Results for basic catalysis conditions are shown in Table 15.1. Over the range of hydrolysis conditions studied, surface area is observed to vary by approximately a factor of 6, pore volume by approximately a factor of 10 and pore diameter by approximately 15 %. The magnitude of such variations on capillary pressure could be calculated considering Eqs. (15.7) and (15.8), if skeletal and relative densities are known. However, it should be remembered that the properties reported

Table 15.1 Effect of R_w on the physical characteristics of acid-catalyzed desiccated PbTiO_3 gels. After [3]

	R_w (mols H_2O /mol alkoxide)				
	2.0	2.5	3.0	3.5	4.0
Surface area (m^2/g)					
BET	20.5	89.1	118.6	133.4	135.7
Langmuir	28.3	123.9	165.7	187.5	192.6
Single point	19.5	84.4	111.4	124.5	127.1
Pore volume (cm^3/g)					
Single point	0.0117	0.0491	0.0716	0.0860	0.0915
BJH cumulative	0.0082	0.0361	0.0617	0.0804	0.0890
Pore size (nm)					
Average diameter (BET)	2.29	2.21	2.41	2.58	2.68

in Table 15.1 are for dried gels, for which pyrolysis was incomplete. In addition, gel properties during, rather than after drying, will dictate the capillary pressures that are developed. Nonetheless, such post-mortem characteristics are likely still evidence of differences earlier in the process. And, as discussed below, because such physical characteristics also impact the free energy state of the material, crystallization behavior may also be impacted, presuming such differences still exist at the temperature at which crystallization onset occurs [42].

15.3.2 Structural Evolution During Pyrolysis

The processes that lead to skeletal densification have their origin in the continued condensation reactions that occur with heat treatment and the associated reduction in free volume of the amorphous phase that lowers the free energy of the material [3, 38, 43]. Following gelation, under commonly employed synthesis conditions, the formation of the oxide network in the gel is incomplete and the M-O-M backbone (skeleton) contains residual OR and OH groups. With heat treatment for pyrolysis of organic species, further condensation reactions occur along the M-O-M network, resulting in the formation of either ROH or H_2O with the simultaneous creation of additional M-O-M linkages. As these additional linkages are formed, skeletal density increases. The elimination of OR and OH groups from the M-O-M backbone also contributes to the consolidation behavior (shrinkage) of the film as shown in Fig. 15.5.

Assuming materials such as PZT and BST could be made by traditional glass processing routes, with continued heat treatment up to the crystallization temperature, the skeletal density *might* approach that of the corresponding melt-prepared glass [43]. However, since these materials are non-traditional glass formers, crystallization most likely occurs before full skeletal densification has been attained, or before viscous flow processes can contribute further to densification. In any case, the properties of the film at this stage of the process, including residual OH content, surface area and skeletal density can impact crystallization behavior [2, 3, 42, 43].

As shown in Fig. 15.1, at higher processing temperatures, crystallization and structural relaxation processes overlap. There is thus a kinetic competition between the processes that contribute to densification and those that contribute to crystallization [44, 45]. The retention of organic groups may inhibit both film densification and crystallization, though there are few reports of the carbon impurity level required to effectively inhibit crystallization. The paper by Nouwen [23] reports that crystallization for gels pyrolyzed under inert gas is limited by residual carbon impurity, but the associated carbon level is not described. The paper by Keddie and Giannelis [44] illustrates the effect of heating rate on densification and crystallization. These researchers utilized TiO_2 prepared by a sol-gel process as a model system to look at the impact of heating rate (0.2 to 8,000 °C/min) on film density. As indicators of film density, the authors used ellipsometry to measure thickness and refractive index and studied Ti atom density (atoms/m^3) using Forward Recoil Spectroscopy (FRES) and Rutherford Backscattering (RBS). The thinnest films (e.g., those demonstrating the greatest shrinkage) with the highest refractive indices were obtained at the highest heating rates. Results obtained from FRES measurements were in agreement with these results. At 0.2 °C/min, a Ti atomic density of 1.67×10^{28} Ti atoms/ m^3 was obtained, while at 8,000 °C/min, a Ti atomic density of 2.30×10^{28} atoms/ m^3 was obtained. The results obtained were attributed to the retarded onset of nucleation of the crystalline phase, until further structural densification had occurred.

Similar observations have been made by a number of other investigators [37, 45]. In a study of ZrO_2 thin films, Schwartz and colleagues observed that high organic content precursors could be heated at rates of 300 °C/min to achieve a refractive index of 2.07 while low organic content precursors heated at a rate of 5 °C/min demonstrated a refractive index of only 1.83 [37]. These values represent approximately 96 and 81 % of theoretical density, respectively. Merklein and coworkers [24] reported that higher heating rates (placing the film directly on the hot plate at 300 °C followed by heat treatment at 500 °C with an ~ 70 °C/min ramp rate) resulted in crack-free PZT films with a higher fraction of the perovskite phase. They attributed this result to the rapid removal of solvent prior followed by rapid film densification.

The various processes that contribute to film densification are governed by their individual kinetic rates. Thus, ramp rate and associated changes in the extent of overlap of each densification process can impact the nature of the material prior to crystallization. However, it is expected that each of the densification processes will increase crosslink density of the M-O-M backbone, and thus contribute to the development of a material that is more like the traditionally prepared glass. Higher ramp rates tend to delay structural changes to higher temperature, resulting in a greater retention of the original gel characteristics and generating noticeable effects with regard to thin film microstructure. Isothermal heat treatment at elevated temperatures and/or the use of rapid thermal annealing (RTA) methods also afford unique opportunities with regard to thin film processing, since the temperature regime over which organic removal, densification and crystallization processes occur is further compressed [20, 21, 46].

15.4 Crystallization and Phase Evolution: Thermodynamic Perspectives

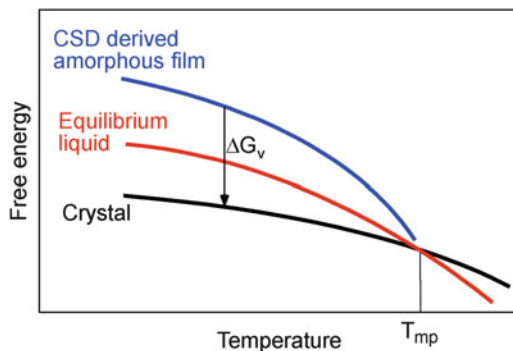
After pyrolysis, the film is typically amorphous, but upon further high temperature heat treatment, transforms to the crystalline state by a nucleation and growth process. However, simply noting that the film is “amorphous” in nature at this processing point is an inadequate description of the nature of the film. Film properties, such as pore size, pore volume, surface area, residual hydroxyl content, residual carbon content, and skeletal density may vary based on both solution chemistry and processing history. Not only thermal history, but even film fabrication conditions such as spin casting speed are known to induce structural and physical differences in the characteristics of the amorphous film [37].

To understand the crystallization process and phase evolution behavior of CSD based films, thermodynamic and kinetic approaches are often coupled with experimental data for in-depth analysis. These fundamental approaches, together with an understanding of intermediate phases and the properties of the amorphous film have led to significant insights into observed variations in crystallization behavior and thin film microstructure. In this section, we review some of the principles used to understand these mechanisms and we discuss how amorphous film properties can impact crystallization.

15.4.1 Free Energy Maps

Two types of free energy maps have been used to understand the crystallization behavior of CSD thin films: free energy vs. temperature and free energy vs. composition. A schematic free energy vs. temperature plot is shown in Fig. 15.6 [1, 47, 48]. There are several aspects of this figure that are pertinent to understanding thin film crystallization behavior. We can see that the free energy of the CSD amorphous thin film is greater than that of either the characteristic equilibrium liquid or the crystalline state. The difference in the free energy between the amorphous film and the crystallized thin film is ΔG_v (volumetric free energy; J/m^3). Chemical, physical and structural factors can each contribute to the free energy of the film. The principal chemical factor is residual hydroxyl content [38, 43]. The principal physical factors are porosity and the associated surface area of the pores (e.g., a surface energy contribution). And the principal structural factor is the lower skeletal density of the M-O-M network compared to the traditional glass (equilibrium liquid). Because of the impact of ΔG_v on nucleation behavior, significant variations in thin film microstructure can be observed for different solution chemistries. This occurs because different solution chemistries cause differences in the chemical, physical and structural characteristics of the amorphous film. We must also, though, not forget the importance of heat treatment schedule. This can impact the persistence of such property variations up to the crystallization

Fig. 15.6 Schematic of free energy vs. temperature for crystalline, equilibrium liquid and chemically-derived amorphous materials. Also indicated is the thermodynamic driving force for the transformation, ΔG_v . After [43, 48]

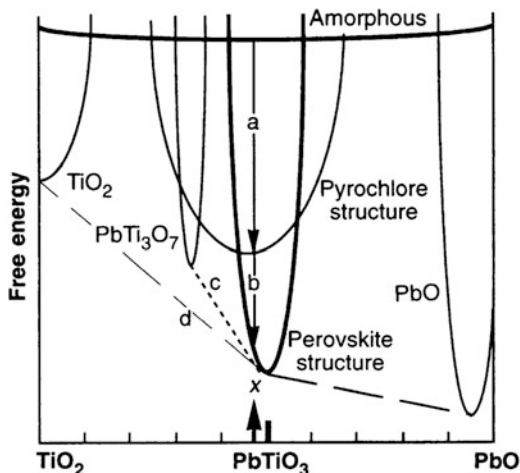


temperature, as discussed by Cooper [42]. Below, the possible magnitude of such variations is discussed and the potential impact on nucleation behavior, and thus, thin film microstructure is demonstrated.

The other type of free energy map that is utilized to understand crystallization behavior is the free energy vs. composition map. A representative map for PT, shown as the TiO_2 - PbO binary phase system, is presented in Fig. 15.7 [49]. This diagram displays the free energies of three stable equilibrium phases (TiO_2 , PbTiO_3 and PbO) and three metastable phases (the amorphous oxide following pyrolysis, the pyrochlore structure, and PbTi_3O_7). As expected, the compositional window over which the perovskite structure exists is narrower than that of the pyrochlore phase. This schematic representation is in agreement with experimental observation that perovskite compounds are known to have a smaller range of tolerance with regard to non-stoichiometry compared to pyrochlore compounds, which are known to exist over a greater range of compositions. The authors discuss crystallization behavior that may be observed based on the concept of kinetically limited (or diffusion limited) crystallization [49, 50]. Under such conditions, the equilibrium phases are not always attained due to the limited diffusion that may occur at the lower heat treatment temperatures associated with the processing and crystallization of CSD thin films. A brief example of the impact of such conditions on phase evolution for composition “x” shown in Fig. 15.7 follows [49, 50].

Composition “x” is slightly non-stoichiometric (TiO_2 -rich) compared to the 1:1 $\text{PbO}:\text{TiO}_2$ stoichiometry of PbTiO_3 , lead titanate. Following film preparation and pyrolysis, the free energy state of the system is defined by the intersection of the amorphous free energy curve and the tail of the arrow (a) associated with the first transformation. The free energy difference between the amorphous state and the (slightly non-stoichiometric) crystalline perovskite state is given by the sum of the arrows a and b and is ΔG_v . Upon further heat treatment following pyrolysis at temperatures between 400 and 800 °C, the initial crystalline phase to form, as shown by this figure, is pyrochlore. As noted, the structure of this compound is more compositionally tolerant, and its formation reduces the overall free energy of the system. The formation of this phase is typically metastable, and with continued heat treatment, either for longer time or at higher temperature, the transformation continues along path b resulting in the formation of the lower free energy, slightly

Fig. 15.7 Free energy versus composition schematic for the PbO-TiO₂ material system for temperatures between 400 and 800 °C. Stable and metastable phases associated with chemically derived materials shown. After [49]



non-stoichiometric perovskite structure [49]. The schematic illustration of this transformation behavior is in good agreement with experimental observation, both with regard to the formation of the metastable pyrochlore (or fluorite) phase and its subsequent disappearance and concomitant formation of perovskite [51–59].

Typically, at the temperatures utilized for CSD thin films, this would be the final state of the material. However, as the authors note, at this point, the material is not under equilibrium conditions; further reductions in free energy are possible, if higher processing temperatures are utilized. For example, for composition “x” if the kinetic constraints on crystallization (diffusion) are removed by using higher temperatures, another step toward equilibrium can be achieved by the formation of the stoichiometric perovskite and PbTi₃O₇ (the material would become diphasic and the free energy would be given by the intersection of the compositional line and dashed line c) [49, 50]. If still higher temperatures are used, a further reduction in free energy is achieved by the transformation into TiO₂ and stoichiometric PbTiO₃ phases. Should this final transformation occur, which requires additional diffusion and either longer time or higher temperature (or both) to achieve true equilibrium, the free energy would then be defined by the intersection of the compositional line and dashed line d.

Free energy maps may be used to understand phase evolution during heat treatment. However, cognizance of the impact of processing conditions on kinetics constraints is also required.

15.4.2 Intermediate Phases

The formation of intermediate phases is important from at least two perspectives. First, depending upon lead loss, the fluorite/pyrochlore phase may exist as a residual phase in the film following processing resulting in degraded dielectric

and ferroelectric properties. Second, as shown in Fig. 15.7, a significant reduction in the free energy of the material occurs upon crystallization of the intermediate phase. As will be seen below, this results in a lower driving force for crystallization, which impacts nucleation rate.

For both BST and PZT material systems, intermediate phases typically form during the transformation process. For PZT, while Pb and PbO phases have been observed as transient phases during processing [9, 26], the most commonly observed phase is a defect fluorite or pyrochlore compound. This intermediate phase, which has been identified by techniques such as XRD and transmission electron microscopy (TEM), typically exist as a nanocrystalline phase that is subsequently consumed in the formation of the desired perovskite phase [51–56]. As shown by Voigt [51] and others, the defect fluorite/pyrochlore phase is nanocrystalline, consisting of grains in the 2–5 nm range. With further heat treatment, this phase typically transforms to perovskite, though if inappropriate processing conditions are utilized, a residual pyrochlore phase may remain after heat treatment. Careful balance of excess lead precursor concentration, film thickness, heat treatment conditions and PZT composition are required to achieve phase pure perovskite films.

The factors that contribute to the initial formation of the defect fluorite/pyrochlore phase are reviewed in a thorough article by Bursill and Brooks [19]. In this paper, the authors consider PbO-Pb₃O₄ equilibrium as related to pO₂ during processing, the role of excess PbO incorporated into the precursor solutions to compensate for lead loss during heat treatment, the added complexity of the PZT material system, and the role of the substrate. A focus of the paper, which has been widely used in interpreting the appearance of the transitory pyrochlore phase and its conversion to perovskite, is the impact of the limited tolerance of the perovskite structure to non-stoichiometry and the ability of the pyrochlore structure to tolerate significant non-stoichiometry. It is the combination of these factors that results in pyrochlore being the first crystalline phase to form as a result of the atomic level compositional heterogeneity that is expected in solution derived thin films [19].

Specifically, the authors point to both lead (excess or deficient) and oxygen non-stoichiometry compared to the ABO₃ chemical formula of perovskite as factors leading to pyrochlore formation in the 350–550 °C heat treatment temperature regime. This is in agreement with the proposed model of Lange and coworkers for kinetically limited crystallization leading to pyrochlore formation [49, 50]. Then, as heat treatment temperature is further increased, if thermal and atmospheric processing conditions leading to the appropriate stoichiometry for both lead and oxygen species are developed, the perovskite phase is formed. Interestingly, while the typical focus of pyrochlore formation has been on lead, the authors clearly demonstrate that oxygen stoichiometry is also critical. They do so by showing that even at 700 °C, pyrochlore is the only crystalline phase present when atmospheric conditions leading to non-ABO₃ stoichiometry (oxygen excess) exist. Lastly, these authors also suggest, as we should expect, that little is known about the oxygen content of the amorphous phase. Compared to the ABO₃ stoichiometry, we should expect the amorphous structure to be non-stoichiometric with

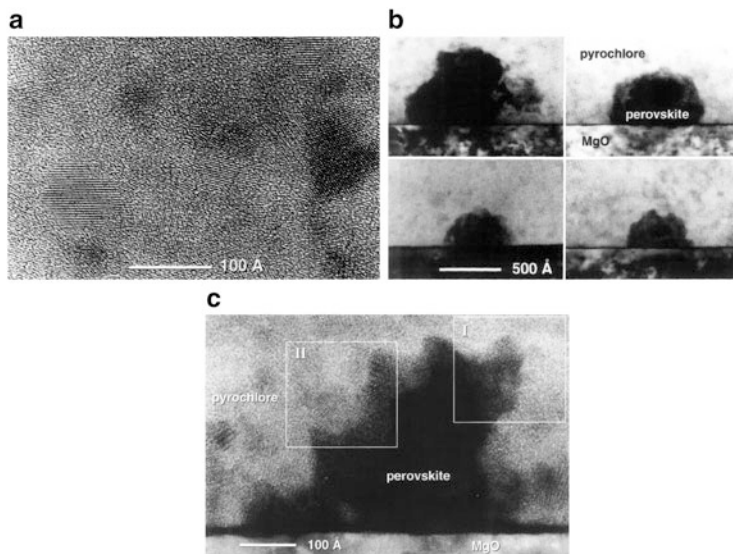


Fig. 15.8 Transmission electron photomicrographs illustrating pyrochlore and perovskite phases in PZT 20/80 thin films: (a) Pyrochlore matrix, (b) pyrochlore and perovskite phase nucleated at MgO substrate surface (525 °C; 15 s heat treatment), and (c) high-resolution image of perovskite/pyrochlore interface illustrating areas of fast (I) and slow (II) perovskite growth. After [51]

respect to oxygen, yet another factor that could contribute to the formation of the intermediate pyrochlore phase.

Transmission electron microscopy (TEM) images of the pyrochlore matrix and perovskite growth into the matrix for PZT 20:80 (20 mol% PbZrO_3 /80 mol% PbTiO_3) thin films prepared by a hybrid process are shown in Fig. 15.8 [51]. These images illustrate a uniform pyrochlore matrix with a grain size of approximately 10 nm (Fig. 15.8a) and the growth of the perovskite phase into the pyrochlore matrix initiating at the surface of the MgO substrate (Fig. 15.8b). The abnormal shape of the interface between the perovskite and pyrochlore phases is due to the fact that growth in different crystallographic directions proceeds at different rates. Figure 15.8c shows the perovskite nucleus later in the transformation process. The growth of the perovskite nuclei may proceed as a growth front through the film from the surface of the substrate to the film surface [57]. Under certain processing (solution chemistry and film thickness) and heat treatment conditions, nucleation of the perovskite phase may also occur at the film surface, or within the bulk of the film for thicker layers [8, 58, 59].

For BT, SrTiO_3 (ST) and BST materials, observed intermediate phases include barium carbonate (BaCO_3), barium peroxy monocarbonate (BaCO_4), barium titanium oxycarbonate ($\text{Ba}_2\text{Ti}_2\text{O}_5\text{CO}_3$) or strontium titanium oxycarbonate ($\text{Sr}_2\text{Ti}_2\text{O}_5\text{CO}_3$). The carbonate and oxycarbonate phases are the most commonly observed [13, 17, 60–64], and thorough investigations of the transformation pathway, as well as the influence of the precursor compounds have been carried out.

Hasenkox and coworkers [61] have carried out a detailed study of such effects in BT and ST thin film preparation using acetate, propionate, 2-methylpropionate, and 2-ethylhexanoate precursors for Ba and Sr. As a titanium source, titanium tetra-n-butoxide was added to a carboxylic acid solution of the respective carboxylate or was first stabilized using acetylacetone. Various solvents were then added to prepare solutions of 0.3 M. These researchers noted the following general effects:

- The titanium precursor decomposed first leaving an amorphous titanium oxide network and distributed alkaline earth carbonate;
- Decomposition of the metal carboxylates was dependent on precursor with the 2-ethylhexanoate decomposing at approximately 400 °C (Ba) and 370 °C (Sr) and the acetate and propionate decomposing at 500 °C (Ba) and 470 °C (Sr);
- The formation of the oxycarbonate phase in the BT system delayed perovskite crystallization to higher temperature, which contributed to greater densification and a larger grain size; and
- The growth of the intermediate phase, and its transitory nature, are influenced by the distribution and structure of the pyrolysis products and the carboxylate decomposition mechanism.

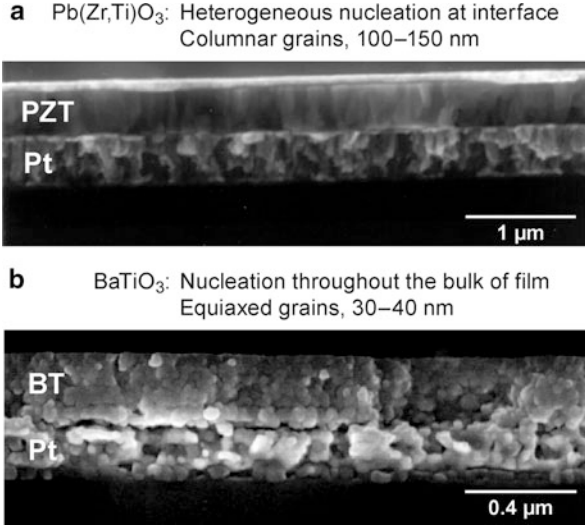
While not discussed by these researchers, local pO_2 effects resulting from the nature of the organic phase that is being removed may also play a role in the observed effects [63].

The nature and distribution of the intermediate phases in BT, ST and BST film processing result in homogenous nucleation of the perovskite phase through the film compared to the columnar microstructure of PT and PZT materials. In PZT materials, the relatively lower thermodynamic stability of $PbCO_3$ compared to $BaCO_3$ and $SrCO_3$, together with its disappearance and the formation of the fluorite/pyrochlore phase make heterogeneous nucleation at the interface with the substrate more important than in BT, ST and BST. These factors contribute to the generally different microstructures shown in Fig. 15.9: (a) columnar for PZT materials and (b) equiaxed grains for BST. It is worth noting, however, that by understanding the role of such phases, it has been possible to develop novel processing strategies to fabricate columnar BT, ST, and BST films [65–67].

15.4.3 Nucleation and Growth

Although the processing methodologies employed in CSD are different from traditional mixed oxide ceramic and glass processing, classical principles used to describe nucleation and growth mechanisms are still useful in describing crystallization behavior. The reduction or minimization in the Gibbs free energy, as shown in Fig. 15.6, by forming a new phase is the driving force for both nucleation and growth. Although we have already noted the importance of intermediate phases during crystallization, various authors have demonstrated that using classical approaches to describe nucleation and growth behavior from the amorphous state

Fig. 15.9 Typical microstructures for (a) PZT and (b) BST thin films. After [67, 68]



to the perovskite phase can still provide useful insights into the various factors contributing to microstructural evolution [54, 68–70].

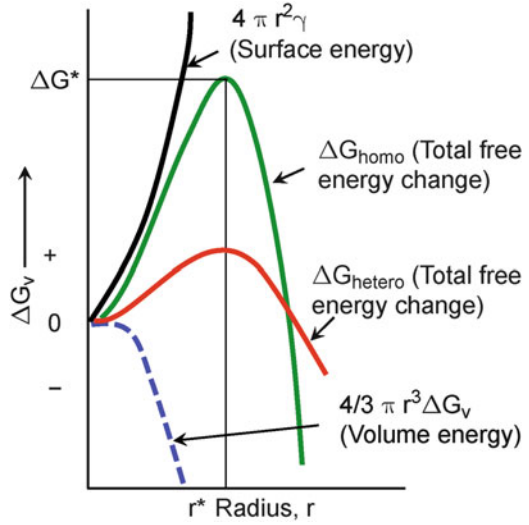
The nucleation process has been widely reported on and the reader is referred to [71] through [74] for a detailed discussion of this topic. The governing equation for homogeneous nucleation of a spherical crystalline nucleus, with radius ‘ r ’, in a uniform amorphous host is given by:

$$\Delta G = -\frac{4}{3}\pi r^3 \Delta G_v + 4\pi r^2 \gamma \quad (15.10)$$

where the first and second terms are known as ‘volume’ and ‘surface’ free energy, respectively. ΔG_v , the Gibbs free energy per unit volume, is the driving force for crystallization, which is the difference in the free energies of the amorphous and crystalline states, and γ is the surface energy per unit area associated with the formation of the nucleus. In describing the free energy change associated with nucleation, it is also possible to include a strain energy term to account for the formation of the crystalline nucleus in the amorphous host. We neglect that contribution in the analysis presented below.

Figure 15.10 shows the change in the volume, surface and total free energy as a function of the radius of the nucleus. It can be seen that there exists a critical radius (r^*) below which the newly formed nucleus is not stable, while for $r > r^*$, the nucleus is stable and continues to grow. The energy barrier, ΔG^* , that the nucleation process must overcome to form a stable nucleus is given by:

Fig. 15.10 Volume and surface energy contributions to the barriers for homogeneous and heterogeneous nucleation



$$\Delta G^* = \frac{16\pi\gamma^3}{3(\Delta G_v)^2} \tag{15.11}$$

Before proceeding with the discussion it is worth noting that Eq. (15.11) indicates that the barrier for the formation of a stable nucleus increases with increasing surface energy and decreases with increasing free energy difference between the amorphous and crystalline states.

For heterogeneous nucleation, Eqs. (15.10) and (15.11) may be multiplied by a contact angle term that is dependent on the surface energies of the interfaces associated with the growth surface (which for CSD films is most often the substrate), crystal and amorphous phases, as in Eq. (15.12):

$$\Delta G_{hetero}^* = \Delta G^* \cdot f(\theta);$$

$$f(\theta) = \frac{2 - 3 \cos \theta + \cos^3 \theta}{4} \tag{15.12}$$

where, θ is the contact or wetting angle measured between crystal and the substrate surface. Energetically, heterogeneous nucleation will always be preferred (see Fig. 15.10) because preferential nucleation sites, such as the substrate surface, impurity phases or grain boundaries require less energy due to a lower effective surface energy. However, it is important to note that while r^* remains unchanged for heterogeneous vs. homogeneous nucleation, the volume of the crystalline nuclei can be significantly less for heterogeneous nucleation due to the wetting angle affecting the shape of the nuclei. (Recall Fig. 15.8 that demonstrates a hemispherical nucleus formed on the substrate surface.)

While the energy barrier is important in understanding the changes in the energy of the system as a function of nuclei radius, for thin film microstructure, we are also interested in the nucleation rate. Higher nucleation densities produce films with finer grain sizes, whereas lower nucleation densities produce larger grain size materials. As would be expected, greater barrier heights decrease nucleation density. The relationship between barrier height, temperature and nucleation density is given by:

$$n^* \propto \exp(-\Delta G^*/RT) \quad (15.13)$$

where n^* is the nucleation density (number of nuclei per cubic meter). At lower temperatures, in traditional glasses, nucleation density is low due to the high viscosity of the amorphous matrix. As temperature increases, RT increases, providing greater energy for the nucleation barrier to be overcome, thus increasing the nucleation density. With further increases in temperature, nucleation density again decreases. Such characteristic behavior is shown by a bell-shaped curve for nucleation. Growth rate displays a similar characteristic and the two curves are displaced with respect to each other with the curve for nucleation rate dominating at lower temperatures and the curve for growth rate being dominant at higher temperatures [74]. Schematic representations, as well as actual experimental results for nucleation and growth curves may be found in [71] through [74]. Calculated nucleation density curves as a function of changes in γ and ΔG_v , as may be expected based on different physical, chemical and structural differences for the amorphous state are discussed in greater detail below.

At constant temperature, the fraction of amorphous material transformed (x) to the crystalline state in a given time (t) can be described using the *Johnson-Mehl-Avrami* model as given below [75, 76]:

$$x = 1 - \exp(-kt^n) \quad (15.14)$$

where n is the reaction order, and k is the reaction rate constant described by the Arrhenius expression:

$$k = k_0 \exp(-E_a/RT) \quad (15.15)$$

where E_a is the activation energy, k_0 is the pre-exponential constant, T is the temperature and R is the gas constant. The reaction order can be correlated to the mode of nucleation with value ranging between 1 and 4. For bulk homogeneous nucleation (1D, 2D, and 3D), n ranges between 2 and 4, whereas for heterogeneous surface nucleation it is unity. Many other empirical kinetic models with different functions have also been reported in the literature [77, 78].

The growth process is governed by related thermodynamic factors to those discussed for nucleation, including the thermodynamic driving force for growth [71, 74]. Depending on the analysis used to describe growth, other factors such as jump distance, jump frequency across the interface between the crystal and

amorphous matrix, and surface energy also play a role. Growth behavior is not considered further here because in the analysis below we only discuss the impact of amorphous material properties on nucleation.

15.4.4 Chemical, Physical, and Structural Effects

As shown in Fig. 15.6, the free energies of the CSD amorphous film and perovskite crystal are dependent on temperature. Therefore, crystallization temperature, as well as the chemical, physical and structural properties of the amorphous state will dictate the thermodynamic driving force (ΔG_v) for crystallization. As mentioned earlier, these properties may be influenced by solution precursor chemistry and heat treatment history. Observed differences in microstructural properties are thus dependent on any residual differences in the structure of the amorphous material. As would be expected, higher heating rates or shorter heat treatment times leading up to crystallization would be expected to preserve greater chemical, physical and structural differences, whereas longer thermal soaks at temperatures below the crystallization temperature tend to reduce such differences. Cooper [42] explores this issue in detail. To fully understand observed variations in crystallization behavior requires a full analysis of amorphous film properties immediately prior to the onset of crystallization. To the knowledge of the authors, such a study has not been carried out for ferroelectric films. However, there are a number of studies that have looked at material properties at temperatures of 25–50 °C below the crystallization temperature [3, 79]. These studies have demonstrated the significant differences that can exist in amorphous gel properties following heat treatment. In this section, examples of the magnitude of these effects are presented, but first, the contributing factors are described.

15.4.4.1 Chemical Factors

Hydroxyl Content

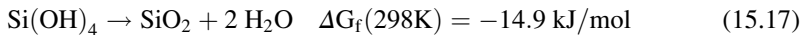
The chemical factor for CSD amorphous films that has been considered most extensively is hydroxyl content [1, 38, 43]. This may be considered from the perspective of the following general reaction that demonstrates the removal of water from the structural backbone of the amorphous material as two hydroxyl species react to form a water molecule and a new M-O-M bond (a dehydration condensation reaction):



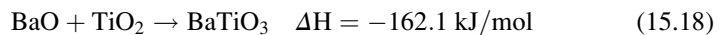
where OR is the alkoxy group. Because the above reaction is typically exothermic, structures with higher levels of hydroxyl species have greater excess free energy, or

greater ΔG_v upon crystallization, all other factors being held constant. These reactions and their associated reaction enthalpies (or free energies) are noted below for specific cases as examples of the magnitude of the contribution to the free energy of the material.

For SiO_2 [38]:



For BaTiO_3 (note the reaction involving the elimination of a water molecule is more exothermic) [17, 80]:



It should be noted that (15.20) is highly temperature dependent, unlike (15.18), which is relatively independent of temperature [17]. For temperatures above approximately $600 \text{ }^\circ\text{C}$, (15.19) is more exothermic in nature than (15.18).

Other investigators have noted that H_2O introduced into either the firing atmosphere [54] or during solution preparation [81] can also impact crystallization temperature and film orientation. Keddie and Giannelis have shown the impact of ramp rate on retained hydroxyls for TiO_2 thin film processing and have reported that slower ramp rates do, in fact, result in lower hydroxyl concentrations, but they do not report on the impact of this chemical characteristic on crystallization behavior [44]. The more extensive removal of hydroxyl species for slower ramp rates though does agree with the expectation that the chemical solution derived material would become more like the traditionally processed material under conditions that are less kinetically limiting.

Organic Content

Another chemical factor that can impact crystallization behavior is organic content. Retained organic content can delay crystallization to higher temperatures, resulting in a reduced thermodynamic driving force (ΔG_v) for crystallization. This, in turn, results in an increased energy barrier for nucleation (ΔG^*), and as reported by Schwartz and coworkers, can impact the relative differences in the energy barriers for heterogeneous versus homogenous nucleation [68]. Comparing the energy barriers to ramp rate can lead to understanding of the nucleation sites that can define thin film microstructure.

This is shown schematically in Fig. 15.11 for (a) lower temperature and (b) higher temperature crystallization conditions and possible substrate and film surface nucleation events. The resulting thin film microstructures are shown in Fig. 15.12.

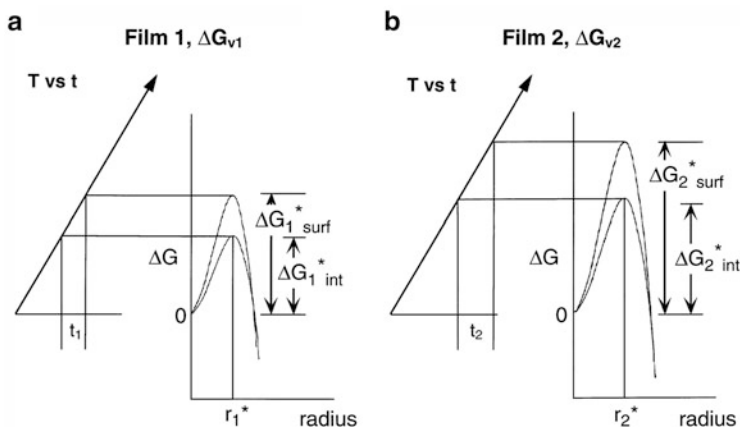


Fig. 15.11 Energy barriers for interface and surface nucleation in thin films with (a) lower and (b) higher pyrolysis and crystallization temperatures. Also shown is a comparison of the energy barriers to ramp rate and suggested time intervals (t_1 and t_2) between the interface and surface nucleation events. After [68]

The film shown in Fig. 15.12a was prepared from a solution that resulted in a lower crystallization temperature [68]. Nucleation at both the substrate interface and film surface is observed. It is believed that nucleation at the substrate occurs first, leading to the growth of columnar grains toward the surface of the film. Subsequent to this nucleation and growth event, nucleation at the film surface also occurs. Nucleation density is lower here than at the substrate surface. Large hemispherical grains, that grow toward the substrate, result from this second nucleation event. Figure 15.11a shows that for the low crystallization temperature films, there is a smaller difference in the energy barriers for the two nucleation events than for films that crystallize at higher temperatures (Fig. 15.11b and 15.12b), which exhibit a greater difference in the energy barriers [68]. Evidently, for the high crystallization temperature film, growth of the grains nucleated at the substrate surface proceeds to completion prior to nucleation at the film surface.

We may speculate that if a thicker film had been prepared from the higher crystallization temperature precursor solution we might again observe grains nucleated at the surface of the film, due to the longer time required for the growth of the grains nucleated at the substrate to transform the film. This “kinetic” aspect, which is also to be expected, is highlighted in Fig. 15.11. Because the onset of crystallization likely occurs during the ramp to the firing temperature, we can see the relationship between nucleation behavior, thermal input, and the differences in the energy barrier heights [68]. Compared to Fig. 15.11a, longer time and higher temperature are required to induce surface crystallization, which did not occur for the film thickness studied. Stated otherwise, grain growth of the columnar grains nucleated at the substrate completely transforms the film into the perovskite structure in a time interval less than t_2 in Fig. 15.11b [68].

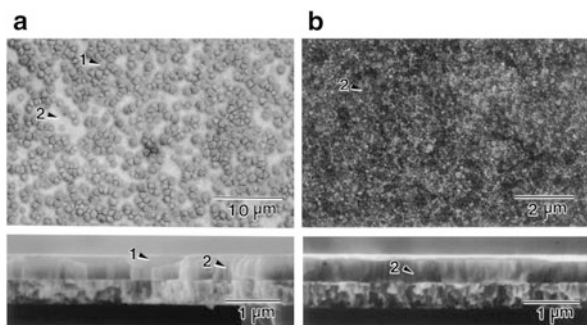


Fig. 15.12 Surface and cross-sectional scanning electron photomicrographs for the thin films associated with Fig. 15.11: (a) lower and (b) higher pyrolysis and crystallization temperatures. Film (a) cross-section demonstrates lower electrode and film (b) demonstrates both lower and surface Pt electrodes. After [68]

15.4.4.2 Physical Factors

The predominant physical factor that may impact crystallization behavior is the surface area of the film. As was discussed in Sect. 15.3.1, in the as-deposited state, the film consists of a viscoelastic solid with entrapped organic species. As these species are removed during pyrolysis, a pore structure develops within the film, potentially creating a high surface area, high pore volume material. Due to surface energy, films with higher surface areas have higher free energies than films with lower surface areas (all other variables being held constant). This concomitantly impacts ΔG_v , ΔG^* , and n^* .

We noted earlier that precursor differences can result in differences in the characteristics of dried gels, which may be retained to higher heat treatment temperatures. One report of the retention of differences in gel physical characteristics with heat treatment to temperatures within 50 °C of crystallization is that of Schwartz et al. [79]. The observed changes in surface area for PT gels between desiccation at 140 °C and heat treatment at 400 °C are illustrated in Fig. 15.13a. As anticipated, surface area is decreased. However, over the range of synthesis conditions utilized, a variation in surface area from approximately 35 to 70 m²/g is still observed. If we assume a value of 1 J/m² for the surface energy of the amorphous PT phase [82, 83], contributions to ΔG_v of 10.6 and 21.2 kJ/mol, respectively would be anticipated.

Of course, the key issue, as noted by Cooper [42] is what property differences persist to the onset of crystallization? To address this question, physical properties of these gels were studied as a function of long heat treatment times (up to 10 h) at 410 °C. This temperature was selected since it is close to the anticipated crystallization temperature of 425 °C. As illustrated in Fig. 15.13b, even after extended heat treatment times at 410 °C, differences in the surface areas of chemically-derived PT remain [79]. Considering the observed range of surface areas from 25 to 40 m²/g, we would expect contributions to ΔG_v of 7.6 to 12.1 kJ/mol, respectively. Other parts of the figure (Fig. 15.3c, d) are discussed in Sect. 15.4.4.3.

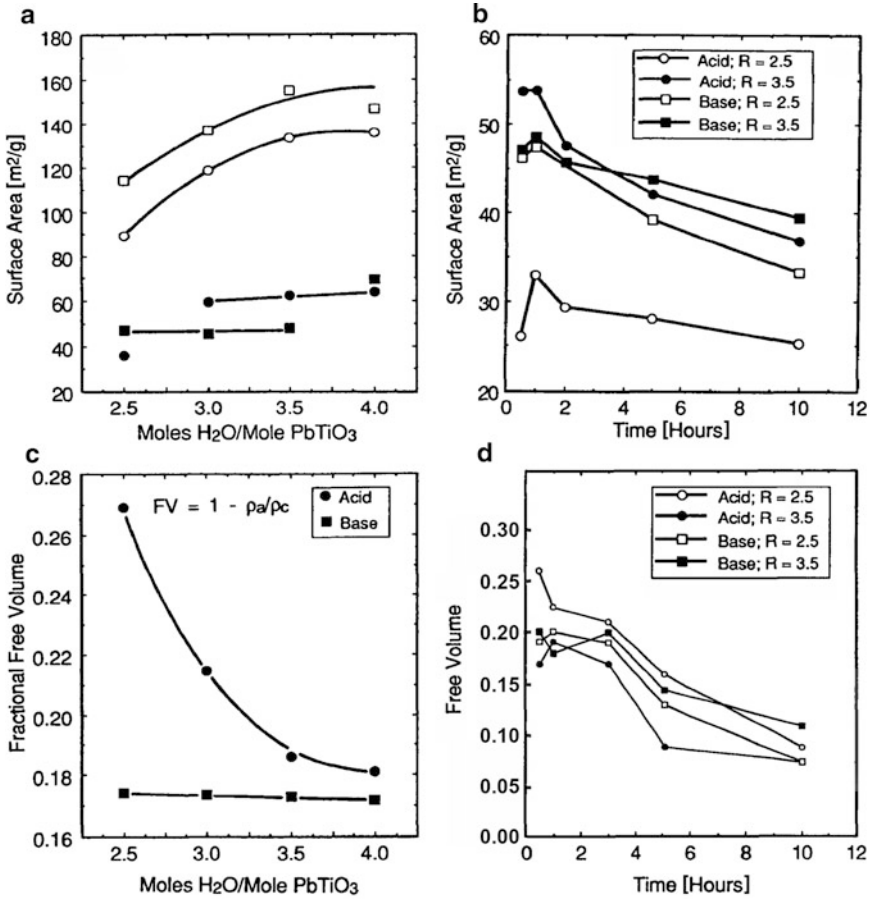


Fig. 15.13 Physical properties of desiccated and heat-treated sol-gel derived lead titanate powders prepared under various catalysis and hydrolysis conditions: (a) surface area of room temperature (*open symbol*) and 400 °C heat treated (*closed symbol*) powders; *circles*—acid catalysis and *squares*—base catalysis; (b) surface area as a function of heat treatment time at 410 °C; (c) free volume following heat treatment at 400 °C; and (d) free volume as a function of heat treatment time at 410 °C. After [79]

Other authors have noted that differences in surface energies between different crystallographic directions can impact thin film orientation following heat treatment. While this does not contribute to a difference in ΔG_v , it does contribute to the change in ΔG associated with nucleation. Norga and Fe have reported such effects for PZT thin film growth on Pt-coated Si substrates and have noted that the (111) orientation is energetically favored compared to the (100) orientation because of a lower barrier height for nucleation [54].

15.4.4.3 Structural Factors

Compositional uniformity and bonding arrangements of the metallic species in amorphous CSD films have been sparingly studied, but there are a few reports of such film properties in the literature [84–87]. Sengupta et al. used extended X-ray absorption fine structure (EXAFS) analysis (cp. Chap. 8) to probe the nature of amorphous PZT films [84]. This investigation suggests that the A-site species (Pb) does not form M-O-M linkages such as Pb-O-Zr and Pb-O-Ti. In contrast, Arçon notes such linkages definitely exist in the precursor solutions for PZT films, which suggests they would also exist in the amorphous structure [85]. Other authors have reported on structural changes during pyrolysis. For example, Lakeman et al. [85] note the development of medium range order and additional heterogeneities during heat treatment. Such local atomic level heterogeneities may be expected to impact crystallization behavior, but here, we take a broader look at structural effects in the context of structural free volume.

Structural free volume is calculated using the densities of the amorphous material and the pure crystalline compound of the parent material according to:

$$FV = 1 - (\rho_a/\rho_c) \quad (15.21)$$

where FV is the free volume, ρ_a the density of the amorphous phase and ρ_c the density of the crystalline compound. Higher free volumes imply greater openness in the structure and greater ease of structural rearrangement toward the metastable liquid [38]. Brinker and colleagues note that structural relaxation occurs by diffusive motions of the network that result in irreversible shrinkage [38, 43]. These authors present shrinkage, thermal data (differential scanning calorimetry; DSC) and changes in surface area to demonstrate that that the irreversible shrinkage associated with structural relaxation is exothermic in nature. For the material studied (SiO_2) the net energy change reported for the temperature range of 400–700 °C was approximately -19.7 J/g [38]. This value includes contributions from the reduction in surface energy, the heat of dehydration and structural relaxation. Based on typical values of surface energy for oxide glasses and ceramics and the known exothermic nature of dehydration [Eq. (15.17)], we estimate the exothermic nature of the structural relaxation process to be -5 J/g for the sol-gel derived materials of the reported studies [38, 43].

Figure 15.13c, d show that differences in structural free volume induced through variations in solution preparation conditions persist after heat treatment in the 400–410 °C temperature regime [79]. As noted for the SiO_2 materials in the above reports, even after thermal treatment at 400 °C, free volume varies widely, from approximately 0.17 to 0.27 (Fig. 15.13c). With extended heat treatment times at 410 °C (Fig. 15.13d), after 10 h, free volume differences range from 0.08 to 0.15.

Assuming such differences still exist within the gel structure at the onset of crystallization, we still need to make a number of further assumptions in order to estimate the contributions of differences in structural free volume to the driving force for crystallization. First, we wish to make a conservative estimate, so in

carrying out this analysis, we first assume that the -5 J/g exothermic energy associated with structural relaxation in SiO_2 is representative of that for PT with the highest observed free volume at 400°C , which is $\text{FV} = 0.27$ (the acid-catalyzed material prepared with an R_W value of 2.5). Materials with lower free volume would, therefore, only be capable of smaller contributions to the free energy state of the amorphous material. Assuming this value varies linearly with free volume, the variation in energetic contributions range from -1.5 to -2.8 J/g, or converting to mols, from approximately -0.5 to -0.9 kJ/mol. We note here that this is a speculative conclusion, but presuming some validity to the assumptions and values utilized, compared to the other possible contributions to crystallization driving force, the contribution from structural factors is the smallest of the three contributions.

We show below that the magnitude of these contributions (hydroxyl content, surface area/energy and structural free volume) are not insignificant compared to the heats of fusion of these materials. Thus, variations in such properties can have an impact on the driving force for crystallization, the observed crystallization behavior and the resulting thin film microstructure.

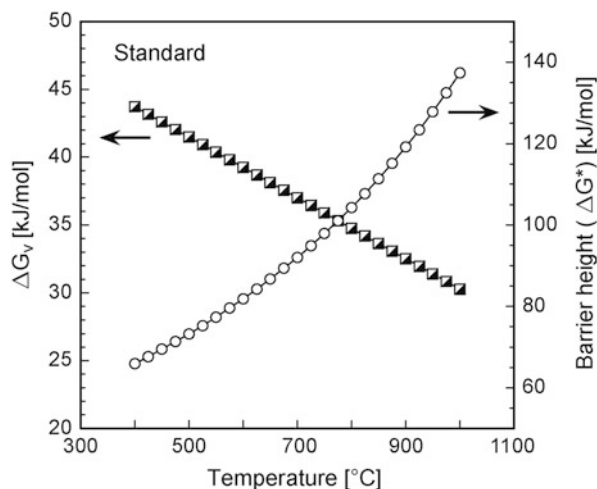
15.4.4.4 Magnitude of Factor Effects on Nucleation and Growth

To illustrate the effect of these individual contributions to thin film nucleation and growth (microstructure), we study the case of ST, a room temperature paraelectric material. Here we neglect the formation of any intermediate phase and simply present an analysis of the magnitude of property variations on crystallization as an illustrative example. For ST, the driving force between 400 and $1,000^\circ\text{C}$ was calculated using the Turnbull equation [88]:

$$\Delta G_v = \Delta H_f [(T_m - T)/T_m] \quad (15.22)$$

where ΔH_f is the heat of fusion, T_m the melting point and T the temperature (below the melting point). The following data were utilized: $T_m = 2,626$ K, $T_g = 673$ K, and $\Delta H_f = 58.7$ kJ/mol and the analyses for ΔG_v and ΔG^* are reported in Fig. 15.14. The barrier height and nucleation density were calculated using Eq. (15.11) and (15.13), respectively. It can be noticed in Fig. 15.6 that the driving force for crystallization decreases as the temperature approaches the melting temperature. This causes the barrier height for nucleation to increase with temperature. Since we know that the driving force for transformation and the transformation pathway depends on the thermal history of the sample and solution chemistry, differences in the free energy state of amorphous CSD films processed under various conditions are expected, as already discussed. Considering the factors noted above and the reported heat of fusion for ST, we see that if simply structural differences exist between materials, ΔG_v may only vary by a few percent. However, if significant differences in surface energies or hydroxyl content exist between different materials, differences in ΔG_v , exceeding 10% may easily result.

Fig. 15.14 ΔG_v and ΔG^* values for strontium titanate calculated from the Turnbull equation



To illustrate the effect of differences in amorphous state free energy on nucleation density, we assume an increase in the free energy of 5, 10 and 15 %. The corresponding changes in calculated nucleation density are shown in Fig. 15.15a where 'standard' represents the relative nucleation density corresponding to the free energy calculated in Fig. 15.14. The nucleation density changes significantly with a 15 % increase in the free energy of the amorphous phase. For example, at 600 °C, the nucleation density increases by approximately a factor of 25.

Likewise, to demonstrate the effect of a decrease in surface energy on nucleation density, a decrease of 5–15 % was assumed in the calculations. Results are represented in Fig. 15.15b. Here, we note that this is not the physical surface area as discussed in detail above, but the surface area between the crystalline nucleus and amorphous matrix, as related to the preferred growth direction of [111] compared to [100] noted by Norga and Fe [54]. Such a surface energy effect can be seen to be even more important than the physical surface energy or hydroxyl effect, changing relative nucleation density from a value of less than 5 to nearly 150 at 600 °C.

15.4.5 Control of Crystallization and Film Orientation (Seeding and Lattice Matching)

Above we discussed preferred growth directions from an energetic perspective. Through their impact on the nature of the heterogeneous nucleation event, seeding and lattice matching can have a significant effect on crystallization behavior and thin film microstructure. Many researchers have observed a change in the crystallization kinetics and temperature of lead-based perovskite materials deposited on different substrates or buffer layers. Tong [89] reported a difference of >50 °C in

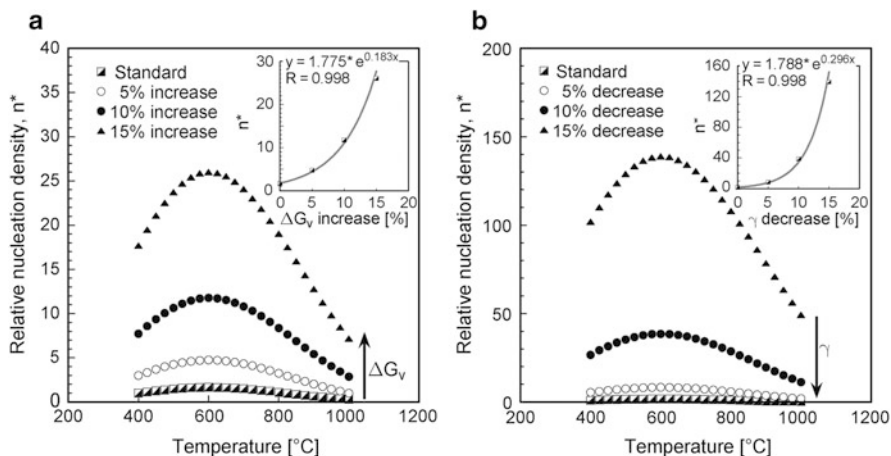
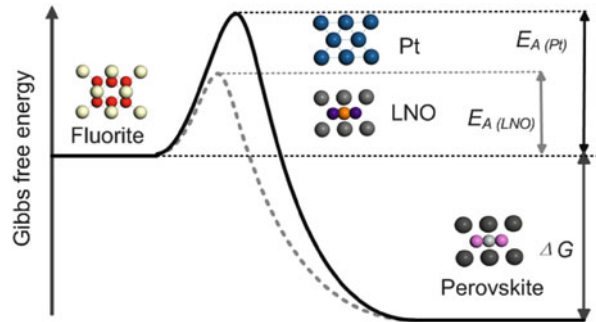


Fig. 15.15 Relative nucleation densities as a function of 5, 10 and 15 % changes in (a) thermodynamic driving force (ΔG_v) and (b) surface energy (γ)

crystallization temperature (T_{cryst}) for PLZT (lanthanum-doped PZT) films deposited on platinum and lanthanum nickel oxide (LNO) bottom electrodes. Similar results were reported by Cheng et al. [90] for PZT on an iron substrate with a PT buffer layer. These investigators found that the pyrochlore phase was absent at T_{cryst} as low as 550 °C, suggesting that the perovskite phase is favored over pyrochlore by nucleation and growth on a buffer layer with perovskite structure. Kwok et al. [91] employed PT as the seed layer for PZT films deposited on sapphire substrates and observed a 100 °C decrease in the conversion temperature for pyrochlore to perovskite ($T_{\text{py-pe}}$). They concluded that this effect was not related to the strain energy of the deposited films. Shareef et al. [92] reported the opposite effect for PZT films deposited on RuO_2 . Through TEM studies, these investigators determined that the density of perovskite nuclei on RuO_2 is significantly smaller than on Pt/Si substrates. They observed the $T_{\text{py-pe}}$ to be 50 °C lower for PZT films deposited on Pt/Si compared to those on RuO_2 . These results can be explained by the similar structure of RuO_2 (rutile) to pyrochlore (fluorite) phase and the transformation pathway of perovskite from the amorphous state, as discussed below.

Figure 15.16 shows schematically the thermodynamics associated with the phase transition for PLZT films on Pt and LNO surface at the same T_{cryst} . The composition and lattice structure in the initial (fluorite) and final (perovskite) states of the film remain the same for transformation on each substrate. Similarly, the interfacial energy between these two states, γ , is a constant. Thus, the nucleation barriers in the two situations are determined solely by $f(\theta)$. Although θ is properly defined as the wetting contact angle of liquid with the surface (Pt or LNO), $f(\theta)$ can be considered to decrease the nucleation energy in a solid state reaction as discussed here; e.g., elimination of the interfacial energy between a new phase and the substrate. Since

Fig. 15.16 Variation in free energy for the fluorite to perovskite transformation on Pt and LaNiO₃ substrates



PLZT and LNO have the same perovskite structure, similar ionic radii and electronegativity, a coherent or semi-coherent interface will form. Compared with an incoherent interface, like that of PLZT on Pt, a coherent or semi-coherent interface will have a lower ΔG^* , and therefore, nucleation will be easier. Since ΔG is a constant for the fluorite-perovskite transition, only the bottom electrode determines ΔG^* for the phase transition, as shown in Fig. 15.16. If the bottom electrode (LNO- ABO_3 perovskite) has a crystal structure (and lattice matching) similar to that of the deposited film, ΔG^* is lowered by providing preferred nucleation sites, which decreases $T_{\text{py-pe}}$. In contrast, as shown by the solid line of Fig. 15.16, if the bottom electrode (Pt-FCC) has a dissimilar crystalline structure to the perovskite phase, nucleation requires a larger ΔG^* , which raises $T_{\text{py-pe}}$, because greater thermal energy is required to exceed the energy barrier for crystallization. As a result, $T_{\text{py-pe}}(\text{Pt}) > T_{\text{py-pe}}(\text{LNO})$ because $\Delta G^*(\text{Pt})$ is greater than $\Delta G^*(\text{LNO})$, due to the mismatch of lattice structures between the substrate/bottom electrode and coated films.

15.5 Kinetic Competition During Heat Treatment

A final aspect of pyrolysis and crystallization worth considering is the concept of the “kinetic competition” between various processes and the role of film thickness. Processes that occur concurrently during film processing are highlighted in Fig. 15.1. Beyond the overlap [and thus the time (t), and temperature (T) competition] between processes such as organic removal and structural collapse, numerous other processes are in competition with one another during higher heat treatment temperatures. While it is simple to note that the thermodynamic and kinetic aspects of these processes will serve to dictate the final thin film microstructure, obviously, significant research into such effects has been ongoing since the early investigations into the solution deposition of ferroelectric films in the mid-1980s. Some of the other competing processes that occur during film processing include densification, nucleation, grain growth, interfacial reactions, formation and consumption of intermediate phases, diffusion of film constituents into the substrate and the loss

of volatile species. There are many examples regarding approaches developed to address problems caused when one process in competition with another results in undesirable film characteristics.

One such example is the case of the undesired surface nucleation event shown in Fig. 15.12 [79]. Here, the researchers resorted to the addition of a higher boiling structural modifier to delay organic removal, reduce ΔG_v , and shift crystallization to a higher temperature, thus suppressing the second nucleation event at the surface. Another interesting example is found in the work of Hoffman et al. in the processing of BT, ST and BST materials [65]. These investigators were able to prepare columnar BT and ST materials and thus “get around” bulk nucleation within the film (which produces the typical, fine grain equiaxed microstructure) by reducing the thickness of the individual layers that are deposited and using a high heat treatment temperature after deposition of each of the thinner layers to induce film crystallization. This approach resulted in an epitaxial overgrowth of subsequent layers and the columnar microstructure that had been sought by the authors. A final interesting example involves the challenge of balancing crystallization kinetics of the PZT materials with the volatility of lead oxide during processing. If improperly done, a residual pyrochlore phase may exist at the surface of the film, degrading electrical properties. The most common strategy to address this problem has been to incorporate excess lead into the precursor solution, though Bursill and Brooks have shown some of the possible problems of this approach with regard to the narrow range of stoichiometry of the perovskite compounds [19]. Novel strategies to prevent residual pyrochlore at the surface of the film, such as using a final top deposited layer with a solution of only the lead precursor, have proven effective [93]. Others have noted how such problems can develop, or be reduced based on the Zr/Ti ratio in the PZT material. Numerous examples of such kinetic competition effects are reported in the literature.

15.6 Summary and Conclusions

All aspects of the CSD processing of thin films, ranging from solution characteristics to patterning can impact the resultant film properties. The pyrolysis and crystallization conditions utilized in film processing are certainly among the more important parameters that will serve to define thin film microstructure, and thereby, dielectric, ferroelectric and even optical properties. In this chapter, we have attempted to give a fundamental view of the reactions and transformation behavior that occur during heat treatment. We have also attempted, as possible, and hopefully as appropriate, to both explore and speculate about how some of these factors may contribute to the differences in film microstructure that have been observed. Since the early investigations of such processing routes for thin ferroelectric films, significant progress in both scientific understanding and engineering advancement for devices has been achieved. It is also our opinion, however, that many opportunities remain to gain additional insights into film processing, which

may lead to better process control, and thus, greater adoption of CSD as a mainline fabrication strategy. The vast number of studies that have been carried out regarding pyrolysis and crystallization behavior provide an expansive foundation on which to draw for further study, as well as for the fabrication of films with excellent dielectric, ferroelectric, and optical properties.

References

1. Schwartz RW, Narayanan M (2009) Chemical solution deposition – basic principles. In: Mitzi D (ed) *Solution processing of inorganic materials*. Wiley, New York, pp 33–76
2. Schwartz RW, Schneller T, Waser R (2004) Chemical solution deposition of electronic oxide films. *CR Chim* 7:433–461
3. Schwartz RW (1989) Chemical processing of PbTiO_3 by co-precipitation and sol-gel methods: the role of powder and gel characteristics on crystallization behavior. Dissertation, University of Illinois at Urbana-Champaign, Champaign, IL
4. Budd KD, Dey SK, Payne DA (1986) Effect of hydrolysis conditions on the characteristics of PbTiO_3 gels and thin films. *Mater Res Soc Symp Proc* 73:711–716
5. Budd KD, Dey SK, Payne DA (1985) Sol-gel processing of PbTiO_3 , PbZrO_3 , PZT, and PLZT thin films. *Br Ceram Soc Proc* 36:107–121
6. Dey SK, Budd KD, Payne DA (1988) Thin-film ferroelectrics of PZT by sol-gel processing. *IEEE Trans UFFC* 35:80–81
7. Braunstein G, Paz-Pujalt GR, Mason MG, Blanton T, Barnes CL, Margevich D (1993) The processes of formation and epitaxial alignment of SrTiO_3 thin films prepared by metallo-organic decomposition. *J Appl Phys* 73:961–970
8. Schwartz RW, Assink RA, Dimos D, Sinclair MB, Boyle TJ, Buchheit CD (1995) Effects of acetylacetone additions on PZT thin film processing. *Mater Res Soc Symp Proc* 361:377–387
9. Polli AD, Lange FF (1995) Pyrolysis of $\text{Pb}(\text{Zr}_{0.5}\text{Ti}_{0.5})\text{O}_3$ precursors: avoiding lead partitioning. *J Am Ceram Soc* 78:3401–3404
10. Neumayer DA, Duncombe PR, Laibowitz RB, Grill A (1997) Chemical solution deposition of BaSrTiO_3 films. *Int Ferro* 18:297–309
11. Li S, Condrate RA, Spriggs RM (1988) A FTIR and Raman spectral study of the preparation of lead titanate (PbTiO_3) by a sol-gel method. *Spectrosc Lett* 21:969–980
12. Seth VK, Schulze WA (1990) Fabrication and characterization of ferroelectric PLZT 7/65/35 ceramic thin films and fibers. *Ferroelectrics* 112:283–307
13. Ousi-Benommar W, Xue SS, Lessard RA, Singh A, Wu ZL, Kuo PK (1994) Structural and optical characterization of BaTiO_3 thin films prepared by metal-organic deposition from barium 2-ethylhexanoate and titanium dimethoxy dineodecanoate. *J Mater Res* 9:970–979
14. Klee M, Eusemann R, Waser R, Brand W, van Hal H (1992) Processing and electrical properties of $\text{Pb}(\text{Zr}_x\text{Ti}_{1-x})\text{O}_3$ ($x = 0.2-0.75$) films: comparison of metallo-organic decomposition and sol-gel processes. *J Appl Phys* 72:1566–1576
15. Haertling GH (1991) PLZT thin films prepared from acetate precursors. *Ferroelectrics* 116:51–63
16. Tahan DM, Safari A, Klein LC (1996) Preparation and characterization of $\text{Ba}_x\text{Sr}_{1-x}\text{TiO}_3$ thin films by a sol-gel technique. *J Am Ceram Soc* 79:1593–1598
17. Kumar S, Messing GL, White WB (1993) Metal organic resin derived barium titanate. I, formation of barium titanium oxycarbonate intermediate. *J Am Ceram Soc* 76:617–624
18. Fox GR, Krupanidhi SB (1994) Dependence of perovskite/pyrochlore phase formation on oxygen stoichiometry in PLT thin films. *J Mater Res* 9:699–711

19. Bursill LA, Brooks KG (1994) Crystallization of sol-gel derived lead-zirconate-titanate thin films in argon and oxygen atmospheres. *J Appl Phys* 75:4501–4509
20. Reaney IM, Brooks K, Klissurska R, Pawlaczyk C, Setter N (1994) Use of transmission electron microscopy for the characterization of rapid thermally annealed, solution-gel, lead zirconate titanate films. *J Am Ceram Soc* 77:1209–1216
21. Brooks KG, Reaney IM, Klissurska R, Huang Y, Bursill L, Setter N (1994) Orientation of rapid thermally annealed lead zirconate titanate thin films on (111) Pt substrates. *J Mater Res* 9:2540–2553
22. Coffman PR, Barlingay CK, Gupta A, Dey SK (1996) Structure evolution in the PbO-ZrO₂-TiO₂ sol-gel system: part II-pyrolysis of acid and base-catalyzed bulk and thin film gels. *J Sol-Gel Sci Technol* 6:83–106
23. Nouwen R, Mullens J, Franco D, Yperman J, Van Poucke LC (1996) Use of thermogravimetric analysis – Fourier transform infrared spectroscopy in the study of the reaction mechanism of the preparation of Pb(Zr, Ti)O₃ by the sol-gel method. *Vib Spectrosc* 10:291–299
24. Merklein S, Sporn D, Schönecker A (1993) Crystallization behavior and electrical properties of wet-chemically deposited lead zirconate titanate thin films. *Mater Res Soc Symp Proc* 310:263–269
25. Schneller T, Waser R (2007) Chemical modifications of Pb(Zr_{0.3}Ti_{0.7})O₃ precursor solutions and their influence on the morphological and electrical properties of the resulting thin films. *J Sol-Gel Sci Technol* 42:337–352. doi:[10.1007/s10971-007-0764-2](https://doi.org/10.1007/s10971-007-0764-2)
26. Chen S, Chen I (1994) Temperature-time texture transition of Pb(Zr_{1-x}Ti_x)O₃ thin films: I, Role of Pb-rich intermediate phases. *J Am Ceram Soc* 77:2332–2336
27. Tani T, Xu Z, Payne DA (1993) Preferred orientations for sol-gel derived PLZT thin layers. *Mater Res Soc Symp Proc* 310:269–274
28. Huang Z, Zhang Q, Whatmore RW (1999) Low temperature crystallization of lead zirconate titanate thin films by a sol-gel method. *J Appl Phys* 85:7355–7361
29. Losego MD, Ihlefeld JF, Maria J (2008) Importance of solution chemistry in preparing sol-gel PZT thin films directly on copper surfaces. *Chem Mater* 20:303–307
30. Losego MD, Jimison LH, Ihlefeld JF, Maria J (2005) Ferroelectric response from lead zirconate titanate thin films prepared directly on low-resistivity copper substrates. *Appl Phys Lett* 86:172906
31. Laughlin B, Ihlefeld J, Maria J (2005) Preparation of sputtered (Ba_xSr_{1-x})TiO₃ thin films directly on copper. *J Am Ceram Soc* 88:2652–2654
32. Narayanan M, Kwon D-K, Ma B, Balachandran U (2008) Deposition of sol-gel derived lead lanthanum zirconate titanate thin films on copper substrates. *Appl Phys Lett* 92:252905. doi:[10.1063/1.2945887](https://doi.org/10.1063/1.2945887)
33. Yang GY, Lee SI, Liu ZJ, Anthony CJ, Dickey EC, Liu ZK, Randall CA (2006) Effect of local oxygen activity on Ni–BaTiO₃ interfacial reactions. *Acta Mater* 54:3513–3523
34. Kingon AI, Srinivasan S (2005) Lead zirconate titanate thin films directly on copper electrodes for ferroelectric, dielectric and piezoelectric applications. *Nat Mater* 4:233–237
35. Gaskell DR (1981) Introduction to metallurgical thermodynamics, 2nd edn. Hemisphere Publishing Corporation, New York
36. Hirano SI, Yogo T, Kikuta K, Araki Y, Saitoh M, Ogasahara S (1992) Synthesis of highly oriented lead zirconate-lead titanate film using metallo-organics. *J Am Ceram Soc* 75:2785–2789
37. Schwartz RW, Boyle TJ, Voigt JA, Buchheit CD (1994) Densification and crystallization of zirconia thin films prepared by sol-gel processing. In: Bhalla AS, Nair KM, Lloyd IK, Yanagida H, Payne DA (eds) Ferroic materials: design, preparation, and characteristics. *Ceramic Trans* 43:145–163
38. Brinker CJ, Scherer GW (1990) Sol-gel science: the physics and chemistry of sol-gel processing. Academic, Boston
39. Scherer GW (1987) Drying gels V. rigid gels. *J Non Cryst Solids* 92:122–144

40. Garino TJ, Harrington M (1992) Residual stress in PZT thin films and its effect on ferroelectric properties. *Mater Res Soc Symp Proc* 243:341–347
41. Zarzycki J (1982) Gel – glass transformation. *J Non Cryst Solids* 48:105–116
42. Cooper AR (1986) Differences between gel-derived melts and those produced by batch melting. *Mater Res Soc Symp Proc* 73:421–430
43. Brinker CJ, Roth EP, Tallant DR, Scherer GW (1986) Relationships between sol to gel and gel to glass conversions: structure of gels during densification. In: Hench LL, Ulrich DR (eds) *Science of ceramic chemical processing*. Wiley, New York, pp 37–51
44. Keddie JL, Giannelis EP (1991) Effect of heating rate on the sintering of titanium dioxide thin films: competition between densification and crystallization. *J Am Ceram Soc* 74:2669–2671
45. Panda PC, Mobley WM, Raj R (1989) Effect of the heating rate on the relative rates of sintering and crystallization in glass. *J Am Ceram Soc* 72:2361–2364
46. Pascual R, Sayer M, Vasant Kumar CVR, Zou L (1991) Rapid thermal processing of zirconia thin films produced by the sol-gel method. *J Appl Phys* 70:2348–2352
47. Brinker CJ, Scherer GW (1984) Relationships between the sol-to-gel and gel-to-glass conversions. In: Hench LL, Ulrich DR (eds) *Ultrastructure processing of ceramics, glasses, and composites*. Wiley, New York, pp 43–59
48. Roy R (1969) Gel route to homogeneous glass preparation. *J Am Ceram Soc* 52:344
49. Lange FF (1996) Chemical solution routes to single-crystal thin films. *Science* 273:903–909
50. Seifert A, Lange FF, Speck JS (1995) Epitaxial growth of PbTiO_3 thin films on (001) SrTiO_3 from solution precursors. *J Mater Res* 10:680–691
51. Voigt JA, Tuttle BA, Headley TJ, Lamppa DL (1995) The pyrochlore-to-perovskite transformation in solution-derived lead zirconate titanate thin films. *Mater Res Soc Symp Proc* 361:395–402
52. Kwok CK, Desu SB (1992) Pyrochlore-perovskite phase transformation of lead zirconate titanate (PZT) thin films. *Ceramic Trans* 25:85–96
53. Lefevre MJ, Speck JS, Schwartz RW, Dimos D, Lockwood SJ (1996) Microstructural development in sol-gel derived lead zirconate titanate thin films: the role of precursor stoichiometry and processing environment. *J Mater Res* 11:2076–2084
54. Norga GJ, Vasiliu F, Fe L, Wouters DJ, Van der Biest O (2003) Role of fluorite phase formation in the texture selection of sol-gel-prepared $\text{Pb}(\text{Zr}_{1-x}\text{Ti}_x)\text{O}_3$ films on Pt electrode layers. *J Mater Res* 18:1232–1238
55. Schwartz RW, Boyle TJ, Lockwood SJ, Sinclair MB, Dimos D, Buchheit CD (1995) Sol-gel processing of PZT thin films: a review of the state-of-the-art and process optimization strategies. *Int Ferro* 7:259–277
56. Wilkinson AP, Speck JS, Cheetham AK, Natarajan S, Thomas JM (1994) In situ x-ray diffraction study of the crystallization kinetics in $\text{PbZr}_{1-x}\text{Ti}_x\text{O}_3$ (PZT, $x = 0.0, 0.55, 1.0$). *Chem Mater* 6:750–754
57. McCauley RA (1980) Structural characteristics of pyrochlore formation. *J Appl Phys* 51:290–294
58. Tu YL, Calzada ML, Phillips NJ, Milne SJ (1996) Synthesis and electrical characterization of thin films of PZT made from a diol-based sol-gel route. *J Am Ceram Soc* 79:441–448
59. Phillips NJ, Calzada ML, Milne SJ (1992) Sol-gel-derived lead titanate films. *J Non Cryst Solids* 147&148:285–290
60. Kumar S, Messing GL (1994) Metal organic resin derived barium titanate: II, kinetics of BaTiO_3 formation. *J Am Ceram Soc* 77:2940–2948
61. Hasenkox U, Hoffmann S, Waser R (1998) Influence of precursor chemistry on the formation of MTiO_3 ($M = \text{Ba, Sr}$) ceramic thin films. *J Sol-Gel Sci Technol* 12:67–79
62. Gopalakrishnamurthy HS, Subba Rao M, Narayanan Kutty TR (1975) Thermal decomposition of titanyl oxalates-I; barium titanyl oxalate. *J Inorg Nucl Chem* 37:891–898
63. Tsay J, Fang T (1996) Effects of temperature and atmosphere on the formation mechanism of barium titanate using the citrate process. *J Am Ceram Soc* 79:1693–1696

64. Frey MH, Payne DA (1995) Synthesis and processing of barium titanate ceramics from alkoxide solutions and monolithic gels. *Chem Mater* 7:123–129
65. Hoffman S, Hasenkox U, Waser R, Jia JL, Urban K (1997) Chemical solution deposition of BaTiO₃ and SrTiO₃ with columnar microstructure. *Mater Res Soc Symp Proc* 474:9–14
66. Jia CL, Urban K, Hoffmann S, Waser R (1998) Microstructure of columnar-grained SrTiO₃ and BaTiO₃ thin films prepared by chemical solution deposition. *J Mater Res* 13:2206–2217
67. Schwartz RW, Clem PG, Voigt JA, Byhoff ER, Van Stry M, Headley TJ, Missert NA (1999) Control of microstructure and orientation in solution deposited BaTiO₃ and SrTiO₃ thin films. *J Am Ceram Soc* 82:2359–2367
68. Schwartz RW, Voigt JA, Tuttle BA, DaSalla RS, Payne DA (1997) Comments on the effects of solution precursor characteristics and thermal processing conditions on the crystallization behavior of sol-gel derived PZT thin films. *J Mater Res* 12:444–456
69. Schwartz RW, Dobberstein H (2003) Modeling structural evolution in ferroelectric thin films. In: *Proceedings of the 11th US-Japan Sem Dielect Piezo Ceram*. Sapporo, Japan, pp. 215–218
70. Dobberstein H (2002) A thermodynamic and kinetic model for nucleation and growth in solution derived thin films. Dissertation, Clemson University
71. Kingery WD, Bowen HK, Uhlman DR (1960) *Introduction to ceramics*. Wiley, New York
72. Chiang YM, Birnie D III, Kingery WD (1997) *Physical ceramics, principles for ceramic science and engineering*. Wiley, New York
73. Doremus RH (1994) *Glass science*, 2nd edn. Wiley, New York
74. McMillan PW (1979) *Glass-ceramics*, 2nd edn. Academic, London
75. Johnson WA, Mehl RF (1939) Reaction kinetics in processes of nucleation and growth. *Trans Am Inst Miner (Metall) Eng* 135:416–458
76. Avrami M (1939) Kinetics of phase change. *J Chem Phys* 7:1103–1112
77. Malek J, Criado JM (1992) Empirical kinetic models in thermal analysis. *Thermochim Acta* 203:25–30
78. Malek J, Criado JM (1994) A simple method of kinetic model discrimination. Part 1. analysis of differential non-isothermal data. *Thermochim Acta* 236:187–197
79. Schwartz RW, Lakeman CDE, Payne DA (1990) The effects of hydrolysis conditions, and acid and base additions, on the gel-to-ceramic conversion in sol-gel derived PbTiO₃. *Mater Res Soc Symp Proc* 180:335–340
80. Leikina BB, Kostikov YP, Olesk AO (1989) Effect of the chemical composition of titanium-containing raw material on the properties of BaTiO₃. *Neorg Mater* 25:2050–2052
81. Gust MC, Momoda LA, McCartney ML (1994) Microstructure and crystallization behavior of sol-gel prepared BaTiO₃ thin films. *Mater Res Soc Symp Proc* 346:649–653
82. Meyer B, Padilla J, Vanderbilt D (1999) Theory of PbTiO₃, BaTiO₃ and SrTiO₃ surfaces. *Faraday Discuss* 114:395–405
83. Eglitis RI, Vanderbilt D (2007) Ab initio calculations of BaTiO₃ and PbTiO₃ (001) and (011) surface structures. *Phys Rev B* 76:155439-1-9
84. Sengupta SS, Ma L, Adler DL, Payne DA (1995) Extended x-ray absorption fine structure determination of local structure in sol-gel-derived lead titanate, lead zirconate and lead zirconate titanate. *J Mater Res* 10:1345–1348
85. Arčon I, Malič B, Kosec M, Kodre A (1999) Study of the lead environment in liquid and as-dried precursors of PZ, PT and PZT thin films. *J Sol-Gel Sci Technol* 13:861–864
86. Lakeman CDE, Xu Z, Payne DA (1995) On the evolution of structure and composition in sol-gel-derived lead zirconate titanate thin layers. *J Mater Res* 10:2042–2051
87. Mosset A, Gautier-Luneau I, Galy J, Strehlow P, Schmidt H (1988) Sol-gel processed BaTiO₃: structural evolution from the gel to the crystalline powder. *J Non-Cryst Solids* 100:339–344
88. Turnbull D (1950) Formation of crystal nuclei in liquid metals. *J Appl Phys* 21:1022–1028
89. Tong S (2012) Dielectric and ferroelectric properties of lead lanthanum zirconate titanate thin films for capacitive energy storage. PhD dissertation, University of Cincinnati

90. Cheng J, Zhu W, Li N, Cross LE (2002) Electrical properties of sol-gel-derived Pb($Zr_{0.52}Ti_{0.48}$)O₃ thin films on a PbTiO₃-coated stainless steel substrate. *Appl Phys Lett* 81:4805–4807
91. Kwok CK, Desu SB (1993) Low temperature perovskite formation of lead zirconate titanate thin films by a seeding process. *J Mater Res* 8:339–344
92. Al-Shareef HN, Bellur KR, Auciello O, Kingon AI (1994) Effect of electrodes on the phase evolution and microstructure of Pb($Zr_{0.53}Ti_{0.47}$)O₃ films. *Ferroelectrics* 152:85–90
93. Tani T, Lakeman CDE, Li JF, Xu Z, Payne DA (1994) Crystallization behavior and improved properties for sol-gel derived PZT and PLZT thin layers processed with a lead oxide cover coating. *Ceramic Trans* 43:89–106

Chapter 16

Epitaxial Films

Fred Lange

16.1 Introduction

Physicists, who call materials “condensed matter”, have synthesized single crystal thin films for many years using a variety of vapor phase methods. Within the last 20 years, several chemical solution methods have been developed. One, the chemical solution deposition (CSD) method is the theme of this review. CSD is also called metal organic deposition (MOD), a term commonly used by people developing ‘reel to reel’ superconducting wires [1]. Although CSD is a relatively recent method for synthesizing epitaxial films, its application to manufacture kilometer lengths of superconductor wires has been demonstrated [1]. Literature that describes other solution routes, such as the high temperature hydrothermal synthesis method and the low temperature chemical bath deposition (CBD) method (see Chap. 14), where epitaxial films and crystals are directly synthesized within a solution, can be found elsewhere [2–4]. The CSD method starts with a solution of dissolved molecules, mixed at the molecular level, that will of form a multi-element, inorganic material during heating. These molecules are similar to those used for different vapor phase methods, but differ in the fact that they do not volatilize during heating, but, instead, decompose during heating (pyrolysis) to form an inorganic material. Many different molecules, each containing at least one metal atom bonded to either an oxygen, sulfur, nitrogen, carbon, etc., which, in turn, is bonded to an organic ligand, can be mixed in a common solvent to form a multi-element inorganic compound during pyrolysis. Substrates are coated with the solution by one of a number of methods. The technologies for producing coatings with a uniform thickness over large areas via spin-coating has been well developed in the electronic industry where photoresist coatings are commonly used to make patterns, and in the glass industry where SnO₂ anti-reflective coatings are produced

F. Lange (✉)

Materials Department, University of California, Santa Barbara, CA, USA
e-mail: maryannelange41@gmail.com

via dip coating large sheets of glass with an alkoxide precursor [5]. Spin-coating and ultrasonic spray deposition (spray pyrolysis) [6] are popular coating methods for experimentalists. During coating, the solvent evaporates to produce a solid, precursor film with mechanical properties that depend on the precursor, e.g., 'soapy' for some surfactant-like precursors such as the hexanoates, and brittle for gel forming precursors. It has been demonstrated that dip coating and, more recently, slot coating can be used in the production of long lengths (reel to reel) of epitaxial, superconductor wires [7]. Soft lithographic and photolithographic methods have been used to pattern the precursor on a substrate [8–10]. The science and engineering of all solution coating methods involve rheology and evaporation, which governs film thickness, capillarity, which governs wetting and surface defects, and fracture mechanics, which explains the critical thickness needed to extend small flaws into large cracks. Although the CSD method has primarily been used to synthesize a large variety of oxides, it has also been used to synthesize GaN, different sulfides and selenides. Single crystal substrates that are atomic templates for the structure of the coating are required to form epitaxial films. As discussed below, epitaxy can take place even when the crystalline structures of the substrate and film are dissimilar.

The review begins with a summary of the different precursors chemistries, which is generally only limited by the imagination of the chemist. Because mud cracks commonly arise during substrate coating, the second subject will explain why cracking is likely when the film exceeds a critical thickness. It is shown that films generally crack when the solvent evaporates. Since the critical thickness is generally ~ 100 nm, the cracking phenomenon is the limiting feature of the CSD method to form epitaxial films with minimal defects. Thicker film, generally containing more defects, can be produced by multiple precursor deposition, pyrolysis cycles.

Heating causes the precursor film to pyrolysis (decomposition during heating), forming an amorphous film, which then crystallizes into a porous, polycrystalline film with a nano-grain size. The reason for the nano-grain size will be detailed below. Spontaneous crystallization at low temperatures is generally diffusion limited. Namely, since crystallization only requires small atomic displacements, and not long range diffusion, metastable structures and extended solutions are likely to form at low temperature, before they form thermodynamic stable phases produced when heated to higher temperatures.

The review discusses the different phenomena that can be used to convert the polycrystalline film, first formed after pyrolysis, into a single crystal. Generally, the structure of the single crystal substrate is either identical or very similar (namely, different in composition and lattice parameters) to the structure of the material that crystallizes after pyrolysis. But, epitaxial films can also be formed when the crystalline structure of the film is different relative to the single crystal substrate. It will be shown that either epitaxial or highly oriented films can be produced despite the mismatch between structures, let alone, the mismatch between lattice parameters.

16.2 Precursor Chemistries

Different solution precursor chemistries can be used to produce the same inorganic material. The different precursors used for coating substrates can have different properties that include different rheological behaviors that influence coating coverage, different mechanical properties that effect cracking during solvent evaporation and different decomposition products that can alter the composition of the inorganic formed during pyrolysis. Because the inorganic material is formed by pyrolysis at low temperatures where diffusion is kinetically limited, metastable phases can crystallize to affect epitaxy during their transformation to the stable phase.

One advantage of solution routes is the economics that ‘beakers and benches’ chemistry offer relative to capital intensive vapor phase routes. A second advantage is the high degree of compositional control inherent with the solution synthesis of multi-element, inorganic materials. As reviewed by Schwartz et al. [11], common precursor chemistries are generally defined by their ligand, e.g., carboxylates, alkoxides, and β -diketonates. Carboxylates (see Chap. 2), $M^{n+}(\text{OOCR})_n$, are salts of carboxylic acids, where n is the valence of the cation (M) and R is an alkyl group, viz., a hydrocarbon chain. When $R=\text{CH}_3$, the carboxylate is a metal acetate, which, because of its very small ‘hydrocarbon chain’, can be soluble in either water or its carboxylic acid, namely, acetic acid. Longer chain carboxylates such as 2-ethylhexanoates ($R=\text{C}_7\text{H}_{15}$) can solubilize in their carboxylic acid and non-polar solvents such as toluene and xylene. Commercial carboxylates are available for most all metals. Multi-element compounds can be formulated by mixing different carboxylates in a common solvent. Evaporation of the solvent from longer chain carboxylates produces a waxy precursor, where the different carboxylates are mixed at the molecular scale without separation. An example is the cuprate superconductor, $\text{Bi}_{2.1}\text{Sr}_{1.6}\text{Ca}_{0.9}\text{Cu}_2\text{O}_x$, synthesized by mixing Bi, Sr, Ca and Cu 2-ethyl-hexanoates, each assayed for their specific metal oxide, in toluene [12]. Some acetates like zirconium acetate, do not cleanly pyrolyze to ZrO_2 , but produce residual carbon, which must be removed by oxidation [5]. Noble metals, Ag, Au, Pt, etc., can also form via the pyrolysis of carboxylate precursors. These ‘resin’ precursors are commonly used as ‘inks’ to produce decorative coatings on ‘up-market’ products.

Although not as convenient to synthesize multi-element compounds as it is with carboxylates, alkoxides, $M^{n+}(\text{OR})_n$, the metal salts of alcohols, are another common group of precursors. The great popularity of alkoxide precursors stems from their ability to form polymeric species composed of metal-oxygen-metal bonds when reacted with water [13, 14]. Two reactions occur to form a three dimensional network with branched -O-M-O-M- bonds. One occurs when a water molecule partially hydrolyzes the alkoxide molecule to form $M^{n+}(\text{OR})_{n-1}(\text{OH})$. The second occurs when a partially hydrolyzed molecule reacts with another alkoxide molecule. These two reactions form the crossed-linked metal oxide network. The first of these reactions is called hydrolysis, and the second, condensation (or polymerization). The viscosity of the solution increases with the molecular

weight of the reacted species. The cross-linked polymeric species eventually forms a gel composed of a three dimensional metal-oxide network [13, 14] within alcohol, with a substantial fraction of un-reacted, -M-OH and -M-OR groups. If it were not due to the many un-reacted -M-OR and -M-OH groups ‘hidden’ within the tangled, molecular gel, it would cleanly transform to an oxide when heated with a weight loss only due to the alcohol, or some other solvent for the alkoxide, such as 2-methoxyethanol ($\text{CH}_3\text{OCH}_2\text{CH}_2\text{OH}$), that ‘holds’ the gel apart. Unlike precursor solutions containing mixed 2-ethyl-hexanoates that evaporate to form a soft, soapy substance, alkoxide solutions form brittle gels that are more prone to ‘mud-cracking’.

The major objective of using solutions precursors is to allow the mixing of different precursor molecules, each containing a different metal element, at the molecular level so that long range diffusion is not required to synthesize a multi-element compound. Mixing on the molecular scale enables compound synthesis at low temperatures, following pyrolysis. This goal is easy to achieve, provided the different molecules do not segregate. Small precursor molecules, such as acetates (a short chain carboxylate) can crystallize and thus, phase separate during evaporation. Phase separation involves longer diffusion distances. Metal nitrates also crystallize during water evaporation, and should be avoided unless the nitrates have an identical structure enabling a solid-solution after pyrolysis. As pointed out by Mantese et al. [15], metal carboxylates can directly produce certain metals, including Pb, Bi, Sn, and Cu, because they can cleanly pyrolyzed within a ‘window’ of low oxygen partial pressure, where the metal, instead of its oxide, is thermodynamically stable. The loss of volatile Pb during the synthesis of oxide compounds is caused by the low oxygen partial pressure produced by the volatilized hydrocarbon gas that arise during pyrolysis [16].

16.3 Mechanical Instability (Avoiding ‘Mud-Cracking’)

After coating the substrate with the precursor solution, solvent evaporation causes the precursor molecules to consolidate and form a film that is sufficiently elastic to support stresses. At this point, further evaporation will further reduce the volume of the film causing shrinkage. Because the film is bound to the substrate, the decreased volume is biaxially constrained, producing biaxial tensile stresses. Alkoxide precursors form brittle gels that easily support tensile stresses. Although large chain carboxylates form waxy films that appear not to support large stress, they undergo a large volume change during pyrolysis to an elastic, inorganic material which can support biaxial tensile stresses. As illustrated below, the biaxial tensile stresses will lead to the formation of ‘mud’ cracks if the film thickness is greater than a critical value. For precursors that produce brittle gels, the critical thickness is generally ≈ 100 nm.

The reason for a critical thickness can be understood with the help of Fig. 16.1, which shows a thin film of thickness, ‘t’, containing a small crack of length ‘c’, that

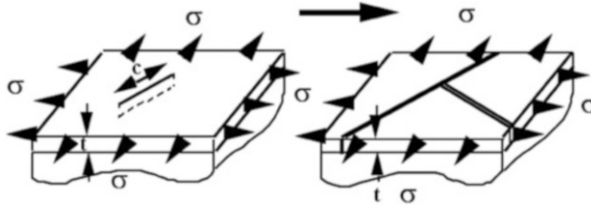


Fig. 16.1 Portion of a thin film bonded to a thicker substrate containing a crack of length c , which extends (*right hand view*) along the length of the film to form a ‘mud crack’ pattern with the extension of other cracks

extends from the surface to the substrate. The film has an elastic modulus, E and a Poisson’s ratio, ν and is subjected to a biaxial tensile stress, σ due to the constrained shrinkage. Since the tensile forces within the film, times the cross-sectional area of the film, must be equal to the compressive forces within the substrate, times the cross sectional area of the substrate, the compressive stresses within the substrate will be extremely small when the film is very thin relative to the substrate. That is, only the tensile stresses within the film need be considered.

The strain energy stored in the film, per unit volume, is:

$$\frac{\sigma^2(1 - \nu)}{2E} = \frac{\sigma^2}{2E^*} \tag{16.1}$$

The strain energy within the film of area A , containing the small crack of length c is:

$$\left[\frac{\sigma^2}{2E^*} \right] At - \left[\frac{\sigma^2}{2E^*} \right] Zct^2 \tag{16.2}$$

where Zct^2 is the volume of material around the crack where strain energy is relieved as shown in the second term. The energy needed to form the crack’s surface is ctG_C , where G_C is the energy needed to form two crack surfaces per unit area, and ct is the area of the crack. Thus, the total energy associated with the cracked film is:

$$U_t = \left[\frac{s^2}{2E^*} \right] At - \left[\frac{s^2}{2E^*} \right] Zct^2 + ctG_C \tag{16.3}$$

To find the conditions for crack extension along the film, we apply the concept introduced 90 years ago by A.A. Griffith, namely, a crack can only extend if it reduces the free energy of the system. Assuming that the stress, elastic properties and strain energy release rate (G_C) are constants of the film, the only variables are the thickness and crack length. Applying Griffith’s criterion, one needs to determine when $\partial U_t / \partial c \partial t \leq 0$. Differentiating the free energy function [Eq. (16.3)] with respect to the crack length and film thickness, one finds that the condition for

crack extension does not depend on the *length of the crack*, but instead, depends on the *film thickness* as expressed by

$$\frac{\partial U_t}{\partial c \partial t} \leq G_c - Z \frac{\sigma^2}{E^*} t \quad (16.4)$$

Setting Eq. (16.4) equal to zero, one can now understand why a crack cannot extend until the film thickness exceeds a critical value:

$$t \geq t_c = \frac{G_c E^*}{Z \sigma^2} \quad (16.5)$$

A more rigorous analyses [17–19] for a variety of different crack geometries, e.g., cracks that not only extend across the film, but concurrently extend either along the interface or into the substrate, leads to the same equation, where Z changes with the crack geometry [19]. Thus, crack extension can be avoided when the film thickness does not exceed a critical value.

For a given stress (or shrinkage strain), Eq. (16.5) shows that the critical thickness can be increased by increasing the crack growth resistance of the precursor film, i.e., increasing G_c . Observations suggest that brittle precursors (gels) form their ‘mud’ crack pattern during drying when G_c apparently has its smallest value. Using this knowledge, Roeder and Slamovich [20] showed that when 10 wt% of an elastomeric polymer was mixed with a precursor solution formulated with a hybrid alkoxide, they could increase the critical thickness by an order of magnitude (0.1–1 μm). The elastomer would be expected to increase the G_c of the film. Evidence also suggests that if a eutectic melt can be formed prior to epitaxy, the melt can heal any cracks produced during the earlier stages, thus, enabling thicker films [12]. Today, processors who use CSD, generally form thicker films by building up the film thickness with cyclic coating and pyrolysis steps, avoiding cracking during each cycle. This cyclic coating procedure is known to introduce defects.

16.4 Kinetic Limited Crystallization

Crystallization of the inorganic phase can occur either during or after pyrolysis. If crystallization occurs after pyrolysis, the inorganic is a porous, amorphous material. Crystallization requires the formation of a critical nucleus that can grow when it spontaneously lowers its free energy. The size of the critical nucleus is determined in a similar manor as for the condition for crack extension detailed above. Namely, the free energy per unit volume ΔG_c that is driving the crystallization, is negative below the melting temperature, whereas the growing nucleus introduces a new interface, and thus growth also increases the free energy, as the nucleus becomes larger. In addition, because nucleation occurs within a porous

solid, strain energy arises both within and around the growing nucleus. The strain energy per unit volume, U_{se} , always increases the free energy. The free energy function can be described by

$$\Delta G = (U_{se} - |\Delta G_c|) \frac{4\pi}{3} r^3 + 4\pi r^2 \gamma \quad (16.6)$$

where r is the radius of the nucleus, γ is the surface energy per unit area, and $|\Delta G_c|$ is the absolute value of ΔG_c , which is assumed to be negative below the melting temperature. It can be seen that Eq. (16.6) has a maximum value, which can be determined by its differential with respect to r , namely,

$$\frac{\partial \Delta G}{\partial r} = (U_{se} - |\Delta G_c|) 4\pi r^2 + 8\pi r \gamma \quad (16.7)$$

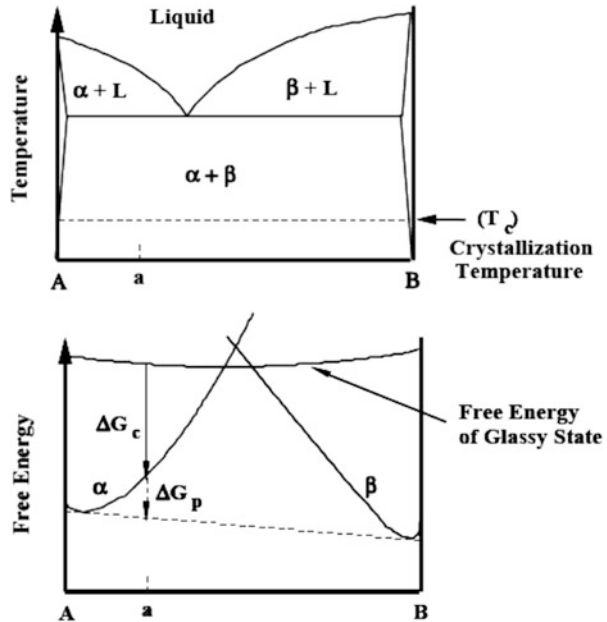
The critical nucleus that allows the free energy of the system to decrease as it grows is determined by setting Eq. (16.7) equal to zero. Thus, the critical nucleus is estimated with

$$r_c = \frac{2\gamma}{(|\Delta G_c| - U_{se})} \quad (16.8)$$

Because the difference between the pyrolysis temperature (generally between 200 and 400 °C) and the melting temperature of the inorganic is very large, $|\Delta G_c|$ will be very large, and thus, r_c will be very small. Thus, the crystallization of a connective (partially sintered) network of nano-crystallites (<2 nm) is generally observed.

Because crystallization occurs at low temperatures, where diffusion is kinetically limited, metastable phases (extended solid-solutions and non-equilibrium structures) can crystallize [21, 22]. The concept of kinetic limited crystallization, detailed by Levi [23], can be illustrated with the help of a free energy vs. composition plot shown in Fig. 16.2 (lower figure), which schematically shows the free energy of two phases, with the α and β structures, that forms in a simple binary system with a single eutectic (upper figure). It is assumed that the lower plot represents the free energy of both α and β and the amorphous phase (upper curve) as a function of composition, at the crystallization temperature. The equilibrium composition of both crystalline phases occurs at their minimum free energy. Let us assume we formulate a precursor that has the composition 'a', which produces an amorphous phase after pyrolysis. Under equilibrium conditions, this composition would crystallize as two phases, α and β , each with their equilibrium composition, as shown in the upper plot. Instead, one experimentally finds only one crystalline phase, α , that contains all of the B atoms with different lattice parameters than what would be expected. Using the TEM, no amorphous phase can be found [22].

Fig. 16.2 Simple binary phase diagram with a eutectic (*upper figure*) showing two phases, A and B, with the respective crystal structures, α and β . *Lower figure* shows that free energy of α , β and the amorphous phase as a function of composition at the temperature where the amorphous phase, with the composition 'a' will crystallize



Because diffusion is kinetically limited at temperatures just above the pyrolysis temperature and the free energy (ΔG_c) driving crystallization is large, a nano-sized, single phase polycrystalline material with a metastable composition, forms and lowers the free energy of the system. As the temperature is increased and diffusion is unleashed, partitioning begins by the precipitation of the β phase with its equilibrium composition. The free energy change driving partitioning is ΔG_p . During partitioning, the α phase loses its excess B atoms as the β phase increases its volume fraction within the two phase material. After partitioning ceases, the precursor derived material consists of two phases, consistent with the phase diagrams (upper figure), each with their equilibrium composition.

When the composition of the precursor 'a' is closer to the equilibrium composition (composition with the minimum in free energy), ΔG_c is larger, and thus, the size of the critical nucleus is small. On the other hand, when the composition 'a' moves further away from the equilibrium composition, ΔG_c becomes smaller and smaller, requiring larger and larger nuclei to enable spontaneous crystallization. Experiments [22] have shown that as the composition moves further away from the equilibrium composition, crystallization takes place at higher and higher temperatures, presumably due to the larger and larger size of the nuclei needed for spontaneous crystallization.

Besides forming metastable, extended solid-solutions, single phase materials synthesized from precursors are well known to crystallize with a metastable crystal structure. Single oxide examples include the crystallization of Al_2O_3 with the metastable γ (spinel) structure instead of the stable α structure, and the crystallization of TiO_2 as the anatase structure, instead of the stable rutile structure.

These metastable structures enable larger distortions in the atomic arrangements [23]. Mixed oxide compounds also form metastable phases. Important examples include the series of solid solution $\text{Pb}(\text{Ti},\text{Zr})\text{O}_3$ materials, which will crystallize with the pyrochlore structure, instead of the stable perovskite structure from which it derives its ferroelectricity. Why the metastable pyrochlore structure is chosen could be because it offers greater freedom for placement of Pb and Ti ions on cation sites and offers the greater possibility of vacancies on oxygen sites. That is, at temperatures where diffusion is severely limited, the pyrochlore structure is kinetically more favorable, and offers a structure that does not require exact placement of elements, relative to the stable structure. In one precursor study of the $\text{PbO}-\text{TiO}_2$ binary system [16], where a TiO_2 rich PbTiO_3 composition was synthesized, a large number of metastable phases were formed. Despite the excess TiO_2 , a metastable pyrochlore crystallized first. When heated to higher temperatures, the metastable pyrochlore structure transformed to the perovskite structure, but retained its metastable, Ti-rich composition. At still higher temperatures, the metastable perovskite partitioned into two phases: a metastable Ti-rich phase (PbTi_3O_7) and a perovskite phase with a composition that approached the stoichiometric, equilibrium phase, PbTiO_3 . At still higher temperatures, the two phases react to finally form the two stable phases, TiO_2 (rutile) and PbTiO_3 (perovskite). The free energy is sequentially decreased during each of these kinetically limited steps.

16.5 Epitaxial Grain Growth

Although a number of different phenomena are known to convert the polycrystalline film, first formed during crystallization, into a single crystal film, the most common is enabled by grain growth. If the film material and substrate have identical structures, despite different chemistries, and their lattice mismatch is small ($<5\%$), the nanometer grains at the film/substrate interface will crystallize with the orientation of underlying substrate [24]. That is, the substrate acts as a large nucleus for the crystallization of the amorphous material formed after pyrolysis. All other grains not in direct contact with the substrate will have no special orientation. This is shown in Fig. 16.3a where the darker grains at the interface have lattice fringes that extend from the substrate. After crystallization and further heat treatment, the oriented grains at the interface, which have a lower free energy, will systematically grow to consume the grains above them to eventually convert the polycrystalline film into a single crystal via grain growth. Miller et al. [24] uncovered this growth mechanism during studies where aqueous solutions of Zr-acetate + Y-nitrate were used to coat (100) cubic- $\text{Zr}(\text{Y})\text{O}_2$ (9.5 mol% Y_2O_3) substrates. Film compositions within the range cubic- $\text{Zr}(\text{Y})\text{O}_2$ (6–40 mol% Y_2O_3) had a lattice mismatch up to 1.59%. Miller et al. showed that although the nanometer, epitaxial grains are produced at the film/substrate interface during pyrolysis ($\approx 400^\circ\text{C}$), higher temperatures were needed to sufficiently densify the film to allow the epitaxial grains to grow to the surface by consuming all other misoriented grains.

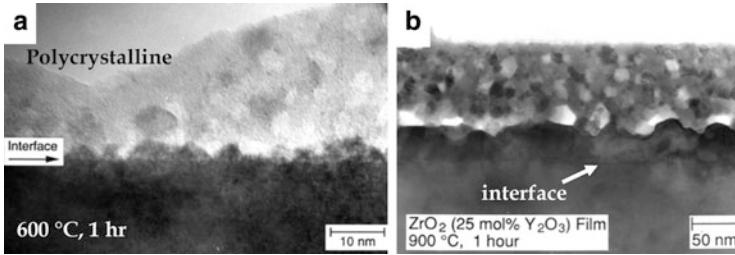


Fig. 16.3 (a) A cross-sectional view of a polycrystalline Zr(Y)O₂ film formed on a (100) cubic-Zr (Y)O₂ single crystal substrate grains at the substrate interface that have nucleated with the same orientation during pyrolysis (distance between lattice fringes is ≈ 2.5 nm) and (b) dark field TEM of the same film heat treated at 900 °C showing partial conversion of the polycrystalline film to a single crystal by grain growth [24]

The elimination of grain boundaries in the initial, polycrystalline film is the apparent driving free energy for this epitaxial grain growth phenomenon.

Figure 16.3b, a dark field transmission electron microscopy (TEM) image, shows that at 900 °C, the epitaxial layer (mismatch = 0.81 %) has grown approximately half-way to the surface. The top half is still polycrystalline. Most of the epitaxial film and substrate are brighter because the image is taken with a common diffraction beam (dark field) from the substrate and epitaxial film. Grains that have a small misorientation were not consumed during epitaxial grain growth and appear as darker, defect ‘grains’. For this system, higher temperatures ($\approx 1,100$ °C) were needed to fully grow the film to the surface and to eliminate many of the internal defects observed at lower temperatures. At 1,100 °C, the surface was not smooth, but contained pits caused by remnant pores ‘pushed’ to surface by the moving, epitaxial front. Surface diffusion produced smooth surfaces at higher temperatures ($>1,200$ °C).

Miller et al. [25] also observed that when the film and substrate had nearly the same composition and thus, nearly no mismatch strain, the epitaxial grain growth phenomenon initiated at a lower temperature relative to compositions with a larger mismatch. For this case, pores within the partially dense, polycrystalline film, would become internally trapped as it was converted into a single crystal film. Trapped pores were difficult to remove via heat treatment because of the lack of intersecting grain boundaries, which are rapid paths for mass transport [25]. This observation suggested that the strain energy associated with the initial epitaxial growth helps retard growth to a higher temperature, were pores were able to move with the epitaxial front [25].

Miller et al. [24] showed that much of the strain energy within the film due to lattice mismatch was relieved by the formation of a dislocation network at the film/substrate interface as observed for vapor grown films [26, 27]. To a first approximation, the interfacial energy might be estimated to be solely due to the dislocation network. For atomic layer by layer growth in vapor phase epitaxy, it is believed that the dislocations move from the surface to the interface [26]. The mechanism of how the dislocation network forms at the interface is still unknown for the CSD method.

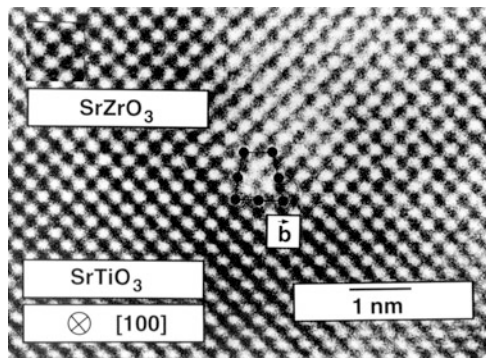


Fig. 16.4 Cross-sectional view, $\langle 100 \rangle$ zone axis, of an interface between epitaxial SrZrO_3 film and (001) SrTiO_3 substrate, showing periodic missing planes in SrZrO_3 crystal that compensates for much of the lattice mismatch strain due to the larger (5 %) lattice parameter of the SrZrO_3 . Note Burgers circuit around the dislocation at the interface [28]

Several studies were undertaken to understand how the epitaxy mechanism might change with lattice mismatch. One involved the epitaxy of metal oxides (CdO , CaO , SrO) on MgO ; all have the NaCl structure with lattice mismatch between 11 and 23 %. [28] The second involved a series of solid-solution compositions $(\text{Sr},\text{Ba})(\text{Ti},\text{Zr},\text{Ce})\text{O}_3$ grown on either SrTiO_3 or LaAlO_3 [29], with a lattice mismatch between 0 to 16 %. In both studies, both films and substrates have the perovskite structure and 2-ethyl-hexanoate/toluene were the precursor solutions. Figure 16.4 shows the closely spaced and periodic dislocations at the $\text{SrZrO}_3/\text{SrTiO}_3$ interface [30]. The dislocation spacing 's' is nearly identical to that predicted with the relation, $s = b/\epsilon$, where b is the Burger's vector of the dislocation and ϵ is the strain associated with the lattice mismatch [27]. It should be noted that since the film has a larger lattice parameter relative to the substrate, the edge dislocations that terminate at the interface are missing planes within the film.

In a third study of epitaxy mechanisms, LiNbO_3 (precursor: hybrid alkoxide) was grown on basal plane Al_2O_3 substrates [31]. Both have similar structures with Li and Nb systematically replacing Al. The large lattice mismatch ($\approx 8\%$) appears to be responsible for the 'mosaic' character of the film and a second epitaxy orientation described by an in-plane rotation of 60° . 'Mosaic' character describes a film composed of small regions that are slightly rotated relative to one another and the substrate (up to 5 % in this case) [31]. 'Mosaic' regions are undesirable because their boundaries scatter light, and the grooves formed where the boundaries intersect the surface produces a 'rough' surface which also scatters light. Films grown by vapor routes have similar defects. A Fe_2O_3 epitaxial buffer layer (produced with a Fe-hexanoate precursor) between the Al_2O_3 substrate and LiNbO_3 film, which reduces the lattice mismatch to 2 %, lowers the 'mosaic' character and eliminates the in-plane, 60° rotation variant [31]. This evidence suggests that when the mismatch strain exceeds $\approx 8\%$, the epitaxy phenomena is not the grain growth phenomenon described above, but appears to occur by concurrent abnormal grain growth and an instability phenomena described in the section detailing instabilities.

Non-oxide epitaxial films can also be produced by the CSD method. A good example is the epitaxy of GaN on basal-plane [32, 33] and R-plane [34] sapphire and LiGaO₂ [35]. The GaN films were produced using two different precursors: gallium dimethyl amide, containing gallium–nitrogen bonds and gallium isopropoxide, containing gallium oxygen bonds [36]. Pyrolysis of the gallium dimethyl amide film at 600 °C produced a continuous layer of GaN grains with a single orientation relation with the substrate, identical to that of the GaN epitaxially grown on basal plane sapphire via MOCVD. Above this layer of epitaxial GaN grain was an overlying polycrystalline film similar to that discussed above. Namely, when the precursor crystallizes, only the grains in contact with the substrate have the preferred orientation dictated by the substrate. But the growth of the oriented grains into a single crystal thin film occurred by a very different mechanism. At temperatures greater than 600 °C, the oriented grains consumed the polycrystalline layer via evaporation–condensation mass transport. Evaporation-condensation occurs because GaN decomposes in the environment used for synthesis [36]. Pyrolysis at 600 °C of the films made with the alkoxide precursor, usually used to synthesize Ga₂O₃, produced a continuous layer of gallium oxynitride grains with the corundum structure in the NH₃ atmosphere, which was epitaxial relative to the corundum substrate. The epitaxial grains had an overlying polycrystalline gallium oxynitride film with a spinel structure. Increasing the temperature caused growth of oriented grains in contact with the substrate and their conversion of the oxynitride to wurtzite GaN at 800 °C. It is interesting to note that the reaction of Ga₂O₃ with ammonium would not be expected to produce GaN due to the positive change in free energy. The reason GaN does form is that the gaseous reaction product, H₂O, is swept out of the furnace and thus, cannot maintain an equilibrium partial pressure.

16.5.1 Multilayered, Epitaxial Films

Within the last decade, the use of the CSD method for producing epitaxial films has played an increasing role in the development of the ‘reel to reel’ processing of superconducting wires. The US Department of Energy has supported several large programs. Initially, all programs used metal substrates on which different epitaxial layers including the superconductor, YBa₂Cu₃O_{7-δ} (YBCO), was deposited by one of several vapor phase methods. In one program, a group at Oak Ridge National Laboratory (ORNL) lead by Goyal and colleagues [37], developed a highly textured ribbon of a Ni-W (5 atom %) as a substrate. To reduce the costs inherent to vapor phase processing, the ORNL program took the chance to explore the CSD method [1]. The superconducting wire produced at ORNL has a layered architecture on top of the Ni-W ribbon. Prior to any deposition, the textured substrate is sulfurized by annealing in H₂S gas to obtain a textured, $c(2 \times 2)$, monolayer of sulfur on the Ni–W surface. The sulfur imitates an epitaxial layer of oxygen that enables the deposition of the first epitaxial layer of an oxide. A series of epitaxial layers are then deposited on top of the Ni-W substrate. Currently, a ‘seed layer’ of Y₂O₃ is first placed on the sulfurized Ni-W substrate; it enables the epitaxial growth of the

second layer, a yttrium stabilized ZrO_2 , which is the buffer layer that inhibits the oxidation of the substrate. The third epitaxial layer is CeO_2 which enables the epitaxy of YBCO. With the exception of the YBCO, all layers are deposited using reactive sputtering.

Since ~2000, the fourth epitaxial layer, YBCO, has been synthesized with a CSD method (for details see Chap. 27). Because it was expected that Ba precursors would form BaCO_3 , which is stable to ~900 °C and would not react with the Y and Cu precursors at lower temperatures, a $\text{Ba}(\text{O}_2\text{CCF}_3)_2$ precursor, which forms BaF_2 , was shown by Gupta et al. [38] to be effective when water vapor was introduced between 200 to 400 °C. This process, known as the trifluoroacetate process, because all three elements were introduced as trifluoroacetates, is used by American Superconductors Inc. [39] to manufacture a commercial product known as the ‘second generation’ superconductor wire. In Xu et al. [40] showed that trifluoroacetates could be abandoned by simply using $\text{Ba}(\text{OH})_2$ and simpler, trimethyl acetate salts of copper, yttrium, ($\text{Y}(\text{C}_4\text{H}_9\text{COO})_3$ and $\text{Cu}(\text{C}_4\text{H}_9\text{COO})_2$). Later Xu et al. [41] showed that this precursor route will produced a good superconductor on a layered (Y_2O_3 , $\text{Zr}(\text{Y})\text{O}_2$, CeO_2) Ni-W substrate. It should be noted that the anhydrous form of $\text{Ba}(\text{OH})_2$ melts at ~400 °C, i.e., the temperature where water vapor is still being introduced during the trifluoroacetate process. This melt could be responsible for the thicker films that can be formed in this system. Most recently Wesolowski et al. [42] reported that some sort of melt phase is observed in both the trifluoroacetate and trimethyl acetate precursor approaches to YBCO synthesis.

In recent years, Paranthaman and colleagues [43] at ORNL first demonstrated that the barrier properties and the performance of a CSD epitaxial layer of $\text{La}_2\text{Zr}_2\text{O}_7$ (LZO) produced on top of the sputtered Y_2O_3 layer, matched that of the sputtered Zr ($\text{Y})\text{O}_2$ layer. More recently the same group has grown a La_3TaO_7 (LTO) seed layer directly on the biaxially textured Ni-W substrate that not only replaces the sputtered Y_2O_3 layer, but also improves the epitaxial texture of the next layer, LZO, also produced by the CSD method. Their current effort is to replace the sputtered CeO_2 layer with a CSD CeO_2 layer, to enable each successive CSD layer to be deposited by industrially scalable methods such as slot-die coating of metal-organic precursors [7].

The first non-government supported commercial product using the ‘second generation’ superconductor wire is a Magnetic Billet Heater manufactured by Zenergy Power, which is used for extruding aluminum billets [44].

Although not as profound as the application of CSD to superconducting wires, McNally et al. [45] demonstrated a three layer ferroelectric FRAM device, where each of the three layers were epitaxially synthesized on top of one another via the CSD method. The active material was $\text{Pb}(\text{Zr}_{0.5}\text{Ti}_{0.5})\text{O}_3$ (PZT), which was sandwiched between the oxide conductor, $\text{La}_{0.7}\text{Sr}_{0.3}\text{MnO}_3$ (LSMO). The first LSMO layer was epitaxially grown on a SrTiO_3 (STO) single crystal substrate. The LSMO/PZT/LSMO/ SrTiO_3 multilayered specimens were compared to devices in which the top electrode was a metal instead of the LSMO oxide electrode. The addition of a top oxide electrode to PZT/LSMO/ SrTiO_3 specimens was found to give larger polarization, lower coercive field values, and superior fatigue behavior

relative to metal electrodes. These values were similar to those obtained for oxide electrode-PZT combinations fabricated using vapor deposition techniques.

16.5.2 Thermodynamics of Morphological Instabilities

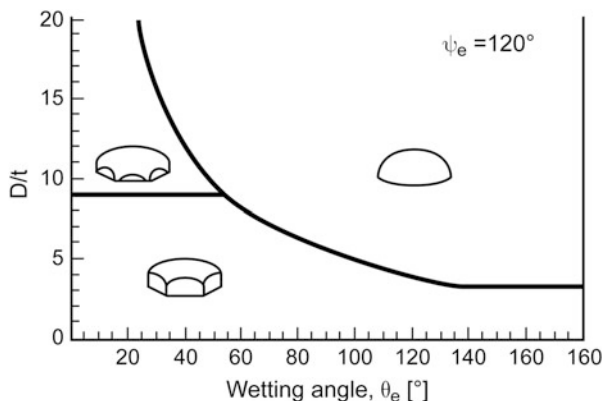
The most general case where the idea of templating becomes obscure, the film and substrate do not have the same structure. A polycrystalline film, which does not produce epitaxial grains, will undergo grain growth during heating as any other polycrystalline material until the grain size is equivalent to the film thickness. Once the in-plane dimension of the grains is larger than the film thickness, grains with specific orientations will undergo abnormal grain growth because of their lower surface and/or interfacial energy [46]. Namely, these grains will have a lower free energy relative to all other grains, and thus ‘consume’ neighboring grains by grain boundary motion. Thus, polycrystalline films with columnar microstructures are expected to undergo abnormal grain growth and to develop at least one preferred orientation even when the substrate is amorphous.

In addition to abnormal grain growth, the film can also undergo a morphological instability that causes it to uncover the substrate during grain growth. This phenomenon eventually produces a microstructure where every grain is an island and separated from one another. Srolovitz and Safran [47] were the first to predict this instability phenomena. They showed that a pin hole could grow in a polycrystalline thin film by the deepening of the grain boundary grooves at a three grain junction during grain growth. Miller et al. [48] confirmed this uncovering phenomenon with polycrystalline $Zr(Y)O_2$ thin films on sapphire substrates. They also presented a thermodynamic analysis showing that the break-up process lowers the free energy of the system when the grain size (D) to film thickness (t) ratio exceeds a critical value, $(D/t)_c$, which depends on the dihedral angle (a measure of the grain boundary to surface energy ratio) and the solid-state ‘wetting angle’ of the isolated grains ‘sitting’ on the substrate.

Miller et al. [48] summarized their thermodynamic calculations with an equilibrium, configurational diagram, shown in Fig. 16.5, where the D/t ratio is plotted as a function of the solid-state ‘wetting angle’ for a specific value of the ratio of the surface to grain boundary energies. One boundary in this diagram represents the condition (values of D/t and solid-state wetting angle) where the free energy of the coherent film (represented by hexagonal, truncated grains) is equal to that of the film broken into isolated, single crystal islands (spherical caps). A third configuration also exists where grains are still joined by grain boundaries, but the substrate is uncovered where three grains meet. As illustrated, the coherent film only exists over a small range of D/t . For very thin films, only a small amount of grain growth is required to cause the polycrystalline film to break-up, uncover the substrate and reduce the free energy of the system.

For most film applications, the instability phenomenon is unwanted. For example, if the polycrystalline film were to be used as an electrode, its break-up into

Fig. 16.5 Equilibrium configuration diagram for polycrystalline thin films with columnar microstructures. Boundaries represent the conditions (grain size/film thickness ratio and solid-state wetting angle) where different configurations have the same free energy [48]



isolated islands would prohibit in-plane connectivity and thus, conductivity. On the other hand, the break-up into isolated, highly oriented single crystal islands can be used for a variety of applications. In one, if the single crystal islands are truly epitaxial, with a single orientational relation with the substrate both in-plane and out of plane, they can be used to produce ‘seeds’ to grow another material as a thin film. This was first accomplished by Kim and Lange [49] when it was found that the lattice mismatch between the PbTiO_3 and LaAlO_3 , two perovskites, was too large to produce an epitaxial film without many defects. To reduce the defects, a very thin polycrystalline film of PbTiO_3 was produced and heat treated to break-up the film into oriented single crystal islands on the LaAlO_3 substrate. A second coating of the PbTiO_3 precursor was then applied to the substrate containing oriented islands. After a second heat treatment, the large oriented islands consumed the very small grains within the film to produce a single crystal film with fewer defects. In another application of this ‘seeding’ method, ‘seeds’ of ZrO_2 were produced on a basal plane sapphire substrate, where all grains had a single out-of-plane orientation, but due to the threefold symmetry axis of the underlying substrate, the cubic ZrO_2 seeds had three in-plane variants, each related to one another by 120° [50]. In a third example [31], because of the large lattice mismatch ($\sim 9\%$) between LiNbO_3 , which has an ‘ α -alumina like’ structure, and a basal-plane alumina substrate, a poly-variant LiNbO_3 forms. To avoid this, it was discovered that a single variant film could be produced using a two-step process. Namely, the first step produced a single variant at a lower temperature, whereas recoating produced an epitaxial film with the single variant [31]. One might comment on the La_3TaO_7 (LTO) seed layer reported by Bhuiyan et al. [51] discussed above. The published micrographs suggest that the isolated ‘seeds’ act in the same way as discussed for the last three examples. Namely, isolated LTO single crystal islands, produced by the grain growth phenomenon sited above, were the ‘seeds’ for the growth of the $\text{La}_2\text{Zr}_2\text{O}_7$ (LZO) buffer layer, which is one part of the layered architecture of the superconductor wire. One more example can be given where lead titanate nano islands were produced by breaking up a film produced by the CSD method on a polycrystalline Pt substrate [52].

A second type of morphological instability, which causes a single crystal film to uncover the substrate, was recently discovered [53] when very thin, single crystal PbTiO_3 films were grown on a SrTiO_3 . This instability is observed when the surface of a hole has a lower specific energy than the surface of the film. Experimental observations showed that three different film-configurations may exist, which depends on the film thickness: thick films completely cover the substrate whereas pre-existing holes in thinner films can grow to either form a continuous film containing an equilibrium area fraction of holes or they can grow together to cause the film to break-up into single crystal islands. A free energy model, which includes surface energy anisotropy and the spacing between pre-existing holes, was used to explain this instability phenomenon [54]. The model showed, similar to the experimental results, that pre-existing holes in thinner films will uncover the substrate. It was also found that for the range of surface energies commonly observed in the inorganic materials of interest, pre-existing holes, greater than a critical size, are necessary to initiate the instability.

16.5.3 *Epitaxy of Dissimilar Structures*

The different examples for epitaxial materials discussed above neglected to comment that the structure of the film material was different than that of the substrate. Two examples taken from the discussion of superconductors above are, from the substrate to the top, $\text{Ni-W}/\text{Y}_2\text{O}_3/\text{Zr}(\text{Y})\text{O}_2/\text{CeO}_2/\text{YBa}_2\text{Cu}_3\text{O}_{7-\delta}$, and $\text{Ni-W}/\text{La}_2\text{Zr}_2\text{O}_7/\text{La}_2\text{Zr}_2\text{O}_7/\text{CeO}_2/\text{YBa}_2\text{Cu}_3\text{O}_{7-\delta}$. Another is the epitaxy of ZrO_2 on Al_2O_3 [50, 55]. The question is why does one structure template a totally different structure? And, how can one predict this occurrence?

For identical structures, with different lattice spacing, e.g., BaTiO_3 epitaxially grown on SrTiO_3 (both perovskites), the misfit strain due to their differential lattice spacing can be conceptually related to the excess energy associated with the interface, due to the predictable dislocation density at the interface. This conceptual relation is not apparent when the two structures are different, and thus differential strain cannot be the only tool used to explain special crystallographic relations between two dissimilar structures.

The coincident site lattice (CSL) model has often been used to understand the frequent occurrence of special interfaces between two lattices [27]. It was first used to understand the interfaces that join together two identical crystals, namely grain boundaries. The CSL model was of limited success in predicting the formation of special grain boundaries in metals. With this limited success, it has been assumed that the plane with the largest number of coincident sites might have the lowest free energy. Later, the CSL model has been used to explain the special interfaces observed between two crystals with dissimilar structures [55]. When applied to dissimilar structures, the requirement for exact coincidence of lattice sites is usually

relaxed, such that when lattice vectors in the two structures are compared, some differential is allowed, giving rise to the term near coincident site lattice (NCSL) model.

Determining a CSL (or NCSL) starts by rotating the two lattices about an invariant direction (normal to the interface) to seek a rotation, via a computer search, with the greatest density of coincident lattice sites, i.e., sites in one lattice that overlay sites in the second lattice [55]. Alternately, one can seek a rotation vector and a rotation angle to determine the plane that would contain the largest number of coincident sites. For the near coincidence site lattice (NCSL) principle, translation vectors in both lattices need not perfectly match one another. It was anticipated that planes with the largest density of coincident sites (or near coincident sites) would have a low interfacial energy. Although CSL (or NCSL) representations can be formed with known epitaxial relations between dissimilar structures, other possible, however, not observed, NCSL relations can be formed with the same invariant rotational axis that produces identical coincident site densities with similar misfit allowances [55, 56]. Thus, the NCSL model cannot necessarily predict an epitaxial relation even when the invariant rotation axis is known. In addition the NCSL model does not address the coordination of atoms of one type by those of the other type, at the interface.

Recently, a new understanding was discovered [54, 57, 58]. It uses the two simple rules of crystal chemistry to understand epitaxial orientation relations between dissimilar structures formed by non-metallic, inorganic materials. The first rule pertains to the fact that the (generally smaller) cations are coordinated by a specific number of anions, referred to as the coordination number, which depends on the size ratio of the cations to anions. With this simple rule, it was hypothesized that the first, and most important, rule must be obeyed for cations and anions that make up the interface. The second rule states that the charge associated with the cations and anions within a space that includes the interface, should balance to zero. These two rules are commonly used to select a stable of different cations and anions that substitute for one another to form specific structures.

The two rules, coordination number and charge balance, are the important first two of the five statements known as “Pauling’s rules” [59–61]. The first rule states that a coordination polyhedron of anions is formed about each cation in the structure, where the coordination number is determined by the ratio of the radii of the two ions. Although this appears to imply purely ionic bonding, it also applies to a mixture of ionic/covalent bonding, and covalent bonding between like atoms, e.g., Si, C, etc. In a crystal structure, the polyhedra formed by anions and coordinated cations are arranged in three dimensions to optimize the nearest neighbor interactions. A stable structure must be electrically neutral at the unit cell level. Pauling’s second rule describes the base for evaluating charge neutrality. Pauling’s third rule further describes the linking of different (or like) polyhedra. Although all linkages are possible, more stable structures link at corners, relative to edges and faces, etc. The fourth and fifth rules further express the linkage and the joining of different polyhedra. Pauling and Brown further elaborated the bonding as a ‘Valence-Bond’ rule [62]. It can be shown that these same rules govern the epitaxial relation between two dissimilar structures. Namely, as detailed elsewhere [58],

what explains the relative placement of atoms in a three dimensional structure, must also apply to their placements at interfaces between two different structure, where each has a special orientation relation to one another.

16.6 Patterning

Many device applications, e.g., optical wave guides, require patterned thin films. After forming a precursor film produced with mixed, metal carboxylates, such as hexanoates, Mantese et al. [15] have formed useful device patterns by only pyrolyzing the selected regions with a scanning laser. Un-scanned areas can be simply washed away with the same solvent used to formulate the initial precursor solution. Yogo et al. [63] have applied photolithography techniques to form patterns by adding a photo sensitive chemical (1-phenyl-1,3-butanedione), designed to have a specific ultraviolet absorption at 330 nm, to their mixed alkoxide precursor to form patterned, single crystal films of LiNbO_3 on sapphire substrates by masking and exposure.

Jeon et al. [10] adopted the innovative method developed by Kumar and Whitesides [64] of stamping hydrophobic patterns on nearly any surface to produce patterned, epitaxial LiNbO_3 films on sapphire. This method uses a rubber stamp and an 'ink' that renders the stamped surface hydrophobic. The rubber stamp is produced from a relief pattern formed on a Si substrate by conventional photolithography and etching techniques, and thus has the potential for sub-micron resolution. The inks are bi-functional molecules; one end reacts with the -metal-OH surface sites to chemically attach a hydrocarbon chain, which renders the surface it prints, hydrophobic. Jeon et al. [10] demonstrated that a spun-on precursor does not bond to the substrate at hydrophobic sites, and thus is easily removed after pyrolysis.

Moran and Lange [8] developed a method using the PDMS stamp procedure developed by Kumar and Whitesides [64], but instead of using the raised plateaus to define the pattern, they used the channels. Namely, the channels were filled with the precursor solution by spin coating the PDMS stamp. During spin coating, the solution evaporates leaving the precursor molecules behind within the channels. The material within the channels is then transferred to the substrate by stamping. Moran and Lange showed that during solvent evaporation, the precursor shrinks away from the channels, forming cracks along the sidewalls. During stamping, the solid precursor within the channel makes contact with the substrate. When the stamp is lifted away from the substrate, and the precursor within the channel adheres to the substrate, the crack between the precursor, the side walls and bottom of the channel will extend. They detailed the fracture mechanics of this process to enable the design of surface adhesion of the precursor molecules with the PDMS and substrate that will produce stamped patterns without defects. They also showed that photoresist could be easily stamped onto different substrates with this method they called "Channel Stamping", thus avoiding costly photolithography. Kim et al. [65] showed that they could pattern the lead-free ferroelectric, $\text{SrBi}_2\text{Ta}_2\text{O}_9$,

on SrTiO₃ substrates via Channel Stamping. More recently, Clemens et al. [66] developed a ‘bottom-up’ method of growing periodic Pb(Zr,Ti)O₃ ferroelectric nano-crystals that are epitaxial with the underlying substrate. In this approach, a number of different steps and chemical processes were involved, centered around the use of electron lithography to define the periodic, nano-pattern.

16.7 Looking Forward

As discussed above, the major limitation of CSD is film thickness. In general, films thicker than 100–200 nm must be formed by multiple deposition/pyrolysis cycles, which is not only costly, but also introduces defects. Routes to solve this problem have been identified. One, the incorporation of a polymer that increases the precursor film’s crack growth resistance has been introduced [20], but not followed up to this author’s knowledge. A second route where the pyrolyzed precursor forms a melt has also been identified [20], and is more than likely why YBCO films are generally much thicker than other materials formed by the CSD method. This route should be further explored. Innovations in this area are needed.

It appears that if superconducting wires will ever be universally commercialized, it will be due to the relatively inexpensive CSD method used in its manufacture. The question is: what other large scale commercial opportunities exist for epitaxial CSD films. As pointed out by several research groups, CSD could impact the further development of non-volatile ferroelectric random access memory (FeRAM) devices [67] as well as ferroelectric mass-storage [68]. The Waser Group at RWTH-Aachen [66] is working towards this commercial goal using CSD.

ZnO offers one of the greatest opportunities for epitaxial CSD processing. ZnO is a wideband gap, transparent semiconductor, and resembles GaN in many ways, viz., structure, band gap, etc., the semiconductor used for white lighting. The bandgap of ZnO can be engineered between 3 and 4 eV by substituting Mg and Cd for Zn, respectively [69]. Band gap engineering is required for obtaining different colors. Unlike GaN, ZnO is currently processed by all methods only as a n-type semiconductor; consistent synthesis p-type, by any means, has yet to be accomplished. But, unlike GaN, large single crystal substrates of ZnO can be produced by several methods [2]. Single crystal substrates of the same material are important in reducing threading dislocations that trap electrons and holes, reducing the luminescence efficiency. The lack of large GaN single crystal is one factor that is currently limiting the mass production of large, white LEDs needed for the economic replacement of florescent lighting, at great energy savings. Assuming a p-ZnO will be developed, several research objectives will need to be implemented to enable ZnO Light Emitting Diode (LED) production via CSD. First, high purity precursors need to be developed. This objective should be easy since Metal Organic Chemical Vapor Deposition (MOCVD), a commercial production method of current GaN LEDs, uses similar, but volatile, metal organic molecules. Namely, if one can commercially produce high purity volatile precursors, one should be able to

produce pure, non-volatile precursors. It should be noted here that a large fraction of these expensive volatile precursors are lost in the MOCVD process as they 'shower' the substrate. Second, sophisticated LEDs are not a simple, single p-n junction, but are formed of multiple layers with nanometer dimensions. One reason for the multiple layers is to grade lattice mismatch between different materials, namely, substrate to semiconductor, etc. The principle reason is that single and multiple quantum wells are used to better 'collect' electrons and holes. Thus, to implement this multiple layered architecture for ZnO (or GaN) CSD technology must become more sophisticated to produce the desired, multiple nano layers. No theoretical or experimental limitation to this object can be seen to impede this paradigm shift.

References

1. Paranthaman MP, Izumi T (2004) High-performance YBCO-coated superconductor wires. *MRS Bull* 29:533–541
2. Ehretraut D, Sato H, Kagamitani Y, Sato H, Yoshikawa A, Fukuda T (2006) Solvothermal growth of ZnO. *Prog Cryst Growth Char Mater* 52:280–335
3. Lange FF, Goh GKL (2001) Hydrothermal epitaxial growth of perovskite films. *J Ceram Proc Res* 2:4–8
4. Richardson JJ, Lange FF (2009) Controlling low temperature aqueous synthesis of ZnO. Part I and II. *Cryst Growth Des* 9:2570–2575
5. Leroy E, Robin-Brosse C, Torre TP (1984) In: Hench LL, Ulrich DR (eds) *Ultrastructure processing of ceramics, glasses, and composites*. Wiley, New York
6. Pike RD, Cui H, Kershaw WR, Dwight K, Wold A, Blanton TN, Wernberg AA, Gysling HJ (1993) Preparation of ZnS thin films by ultrasonic spray pyrolysis from bis(diethylthiocaramoto) Zinc(II). *Thin Solid Films* 224:221–226
7. Heatherly L, Hsu H, Wee SH, Li J, Sathyamurthy S, Paranthaman M, Goyal A (2007) Slot die coating and conversion of LZO on rolling assisted biaxially textured Ni-W substrates with and without a very thin seed layer in low vacuum. *IEEE Trans Appl Supercond* 17:3417–3419
8. Moran PM, Lange FF (1999) Microscale lithography via channel stamping: relationships between capillarity, channel filling and debonding. *Appl Phys Lett* 74:1332–1334
9. Trau M, Yao N, Kim E, Xia Y, Whitesides GM, Aksay IA (1997) Microscopic patterning of orientated mesoscopic silica through guided growth. *Nature* 390:674–676
10. Jeon NL, Clem PG, Payne DA (1996) A monolayer-based lift-off process for patterning chemical vapor deposition copper thin films. *Langmuir* 12:5350–5355
11. Schwartz RW, Schneller T, Waser R (2004) Chemical solution deposition of electronic oxide films. *C R Chim* 7:433–461
12. Golden SJ, Lange FF, Clarke DR, Chang LD, Necker CT (1992) Metalorganic deposition of high J_c thin films in the Bi-Pb-Sr-Ca-Cu-O system on 100 LaAlO₃ substrates. *Appl Phys Lett* 61:351–353
13. Livage J, Henry M, Sanchez C (1988) Sol-gel chemistry of transition-metal oxides. *Prog Solid State Chem* 18:259–341
14. Brinker CJ, Scherer GW (1990) *Sol-gel science*. Academic, New York
15. Mantese JV, Micheli AL, Hamdi AH, Vest RW (1989) Metalorganic deposition (MOD): a non vacuum, spin-on, liquid-based, thin film method. *MRS Bull* 14:48–53
16. Polli AD, Lange FF, Levi CG (2000) Metastability of the fluorite, pyrochlore and perovskite structures in the PbO-ZrO₂-TiO₂ system. *J Am Ceram Soc* 83:873–881

17. Evans AG, Dory MD, Hu MS (1988) Cracking and decohesion of thin films. *J Mater Res* 3:1043–1049
18. Gille G (1985) In: Kaldis E (ed) *Current topics in materials science*. Amsterdam, North Holland
19. Hutchinson JW, Suo Z (1991) In: Hutchinson JW, Wu TY (eds) *Advances in applied mechanics*. New York, Academic
20. Roeder RK, Slamovich EB (1999) Measuring the critical thickness of thin metalorganic precursor films. *J Mater Res* 14:2364–2368
21. Leung DK, Chang CJ, Rühle M, Lange FF (1991) Metastable crystallization, phase partitioning, and grain growth of ZrO_2 - Gd_2O_3 materials processed from liquid precursors. *J Am Ceram Soc* 74:2786–2792
22. Balmer ML, Lange FF, Levi CG (1992) Metastable phase selection and partitioning in ZrO_2 - Al_2O_3 processed from liquid precursors. *J Am Ceram Soc* 75:946–952
23. Levi CG (1998) Metastability and microstructure evolution in the synthesis of inorganics from precursors. *Acta Mater* 46:787–800
24. Miller KT, Chan CJ, Cain MG, Lange FF (1993) Epitaxial zirconia thin films from aqueous precursors. *J Mater Res* 8:169–177
25. Müller KT, Lange FF (1989) Single crystal zirconia thin films from liquid precursors. In: Aksay IA, McVay GL, Ulrich DR (eds) *Processing science of advanced ceramics*, vol 155. MRS, Pittsburgh, p 191
26. Bauer EG, Dodson BW, Ehrlich DJ (1990) Fundamental issues in heteroepitaxy—a department of energy council-on-materials science panel report. *J Mater Res* 5:852–894
27. Sutton AP, Balluffi RW (1995) *Interfaces in crystalline materials*. Clarendon, Oxford
28. Langjahr PA, Wagner T, Lange FF, Rühle M (2003) Epitaxial growth and structure of highly mismatched oxides with rock-salt structure on MgO. *J Cryst Growth* 256:162–173
29. Langjahr PA, Wagner T, Rühle M, Lange FF (1996) Epitaxial growth and structure of cubic and pseudocubic perovskite films on perovskite substrates. In: Speck JS, Fork DK, Wolf RM, Shiosaki T (eds) *Materials research society symposium proceedings, Epitaxial oxide thin films II*, vol 401. Pittsburgh, PA, pp 109–114
30. Langjahr PA, Lange FF, Wagner T, Rühle M (1998) Lattice mismatch accommodation in perovskite films on perovskite substrates. *Acta Mater* 46:773–785
31. Derouin TA, Lakeman CDE, Wu XH, Speck JS, Lange FF (1997) Effect of lattice mismatch on the epitaxy of sol-gel $LiNbO_3$ thin films. *J Mater Res* 12:1391–1400
32. Puchinger M, Wagner T, Fini P, Kisailus D, Beck U, Bill J, Aldinger F, Arzt E, Lange FF (2001) Chemical solution deposition derived buffer layers for MOCVD-grown GaN films. *J Cryst Growth* 233:57–67
33. Puchinger M, Wagner T, Rodewald D, Aldinger F, Lange FF (2000) Gallium nitride thin layers via a liquid precursor route. *J Cryst Growth* 208:153–159
34. Puchinger M, Kisailus DJ, Lange FF, Wagner T (2002) Microstructural evolution of precursor-derived gallium nitride thin films. *J Cryst Growth* 245:219–227
35. Kisailus D, Lange FF (2001) Growth of epitaxial GaN on $LiGaO_2$ substrates via a reaction with ammonia. *J Mater Res* 16:2077–2081
36. Kisailus D, Choi JH, Lange FF (2002) Chemical solution deposited GaN films from oxygen- and nitrogen-based precursors. *J Mater Res* 17:2540–2548
37. Goyal A, Budai JD, Kroeger DM, Norton DP, Specht ED, Christen DK (1998) Structures having enhanced biaxial texture and method to fabricating same—I. US Patent 5,739,086
38. Gupta A, Jaganathan R, Cooper EI, Giess EA, Landman JI, Hussey BW (1988) Superconducting oxide-films with high transition temperatures prepared from metal trifluoroacetate precursors. *Appl Phys Lett* 52:2077
39. Rupich MW, Verebelyi DT, Zhang W, Kodenkandath T, Li XP (2004) High-temperature superconductor wires. *MRS Bull* 29:572–578

40. Xu YL, Shi DL, McClellan S, Buchanan R, Wang SX, Wang LM (2001) Deposition of epitaxial YBCO thin film on single domain YBCO substrate for the development of RF components. *IEEE Trans Appl Supercond* 11:2865–2868
41. Xu Y, Goyal A, Leonard KJ, Specht ED, Shi D, Paranthaman M (2006) Processing dependence of texture, and critical properties of $\text{YBa}_2\text{Cu}_3\text{O}_{7-\delta}$ films on RABiTS substrates by a non-fluorine MOD method. *J Am Ceram Soc* 89:914–920
42. Wesolowski DE, Patta YR, Cima MJ (2009) Conversion behavior comparison of TFA–MOD and non-fluorine solution-deposited YBCO films. *Phys C* 469:766–773
43. Paranthaman MP, Bhuiyan MS, Sathyamurthy S, Heatherly L, Cantoni C, Goyal A (2008) Improved textured $\text{La}_2\text{Zr}_2\text{O}_7$ buffer on La_3TaO_7 seed for all-MOD Buffer/YBCO coated conductors. *Phys C* 468:1587–1590
44. Kellers J, Bührer C, Hagemann H, Ostermeyer B, Witte W (2009) Magnetic billet heating rivals conventional furnaces. *Heat Process* 7:205–210
45. McNally F, Kim JH, Lange FF (2000) Fatigue properties of lanthanum strontium manganate-lead zirconate titanate epitaxial thin film heterostructures produced by a chemical solution deposition method. *J Mater Res* 15:1546–1550
46. Thompson CV (1990) Grain growth in thin films. *Annu Rev Mater Sci* 20:245–268
47. Srolovitz DJ, Safran SA (1986) Capillary instabilities in thin films. Part I energetics and part II kinetics. *J Appl Phys* 60:247–260
48. Miller KT, Lange FF, Marshall DB (1990) The instability of polycrystalline thin films: experiment and theory. *J Mater Res* 1:151–160
49. Kim JH, Lange FF (1999) Seeded epitaxial growth of PbTiO_3 thin films on (001) LaAlO_3 using the chemical solution deposition method. *J Mater Res* 134:1626–1633
50. Miller KT, Lange FF (1991) Highly oriented thin films of cubic zirconia on sapphire through grain growth seeding. *J Mater Res* 6:2387–2392
51. Bhuiyan MS, Paranthaman M, Sathyamurthy S (2007) All solution-based epitaxial oxide films on biaxially textured Ni-W substrates with improved out-of-plane texture for YBCO-coated conductors. *J Electron Mater* 36:1270–1274
52. Clemens S, Schneller T, Waser R, Ruediger A, Peter F, Kronholz S, Schmitz T, Tiedke S (2005) Integration of ferroelectric lead titanate nanoislands for direct hysteresis measurements. *Appl Phys Lett* 87:142904
53. Seifert A, Vojta A, Speck J, Lange FF (1996) Microstructural instability in single-crystal thin films. *J Mater Res* 11:1470–1482
54. Andeen D, Loeffler L, Padture N, Lange FF (2003) Crystal chemistry of epitaxial ZnO (111) MgAl_2O_4 produced by hydrothermal synthesis. *J Cryst Growth* 259:103–109
55. Cain MC, Lange FF (1994) Heteroepitaxy of cubic zirconia on basal and prismatic planes of sapphire. *J Mater Res* 9:674–686
56. Navaco AD, McTague JP (1977) Orientational epitaxy – the orientational ordering of incommensurate structures. *Phys Rev Lett* 38:1286–1289
57. Jewhurst SA, Andeen D, Lange FF (2005) Crystal chemistry of the epitaxy of cristobalite (SiO_2) on basal plane sapphire. *J Cryst Growth* 280:168–172
58. Andeen D, Lange FF (2007) Crystal chemistry of interfaces formed between two different non-metallic, inorganic structures. *Int J Mater Res* 98:1222–1230
59. Pauling L (1960) Nature of the chemical bond, 3rd edn. Cornell University Press, Ithaca, NY
60. Evans RC (1964) An introduction to crystal chemistry, 2nd edn. Cambridge University Press, London
61. Roy R, Muller O (1974) Crystal chemistry of non-metallic materials: the major ternary structural families. Springer, Heidelberg
62. Brown ID, Altermatt D (1985) Bond-valence parameters obtained from a systematic analysis of the inorganic crystal structure database. *Acta Crystallogr B Struct Sci* 41:244–247
63. Yogo T, Takeichi Y, Kikuta K, Hirano SI (1995) Ultraviolet patterning of alkoxy-derived lithium niobate film. *J Am Ceram Soc* 78:1649–1652

64. Kumar A, Whitesides GM (1993) Features of gold having micrometer to centimeter dimensions can be formed through a combination of stamping with an elastomeric stamp and an alkanethiol ink, followed by chemic etching. *Appl Phys Lett* 63:2002–2004
65. Kim JH, Lange FF, Cheon C-I (1999) Epitaxial growth of patterned $\text{SrBi}_2\text{Ta}_2\text{O}_9$ lines by channel stamping. *J Mater Res* 14:1194–1196
66. Clemens S, Schneller T, van der Hart A, Peter F, Waser R (2005) Registered deposition of nanoscale ferroelectric grains by template-controlled growth. *Adv Mater* 17:1357–1361
67. Auciello O, Scott JF, Ramesh R (1998) Processing technologies for ferroelectric thin films and heterostructures. *Annu Rev Mater Sci* 28:501–531
68. Tybell T, Paruch P, Giamarchi T, Triscone JM (2002) Domain wall creep in epitaxial ferroelectric $\text{Pb}(\text{Zr}_{0.2}\text{Ti}_{0.8})\text{O}_3$ thin films. *Phys Rev Lett* 89:097601
69. Makino T, Segawa Y, Kawasaki M, Ohtomo A, Shiroki R, Tamura K, Yasuda T, Koinuma H (2001) Band gap engineering based on $\text{Mg}_x\text{Zn}_{1-x}\text{O}$ and $\text{Cd}_y\text{Zn}_{1-y}\text{O}$ ternary alloy films. *Appl Phys Lett* 78:1237–1239

Chapter 17

Orientation and Microstructure Design

Susanne Hoffmann-Eifert and Theodor Schneller

17.1 Introduction

Crystalline film formation typically occurs from the amorphous phase through a *nucleation & growth* process. In Chap. 15 ‘*Thermodynamics and Heating Processes*’ it has been shown that for chemical solution deposited (CSD) thin films already the first pyrolysis step has an impact on the film densification process and thereby on the film microstructure and orientation. In most cases CSD films have to be heated to even higher temperatures for crystallization into the final structure to occur. The high temperature steps involve thermolysis and structural relaxation reactions, crystallization and dissolution of intermediate phases, and finally the crystallization of the desired phase. All intermediate steps influence the nucleation and growth process of the crystalline structure and by this affect the grain size and orientation, in other words the morphology of the films. Therefore a careful understanding of the crystallization process of a given material system depending on the applied precursor chemistry, the heating processes and atmospheres, and the underlying substrate material is inevitable for the growth of thin films of high and reproducible quality. At the same time the strong effect of external processing parameters on crystallization opens up the possibility to tailor the final microstructure and orientation of thin films deposited by CSD if the decisive controlling parameters are once known. For the thermodynamic basics of nucleation theory the reader may be referred to Chaps. 15 and 16 where crystallization processes are described fundamentally in the model of glass crystallization theory. For many practical applications of oxide thin films, the adjustment of a certain microstructure

S. Hoffmann-Eifert (✉)

Peter Grünberg Institut and JARA-FIT, Forschungszentrum Jülich, Germany

e-mail: su.hoffmann@fz-juelich.de

T. Schneller

Institut für Werkstoffe der Elektrotechnik II, RWTH Aachen University, Aachen, Germany

and a certain orientation is of utmost importance to obtain the desired properties of thin films, especially for materials with anisotropic physical properties as is shown in several chapters of this book.

17.2 Crystallization of Amorphous Films

Briefly crystallization is characterized by a competition between homogeneous nucleation events within the volume of amorphous films and heterogeneous nucleation events at the interfaces (substrate-film and/or substrate-atmosphere) or at seeds (foreign particles or intermediate phases) within the amorphous matrix. The initial stages of growth of the desired phase starting from an amorphous matrix are schematically shown in Fig. 17.1a–c. Each of these events has its specific nucleation and growth rate and one might dominate over the other (for comparison see [1–3]). Columnar growth in CSD derived films can only be obtained if the possibility for heterogeneous nucleation at the interface (preferably substrate/film) is favored over all other basically possible nucleation events. It should be mentioned that during the crystallization of an initially amorphous matrix also a competition of the nucleation of different phases may occur, which of course affects the crystallization of the desired phase. In certain cases, the formation of a metastable intermediate phase is advantageous for the crystallization of the desired phase with a certain texture (e.g. crystallization of PZT via the fluorite phase [4]). The competition of the nucleation of different phases can for example be initialized by tiny inhomogeneities of the cation or anion stoichiometry at the nanoscale.

Another important parameter for the phase formation is the control of the partial pressure of volatile species during crystallization. In thin film production lines this can be a rather difficult task because the thin film crystallization is mostly not performed in a sealed environment but in a continuous gas stream. Therefore different alternatives have been proposed to compensate evaporation of volatile compounds in order to avoid the formation of non-desired phases during crystallization like for example adding a well-controlled excess of the volatile compound, making use of as deposited gradients or depositing an enriched capping layer. Some of these ‘tricks’ will be found in next paragraphs which deal with the case studies of ferroelectric $\text{Pb}(\text{Zr},\text{Ti})\text{O}_3$ and high- k $(\text{Ba},\text{Sr})\text{TiO}_3$ thin films.

Beside the control of compositional homogeneity also the control of grain size and texture are of predominant importance for the application of ferroelectric and high- k thin films. Basically, this is originating from the non-centro-symmetric materials properties which are inherent to ferroelectrics. Again different technological approaches are available to address these topics. In the case study of high- k $(\text{Ba},\text{Sr})\text{TiO}_3$ thin films it will be shown how the grain size can be adjusted by the control of the nucleation events resulting in thin film morphologies which range from nanocrystalline to columnar shaped grains. In the case study of ferroelectric $\text{Pb}(\text{Zr},\text{Ti})\text{O}_3$ thin films the texture control will be addressed by demonstrating the importance of the underlying substrate material for the initialization of textured growth. In this case a control with regard to texture selection might be enabled if the

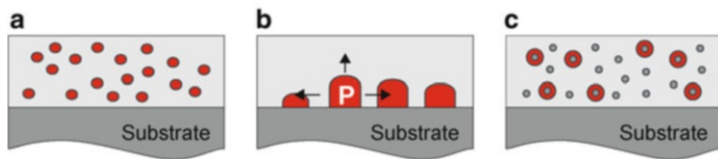


Fig. 17.1 Schematic illustrations of the different nucleation events which can take place during crystallization of amorphous CSD thin films. (a) homogeneous nucleation, (b) heterogeneous nucleation events at the interface, and (c) heterogeneous nucleation events at seeds

lattice constants of the substrate and the crystalline film are matching. Table 17.1 summarizes exemplarily some lattice constants of alkaline earth and lead based titanates and the corresponding misfit of the (111) oriented unit cells to (111) textured platinum to show where textured growth should be possible.

As will be shown in the next sections, sometimes, in spite of relatively good lattice matching, special tricks like artificial seeds or seed layers are necessary to force the textured growth in a certain direction (see also Chap. 21).

Thus, important parameters which govern the microstructure and orientation evolution are (1) precursor chemistry, (2) atmosphere, (3) processing temperature, (4) heating ramp, (5) seed layers, (6) compositional inhomogeneities, and (7) the underlying substrate material. In the following sections the evolution of different morphologies and textures, respectively, will be explained by taking the influencing factors mentioned above into account. By means of two technologically important case study materials, i.e. ferroelectric $\text{Pb}(\text{Zr,Ti})\text{O}_3$ (PZT) and high- k $(\text{Ba,Sr})\text{TiO}_3$ (BST) it will be discussed how the detailed knowledge of the effects of these different parameters enables the design of microstructure and orientation.

17.3 Case Study I: Crystallization of $\text{Pb}(\text{Zr}_x\text{Ti}_{1-x})\text{O}_3$ Films

Lead titanate based material systems will serve in this section as prime example to explain different facets of heterogeneous nucleation. Since lead titanate itself is relatively difficult to grow crack free on platinized silicon substrates and since the coercive voltage is relatively high, which makes it less attractive for device integration, most work in the field of ferroelectric and piezoelectric thin films has been directed to zirconia substituted lead titanate ($\text{Pb}(\text{Zr}_x\text{Ti}_{1-x})\text{O}_3$) with various compositions. For memory applications typically tetragonal compositions ranging from 20 to 40 % substitution of Ti by Zr are preferred since they feature high remanent polarization and relatively low coercive voltage. From a look to the tetragonal distortion of the unit cell (Table 17.1) it becomes clear that the highest remanent polarization is expected if the PZT grains grow along the c -axis direction perpendicular to the substrate surface, i.e. (001) oriented grains. This however is typically not possible on platinized silicon substrates due to ~ 150 MPa tensile stress arising in the crystallized film during cooling through the Curie temperature caused

Table 17.1 Lattice constants of selected materials and compositions

Material/ composition	System at RT	Lattice constants		Inplane distance (111) d_i [Å]	Misfit to ^a (111) Pt [%]	References
		a [Å]	c [Å]			
Pt	Cubic	3.92(4)	–	5.55	0	[5]
Pt _x Pb	Cubic	4.05	–	5.73	+3.24	[6]
PbTiO ₃	Tetragonal	3.902	4.156	5.64	+1.62	[7]
Pb(Zr _{0.2} Ti _{0.8})O ₃	Tetragonal	3.965	4.110	5.68	+2.34	[8]
Pb(Zr _{0.3} Ti _{0.7})O ₃	Tetragonal	3.992	4.108	5.70	+2.70	[9]
Pb(Zr _{0.44} Ti _{0.46})O ₃	Tetragonal	4.017	4.139	5.74	+3.42	[10]
SrTiO ₃	Cubic	3.905	–	5.52	–0.54	[11]
(Ba _{0.6} Sr _{0.4})TiO ₃	Cubic	3.965	–	5.61	+1.08	[12]
(Ba _{0.67} Sr _{0.33})TiO ₃	Tetragonal	3.972	3.970	5.62	+1.26	[13]
BaTiO ₃	Tetragonal	3.994	4.038	5.67	+2.16	[14]

^aSince platinized silicon substrates are a very typical and often applied substrate for CSD, the lattice mismatch is calculated with regard to the usual (111) texture of the Pt-layer. For this purpose averaged distances (d_i) of the atoms (ions) in the (111) plane were calculated from the lattice constants of each material according to $d_i = \left(\sqrt{2a^2} + 2\sqrt{a^2 + c^2} \right) / 3$ ($c = a$ in cubic case).

Then the misfit was determined according to $Misfit = \frac{(d_i(\text{Material}) - d_i(\text{Pt}))}{d_i(\text{Pt})} \cdot 100 \%$

by the thermal expansion mismatches between the film and substrate [15]. Hence the second best growth direction would be along the body diagonal. In particular for memory applications, where a high remanent polarization is a major issue, the processes have to be designed to obtain highly (111) textured PZT films. In addition a columnar microstructure is preferred over a grainy microstructure because it eliminates grain boundaries in a direction perpendicular to the switched field. For piezoelectric applications (for details see Chap. 25) compositions around the morphotropic phase boundary (~PZT 53/47) are advantageous. As will be shown there texture orientation control requires special measures, such as seed layers etc. In the following the “natural” orientation development, i.e. after film deposition on bare platinized silicon substrates is described. For details to the different applied tricks the reader is referred to the Chaps. 21 and 25.

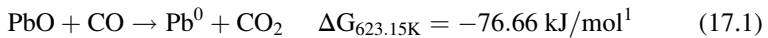
At first the different stages of the processing are briefly described to show crucial factors which influence the microstructure evolution process. Starting point is always the precursor solution. Most of the PZT precursor solutions (for details see Chap. 3) are based on lead (II) acetate (with and without crystal water), zirconium tetra n-propoxide and titanium tetra iso-propoxide dissolved in a solvent which is very often an ethalcohol (R-O-CH₂CH₂-OH). Since it is a chemical deposition process the precursor chemistry may play an important role. This aspect is partly controversy discussed [1] but a recent comparison of studies on similar precursor solutions with moderately modified educts shows a clear dependence on this parameter (Fig. 17.4) [16]. After the deposition onto a substrate which is often done by spin coating, the films are thermally treated which is typically performed in a two-step process where at first a drying/pyrolysis (range 200–450 °C) step is

performed and the as-pyrolyzed film is finally transferred to the crystalline film by annealing in a furnace at 600–700 °C. As briefly pointed out in the introduction nucleation has to take place in the as-pyrolyzed film, which is mainly X-ray amorphous, but could still contain carbon residues or nanocrystalline secondary phases depending on the process conditions. Thus it is instructive to begin with a view on this amorphous phase. In the early days of PZT film preparation, often secondary pyrochlore and fluorite phases, respectively, [17–19] were observed in the films. These were commonly lead deficient if stoichiometric coating solutions were applied due to the volatility of PbO at temperatures above approximately 500 °C. In order to avoid this lead deficiency either a lead excess between 10 and 20 % can be added to the precursor solutions, a PbO overcoat [20] on top of the PZT film before crystallization can be deposited, or a PbO rich atmosphere in the furnace during crystallization may be applied. These procedures were successfully applied to avoid lead deficiencies, nevertheless pyrochlore or fluorite phases may occur when indicated in nanocrystalline form, which means they cannot be detected by conventional X-ray analysis. The origin of these metastable intermediate phases can be explained by the model of the kinetically limited crystallization which is described in detail in Chap. 15. This means that the applied temperature is not sufficient to allow for long-range diffusion which in turn would be necessary to form the thermodynamically stable perovskite. Instead (nano)crystalline fluorite or pyrochlore intermediate phases are often observed [17–22], because these intermediate phases are compositionally more flexible than the perovskite phase and hence form more easily [23]. Further factors which affect the kinetic competition between different nucleation events are the Zr content, the type and orientation of substrate, and the roughness. For example, increasing the Zr content is known to reduce the perovskite crystallization rate. Therefore, increasing the Zr to Ti ratio should increase the time for PbO loss and thus increase the likelihood of forming residual surface fluorite. All these factors will influence the final microstructure [24, 25].

Interestingly these nanocrystalline fluorite or pyrochlore phases which may be distributed homogeneously in the volume of the film do not act as nucleation sites for the perovskite structure [23, 26] and therefore the favored nucleation event is the heterogeneous nucleation at the substrate/film interface (Fig. 17.1b). Under certain conditions heterogeneous nucleation at the film/atmosphere interface is basically also possible. Schwartz et al. observed for example surface nucleated grains in case of the use of aged PZT 40/60 precursor solutions [1]. Fortunately this kind of nucleation is rarely observed and will therefore not be considered further in this chapter. In fact most PZT films grow in a columnar way as the outcome of the predominant heterogeneous nucleation, which in turn is the important precondition to gain control over the orientation of the grains in the film. The current models for texture selection of PZT thin films on platinized silicon substrates are discussed in the following paragraphs. Thereby the most prominent model which is based on the formation of an intermediate Pt_xPb phase will be described in detail but other proposed models will be also mentioned for completeness.

For the intermetallic phase model two specific features of the CSD process, namely the burnout of the organic material in the as-deposited film and the ease of

change of the oxidation state between 0, +2, and +4 of lead have to be taken into account. The latter is one reason for the suitability as electrode material in batteries. During pyrolysis typically the organic matrix around the metal ions is decomposed into carbon dioxide and water and maybe to a certain extent, depending on the oxygen partial pressure to carbon monoxide. A low oxygen partial pressure corresponding to a reducing atmosphere nearby the substrate PZT film interface is self-evident either in the first time after starting the pyrolysis or if thicker films are deposited, simply because oxygen diffusion from the surface through the film to the interface needs a certain time. Thus Pb^{2+} could easily be reduced to metallic lead (+0). Although the exact mechanism is not known yet the following well known exothermic reaction may illustrate that thermodynamically this reaction is reasonable in such a reducing ambience at a typical temperature for pyrolysis (350 °C).



Furthermore in the given metal oxide system, according to the Ellingham diagram (Fig. 23.1), PbO is more easily reduced than TiO_2 and ZrO_2 [28]. In the subsequent step the metallic lead will form an epitaxial (111) oriented Pt_xPb alloy in the interface near region. This (111) Pt_xPb phase has a smaller lattice mismatch to PZT (111) as the pure Pt (111) (Table 17.1) and is therefore beneficial for the heteroepitaxial nucleation of PZT. Although the exact composition of this intermetallic phase is not completely clear yet there are several literature reports which unambiguously point to this reaction. Chen et al. where the first, who investigated this mechanism in order to explain the texture selection of their MOD derived films [29]. They postulated a composition Pt_{5-7}Pb while others found Pt_3Pb [30, 31] (Fig. 17.2d) or similar Pt_{3-4}Pb [32] during thermal processing of sol-gel derived PZT films. Brooks et al. also detected the formation of the intermetallic phase in sol-gel derived PZT films, but only if the atmosphere was reducing (argon). They found no evidence in their experiments that the Pt_xPb phase is formed when processed under air and hence concluded that other mechanisms must govern the texture selection [17]. However a closer look to the pyrolysis times in this work and a comparison with studies, which investigate shorter pyrolysis times of sol-gel derived PZT films [33, 34], show that the pyrolysis time in the study of Brooks et al are probably too long to be able to observe the Pt_xPb phase, since under oxidizing conditions the probably initially formed Pt_xPb phase was easily re-oxidized. Interestingly this Pt_xPb alloy was at first found in a MOD derived film maybe due to the fact that there is much more organic material in the as deposited film which has really to be thermally decomposed and burned out, respectively.

¹ Calculated according to thermodynamic functions from textbook knowledge. Thermodynamic basic data from [27].

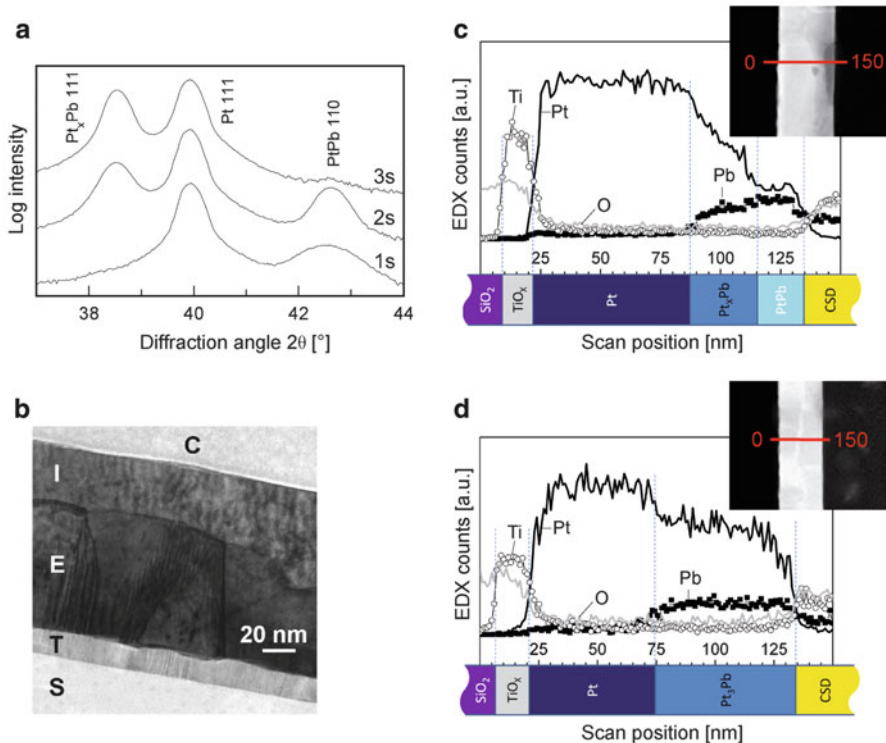


Fig. 17.2 Combined transmission electron microscopic and XRD study on the early stage of lead titanate crystallisation. (a) X-ray diffraction patterns of comparably thick sol-gel type PbTiO_3 layers heat treated at $650\text{ }^\circ\text{C}$ for untypically short times. Durations and emerging phases are indicated in the graph. (b) Bright field TEM image of a sample exhibiting the intermediate lead platinum compound. Capital letters indicate the different layer materials S— SiO_2 , T— TiO_2 adhesion layer, E—Pt bottom electrode, I—intermediate Pt_xPb layer and C—CSD derived film. (c) and (d) High-angle annular dark field (HAADF) images and EDX scan lines (red in nm) of the sample showing both intermetallic phases in the XRD pattern recorded at different positions. The corresponding analysis of the EDX signals shows in case of (c) both intermediate phases (PtPb and Pt_xPb), while in (d) only Pt_3Pb could be detected. The bar at the bottom of the EDX profiles shows schematically the layer sequence. Modified after [30]

This means that the typically applied pyrolysis times in the range of few minutes are simply not long enough to obtain already oxidizing conditions nearby the Pt/film interface. Hence the probability for detecting the Pt_xPb phase in the XRD's of these MOD films is higher than in sol-gel² derived films after similar

² In the systematic of the CSD terminology PZT precursor solutions, which are often denoted with “sol-gel”, belong to the mixed metallo-organic precursor systems (Chap. 3). They contain lead carboxylate and the alkoxides of titanium and zirconium, which still undergo hydrolysis and condensation reactions. Hence they can react in a sol-gel manner, which is different to MOD.

pyrolysis times since in the latter case a larger portion of the organic material may be removed already at lower temperatures due to simple evaporation of released alcohols stemming from the hydrolysis/condensation reactions. However if sufficiently short pyrolysis times and slightly thicker film thicknesses were chosen, intermetallic lead platinum phases could be also observed in sol-gel type solutions. Thus recently, hints to the kinetics of the alloy formation were found by using untypically short heat treatment times in the range of few seconds. By a combined transmission electron microscopic and X-ray diffraction study on CSD derived lead titanate films the occurrence of a Pt_xPb phase could be proven and even a hitherto not observed phase with the composition of Pb:Pt of 1:1 was found in the very early stage of the thermal process, i.e. after 1–2 s (Fig. 17.2). From the obtained data the following improved model for the phase evolution was developed. In the early phase of thermal processing a thin lead platinum alloy develops at the CSD film-platinum electrode interface. With increasing temperature the lead atoms gain a higher mobility leading to further diffusion into the Pt layer forming progressively the intermetallic compound in sub-stoichiometric ratio. After a certain period of coexistence the equimolar Pt-Pb composition vanishes leaving behind the Pt rich composition.

Another alloy, namely Pt_3Ti , proposed by Tani et al. [35], has to be mentioned in this context as well. It is formed on Pt/Ti/SiO₂/Si substrates by Ti outward diffusion and reaction with Pt. This also decreases the interfacial energy between Pt electrode and PZT(111) planes, due to the closer lattice matching similar to the Pt_xPb phase [35, 36]. However this intermetallic phase can only form in case of a metallic Ti adhesion layer. In case of the often used TiO₂ adhesion layer the formation can be practically excluded for two reasons. Firstly TiO₂ does not move along the Pt grain boundaries to the top of the Pt [37] and secondly the reduction of TiO₂ to metallic Ti under the given conditions can also be ruled out due to the thermodynamic reasons mentioned above. A comparison of PZT films deposited by the same CSD process on platinized silicon substrates with TiO₂, ZrO₂, and Al₂O₃ adhesion layers featured the same morphologic and ferroelectric properties irrespective of the underlying adhesion layer [16]. This yields another argument why Pt_3Ti as orientation promoting phase can be disregarded in most cases.

Besides these alloy models the (111) oriented nucleation and growth was also explained by PZT seeds, which nucleate directly on Pt due to the lattice matching between PZT (111) and Pt (111) (Table 17.1) at the film/Pt interface [38–40] or by a model where at first a well-crystallized PZT-fluorite-structure $Pb_2(Zr,Ti)_2O_{7-x}$ forms at the PZT/Pt interface in the as pyrolyzed film [41]. Since the (111) planes are minimum energy planes in the fluorite lattice, it is concluded that these fluorite crystallites grow with a preferential (111) orientation. During the subsequent crystallization, (111) oriented perovskite nuclei form by conversion of the (111)-oriented fluorite grains.

The case of (100) oriented growth of PZT films is often explained by an energetically favored (100) growth plane [20, 39, 42].

In the last part of this paragraph some other factors will be shown which influence the texture and microstructure development during CSD processing of

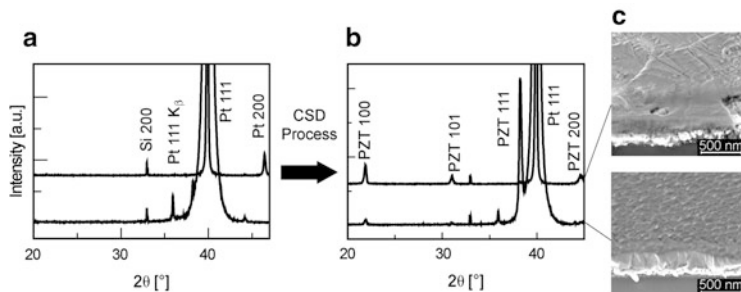


Fig. 17.3 Influence of substrate. (a) XRD pattern from platinized silicon substrates obtained from different suppliers after preannealing at 700 °C. The *upper diffractogram* stems from a less well (111) oriented Pt layer with a considerable amount of (200) oriented grains in the Pt film. (b) XRD results from PZT 53/47 films prepared with the same precursor solution (prepared according to [43]) and the same processing conditions (spin on at 3,000 rpm, pyrolysis at 420 °C, 10 min, crystallization in a RTA at 700 °C for 30 min) on these different substrates. (c) Corresponding cross section SEM images showing quite different morphologies. The *upper parts* of the graphs in each case show the films with less good properties. Modified after [44]

PZT thin films. Certainly the thermodynamics and heat treatment conditions play a crucial role. Therefore however the reader is referred to Chap. 15, where the corresponding aspects are described in detail.

17.3.1 Influence of the Substrate

In order to get columnar grown PZT films with a preferred orientation such as (111) for memory applications, predominant heterogeneous nucleation at the Pt/PZT interface including transfer of grain orientation is of utmost importance. This directly implies that the Pt film must have excellent surface properties, i.e. high degree of (111) orientation, low roughness, and no hillocks or pin holes. The latter two points are especially important for getting finally short circuit free ferroelectric thin film capacitors. Figure 17.3 illustrates the impact of the quality of the platinum bottom electrodes on morphologies and orientations of the grown PZT films.

If the platinum layer possesses a low degree of (111) orientation along with a significant amount of (200) oriented grains (Fig. 17.3a), the resulting PZT film shows a preferred (100) orientation and consists of large not well defined grains (Fig. 17.3 upper lines and SEM image) [44]. In contrast, in case of optimized substrates with highly (111) oriented Pt layers, correspondingly oriented PZT films with well-defined columnar microstructures could be obtained (Fig. 17.3 lower graphs and image).

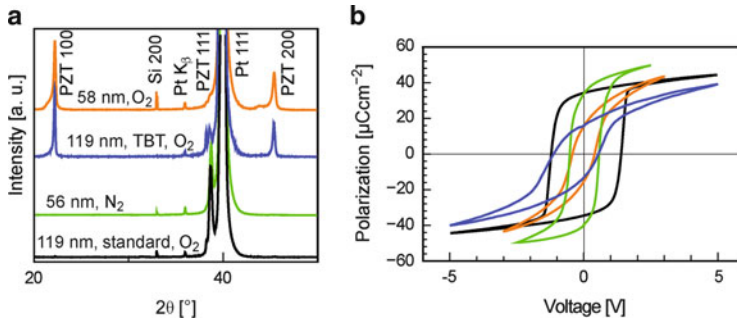


Fig. 17.4 Impact of film thickness and precursor chemistry on the orientation and the ferroelectric properties of PZT 30/70. (a) XRD pattern of differently processed PZT 30/70 films. (b) Corresponding ferroelectric hysteresis curves. *Black graphs*: 119 nm thick films prepared by an optimized standard CSD process (0.5 mol/l concentration) with annealing under oxygen [16]. *Green graphs*: 56 nm thick films prepared by a modified CSD process with annealing under nitrogen [45]. *Blue graphs*: 119 nm thick films prepared by a precursor modified CSD process with annealing under oxygen. Here $\text{Ti}(\text{O}^i\text{Pr})_4$ has been replaced by (TBT). *Orange graphs*: 56 nm thick films prepared by a modified CSD process with annealing under oxygen [45]

17.3.2 Influence of Film Thickness and Precursor Chemistry

Depending on the application of the final PZT films, different film thicknesses are required. While in case of piezoelectric applications thicker films are beneficial due to the larger piezoelectric response, for memory applications thinner films are aimed due to e.g. lower coercive voltage (see Fig. 17.4), which helps to reduce the operation voltage of the device. In order to prepare such thinner films by CSD the simplest approach is a reduction of the number of coatings and dilution of the precursor solution with the corresponding solvent. According to the before discussed effect of the Pt_xPb phase on the texture of the grown PZT films it can be easily anticipated that the dilution of coating solution may affect the resulting orientation of the PZT grains. The orange graphs in Fig. 17.4a, b show a typical result of this procedure [45]. Here a 2-butoxyethanol based precursor solution [16, 46] was diluted to a concentration of 0.37 mol/l and processed in an oxygen containing environment. Highly (100) oriented PZT films were obtained featuring indeed a lower coercive voltage but also a significantly lower remanent polarization and a slanted loop compared to the optimized 119 nm thick (111) textured films (black graphs in Fig. 17.4). This can be understood in terms of a suppressed formation of the (111) orientation promoting Pt_xPb intermediate phase due to faster oxygen diffusion through the thinner film. Less reducing conditions at the PZT/Pt interface might lead to a suppression of the Pb^{2+} to Pb^0 reduction, or a shorter lifetime of a once formed lead platinum alloy. As the result the films grow predominantly in (100) direction which give the lower ferroelectric response.

Taking this into account Norga et al. [47] suggested a reducing annealing in N_2 atmosphere and could show the beneficial effect on the orientation, but only

Ellerkmann et al. [45] could measure the improved ferroelectric response (green graphs in Fig. 17.4).

Although not fully understood on the microscopic scale yet, the impact of a small change of the educts in precursor solution synthesis may be explained by a similar mechanism. The simple exchange of the typically used $\text{Ti}(\text{O}^i\text{Pr})_4$ by $\text{Ti}(\text{O}^n\text{Bu})_4$ (TBT) during solution synthesis and otherwise unchanged processing conditions compared to the standard route also led to an increased degree of (100) orientation. As a consequence again a reduced remanent polarization is measured (blue graphs in Fig. 17.4), although the thickness remained unchanged with respect to the standard. This could be explained by different overall hydrolysis-condensation-decomposition behavior of Pt of the latter, which may lead to slightly more oxidizing conditions at the Pt/PZT film interface [16]. This in turn prohibits the effective formation of the Pt_xPb phase similar to the situation if very thin films (<100 nm) are annealed under oxidizing conditions.

17.4 Case Study II: Crystallization of $(\text{Ba}_{1-x}\text{Sr}_x)\text{TiO}_3$ Films

Barium strontium titanate thin film systems will serve in this section as prime example for a material system for which the crystallization of the pyrolyzed, amorphous film into the perovskite structured titanate predominantly occurs via homogeneous nucleation (see Fig. 17.1a, c). Nevertheless it will be shown how the thin film morphology can be affected by the control of CSD processing (1) by the choice of alkaline earth and titanium precursors, (2) by the heating procedure and solution concentration.

Whereas the fundamental theory on ‘*Thermodynamics and Heating Processes*’ is discussed in Chap. 15, the present chapter should give a more detailed view on the technologically interesting high- k material barium strontium titanate. Within the solid solution system $(\text{Ba}_{1-x}\text{Sr}_x)\text{TiO}_3$, the phase transition from the low temperature ferroelectric to the high temperature cubic phase is continuously shifted from about $(-260)^\circ\text{C}$ for SrTiO_3 to about 123°C for BaTiO_3 (see Fig. 17.5a) [48]. The composition $(\text{Ba}_{0.7}\text{Sr}_{0.3})\text{TiO}_3$ exhibits a high technological potential because of its high dielectric permittivity at room temperature which is of superior interest for high- k capacitors as for example in monolytic integrated decoupling devices.

A challenge in the utilization of this type of high- k material in thin film devices is the dependence of the dielectric and ferroelectric properties on the microstructure of the crystalline material, i.e. the grain size, texture, and intrinsically incorporated defects (Fig. 17.5b) [49]. In Chap. 23 it is demonstrated how the increase of the crystallization temperature can improve the dielectric properties of BaTiO_3 thin films for integration into multilayer ceramic capacitors (MLCC). Whereas in this chapter we will concentrate on the temperature regime below 800°C which is the maximum temperature for the integration of BST thin film capacitors onto silicon based devices [50].

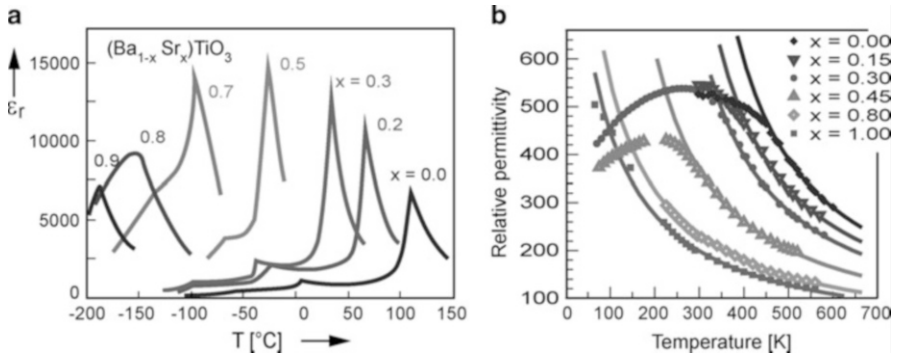


Fig. 17.5 Temperature dependence of the relative dielectric permittivity for (a) coarse grained $(\text{Ba}_{1-x}\text{Sr}_x)\text{TiO}_3$ ceramics and (b) CSD grown thin films with a thickness of about 200 nm integrated into Pt/BST/Pt devices [49]. With kind permission of The European Physical Journal (EPJ)

17.4.1 Influence of Precursor Chemistry

Well established synthesis routes for precursor solutions containing barium, strontium and titanium are typical hybrid routes (see Chap. 3) utilizing alkaline earth carboxylates in combination with stabilized or non-stabilized titanium alkoxides dissolved in a mixture of carboxylic acid and a parent alcohol or glycol [51–54]. In order to prepare high quality BST thin films, Hasenkox et al. [55] optimized and studied this approach in detail in particular with regard to decomposition and phase formation behavior of precursors with different chain lengths of the carboxylates. The details of the CSD process may be found in Sect. 3.4. In general a complex sequence of decomposition and densification steps accompanied by eventual formation of metastable intermediate phases occurs during the heating procedure which is roughly comprised in Table 17.2.

For alkaline earth carboxylates the length of the alkyl chain significantly affects the chemical and physical properties of the compound [56] such as the polarity or solubility and the thermal decomposition behavior (for details see Chap. 2).

It could be shown [55, 57] that one key point for the understanding of the crystallization behavior of BST thin films from a carboxylic route is the knowledge about the decomposition of the alkaline earth carboxylate precursor in relation to the decomposition of the titanium precursor and thus the formation of the titanium oxide skeleton. For this purpose the regimes of thermal decomposition were determined from thermogravimetric analyses of the different precursors. From the systematic summary given in Fig. 17.6 two types of barium and strontium carboxylate precursors have been identified. Type I precursors which are given above the Ti compounds in Fig. 17.6 show a slightly lower or comparable decomposition temperature compared to the titanium precursors and Type II precursors which are listed below the Ti compounds decompose at slightly higher temperatures relative to the titanium compound.

The effect of the decomposition behavior of the alkaline earth precursors on the crystallization of the barium-titanium and strontium-titanium based films into the

Table 17.2 General effects occurring during the crystallization of BST thin films (see [55])

Step	Effect
1	Hydrolysis and decomposition of the titanium precursor
2	Formation of an amorphous titanium-oxide skeleton with alkaline earth carbonates sitting in the pores of the network
3	Decomposition of the Ba- and Sr-carboxylates
4	Growth of intermediate phases which affect the crystallization of the perovskite phase
5	Densification and crystallization of the final perovskite phase

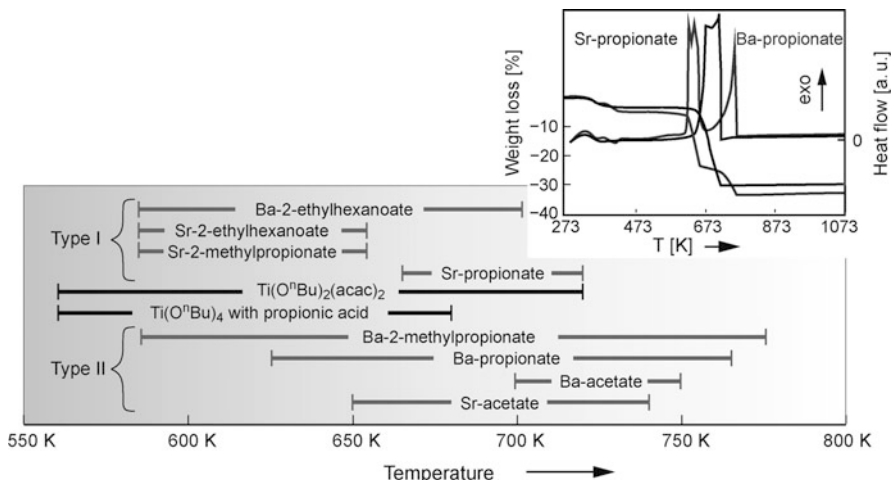


Fig. 17.6 Decomposition regimes of the barium and strontium carboxylates in air in comparison to titanium tetra n-butoxide. The *inset* shows representative TG/DTA curves of Sr and Ba propionate

respective perovskite structures, SrTiO₃ and BaTiO₃, has been studied in detail by means of a series of crystallization temperatures in combination with infrared spectroscopy (FTIR) and X-ray diffraction (XRD) analyses of the obtained thin films [55]. Figure 17.7 shows the results for three representative precursors, the type I precursor Sr-propionate in comparison to the type II precursors Sr-acetate and Ba-acetate. In accordance to the low decomposition temperature of the Sr-propionate precursor, the respective CSD process gives SrTiO₃ thin films of crystalline perovskite phase at very low growth temperatures of about 450 °C (723 K). In contrast, the crystallization into the SrTiO₃ or BaTiO₃ phase, respectively, is delayed up to temperatures of about 650 °C (923 K) if type II precursors are used. A very interesting feature is the appearance of an intermediate phase (ZP) which is observed for both type II precursors irrespective of the difference of the alkaline earth cation. By combination of the FTIR and XRD diagrams with literature data an alkaline earth titanium oxocarbonate phase [58] was proposed [55] which was also confirmed by other groups [59].

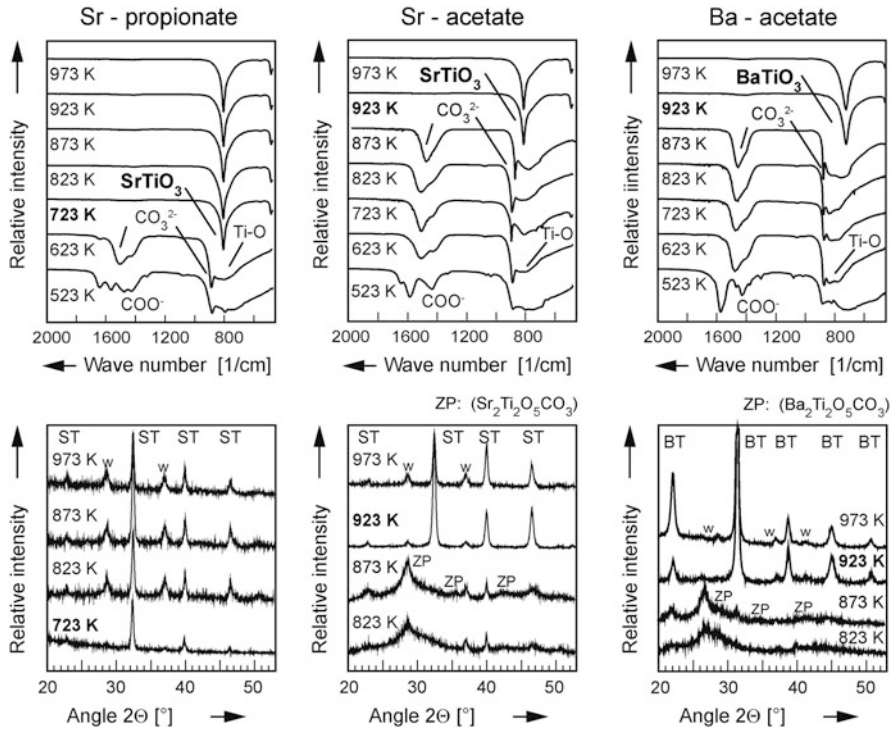


Fig. 17.7 Crystallization behavior of SrTiO_3 and BaTiO_3 thin films derived from different alkaline earth precursors which can be classified with respect to their decomposition behavior into type I, Sr-propionate, and type II, Sr-acetate and Ba-acetate, according to Fig. 17.6. ‘w’ assigns peaks of the substrate material. (rearrangement of diagrams from [55] with kind permission from Springer Science and Business Media)

Thus, two mechanisms have to be distinguished in respect of the nucleation of the SrTiO_3 , BaTiO_3 , and BST thin films obtained from alkaline earth carboxylate/Ti butoxide based CSD solutions. For the type I Sr- and Ba-precursors, the crystallization process may be described as a homogeneous nucleation which occurs at low temperatures (compare Fig. 17.1a) [60]. In contrast, the crystallization into the final perovskite phase is delayed to higher temperatures for the type II Sr- and Ba-precursors, and in addition, the formation of an intermediate alkaline earth titanium oxocarbonate phase is observed [61, 62]. The intermediate phase formation is identified as the main origin for the increase of the temperature for crystallization of the perovskite phase to values of about 650°C (923 K) which is even higher than the decomposition temperatures of the individual precursors. In analogy to the crystallization process of CSD PZT thin films described in case study I, it is of superior importance to identify the role of the intermediate phase for the nucleation behaviour of the BST thin films. Hasenkox et al. [55] showed that the intermediate metal-Ti-oxo-carbonate phase influences the perovskite phase formation in two respects. Firstly, the crystallization of the perovskite phase is delayed to higher

temperatures. Secondly, the metal-Ti-oxo-carbonate nanograins act as homogeneous seeds for preferred crystallization of the perovskite phase. Thus the crystallization mechanism of perovskite type BST thin films from carboxylate-alkoxide-based CSD routes has basically to be described as homogeneous. For type I alkaline earth precursors which decompose at low temperature a nucleation of randomly oriented perovskite grains can be observed at temperatures of about 450 °C. For type II alkaline earth precursors crystallization of the perovskite phase is delayed due to the intermediate formation of a metal-Ti-oxo-carbonate phase. The nucleation of this phase appears in a homogeneous manner throughout the amorphous film matrix and these metal-Ti-oxo-carbonate nano crystals serve as seeds for the nucleation of the perovskite BST phase [60]. The nucleation processes may be schematically comprised by the pictures in Fig. 17.8.

In summary, homogeneous nucleation events are dominating the microstructure of CSD derived perovskite-type BST thin films irrespective of the choice of alkaline earth carboxylic precursor. Nevertheless, the nucleation density and subsequently the grain size are affected by the decomposition temperature of the alkaline earth carboxylate compound. While CSD processes utilizing type I precursors result in a high density of perovskite type nuclei formed at low temperatures, the use of type II precursors results in nucleation of oxo-carbonate seeds at higher temperatures and in a lower density of nanograins. These intermediate phase nuclei may then act as seeds for the crystallization of the perovskite phase. This model can explain the morphological difference in grain size between the films obtained from different precursors.

17.4.2 Influence of Heating Procedure and Solution Concentration

As it has been discussed in detail by Schwartz and Narayanan in Chap. 15 there is a strong kinetic competition of homogeneous and heterogeneous nucleation events and thus, the heating rate and the crystallization temperature of the desired phase strongly influence the final microstructure of the thin films. From thermodynamic perspectives of crystallization events and phase evolution processes it becomes apparent that heterogeneous nucleation events are favored for high heating rates and high crystallization temperatures [1]. In this case the driving force for crystallization is small and thus the number of homogeneous nucleation events is strongly decreased shifting the competition between the nucleation events to the side of heterogeneous nucleation [63]. Experimental evidence for this model has already been indicated in Sect. 17.4.1 where it was shown that the increase of the crystallization temperature for the perovskite phase for the case of type II precursors resulted in more coarse grained films as compared to fine grained polycrystalline films which are obtained by low temperature processing utilizing the type I precursors.

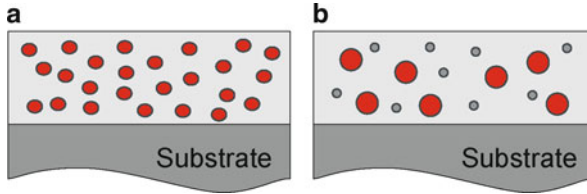


Fig. 17.8 Schematic illustration of the early state of nucleation of the perovskite phase in CSD grown SrTiO_3 and BaTiO_3 thin films obtained from an alkaline-earth-carboxylate/Ti alkoxide based route for (a) Type I alkaline earth precursor and (b) Type II alkaline earth precursor. The grey film represents the amorphous matrix, and the red and grey circles refer to the perovskite and to the metal-Ti-oxo-carbonate phase, respectively

But in order to change the microstructures of the BST thin films significantly, one more step is necessary. This is accessible by means of one more independent parameter of the CSD processing: the concentration of the CSD solution which affects the thickness of the single deposited layer. The reduction of the thickness of the amorphous layer will increase the probability of heterogeneous nucleation events at the cost of homogeneous nucleation events as a consequence of the increase of the surface to volume ratio. And this parameter is directly accessible by the thickness of the single coating in CSD [57]. Results of the corresponding experiments for the case of BaTiO_3 and SrTiO_3 thin films are shown in Fig. 17.9.

The columnar structure of the alkaline earth titanate films grown from CSD has been confirmed by transmission electron microscopic studies on thin film cross sections [64]. From the high resolution micrographs the epitaxial overgrowth of subsequent layers forming the columnar microstructure could be revealed; examples are shown in Fig. 17.10.

This case study on the crystallization behavior of CSD grown $(\text{Ba}_{1-x}\text{Sr}_x)\text{TiO}_3$ thin films may show the huge variety of process parameters which are accessible in chemical solution deposition techniques and which in combination with a fundamental understanding of the decisive chemical and physical mechanisms may be utilized to tune the microstructure of the film with respect to the need of the final application.

The proposed growth mechanism for CSD grown BST thin films is in good agreement to the empirical ‘structure zone model for sol-gel films’ which has been recently proposed by Schuler and co-workers [65]. The authors defined an empirical number $q = \text{ICS}/\text{SLT}$ as the ratio of the ‘intrinsic crystallite size (ICS)’ and the ‘single layer thickness (SLT)’. From statistical analysis of the q -parameter as a function of the film crystallization temperature for a variety undoped and doped TiO_2 , SnO_2 , and ZnO_2 thin films they could identify different zones representing the three main structures of thin films: columnar, layered and granular. For CSD accessible processing temperatures which result in crystallized thin films the three main microstructures can be identified by the q -parameter. For $q \ll 1$, a fine grained morphology is observed, while for $0.42 < q < 1$ a layer-type film microstructure appears, and for $q \gg 1$ the grain structure becomes columnar type.

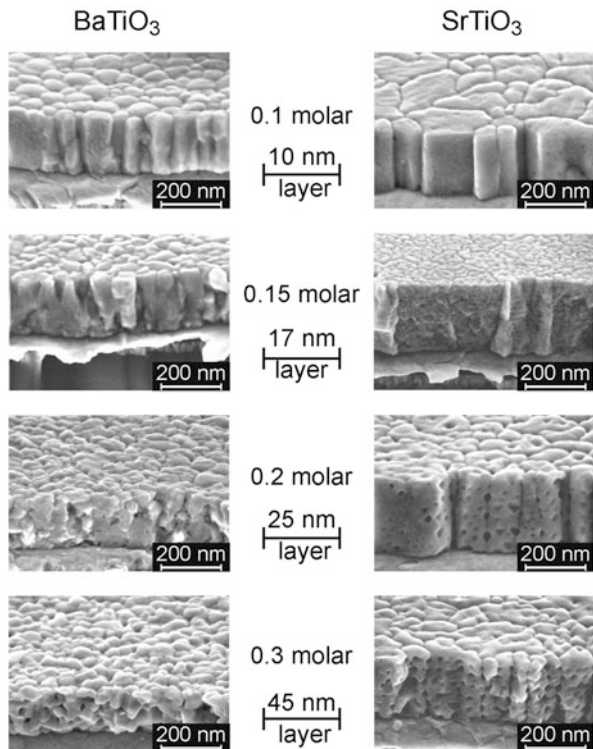


Fig. 17.9 Morphologies of BaTiO_3 and SrTiO_3 thin films grown from CSD solutions with different concentrations which result in different thicknesses of the individual layers. The perovskite thin films were grown from type II carboxylate Ti-alkoxide solutions using Ba-propionate and Sr-acetate, respectively. The single layers were crystallized at 750°C and the final annealing of the about 250 nm thick films was performed at 800°C (rearrangement of diagrams from [57] with kind permission from Cambridge University Press)

From the glass crystallization theory described in Chap. 15 and from our studies it is obvious that this classification by means of the q ratio holds for the categorization of thin film structures for which the homogeneous nucleation is dominating over the heterogeneous one. While the ‘structure zone model’ is an empirical approach, the results confirm those derived from the thermodynamic and kinetic description of the crystallization process and the phase evolution. The empirical ‘structure zone model’ may therefore be utilized where a new CSD route should be applied to the growth of a crystalline thin films with a certain desired microstructure.

The necessity for the control of the microstructure of high- k thin films is becoming obvious from the graph in Fig. 17.11. Here the temperature dependence of the permittivity of Pt/ BaTiO_3 /Pt capacitors is shown for films of the same thickness of 200 nm, but significant differences in the morphology and grain size (see [66, 67]).

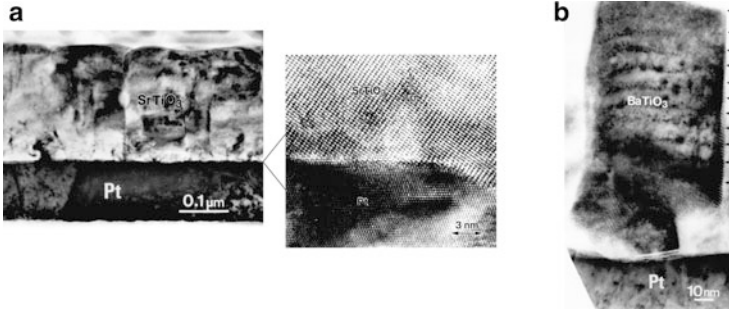


Fig. 17.10 (a) Transmission electron micrographs of a columnar structured SrTiO₃ thin film revealing straight columns, a clear interface between the Pt substrate and the STO film and even a heteroepitaxial relationship between the (111) Pt texture and the (111) STO texture of the SrTiO₃ thin film. (b) The high resolution transmission electron micrograph of a columnar structured BaTiO₃ grain clearly resolves the epitaxial overgrowth of subsequent layers during CSD processing (rearrangement of diagrams from [64] with kind permission from Cambridge University Press)

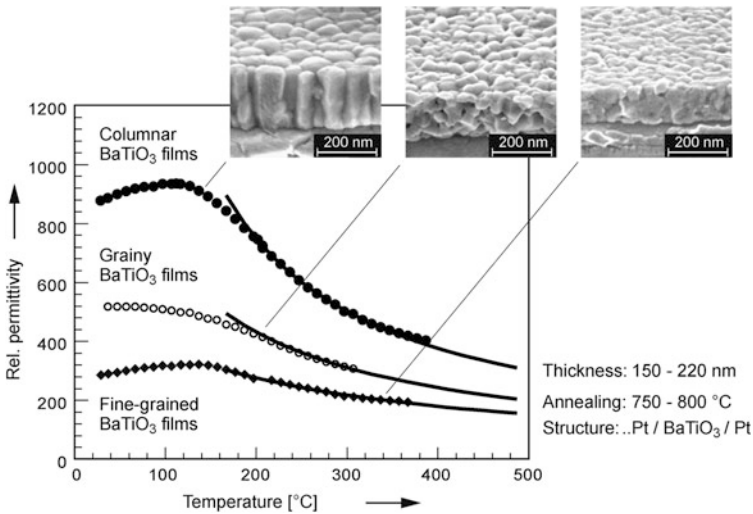


Fig. 17.11 Effect of microstructure and grain size on the relativity permittivity values of Pt/BaTiO₃/Pt capacitors (rearrangement of diagrams from [66] with permission from Elsevier)

The principle has been also applied to (Ba_{0.7}Sr_{0.3})TiO₃ thin films by Liedtke et al. [68–70] who could demonstrate the growth of 30 nm thin columnar structured BST thin films from CSD technique (see Fig. 17.12) [69], which showed comparable high insulation resistance and high-*k* values as compared to state of the art MOCVD grown BST films [71] for integrated capacitor applications.

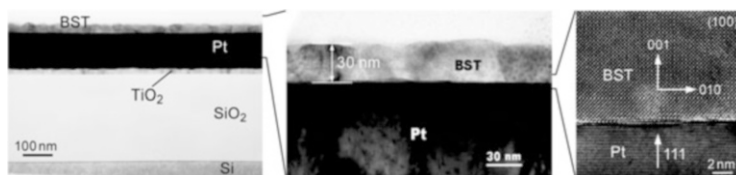


Fig. 17.12 Columnar structured $(\text{Ba}_{0.7}\text{Sr}_{0.3})\text{TiO}_3$ thin films of 30 nm thickness prepared by a propionate based CSD route. The films exhibit density values as well as permittivities and leakage currents which are comparable to high quality BST films obtained from metal organic chemical vapor deposition. Modified after [72]

Beyond the high- k materials, the microstructure tuning approach of multiple coatings of ultrathin individual layers has been successfully applied to a variety of other functional oxide layers, which show a predominately homogeneous crystallization behavior. Among these are transparent conducting oxides (TCO—see Chap. 26) [73–75], higher- k materials [76], and proton conducting perovskites [77], to name a few examples.

17.5 Summary

For functional oxide thin films the microstructure and orientation of the films' grains is of superior importance with regard to a control of the desired electrical properties. In this chapter, we have attempted to give a more detailed insight into the microstructure control of technical relevant $\text{Pb}(\text{Zr},\text{Ti})\text{O}_3$ thin films for ferroelectric and piezoelectric applications and $(\text{Ba},\text{Sr})\text{TiO}_3$ films for high- k capacitors. The main difference between the two perovskite thin films is their preferred nucleation when deposited on technical relevant platinum coated silicon substrates. While the crystallization of PZT films is a predominant example for a *heterogeneous nucleation* the crystallization of BST films can be regarded as a classical example for *homogeneous nucleation*. Thus, the two case studies dealt with in this chapter, highlight different important aspects which might be utilized to achieve a certain microstructure. For the heterogeneously crystallizing PZT films grown on Pt coated silicon substrates the formation of a textured Pt_xPb phase is of great importance because of the better lattice matching to PZT. We showed that beside the preference of heterogeneous nucleation events the atmosphere during processing and the chemistry of the CSD PZT solution are significant factors in order to establish an oxygen deficient environment at the Pt/PZT interface to favor the development of the Pt_xPb phase. For the homogeneously crystallizing BST films grown on Pt coated silicon substrates the orientation of the Pt layer is of lower importance. Nevertheless, the microstructure of these films can be tailored from fine grained random oriented, via coarse grained to columnar structured grains with preferred texture by changing the solution chemistry, the concentration of the

solution and the heating rate. It should be mentioned that the formation of an intermediate metal-Ti-oxo carbonate phase is necessary to shift the crystallization temperature of the perovskite phase to higher temperatures. This in consequence favors heterogeneous nucleation, although in a very limited processing regime. In recent years the 'dissolution principle' has been successfully transferred to other material systems in order to control the microstructure and hence the desired properties of the thin films. This in turn nicely demonstrates the more general applicability of this method.

References

1. Schwartz RW, Voigt JA, Tuttle BA, DaSalla RS, Payne DA (1997) Comments on the effects of solution precursor characteristics and thermal processing conditions on the crystallization behavior of sol-gel derived PZT thin films. *J Mater Res* 12:444–456
2. Gust MC, Momoda LA, McCartney ML (1994) Microstructure and crystallization behavior of sol-gel prepared BaTiO₃ thin films. *Mater Res Soc Symp Proc* 346:649–653
3. Sporn D, Merklein S, Grond W, Seifert S, Wahl S, Berger A (1995) Sol-gel processing of perovskite films. *Microelectron Eng* 29:161–168
4. Seifert A, Lange FF, Speck JS (1995) Epitaxial growth of PbTiO₃ thin films on (001) SrTiO₃ from solution precursors. *J Mater Res* 10:680–691
5. Database of the International Center of Diffraction Data (ICDD) (2001) File Card No. 87-0646
6. Database of the International Center of Diffraction Data (ICDD) (2001) File Card No. 06-0574
7. Database of the International Center of Diffraction Data (ICDD) (2001) File Card No. 78-0298
8. Klee M, Eusemann R, Waser R, Brand W, van-Hal H (1992) Processing and electrical properties of Pb(Zr_xTi_{1-x})O₃ (x = 0.2–0.75) films: comparison of metallo-organic decomposition and sol-gel processes. *J Appl Phys* 72:1566–1576
9. Wang ZJ, Aoki Y, Yana LJ, Kokawa H, Maeda R (2004) Crystal structure and microstructure of lead zirconate titanate (PZT) thin films with various Zr/Ti ratios grown by hybrid processing. *J Cryst Growth* 267:92–99
10. Database of the International Center of Diffraction Data (ICDD) (2001) File Card No. 50-0346
11. Database of the International Center of Diffraction Data (ICDD) (2001) File Card No. 84-0444
12. Database of the International Center of Diffraction Data (ICDD) (2001) File Card No. 34-411
13. Database of the International Center of Diffraction Data (ICDD) (2001) File Card No. 89-0274
14. Database of the International Center of Diffraction Data (ICDD) (2001) File Card No. 75-1169
15. Brennecka GL, Huebner W, Tuttle BA, Clem PG (2004) Use of stress to produce highly oriented tetragonal lead zirconate titanate (PZT 40/60) thin films and resulting electrical properties. *J Am Ceram Soc* 87:1459–1465
16. Schneller T, Waser R (2007) Chemical modifications of Pb(Zr_{0.3}Ti_{0.7})O₃ precursor solutions and their influence on the morphological and electrical properties of the resulting thin films. *J Sol-Gel Sci Technol* 42:337–352
17. Brooks KG, Reaney IM, Klissurska R, Huang Y, Bursill L, Setter N (1994) Orientation of rapid thermally annealed lead zirconate titanate thin films on (111) Pt substrates. *J Mater Res* 9:2540–2553
18. Carim AH, Tuttle BA, Doughty DH, Martinez SL (1991) Microstructure of solution-processed lead zirconate titanate (PZT) thin films. *J Am Ceram Soc* 74:1455–1458
19. Tuttle BA, Schwartz RW, Doughty DH, Voigt JA, Carim AH (1990) Characterization of chemically prepared PZT thin films. *Mater Res Soc Proc* 200:159–165

20. Tani T, Payne DA (1994) Lead oxide coatings on sol-gel-derived lead lanthanum zirconium titanate thin layers for enhanced crystallization into the perovskite structure. *J Am Ceram Soc* 77:1242–1248
21. Chang J, Desu SB (1994) Effects of dopants in PZT films. *J Mater Res* 9:955–969
22. Wilkinson AP, Speck JS, Cheetham AK, Natarajan S, Thomas JM (1994) An in situ X-ray diffraction study of the crystallization kinetics in PZT, $\text{PbZr}_{1-x}\text{Ti}_x\text{O}_3$ ($x = 0.0, 0.55, 1.0$). *Chem Mater* 6:750–754
23. Seifert A, Lange FF, Speck JS (1995) Epitaxial growth of PbTiO_3 thin films on (001) SrTiO_3 from solution precursors. *J Mater Res* 10:680–691
24. Tuttle B, Voigt JA, Headley TJ, Potter BG, Dimos D, Schwartz RW, Dugger MT, Michael J, Nasby RD, Garino TJ, Goodnow DC (1994) Ferroelectric thin film microstructure development and related property enhancement. *Ferroelectrics* 151:11–20
25. Voigt JA, Tuttle BA, Headley TJ, Eatough MO, Lamma DL, Goodnow D (1993) Oriented lead zirconate titanate thin films: characterization of film crystallization. *Mater Res Soc Proc* 310:15–22
26. Lefevre MJ, Speck JS, Schwartz RW, Dimos D, Lockwood SJ (1996) Microstructural development in sol-gel derived lead zirconate titanate thin films: the role of precursor stoichiometry and processing environment. *J Mater Res* 11:2076–2084
27. Atkins PW (1986) *Physical chemistry*, 3rd edn. Oxford University Press, Oxford
28. Darken LS, Gurry RW (1953) *Physical chemistry of metals*. McGraw-Hill, New York
29. Chen SY, Chen IW (1994) Phase transformations of oriented $\text{Pb}(\text{Zr}_{1-x}\text{Ti}_x)\text{O}_3$ thin films from metalloorganic precursors. *Ferroelectrics* 152:25–30
30. Dippel AC, Schneller T, Waser R, Park D, Mayer J (2010) Formation sequence of lead platinum interfacial phases in chemical solution deposition derived $\text{Pb}(\text{Zr}_{1-x}\text{Ti}_x)\text{O}_3$. *Chem Mater* 22:6209–6211
31. Huang Z, Zhang O, Whatmore RW (1998) The role of an intermetallic phase on the crystallization of lead zirconate titanate in sol-gel process. *J Mater Sci* 17:1157–1159
32. Kaewchinda D, Chairaungsri T, Naksata M, Milne SJ, Brydson R (2000) TEM characterisation of PZT films prepared by a diol route on platinised silicon substrates. *J Eur Ceram Soc* 20:1277–1288
33. Huang Z, Zhang O, Whatmore RW (1999) Structural development in the early stages of annealing of sol-gel prepared lead zirconate titanate thin films. *J Appl Phys* 86:1662–1669
34. Huang Z, Zhang O, Whatmore RW (1998) The role of an intermetallic phase on the crystallization of lead zirconate titanate in sol-gel process. *J Mater Sci* 17:1157–1159
35. Tani T, Xu Z, Payne DA (1993) Preferred orientations for sol-gel derived PLZT thin layers. *Mater Res Soc Symp Proc* 310:269–274
36. Song YJ, Zhu Y, Desu SB (1998) Low temperature fabrication and properties of sol-gel derived (111) oriented $\text{Pb}(\text{Zr}_{1-x}\text{Ti}_x)\text{O}_3$ thin films. *Appl Phys Lett* 72:2686–2688
37. Al-Shareef HN, Gifford KD, Rou SH, Hren PD, Auciello O, Kingon A (1993) Electrodes for ferroelectric thin films. *Integr Ferroelectr* 3:321–332
38. Reaney IM, Brooks K, Klissurska R, Pawlaczyk C, Setter N (1994) Use of transmission electron microscopy for the characterization of rapid thermally annealed, solution-gel, lead zirconate titanate films. *J Am Ceram Soc* 77:1209–1216
39. Liu Y, Phule PP (1996) Nucleation- or growth-controlled orientation development in chemically derived ferroelectric lead zirconate titanate ($\text{Pb}(\text{Zr}_x\text{Ti}_{1-x})\text{O}_3$, $x = 0.4$) thin films. *J Am Ceram Soc* 79:495–498
40. Spierings GACM, Ulenaers MJE, Kampschöer GLM, van Hal HAM, Larsen PK (1991) Preparation and ferroelectric properties of $\text{PbZr}_{0.53}\text{Ti}_{0.47}\text{O}_3$ thin films by spin coating and metalorganic decomposition. *J Appl Phys* 70:2290–2298
41. Norga GJ, Vasiliu F, Fè L, Wouters DJ, Van der Biest O (2003) Role of fluorite phase formation in the texture selection of sol-gel-prepared $\text{Pb}(\text{Zr}_{1-x}\text{Ti}_x)\text{O}_3$ films on Pt electrode layers. *J Mater Res* 18:1232–1238

42. Chen SY, Chen IW (1998) Texture development, microstructure evolution, and crystallization of chemically derived PZT thin films. *J Am Ceram Soc* 81:97–105
43. Budd KD, Dey SK, Payne DA (1985) Sol-gel processing of PbTiO_3 , PbZrO_3 , PZT, and PLZT thin films. *Br Ceram Proc* 36:107–121
44. Waser R, Schneller T, Ehrhart P, Hoffmann-Eifert S (2001) Chemical deposition methods for ferroelectric thin films. *Ferroelectrics* 259:205–214
45. Ellerkmann U, Schneller T, Nauenheim C, Böttger U, Waser R (2008) Reduction of film thickness for chemical solution deposited $\text{PbZr}_{0.3}\text{Ti}_{0.7}\text{O}_3$ thin films revealing no size effects and maintaining high remanent polarization and low coercive field. *Thin Solid Films* 516:4713–4719
46. Nouwen R, Mullens J, Franco D, Yperman J, Van Poucke LC (1996) Use of thermogravimetric analysis - Fourier transform infrared spectroscopy in the study of the reaction mechanism of the preparation of $\text{Pb}(\text{Zr},\text{Ti})\text{O}_3$ by the sol-gel method. *Vib Spectrosc* 10:291–299
47. Norga GJ, Fe L (2001) Orientation selection in sol-gel derived PZT thin films. *Mater Res Soc Symp Proc* 655:CC9.1.1–CC9.1.11
48. Smolenskii GA, Rozgachev KI (1954) Seignettelectric properties of solid solutions in the system barium titanate-strontium titanate. *Zh Tekh Fiz* 24:1751–1760
49. Hoffmann S, Waser R (1998) Curie-Weiss law of $(\text{Ba}_{1-x}\text{Sr}_x)\text{TiO}_3$ thin films prepared by chemical solution deposition. *J Phys IV* 8:221–224
50. Kotecki DE, Baniecki JD, Shen H, Laibowitz RB, Saenger KL, Lian JJ, Shaw TM, Athavale SD, Cabral C Jr, Duncombe PR, Gutsche M, Kunkel G, Park YJ, Wang YY, Wise R (1999) $(\text{Ba}, \text{Sr})\text{TiO}_3$ dielectrics for future stacked capacitor DRAM. *IBM J Res Dev* 43:367–382
51. Joshi PC, Ramanathan S, Desu SB, Stowell S (1997) Microstructural and Electrical Characteristics of Rapid Thermally Processed $(\text{Ba}_{1-x}\text{Sr}_x)\text{TiO}_3$ Thin Films prepared by Metalorganic Solution Deposition Technique. *Phys Stat Sol* 161:361–370
52. Mohammed MS, Naik R, Mantese JV, Schubring NW, Micheli AL, Catalan AB (1996) Microstructure and ferroelectric properties of fine grained $(\text{Ba}_x\text{Sr}_{1-x})\text{TiO}_3$ thin films prepared by metalorganic decomposition. *J Mater Res* 11:2588–2593
53. Tahan DA, Safari A, Klein LC (1996) Preparation and characterization of $(\text{Ba}_x\text{Sr}_{1-x})\text{TiO}_3$ thin films by a sol-gel-technique. *J Am Ceram Soc* 79:1593–1598
54. Hoffmann S, Klee M, Waser R (1995) Structural and electrical properties of wet-chemically deposited $\text{Sr}(\text{Ti}_{1-y}\text{Zr}_y)\text{O}_3$ thin films. *Integr Ferroelectr* 10:155–164
55. Hasenkox U, Hoffmann S, Waser R (1998) Influence of precursor chemistry on the formation of MTiO_3 ($\text{M} = \text{Ba}, \text{Sr}$) ceramic thin films. *J Sol-Gel Sci Technol* 12:67–79
56. Mehrotra RC, Bohra R (1983) Metal carboxylates. Academic, London
57. Hoffmann S, Hasenkox U, Waser R, Jia CL, Urban K (1997) Chemical solution deposited BaTiO_3 and SrTiO_3 thin films with columnar microstructure. *Mater Res Soc Symp Proc* 474:9–14
58. Gopalakrishnamurthy HS, Subba Rao M, Narayanan Kutty TR (1975) Thermal decomposition of titanyl oxalates-I; barium titanyl oxalate. *J Inorg Nucl Chem* 37:891–898
59. Schwartz RW, Clem PG, Voigt JA, Byhoff ER, Van Stry M, Headley TJ, Missert NA (1999) Control of microstructure and orientation in solution deposited BaTiO_3 and SrTiO_3 thin films. *J Am Ceram Soc* 82:2359–2367
60. Gust MC, Evans ND, Momoda LA, Mecartney ML (1997) In-situ transmission electron microscopy crystallization studies of sol-gel-derived barium titanate thin films. *J Am Ceram Soc* 80:2828–2836
61. Kumar S, Messing GL, White WB (1993) Metal organic resin derived barium titanate: I. Formation of barium titanium oxocarbonate intermediate. *J Am Ceram Soc* 76:617–624
62. Gust MC, Momoda LA, Evans ND, Mecartney ML (1997) Crystallization of sol-gel-derived barium strontium titanate thin films. *J Am Ceram Soc* 84:1087–1092
63. Schwartz RW, Clem PG, Voigt JA, Byhoff ER, Van Stry M, Headley TJ, Missert NA (1999) Control of microstructure and orientation in solution deposited BaTiO_3 and SrTiO_3 thin films. *J Am Ceram Soc* 82:2359–2367

64. Jia CL, Urban K, Hoffmann S, Waser R (1998) Microstructure of columnar-grained SrTiO₃ and BaTiO₃ thin films prepared by chemical solution deposition. *J Mater Res* 13:2206–2217
65. Schuler T, Krajewski T, Grobelsek I, Aegerter MA (2004) A microstructural zone model for the morphology of sol-gel coatings. *J Sol-Gel Sci Technol* 31:235–239
66. Hoffmann S, Waser R (1999) Control of the morphology of CSD-prepared (Ba,Sr)TiO₃ thin films. *J Eur Ceram Soc* 19:1339–1343
67. Waser R, Hoffmann S (1998) Microstructure-property relationships of (Ba,Sr)TiO₃ films. *J Korean Phys Soc* 32:S1340–S1343
68. Qin YL, Jia CL, Liedtke R, Waser R, Urban K (2003) Transmission electron microscopy investigation of Pt/Ba_{0.7}Sr_{0.3}TiO₃/Pt capacitors with different annealing process. *J Am Ceram Soc* 86:1190–1195
69. Ellerkmann U, Liedtke R, Boettger U, Waser R (2004) Interface-related thickness dependence of the tunability in BaSrTiO₃ thin films. *Appl Phys Lett* 85:4708–4710
70. Ellerkmann U, Liedtke R, Waser R (2002) Influence of the film-electrode interface in thin-film capacitors. *Ferroelectrics* 271:315–320
71. Basceri C, Streiffer SK, Kingon AI, Waser R (1997) The dielectric response as a function of temperature and film thickness of fiber-textured (Ba,Sr)TiO₃ thin films grown by chemical vapor deposition. *J Appl Phys* 82:2497–2504
72. Waser R, Schneller T, Hoffmann-Eifert S, Ehrhart P (2001) Advanced chemical deposition techniques - from research to production. *Integr Ferroelectr* 36:3–20
73. Dippel AC, Schneller T, Gerber P, Waser R (2007) Morphology control of highly-transparent indium tin oxide thin films prepared by a chlorine-reduced metallo-organic decomposition technique. *Thin Solid Films* 515:3797–3801
74. Mottern M, Tyholdt F, Ulyashin A, van Helvoort ATJ, Verweij H, Bredesen R (2007) Textured indium tin oxide thin films by chemical solution deposition and rapid thermal processing. *Thin Solid Films* 515:3918–3926
75. Schuler T, Aegerter MA (1999) Optical, electrical and structural properties of sol gel ZnO:Al coatings. *Thin Solid Films* 351:125–131
76. Kambara H, Schneller T, Sakabe Y, Waser R (2009) Dielectric properties of highly c-axis oriented chemical solution deposition derived SrBi₄Ti₄O₁₅ thin films. *Physica Status Solidi A* 206:157–166
77. Lenrick F, Griesche D, Kim J, Schneller T, Wallenberg L (2012) Electron microscopy study of single crystal BaZr_{0.9}Y_{0.1}O_{3-x} films prepared by chemical solution deposition. *ECS Trans* 45:121–127

Chapter 18

Low-Temperature Processing

Sebastjan Glinšek, Barbara Malič, and Marija Kosec[†]

18.1 Introduction

Functional oxides typically consist of at least two metal ions, such as a large group of transition-metal perovskites, including $(\text{Ba,Sr})\text{TiO}_3$ (BST) and $\text{Pb}(\text{Zr,Ti})\text{O}_3$ (PZT). While in CSD of single-metal oxides the crystallization from the amorphous phase is the process which mainly determines the final heating temperature, in complex oxides the thermodynamically stable phase composition and absence of chemical heterogeneities are additional requirements to be fulfilled.

The design of the heterometallic precursor solution, which results in a homogeneous distribution of constituent species, and the heating profile, which allows an effective removal of functional groups without any phase segregation, are the key parameters which contribute to decreasing the processing temperature in ‘classical’ CSD of complex-oxide thin films [1–3].

The choice of the substrate and/or the nucleation layer or seeds has contributed to decreasing the crystallization temperature of materials which crystallize predominantly via heterogeneous nucleation, with PZT as the most studied example [4–11]. In contrast, in films with prevailing homogeneous nucleation, such as BST, lowering of the crystallization temperature could be influenced either by solution chemistry or heating profile [2, 12].

[†] Author was deceased

S. Glinšek (✉)

School of Engineering, Brown University, 184 Hope Street Box D, Providence, RI 02906, USA

Centre of Excellence SPACE-SI, Ljubljana, Slovenia

e-mail: sebastjan_glinsek@brown.edu

B. Malič

Jožef Stefan Institute, 1000 Ljubljana, Slovenia

Centre of Excellence SPACE-SI, Ljubljana, Slovenia

Due to application requirements the functional-oxide films have been generally deposited on platinized silicon substrates with the following structure: Pt/TiO_x/SiO_x/Si. The main obstacle for successful integration of the films into silicon technology is their relatively high processing temperature, usually between 500 and 750 °C for PZT [5] and at least 650 °C for BST [2, 13]. At temperatures above 500 °C, various interface reactions contribute to a decreased functional response of the films, including diffusion of titanium through the substrate [7, 14] and/or diffusion of lead through the platinum in case of the PZT [15].

Halder and co-workers [16] showed that the temperature stability of the platinum electrodes can be enhanced up to 1,000 °C by the exchange of TiO_x adhesion layer with Al₂O₃. Despite strongly enhanced functional properties of the BST films deposited on such substrates, this approach still does not solve the problem of high-temperature stability of other components and therefore the need for lower processing temperatures of functional-oxide thin films remains.

In recent years, many combined approaches have been employed to prepare functional-oxide films at temperatures around 400–450 °C. In these cases other methods have been included into the chemical solution deposition process, such as hydrothermal processing, photochemical activation, or laser activation [17–19].

Further approaches, such as multiphase ferroelectric films (ferrons model) [20], ultra-thin films of solid solutions of Bi₂SiO₅ and ferroelectrics (Bi₄Ti₃O₁₂, SrBi₂Ta₂O₉, Pb(Zr,Ti)O₃) with crystallization temperatures at 150–200 °C [21], or low-pressure rapid thermal annealing (RTA) [22] have been reported and the interested reader is directed to references listed above.

Flexible, transparent, lightweight, and mechanically robust electronics for so-called “invisible electronic circuits”, such as displays or identification tags, are based on oxide semiconductor films on polymer substrates which typically require processing temperatures below 150–200 °C. Amorphous ZnO-based thin films have been deposited by physical vapor deposition routes even at room temperature [23, 24], however solution approaches to deposit organics-free amorphous films at such temperatures are still a challenge [25, 26].

18.2 Solution Chemistry

One of the main advantages of CSD is that by designing the solution chemistry the phase composition, orientation, microstructure and functional properties of the films are modified. Lowering the crystallization temperature can be achieved by forming the metal complexes or coordination compounds, which have the same arrangement of metal and oxygen ions as in the final crystalline state already in the solution, and/or by increasing the homogeneity of the solution.

Hirano and Kato [1, 27] prepared LiNbO₃ thin films on silicon and sapphire single-crystal substrates from the 24 h-refluxed solutions of lithium and niobium ethoxides in ethanol solvent. The films, deposited from the partially hydrolyzed solutions, started to crystallize after heating as low as 250 °C and were fully crystallized upon heating at 400 °C. The heating was performed in a flow of

water vapor-enriched oxygen, which promoted both hydrolysis of the remaining alkoxide groups in the gel film and oxidation of residual organic species. As it was shown later by Eichorst and Payne [28], the bimetallic alkoxide $\text{LiNb}(\text{OEt})_6$ was formed during the reflux, which served as the “molecular building block” for the crystallization of LiNbO_3 thin films. The films deposited on (100) silicon substrates and heated at 400°C reached the values of dielectric permittivity ϵ' and dielectric losses $\tan\delta$ at 100 kHz of 35 and 0.004, respectively [29].

The crystallization of the perovskite phase often occurs via a transient non-ferroelectric phase and if such phase persists in the final film it can lower its functional response. In the process of crystallization of BaTiO_3 and SrTiO_3 thin films from short alkyl-chain carboxylate-alkoxide based precursors, a transient oxocarbonate phase is formed which shifts the crystallization of the perovskite phase to higher temperatures. This is not the case if longer-chain carboxylates are used. For example, BaTiO_3 films, prepared from barium propionate or acetate, crystallize at 700°C , while the films prepared from barium ethylhexanoate crystallize at 600°C [2]. But even when carboxylate free precursors are used and the formation of the transient oxocarbonate phase is avoided BaTiO_3 -based films were found not to crystallize below 600°C [30].

In the case of PZT, a non-ferroelectric pyrochlore-type phase is stable up to 550°C , depending on the composition, as shown in Fig. 18.1 [5].

The crystallization temperature of the perovskite phase decreases with the decreasing Zr/Ti ratio, as shown in Fig. 18.1. The influence of the Zr/Ti ratio on the crystallization kinetics is also illustrated by the cross-section transmission electron microscope (TEM) micrographs of the Zr-rich $\text{Pb}_{0.905}\text{La}_{0.095}\text{Zr}_{0.65}\text{Ti}_{0.35}\text{O}_3$ (PLZT 9.5/65/35) and Ti-rich $\text{PbZr}_{0.3}\text{Ti}_{0.7}\text{O}_3$ (PZT 30/70) films on platinized silicon heated at 400°C (Fig. 18.2). In the Zr-rich film, only a thin part of the film close to the substrate crystallized into the perovskite phase, indicating the prevalence of heterogeneous nucleation, while the bulk of the film remained amorphous after heating for 5 h. In contrast, the Ti-rich film was fully crystallized and consisted of columnar grains after only 1 h at 400°C . The influence of the solution chemistry on the perovskite crystallization at 400°C was further studied in the Ti-rich PZT and La-doped PZT films [31, 32]. PZT 30/70 films, prepared from lead oxide, zirconium, and titanium *n*-butoxides in 2-methoxyethanol on platinized silicon substrates, crystallized in (111) oriented perovskite phase after heating at 400°C and showed good ferroelectric properties with remanent polarization P_r , $20\ \mu\text{C cm}^{-2}$ and coercive field E_c , $160\ \text{kV cm}^{-1}$.

The reactivity of zirconium alkoxide, *n*-propoxide in the specific study, was found to be the critical issue for enhancing the homogeneity of the PZT 53/47 sols prepared by the 2-methoxyethanol route [3]. The investigation by extended X-ray absorption fine structure spectroscopy (EXAFS—see Chap. 8) pointed to segregation of the zirconium species already upon the PZT solution synthesis. By modification of the zirconium *n*-propoxide by acetic acid prior the PZT synthesis, the original dimeric structure of the alkoxide was preserved throughout the solution processing and also in the amorphous film. Consequently, such films had a more homogeneous microstructure (Fig. 18.3) and exhibited enhanced dielectric properties than conventionally prepared films [35].

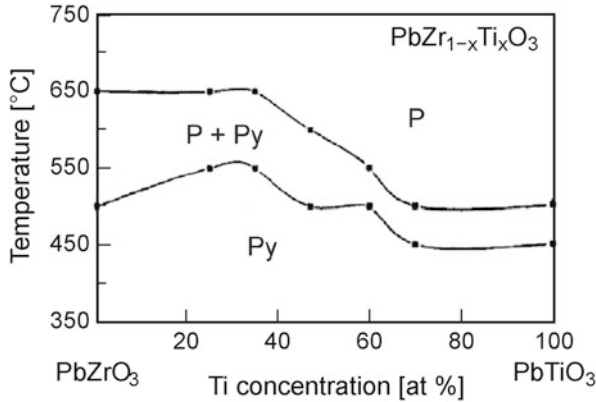


Fig. 18.1 Pyrochlore to perovskite transformation temperatures as a function of the PbZrO_3 – PbTiO_3 solid solution composition. *Py* pyrochlore phase, *P* perovskite phase [5]. Reprinted with permission of the author and MRS©1992

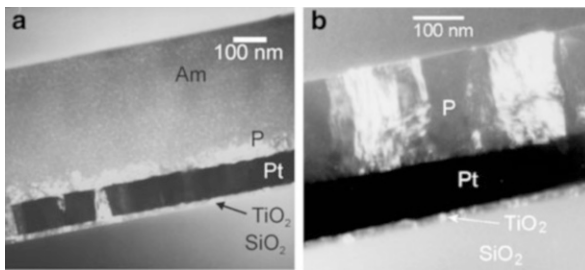


Fig. 18.2 Influence of the composition (Zr/Ti ratio) on the crystallization kinetics of the PZT-based thin films on platinumized silicon substrates (a) TEM micrograph of the PLZT 9.5/65/35 thin film after heating at 400 °C for 5 h [33], (b) PZT 30/70 thin film after heating at 400 °C for 1 h [34]. *Am* amorphous phase, *P* perovskite phase. Reprinted with the author's permission

18.3 Seeding Layers and Crystallization Seeds

The principle of this approach in processing of PZT thin films is that the nucleation is the rate limiting step for the crystallization of the perovskite phase, i.e., the activation energy of the nucleation is much higher than that for the growth of the crystallites [36]. Kwok and Desu [5] successfully lowered the perovskite crystallization temperature of the PZT 53/47 thin films on sapphire substrates for 100 °C, that is to 500 °C, by introducing a thin PbTiO_3 seeding layer (~45 nm), selected on the basis of the lowest crystallization temperature in the PZT solid solution (Fig. 18.1).

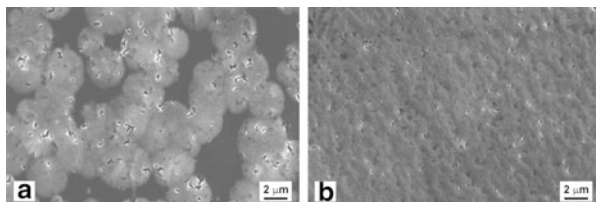


Fig. 18.3 Plane view SEM micrographs of the PZT 53/47 thin films on platinized silicon substrates after heating at 650 °C for 15 min in RTA furnace, prepared from (a) nonmodified precursor solution, (b) acetic acid-modified zirconium *n*-propoxide [30]. Reprinted with permission of Elsevier©2003

In the lead-based perovskite films, another effect has been implemented to promote the heterogeneous nucleation at the film/electrode interface and consecutively to lower the energy barrier for the nucleation of perovskite phase. Upon heating of the as-deposited ('gel') film, a reducing local atmosphere may form as a consequence of the oxygen consumption in the process of thermal decomposition/oxidation of organics. A fraction of Pb^{2+} species may be reduced to Pb^0 (see preceding chapter). In case of the film on platinized silicon substrate, a Pt-Pb intermetallic phase, described as $\text{Pt}_{5.7}\text{Pb}$ [8], Pt_3Pb [37], or Pt_6Pb [38], may form. The TEM micrograph and XRD patterns of the amorphous PZT films after heating to 400 °C in different atmospheres, revealing the presence of the Pt-Pb intermetallic phase, are collected in Fig. 18.4. The intermetallic phase serves as an efficient nucleation layer for the (111) oriented perovskite phase due to a good lattice match to the PZT. For example, the lattice mismatch between the PZT 30/70 ($a_0 = 4.035 \text{ \AA}$ for pseudocubic perovskite phase) and Pt_3Pb phase ($a_0 = 4.05 \text{ \AA}$) is only 0.37 %. Upon further heating the Pb^0 may re-oxidize again to Pb^{2+} . By implementing this approach, the (111) oriented PZT 30/70 films with the values of remanent polarization, P_r , coercive field E_c , and pyroelectric coefficient γ of $36 \mu\text{C cm}^{-2}$, 66 kV cm^{-1} , and $1.8 \times 10^{-4} \text{ C m}^{-2} \text{ K}^{-1}$, respectively, have been prepared at 480 °C [4].

The amount of the intermetallic Pt-Pb phase formed during heating can be controlled by the choice of the starting compounds [39]. PZT 30/70 films on platinized silicon were prepared from transition metal *n*-butoxides in 2-methoxyethanol. When the PbO was used, the films were (111) oriented after heating at 400 °C, while the films prepared from the lead acetate had a mixed (111)/(100) orientation of the perovskite phase. The difference was explained by the thermal decomposition pathways of the lead oxide- and lead acetate-derived gel films. In the former case, the local atmosphere was much more reducing than in the latter case. As a consequence, a larger amount of intermetallic Pt-Pb phase was formed during heating which remained stable in a wide temperature range, between 350 and 450 °C. In the latter case, the amount of the as-formed Pb^0 was lower and it re-oxidized to Pb^{2+} in a narrower temperature interval.

Wu and co-workers [5] used another approach to lower the activation energy for nucleation of the perovskite phase. They introduced the perovskite PZT 52/48 particles as the nucleation seeds into the sol of the same composition. The films, prepared from the sols with 5 mol% of the seeds, crystallized into the single-phase

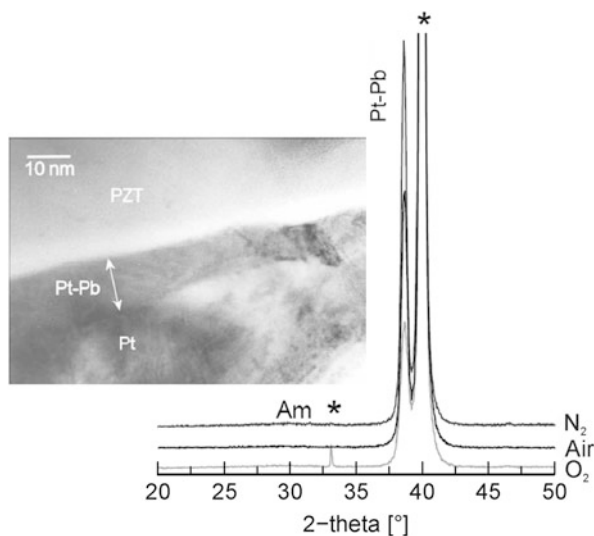


Fig. 18.4 XRD patterns of the amorphous PZT 30/70 thin films prepared from transition metal *n*-butoxides and PbO in 2-methoxyethanol deposited on platinized silicon substrates. The films were heated to 400 °C in nitrogen, air, or oxygen atmospheres. Inset: TEM micrograph of the film heated to 400 °C in air revealing the intermetallic Pt-Pb phase between the amorphous PZT and platinum electrode [33, 40]. *Am* amorphous phase, *asterisk* substrate. Reprinted with permission of the author and MRS©2006

perovskite with preferential (111) orientation after heating at 400 °C for 40 h. The films heated at 430 °C for 40 h reached the values of remanent polarization P_r , and coercive field E_c of $6.71 \mu\text{C cm}^{-2}$, and 80 kV cm^{-1} , respectively.

Maki et al. [41] combined the seeding approach with the RTA heating to prepare high quality PZT 40/60 thin films on platinized silicon substrates at as low as 420 °C. First, they deposited a thin ($\sim 3 \text{ nm}$) PbTiO_3 seeding layer. In the second step, they deposited the PZT solution on it and crystallized it on a hot-plate at 420 °C for 2 h. They repeated the deposition/heating steps for four times and therefore each crystallized layer served as the seeding layer for the following one. The 135 nm thick films showed promising ferroelectric properties with the P_r $15 \mu\text{C cm}^{-2}$ and E_c 59 kV cm^{-1} .

18.4 Sol-Gel Hydrothermal Processing

An interesting approach to low temperature processing of thin films is a combination of sol-gel, or more generally CSD, and hydrothermal methods. This method offers advantages of both techniques, control of the film stoichiometry and thickness, deposition of uniform layers over large areas of the former, and low

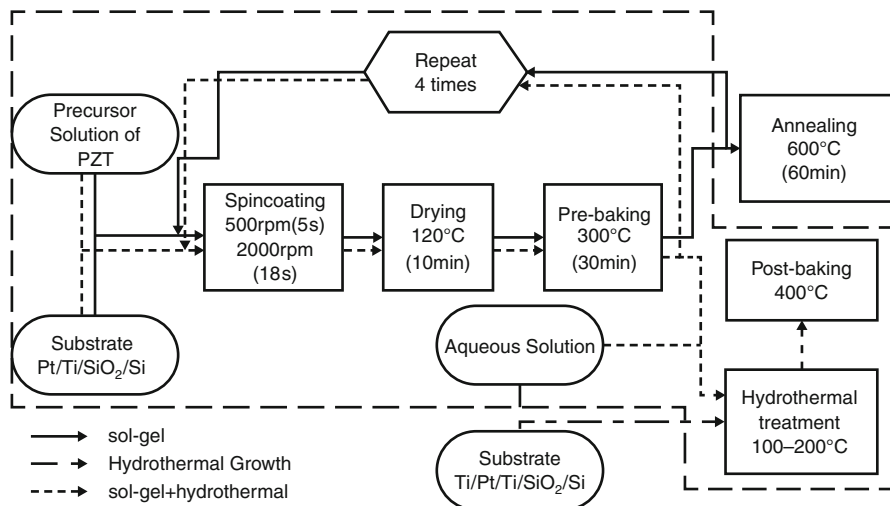


Fig. 18.5 Flow chart presentation of the conventional sol-gel, hydrothermal methods and comparison to the “hybrid” sol-gel hydrothermal process as reported by Wei and co-workers for PZT 52/48 films [42]. Reprinted with permission of JSAP©2001

temperature crystallization of the latter. A comparison of the three approaches, sol-gel, hydrothermal, and ‘combined’, for the processing of PZT 52/48 films is shown in Fig. 18.5 [17, 42].

Amorphous gel film, containing Pb/Zr/Ti in the stoichiometric ratio corresponding to PZT 52/48, on platinized silicon substrate was immersed into the 2 M KOH + 0.1 M Pb(OH)₂ solution and hydrothermally treated in an autoclave at 160 °C for 1 h. The KOH supplied a large enough amount of OH⁻ ions for the reaction as the solubility of the Pb(OH)₂ was not high enough. The perovskite phase with (111) preferred orientation crystallized upon hydrothermal treatment. The authors proposed a dissolution-reaction-crystallization mechanism for the perovskite formation. The Pb-species dissolved in the KOH + Pb(OH)₂ mixture, while the dissolution of ZrO₂ and TiO₂ was slower, and consequently a porous skeleton of these two compounds remained on the substrate. PZT as the product of the hydrothermal reaction in the solution precipitated on the substrate. The as-prepared films had poor ferroelectric properties. However, after post-heating at 400 °C the P_r 26 $\mu\text{C cm}^{-2}$ and E_c 40.1 kV cm^{-1} were obtained. The improvement was most probably due to the removal of the adsorbed water [42].

Besides PZT, BaTiO₃ films were also deposited at low temperatures using this approach. Similarly, post-annealing at 500 °C contributed to improved dielectric properties [43].

A low-temperature water-based synthesis was used for the preparation of epitaxial ZnO structures on (111) MgAl₂O₄ substrates [44]. The synthesis was performed in two steps. In the first step, the substrate was submerged into a sealed aqueous solution of zinc nitrate and ammonium nitrate at 90 °C. Simultaneously,

the pH of the solution was raised from 4.5 to 7.5 (room temperature values, pH was approximated to be invariant with the temperature) to produce a supersaturated solution with a large number of nuclei. This step resulted in a thin ZnO film composed of small epitaxial grains which served later as the seeding layer. Before the second step, the film was covered by a photoresist and patterned to obtain periodic circular windows where anisotropic growth of the ZnO could occur. Consequently, the epitaxial growth on the seeding layer was achieved by submerging the film into a sealed solution of zinc nitrate and ammonia at room temperature, then the temperature was raised to 90 °C. Somehow contra-intuitive decrease of ZnO solubility with increase of the temperature in the aqueous ammonia solution was confirmed also by a thermodynamical model [45].

18.5 Photochemical Solution Deposition

A combination of photochemical activation and CSD has been employed in low-temperature processing of functional-oxide films. The decomposition of organic species in the gel film upon pyrolysis was promoted by a high-power irradiation in the ultraviolet (UV) range. This resulted in a decrease of the crystallization temperature of the target phase. To modify the organics decomposition pathway by the UV radiation, the starting solution should contain UV absorbing species. Metal alkoxides, which are often used as metal sources in the CSD, do not have significant absorption in this wavelength range. On the other hand, UV radiation causes photoexcitation of $\pi - \pi^*$ transitions in β -diketonate complexes and dissociation of the chelate bonds [46, 47]. Thus UV radiation can also be used for patterning as described in more detail in Chap. 20.

The photochemical solution deposition has been implemented in processing of different single-oxide films, such as ZrO₂ and SiO₂ [48, 49], as well as complex oxides, such as Pb_{0.76}Ca_{0.24}TiO₃ (PCT). Calzada and co-workers [18] prepared PCT films on platinized silicon substrates by the diol-based sol-gel route where the titanium alkoxide was modified with β -diketonate, as shown in Fig. 18.6a. The gel films were exposed to UV radiation at 250 °C for 4 min (Fig. 18.6b).

Fourier-transform infrared spectroscopy (FTIR) patterns of the gel films prepared without or with UV radiation revealed decreased intensities of the absorption bands, characteristic for the stretching vibrations of the CH₂ and CH₃ groups, in the latter (Fig. 18.6c). This indicated that the UV radiation contributed to the enhanced elimination of the organics. Single phase perovskites were prepared at 450 °C using an RTA furnace without any organic residues [50].

In the sequel work the authors reported the enhanced electrical properties by processing the films in oxygen, which was attributed to the presence of ozone O₃ and active oxygen species O(¹D) formed upon dissociation of oxygen under the UV light [51]. PCT films, prepared by UV radiation and heating at 450 °C, had time-stable remanent polarization P_r , 11 $\mu\text{C cm}^{-2}$, and the values of coercive field E_c and pyroelectric coefficient γ 164 kV cm^{-1} and $3.1 \times 10^{-8} \text{ C cm}^{-2} \text{ K}^{-1}$, respectively.

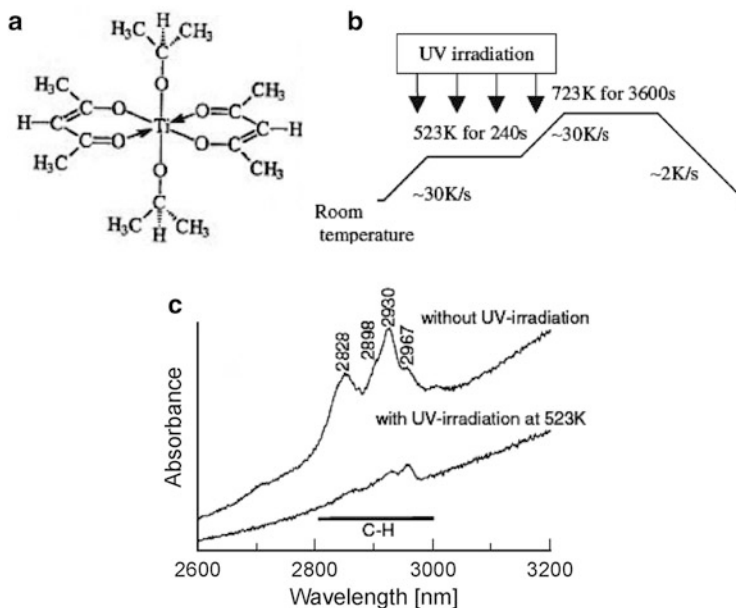


Fig. 18.6 (a) Structure of the titanium di-isopropoxide bis-acetylacetonate; (b) scheme of the UV-assisted thin films heating regime; (c) FTIR spectra of the $\text{Pb}_{0.76}\text{Ca}_{0.24}\text{TiO}_3$ gel layers prepared with and without UV radiation [18]. Reprinted with permission of the author and Wiley-VCH©2007

These properties were still somehow inferior to the properties of the films prepared at high temperatures ($\gamma \approx 42 \times 10^{-9} \text{ C cm}^{-2} \text{ K}^{-1}$ [52]), but fulfilled requirements for some applications. Recently Bretos et al. [53] reported the successful preparation of the PCT films from the stoichiometric solutions, i.e., without any lead-oxide excess, which is usually necessary to obtain phase-pure perovskite films.

18.6 Laser-Assisted Low Temperature Crystallization

Laser-assisted heating is a well known method in semiconductor industry to enable crystallization of ion-implanted amorphous silicon films on different substrates at low temperatures [54]. The benefit of the method lies in the absorption of the laser light which produces strong heating only in a thin surface layer while the substrate remains cold. Strictly speaking, the approach is not really a “low” temperature one, since the calculations showed that the surface temperature can be as high as 3,400 K [19]. The approach has not been widely used in processing of electroceramic thin films and the amount of studies in the literature is very limited. The reasons are poor thermal conductivity and a very high absorption coefficient of ferroelectric materials at excimer laser wavelengths, which may cause melting and therefore

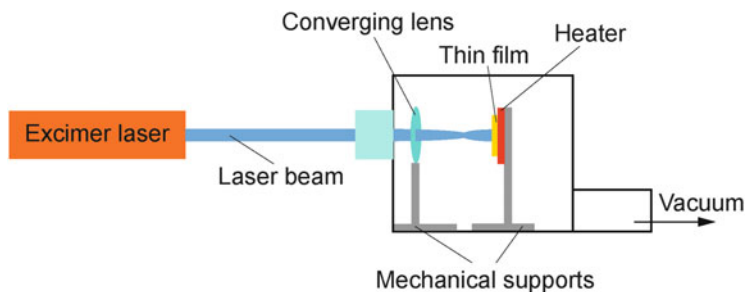


Fig. 18.7 Schematic of a laser-assisted crystallization setup [19]. Reprinted with permission of Wiley-Blackwell@2008

deterioration of the film surface [55]. Most often used excimer lasers are based on ArF and KrF gases, which provide wavelengths of 193 and 248 nm, respectively, and energy densities used are usually around $\sim 100 \text{ mJ cm}^{-2}$. The experimental setup for laser-assisted crystallization is shown in Fig. 18.7.

Baldus and Waser [56] prepared BST 70/30 films on platinized silicon substrates by the laser-assisted crystallization of amorphous films. They studied the influence of the film thickness on final properties. In case of 200 nm thick films cracking occurred. The 30 nm thick films melted during processing. The authors successfully prepared 130 nm thick films using the energy density of 100 mJ cm^{-2} and obtained the values of dielectric permittivity ϵ' 180 and dielectric losses $\tan\delta$ 0.01 at 10 kHz.

The influence of the substrate temperature on the crystallization kinetics during laser annealing was described by Donohue and co-workers [54, 57]. The amorphous PZT 30/70 thin films on platinized silicon substrates were activated by energy density of 80 mJ cm^{-2} when the substrates were held at 300°C . Both perovskite and pyrochlore phases were detected by X-ray diffraction. The films could not be crystallized when the substrates were kept at room temperature whatever energy density was used.

Cheng et al. [58] prepared $\text{Bi}_{1.5}\text{Zn}_{0.5}\text{Nb}_{1.5}\text{O}_{6.5}$ thin films on platinized silicon substrates using a combination of laser-assisted crystallization and conventional heating. High quality films were obtained using the energy density of 27 mJ cm^{-2} , the temperature of the substrate 400°C , and post-annealing at 400°C for 2 h in an oxygen atmosphere. The films had dielectric permittivity ϵ' 156, dielectric losses below 0.2 %, and tunability $(\epsilon'_{(0)} - \epsilon'_{(2.24 \text{ MV/cm})})/\epsilon'_{(0)}$ of 33 %, measured at 100 kHz. These values are comparable to those obtained for rapid thermally annealed $\text{Bi}_{1.5}\text{Zn}_{0.5}\text{Nb}_{1.5}\text{O}_{6.5}$ films prepared at T exceeding 600°C .

Finally, Hawelka and co-workers [59] recently proposed the use of size- and cost-efficient diode laser module for drying and hardening of ZrO_2 nano-dispersions spin-coated on steel substrates. Four-time increase in hardness as compared to a non-treated coating was achieved by using laser intensity of $5 \times 10^3 \text{ W cm}^{-2}$.

18.7 Amorphous Functional-Oxide Films

As mentioned earlier functional-oxide thin films on flexible polymer substrates are interesting for some applications in electronics, namely in transparent electronic devices. Oxide semiconductors, including $\text{In}_2\text{O}_3:\text{Sn}$ (ITO) or compositions based on ZnO, such as In-Zn-O or In-Zn-Ga-O, are an alternative to classical silicon semiconductors and are prepared in the form of transparent films at low temperatures, mainly by physical vapor deposition routes [23, 24], taking into account the fact that the mobility of the amorphous materials is comparable to that of the crystalline phases [60]. Amorphous ZnO films have been prepared from zinc acetate dihydrate and 2-methoxyethanol as a solvent at as low as 150 °C. The films on polyethylene naphthalate substrates did not contain any residual organics as confirmed by X-ray photoelectron spectroscopy, and showed reasonable optical and electrical properties [61]. Similarly, amorphous ZrO_2 films have been prepared from the zirconium *n*-propoxide based solutions on glass substrates at 200 °C in oxygen atmosphere [62].

18.8 Summary

In this chapter some approaches to lower the processing temperature of functional complex-oxide thin films by CSD have been introduced. The optimized solution chemistry and/or the heating profile have contributed to successfully decreasing the crystallization temperature of a number of complex oxides. In processing of PZT thin films, nucleation layers—either prepared before the deposition of the active material or formed in-situ during processing have majorly contributed to achieving both a lower crystallization temperature and a selected orientation of the perovskite phase. Hydrothermal processing resulted in crystallization of functional-oxide thin films already in solution, but required an additional heating step to achieve suitable functional properties. Photochemical activation of the as-deposited films promoted the decomposition of organic groups and contributed to a decrease of crystallization temperature of PbTiO_3 -based films, even without any lead-oxide excess in the coating solution. Laser activation of the as-deposited films could result in film crystallization without over-heating the underlying substrate and could be therefore implemented with temperature-unstable substrates such as glass and polymers. The challenge in CSD of oxide semiconductors on polymer substrates is to design liquid precursors which decompose at temperatures not exceeding 150–200 °C.

References

1. Hirano S, Kato K (1988) Preparation of crystalline LiNbO_3 films with preferred orientation by hydrolysis of metal alkoxides. *Adv Ceram Mater* 3:503–506
2. Hasenkox U, Hoffmann S, Waser R (1998) Influence of precursor chemistry on the formation of MTiO_3 ($M = \text{Ba}, \text{Sr}$). *J Sol-Gel Sci Technol* 12:67–79
3. Malič B, Arčon I, Kodre A, Kosce M (2006) Homogeneity of $\text{Pb}(\text{Zr},\text{Ti})\text{O}_3$ thin films by chemical solution deposition: extended x-ray absorption fine structure spectroscopy study of zirconium local environment. *J Appl Phys* 100:051612
4. Huang Z, Zhang Q, Whatmore RW (1999) Low temperature crystallization of lead zirconate titanate thin films by a sol-gel method. *J Appl Phys* 85:7355–7361
5. Kwok CK, Desu SB (1992) Low temperature perovskite formation of lead zirconate titanate thin films by a seeding process. *J Mater Res* 8:339–344
6. Wu A, Vilarinho PM, Reaney I, Miranda Salvado IM (2003) Early stages of crystallization of sol-gel derived lead zirconate titanate thin films. *Chem Mater* 15:1147–1155
7. Brooks KG, Reaney IM, Klissurska R, Huang Y, Bursill L, Setter N (1994) Orientation of rapid thermally annealed lead zirconate titanate thin films on (111) Pt substrates. *J Mater Res* 9:2540–2553
8. Chen SY, Chen IW (1994) Temperature-time texture transition of $\text{Pb}(\text{Zr}_{1-x}\text{Ti}_x)\text{O}_3$ thin films: I, role of Pb-rich intermediate phases. *J Am Ceram Soc* 77:2332–2336
9. Muralt P, Maeder T, Sagalowicz L, Scalse S, Naumovic D, Agostino RG, Xanthopoulos N, Mathieu HJ, Patthey L, Bullock EL (1998) Texture control of PbTiO_3 and $\text{Pb}(\text{Zr},\text{Ti})\text{O}_3$ thin films with TiO_2 seeding. *J Appl Phys* 83:3835–3841
10. Tani T, Xu Z, Payne DA (1993) Preferred orientations for sol-gel derived PLZT thin layers. In: Myers ER, Tuttle B, Desu SB, Larsen PK (eds) *Ferroelectrics thin films III*. Materials research society symposium proceedings, vol 310, pp 269–274
11. Hiboux S, Muralt P (2004) Mixed titania-lead oxide seed layers for PZT growth on Pt(111): a study on nucleation, texture and properties. *J Eur Ceram Soc* 24:1593–1596
12. Hofmann S, Waser R (1999) Control of the morphology of CSD-prepared $(\text{Ba},\text{Sr})\text{TiO}_3$ thin films. *J Eur Ceram Soc* 19:1339–1343
13. Malič B, Boerausu I, Mandeljc M (2007) Processing and dielectric characterization of $\text{Ba}_{0.3}\text{Sr}_{0.7}\text{TiO}_3$ thin films on alumina substrates. *J Eur Ceram Soc* 27:2945–2948
14. Park KH, Kim CY, Jeong YW, Kwon HJ, Kim KY, Kim ST (1995) Microstructures and interdiffusions of Pt/Ti electrodes with respect to annealing in the oxygen ambient. *J Mater Res* 10:1790–1794
15. Atsuki T, Soyama N, Sasaki G, Yonezawa T, Ogi K, Sameshima K, Hoshiba K, Nakao Y, Kamisawa A (1994) Surface morphology of lead-based thin films and their properties. *Jpn J Appl Phys* 33:5196–5200
16. Halder S, Schneller T, Waser R (2007) Enhanced stability of platinumized silicon substrates using an unconventional adhesion layer deposited by CSD for high temperature dielectric thin film deposition. *Appl Phys A* 87:705–708
17. Zeng J, Zhang M, Song Z, Wang L, Li J, Li K, Lin C (1999) Lead-zirconate-titanate thin films deposited on silicon using a novel technique at low temperature. *Appl Surf Sci* 148:137–141
18. Calzada ML, Bretos I, Jiménez R, Guillon H, Pardo L (2004) Low-temperature processing of ferroelectric thin films compatible with silicon integrated technology. *Adv Mater* 16:1620–1624
19. Bharadwaja SSN, Dechakupt T, Trolier-Mckinstry S (2008) Excimer laser crystallized $(\text{Pb},\text{La})(\text{Zr},\text{Ti})\text{O}_3$ thin films. *J Am Ceram Soc* 91:1580–1585
20. Bescher E, Xu Y, Mackenzie JD (2001) New low temperature multiphase ferroelectric films. *J Appl Phys* 89:6341–6348
21. Kijima T, Ishiwara H (2002) Si-substituted ultrathin ferroelectric films. *Jpn J Appl Phys* 41:L716–L719

22. Fujimori Y, Nakamura T, Takasu H (1999) Low-temperature crystallization of sol-gel-derived $\text{Pb}(\text{Zr},\text{Ti})\text{O}_3$ thin films. *Jpn J Appl Phys* 38:5346–5349
23. Martins R, Almeida P, Barquinha P, Pereira L, Pimentel A, Ferreira I, Fortunato E (2006) Electron transport and optical characteristics in amorphous indium zinc oxide films. *J Noncryst Solids* 352:1471–1474
24. Lim W, Wang YL, Ren F, Nortona DP, Kravchenko II, Zavada JM, Peartona SJ (2008) Indium zinc oxide thin films deposited by sputtering at room temperature. *Appl Surf Sci* 254:2878–2881
25. Hoffman RL, Norris BJ, Wager JF (2003) ZnO-based transparent thin-film transistors. *Appl Phys Lett* 82:733–735
26. Choi MC, Kim Y, Ha CS (2008) Polymers for flexible displays: from material selection to device applications. *Prog Polym Sci* 33:581–630
27. Hirano S, Kato K (1988) Formation of LiNbO_3 films by hydrolysis of metal alkoxides. *J Non Cryst Solids* 100:538–541
28. Eichorst DJ, Payne DA (1990) Evolution of molecular structure in alkoxide-derived lithium niobate. In: Brinker CJ, Zelinski BJJ, Clark DF, Ulrich DR (eds) *Better ceramics through chemistry IV. Materials research society symposium proceedings*, vol 180, pp 669–674
29. Joshi V, Roy D, Mecartney ML (1993) Low temperature synthesis and properties of lithium niobate thin films. *Appl Phys Lett* 63:1331–1333
30. Halder S, Schneller T, Waser R (2005) Crystallization temperature limit of $(\text{Ba},\text{Sr})\text{TiO}_3$ thin films prepared by a nonoxocarbonate phase forming CSD route. *J Sol-Gel Sci Technol* 33:299–306
31. Kosec M, Malič B, Mandeljc M (2002) Chemical solution deposition of PZT thin films for microelectronics. *Mater Sci Sem Proc* 5:97–103
32. Mandeljc M, Kosec M, Malič B, Samardžija Z (2000) Low temperature processing of lanthanum doped PZT thin films. *Integr Ferroelectr* 30:149–156
33. Mandeljc M (2000) Priprava tankih plasti $(\text{Pb},\text{La})(\text{Zr},\text{Ti})\text{O}_3$ pri nizkih temperaturah (=Low temperature preparation of the $(\text{Pb},\text{La})(\text{Zr},\text{Ti})\text{O}_3$ thin films), MSc thesis, University of Ljubljana, Ljubljana
34. Mandeljc M (2006) Študij kristalizacije tankih plasti na osnovi $\text{Pb}(\text{Zr},\text{Ti})\text{O}_3$ (=Study of crystallization of $\text{Pb}(\text{Zr},\text{Ti})\text{O}_3$ thin films) PhD thesis, University of Ljubljana, Ljubljana
35. Malič B, Kosec M, Arčon I, Kodre A, Hiboux S, Mural P (2000) PZT thin films prepared from modified zirconium alkoxide. *Integr Ferroelectr* 35:81–89
36. Chen K, Mackenzie J (1990) Crystallization kinetics of metallo-organics derived PZT thin film. In: Zelinsky BJJ, Brinker CJ, Clark DE, Ulrich DR (eds) *Better ceramics through chemistry IV. Materials research society symposium proceedings*, vol 180, pp 663–668
37. Huang Z, Zhang Q, Whatmore RW (1999) Structural development in the early stages of annealing of sol-gel prepared lead zirconate titanate thin films. *J Appl Phys* 86:1662–1669
38. Impey SA, Huang Z, Patel A, Beanland R, Shorrocks NM, Watton R, Whatmore RW (1998) Microstructural characterization of sol-gel lead-zirconate-titanate thin films. *J Appl Phys* 83:2202–2208
39. Malič B, Mandeljc M, Dražič G, Škarabot M, Muševič I, Kosec M (2008) Strategy for low-temperature crystallization of titanium-rich PZT thin films by chemical solution deposition. *Integr Ferroelectr* 100:285–296
40. Mandeljc M, Malič B, Kosec M, Dražič G (2006) Influence of the lead-compound on PZT 30/70 thin film orientation. In: Ramesh R, Maria JP, Alexe M, Joshi V (eds) *Ferroelectric thin films XIII. Materials research society symposium proceedings*, vol 902E, pp 0902-T03–37
41. Maki K, Soyama N, Nagamine K (2001) Low-temperature crystallization of sol-gel derived $\text{PbZr}_{0.4}\text{Ti}_{0.6}\text{O}_3$ thin films. *Jpn J Appl Phys* 40:5533–5538
42. Wei Z, Yamashita K, Okuyama M (2001) Preparation of $\text{Pb}(\text{Zr}_{0.52}\text{Ti}_{0.48})\text{O}_3$ thin films at low-temperature of less than 400 °C by hydrothermal treatment following sol-gel deposition. *Jpn J Appl Phys* 40:5539–5542

43. Xu J, Zhai J, Yao X (2006) Structure and dielectric properties of barium titanate thin films grown by sol-gel-hydrothermal process. *Appl Phys Lett* 89:252902
44. Richardson JJ, Lange FF (2009) Controlling low temperature aqueous synthesis of ZnO. 2. A novel continuous circulation reactor. *Cryst Growth Des* 9:2576–2581
45. Richardson JJ, Lange FF (2009) Controlling low temperature aqueous synthesis of ZnO. 1. Thermodynamic analysis. *Cryst Growth Des* 9:2570–2575
46. Barnum DW (1961) Electronic absorption spectra of acetyl-acetonato complexes–I: complexes with trivalent transition metal ions. *J Inorg Nucl Chem* 21:221–237
47. Tohge N, Shinmou K, Minami T (1994) Effects of UV-irradiation on the formation of oxide thin films from chemically modified metal-alkoxides. *J Sol-Gel Sci Technol* 2:581–585
48. Hirai S, Shimakage K, Sekiguchi M (1999) Zirconium oxide coating on anodized aluminium by the sol-gel process combined with ultraviolet irradiation at ambient temperature. *J Am Ceram Soc* 82:2011–2016
49. Makeawa S, Ohishi T (1994) Evaluation of SiO₂ thin films prepared by sol-gel method using photoirradiation. *J Non Cryst Solids* 169:207–209
50. Bretos I, Jiménez R, Rodríguez-Castellón E, Garcia-Lopez J, Calzada ML (2008) Heterostructure and compositional depth profile of low-temperature processed lead titanate-based ferroelectric thin films prepared by photochemical solution deposition. *Chem Mater* 20:1443–1450
51. Calzada ML, Bretos I, Jiménez R, Guillona H, Ricote J, Pardo L (2007) Low-temperature ultraviolet sol-gel photoannealing processing of multifunctional lead-titanate-based thin films. *J Mater Res* 22:1824–1833
52. Poyato P, Calzada ML, Pardo L (2003) Effects of substrate annealing and post-crystallization thermal treatments on the functional properties of preferentially oriented (Pb,Ca)TiO₃ thin films. *J Appl Phys* 93:4081–4090
53. Bretos I, Jiménez R, García-López J, Pardo L, Calzada ML (2008) Photochemical solution deposition of lead-based ferroelectric films: avoiding the PbO-excess addition at last. *Chem Mater* 20:5731–5733
54. Baeri P, Campisano SU, Foti G, Rimini E (1979) A melting model for pulsing-laser annealing of implanted semiconductors. *J Appl Phys* 50:788–797
55. Donohue P, Todd MA (2000) Pulse-extended excimer laser annealing of lead zirconate titanate thin films. *Integr Ferroelectr* 31:285–296
56. Baldus O, Waser R (2004) Laser crystallization studies of barium strontium titanate thin films. *J Eur Ceram Soc* 24:3013–3020
57. Lai SC, Lue HT, Hsieh KY, Lung SL, Liu R, Wu TB, Donohue PP, Rumsby P (2004) Extended-pulse excimer laser annealing of Pb(Zr_{1-x}Ti_x)O₃ thin film on LaNiO₃ electrode. *J Appl Phys* 96:2779–2784
58. Cheng JG, Wang J, Dechakupt T, Trolrier-McKinstry S (2005) Low-temperature crystallized pyrochlore bismuth zinc niobate thin films by excimer laser annealing. *Appl Phys Lett* 87:232905
59. Hawelka D, Stollenwerk J, Pirch N, Büsing L, Wissenbach K (2011) Laser based inline production of wear protection coatings on temperature sensitive substrates. *Phys Proc* 12:490–498
60. Hosono H (2007) Recent progress in transparent oxide semiconductors: materials and device application. *Thin Solid Films* 515:6000–6014
61. Tellier J, Kuščer D, Malič B, Cilenšek J, Škarabot M, Kovač J, Gonçalves G, Muševič I, Kosec M (2010) Transparent, amorphous and organics-free ZnO thin films produced by chemical solution deposition at 150 °C. *Thin Solid Films* 518:5134–5139
62. Brenier R (2002) Stress and moisture-sorption in ozone-annealed films of zirconium oxide obtained from sol-gel. *J Sol-Gel Sci Technol* 25:57–63

Chapter 19

Composite Film Processing

Robert Dorey, Subhasis Roy, A. Sharma, Chandan Ghanty,
and Subhasish B. Majumder

19.1 Composites from Particles Larger than 100 nm

19.1.1 Introduction: Why Thick Films

As will be shown in Chap. 24, piezoelectric films are of interest as they can be used to act upon or sense the surrounding environment. Thicker films are of particular interest due to the higher forces and strains that can be exerted [1, 2] and due to the higher signals that they generate [3–5] when acted upon. Of special interest are films with thicknesses between 1 and 100 μm due to the combined high sensitivity and high power that can be achieved.

Films typically below 1 μm are most commonly deposited using physical and chemical vapour deposition or chemical solution deposition routes, while films thicker than 100 μm are most readily produced by machining bulk materials [6]. The main route for achieving thick films between 1 and 100 μm is through the use of powder based deposition routes where powder is deposited onto the surface of the substrate and then processed to produce a thick film. A variety of different techniques can be used to deposit the film including screen printing, electrophoresis and spray coating.

The most common of the deposition processes is screen printing as it is considered to be a relatively simple process and is able to create films up to 100 μm thick with relative ease [7]. In its simplest configuration screen printing consists of creating an ink containing the active powder, an organic carrier fluid (such as pine oil), dispersing agent and ceramic binder [8]. This ink is printed onto the

R. Dorey (✉)
Cranfield University, Cranfield, Bedfordshire MK43 0AL, UK
e-mail: r.a.dorey@cranfield.ac.uk

S. Roy • A. Sharma • C. Ghanty • S.B. Majumder (✉)
Materials Science Centre, Indian Institute of Technology, Kharagpur 721 302, India
e-mail: subhasish@matsc.iitkgp.ernet.in

substrate and dried to remove the carrier fluid. The active powder, along with any non volatile materials, is then left behind in a loosely bound state. A high temperature sintering stage is used to densify the powder and bond it to the surface of the substrate. Due to the nature of ceramic materials such sintering stages typically occur at relatively high temperatures of between 1,000 and 1,400 °C [7, 9]. This poses a number of challenges when the whole system consisting of film, substrate and electrodes is considered.

19.1.2 Challenges

The challenges associated with integrating functional thick films with the required electrical connections and mechanical support structures can be grouped under three main headings depending on the origin of the failure mechanism that arises.

- **Thermal:** Failure arises purely due to thermally induced degradation of one, or more, of the materials in the system. Examples of degradation include melting, vaporising, and softening of materials. Such a failure mechanism occurs when the processing requirements for one material (normally the ceramic) exceed the safe working conditions for one of the other materials within the system. An example of this type of failure would be that of a polymer melting during processing at elevated temperatures. Such failure can also occur in more thermally robust systems. A critical concern for lead-containing ceramics is that of loss of lead at elevated temperatures [9]. While not inducing structural failure, this loss of lead due to evaporation changes the stoichiometry of the materials and significantly alters the functional properties of such materials.
- **Thermo-chemical:** Failure through chemical reactions occurs when neighbouring materials are chemically incompatible. Such incompatibilities can also occur between a material and the surrounding environment. Failure will proceed either through the removal of material (e.g. transformation into a liquid or gas which is unable to act as a linking material) or creation of a weak interface material (e.g. creation of a poor adhesion material).

The role of temperature is to control the rate at which such reactions occur or to allow such a reaction mechanism to be activated. So, while a chemical reaction is a prerequisite for this type of failure mode, the presence of elevated temperatures is not necessarily required as many such reactions can occur at ambient temperatures. The term thermo-chemical is used as both atomic diffusion and chemical reactions are accelerated at elevated temperatures which means that degradation will tend to occur where both chemical incompatibility and high temperatures are present. In the majority of solid-solid interfaces reactions typically occur at very slow rates (if at all) at ambient temperatures. In such situations elevated temperatures are required to initiate failure. However, across liquid–solid or gaseous-solid interfaces such reactions can occur at much faster rates, even at ambient temperatures, due to the enhanced atomic diffusion

of liquids and gases. Examples of such failure include oxidation of metals [9] and formation of liquid phases in interfacial regions such as found between silicon and lead containing materials at temperature in excess of 714 °C [1, 3, 10].

- **Thermo-chemo-mechanical:** Mechanical strains, generated due to the thermal and/or chemical processing of materials, can give rise to mechanical stresses within a system when there is a mismatch between the strains in different materials. Differential strains arise due to volume changes caused by thermal expansion mismatch, oxidation, reactions, densification and drying. When the system is subjected to stresses failure modes, include bowing, cracking and delamination, can occur. Even when failure does not occur initially, delayed failure can occur in a system due to sub-critical crack growth where defects continue to grow under the action of stress until they reach a critical size and failure of the system occurs. The term thermo-chemo-mechanical failure is used as the mechanical failure is driven by thermal and/or chemically generated stresses.

Underlying the separate failure mechanisms highlighted above are a series of common causes. The most influential of these is that of temperature as it has a direct influence on the majority of the issues. It is for this reason that a reduction in the processing temperature is the most beneficial action that can be undertaken to minimise the challenges faced in integrating thick ceramic films with structural materials. Other mitigation measures that can be undertaken include the use of an inert atmosphere to prevent oxidation, diffusion/adhesion barriers to prevent interfacial reactions and delamination and decreasing the amount of densification required during processing to reduce the stresses generated.

In the first instance, the reduction in processing temperature can be viewed as the primary way to minimise the probability of failure. To start with this chapter will examine some conventional routes, taken from bulk ceramic processing, which have also been successfully used to reduce the sintering temperature of ceramic thick films.

19.1.3 Reduction in Sintering Temperature

19.1.3.1 Sintering Aid

The processing temperature can be reduced very effectively through the use of low melting temperature sintering aids (Table 19.1). These sintering aids melt at moderate temperatures and coat the active powder. As atomic diffusion is significantly faster in a liquid than it is in a solid, the rate of material diffusion is increased allowing densification to occur at a much increased rate or at a reduced temperature.

Table 19.1 Examples of sintering aids, level of addition and processing temperature used in the densification of lead containing piezoelectric and ferroelectric films

Sintering aid	Addition	Processing temperature	References
PbO	6 wt%	850 °C	[7]
($T_m = 800$ °C)	5wt%	925 °C	[9]
Pb ₅ GeO ₁₁	2 wt%	800 °C	[7]
($T_m = 738$ °C)		850 °C	
Bi ₂ O ₃ -Li ₂ O	1 wt%	925 °C	[9]
Cu ₂ O:4PbO	5 wt%	710 °C	[12]
($T_m = 680$ °C)			
Bi ₂ O ₃ -ZnO		950 °C	[10]
Borosilicate glass			

In addition, because the particles are surrounded by a lubricating liquid they can reorient themselves more easily to relieve stress and increase density.

The most straightforward approach is to use a relatively high level (up to 30 vol%) of ceramic binder such as lead borosilicate glass [8]. The disadvantage of using such sintering aids is that they are non functional and so represent an inactive phase which reduces the functional properties of the film [8, 9, 11]. Conversely, minimising the quantities added makes it difficult to get the homogenous mixing of materials that is required for short processing times at low temperatures [9]. In addition, the lower levels of liquid phase result in a reduction in the ability of particles to reorientate. Due to these conflicting actions there is often an optimum level of sintering aid that can be added. This varies from system to system and depends on a number of parameters including particle sizes, shapes and chemistry of the system. Typically additions of between 1 and 10 vol% of sintering aid are added to enhance densification (Table 19.1).

19.1.3.2 Small Powder Sizes

As with conventional sintering processes, decreasing the size of the powder particles leads to an increased driving force and sintering kinetics which manifests itself in enhanced sintering and the ability to process films at lower temperatures. By using nanoscale powder systems the sintering temperatures can be reduced by a few hundred Kelvin.

19.1.3.3 Mixed Powder Sizes

When powders are compacted together (irrespective of the size of particles) small interstitial voids will remain within the structure. It is the role of the sintering process to remove these voids through densification. If these voids can be filled with smaller particles the level of densification required can be reduced. By mixing two powders of different size it is possible to increase the density of the unsintered film

as the smaller particles fill the gaps between the larger particles [13]. Not only do the smaller particles help to increase the green density by filling in the voids, they also help to accelerate the densification process due to their higher densification kinetics. Care needs to be taken to ensure that a homogenous distribution of the different sizes of particles obtained otherwise some areas will sinter at different rates to other areas giving rise to differential strains and stresses being generated.

19.1.3.4 Sol Infiltration

A logical evolution of the mixed powder sizes is the use of sol–gel systems [14]. Conventionally screen printed PZT ceramics can be processed at lower temperatures through the use of a sol infiltration stage [15]. This builds on the notion of using a mixed powder sized distribution and makes use of the nano-particulate and low temperature processing nature of sol–gel materials to both fill the interstitial voids and bind the larger ceramic particles together and to the substrate. A conventional screen printing route with high temperature (1050 °C/2 h) sintering can first be used to create a thick film material. The functional properties of the system can then be increased by infiltrating a PZT producing sol into the screen printed structure prior to drying at 300 °C for 30 min and sintering at 650 °C for 1 h. Increasing the number of infiltrations results in an increase in remnant polarisation, coercive field, and relative permittivity. The piezoelectric coefficient, however, tends to decrease due to increased clamping of the substrate and internal stresses. Increasing the concentration of the sol results in an increased effectiveness of the infiltration process as more PZT is produced within the pores for each infiltration stage. However, increasing the concentration of the sol too much (above 1–1.5 M) does not result in an increase in properties as the sol becomes too viscous to infiltrate the porous structure [16]. Instead, the sol remains at the surface of the film, effectively trapping the porosity within the layer.

A similar approach, using repeated sol infiltration prior to sintering, can be used to reduce the sintering temperature to between 750 and 950 °C [3]. This is obviously an advantage over the pre-sintering route in that the maximum temperature that the film experiences is reduced. The infiltration of the sol prior to sintering increases the sinterability of the film allowing higher densities at a given sintering temperature to be achieved. As with the previous post-sintering infiltration, pre-sintering infiltration leads to an increase in both relative permittivity and remnant polarisation as a result of improvements in density.

It is not just the active material that can be infiltrated to improve the final properties of the films. A sintering aid, in the form of a PbO producing sol, can be infiltrated into a presintered electrophoretically deposited film to increase the density and properties of the native film [17]. In this way the sintering aid was directly deposited on the surface of the PZT particles.

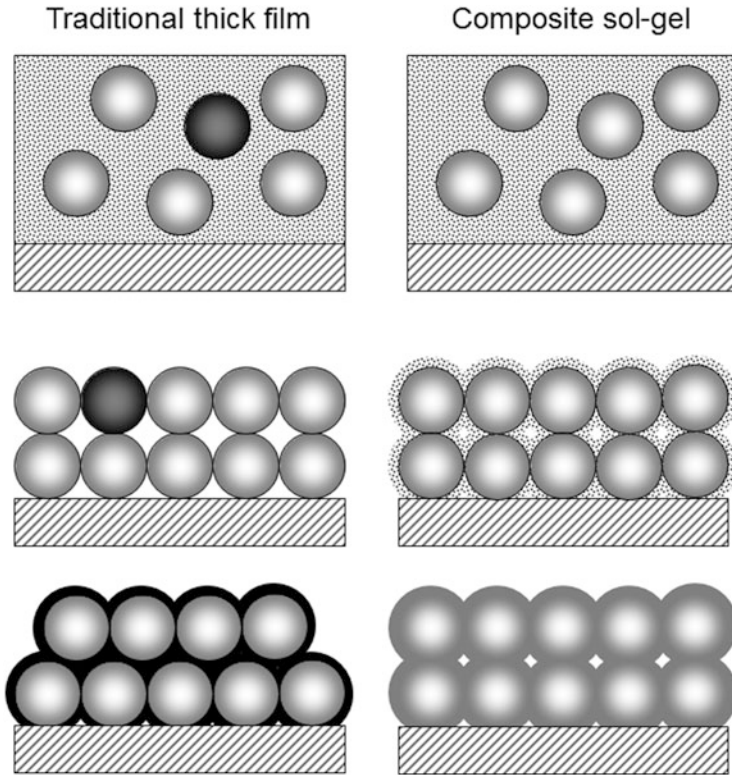


Fig. 19.1 Schematic showing a comparison between the conventional ceramic film technologies (*left*) and composite sol-gel system (*right*)

19.1.4 Composite Sol-Gel Approach

The basic premise behind the use of composite sol-gel processing is the combination of the sol infiltration and powder processing stages into a single step to enhance sintering [18, 19]. By creating an ink where the conventional inert carrier fluid and binder are replaced by a ceramic producing sol it is possible to produce a system where the sol serves the dual role of carrier fluid and binder. The added advantage of this approach is that the binder system can be compositionally matched to the parent ceramic powder ensuring a homogenous system [20] without inactive or detrimental phases (Fig. 19.1).

As the composite sol-gel system is essentially a mixture of sol and powder it is possible to produce inks with very different fluidic properties by varying both the sol concentration and the ratio of sol to powder. In this way a diverse system of inks can be produced that range from very fluid systems through to very viscous pastes. This ability to tailor the properties of the ink allows a range of deposition techniques to be employed for producing thick films.

Irrespective of the route used to deposit the film there are a number of key stages in the processing which need to be considered if the optimum film is to be obtained.

- Deposition, where the ink is deposited onto the substrate using on the techniques outlined below.
- Drying where the solvent is removed from the system at temperatures below 250 °C. This stage sees a significant reduction in the volume of the system and needs to be carefully controlled in order to prevent cracking of the films. During the early stages of drying the system is relatively fluid and particle reorientation is possible with relative ease. As more liquid is removed from the system this reorientation becomes progressively more difficult. Indeed, in the very late stages of drying the capillary forces between individual particles can build to such a level that the film will fail.
- Pyrolysis stage involves the conversion of the metal organic gel into an amorphous ceramic material through the application of heat. Typically pyrolysis occurs in the temperature range 250–550 °C. Further volume reduction occurs during this stage as the organic component of the sol removed. Rapid changes in strength and increases in stress can again lead to cracking.
- Crystallisation of the amorphous ceramic material into a crystalline ceramic material. Typically a temperature range of 550–700 °C is required to accomplish this transformation. A slight change in volume is often observed during the crystallisation of the ceramic material.

Due to the volume changes experienced during the processing of these composite sol–gel systems it is often necessary to deposit films using a layer-by-layer process with intermediate thermal treatments. In this way stresses within the film are managed and cracking is retarded.

While one of the stated advantages of the composite sol–gel system is the ability to create homogenous films, it is equally possible to create heterogeneous active films by combining multiple active materials such that the sol is used to produce one materials while the powder is composed on another material. An examples of such a heterogeneous film is PMN-PT powder in a PZT sol matrix [21] to enhance the dielectric properties of the thick film. This approach opens up an exciting possibility to create multifunctional systems.

19.1.4.1 Spin Coating

Perhaps the most frequently used approach for depositing composite sol–gel films is that of spin coating owing to the ability to achieve uniform film thicknesses and the readily transferrable know-how from the microelectronics industry where spin coating is frequently used for conformal coating. The process involves covering the substrate with the ink and then spinning the excess off at high speed to produce a uniform layer.

A number of different powder loadings have been employed with the spin coating approach to yield films with markedly different microstructures [22].

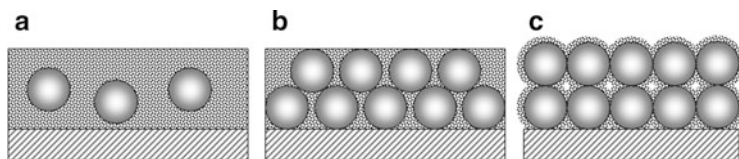


Fig. 19.2 Schematic showing possible arrangements of powder, sol-gel derived material and porosity in a thick film (a) powder embedded in a ‘sea’ of sol-gel derived material; (b) sol-gel material completely filling the interstitial pores between powder particles; (c) powder particles bonded together with sol-gel derived material with remnant porosity between powder particles

Where the ink contains an excess of sol the resultant microstructures are typically characterised by individual powder particles embedded in a ‘sea’ of sol-gel derived material [22]. Conversely, where the powder loading is much higher the microstructure is composed of easily discernable powder particles bonded together by the sol-gel phase [23]. This gives rise to a range of reported properties as the different phases contribute to different degrees depending on the exact arrangement of sol-gel derived phase, ceramic powder and porosity (Fig. 19.2).

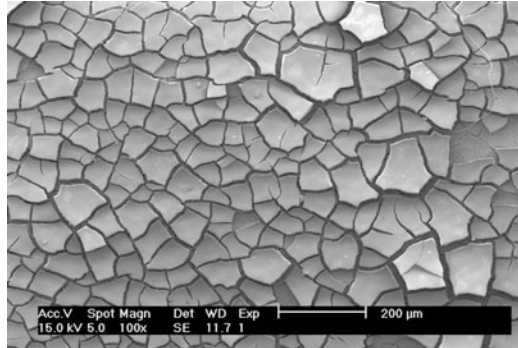
The choice of powder to sol ratio is dictated by the often conflicting requirements for the final film. Examples of common constraints places upon the final film include thickness, uniformity, surface quality, and properties.

For given processing conditions, the **thickness** of the film achieved using spin coating is dictated by the viscosity of the ink. As the viscosity of the ink increases so does the thickness of the film. In this way increases in film thickness can be achieved by increasing the powder loading [2]. This needs to be conducted with caution as there is an increased risk that films will crack when the film thickness increases (Fig. 19.3). This is mitigated to a slight degree by the reduced shrinkage exhibited by inks with high powder loading. However, generally this reduction in shrinkage is insufficient to prevent fracture of the films as the film thickness increases at a much faster rate.

While increasing the powder loading leads to an increase in thickness it also results in a change in shear thinning behaviour of the ink which can have an effect on the **uniformity** of the film. Shear thinning liquids are characterised by a large decrease in viscosity as the shear force is increased. This behaviour becomes more prevalent when the powder loading is increased. In a spin coating system the shear forces are at a minimum in the centre of the spinning substrate and increase towards the edges. The effect of this is to cause the ink to exhibit a higher viscosity, and hence thicker deposition, at the centre than compared to the periphery. This can result in a significant variation in thickness across the film. So while spin coating can be used to achieve relatively uniform thickness coatings in many systems, problems can arise in the composite sol-gel system if the powder loading is increased too far.

The **surface quality** of the film is affected by perturbations in the film and by cracking. It is known that spin coating of pure sol system results in very high quality surface finishes. When a small amount of powder is added to the sol to produce a

Fig. 19.3 SEM micrograph showing a cracked PZT thick film with an excessively high powder loading



composite sol–gel system the viscosity of the ink may only be increased slightly such that when it is spun the film thickness is less than the size of the ceramic particles. The resultant structure will then have a very poor surface quality and be composed of a thin film with large particles sitting proud of the film surface. Only as the powder loading increases does the film thickness increase to allow the particles to be fully embedded. The highest surface quality is obtained when powder particles are fully embedded in the structure and the sol forms a conformal layer at the top of the film. As the powder loading is increased still further the surface roughness increases again due to the profile of the powder particles dominating.

Along with the geometric constraints outline above, the final **properties** of the film are of great importance. Within a composite system each individual phase exhibits unique properties. Within the composite sol–gel system the three dominant phases are the sol–gel derived PZT (medium functional properties), the PZT powder (high functional properties) and the porosity (air—negligible functional properties). The final properties of the film will be a complex function of the system geometry and relative proportions of each phase [24]. The ceramic particle phase tends to exhibit a greater contribution than the sol–gel derived phase due to the larger grain size. The porosity will only have a negligible contribution to the functional properties. The result of these different contributions is that for inks with very low powder content the functional properties are relatively low and dominated by the sol–gel derived phase. As the powder content increases the functional properties are increased until the sol–gel derived phase just fills all of the pores between the ceramic particles. Further increases in powder content will cause progressively more porosity to be introduced into the system and a decrease in properties. The exact tipping point when properties begin to decrease will depend on the balance between the proportions and relative properties of each phase. Within a relatively narrow range of compositions increasing the powder loading or sol concentration leads to thicker films which exhibit higher relative permittivities and remnant polarisations [2]. As with sol infiltration treatments of screen printed materials, the increase in sol concentration results in a more effective filling of the pores. Increasing the powder loading results in improved properties due to the higher proportion of powder present.

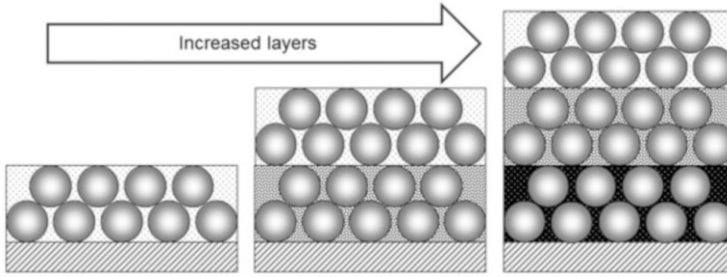


Fig. 19.4 Schematic showing the through thickness variation in density of the films caused by successive infiltration of sol from subsequent deposition stages

The through thickness microstructural **homogeneity** can be affected by the repeated deposition process due to infiltration of sol into lower levels [23, 25, 26]. Consider a four layer system where each layer has a degree of porosity following pyrolysis. The first layer deposited will have three layers above it where each will have infiltrated some sol into lower the levels during deposition. The effect of this is that the bottom layer will have been infiltrated three times, the second layer two times and the third layer once giving rise to a density gradient through the thickness of the film (Fig. 19.4).

As stated earlier, another variable of the composite sol–gel ink is the concentration of the sol used to disperse the powder. As the concentration of the sol is increased, the viscosity of the sol, and hence the ink, increases leading to an increase in thickness of the resultant film [2, 22]. While this also results in an increase in density, due to reduced sol shrinkage, aggregation of powder [22] and risk of cracking are increased (due to the increased thickness).

Spin coating is a relatively inefficient fabrication technique due to the material wastage during the spin-off stage where as much as 90 % of the material is discarded. This can pose problems with environmentally unfriendly or expensive materials. In an effort to alleviate the issue of thickness variation and cracking, other techniques have also be used to deposit ceramic thick films using the composite sol–gel approach. Techniques include screen printing, dip and spray coating and interfacial reaction techniques.

19.1.4.2 Screen Printing

Screen printing inks are characterised by high viscosity and deliberate shear thinning behaviour. The ink behaves like a thick paste when placed on top of the screen printing mesh preventing it from passing through the small holes. When the squeegee moves across the printing frame the applied shear stress causes the ink to shear thin and reduce in viscosity. At this stage the ink is able to pass through the mesh and make contact with the underlying substrate. The removal of the shear stress, once the squeegee has passed, causes the ink to once again increase in

viscosity preventing further spreading of the ink on the substrate. In conventional screen printing inks such shear thinning behaviour is caused by a high powder loading and selection of appropriate carrier fluids. In the case of the composite sol–gel system similar behaviour can be created by increasing the powder loading of the ink.

One factor that must be considered in addition to the powder loading is the volatility of the carrier fluid. In screen printing it is common to use carrier fluids such as pine oil with a relatively low volatility. This is to ensure that the ink does not dry out prior to passing through the mesh. Many sol–gel systems are based on low boiling point solvents such as ethanol, methanol and propanol. While suitable for spin coating, where drying time is expected to be relatively rapid, they are unsuitable for screen printing applications where the major solvent should have a boiling point above 100 °C to minimise evaporation. A slow evaporation rate also ensures that the rheological properties of the ink do not change in an uncontrolled manner during the printing process. Such composite sol–gel based screen printing inks can be achieved using systems based on 2-methoxyethanol [27, 28], butanol or other high boiling point solvents. The use of such solvents, does however lead to a slight increase in shrinkage on pyrolysis as more organic matter needs to be removed from the system.

Screen printing of composite sol–gel systems has not been examined in great detail due to the tendency of the sols to be sensitive to moisture which in turn makes cleaning the fine printing screens problematic. Other deposition processes do not require such a screen and so can tolerate composite sol–gel inks more readily.

19.1.4.3 Dip Coating

Dip coating ink occupies the opposite spectrum of the composite sol–gel inks in terms of powder loading and viscosity. In these systems [24, 29] dilute suspension of particles (0.01–10 g/ml) are used such that each dipping stage results in the deposition of a thin layer of material. Repeated deposition with intermediate drying stages is then used to build up the final film thickness. Care needs to be taken to ensure that the viscosity of the system is sufficiently high to prevent particle sedimentation and creation of very thin pure sol–gel layers. This can be accomplished either by adding an organic viscosity enhancer or by continuously agitating the dip coating bath [29]. Addition of significant levels of organic phase will result in the generation of porosity in the system when it is burned out. Relatively high density films are obtained using this approach as sol is able to infiltrate the interstitial pores during subsequent infiltration stages.

19.1.4.4 Electrophoretic Deposition

Comparable to dip coating in terms of the inks used, electrophoretic deposition makes use of the fact that charged particles in suspension can be deposited onto a

substrate through the application of an applied field. The advantage of this approach is that non-planar substrates can be coated with relative ease providing that they are electrically conducting or can be coated with an electrically conducting material.

The speed at which the charged particles move in the suspension, and hence their deposition, will depend on their physical attributes such as shape, size and density and the level of charge associated with them. This can lead to differences in deposition when mixed particles are deposited simultaneously. Due to the nature of the sol in the ink, it does not deposit at the same rate (if at all) as the suspended powder. However, as it is part of the carrier fluid the EPD process intrinsically ensures that the sol material is embedded in the resultant film. During EPD the powder particles will be deposited in a semi compacted arrangement on the surface of the substrate with the sol in the interstitial voids. On drying this sol will shrink considerably so that the resultant structure will be comparable to a high powder loading spin coated system (Fig. 19.2c). Alternatively a standard EPD film can be infiltrated with sol following deposition in a standard EPD solution [17]. This approach has the advantage that a more concentrated sol can be used to infiltrate the porous film, resulting in greater filling efficiency, and there are no issues of disposal of the remaining sol in the EPD solution.

19.1.4.5 Sedimentation

Instead of using an electric field to deposit the PZT thick film, a sedimentation route can be employed. In this case a low concentration powder suspension (~0.5 mg/ml) [24] is centrifuged at a few thousand rpm to cause the powder system to sediment. After each cycle the film is dried and pyrolysed until the final film thickness is achieved.

19.1.4.6 Spray Coating

A number of approaches can be used to create an atomised aerosol of ink for spraying including ultrasonic nebuliser, air atomizer [30], or electrospray [31]. Irrespective of the route used to create the aerosol the basic requirements of the ink are broadly similar and require a relatively dilute suspension of powder in a carrier fluid with a moderate evaporation rate. The key requirement is that the droplets created are sufficiently stable that they remain liquid during the transit from the spray apparatus to the substrate. If the droplets dry out during flight they will not spread on contact with the substrate and a highly porous film will be produced [31, 32]. Even when the spraying is managed effectively to ensure wet droplets arrive at the surface of the substrate, porosity can still arise due to shrinkage of the sol-gel phase during pyrolysis [30].

As with spin coating, intermediate drying, pyrolysis and crystallisation stages are often performed to manage the stresses within the films.

19.1.4.7 Interfacial Polymerisation

An alternative approach to building up the thick film on the surface of the substrate is to first create the film and then bring it into contact with the substrate. This can be achieved by using an interfacial polymerisation type approach [33, 34] using two immiscible liquids. The PZT producing sol and powder are mixed with a non-water soluble solvent such as hexane. A suitable substrate is then immersed in a container of water and the composite ink gently poured on top of the water. At the interface between the water and composite solution an interfacial polymerisation reaction occurs forming a composite film. When the water is drained off, the composite film is gently lowered onto the waiting substrate. Controlled heating in stages at room temperature, 400 and 950 °C are used to dry, pyrolyse and sinter the films. The resultant films are similar to the other high powder loaded composite films in appearance and characterised by PZT powder bound by the sol–gel phase with interstitial porosity. As with the other high powder loading systems, the porosity arises due to the shrinkage of the sol material during drying and pyrolysis.

19.1.5 Enhancements to the Composite Sol–Gel Process

19.1.5.1 Infiltration

As discussed above, the presence of porosity within the film results in a reduction in functional properties. This can be countered by incorporating an infiltration process whereby the pores are filled with PZT producing sol prior to converting the sol to ceramic through a heat treatment process. The infiltration process can be conducted at the end of the deposition process [24] or at intermediate coating stages [1, 23, 35, 36]. Using an intermediate deposition process can help to improve the surface finish of the films [23], but also has the effect of slowing the film forming process down.

The process can be described by considering a ‘standard’ repeat building block as the composite ink layers with corresponding infiltration cycles. Such that 2C + 2S would describe a process where two composite ink layers were deposited and infiltrated twice using sol.

Following the infiltration of the porous network the excess sol–gel material is removed to leave only the pores filled with sol. Subsequent drying and pyrolysis converts the sol to a ceramic and also causes a significant loss of material the effect of which is to leave a degree of porosity. Subsequent infiltration will again only fill some of the remaining porosity. In this respect sol–gel infiltration operates on a case of diminishing returns as each successive infiltration treatment will remove progressively less porosity from the system. Depending on the concentration of the sol the point at which infiltration no longer brings a benefit can occur after only a few cycles.

Another feature of the sol infiltration process is the formation of interlayers of pure sol–gel material between layers of composite sol–gel. This occurs at the stage where sol can no longer infiltrate the composite sol–gel layer and instead remains on the surface of the film and blocks the surface pores preventing further infiltration. Further infiltration treatments only result in an increase in the thickness of these interlayers and a decrease in the properties of the film as while due to the lower functional properties associated with pure sol–gel derived material.

19.1.5.2 Sintering Aids

As with the conventional screen printing approach, the application of sintering aids can be used to increase densification and reduce the sintering temperature. The key parameter again is to ensure that the melting temperature of the sintering aid is below that of the proposed processing temperature. Given the low temperatures at which sol–gel systems are converted to ceramics the sintering aids used in screen printing are often ineffective. Two low temperature sintering aids that have been used successfully with thick PZT films include the eutectic mixture of PbO/Cu₂O ($T_m = 678\text{ }^\circ\text{C}$) [23] processed at 710 °C and PGO ($T_m = 738\text{ }^\circ\text{C}$) [37] processed at 770 °C.

While adding a sintering aid has been shown to lead to an improvement in densification, the formation of the liquid phase increases interfacial reactions making it necessary to introduce a barrier layer into the system. This is particularly important when integrating lead containing materials with silicon based materials [7] where interdiffusion of the lead in silicon can lead to the formation of low permittivity lead silicates. The presence of such reaction phases can lead to significant reduction on properties. Examples of diffusion barrier materials employed to prevent such reactions include ZrO₂ [38], TiO₂ [39], and Al₂O₃ [7].

As the sintering aid is added to the composite sol–gel system it is possible to combine the use of sintering aids and sol infiltrations to get enhanced densification.

19.1.5.3 Pressure

The application of uniaxial pressure to the film during sintering has also been proposed as a way to increase the density of the film in a similar manner to how hot pressing is used in the manufacture of bulk ceramics. Improvements in density were observed using this process, but care needs to be taken to ensure that the substrate material is not damaged and that uniform pressure is applied across the film to prevent inhomogeneities in density from developing. These two constraints have tended to limit the tackle up of this approach.

To maintain a reasonable surface finish and functional properties in films only a few microns thick requires the size of the powder additions to be reduced to sub 100 nm. In this way it is still possible for the films to be many particles thick such that the random packing of the particle allows a homogenous surface to be

maintained. When the particles are too big variations in particle packing can result in significant inhomogeneities in thickness and density across the film.

19.2 Composites from Sub-100 nm Particles/ (Or Nano-composite Electro-Ceramic Thin Films)

19.2.1 Why Nano-composite Thin Films

Oxide thin films exhibit a wide range of functional properties including but not limited to ferroelectricity, multiferroic characteristics, high temperature superconductivity, spintronic characteristics, colossal magneto-resistance etc [40]. Synthesis of nano-composite thin films using two or more oxides are found to be very attractive either to enhance the individual properties of these oxide characteristics or to yield new functionality which otherwise is not available in the constituent oxide forming the composite. As for example the electrochromism characteristics are significantly improved in Nb_2O_5 -ITO based nano-composite thin films [41]. Also relaxor and multiferroic characteristics are reported in BaTiO_3 - ZrO_2 and $\text{Pb}_{0.85}\text{La}_{0.15}\text{TiO}_3$ (PLT) - CoFe_2O_4 (CFO) [42, 43] nano-composite thin films, where, neither BaTiO_3 (BTO) nor ZrO_2 shows relaxor behavior, similarly, neither PLT nor CFO are multiferroic. For such nano-composite thin films, understanding on the compositional, morphological, and size effect of the individual oxide component is crucial to comment on their physical and chemical interaction that leads to either the enhancement of properties or evolution of new properties. In view to this several new discoveries including interface induced high temperature superconductivity [44], enhanced polarization and magnetism at the interface [45] etc. have recently been reported in literature.

In the present section various process methodologies to grow nano-composite thin films are reviewed. First the micro-emulsion mediated synthesis of BaTiO_3 - ZrO_2 nano-composite thin films suitable for miniaturized multi-layered capacitor thin films is described. Second self-assembled oxide nano-composite thin films and their functionalities reported in recent literatures are reviewed. Third nano-composites of piezoelectric and ferrites form multiferroic composite materials. The strain mediated interaction between these phases' results in a magnetoelectric coupling. Multiferroic thin films are proposed to be attractive material candidates for next generation computer memories and tunable devices. The magnetoelectric coupling coefficients are dependent on the phase distribution of the magnetostrictive and piezoelectric phases. When one of these phases is distributed homogeneously at the nano-scale into the bulk matrix it is called a 0–3 type composite. When such a phase distribution is of columnar type in the bulk matrix it is called 1–3 type composite. Finally the multilayered thin film configuration of these phases is termed as 2–2 composite. Next the material characteristics of layered oxide intercalating compounds with super-lattice cation ordering is described.

$\text{Li}[\text{Li}_{x/(2+x)}\text{Mn}_{2x/(2+x)}\text{M}'_{(2-2x)/(2+x)}]\text{O}_2$ [where $\text{M}' = (\text{Mn}_{0.375}\text{Ni}_{0.375}\text{Co}_{0.25})$] thin films with super-lattice ordering between Li and Mn ions (forming Li_2MnO_3 type domains) demonstrated to be attractive cathode materials for lithium rechargeable micro-batteries. Finally, the challenges involved and application prospective of these nano-composite thin films are summarized.

19.2.2 Micro-emulsion Mediated Synthesis of Nano-composite Thin Films

The advent of portable electronic devices with a steadily increasing number of functions (in the same available space) necessitates the further miniaturization of passive components such as low temperature co-fired ceramics (LTCC), micro electro mechanical systems (MEMS), multilayer ceramic capacitors (MLCC), etc., fabricated by multi-layer technology. The trend towards miniaturization of microelectronic modules requires continuous reduction of layer thickness and use of nano-crystalline ceramic powders. State of the art MLCCs fabricated by conventional tape casting or screen printing techniques consist of a multitude of dielectric layers with an individual thickness down to $\sim 1\text{--}3\ \mu\text{m}$ separated by base metal electrodes ($\sim 0.3\text{--}0.5\ \mu\text{m}$ thick) of Ni, Cu etc. [46, 47]. For the required miniaturization of MLCCs, however, the reduction of the individual dielectric layers thickness remains the most promising approach [48], since alternative thin film materials with higher permittivity than chemically modified BTO, which is typically used in industry, are hard to find. In Chap. 22 details to the status of MLCCs and the issues for the required reduction of thickness are discussed. Hence novel processing techniques should be sought to deposit tailor-made dielectric layers in the mesoscopic thickness range of 500–800 nm for miniaturized and highly volume-efficient MLCCs. In this context the use of water in oil type reverse micelle (microemulsions) nano-reactors to synthesize nano-sized BaTiO_3 (BTO) particles and corresponding films has been suggested [49]. Basically the microemulsion mediated synthesis of BTO films results in dielectric properties that are attractive to MLCC applications (cp. Chap. 22). Also as compared to standard chemical solution derived films, the microemulsion mediated routes allow to deposit thicker films per coating/firing cycle significantly reducing the processing cost. For commercial MLCCs the most widely used types are based on ceramic formulations meeting the Y5V and X7R specifications of the EIA (Electronic Industry Association) [50]. Ceramic capacitors of the Y5V type exhibit a strong voltage and temperature dependence of capacitance whereas X7R type MLCCs exhibit a minimal frequency, temperature as well as voltage dependence of their capacitance values. This means that for micro-emulsion derived pure barium titanate thin films, further material optimization is needed in order to reduce both the frequency and temperature dependence of the measured capacitance.

In the following section the synthesis and electrical properties of micro-emulsion derived nano-composite films with tailor made dielectric properties are described in more detail.

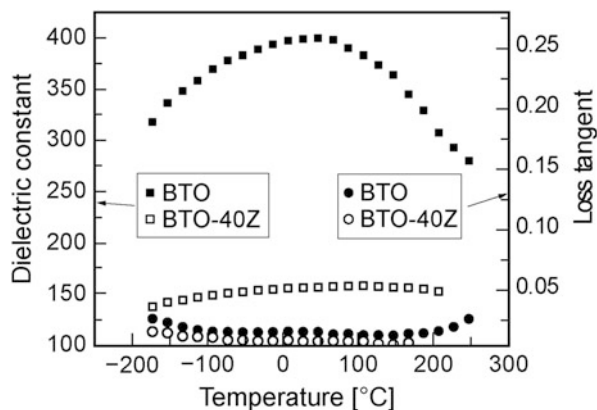
19.2.2.1 Micro-emulsion Mediated Nano-composite Films with Tailor Made Dielectric Properties

The incorporation of a linear dielectric material in a non-linear dielectric matrix has been found to significantly reduce the frequency dispersion of the capacitance, loss tangent as well as leakage current densities. Realization of these effects strongly depends on the thin film geometry and dispersion of a low loss linear dielectric within the non-linear dielectric matrix [51]. Only a broad temperature dependent dielectric anomaly was obtained in these engineered thin film structures. For a significant reduction of the temperature coefficient of capacitance (TCC), local variation of the Curie temperature of barium titanate is essential. Substitution of Ti^{4+} cations in the BTO lattice by Zr^{4+} is known to reduce the paraelectric to ferroelectric phase transition temperature. However, it remains challenging to use this Curie point shifter cation to locally vary the transition temperature (T_c) in order to achieve an almost flat temperature characteristic of the dielectric response [48]. The relatively low sensitivity of the measured dielectric constant as a function of frequency, dc bias voltage and temperature can be achieved in heterogeneous BTO (core)- ZrO_2 (shell) nano-composite thin films.

So-called BTO:metal alkoxide hybrid precursor sols using microemulsion derived BTO nano-particles dispersed homogeneously in zirconia tetra-n-butoxide precursor solutions have been prepared. At first the required stable BTO nanoparticle dispersions were prepared by stoichiometric hydrolysis of a mixed Ba-Ti-methoxide precursor inside reverse micelles formed from the cationic surfactant cetyl trimethyl ammonium bromide (CTAB). Homogeneous dispersions of nano-crystalline BTO particles with surfactant molecules adsorbed at the surface were obtained. The typical particle size of these dispersed BTO particles, measured by dynamic light scattering, was found to be 5 ± 0.5 nm. Their concentration was adjusted to be ~ 0.17 mol/l. To prepare the hybrid precursor solutions, stoichiometric amounts of the Zr alkoxide precursor solution and BTO nanoparticle dispersion were mixed together to yield in 0.0, 1.0, 5.0, 10.0, 20.0, 30.0, and 40.0 wt% ZrO_2 in the final nano-composite film. Details of the preparation of surfactant stabilized water droplets, dispersed in cyclohexane may be found elsewhere [43, 49].

Before mixing the Zr-alkoxide with the BTO particulate sol, the alkoxide solution was aged for 2–3 days. Using the hybrid precursor sols thin films were spin coated on platinized silicon substrates. Just after deposition films were directly inserted in a preheated diffusion furnace and annealed at 700 °C for 30 min. The coating and firing schedule was repeated for 1–4 times to yield films about 500 nm thick. Circular platinum top contacts (approximately 200 μm in diameter) were deposited on the film surface and parts of the films and parts of the films were chemically etched to expose the underlying platinum layer as bottom contact. The

Fig. 19.5 Temperature dependence of the dielectric constant and loss tangent of BTO and BTO-40Z nano-composite films



dielectric properties of the annealed films were measured as a function of frequency (100 Hz to 100 kHz) and temperature (RT – 350 °C). Figure 19.5 compares the temperature dependence of the dielectric constant and the loss tangent of pure BTO and BTO-40Z thin films. As shown in the figure, the pure BTO film shows a broad dielectric anomaly with low loss tangent coefficients in the studied temperature range. As compared to pure BTO, BTO-Z film exhibits a temperature independent dielectric constant and lower loss tangent in a wide range of temperature (–174 to +200 °C). Such flat dielectric response is extremely desirable in many practical device applications including MLCC and voltage tunable frequency agile microwave electronic (FAME) devices. Additionally, in BTO-Z composite thin films the dielectric constant becomes more and more insensitive to the measurement frequency and dc bias with progressive increase of the zirconia content (not shown). All these material characteristics are attractive for the use of such composite thin films in miniaturized multilayered ceramic capacitors. The plausible mechanism of the formation of core-shell microstructure in BTO-Z composite films and their lower sensitivity of the measured dielectric constant as a function of frequency, dc bias voltage and temperature is explained in the following subsection.

19.2.2.2 Plausible Mechanism of the Formation of Core-Shell Nano-composite Films

Mainly two different types of mechanism have been invoked in the literature to explain the formation of nano-crystalline core-shell structures via reverse micelle route [52]. For Cds:Ag based system, the addition of Ag^+ to CdS micro-emulsion partially replace Cd^{2+} resulting a monolayer shell of Ag_2S on the core of CdS. In another plausible mechanism CdS particles act as heterogeneous site for the nucleation and subsequent growth of a surrounding Ag_2S shell. None of the above two mechanism seems to be operative to form BTO (core)- ZrO_2 (shell)

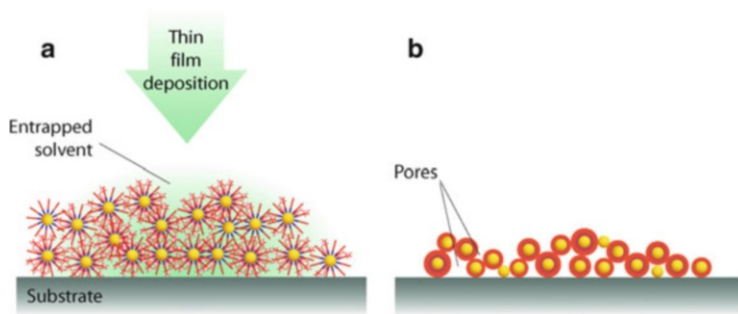


Fig. 19.6 Schematic of micro-emulsion mediated thin film processing (a) after deposition and (b) after firing (adapted from [43])

based nano-composite films described above. As for example, the ionic exchange can be ruled out as it is unlikely that Zr^{4+} ions would be separated from acetyl acetone stabilized zirconia oligomers in the hybrid precursor sol used in this study [43].

As the steric strain of the acetyl acetone chelated alkoxide is much larger, mainly due to Coulombic attraction, the zirconia oligomers are expected to be floccled in the vicinity of the surfactant stabilized BTO core to form a core-shell structure in the hybrid sol. Once the hybrid sol was spin coated onto the platinized silicon substrates (Fig. 19.6a), the core-shell structures of the hybrid sol come into close proximity in the deposited film with the oil phase, surfactant, and the solvent trapped in between. Now depending on the concentration of oligomers surrounding the BTO cores in the hybrid sol, the thickness of the shell is varied around each core particle. During intermediate heat treatment, the solvent, oil phase as well as the surfactants are evaporated instantaneously and a zirconia shell forms as an oxide skeleton on BTO core (see Fig. 19.6b). As shown in the schematic Fig. 19.6b, the nano-composite thin films at this stage has a porous microstructure and each BTO core is surrounded by a ZrO_2 based shell layer with varying thickness. During sintering, Zr^{4+} ions from the reactive oxide skeleton of the shell diffuse inwards to the BTO cores. Such diffusion is driven by the concentration gradient of the diffusing species. Due to the unequal thickness of the shell layer, the said concentration gradient varies among the dispersed BTO cores. Since the annealing temperature and time are kept relatively low, the diffusion rate of the dopant is slow along the nano-sized BTO core. The slow diffusion rate of the dopant cation in turn yields an inhomogeneous dopant distribution within as well as among the BTO cores. In other words each BTO core is expected to have Ti:Zr compositional heterogeneity in these micro-emulsion derived nano-composite thin films.

Micro-emulsion mediated synthesis demonstrated to be one of the most versatile and attractive methods to synthesize $BaTiO_3$ (BTO) nano-particles as well as mesoscopic thin films with excellent dielectric properties. Using mixed precursor sols based on zirconium alkoxide and micro-emulsion synthesized BTO, nanocomposite $BaTiO_3$ - ZrO_2 (BTO-Z) thin films have successfully been prepared.

It has been proposed that a ZrO_2 oligomer shell already forms on the nanocrystalline BTO core in the hybrid precursor sol used for thin film deposition. The compositional heterogeneity in the precursor sol is found to be maintained in crystalline BTO-Z nano-composite films avoiding the formation of $\text{BaZr}_x\text{Ti}_{1-x}\text{O}_3$ solid solution. The heterogeneity has been confirmed by Raman spectroscopy in conjunction with X-ray diffraction and high resolution transmission microstructure analyses [43]. It was proposed that such nano-composite films would be able to close the gap between conventional particulate fabrication routine (to yield films down to ~ 800 nm) and classical wet chemical synthesis technique (to yield films up to 300 nm thick) to grow composite films for multi-layered ceramic capacitors. In principle, such nano-composite films can also be used for several other applications where nano-scale heterogeneity of the functional thin films is required. As one example, BaZrO_3 nanoparticles acting as flux pinning centers in superconducting $\text{YBa}_2\text{Cu}_3\text{O}_{7-\delta}$ layers are briefly described in Chap. 27.

19.2.3 Self-Assembled Oxide Nano-composite Thin Films

Achieving self-assembling or self-organized organic systems have been studied intensively in the last two decades. As for example polystyrene and polymethyl methacrylate has been made phase separated by spinodal decomposition of a polymer blend. Several self-assembled nanostructures in the form of lamellae, cylinders embedded in a matrix etc. with spatial dimensions in the order of 20 nm have been reported in these organic systems [53, 55]. Controls of the parameters such as temperature, bond energies, composition etc. are required to control the overall energy of the system to yield desired nano-composite structures. The kinetics of the system is controlled to yield the desired length scale of the self assembled organic nanostructures.

Compared to organic self-assembled nano-composites, very limited research works have been performed on oxide based inorganic systems. As outlined in the following section, the majority of the self-assembled oxide nano-composite films have been grown by physical vapor deposition routes. Limited attempt so far been made to synthesize such films by CSD routes. It is believed that CSD could qualify as a viable synthesis route to synthesize nano-composite oxide films on large area substrates. Using suitable lattice matched single-crystalline substrates it is also possible to grow vertical hetero-epitaxial nano-composite (VHN) oxide thin films. As a proof of concept, polycrystalline lead lanthanum titanate—cobalt iron oxide nano-composite thin films on platinized silicon substrates utilizing a hybrid sol–gel technique have been grown. A percolative distribution of cobalt iron oxide in a lead lanthanum titanate matrix (with percolation threshold ~ 8 vol%) is identified in these in these nano-composite thin films. The structural, microstructural, electrical, magnetic, magnetoelectric and optical characteristics of these films are described as follows.

19.2.3.1 Self-Assembled Thin Film Growth: Sol–Gel Grown Lead Lanthanum Titanate-Cobalt Iron Oxide Multiferroic Composite Thin Films as a Case Study

In general self-assembled oxide thin films are grown using physical vapor deposition routes (e.g. pulsed laser deposition) using a target composed of two intermixed oxides of interest. For hetero-epitaxial growth of the oxide, lattice matched single crystalline substrates are used. Plausible growth mechanism of these films are recently been reviewed by Judith et al. [40]. Depending on the nature of constituent oxides, three different self-assembly growth mechanisms have been identified. These mechanisms are summarized for four different types of oxide combinations. First, for oxides with no solid solubility, individual oxides may be grown on the underlying substrate by nucleation and growth. If there exists sufficient miscibility of the constituent cations and oxygen, a single phase oxide film may be nucleated and grown on the substrate. For oxide systems which are miscible at higher temperature and a tendency towards clustering at relatively lower temperatures, then depending on the overall composition of the starting mixture, two phases may form either by nucleation and growth or by spinodal growth. Finally, for partially miscible oxides, coherent precipitation of a lower symmetry oxide phase is obtained in the matrix of a higher symmetry phase.

Guided by the above summary we thought that it would be interesting to grow nano-composite films by mixing molecular precursors of constituent oxides. As outlined earlier, for all of those four types of oxide systems, nano-composite thin films are primarily grown using physical vapor deposition techniques. The growth of such thin films using molecular precursors using wet chemical synthesis routes has grossly been neglected. Therefore, as a case study lanthanum doped lead titanate (PLT) (piezoelectric constituent) and cobalt iron oxide (CFO) (magnetostrictive constituent) precursor sol to prepare PLT-CFO composite thin films have been mixed. The individual precursor sols have been synthesized by mixing nitrate salts of cobalt and iron for cobalt iron oxide and, lead acetate and lanthanum nitrate are mixed with titanium butoxide for lead lanthanum titanate. The salient features of synthesizing piezoelectric:magnetostrictive composite thin films using PLT-CFO mixed precursor sols are as follows: *First*, in this kind of processing, the magnetostrictive (CFO) and piezoelectric (PLT) precursors are mixed in molecular level; hence a homogeneous phase mixing (at nano-scale) between the constituent phases is expected. *Second*, the crystallization kinetics of the perovskite (PLT) and spinel (CFO) phases in a mixed precursor sol could be very different as compared to respective pure precursor sols. *Third*, although the spinel and perovskite phase are not expected to react (during calcination) to form any impurity phase/(s), due to molecular level mixing of the precursors, possible interfacial reaction between piezoelectric and magnetostrictive phases cannot be ruled out during calcination.

Composite multiferroic films are being studied actively for their possible applications in magnetic field sensors, transducers, filters, oscillators, phase shifters and memory devices. Traditional magneto-resistive read heads requires a constant

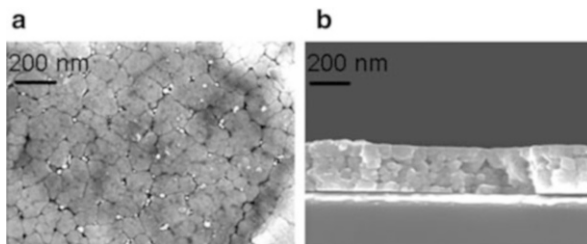
dc current to detect the resistance change during operation. As proposed by Vopsaroiu et al. theoretically [55], in a novel magnetic record head, constant dc current is not required as the data are read back directly as an induced magneto-electric output voltage. Use of multiferroic composites in such application would lead to lowering of power consumption. A prototype of such magneto-electric recoding head has recently been demonstrated using $\text{CoFe}_2\text{O}_4/\text{BaTiO}_3$ bi-layer film [56]. Also, the magneto-electric coupling in multiferroic composite thin films is considered to be very attractive to make electrically tunable microwave magnetic devices such as filters, resonators, phase shifters etc. Thus by fabricating $\text{Fe}_3\text{O}_4/\text{PMN-PT}$ and $\text{Fe}_3\text{O}_4/\text{PZN-PT}$ composite films Liu et al. [57] achieved a shift in FMR absorption spectra by applying an electric field. Magnetoelectric multiferroic films are also attractive for next generation memory devices. In these devices data could be written electrically and read magnetically. Possibilities of several such novel type memory elements are reported in the open literature [58, 59]. In these proposed memory devices the electrical control of magnetization via ME coupling offers the opportunity to combine the respective advantages of FeRAM and MRAM devices. In the subsequent sections the characteristics of lead lanthanum titanate (PLT)-cobalt iron oxide (CFO) nano-composite multiferroic thin films are presented.

19.2.3.2 Structural and Micro-structural Characteristics

Two interesting observations are made while analyzing the X-ray diffraction patterns of $(1-x)\text{Pb}_{0.85}\text{La}_{0.15}\text{TiO}_3 - x\text{CoFe}_2\text{O}_4$ nano-composite films. First, in all the synthesized composite thin films, the diffraction peaks corresponding to the perovskite PLT are readily detected; however, diffraction peaks corresponding to the spinel CFO are too weak to be detected. Second: with the increase of CFO volume content up to 8.3 %, the diffraction peaks of the perovskite (PLT) phase is shifted to higher diffraction angle (2θ). Beyond 8.3 % volume content of the magnetostrictive phase, the peak shift, however, is less prominent. The systematic shifts of the PLT diffraction peaks indicate the shrinkage of the lattice parameter of perovskite PLT in the nano-composite films. In piezoelectric:magnetostrictive based composite thin films, mechanical interaction between the constituent phases introduces stress in each other resulting in such reduction of lattice parameters. During the annealing of such nano-composite films, diffusion of transition metal cation/(s) [viz. Co^{2+} , Fe^{3+}] from the ferrite to perovskite phase is also possible. Such cationic diffusion would indeed reduce the lattice parameter of perovskite phase as the transition metal cations have smaller ionic radii than Ti^{4+} ions in PLT lattice. Further research effort is needed to delineate if the lattice contraction is due to strain or dopant induced.

Figure 19.7 shows (a) the surface and (b) cross sectional morphology of PLT-CFO composite thin films. In the PLT-CFO nano-composite films, CFO grains (white nano-crystals) are found to be uniformly dispersed in the PLT matrix. The cross sectional surface morphologies of PLT-CFO composite films are found to be

Fig. 19.7 FESEM micrograph of the (a) surface and (b) cross-section morphology of a PLT-CFO (5.94 vol%) nano-composite thin film

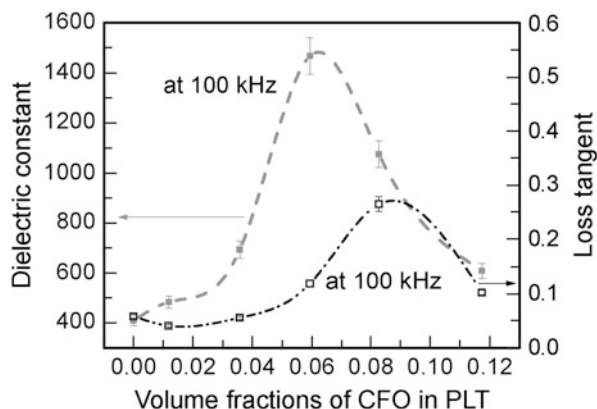


equiaxed. The distribution of CFO and PLT phases, however, remain undistinguishable in the cross section micrographs. The line scans analysis on the white regions (not shown) yield signals only from Co, Fe and O confirming them to be the CFO phase. When the line scan is performed in the greyish region then the elemental signal corresponds to Pb, Ti, La, and O; confirming it to be the PLT matrix. Finally when the span of the line scan is increased to cover both white (CFO) and grey (PLT) regions then signals from all the constituent elements are achieved. EDS analyses are performed to determine the atomic contents of the constituent elements in these films. A close agreement between the nominal and EDS estimated compositions of pure PLT and PLT-CFO composite films has been observed.

19.2.3.3 Electrical Characteristics

$(1-x)\text{Pb}_{0.85}\text{La}_{0.15}\text{TiO}_3 - x\text{CoFe}_2\text{O}_4$ ($x \sim 0.0-0.12$) nano-composite films were characterized in terms of dielectric, ferroelectric and leakage current characteristics. The remarkable difference in the dielectric permittivity and conductivity between PLT and CFO phases together with their nano-scale mixing lead to Maxwell-Wagner polarization in the nano-composite thin films. Strong frequency dispersion in both dielectric constant and loss tangent is found in these films and it is inferred that both space charge polarization and dipolar response contribute to the observed frequency dispersion. The dielectric constant of such composite films depends both on space charge polarization, dominated by the magnetostrictive phase component, and dipolar polarization dominated by the piezoelectric phase. For PLT-CFO nano-composite films, the measured dielectric constant and loss tangent initially increase and maximize at certain specific CFO volume contents and then both these parameters are steadily decreased (see Fig. 19.8). According to a general percolation theory developed for ceramic—metal composites, the dielectric constant of a composite is strongly dependent on the conductivity ratio of the matrix and dispersed phase. As reported elsewhere in details, the increase of dielectric constant and loss tangent fits well to the general empirical equations of the respective parameters, developed originally for ceramic—metal composites [60]. At the percolation threshold (~ 8.6 vol% of CFO contents, derived from non-linear curve fitting of general empirical equations) both

Fig. 19.8 Variation of dielectric constant and loss tangent of PLT-CFO nano-composite films measured at 100 kHz

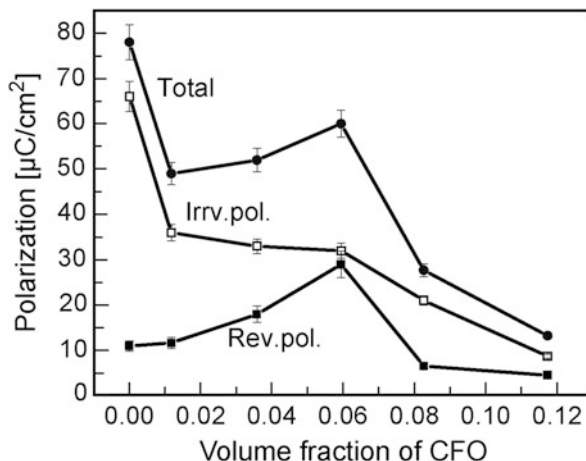


the dielectric constant and loss tangent of PLT-CFO composite film are found to be increased significantly as compared to pure PLT thin films. The sharp drop in the dielectric constant with further increase in CFO volume contents beyond the percolation threshold is thought to be related to the sudden drop in the resistivity of the composite films.

The polarization hysteresis characteristics of these composite films are characterized by capacitance (C)-dc voltage (V) (C-V loop) and polarization (P)-electric field (E) (P-E loop) measurements. In PLT-CFO composite films, the saturation polarization increases up to ~6.0 vol% CFO contents and then starts to decrease with further increase of CFO contents. The coercive field, however, does not have any definite correlation with the CFO volume contents in these composite films. The ferroelectric polarization consists of reversible and irreversible components. It is accepted that the irreversible polarization component is useful for potential applications. By integrating a C-V curve and dividing by the area of the capacitor in a point to point basis, the reversible polarization contribution has been estimated. Such an estimation is based on the fact that a small ac signal (~50 mV used for capacitance measurements) superimposed on the slowly varying dc bias allows only for small reversible displacements of the domain wall. The measured quasistatic P-E hysteresis is a sum of reversible and irreversible contributions. By subtracting the reversible polarization the irreversible polarization components have been obtained. In Fig. 19.9 the variation of the reversible, irreversible and total polarization (at V_{max}) with CFO volume contents in PLT-CFO composite thin films is compared. It is interesting to note that with the increase in CFO volume contents the irreversible polarization component is reduced. The reversible polarization component, however, increases up to 6 vol% CFO contents and reduced thereafter with the further increase in CFO volume contents.

Due to the variation of the reversible polarization component, at lower CFO contents (<6.0 vol% CFO), the total polarization increases with CFO contents (although for all these nano-composite films, the total polarization still remains less as compared to pure PLT film). Two accepted mechanisms exist to explain the

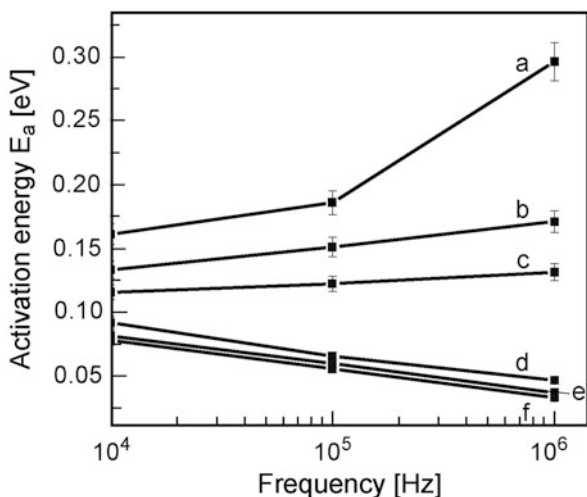
Fig. 19.9 Plot of the reversible (rev.), irreversible (irr.), and total polarization of PLT-CFO composite films with varying CFO volume contents



irreversible polarization (1) the intrinsic defects could pin the domain wall and hence after removing the electric field the domain wall does not return back to their original position. In other words, the domain walls are pinned by the defect. (2) Another possible mechanism is the application of electric field initiates the nucleation and growth of new domains which do not disappear when the field is removed. However, these are simplified assumptions made originally for ferroelectric thin films. In ferroelectric:ferrite based composite films the phenomenon is further complicated by the presence of a magnetostrictive phase, possibilities of cation diffusion from the ferrite to perovskite grains etc. The presence of defect dipoles and free charges also contribute to the measured polarization (in low frequency measurement), and, in addition, they would also interact with domain walls. The reversible polarization is influenced by the defect density and the perovskite phase content in the composite thin films. Among all these possible factors, the increase of the magnetostrictive (CFO) phase contents clearly would have pronounced influence on increasing the reversible polarization components of PLT15-CFO nano-composite thin films with lower CFO volume contents (up to 5.94 vol%). In the vicinity of the percolation threshold, a decrease in the reversible polarization component with the increase in CFO volume contents has been observed. More detailed studies are required to fully understand the role of the magnetostrictive phase distribution in controlling the domain wall motion in these nano-composite films. The leaky hysteresis loop of the PLT15-CFO (11.74 vol%) nano-composite film clearly indicates the decrease of dc resistivity of this film.

The operative conduction mechanisms in insulating films can be grouped into either electrode or bulk limiting. For piezoelectric:magnetostrictive nano-composite films it is not clear whether the primary current conduction mechanism is electrode or bulk limiting. By measuring both field as well as temperature dependence of leakage current, Schottky emission is found to be the dominant current conduction mechanism in the PLT15-CFO composite thin films. Interestingly, similar to the dielectric constant, the increase in conductivity could also be

Fig. 19.10 The variation of the estimated activation energies (for ac conduction) with the measurement frequencies in PLT-CFO composite thin films of different composition (a) PLT15, (b) 98.82 PLT15-1.18 CFO, (c) 96.42 PLT15-3.58 CFO, (d) 94.06 PLT15-5.94 CFO, (e) 91.74 PLT15-8.26 CFO, (f) 88.26 PLT15-11.74 CFO



fitted using an empirical equation originally developed for ceramic metal composites. As reported in details in a recent publication, a good agreement is achieved between the percolation threshold from dielectric and conductivity data [61].

The ac conductivity of PLT-CFO composite films in a temperature range between 25 and 200 °C has also been measured. Additionally these films are also characterized using impedance and modulus spectroscopy analyses. Interesting features in the ac conductivities, impedance and modulus parameters are only observed beyond the percolation threshold. The frequency dependent ac conductivity in the mentioned temperature range is fitted to a double power universal Power law. For PLT-CFO composite films, irrespective of the measurement frequencies, the ac conductivity is found to increase with the increase in temperature. For a particular frequency, the temperature dependence of the ac conductivity obeys the Arrhenius relation. Accordingly, from the estimated slope of the linear fit of the logarithmic variation of ac conductivities vs inverse of measurement temperatures, activation energy for ac conduction was estimated for PLT-CFO composite films. For these films, Fig. 19.10 shows the variation of the estimated activation energies (for ac conduction) with the measurement frequencies. Two interesting features are identified in Fig. 19.10. First, at lower CFO contents (up to 3.6 vol%), E_{ac} increases with the increase in frequency, however, in composite films with higher CFO volume contents, a reverse trend is observed. Second, irrespective to the measurement frequencies, E_{ac} decreases systematically with the increase in CFO volume contents. The range of activation energy (0.07–0.16 eV at 10 kHz) is lower as compared to that estimated at higher frequency (0.03–0.3 eV). The comparatively lower activation energy is indicative to hopping conduction at intermediate frequency range. The fact that activation energy is reduced systematically with the

increase in CFO volume contents in PLT-CFO composite films is consistent with the increase of ac conductivity with CFO volume contents in these films.

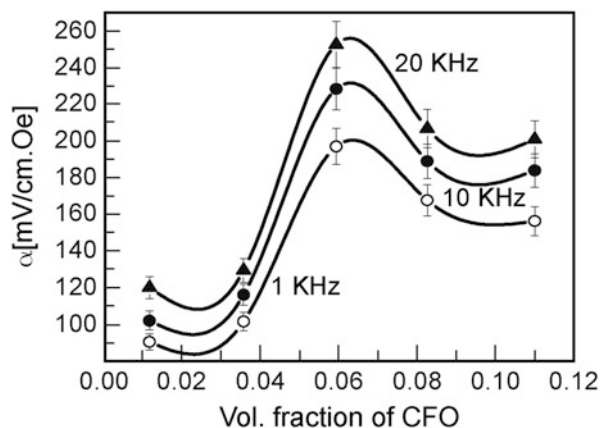
For impedance and modulus spectroscopy analyses the frequency dispersion (42 Hz–1 MHz) of impedance (Z) and phase angle (θ) in the temperature range between 30 and 200 °C has been measured. From the measured Nyquist plots of PLT and PLT-CFO nano-composite thin films it is observed that the bulk resistance is suddenly reduced in nano-composite film with 8.2 vol% CFO content. Thus the ac impedance spectroscopy analyses support the percolative model of magnetostrictive phase distribution. For nano-composite thin films with higher CFO volume content, the broad nature of Z'' - f peak and its shift to higher frequencies with the increase in temperature ascertain the distribution of relaxation time. It is known that for an ideal Debye-type relaxation for a particular temperature, both Z'' and M'' should peak at identical frequencies. Since in the present case it has been found that Z'' and M'' peak at different frequencies, a non-Debye type relaxation process in the composite films with higher CFO contents can be inferred.

19.2.3.4 Magnetic and Magnetoelectric Characteristics

The magnetic properties and magneto-electric coupling characteristics of $(1-x)\text{Pb}_{0.85}\text{La}_{0.15}\text{TiO}_3 - x\text{CoFe}_2\text{O}_4$ ($x \sim 0.0$ – 0.12) composite films have also been characterized. The magnetic hysteresis at room temperature is measured by applying a magnetic field perpendicular to the plane of PLT-CFO composite films using a vibrating sample magnetometer. It is interesting to note that PLT-CFO composite films exhibit both polarization and magnetic hysteresis loops at room temperature. Thus for 91.7 PLT-8.3 CFO film, the measured saturation and remnant magnetization of these films are ~ 15.0 and 5 emu/cm^3 with a coercive field $\sim 336 \text{ Oe}$. Beyond 12.0 vol% CFO contents, the polarization hysteresis loop turns leaky; however, magnetization is increased yielding well saturated hysteresis loops. The field cooled (FC), zero field cooled (ZFC), magnetization (M)- temperature (T) characteristics of PLT-CFO composites have also been measured. For PLT-CFO (5.9 vol%) composite a bifurcation of ZFC and FC curve is clearly visible $\sim 180 \text{ K}$. Similar feature has also been observed in PLT-CFO composites with relatively higher CFO volume contents. Such FC:ZFC magnetization behavior is probably related to the nano-scale distribution of CFO phase in PLT matrix forming a 0–3 type composite [62].

To measure magneto-electric coupling coefficient (dE/dH), the composite films are put in a dc magnetic field that is varied up to 3 kOe. The measurements are done with superimposed small amplitude of ac magnetic fields generated by Helmholtz coils. Both ac and dc magnetic fields are kept parallel to the direction of polarization (longitudinal mode). The output voltage generated by the composite film is measured using a lock in amplifier. A maximum magnetoelectric coupling coefficient (α_{max}) is obtained at an optimized dc magnetic field. The magnetic bias field dependence of the magnetoelectric coupling coefficient is found to be due to the

Fig. 19.11 The variation of the estimated α_{\max} with CFO volume contents at three different ac frequencies



magnetic field dependence of the piezomagnetic coefficient of the CFO phase. Figure 19.11 shows the dc magnetic field dependence of the estimated magneto-electric coupling coefficients for PLT-CFO thin films with varying CFO volume contents. It is interesting to note that α_{\max} is significantly increased in nano-composite films with CFO volume content in the vicinity (within 2.0 vol% of CFO contents) of the percolation threshold. With further increase in CFO volume contents α_{\max} drops and probably levels off. Thus for $x \sim 0.06$, α_{\max} is measured to be ~ 250 mV/cm Oe (at 20 kHz). As compared to the magneto-electric coupling coefficients reported for ferroelectric-ferrite nano-composite films, the present films yield significantly larger magneto-electric coupling coefficients.

19.2.3.5 Optical Characteristics

Finally, the optical properties of $(1-x)\text{Pb}_{0.85}\text{La}_{0.15}\text{TiO}_3 - x\text{CoFe}_2\text{O}_4$ ($x \sim 0.0-0.12$) composite films have been studied. Optical characterization of these nano-composite thin films can be used as an effective diagnostic tool to assess the quality of these films. In case of ferroelectric:ferrite based nano-composite films with dilute magnetostrictive phase the optical constants of these thin films have been systematically investigated.

The optical properties of these nano-composite films are investigated using both transmission and reflection spectra in the wavelength range 200–900 nm. The refractive index (n), extinction coefficient (k) and thickness of the film (d) are determined from the measured transmission spectra. Thickness of the films obtained from the interference fringes in transmission or reflection spectra agree well with those obtained from other characterization methods. The appearance of interference fringes itself is an indication of the thickness uniformity of these films. The low value of extinction coefficient (in the order of 10^{-2}) as observed in our films is a qualitative indication of excellent surface smoothness of the films. The densities of the films have also been estimated from their packing fraction values.

The packing fractions of the films are calculated from their refractive indices using effective medium approximation (EMA). The average oscillator strength and its associated wavelength are estimated using a Sellmeier-type dispersion equation. It could be demonstrated that analysis of multiferroic nano-composite films in terms of its dispersion of refractive indices could be an effective tool to comment on the magnetostrictive phase distribution in perovskite matrix. Thus in case of 0–3 type PLT-CFO nano-composite films it has been shown that as long as the CFO phase is distributed homogeneously in the PLT matrix, the measured refractive indices follow Sellmeier dispersion formalism. Interestingly, when the percolation of the magnetostrictive phase (CFO) initiates, then the dispersion deviates from the Sellmeier type dispersion (for one dominant electronic oscillator) [63].

Absorption coefficient (α) and the band gap energy (E_g) are obtained for PLT and PLT-CFO composite films with varying CFO volume contents. Both refractive indices and the packing fraction of PLT-CFO composite films are found to be marginally reduced with the increase in CFO volume contents. The band gap (E_g) of these films is found to be systematically reduced with the increase in CFO volume contents. The observed change in band gap is argued to be due to a combined effect involving microstructure and cation/(s) diffusion across the PLT/CFO interfacial regions.

The salient features of the results presented above are summarized as follows: Multiferroic lead lanthanum titanate-cobalt iron oxide nano-composite thin films are synthesized by a sol-gel route. A percolative distribution of cobalt iron oxide phase, with percolation threshold ~ 8 vol%, is identified through unified microstructural, electrical and optical characterizations. Large magnetoelectric coupling coefficient (~ 250 mV/cm Oe) is found in the nano-composite films with cobalt iron oxide volume contents in the vicinity of its percolation threshold. The composite films with dilute magnetostrictive volume contents yield superior multiferroic properties to its counterparts with relatively higher magnetostrictive volume contents. Using various theoretical formalisms it is predicted that 1–3 type vertical heterostructures with low leakage current would yield large magnetoelectric coupling coefficient whereas 2–2 type laminated composite would yield poor coupling coefficient due to substrate constraint effect. Such theoretical prediction has been experimentally verified. We could not find any comprehensive theoretical model predicting the magnetoelectric coupling coefficient of 0–3 type composite films. It is therefore necessary to develop a theoretical model for such 0–3 nano-composites to check if our experimental observations that the composite film with dilute magnetostrictive phase content would exhibit percolation and large magnetoelectric coupling in the vicinity of percolation threshold are in line to the theoretical prediction or not. Additionally, by cross-sectional high-resolution transmission electron microscopy (HRTEM) in conjunction with compositional line analyses we need to verify if indeed cation/(s) diffusion is operative across the piezoelectric/magnetostrictive inter-phase boundary. Analyses the nature of the interface is very important to understand the strain-mediated magnetoelectric coupling. Finally, to yield effective magnetoelectric coupling, one can synthesize ferroelectric:ferrite core-shell nano-crystalline particles with ferrite as core and

ferroelectric materials as shell. The synthesis of such particles could be micro-emulsion mediated, as outline in Sect. 19.2.2. Multiferroic films grown from such core-shell nano-particles would probably yield excellent magnetoelectric coupling.

19.2.4 *Nano-composite Thin Films with Super-Lattice Ordering*

19.2.4.1 Introduction to Bulk Nano-composite with Super-Lattice Ordering

Due to the enormous growth of various portable electronic devices cheaper, environmentally benign lithium rechargeable micro-batteries with higher capacities and energy densities are in large demand. As for example, to power the devices like high density computer memories such micro-batteries are proposed to be integrated into the electronics at chip level [64]. The heart of these micro-batteries is the cathode material used in the cell construction. Due to their higher discharge capacities and thermal stability, hexagonal layered structured $\text{Li}(\text{Ni}_{0.5}\text{Mn}_{0.5})\text{O}_2$ has been considered to be one of the most important material candidates for such applications [65]. In these cathode materials, oxygen octahedra containing transition metal cations (Ni, Mn, or Co) are separated to each other by another oxygen octahedra containing Li ions. Unlike conventional LiCoO_2 cathode, $\text{Li}(\text{Ni}_{0.5}\text{Mn}_{0.5})\text{O}_2$ is able to incorporate excess lithium ions in transition metal site. The ability to incorporate excess lithium ions in the transition metal site is attributed to the +2 valence state in nickel and +4 valence state in manganese. In conventional layered oxides (viz. LiCoO_2 , LiNiO_2 , LiMnO_2 etc.), the transition metal cations remain in the +3 valence state and therefore excess lithium incorporation in transition metal sites is improbable [66]. Interestingly, when lithium ions exist in the transition metal site containing Mn^{4+} as major constituent, they have a strong tendency to form a cation ordering with Mn^{4+} ion to form Li_2MnO_3 type nano-domains. As has recently been reported for $\text{Li}(\text{Li}_{0.2}\text{Mn}_{0.55}\text{Ni}_{0.15}\text{Co}_{0.1})\text{O}_2$ powders (calcined at 800 °C for 12 h in air) Arrhenius super lattice peaks (marked by asterisk in Fig. 19.12a) around 20–25° are due to the ordering of Li and Mn ions to form a Li_2MnO_3 like regions [67]. For similar cathode compositions, identification of Li_2MnO_3 -type domain in active-cathode matrix has also been confirmed by high-resolution transmission electron microscopy and other characterization tools such as nuclear magnetic resonance, X-ray absorption spectroscopy, etc. [68].

For example, as shown in the transmission electron micrographs of $\text{Li}(\text{Li}_{0.111}\text{Mn}_{0.471}\text{Ni}_{0.249}\text{Co}_{0.166})\text{O}_2$ cathode particles (Fig. 19.12b) two distinctly different lattice fringes are identified in the individual particles. Thus, along with the well ordered fringes there are regions with disturbed lattice fringes (marked with circles in the micrograph). These disorder regions correspond to the nano-domains of Li_2MnO_3 [67, 69]. The nano-domains (form due to the ordering of lithium and

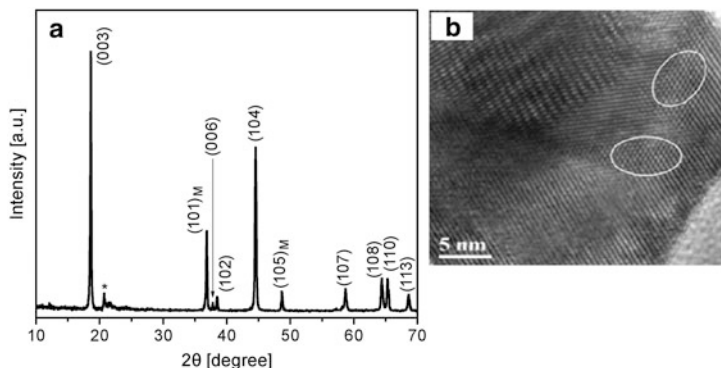


Fig. 19.12 (a) XRD profile of $\text{Li}(\text{Li}_{0.2}\text{Mn}_{0.55}\text{Ni}_{0.15}\text{Co}_{0.1})\text{O}_2$. Super-lattice peaks are marked by asterisk. (b) High resolution transmission electron micrograph of $\text{Li}(\text{Li}_{0.111}\text{Mn}_{0.471}\text{Ni}_{0.249}\text{Co}_{0.166})\text{O}_2$ powder. Regions correspond to Li_2MnO_3 nanodomains are marked in the micrograph

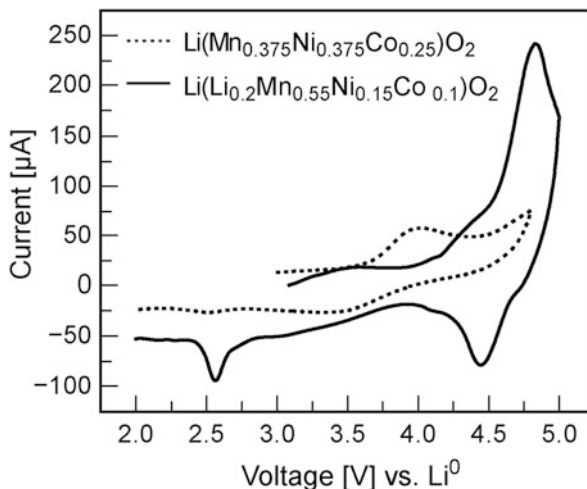
manganese ions in transition metal layer) are large enough to yield coherent X-ray diffraction. The diffraction peaks corresponding to the super-lattice ordering has clearly been identified in the X-ray diffractograms presented earlier. In bulk form, these nano-composite cathodes with super-lattice cation ordering, yield much higher discharge capacity as compared to conventional layered and spinel oxide based cathodes. Little efforts has so far been attempted to investigate the electrochemical characteristics of such nano-composites cathodes in thin film form. Preliminary structural and electrochemical characteristics of such thin film cathodes are described as follows.

19.2.4.2 Nano-composite Thin Films for Lithium Rechargeable Batteries

To prepare the precursor solution for thin film deposition, stoichiometric amounts of lithium acetate, nickel acetate, cobalt acetate and manganese acetate were co-dissolved in warm acetic acid through continuous stirring. To avoid precipitation few drops of nitric acid was added into the mixed precursor sol. The molar concentration of the precursor solution was maintained to ~ 0.5 mol/l, and it was spin coated on polished platinum substrates at 2,500 rpm for 10 s. Just after deposition, the films were directly inserted into a pre-heated furnace kept at 450°C and fired for 5 min to remove the associated organics. The coating and firing schedule was repeated for 25 times to yield films about $1\ \mu\text{m}$ thick. After final firing, these films were annealed at 700°C for 360 min for crystallization. The firing and annealing temperatures were decided on the basis of thermo-gravimetric analysis of gel derived powder of the precursor sol.

The electrochemical properties of these films were evaluated in a two electrode split cell using Li foil both as counter and reference electrodes and deposited thin

Fig. 19.13 Cyclic voltammograms of $\text{Li}(\text{Mn}_{0.375}\text{Ni}_{0.375}\text{Co}_{0.25})\text{O}_2$, and $\text{Li}(\text{Li}_{0.2}\text{Mn}_{0.55}\text{Ni}_{0.15}\text{Co}_{0.1})\text{O}_2$ thin film cathodes

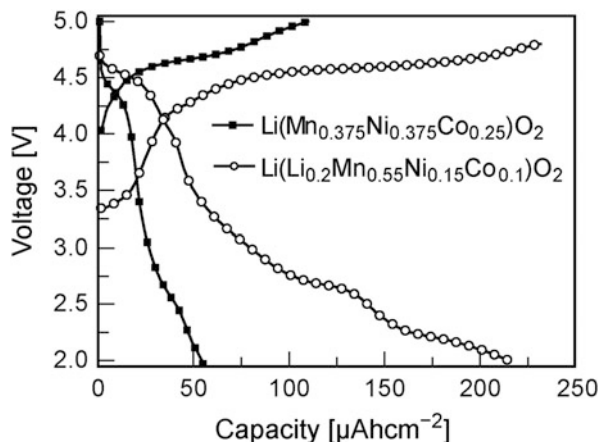


film on platinum substrate as working electrode. The electrolyte solution was 1 M LiPF_6 salt mixed with ethylene carbonate (EC) and diethyl carbonate (DEC) in 1:1 molar ratio. All the electrochemical experiments were performed inside a moisture-controlled glove box. The films were about $1.0 \mu\text{m}$ thick unless specified otherwise and the electrode area inside the electrolyte solution was $\sim 0.56 \text{ cm}^2$. A computer-controlled potentiostat–galvanostat system was utilized for the electrochemical measurements. The cyclic voltammograms were recorded at a voltage scan rate (v) of 0.5 mV/s in a cut-off limit of $5.0\text{--}2.0 \text{ V}$. The charge–discharge measurements were performed at constant current densities ranging 0.05 mA/cm^2 in a cut-off voltage limit of $5.0\text{--}2.0 \text{ V Li/Li}^+$. The discharge capacity was estimated from these measurements.

The X-ray diffraction peaks of thin film cathode materials are too weak to estimate their phase formation behavior. However, comparing with its bulk counterpart it can be concluded that due to the presence of high content of lithium and manganese ions, super lattice ordering between lithium and manganese ions leads to formation of inactive Li_2MnO_3 like regions embedded inside the active $\text{Li}(\text{Mn}_{0.375}\text{Ni}_{0.375}\text{Co}_{0.25})\text{O}_2$ matrix. This eventually can be visualized as a nano-composite structure.

The occurrence of Li_2MnO_3 domains embedded in the $\text{Li}(\text{Mn}_{0.375}\text{Ni}_{0.375}\text{Co}_{0.25})\text{O}_2$ phase can be realized from the electrochemical measurements. For example, cyclic voltammetry (CV) measurements are performed to identify the redox reactions during the charging and discharging of these nano-composite cathode thin films. Figure 19.13 compares the CV characteristics of $\text{Li}(\text{Mn}_{0.375}\text{Ni}_{0.375}\text{Co}_{0.25})\text{O}_2$, and $\text{Li}(\text{Li}_{0.2}\text{Mn}_{0.55}\text{Ni}_{0.15}\text{Co}_{0.1})\text{O}_2$. For $\text{Li}(\text{Mn}_{0.375}\text{Ni}_{0.375}\text{Co}_{0.25})\text{O}_2$ thin films, the said super lattice ordering is absent. During charging of this film, the broad oxidation peak $\sim 4.0 \text{ V}$ is due to the oxidation of nickel and cobalt cations in the transition metal cation layer of this layered oxide cathode. In pristine $\text{Li}(\text{Mn}_{0.375}\text{Ni}_{0.375}\text{Co}_{0.25})\text{O}_2$ cathode, nickel and cobalt ions are in the $+2$ and $+3$ valence state, respectively,

Fig. 19.14 Charge discharge profile of $\text{Li}(\text{Mn}_{0.375}\text{Ni}_{0.375}\text{Co}_{0.25})\text{O}_2$ and $\text{Li}(\text{Li}_{0.2}\text{Mn}_{0.55}\text{Ni}_{0.15}\text{Co}_{0.1})\text{O}_2$ thin film cathodes



and during charging they are oxidized to the +4 valence state. As seen in Fig. 19.13, the reduction potential of these cations is found to be ~ 3.4 V. During the discharge cycle, the broad hump at ~ 4.5 V probably indicates the insertion of lithium ions in the vacant tetrahedral site of the layered oxide lattice. In pure Li_2MnO_3 thin films a loss of lattice oxygen takes place with concomitant (electrochemical) extraction of lithium from the monoclinic Li_2MnO_3 lattice. In the composite thin film, (where super lattice ordering takes place to form Li_2MnO_3 like region) Li can be extracted from the Li_2MnO_3 domain through the release of lattice oxygen (indicated by a oxidation peak at ~ 4.8 V) to form activated MnO_2 . The MnO_2 is reported to be structurally integrated with an active component. Upon discharge Mn ions are reduced to the +3 states and subsequently oxidized to the +4 valence state in the next charge cycle. The capacity of these composite cathodes is increased due to the occurrence of both $\text{Mn}^{3+}/\text{Mn}^{4+}$ along with usual $\text{Ni}^{2+}/\text{Ni}^{4+}$ and $\text{Co}^{3+}/\text{Co}^{4+}$ redox couples in these nano-composite cathodes.

In line to this, as shown in Fig. 19.14 the specific capacity of the nano-composite $\text{Li}(\text{Li}_{0.2}\text{Mn}_{0.55}\text{Ni}_{0.15}\text{Co}_{0.1})\text{O}_2$ cathode is much higher than the $\text{Li}(\text{Mn}_{0.375}\text{Ni}_{0.375}\text{Co}_{0.25})\text{O}_2$ thin film. The voltage plateau obtained in the ~ 3 V regions is due to the reduction of Mn^{4+} to Mn^{3+} . The formation of Li_2MnO_3 type nano-domains (due to the incorporation of excess lithium in the transition metal site) in these nano-composite thin films helps to increase the discharge capacity significantly.

19.3 Summary

Composite film processing offers many exciting possibilities to optimize and tailor the resulting functional layers not only with regard to economic production of high performance thicker films as described in Sect. 19.1, but also as presented in the second part the potential of modifying the microstructure on a nanoscale, i.e. nano-composites in the sub-100 nm regime.

The ability to create high density thick films at moderate temperatures between 550 and 750 °C was shown impressively in the first part. This reduction in processing temperature is brought about by the move away from classical sintering relying on solid state diffusion of atoms. Instead, film formation is accomplished through a gluing type approach where the conversion of metallo-organic precursors to ceramic materials through the action of heat. Small scale atomic diffusion, possible at these moderate temperatures, still occurs but is insufficient for large scale densification required to densify a collection of ceramic particles. High density thick films are either achieved by having a high proportion of sol-gel material such that the final films structure consists of isolated ceramic powder particles embedded in a 'sea' of sol-gel derived material, or where subsequent sol infiltration treatments are used to fill remnant porosity directly. Further densification can also be achieved by using a low melting point sintering aid to enhance local diffusion or through the action of an externally applied pressure. The use of an applied pressure should, however, be used with caution to prevent damage to underlying substrate materials.

In the second part of the chapter recent approaches to generate nano-composite films with a tailored heterogeneity are reviewed. Nano-composite $\text{BaTiO}_3\text{-ZrO}_2$ (BTO-Z) thin films have successfully been prepared using mixed precursor sols based on zirconium alkoxide and micro-emulsion synthesized BTO nanoparticle dispersions. It has been proposed that a ZrO_2 oligomer shell forms on the nanoparticle BTO core in the hybrid precursor sol used for thin film deposition. The compositional heterogeneity in the precursor sol is found to be maintained in crystalline BTO-Z nano-composite films. It was proposed that such nano-composite films would be able to close the gap between conventional particulate fabrication routine (to yield films down to ~800 nm) and classical wet chemical synthesis technique (to yield films up to 300 nm thick) to grow nano-composite films for multi-layered ceramic capacitors. Such nano-composite films can also be used for several other applications, such as superconducting tape conductors, where nano-scale heterogeneity of the functional thin films is required.

Multiferroic lead lanthanum titanate-cobalt iron oxide nano-composite thin films are synthesized by a sol-gel route. A percolative distribution of the cobalt iron oxide phase, with a percolation threshold of ~8 vol%, is identified through unified microstructural, electrical and optical characterizations. A large magnetoelectric coupling coefficient (~250 mV/cm Oe) is found in the nano-composite films with cobalt iron oxide volume contents in the vicinity of its percolation threshold. The nano-composite films with dilute magnetostrictive volume contents yield superior multiferroic properties to its counterparts with relatively higher magnetostrictive volume contents.

Finally the synthesis and electrochemical characteristics of lithium excess hexagonal layered oxide thin film cathodes for lithium rechargeable micro-batteries has been outlined. The excess lithium forms Li_2MnO_3 type nano-domains in the layered oxide matrix forming a nano-composite structure. Extraction of lithium from these nano-domains during high voltage charging is found to be the key to achieve sufficiently larger discharge capacity from these nano-composite cathodes.

Acknowledgments One of the authors S.B. Majumder wishes to thank Alexander von Humboldt foundation for the partial financial support to carry out the research work. Mr. C. Ghanty, would also like to acknowledge CSIR, Govt. of India for providing him a Research Fellowship under CSIR-NET scheme.

References

1. Perez J, Vyshatko NP, Vilarinho PM, Kholkin AL (2007) Electrical properties of lead zirconate titanate thick films prepared by hybrid sol-gel method with multiple infiltration steps. *Mater Chem Phys* 101:280–284
2. Wang Z, Miao J, Zhuh W (2007) Piezoelectric thick films and their application in MEMS. *J Eur Ceram Soc* 27:3759–3764
3. Kwon TY, Park JH, Kim YB, Yoon DS, Cheon CI, Lee HL, Kim TS (2006) Preparation of piezoelectric $0.1 \text{Pb}(\text{Zn}_{0.5}\text{W}_{0.5})\text{O}_3$ - $0.9 \text{Pb}(\text{Zr}_{0.5}\text{Ti}_{0.5})\text{O}_3$ solid solution and thick films for low temperature firing on Si-substrate. *J Cryst Growth* 295:172–178
4. Zhu H, Miao J, Wang Z, Zhao C, Zhu W (2005) Fabrication of ultrasonic arrays with $7 \mu\text{m}$ PZT thick films as ultrasonic emitter for object detection in air. *Sens Actuators A* 123–124:614–619
5. Zhong-Xia D, Jie Y, Quan-Liang Z, Hong-Mei L, Hai-Bo L, Wen-Tong Z, Mao-Sheng C (2008) Preparation and ferroelectric properties of double-scale PZT composite piezoelectric thick film. *Chin Phys Lett* 25:1472–1475
6. Dorey RA, Whatmore RW (2004) Electroceramic thick film fabrication for MEMS. *J Electroceram* 12:19–32
7. Hrovat M, Holc J, Drnovsek S, Belavic D, Cilensek J, Kosec M (2006) PZT thick films on LTCC substrates with an interposed alumina barrier layer. *J Eur Ceram Soc* 26:897–900
8. Torah RN, Beeby SP, Tudor MJ, White NM (2007) Thick-film piezoceramics and devices. *J Electroceram* 19:95–110
9. Yao K, He X, Xu Y, Chen M (2005) Screen-printed piezoelectric ceramic thick films with sintering additives introduced through a liquid-phase approach. *Sens Actuators A* 118:342–348
10. Gebhardt S, Seffner L, Schlenkrich F, Schönecker A (2007) PZT thick films for sensors and actuator applications. *J Eur Ceram Soc* 27:4177–4180
11. Menil F, Debeda H, Lucat C (2005) Screen-printed thick-films: from materials to functional devices. *J Eur Ceram Soc* 25:2105–2113
12. Corker DL, Zhang Q, Whatmore RW, Perrin C (2002) PZT ‘composite’ ferroelectric thick films. *J Eur Ceram Soc* 22:383–390
13. Villegras M, Moure C, Jurado JR, Duran P (1994) Improvement of sintering and piezoelectric properties of soft lead zirconate titanate ceramics. *J Mater Sci* 29:497–4983
14. Tu WC, Lange FF (1995) Liquid precursor infiltration processing of powder compacts: II, fracture toughness and strength. *J Am Ceram Soc* 79:3283–3289
15. Lee SG (2007) Effects of sol infiltration on the screen-printed lead zirconate titanate thick films. *Mater Lett* 61:1982–1985
16. Dorey RA, Duval FFC, Haigh RD, Whatmore RW (2002) The effect of repeated sol infiltrations on the microstructure and electrical properties of PZT composite sol-gel films. *Ferroelectrics* 267:373–378
17. Wu A, Vilarinho PM, Srinivasan S, Kingon AI, Reaney IM, Woodward D, Ramos AR, Alves E (2006) Microstructural studies of PZT thick films on Cu foils. *Acta Mater* 54:3211–3220
18. Kindl B, Carlsson DJ, Deslandes Y, Hoddenbagh JMA (1991) Preparation of α -alumina ceramics: the use of boehmite sols as dispersing agents. *Ceram Int* 17:347–350
19. Wu J, Chen M, Jones FR, James PF (1993) Mullite and alumina-silica matrices for composites by modified sol-gel processing. *J Non Cryst Solids* 162:197–200

20. Barrow DA, Petroff TE, Sayer M (1995) Thick ceramic coatings using a sol-gel based ceramic-ceramic 0-3 composite. *Surf Coat Technol* 76-77:113-118
21. Dorey RA, Whatmore RW (2004) Electrical properties of high density PZT and PMN-PT/PZT thick films produced using ComFi technology. *J Eur Ceram Soc* 24:1091-1094
22. Ohno T, Kunieda M, Suzuki H, Hayashi T (2000) Low-temperature processing of $\text{Pb}(\text{Zr}_{0.53}\text{Ti}_{0.47})\text{O}_3$ thin films by sol-gel casting. *Jpn J Appl Phys* 39:5429-5433
23. Dorey RA, Stringfellow SB, Whatmore RW (2002) Effect of sintering aid and repeated sol infiltrations on the dielectric and piezoelectric properties of a PZT composite thick film. *J Eur Ceram Soc* 22:2921-2926
24. Kholkin AL, Yarmarkin VK, Wu A, Avdeev M, Vilarinho PM, Baptista JL (2001) PZT-based piezoelectric composites via a modified sol-gel route. *J Eur Ceram Soc* 21:1535-1538
25. Dorey RA, Haigh RD, Stringfellow SB, Whatmore RW (2002) Effect of sol infiltrations on the electrical properties of PZT. *Br Ceram Trans* 101:146-148
26. Dorey RA, Whatmore RW (2002) Apparent reduction in the value of the d_{33} piezoelectric coefficient in PZT thick films. *Integr Ferroelectr* 50:111-119
27. Dorey RA, Whatmore RW, Beeby SP, Torah RN, White NM (2003) Screen printed PZT thick films using composite film technology. *Integr Ferroelectr* 54:651-658
28. Dorey RA, Whatmore RW, Beeby SP, Torah RN, White NM (2004) Screen printed PZT composite thick films. *Integr Ferroelectr* 63:601-604
29. Kholkin AL, Yarmarkin VK, Wu A, Vilarinho PM, Baptista JL (2000) Thick piezoelectric coatings via modified sol-gel techniques. *Integr Ferroelectr* 30:245-252
30. Kobayashi M, Olding TR, Sayer M, Jen CK (2002) Piezoelectric thick film ultrasonic transducer fabricated by a sol-gel spray technique. *Ultrasonics* 39:675-680
31. Wang D, Edirisinghe MJ, Dorey RA (2008) Formation of PZT crack-free thick films by electrohydrodynamic atomization deposition. *J Eur Ceram Soc* 28:2739-2745
32. Sun D, Rocks SA, Wang D, Edirisinghe MJ, Dorey RA (2008) Novel forming of columnar lead zirconate titanate structures. *J Eur Ceram Soc* 28:3131-3139
33. Yamane M (1998) Preparation of thick PZT ceramic film by an interfacial polymerisation. *J Sol-Gel Sci Technol* 13:821-825
34. Tsurumi T, Ozawa S, Abe G, Ohashi N, Wada S, Yamane M (2000) Preparation of $\text{Pb}(\text{Zr}_{0.53}\text{Ti}_{0.47})\text{O}_3$ thick films by an interfacial polymerisation method on silicon substrates and their electric and piezoelectric properties. *Jpn J Appl Phys* 39:5604-5608
35. Li K, Chan HLW, Lee KW, Choy CL (2000) Preparation of thick PZT films on stainless steel substrates. *Integr Ferroelectr* 30:253-260
36. Wang Z, Zhao C, Zhu W, Tan OK, Yao X (2002) Processing and characterization of $\text{Pb}(\text{Zr,Ti})\text{O}_3$ thick films on platinum-coated silicon substrates derived from sol-gel deposition. *Mater Chem Phys* 75:71-75
37. Duval FFC, Dorey RA, Zhang Q, Whatmore RW (2003) Lead germanium oxide sinter assisted PZT composite thick film. *J Eur Ceram Soc* 23:1935-1941
38. Dauchy F, Dorey RA (2007) Thickness mode high frequency MEMS piezoelectric micro ultrasound transducers. *J Electroceram* 19:383-386
39. Duval FFC, Dorey RA, Haigh RH, Whatmore RW (2003) Stable TiO_2/Pt electrode structure for lead containing ferroelectric thick films on silicon MEMS structures. *Thin Solid Films* 444:235-240
40. MacManus-Driscoll JL (2010) Self-assembled heteroepitaxial oxide nanocomposite thin film structures: designing interface-induced functionality in electronic materials. *Adv Funct Mater* 20:2035-2045
41. Granqvist CG (2008) Oxide electrochromics: why, how, and whither. *Sol Energ Mater Sol Cells* 92:203-208
42. Roy S, Chatterjee R, Majumder SB (2011) Magnetolectric coupling in sol-gel synthesized dilute magnetostrictive-piezoelectric composite thin film. *J Appl Phys* 110:036101-1-036101-4
43. Schneller T, Halder S, Waser R, Pithan C, Dornseiffer J, Shiratori Y, Houben L, Vyshnavi N, Majumder SB (2011) Nanocomposite thin films for miniaturized multi-layer ceramic

- capacitors prepared from barium titanate nanoparticle based hybrid solutions. *J Mater Chem* 21:11631–11638
44. Logvenov G, Gozar A, Bozovic I (2009) High-temperature superconductivity in a single copper-oxygen plane. *Science* 326:699–702
 45. Bousquet E, Dawber M, Stucki N, Lichtensteiger C, Hermet P, Gariglio S, Triscone JM, Ghosez P (2008) Improper ferroelectricity in perovskite oxide artificial superlattices. *Nature* 452:732–737
 46. Hennings DFK (2001) Dielectric materials for sintering in reducing atmospheres. *J Eur Ceram Soc* 21:1637–1642
 47. Sato S, Nakano Y, Sato A, Nomura T (1999) Mechanism of improvement of resistance degradation in Y-doped BaTiO₃ based MLCCs with Ni electrodes under highly accelerated life testing. *J Eur Ceram Soc* 19:1061–1065
 48. Liu X, Cheng S, Randall CA (1998) The core-shell structure in ultrafine X7R dielectric ceramics. *J Korean Phys Soc* 32:S312–S515
 49. Pithan C, Schneller T, Shiratori Y, Majumder SB, Haegel FH, Dornseiffer J, Waser R (2006) Microemulsion mediated synthesis of nanocrystalline BaTiO₃: possibilities, potential and perspectives. *Int J Mater Res* 5:499–507
 50. Kishi H, Mizuno Y, Chazono H (2003) Base-metal electrode-multilayer ceramic capacitors: past, present and future perspectives. *Jpn J Appl Phys* 42:1–15
 51. Sahoo SK, Agrawal DC, Mohapatra YN, Majumder SB, Katiyar RS (2004) Changes in the leakage currents in Ba_{0.8}Sr_{0.2}TiO₃ZrO₂ multilayers due to modulations in oxygen concentration. *Appl Phys Lett* 85:5001–5003
 52. Shukla D, Mehra A (2006) Modeling shell formation in core – shell nanocrystals in reverse micelle systems. *Langmuir* 22:9500–9506
 53. Li M, Ober CK (2006) Block copolymer patterns and templates. *Mater Today* 9:30–39
 54. Bates FS (1991) Polymer-polymer phase behavior. *Science* 251:898–905
 55. Vopsaroiu M, Blackburn J, Cain MG (2007) A new magnetic recording read head technology based on the magneto-electric effect. *J Phys D* 40:5027–5033
 56. Zhang Y, Li Z, Deng C, Ma J, Lin Y, Nan CW (2008) Demonstration of magnetoelectric read head of multiferroic heterostructures. *Appl Phys Lett* 92:152510–152512
 57. Liu M, Obi O, Lou J, Chen Y, Cai Z, Stoute S, Espanol M, Lew M, Situ X, Ziemer KS, Harris VG, Sun NX (2009) Giant electric field tuning of magnetic properties in multiferroic ferrite/ferroelectric heterostructures. *Adv Funct Mater* 19:1826–1831
 58. Bibes M, Barthélemy A (2008) Multiferroics: towards a magnetoelectric memory. *Nat Mater* 7:425–426
 59. Gajek M, Bibe M, Fusi S, Bouzouane K, Fontcuberta J, Barthélemy A, Fert A (2007) Tunnel junctions with multiferroic barriers. *Nat Mater* 6:296–302
 60. Roy S, Majumder SB (2011) Percolative dielectric behavior of wet chemical synthesized lead lanthanum titanate – cobalt iron oxide composite thin films. *Phys Lett A* 375:1538–1542
 61. Roy S, Chatterjee R, Majumder SB (2011) Magnetoelectric coupling in sol–gel synthesized dilute magnetostrictive-piezoelectric composite thin films. *J Appl Phys* 110:036101–036103
 62. Li XH, Xu CL, Han XH, Qiao L, Wang T, Li FS (2010) Synthesis, and magnetic properties of nearly monodisperse CoFe₂O₄ nanoparticles through a simple hydrothermal condition. *Nano-scale Res Lett* 5:1039–1044
 63. Roy S, Majumder SB (2012) Optical characteristic of sol–gel synthesized lead lanthanum titanate-cobalt iron oxide multiferroic composite thin film. *J Appl Phys* 112:043520–043528
 64. Patil A, Patil V, Shin DW, Choi JW, Paik DS, Yoon SJ (2008) Issues and challenges facing rechargeable thin film lithium batteries. *Mater Res Bull* 43:1913–1942
 65. Xu B, Qian D, Wang Z, Meng YS (2012) Recent progress in cathode materials research for advanced lithium ion batteries. *Mater Sci Eng R* 73:51–65
 66. Sivaprakash S, Majumder SB (2010) Spectroscopic analyses of 0.5Li[Ni_{0.8}Co_{0.15}Zr_{0.05}]O₂–0.5Li[Li_{1/3}Mn_{2/3}]O₂ composite cathodes for lithium rechargeable batteries. *Solid State Ion* 181:730–739

67. Ghanty C, Basu RN, Majumder SB (2012) Performance of wet chemical synthesized $x\text{Li}_2\text{MnO}_3-(1-x)\text{Li}(\text{Mn}_{0.375}\text{Ni}_{0.375}\text{Co}_{0.25})\text{O}_2$ ($0.0 \leq x \leq 1.0$) integrated cathode for lithium rechargeable battery. *J Electrochem Soc* 159:A1125–A1134
68. Amalraj F, Kovacheva D, Talianker M, Zeiri L, Grinblat J, Leifer GG, Markovsky B, Aurbach D (2010) Synthesis of integrated cathode materials $x\text{Li}_2\text{MnO}_3-(1-x)\text{LiMn}_{1/3}\text{Ni}_{1/3}\text{Co}_{1/3}\text{O}_2$ ($x = 0.3, 0.5, 0.7$) and studies of their electrochemical behavior. *J Electrochem Soc* 157: A1121–A1130
69. Sivaprakash S, Majumder SB (2010) Synthesis and electrochemical characteristics of Li $[\text{Ni}_{0.375}\text{Mn}_{0.375}\text{Co}_{0.2}]\text{O}_2-[\text{Li}_{1/3}\text{Mn}_{2/3}]\text{O}_2$ cathode materials for Li rechargeable batteries. *J Electrochem Soc* 157:A418–A422

Chapter 20

UV and E-Beam Direct Patterning of Photosensitive CSD Films

Kiyoharu Tadanaga and Mohammad S.M. Saifullah

20.1 UV Patterning

20.1.1 Introduction

Fine patterning techniques of thin films derived by chemical solution deposition process have attracted much attention for the practical applications of these films to devices like integrated optical circuits and micro-electronic memories. Several approaches, such as UV-irradiation on photosensitive precursor films, embossing, micro-contact printing (cp. Chap. 13) or UV-patterned self-assembled monolayers, have been proposed.

In this section, direct UV-patterning process using photosensitive precursor films is reviewed. Figure 20.1 portrays the fine-patterning process using photosensitive precursor films. Table 20.1 lists examples of materials, in which micropatterns were prepared by the direct UV-patterning process, together with precursors. Precursors for the photosensitive films, preparation of multi-component systems, some applications of direct UV-patterning, and limitation of this process will be discussed.

K. Tadanaga (✉)

Faculty of Engineering, Hokkaido University, Sapporo, Hokkaido 060-8628, Japan
e-mail: tadanaga@eng.hokudai.ac.jp

M.S.M. Saifullah (✉)

Patterning and Fabrication Capability Group, Institute of Materials Research and Engineering, A*STAR (Agency for Science, Technology and Research), 3 Research Link, Singapore 117602, Republic of Singapore
e-mail: saifullahm@imre.a-star.edu.sg

Fig. 20.1 Fine-patterning process using a photosensitive precursor film

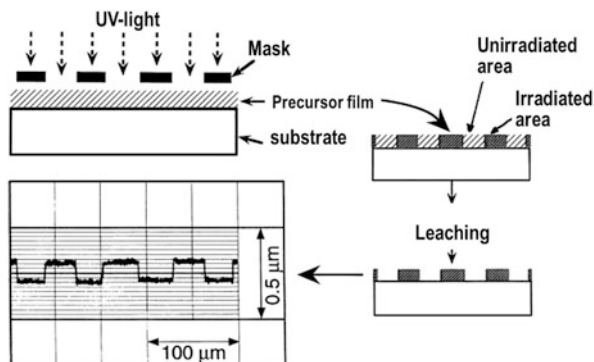


Table 20.1 Precursors for UV-micropatterning of oxide thin films

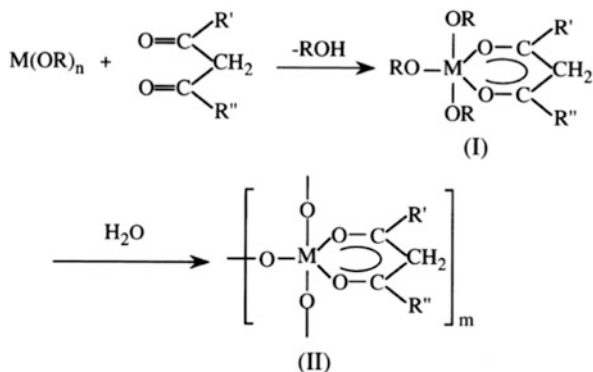
Oxides	Precursors	References
TiO ₂	Ti-alkoxide + β-diketone	[1, 3, 10, 14, 15]
	Ti-alkoxide + alkanolamine	[27]
ZrO ₂	Zr-alkoxide + β-diketone	[1–3, 10–13]
Al ₂ O ₃	Al-alkoxide + β-diketone	[4, 6, 10, 20]
ZnO	Zn-acetate + β-diketone	[8, 9]
SnO ₂	SnCl ₂ + β-diketone	[16]
	Sn-2-ethylhexanoate	[23]
	Sn-alkoxide + β-diketone	[25]
	Sn-alkoxide + alkanolamines	[28]
Cu ₂ O	Cu-2-ethylhexanoate	[17]
In ₂ O ₃	In-2-ethylhexanoate	[18]
UO ₃	U-2-ethylhexanoate	[19]
Al ₂ O ₃ -SiO ₂	Al-alkoxide + β-diketone	[5]
Pb(Zr _x Ti _{1-x})O ₃	Zr, Ti-alkoxide + β-diketone	[7]
	Pb, Zr-2-ethylhexanoate	[21]
(Pb _x La _{1-x})(Zr _y Ti _{1-y})O ₃	Zr, Ti-alkoxide + β-diketone	[10]
	Pb, Zr-2-ethylhexanoate	[22]
Bi _{4-x} La _x Ti ₃ O ₁₂	Bi-, La-2-ethylhexanoate	[24]
LiNbO ₃	Li-Nb double-alkoxide + β-diketone	[26]

20.1.2 Precursors for Photosensitive Precursor Films

20.1.2.1 Metal-Alkoxide with β-Diketones

When metal alkoxides $M(OR)_n$ or metal salts are reacted with β-diketones, metal atoms are coordinated with β-diketones to form chelate rings (cp. Chap. 1). Chelate rings are durable against hydrolysis, and thus gel films derived by the hydrolysis of modified metal alkoxides contain chelate bonds. These gel films exhibit absorption bands, which are characteristic of the π - π^* transition in the chelate rings, at wavelength in a UV-range depending on a combination of metal and β-diketones.

Scheme 20.1 Model of a reaction of β -diketone with metal alkoxide



Moreover such or related compounds are sensitive to electron beam exposure as well, which is also used for patterning (see Sect. 20.2). Typical β -diketones used for micropatterning are acetyl acetone (AcAc), ethyl acetoacetate (EAcAc), benzoyl acetone (BzAc). By UV-irradiation on gel films, chelating bonds in gel films are decomposed, and usually, the films become dense because of formation of metal-oxygen-metal bonds in the gel films. Any type of UV-source can be used such as high pressure mercury lamps, excimer lamps, and UV-lasers. The reaction model is described in Scheme 20.1.

Figure 20.2 shows the absorption spectra of the ZrO_2 gel films modified chemically with four different β -diketones [11]. The characteristic absorption bands of these gel films lay at 280, 302, 334 and 365 nm for ethyl acetoacetate (EAcAc), acetylacetone (AcAc), benzoyl acetone (BzAc) and dibenzoyl methane (DBzMe) ligands, respectively; the absorption bands observable in a range from 240 to 280 nm for BzAc and DBzMe ligands originate from phenyl group, showing that the incorporation of phenyl group in chelate rings shifts the characteristic absorption band to longer wavelengths due to induction effect of phenyl group. Thus, suitable β -diketones should be selected according to combination of center metal and UV source.

Figure 20.3 shows the change of optical absorption spectra of ZrO_2 films modified with acetylacetone, AcAc, with UV-irradiation [2]. The ZrO_2/AcAc gel films shows the absorption band at around 300 nm because of π - π^* transition in the chelating bonds of AcAc. The absorption of the band decreased with an increase in UV-irradiation time, and the band disappeared after 5 min irradiation. The disappearance of the band shows that the chelate bonds dissociate with UV-irradiation. Because these chelating bonds are confirmed to be stable at room temperature, the dissociation of the chelate bonds is accelerated by the excitation of π - π^* transition.

In the gel films prepared by metal alkoxide modified with β -diketones, the solubility of the gel film is controlled by the photochemically-induced reactions of chelates bond to metal centers. The photo-dissociation of the chelate rings is accompanied by the change in solubility of the gel films, because of formation of metal-oxygen-metal bonds in the gel films.

Fig. 20.2 Optical absorption spectra of ZrO_2 gel films derived from $Zr(O-n-Bu)_4$ modified with different β -diketones

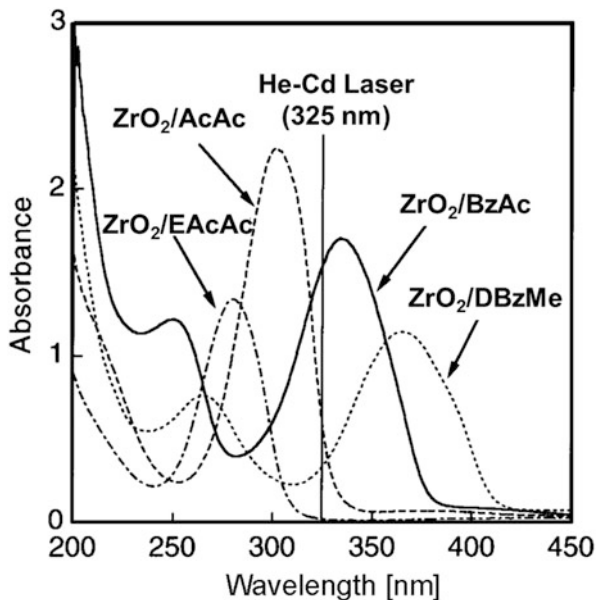
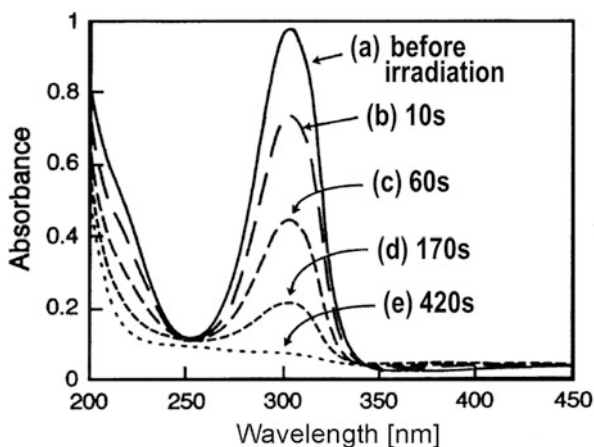


Fig. 20.3 Change of optical absorption spectra of ZrO_2 gel films derived from $Zr(O-n-Bu)_4$ modified with acetylacetone, with UV irradiation [2]



The change of solubility enables the formation of micropatterns through UV-irradiation. Gel films were irradiated through a mask with UV-light and then leached with appropriate solutions. The irradiated part of the gel films remained after the leaching, while the unirradiated part was leached out, which gave a negative pattern of the mask used. As leaching solutions, organic solvents such as methanol, ethanol, 2-propanol, or appropriate pH of acid- and base-solution have been used.

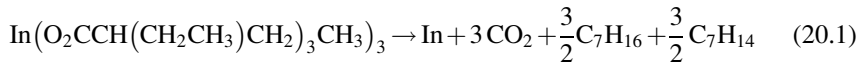
Patterning of oxide thin films using metal-alkoxide- β -diketone systems was firstly reported by Tohge's group, and the other groups are following using similar

process. As a simple oxide system, micropatterning of ZrO_2 , TiO_2 , Al_2O_3 , SnO_2 have been reported as shown in Table 20.1.

20.1.2.2 Metal Complex of Carboxylic Acid

Metal complexes of carboxylic acids are known to show absorption bands in UV or near UV region because of ligand-to-metal charge transfer (LMCT). These complexes undergo photoreduction in solution and the solid state. Patterning of oxide thin films using these metal complexes has been proposed as photochemical metal organic deposition (PMOD) process [18]. In this process, precursor amorphous films are formed from these metal complexes. Photolysis of these films results in the loss of the ligands from the metal center, leaving metal on the surface under inert gas, and metal oxides under the ambient atmosphere because of the oxidation of metals.

For example, photolithographic deposition of indium oxide from indium 2-ethylhexanoate has been reported [18]. The complex shows absorption maximum at 260 nm, and UV light of 254 nm was used for irradiation. The photoreaction was monitored with FT-IR spectra and the mass spectroscopy, the photolysis reaction is clarified as follows:



After UV irradiation using a contact mask, the patterns were developed using methylene chloride. As leaching solutions, organic solvents such as methanol, hexane, methylene chloride have been used.

Using this type of complex with 2-ethylhexanoate, formation of patterns of oxides such as CuO , InO_x , SnO_2 , UO_3 , PZT, PLZT, and so on has been reported as shown in Table 20.1.

20.1.3 Binary and Multi-Component Systems

Not only single oxide films, micropatterns of several binary oxides and multi-component oxide systems have been reported. Especially, thin films of ferroelectric materials such as PZT, PLZT are very important target of the micropatterning. In the preparation of multi-component oxides, not all the precursor should be photosensitive precursor. For example, in the preparation of PZT using β -diketones-modified gel films, Zr and Ti are modified with β -diketones, but lead acetate, for example, is used for precursor [7]. In the preparation of PZT using PMOD process,

Pb and Zr complexes with 2-ethylhexanoate, and Ti-alkoxide are used as precursors [21].

Tohge's group reported that preparation of Al_2O_3 - SiO_2 binary oxide system using tetraethoxysilane, which is not photosensitive precursor, and Al-alkoxide with a β -diketone [5]. They show that gel films with a composition of x larger than 30 in $x \text{ Al}_2\text{O}_3 (100-x)\text{SiO}_2$ showed difference in solubility between irradiated- and unirradiated- areas to form micropatterns. This proves the feasibility of direct fine patterning process of multi-component oxide thin films using photosensitive gel films.

20.1.4 Positive-Type Patterning

Kawahara et al. reported the formation of positive-type patterned ZnO films [8, 9]. Usually, photo-irradiated areas become dense after photo-decomposition of precursors. However, irradiation of UV-light on precursor films prepared from Zn^{2+} modified with benzoylacetone yields hydrophilic moieties in the gel films, and irradiated area were easily leached out with an aqueous solution of HNO_3 .

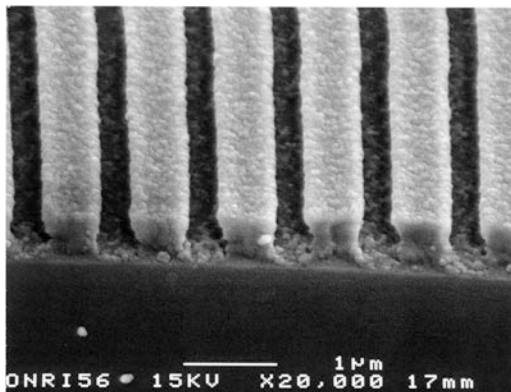
20.1.5 Applications

Finely patterned thin films derived by CSD have attracted much attention for the practical applications of these films to devices like integrated optical circuits and micro-electronic memories. For example, Tohge's group applied the process for the UV patterning of photosensitive gel films to the formation of several types of diffraction gratings [6, 10–13]. Surface-relief gratings were fabricated on silica glass and Si substrates by the irradiation of the modified gel films with a XeF excimer laser through a phase mask, or diffraction gratings of arbitrary periods have been prepared by using two-beam-interference method using He-Cd laser.

In the two-interference method, linearly polarized laser beam is split into two beams, which are then condensed on the sample surface to form straight interference fringe. Changing the incidence angle of the two beams can control the spacing of the fringe. By using two-beam-interference method, very uniform diffraction gratings with a pitch of about 0.5–1.0 μm were produced for oxide thin films such as Al_2O_3 , ZrO_2 , TiO_2 , and PLZT [6, 10–13]. Figure 20.4 shows the SEM photograph of 1.0 μm diffraction gratings prepared from ZrO_2 gel film modified with BzAc [11]. The grooves formed are uniform and their cross sectional shape is rectangular.

By double exposures with rotation of the photosensitive gel films between exposures, two-dimensional gratings can be also fabricated [12]. If the irradiation by one exposure is rather below the threshold to make irradiated area to be insoluble in a leaching solution, and the second irradiation ensures the doubly irradiated area to be insoluble in leaching solutions, then. The doubly irradiated areas with 90°

Fig. 20.4 SEM photograph of 1.0 μm diffraction gratings prepared from a ZrO_2 gel film modified with BzAc [11]



rotation between exposure can remain after the leaching, whereas both unirradiated and singly irradiated regions are soluble in the leaching solution. In this case, the island type patterns can be formed. When the dose of one exposure is strong enough to make irradiated region insoluble in a leaching solution, both singly and doubly irradiated regions after rotation remain after the leaching. In this case, grating of lattice type can be obtained. The island type two dimensional surface relief gratings showed excellent antireflection effect in a range of wavelength longer than the period of gratings, because of so-called the “moth eye effect” [12].

20.1.6 Limitation of UV-Patterning

As pointed out in a review by Martin and Aksay [29], the limitation of the patterning process should be discussed in terms of materials, resolution, and thickness or cracking.

As to the material limitation, a precursor gel film must have photosensitivity in the UV-region. Most of metals can form complexes with β -diketones or carbonyl compounds, and thus, photosensitivity can be introduced to the gel films prepared from those precursors. However, for the nonmetallic elements, formation of such photosensitive absorption band in the UV region is very difficult, and thus, formation of micropatterns of such oxides is very difficult. For example, although pure SiO_2 micropatterning must be very important, it is very difficult to make pattern of pure SiO_2 because there are no good photosensitive precursors for SiO_2 . By using organically modified alkoxysilanes with $\text{C}=\text{C}$ in organic group, or by using photosensitive solvents such as photo curable monomers, micropatterns can be prepared, but organic groups must be removed from the pattern.

As in the photolithography in semiconductor industry, the resolution of micropatterns is limited by the resolution of photomask, equipment optics, and the wavelength of the light source. As mentioned above, by using two-beam

interference process, very uniform diffraction gratings with a pitch of about 0.5–1.0 μm were produced using He-Cd laser (325 nm).

Because continuous thin films must be prepared before the formation of the final pattern, the height of the final patterns is limited by the thickness of the precursor thin films. In the CSD process, the critical thickness without cracking is in the order of 0.1 μm . Thus repeated coating and heat-treatment cycles are required to get thicker films. If micropatterns are formed with thicker photosensitive gel films, this pattern can be cracked with heat-treatment after development with the leaching solution.

In order to overcome in particular the limitations of the minimal structure size of the patterned structure, electron beams which exhibit a significantly smaller wavelength have been introduced into patterning processes. Hence in Sect. 20.2 the features of electron beam lithography are discussed in detail.

20.2 Electron Beam Lithography

20.2.1 Introduction

Electron beam lithography is a process where a beam of electrons is scanned ('exposure') in a patterned fashion across a surface ('substrate') coated with a film (called the 'resist') and then selectively removing ('development') either the unexposed or exposed regions to create very fine structures in the film. 'Positive' electron resist produces the image that is the same as the pattern drawn by an electron beam, while 'negative' one produces the reverse image of the pattern drawn. Positive resists undergo bond-breaking when exposed to electrons, thus become more soluble in a developer solution. On the other hand, negative resists form bonds or cross-links between polymer chains which render them less soluble in a developer. The structure created in the resist can be subsequently transferred to a substrate by either 'wet' or 'dry' etching. Alternatively, metals or oxides can be deposited on the patterned resist and, subsequently, the resist can be "lifted-off" or dissolved in organic solvents to obtain patterned metals or oxides. A typical electron beam lithography system consists of an electron gun, focusing condenser lenses, beam blanker unit, beam deflection unit and a stage holder for substrate. The principal advantage of electron beam lithography is its ability to beat the diffraction limit of light. The resolution is related to the extremely small de Broglie wavelength of the electrons (the wavelength at an accelerating voltage of 50 kV is ~ 0.01 nm). Furthermore, the electron beam also has a greater depth of focus. In spite of these advantages, the key limitation of electron beam lithography is that it is a serial process and, therefore, the throughput suffers as it takes a very long time to expose an entire silicon wafer or a chrome-coated glass substrate. A long exposure time means that the process of writing is vulnerable to beam drift or instability which may occur during the exposure. Conventional electron beam lithography uses poly

(methylmethacrylate), or PMMA as it is commonly abbreviated, as resist and has a resolution ~ 4 nm [30]. At this resolution, the lift-off step is delicate and the line edge roughness poor. The limiting factors for not achieving the theoretical resolution as per the de Broglie wavelength are spherical aberrations, scattering of electrons (both forward scattering in the resist and backscattering from substrate) and the range of secondary electrons generated by inelastic interaction of primary electrons with the resist molecules. These effects tend to ‘increase’ the beam size and also lead to unwanted additional exposure known as the proximity effect. Furthermore, the chemical nature of the resist, its molecular size and the choice of developer also determines the maximum achievable resolution in the resist. Using a thin resist and a thin substrate in combination with appropriate lithography conditions such as high accelerating voltage, smaller apertures can reduce the scattering and aberration effects, while the proximity effect can be compensated by dose control. The advantage of an inorganic resist over an organic one is that it offers a resolution better than 1 nm and requires little or no chemical development. To attain such sort of resolution, researchers around the world have been studying various materials and their behaviour under an electron beam for potential application as inorganic resists. The suitability of these materials as resists depends upon their ease of deposition on the substrate, their electron beam sensitivity and damage (or exposure) characteristics in an electron beam, and ease of pattern transfer on silicon substrates after exposure. Here we provide an overview of the studies so far carried out in the development of inorganic resists for high resolution electron beam nanolithography.

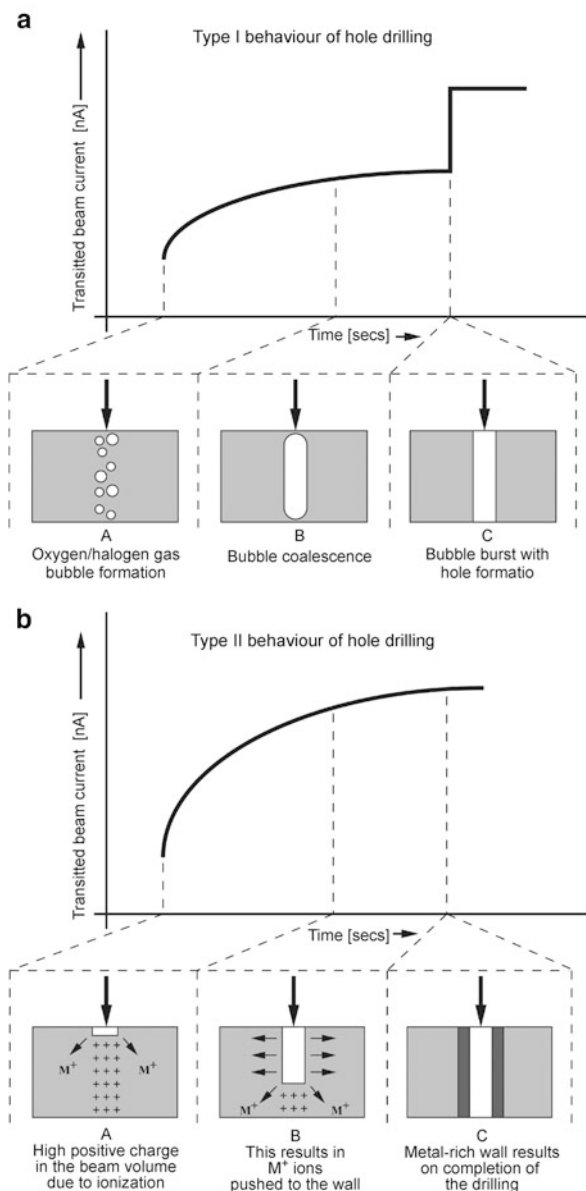
20.2.2 Patterning of Inorganic Materials by an Electron Beam: a Brief History

The origin of patterning of inorganic materials used as resists goes back to about 30 years. The earliest efforts to find suitable inorganic resists for electron beam lithography were largely confined to using instruments fitting with intense electron probes and their ability to drill holes through a thin specimen. The use of a highly intense and small probe, such as that provided by a Vacuum Generators 501HB dedicated Scanning Transmission Electron Microscope (VG-STEM) and a Field Emission Gun-equipped Scanning Electron Microscope (FEG-SEM) to directly form nanoscale features in a physically deposited film of ionic materials has been an exciting discovery.

20.2.2.1 In the Beginning: Metal Halides as High Resolution Resists

In 1978 Broers et al. first drilled holes of 5 nm in diameter in a 250 nm thick NaCl film using a focused electron probe in a STEM with LaB₆ filament [31]. The holes

Fig. 20.5 The transmitted current versus time curves (or the drilling curves) in some halides and oxides indicate that broadly two types of materials exist in terms of their mass loss behaviour during the exposure to an electron beam. (a) Type 1: Here an abrupt mass loss is observed during drilling. This is caused by the formation of gas bubbles in the irradiated volume of the sample which ‘pop’ to form a hole after sufficient irradiation. Metal cations are displaced from the irradiated volume to surround the hole. Drilling time shows a nearly linear behaviour with accelerating voltage and is relatively temperature and thickness independent. Examples include amorphous AlF_3 , amorphous Al_2O_3 and MgF_2 . (b) Type 2: In this case continuous mass loss is observed during drilling. Material may be lost from both surfaces of the specimen. Drilling time shows highly non-linear accelerating voltage dependence but mass loss is accelerated at higher temperatures. Examples are crystalline CaF_2 , TiO_2 , NaCl , MgO , and sodium β -alumina



required an exposure dose of 0.1 C m^{-2} . This observation was attributed to evaporation of the material. In 1981, Isaacson and Muray studied the drilling mechanism in thinner NaCl crystalline films evaporated on carbon support grids using electron energy loss spectroscopy (EELS) [32]. They could drill holes of 2 nm diameter. EELS analysis of an intermediate, partially drilled hole suggested that sodium metal was left. The mechanism of drilling is schematically shown in

Fig. 20.5b. These holes were not permanent structures due to the attack of NaCl by atmospheric water vapour.

The first permanent hole drilling was performed by Mochel et al. in sodium β -alumina using a field emission gun [33]. Devenish et al. have shown that holes may be drilled in sodium β -alumina by using a standard thermionic source [34]. The acronym SCRIBE (Sub-nanometer Cutting and Ruling by an Intense Beam of Electrons) was coined by Salisbury et al. to differentiate this process from conventional electron beam lithography [35]. Various metal halides, oxides and pure metals undergo this process, albeit exhibiting different damage mechanisms (Fig. 20.5).

Muray et al. found that in AlF_3 , a dose of about $1 \times 10^5 \text{ C m}^{-2}$ was required to remove aluminium and fluorine from the irradiated areas of 80 nm thick film [36]. They used AlF_3 film to mask a 50 nm thick silicon nitride film against reactive ion etching in a CHF_3 plasma. After reactive ion etching, features with dimensions of $8 \times 10 \text{ nm}$ were produced by removing the AlF_3 with an aqueous solution of HCl. On the other hand, studies by Kratschmer and Isaacson have found that metallic aluminium was formed in the irradiated areas of AlF_3 after a dose of only $\sim 2 \text{ C m}^{-2}$ [37]. Aluminium wires about 20 nm wide were produced by subsequently dissolving the resist in water. They also investigated the use of AlF_3 , FeF_2 , BaF_2 , SrF_2 , CrF_2 , and CsF as both positive and negative resists [38]. They were all found to act acceptably in both fashions, albeit FeF_2 tended to crack due to internal stresses set-up due to mass loss and CrF_2 could not be used as an etch mask as a positive resist due to a residual thin layer of chromium on Si_3N_4 substrate. LaF_3 was found not to drill well, instead producing voids and cracking next to the exposed area. Scherer and Craighead showed that BaF_2 and SrF_2 films could indeed act as negative resists [39]. In situ EELS analysis on both materials showed a distinct decline in the fluorine K-edge signal, together with a corresponding increase in the oxygen K-edge intensity—oxygen coming from the vacuum of the microscope chamber. Using BaF_2 and SrF_2 developed in water, feature sizes of about 100 nm were achieved on GaAs, the limiting factor being the grain size of the resist film. The work was continued by Scherer et al. who attempted to optimise the negative fluoride resists by grain size control [40]. The best balance was struck with a SrF_2 film containing 8 at.% of AlF_3 to reduce the grain size.

CaF_2 and MgF_2 were used as positive resists and developed in water or other suitable agents to chemically strip radiolysis-induced products. Such resists require relatively high doses of typically 1×10^4 to $1 \times 10^6 \text{ C m}^{-2}$, since chemical conversion of fluorides to other products has to occur before exposure is complete. Mankiewich et al. had demonstrated the use of CaF_2 as a high resolution inorganic resist with 30 nm resolution using water as developer [41]. They found that the end product of CaF_2 radiolysis was CaO when the exposure was carried out in a STEM at $\sim 5 \times 10^{-7}$ Torr. They suggested that the product of electron-induced radiolysis of CaF_2 was Ca, which was rapidly oxidised at $\sim 5 \times 10^{-7}$ Torr by oxygen and/or oxygen containing residual gases. The chemical conversion took $1 \times 10^5 \text{ C m}^{-2}$ to complete. CaO is about hundred times more soluble in water than CaF_2 , therefore

H₂O could be used as developer. The work on a CaF₂ etch mask was continued by Zanetti et al. who used molecular beam epitaxy to deposit CaF₂ as a resist for etching GaAs [42]. CaF₂ was chosen as it has a good lattice match with GaAs and hence epitaxial films should be attainable.

Sub-10 nm electron beam nanolithography using a FEG-SEM was carried out by Fujita et al. on AlF₃-doped LiF inorganic resists. They were able to delineate 5 nm linewidths patterns with 60 nm periodicity using a 30 kV electron beam [43]. Electron stimulated desorption studies on these resists showed that a metal rich layer is formed by preferential desorption of fluorine which suppresses the subsequent fluorine desorption. The surface diffusion of the residual metal film plays an important role in the self-developing reaction [44]. Although metal halides demonstrated a very high resolution, they suffered from two main drawbacks: firstly, they are highly hygroscopic and, secondly, the dose requirement to drill a hole or expose the resist is very steep. In order to eliminate these drawbacks, metal oxides were looked into as potential resists for high resolution electron beam nanolithography.

20.2.2.2 Metal Oxides as High Resolution Resists

It was mentioned earlier that Mochel et al. found that a highly intense focused electron probe could drill 2 nm holes and cut 2 nm lines through a 200 nm thick crystalline sample of sodium β-alumina in a few seconds [33]. If the irradiation was stopped before the hole was completed, a stable partially formed hole could be observed. A plot of the transmitted current versus time curve during hole drilling shows an initial fairly constant rate of mass loss, followed by decrease of mass loss rate and ending with the formation of a hole (schematically shown in Fig. 20.5b). Berger et al. used the techniques of EELS and energy filtered imaging, together with transmitted current versus time curves, to study drilling process in crystalline sodium β-alumina [45]. They suggested that the hole was produced by material removed atom plane by atom plane from both surfaces, with oxygen being desorbed following ionisation by the incident beam, and aluminium migrating to the sides of the hole.

Similar work performed by Mochel et al. [46] and Berger et al. [45] showed that drilling of a nanometer-sized hole in anodised amorphous Al₂O₃ occurred in a different way from that of crystalline sodium β-alumina. A plot of transmitted current versus time shows a swift increase in current followed by a slowly rising plateau region, which slowly increases until the current suddenly jumps to a final value (schematically shown in Fig. 20.5a). This indicates that amorphous Al₂O₃ suffers from initial small loss of mass followed by an interval during which no appreciable mass loss occurs. Finally, an abrupt transition to a complete hole takes place. If the beam was switched off in the plateau region, then the partially drilled hole healed up quickly and no sign of the embryonic hole remained.

Devenish et al. attempted to drill amorphous Al₂O₃ using a conventional thermionic source in a conventional transmission electron microscope, and consequently

at much lower current density [34]. It was found that at room temperature the material suffered some damage but no holes could be drilled. At liquid nitrogen temperature, however, holes were easily drilled. One possibility is that at low temperatures gases in the column vacuum (water vapor, oxygen, etc.) may be condensed or adsorbed on the specimen. The electron beam ionizes the adsorbed species, and the reactive ions enhance the hole drilling. Another explanation was proposed when some partially drilled holes were observed to heal up. It was proposed that the drilling process was a balance between material removal and diffusion of aluminium back to the hole which reacts to give Al_2O_3 . Lowering the temperature should decrease the rate of back diffusion of aluminium and hence increase the drilling rate.

Hollenbach and Buchanan studied the response of RF sputtered thin films of amorphous Al_2O_3 in a VG-STEM [47]. They found that the sensitivity was significantly increased in sputtered amorphous Al_2O_3 films relative to anodised Al_2O_3 films and the hole formation time could be dramatically reduced to 50 ms rather than tens of seconds. This reduction of dose requirement for the two materials indicates that microstructural characteristics strongly affect the speed of the material removal process. One obvious chemical difference in sputtered films is the incorporation of argon. Argon, which has a relatively large ionic size, is believed to be incorporated as a neutral species. Hence argon can act as a structural modifier. Thus the improved rate of material removal can be a result of more open structure of amorphous materials, particularly when modified by entrapped argon, via an increase of atomic diffusion rates. Further investigations of this material by Morgan et al. showed that electron irradiation with a high magnification raster (>500 k) causes the holes to heal up [48]. They found that when the holes were produced closer together than a critical separation then a proximity effect occurred causing pear-shaped holes. These effects are not observed in crystalline Al_2O_3 [49].

Chen et al. [50] and later Saifullah et al. [51] showed that self-supporting thin films of SiO_2 produced by electron beam evaporation can be directly reduced to silicon with an intense 100 kV electron probe in a VG-STEM. Windowless energy dispersive X-ray spectroscopy and EELS studies showed that although both silicon and oxygen are lost, the latter is lost faster than the former. They proposed the fabrication of nanoscale structures such as columns and plates of silicon that can be used in microelectronics. Using a FEG-SEM, Fujita et al. have shown that the selective thermal desorption of thermally grown SiO_2 on Si (111) substrate can be induced by an intense electron probe in an ultra-high vacuum (UHV) chamber [52]. Change of contrast during selective thermal desorption was observed using scanning reflection electron microscopy (SREM) as well as microprobe reflection high energy electron diffraction (μ -RHEED). It was proposed that this was caused by the existence of a near-surface region with high Si content produced by electron beam irradiation and its interaction with SiO_2 .



By using this technique of selective thermal desorption, 10 nm wide open windows could be produced. A pattern transfer from the open windows to thin Si films was performed by Si growth and subsequent heating. This had produced Si wires of 10 nm width.

Salisbury et al. first studied the SCRIBE process in MgO [35]. They found that it is possible to machine holes and steps on the nanometer scale on the surface of MgO smoke cubes with {100} faces oriented parallel to the electron beam. Further studies by Turner et al. and Devenish et al. have found that rastering a focused electron beam over the surface of the crystal results in the formation of atomically smooth surface faces [53, 54]. The holes produced in MgO formed by a deep indentation on the electron exit surface grow towards a much shallower indentation on the entrance surface. Energy dispersive X-ray spectroscopy showed that the Mg:O ratio remained constant during drilling suggesting that the material is removed in stoichiometric groups.

SCRIBE studies in TiO₂, TiO and Ti₂O₃ showed that drilling was accompanied by the gradual loss of oxygen and displacement of titanium under the beam in a process that is similar to that observed in metal β-aluminas [55]. The holes did not penetrate through the film and the hole drilling stopped when a critical Ti:O ratio was reached. A comparative study of amorphous and crystalline TiO₂ films suggested that, contrary to what has been observed, crystalline TiO₂ film is more amenable to electron beam damage. Time-resolved EELS studies suggested that both amorphous and crystalline TiO₂ films lose oxygen continuously during electron irradiation and that the Ti-L_{2,3} edges shift to lower value indicating an insulator to metal transition [56].

Devenish et al. studied hole drilling in ZnO crystals and they found that it gives rise to faceted holes, but the indentation formed equally at both entrance and exit surfaces [54]. Other oxides where hole drilling has been studied are MoO and the YBa₂Cu₃O₇ system [34]. In YBa₂Cu₃O₇ under electron irradiation, oxygen can be removed transforming it into a semiconductor. Since this process can be done on a nanometer scale, Devenish et al. suggested that Josephson junctions could be produced using the SCRIBE technique [34]. Pauza et al. used electrons to create a narrow damaged section on YBa₂Cu₃O₇ film and showed that weak links can be written directly on this material [57].

With the exception of few studies, almost all the work on metal oxides as electron beam resists were carried out using free-standing thin films. In order to understand the electron beam exposure behaviour of inorganic resists on a substrate, Saifullah et al. conducted series of experiments using sputtered Al₂O₃ resist on silicon [58]. The changes taking place in the resists as a function of electron dose were recorded from a 6 × 6 nm² area using EELS. Before exposure both the Al and Si (from the substrate) L_{3,2} edges and the O-K edge are visible (Fig. 20.6a, b). After a 10 s exposure the Al-L_{3,2} and O-K edges are much reduced, indicating that both aluminium and oxygen are lost from the damaged area, whilst the Si-L_{3,2} edge becomes much clearer owing to the reduced resist thickness. However, even after a prolonged exposure some of aluminium and oxygen remains. It should be noted that the Si-L_{3,2} edge shows no evidence of the shift to higher energies which would be

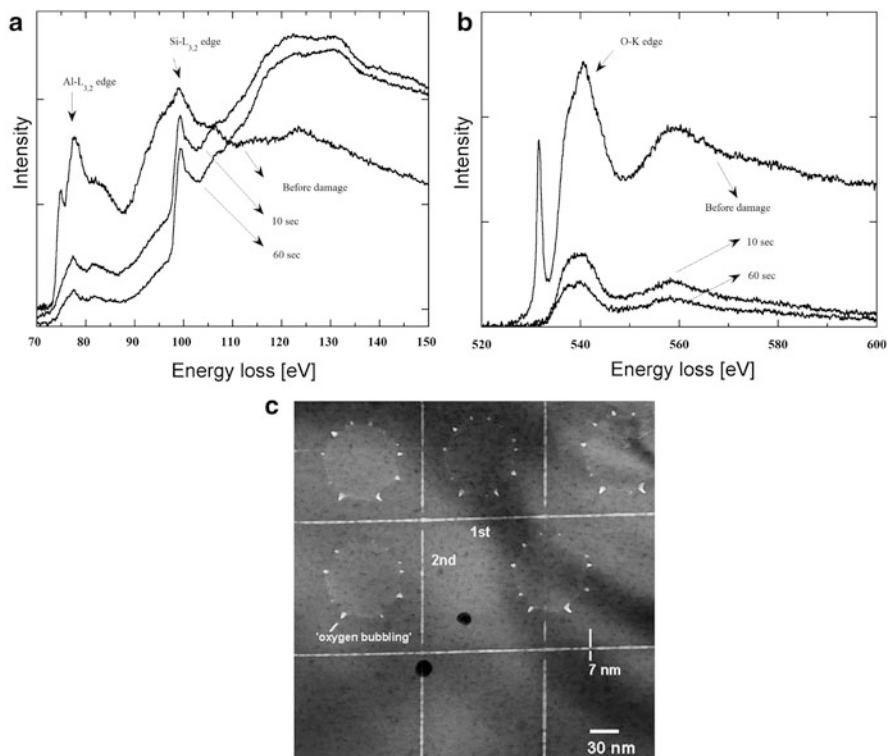


Fig. 20.6 EELS spectra showing (a) Al-L_{3,2} and (b) O-K edges before and after exposure of amorphous Al₂O₃ on silicon substrate to a high magnification raster. (c) Lines cut through an amorphous Al₂O₃ resist with a line dose of $1.80 \times 10^{-3} \text{C m}^{-1}$. It is seen that the second line drawn is discontinuous when it crosses the first line

seen if the surface of the silicon was oxidising. The presence of the remaining oxide on the substrate surface after a prolonged exposure could be due to two reasons (a) Previous studies using micro-diffraction patterns acquired using a nanoprobe in a STEM from a newly created structure in an amorphous Al₂O₃ film were found to be of metallic aluminium [47]. The oxide formation could be because of the appearance of atomic species of oxygen under the electron beam which then quickly reacts with the aluminium on the silicon substrate. (b) The amorphous Al₂O₃ itself becomes resistant to damage before it is completely reduced to aluminium. This is supported by the fact that if two lines are drawn intersecting each other, then there is a region about 8 nm from the first line on which a second line cannot be drawn (Fig. 20.6c). The non-connectivity of the two lines is also shown in amorphous Al₂O₃ self-supporting films [59]. In self-supporting films, this proximity effect is attributed to the migration of aluminium from the damaged areas to the edges of the line. The presence of oxide in the damaged region has implications for the fabrication of nanostructures using reactive ion etching. Amorphous Al₂O₃ is resistant to reactive ion etching in fluorine containing plasmas.

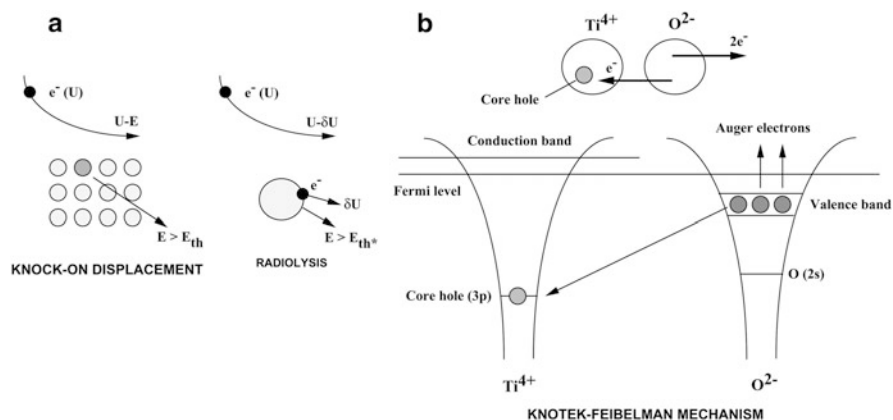


Fig. 20.7 Mechanisms of permanent displacement of atoms under an electron beam. (a) The processes of knock-on displacement and radiolysis. E_{th} and E_{th}^* are threshold energies for knock-on displacement and radiolysis, respectively. (b) Knotek-Feibelman Mechanism. Schematic of desorption induced by interatomic Auger decay of a maximal valency ionic solid (TiO_2). In these systems electrons are always removed from anion species in Auger events resulting in highly repulsive final states and subsequent desorption

Presence of small amount of amorphous Al_2O_3 on the substrate can result in the lack of pattern transfer.

Although the oxide resists did not suffer from the problem of hygroscopic behaviour of metal halides, they still required a very high electron dose for their exposure. The reason for such a high exposure dose can be understood by studying the electron beam damage mechanisms in these materials.

20.2.2.3 Mechanisms for the Electron Beam Damage Processes

The mechanisms by which an inorganic material is damaged on exposure to an intense electron beam are intriguing and variable. For example, Devenish et al. showed that a less intense electron beam from a tungsten filament or a LaB_6 filament could easily drill holes in an amorphous Al_2O_3 at liquid nitrogen temperatures even though the current density of the incident electron beam was well below the threshold for hole drilling [34]. There may be many different mechanisms involved during the SCRIBE process and different mechanisms may be dominant in different materials. In this section, the mechanisms of electron beam damage are chosen and discussed to illustrate their wide variety.

Knock-On Displacement and Radiolysis

Knock-on displacement is produced by direct momentum transfer from the incident electron to the atomic nucleus. Figure 20.7a shows that the energy transferred to an

atom E must be greater than the threshold for knock-on displacement, E_{th} to permanently displace a lattice atom from its normal site, thus forming an interstitial vacancy Frenkel pair defect. This defect constitutes the fundamental unit of radiation damage in the knock-on displacement process. The knock-on threshold energy depends on bond strength, specimen temperature, space available for accommodating an interstitial atom in the structure, the form of interstitials and the orientation of the crystal with respect to the incident electrons.

Radiolysis occurs with relatively high efficiency in almost all alkali and alkaline earth halides as well as in a variety of other inorganic materials [60] and is the main damage mechanism in the SCRIBE process [33, 36, 38, 41]. Pooley proposed a model that the decay of an exciton could transfer its energy to an alkali halide molecule to induce molecular dissociation [61]. Kabler and Williams also showed the radiolytic displacement in alkali halides (MX) resulted from the decay of excitons from which an $[X_2^-]$ and halogen vacancy (F centre) were formed. They proposed an energy to momentum transfer mechanism [62]. The released energy could be used in crowdion translation or off-centre rotation forming an $[X_2^-]_x$ crowdion interstitial (H centre). The $[X_2^-]_x$ interstitial and halogen vacancy together form the fundamental Frenkel pair defect in the halogen sub-lattice. This mechanism is remarkably efficient because it involves only a single sub-lattice.

The permanent displacements through knock-on and radiolysis processes suggest that the dissociation of “internal” molecules results in the production of Frenkel pair defects. Molecules on or near surfaces can be displaced more easily than internal molecules because of reduced interatomic bonding. Surface knock-on displacement can occur as a result of direct momentum transfer. Surfaces can also be rendered unstable when irradiated with an electron beam.

Knotek-Feibelman Mechanism

Surface desorption of materials is induced by electron excitation of surface bonds. The Knotek and Feibelman desorption mechanism involves the excitation of core levels followed by interatomic decay to complex desorptive final states [63, 64]. Knotek and Feibelman observed in materials like TiO_2 that if an electron is removed by ionisation from Ti then an intermediate Auger process can cause the loss of up to three electrons from an O^{2-} ion to give an O^+ ion. This results in a repulsive Madelung term and therefore oxygen gets desorbed (Fig. 20.7b).

Mochel et al. suggested that the hole in crystalline sodium β -alumina was produced by material being removed atom plane by atom plane from both surfaces, with oxygen being desorbed by the Knotek-Feibelman mechanism under the electron beam, and aluminium migrating to the sides of the hole [33]. Humphreys et al. reiterated this proposed mechanism by delineating the energy levels of Al_2O_3 , showing that the highest occupied level of the Al^{3+} ion is the 2p level, which is deep enough to provide energy to remove one or two electrons from O^{2-} [65].

Although the advantage of an inorganic resist over an organic one is that it offers a resolution better than 1 nm and requires little or no chemical development, it was

noted that the former suffered from the requirement of a heavy electron dose especially when the resist was deposited on a substrate. In order to minimize the dose required, sputtered oxides such as Fe_2O_3 and WO_3 were investigated [66–68]. These oxides undergo amorphous to crystalline transition under an electron beam which results in change in their solubility in basic or acidic aqueous solutions. Although lowering of dose to exposure was obtained by several orders of magnitude, the amorphous to crystalline transition also resulted in increased line edge roughness after development. Thus the benefit of higher resolution was lost in spite of gaining higher sensitivity.

20.2.3 From Physical Deposition to Chemical Solution Deposition: A Paradigm Shift

By 1990s, a stalemate was reached for inorganic resists. A paradigm shift was needed in order to achieve not only higher resolution and low line edge roughness but also higher sensitivity to electrons. It was suggested by us that instead of starting from a pure inorganic resist, whether a halide or an oxide, which is relatively stable in an electron beam and hence requires a higher dose to damage (or exposure), it is better to start from a relatively unstable material that has both inorganic and organic components, and more importantly, it should be spin-coatable. Exposure to an electron beam would enrich the inorganic component of the material because the organic part is removed in the form of volatile compounds. Such a proposal resulted in the introduction of metal alkoxides to high resolution electron beam nanolithography.

20.2.3.1 Spin-Coatable Metal Alkoxides for High Resolution Electron Beam Nanolithography

Metal alkoxides (cp. Chap. 1) are very reactive compounds because of the presence of electronegative alkoxy groups, making the metal atoms highly prone to nucleophilic attack. Due to the high affinity of alkoxides to water, the hydrolysis reaction results in the formation of molecular aggregates of hydrated metal oxide alkoxides. However, under carefully controlled conditions, it is possible to form soluble polymeric intermediates (or sols) which undergo further polymerization to form a clear electron beam-sensitive gel. The hydrolytic reactivity of metal alkoxides can be controlled by complexation with β -diketones (e.g., acetylacetone, benzoylacetone, etc.) and β -ketoesters (e.g., methyl acetoacetate, ethyl acetoacetate, etc.) capable of *keto-enol* tautomerism. The *enol* form of β -diketones or β -ketoesters is stabilized by chelation with metal alkoxides. Further, the reaction also results in the partial replacement of the alkoxy group by a β -diketonato ligand, as shown Fig. 20.8a. The hydrolytic activity of stabilized metal alkoxides is substantially reduced perhaps due to the steric hindrance.

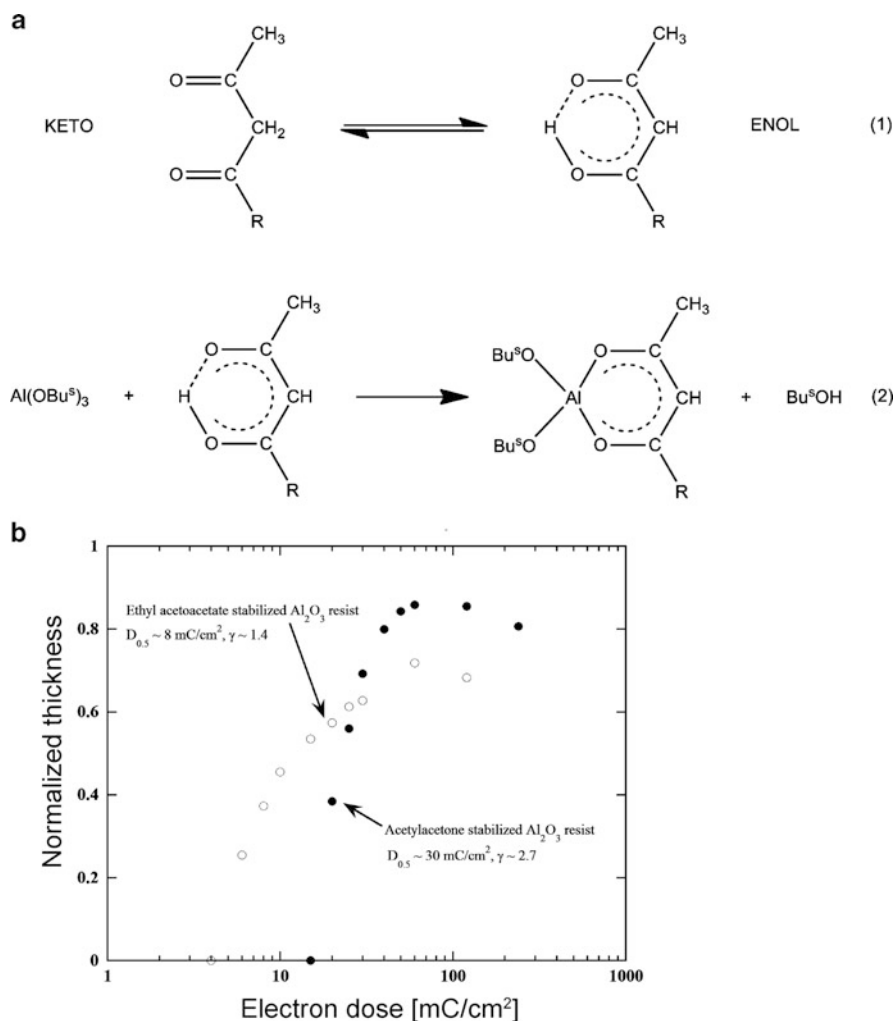


Fig. 20.8 (a) Principle of stabilizing of a metal alkoxide resist using β -diketones and β -ketoesters. Here the stabilization of aluminium *tert*-butoxide with β -diketone ($R = \text{alkyl group}$) or β -ketoester ($R = \text{alkoxy group}$) is shown. The stabilized product is used as spin-coatable Al_2O_3 resist. (b) Electron beam exposure response curves for Al_2O_3 resist stabilized by β -diketone and β -ketoester. The accelerating voltage of the electron beam was 80 kV

This also enables the stabilized alkoxide to be spin-coatable on a substrate in a conventional manner for electron beam nanolithography.

The first stabilized metal alkoxide studied for electron beam nanolithography was aluminium *sec*-butoxide reacted with acetylacetone and ethylacetoacetate [69,70], which was already used for UV-patterning [4–6] (see Sect. 20.1.2). The final product was a gel, which on spin-coating on a silicon substrate gave Al_2O_3 resist for electron beam writing. Figure 20.8b shows the electron beam exposure

response curves for Al_2O_3 resist stabilized by acetylacetone (β -diketone) and ethyl acetoacetate (β -ketoester). Exposure response curve of a resist gives an idea of its sensitivity and contrast. Sensitivity, by definition, is an exposure that provides thickness of the remaining film equal to 50 % of its original value. For negative tone resists, contrast is defined as $\gamma = \log(D_1/D_0)^{-1}$, where D_0 and D_1 correspond to electron doses at 0 and 100 % of remaining film thickness, respectively. It was found that the Al_2O_3 resist was $\sim 10^6$ times more electron beam-sensitive (sensitivity at 80 kV, $D_{0.5} = \sim 8 \text{ mC cm}^{-2}$ and contrast, $\gamma \sim 1.4$) than sputtered amorphous Al_2O_3 resists [58], thus bringing the former's sensitivity closer to some of the conventional electron beam resists such as calixerene.

Around the same time, Mitchell and Hu performed electron beam nanolithography on the *condensed* titanium isopropoxide films to obtain TiO_2 patterns. These films showed a high sensitivity to an electron beam, close to what is seen for conventional organic resists such as PMMA, but cumbersome deposition of titanium isopropoxide required a high vacuum chamber and cooling of the wafer for alkoxide deposition [71–73]. Although it was an interesting approach, it failed to gain traction because it could not be used for wide variety of alkoxides. It also lacked the features such as environmental stability and spin-coatability of stabilized alkoxides.

It was seen that the spin-coatable Al_2O_3 resist was capable of $\sim 10 \text{ nm}$ resolution over the entire $500 \mu\text{m} \times 500 \mu\text{m}$ main field, a unique distinction for a newly introduced resist (Fig. 20.9) [74]. Using the model of Al_2O_3 resist, spin-coatable electron-beam sensitive resists of TiO_2 [75], ZrO_2 [76], HfO_2 [77], Nb_2O_5 [78], VO_2 [79], PbTiO_3 , PZT, yttrium iron garnet (YIG) among others were developed [80]. Particularly interesting are the cases of TiO_2 and ZrO_2 resist where not only high density sub-10 nm patterns of low line edge roughness were achieved (Fig. 20.10a, c) but also little deviation of the patterned structures from the designed widths was seen (Fig. 20.10b).

An interesting variation in patterning $\text{La}_{0.7}\text{Sr}_{0.3}\text{MnO}_3$ involved the use of metal nitrates and polyvinyl alcohol as the starting materials instead metal alkoxides. Depending upon the electron dose, the spin-coatable $\text{La}_{0.7}\text{Sr}_{0.3}\text{MnO}_3$ acted as a positive or negative resist [81, 82]. Upon heat-treatment at 900°C for 4 h, periodic arrays of magnetic $\text{La}_{0.7}\text{Sr}_{0.3}\text{MnO}_3$ were formed.

Mechanism for the Electron Beam Exposure Process in Spin-Coatable Metal Alkoxide Resists

The behavior of stabilized metal alkoxides under an electron beam is different from the oxide and halide resists studied in the earlier sections “Knock-On Displacement and Radiolysis” and “Knotek-Feibelman Mechanism”. In the case of stabilized metal alkoxides, it is seen that with increasing electron dose the peaks associated with $\nu(\text{C}=\text{C})$ and $\nu(\text{C}=\text{O})$ vibrations in the chelate ring decrease in intensity, suggesting their rapid breakdown under an electron beam (Fig. 20.11).

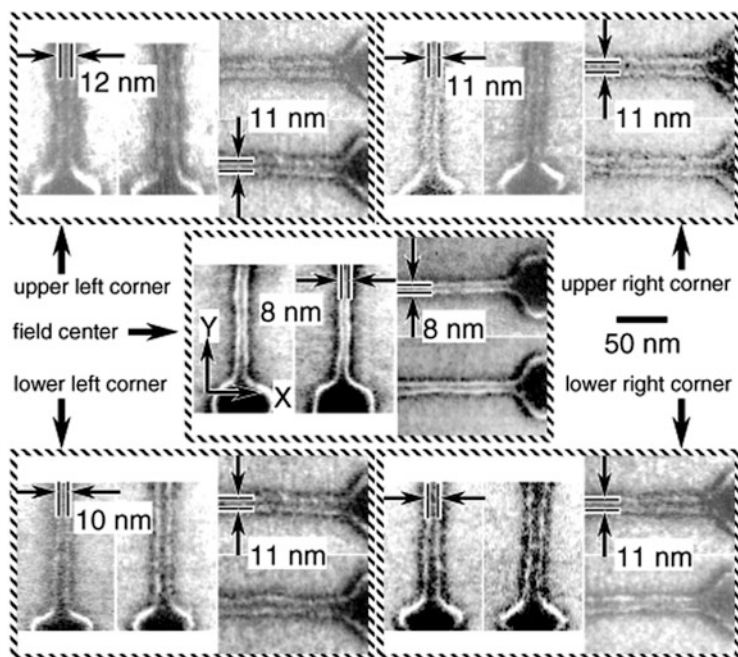


Fig. 20.9 ~8–11 nm lines of Al_2O_3 formed in the centre as well as the corners of the main field (with permission from K. Yamazaki). The resist was prepared by stabilizing aluminium *tert*-butoxide with ethyl acetoacetate

The Fourier Transform Infrared (FTIR) spectra become “flattened” with increasing dose indicating that the organic component is decomposed and removed from under the electron beam. The breakdown of the chelate rings makes the resist insoluble in organic solvents such as methanol, ethanol and acetone. This behavior was used for the direct electron beam writing of stabilized metal alkoxide resists. A tentative exposure mechanism of Al_2O_3 resist is shown in Fig. 20.12.

A comment needs to be added concerning the sensitivity and contrast of the spin-coatable oxide resists. It was observed that the sensitivity of the spincoatable Al_2O_3 resist was dependent upon the choice of stabilizer used for suppressing the hydrolysis of aluminium *tert*-butoxide [83]. The nature of the stabilizer in turn modifies the stability of the chelate ring. This stability can be decreased either by adding or removing electrons from the chelate ring. The alkyl group’s ability to release electrons increases in intensity among the normal and branched chain homologues is as follows [84]:



The number of available electrons on the chelate ring increases with increasing molecular weight of R (Fig. 20.8a). This increased availability of electrons can

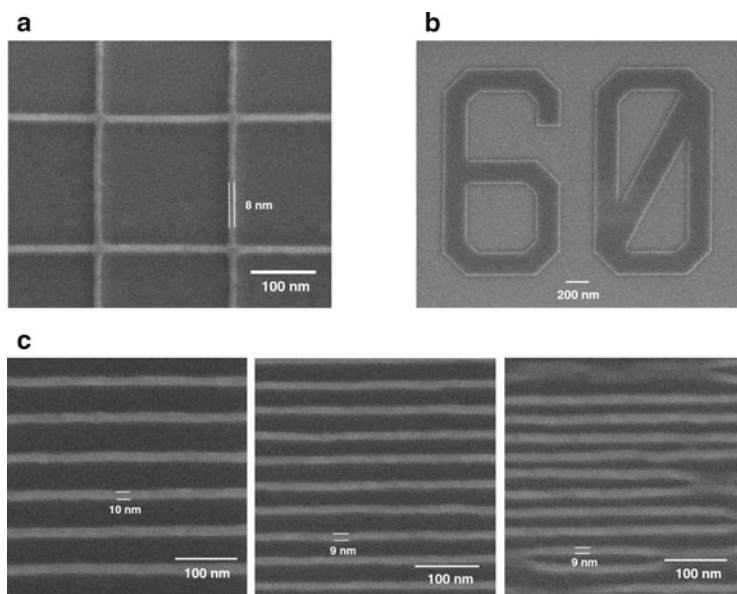


Fig. 20.10 (a) SEM images of an 8 nm wide line written with spin-coatable TiO_2 resist. (b) An example of close tolerances (design width = 200 nm) that can be achieved (obtained width = ~ 200 nm) when directly writing complex features using this resist. (c) Patterning density achievable in this resist with (*left to right*) 60 nm, 40 nm, and 30 nm pitches

result in weakening of the link between alkoxide and β -ketoester ligand. A stream of high energy electrons could break this weak link easily and this would in turn facilitate the breakdown of chelate bonds.

The higher contrast of an acetylaceton-stabilized aluminium *tert*-butoxide as opposed to a β -ketoester-stabilized aluminium *tert*-butoxide is *perhaps* due to the amount of *enol* content (Fig. 20.8b). Acetylaceton and ethyl acetoacetate have 76.4 and 8 % *enol* contents, respectively [85]. Hence a large fraction of aluminium *tert*-butoxide would be chelated when reacted with acetylaceton unlike ethylacetoacetate. A large chelated fraction means that the resist would get exposed at a particular threshold dose of electrons, thus giving rise to higher contrast. Not surprisingly, it was also observed that an acetylaceton-stabilized aluminium *tert*-butoxide was more stable than an ethyl acetoacetate-stabilized aluminium *tert*-butoxide in an atmosphere containing 45 % relative humidity [70].

Applications of Spin-Coatable Metal Alkoxide Electron Beam Resists

Resists based on stabilized metal alkoxides such as spin-coatable Al_2O_3 , TiO_2 and ZrO_2 have found applications in pattern transfer in semiconductors [70, 86, 87]. Electron beam-patterned TiO_2 , ZrO_2 and HfO_2 resists were used as gate dielectrics in a field effect transistor (FET), and showed similar behavior

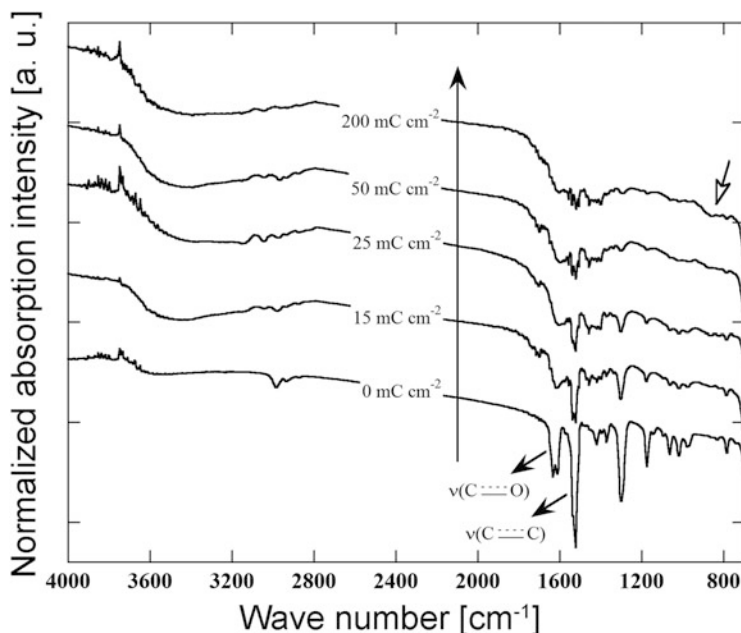


Fig. 20.11 Time-resolved FTIR spectra of electron beam exposure of Al_2O_3 resist prepared by stabilizing aluminium *tert*-butoxide with ethyl acetoacetate. The normalized absorption intensity is plotted on a reverse scale. Notice the reduction of bands arising due to chelate rings at $\sim 1,600\text{ cm}^{-1}$ and $\sim 1,525\text{ cm}^{-1}$ with increasing dose. The arrow marked on the right hand side shows a broad band that is likely due to appearance of Al-O bonding

[77, 88, 89]. In these FETs, the oxide dielectric layer allowed too large a gate leakage current for good device operation at room temperature due to the presence of defects, but the leakage current was strongly suppressed at cryogenic temperatures and good transistor characteristics were observed (Fig. 20.13). Investigation of the lifetime of a single electron trapped in the TiO_2 dielectric layer of a FET under the influence of a short microwave pulse suggests promise for quantum information processing [90]. A single FET with a sol-gel-based TiO_2 as gate dielectric contains a large number of excitations that can act as potential qubits, which can be separately addressed in the frequency domain [89]. This provides the possibility of constructing a multi-qubit quantum computer.

More complicated alkoxide-based multicomponent materials have been electron beam-patterned with interesting results. Alexe et al. used such a system to electron beam pattern periodic arrays of ferroelectric cells of $\text{SrBi}_2\text{Ta}_2\text{O}_9$ (SBT) and PZT, yielding 1 Gbit/cm^2 density as shown in Fig. 20.14a [91].

After developing in xylene, the patterns were subsequently transformed into an oxide by annealing in air for 5 min at $300\text{ }^\circ\text{C}$ and further crystallized into the ferroelectric phase by heat-treating at temperatures ranging from 600 to $850\text{ }^\circ\text{C}$. The properties of patterned ferroelectric material were studied by a scanning probe

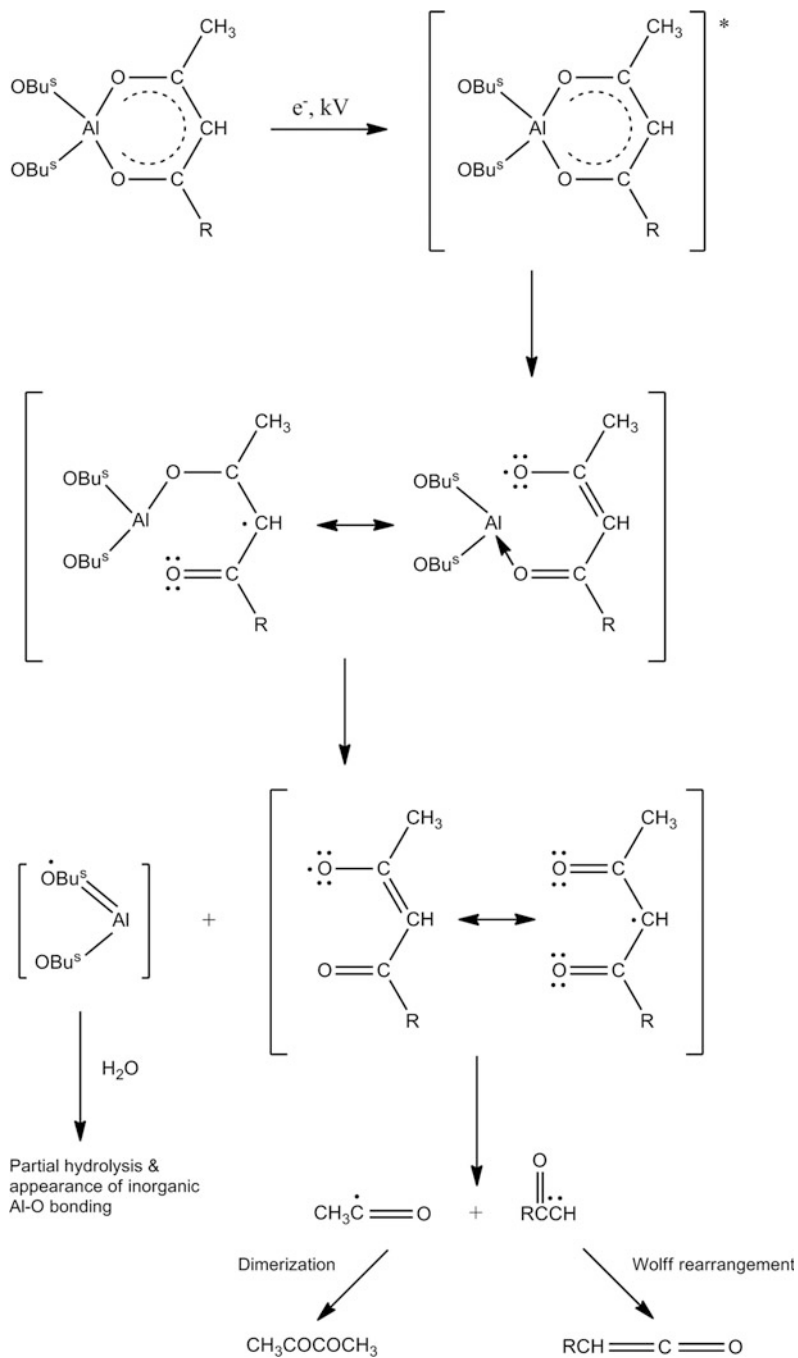


Fig. 20.12 Tentative proposal of chemical changes occurring in a spin-coatable Al_2O_3 resist under an electron beam

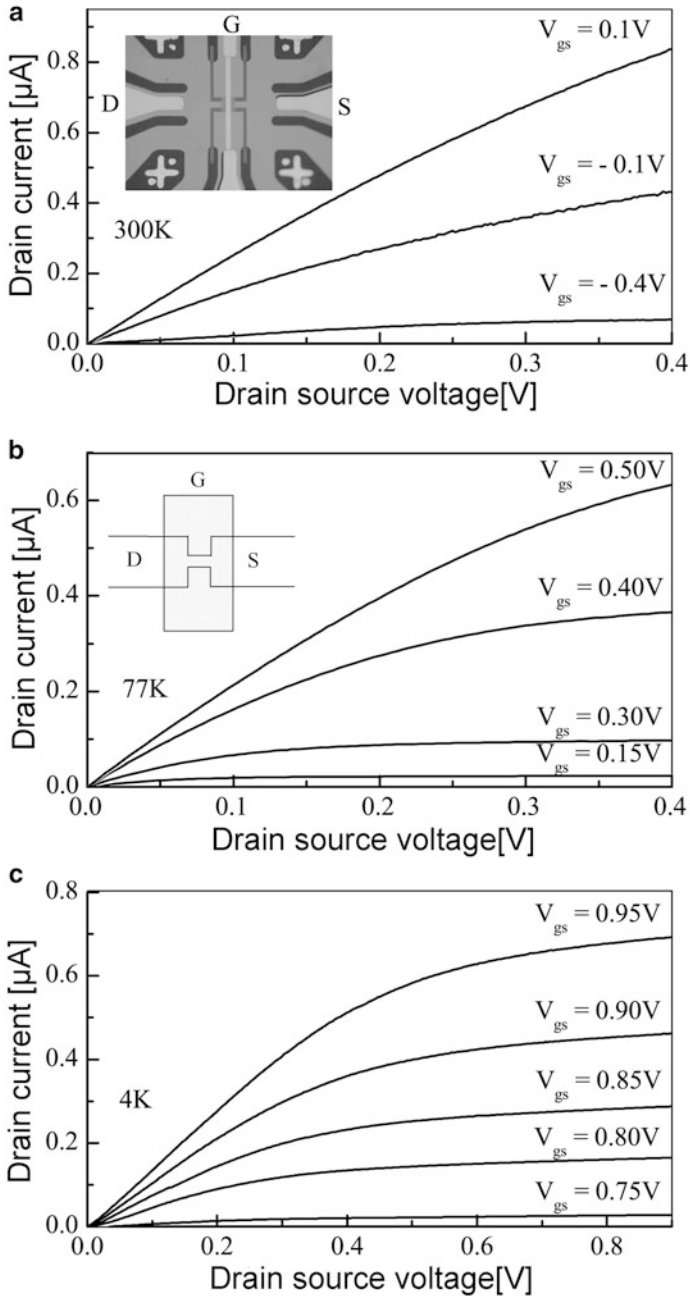


Fig. 20.13 I_d - V_{ds} characteristics of sol-gel TiO_2 gate oxide-based FET at (a) room temperature, inset: optical image of the device (b) 77 K, inset: the schematic layout and (c) 4 K (with permission from M.Z.R. Khan)

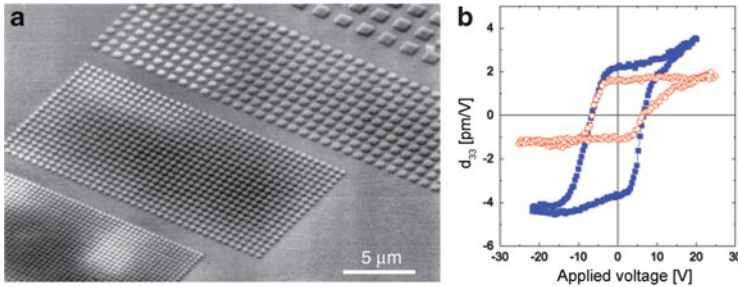


Fig. 20.14 (a) Metallo organic SBT test structures fabricated with an electron dose of 3 mC cm^{-2} and subsequently developed in xylene. (b) Piezoelectric hysteresis loops of a $1 \mu\text{m}$ PZT cell (*open circle*) and of a 100 nm PZT cell (*filled squares*). Each point of the hysteresis was acquired at zero dc bias after polarizing the sample with a bias pulse (100 ms width) at the desired voltage (with permission from M. Alexe and the American Institute of Physics)

microscope working in piezoresponse mode. Figure 20.14b shows the piezoelectric hysteresis loop of a $1 \mu\text{m}$ and a 100 nm PZT cell, respectively. Both cell sizes exhibit well-defined hysteresis loops having exactly the same coercive voltages, which indicates that shrinking the cell down to 100 nm does not modify the coercive field. However, the piezoelectric coefficient at zero field decreases as the size decreases, the value for the $1 \mu\text{m}$ cell being about two times larger than that of the 100 nm cell.

20.2.3.2 Metal Naphthenates as High Resolution Electron Beam Resists

Another class of electron beam sensitive materials which have attracted attention for direct writing of oxides is metal naphthenates. Metal naphthenates are stable viscous liquids at room temperature. They consist of cyclopentanes or cyclohexanes, methylene chains $[-(\text{CH}_2)-]$, carboxylates and metals. They are represented as $[(\text{cyclopentane})-(\text{CH}_2)_n-\text{COO}]^m-\text{M}^{m+}$, where M is a metal atom. The infrared absorption study on a naphthenate resist suggests that its exposure to an electron beam results in naphthenate molecules building bridges between each other at $-\text{C}=\text{O}$ and/or $-(\text{CH}_2)_n-$ thereby cross-linking and increasing the molecular weight of the resist, making it insoluble in toluene. This gives rise to negative-tone patterning [92]. The low molecular weights of metal naphthenates make them excellent candidates for high-resolution electron beam nanolithography.

The earliest oxide to be written using a mixture of metal naphthenates was $\text{YBa}_2\text{Cu}_3\text{O}_7$ [93]. Here individual metal naphthenates were mixed in the required ratio, spin-coated on a substrate, and patterned using an electron beam. Toluene was used a developer to removed the unexposed areas. The patterned film was pyrolyzed to give $\text{YBa}_2\text{Cu}_3\text{O}_7$. Using similar method, Kakimi et al. showed that ferroelectric $\text{Bi}_4\text{Ti}_3\text{O}_{12}$ patterns can also be written using an electron beam from naphthenate

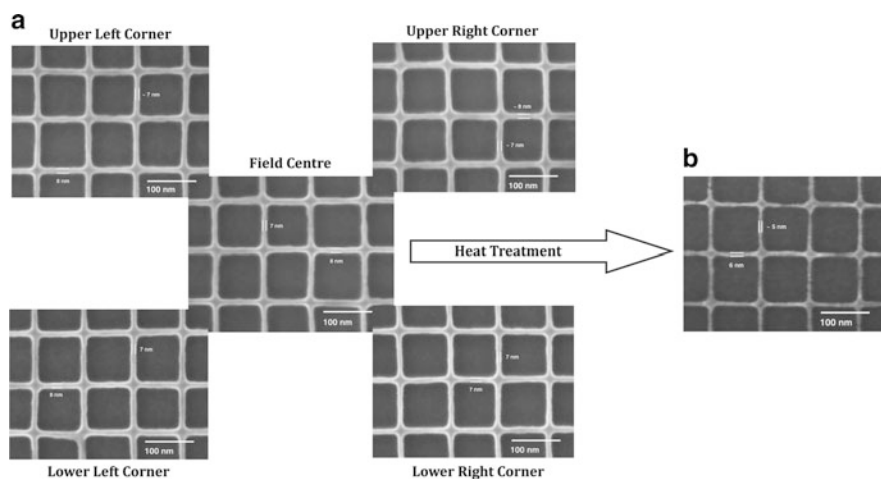


Fig. 20.15 (a) Patterned zinc naphthenate resist showing sub-10 nm linewidths in the centre as well as at the edges of the main deflection field. These lines show a line edge roughness (3σ) of about 2.8 nm, the lowest value for any electron beam resist studied so far. (b) Reduction of linewidth to ~ 5 nm after heat-treatment at 500 °C for 1 h to form ZnO

precursors [92]. It was the work of Saifullah et al. that showed that zinc naphthenate (sensitivity at 100 kV, $D_{0.5} = \sim 15 \text{ mC cm}^{-2}$ and contrast, $\gamma \sim 3.3$) was capable of forming 7 nm lines with an aspect ratio of ~ 9 over the entire $500 \mu\text{m} \times 500 \mu\text{m}$ main field (Fig. 20.15a) [94, 95]. These lines also showed a very low line edge roughness ($3\sigma = 2.8 \text{ nm}$). Heat-treatment of these naphthenate patterns gave ~ 5 nm wide ZnO nanolines (Fig. 20.15b).

Naphthenates of iron, nickel and copper were also patterned using an electron beam, and like zinc naphthenate, they also showed very high resolution ($\sim 11 \text{ nm}$ wide lines with aspect ratios of ~ 8) [96]. The advantage of these naphthenates is that they can be converted to either oxides or native metals depending upon the type of heat-treatment used. For example, patterned nickel naphthenate can be converted to nickel oxide when heat-treated in air. However, when a hydrogen-rich gas is used for heat-treatment, the patterned structure transforms to metallic nickel. Such flexibility offers interesting possibilities for using patterned oxide or metal as a catalyst to grow other materials. For example, vertically aligned, densely packed, equal in height, three- to four-walled and 5–7 nm inner diameter carbon nanotubes were grown on the nanoscale stripe patterns generated from iron naphthenate by water-assisted chemical vapour deposition [97].

Metal octylates are another class of materials, similar to naphthenates, which are electron beam-sensitive and hence can be used to pattern oxides. $\text{Bi}_4\text{Ti}_3\text{O}_{12}$ was patterned by electrons by exposing a spin-coated film containing a suitable ratio of bismuth and titanium octylates. The patterned metal organic was heat-treated in air to give crystalline ferroelectric $\text{Bi}_4\text{Ti}_3\text{O}_{12}$ [98].

Patterned composite metal naphthenates ($\text{YBa}_2\text{Cu}_3\text{O}_7$, $\text{Bi}_4\text{Ti}_3\text{O}_{12}$, BaTiO_3) and metal octylates ($\text{Bi}_4\text{Ti}_3\text{O}_{12}$, BaTiO_3) were investigated for their capability as an etch mask to pattern chemical vapour deposited diamond films. It was observed that the etch selectivity of composite metal octylates was better than metal naphthenates under the plasma etching conditions of microwave power of 300 W and O_2 gas flow rate of 3 sccm. In particular, the $\text{Bi}_4\text{Ti}_3\text{O}_{12}$ octylate film showed the best etch selectivity [99].

20.3 Conclusions and Future Perspectives

The direct patterning of chemical solution derived functional oxide precursor resists by exposure to irradiation (UV light or electron beam) for use in micro-optical components, MEMS, and other applications is of great interest. Depending on the required minimum feature size UV light or electron beams (<10 nm) may be applied to the inorganic resists. In the first part of the present chapter the use of UV-patterning of photosensitive precursor films is reviewed. It was shown that not only single oxide films but also micropatterns of multi-component oxide systems can be prepared.

In Sect. 20.2 electron beam direct writing which enables patterns in the sub-10 nm region was discussed starting with a brief history. Hence 30 years ago, the foundations of high resolution electron beam patterning of inorganic resists were laid with the writing of 5 nm holes in a physically deposited NaCl film [31]. Eventually, many metal oxides and metal halides were studied for their suitability as high resolution inorganic resists. Despite their ability to attain sub-10 nm resolution, the dose requirement was very steep—almost more than million times than that of conventional organic resists such as PMMA. However, with a shift from physical deposition to chemical solution deposition resulting from the development of stabilized metal alkoxide and metal naphthenate resists, whose sensitivity matched closely to conventional electron beam resists, the research shifted away from mere academic curiosity. These resists displayed not only superior sensitivity to electrons but also showed very low line edge roughness at sub-10 nm resolution. Moreover, the ability to directly write metal oxides down to sub-10 nm scale resulted in the removal of the delicate lift-off step.

Electron beam-sensitive stabilized metal alkoxide and metal naphthenate resists have found several applications, especially in device fabrication. Their ability to be patterned on a sub-10 nm scale has opened up new vistas in the world of miniaturization of devices and the potential to study them on such a small scale.

In spite of such a good performance, higher electron beam sensitivity is desired for the stabilized metal alkoxide and metal naphthenate resists. Furthermore, apart from the alkoxides of aluminium, titanium and zirconium, all other alkoxides are expensive and some of them are insoluble in common alcohols. This restricts their broad usage. Further research in cheaper production of some of the metal alkoxides would boost their usage in direct writing of oxides.

References

1. Tohge N, Shinmou K, Minami T (1994) Photolysis of organically modified gel films and its application to the fine-patterning of oxide thin films. In: Mackenzie JD (ed) Sol-gel optics III, Proc SPIE 2288, p 589
2. Shinmou K, Tohge N, Minami T (1994) Fine-patterning of ZrO_2 thin films by the photolysis of chemically modified gel films. *Jpn J Appl Phys* 33:L1181
3. Tohge N, Shinmou K, Minami T (1994) Effects of UV-irradiation on the formation of oxide thin films from chemically modified metal-alkoxides. *J Sol-Gel Sci Tech* 2:581
4. Zhao G, Tohge N (1995) Fine patterning of Al_2O_3 thin films by the photolysis of gel films chemically modified with benzoylacetone. *J Ceram Soc Jpn* 103:1293 (in Japanese)
5. Zhao G, Tohge N (1998) Preparation of photosensitive gel films and fine patterning of amorphous Al_2O_3 - SiO_2 thin films. *Mater Res Bull* 33:21
6. Zhao G, Tohge N, Nishii J (1998) Fabrication and characterization of diffraction gratings using photosensitive Al_2O_3 gel films. *Jpn J Appl Phys* 37(part 1):1842
7. Tohge N, Takama Y (1999) Direct fine-patterning of PZT thin films using photosensitive gel films derived from chemically modified metal-alkoxides. *J Mater Sci Mater Electron* 10:273
8. Kawahara T, Ishida T, Tada H, Tohge N, Ito S (2002) Positive-type patterned ZnO films prepared by a chemically modified sol-gel method. *J Mater Sci Lett* 21:1423
9. Kawahara T, Ishida T, Tada H, Noma N, Tohge N, Ito S (2003) Photoreaction of a ZnO gel film chemically modified with beta-diketones. *J Mater Sci* 38:1703
10. Tohge N, Zhao G, Chiba F (1999) Photosensitive gel films prepared by the chemical modification and their application to surface-relief gratings. *Thin Solid Films* 351:85
11. Tohge N, Ueno R, Chiba F, Kintaka K, Nishii J (2000) Characteristics of diffraction gratings fabricated by the two-beam interference method using photosensitive hybrid gel films. *J Sol-Gel Sci Technol* 19:119
12. Nishii J, Kintaka K, Tohge N, Noma N, Hasegawa M, Mizutani A, Kikuta H (2002) Low-reflection microstructure formed by sol-gel process. *Jpn J Appl Phys* 41(part 1):5210
13. Tohge N, Hasegawa M, Noma N, Kintaka K, Nishii J (2003) Fabrication of two-dimensional gratings using photosensitive gel films and their characterization. *J Sol-Gel Sci Technol* 26:903
14. Imano T, Horiuchi T, Noma N, Ito S (2006) Preparation of new photosensitive TiO_2 gel films using chemical additives including nitrogen and their patterning. *J Sol-Gel Sci Technol* 39:119
15. Kowada Y, Noma N (2009) Electronic state and photosensitivity of metal alkoxides chemically modified with beta-diketones. *J Solgel Sci Technol* 52:166
16. Tadanaga K, Owan T, Morinaga J, Urbanek S, Minami T (2000) Fine patterning of transparent, conductive SnO_2 thin films by UV-irradiation. *J Sol-Gel Sci Technol* 19:791
17. Avey AA, Hill RH (1996) Solid state photochemistry of $Cu_2(OH)_2(O_2C(CH_2)_4CH_3)_4$ in thin films: the photochemical formation of high-quality films of copper and copper(I) oxide. Demonstration of a novel lithographic technique for the patterning of copper. *J Am Chem Soc* 118:237
18. Ching CLW, Hill RH (1998) Photolithographic deposition of indium oxide from metalorganic films. *J Vac Sci Technol* A16:897
19. Gao M, Hill RH (1998) High efficiency photoresist-free lithography of UO_3 patterns from amorphous films of uranyl complexes. *J Mater Res* 13:1379
20. Law WL, Hill RH (2000) Photolithographic deposition of insulating Al_2O_3 films from thin amorphous films of aluminum complexes on silicon surfaces. *Thin Solid Films* 375:42
21. Park HH, Yoon S, Park HH, Hill RH (2004) Electrical properties of PZT thin films by photochemical deposition. *Thin Solid Films* 447-448:669
22. Park HH, Kim WS, Yang JK, Park HH, Hill RH (2004) Characterization of PLZT thin film prepared by photochemical deposition using photosensitive metal-organic precursors. *Microelectron Eng* 71:215
23. Park HH, Park HH, Hill RH (2006) Direct-patterning of SnO_2 thin film by photochemical metal-organic deposition. *Sens Actuators A* 132:429

24. Park HH, Lee HS, Park HH, Hill RH, Hwang YT (2009) Ferroelectric properties of direct-patternable La substituted $\text{Bi}_4\text{Ti}_3\text{O}_{12}$ thin films formed by photochemical metal-organic deposition. *J Ceram Soc Jpn* 117:604
25. Kololuoma T, Karkkainen AHO, Tolonen A, Rantala JT (2003) Lithographic patterning of benzoylacetone modified SnO_2 and $\text{SnO}_2\text{:Sb}$ thin films. *Thin Solid Films* 440:184
26. Yogo T, Takeichi T, Kikuta K, Hirano S (1995) Ultraviolet patterning of alkoxy-derived lithium-niobate film. *J Am Ceram Soc* 78:1649
27. Kikuta K, Takagi K, Hirano S (1999) Photoreaction of titanium-based metal-organic compounds for ceramic fine patterning. *J Am Ceram Soc* 82:1569
28. Kikuta K, Suzumori K, Takagi K, Hirano S (1999) Patterning of tin oxide film from photoreactive precursor solutions prepared via the addition of N-phenyldiethanolamine. *J Am Ceram Soc* 82:2263
29. Martin CR, Aksay IA (2004) Submicrometer-scale patterning of ceramic thin films. *J Electroceram* 12:53
30. Yasin S, Hasko DG, Ahmed H (2001) Fabrication of <5 nm width lines in poly (methylmethacrylate) resist using a water:isopropyl alcohol developer and ultrasonically-assisted development. *Appl Phys Lett* 78:2760–2762
31. Broers AN, Cuomo J, Harper J, Molzen W, Laibowitz R, Promerantz M (1978) High resolution electron beam fabrication using STEM. In: Sturgess JM (ed) *Proceedings of the 9th international congress on electron microscopy*, vol 3, Imperial, ON, pp 343–354
32. Isaacson M, Murray A (1981) In situ vaporization of very low molecular weight resists using $\frac{1}{2}$ nm diameter electron beams. *J Vac Sci Technol* 19:1117–1120
33. Mochel ME, Humphreys CJ, Eades JA, Mochel JM, Petford AM (1983) Electron beam writing on a 20 Å scale in metal β -aluminas. *Appl Phys Lett* 42:392–394
34. Devenish RW, Eaglesham DJ, Maher DM, Humphreys CJ (1989) Nanolithography using field emission and conventional thermionic electron sources. *Ultramicroscopy* 28:324–329
35. Salisbury IG, Timsit RS, Berger SD, Humphreys CJ (1984) Nanometer scale electron beam lithography in inorganic materials. *Appl Phys Lett* 45:1289–1291
36. Murray A, Isaacson M, Adesida I (1984) AlF_3 – a new very high resolution electron beam resist. *Appl Phys Lett* 45:589–591
37. Kratschmer E, Isaacson M (1986) Nanostructure fabrication in metals, insulators, and semiconductors using self-developing metal organic resist. *J Vac Sci Technol B* 4:361–364
38. Kratschmer E, Isaacson M (1987) Progress in self-developing metal fluoride resists. *J Vac Sci Technol B* 5:369–373
39. Scherer A, Craighead HG (1987) Barium fluoride and strontium fluoride negative electron beam resists. *J Vac Sci Technol B* 5:374–378
40. Scherer A, Van de Gaag BP, Beebe ED, Lin PSD (1990) Fluoride etch masks for high-resolution pattern transfer. *J Vac Sci Technol B* 8:28–32
41. Mankiewich PM, Craighead HG, Harrison TR, Dayem AH (1984) High resolution electron beam lithography on CaF_2 . *Appl Phys Lett* 44:468–469
42. Zanetti R, Bleloch AL, Grimshaw M, Paterson JH, Jones GAC (1993) *Inst Phys Conf Ser* 138:67
43. Fujita J, Watanabe H, Ochiai Y, Manako S, Tsai JS, Matsui S (1995) Sub-10 nm lithography and development properties of inorganic resist by scanning electron beam. *Appl Phys Lett* 66:3065–3067
44. Fujita J, Watanabe H, Ochiai Y, Manako S, Tsai JS, Matsui S (1995) Sub-10 nm lithography and development properties of inorganic resist by scanning electron beams. *J Vac Sci Technol B* 13:2757–2761
45. Berger SD, Salisbury IG, Milne RH, Imeson D, Humphreys CJ (1987) Electron energy-loss spectroscopy studies of nanometer-scale structures in alumina produced by intense electron-beam irradiation. *Philos Mag B* 55:341–358
46. Mochel ME, Eades JA, Metzger M, Meyer JI, Mochel JM (1984) Electron beam cutting in amorphous alumina sheets. *Appl Phys Lett* 44:502–504

47. Hollenbech JL, Buchanan RC (1990) Oxide thin films for nanometer scale electron beam lithography. *J Mater Res* 5:1058–1072
48. Morgan CJ, Bailey SJ, Preston AR, Humphreys CJ (1991) Electron beam nanolithography of sputtered amorphous Al_2O_3 and the proximity effect. *Inst Phys Conf Ser* 119:503–506
49. Morgan CJ, Chen GS, Boothroyd CB, Bailey S, Humphreys CJ (1992) Ultimate limits of lithography. *Phys World* 5:28–32
50. Chen GS, Boothroyd CB, Humphreys CJ (1993) Novel fabrication method for nanometer-scale silicon dots and wires. *Appl Phys Lett* 62:1949–1951
51. Saifullah MSM, Boothroyd CB, Botton GA, Humphreys CJ (1998) Electron energy loss spectroscopy of silicon nanostructures in a scanning transmission electron microscope. In: *Electron microscopy 96*, vol 2. Committee of European Societies of Microscopy, Brussels
52. Fujita J, Maruno S, Watanabe H, Ichikawa M (1996) Nanostructure fabrication using the selective thermal desorption of SiO_2 induced by electron beams. *Appl Phys Lett* 69:638–640
53. Turner PS, Bullough TJ, Devenish RW, Maher DM, Humphreys CJ (1990) Nanometre hole formation in MgO using electron beams. *Philos Mag Lett* 61:181–193
54. Devenish RW, Bullough TJ, Turner PS, Humphreys CJ (1990) Electron-beam machining of MgO and ZnO in the STEM. *Inst Phys Conf Ser* 98:215–218
55. Berger SD, Macaulay JM, Brown LM (1987) Radiation damage in TiO_x at high current density. *Philos Mag Lett* 56:179–185
56. Saifullah MSM, Boothroyd CB, Botton GA, Humphreys CJ (1997) Electron beam damage in titanium dioxide films. *Inst Phys Conf Ser* 153:167–170
57. Pauza AJ, Barber Z, Campbell AM, Evetts JE, Somekh RE, Moore DF, Broers AN (1991) Direct writing of weak links in high T_c superconductors with electrons. In: *Proceedings of the third international superconductive electronics conference*, University of Strathclyde, Glasgow, Scotland, Meeting Makers, Glasgow
58. Saifullah MSM, Boothroyd CB, Botton GA, Humphreys CJ (1998) Irradiation damage of inorganic resists on a silicon substrate. In: Kirkland A, Brown PD (eds) *The electron – proceedings of the international centennial symposium on the electron*, IOM Communication Ltd, London
59. Morgan CJ, Humphreys CJ (1995) The proximity effect for electron beam lithography of aluminium oxide. *Inst Phys Conf Ser* 147:575–578
60. Hobbs LW (1987) Radiation effects in analysis by TEM. In: Hren JJ, Goldstein JI, Joy DC (eds) *Introduction to analytical electron microscopy*. Plenum, New York, pp 399–445
61. Pooley D (1966) F-centre production in alkali halides by electron–hole recombination and a subsequent [110] replacement sequence: a discussion of the electron–hole recombination. *Proc Phys Soc (Lond)* 87:245–256
62. Kabler MN, Williams RT (1978) Vacancy-interstitial pair production via electron–hole recombination in halide crystals. *Phys Rev B* 18:1948–1960
63. Knotek ML, Feibelman PJ (1978) Ion desorption by core-hole Auger decay. *Phys Rev Lett* 40:964–967
64. Knotek ML, Feibelman PJ (1979) Stability of ionically bonded surfaces in ionizing environments. *Surf Sci* 90:78–90
65. Humphreys CJ, Bullough TJ, Devenish RW, Maher DM, Turner PS (1990) Electron beam nano-etching in oxides, fluorides, metals and semiconductors. *Scanning Microsc Suppl* 4:185–192
66. Kammlott GW, Sinclair WR (1974) Fe_2O_3 – an inorganic electron resist material. *J Electrochem Soc* 121:929–932
67. Baba M, Ikeda T (1981) A new inorganic electron resist using amorphous WO_3 film. *Jpn J Appl Phys* 20:L149–L152
68. Carcenac F, Vieu C, Haghiri-Gosnet AM, Simon G, Mejjias M, Launois H (1996) High voltage electron beam nanolithography on WO_3 . *J Vac Sci Technol B* 14:4283–4287
69. Saifullah MSM, Namatsu H, Yamaguchi T, Yamazaki K, Kurihara K (1999) Spin-coatable aluminum oxide resists in electron beam nanolithography. *Proc SPIE* 3678:633–642

70. Saifullah MSM, Namatsu H, Yamaguchi T, Yamazaki K, Kurihara K (1999) Effect of chelating agents on high resolution electron beam nanolithography of spin-coatable alumina gel films. *Jpn J Appl Phys* 38:7052–7058
71. Mitchell WJ, Hu EL (1999) Selective area chemical vapor deposition of titanium oxide films: characterization of $\text{Ti}(\text{OC}_3\text{H}_7)_4$ as an electron beam resist. *J Vac Sci Technol B* 17:1622–1626
72. Mitchell WJ, Hu EL (1999) In situ electron-beam lithography on GaAs substrates using a metal alkoxide resist. *Appl Phys Lett* 74:1916–1918
73. Mitchell WJ, Hu EL (2002) High-resolution in situ electron beam patterning using $\text{Ti}(\text{OC}_3\text{H}_7)_4$ as a negative-type resist. *J Vac Sci Technol B* 20:596–603
74. Yamazaki K, Saifullah MSM, Namatsu H, Kurihara K (2000) Sub-10 nm electron beam lithography with sub-10 nm overlay accuracy. *Proc SPIE* 3997:458–466
75. Saifullah MSM, Subramanian KRV, Tapley E, Kang DJ, Welland ME, Butler M (2003) Sub-10 nm electron beam nanolithography using spin-coatable TiO_2 resists. *Nano Lett* 3:1587–1591
76. Subramanian KRV, Saifullah MSM, Tapley E, Kang DJ, Welland ME, Butler M (2004) Direct writing of ZrO_2 on a sub-10 nm scale using an electron beam. *Nanotechnology* 15:158–162
77. Saifullah MSM, Khan MZR, Hasko D, Leong ESP, Neo XL, Goh ETL, Anderson D, Jones GAC, Welland ME (2010) Spin-coatable HfO_2 resist for optical and electron beam lithographies. *J Vac Sci Technol B* 28:90–95
78. Liang LXY (2008) Synthesis and characterization of new oxide materials. Dissertation (BSc), National University of Singapore
79. Sim KS, Shahid M, Saifullah MSM, Subramanian KRV, Leong ESP, Sohn JI, Anderson D, Jones GAC, Welland ME, Kang DJ, unpublished work
80. Subramanian KRV (2006) Spin-coatable oxide resists for electron beam nanolithography, Dissertation (PhD), University of Cambridge
81. Chuang CM, Wu MC, Huang YC, Cheng KC, Lin CF, Chen YF, Su WF (2006) Nanolithography made from water-based spin-coatable LSMO resist. *Nanotechnology* 17:4399–4404
82. Wu MC, Chuang CM, Chen YF, Su WF (2008) Fabrication and optical properties of periodical structures based on a water-developable and tunable $\text{La}_{0.7}\text{Sr}_{0.3}\text{MnO}_3$ resist. *J Mater Chem* 18:780–785
83. Saifullah MSM, Kang DJ, Subramanian KRV, Welland ME, Yamazaki K, Kurihara K (2004) Electron beam nanolithography of β -ketoester modified aluminium tri-*sec*-butoxide. *J Sol-Gel Sci Technol* 29:5–10
84. Ingold CK (1953) Structure and mechanism in organic chemistry. G. Bell & Sons Ltd, London
85. Gero A (1954) Studies on enol titration. II. Enol contents of some ketones and esters in the presence of methanol. *J Org Chem* 19:1960–1970
86. Liu BY, Ho ST (2008) Sub-100 nm nanolithography and pattern transfer on compound semiconductor using sol-gel-derived TiO_2 resist. *J Electrochem Soc* 155:P57–P60
87. Liu BY, Huang YY, Xu GY, Ho ST (2008) Nanolithography using spin-coatable ZrO_2 resist and its application to sub-10 nm direct pattern transfer on compound semiconductors. *Nanotechnology* 19:155303
88. Khan MZR, Hasko DG, Saifullah MSM, Welland ME (2008) Characterization of a sol-gel based high-*k* dielectric field effect transistor for cryogenic operation. *J Vac Sci Technol B* 26:1887–1891
89. Khan MZR, Hasko DG, Saifullah MSM, Welland ME (2009) Trapped charge dynamics in a sol-gel based TiO_2 high-*k* gate dielectric silicon metal-oxide-semiconductor field effect transistor. *J Phys Condens Matter* 21:215902
90. Khan MZR, Hasko DG, Saifullah MSM, Welland ME (2008) Single shot measurement of the lifetime of a trapped electron in the gate dielectric of a high-*k* FET. *Appl Phys Lett* 93:193501
91. Alexe M, Harnagea C, Hesse D, Gösele U (1999) Patterning and switching of nano-size ferroelectric memory cells. *Appl Phys Lett* 75:1793–1795

92. Kakimi A, Okamura S, Yagi Y, Mori K, Tsukamoto T (1994) Fabrication of ferroelectric $\text{Bi}_4\text{Ti}_3\text{O}_{12}$ thin films by dipping pyrolysis of metal naphthenates and micropatterns by an electron beam. *Jpn J Appl Phys* 33:5301–5304
93. Mori K, Okamura S (1992) Electron-beam-induced structuring of composite oxides by means of dipping pyrolysis of metal naphthenate films. *Jpn J Appl Phys* 31:L1143–L1145
94. Saifullah MSM, Subramanian KRV, Kang DJ, Anderson D, Huck WTS, Jones GAC, Welland ME (2005) Sub-10 nm high aspect ratio patterning of ZnO by an electron beam. *Adv Mater* 17:1757–1761
95. Saifullah MSM, Subramanian KRV, Anderson D, Kang DJ, Huck WTS, Jones GAC, Welland ME (2006) Sub-10 nm high aspect ratio patterning of ZnO in a 500 μm main field. *J Vac Sci Technol B* 24:1215–1218
96. Nedelcu M, Saifullah MSM, Hasko DG, Jang A, Anderson D, Kang DJ, Huck WTS, Jones GAC, Welland ME, Steiner U (2010) Fabrication of sub-10 nm metallic lines of low line-width roughness by hydrogen reduction of patterned metal-organic materials. *Adv Funct Mater* 20:2317–2323
97. Patole SP, Patole AS, Rhen DS, Shahid M, Min H, Kang DJ, Kim TH, Yoo JB (2009) Patterned carbon nanotube growth using an electron beam sensitive direct writable catalyst. *Nanotechnology* 20:315302
98. Okamura S, Yagi Y, Kakimi A, Ando S, Mori K, Tsukamoto T (1996) Crystallization of precursor micropatterns of ferroelectric $\text{Bi}_4\text{Ti}_3\text{O}_{12}$ fabricated by electron beam scanning. *Jpn J Appl Phys* 35:5224–5228
99. Kiyohara S, Takamatsu H, Motoishi T, Mori K (2004) Nanopatterning of diamond films with composite oxide mask of metal octylates in electron beam lithography. *J Mater Sci Mater Electron* 15:99–102

Chapter 21

Template Controlled Growth

Sven Clemens and Theodor Schneller

21.1 Introduction

As already pointed out in the general introduction of this book in case of CSD processing the genesis of crystalline oxide thin films or structures occurs through a nucleation and growth process from an initially amorphous thin film on a substrate. This enables engineering of the nucleation process by artificial nucleation sites within the film or at the substrate/amorphous film interface. For certain applications it is important to generate not only crystalline films but also highly oriented films and/or registered deposition of functional oxides.

Gaining control on the orientation of the crystalline thin film allows for tailoring the films physical properties within certain limits. Laterally well defined structures are of particular interest for applications in information and semiconductor industry, where in order to stay competitive, the markets need for ever growing integration densities has to be followed [1]. Achieving this by controlling the thin films nucleation process yields the elegant opportunity to do without any erosive and therefore deteriorating post-deposition patterning processes, i.e. cutting laterally defined ceramic cells from continuous films. This might become a key factor for processing as the physical properties of ceramic materials directly rely on their crystal lattice structure. Especially in case of ferroelectrics, where size effects are expected to occur intrinsically due to the ferroelectric nature of collective dipole-dipole interactions, stabilization of the ferroelectric phase by tailoring, stabilization or at least perpetuation of the crystal lattice is in focus of research [2, 3]. One has to

S. Clemens (✉)

Robert Bosch GmbH, Reutlingen, Germany

Institut für Werkstoffe der Elektrotechnik II, RWTH Aachen University, Aachen, Germany

e-mail: sven_clemens@web.de

T. Schneller

Institut für Werkstoffe der Elektrotechnik II, RWTH Aachen University, Aachen, Germany

e-mail: schneller@iwe.rwth-aachen.de

consider, that even when dealing with a stable ferroelectric phase, the switching charge scales with the cells surface. A surface charge of a 100 nm^2 capacitor that features a $30 \text{ } \mu\text{C}/\text{cm}^2$ polarization is compensated by merely 180 electrons for example.

Regarding CSD processing routes, ceramic nanocells can be prepared using self-assembly routes based on a microstructural instability of thin films [4]. The underlying principle is that with shrinking amorphous film thickness, a three dimensional island configuration becomes energetically more favourable during crystallization compared to a continuous thin film configuration. Using such a bottom-up growth technique, smallest ceramic nanocells can be patterned in effective manners [5–7]. However, the resulting cells grow self-assembled with a poor level of registration and a wide size distribution. In order to gain a high degree of registration, some kind of pre-patterned field, i.e. a specially prepared substrate, becomes essential [8].

Controlling the nucleation process during ceramic oxide thin film growth by using artificial pre-patterned nucleation sites on the substrate, ceramic cell arrays featuring dimensions from microns down to a few nanometers could be generated [9, 10]. Within this chapter the use of templates or seeds will be explained on the example of a registered growth of ferroelectric lead titanate nanograins and the use of isolated alkaline earth titanate nanograins to support the texture selection in case of alkaline earth titanate thin films.

21.2 Seed Layers and Seeds for Orientation Selection

For thin film materials with anisotropic properties such as ferroelectrics or superconductors the relative orientation of the film on its substrate plays a crucial role for the final device properties as already pointed out in some chapters of this book (Chaps. 17 and 27). In order to gain control on the orientation one has to take into account that the different materials (substrate and film) may have good and excellent, respectively, or poor lattice match.

In the first case it is often comparatively easy to get a reasonable orientation of the films but even then sometimes special techniques have to be applied to control the texture selection of the deposited films. Tetragonal PZT thin films on platinumized silicon wafers where the Pt layer is highly (111) oriented may serve as an example. Although the lattice mismatch between tetragonal (111) PZT (e.g. PZT 20/80) and cubic (111) Pt is only 2, 3 % one can get all different orientations depending on various factors (for details see Chap. 17). In the early days of wet chemical PZT deposition getting the preferred (111) orientation was therefore one big issue. One solution is the finding, that crystalline few nanometer thick Ti, or TiO_2 films, respectively, on top of the (111) Pt surface are very efficient seed-layers for the (111) oriented growth of PZT [11–14]. Murali et al. [14] were the first who investigated this phenomenon in more detail and found, that ultrathin titania layers lower the nucleation energy of the perovskite phase, promote crystal growth in

(111) orientation and are finally transformed into the perovskite phase during crystallization. A scenario that was suggested for this seeded growth by sputter deposition of lead zirconate titanate (PZT) describes an affinity layer that actively takes part in the chemical reactions. Briefly, PbO is attached to the TiO₂ surface, preventing its desorption and providing the correct hexagonal coordination of the (111)-oriented perovskite lattice. While the promoted embryonic nuclei grow, PbO sinks into the seeding layer and the TiO₂ becomes unstable, transforming into the (111)-oriented perovskite phase [15].

In the second case of larger lattice mismatch it is mostly impossible without processing tricks to get highly textured films. Thus seed concepts have been developed in order to gain control over nucleation and growth. In the following the seed concept, which was already introduced in Chap. 16 by Fred Lange, is briefly repeated by means of oriented BST and SrBi₄Ti₄O₁₅ films in order to have the basis present for the templated growth approach described in the next section. This seed concept relies in the first step on the microstructure instability phenomenon of polycrystalline thin films [16], which means that if the thin film falls below a certain value it breaks up into islands due to thermodynamic reasons (for details see Chap. 16). During the breakup process grains with unpropitious orientations relative to the substrate are eliminated. In the second coating step a thicker layer is deposited onto the remaining highly oriented grains at which these oriented grains act as seeds for the growing grains of the second and any further layer during the crystallization step. According to Miller et al. [17] for this process a lattice matching of the film and the substrate is not required.

Besides the examples presented in detail in Chap. 16, two further examples may illustrate this approach. In case of SrBi₄Ti₄O₁₅ it was possible by a careful control of the process parameters, namely concentration of the precursor solution and heating ramp, to obtain highly c-axis oriented thin films on platinized silicon wafers although the ceramic film has a quite different texture and lattice constant compared to the underlying (111) Pt bottom electrode [18]. The seed technique was also successfully applied for the CSD fabrication of highly (100) oriented SrTiO₃ films on highly (200) textured Ni-tapes under reducing annealing conditions in spite of the large lattice mismatch of 11.1% [19]. Such films are investigated for the use as alternative buffer layer for the manufacturing of coated conductors (see Chap. 27). By a suitable combination of the “material effect” (matched rutile structure on (111) platinum) of the TiO₂ seed layer and the thermodynamic nucleation aspect of the seeds concept, templates can be generated which may enable the control of registration and orientation on a sub 100 nm scale. This approach will be discussed in the following section.

21.3 Templated Growth of Ferroelectric Nanograins

As already mentioned within the introductory part of this chapter, using the CSD technique, in particular the microstructural instability in case of thinnest films, is a promising approach to grow laterally insulated ceramic nanocells. It is

straightforward and yields nanoscaled ceramic structures without the need for sophisticated, time consuming and usually expensive top-down patterning steps. Besides, being a bottom-up technique, no post-deposition patterning steps are employed, which reduces the risk of inducing damage to the functional structures.

The already mentioned microstructural instability of ultrathin perovskite films during CSD processing was first reported by Seifert et al. [4] by growing epitaxial PTO films on single crystal (001) STO substrates. They found that for film thicknesses < 80 nm holes developed during crystallization. Towards thinner films these holes grew and caused breaking of the film into single-crystal PTO islands. This phenomenon was described by a free energy model based on the minimization of the overall surface and interface energies. The principle was adapted to polycrystalline substrates by Roelofs et al. in order to grow PTO islands on Pt(111)/TiO₂/SiO₂/Si(100) and study size-effects [5, 6] PTO grains of sizes below 15 nm were fabricated and it was found, that grains smaller than approximately 20 nm in lateral dimension exhibited no piezoelectric response whereas larger grains clearly showed ferroelectric behavior. This was attributed to a size dependent phase transition into a superparaelectric state. Using the same approach, Szafraniak et al. grew PZT crystals epitaxially on single crystalline Nb-doped (001)-oriented STO substrates [7]. The lowest initial film thickness resulted in grains with lateral dimensions ranging from 40 to 90 nm and a thickness of around 10 nm. Grains below 25 nm in height showed no piezoelectric hysteresis which was attributed to defects like interface dislocations.

However, regarding possible applications of the resulting structures, the self-assembly technique is hampered for a few reasons. This is, as the ceramic cells show no alignment or ordering and feature a statistical governed size distribution. For integration in prospective device architectures however, a high registration and a narrow grain size distribution is mandatory. In order to preserve the advantages of bottom-up growth approaches (i.e. down-scaling of structural dimensions and minimization of damage), guiding the nucleation and growth process on the substrate becomes essential. As already mentioned, this can be achieved by a pre-patterned field on the substrate, i.e. a specially engineered substrate [8]. A promising option within this context is the use of artificial nucleation spots. The basic idea behind the nucleation site concept is to engineer the substrate in such a way that nucleation and growth takes place at predefined sites with reduced activation energies for nucleation. Such preferential nucleation sites can for example be generated by strain fields [8] or by topographic surface features [20]. As soon as these sites are highly ordered the ceramic thin film will grow highly arranged as well. Beyond, when such sites allow for guiding the crystallographic orientation of the growing cells, tuning of the highly anisotropic physical properties of the emerging cells becomes possible as well.

In the following, the realization of a template-based concept for a registered growth of lead based perovskite islands deposited by CSD is presented. The concept is deduced from a combination of ultrathin TiO₂ layers and the isolated seeds described above, i.e. it utilizes the preparation of predefined nanosized TiO₂

patterns on (111)-oriented platinized substrates to act as seeds for the subsequent deposition of lead based perovskites.

In the course of the next subchapters, we will show how tailor-made TiO_2 nucleation sites can be generated on platinised silicon substrates and how such sites feature guidance for bottom-up grown ferroelectric PTO nanocell arrays by CSD and/or other deposition methods. As we will see, the resulting matrices feature ferroelectric cells with smallest structural dimensions below 100 nm in lateral dimensions and can achieve integration densities far into the Gbit/cm² regime. Setting a step towards further integration, we subsequently present an embedding technique based on flowable oxides as dielectric matrix layers that allow for equipping bottom-up grown ferroelectric structures with top electrodes—a necessary requirement for prospective direct electrical characterization, which is currently hampered as the surface charge to detect scales with lateral cell dimensions. In order to characterize ferroelectric nanostructures, different scanning probe microscopy (SPM) techniques (vide infra) are currently the method of choice.

21.3.1 Template Controlled Growth Approaches

The concept of using nanosized TiO_2 patterns on platinum (111)-oriented substrates to guide nucleation and growth of lead based perovskites was followed in few publications so far. Basically two approaches for structuring the nucleation site templates were presented: generation of the templates by e-beam lithography [9, 10] or by self-assembly based on diblock-copolymer micelles and gold hard masks [21]. Both approaches will be presented in the following in more detail.

In addition it should be mentioned here, that also a reversed nucleation site concept has been suggested in literature [22]. Based on the findings that only adequately thin, crystalline TiO_2 layers are effective in seeding the perovskite phase, amorphous, 50 nm thick TiO_2 layers on platinized silicon substrates were provided with holes ranging from 100 to 500 nm using a focused ion beam (FIB) technique. Subsequent crystallization of a low temperature PZT precursor (400 °C) yielded a perovskite PZT phase that only emerged within the milled holes. This effect was explained by an amorphous TiO_2 layer that actively drives away the PZT nucleation to the FIB generated holes where bare platinum is present. The platinum reacts with metallic lead which forms during the reducing conditions of pyrolysis an intermetallic PbPt_x phase (cp. Chap. 17) which serves as an excellent nucleation seed for the ferroelectric PZT phase. Thus it is mandatory to keep the annealing temperature as low as possible in order to just enable crystallization of the PZT but inhibit crystallization of the glassy TiO_2 (Fig. 21.1).

A notable side effect of the method is that the patterned ferroelectrics are readily integrated within a dielectric matrix layer after deposition as will be discussed in Sect. 21.3.3.

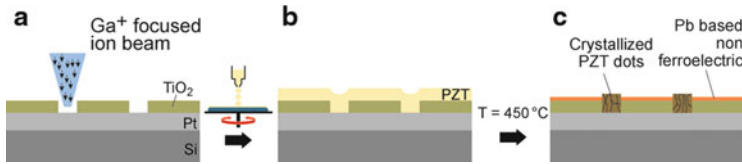


Fig. 21.1 Schematic diagram of the processing steps used in the fabrication of ferroelectric nanostructures. (a) FIB patterning of the spun-on-TiO₂ coated platinized silicon wafer. (b) The structure after spin-coating of the PZT precursor solution. (c) Actual structure after annealing at 450 °C. It has been shown that the PZT material inside the dot is raised above the surrounding matrix and that it has individual crystallites. Figure modified after [22]

21.3.1.1 Nucleation Site Concept by e-Beam Lithography

One possible way to pattern TiO₂ nucleation site arrays with nanoscale dimensions is based on electron beam lithography. Here, basically two approaches were followed. Initially, the functionality of the seed concept was demonstrated for sputter deposited lead based ferroelectric perovskites. 120–150 nm wide PZT crystals were grown onto 150 nm wide TiO₂ nucleation sites that featured a 500 nm pitch distance [9]. The merely 2 nm thick TiO₂ seed layer was epitaxially grown onto (111)-oriented Pt/STO substrates and structured by means of a Cr hard mask and electron-beam lithography (EBL). With varying initial PbO flux, either square shaped grains indicating a (100) orientation (large PbO flux) or triangular shaped grains indicating a (111) orientation (low PbO flux) were grown (cp. Sect. 24.3).

While the structuring of the TiO₂ layer was done here indirectly by means of a dry etching process to gain epitaxial TiO₂ seed structures, the TiO₂ layer can also be patterned directly by lift-off processing [10]. In this case, the structures to be transferred were directly written into a two-layer e-beam resist system, consisting of a conventional PMMA polymer top layer with a (relatively high) molecular weight of 950 kg/mol in combination with a copolymer of PMMA and methacrylic acid (MAA) bottom layer. Due to the much higher sensitivity of the PMMA/MAA copolymer (the methacrylic acid reduces re-polymerization during electron exposure), negative resist profiles were obtained after exposure and development. Such a resist profile is especially suitable for lift-off processing. As the TiO₂ seed structures to be transferred were below 100 nm in lateral dimensions, the overall resist thickness was adjusted to the same range (Fig. 21.2).

For structural transformation into TiO₂, an about 1.2 nm thick layer of titanium was thermally evaporated on top of the developed resist mask. Subsequently the resist was removed in an organic solvent, yielding titanium dot arrays on the polycrystalline Pt(111)[100nm]/TiO₂[15nm]/SiO₂[450nm]/Si(100) substrates (denoted as Pt/Si). In order to ensure full transformation of the titanium into TiO₂, the seeded substrates were subsequently heat treated at 700 °C in oxygen atmosphere (Fig. 21.3).

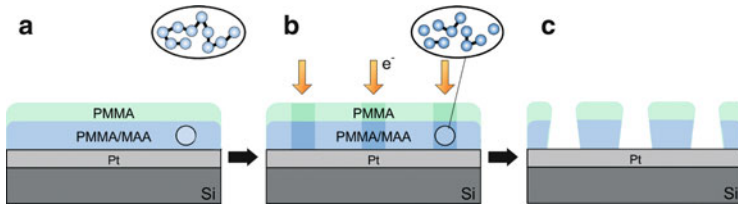


Fig. 21.2 Schematic of the two-layer resist process based on PMMA polymer resists. (a) A two layer resist system consisting of a PMMA top layer and a PMMA/MAA bottom layer is spin coated onto platinumized silicon substrates; (b) The resist layers are exposed by electron-beam; (c) After development, an undercut resist profile is obtained as the lower copolymer resist is higher in sensitivity. Figure modified after [10]

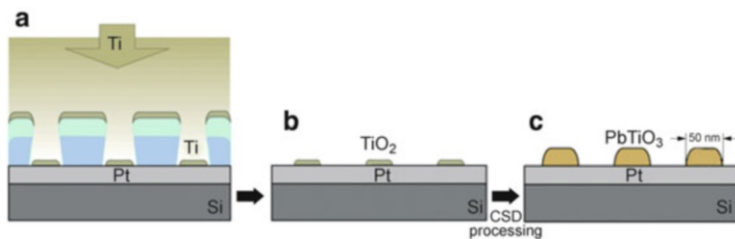


Fig. 21.3 Schematic of the TiO_2 nucleation site patterning. (a) A $12\text{--}20^\circ\text{A}$ thick layer of titanium is thermally evaporated on top of the structured resist mask with an evaporation rate of $0.8\text{ A}^\circ/\text{s}$; (b) The resist mask is removed in an organic solvent using N-methyl-2-pyrrolidone (NMP) for 24 h followed by slight ultrasonic agitation for 3 min. The titanium seed patterns on the substrate are then heat treated at 700°C in oxygen atmosphere using a RTP unit to ensure full oxidation of the titanium. (c) CSD processing of a low concentrated PTO precursor solution finally yielded well registered PTO nanograins. Figure modified after [10]

The smallest dots that were fabricated with this method were 30 nm in diameter on a 75 nm pitch which corresponds to an integration density of approx. $17.8\text{ Gbit}/\text{cm}^2$. Higher integration densities resulted in an increased loss of contrast during exposure and development (Fig. 21.4).

Subsequently, PTO islands were grown onto the seeded substrates by CSD using highly diluted, modified 2-butoxyethanol based precursor solutions. After pyrolysis at 350°C , crystallization of the amorphous PTO films was carried out at 700°C for 15 min in oxygen atmosphere. By carefully adapting the processing parameters, the growth of PTO islands could be tuned in such a way that it only took place on the TiO_2 nucleation sites (Fig. 21.5).

It was found, that towards higher TiO_2 seed layer thicknesses, an increased amount of PTO crystals lost their piezoelectric and therefore ferroelectric properties, possibly due to a lead-deficient, non-stoichiometric and therefore non-ferroelectric phase emerging as the nucleation sites are incorporated into the growing perovskite during crystallization. Anyway, also loss of the epitaxial relationship between the polycrystalline (111)-oriented platinum substrate and a

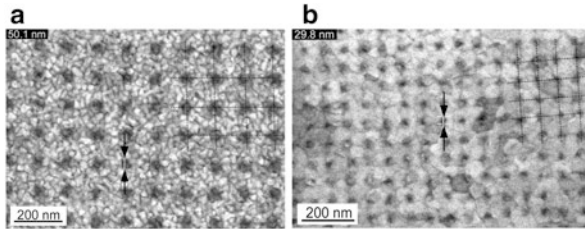


Fig. 21.4 SEM images of TiO_2 dot structures appearing as round shadows on the bright platinum substrate. (a) The dots are 50 nm in diameter and have a distance of 125 nm. (b) The smallest TiO_2 dot structures that were patterned were 30 nm in diameter with a 75 nm pitch. The nucleation site arrangement is marked by dashed lines on the top right of both images. Figure modified after [10]

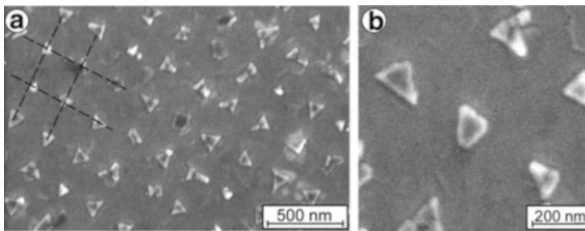


Fig. 21.5 SEM images of separated PTO nanoislands deposited with a 0.032 M precursor solution on 100 nm wide TiO_2 seed structures. The nucleation of the PTO crystals exclusively took place on the TiO_2 seed pattern, whereas there is no crystallization at the grain boundaries of the platinumized substrate. To point out the alignment of the deposited PTO crystals, *grid lines* are plotted in (a). Figure adapted from [10]

postulated rutile TiO_2 phase towards thicker TiO_2 layers could explain this finding. Ferroelectric switching of the islands was exemplarily verified on single cells using piezoelectric force microscopy (PFM) as will be explained in Sect. 21.3.2. Upon optimization of the seed layer thickness, 90 % of the deposited crystals displayed piezoelectric activity, coming along with a distinct triangular faceting of the crystals, which in turn indicate a preferred (111)-orientation (Fig. 21.6).

By carefully adapting the CSD process to the nucleation site dimensions and densities, highly ordered PTO nanocrystals down to 50 nm in lateral dimensions were successfully grown onto the TiO_2 arrays featuring a 125 nm pitch, which corresponds to a grain density of 6.4 Gbit/cm².

21.3.1.2 Ferroelectric Nanotubes by Soft-Template Infiltration

Recently a further combination of EBL with CSD processing to generate arbitrary arranged ferroelectric nanostructures was presented [23]. In this bottom-up approach a sol-gel type $\text{PbZr}_{0.52}\text{Ti}_{0.48}\text{O}_3$ (PZT52/48) precursor solution, was infiltrated into a polymeric template under reduced pressure, yielding ferroelectric

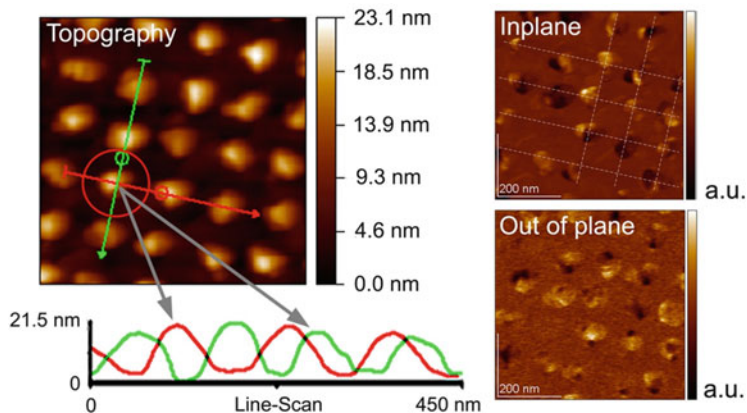


Fig. 21.6 Topographic AFM scan (*left*) of PTO crystals grown onto 50 nm wide seeds on a 125 nm separation distance. Piezoelectric in-plane (*top*) and out-of plane (*bottom*) response of the island array are displayed on the *right*, showing the amplitude times phase in arbitrary units. PFM scans were carried out with an excitation signal of 1 V at 7 kHz applied to the probe tip. Note that the effective lateral grain dimensions are displayed enlarged due to the tip radius. The high registration of grains is clearly visible in topography and *dashed lines* mark the arrangement of PTO grains in the in-plane PFM scan. Up to 90 % of the depicted islands show piezoelectric activity. As indicated by the topographic line-scan on the *left*, grain heights are uniform and reach a maximum level of about 20 nm. Figure adapted from [54]

PZT nanotubes after two step thermal processing (pyrolysis at 300 °C and crystallization in a ramp from 600 to 800 °C). During the high temperature annealing PZT crystallization and decomposition of the organic resist simultaneously took place. The required soft-template was manufactured by EBL of a spin coated negative e-beam resist with subsequent thin Al₂O₃-layer coating by atomic layer deposition. This less than 10 nm thick alumina layer leads to mechanical consolidation and prevents chemical reactions between the PZT precursor solution and the polymeric template. After the high temperature annealing, the thin Al₂O₃ layer connects the build adjacent PZT nanotubes. The aspect ratio of the generated PZT nanostructures is determined by the height and the width of the pattern in the e-beam resist, which can be independently controlled. By varying the rotation speed during the spin on process of the e-beam resist the polymer template thickness and hence the height of the PZT nanotubes could be altered. Aspect ratios from 1.2:1 up to 5:1 have been demonstrated so far. Micro-Raman spectroscopy and PFM methods were applied in order to proof crystallinity and the ferroelectric nature of the fabricated nanostructures [23]. The authors conclude that their approach can be tailored for a variety of ceramic materials by appropriate choice of CSD conditions (precursors and annealing temperatures) and may be easily scaled for larger patterned areas, by the use of nanoimprint lithography (NIL) instead of EBL for creation the required soft templates.

21.3.1.3 Copolymer Micelle Lithography Derived Gold Nanoparticle Hard Masks

Although the e-beam lithography mediated nucleation site concept described above yields excellent results there are still drawbacks such as the serial working principle i.e. time consumption, relatively high cost, and the typically covering of only small surface areas. Self assembly approaches on the other hand allow for efficient parallel generation of nanopatterns. The aim is here at first to implement a suitable process that allows a high degree of structural ordering which is then transferred in suitable templates with dimensions of a few nanometers. Möller et al. [24–26] made considerable progress in the fabrication of such highly ordered nanostructures by using “copolymer micelle lithography”. The used copolymers consists of two chemically different macromolecular chain segments which do not mix, but form microdomains. The size and mesomorphic order of these so called A-B diblock copolymers largely depend on the length of the blocks and their molecular weight distribution [27–29]. For a review on the use of such polymers for nanomaterial fabrication the reader is referred to the literature [30]. Typical periodicities are in the range of 10 ± 200 nm. In thin films, the domain structure is affected by the interfacial energies and the geometrical constraints introduced by the flat interfaces [31–34].

In order to explore the potential of this method for bottom up-fabrication of sub-100 nm structures and functional oxide particles, Kronholz et al. used gold loaded diblock-copolymer micelles, which arrange in a hexagonal pattern according to the balance of different forces (e.g. capillary forces, long range van der Waals interactions and adhesion forces), for the generation of such defined oxidic nanostructures [21]. The first steps of the preparation process involved the formation of micelles from poly(vinylpyridine)-b-poly(styrene) (PVP-b-PS) diblock copolymers and the loading of the micellar core with the gold salt. Dip coating of an ultrathin titania layer coated platinized silicon substrate ($\text{TiO}_2[2\text{nm}]/\text{Pt}/\text{Si}$) yielded a monolayer micellar film. In the subsequent process step the organic compounds are removed by reactive ion beam etching (RIBE) with an oxygen-plasma. The plasma treatment leads to a reduction of the Au salt and finally to one Au nanocluster per micelle by thermal annealing. The resulting Au nanoparticles are suitable as hard mask for the patterning of the ultrathin TiO_2 -film on top of the Pt electrode with reactive ion etching (RIE) using a CF_4 -plasma. Subsequently the residual Au nanoparticles are removed by a RIBE Ar-plasma treatment step (Fig. 21.7).

As the result, TiO_2 seeds are produced for the controlled growth of PbTiO_3 nanograins by the basically same chemical solution deposition technique which has already been applied for e-beam patterned TiO_2 described in Sect. 21.3.1.1. Figure 21.8 shows the atomic force microscope (AFM) photographs and inter-particle distances obtained from line scans taken for samples at different steps of the preparation process.

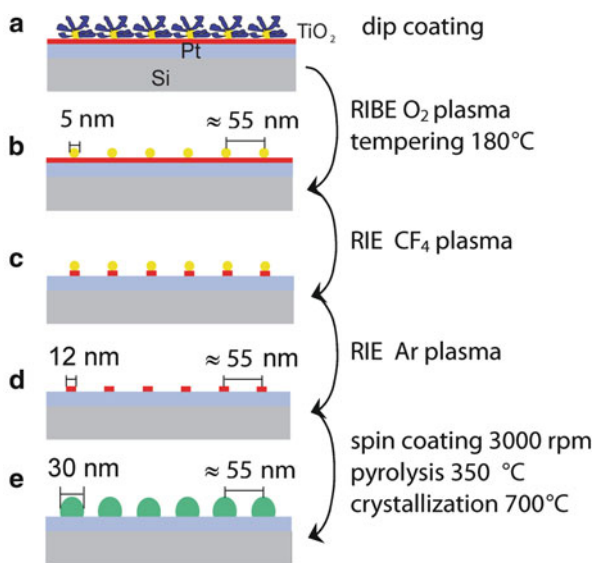


Fig. 21.7 Process flow for the template-based preparation of PbTiO_3 nanograins (a) self-assembled gold-loaded PVP-*b*-PS micelles; (b) gold nanoparticles after reduction and temperature treatment (RIBE: reactive-ion-beam etching); (c) gold-covered TiO_2 seeds after reactive-ion etching (RIE); (d) elimination of the Au template by RIE; and (e) PbTiO_3 grains grown on TiO_2 seeds. Figure adapted from [21]

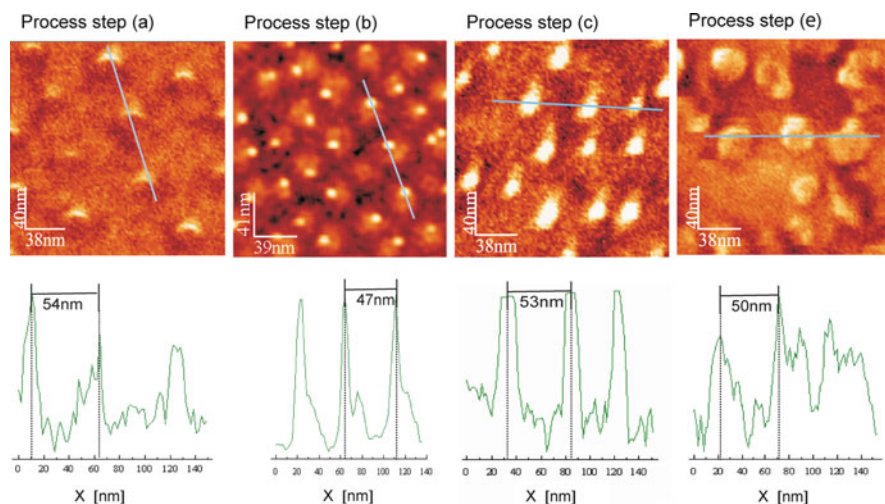


Fig. 21.8 AFM photographs and results of line scans yielding the inter-particle distances taken at process steps (a), (b), (c) and (e) (see Fig. 21.7) during the preparation of PbTiO_3 nanograins on a TiO_2 surface. For the monolayer film preparation a withdrawal speed of $v = 5$ mm/min was used. Figure adapted from [21]

It is self evident that the quality of the template is essential for the success of the patterning process. The great interest of using diblock-copolymer micelles as templates was partly based on the idea that the spacing can be easily varied by increasing the length of the block which builds the shell. By a combined approach of scattering experiments on the solution properties of the Au loaded micelles and surface characterizations of the dried monolayer films it has been possible to determine which impact the diblock-copolymer architecture and the monolayer film preparation conditions have on the characteristics of the present template [21]. By dynamic light scattering and also small-angle neutron scattering experiments information about the full form factor has been obtained, which allowed to determine the overall shape of the micelles in solution and the distribution of the gold load in the micelles. No hints for agglomeration have been found.

The micelle dimensions and average inter-micelle spacing in solutions have been compared with those obtained from dried monolayer films. The inter-micelle spacing in the dried film is much smaller than the micelle dimension in solution and approaches the dimension of a fully collapsed micelle in case the dipping process is performed slowly enough. The micelles collapse, but they still have a certain mobility to rearrange on the surface during the drying process resulting in a higher degree of order of the pattern. It turned out that inter-micelle distances and the degree of order of the dried monofilm is mainly determined by the preparation condition such as the pulling velocity of the dipping process and the strength of the surface-micelle interaction and not necessarily by the architectural properties (block length and ratio) of the diblock copolymers building the micelles. In conclusion this additive growth technique results in registered nanocrystals with natural growth facets. As an example TiO_2 seeds and PbTiO_3 grains with a diameter of 12 and 30 nm, respectively, have been prepared without any e-beam lithographic step.

21.3.2 Ferroelectric Characterization by SPM Techniques

In order to characterize the piezo-, and ferroelectric properties of crystalline thin films, usually patterned top electrodes are deposited and afterwards ferroelectric characterization is performed by contacting top and bottom electrode and measuring the ferroelectric (and dielectric) displacement currents while cycling an external electric field. Integration of the current response yields a characteristic ferroelectric hysteresis loop as the ferroelectric polarization P_i is the dominant contribution to the dielectric displacement charge D_i [35].

However, in case of sub-100 nm lead titanate islands the deposition of well defined individual top electrodes is quite complex. Therefore characterization of such nanoscopic structures is ideally performed by scanning force microscopy (SFM) which builds a subcategory of the scanning probe microscopy family. The principle of SPM is as elegant as simple: a sharp tip raster scans a sample surface and the interactions between probe tip and sample are spatially recorded. These

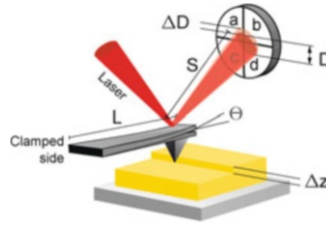


Fig. 21.9 Schematic of a SFM that utilizes an optical lever arm for detection of the cantilever bending. The laser beam is reflected from the backside of the cantilever. Any movement of the cantilever is optically detected as the laser beam changes its position on the photosensitive diode. Figure adapted from [39]

interactions can be of various nature (e.g. electrical, magnetic, mechanical etc.). The first SPM based method, scanning tunneling microscopy (STM), was developed by Binnig and Rohrer at IBM R schlikon [36]. It was Nobel Price awarded because they achieved atomic resolution on Si(111) 7×7 surfaces [37]. Anyway, the necessity of a tunneling current between probe tip and sample restricts the method to conducting or at least semi-conducting sample surfaces.

In SFM, a force interaction between tip and sample surface is recorded by mounting the probe tip underneath a flexible cantilever and measuring its deflections (Fig. 21.9). As this method is not restricted to conducting samples, it is the most widely used scanning probe based method today. Depending on the force that is detected, SFM is subdivided into special applications, atomic force microscopy (AFM) and PFM for example.

PFM is the most widely used tool for nanoscale studies on ferroelectrics as it features a high spatial resolution and allows for effective ferroelectric domain imaging and manipulation [38]. Basically, it is an AFM working in contact mode. Here, the sharp cantilever tip is in permanent contact with the sample surface—it scratches the sample. The PFM setup is in contrast to an AFM setup extended to detect deflections on the sample surface due to the converse piezoelectric effect according to Eq. (21.1), which describes the strain S_{ij} that is generated in a piezoelectric material due to an applied electric field E [V/m]:

$$S_{ij} = d_{ijk}^t E_k \quad (21.1)$$

Here, d_{ijk}^t [m/V] is the transposed tensor of piezoelectric coefficients [35].

The cantilever fulfills two functions: it is used as temporary top electrode for applying the excitation voltage to the sample while simultaneously recording the voltage induced piezoelectric deformation. Due to the setup of the cantilever, two types of mechanical response can be distinguished: out-of-plane and in-plane deformations. In case of ferroelectric perovskite crystals, both in and out-of-plane response are directly related to the polarization vector of the crystal. Here, for crystal symmetry reasons the initially third rank tensor of piezoelectric constants d_{ijk} [C/N] is reduced to merely three independent, non-zero piezoelectric

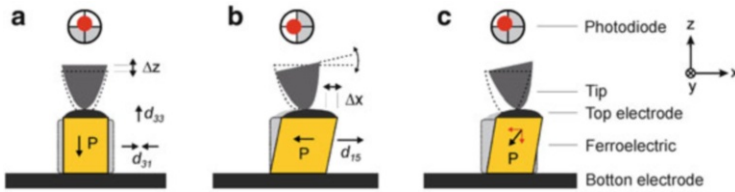


Fig. 21.10 Converse piezoelectric effect in ferroelectric perovskites. (a) When the electric field E between cantilever and bottom electrode is in parallel to the polarization direction P , the cantilever is deflected in out-of-plane direction and the laser spot on the photosensitive diode moves in the vertical direction. An additional lateral deformation of the ferroelectric structure due to d_{31} cannot be detected for symmetry reasons. (b) In case of a polarization direction perpendicular to the applied electric field, the grain is sheared due to d_{15} . This causes a lateral torsional deformation of the cantilever and the laser spot moves in lateral direction on the four quadrant photodiode. (c) A ferroelectric crystal with a polarization vector in the x - z plane will contribute to both the out-of-plane and in-plane signal. Figure adapted from [40]

coefficients: d_{33} , d_{31} and d_{15} [35]. The possible piezoelectric deflections of such a crystal under an applied electric field are depicted in Fig. 21.10.

When the vector of spontaneous polarization of the crystal is in parallel to the applied electric field in z -direction, the crystal will elongate or contract in out-of-plane direction according to the piezoelectric coefficient d_{33} . Is the spontaneous polarization perpendicular to the electric field, d_{15} will force the crystal to shear in x -direction (in-plane), resulting in a lateral torsion of the cantilever. Both lateral and vertical movements of the cantilever can be resolved by using a photodiode resolving the laser movement in four quadrants as illustrated in Fig. 21.10.

The first harmonic of the deflection signal on the photosensitive diode is extracted using lock-in amplifiers. This part of the signal equals the piezoelectric response of the sample. The output signal of the lock-in amplifiers V_{out} can be represented either by complex amplitudes X (real part) and Y (imaginary part) or alternatively by an amplitude R and a phase shift ϕ between the excitation voltage and the detected signal.

PFM is of particular interest as it can be used to monitor ferroelectric switching with highest lateral resolution. In contrast to piezoelectric materials, the direction of polarization P in ferroelectrics determines the phase between excitation voltage and deformation of the crystal as illustrated in Fig. 21.11.

Here, switching the polarization vector by 180° results in a 180° phase shift of the corresponding out-of-plane signal. The same effect is obtained for the in-plane signal when switching the polarization vector in in-plane direction.

In order to verify the ferroelectric properties of the template grown PTO islands as described in Sect. 21.3.1.1 PFM measurements upon switching were carried out as displayed in Fig. 21.12 [10]. Here, the switching of a 50 nm wide PTO grain on a 125 nm pitch is monitored. The polarization vector and thus the piezoelectric tensor of the highlighted grain was switched bi-directionally by applying an external DC voltage in between the single PFM scans. The two stable polarization states of the structure demonstrate ferroelectricity.

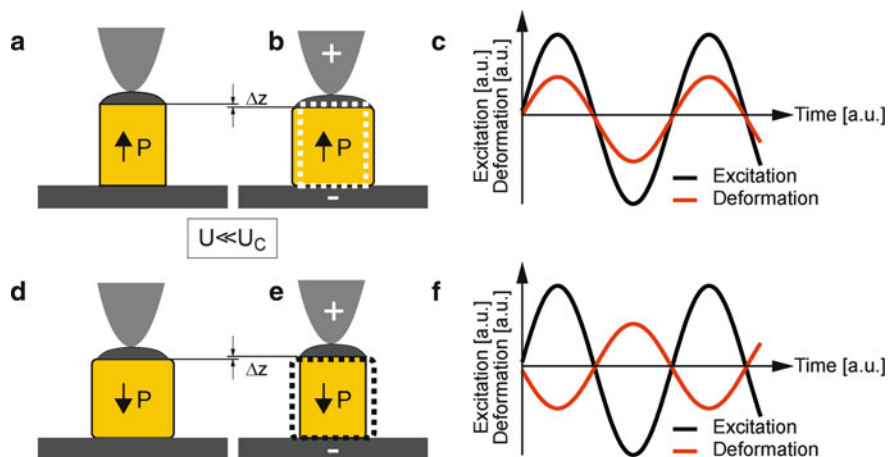


Fig. 21.11 Schematic of the detectable phase shift in ferroelectric crystals due to a change in polarization direction. In the *upper case* [parts (a, b)], the electric field is applied antiparallel to the polarization. This leads to a contraction of the ferroelectric crystal. When switching the polarization in the opposite direction [as depicted in (d, e)], the crystal is stretched as the electric field and polarization point into the same direction. This results in a phase shift of 180° between electric field and crystal deformation analog to (c) and (f). Here, a contraction in z is defined as positive deformation. Figure adapted from [39]

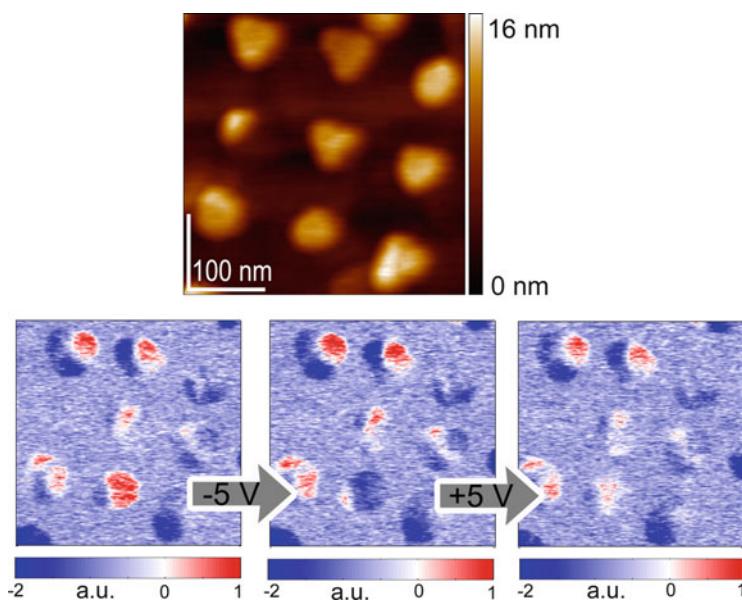


Fig. 21.12 Top: AFM image of PTO grains that nucleated on 50 nm wide TiO_2 seeds having a pitch distance of 125 nm . Bottom line: In-plane piezoresponse signals of the depicted grains. The polarization state of the accentuated grain was switched bi-directionally in between single PFM scans by applying a DC voltage of -5 V and 5 V respectively to the grain. The PFM scans were carried out using an excitation signal of 1 V at 7 kHz . The out-of plane polarization of the highlighted grain switched as well (not shown). Figure modified after [10]

Note, that PFM is not or at least not yet an appropriate tool for any quantitative evaluation of ferroelectric characteristics. The evaluation of the coercive field E_c is hampered as the electrical field underneath the tip is often insufficiently quantified [41]. Besides, the piezoelectric coefficient d_{33} gives yields no quantitative information on the spontaneous polarization P_s of the crystal [43]. For a quantitative analysis, direct electrical characterization by applying an alternating external electric field and measuring the current response remains mandatory.

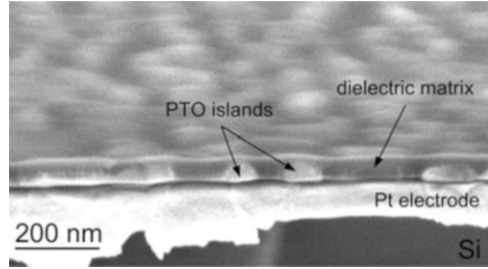
21.3.2.1 Heated AFM Cantilever Tips

It has to be mentioned that the AFM setup can not only be used for characterization but also for generating nanostructures after technical adaption. One interesting approach which became popular is the use of resistively heated AFM cantilever tips [44]. This technique allows controlled local deposition of materials, which are normally immobile at room temperature, and local chemical reactions such as conversion to other functional groups [45, 46] or local reduction of e.g. graphene oxide [47]. This so-called thermochemical nanolithography was recently also employed to locally crystallize a ferroelectric CSD derived amorphous precursor film [48]. The amorphous PZT films have been prepared by spin coating and a subsequent short drying/pyrolysis step at moderate temperatures of 250–300 °C. Thus beyond the standards silicon based substrates a large variety of typically too temperature sensitive substrates such as plastics (e.g. Kapton) or soda-lime glass can be used. In summary this maskless method enabled the direct creation of ferroelectric lines with widths >30 nm and spheres with a diameter >10 nm and densities up to ~ 33 Gbit/cm² (~ 213 Gbit/in.) [48]. The authors conclude that the method can potentially parallelized in order to have high registry and alignment quality for fabrication of real devices.

21.3.3 Embedding Concepts

In order to enable direct electrical characterization of single ferroelectric nanoislands, integration has to be pushed to a level where the bottom-up prepared ferroelectric cells can be provided with top-electrodes, i.e. nanocapacitors can be fabricated. For this, a dedicated process based on flowable oxides in combination with chemical mechanical polishing (CMP) [49] will be presented in the following [53–55]. As we will see, the process yields ferroelectric nanocells which are electrically insulated within a dielectric matrix layer but at the same time feature electrically accessible tops—a configuration that allows for the deposition of top electrodes and hence, quantitative direct electrical hysteresis measurements. Flowable spin-on glass (SOG) dielectrics were used as dielectric matrix layers for embedding the ferroelectric nanocells as they feature excellent gap-fill and planarization properties. The processing route is likewise a CSD route where the

Fig. 21.13 Cross-sectional SEM image of PTO islands on a platinized silicon substrate. The low-k dielectric HSQ layer on top was spin coated to a thickness of about 70 nm, just surmounting the maximum grain heights



SOG materials are dispensed in a liquid state, i.e. they are spin-coated onto the substrate. After curing, a layer of low permittivity glass ($\epsilon_r \approx 4$) with characteristics similar to those of SiO_2 is formed. For this, low-k SOG dielectrics are widely used as inter-layer dielectric (ILD) or overcoat passivation in the manufacture of IC's in semiconductor industry [50].

For embedding and integration of the ferroelectric nanoislands, different low-k dielectric SOG materials like hydrogen silsesquioxane (HSQ) or methyl silsesquioxane (MSQ) were applied—polymers with the empirical formula $(\text{R-SiO}_{3/2})_n$ [51, 52]. The name silsesquioxane is derived from the one and a half (sesqui) stoichiometry of oxygen bound to silicon. HSQ is an inorganic polymer that contains hydrogen bonded to the silicon atoms in the Si-O backbone ($\text{R}=\text{H}$). MSQ includes an organic substitution of 10 wt% CH_3 groups to silicon ($\text{R}=\text{CH}_3$). The low dielectric constant of the materials is due to the low polarizability of the Si-R bond in comparison to the Si-O bond in SiO_2 [52]. Moreover, the presence of cage structures increases the larger free volume of the films compared to films of amorphous SiO_2 networks. In order to obtain mechanically stable films, cross-linking of the silsesquioxane polymer structures was achieved by thermal curing of the films after deposition at temperatures around 400 °C in inert (nitrogen) atmosphere in order to prevent oxidation of the films.

The dielectric layers were spin coated to thicknesses that just covered the highest PTO grain tops as depicted in Fig. 21.13.

The excessive dielectric material on top of the grains was subsequently removed by CMP [53]. Due to the planarizing properties of the matrix layers and the marginal surface corrugation after embedding, the polishing process could be carried out on a commercial tabletop polisher (which in contrast to a dedicated CMP tool barely features any global planarization impact). Gaining a high local and global uniformity in polishing abrasion, piezoresponse force microscopy scans (see Sect. 21.3.2 for the working principle) were carried out for identifying the percentage of electrically addressable ferroelectric grain tops after polishing. Figure 21.14 illustrates the gain in piezoelectric activity with respect to the polishing time compared to a sample with an embedding HSQ layer on top of the PTO grains. Here, the piezoelectric signal proves the electrical contact between the conducting probe tip of the microscope and the PTO islands after polishing.

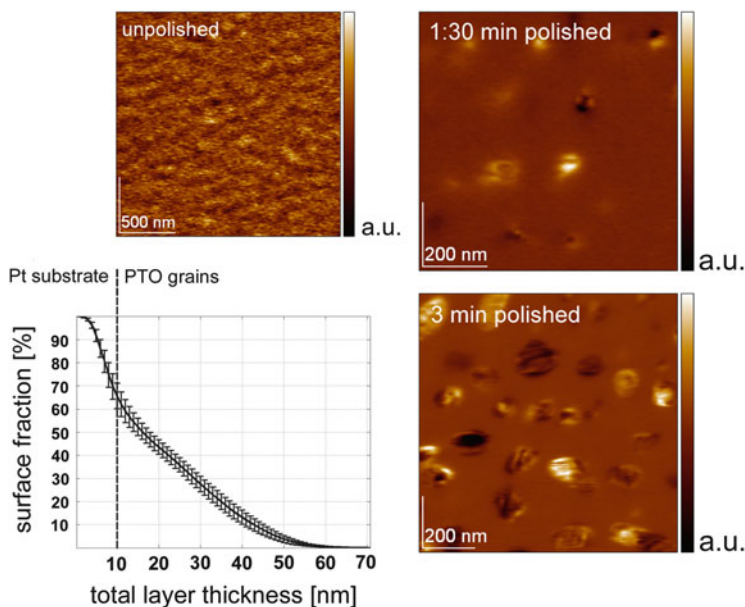


Fig. 21.14 In-plane PFM images demonstrating the gain in piezoelectric active surface fraction with increasing polishing time. No piezoelectric activity is recorded on the unpolished samples as displayed on the *top left*. After 90 s of CMP small piezoelectric spots emerge in the PFM scans and after 3 min large parts of the embedded islands are visible. The graph inset on the *bottom left* displays the expected surface fraction of polished PTO grains against the remaining layer thickness (derived from statistical topographic information of the PTO islands deposited with a 0.17 M precursor and a single coating). As the platinum bottom electrode is not entirely flat, the remaining layer strength of the HSQ matrix is about 10 nm less compared to the total layer thickness. Reprinted with permission from [53]. Copyright 2005 American Institute of Physics

Figure 21.15 displays a ferroelectric nanostructure array of highly arranged about 100 nm wide and 15 nm high PTO cells on a 250 nm pitch that were embedded in MSQ and made electrically accessible by polishing [54]. Although the embedding process is obviously not restricted to smallest structural dimensions, direct electrical characterization of such structures is hampered as the electric charge to detect scales with lateral cell dimension. As this charge readily drops below any background noise, parasitic capacitances and leakage during measurement, the method of choice for proving ferroelectricity on nanoscaled ferroelectrics still is piezoresponse force microscopy.

Anyway, direct electrical characterization of sub-100 nm ferroelectric islands becomes feasible when measuring several structures in parallel. For this, collective Au and Pt top electrodes with diameters in the range of 100 μm were deposited onto embedded and electrically accessible PTO nanoislands of typically below 100 nm in lateral dimensions that were grown by self-assembly routes [55].

I-V plots as shown in Fig. 21.16 were recorded that show displacement current peaks close to those measured on continuous PTO thin films with related characteristics regarding frequency and applied voltage.

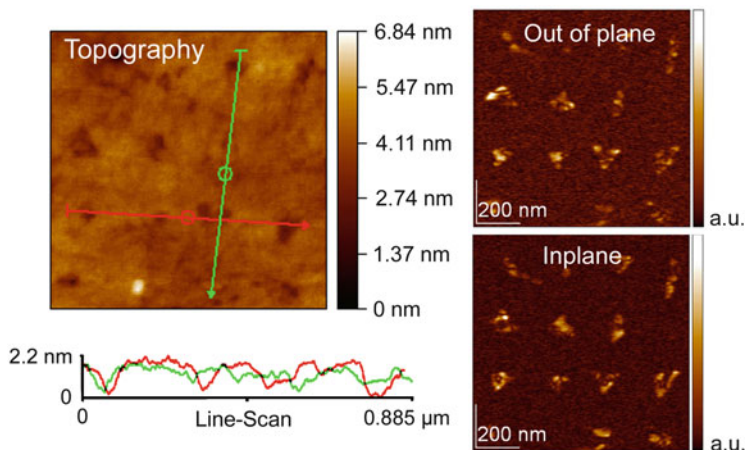


Fig. 21.15 PFM scan of a in MSQ embedded PTO grain array after 40 s of CMP. The islands were grown onto 100 nm nucleation sites. The topographic image on the *left* displays an almost perfectly plain surface, only disrupted by minuscule holes (around 2 nm in depth as indicated by the line-scan) on the grain sites. Piezoresponse scans taken with 1 V at 7 kHz applied to the probe tip show distinct piezoelectric activity of the embedded islands and hence, prove the electrical accessibility after polishing. Note the height registration of piezoelectric active regions while the surface topography is almost entirely flat. Figure adapted from [54]

While values for the coercive field E_c can directly be extracted from the I-V plots, a first evaluation of the remanent polarization P_r of the nanosized PTO islands was derived by integration of the displacement current peaks. In this context it was found, that the actual switching charge closely corresponded to the piezoelectric active surface fraction of the embedded grains as verified by PFM and illustrated in Fig. 21.17. The excellent agreement with literature values when the surface fraction of ferroelectric nanoislands approaches unity is a strong hint on the eligibility of the applied integration route.

21.4 Concluding Remarks

The continuing trend of miniaturization of functional oxide materials down to a few tens of nanometers or even less is a necessity to increase the density of devices. In order to figure out the limits of the corresponding device concept, the detailed knowledge of the size effects, i.e. the physical behavior of the material which has been scaled down to these dimensions, is required. Suitable manufacturing methods as well as characterization methods have to be sought out. On an industrial scale highly expensive XUV-lithography tools are used to fabricate such small structures by typical top-down approaches, which are consequently not available in normal research institutions. By means of the registered growth of ferroelectric nanostructures, a number of template based bottom-up approaches have been

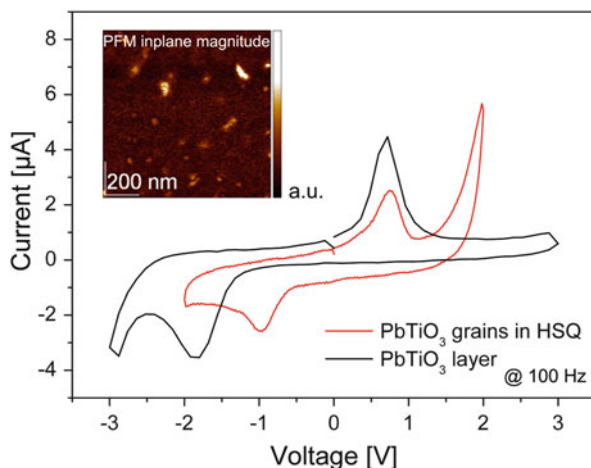


Fig. 21.16 I-V curves of HSQ embedded PTO grains (*red*) of about 40 nm in height and of an approximately 80 nm thick continuous PTO thin film (*black*). Both curves were measured at 100 Hz using Pt top-electrodes of 200 μm (grains) and 80 μm (layer) in diameter. The PFM inset on the *top left* displays the percentage of piezoelectric activity that could be recorded on the embedded PTO grain surface. Reprinted with permission from [55]. Copyright 2008 American Institute of Physics

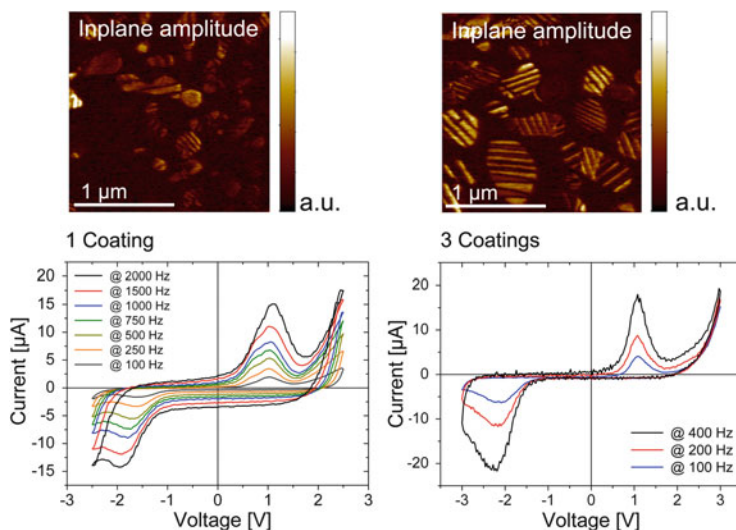


Fig. 21.17 Frequency dependent I-V curves measured on MSQ embedded PTO grains that were deposited by a single (*left*) respectively three (*right*) coatings of a 0.29 M precursor solution. The layer thicknesses after polishing are in the range of 50 nm for the single coating and about 80 nm for the multiple coating approach. With an increased surface fraction of uncovered islands, as displayed by the PFM insets on top of the particular I-V curves, the displacement current peaks become more pronounced. In case of the single coating about 12 $\mu\text{C}/\text{cm}^2$ switch and this charge rises to 35 $\mu\text{C}/\text{cm}^2$ in case of the multiple coating approach

reviewed in the present chapter. They enable in an academic environment the fabrication of nanometer structures from the bottom up by creating e.g. arbitrary seed pattern of TiO_2 , which can be subsequently CSD processed to the corresponding PTO nanograins, or by infiltrating an EBL patterned soft template with a PZT precursor solution and subsequent crystallization of only the predefined amorphous PZT nanomaterial. In both cases a deteriorating influence of the patterning method itself on the physical properties could be excluded. AFM techniques in various modes have been shown to be the methods of choice to characterize and even produce individual nanograins. Embedding approaches showed that the ferroelectric nanograins remain functional. Overall the presented template based growth concepts and characterization techniques may inspire researchers to transfer and modify them to other nanoscaled functional oxide materials.

References

1. Waser R (2012) *Nanoelectronics and information technology*, 3rd edn. Wiley-VCH, Weinheim
2. Setter N, Damjanovic D, Eng L, Fox G, Gevorgian S, Hong S, Kingon A, Kohlstedt H, Park NY, Stephenson GB, Stolitchnov I, Tagantsev AK, Yamada DV, Taylor T, Streiffer S (2006) Ferroelectric thin films: review of materials, properties and applications. *J Appl Phys* 100:51606-1-46
3. Rüdiger A, Schneller T, Roelofs A, Tiedke S, Schmitz T, Waser R (2005) Nanosize ferroelectric oxides – tracking down the superparaelectric limit. *Appl Phys Mater Sci Process* 80:1247–1255
4. Seifert A, Vojta A, Speck JS, Lange FF (1996) Microstructural instability in single crystal thin films. *J Mater Res* 11:1470–1482
5. Roloefs A, Schneller T, Szot K, Waser R (2002) Piezoresponse force microscopy of lead titanate nanograins possibly reaching the limit of ferroelectricity. *Appl Phys Lett* 81:5231–5233
6. Roelofs A, Schneller T, Szot K, Waser R (2003) Towards the limit of ferroelectric nanosized grains. *Nanotechnology* 14:250–253
7. Szafraniak I, Harnagea C, Scholz R, Bhattacharyya S, Hesse D, Alexe M (2003) Ferroelectric epitaxial nanocrystals obtained by a self-patterning method. *Appl Phys Lett* 83:2211–2213
8. Dawber M, Szafraniak I, Alexe M, Scott JF (2003) Self-patterning of arrays of ferroelectric capacitors: description by theory of substrate mediated strain interactions. *J Phys Condens Matter* 15:L667–L671
9. Bühlmann S, Muralt P, Von Allmen S (2004) Lithography modulated self assembly of small ferroelectric $\text{Pb}(\text{Zr,Ti})\text{O}_3$ single crystals. *Appl Phys Lett* 84:2614–2616
10. Clemens S, Schneller T, van der Hart A, Peter F, Waser R (2005) Registered deposition of nanoscale ferroelectric grains by template-controlled growth. *Adv Mater* 17:1357–1361
11. Aoki K, Fukuda Y, Numata K, Nishimura A (1995) Effects of the titanium buffer layer on PZT crystallization process in sol–gel deposition technique. *Jpn J Appl Phys* 34:192–195
12. Frey J, Schlenkrich F, Schönecker A (2001) Self-polarization and texture of wet chemically derived lead zirconate titanate thin films. *Integr Ferroelectr* 35:105–113
13. Seifert A, Ledermann N, Hiboux S, Baborowski J, Muralt P, Setter N (2001) Processing optimization of solution derived $\text{PbZr}_{1-x}\text{Ti}_x\text{O}_3$ thin films for piezoelectric applications. *Integr Ferroelectr* 35:159–166

14. Murali P, Maeder T, Sagalowicz L, Hiboux S, Scalse S, Naumovic D, Agostino RG, Xanthopoulos N, Mathieu HJ, Patthey L, Bullock EL (1998) Texture control of PbTiO_3 and $\text{Pb}(\text{Zr,Ti})\text{O}_3$ thin films with TiO_2 seeding. *J Appl Phys* 83:3835–3841
15. Murali P (2006) Texture control and seeded nucleation of nanosize structures of ferroelectric thin films. *J Appl Phys* 100:051605
16. Miller KT, Lange FF, Marshall DB (1990) The instability of polycrystalline thin films: experiment and theory. *J Mater Res* 5:151–160
17. Miller KT, Lange FF (1991) Highly oriented thin films of cubic zirconia on sapphire through grain growth seeding. *J Mater Res* 6:2387–2392
18. Kambara H, Schneller T, Sakabe Y, Waser R (2009) Dielectric properties of highly c-axis oriented chemical solution deposition derived $\text{SrBi}_4\text{Ti}_4\text{O}_{15}$ thin films. *Phys Status Solidi A* 206:157–166
19. Dawley JT, Ong RJ, Clem PG (2002) Chemical solution deposition of $\langle 100 \rangle$ -oriented SrTiO_3 buffer layers on Ni substrates. *J Mater Res* 17:1678–1685
20. Vasco E, Karthäuser S, Dittmann R, He J-Q, Jia C-L, Szot K, Waser R (2005) SrZrO_3 nanopatterning using self-organized SrRuO_3 as a template. *Adv Mater* 17:281
21. Kronholz S, Rathgeber S, Karthäuser S, Kohlstedt H, Clemens S, Schneller T (2006) Self-assembly of diblock-copolymer micelles for template-based preparation of PbTiO_3 nanograins. *Adv Funct Mater* 16:2346–2354
22. Nagarajan V, Stanishevsky A, Ramesh R (2006) Ferroelectric nanostructures via a modified focused ion beam technique. *Nanotechnology* 17:338–343
23. Bernal A, Tselev A, Kalinin S, Bassiri-Gharb N (2012) Free-standing ferroelectric nanotubes processed via soft-template infiltration. *Adv Mater* 24:1160–1165
24. Spatz JP, Mossmer S, Hartmann C, Möller M, Herzog T, Krieger M, Boyen HG, Ziemann P, Kabius B (2000) Ordered deposition of inorganic clusters from micellar block copolymer films. *Langmuir* 16:407–415
25. Haupt M, Miller S, Ladenburger A, Sauer R, Thonke K, Spatz JP, Riethmüller S, Möller M, Banhart F (2002) Semiconductor nanostructures defined with self-organizing polymers. *J Appl Phys* 91:6057–6059
26. Glass R, Möller M, Spatz JP (2003) Block copolymer micelle nanolithography. *Nanotechnology* 14:1153–1160
27. Bates FS, Frederickson GH (1990) Block copolymer thermodynamics: theory and experiment. *Annu Rev Phys Chem* 41:525–557
28. Milner ST (1991) Polymer brushes. *Science* 251:905–914
29. Leibler L (1980) Theory of microphase separation in block copolymers. *Macromolecules* 13:1602–1617
30. Lazzari M, López-Quintela MA (2003) Block copolymers as a tool for nano material fabrication. *Adv Mater* 15:1583–1594
31. Kellogg GJ, Walton DG, Mayes AM, Lambooy P, Russell TP, Gallagher PD, Satija SK (1996) Observed surface energy effects in confined diblock copolymers. *Phys Rev Lett* 76:2503–2506
32. Morkved TL, Lu M, Urbas AM, Ehrichs EE, Jaeger H, Mansky P, Russell TP (1996) Local control of microdomain orientation in diblock copolymer thin films with electric fields. *Science* 273:931–933
33. Mansky P, Russell TP, Hawker CJ, Mays J, Cook DC, Satija SK (1997) Interfacial segregation in disordered block copolymers: effect of tunable surface potentials. *Phys Rev Lett* 79:237–240
34. Mansky P, Liu Y, Huang E, Russell TP, Hawker C (1997) Controlling polymer-surface interactions with random copolymer brushes. *Science* 275:1458–1460
35. Damjanovic D (1998) Ferroelectric, dielectric and piezoelectric properties of ferroelectric thin films and ceramics. *Rep Prog Phys* 61:1267–1324
36. Binnig G, Rohrer H, Gerber C, Weibel E (1982) Tunneling through a controllable vacuum gap. *Appl Phys Lett* 40:178–180

37. Binning G, Rohrer H, Weibel E (1983) 7x7 Reconstruction on Si(111) resolved in real space. *Phys Rev Lett* 50:120–123
38. Gruverman A, Kholkin A (2006) Nanoscale ferroelectrics processing, characterization and future trends. *Rep Prog Phys* 69:2443–2474
39. Peter F (2006) Piezoresponse force microscopy and surface effects of perovskite ferroelectric nanostructures. Dissertation RWTH Aachen
40. Roelofs A (2004) Size effects in ferroelectric thin films. Dissertation RWTH Aachen
41. Peter F, Szot K, Waser R, Reichenberg B, Tiedke S, Spade J (2004) Piezoresponse in the light of surface adsorbates: Relevance of defined surface conditions for perovskite materials. *Appl Phys Lett* 85:2896–2898
42. Peter F, Kubacki J, Szot K, Reichenberg B, Waser R (2006) Influence of adsorbates on the piezoresponse of KNbO_3 . *Phys Status Solidi A* 203:616–624
43. Rüdiger A, Schneller T, Roelofs A, Schmitz T, Waser R (2005) Nanosize ferroelectric oxides—tracking down the superparaelectric limit. *Appl Phys A* 80:1247–1255
44. Sheehan PE, Whitman LJ, King WP, Nelson BA (2004) Nanoscale deposition of solid inks via thermal dip pen nanolithography. *Appl Phys Lett* 85:1589–1591
45. Szoszkiewicz R, Okada T, Jones SC, Li TD, King WP, Marder SR, Riedo E (2007) High-speed, sub-15 nm feature size thermochemical nanolithography. *Nano Lett* 7:1064–1069
46. Wang D, Kodali VK, Underwood WD II, Jarvholm JE, Okada T, Jones SC, Rumi M, Dai Z, King WP, Marder SR, Curtis JE, Riedo E (2009) Thermochemical nanolithography of multifunctional nanotemplates for assembling nano-objects. *Adv Funct Mater* 19:3696–3702
47. Wei Z, Wang D, Kim S, Kim S-Y, Hu Y, Yakes MK, Laracuente AR, Dai Z, Marder SR, Berger C, King WP, de Heer WA, Sheehan PE, Riedo E (2010) Nanoscale tunable reduction of graphene oxide for graphene electronics. *Science* 328:1373–1376
48. Kim S, Bastani Y, Lu H, King WP, Marder S, Sandhage KH, Gruverman A, Riedo E, Bassiri-Gharb N (2011) Direct fabrication of arbitrary-shaped ferroelectric nanostructures on plastic, glass, and silicon substrates. *Adv Mater* 23:3786–3790
49. Steigerwald JM, Murarka SP, Gutmann RJ (1997) Chemical mechanical planarization of microelectronic materials. Wiley, New York
50. ITRS (2011) The International Roadmap for Semiconductors: Interconnect. <http://www.itrs.net/Links/2011ITRS/2011Chapters/2011Interconnect.pdf>. Accessed 18 Feb 2013
51. Baney RH, Itoh M, Sakakibara A, Suzuki T (1995) Silsesquioxanes. *Chem Rev* 95:1409–1430
52. Maex K, Baklanov MR, Shamiryan D, Iacopi F, Brongersma SH, Yanovitskaya ZS (2003) Low dielectric constant materials for microelectronics. *J Appl Phys* 93:8793–8841
53. Clemens S, Schneller T, Waser R, Rüdiger A, Peter F, Kronholz S, Schmitz T, Tiedke S (2005) Integration of ferroelectric lead titanate nanoislands for direct hysteresis measurements. *Appl Phys Lett* 87:142906
54. Clemens S, Röhrig S, Rüdiger A, Schneller T, Waser R (2009) Embedded ferroelectric nanostructure arrays. *Nanotechnology* 20:075305–075310
55. Clemens S, Dippel A-C, Schneller T, Waser R, Rüdiger A, Röhrig S (2008) Direct electrical characterization of embedded ferroelectric lead titanate nanoislands. *J Appl Phys* 103:034113

Part V

Functions and Applications

The last part will summarize the different application areas of CSD derived functional oxide thin films. Because this area is huge, the focus is laid on those applications which are suitable for wet chemical processing. In general CSD is applicable, where no extremely small lateral dimensions, and 3-D folding have to be conformally coated. Thus for memory application gas phase based methods such as sputter deposition, metal organic chemical vapor deposition (MOCVD), atomic layer deposition (ALD), molecular beam epitaxy (MBE) are methods of choice. For small substrates, pulsed laser deposition (PLD) represents a very versatile technique. Another obstacle may be the requirement of ultrathin coatings. Although not impossible, there may occur difficulties in case of ultrathin coatings, i.e. thicknesses below $\sim 20\text{--}30$ nm. On the other hand this means that in almost all other cases CSD offers the potential to fabricate device quality films at moderate investment and precursor cost. Due to the high flexibility with regard to the coating method and stoichiometry, as well as the economic advantage, CSD offers moreover excellent possibilities in research labs for exploring new thin film materials or modifying compositions by addition of dopants for example. CSD methods can also enable the miniaturization of classical bulk devices such as multilayer ceramic capacitors (MLCCs—see Chap. 22) or solid oxide fuel cells (SOFCs—see Chap. 25) by replacement or supplementation of the standard oxide ceramic powder based technologies.

Ferroelectric capacitors consisting of PZT or strontium bismuth tantalates (SBT) are utilized as binary polarization state storage element in non-volatile ferroelectric random access memories (FeRAM). In low memory density FeRAM products, as well as in the early period of prototype production for high-density 4- or 32-Mbit FeRAMs, CSD was used by the industry to fabricate the functional ferroelectric oxide thin films [1–3]. Micro-electro-mechanical systems (MEMS) enable a direct and efficient transformation of mechanical to electric energy and vice versa. Using the piezoelectric and pyroelectric properties of PZT and related thin film materials for integration into MEMS provides in contrast to FeRAMs an almost ideal field for CSD. The processing and features of MEMS are detailed in Chap. 24. Meanwhile it is possible to automatize the deposition and crystallization process of PZT films on

wafer sizes up to 8 in. [4], which basically facilitates industrial fabrication. In general, MEMS devices are useful for various motion and force sensors, linear actuators, micromotors, acoustic and ultrasound devices, electromechanical microwave resonators, microcavity pumps, energy harvesting etc.

The pyroelectric effect of materials is exploited to detect temperature changes with an extremely high sensitivity. The most common devices are uncooled infrared (IR) detectors. Pyroelectric thin films based on perovskite-type complex oxides have been deposited by CSD, to be integrated into 1-D and 2-D arrays for intruder alarms, gas sensors, and IR cameras.

Although never applied in capacitors for DRAM applications, the success in fabrication of excellent high-permittivity films on noble metal (e.g. Au or Pt) coated semiconductor substrates enabled the integration of ferroelectric capacitors in GaAs MMICs (microwave monolithic integrated circuits) [5, 6] and decoupling capacitors [7, 8]. More recently it has been demonstrated BST and even PZT can be deposited in excellent quality on base metal substrates such as nickel and copper foils using carefully controlled crystallization conditions (temperature and corresponding atmosphere) [9–12]. The prerequisites and details of this approach are summarized in Chap. 23. Utilizing these substrates for ferroelectric thin films provides a viable solution for integrating embedded passive components into printing wiring boards (PWB). These results are also encouraging for lowering the individual layer thicknesses in MLCCs, in which the interlayer electrodes consist of nickel as well.

It is even possible to grow epitaxial superconducting yttrium barium copper oxide (YBCO) layers on highly textured nickel tapes of great lengths by combining the knowledge of (1) growing epitaxial films by CSD, (2) the specific requirement for growing YBCO on nickel, and (3) advanced coating techniques such as inkjet printing. The commercialization of this technique will significantly increase the energy efficiency of cables, motors, and generators and could hence contribute to the reduction of carbon dioxide emissions. All aspects of superconducting layers and examples for devices are reviewed in Chap. 27.

Other conducting films represent a further important class of functional thin film oxide materials the fabrication of which can be addressed by CSD. They comprise ion conducting (oxygen ion and proton conducting), electronically conducting, and mixed electronic/ionic conducting materials, as well as transparent conducting oxides (TCOs). Ion conducting oxides are frequently used as electrolytes in solid oxide fuel cells and sensors, and the mixed electronic/ionic conductors serve as cathode materials for the catalytic dissociation and reduction of the molecular oxygen in these devices. CSD methods can be applied to reduce the layer thicknesses and the annealing temperatures of these functional films. On the one hand this enables the fabrication of miniaturized SOFCs, “ μ -SOFC”. On the other hand a lowering of the operation temperatures of bulk SOFCs is expected, which in turn reduces deteriorating influences on the materials of the stack. The aspects of these materials and devices, as well as electronically conducting oxides, e.g. LaNiO_3 , including magnetoresistive films, e.g. $\text{La}_{0.67}\text{Ca}_{0.33}\text{MnO}_3$, are reviewed in Chap. 25. Due to their simultaneous transparency, TCOs represent an extra class

of conducting oxides and are thus presented in detail separately in Chap. 26. They are produced industrially on a large scale by sputtering methods for all kinds of display applications. Furthermore they are used in photoelectrochemical (PEC) devices for alternative energy conversion. As will be shown in Chap. 26, there are a number of innovative fields such as printed electronics and transparent p-n junctions where CSD processing of TCO thin films may play an important role, if combined with direct writing approaches such as inkjet printing.

The last two book chapter deal with optical applications of CSD derived thin films. Chapter 28 gives a survey on general strategies for antireflective (AR) coatings and how single- and multilayer interference-type films can be produced by sol-gel coating techniques. Finally, Chap. 29 reviews the possibilities of wet-chemical synthesis of luminescent thin films for integrated optical and optoelectronic devices. Examples for the application in devices such as active waveguides, displays, X-ray imaging systems, and solar cells are given.

The functions and applications presented above represent the most frequently studied areas in CSD technology. Although they cover the largest part of devices, which are accessible to CSD processing, there are certainly further fields of applications which have potential, but are less intensively studied by means of CSD yet. Besides the classical ferroelectric capacitor and piezo-MEMS applications it may be concluded that the application of CSD film processing for alternative energy device is a strong and growing domain for this technique.

In this sense the direct conversion of sun light to electrical power or chemical fuels has to be mentioned. Photoelectrochemical (PEC) water splitting yielding hydrogen, which can be stored and used as clean fuel, is of particular interest [13]. Among the plethora of functional oxide materials, which are reviewed concerning suitability for PEC water splitting in [14], TiO_2 and Fe_2O_3 are the most frequently studied wide-band gap semiconductors. Their advantages comprise abundance, nontoxicity, and electrochemical stability, but issues remain, which still lead to poor conversion efficiencies. Hematite ($\alpha\text{-Fe}_2\text{O}_3$) possesses a band gap of ~ 2.2 eV, which is suitable for visible light, but still has low photon conversion efficiency (IPCE) due to short hole diffusion lengths of 2–4 nm, low absorption coefficient, and very short excited state lifetime. For a recent review on the progress of hematite photoanodes the reader is referred to [15]. On the other hand TiO_2 , which was the first photoanode material where the PEC water splitting reaction was demonstrated [16], performs better but uses only a part of the solar spectrum due to the band gap in the UV range (3.2 eV). In order to improve and optimize these devices further basic research in various areas from materials and physical aspects to design criteria is required [17]. Besides new materials, which may be found by solution based combinatorial approaches [18], nanostructuring and bandgap engineering of hematite and titania are two promising possibilities to optimize the photoanodes. CSD offers a large potential because of cost efficiency, possibility of micro-/nanostructure control, and flexibility with regard to composition including the ease of dopant addition for tuning the bandgap. Two examples may serve to illustrate this potential without claiming to be comprehensive. In case of TiO_2 , mesoporous photoanode films prepared from a sol-gel type CSD process (EISA

process, see Chap. 10) featured a much higher maximum photocurrent density ($j_{\text{ph}} = 3.5 \text{ mA/cm}^2$) than the film which was classically prepared from pre-formed nanoparticles ($j_{\text{ph}} = 0.35 \text{ mA/cm}^2$) [19]. The other example concerns undoped and titania-doped hematite films, which were prepared by spin coating of the corresponding precursor solutions onto FTO¹-coated glass substrates and subsequent annealing at 500 °C [20]. The doped film showed the better PEC response.

References

1. Kato Y, Kaneko Y, Tanaka H, Kaibara K, Koyama S, Isogai K, Yamada T, Shimada Y (2007) Overview and future challenge of ferroelectric random access memory technologies. *Jpn J Appl Phys* 46:2157–2163
2. Lee SY, Kim HH, D. Jung DJ, Song YJ, Jang NW, Choi MK, Jeon BK, Lee YT, Lee KM, Joo SH, Park SO, Kim K (2001) Highly scalable sub-10F² 1T1C COB cell for high density FRAM. In: Symposium on VLSI technology digital technical papers, pp 111–112
3. Lee SY, Kim K (2002) Future 1T1C FRAM technologies for highly reliable, high density FRAM. In: IEDM technical digest, pp 547–550
4. Solarsemi product-flyer (2010) Microcluster automatic system platform. http://www.solarsemi.com/images/stories/flyer/02_MICROCLUSTER_flyer.pdf. Accessed 16 May 2013
5. Koizumi H, Noma A, Tanaka T, Kanazawa K, Ueda D (1996) A GaAs MMIC chip-set for mobile communications using on-chip ferroelectric capacitors. *IEEE J Solid-State Circuits* 31:835–840
6. Nagata S, Ueda T, Noma A, Koizumi H, Kanazawa K, Ishida H, Tanaka T, Ueda D, Kazumura M, Kano G, Paz De Araujo C (1993) A GaAs MMIC chip-set for mobile communications using on-chip ferroelectric capacitors. In: Proceedings IEEE international solid-state circuits conference digest of technical papers, pp 172–173
7. Imanaka Y, Shioga T, Baniecki JD (2002) Decoupling capacitor with low inductance for high-frequency digital applications. *FUJITSU Sci Tech J* 38:22–30
8. Dimos D, Lockwood SJ, Garino TJ, Al-Shareef HN, Schwartz RW (1996) Integrated decoupling capacitors using Pb(Zr,Ti)O₃ thin films. *Mater Res Soc Proc* 433:305–316
9. Kingon AI, Srinivasan S (2005) Lead zirconate titanate thin films directly on copper electrodes for ferroelectric, dielectric and piezoelectric applications. *Nat Mater* 4:233–237
10. Ihlefeld J, Laughlin B, Hunt-Lowery A, Borland W, Kingon A, Maria J-P (2005) Copper compatible barium titanate thin films for embedded passives. *J Electroceram* 14:95–102
11. Dawley JT, Clem PG (2002) Dielectric properties of random and < 100 > oriented SrTiO₃ and (Ba,Sr)TiO₃ thin films fabricated on < 100 > nickel tapes. *Appl Phys Lett* 81:3028–3030
12. Maria J-P, Cheek K, Streiffer S, Kim SH, Dunn G, Kingon A (2001) Lead zirconate titanate thin films on base-metal foils: an approach for embedded high-permittivity passive components. *J Am Ceram Soc* 84:2436–2438
13. Graetzel M (2001) Photoelectrochemical cells. *Nature* 414:338–344
14. Osterloh FE (2007) Inorganic materials as catalysts for photochemical splitting of water. *Chem Mater* 20:35–54
15. Sivula K, Le Formal F, Grätzel M (2011) Solar water splitting: progress using hematite ($\alpha\text{-Fe}_2\text{O}_3$) photoelectrodes. *ChemSusChem* 4:432–449

¹ Fluorine doped tin oxide (FTO) represents a TCO, which is frequently used in PEC devices.

16. Fujishima A, Honda K (1972) Electrochemical photolysis of water at a semiconductor electrode. *Nature* 238:37–38
17. Frank E, Osterloh FE, Parkinson BA (2011) Recent developments in solar water-splitting photocatalysis. *MRS Bull* 36:17–22
18. Woodhouse M, Herman GS, Parkinson BA (2005) Combinatorial approach to identification of catalysts for the photoelectrolysis of water. *Chem Mater* 17:4318–4324
19. Hartmann P, Lee D, Smarsly BM, Janek J (2010) Mesoporous TiO₂: comparison of classical sol-gel and nanoparticle based photoelectrodes for the water splitting reaction. *ACS Nano* 4:3147–3154
20. Lian X, Yang X, Liu S, Xu Y, Jiang C, Chen J, Wang R (2012) Enhanced photoelectrochemical performance of Ti-doped hematite thin films prepared by the sol-gel method. *Appl Surf Sci* 258:2307–2311

Chapter 22

Thin Film Multilayer Capacitors

Hiroyuki Kambara, Theodor Schneller, and Rainer Waser

22.1 Introduction

Capacitors such as ceramic capacitors, plastic film capacitors, mica capacitors, electrolytic capacitors, and electric double-layer capacitors (EDLC) in general play an important role in various kinds of electronic devices used in modern societies. They are produced in huge quantities, various shapes and either directly integrated on a suitable substrate like silicon or as discrete capacitors which are later mounted on the printed wiring boards by soldering (nowadays mainly by surface mounting—SMD technology). Typical examples for the latter case are different types of electrolytic capacitors and multilayer ceramic capacitors (MLCCs, Fig. 22.1). Especially MLCCs are one of the most widely used capacitors and more than 80 billion MLCC chips are manufactured worldwide each year [1].

Within the present chapter the application of ferroelectric and dielectric materials for capacitors will be reviewed with a focus on multilayer stacks. These multilayer stacks consist of alternating layers of electrode and dielectrics or ferroelectrics, respectively.

The continuing demand for further functionalities of the electronic devices in less space is a strong driving force for the increase of the capacitance per volume (volumetric efficiency—VE). This means that the layer thicknesses of the ceramic as well as the electrode layers need to decrease more and more. Figure 22.2

H. Kambara (✉)
Murata Manufacturing Co., Ltd., 10-1, Higashi Kotari 1-chome, Nagaokakyo-shi, Kyoto
617-8555, Japan
e-mail: kambara@murata.co.jp

T. Schneller • R. Waser
Institute of Electronic Engineering Materials (IWE II), RWTH Aachen University, D-52055
Aachen, Germany

JARA – Fundamentals of Future Information Technology, Jülich, Germany

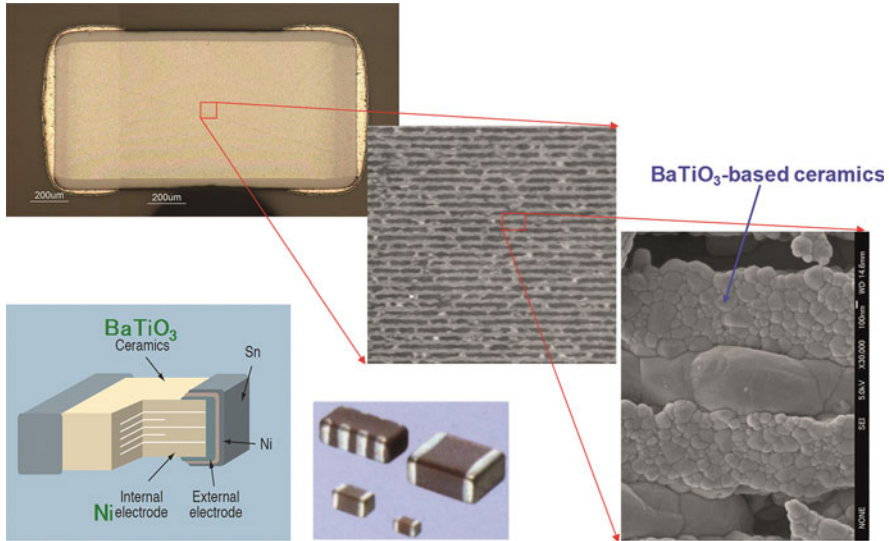


Fig. 22.1 Cross-section of a 1,608 size (external dimension of the chip $1.6 \text{ mm} \times 0.8 \text{ mm} \times 0.8 \text{ mm}$) MLCC consisting of $1 \mu\text{m}$ thick dielectrics with 400 layers and their illustrative pictures (Murata Manufacturing Co., Ltd.)

schematically summarizes the typical thickness ranges used for the ceramic layer material and the corresponding manufacturing technologies.

Films are typically differentiated into *thin films* comprising typical layer thicknesses below approx. $1 \mu\text{m}$ and *thick films* above approx. $1 \mu\text{m}$ (Fig. 22.2). This distinction is also related to the technologies which can be reasonably applied to fabricate the corresponding films. Although these are no absolute limits, it often makes economically no sense to use for example a classical thin film technique to prepare relatively thick films in the order of e.g. $5 \mu\text{m}$ due to possibly expensive equipment (vapor phase methods) and long deposition times or the tedious number of sequential coating steps in case of classical chemical solution deposition (CSD) [2]. On the other hand mature thick film technologies like tape casting of slurries containing ceramic particles reach limits in the thickness range below $\sim 0.8 \mu\text{m}$ due to the mechanical instability of the produced green foil for example and the need of using smaller and smaller ceramic particles in the diameter range below $150\text{--}200 \text{ nm}$ to maintain a minimum number of grains per layer of 5–6 [3]. The transition zone from $\sim 500 \text{ nm}$ to $\sim 0.8 \mu\text{m}$ might be denoted as *mesoscopic thickness* range which corresponds to the frontier zone of future MLCCs.

As said thin film ferroelectrics and dielectrics are generally defined as less than $1 \mu\text{m}$ (more typically less than $\sim 0.3 \mu\text{m}$) thickness. They require thick and sustainable substrates such as Si and Al_2O_3 beneath them because they are too thin to sustain themselves. Hence thin films need to grow on these thick substrates and the characteristics of the thin films are strongly influenced by structure, morphology, and thermal stress of the substrates. Highly oriented or epitaxial thin films can be

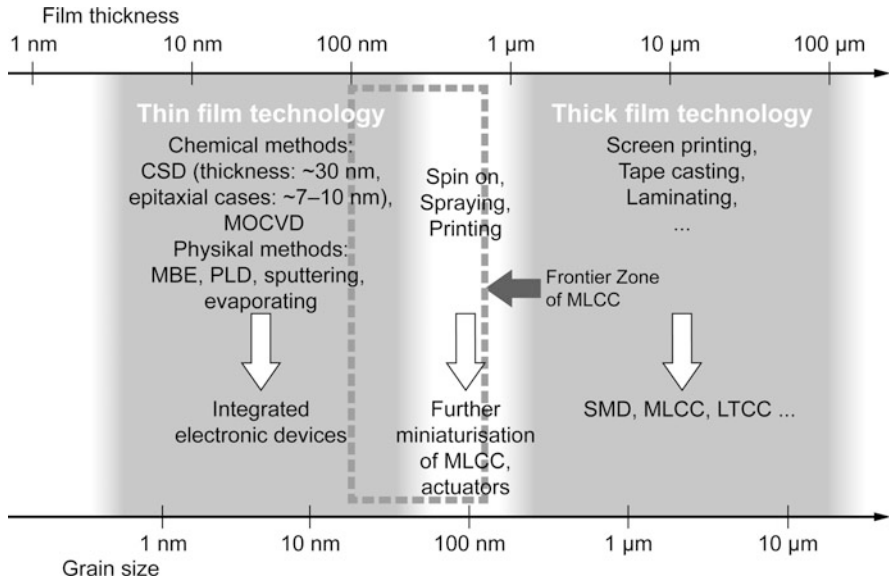


Fig. 22.2 Typical thickness ranges used for the ceramic layer material and the corresponding manufacturing technologies. Further miniaturization of MLCCs is required to achieve the “Frontier Zone” by advancing and utilizing film technologies

formed when the thin film and the substrate have similar lattice constant and structure. In addition the characteristics of the thin films depend on the thickness and most of the unique characteristics are attributed to their low thickness. Thin film capacitors of ~1,000 nm thickness have recently been studied in terms of film behavior for specific device application such as piezoelectric thin films for microelectromechanical systems (MEMS, see Chap. 24) [4] and ferroelectric thin films for nonvolatile memories [5].

In the following at first a short overview on the mature technology for the fabrication of multilayer ceramic capacitors (MLCC) is given. Then the question of further miniaturization will be addressed which gives the reasons for the introduction of new concepts by using thin film deposition technologies to prepare miniaturized multilayer capacitors—*thin film multilayer capacitors* (TMC). Hence some background information on the different thin film deposition technologies will be shortly reviewed. Finally the concepts for TMC’s will be described in more detail and the corresponding literature will be reviewed.

22.2 State of the Art MLCC's

As electronic devices have been downsized and more highly densified, the demand for MLCCs has been rapidly raised. The MLCC technology continues to be developed with respect to further miniaturization and higher capacitance. Conventional ceramic capacitors offer low dielectric loss and superior dielectric behavior at high frequency. However, the capacitances of the ceramic capacitance are below 10 μF , which lead to limited application. In contrast MLCCs have achieved higher capacitance up to 100 μF and realized wider range of applications substituting for tantalum capacitors and electrolyte capacitors. Furthermore superior characteristics such as high reliability, low equivalent series resistance (ESR) and low impedance can be obtained by MLCCs.

Originally in 1950s MLCCs started with Pt inner electrodes which are stable at high temperature and under oxidizing atmosphere. In 1970s Ag-Pd electrodes were newly introduced to MLCCs substituting for expensive Pt electrodes, which lowered the price of MLCCs drastically. Thereafter the technology for the mass-production of MLCCs improved rapidly and the price decreased drastically, which contributed to many electric devices. As MLCCs became more multi-layered, however, the cost of the inner electrode became more dominant due to the increase of price for the noble metals through energy crises in that time. Hence the technology for using base metal electrodes like Ni instead of the noble metals was required. The shift from Ag-Pd to Ni electrode was achieved in 1980s by modifying the composition of dielectrics and the annealing condition to suppress the reduction of dielectric layers under lower oxygen partial pressure.

MLCCs have met the requirement of high performance devices for mountability, performance, reliability, and low price substituting for parallel-plate capacitors since 1980s. The trends of MLCC products are downsizing, high capacitance, high frequency, high voltage, high electric power, and multi function. As for the material and processing technology, the introduction of base metal electrodes, fine grains for both ceramic materials and electrodes, and technology for thinner layer and multi layer, have improved the mass-production process and lowered the cost.

In order to achieve these goals one may take the following formula into account which allows one to estimate the capacitance of a MLCC (C_{MLCC}) [6]:

$$C_{MLCC} = [\epsilon_r \cdot \epsilon_0 \cdot (n - 1) \cdot s] / t \quad (22.1)$$

t denotes the thickness of the dielectric layer, s represents the overlapping area of the internal electrode, n is the number of dielectric layers, ϵ_0 is the permittivity of the free space, and ϵ_r is the relative permittivity of the dielectric film material.

Thus the key to increase the capacitance per volume (F/mm^3) of MLCCs is to stack as thin film as possible with as many layers as possible. In 1970s the thickness of the MLCC was 30–40 μm [7]. Thereafter the advance in thin film sheet technology and the improvement in dielectric materials and multi-layer technology brought about the thinner and more layered films in 1990s. Much thinner films such

as 3 μm thick films in the late 1990s and 1 μm in the early 2000s, of which capacitance per volume $20 \mu\text{F}/\text{mm}^3$ are comparable to those of tantalum capacitor and aluminum electrolytic capacitor, were realized [8].

22.2.1 *Trend to Miniaturization*

As high-tech electronic devices such as portable video cameras, lap top PCs and cell phones have been downsized in recent years, electric parts mounted in them have also been required to be smaller. The miniaturization of electronic devices and electric parts makes it possible to design the electronic circuits more flexible and manufacture new products of high value and new functions as well as to scale down the devices.

The surface area of chip capacitors has gotten smaller year by year from 1005 (external dimension of chip $1.0 \text{ mm} \times 0.5 \text{ mm}$) to 0402 ($0.4 \text{ mm} \times 0.2 \text{ mm}$). The latest ceramic coating technology has realized micron-order thick green sheets. However, it would be difficult to produce even thinner ceramic green sheet due to the difficulty in dispersing ceramic particles homogeneously and suppressing defect formation in such a thinner sheet. Furthermore it has generally been recognized that the properties of bulk dielectric material are often poor in thin films due to the intrinsic dead layers, defects, film stress, etc. Therefore the development of new methods to produce submicron dielectric layer have already been undertaken in order to achieve even higher capacitance densities. Hence classical thin film technologies were investigated due to their following typical advantages:

Classical thin film technologies can. . .

- control the orientation of the film by epitaxial nucleation (cp. Chap. 16) e.g. [9]
- lower the processing temperature.
- apply lower voltages to films.
- form microstructure and thin films like LSI (Large Scale Integration) and increase the element density.
- take advantage of the unique characteristics of thin films: for example, films consisting of a few atoms show unique characteristics called “size effect”.
- modify the film property maintaining the workability and the property of the substrates.
- make the most of the smooth surface, for example SAW device.
- deposit amorphous and crystalline films depending on the process condition.

Thin film dielectrics and ferroelectrics can be formed via the state of atom, and ion, respectively, or molecules by depositing raw materials on the substrate. Depending on the deposition method, they either directly nucleate and grow or form at first an amorphous layer which afterwards nucleates and grows into a crystalline thin film. Thin film methods basically allow one to form oriented materials on larger areas of the substrates.

Typically thin films can be prepared by a variety of methods such as metal-organic chemical vapor deposition (MOCVD) [10], aerosol chemical vapor deposition (ASCVD) [11], pulsed laser deposition (PLD) [12], sputtering, electrophoretic deposition (EPD) [13], hydrothermal-electrochemical method or chemical solution deposition (CSD) consisting of sol-gel and metallo-organic decomposition routes [2].

By gas phase techniques the raw materials are heated and then evaporated onto the substrates. Advantages of the MOCVD method are conformal coverage, high rate of film formation, and relatively precise control of composition. However, this method cost much with expensive devices and the productive efficiency is low, although the high cost can be lowered to some extent by mass-production. Therefore this method will be first introduced to products of high value such as ultra-small high capacitance capacitor on Si substrates or LCR circuit (electric circuit consisting of inductor L, capacitor C, and resistor R) multifunction device.

Electrophoresis is a coating method where electrically-charged ceramic particles or metal particles in a solvent are deposited as a thin film on a substrate by electric field. This method employs nonconductive substrate such as glass or carrier tape of which surface is given electrical conductivity by e.g. sputtering. Electrophoresis can control the thickness of the film easily by applied voltage and duration. More uniform and denser films without defects and higher rate of film formation compared to the conventional screen printing and doctor blade method can be realized [13]. This method will possibly lead to high productivity, for instance for inner electrodes of MLCCs.

The CSD method overcomes some of the limitations of thin film fabrication and offers advantages such as low cost, precise control of composition, relatively simple and flexible synthesizing route and conformal, continuous, large-area deposition via aerosol or dip coating. In CSD several dielectric layers are deposited subsequently, and therefore the dielectric properties such as dielectric constant and temperature coefficient of the capacitance can also be controlled by a deposition of graded compositions, which will be capable for the preparation of functional ceramic thin films.

Table 22.1 gives an overview on the pros and cons of the different main thin film deposition methods:

22.3 Design of TMC's

The requirement for multilayer structures of the ceramic capacitors with smaller size and larger capacitance has been raised for the application of integrated devices. The purpose of this miniaturization is to achieve a maximum capacitance per unit volume of MLCCs, i.e. volumetric efficiency (VE) with a larger dielectric constant, smaller dielectric and internal electrode thickness, and a larger number of layers.

Table 22.1 Comparison of characteristics of thin film deposition methods [9]

	Initial investment	Reproducibility of source compositions	Coating area	Epitaxy
Solution methods	Excellent	Excellent	Excellent	Not good ^a
MOCVD	Good	Not good	Good	Good
Sputtering	Good	Good	Excellent	Excellent
Laser ablation	Not good	Excellent	Not good	Excellent

^aIn the early days of CSD processing ultrathin films and epitaxial films were hardly possible to process. In the meantime the knowledge of the technology has improved considerably so that epitaxial [14, 15] and highly textured films, respectively, even on base metal substrates are possible [16]

The minimum layer thickness of MLCCs obtained by traditional powder-based fabrication techniques such as tape casting or printing processes has decreased to the micron order (Fig. 22.3).

Core-shell structures (Fig. 22.4), where grains consist of a ferroelectric “core” inside and a non-ferroelectric “shell” on the surface have been introduced to modify the dielectric properties without increasing the thickness of the layers. The so-called X7R materials (X7R: specification of EIA, Electronic Industry association) may serve as one practical example. High values of the dielectric constant ϵ_r (e.g. $\epsilon_r(25^\circ\text{C}) \approx 3,000$) result for these materials from the presence of ferroelectric cores inside the grains (“Core”) with a temperature coefficient ($\Delta\epsilon_{\text{max}}/\epsilon_r(25^\circ\text{C})$) of ϵ_r of -15% to $+15\%$ in the temperature range of -55°C to 125°C . Such structures can be obtained for example from Dy-doped BaTiO_3 , which shows a non-ferroelectric Dy-doped BaTiO_3 shell and a ferroelectric BaTiO_3 core in one grain. This exhibits smaller temperature dependence of the dielectric constant compared to those of pure BaTiO_3 and Dy-doped BaTiO_3 grains [17].

However, it is doubtful that the hitherto applied conventional ceramic methods using powders will be further applicable for the fabrication of submicron films, because the dielectric layer needs to have several grains (5–6) throughout the thickness of each dielectric layer in order to be suitably reliable [18]. If the number of dielectric grains per layer is too small, the resistivity of the film is lowered due to the generation of oxygen vacancies in the grains and therefore the leakage current increases when electric field concentrates on the vacancies especially at higher temperatures. Hence grains should be small enough in terms of reliability to compose the dielectric layer with as many grains as possible.

Therefore alternative techniques for the formation of thin film multilayer capacitors are required to decrease the film thickness down to the submicron order and the mesoscopic thickness range, respectively. Moreover simultaneously the temperature characteristics have to be controlled in order to fulfill the specifications of the capacitors. A design is applied with alternately arranged dielectric and electrode layers, which leads to an equivalent circuit of several capacitors in parallel. This principle is already well established for the standard ceramic multilayer capacitors used as surface mount devices. Additionally, the integrated capacitor is deposited on a SiO_2/Si substrate, which is compatible to

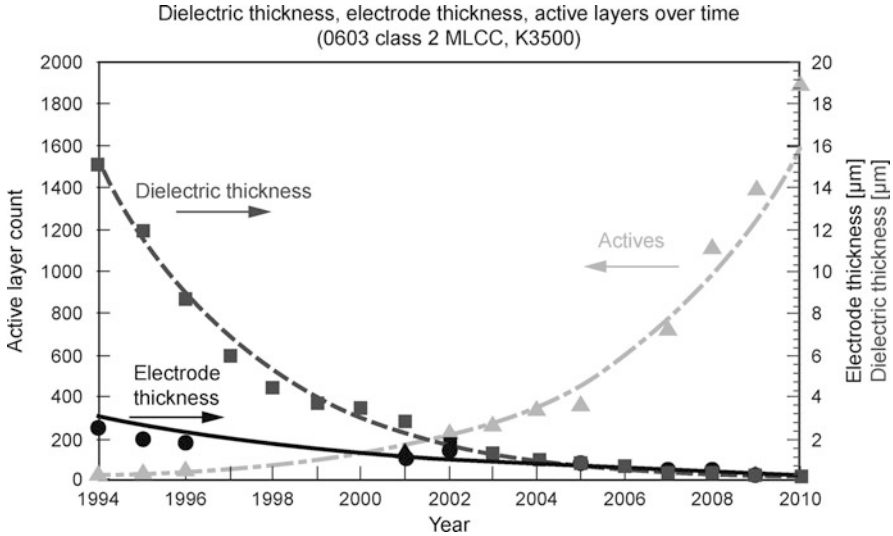


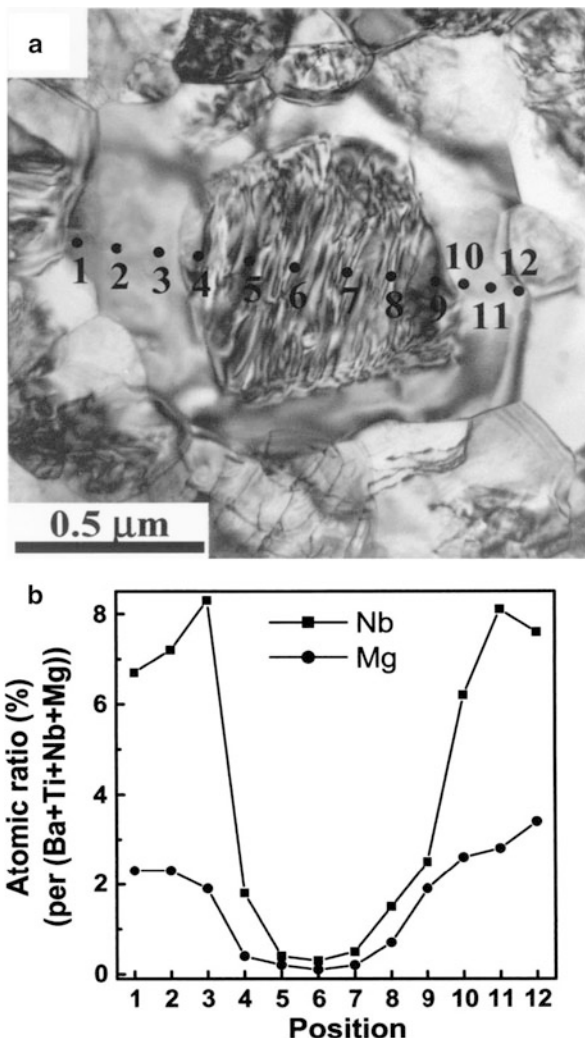
Fig. 22.3 Chart showing evolution and projection of major design parameters for MLCCs. Dielectric and electrode thicknesses decreased over the years as the capacitance has increased. This trend in decreasing thickness will slow down later than 2010 due to technical difficulties. Downsizing of external dimension of chips, however, still continues. Modified after [18]

the substrates used in the semiconductor industry [20–22] and allows basically for an integration of these capacitors into semiconductor devices.

22.3.1 Electrode Materials

Oxidation resistant electrodes such as Pt, Pd, and Ag/Pd have been mainly used for thin film dielectrics. These electrodes are expensive and therefore the requirement for low cost electrode materials is raised. However low cost base materials such as Ni, Cu, and Al have a lower oxidation resistance and a sensitivity of dielectric loss to low partial oxygen pressure [23]. The motivation for the use of base metal electrodes originates from MLCCs where noble metals have been replaced with Ni electrodes in BaTiO₃ based capacitors. Integration of such base-metal electrodes into multilayer capacitors and other bulk ceramic dielectric applications is nowadays well established [24], but development of thin-film integration on base metals has been more limited. Although complicated, the growth of thin dielectric layers on base-metal substrates in reducing atmospheres has often been successfully demonstrated and for details the reader is referred to Chap. 23 of this book. Beside the temperature/atmosphere profiles the selection of appropriate substrate materials is crucial; the metal should possess a high melting point, exhibit a close match of the linear coefficient of thermal expansion to the dielectric film, show low reactivity with the film, and permit good adhesion to the film [25]. BaTiO₃ and BST films with

Fig. 22.4 Example of a core shell structure of Nb- and Mg-doped BaTiO_3 [19]. The core shell structure of the grain is clearly observed from the TEM image (a) and Nb and Mg high concentrations at the shell region are indicated by STEM/EDS results below (b). Reproduced with permission from [19]. Copyright © 2004, John Wiley and Sons



sputtered-Ni bottom electrodes, for example, show that there is an increased grain growth and globulization of Ni electrodes with increase of annealing temperature at 700–900 °C under 3 % forming gas. The Ni layer annealed at 900 °C disintegrates already after 5-min duration; therefore Ni bottom electrodes should be annealed at 800 °C or less [26]. Furthermore the precise control of the oxygen partial pressure within the processing window is necessary to avoid the formation of base metal oxidation, oxygen vacancy-related increases in dielectric loss, and suppression of film dielectric constants [23] and to form simultaneously oxide ceramic thin film capacitors on the base metal. In a reducing atmosphere, the electron concentration increases with dissociation of oxygen atoms from e.g. BaTiO_3 , which is expressed

by the following reduction reaction [Eq. (22.2)] of the Kröger-Vink defect notation [27].



(O_o : neutral oxygen atom, V_o'' : oxygen vacancy, e^- : electron).

The generated electron enhances the conductivity of BaTiO_3 by electron hopping between $\text{Ti}^{4+}/\text{Ti}^{3+}$ [Eq. (22.3)].



The defect chemistry of BaTiO_3 was studied focusing on the development of Ni-MLCCs. Conduction electrons generated under reducing conditions are trapped by acceptors [e.g., Mn^{2+} , Ca^{2+} , and Cr^{3+}] on the B site of the perovskite improving the insulating resistance of the material. Bretos et al. proved that this principle also applies to CSD-derived BST thin films on Ni-foils by doping Mn^{2+} as acceptor according to the theory mentioned above and Nb^{5+} as B-site donor into already acceptor-doped BST, which reduced both the number of oxygen vacancies and their respective migration [28]. The leakage current density measured in the Mn, Nb-BST film reveals a decrease of almost one order of magnitude with respect to the undoped composition while maintaining low loss tangent of 0.02 and acceptable values of permittivity.

Even the formation of sol-gel derived PZT thin films directly on Cu foils has been demonstrated by a careful control of the oxygen partial pressure within a narrow processing window [29] and a specific optimization of the solution chemistry by e.g. chelating agent strength in order to avoid interfacial reactions [30].

Alternatively, conductive oxide electrodes such as LaNiO_3 and SrRuO_3 can be used instead of metal electrodes. Using chemical solutions for both the dielectric and electrode layers is an economical means of preparing thin films for TMCs. Multilayer capacitors of 100 nm-thick BaTiO_3 dielectrics and 20–30 nm-thick LaNiO_3 electrodes (Fig. 22.5) were successfully prepared by CSD without the need of using reducing atmospheres (Sect. 22.3.3) [31].

22.3.2 Dielectric Film Processing Issues

As already shortly pointed out in the introduction, there is a series of deposition techniques available for the fabrication of functional ceramic layers for the TMC. Although gas phase based deposition methods might sometimes yield slightly better performance of the ceramic thin films, these techniques are most probably too expensive for the later mass production of TMC's. Therefore in this section some aspects which are important for the wet chemical processing of the dielectric layer for TMC's are briefly summarized. For more details the reader is referred to the corresponding chapters of the present book.

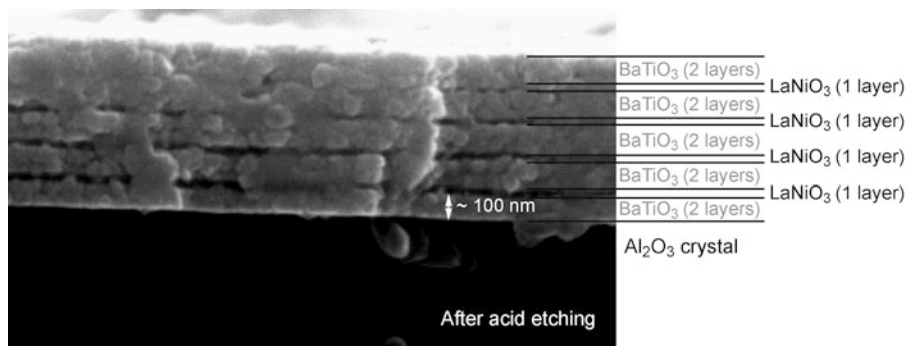


Fig. 22.5 Cross-section of multilayer capacitor consisting of BaTiO₃ and LaNiO₃ layers. Each layer is successively formed from 0.1 M BaTiO₃ and 0.3 M LaNiO₃ solution, respectively, by spin-coating, drying at 180 °C for 3 min, pyrolyzing at 260 °C for 3 min, and crystallization in RTA in O₂ at 650 °C for 1 min for the electrode layers and at 750 °C for 1 min for the BaTiO₃ layers. Reproduced with permission from [31]. Copyright © 2006, John Wiley and Sons

Basically in CSD processing films are fabricated by repeated coating/thermal annealing steps of a suitable precursor solution onto the substrate under various atmospheres (oxygen for noble metal substrates or in *p*O₂-controlled atmosphere for base metal substrates). Thereby the film micro structure is influenced by coating process, precursor chemistry, structure of the substrate and thermal processing such as crystallization temperature, heating ramp, and annealing atmosphere [2]. Usual thicknesses per individual coating step are in the range of 10–50 nm, which means that for a mesoscopic film thickness up to 50 coating cycles could be necessary, which of course is not practicable.

Different ways have been proposed to circumvent this. One possibility is to modify the chemistry of the precursor solutions (educts and viscosity-enhancing solvents). Thus, thicker layers of about 1 μm per coating step can be principally made by substitution of the usually used primary alcohols by multifunctional alcohols like e.g. 1,2-ethylenediol [32] or 1,3-propanediol [33]. Owing to the higher content of organics in these layers which has to be burned out, however, relatively high porosity is often found which leads to the limitation of the functionality of the resulting ceramic films. Furthermore the formation of cracks must be minded.

It should be noted that in case of PZT based films the control of microstructure and orientation is easier to obtain relatively independent on the layer thickness, due to the tendency to heterogeneous nucleation (see Chap. 17). Unlike in case of alkaline earth titanate based materials, the grain size and microstructure (columnar-grainy) is strongly dependent on the precursor chemistry, solution concentration, and the heating schedule [34, 35]. If one considers barium titanate, which is a preferred material due to its high dielectric constant, its low dielectric loss, and its low leakage current at simultaneous long-term stability, often carboxylate based precursors are used for CSD processing (see Chaps. 2 and 3). They all decompose via carbonate-like intermediates; however the decomposition pathway

and therefore their crystallization behaviours are dependent on the chain length of the hydrocarbon chain. “Long-chain” carboxylates like 2-ethylhexanoates decompose at lower temperatures ($\sim 450\text{--}550\text{ }^{\circ}\text{C}$) than “short-chain” carboxylates such as acetate and propionate, which means that the carbonates of the former are completely decomposed at $\sim 550\text{ }^{\circ}\text{C}$ and already at least partly crystalline while the latter decompose and crystallize only above $\sim 650\text{ }^{\circ}\text{C}$ [34].

This has also consequences on the microstructure. As already mentioned above higher porosity may result if more hydrocarbons have to be removed as gaseous CO_2 and H_2O . Moreover a high crystallization temperature leads to an increased densification and to larger grains. This is obviously due to the temperature activated mobility of the ions. Due to the tendency to nucleate in a homogeneous nucleation manner, the layer thickness of each coating is another factor influencing the microstructure of BTO films (see Chap. 17). If the individual layer thickness exceeds a critical value of approx. 10 nm/per coating a fine grained morphology is obtained with lower permittivity values compared to a columnar morphology [34]. $\text{SrBi}_4\text{TiO}_{15}$ may serve as further example where the strategy of ultrathin individual layer deposition is crucial. Thus highly c-axis oriented columnar $\text{SrBi}_4\text{Ti}_4\text{O}_{15}$ films on (111)Pt bottom electrodes could be obtained in spite of the quite different texture and lattice constants of the electroceramic thin film material and the electrode material ($\text{Pt} = 3.9\text{ \AA}$, $\text{SrBi}_4\text{Ti}_4\text{O}_{15} = 5.4\text{ \AA}$) [36]. These c-axis oriented $\text{SrBi}_4\text{Ti}_4\text{O}_{15}$ films show a unique property of stable dielectric constant at 200 in the range of -500 to 500 kV/cm , at a temperature of $25\text{--}200\text{ }^{\circ}\text{C}$, and in the thickness range of $55\text{--}160\text{ nm}$ [36].

In the P(L)ZT system a careful control of the Pb stoichiometry is essential to achieve phase purity and optimum dielectric properties [37]. Films with too little Pb-content form a low-K Pb-deficient pyrochlore phase which degrades the dielectric constant. The interaction between Pb and Pt bottom electrode and PbO volatilization from the surface of the film during thermal processing cannot be solved by simply increasing the amount of excess Pb in solution especially for Zr-rich compositions. The large amount of excess Pb results in the formation of a Pb rich intergranular phase. Therefore a combination of excess Pb in solution and post-pyrolysis deposition of a PbO cover coat improves film stoichiometry and dielectric properties.

These are only some examples of how the processing of precursor chemistry, coating method, and heating schedule affect the film morphology and orientation. In general CSD processes employ lower crystallization temperatures at $600\text{--}800\text{ }^{\circ}\text{C}$ compared to that of the conventional MLCCs at $1,000\text{--}1,300\text{ }^{\circ}\text{C}$ or more. This has a great advantage when putting them into mass-production because this process can reduce the production cost considerably and moreover decrease the damage of the film and film/electrode interfaces, respectively, while annealing.

Besides the classical CSD processes, thin ceramic or mesoscopic BTO layers can basically be also made by means of colloidal solutions of correspondingly composed nanoparticles with dispersed primary particle size of less than 100 nm [38, 39]. Such dispersions or colloidal solutions, respectively, can in principle be made by various methods. A very energy and cost consuming method is the

down-milling of coarse-grained ($>1 \mu\text{m}$) oxide ceramic powders, which are e.g. obtained by the so-called mixed oxide process with high-power mills by use of organic dispersing agents [40]. The redispersion of nanopowder aggregates made by hydrothermal or oxalate method with high-power stirrers or mills also by addition of organic stabilizers is known, too. For both methods normally suspensions with a polydisperse particle size distribution and primary particles scarcely smaller than 50 nm are obtained. Typically with such solutions, usable functional ceramic films can only be made with layer thickness around 1 μm . Thus for the manufacturing of mesoscopic ceramic films, colloidal solutions with narrow particle size distribution and average particle size of ca. 5–10 nm may be more favoured. Microemulsion mediated synthesis of BTO nanoparticles is one excellent possibility to prepare such particles in the desired grain size range [38, 39, 41]. In this approach the type of surfactant and co-surfactant as well as their concentration generally play an important role in the maximum amount of stable dispersed solid content. The 658 nm thick BTO film, displayed in Fig. 22.6, was prepared by only five subsequent spin-coating/annealing steps of a 5 weight percent BTO containing coating solution.

In this case a cationic surfactant, namely cetyltrimethyl ammonium bromide (CTAB) enabled a significantly higher solid content [42, 43] compared to the non-ionic surfactant used in [39]. Therefore less number of coatings is necessary to reach the desired thickness. The film shows a permittivity of around 400 which is comparable to other BTO-films with the same morphology prepared by classical CSD on the same type of substrate [34].

22.3.3 *Patterning Aspects*

At present, most MLCCs are prepared by tape casting layers of dielectric using dispersions of submicrometer ceramic powders. Metal electrodes are then screen printed in the desired patterns, and the devices are laminated, fired, and terminated [31]. For the case of thin film processes, it is more important that the deposition technique exhibit high precision of deposition to achieve the targeted capacitance value with great accuracy and repeatability [18], and the dielectric and electrode layers must be repetitively stacked without delamination or cracking [31].

High resolution patterning using photolithography or the like enables the production of structures with very fine spatial detail [18]. The photolithography which is a typical method for top down patterning requires a great deal of photoresist, developer, etching liquid, and remover, and has to use a photo mask for each layer. Figure 22.7 shows processing of TMC's by using photolithography, where a SrTiO_3 precursor solution is deposited onto a platinumized Si/SiO₂ wafer by spin coating and then the first intermediate Pt electrode layer is sputter-deposited.

After the deposition of the second dielectric layer a contact hole is wet-chemically etched to connect the bottom electrode to the intermediate electrode, which is deposited in the following step. These steps are subsequently

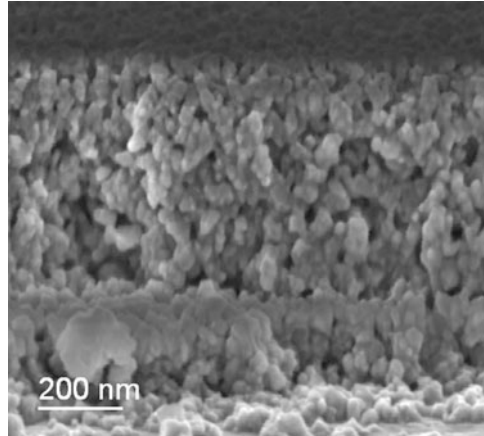


Fig. 22.6 Cross section SEM image of a 658 nm thick BTO film which was deposited by only five coating and annealing steps. After each coating step the film was annealed at 750 °C in a diffusion furnace. The film shows a polycrystalline microstructure with a relatively narrow grain-size distribution in the range of ~40 to 60 nm

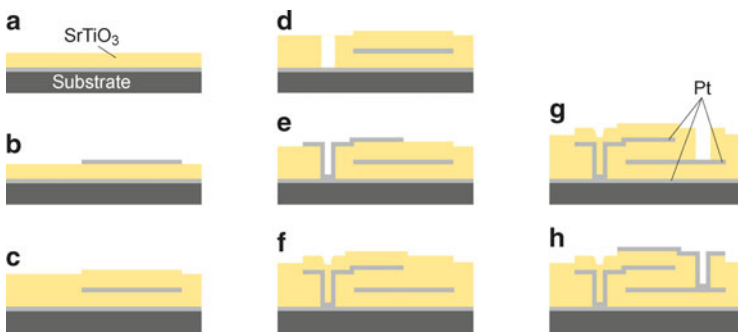


Fig. 22.7 Processing of the TMC: (a) sputter deposition of the Pt bottom electrode on a Ti/TiN adhesion layer and subsequently the dielectric SrTiO₃ deposition; (b) Pt electrode deposition; (c) deposition of the second SrTiO₃ layer; (d) wet-chemically etching of the contact hole; (e) Pt electrode deposition; (f) deposition of the third SrTiO₃ layer; (g) see (d); (h) see (e). Modified after [21]

repeated until the TMC consists of at least three dielectric and four electrode layers [21] as shown in Fig. 22.8. While this process has excellent alignment capabilities, it is expected to cost much when producing thin, light, and high density multilayered devices and to extend times for stack buildup.

Consequently, it is important to consider inexpensive, manufacturable approaches to making multilayer samples on a basis that will enable continued down-scaling of MLCC dielectric thicknesses [31].

Examples of thin film techniques realizing a uniform coating of large areas with relative ease, and with low cost are anodization, electrophoretic deposition and dip

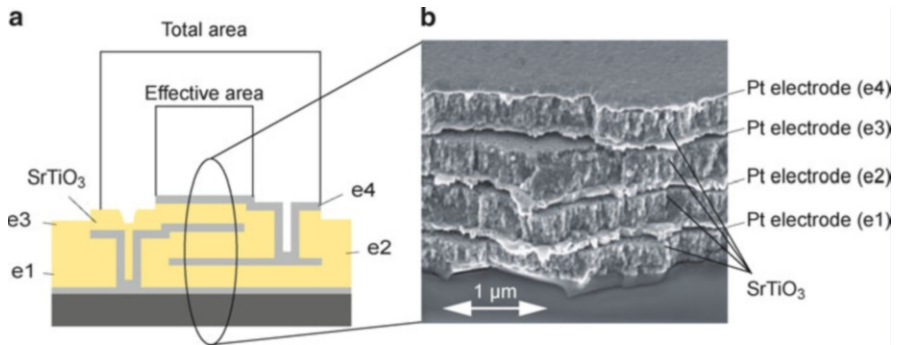


Fig. 22.8 (a) Schematic cross section (not to scale) of a TMC with three dielectric and four electrode layers (e1...e4) and introduction of the effective and total capacitor area; (b) the corresponding SEM micrograph. Modified after [21]

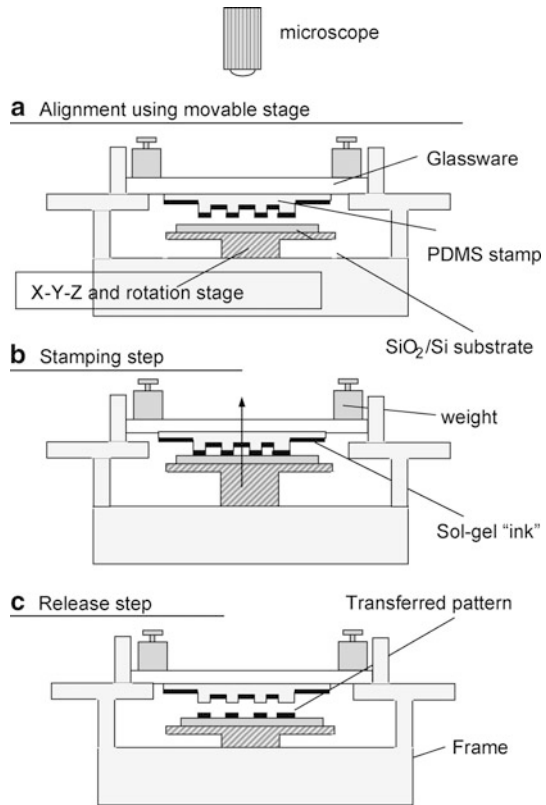
coating, or micropad stamping of sol-gel materials, ink jet deposition and the like [18].

Inkjet technology is becoming an increasingly attractive material deposition method which is capable of generating and placing droplets of polymers, solder, metallorganics, and metal nanoparticle solutions (see Chap. 13). This additive method employs less amount of raw materials compared to the conventional photolithography process, since it describes fine patterns only for necessary places and does not use photo masks, as a result this method leads to a cost effective, flexible, and data driven way to manufacture a wide variety of products in small quantities. Moreover direct patterning is also introduced for via holes between layers, therefore it is easy and environmentally friendly to stack multi-layers without using chemical solutions for etching [44].

BST films can be obtained by inkjet printing of metallo-organic precursors. By printing multiple stacks of the inkjet-printed layers, increasing thicknesses are achieved, which results in larger dielectric constants up to 1,000. Spray-printed silver contacts are also employed and demonstrated good adhesion and good electrical contact to the inkjet-printed BST films as a useful direct-write printing method [45].

Microcontact printing (μ CP) was first reported by Kumar and Whitesides using self-assembled monolayer (SAM) [46]. An inked patterned stamp [e.g. polydimethylsiloxane (PDMS)] is used to transfer self-assembled moieties [e.g. thiol] to flat or curved material surfaces to fabricate selective nano-structures. Then μ CP of electroceramic thin films such as PZT, LiNbO_3 , and Ta_2O_5 was introduced by using sol-gel deposition of ceramic oxides, followed by lift-off from the monolayer [47]. This process does not require complicated post-deposition ion beam or chemical etching. Further modification of μ CP has been done by Nagata et al. [31] for the fabrication of MLCCs without photolithography as shown schematically in Fig. 22.9.

Fig. 22.9 Schematic diagram of the alignment system (a) alignment, (b) stamping, and (c) release. Reproduced with permission from [31]. Copyright © 2006, John Wiley and Sons



μ CP of chemical solutions of both the dielectric [e.g. BaTiO₃] and electrode [e.g. LaNiO₃] layers was explored as an economical means for directly preparing patterned thin films for MLCCs. This process can produce features of sufficient flatness, homogeneity, and edge definition for dielectric and electrode layers in ultra-thin MLCCs with layer thickness in the range of $<0.2 \mu\text{m}$ [31]. However, in any printing method, it is difficult to develop thin film systems with very high layer counts, because thin film deposition rates are typically slower in the order of minutes per micron than that of the traditional MLCCs and thin film ceramic systems typically must be thermally processed every few layers to prevent the venting or shrinkage cracks during co-fire of the entire monolith.

Therefore, thin film printing methods will start with several layers for example for high frequency applications in order to address future demand of the very high VE application portion of the capacitor industry or the manufacture of embedded or integrated MLCC [18].

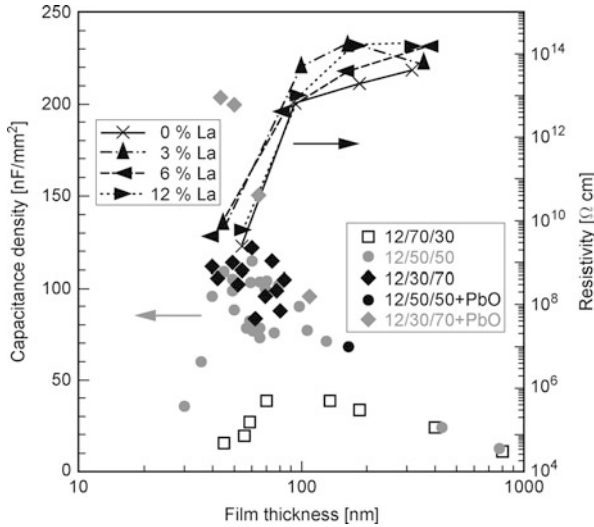


Fig. 22.10 Capacitance density and resistivity as a function of PLZT film thickness. The *numbers* indicated in the inset boxes show the La content and Zr/Ti ratio. Both decreases below 40–100 nm in ultrathin films. Post-annealing PbO treatment increases the value of the capacitance density (*full black circles and grey squares*), but has not yet been shown to reduce the observed threshold thickness. The capacitance is maximized near 100 nm because the decrease in dielectric constant is more rapid than the increase by reducing the layer thickness. Modified after [48]

22.3.4 Electrical Properties

As the thickness of dielectric thin films such as BaTiO₃-based and PZT-based perovskite materials decrease, the dielectric constant decreases significantly. This belongs to the so-called *size effects*. The magnitude of degradation and thickness ranges of the *size effects* often varies widely, depending on processing method, processing condition, and interaction between the film and substrate or electrode. For example, (Pb_x,La_{1-x})(Zr_y,Ti_{1-y})O₃(PLZT) films prepared by a CSD route on Pt/Ti/SiO₂/Si substrates show a decrease in capacitance [capacitance is directly proportional to dielectric constant, cp. Eq. (22.1)] at a thickness below 40–100 nm (Fig. 22.10) [48].

Another example shows decreasing dielectric constants of well known (Ba_{0.5}Sr_{0.5})TiO₃ (BST) films with a decrease of film thickness. Films prepared by RF magnetron sputtering on Pt/TiO₂/SiO₂/Si substrates show ϵ_r -values of 110 at 24 nm, 180 at 48 nm, 300 at 96 nm, 350 at 204 nm, and dielectric constant saturates for film thickness greater than 200 nm [49]. On the other hand some exceptions have also been reported concerning degradation-free material. Stable dielectric characteristics can be achieved with c-axis oriented bismuth layer-structured dielectric materials such as SrBi₄Ti₄O₁₅ thin films mentioned in Sect. 22.3.2, where the dielectric constant shows a constant value of 200 in the thickness range of 55–160 nm [36].

In general the decrease in dielectric constant is more rapid than the increase in capacitance gained by reducing the dielectric layer thickness, and therefore the areal capacitance density also maximizes near the threshold thickness [48]. This disadvantage of monolayered-thin film in dielectric property is overcome by a TMC structure. One example of such a thin film multilayer capacitor comprises BST thin layers deposited on MgO substrates by MOCVD and Pt electrodes patterned in a line shape [20]. Pt line patterns are successively RF magnetron sputtered on the Pt pattern lines below at a right angle. The capacitance of the multilayer capacitor increases with increase of the number of BST layers reaching 20 nF with five BST layers.

Another example for the TMC concept with three CSD-derived SrTiO₃ dielectric and four Pt electrode layers is shown in Fig. 22.9 [21]. One advantage of this design is the good ratio between the effective capacitance area and the total area (>40 % for a total area of 0.725 mm²). Dielectric properties of each dielectric layer show no significant difference. With this TMC design a further reduction of the capacitor size seems feasible, and possible applications would be decoupling or bypass capacitors in integrated circuits (ICs).

Watt compared these two different TMC approaches to his group's research based on top-down patterning methods (Table 22.2, columns 1–3) [50, 51]. The top-down mesa (table-like structure with a flat top) patterning approach is favorable with respect to the control of materials and interface properties since all deposition steps are completed on a flat substrate and without interference of patterning steps. Particulate contamination hazards are inherently reduced. The bottom-up approaches offer patterning simplicity but introduce complex material flow and more contamination hazards. As for process technology, CSD-based methods generally require less expensive equipment compared to chemical vapor deposition approaches.

Besides the predominantly for TMC investigated alkaline earth titanate based thin film materials, PLZT as alternative material was investigated in detail by Brenneka et al. [22, 37, 48]. The capacitance of such CSD-derived multilayer stacks of PLZT connected in parallel also increases essentially linearly with the number of layers, e.g. from 130 nF with one layer to 210 nF with two layers, and 290 nF with three layers of 120 nm thickness per layer as shown by Brenneka et al. [22] (full black circles in Fig. 22.11a).

By optimizing this approach multilayer stacks with up to ten layers and individual layers down to 20 nm have been prepared. Dissipation factors of the films measured at 1 kHz ranges from 0.02 to 0.03 and are independent of both film thickness and the number of dielectric layers [22].

However, it should be noted that the surface morphology of the top layer is in many cases rougher than that of single-layered films. The roughness of the films increased with increase of layer numbers, resulting in enhancement of leakage current from 10⁻⁷ A/cm² at 3 V with a single-layered BST thin film to 10⁻⁵ A/cm² with a five-layered film [20].

A thin film MLCC with 11 layers of amorphous STO dielectric layers prepared by aerosol chemical vapor deposition (ASCVD, cp. Chap. 12) overcomes this

Table 22.2 Updated comparative review of reports on different TMC concepts based on [50]

Features	Takeshima et al. (1997) [20]	Grossmann et al. (1998) [21]	Watt et al. (1998) [49]	Brennecka et al. (2008) [22]	Nagata et al. (2006) [31]	Wang et al. (2006) [11]
Substrate	Pt(111)/MgO	Pt/SiO ₂ /Si	Pt/SiO ₂ /Si	Pt/Ti/SiO ₂ /Si	LaNiO ₃	Pt/Al ₂ O ₃
Ferroelectric material	Ba _{0.6} Sr _{0.4} TiO ₃	SrTiO ₃	Ba _{0.7} Sr _{0.3} TiO ₃	Pb _{0.12} La _{0.88} Zr _{0.3} Ti _{0.7} O ₃	BaTiO ₃	SrTiO ₃
Deposition method	MOCVD	CSD	CSD	CSD	μCP assisted CSD	ASCVD
Deposition-pattern-termining-sequence	Bottom-up dep.-pattern level-by-level	Bottom-up dep.-pattern level-by-level	Top-down patterning after all depositions	Bottom-up dep.-level-by-level	Bottom-up dep.-pattern level-by-level	Bottom-up dep.-pattern level-by-level
Electrode configuration	Intersecting rectangles	Intersecting rectangles	Mesa (pyramid) structure	Alternate-layer electrode	alternate-layer electrode ^a	alternate-layer electrode
Multi-level electrode access	Overlapping pads at die-edge	Vias in high-dielectric	Vias in low-e inter-layer dielectric	Vias in high-e dielectric	Vias in high-e dielectric ^b	Vias in high-e dielectric
No. of MLC levels	5	3	4	3 ^c	1 ^d	10
Capacitance density @1 kHz	126 nF/mm ²	15 nF/mm ²	120 nF/mm ²	600 nF/mm ^{2e}	(ε _r = 800 at <200 nm on Ni foil)	9 nF/mm ²

^aThe feasibility of the μ-CP approach is presented [31] by means of an array of single layer LNO/BTO/LNO capacitors. From this setup an alternate layer approach similar to that presented in [22] may be assumed for real multilayer stacks fabricated by μ-CP

^bIn [31] no direct information about the electrode access is given. Probably it can be realized by further aligned μ-CP processing, where the bottom and top contacts are naturally brought into contact by this additional processing approach

^cUp to five levels are demonstrated, but the capacitance value given here corresponds to that of three level

^dAccording to (a) only one level is shown. However in another part of [31] it is demonstrated by means of five alternating LNO-BTO layers that multilayer stacking of these material combination is basically possible

^eThis is the maximum capacitance density calculated from the film with 50 nm dielectric layer thickness in Fig. 2.2.11a, three levels and the electrode size of 1 mm² given in [22]

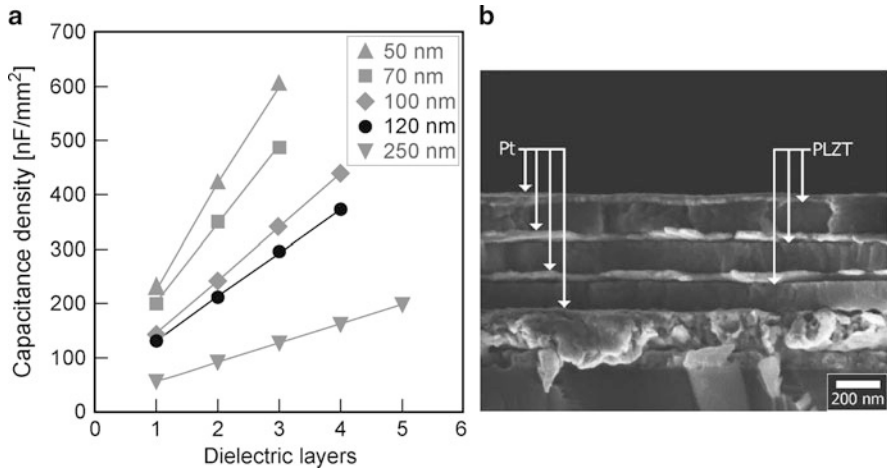


Fig. 22.11 (a) Capacitance measurements of various multilayer stacks with different individual layer thicknesses and number of multilayers connected in a parallel electrode configuration. They show a linear increase with the number of dielectric layers, regardless of the film thickness. (b) Exemplary SEM image of a corresponding Pt/PLZT/Pt multilayer stack with three 120 nm thick PLZT layers as indicated in the image. Reproduced with permission from [22]. Copyright Cambridge University Press

degradation showing slightly changed surface roughness with increasing number of layers [11]. Moreover leakage currents of both, ten layers and the single layer show an excellent low value of less than 10^{-7} A/cm² at 5 V_{DC}. The capacitance density, however, indicates a little bit low value of 900 nF/cm² at 1–100 kHz with ten layers and abrupt degradation of capacitance and dielectric loss at >100 kHz, which could be related to the effect of larger electrode resistance due to the larger effective electrode area (2×2 mm²).

Difficulties with property degradation and/or reliability shown above have to be improved by devising the design of the TMC and limiting the thickness of the structure in order to take advantage of the increased capacitance that should accompany thinner layers. Hence one idea could be proposed by utilizing the “*transferring method*” which was originally developed for 3-dimensional packaging [52]. To meet the demand for miniaturization of printed circuit boards, thin film capacitors should be packaged 3-dimensionally rather than surface-mounted on the board. However, ceramic capacitors typically need high-temperature annealing to be crystallized, which leads to degradation of the substrates with low melting point. Thus, ceramic capacitors have to be annealed in advance on a substrate with high melting point such as Pt/SiO₂/Si. Then dielectric layers (PZT) are formed by CSD with sputtered Pt top electrodes. This set of “Pt/PZT/Pt” can be removed from the SiO₂/Si substrate due to the weak adhesion strength between Pt bottom electrode and SiO₂ that is inversely proportional to the thickness of the Pt bottom electrode. Lastly the set of Pt/PZT/Pt is transferred into a package as a thin film capacitor which does not need thermal treatment any more.

By taking advantage of this method, it might be possible to form TMC structures by stacking the preformed set of electrode/dielectric/electrode layers instead of the conventional layer by layer deposition/annealing process. Furthermore, this method could increase the chance of introducing base metal electrodes for TMCs. For the example of the PZT/Pt bottom electrode, a base metal top electrode such as Cu can be evaporated onto PZT to form Cu/PZT/Pt layer and then these sets are stacked to form the TMC structure.

Table 22.2 shows a summary of the results obtained in the field of TMC's so far.

22.4 Summary and Outlook

As electronic devices have been downsized and more highly densified, the demand for MLCCs has been rapidly raised. The MLCC technology continues to be developed with respect to further miniaturization and higher capacitance. However mature thick film technologies like tape casting of slurries containing ceramic particles reach limits in the thickness range below $\sim 0.8 \mu\text{m}$. Therefore the development of new methods to produce submicron dielectric layer have already been undertaken in order to achieve even higher capacitance densities.

The CSD method overcomes some of the limitations of thin film fabrication and offers advantages such as low cost, precise control of composition, relatively simple and flexible synthesizing route, and continuous, large-area deposition. Thin film techniques realizing uniform coating with relative ease and low cost are anodization, electrophoretic deposition and dip-coating, or micropad stamping of sol-gel materials, inkjet deposition and the like.

A TMC design is applied with alternately arranged dielectric and electrode layers, which leads to an equivalent circuit of several capacitors in parallel. In general the decrease in dielectric constant is more rapid than the increase in capacitance gained by reducing the dielectric layer thickness. This disadvantage concerning dielectric properties of monolayered-thin films may be surmounted by the TMC approach. The capacitance of BST, STO, and PLZT multilayer stacks increases with the number of layers. Difficulties with reliability have to be improved by devising the design of the TMCs and limiting the thickness of the structure in order to take advantage of increased capacitance that should accompany thinner layers.

References

1. Carter CB, Norton MG (2007) Ceramic materials: science and engineering. Springer, New York, NY
2. Schwartz RW, Schneller T, Waser R (2004) Chemical solution deposition of electronic oxide films. *C R Chim* 7:433–461

3. Tsurumi T (2008) Technology in the future of high capacity multilayer ceramics capacitor. *Mater Integr* 21:59–70
4. Trolrier-Mckinstry S, Muralt P (2004) Thin film piezoelectrics for MEMS. *J Electroceram* 12:7–17
5. Kim SH, Kim DJ, Im J, Kim CE, Kingon AI (1999) Ferroelectric properties of new chemical solution derived SBT thin films for non-volatile memory devices. *J Sol-Gel Sci Technol* 16:57–63
6. Kishi H, Mizuno Y, Chazono H (2003) Base-metal electrode-multilayer ceramic capacitors: past, present and future perspectives. *Jpn J Appl Phys* 42:1–15
7. Fabricius JH, Olsen AG (1958) Monolithic structure – a new concept for ceramic capacitors. *Sprague Technical Paper* 58-6, pp. 85–96
8. Wakino K, Sato S, Ushiro T, Sakabe Y (1983) Large capacitance multilayer ceramic capacitor with base metal electrode. In: *Proceedings of the 3rd, CARTS, capacitor and resistor symposium*, pp. 169–172
9. Tani T (1994) Solution-derived ferroelectric thin films. *Toyota Central Res Cent R&D Rev* 29 (4):1–12
10. Watanabe T, Funakubo H (2006) Controlled crystal growth of layered-perovskite thin films as an approach to study their basic properties. *J Appl Phys* 100:051602
11. Wang S, Kawase A, Ogawa H (2006) Preparation and characterization of multilayer capacitor with SrTiO₃ thin films by aerosol chemical vapor deposition. *Jpn J Appl Phys* 45:7252–7257
12. Tay ST, Huan CH, Wee ATS, Liu R, Goh WC, Ong CK, Chen GS (2002) Substrate temperature studies of SrBi₂(Ta_{1-x}Nb_x)₂O₉ grown by pulsed laser ablation deposition. *J Vac Sci Technol* 20:125–131
13. Randall CA (1999) In: *Proceedings of 9th US-Japan seminar on dielectric and piezoelectric ceramics*, pp. 7–14
14. Lange FF (1996) Chemical solution routes to single-crystal thin films. *Science* 273:903–909
15. Hasenkox U, Mitze C, Waser R, Arons RR, Pommer J, Güntherodt G (1999) Chemical solution deposition of epitaxial La_{1-x}(Ca,Sr)_xMnO₃ thin films. *J Electroceram* 3:255–260
16. Dawley JT, Ong RJ, Clem PG (2002) Chemical solution deposition of <100>-oriented SrTiO₃ buffer layers on Ni substrates. *J Mater Res* 17:1678–1685
17. Yoneda Y, Hosokawa T, Omori N, Takeuchi S (1996) Relationship between microstructure and characteristics of multilayer capacitors having core-shell structure. In: *The 10th European passive components symposium, CARTS EUROPE '96, Nice, France, 7–11 Oct 1996*, pp. 11–16
18. Randall M, Skamser D, Kinard T, Qazi J, Tajuddin A, Trolrier-McKinstry S, Randall C, Ko SW, Dechakupt T (2007) Thin film MLCC. In: *Electronic components, assemblies and materials association (ECA), Arlington, VA CARTS 2007 symposium proceedings, Albuquerque, NM, March 2007*, pp. 1–12
19. Yoon SH, Lee JH, Kim DY, Hwang NM (2002) Core-shell structure of acceptor-rich, coarse barium titanate grains. *J Am Ceram Soc* 85:3111–3113
20. Takeshima Y, Shiratsuyu K, Takagi H, Sakabe Y (1997) Preparation and dielectric properties of the multilayer capacitor with (Ba,Sr)TiO₃ thin layers by metalorganic chemical vapor deposition. *Jpn J Appl Phys* 36:5870–5873
21. Grossmann M, Slowak R, Hoffmann S, John H, Waser R (1999) A novel integrated thin film capacitor realized by a multilayer ceramic electrode sandwich structure. *J Eur Ceram Soc* 19:1413–1415
22. Brennecka GL, Parish CM, Tuttle BA, Brewer LN (2008) Multilayer thin and ultrathin film capacitors fabricated by chemical solution deposition. *J Mater Res* 23:176–181
23. Dawley JT, Clem PG (2002) Dielectric properties of random and <100> oriented SrTiO₃ and (Ba,Sr)TiO₃ thin films fabricated on <100> nickel tapes. *Appl Phys Lett* 81:3028–3030
24. Hennings DFK (2001) Dielectric materials for sintering in reducing atmospheres. *J Eur Ceram Soc* 21:1637–1642

25. Zou Q, Ruda HE, Yacobi BG, Saegusa K, Farrell M (2000) Dielectric properties of lead zirconatetitanate thin films deposited on metal foils. *Appl Phys Lett* 77:1038–1040
26. Halder S, Schneller T, Waser R, Thomas F (2007) Microstructure and electrical properties of BaTiO₃ and (Ba,Sr)TiO₃ ferroelectric thin films on nickel electrodes. *J Sol-Gel Sci Technol* 42:203–207
27. Kröger FA, Vink HJ, Seitz F, Turnbull D (eds) (1956) *Solid State Physics*, vol 3. Academic, New York, NY, pp 307–435
28. Bretos I, Schneller T, Waser R, Hennings DF, Halder S, Thomas F (2010) Compositional substitutions and aliovalent doping of BaTiO₃-based thin films on nickel foils prepared by chemical solution deposition. *J Am Ceram Soc* 93:506–515
29. Kingon AI, Srinivasan S (2005) Lead zirconate titanate thin films directly on copper electrodes for ferroelectric, dielectric and piezoelectric applications. *Nat Mater* 4:233–237
30. Losego MD, Ihlefeld JF, Maria JP (2008) Importance of solution chemistry in preparing sol-gel PZT thin films directly on copper surfaces. *Chem Mater* 20:303–307
31. Nagata H, Ko SW, Hong E, Randall CA, Trolrier-McKinstry S, Pinceloup P, Skamser D, Randall M, Tajuddin A (2006) Microcontact printed BaTiO₃ and LaNiO₃ thin films for capacitors. *J Am Ceram Soc* 89:2816–2821
32. Yi G, Wu Z, Sayer M (2005) Preparation of Pb(Zr,Ti)O₃ thin films by sol gel processing: Electrical, optical, and electro-optical properties. *J Appl Phys* 64:2717–2724
33. Tu YL, Milne SJ (1995) Characterization of single layer PZT (53/47) films prepared from an air-stable sol-gel route. *J Mater Res* 10:3222–3231
34. Hasenkox U, Hoffmann S, Waser R (1998) Influence of precursor chemistry on the formation of MTiO₃ (M = Ba, Sr) ceramic thin films. *J Sol-Gel Sci Technol* 12:67–79
35. Hoffmann S, Waser R (1999) Control of the morphology of CSD-prepared (Ba,Sr)TiO₃ thin films. *J Eur Ceram Soc* 19:1339–1343
36. Kambara H, Schneller T, Sakabe Y, Waser R (2009) Dielectric properties of highly c-axis oriented chemical solution deposition derived SrBi₄Ti₄O₁₅ thin films. *Phys Stat Solidi A* 206:157–166
37. Brennecka GL, Tuttle BA (2007) Fabrication of ultrathin film capacitors by chemical solution deposition. *J Mater Res* 22:2868–2874
38. Pithan C, Schneller T, Shiratori Y, Majumder SB, Haegel FH, Dornseiffer J, Waser R (2006) Microemulsion mediated synthesis of nanocrystalline BaTiO₃: possibilities, potential and perspectives. *Int J Mat Res (formerly Z Materialkd)* 97:499–507
39. Yamashita Y, Yamamoto H, Sakabe Y (2004) Dielectric properties of BaTiO₃ thin films derived from clear emulsion of well-dispersed nanosized BaTiO₃ particles. *Jpn J Appl Phys* 43:6521–6524
40. Pithan C, Hennings D, Waser R (2005) Progress in the synthesis of nano-crystalline BaTiO₃ powders for MLCC. *Int J Appl Ceram Technol* 2:1–14
41. Beck C, Härtl W, Hempelmann R (1998) Size-controlled synthesis of nano-crystalline BaTiO₃ by a sol-gel type hydrolysis in microemulsion provided nanoreactors. *J Mater Res* 13:3174–3180
42. Schneller T, Pithan C, Dornseiffer J, Hägel FH, Waser R (2006) Herstellung von Beschichtungs-lösungen nebst hergestellten Produkten. DE 102006025770.7
43. Schneller T, Halder S, Waser R, Pithan C, Dornseiffer J, Shiratori Y, Houben L, Vyshnavi N, Majumder SB (2011) Nanocomposite thin films for miniaturized multi-layer ceramic capacitors prepared from barium titanate nanoparticle based hybrid solutions. *J Mater Chem* 21:7953–7965
44. Shah VG, Hayes DJ (2002) Fabrication of passive elements using ink-jet technology. IMAPS ATW on passive integration. MicroFab Technologies, Inc., Plano, TX, pp 1–6
45. Kaydanova T, Miedaner A, Perkins JD, Curtis C, Alleman JL, Ginley DS (2007) Direct-write inkjet printing for fabrication of barium strontium titanate-based tunable circuits. *Thin Solid Films* 515:3820–3824

46. Kumar A, Whitesides GM (1993) Features of gold having micrometer to centimeter dimensions can be formed through a combination of stamping with an elastomeric stamp and an alkanethiol “ink” followed by chemical etching. *Appl Phys Lett* 63:2002–2004
47. Payne D, Clem PG (1999) Monolayer-mediated patterning of integrated electroceramics. *J Electroceram* 3(2):163–172
48. Brenneka GL, Parish CM, Tuttle BA, Rodriguez MA, Brewer LN, Wheeler JS (2008) TF026. In: Proceedings of the 17th IEEE international symposium on the applications of ferroelectrics (ISAF 2008), vol 3, pp. 1–4
49. Padmini P, Taylor TR, Lefevre MJ, Nagra AS, York RA, Speck JS (1999) Realization of high tunability barium strontium titanate thin films by rf magnetron sputtering. *Appl Phys Lett* 75:3186–3188
50. Watt MM (1999) Process engineering issues of CSD-based thin-film multi-level ceramic capacitors. *Integr Ferroelectr* 26:163–186
51. Watt MM, Woo P, Rywak T, McNeil L, Kassam A, Joshi V, Cushiario JD, Melnick BM (1998) Feasibility demonstration of a multi-level thin film BST capacitor technology. In: ISAF98. Proceedings of the 11th IEEE international symposium on applications of ferroelectrics, pp. 11–14
52. Tomioka F, Hosono T, Iimura K, Ichiki M, Suga T, Itoh T (2011) Peeling property and application of ferroelectric thin film structure. In: Proceedings of the 25th spring conference for Japan institute of electronics packaging, pp. 343–344

Chapter 23

Base Metal Bottom Electrodes

Jon F. Ihlefeld, Mark D. Losego, and Jon-Paul Maria

23.1 Introduction: Integrating Electroceramic Thin Films with Base Metals

For a number of applications, rigid substrates and the expense associated with noble metal electrodes are not consistent with preferred manufacturing methods or cost considerations. It would be desirable in these cases to be able to transfer the established deposition processes to flexible and inexpensive substrates. Several groups have investigated the integration of chemical solution deposited electroceramic thin films with base metal substrates. Initial efforts focused on depositing low crystallization temperature ferroelectric films based upon $\text{Pb}(\text{Zr},\text{Ti})\text{O}_3$ onto non-noble metallic substrates, such as titanium, aluminum, nickel alloys, brass, and stainless steel [1–6]. With few exceptions these efforts focused on limiting processing temperatures in an attempt to prevent substrate oxidation and subsequent reactions. Later studies focused on utilizing buffer layers to minimize reactions with underlying base metal substrate. Two general groups of buffer layers were investigated: insulating or poorly conducting buffers [7, 8] and conductive buffer layers [9–14]. Both have been used with varying degrees of success. Insulating buffers allow for oxide film integration while preventing degradation of the metallic substrate, but at the expense of other properties such as capacitance density. Conductive buffer layers allow for films to be

J.F. Ihlefeld (✉)

Sandia National Laboratories, Albuquerque, NM 87185, USA

e-mail: jihlefe@sandia.gov

M.D. Losego

Department of Chemical and Biomolecular Engineering, North Carolina State University, Raleigh, NC 27695, USA

J.-P. Maria

Department of Materials Science and Engineering, North Carolina State University, Raleigh, NC 27695, USA

processed while maintaining the desired dielectric characteristics, but add complexity to processing that may limit mass production.

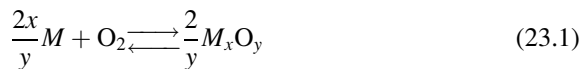
In this chapter we describe two methods for integrating electroceramic thin films with base metal substrates with a resulting embodiment devoid of deleterious interfacial phases. The two methods can be divided into an approach based on utilizing the thermodynamics of oxidation of conventional thin film elements and base metals (Sect. 23.2) and a kinetic approach to preventing interfacial reactions for systems where the thermodynamic equilibrium is less favorable (Sect. 23.3).

23.2 Equilibrium Approaches to Oxide-Base Metal Integration

The methods for equilibrium processing of oxide ceramics with base metals were established in the 1960s for integrating barium titanate with nickel and iron electrodes [15, 16]. By co-firing manganese-doped barium titanate with these electrodes using a hydrogen-rich atmosphere, insulating ceramic monoliths with base-metal electrodes were realized. The success of this approach owes itself to the thermodynamic equilibrium established between the oxides of barium, titanium, and manganese and the base metals under the reductive processing conditions. This method is the basis on which the multilayer capacitor industry manufactures multilayer ceramic capacitors on inexpensive nickel-based electrodes [17] and these same approaches have recently been implemented in thin film technology by several groups [18–21].

23.2.1 Thermodynamics of Oxidation

The equilibrium method to processing oxide films integrated with base metals can be understood by examining oxidation thermodynamics. Generically, the thermodynamic equations for metal oxidation can be expressed by considering the reaction of a metal, M , with oxygen to form a metal oxide, M_xO_y as in Eq. (23.1):



As with any chemical reaction, this will proceed according to an equilibrium constant, K , that is dependent upon the activities of all system components as shown in Eq. (23.2).

$$K = \frac{a_{M_xO_y}^{2/y}}{a_M^{2x/y} pO_2} \approx \frac{1}{pO_2} \quad (23.2)$$

The activities of solids can be assumed to be unity, which reduces the equilibrium constant to an inverse relationship with the oxygen partial pressure. This oxygen partial pressure is the oxide dissociation pressure and is the pressure at which the metal, oxygen, and the metal oxide are all in equilibrium. This pressure can be evaluated for any oxide given the Gibb's free energy of formation, ΔG_f as shown in Eqs. (23.3) and (23.4):

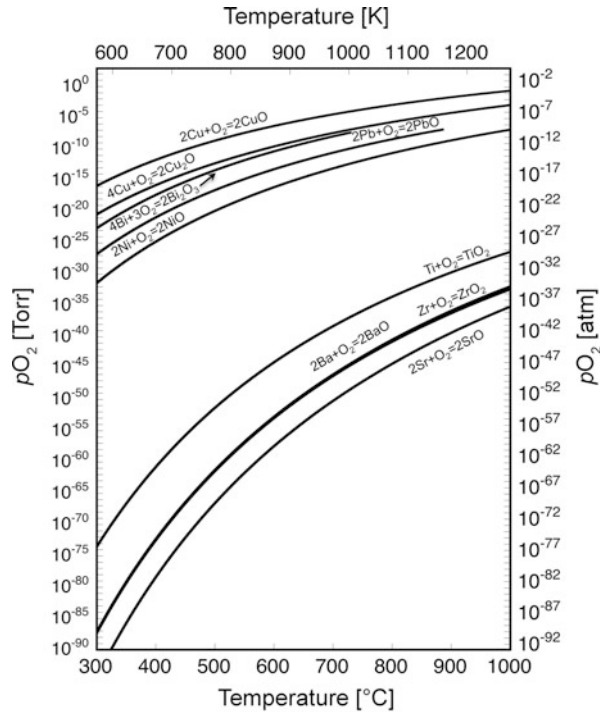
$$\Delta G_f = -RT \cdot \ln K \approx -RT \cdot \ln \frac{1}{pO_2} \quad (23.3)$$

$$pO_2 \approx e^{\frac{\Delta G_f}{RT}} \quad (23.4)$$

where R is the ideal gas constant and T is the absolute temperature. Plotting the temperature dependent dissociation pressures for a given metal, oxygen, and metal oxide results in a Richardson-Ellingham diagram whereby the necessary oxygen pressures to allow/disallow metal oxidation can be easily determined. Figure 23.1 shows a Richardson-Ellingham plot for a number of technologically pertinent metals and oxides, including the constituents of (Ba,Sr)TiO₃, Pb(Zr,Ti)O₃, Bi₄Ti₃O₁₂, and the base metals copper and nickel. For oxygen partial pressures exceeding the dissociation pressures the oxides are thermodynamically stable with oxygen gas. For oxygen partial pressures less than the dissociation pressure the metals are in thermodynamic equilibrium with oxygen. For example, inspection of this diagram reveals temperature-oxygen partial pressure phase space in which all constituents of (Ba,Sr)TiO₃ can be stable as oxides while the base metals remain metallic. The large oxygen partial pressure-temperature window separating M_xO_y and copper/nickel indicates a large processing space where (Ba,Sr)TiO₃ is in thermodynamic equilibrium with the base metals. Alternatively for materials containing more noble components there exists a very narrow equilibrium window. This includes the processing of PbO and Bi₂O₃-containing compounds. This narrow processing space suggests that lead- and bismuth-containing compounds are thermodynamically stable with copper, however the processing space is exceedingly small and requires substantial process controls, and that these compounds cannot be in thermodynamic equilibrium with nickel metal. Owing to the narrow thermodynamic window for PbO-copper equilibrium, a kinetic method to integration will be discussed in Sect. 23.3.

It would be impractical and difficult to achieve the oxygen partial pressures ($< \sim 10^{-11}$ atm) necessary for processing films on base metals using standard semiconductor approaches including vacuum processing equipment. A thermodynamic reaction approach is a more practical solution. The most widely used method is the reaction of oxygen with hydrogen to form water as shown in Eq. (23.5)

Fig. 23.1 Richardson-Ellingham diagram showing the phase space for metal/metal oxide systems important in the integration of functional oxides with base metals. Temperature and oxygen partial pressure (pO_2) are the thermodynamic state variables. *Lines* represent thermodynamic conditions for equilibrium between the metal, oxygen, and metal oxide. When processing conditions are below these equilibrium lines, the element is in the reduced metallic state; when processing conditions are above these equilibrium lines, the element is in the oxidized state



This is accomplished by flowing hydrogen containing forming gas (~1–5 % H_2 balanced by N_2 or another inert gas) through a sealed furnace during film processing. The reaction of H_2 with residual O_2 to form H_2O reduces the oxygen partial pressures to levels sufficient for base metal reduction. The oxygen partial pressure can be tailored by bubbling the source gas through water to drive the reaction toward the reactants and increase the oxygen partial pressure. An alternative approach is the use of CO and CO_2 to establish oxygen partial pressures [22]. The inherent safety and environmental issues associated with handling CO and CO_2 gas may limit the use of this technique.

23.2.2 Solution Chemistry and Processing

Several solution chemistries have been successfully implemented to deposit refractory oxides on base metal electrodes. The most commonly employed chemistry is loosely based upon the inverted-mixing order chemistry originally developed for lead zirconate titanate (PZT) films [23]. This chelate-based chemistry was developed for $(Ba,Sr)TiO_3$ by Schwartz et al. [24] and Hoffmann et al. [25] for use on

platinized-silicon substrates. In general, for barium strontium titanate, the solutions are prepared by dissolving alkaline-earth acetates in acetic acid and separately chelating titanium-carboxylates (titanium isopropoxide or titanium butoxide) with acetic acid or 2,4-pentanedione (also referred to as acetylacetonate or *acac*). Solutions chelated with *acac* tend to have longer shelf lives by slowing hydrolysis, however *acac* may remain in the film due to relatively high temperatures delaying the onset of crystallization [26]. The two precursors are combined and then the solutions are diluted with a suitable solvent including acetone, methanol, ethanol, isopropanol, butanol, or acetic acid to a molarity ranging from 0.05 to 0.4. Additions of high boiling point organic chemicals, including diethanolamine, can allow for strain relief as films are heat treated to drive off solvents [19, 27]. These additions can aid in densification and prevent cracking during gel formation and consolidation.

An alternative solution chemistry that was first used to develop oriented buffer layers for coated-conductors (see for example Chap. 27) involves the use of fluorinated solutions. Two solution preparation methods for fluorinated chemistries have been discussed in the literature. The first is similar to that for the chelate method outlined above, but uses trifluoroacetic acid (TFA) in place of acetic acid to dissolve the carboxylates [18, 28]. The second involves the preparation of a barium trifluoroacetate, $\text{Ba}(\text{CF}_3\text{COO})_2$, powder via reaction of barium acetate with trifluoroacetic acid in an aqueous solution followed by dissolution of the barium trifluoroacetate in alcohol [29]. During heating to crystallization temperatures the fluorine reacts with barium to form BaF_2 . It is suspected that BaF_2 prevents the formation of BaCO_3 or barium titanium oxycarbonates, which delay the onset of perovskite crystallization. This, combined with a suspected transient liquid phase, allows for epitaxial growth and is typically used on oriented nickel tapes [28].

The processing steps involved in gel formation are nearly the same as used for oxide films on refractory or noble substrates. This includes spin casting using a standard photoresist spin coater or dip coating and drying on a hotplate. Rapid drying on a hotplate is the most effective method to quickly volatilize solvents and consolidate precursors before metal-oxygen-metal network formation. Drying in ambient atmospheres is desirable because sufficient water concentrations exist to drive hydrolysis reactions. Some processing restrictions exist on the hotplate solvent extraction and gel consolidation steps. Whereas it is common to use temperatures in excess of 300 °C for films on refractory or noble metal substrates, these conditions can cause oxidation of base metal substrates.

Figure 23.2 shows X-ray diffraction patterns for PZT films on copper substrates dried for 5 min at temperatures ranging from 200 to 325 °C. Cu_2O peaks are present at temperatures in excess of 250 °C, suggesting that this is the upper limit for hotplate gel consolidation before copper oxidation. Although efforts to control drying atmospheres to minimize oxygen concentrations that drive copper oxidation have been investigated, difficulties arise in striking a balance between solvent vapor removal and water content to drive hydrolysis. Thus, a 250 °C hotplate treatment in atmospheric ambient conditions is the practical limit for the drying of CSD films on base metal copper substrates. To increase film thickness, multiple coating and

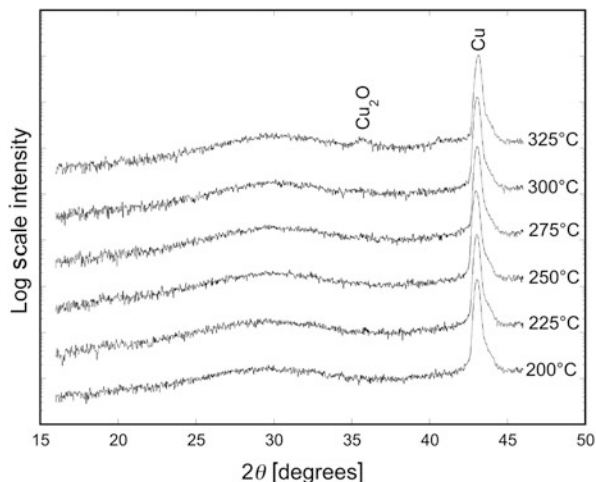
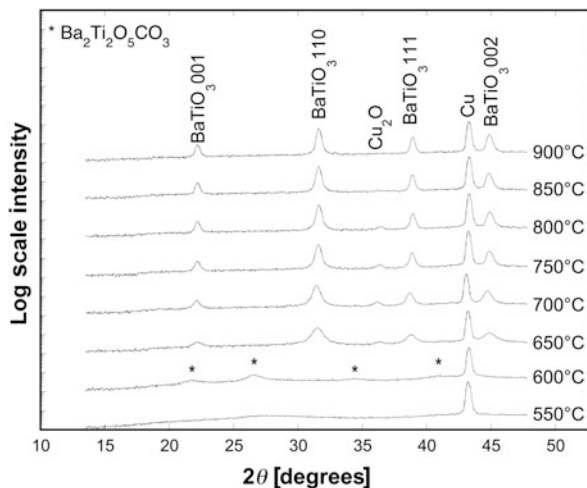


Fig. 23.2 X-ray diffraction patterns collected from six different PZT xerogels prepared on copper foils dried on a hotplate in ambient conditions at different temperatures for 5 min. Copper oxide is detected in structures heated above 250 °C. Reprinted with permission from Mark D. Losego, Leslie H. Jimison, Jon F. Ihlefeld, and Jon-Paul Maria, “Ferroelectric response from lead zirconate titanate thin films prepared directly on low-resistivity copper substrates,” *Applied Physics Letters*, Vol. 86 (17) 172906 (2005). Copyright 2005, American Institute of Physics

drying steps may be conducted, however crystallization anneals following every coating step enable a higher density microstructure, particularly for refractory oxides such as BaTiO_3 [25, 30]. Crystallization anneals are performed in atmospheres described previously. In general, the furnace is evacuated and backfilled or is flushed with the reducing atmosphere gases prior to initiating the temperature ramp. The crystallization pathway of BaTiO_3 and $(\text{Ba},\text{Sr})\text{TiO}_3$ from the gel state is dependent upon the solution chemistry used. Conventional chelate and sol-gel chemistries are known to possess an intermediate barium carbonate (BaCO_3) or barium titanium oxycarbonate ($\text{Ba}_2\text{Ti}_2\text{O}_5\text{CO}_3$) phase prior to the formation of the perovskite BaTiO_3 [25, 31–34].

Figures 23.3 and 23.4 show the phase evolution in BaTiO_3 films ramped to temperature, held for 30 min, and slowly cooled in the furnace and samples ramped to temperature and quickly removed without a dwell, respectively [35, 36]. A $\text{Ba}_2\text{Ti}_2\text{O}_5\text{CO}_3$ signature is evident in both sample sets. In the first set the oxycarbonate is present at 600 °C and has transformed to BaTiO_3 by 650 °C and in the second set it forms at 650 °C and is gone by 800 °C. This disparity demonstrates the kinetic nature of phase formation in this system. Regardless, perovskite crystallization is not observed until a minimum temperature of 650 °C using traditional chemistries. X-ray diffraction patterns showing phase evolution in fluorine-containing chemistries are shown in Fig. 23.5 [28]. Here no transient oxycarbonate or carbonate phases are observed and perovskite crystallization is evident by 500 °C. It should be noted that the data represented in Fig. 23.5 was not

Fig. 23.3 X-ray diffraction patterns for BaTiO₃ films prepared on copper foils using an acetic-acid chelation chemistry and crystallized in a controlled pO₂ furnace at varying temperatures from 550 °C to 900 °C for 30 min. Samples are allowed to cool slowly in the furnace after crystallization. Phase evolution from the carbonate phase (denoted with *asterisks*, Ba₂Ti₂O₅CO₃) to BaTiO₃ is observed



collected at sufficiently low angles to reveal the presence of a BaF₂ phase that was observed by researchers utilizing a fluorinated chemistry on platinumized silicon substrates and air atmospheres [29]. It is possible that the wet atmosphere used in preparing the fluorinated films on nickel substrates aids in BaF₂ decomposition, however this was not confirmed.

23.2.3 Microstructural and Electronic Properties

Typical film morphologies range from polycrystalline equiaxed grains for most metallo-organic based solution deposited films on polycrystalline base metal substrates to columnar crystallographically textured films for seeded metal-organic based solution deposited and fluorinated films. Figure 23.6 shows a plan-view atomic force microscopy (AFM) image of a chelate-chemistry deposited BaTiO₃ thin film processed on a copper foil at 900 °C [19]. Equiaxed grains with average sizes in excess of 100 nm are observed. These grain sizes are larger than those typically observed for similar composition films processed on platinumized silicon substrates, which can be attributed to the greater thermal budget allowed by the base metal electrodes. Films processed on copper substrates generally possess larger grain diameters than films processed on nickel. The mechanism for this is unclear, however may be related to the slightly higher oxygen partial pressures used in processing on copper [37].

Clean interfaces are expected from processing films on base metals under conditions where the films are thermodynamically stable as oxides and the metals remain metallic. For films deposited on copper electrodes, there is no evidence to suggest any interfacial phases, with apparent abrupt interfaces suggested from transmission electron microscopy (TEM) studies of both CSD and sputter deposited

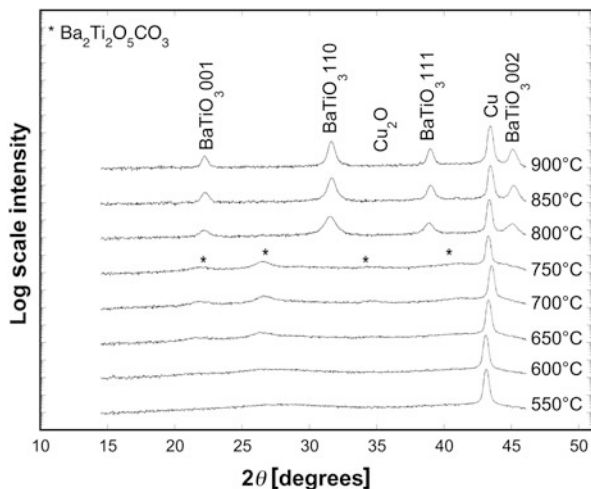


Fig. 23.4 X-ray diffraction patterns for BaTiO₃ films prepared on copper foils using an acetic-acid chelation chemistry and crystallized in a controlled pO_2 furnace at varying temperatures from 550 °C to 900 °C for 30 min. After crystallization, samples are quenched to room temperature by immediately removing from furnace. Phase evolution from the carbonate phase (denoted with asterisks, Ba₂Ti₂O₅CO₃) to BaTiO₃ is observed

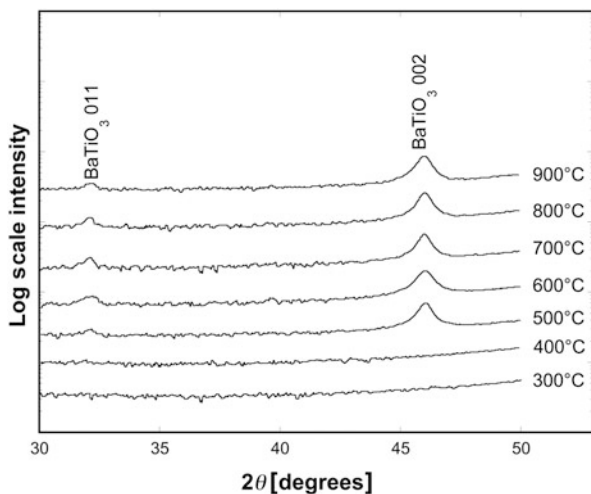
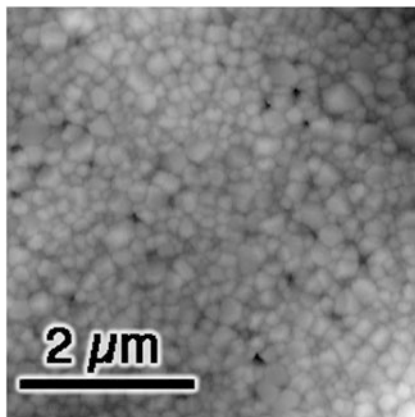


Fig. 23.5 X-ray diffraction patterns for BaTiO₃ films prepared on nickel tapes using a trifluoroacetic acid chemistry and crystallized in a controlled pO_2 furnace at varying temperatures from 300 °C to 900 °C for 30 min. Phase evolution from the gel phase directly to BaTiO₃ is observed. Reprinted from R.J. Ong, J.T. Dawley, and P.G. Clem, “Chemical solution deposition of biaxially oriented (Ba,Sr)TiO₃ thin films on <100 > Ni,” *Journal of Materials Research*, Vol. 18 (10) pages 2310–2317 (2003), with permission Copyright 2003, Materials Research Society

Fig. 23.6 $5\ \mu\text{m} \times 5\ \mu\text{m}$ topographical atomic force microscopy image of a BaTiO_3 film prepared on a copper foil substrate at $900\ ^\circ\text{C}$. Average grain sizes greater than $100\ \text{nm}$ are observed



films [19, 38]. For nickel-based electrodes, however, barium-nickel alloys have been identified in films processed from the conventional chelate method [37]. It has been proposed that the existence of carbon in the gel network locally reduces the interfacial oxygen pressure and results in barium reduction and subsequent reaction with the underlying substrate. The nickel-barium alloy has no apparent detrimental effect on film electrical performance and has been identified previously in bulk multilayer ceramic capacitors [39].

Processing of oxide thin films at low partial pressures of oxygen often results in a finite concentration of oxygen point defects. These defects manifest in higher dielectric loss and electrical leakage. To minimize oxygen vacancy concentrations, reoxidation anneals at lower temperatures and higher oxygen partial pressures can be employed, as have been demonstrated for bulk multilayer ceramic capacitors [40]. The conditions used for reoxidation anneals are in a processing regime where base-metal oxidation may be expected. However, the presence of a dense film coating the substrate kinetically limits the amount of oxygen reaching the oxide/metal interface and conditions may be empirically selected that decrease oxygen defect concentrations while maintaining a clean interface. Typical reoxidation annealing conditions for a $600\ \text{nm}$ thick BaTiO_3 film on copper are $550\ ^\circ\text{C}$ at 10^{-7} atm of oxygen for 30 min.

Figure 23.7 shows X-ray diffraction patterns for an as-fired and reoxidized BaTiO_3 film. No change in film peak intensity or copper oxide phase development is observed. Figure 23.8 shows permittivity and loss tangent versus field measurements for these same films [41]. The high field dielectric loss exceeds 40 % in the as-fired film, while the reoxidized film possesses a high field loss tangent of less than 0.3 %. Additionally, the low-field permittivity is increased in the reoxidized film, likely owing to fewer barriers to domain wall motion and increased extrinsic contributions to permittivity.

As an alternative to the additional processing step required by reoxidation, acceptor and amphoteric doping of solution deposited complex oxide films on base-metal bottom electrodes has been demonstrated to compensate for oxygen

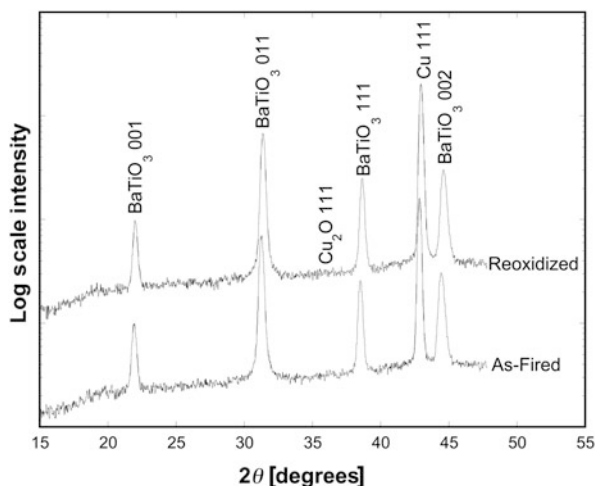


Fig. 23.7 X-ray diffraction patterns for BaTiO₃ films processed at 900 °C in an oxygen partial pressure (p_{O_2}) of 10^{-13} atm (*top*) and subsequently annealed at 550 °C and 10^{-7} atm O₂ (*bottom*). The dense BaTiO₃ film kinetically limits the amount of oxygen reaching the film/copper interface and prevents copper oxidation

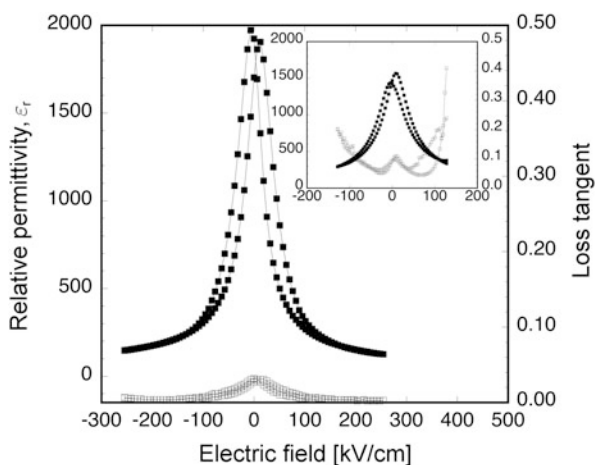


Fig. 23.8 Field dependence of permittivity (*solid markers*) and loss tangent (*open markers*) for BaTiO₃ films processed at 900 °C in an oxygen partial pressure (p_{O_2}) of 10^{-13} atm (*inset*) and subsequently annealed at 550 °C and 10^{-7} atm O₂ (*main figure*). Reprinted from Journal of Materials Science, Vol. 43, pages 38–42, “Defect chemistry of nano-grained barium titanate films,” Jon F. Ihlefeld, Mark D. Losego, Ramón Collazo, William J. Borland, and Jon-Paul Maria, Fig. 1, Copyright 2008. With kind permission of Springer Science and Business Media

vacancies [41, 42]. For example, 100 ppm of magnesium batched to be forced onto the *B*-site of BaTiO₃ was sufficient to eliminate space charge signatures resulting from oxygen vacancies for films processed on copper foil substrates. The resulting films possessed room temperature relative permittivities in excess of 1,400 with low loss tangent values [41]. Likewise, reduced leakage currents and loss tangents have been observed in (Ba,Sr)TiO₃ compositions prepared on nickel foils with manganese acceptor dopants and manganese-niobium acceptor-donor complexes [42], similar to the effects observed in commercial capacitor formulations [15, 22, 43, 44]. Amphoteric rare-earth dopants have not been observed to significantly improve the leakage current or dielectric loss in films processed on base-metal substrates, however low thermal budgets compared to traditional bulk ceramic preparation procedures may play a role [42].

Dielectric properties of films processed via the thermodynamic approach on base metals are generally more closely related to bulk ceramics than thin films processed on traditional substrates. Thermo-physical instabilities in traditional platinized silicon substrates (e.g. those that utilize titanium or titanium oxide adhesion layers) limit processing temperatures effectively to 750 °C. Higher temperatures result in platinum hillocking or delamination from the underlying silicon substrate. Base-metal foils are limited only by proximity to the substrate melting temperature. Films on copper can therefore be processed to greater than 1,000 °C and films on nickel may be processed to greater than 1,100 °C. These higher thermal budgets for films on base metals have resulted in materials with larger grain sizes and higher degrees of crystallinity. This in turn allows for greater extrinsic contributions to ferroelectricity through enhanced domain wall mobility. This is well demonstrated by comparing the field response of permittivity for a BaTiO₃ film processed under conventional thin film temperatures and one processed at a temperature allowed by the base metal.

Figure 23.9 shows the field response of permittivity for a 600 nm thick chelate-chemistry derived BaTiO₃ film processed between 700 and 900 °C [45]. Dielectric tunability increases from ~45 % to ~90 % as peak permittivity increases from 370 to 2,100 while the saturation permittivity is similar for both samples. The increased low-field permittivity can be correlated with enhanced extrinsic ferroelectric contributions owing to improved crystallinity and enlarged grain size. A comparison of grain size and coherent crystal size as measured by atomic force microscopy and x-ray line broadening, respectively, shows that as the processing temperature increases the disparity between grain size and coherent crystal size lessens, as shown in Fig. 23.10. The convergence of grain size and coherent crystal size as temperature increases suggests that the enhanced dielectric response of films processed on base metals is directly related to the ability to process at greater temperatures. It is prudent to mention in this discussion of thermo-physical barriers to preparation of oxide films on metal/metalized substrates that there have been recent adhesion layer advancements for preparing platinum films on SiO₂/Si substrates that enable access to processing temperature in excess of 900 °C. These adhesion layers, solution deposited Al₂O₃ and sputtered ZnO, have been successfully implemented in the solution preparation of (Ba,Sr)TiO₃ and BaTiO₃

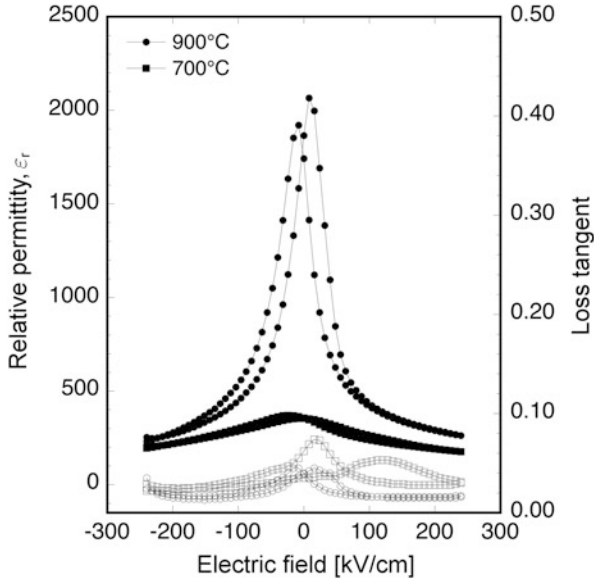


Fig. 23.9 Field dependence of permittivity (*solid markers*) and loss tangent (*open markers*) for BaTiO₃ films processed at 900 °C (*circle markers*) and 700 °C (*square markers*) on copper foil substrates. Reprinted with permission from Jon F. Ihlefeld, Aaron M. Vodnick, Shefford P. Baker, William J. Borland, and Jon-Paul Maria, “Extrinsic scaling effects on the dielectric response of ferroelectric thin films,” *Journal of Applied Physics*, Vol. 103, 074112 (2008). Copyright 2008, American Institute of Physics

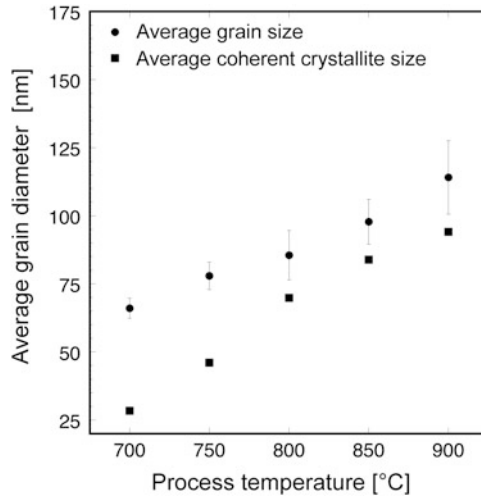


Fig. 23.10 Average grain and coherent crystal sizes determined from plan-view atomic force microscopy and X-ray line broadening, respectively, for BaTiO₃ films processed between 700 °C and 900 °C on copper foil substrates. Reprinted with permission from Jon F. Ihlefeld, Aaron M. Vodnick, Shefford P. Baker, William J. Borland, and Jon-Paul Maria, “Extrinsic scaling effects on the dielectric response of ferroelectric thin films,” *Journal of Applied Physics*, Vol. 103, 074112 (2008). Copyright 2008, American Institute of Physics

films with similarly increased relative permittivities, thus further strengthening the linkage between thermal budget, microstructural refinement, and improved dielectric response [46, 47].

23.3 Kinetic Route to Chemical Solution Deposition of Functional Oxide Films on Base Metals

Having lead or bismuth at the A-site of a perovskite oxide structure increases its spontaneous polarization by introducing additional bonding covalency between lone pair electrons and the oxygen anions. This covalent bonding interaction further stabilizes the unit cell's ferroelectric distortion [48–50]. The large polarization in these materials makes them more attractive for pyroelectric, piezoelectric, and polarization switching applications than the family of BaTiO₃ ferroelectrics. Unfortunately, lead and bismuth have high vapor pressures [51] and are relatively noble. The Ellingham diagram (Fig. 23.1) shows that the temperature/*p*O₂ process window for thermodynamic equilibrium between PbO or Bi₂O₃ and metallic copper is vanishingly narrow compared to the family of (Ba,Sr)TiO₃ perovskites. PbO and Bi₂O₃ are never thermodynamically stable with metallic nickel at atmospheric pressures. Moreover, the temperatures necessary to access thermodynamic equilibrium within a reasonable timeframe (>800 °C) will also volatilize these elemental oxides. High temperature bulk sintering of ceramics containing lead or bismuth typically involves creating an overpressure by heating the component in a sealed container containing a PbO or Bi₂O₃ powder bed. Thus, a thermodynamic equilibrium processing environment for lead or bismuth containing oxides would require controlling both the oxygen vapor pressure and the volatile metal oxide's vapor pressure. For oxides containing these volatile constituents it becomes prudent to ask whether a kinetic approach of avoiding base metal oxidation through a carefully managed thermal budget and design of solution chemistry is possible. Fortunately, the low crystallization temperatures necessary for CSD processing of many lead and bismuth containing oxides facilitate such a kinetic approach to avoiding substrate oxidation.

23.3.1 *Challenges to a Kinetic Route for Processing CSD Oxide Films on Base Metals*

To achieve a kinetic route avoiding substrate oxidation in the CSD processing of oxide films on base metal surfaces, a careful balance of the thermal budget must be struck. Sufficient thermal energy must be supplied to drive gel consolidation and avoid cracking while limiting the amount of time at temperature the substrate has to oxidize. The data of Fig. 23.11 encapsulates this challenge. Here an alkoxide

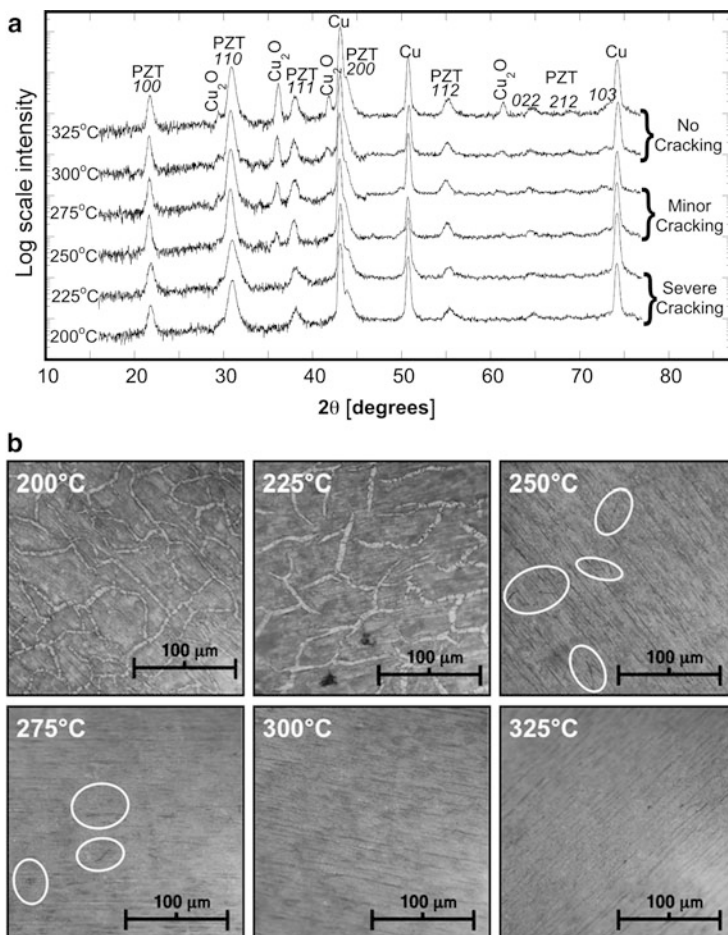


Fig. 23.11 (a) θ - 2θ x-ray diffraction scans and (b) optical microscopy images of CSD PZT films prepared on 18 μm -thick copper foils. All films are 4 spun-cast layers thick, each layer was dried at the temperature indicated, and all films underwent a final crystallization at 650 $^{\circ}\text{C}$ in flowing nitrogen. The white circles for 250 $^{\circ}\text{C}$ and 275 $^{\circ}\text{C}$ in (b) indicate microcracking

precursor $\text{PbZr}_x\text{Ti}_{1-x}\text{O}_3$ (with a nominal composition of $x = 0.52$) solution chelated with acetic acid [23] is prepared at increasing drying temperatures (5 min on a hotplate in air). Each film is four spun-coat layers thick (~ 500 nm) and crystallized at 650 $^{\circ}\text{C}$ in a nitrogen atmosphere. The combination of x-ray diffraction data and optical microscopy images demonstrate that at low drying temperatures (< 250 $^{\circ}\text{C}$) copper oxidation is mitigated, but the films are severely cracked due to insufficient gel consolidation. Cracking results because gel consolidation and network formation are predominantly determined during the drying step by the capillary forces of solvent extraction and thermally activated hydrolysis of metal ligands. At low

temperatures, these processes are not as effective in forming a dense, well-networked gel. Upon crystallization, a large volume shrinkage causes the film to crack. However, these films show no evidence of copper oxide formation (despite the large cracks), indicating that a 30 min anneal in a flowing nitrogen atmosphere at 650 °C is sufficient to protect the base metal.

Typical film processing of this solution chemistry on a noble metal surface requires drying temperatures in excess of 300 °C to achieve films of highest quality. Consequently, the optical images show the diminishing severity of cracking for drying temperatures above 250 °C. However, as discussed in Sect. 23.2.2, such drying temperatures in air are incompatible with a base metal substrate and result in severe substrate oxidation as observed in the XRD scans of Fig. 23.11a. Note that some oxidation is observed even for films dried at 250 °C. This oxidation occurs during the crystallization anneal due to oxidizing species trapped in the gel network. This problem is addressed further in the forthcoming discussion.

Finally, it is prudent to mention that severe cracking is likely not seen in (Ba,Sr)TiO₃ films dried at 250 °C because these perovskites crystallize at much higher temperatures. During the final anneal, the gel has additional time to network and consolidate before crystallization. Thus, managing the gel structure to minimize consolidation stresses during crystallization is more important in PZT films than (Ba,Sr)TiO₃ films.

23.3.2 Methodology for a Kinetic Route to the Processing of CSD Oxide Films on Base Metal

A two-pronged strategy has been effective in achieving the gel structure necessary to prevent cracking within the processing constraints that avoid oxidation of a base metal substrate. The first component to this strategy is the selection of a solution chemistry that can be processed using a low thermal budget. The second component is developing a thermal process flow that protects the base metal substrates during the initial deposition of CSD layers followed by a more aggressive thermal treatment on subsequent layers to achieve a consolidated and networked gel structure.

To kinetically avoid oxidation of a base metal substrate, the solution chemistry must only contain organic constituents that can be extracted at relatively low temperatures. Specifically, organic extraction by a thermolysis route (volatilization without oxidative combustion) is strongly preferred over pyrolysis (oxidative combustion and volatilization of the products). For a chelation solution chemistry, this restriction requires the selection of a low molecular weight and low boiling point chelating ligand. These properties for common chelating ligands are given in Table 23.1.

The solvent should also have high volatility (like methanol or ethanol) to allow rapid solvent extraction and gel consolidation at low drying temperatures. PbZr_xTi_{1-x}O₃ (with a nominal composition of $x = 0.52$, denoted as PZT throughout the remainder of the chapter) solutions using lead acetate and transition metal alkoxides chelated with

Table 23.1 Properties of common chelating ligands to consider when designing a process route to kinetically avoid oxidation of a base metal substrate

Chelating ligand	Molar mass (g/mol)	Boiling point (°C)
Diethanolamine	105	217
Acetylacetone	100	140
2-Methoxyethanol	76	125
Acetic acid	60	118

diethanolamine, acetylacetone, and acetic acid solvated in methanol and spun cast on copper surfaces have been investigated. Our investigations [52] reveal that high volatility of the chelating ligand is necessary for compatibility with a thin film processing route that kinetically avoids substrate oxidation. Figure 23.12 is a schematic rendering of the process space afforded to these different solution chemistries based on our experimental results. In this figure, the shaded regions represent the process space for phase pure, uncracked PZT films; the hatched region represents the process conditions to kinetically avoid copper oxidation. The area of overlap characterizes the process space available for synthesizing device-quality PZT thin films on copper substrates. Note how ligands with lower boiling points push the PZT process window to lower thermal budgets, allowing a kinetic route to avoiding base metal oxidation. Acetylactone, with a boiling point of 140 °C appears to be on the edge of processibility. Thus a true sol–gel processed film using 2-methoxyethanol (bp = 125 °C) is also possible, but will likely depend on the solvent chemistry, as typical solvent components (2-methoxyethanol, water) may lack sufficient volatility during the drying step [53].

Although solution chemistry selection can shift the process window for a single spun coat layer (~100 nm) to a regime compatible with base metal substrates, microcracking persists for multilayer films (>200 nm). These thicker layers are also necessary to kinetically limit substrate oxidation during the high temperature crystallization step. To eliminate microcracking in multilayer films, a “composite gel architecture” approach was developed in which the initial two spun-cast layers are dried at 250 °C in air and thermolyzed (400 °C) in a reducing atmosphere while subsequent layers (usually three layers) are dried at higher temperatures (300 °C) in air [52, 54]. Figure 23.13 shows this process flow.

This composite gel architecture aims to protect the substrate during the deposition of the initial layers while more aggressively consolidating and networking the gel structure in the final layers. The presence of the initial gel layers also acts to kinetically impede substrate oxidation during the higher temperature drying of the final layers. The thermolysis step used for the initial layers is found necessary to remove gel constituents that can oxidize the substrate during the crystallization anneal. Figure 23.14 shows an increase in copper oxidation observed between film drying and film crystallization for films processed at increasing drying temperatures (same set of films presented in Fig. 23.11; note that films dried at 250 °C showed no oxidation prior to the crystallization anneal but show copper oxide after crystallization.). We hypothesize that the increased gel density at higher drying temperatures more effectively traps gel constituents such as water and adsorbed

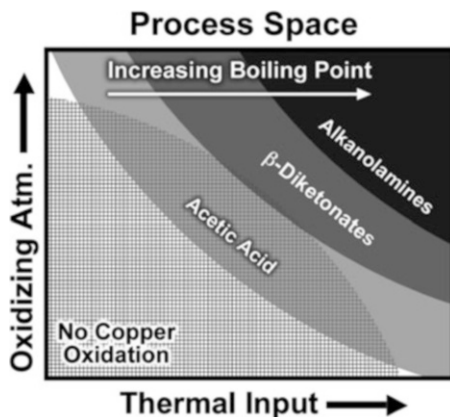


Fig. 23.12 Schematic representation of the process space (thermal inputs and oxidizing atmosphere) available for synthesizing CSD PZT films directly on copper substrates via kinetic avoidance of substrate oxidation. Shaded areas represent conditions necessary to form phase-pure, uncracked PZT films using the indicated chelation chemistry. Hatched area represents the conditions necessary for avoiding oxidation of the substrate. Reprinted in part with permission from Mark D. Losego, Jon F. Ihlefeld, and Jon-Paul Maria, "Importance of solution chemistry in preparing sol-gel PZT thin films directly on copper surfaces," *Chemistry of Materials*, Vol. 20 (1), pages 303–307 (2008). Copyright 2008, American Chemical Society

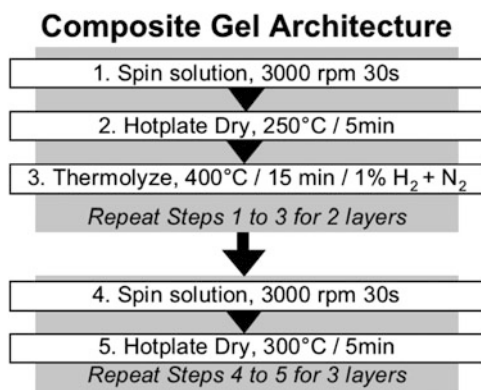


Fig. 23.13 Description of "composite-gel architecture" process flow strategy used to kinetically avoid oxidation of base metal substrates while maintaining high-quality perovskite oxide thin films. Reprinted in part with permission from Mark D. Losego, Jon F. Ihlefeld, and Jon-Paul Maria, "Importance of solution chemistry in preparing sol-gel PZT thin films directly on copper surfaces," *Chemistry of Materials*, Vol. 20 (1), pages 303–307 (2008). Copyright 2008 American Chemical Society

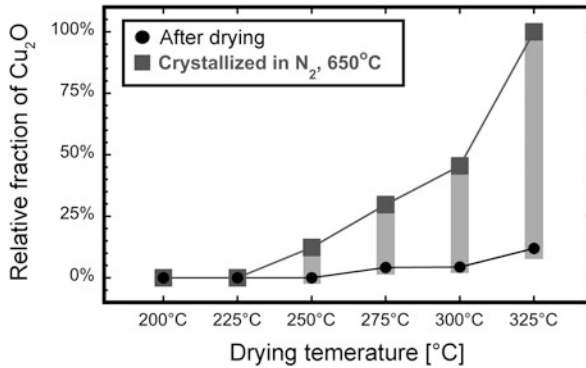


Fig. 23.14 Relative fraction of copper oxide detected by x-ray diffraction for a series of CSD PZT films dried at increasing temperatures both before and after the final crystallization anneal at 650 °C in flowing nitrogen. Values represent the diffraction intensity of the Cu_2O *111* reflection normalized to the Cu_2O *111* diffraction intensity collected for the dried at 325 °C and then crystallize (100%). No copper oxide (0%) was detected for films dried at 200 °C, 225 °C, or 250 °C before annealing nor for 200 °C and 225 °C after annealing

oxygen that can oxidize the substrate upon the final crystallization anneal. All successful examples of PZT films processed on copper have utilized a thermolysis step in a reducing atmosphere that removes such oxidizing constituents and protects the base metal substrate from oxidation during high-temperature crystallization [52–56].

By properly managing CSD film process conditions, kinetic avoidance of base metal substrate oxidation is achievable and ferroelectric oxides films can be fabricated with properties comparable to films processed on noble metal electrodes using more aggressive thermal treatments [54, 56].

For example, Fig. 23.15 compares the polarization hysteresis loops collected from a PZT film deposited directly on copper using the above described “composite gel architecture” strategy to a PZT film deposited on platinized silicon using a standard 300 °C hotplate dry and 650 °C crystallization anneal. Both films were processed from the same acetic acid chelated precursor solution and crystallized in nitrogen to fix both the Zr:Ti ratio and oxygen vacancy concentration. Both hysteresis loops show comparable saturation, remanent polarization, and coercive fields, indicating the PZT film deposited on copper has low current leakage, good microstructure, and is of device-quality.

23.4 Summary

While chemical solution deposition technology is inherently inexpensive and amenable to commercialization, mass production of functional oxide thin films continues to be cost prohibitive due to the high cost of the bottom electrode and its

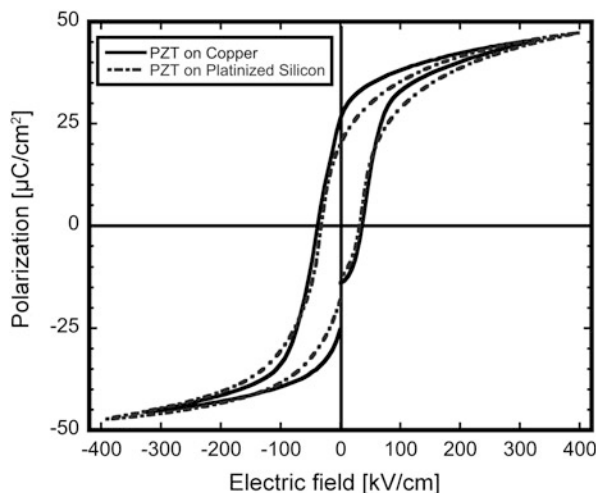


Fig. 23.15 Comparison of polarization hysteresis loops collected from a CSD PZT film prepared via the “composite gel architecture” on a copper foil and a CSD PZT film prepared under more thermally aggressive/oxidizing conditions (300 °C air dry; 650 °C anneal in nitrogen) on a platinized silicon substrate. Reprinted with permission from Mark D. Losego, Leslie H. Jimison, Jon F. Ihlefeld, and Jon-Paul Maria, “Ferroelectric response from lead zirconate titanate thin films prepared directly on low-resistivity copper substrates,” *Applied Physics Letters*, Vol. 86 (17) 172906 (2005). Copyright 2005, American Institute of Physics

rigid nature, which necessitates non-continuous, serial processing. This chapter introduced emerging methods for integrating chemical solution processed electroceramic thin films on flexible base metal foils, which enables cost-effective thin film manufacturing. For the $(\text{Ba,Sr})\text{TiO}_3$ family of oxides, a thermodynamic processing approach is possible in which the CSD film is crystallized under conditions of temperature and oxygen partial pressure that afford equilibrium between the oxide and base metal. Such films can be crystallized at temperatures much higher than traditional bottom electrode technologies, leading to improved film crystallinity and microstructure and electrical performance far exceeding films limited to lower temperatures on noble metal substrates. Because of the narrow or non-existent equilibrium window for functional oxides containing PbO or Bi_2O_3 (e.g. PZT) a kinetic approach to avoiding base metal oxidation is necessary. This strategy requires proper chelation chemistry that permits low-temperature removal of the organic and careful thermal processing strategies that fully consolidate the gel network before crystallization to avoid cracking. Ultimately, both of these strategies can achieve oxide thin films integrated on base metals with functional properties comparable or better than similar films deposited on more traditional and more expensive noble metal bottom electrodes. Thus, these methods offer a bright outlook for realizing full-scale commercialization of thin film functional oxide technology.

Acknowledgments The authors gratefully acknowledge our colleagues and collaborators and would like to thank Dr. Seymen Aygün and Patrick Daniels of North Carolina State University, Drs. Paul Clem and Geoff Brennecka of Sandia National Laboratories, and Dr. Brian Laughlin and Dr. William J. Borland of E.I. DuPont de Nemours and Company for their many discussions and work that contributed to this chapter. Sandia is a multiprogram laboratory operated by Sandia Corporation, a wholly owned subsidiary of Lockheed Martin Company, for the United States Department of Energy's National Nuclear Security Administration under Contract DE-AC04-94AL85000.

References

1. Saegusa K (1997) Preparation by a sol-gel process and dielectric properties of lead zirconate titanate glass-ceramic thin films. *Jpn J Appl Phys* 1(36):3602-3608
2. Zou Q, Ruda HE, Yacobi BG, Saegusa K, Farrell M (2000) Dielectric properties of lead zirconate titanate thin films deposited on metal foils. *Appl Phys Lett* 77:1038-1040
3. Yi G, Sayer M, Wu Z, Jen CK, Bussiere JF (1989) Piezoelectric lead zirconate titanate coatings on metallic wires. *Electron Lett* 25:907-908
4. Yi GH, Wu Z, Sayer M (1988) Preparation of $\text{Pb}(\text{Zr,Ti})\text{O}_3$ thin-films by sol-gel processing - electrical, optical, and electro-optic properties. *J Appl Phys* 64:2717-2724
5. Chen JY, Xu QC, Blaszkiewicz M, Meyer R, Newnham RE (1992) Lead zirconate titanate films on nickel titanium shape memory alloys - smarties. *J Am Ceram Soc* 75:2891-2892
6. Mercado PG, Jardine AP (1995) Thin film multilayers of ferroelastic TiNi-ferroelectric PZT: fabrication and characterization. *J Intell Mater Syst Struct* 6:62-70
7. Kim T, Kingon AI, Maria JP, Crosswell RT (2006) Electrical properties of lead zirconate titanate thin films with a ZrO_2 buffer layer on an electroless Ni-coated Cu foil. *J Am Ceram Soc* 89:3426-3430
8. Ogawa T, Saitoh S, Sugiyama O, Kondoh A, Mochizuka T, Masuda H (1994) Sol-gel barium titanate thin films on nickel alloy electrodes. In: Paper presented at the ISAF '94—Proceedings of the 9th IEEE international symposium on applications of ferroelectrics, New York
9. Es-Souni M, Piorra A, Habouti S, Kumar SR, Faupel F (2005) $(\text{La}_{0.8},\text{Sr}_{0.2})\text{MnO}_3/\text{Ti}$ -metal foil substrate heterostructure effects on the ferroelectric and piezoelectric properties of lead zirconate titanate thin films. *Appl Phys Lett* 87:182910
10. Kim DJ (2007) Effects of barrier layers on the electrical properties of $(\text{Pb,L a})(\text{Zr,Ti})\text{O}_3$ films on nickel foils. *Mater Sci Eng B-Solid State Mater Adv Technol* 141:87-90
11. Ma BH, Kwon DK, Narayanan M, Balachandran U (2009) Chemical solution deposition of ferroelectric lead lanthanum zirconate titanate films on base-metal foils. *J Electroceram* 22:383-389
12. Maria J-P, Cheek K, Streiffer S, Kim SH, Dunn G, Kingon A (2001) Lead zirconate titanate thin films on base-metal foils: An approach for embedded high-permittivity passive components. *J Am Ceram Soc* 84:2436-2438
13. Narayanan M, Ma BH, Balachandran U, Li W (2010) Dielectric spectroscopy of $\text{Pb}_{0.92}\text{La}_{0.08}\text{Zr}_{0.52}\text{Ti}_{0.48}\text{O}_3$ films on hastelloy substrates with and without LaNiO_3 buffer layers. *J Appl Phys* 107:024103
14. Zou Q, Ruda HE, Yacobi BG (2001) Improved dielectric properties of lead zirconate titanate thin films deposited on metal foils with LaNiO_3 buffer layers. *Appl Phys Lett* 78:1282-1284
15. Herbert JM (1963) High-permittivity ceramics sintered in hydrogen. *Brit Ceram Trans J* 62:645-658
16. Herbert JM (1965) Thin ceramic dielectrics combined with nickel electrodes. *Proc IEE* 112:1474-1477

17. Kishi H, Mizuno Y, Chazono H (2003) Base-metal electrode-multilayer ceramic capacitors: past, present and future perspectives. *Jpn J Appl Phys* 1(42):1–15
18. Dawley JT, Clem PG (2002) Dielectric properties of random and $< 100 >$ oriented SrTiO₃ and (Ba,Sr)TiO₃ thin films fabricated on $< 100 >$ nickel tapes. *Appl Phys Lett* 81:3028–3030
19. Ihlefeld J, Laughlin B, Hunt-Lowery A, Borland W, Kingon A, Maria J-P (2005) Copper compatible barium titanate thin films for embedded passives. *J Electroceram* 14:95–102
20. Nagata H, Ko SW, Hong E, Randall CA, Trolrier-McKinstry S (2006) Microcontact printed BaTiO₃ and LaNiO₃ thin films for capacitors. *J Am Ceram Soc* 89:2816–2821
21. Halder S, Schneller T, Waser R, Thomas F (2007) Microstructure and electrical properties of BaTiO₃ and (Ba, Sr)TiO₃ ferroelectric thin films on nickel electrodes. *J Sol-Gel Sci Technol* 42:203–207
22. Burn I, Maher GH (1975) High-resistivity BaTiO₃ ceramics sintered in CO-CO₂ atmospheres. *J Mater Sci* 10:633–640
23. Assink RA, Schwartz RW (1993) H-1 and C-13 NMR investigations of Pb(Zr,Ti)O₃ thin-film precursor solutions. *Chem Mat* 5:511–517
24. Schwartz RW, Clem PG, Voigt JA, Byhoff ER, Van Stry M, Headley TJ, Missert NA (1999) Control of microstructure and orientation in solution-deposited BaTiO₃ and SrTiO₃ thin films. *J Am Ceram Soc* 82:2359–2367
25. Hoffmann S, Waser R (1999) Control of the morphology of CSD-prepared (Ba,Sr)TiO₃ thin films. *J Eur Ceram Soc* 19:1339–1343
26. Schwartz RW (1997) Chemical solution deposition of perovskite thin films. *Chem Mat* 9:2325–2340
27. Dawley JT, Clem PG, Siegal MP, Tallant DR, Overmyer DL (2002) Improving sol-gel YBa₂Cu₃O_{7-δ} film morphology using high-boiling-point solvents. *J Mater Res* 17:1900–1903
28. Ong RJ, Dawley JT, Clem PG (2003) Chemical solution deposition of biaxially oriented (Ba, Sr)TiO₃ thin films on 100 Ni. *J Mater Res* 18:2310–2317
29. Fujihara S, Schneller T, Waser R (2004) Interfacial reactions and microstructure of BaTiO₃ films prepared using fluoride precursor method. *Appl Surf Sci* 221:178–183
30. Aygün SM, Ihlefeld JF, Borland WJ, Maria JP (2011) Permittivity scaling in Ba_{1-x}Sr_xTiO₃ thin films and ceramics. *J Appl Phys* 109:034108
31. Gopalakrishnamurthy HS, Rao MS, Kutty TRN (1975) Thermal-decomposition of titanyl oxalates – I Barium titanyl oxalate. *J Inorg Nucl Chem* 37:891–898
32. Campion JF, Payne DA, Chae HK (1992) Chemical processing of barium titanate powders and thin layer dielectrics. *Ceram Trans* 22:477–489
33. Kumar S, Messing GL, White WB (1993) Metal-organic resin derived barium-titanate: I. Formation of barium titanium oxycarbonate intermediate. *J Am Ceram Soc* 76:617–624
34. Frey MH, Payne DA (1995) Synthesis and processing of barium-titanate ceramics from alkoxide solutions and nonlithic gels. *Chem Mat* 7:123–129
35. Ihlefeld JF (2006) Synthesis and properties of barium titanate solid solution thin films on copper substrates. Ph.D. Dissertation, North Carolina State University, Raleigh
36. Aygün SM (2009) Processing science of barium titanate. PhD Dissertation, North Carolina State University, Raleigh
37. Dechakupt T, Yang G, Randall CA, Trolrier-McKinstry S, Reaney IM (2008) Chemical solution-deposited BaTiO₃ thin films on Ni foils: Microstructure and interfaces. *J Am Ceram Soc* 91:1845–1850
38. Laughlin B, Ihlefeld J, Maria J-P (2004) TEM and electrical analysis of sputtered barium strontium titanate (BST) thin films on flexible copper substrates. *Mater Res Soc Symp P* 784:301–306
39. Yang GY, Lee SI, Liu ZJ, Anthony CJ, Dickey EC, Liu ZK, Randall CA (2006) Effect of local oxygen activity on Ni-BaTiO₃ interfacial reactions. *Acta Mater* 54:3513–3523
40. Yang GY, Dickey EC, Randall CA, Barber DE, Pinceloup P, Henderson MA, Hill RA, Beeson JJ, Skamser DJ (2004) Oxygen nonstoichiometry and dielectric evolution of BaTiO₃ Part I – Improvement of insulation resistance with reoxidation. *J Appl Phys* 96:7492–7499

41. Ihlefeld JF, Losego MD, Collazo R, Borland WJ, Maria JP (2008) Defect chemistry of nano-grained barium titanate films. *J Mater Sci* 43:38–42
42. Bretos I, Schneller T, Waser R, Hennings DF, Halder S, Thomas F (2010) Compositional substitutions and aliovalent doping of BaTiO₃-based thin films on nickel foils prepared by chemical solution deposition. *J Am Ceram Soc* 93:506–515
43. Burn I (1979) Mn-doped polycrystalline BaTiO₃. *J Mater Sci* 14:2453–2458
44. Albertsen K, Hennings D, Steigelmann O (1998) Donor-acceptor charge complex formation in barium titanate ceramics: Role of firing atmosphere. *J Electroceram* 2:193–198
45. Ihlefeld JF, Vodnick AM, Baker SP, Borland WJ, Maria J-P (2008) Extrinsic scaling effects on the dielectric response of ferroelectric thin films. *J Appl Phys* 103:074112
46. Halder S, Schneller T, Waser R (2007) Enhanced stability of platinized silicon substrates using an unconventional adhesion layer deposited by CSD for high temperature dielectric thin film deposition. *Appl Phys A-Mater Sci Process* 87:705–708
47. Shelton CT, Kotula PG, Brenneka GL, Lam PG, Meyer KE, Maria J-P, Gibbons BJ, Ihlefeld JF (2012) Chemically homogeneous complex oxide thin films via improved substrate metallization. *Adv Funct Mater*. doi:10.1002/adfm.201103077
48. Cohen RE (1992) Origin of ferroelectricity in perovskite oxides. *Nature* 358:136–138
49. Jan JC, Tsai HM, Pao CW, Chiou JW, Asokan CK, Kumar KPK, Pong WF, Tang YH, Tsai MH, Kuo SY, Hsieh WF (2005) Direct experimental evidence of hybridization of Pb states with O 2p states in ferroelectric perovskite oxides. *Appl Phys Lett* 87:012103
50. Seshadri R, Hill NA (2001) Visualizing the role of Bi 6s “Lone pairs” in the off-center distortion in ferromagnetic BiMnO(3). *Chem Mat* 13:2892–2899
51. Lamoreaux RH, Hildenbrand DL, Brewer L (1987) High-temperature vaporization behavior of oxides 2. Oxides of Be, Mg, Ca, Sr, Ba, B, Al, Ga, In, Tl, Si, Ge, Sn, Pb, Zn, Cd, and Hg. *J Phys Chem Ref Data* 16:419–443
52. Losego MD, Ihlefeld JF, Maria J-P (2008) Importance of solution chemistry in preparing sol–gel PZT thin films directly on copper surfaces. *Chem Mat* 20:303–307
53. Narayanan M, Kwon DK, Ma B, Balachandran U (2008) Deposition of sol–gel derived lead lanthanum zirconate titanate thin films on copper substrates. *Appl Phys Lett* 92:252905
54. Losego MD, Jimison LH, Ihlefeld JF, Maria J-P (2005) Ferroelectric response from lead zirconate titanate thin films prepared directly on low-resistivity copper substrates. *Appl Phys Lett* 86:172906
55. Kingon AI, Srinivasan S (2005) Lead zirconate titanate thin films directly on copper electrodes for ferroelectric, dielectric and piezoelectric applications. *Nat Mater* 4:233–237
56. Losego MD, Maria JP (2010) Reproducibility and ferroelectric fatigue of lead zirconate titanate thin films deposited directly on copper via a composite gel architecture. *J Am Ceram Soc* 93:3983–3985

Chapter 24

Polar Oxide Thin Films for MEMS Applications

Paul Muralt

24.1 Introduction to Piezoelectric and Pyroelectric Properties and Its Applications in MEMS

If we put the world of sensors and actuators in a more general context, we become aware that humanity has created—and is continuing to expand and perfection—an artificial or digital world existing in our computers and computer networks, not so much as a result of human fantasy, but as a mirror or reflection of the real world. The link between those worlds is not only made by humans operating a computer, but more and more also by myriads of sensors, and devices that can react on the real world. Modern cars with their electronic devices regulating speed, temperature, air conditioning, etc. are just one example.

The device category contributing to converge the real and digital world is often called *smart*, because it brings an intelligent behavior into an otherwise “brainless” apparatus. In microelectronics the expression “more than Moore” was coined to give a name to new types of devices combining digital functionalities with sensing or actuating capabilities. Apart from pure sensor systems, the goal is often to create an *adaptive system*. This is a combination of sensors that notice a change, and actuators that correct or adapt the system to respond to the environment. Such new smart devices are of course essential ingredients to establish robots. In addition, they will serve in any field of human activity to organize fabrication flows, to optimize power distribution, to minimize energy consumption, to detect pollutants for environmental controls, and so on. Apart from the smart devices themselves, which are to a great extent the result of the tremendous research and development activity during the last 20 years in micro-electro-mechanical systems (MEMS), one has to consider wireless communication as an essential ingredient to handle system

P. Muralt (✉)

Ceramics Laboratory, Swiss Federal Institute of Technology EPFL, Lausanne, Switzerland
e-mail: paul.muralt@epfl.ch

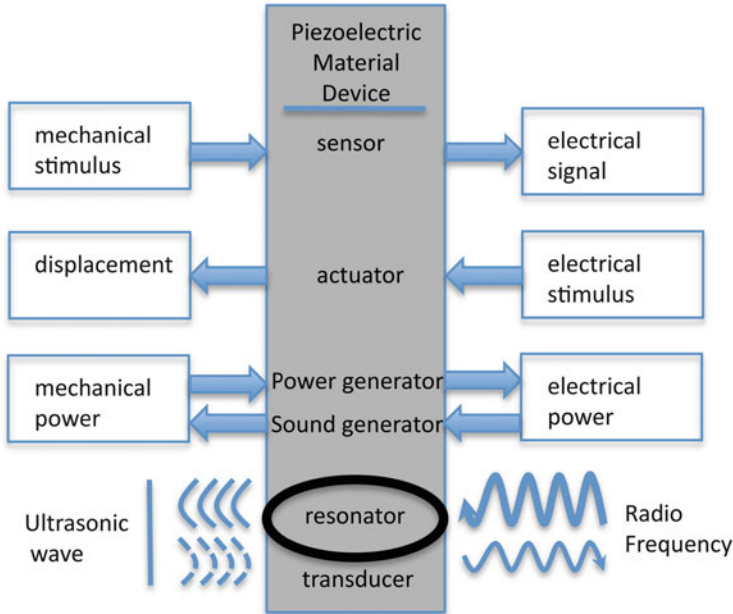


Fig. 24.1 The different conversions and signal generations in piezoelectric materials for sensors, actuators, resonators and transducers

size and complexity, while even reducing energy consumption. Vast wireless sensor networks, or more generally wireless smart systems networks are in the focus of many projects and are being established.

Smart systems need smart materials. Smart materials are materials whose behavior can be controlled by an electrical output parameter of microelectronics, and are able to give a signal in return of how the environment reacts. Most simply, all those signals are directly electrical signals, but can also be governed by magnetic, optical, and thermal interactions. Piezoelectric materials play an important role among these smart materials. They are directly controlled by electrical signals and work in both ways—an ideal solution for adaptive systems. The various exploitations of this effect are sketched in Fig. 24.1. The bi-directional coupling between mechanical and electrical parameters allows the realization of motion and vibration sensors, actuators, transducers, and resonators.

In miniaturized systems, bulk materials are difficult to deal with. Refined machining techniques can typically be used to control dimensions of the order of 10 μm at pieces that are not smaller than 100 μm in diameter. Thick film techniques produce layers of typically 10 to 20 μm thickness, limiting the lateral precision to about the same value. Higher precisions are possible with the techniques known from microelectronics, i.e. thin film deposition, photolithography, and dry and wet etching processes. This brings us to micro-electro-mechanical systems (MEMS). MEMS technology was born as a new technological discipline during the 1980s (for an introductory textbook see [1]). The idea of the pioneers was to enlarge

capabilities of integrated circuits based on silicon beyond pure electronics by adding mechanical elements made of silicon and further materials of semiconductor technology. The addition of mechanics extended the application range of silicon technology to motion sensors, pressure and force sensors, small actuators, and a number of acoustic and ultrasonic devices, most importantly resonators for signal treatment. In order to profit from symbiosis with electronics, those mechanical elements should, of course, be controlled by electronic signals. Evidently, this new silicon technology makes only sense for small, miniaturized devices. The technical advantage comes from the fact that powerful thin film deposition and patterning techniques as used for semiconductor fabrication allow for unprecedented precision of mechanics in the nano to micrometer range. As a large number of devices are produced in parallel on the same wafer (batch processing), the cost level is acceptable in spite of expensive fabrication tools, at least at high production volumes. The chemistry of silicon turned out to be very helpful for micromachining: high etching rates of anisotropic wet etching in a base solution (as e.g. KOH), and anisotropic deep silicon etching in a plasma reactor are crucial issues in efficiently tailoring silicon. Over the last 20 years, MEMS technology became a proven and mature technology with many applications. While “MEMS” is still taken as a standing brand name for the field, the actual MEMS field has become much wider than stipulated by the notion of electro-mechanics, including thermal, optical, magnetic, chemical, biochemical, and further functional properties. Also the main material of the device is not necessarily silicon, but may be glass or plastics, especially in case of bio-medical applications. It is expected that piezoelectric materials with their intrinsic electro-mechanical coupling should and will play an important role in MEMS. Indeed, piezoelectric thin film devices based on ZnO were among the first ones to be demonstrated [2].

Among the most interesting films that can be produced by chemical solution deposition are the ferroelectrics. They are mostly oxides and thus very suited to be synthesized by CSD techniques. There are two properties that are of prime interest for MEMS: piezoelectricity and pyroelectricity. The first property extends mechanical capabilities of MEMS, the second is useful in uncooled thermal infrared detection. This chapter deals with the current status and further research issues in lead zirconate titanate (PZT) thin films for piezoelectric MEMS applications. Focus is given on issues related to processing, integration and characterization, and is thought as a complement to earlier reviews [3–5].

24.1.1 *Pyroelectricity*

Pyroelectricity is a consequence of polar order. In ferroelectrics, it originates from the temperature dependence of the spontaneous polarization P_s . The pyroelectric coefficient p is written as $p = dP/dT$ (see Fig. 24.2). Although any polar material is also pyroelectric, the effect is much stronger in ferroelectrics. The pyroelectric coefficient even diverges at second order ferroelectric phase transitions. To give an

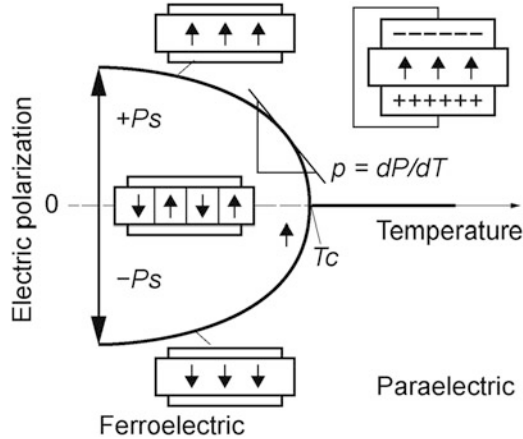


Fig. 24.2 Schematic graph showing the bifurcation (second-order phase transition) of the spontaneous electrical polarization at the critical temperature from $P = 0$ (paraelectric phase) to the two equally probable solutions $\pm P_s$ for the spontaneous polarization in the ferroelectric phase. The inserted capacitor schemes show the cases of maximal positive and negative total polarization, and the case where an equal number of both types of 180° domains results in a zero macroscopic polarization

example: in the rigid polar wurtzite material AlN, the pyroelectric coefficient amounts to $-1 \mu\text{C}/\text{m}^2/\text{K}$ [6], whereas in ferroelectric films of PZT, PLT (lead lanthanum titanate), etc. the coefficient is more than 200 times larger (see, e.g. [7] and refs. therein). The pyroelectric effect is typically used in thermal infrared detectors. The infrared power is absorbed by suitably designed pyroelectric elements that include an absorption layer. The absorbed heat leads to a temperature increase of the pyroelectric element causing the appearance of pyroelectric charges and/or a voltage (see the reviews [8, 9]). The detectability of the IR detector is limited by the signal to noise ratio. The noise contributed by the pyroelectric material is governed by dielectric constant (ϵ) and loss tangent ($\tan\delta$): $\text{noise} \propto \sqrt{\epsilon \tan\delta}$. Hence, an important figure of merit (FM) for the materials is found as: $FM = p/\sqrt{\epsilon \tan\delta}$ (neglecting the thermal heat capacity which varies only weakly from material to material). Considering Fig. 24.2, it looks as if the detection close to the critical temperature would be advantageous. However, in case of a second order phase transition, the product $p\epsilon^{-1/2}$ is temperature independent. Considering that the dielectric loss increases in general as well with the dielectric constant, it is in fact not advantageous to work too close to the critical temperature. In case of first order phase transitions, however, there is no divergence of the dielectric constant at the critical temperature. It was found that when superimposing a DC electric field, and working slightly above the critical temperature where the polarization is induced by the DC electric field, very sensitive IR detectors are obtained [10, 11]. More information on micro-machined thin film pyroelectric detectors and their principles can be found in [7].

In recent years, there is a growing interest in using the pyroelectric effect also for thermal energy harvesting. The pyroelectric materials are subject to thermal cycles that vary the ferroelectric polarization, and thus the electrical energy within the material [12, 13].

24.1.2 Piezoelectricity

In piezoelectric materials, a deformation occurs upon application of an electric field (converse effect). The opposite effect works as well: Upon application of a stress, charges develop on the surfaces of the piezoelectric body (direct effect). Both effects are linear, at least at not too high values of electric field and stress. Strain and stress are symmetrical two-dimensional tensors (see textbook [14]). In engineering, these tensors are given as 1×6 matrices in order to reduce the number of indices. Throughout this chapter, we use the symbols S_k ($k = 1-6$) for the strain tensor, T_k ($k = 1-6$) for the stress tensor, E_k ($k = 1-3$) for the electric field vector, and D_k ($k = 1-3$) for the electric displacement field vector. The equations of state give the relations between electrical and mechanical variables and parameters as follows (see textbook [15])

$$D_i = \epsilon_0 \epsilon_i^S E_i + e_{ik} S_k, \quad T_i = c_{ik}^E S_k - e_{ik} E_k \quad (24.1)$$

$$D_i = \epsilon_0 \epsilon_i^T E_i + d_{ik} T_k, \quad S_i = s_{ik}^E T_k + d_{ik} E_k \quad (24.2)$$

Using E_k and S_k as variables [upper Eq. (24.1)] we must use the dielectric constants at constant strain ϵ_i^S , and the stiffness tensor at constant E -field c_{ik}^E . The piezoelectric tensor in this case is named e_{ik} . Keeping the strain at zero (fully clamped body), e_{ik} relates the produced piezoelectric stress to the applied electric field. In the direct effect, keeping the electric field at zero, e_{ik} relates the produced charge density to the applied strain. In the second set of equations [Eq. (24.2)], we replace the variable strain by the variable stress. We keep the electric field as variable. In this case, the piezoelectric tensor is named d_{ik} and relates the produced strain to the applied electric field at zero stress, i.e. in case of a free body. In the direct effect, it relates the charge density to the applied stress. The elastic relations are defined by the compliance at constant E -field s_{ik}^E , and the dielectric relations with the dielectric constant at constant stress ϵ_i^T . In many polar materials the polar direction follows a 3, 4 or 6 fold symmetry axis. The number of independent piezoelectric coefficients is then reduced to 3 independent values: d_{33} , $d_{31} = d_{32}$, $d_{15} = d_{24}$. In case of a polycrystalline thin film poled perpendicular to the film plane we deal with a cylindrical symmetry giving the same result.

The most frequently applied piezoelectric bulk material is PZT, a solid solution with formula $\text{Pb}(\text{Zr}_x\text{Ti}_{1-x})\text{O}_3$, which exhibits outstanding piezoelectric properties at the morphotropic phase boundary at $x = 0.53$, where the polar direction is changing from [001] to [111] with increasing x , using the notation of the cubic high-symmetry

phase. Considering applications of bulk materials (including thick films), we identify many typical features reflecting their unique characteristics, which may be also unique on the micro or nano scale, and also useful for applications at small dimensions. The use of piezoelectrics in scanning micro probe microscopy is justified by the high rigidity prevailing during deformation, and enabling sub-nanometer precision in all directions. Piezoelectrics are used to generate and sense ultrasonic waves as needed in ultrasonic imaging at frequencies of 1–50 MHz, and in non-destructive testing at similar frequencies, by virtue of the large efficiency in energy conversion between electrical and mechanical energy. In signal filtering, piezoelectric resonators play a dominant role in the range of 0.1 to 10 GHz thanks to their high quality factors, outperforming by far LC resonators. In injection valves for combustion motors, piezoelectric multilayer actuators are applied thanks to large forces and high operation speeds. Without discussing dimensional details one can summarize advantages as follows:

- strong forces, or alternatively large excursions in bending structures;
- low voltage because of high dielectric constants,
- high efficiency in energy conversion, and equivalently low noise detection;
- high speed and high frequency operation possible;
- high acoustic quality of many piezoelectrics (not true in multi-domain ferroelectrics);
- linear behavior in case of not too active ferroelectric domains.

For thin film applications, the same principles remain valid, however, one has to keep in mind that smaller dimensions lead on the one hand to smaller voltages, on the other hand to weaker forces, smaller excursions, and higher resonance frequencies. Piezoelectricity is not the only possible choice. There are also other electro-mechanical phenomena available in the micro world, and not necessarily the same as in the macro world. There is first of all electrostatic interaction across an air or vacuum gap of a capacitor [16, 17] or between comb fingers [18, 19]. Even with the disadvantage of non-linearity, electrostatic interaction can be well used for actuators, and with a bias voltage, also for sensors and transducers. Not so practical in the macro world (very high voltages needed), electrostatics can be a smart solution in the micro world. In theory, electrostatic devices may even reach an electro-mechanical coupling coefficient (or conversion efficiency) k^2 of 100 % in the small signal limit [17], a value that hardly exceeds 60 % in piezoelectrics. A further competing effect is the thermo-mechanical bimorph effect. It can be used for actuation if a micro heater is embedded in the device. The heat dissipation, and thus power consumption of such a device is naturally higher, the application frequency lower, than with a piezoelectric drive. The same holds for shape memory alloy actuators. Further possibilities are offered by electromagnetic interactions, and magnetostrictive materials. Disadvantages of these technologies are in general resistive losses in coils. On the other hand, magnetic interaction can be an advantage if remote power feeding is required [20].

The scientific community was always aware of the importance of piezoelectric MEMS. Interestingly, PZT thin films and their integration were developed in

parallel to main stream MEMS processing. Both fields profited from a general improvement of physical and chemical deposition techniques during the 1980s, and dry etching techniques during the 1990s. However, the main momentum in ferroelectric films came from memory applications (ferroelectric random access memory, FERAM [21, 22]). While PZT FERAM's have now found their niche markets and appear to be more and more established in low power/low voltage non-volatile memories, PZT MEMS have not yet an established place in MEMS. The implied industry is much smaller, and even if physical criteria speak for PZT MEMS, the availability of high quality material, and its price play an important role. Whereas AlN has become well available due to numerous companies and institutes working on thin film bulk acoustic wave RF filters—the first piezo-MEMS success—the ferroelectric $\text{Pb}(\text{ZrTi})\text{O}_3$ thin film is hardly available on a commercial basis. This is not only due to the very limited number of experienced producers (producing mostly for themselves only), but also due to the integration scheme that is often not well mastered and which imposes its rules to the design (see, e.g. [23]). As a result, PZT MEMS is only considered if there is no other, less demanding solution.

24.2 Integration of Ferroelectric Thin Films

Ferroelectric thin films need to be grown or crystallized at relatively high temperatures of 550 to 700 °C. The most economic way is to grow such films directly on the final substrate to be used for MEMS fabrication. Silicon substrates are well suited for this purpose. Glass could also be used provided its melting point is not too low (for instance quartz glass). Processes for silicon micromachining are in general more developed than for any other substrate, meaning that silicon is an ideal choice for ferroelectric MEMS devices. Nevertheless, alternative approaches were and are studied, mostly to increase the film quality or the film thickness beyond possibilities of thin film coatings. The superior quality of PbTiO_3 grown on MgO single crystals was the reason to transfer such PbTiO_3 films onto silicon in a kind of flip chip process at the end of which the MgO single crystal is dissolved [24]. This is of course a very expensive approach. In this chapter we restrict ourselves to integration of thin films on silicon, or more precisely, thermally oxidized silicon. An example is shown in Fig. 24.3. Functional structures as needed in piezo-MEMS are typically cantilevers, bridges, plates and membranes. They contain a passive, elastic layer formed by silicon, and an active layer of a piezoelectric material. The thickness ratio between the two depends on the application, but is typically optimal with respect to the piezoelectric coupling coefficient when silicon is about twice as thick as silicon [25, 26]. A convenient way to define the silicon layer thickness is the use of silicon-on-insulator (SOI) wafers consisting of a several hundred micrometer thick handle wafer, and a device layer of defined thickness (typically few micrometers or less) separated by a thermal oxide layer, called the buried layer. Dry etching of silicon allows for removal of the parts of the handle wafer to liberate the device layer. The buried silicon serves as etch stop layer.

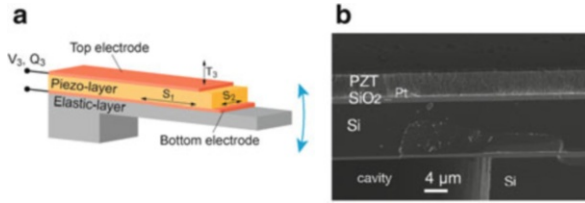


Fig. 24.3 (a) Principle of flexural heteromorph structure driven by piezoelectric parallel plate capacitor configuration. (b) SEM cross section of such an element in SOI technology. The elastic layer of the plate is formed by the device layer (Si) of a SOI wafer (from [27])

There are various integration issues that are important for obtaining an optimal functionality of the film and the device. A first concern is *adhesion* and *phase purity*. On the one hand, no chemical reaction with the substrate is desired in order to obtain a phase pure material. On the other hand, the films must adhere on the substrate. The art is thus to choose and condition the materials as to make chemical bonds across the interfaces without allowing for interdiffusion. This can be delicate when using Pt bottom electrodes on SiO_2 . Adhesion layers of Ti, Zr, or Ta are needed to make Pt layers adhere. During the oxide deposition on top of Pt, oxygen will diffuse through the Pt layer and oxidize the adhesion layer. This provokes Ti diffusion, mechanical stresses and reaction with lead of PZT. It is thus desirable to obtain a certain passivation of the adhesion layer before the deposition of the ferroelectric film [28]. Perovskite materials are enough complex to exhibit a nucleation controlled growth (for details see Chaps. 15 and 17). Nucleation is most easily obtained when growing on other perovskite materials, for instance on a conductive perovskite film such as LaNiO_3 , if it is more easy to grow this one in a given orientation, which seems to be the case with (100)-textured LaNiO_3 [29]. Using Pt(111) as electrode, it is nevertheless possible to grow $\text{PbTiO}_3\{100\}$ as a seed layer for $\text{PZT}\{100\}$. This issue is more discussed in [30]. More recently, interdigitated electrode systems attracted attention for increasing the voltage response [31], or for achieving a negative piezoelectric stress contribution [32]. In this case, the ferroelectric film needs to be grown on an insulating layer, most practically the amorphous thermal oxide on silicon. It is attempted to promote a texture by means of a polycrystalline buffer layer. Besides utility in integration, the requirements of electrical conduction will also influence the choice of a bottom electrode material. Pt is by far a better conductor than the electrically conducting perovskites.

A state of the art version of integrated PZT films on micromachined structures is illustrated in Fig. 24.3(b). Dense and crack free PZT films of $4\ \mu\text{m}$ thickness can be deposited by CSD techniques on wafer level. The measured admittance curves allow for an evaluation of the electro-mechanical coupling factor confirming very well the $e_{31,f}$ of 12 to 14 C/m^2 or even more measured at beams [27, 33, 34].

24.3 CSD Processing of Lead Based Ferroelectric Thin Films for MEMS

Much of PZT processing was learned during FERAM development (see [35, 36]). PZT and related perovskites can be deposited by the major standard methods applied in wafer processing, i.e. metal-organic chemical vapor deposition (MOCVD), sputtering, and CSD. The latter includes the sol-gel techniques. Common to all methods is the thermodynamics of the given materials system, influencing nucleation, growth and phase purity (see Chap. 15).

In case of PZT we deal with a solid solution system composed of PbTiO_3 (PT) and PbZrO_3 (PZ). The free energies of formation for the two corner components is different: PT is more stable than PZ, as revealed by the PbO vapor pressure above PT and PZT. In ceramics annealed above 1100°C , this difference is not so much a concern. Zr and Ti ions do have enough high diffusivities and a statistical distribution is obtained (with the exception of the grain boundaries which might be slightly Zr rich). However, at thin film growth temperatures below 700°C , there is no diffusion of such ions after the perovskite is formed, meaning that the perovskite composition at the growth front (phase boundary between perovskite and vapor (in-situ techniques), or perovskite and amorphous phase (post-annealing) is frozen in. This will in general lead to a compositional gradient, as indeed observed in post-annealed sol-gel films.

The existence of such a gradient was sometimes postulated to explain the moderate peaking of piezoelectric and dielectric properties of thin films at the morphotropic phase boundary [37]. It was once observed by Auger depth profiling [38], and also revealed by etching profiles in PZT MEMS structures [39]. The free energy of formation is significantly more negative (more exothermal) with Ti rich compositions. This means that in the growth front between amorphous and perovskite phase the Ti ions are more likely captured by the crystalline phase than the Zr ions. At a growth temperature of 650°C , the capture probability was estimated to be 56 % for Ti and 44 % for Zr [40]. It turns out that the diffusivity in the amorphous phase is quite high as compared to the propagation speed of the crystallization front. As a consequence, a gradient of composition is established in the amorphous phase leading to a Ti flow to the growth front, and a Zr flow away from the growth front (see Fig. 24.4). Within the perovskite phase there is no diffusion of cations anymore. The gradient can be reduced by a factor 5 if in each individually annealed layer a counter gradient is installed in the amorphous phase, anticipating the problem [40]. One can use for instance four spins of different solutions per one crystallization anneal. The first solution must contain more Zr, the last more Ti than the target composition. Figure 24.4 shows dark field TEM images comparing gradient, and the gradient free films. The contrast arises from the fact that at the morphotropic phase boundary composition (53/47) the symmetry changes from tetragonal (Ti rich) to rhombohedral (Zr-rich). In case of the (standard) gradient film we deal with a well visible tetragonal / rhombohedral phase mixture. The compositional fluctuation was quantitatively measured by EDAX. The Zr

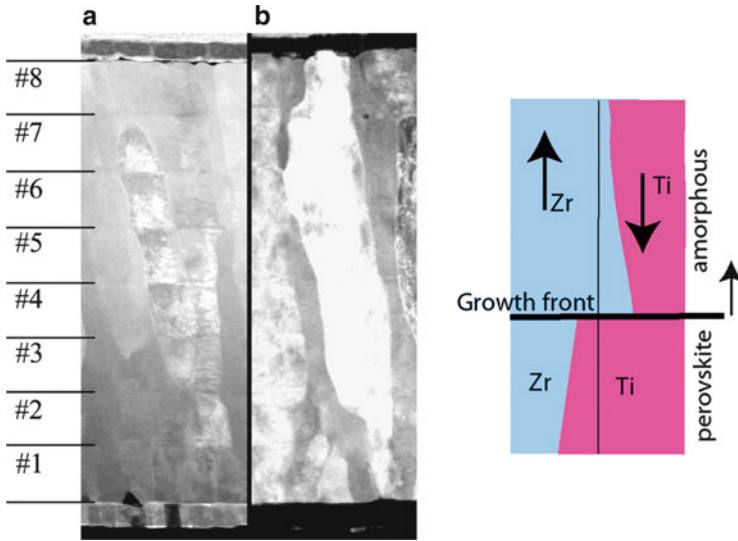
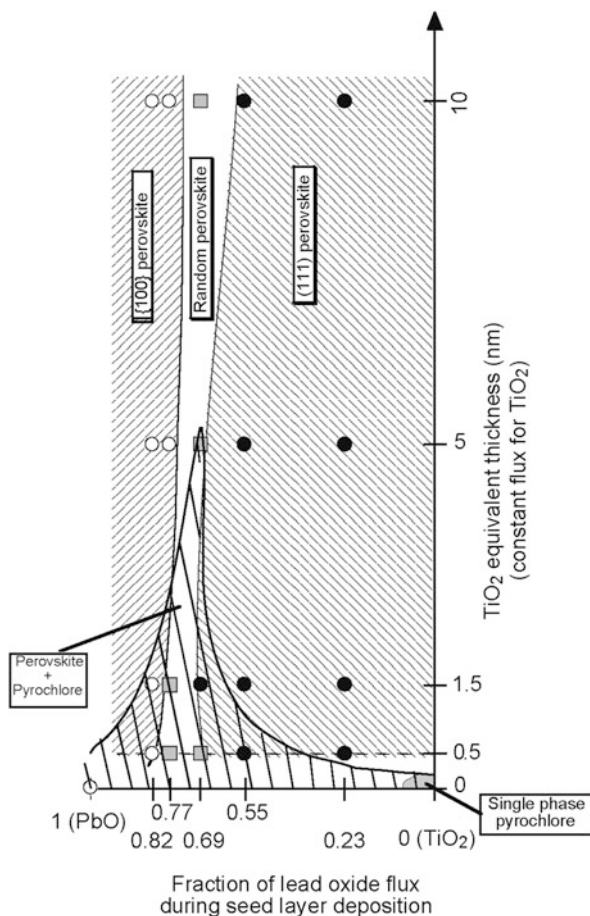


Fig. 24.4 Dark field TEM images of 2 μm thick PZT53/47 films deposited by a sol-gel technique in eight steps. Each step includes 4 spun and pyrolysed layers followed by a crystallization anneal. The image contrast arises from the (201) diffraction from a film of homogeneous 53/47 solution (a), and from a film synthesized with four different solutions anticipating preferential Ti capture for perovskite formation in order to achieve a homogeneous material (b) (from [40]). The schematic to the right depicts the formation of the concentration gradient during crystallization anneal per one single annealed layer of 250 nm

concentration in the gradient film fluctuates between 41 and 65 %, in the gradient-free film between 51.5 and 55.5 %. The removal of the gradient made the dielectric constant rise from 1300 to 1700, and the piezoelectric constant e_{31f} from 13 to 17 C/m². The peaking at the morphotropic phase boundary became more pronounced.

In many other perovskites, homogeneous densification is more of a problem than in sol-gel PZT. In relaxor-type materials there are usually much more disturbing second phases. The related difficulties are well traced in the $\text{Pb}(\text{Sc}_{0.5}\text{Ta}_{0.5})\text{O}_3$ (PST) system [41–43]. The point there is that the first nucleating phase is a Pb-Ta-O pyrochlore, and that there is no stable Pb-Sc-O second phase. As a consequence, the pyrochlore has to be retransformed to form later the PST perovskite, leading to a higher annealing temperature. In addition, not all the lead finds place in the Ta pyrochlore and thus evaporates partially as PbO. The final structure becomes PbO deficient, meaning oxygen vacancies in Sc^{3+} rich zones, and Pb vacancies in Ta^{5+} -rich zones. This type of disorder is different from the disorder obtained by quenching ceramics from 1,200 °C, and not surprisingly, the observed relaxor behavior does not show the large peak in dielectric constant as expected. However, one can refill the missing PbO at 900 °C in a saturated PbO/O_2 atmosphere, and obtains much improved properties [42]. Unfortunately this is not a viable approach for MEMS fabrication. The above described problem of inhomogeneity in thin

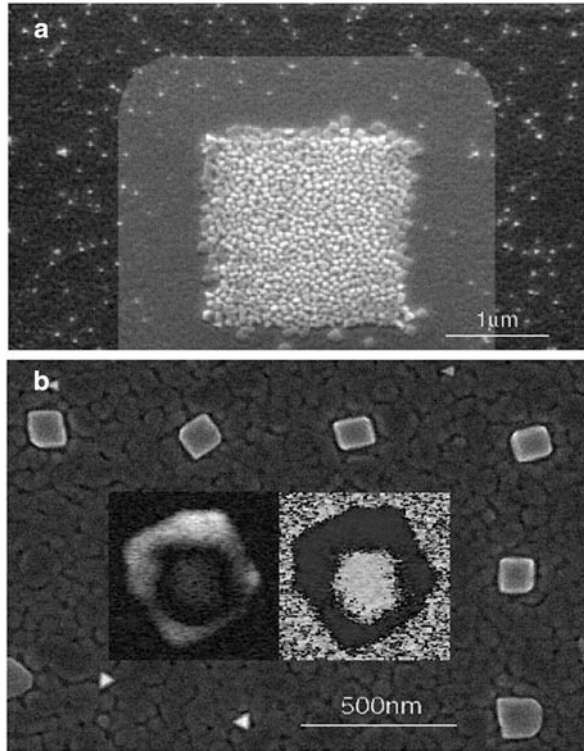
Fig. 24.5 Diagram summarizing PZT texture and presence of pyrochlore as a function of seed layer composition and thickness [46]. Seed layer as well as PZT were obtained by in-situ sputtering from three metal targets. The same trends are also observed in CSD deposition



films resembles in part the findings related to fine grained and porous ceramics of relaxors [44].

The perovskite structure is sufficiently complex to exhibit a so-called nucleation limited growth—at least if we do not deal with homoepitaxy. Hence, substrate structure and chemistry as well as chemical composition of the first monolayers play an essential role (see [45] for details). It is for instance observed that nucleation on Pt(111) needs some lead excess, while no excess is needed for continuing growth on an existing PZT film. This is related to the high vapor pressure of PbO that is not yet incorporated into the perovskite lattice. Another example is the orientation as obtained on Pt(111), which depends on the chemical composition of the first few monolayers. Starting a layer of PbTiO₃ with TiO₂ (or Ti rich) leads rather to (111) orientation, starting with PbO (or lead rich) leads rather to (100)-orientation [46] (see Fig. 24.5). Such behavior allows for a texture control with titania seed layer for achieving (111) growth [47]. On very small TiO₂ islands with 2 nm thick titania (rutile(100)), quasi single crystal platelets were obtained (see Fig. 24.6), allowing

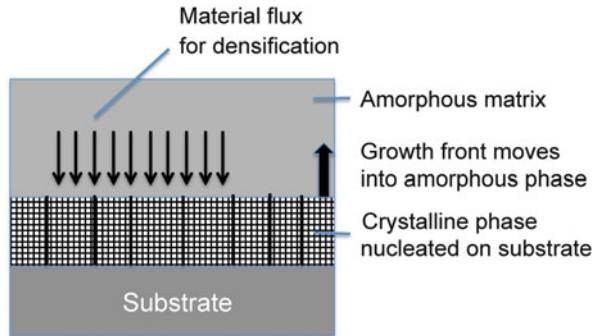
Fig. 24.6 Condensation of PbTiO_3 (nominally 2 nm) on which 18 nm of PZT40/60 is grown. The whole structure was grown on a 100 nm epitaxial Pt(111) film on a SrTiO_3 single crystal. (a) The $2 \times 2 \mu\text{m}$ large square in the center was originally coated by 2 nm TiO_2 . The highlighted area indicates the depletion zone around the affinity square [48]. (b) Nucleation on small affinity spots. The inserts show the piezo-AFM response with amplitude (left) and phase (right) image (from [48])



for a site controlled, or registered growth of ferroelectric nano sized structures by sputtering [48] as well as by sol-gel [49]. Interesting to note that such small islands of titania attract a lot of PbO flux arriving by surface diffusion over a distance of up to about $1 \mu\text{m}$, leading to $\{100\}$ -orientation instead of (111) orientation. It must be inferred that the titania seed layer is transformed to a $\text{PT}\{100\}$ seed layer. On the bare Pt, a much smaller nucleation density is achieved. In addition, the nucleated crystallites show a trigonal symmetry indicating (111) orientation. This shows that lead excess is an important parameter during growth and crystallization anneal. The higher volatility of PbO requires an excess either during growth, or in as-deposited films before post-annealing as required in techniques such as sol-gel. The experiment on the nano scale shows also the importance of seed layers in obtaining orientation and a high density of nucleation sites.

Crystalline phase nucleation is a crucial issue in two respects: First of all it is important to achieve the right crystalline phase of the material. Secondly, for property optimization, the crystalline orientation or texture must be a specific one and needs to be reproducibly controlled. The growth substrate plays of course a very prominent role. It is essential to start with well-defined substrates, meaning bottom electrodes in many cases. A standard solution is a passivated Pt film. This means that the adhesion layer (based on Ti, Ta, Zr, etc.) is oxidized prior to the deposition of the ferroelectric oxide [28, 50]. Alternatively, oxide conductors

Fig. 24.7 Schematic drawing showing the perovskite growth (crystalline phase) and the resulting densification by material diffusion through the amorphous phase



(see Chap. 25) can be used, such as SrRuO_3 , or LaNiO_3 [51]. Of course one has to check if the resistance of the electrode is compatible with the application. The (111) orientation on Pt was also obtained by means of specific steps during crystallization anneal of sol-gel films, provoking Pb-Pt alloying. This alloy was identified as reason for (111)-orientation of the PZT film [52, 53]. For homogeneous nucleation of the (100)-orientation, it turned out to be very useful to use a PbTiO_3 template layer that grows in (100)-orientation on Pt (100) if enough lead flux is assured [54]. PbTiO_3 nucleates much more easily than PZT 50/50, and in addition does not exhibit the competing pyrochlore in the temperature range of interest.

Aside of this concentration issue, sol-gel films of PZT are very well densified during annealing. This is not only seen on TEM or SEM cross sectional images, it is also manifested in the very high e_{31f} [$= d_{31}/(s_{11}^E + s_{12}^E)$ see Eq. (24.3)] coefficient of up to 17 C/m^2 . The material flow is quasi one-dimensional along the z-direction, and allows for an unperturbed columnar growth (Fig. 24.7).

The reason is that we deal with the above mentioned nucleation limited growth, which as a consequence leads to nucleation at interfaces, surfaces, and particles (hetero nucleation) before nucleation within the amorphous phase can take place (homo nucleation). For this reason is it so important to promote nucleation by a suitable substrate, and to work particle free. When PZT films are sputter deposited at lower temperatures, and post-annealed later as in case of sol-gel films, the density seems to be never as good. It appears that during sputtering already the material becomes inhomogeneous by nano-crystallite and roughness formation. The densification is never as homogeneous, leading finally to pores. Sputtering leads to good results only if the film is deposited in-situ, meaning at high temperature (about 600°C) directly in the perovskite phase [55].

24.4 Piezoelectric Coefficients

Thin film microstructure and the electrode system must fit to the operation mode. In MEMS technology, most of the piezoelectric thin films are polycrystalline materials. The piezoelectric effect is averaged over all the grains. At this point

one has to distinguish between ferroelectric (such as PZT) and non-ferroelectric polar materials (such as AlN and ZnO). The latter do not allow reorientation of the polar axis. In this case, the material growth process has to provide for a textured structure that includes the alignment of the polar directions. In ferroelectric materials, the polar axis can be reoriented by an electric field. Although the ideal ferroelectric can be easily switched at room temperature (a property that is used in memories), the ferroelectric thin film is usually better poled (i.e. more remnant polarization) when rising the temperature 100 to 200 °C for moving charged defects, especially oxygen vacancies, in order to un-pin domain walls and comply defect positions with the domains of the poled material [56]. To some degree, the charged defects provoking back switching can also be compensated by electrons and holes generated by UV illumination during poling [57]. Many of the phenomena during poling are not yet fully understood. For the moment we just state that at the end of poling, the polarization is aligned as much as possible with the poling field. Using a parallel plate configuration (bottom and top electrode), the ferroelectric material is poled perpendicular to the film plane. Since for MEMS applications, flexural structures are exploited, the relevant piezoelectric coefficient is the transverse one. Most conveniently one uses the coefficient $e_{31,f}$ defining the in-plane piezoelectric stress T_1 (or T_2) when an electric field in the 3-direction (perpendicular to the plane) is applied under the condition that the out-of-plane stress $T_3 = 0$ [25, 58]:

$$e_{31,f} = d_{31} / (s_{11}^E + s_{12}^E), \quad T_1 = e_{31,f} E_3 \quad (24.3)$$

The direct effect follows as $D_3 = e_{31,f}(S_1 + S_2)$ and is convenient to describe the collected charges upon bending the flexural structure and straining the parallel plate capacitor by S_1 and S_2 . The evaluation of this coefficient without elaborating complicated devices is important for the thin film development. It is often measured in the direct mode through the deformation of wafer thick plates or cantilevers [59–62]. Such measurements have allowed determination of optimal film texture and composition (Fig. 24.8(a)). The $e_{31,f}$ is also a very good indicator of the film density, which is crucial for piezoelectric stress development. Figure 24.8(b) shows its evolution over the years. It is a nice witness of the progress made during the last 14 years, and reflects the various development stages of improving electrode substrates, film density and texture by seeding, and finally compositional improvements within the PZT film.

A more recent variation of electrodes is the use of interdigitated electrodes [77] for ferroelectric films. As the polarization direction follows always the poling field, polarization and electric field are everywhere parallel to each other, and one obtains a kind of “ e_{33} ” or $e_{xx,f}$ effect in the plane of the film. This longitudinal effect is expected to be larger than the transverse effect. Estimations show indeed that a coefficient of 27 C/m² can be expected if poling is fully successful. This mode can be used as alternative to the parallel plate capacitor structure for bending actuation,

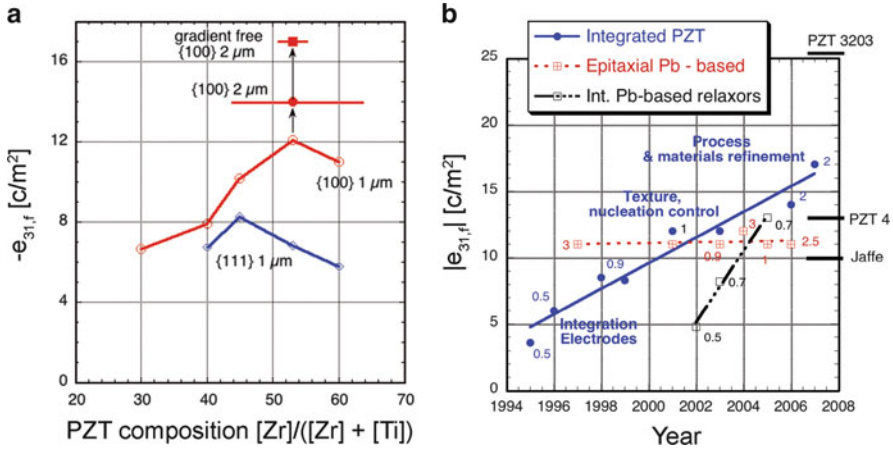


Fig. 24.8 (a) Transverse e_{31f} coefficient as a function of composition and texture of PZT films. Film at morphotropic phase boundary improve by increased film thickness and improved homogeneity of film composition. Combined results from [39, 40, 63]. (b) The evolution of the transverse piezoelectric coefficient e_{31f} as an indicator of the advancement in the field. The films are in the 0.5–2 μm thickness range. PZT thin films integrated on silicon (data from [39, 40, 60, 61, 64–66]) are compared with several types of lead-based epitaxial films (PZT [67, 68]), $\text{BiScO}_3\text{-PbTiO}_3$ [69], $\text{Pb(MgNb)}_2\text{O}_7\text{-PbTiO}_3$ [70–72], relaxor type integrated thin films such as $\text{Pb(Yb,Nb)}_2\text{O}_7\text{-PbTiO}_3$ [73–75]. The values derived from ceramics data refer to early PZT ceramics [76], standard hard PZT 4 (product of Morgan Electroceramics), and modern optimized PZT ceramics, the 3203 of Motorola. The *small numbers* aside of the points are the film thickness in micro meters

or bending strain measurement. In actuators, a larger deflection effect was measured in this configuration [32]. In addition, the compressive piezoelectric stress may yield larger deflections of membranes (which was indeed observed [78]), and does not provoke cracking of PZT, as may occur in very thick, dense PZT thin films. In energy scavenging, the use of interdigitated electrodes in conjunction with ferroelectrics is practically necessary since the harvested voltage must be as large as possible [79, 80].

24.5 Basics of Micromachining and Piezoelectric Thin Film Structures

There is a plethora of applications using piezoelectric laminated structures in the bending mode based on beam and plate structures, as sketched in Figs. 24.9 and 24.10. Rigidity and deflection amplitude can be engineered in a wide range. At the upper frequency range (0.1–15 MHz) we find piezoelectric micromachined ultrasonic transducers (pMUT), realized with ZnO [81] and PZT [82, 83]. A pMUT is a device able to transmit and receive ultrasonic waves. Potential applications are

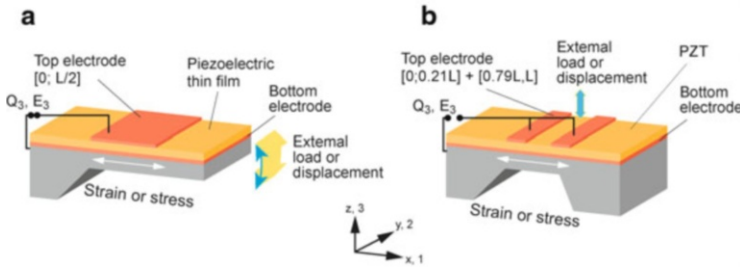


Fig. 24.9 Bending structures for sensors and actuators in the form of cantilever beams (a) and bridges (b) using the transverse piezoelectric coefficient $e_{31,f}$ of with parallel plate electrodes. Silicon micromachining is sketched for the use of anisotropic wet etching (KOH or similar) (from [90])

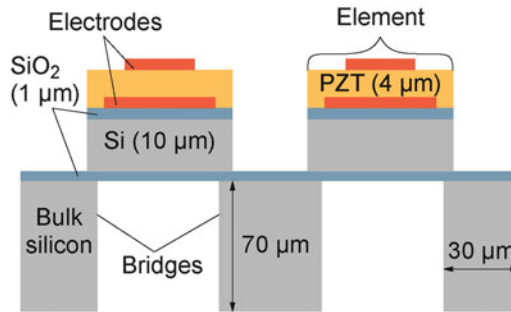


Fig. 24.10 PZT thin film elements for micromachined transducers (pMUT's). In this case the micromachining process is based on deep silicon dry etching (Bosch process) with a stopping layer in the form of a buried oxide layer (from [27])

ultrasonic imaging, non-destructive testing, droplet ejection [84], sensors using ultrasound, ultrasonic micromotors [85–87], and tonpilz transducers [51]. Plates similar to pMUT structures with strong PZT films are very much suited for ink jet printing heads. Resonators of flexural modes have also been proposed for analogue signal processing, as needed for instance at intermediate frequencies (few MHz) in mobile communication [88, 89]. At lower frequencies, flexural structures were demonstrated for applications as microphones in photoacoustic gas sensors [90], as accelerometers [91], and more recently for energy scavenging [79, 80]. A further possible application is active damping of motion sensors. The same PZT film is used in the vibration sensor and the damping actuator [92, 93]. Actuation of optical mirrors is a further possibility. For details on micromachining processes, the reader is referred to textbooks, such as [94].

Much less works are made for devices based on using the $d_{33,f}$ perpendicular to the film plane. Displacements are of course small, but the response can be sufficient for sensor applications. Accelerometers [95] and the sensor part in active damping have been proposed [93]. Resonators in the thickness mode exhibit quite high frequencies in the lower GHz frequency region, where ordinary PZT has too high losses for applications [96]. This application is better suited for AlN.

24.6 Examples of Piezoelectric MEMS Devices

It appears that the typical time to market of a thin film device is about 20 years when counting the time from the first demonstration of a functional thin film for a given device principle. The involvement of a new material complicates the development beyond the known problematic of a new product for a new market. We usually deal with a new product enabled by a new material. When the idea is born, the material is often not ready (the opposite is unlikely, without ideas for applications, no material is optimized). The AlN thin film bulk acoustic wave resonator (TFBAR) for mobile phone RF filters is a good example. The idea goes back to the 1970s; first demonstrations of standing BAW waves in AlN films were made around 1980. However, there was no market yet. At this time RF filters were required for television at some few 100 MHz. Such frequencies are too low for thin film resonators, meaning that too thick films would have been required (frequency goes as inverse film thickness), and specs were much more conveniently achieved with surface acoustic wave filters. The need for RF filters for the second generation mobile phones at 2 GHz was the trigger for starting mass production of TFBAR's in the year 2000. It was thus the increase in frequency that pushed downscaling of a known principle to be implemented with thin piezoelectric films. It looks very likely that similar criteria will lead to the market introduction of ferroelectric PZT thin film MEMS in the field of ink jet printing. Here it is the decrease in pixel size that requires a new approach. Again, the time to market of 20 years would be matched, as the first work of a rudimentary MEMS device with PZT thin film was published in 1990 [97].

When looking at applications of bulk piezoelectrics, we note that the use of PZT ceramics in scanning micro probe microscopy is justified by the high rigidity prevailing during deformation, and enabling sub-nanometer precision in all directions. The large efficiency in energy conversion between electrical and mechanical energy are used to generate and sense ultrasonic waves as needed in ultrasonic imaging at frequencies of 1–50 MHz, and in non-destructive testing at similar frequencies, or at lower frequencies for piezoelectric transformers. The ability of PZT multilayer structures to delivery large forces upon short reaction times and at moderate voltages has allowed for the realization of injection valves that render Diesel motors much cleaner. For thin film applications, the same principles virtues remain valid, however, one has to keep in mind that smaller dimensions lead on the one hand to smaller voltages, on the other hand to weaker forces, smaller excursions, and higher resonance frequencies. In addition, in the micro world piezoelectricity is competing with capacitive devices employing electrostatic interaction across an air or vacuum gap or between comb fingers. Often, piezoelectric structures have an advantage nevertheless, particularly due to better linearity, larger excursions, and because piezoelectric structures do not need a bias voltage to sense motions, or to harvest vibrations energy.

During recent years, energy harvesting from vibration and motion sources has attracted much interest, particular as micropower sources. The main applications are wireless communication and sensors. Supply powers of $< 100 \mu\text{W}$ are sufficient to operate wireless nodes in the silent mode. The duty cycle of such nodes can be quite small, so that mW supply levels enable some autonomy. Motion and vibration are the most versatile and ubiquitous ambient energy source available, if light harvesting is excluded by the application. The mechanical-to-electrical energy transformation is most efficiently done by piezoelectric materials [98]. In a micro-scale generator, an elastic structure containing a piezoelectric film is strained by coupling to the external vibration by means of induced inertial motion at resonance (see Fig. 24.11). Such sources must match their resonance frequency to the external vibration spectrum. Vibrations from machinery usually have a frequency of 100 Hz, i.e. very low for micro systems, as resonant frequencies tend to increase with shrinking dimensions and masses. A useful soft elastic body is a rather thin cantilever with a large mass. The energy transformed from mechanical to an electrical form is proportional to the piezoelectric coupling k^2 , which in the case of MEMS structures is not the material constant of the piezoelectric layer, but includes the rigidities of the other elastic materials involved in the deformation, and the relative dimensions, including the volume fraction of the piezoelectric material in the total elastic body [25]. An evaluation for bimorphs was carried out in [99]. The energy harvesting from the oscillating cantilever is in competition with mechanical losses of the oscillating system. If the system is operated in air the corresponding loss factors are in the percentage range. One can conclude that a k^2 of 5 % would be about adequate. Such high coupling constant can be achieved with PZT thin films [100].

PZT exhibits a high dielectric constant, and thus yields low voltages when using parallel plate electrodes. The rectifying circuit for the harvested AC power needs at least 500 mV for efficient rectification, even when using charge transfer switches for voltage multiplication [103]. As a consequence, it is much better to use interdigitated electrodes for harvesting with high permittivity, ferroelectric piezoelectrics. One could even expect a larger piezoelectric coefficient [5, 32]. Harvesting with interdigitated electrodes was first demonstrated by Kim and coworkers [104]. They reported $1.0 \mu\text{W}$ and 2.4 V output at 14 kHz and 14 nm amplitude with a beam of roughly $200 \times 150 \mu\text{m}$. In subsequent work [105] a spiral beam was proposed exhibiting a much lower resonant frequency of 150 Hz. Theoretical calculations for a bimorph yielded $30 \mu\text{W}/\text{cm}^2$ at 150 Hz and 1 g acceleration. The measurements depicted in Fig. 24.12 show an output voltage of 1.6 V at $1.4 \mu\text{W}$ power (0.6 mm^2 beam, at 2 g acceleration, 870 Hz) [80]. Useful power levels are thus achieved with micro power generators if vibration sources above about 100 Hz and with acceleration levels of 0.1–1 g can be exploited. It is often difficult to match piezoelectric MEMS harvesting structure with its eigenfrequency to the source frequency. To come around this problem, it was proposed to excite the piezoelectric structure not by acceleration, but by direct mechanical contact to a force able to pull the elastic harvesting device. The latter will then oscillate, damped by feeding the piezoelectric current into an external electrical circuit (see

Fig. 24.11 Schematic drawing of piezoelectric thin film vibration energy harvester using ferroelectric materials with interdigitated electrodes

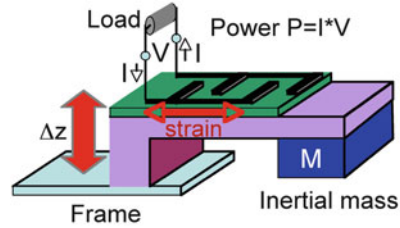


Fig. 24.12 Output voltage and power of 0.6 mm² device (working as shown in Fig. 24.11) as a function of acceleration at 870 Hz (from [101])

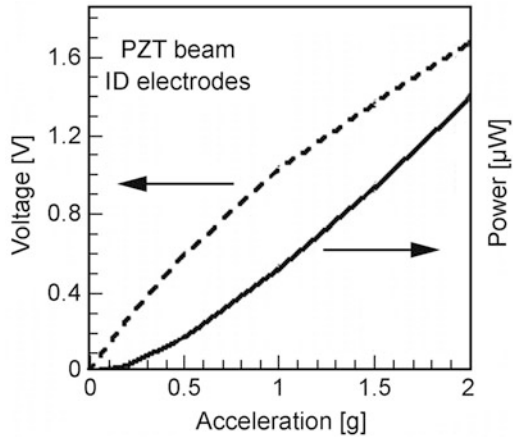


Fig. 24.13). The number of cycles needed to harvest the total elastic energy stored in the elastic harvester structure after deflection, which is equal to the work done by the pulling force, depends directly on the piezoelectric coupling factor k^2 (considering no mechanical losses).

An ingenious example for a linear actuator is an autofocus lens for mobile phone cameras, with a market potential of one billion pieces per year (poLight Technology). The piezoelectric film is deforming a polymer lens to change the focus distance with an impressive speed (Fig. 24.14). This novel lens is 10 to 20 times faster than existing ones, and in addition, it consumes 20 to 40 times less power! It will revolutionize imaging techniques for miniature cameras. Multiple focus distances can be applied for the same snapshot yielding images that are sharp in the fore and background, and improve images of moving objects.

If we supply a linear actuator with an ac voltage, one can hit the oscillation frequency of a mechanical structure, serving for instance as a mirror. The result is an optical scanner. These are not only good for reading barcodes, but also for displaying real time images. Such a miniature apparatus could be used for instance in connection with a mobile phone. The performance depends on how much the mirrors can be tilted, how fast, and also of the width of the mirror. The product of deflection angle times the scanning frequency (how many lines per second can be written) must be large. In a recent work it was shown that piezoelectric thin film

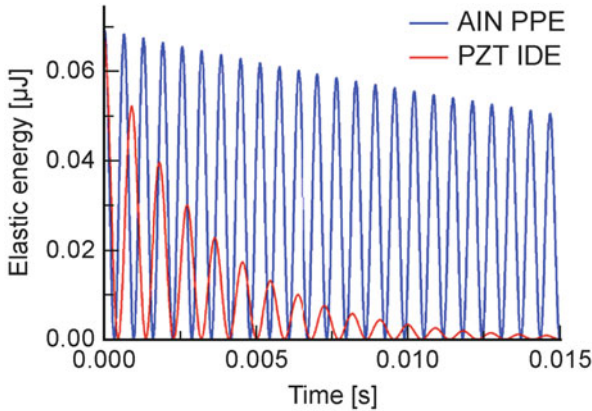


Fig. 24.13 Alternative to resonant vibration harvester: Asynchronous coupling of excitation and harvester eigenvibration in the form of push and release mechanism. The elastic energy stored in a cantilever by an initial deflection (push) is decreasing with time by electrical harvesting (electrical current flows through external resistor). The amount of charge harvested per cycle depends on the piezoelectric coupling factor and is larger in case of a PZT interdigitated electrode (IDE) than in the case of parallel plate electrodes with AlN (from [102])

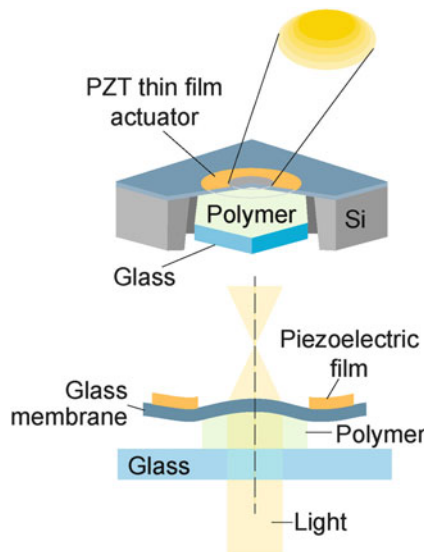


Fig. 24.14 Concept of the poLight tunable lens for small autofocus camera systems. Modified after <http://www.polight.no>

driven, resonant micro mirrors are the fastest ones, faster than electrostatic or electromagnetic drives (Fig. 24.15). In addition, they are smaller, and their power consumption is lower.

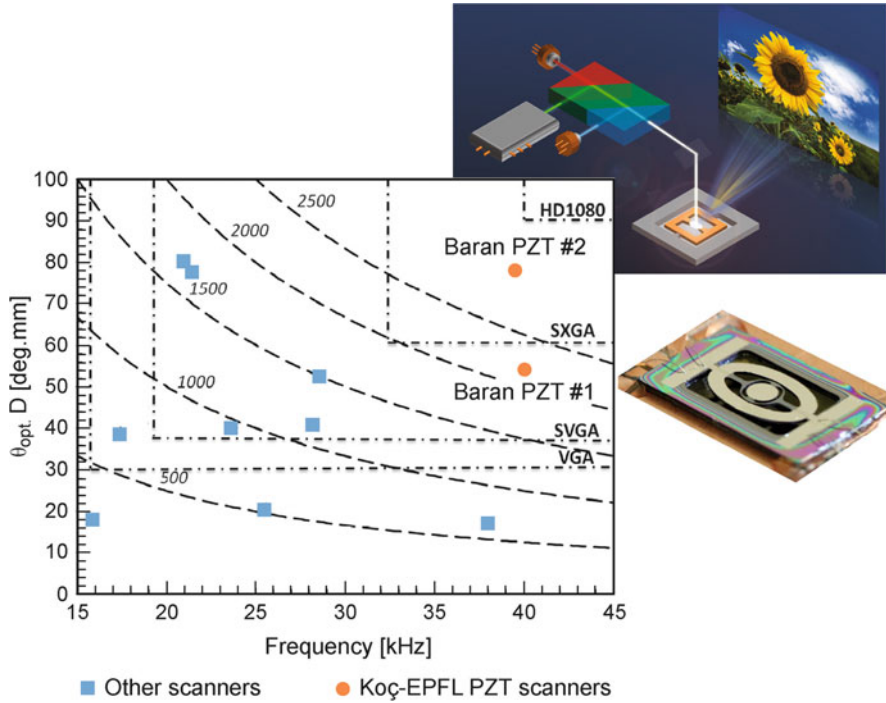


Fig. 24.15 Optical scanner for imaging (from [106]; see also <http://www.microvision.com>)

A further mass product in preparation are ink-jet devices for high-resolution professional printers with 1200 dpi resolution. Practically all companies involved in the fabrication of ink-jet printing heads are currently working on the topic. The high resolution requires linear arrays of high-density droplet ejectors. Diaphragms coated with PZT thin films create a pressure wave in a cavity filled with ink, leading to a droplet ejection at the exit of the cavity (Fig. 24.16). The droplets are timed with micro-second precision and exhibit speeds of typically 10 m/s, before they impact on paper moving with 150 m/min. Apart for printing, ink-jets can also be used for dispensing colors on flat panel displays, or biochemical screening agents on bio-chips for diagnostics. Huge production volumes are expected for all of these fields.

An example of an adaptive system is active damping. A vibration is cancelled by means of active elements making a counter motion. A vibration sensor in the center part of the device, there where the vibration must be kept away, gives the input signal to the regulation circuitry that drives the active elements. PZT thin films can be used for the sensor and the active elements, resulting in a very compact design as shown in Fig. 24.17. It is thought to apply such micro damping stages for vibration sensitive sensors such as gyros (angular revolution sensors).

The piezoelectric thin film beams can also be used for realizing switches. The European project (EPAMO), coordinated by EPCOS-TDK, has the objective to explore the potential of unprecedented ultra-high density MEMS switch arrays to

Fig. 24.16 Schematic cross section through one array element of an ink-jet printing head (after Fujii et al. Panasonic [5, 55])

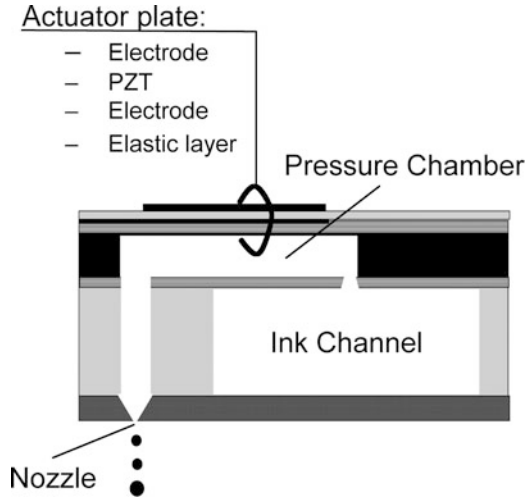
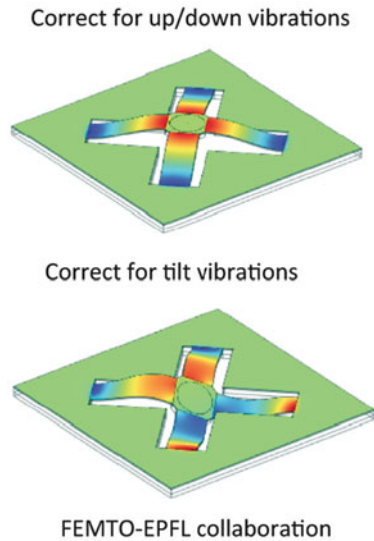


Fig. 24.17 Deformation modes of PZT thin film active damping stage to correct for up-down and tilt vibrations (from [107])



be integrated in an energy-efficient agile radio frequency transceiver with reconfigurable antenna. The goal is to increase very much the antenna efficiency, which will allow for a better reception, and decreasing signal intensities. It is thought that this technique will reduce the power consumption of mobile phones by 50 % and those of the base stations by 10 %. The crucial advantage of piezo-electric films here is again low voltage operation and good scalability to small dimensions.

24.7 Conclusions and Outlook

The integration of piezoelectric materials in micro and nanosystems has made considerable progress during the last 10 years. The thin film material quality approaches, or even surpasses known bulk properties. Piezoelectric MEMS find increasing interest in applications for which piezoelectric actuation or transduction offers superior performance. The most relevant application to date is in analogue signal processing for mobile communication, where bulk acoustic waves in AlN thin films are employed in RF filters. Ferroelectric piezoelectrics are more suited for flexural structures operated at lower frequencies. Important applications are in preparation for liquid delivery and droplet ejectors, as needed in inkjet printing and biomedical devices. Piezoelectrics offer a good stability over a wide temperature range, do not need electric fields across the liquid and can be operated at moderate voltages (PZT). There are many other applications under investigation like energy scavenging, active damping, mirror arrays and scanners, and further more. Especially for PZT, there is still some knowledge gap in reliability issues, such as life time stability in various environments. PZT thin films reached the properties of undoped ceramics. After having solved electrode stability, texture control, and homogeneity issues, it is probably time to advance with doping of PZT thin films, as this is the most obvious difference to superior ceramics. Of particular interest is also domain engineering. The question is whether certain domain configurations are more favorable for a high response than others, and how they can be established by suitable growth conditions, electrode geometries, and electrical treatments.

References

1. Maluf N (2000) An introduction to microelectromechanical systems engineering. Artech House, Boston, London, ISBN 0-89006-581-0
2. Uozumi K, Ohson K, White RM (1983) Generation and detection of ultrasonic Lamb waves in a thin deposited film using interdigital transducers. *Appl Phys Lett* 43:917-919
3. Muralt P (2000) Ferroelectric thin films for microsensors and actuators: a review. *J Micromech Microeng* 10:136-146
4. Kingon A, Muralt P, Setter N, Waser R (2004) Electroceramic thin films for microelectronics and microsystems. In: Buchanan RC (ed) *Ceramic materials for electronics*. Marcel Dekker, New York, NY
5. Muralt P (2008) Recent progress in materials issues for piezoelectric MEMS. *J Am Ceram Soc* 91:1385-1396
6. Dubois MA, Muralt P (1999) Properties of AlN thin films for piezoelectric transducers and microwave filter applications. *Appl Phys Lett* 74:3032-3034
7. Muralt P (2001) Micromachined infrared detectors based on pyroelectric thin films. *Rep Prog Phys* 64:1339-1388
8. Porter SG (1981) A brief guide to pyroelectric detectors. *Ferroelectrics* 33:193-206
9. Whatmore RW (1986) Pyroelectric devices and materials. *Rep Prog Phys* 49:1335-1386

10. Watton R, Todd MA (1991) Induced pyroelectricity in sputtered lead scandium tantalate films and their merit for IR detector arrays. *Ferroelectrics* 118:279–297
11. Hanson CM, Beratan HR, Belcher JF, Udayakumar KR, Soch KL (1998) Advances in monolithic ferroelectric uncooled IRFPA technology. In: SPIE: Infrared detectors and focal plane arrays V, vol 3379. SPIE, Orlando, FL, pp 60–68
12. Ravindran SK, Huesgen T, Kroener M, Woias P (2011) A self sustaining micro thermomechanic-pyroelectric generator. *Appl Phys Lett* 99:104102
13. Moreno RC, James BA, Navid A, Pilon L (2012) Pyroelectric energy converter for harvesting waste heat: simulations versus experiments. *Int J Heat Mass Transfer* 55:4301–4311
14. Nye YF (1985) Physical properties of crystals. Oxford University Press, Oxford
15. Moulson AJ, Herbert JM (1990) Electroceramics. Chapman & Hall, London
16. Soh HT, Ladabaum I, Atalar A, Quate CF, Khuri-Yakub BT (1996) Silicon micromachined ultrasonic immersion transducer. *Appl Phys Lett* 69:3674–3676
17. Ergun AS, Yaralioglu GG, Khuri-Yakub BT (2003) Capacitive micromachined ultrasonic transducers: theory and technology. *J Aerospace Eng* 16:76–84
18. Jaecklin VP, Linder C, de Rooij NF, Moret JM (1993) Comb actuators for xy-microstages. *Sensor Actuat A* 39:83–89
19. Cheung P, Horowitz R, Howe RT (1991) Modelling and position detection of a polysilicon linear microactuator. *ASME Micromech Sensors Actuat Syst* 32:269–278
20. Quandt E, Ludwig A (2000) Magnetostrictive actuation in microsystems. *Sensor Actuat A* 81:275–280
21. Scott JF, Paz de Araujo CA (1989) Ferroelectric memories. *Science* 246:1400–1405
22. Auciello O, Scott JF, Ramesh R (1998) The physics of ferroelectric memories. *Phys Today* 51:22–27
23. Raeder H, Tyholdt F, Booiij W, Calame F, Ostbo NP, Bredesen R, Prume K, Rijnders G, Muralt P (2007) Taking piezoelectric microsystems from the laboratory to production. *J Electroceramics* 19:357–362
24. Fujii S, Kamata T, Hayashi S, Tomita Y, Takayama R, Hirao T, Nakayama T, Deguchi T (1995) Pyroelectric linear infrared sensors made of La-modified PbTiO₃ thin films and their applications. *SPIE* 2552:612–621
25. Muralt P (1997) Piezoelectric thin films for MEMS. *Integr Ferroelectr* 17:297–307
26. Dubois MA, Muralt P (1998) PZT thin film actuated elastic fin micromotor. *IEEE Trans UFFC* 45:1169–1177
27. Belgacem B, Calame F, Muralt P (2007) Piezoelectric micromachined ultrasonic transducers with thick PZT sol gel films. *J Electroceramics* 17:369–373
28. Maeder T, Sagalowicz L, Muralt P (1998) Stabilized platinum electrodes for PZT thin film deposition using Ti, Zr, and Ta adhesion layers. *Jpn J Appl Phys* 37:2007–2012
29. Zhang XD, Meng XJ, Sun JL, Lin T, Ma JH, Chu JH, Kwon DY, Kim CW, Kim BG (2008) Preparation of LaNiO₃ thin films with very low room-temperature electrical resistivity by room temperature sputtering and high oxygen-pressure processing. *Thin Solid Films* 516:919–924
30. Infortuna A, Muralt P, Cantoni M, Setter N (2006) Epitaxial growth of SrBaNb₂O₆ thin films on SrTiO₃ single crystal substrate. *J Appl Phys* 100:104110-1–104110-7
31. Chidambaram N, Mazzalai A, Muralt P (2012) Measurement of effective piezoelectric coefficients of PZT thin films for energy harvesting application with interdigitated electrodes. *IEEE Trans UFFC* 59:1624–1631
32. Hong E, Trolrier-McKinstry S, Smith R, Krishnaswamy SV (2006) Vibration of micromachined circular piezoelectric diaphragms. *IEEE Trans UFFC* 53:697–706
33. Belgacem B, Calame F, Muralt P (2005) Design, modeling, and fabrication of piezoelectric ultrasonic transducers. In: IEEE ultrasonics symposium, vol 1, IEEE, Rotterdam, pp 483–486
34. Muralt P, Ledermann N, Baborowski J, Barzegar A, Gentil S, Belgacem B, Petitgrand S, Bosseboeuf A, Setter N (2005) Piezoelectric micromachined ultrasonic transducers based on PZT thin films. *IEEE Trans UFFC* 52:2276–2288

35. Araujo CA, MacMillan LD, Melnick BM, Cuchiario JD, Scott JF (1990) Ferroelectric memories. *Ferroelectrics* 104:241–256
36. Jones RE, Zürcher P, Chou P, Taylor DJ, Lii YT, Jiang B, Maniar PD, Gillespie SJ (1995) Memory applications based on ferroelectric and high permittivity dielectric thin films. *Microelectr Eng* 29:3–10
37. Klee M, Eusemann R, Waser R, Brand W, van Hal H (1992) Processing and electrical properties of PZT films: comparisons of metallo-organic decomposition and sol–gel processes. *J Appl Phys* 72:1566–1576
38. Amanuma K, Hase T, Miyasaka Y (1994) Crystallization behavior of sol–gel derived PZT thin films and the polarization switching effect on film microstructure. *Appl Phys Lett* 65:3140–3142
39. Ledermann N, Muralt P, Baborowski J, Gentil S, Mukati K, Cantoni M, Seifert A, Setter N (2003) {100}-textured, piezoelectric $\text{Pb}(\text{Zr}_x\text{Ti}_{1-x})\text{O}_3$ thin films for MEMS: integration, deposition and properties. *Sensor Actuat A* 105:162–170
40. Calame F, Muralt P (2007) Growth and properties of gradient free sol–gel lead zirconate titanate thin films. *Appl Phys Lett* 90:062907
41. Huang Z, Battat J, Donohue PP, Todd MA, Whatmore RW (2003) On the phase transformation kinetics in lead scandium tantalate thin films. *J Phys D Appl Phys* 36:3039–3046
42. Brinkman K, Wang Y, Su D, Tagantsev A, Muralt P, Setter NJ (2007) The impact of chemical ordering on the dielectric properties of lead scandium tantalate thin films. *Appl Phys* 102:044110-1–044110-7
43. Huang Z, Todd MA, Watton R, Whatmore RW (1998) Sputtered lead scandium tantalate thin films: a microstructural study. *J Mater Sci* 33:363–370
44. Okazaki K, Nagata K (1973) Effects of grain-size and porosity on electrical and optical properties of PLZT ceramics. *J Am Ceram Soc* 56:82–86
45. Muralt P (2006) Texture control and seeded nucleation of nanosize structures of ferroelectric PZT films. *J Appl Phys* 100:051605
46. Hiboux S, Muralt P (2004) Mixed titania-lead oxide seed layers for PZT growth on Pt(111): a study on nucleation, texture and properties. *J Eur Ceram Soc* 24:1593–1596
47. Muralt P, Maeder T, Sagalowicz L, Hiboux S, Scalse S, Naumovic D, Agostino RG, Xanthopoulos N, Mathieu HJ, Pathney L, Bullock EL (1998) Texture control of PbTiO_3 and PZT thin films with TiO_2 seeding. *J Appl Phys* 83:3835–3841
48. Bühlmann S, Muralt P, VonAllmen S (2004) Site controlled nucleation and growth of small ferroelectric PZT single crystals. *Appl Phys Lett* 84:2614–2616
49. Clemens S, Schneller T, van der Hart A, Peter F, Waser R (2005) Registered growth of nanoscale ferroelectric grains by template-controlled growth. *Adv Mater* 17:1357–1361
50. Sreenivas K, Reaney I, Maeder T, Setter N, Jagadish C, Elliman RG (1994) Investigation of Pt/Ti bilayer metallization on silicon for ferroelectric thin film integration. *J Appl Phys* 76:466–476
51. Zhou QF, Cannata M, Meyer RJ, Van Tol DJ, Tadigadapa S, Hughes WJ, Shung KK, Trolier-McKinstry S (2005) Fabrication and characterization of micromachined high-frequency tonpizl transducers derived by PZT thick films. *IEEE UFFC* 52:350–357
52. Chen SY, Chen IW (1994) Temperature-time texture transition of PZT thin films: II, heat treatment and composition effects. *J Am Ceram Soc* 77:2337–2344
53. Huang Z, Zhang Q, Whatmore RW (1999) Structural development in the early stages of annealing of sol–gel prepared lead zirconate titanate thin films. *J Appl Phys* 86:1662–1669
54. Maeder T, Muralt P, Kohli M, Kholkin A, Setter N (1995) $\text{Pb}(\text{Zr,Ti})\text{O}_3$ thin films by in-situ reactive sputtering on micromachined membranes for micromechanical applications. *Br Ceram Proc* 54:206–218
55. Fujii E, Takayama R, Nomura K, Murata A, Hirasawa T, Tomozawa A, Fujii S, Kamada T, Torii H (2007) Preparation of (001)-oriented PZT thin films and their piezoelectric applications. *IEEE Trans UFFC* 54:2431–2438
56. Kohli M, Muralt P (1998) Poling of ferroelectric films. *Ferroelectrics* 225:155–162

57. Kholkin AL, Setter N (1997) Photo induced poling of PZT thin films. *Appl Phys Lett* 71:2854–2856
58. Muralt P, Kholkin A, Kohli M, Maeder T (1996) Piezoelectric actuation of PZT thin film diaphragms at static and resonant conditions. *Sensor Actuat A* 53:397–403
59. Dubois MA, Muralt P, Taylor DV, Hiboux S (1998) Which PZT thin films for piezoelectric microactuator applications? *Integr Ferroelectr* 22:535–543
60. Shepard JF, Moses PJ, Trolrier-McKinstry S (1998) The wafer flexure technique for the determination of the transverse piezoelectric coefficient (d_{31}) of PZT thin films. *Sensor Actuat A* 71:133–138
61. Dubois MA, Muralt P (1999) Measurement of the effective transverse piezoelectric coefficient e_{31} , f of AlN and PZT thin films. *Sensor Actuat A* 77:106–112
62. Prume K, Muralt P, Calame F, Schmitz-Kempen T, Tiedke S (2007) Piezoelectric thin films: evaluation of electrical and electromechanical characterizations for MEMS devices. *IEEE Trans UFFC* 54:8–14
63. Seifert A, Ledermann N, Hiboux S, Baborowski J, Muralt P, Setter N (2001) Processing optimization of solution derived PZT thin films for piezoelectric applications. *Integr Ferroelectr* 35:159–166
64. Luginbuhl P, Racine GA, Lerch P, Romanowicz B, Brooks KG, Rooij NFD, Renaud P, Setter N (1996) Piezoelectric cantilever beams actuated by PZT sol–gel film. *Sensor Actuat A* 53:530–536
65. Tyholdt F, Calame F, Prume K, Raeder H, Muralt P (2007) Chemically derived seeding layer for {100}-textured PZT thin films. *J Electroceram* 19:311–314
66. Seifert A, Ledermann N, Hiboux S, Muralt P (2000) Study of the transverse piezoelectric coefficient of PZT thin films as a function of texture and composition. *Mat Res Soc Symp Proc* 596:535–540
67. Kanno I, Fujii S, Kamada T, Takayama R (1997) Piezoelectric properties of c-axis oriented PZT thin films. *Appl Phys Lett* 70:1378–1380
68. Kanno I, Yokoyama Y, Kotera H, Wasa K (2004) Thermodynamic study of c-axis oriented epitaxial PZT thin films. *Phys Rev B* 69:064103-1-064103-7
69. Nino JC, Trolrier-McKinstry S (2004) Dielectric, ferroelectric, and piezoelectric properties of (001) BiScO₃-PbTiO₃ epitaxial films near the morphotropic phase boundary. *J Mat Res* 19:568–572
70. Yoshimura T, Trolrier-McKinstry S (2001) Transverse piezoelectric properties of epitaxial PbYbNbO₃-PbTiO₃ thin films. *J Cryst Growth* 229:445–449
71. Maria JP, Shepard JF, Trolrier-McKinstry S, Watkins TR, Payzant AE (2005) Characterization of the piezoelectric properties of (Pb,Ba)(Mg,Nb)O₃-PbTiO₃ epitaxial thin films. *Int J Appl Ceram Technol* 2:51–58
72. Yokoyama S, Okamoto S, Funakubo H, Iijima T, Saito K, Okino H, Yamamoto T, Nishida K, Katoda T, Sakai J (2006) Crystal structure, electrical properties, and mechanical response of (100)/(001)-oriented epitaxial Pb(MgNb)O₃-PbTiO₃ films grown on SrRuO₃/SrTiO₃ substrates by metal-organic chemical vapor deposition. *J Appl Phys* 100:054110-1-054110-7
73. Zhou QF, Zhang QQ, Trolrier-McKinstry S (2003) Structure and piezoelectric properties of sol–gel derived (001)-oriented PbYbNbO₃-PbTiO₃ thin films. *J Appl Phys* 94:3397–3402
74. Zhang QQ, Zhou QF, Trolrier-McKinstry S (2002) Structure and piezoelectric properties of sol–gel derived PbYbNbO₃-PbTiO₃ thin films. *Appl Phys Lett* 80:3370–3372
75. Bassiri Gharb N, Trolrier-McKinstry S (2005) Dielectric nonlinearity of Pb(Yb,Nb)O₃-PbTiO₃ thin films with {100} and {111} crystallographic orientation. *J Appl Phys* 97:064106-1-064106-7
76. Jaffe B, Cook WR, Jaffe H (1971) *Piezoelectric ceramics*. Academic, London
77. White RM, Voltmer VW (1965) Direct piezoelectric coupling to surface elastic waves. *Appl Phys Lett* 17:314–316

78. Hong E, Trolrier-McKinstry S, Smith RL, Krishnaswamy SV, Freidhoff CB (2006) Design of MEMS PZT circular diaphragm actuators to generate large deflections. *J Microelectromech Syst* 15:832–839
79. Jeon YB, Sood R, Jeong JH, Kim SG (2005) MEMS power generator with transverse mode thin film PZT. *Sensor Actuat A* 122:16–22
80. Marzencki M, Basrou S, Belgacem B, Mural P, Colin M (2007) Comparison of piezoelectric MEMS mechanical vibration energy scavengers. In *Nanotech 2007 Santa Clara* 3:21–24
81. Perçin G, Atalar A, Degertekin FL, Khuri-Yakub BT (1998) Micromachined two-dimensional array piezoelectrically actuated transducers. *Appl Phys Lett* 72:1397–1399
82. Maeder T, Mural P, Sagalovicz L, Reaney I, Kohli M, Kholkin A, Setter N (1996) PZT thin films on Zr membranes for micromechanical applications. *Appl Phys Lett* 68:776–778
83. Bernstein JJ, Finberg SL, Houston K, Niles LC, Chen HD, Cross LE, Li KK, Udayakumar K (1997) Micromachined high frequency ferroelectric sonar transducers. *IEEE Trans UFFC* 44:960–969
84. Percin G, Khuri-Yakub BT (2002) Micromachined droplet ejector arrays for controlled ink-jet printing and deposition. *Rev Sci Instr* 73:2193–2196
85. Flynn AM, Tavrow LS, Bart SF, Brooks RA, Ehrlich DJ, Udayakumar KR, Cross LE (1992) Piezoelectric micromotors for microrobots. *J Microelectromech Syst* 1:44–51
86. Damjanovic D, Brooks KG, Kholkin A, Kohli M, Maeder T, Mural P, Setter N (1995) Properties of piezoelectric PZT thin films for microactuator applications. *MRS Symp Proc* 360:429–434
87. Mural P, Kohli M, Maeder T, Kholkin A, Brooks KG, Setter N, Luthier R (1995) Fabrication and characterization of PZT thin-film vibrators for micromotors. *Sensor Actuat A* 48:157–165
88. Piekarski BH, DeVoe D, Dubey M, Kaul R, Conrad J, Zeto R (2001) Surface micromachined piezoelectric resonant beam filters. *Sensor Actuat A* 91:313–320
89. Piazza G, Abdolvand R, Ho GK, Ayazi F (2004) Voltage-tunable piezoelectrically-transduced single crystal silicon micromachined resonator. *Sensor Actuat A* 111:71–78
90. Ledermann N, Mural P, Baborowski J, Forster M, Pellaux JP (2004) Piezoelectric PZT thin film cantilever and bridge acoustic sensors for miniaturized photoacoustic gas detector. *J Micromech Microeng* 14:1650–1658
91. Baborowski J, Hediger S, Mural P, Wüthrich C (1999) Micromachined fabrication and characterization of accelerometers based on PZT thin films. *Ferroelectrics* 224:283–290
92. Wu XM, Ren TL, Liu LT (2006) Active damping of a piezoelectric MEMS acoustic sensor. *Integr Ferroelectr* 80:317–329
93. Meyer Y, Verdoot C, Collet M, Baborowski J, Mural P (2007) Active acoustic isolation of electronic microcomponents with piezoelectrically transduced silicon MEMS devices. *Smart Mat Struct* 16:128–134
94. Madou M (1997) *Fundamentals of microfabrication*. CRC, Boca Raton, FL
95. Nemirovsky Y, Nemirovsky A, Mural P, Setter N (1996) Design of a novel thin film piezoelectric accelerometer. *Sensor Actuat A* 56:239–249
96. Conde J, Mural P (2008) Characterization of sol-gel PZT thin film bulk acoustic resonators. *IEEE Trans UFFC* 55:1373–1379
97. Flynn AM, Tavrow LS, Bart SF, Brooks RA, Ehrlich DJ, Udayakumar KR, Cross LE (1990) Piezoelectric micromotors for microrobots. In: *IEEE ultrasonics symposium*, vol 3, IEEE, Honolulu (HI), USA, pp 1163–1172
98. Mitcheson PD, Yeatman EM, Rao GK, Holmes AS, Green TC (2008) Energy harvesting from human and machine motion for wireless electronic devices. *Proc IEEE* 96:1457–1486
99. Roundy S, Wright PK, Rabaey J (2003) A study of low level vibrations as a power source for wireless sensor nodes. *Comput Commun* 26:1131–1144
100. Mural P, Marzencki M, Belgacem B, Calame F, Basrou S (2009) Vibration energy harvesting with PZT micro device. *Procedia Chem* 1:1191–1194

101. Marzencki M, Basrour S, Belgacem B, Muralt P, Colin M (2007) Comparison of piezoelectric MEMS mechanical vibration energy scavengers. *Nanotech Santa Clara* 3:21–24
102. Mazzalai A, Chidambaram N, Muralt P (2011) Conception of an interdigitated electrodes based cantilever for piezoelectric energy harvesting. In: Mitcheson PD, Oh YS (ed) *Proceedings power MEMS 2011*, Seoul (Korea), pp 233–236
103. Torah R, Glynne-Jones P, Tudor M, O'Donnell T, Roy S, Beeby S (2008) Self-powered autonomous wireless sensor node using vibration energy harvesting. *Measur Sci Technol* 19:125202-1–125202-8
104. Jeon YB, Sood R, Jeong JH, Kim SG (2005) MEMS power generator with transverse mode thin film PZT. *Sensor Actuat A* 122:16–22
105. Choi WJ, Jeon Y, Jeong JH, Sood R, Kim SG (2006) Energy harvesting MEMS device based on thin film piezoelectric cantilevers. *J Electroceram* 17:543–548
106. Baran U, Brown D, Holmstrom S, Balma D, Chidambaram N, Davis WO, Muralt P, Urey H (2012) Resonant PZT MEMS scanner for high resolution displays. *J Microelectromech Syst* 21:1303–1309
107. Verdot T, Collet M, Muralt P (2012) Optimization, design and characterization of a piezoelectric micro suspension. *Int J Smart Nano Mat* 3:123–140

Chapter 25

Conducting Oxide Thin Films

Camilla Haavik and Per Martin Rørvik

25.1 Introduction

Electrical conduction occurs by the long range migration of either electrons (electronic conductors) or ions (ionic conductors). Functional oxide thin films exhibit the full spectrum of electrical properties spanning the entire range from superconducting to insulating electronic conductors and from fast ionic to insulating ionic conductors. This chapter will present examples of oxide thin films with electronic and ionic conductivities in the upper end of the conductivity scale. Such oxide films are promising for application in a range of different devices. Examples of potential (and actual) utilization are:

- Base electrodes for ferroelectrics
- Transparent electrodes for electronics and photovoltaics
- High temperature superconductors
- Magnetoresistive devices and random access memory
- Electrodes and electrolytes for solid oxide fuel cells
- Electrolytes for electro-chemical sensors

In general, conducting oxides are quite complex. They are often solid solutions of two (or more) oxides and their transport properties are highly dependent on their composition. Subtle variations in stoichiometry may lead to large variations in properties. To successfully integrate the conducting oxides in real devices, it is therefore crucial to develop thin film fabrication methods resulting in a precise and homogenous oxide composition over a large area. Among the thin film fabrication techniques, chemical solution deposition (CSD) is well known for both its excellent stoichiometry control and for the possibility to cover large areas.

C. Haavik • P.M. Rørvik (✉)
SINTEF Materials and Chemistry, Box 124 Blindern, O314 Oslo, Norway
e-mail: per.martin.rorvik@sintef.no

In addition to the composition of the oxide, the thin film microstructure is highly important for the transport properties. Grain boundaries are crystallographically and compositionally different from the grain interior, and so is the electron and ion transport within these regions. For some applications, it is crucial to deposit high quality epitaxial oxide films, for others highly textured polycrystalline films are the goal and for some applications polycrystalline films with random orientation are sufficient and even also desirable. Depending on the oxide system, CSD may result in high quality oxide films with all of these growth scenarios.

The main focus in this chapter will be on CSD of ionic, electronic and mixed ionic electronic conductors used as electrodes and electrolytes in solid oxide fuel cells. CSD of metallic oxide electrodes for other devices than fuel cells as well as magnetoresistive oxide thin films will also be presented. Other important conducting oxide thin films are transparent conducting electrodes and high temperature superconductors. These topics will be treated separately in the following Chaps. 26 and 27 of this book.

25.2 Metallic Oxide Base Electrodes

Lead zirconate titanate ($\text{PbZr}_{1-x}\text{Ti}_x\text{O}_3$, PZT) thin films have excellent ferroelectric and piezoelectric properties making them highly interesting for miniaturized sensors and actuators as well as for memory applications. Generally the PZT films are grown on Pt/Ti/SiO₂/Si substrates. Using Pt as a bottom electrode in the devices has many advantages: Pt has high electrical conductivity, results in low leakage current and has high stability at the temperatures needed for PZT processing. On the down side is the high cost, large thermal expansion mismatch with PZT, poor adhesion to Si, but most importantly: a serious ferroelectric fatigue has often been observed after 10^4 – 10^7 operating cycles. The origins and mechanisms of the fatigue are complicated and still under discussion [1, 2]. Several approaches have been tested to prevent the fatigue: depositing barrier layers between Pt and PZT [3] and also implanting oxygen in Pt [4]. Another alternative is to avoid the use of Pt entirely and look for alternative materials as bottom electrodes. RuO₂ that shows electronic conduction has been studied extensively as metallic oxide base electrode for ferroelectrics [1, 5, 6]. Other promising candidates are found among metallic oxides with similar crystal structure as PZT. Like PZT, YBa₂Cu₃O_{7-x}, La_{1-x}Sr_xCoO₃, LaNiO₃ (LNO) and SrRuO₃ (SRO) crystallize in the perovskite type structure. All of these compounds exhibit high electronic conductivities at room temperature and they have been shown to improve the fatigue properties of PZT when used as base electrodes. LNO and SRO are particularly interesting as they have a very good lattice match with PZT with morphotropic phase-boundary composition.

The properties of PZT are highly dependent on the stoichiometry and on the PZT thin film texture. When using CSD to deposit PZT, it is possible to carefully control the stoichiometry over large areas [7] and also to grow the desired film texture [8].

CSD is therefore a viable approach for the deposition of high quality PZT and is widely implemented today. More details on CSD of PZT are found in other chapters of this book. Also for the metallic oxide base electrode, it is important with good control of the texture and stoichiometry. The texture of the base electrode will influence the texture, and in turn, the ferro- and piezoelectric properties of PZT. The stoichiometry of the base electrode is important because of its influence on the electronic properties. Adding to this is the advantage of preparing the base electrode layer and the ferro-/piezoelectric film in one operation. Indeed, CSD turns out to be a very promising fabrication route also for metallic oxide electrodes.

Using CSD, LNO can be deposited with random orientation, with preferred (110) orientation or with highly (100) orientation. Yang and co-workers [9] prepared a LNO sol from lanthanum nitrate, nickel nitrate, acetic acid and water. After annealing at 750 °C, the LNO films exhibited the perovskite structure with preferred (110) orientation. By decreasing the sol concentration from 0.3 M to 0.1 M, the crystallinity of the LNO film improved. On these LNO films, the texture of PZT also varied with the LNO sol concentration. For an LNO sol concentration of 0.3 M, PZT grew with random orientation with a slight tendency towards (110) orientation. When the concentration of the LNO sol was decreased, the PZT (100) diffraction peak increased in intensity, but the film never became purely (100) oriented. The best performing PZT films of Yang and co-workers exhibited a dielectric constant (ϵ_r) of 747, and dielectric loss ($\tan \delta$) of 0.03 at 10^3 Hz. The remnant polarization (P_r) and coercive field (E_c) were $16 \mu\text{C cm}^{-2}$ and 55 kV cm^{-1} , respectively [9].

Chen and co-workers reported that the heating rate between 200 °C and 400 °C determined if the resulting LNO film was (100) or (110) oriented [10]. A heating rate above 10 °C s^{-1} resulted in preferential (100) orientation whereas a heating rate of 6.67 °C s^{-1} resulted in preferred (110) orientation. The resistivity of these films was $2 \times 10^{-3} \Omega \text{ cm}$. The sol was in this case made from lanthanum nitrate, nickel acetate, acetic acid and water, with a final concentration of 0.2 M.

On top of (100)-oriented LNO, PZT seem to grow in the (100) direction which is desirable for piezoelectric applications [8]. On Si(100) substrates, Meng and co-workers grew highly (100)-oriented LNO with a resistivity of $7.6 \times 10^{-4} \Omega \text{ cm}$ [11]. The solution was made from lanthanum nitrate, nickel acetate, acetic acid and water. On top of these LNO films, they deposited highly (100)-oriented PZT exhibiting a symmetrical polarization-electric field (P - E) hysteresis loop with P_r of $18.2 \mu\text{C cm}^{-2}$ and E_c of 40.2 kV cm^{-1} [11]. In a later study, Wang and co-workers used a similar fabrication method and tested the fatigue properties for the PZT/LNO/Si capacitor structures; at an applied maximum field of 300 kV cm^{-1} , no fatigue was observed after 10^8 cycles [12].

In all the above examples, water was used as solvent. High quality (100)-oriented LNO has also been deposited using organic solvents. Suzuki and co-workers dissolved lanthanum nitrate and nickel acetate in a mixture of 2-methoxyethanol and 2-aminoethanol [13]. The resulting LNO films were highly (100)-oriented with a resistivity of about $2 \times 10^{-3} \Omega \text{ cm}$ when the films were annealed in air at 700 °C. If the final annealing of the LNO layers was done in

pure oxygen instead of in air, the resistivity of LNO dropped to $7.27 \times 10^{-4} \Omega \text{ cm}$. On top of these LNO films, highly (100)-oriented PZT was deposited with P_r of $18 \mu\text{C cm}^{-2}$ and E_c of 36 kV cm^{-1} . At 1 kHz, the dielectric constant of PZT was 900. Suzuki and co-workers compared the fatigue of PZT deposited on LNO with PZT on Pt; after 10^8 cycles, no fatigue was observed for PZT on LNO, whereas for (100)-oriented PZT film on Pt/Si fatigue started at 10^6 cycles [13].

Thin film PZT fabricated by CSD is normally crystallized between 600°C and 700°C . The relatively high processing temperature may lead to inter-diffusion between the layers, potentially detrimental to the PZT performance. Shturman and co-workers studied the interface between CSD-deposited LNO and PZT after final annealing at 700°C and observed Pb, Zr and Ti from PZT within the entire LNO electrode thickness [14]. For Ni and La, diffusion lengths of 50 nm into the PZT film and 20 nm into the Si substrate were reported. For their PZT/LNO/Si capacitor structures Shturman and co-workers reported a quite high P_r of $50 \mu\text{C cm}^{-2}$, with no fatigue until 7×10^8 cycles, despite a large degree of inter-diffusion between the badly defined interfaces. They also compared the crystallization process of PZT on LNO with PZT on Pt and found that PZT crystallizes faster and at a much lower temperature on LNO than on Pt [14]. This finding indicates the possibility of realizing a lower PZT processing temperature by the use of LNO base electrodes.

A final note should be made on the stability of LNO at high temperatures and/or reducing conditions. The high valence state of Ni in LNO, Ni(III), is relatively unstable and LNO has a strong tendency to lose oxygen [15]. The oxygen non-stoichiometry decreases the electronic conductivity of LNO [16] and LNO may eventually form La_2NiO_4 which is insulating [15]. Qiao and co-workers propose that oxygen deficiency may lead to charge accumulation at the PZT-LNO interface inducing interfacial depolarization fields and eventually degradation of the dielectric properties of the thin-film capacitor system [15].

In addition to controlling the stoichiometry, the microstructure and the texture of the base electrode, the thickness of the electrode has been reported to influence the electrical properties of the succeeding PZT layer. Ohno and co-workers used CSD to deposit PZT thin films on top of LNO/Pt/Ti/SiO₂/Si stacks [17]. The thickness of the LNO layer was varied between 40 nm and 160 nm. The PZT films deposited on top of these structures were all reported to be highly (100)-oriented and to have almost identical film thickness, microstructure and texture. For these seemingly equal PZT thin films, the authors measured a large variation in the PZT dielectric constant. The PZT dielectric constant was reported to decrease with increasing LNO thickness. This observation was correlated to a measured increase in the residual stress in the PZT thin film. As the LNO film became thicker, the residual compressive stress in this layer increased, and upon relaxation of the LNO residual stress, the residual stress in the PZT layer increased and altered the dielectric constant [17].

SrRuO₃ (SRO) is an alternative to LaNiO₃ as base electrode. Suzuki and co-workers demonstrated the possibility of obtaining (100)-oriented SRO by CSD using RuCl₃ and Sr (or SrCl₂) as precursors and 2-methoxyethanol as solvent [18].

In analogue to PZT/LNO/Si capacitor structures, no polarization fatigue was observed for CSD-derived PZT/SRO/Si stacks after 10^8 cycles [19].

25.3 Magnetoresistive Materials

The scattering of electrons within a material is spin-dependent. The result is that all metals and semiconductors show a change in their electrical resistivity in the presence of an external magnetic field. This effect is called magnetoresistance (MR). MR is generally defined by the equation

$$MR\% = \frac{\Delta\rho}{\rho_0} \times 100 = \frac{(\rho_H - \rho_0)}{\rho_0} \times 100 \quad (25.1)$$

Here ρ_0 and ρ_H are the resistivities in zero field and in an applied field, respectively, at a given temperature. Depending on the system and the strength and orientation of the applied field, MR varies between a few percent and an exceptionally high value. A giant magnetoresistive (GMR) effect is obtained in thin film multi-layers of alternating ferromagnetic and non-magnetic layers [20]. When the magnetic alignment of the magnetic layers is parallel, the overall resistance is relatively low, while the resistivity becomes relatively high for anti-parallel alignment. The magnetic coupling between the magnetic layers depends on the design of the heterostructures. By optimizing the multilayer stacks, IBM has developed highly efficient GMR heterostructures working at useful magnetic fields at room temperature [21]. The GMR structures have been exploited extensively in read heads in modern hard drives and in magnetic sensors.

In addition to the engineered GMR multilayers, there exist another class of materials that exhibit a large intrinsic MR effect: the p-doped perovskite type manganites. These manganites take the form $RE_{1-x}AE_xMnO_3$, where RE is a trivalent rare earth cation (La, Pr, Nd) and AE is a divalent alkaline earth cation (Ca, Ba, Sr). For these materials, the resistivity can decrease many orders of magnitude in the vicinity of the Curie temperature (T_C) upon application of relatively small magnetic fields [22–25]. This intrinsic and large negative MR effect in the manganites is called colossal magnetoresistance (CMR). In 1994, Jin and co-workers reported an MR of $\sim 1,400\%$ at 200 K and above $100,000\%$ at 77 K for $La_{0.67}Ca_{0.33}MnO_3$ (LCM) thin films grown by pulsed laser deposition [26], which inspired further research. LCM is a member of the most studied CMR material system. The manganite parent compound, $LaMnO_3$, crystallizes in the perovskite-type structure and is an antiferromagnetically ordered insulator below its Neel temperature around 140 K. Exchanging La^{3+} with Ca^{2+} (p-doping) leads to formation of a mixed valence state for the Mn cation; Mn^{3+} and Mn^{4+} . At intermediate doping levels ($0 < x < 0.5$) the orbital ordering in the parent compound becomes frustrated and the ground state of the intermediately doped phase is metallic and ferromagnetic. Above T_C , LCM is magnetically disordered and an

insulator (semiconductor). The metal-insulator temperature (T_{MI}) coincides with T_C and also with a maximum in the MR effect. Among the intermediately doped LCMs, $\text{La}_{0.67}\text{Ca}_{0.33}\text{MnO}_3$ is, together with the Sr-doped equivalent, the most studied material because of its relatively high T_C . A high T_C , potentially resulting in high MR effect close to room temperature, is interesting from an application point of view. Extreme doping levels lead to formation of antiferromagnetic ordering and insulating phases and also long-range charge and/or orbitally ordered phases. Metallic ferromagnetic phases are absent at these doping levels. For extensive reviews on the CMR manganites and their properties, see for example [22–25].

As indicated above, the doped perovskite type manganites are complex. Their phase diagrams are rich, exhibiting a variety of phases, with unusual spin, charge, lattice and orbital order. In addition, phase competition at the boundaries between the phases produces new and interesting phenomena. The balance between competing phases is often subtle and small changes in composition can lead to large changes in material properties. The coexistence and competition between different kinds of order involving charge, orbital, lattice and spin degrees of freedom, leads to physical complexity, but it also results in a great opportunity for tuning and optimizing properties. Clearly, the characteristic properties of the doped manganites including the CMR effect are all strongly related to the ratio between the Mn^{3+} and Mn^{4+} ions. When fabricating CMR manganites, it is therefore crucial to carefully control the stoichiometry of the compound. CSD is known for its excellence in composition control and has therefore been explored as a viable approach for fabricating CMR thin films. For application in devices, both single-crystal epitaxial films and polycrystalline films have been considered promising. To obtain the high intrinsic CMR effect at T_C high quality epitaxial films are required. In addition to the intrinsic CMR effect at T_C there has also been reported another promising MR effect that is caused by grain boundaries and which is extrinsic in its nature. A very small field is needed to induce this effect which makes it highly interesting from an application point of view [25]. The extrinsic MR effect in manganites is called low field magnetoresistance (LFMR). Since the LFMR is related to grain boundaries, also polycrystalline manganite bulk and film samples have been studied extensively. In the remains of this subchapter, we will present some examples of the preparation of epitaxial and polycrystalline manganite thin films by means of CSD.

In general epitaxial manganite films can be fabricated by CSD if the film is deposited on single-crystal substrates with a good lattice match, which in most cases mean LaAlO_3 or SrTiO_3 substrates. Bae and Wang spin-coated 100 nm thick $\text{La}_{0.67}\text{Ca}_{0.33}\text{MnO}_3$ films on LaAlO_3 (100), MgO (100) and on SiO_2/Si [27]. The precursors were made of metal salts (nitrates and acetates) dissolved in 2-methoxyethanol. On the LaAlO_3 substrates, very good epitaxy was obtained after annealing the films in O_2 between 600 °C and 1,000 °C. After annealing, the films had low surface roughness (6–8 nm) and consisted of uniformly distributed spherical grains, with diameters ranging from 10 nm to 100 nm, depending on the annealing temperature. The films deposited on MgO were also epitaxial, although

there is a 10 % lattice mismatch between MgO and LCM. On SiO₂/Si the LCM films were polycrystalline with randomly oriented grains. The epitaxial films on LaAlO₃ showed the typical behaviour of CMR oxides: a semiconductor–metal transition accompanied by magnetic transition and a peak in the MR ratio near the transition temperatures. In presence of a magnetic field of 9,000 gauss the peak MR ratio for LCM on LaAlO₃ varied from 30 % to 90 % depending on the annealing temperature. Optimized properties (transport, T_C and peak MR ratio) were observed for films deposited at 900 °C. This was explained by an increase of grain size combined with a better O₂ incorporation in the lattice [27].

Later Hasenkox and co-workers [28] deposited La_{0.7}Ca_{0.3}MnO₃ and La_{0.7}Sr_{0.3}MnO₃ on LaAlO₃ by spin coating using a different set of precursors than Bae and Wang. Precursor solutions were in this case prepared by dissolving metal propionates in propionic acid. Hasenkox and co-workers demonstrated the influence of the concentration of metal ions in the precursor solution on the film quality; a low concentration (0.1 M with respect to Mn) resulted in high quality 110 nm thick films with low surface roughness, good crystallinity and high degree of epitaxy after annealing at 850 °C in O₂. When more concentrated solutions (0.3 M) were used, the resulting films showed less adherence to the substrate, they had a rough surface with large pores, and the crystallinity and the epitaxy were inferior compared to the films deposited with a less concentrated precursor solution. For their highest quality LCM films, Hasenkox and co-workers [28] reported a higher metal-insulator transition temperature (T_{MI}) than Bae and Wang [27]. Hasenkox observed a transition at 275 K, whereas Bae observed a transition around 230 K. In accordance with Bae, Hasenkox reported T_C to be close to T_{MI} , demonstrating the coupling between the ferromagnetism and electrical conductivity. In the presence of a field of 4 T, Hasenkox observed a peak MR ratio of 80 % at 265 K for LCM. For Sr-doped LaMnO₃ (LSM) thin films, the metal-insulator transition took place at 430 K, a temperature that is remarkably high compared to LCM. The T_C and the peak MR value was found at 360 K, much lower than the T_{MI} , in contrast to the LCM thin films [28].

Yet another CSD route was reported by Fors and co-workers [29]. Using all-alkoxide precursors and spin coating, they also deposited epitaxial La_{0.67}Ca_{0.33}MnO₃ on LaAlO₃ substrates. Their films were 50 nm thick, highly porous and had high surface roughness. The growth was columnar but the films showed high epitaxy. The magnetoresistive properties of these CSD films were compared to a film deposited by pulsed laser deposition (PLD). The PLD film was also grown on LaAlO₃ and it had similar composition. The PLD film was thicker (200 nm) than the CSD film and it had a much denser microstructure and lower surface roughness, but slightly inferior epitaxy. The peak in MR values were close to identical for the two types of films: 32 % for the CSD film and 35 % for the PLD film at peak temperatures of 246 K and 249 K, respectively. T_{MI} for the PLD film was higher than for the CSD film, 274 K versus 258 K.

To avoid organic solvents, Jain and co-workers developed a polymer-assisted deposition (PAD, see Chap. 6) approach to prepare epitaxial LSM and LCM films [30, 31]. Spin coating of the precursor solutions on LaAlO₃ resulted in

homogenous, crack-free and epitaxial films. The resistivity and magnetic properties of the films were reported to be highly affected by the post-annealing conditions. Jain and co-workers annealed their films in air at 750 °C, 850 °C and 950 °C and it was the highest annealing temperature that resulted in the highest quality films. For LCM films annealed at 950 °C, T_C coincided with T_{MI} around 250 K. This value is somewhat higher than the value observed by Bae and Wang [27] but lower than the T_C observed by Hasenkox and co-workers [28]. For LSM, Jain and co-workers reported T_C to be 340 K, also lower than the value reported by Hasenkox. But in contrast to Hasenkox, Jain observed the T_{MI} and T_C of LSM to coincide. The maximum MR value near the T_C of the LCM and LSM films annealed at 950 °C showed single-crystal-like behaviour with a maximum value of 88 % and 50 %, respectively (at 5 T).

Also spray pyrolysis has been demonstrated to be a viable CSD approach for depositing epitaxial LaMnO₃-based thin films. Raju and co-workers used spray pyrolysis to deposit La_{1-x}MnO₃ on LaAlO₃ and La_{0.7}Pb_{0.3}MnO₃ on SrTiO₃ [32]. Acetylacetonates were used as precursors and methanol as solvent. The substrates were kept at 400 °C during deposition and post-annealing was done at 800 °C. Both the La_{1-x}MnO₃ and the La_{0.7}Pb_{0.3}MnO₃ films were epitaxial after post-annealing. For the La_{1-x}MnO₃ film, the metal-insulator transition was observed around 210 K in absence of a magnetic field. A peak MR of 95 % was reported at temperatures close to T_{MI} . For La_{0.7}Pb_{0.3}MnO₃ T_{MI} was higher, around 330 K.

The CMR effect discussed above is observed for high quality single-crystals or epitaxial thin film manganites in the vicinity of T_C/T_{MI} in the presence of relatively large external magnetic fields. In the presence of much weaker magnetic fields (<0.1 T) significant low field magnetoresistance (LFMR) is reported for polycrystalline manganite bulk and thin film samples. LFMR it is interpreted in terms of spin-polarized tunnelling across the grain boundaries. The nature and the number of the grain boundaries are therefore very important for this property. In general, deposition of manganite thin films on polycrystalline substrates or on substrates with low lattice match results in polycrystalline films. Singh and co-workers [33] deposited polycrystalline La_{0.67}Ca_{0.33}MnO₃ thin films on single-crystalline yttria-stabilized zirconia substrates using aqueous nitrate precursors and spray pyrolysis. In accordance with the literature on the behaviour of polycrystalline manganite, Singh observed that at low temperatures and at low fields, the MR increases significantly with decreasing temperature. At an applied dc magnetic field of 3 kG, MR was 17.75 % at 77 K and 9 % at 133 K [33].

The studies presented above have all demonstrated successful CSD routes for depositing both high quality epitaxial and polycrystalline LaMnO₃-based thin films. It is not surprising that the reported properties are differing; for films with the same RE/AE ratio, the resistivity, the magnetic anisotropy and the T_C have been shown to be highly dependent on the film microstructure, on the oxygen stoichiometry and on the substrate-induced strain and therefore also the film thickness [25, 27, 31, 34].

25.4 Conducting Thin Films in Solid Oxide Fuel Cells

Conducting oxide thin films are interesting for solid oxide fuel cells (SOFCs) mainly for two reasons:

- They help making the high temperature conventional SOFCs operate efficiently at a lower temperature than they do today [35, 36].
- They are crucial for realising small micro-SOFCs (μ -SOFC) for portable devices [37].

Both the conventional SOFC and the μ -SOFC rely on relatively high oxygen ion conductivity to operate. This means that we now leave room temperature operation and introduce new and severe challenges when it comes to thermo-mechanical and chemical stability as well as nano-structural stability at high temperatures.

The core of a SOFC consists of a cathode, a solid oxide electrolyte and an anode. In the fuel cell, oxygen reacts at the cathode and fuel reacts at the anode. The electrolyte conducts oxygen ions via oxygen vacancies in the oxygen sublattice and can thereby transport oxygen ions from the cathode side (high pO_2) to the anode side (low pO_2). If the electrolyte simultaneously is electronically insulating, an electrical potential difference is created, which drives an electrical current in the external circuit. In the most used design of the SOFC; the dual chamber, the electrolyte constitutes the gas-tight seal between the oxygen-containing and the fuel-containing chambers, see Fig. 25.1.

For efficient operation of the SOFC, the requirements on the electrolyte layer are demanding: the electrolyte needs to exhibit high oxygen ion conductivity and negligible electronic conductivity. It needs to be dense and gas-tight upon operation which means that it needs to be thermo-mechanically and chemically stable under operating conditions. Adding to this that today's operating temperature of such cells are between 800 °C and 1,000 °C, and that the atmosphere on the cathode side is highly oxidizing while the atmosphere on the anode side is highly reducing, it is evident that only a few materials can fulfil the demanding requirements.

A set of materials and processing routes are already established for fabricating efficient SOFCs operating between 800 °C and 1,000 °C [38]. The electrolyte material of choice today is ZrO_2 doped with approximately 8 mol% Y_2O_3 . Adding Y_2O_3 to ZrO_2 stabilizes ZrO_2 in the cubic fluorite structure that exhibits fast oxygen ion conductivity at high temperatures, see for example [39]. This material is called yttria-stabilized zirconia (YSZ). The anode used together with YSZ is a mixture of YSZ and metallic Ni (YSZ-Ni cermet). The cathode for high temperature operation is the perovskite type lanthanum manganite in which La is partly replaced by Sr ($La_{1-x}Sr_xMnO_3$, LSM). The sandwich structure of anode-electrolyte-cathode is often called the membrane-electrode assembly (MEA). A schematic illustration of a typical MEA is shown in Fig. 25.2. The materials constituting the MEA are fabricated by conventional ceramic thick film processing. Examples are solid state co-sintering, tape casting and screen-printing of slurries, followed by high temperature annealing. Using these conventional routes, YSZ is typically densified at 1,400–1,500 °C in air.

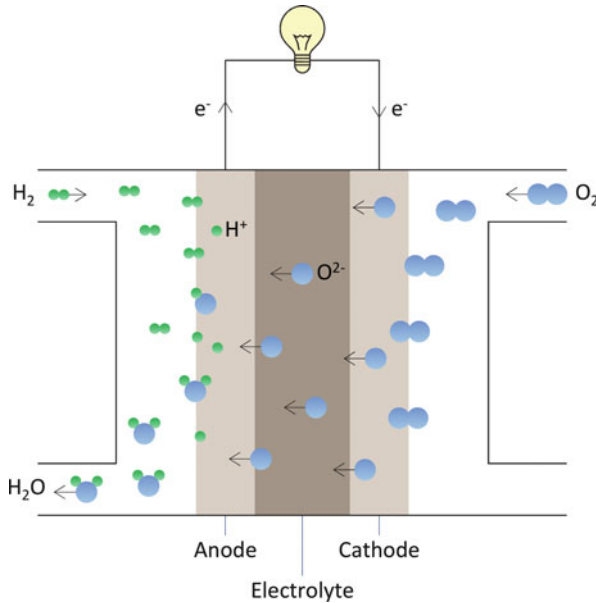


Fig. 25.1 Schematic illustration of the working principle of the solid oxide fuel cell (SOFC). Oxygen enters the fuel cell at the cathode side where the O_2 molecules dissociate and react with electrons to form oxygen ions, which are transported through the gas-tight and electronically insulating electrolyte. The oxygen ions react with hydrogen ions at the anode side, producing water. The electrons go from the anode to the cathode through an external circuit

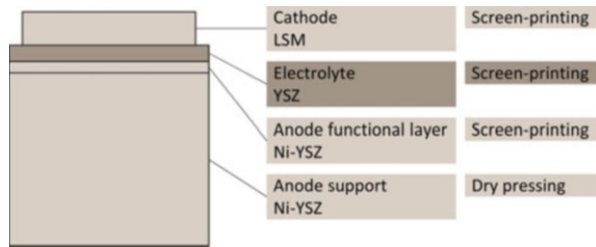


Fig. 25.2 Schematic illustration of the membrane-electrode assembly (MEA) in an anode-supported conventional SOFC with flat plate design

Even though the SOFC based on the MEA described above works well, a wide-spread use of this technology has not yet been reached. There are two major factors preventing a wide-spread market uptake: high production cost and problems with long time degradation. Both the high production cost and the long time degradation is to a large extent caused by the high fabrication and operating temperatures. If the operation temperature of the SOFC is lowered, the ionic conductivity of YSZ falls rapidly. The oxygen ions will spend longer time crossing the electrolyte layer, resulting in high ohmic loss and lower efficiency of the cell. There are two ways of solving this. One is finding a material with higher oxygen ion conductivity than YSZ

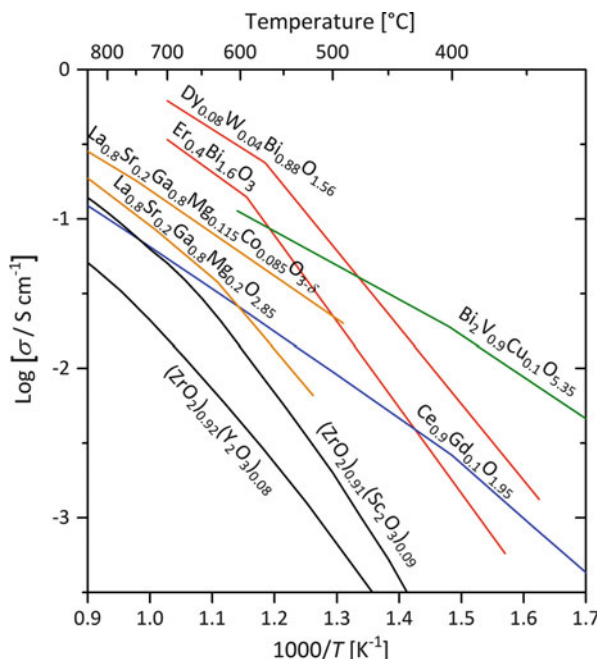


Fig. 25.3 Comparison of the electrical conductivity of various oxygen ion-conducting electrolytes: $(\text{ZrO}_2)_{0.92}(\text{Y}_2\text{O}_3)_{0.08}$ and $(\text{ZrO}_2)_{0.91}(\text{Sc}_2\text{O}_3)_{0.09}$ [40]; $\text{Ce}_{0.9}\text{Gd}_{0.1}\text{O}_{1.95}$ [41]; $\text{La}_{0.8}\text{Sr}_{0.2}\text{Gd}_{0.8}\text{Mg}_{0.2}\text{O}_{2.85}$ and $\text{La}_{0.8}\text{Sr}_{0.2}\text{Gd}_{0.8}\text{Mg}_{0.115}\text{Co}_{0.085}\text{O}_{3-\delta}$ [42]; $\text{Bi}_2\text{V}_{0.9}\text{Cu}_{0.1}\text{O}_{5.35}$ [43]; and $\text{Er}_{0.4}\text{Bi}_{1.6}\text{O}_3$ and $\text{Dy}_{0.08}\text{W}_{0.04}\text{Bi}_{0.88}\text{O}_{1.56}$ [44]

at lower temperatures, within what the fuel cell community denotes as the intermediate temperature region (500–750 °C). SOFCs that operate in this intermediate temperature region are called IT-SOFCs. Many promising materials with higher oxygen ion conductivity than YSZ in this temperature region have been identified. The conductivities of a range of these materials are given in Fig. 25.3. So far none of these materials simultaneously meet the requirements of high oxygen ion conductivity, low electronic conductivity, high thermo-mechanical and high chemical stability under operating conditions. The Bi_2O_3 -based electrolytes typically decompose to metallic Bi under the reducing fuel environment. Gd-doped CeO_2 (CGO) is currently the most promising alternative to YSZ, although the material becomes electronically conducting in reducing atmosphere and at high temperature. Bilayered structures combining two electrolyte materials can be a solution to these challenges.

The other option for realizing an IT-SOFC is making the YSZ electrolyte even thinner than today's state of the art. When the temperature is lowered and the YSZ conductivity decreases, minimizing the distance the ions have to travel by minimizing the thickness of the electrolyte layer could make up for the loss in conductivity. In order to decrease the YSZ thickness from today's state of the art, that is 10–20 μm , to below 5 μm , a new set of fabrication techniques must be considered. To exchange the conventional high temperature thick film fabrication routes with more “gentle” low temperature thin film deposition technology, such as

sputtering, electron beam evaporation, pulsed laser deposition (PLD), chemical vapour deposition (CVD) or CSD has been proposed as a promising future path [35, 36]. Please note that within the SOFC research literature, today's state of the art electrolyte with a thickness between 10 μm and 20 μm is most often denoted a thin film or a thin membrane as the thickness of the first SOFC electrolytes was much higher; between 100 μm and 200 μm [36]. In the present chapter, a film with thickness in the 10–20 μm range will be denoted a thick film, while films that are below 5 μm will be denoted thin films.

In addition to potentially lowering the operation temperature of the SOFC, the thin film techniques will also reduce the electrolyte processing temperature. A reduced processing temperature will allow the use of less costly material in the surroundings of the MEA, in turn lowering the total fabrication cost of the SOFC. A lower processing temperature will also cause much less damage of interfaces between electrolyte and electrodes during processing. Good interfaces improve the performance of the MEA substantially and will also facilitate a lower operating temperature.

Both for YSZ, for the alternative electrolyte materials and for the other constituents of the MEA, the electrochemical properties are highly dependent on composition and doping content. For instance, for YSZ, the optimized oxygen ion conductivity is found around 8 mol% Y_2O_3 content. For lower or higher doping content, the ionic conductivity falls drastically. This means that it is important to choose fabrication methods that give good control of the material composition across the total MEA area. Among the variety of thin film techniques, CSD is the technique that gives the best stoichiometry control. In addition, CSD is characterized by up-scalability, cost-efficiency and flexibility, which are crucial aspects for mass production of MEA components.

The following sections will present some of the work within CSD of conducting thin films for SOFC applications. The presentation will treat CSD thin films both for improvement of MEAs in conventional SOFC and for integration in μ -SOFCs. For more thorough and extensive reviews on SOFC materials and processing routes see for example [35–39, 45–49].

25.4.1 CSD of Thin Film Electrolytes

The MEA in a conventional SOFC consists of a dense electrolyte layer sandwiched between two porous electrodes. This means that a thin dense electrolyte layer must somehow be deposited on a porous support. To deposit a thin dense film on top of a structure with relatively large pores is not straightforward. An alternative is to make the support porous after deposition; for instance, a dense NiO-YSZ anode support will become porous after reduction of NiO to Ni in reducing atmosphere.

Jasinski and co-workers have developed a two stage spin coating procedure to deposit thin YSZ films onto a porous substrate (Fig. 25.4) [50]. In the first stage, a colloidal suspension containing fine YSZ particles is spin coated onto the substrate. The fine particles are expected to seal the large pores. After drying and heat-treating this first layer ($T < 400\text{ }^\circ\text{C}$), a porous ceramic skeleton is left on the substrate. The next step(s) involves spin coating this layer with a polymeric precursor until a dense

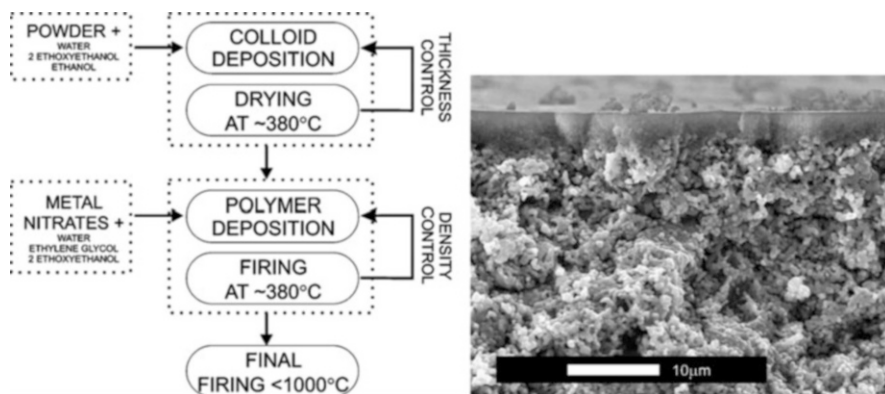


Fig. 25.4 (Left) Flow diagram of the two-stage spin coating procedure described by Jasinski and co-workers [50] for deposition of a thin electrolyte layer on a porous substrate. (Right) Scanning electron microscopy image of a cross-section of YSZ electrolyte deposited on $\text{La}_{0.6}\text{Sr}_{0.4}\text{FeO}_3$ support by the two-stage procedure. Reprinted with permission from Elsevier

layer is formed. After each deposition heat treatment at low temperatures decomposes the polymer. After the deposition of all layers, a final heat-treatment is necessary to crystallize and densify the film. Jasinski and co-workers used this procedure to deposit YSZ layers directly on a porous $\text{La}_{0.6}\text{Sr}_{0.4}\text{FeO}_3$ cathode. The YSZ layer was fully crystalline and dense, with a grain size below 100 nm after a final heat-treatment at 900 °C. By using such a low annealing temperature, they effectively avoided formation of the insulating SrZrO_3 phase, which usually forms between the cathode and the electrolyte at high processing and operation temperatures [50].

Moving from the slurry-based CSD of Jasinski and co-workers to pure solutions may lower the processing temperature of dense films further. Perednis and Gauckler employed two spray pyrolysis methods, electrostatic spray deposition (ESD) and pressurized spray deposition (PSD), to deposit YSZ and bi/multilayer combinations of YSZ and yttria-doped CeO_2 (CYO) on porous YSZ-NiO anode supports [36]. The mean pore size in these substrates was 1.5 μm , and the total electrolyte layer was approximately 1 μm thick. The as-deposited electrolyte films were amorphous. To densify and crystallize the electrolyte layer(s), the films were annealed at 700 °C. The resulting films were dense and crack-free. For the bi-layer electrolytes (anode/YSZ/CYO/cathode) the obtained open circuit voltage (OCV) was close to the theoretical one, with a maximum power density of $\sim 760 \text{ mW cm}^{-2}$ at 770 °C. The films prepared with PSD showed higher OCV than the ones prepared with ESD. Under optimized conditions they managed to coat 3 μm large pores with a 500 nm thick electrolyte film [36].

Perednis and Gauckler obtained better performance for MEAs consisting of a bi-layered YSZ/CYO electrolyte compared to MEA with a single YSZ electrolyte layer [36]. The advantages of such bi-layered electrolytes are several. Firstly, at high temperatures, YSZ reacts with the cathode and forms insulating and deleterious phases, mainly SrZrO_3 and $\text{La}_2\text{Zr}_2\text{O}_7$, at the interface. A thin barrier layer of

CGO or CYO between YSZ and the cathode prevents these reactions from taking place. Additionally a thin barrier layer can improve the gas-tightness of a thick film electrolyte layer. In sum such a barrier layer has been reported to increase the performance of the MEA significantly. Stoermer and co workers increased their power output with more than 20 % by depositing a 200 nm thick CGO barrier layer between thick film YSZ and LSM [51]. A bi-layered electrolyte is also useful if CGO is used as the main electrolyte. CGO has higher ionic conductivity than YSZ in the intermediate temperature region and is therefore a highly promising electrolyte candidate for IT-SOFCs. But if CGO alone is used as an electrolyte, short-circuiting because of the electronic conductivity of CGO at temperatures above 500 °C or under reducing conditions is a challenge. The electronic conductivity of CGO can be blocked by a thin layer with the electronically insulating YSZ. Mehta and co-workers deposited thin (1–3 μm) YSZ films on polished sintered disks of CGO by spin coating alkoxide solutions [52]. After a final heat-treatment at 600 °C the YSZ films were dense and uniform and improved the OCV from 0.6 V to 0.8 V at 700 °C.

Oh and co-workers recently demonstrated that a dense and gas-tight YSZ electrolyte as thin as 100 nm could be produced on a rigid NiO-YSZ substrate by spin-coating of a chemical solution containing 5 vol% YSZ nanoparticles and low-temperature sintering [53]. Nanoparticles were employed in the chemical solution in order to counteract the external constraint and decrease the degree of differential densification because the nanoparticles are expected to sinter at a substantially lower rate than the precursor powders derived from the chemical solution. A similar approach was used to deposit a CGO interdiffusion barrier layer (second electrolyte layer) and a $\text{La}_{0.6}\text{Sr}_{0.4}\text{Co}_{0.2}\text{Fe}_{0.8}\text{O}_{3-\delta}$ cathode layer. The OCV was above 1 V for the temperature range studied (500–650 °C) which indicates gas-tightness of the bilayered electrolyte. The maximum power density was $\sim 1,300 \text{ mW cm}^{-2}$ at 650 °C [53].

What we have learned from decades of work with conventional SOFC electrolytes is that the microstructure of the electrolyte has a large influence on its electrical performance. In the grain boundary region one might find a large lattice mismatch, impurities or second phase segregation, space charge regions and microcracks. These factors affect both the mobility and the density of the charge carriers. As a result, grain boundaries and interfaces can be highly resistive and blocking, but in some polycrystalline materials grain boundaries may provide a region with relatively rapid transport compared to the grain interior. With decreasing grain size the importance of the grain boundaries increase and new type of behaviour can be expected. A lot of work is currently going on in order to understand the relation between deposition conditions, the microstructure and the resulting electrical properties of electrolyte thin films. In the majority of this work, the thin film electrolytes have been deposited on dense and smooth substrates. Thin films on dense (and patternable) substrates are also interesting for the μ -SOFC that is presented later in this chapter. Spin, dip and spray coating of solutions, using a range of different precursors have been applied successfully to deposit high quality YSZ and CGO thin films on dense substrates. The thickness of these films varies

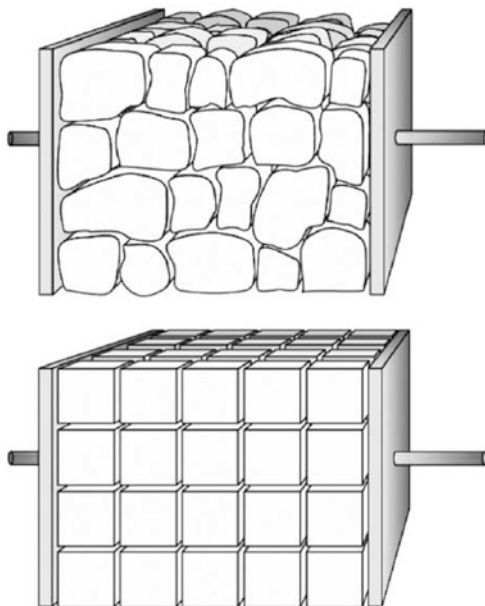
from a few nm to a few μm . The films can be polycrystalline, normally with nano-sized grains, they can be textured with columnar growth or even epitaxial. In general, CSD of these materials results in polycrystalline films with non-columnar microstructures [54] as opposed to vacuum deposition techniques (PLD and CVD), that often result in a columnar texture.

Using polymeric precursors, Kosacki and co-workers spin coated YSZ on sapphire and polycrystalline Al_2O_3 substrates [55]. Upon annealing at temperatures between $300\text{ }^\circ\text{C}$ and $1,200\text{ }^\circ\text{C}$, the films crystallized in the cubic fluorite structure. The films were dense with grain sizes between 1 nm and 220 nm, depending on the annealing temperature. Kosacki and co-workers measured the in-plane conductivity of the YSZ film with 20 nm large grains (on polycrystalline Al_2O_3). Similar conductivity measurements were done with a microcrystalline bulk sample with 2,400 nm large grains. Both samples had the same doping level and should therefore exhibit the same concentration of charge carriers. At $600\text{ }^\circ\text{C}$, the measured electrical conductivity was one order of magnitude higher for the nanocrystalline thin films compared to the microcrystalline bulk sample. The derived activation energy for conduction was also considerably lower in the thin film sample. An activation energy of 0.92 eV was reported for conduction in the thin film and 1.23 eV for the microcrystalline bulk sample. The authors also used the polymer precursor spin coating method to deposit un-doped CeO_2 and CGO thin films [56]. In the Gd-doped films, the ionic conductivity was reported to increase with decreasing grain size, in analogue to what they observed for YSZ in [55]. For the un-doped CeO_2 film the situation was different: in this case it was the undesirable electronic conductivity that increased with decreasing grain size.

These studies [55, 56] and also many other thin film studies clearly demonstrate the close relation between the thin film microstructure and its electrical properties. In order to minimize the resistance across the thin films, it is important to understand the role of the grain boundaries, both because the density of grain boundaries is high in nanocrystalline materials and also because the grain boundary contribution to the total resistance is more significant at the low temperatures where the thin films are intended to operate. A few important aspects of the electrical properties of the grain boundaries are given below. A thorough discussion about the role of the grain boundaries in acceptor-doped ZrO_2 and CeO_2 is given by Guo and Waser [57].

In a simplistic view, a polycrystalline material can be described using a brick layer model, in which the grain boundaries are either parallel or perpendicular to the current direction during the electrical characterization (Fig. 25.5). The specific conductivities in the bulk of the grain are different from the conductivities in the grain boundary region. In acceptor-doped ZrO_2 and CeO_2 , the ionic grain boundary conductivity is usually at least two orders of magnitude lower than the bulk value, such that the grain boundaries in these materials present a blocking effect to the ionic transport across them; see [57] and references therein. There are two main contributions to the (total) grain boundary resistance: i) an extrinsic resistance resulting from current constriction by impurity phases and ii) an intrinsic resistance caused by space-charge layers at the grain-to-grain contact layer. The extrinsic

Fig. 25.5 Schematic illustrations of: (*top*) a real ceramic microstructure, and (*bottom*) the brick layer model of the microstructure in ceramic materials [57]. Reprinted with permission from Elsevier



impurity contribution will of course vary with the processing technology. In acceptor-doped ZrO_2 and CeO_2 , a large contribution to this extrinsic resistance has been reported for samples with the presence of SiO_2 -containing insulating phases [58–60]. In high-purity samples, the intrinsic effect is the main contribution to the grain boundary resistance [57, 61–63]. The intrinsic blocking effect is caused by depletion of positively charged oxygen vacancies in a space-charge region surrounding the grain boundary core.

The understanding we have of the role of the grain boundaries in acceptor-doped ZrO_2 and CeO_2 is a result of a range of studies of bulk material. A similar understanding of grain boundary effects in the thin films is lacking. For bulk-type materials, the grain boundary conductivity and also the grain interior conductivity are reported to be grain size dependent [64, 65]. At 550 °C, Guo and Zhang reported the YSZ grain boundary conductivity to increase and the grain interior conductivity to decrease with decreasing grain size [64]. Grain size dependent effects were also reported for nanocrystalline doped and un-doped ceria, see for example [65]. Chiang and co-workers proposed that in nanocrystalline acceptor-doped CeO_2 , a size-dependent grain boundary segregation causes a de-doping of the grain interior [65]. In the thin films, the grain size (of the polycrystalline films) is also in the nano-regime and there is, in polycrystalline films with randomly oriented grains, a high density of interfaces. If these interfaces are blocking and contribute to a lowering of the total conductivity or if they do the opposite: constitute fast pathways for transport and therefore increases the total conductivity of the film, is currently debated. The (total) ionic conductivity for nanocrystalline thin film YSZ and CGO has been reported to be higher than the bulk value [55, 66–69], it has

been reported to be equal to bulk and independent of grain size [70] and finally it has been reported to be lower than the bulk value [71, 72]. As some thin film deposition techniques result in polycrystalline films with randomly oriented nanocrystalline grains, some in textured films with columnar grains and some even in epitaxial films, it is evident that the fraction of parallel and perpendicular grain boundaries will vary with the deposition technique and the measurement set-up chosen: is the thin film conductivity measured in film plane or across the film plane? One explanation for the diverging conclusions about the relation between the YSZ thin film microstructure and electrical properties may therefore be found in the different thin film microstructure resulting from the different deposition techniques coupled with the varying measurement set-ups used for electrical characterization. Another explanation for the diverging conclusions might be the YSZ thin film stoichiometry. The ionic conductivity of YSZ varies strongly with the Y_2O_3 content. If homogenous doping is not achieved during film deposition, the resulting conductivity will be affected. Films with nominally equal compositions might not be equal after all. A final factor that has been proposed to influence the thin film conductivity is the film strain. The film is clamped to the substrate and a difference in thermal expansion coefficient (TEC) between the electrolyte and the substrate will lead to either compressive or tensile strain in the electrolyte thin film. Chun and Mizutani deposited 4.9 mol% yttria-doped zirconia (4.9-YSZ) thin films on substrates with different TECs: Al_2O_3 (102), MgO (100) and SiO_2 glass [73]. The films were deposited by metalorganic chemical vapour deposition (MOCVD) at 600 °C, they all had the same thickness and similar average grain size. The conductivity was measured at 600–900 °C (above the deposition temperature). They found that the MgO substrate gave the highest conductivity and the lowest activation energy; this can be attributed to tensile stress in the film at the measuring temperatures since the TEC of MgO ($\sim 13 \times 10^{-6} K^{-1}$) is higher than the TEC of 4.9-YSZ ($\sim 8 \times 10^{-6} K^{-1}$). The tensile stress can "open up" the YSZ crystal structure, giving the oxygen ions more space to move and thus increasing the conductivity. For SiO_2 glass with a TEC of $\sim 0.5 \times 10^{-6} K^{-1}$ the opposite effect was observed; lower conductivity values and higher activation energy [73].

An overview of the relation between microstructure and electrical properties of chemical solution-deposited YSZ and CGO is given in Table 25.1. Electrical properties of a few films deposited by other techniques and also the properties of bulk material are given for comparison. Please note that the reported conductivities are not necessarily directly comparable, as the measurement methodologies are different, and will thus include different contributions to the measured conductivity. In general, CSD and maybe in particular spray pyrolysis, results in high quality YSZ and CGO films.

From Table 25.1 it is not clear whether small grains are beneficial for optimizing the ion conductivity of YSZ and CGO thin films. One should note that in nanocrystalline CGO thin films, the electrolytic domain shifts towards higher oxygen partial pressures with decreasing grain size [78]. It is important to avoid a deleterious electronic conductivity in the electrolyte. When decreasing the grain

Table 25.1 Microstructure and electrical properties of thin film YSZ and CGO

Material	Deposition method	Substrate	Film thickness [nm]	Grain size [nm]	E_A [eV]	σ_{tot} at 700 °C [$S m^{-1}$]	Refs.
$(ZrO_2)_{0.92}(Y_2O_3)_{0.08}$	Bulk polycrystalline	–	–	2,400	1.23	$\sim 0.4^a$	[55]
$(ZrO_2)_{0.90}(Y_2O_3)_{0.10}$	Single crystal	–	–	–	1.1 ($T < 650$ °C) 0.9 ($T < 650$ °C)	1.58	[66]
$(ZrO_2)_{0.84}(Y_2O_3)_{0.16}$	Spin coating	MgO	100–600	–	1.1	3.64	[74]
$(ZrO_2)_{0.92}(Y_2O_3)_{0.08}$	Spin coating	Polycrystalline Al_2O_3	–	20	0.93	$\sim 10^a$	[55]
$(ZrO_2)_{0.92}(Y_2O_3)_{0.08}$	Dip coating	Sapphire	240–390	232–728	1.085 (grain) 1.145 (GB)	0.015 ^b (grain) 0.00015 ^b (GB)	[72]
$(ZrO_2)_{0.92}(Y_2O_3)_{0.08}$	PSD	Sapphire	100–500	–	1.19	0.37	[75]
$(ZrO_2)_{0.83}(Y_2O_3)_{0.17}$	USD	Si (100)	~ 200	10	1.14 (grain) 0.79 (GB)	3.3 ^c	[67]
$(ZrO_2)_{0.91}(Y_2O_3)_{0.09}$	USD	Si (111)	340	80–100 textured	1.08	0.157	[76]
$(ZrO_2)_{0.90}(Y_2O_3)_{0.10}$	PLD	MgO (001)	15	Epitaxial	0.62	32	[66]
$(ZrO_2)_{0.90}(Y_2O_3)_{0.10}$	PLD	MgO (001)	29	Epitaxial	1.1 ($T < 650$ °C) 0.62 ($T > 650$ °C)	14	[66]
$(ZrO_2)_{0.90}(Y_2O_3)_{0.10}$	PLD	MgO (001)	60–2,000	Epitaxial	1.1 ($T < 650$ °C) 1 ($T > 650$ °C)	1.58	[66]
$Ce_{0.8}Gd_{0.2}O_{2-x}$	Spin coating	Sapphire	110–630	9	1	0.63	[56]
$Ce_{0.8}Gd_{0.2}O_{2-x}$	Spin coating	Sapphire	110–630	15	1.2	0.319	[56]
$Ce_{0.8}Gd_{0.2}O_{2-x}$	Spin coating	Sapphire	110–630	36	1.3	0.039	[56]
$Ce_{0.8}Gd_{0.2}O_{2-x}$	PSD	Sapphire	200–400	29	0.76	2.01	[69]
$Ce_{0.8}Gd_{0.2}O_{2-x}$	PSD	Sapphire	200–400	59	0.93	3.193	[69]
$Ce_{0.8}Gd_{0.2}O_{2-x}$	PSD	Sapphire	200–400	76	1.04	0.909	[69]
$Ce_{0.8}Gd_{0.2}O_{2-x}$	PVD	Polycrystalline Al_2O_3	110	–	0.95–1.05	0.251	[77]
$Ce_{0.8}Gd_{0.2}O_{2-x}$	PLD	Sapphire	200–800	46	0.81	2.139	[69]
$Ce_{0.8}Gd_{0.2}O_{2-x}$	PLD	Sapphire	200–800	55	0.88	1.783	[69]
$Ce_{0.8}Gd_{0.2}O_{2-x}$	PLD	Sapphire	200–800	75	1.01	0.754	[69]

The activation energy (E_A) is based on the total conductivity (σ_{tot})

GB grain boundary; PSD pressurized spray deposition; USD ultrasonic spray deposition; PLD pulsed laser deposition; PVD physical vapour deposition

^a600 °C

^b400 °C

^c650 °C

size and increasing the grain boundary density it is particularly important to fabricate clean and high quality grain boundaries. Small amount of impurities, like the insulating siliceous phases, lowers the electrolyte performance. Thorough removal of all residuals from the synthesis is also important. Finally, proper crystallization of the electrolyte phase by careful final annealing is crucial when fabricating electrolytes by means of CSD. In analogue to impurity phases, residual amorphous phases may also act as resistive and blocking phases in the grain boundaries. Time-temperature-transformation diagrams as introduced by Rupp and co-workers for CeO_2 and CGO thin films [79] could be useful to predict the crystallization degree of a thin film for pure isothermal or non-isothermal annealing and to reduce the annealing temperature.

The discussion above has focused on the conductivities at the operating temperatures of conventional SOFC or IT-SOFC. Recently it has been shown that YSZ and CeO_2 -based ceramics with extremely small grain sizes show significant proton conduction at low temperatures ($<200^\circ\text{C}$) in wet atmosphere [80–82]. Dense ceramics with grain size ~ 15 nm have been made by spark plasma sintering, yielding materials dominated by grain boundaries which facilitate proton conduction. Although the conductivity is relatively low compared to higher temperatures, such as those reported in Table 25.1, the low temperature operation is very interesting if thin enough electrolytes can be made. For making such electrolyte films CSD and low-temperature annealing processes are natural choices. For instance, Avila-Paredes and co-workers made $1\ \mu\text{m}$ thick polycrystalline films of YSZ prepared on sapphire substrate using a spin coating process [83]. The YSZ film had an average grain size of 17 nm. The protonic conductivity of the films was found to be higher by over an order of magnitude (at 30°C) than earlier reported values for nanocrystalline YSZ bulk ceramics with a similar grain size. The observed conductivity is comparable to the oxygen-ionic conductivity of the same material at around 400°C . The exact mechanism for the low-temperature proton conduction is not fully understood and is being studied.

The high chemical and thermo-mechanical stability of YSZ has made thin films of this material attractive for a range of other applications than fuel cells. Thin film YSZ may for instance be used to protect metallic surfaces towards high-temperature oxidation or wet corrosion or as thermal barrier coatings on alloy surfaces. Both YSZ and CeO_2 have been used as buffer layers for high temperature superconductors. For all of these applications, CSD has been considered as a promising fabrication technique and various CSD approaches have been tested to optimize the properties for a given application. High quality, dense, textured and even epitaxial ZrO_2 - and CeO_2 -based films have been obtained on a wide range of dense and smooth substrates [84–96].

From Fig. 25.3, it is evident that for intermediate temperature operation of the SOFC, there exist other promising alternatives to YSZ than the ceria-based materials. One promising candidate is scandia-stabilized zirconia (ScSZ). In the intermediate temperature region, ScSZ shows the highest ionic conductivity among the ZrO_2 -based electrolytes, but a phase transition from the high temperature cubic phase to a rhombohedral phase takes place at 600°C giving rise to an change in the

thermal expansion and also in the conductivity of this material [40]. It has been proposed that in thin film form, ScSZ behave differently, and that the structural transition might be prevented. Joo and Choi compared a 10 mol% ScSZ bulk sample with a thin film deposited by PLD (thickness 400 nm) [97]. With decreasing temperature the conductivity of the bulk sample suddenly dropped almost three orders of magnitude at approximately 550 °C, while the conductivity of the thin film gradually decreased [97]. Kosacki and co-workers prepared ScSZ thin films on polycrystalline Al₂O₃ by a polymer precursor spin coat technique [98]. They observed similar conductivities for bulk and thin film both above and below the phase transition; conductivity activation energies of 0.78 eV and 1.13 eV were obtained for high- and low-temperature region, respectively. However, the electronic conductivity was enhanced in the ScSZ thin film compared to bulk. This was related to the nanocrystalline structure of the thin film [98].

The oxygen ion-conducting perovskite La_{0.8}Sr_{0.2}Ga_{0.8}Mg_{0.2}O_{3-δ} (LSGM) has been considered as another promising electrolyte candidate for IT-SOFC [42, 45, 99, 100]. LSGM has higher oxygen ion conductivity than YSZ and ScSZ (Fig. 25.3), negligible electronic conduction and high chemical stability in a wide *p*O₂ range (10⁻²⁰ atm to 1 atm) [42]. The challenge with implementing LSGM in SOFC is that LSGM reacts with Ni in the anode during processing at high temperatures. A buffer layer of Ce_{0.8}Sm_{0.2}O_{2-δ} (CSO) was used by Yan and co-workers to avoid reaction between LSGM thin film grown by PLD and NiO-Fe₂O₃-CSO anode substrate [101]. The anode support was dense during deposition, but since NiO and Fe₃O₄ were reduced to Ni and Fe by H₂ treatment, the dense substrate was changed to a porous one and could be used as a porous anode substrate for SOFC. The LSGM film thickness was 5 μm and the peak power density reached 1,951 mW cm⁻² at 600 °C [101]. LSGM thin films have also been deposited by magnetron sputtering [102], but there are few reports on CSD routes. Taniguchi and co-workers deposited LSGM by electrostatic spray deposition, but the resulting films were porous and unsuited as a gas-tight electrolyte layer [103].

Finally, other examples of promising electrolytes for IT-SOFCs are found among the proton-conducting solid oxides [104–108]. In an SOFC where the solid electrolyte conducts protons instead of oxygen ions, the protons from the fuel travel from the anode side, through the electrolyte and reacts with oxygen to form water on the cathode side. These cells are sometimes denoted protonic ceramic fuel cells (PCFC). High proton conductivities are characteristic of the doped barium cerates, BaCe_{1-x}M_xO_{3-δ} (*M* = Y³⁺, Gd³⁺), but the use of barium cerates as SOFC electrolytes is unfortunately hampered by their low stability in CO₂-containing atmospheres. Agarwal and Liu prepared dense and crack-free BaCe_{0.8}Gd_{0.2}O₃ thin films on glass and porous alumina substrates by a modified Pechini process using an aqueous solution of nitrates, ethylene glycol and ethylene diamine tetraacetic acid (EDTA) [109]. A related class of material that shows relatively good proton conductivity and that also shows much better stability in CO₂-containing atmospheres is the doped barium zirconates, BaZr_{1-x}M_xO_{3-δ} (*M* = Y³⁺, Gd³⁺). Somroop and co-workers used ESD to deposit dense BZY films on SiO₂/Si and polycrystalline YSZ substrates from a solution of zirconium

acetylacetonate, barium chloride dihydrate and yttrium chloride hexahydrate dissolved in a water/butyl carbitol solvent mixture [110]. Using propionate-based precursors, Schneller and Schober developed a hybrid-type CSD spin coating process for fabrication of dense proton-conducting $\text{BaZr}_{0.80}\text{Y}_{0.20}\text{O}_{3-\delta}$ (BZY) thin films [111]. The films were deposited on platinised Si substrates. After a final annealing at 980 °C, the films were 630 nm thick, they showed single phase randomly oriented BZY and had a dense microstructure. The grain size was reported to be ~500 nm although the shown images indicate much smaller grain size. The measured conductivity of these films was much lower than the corresponding values for bulk samples [111]. While the grain interior conductivity of BZY is high, the grain boundaries contain a positively charged core which strongly reduces the grain boundary proton conduction [112]. Pergolesi and co-workers demonstrated that grain-boundary-free BZY thin films show a very high proton conductivity of 0.11 S cm^{-1} at 500 °C [113]; these BZY films were deposited onto (100)-oriented MgO substrates by PLD and were highly textured and epitaxially oriented. The lattice match between BZY and MgO is very good, ensuring the epitaxial film growth. Films were also grown on R-cut (1102) Al_2O_3 with a larger lattice mismatch and those films showed a significantly lower proton conductivity [113]. Recently, Lenrick and co-workers [114] deposited BZY films on MgO substrates using a CSD method similar to the one used by Schneller and Schober [111]. The films were studied in detail by electron microscopy and were found to be epitaxial with a cube on cube type interface between BZY and MgO. For the film annealed at 1,000 °C a layered pattern of lower intensity was observed and attributed to partially repeating voids [114].

25.4.2 CSD of Thin Film Cathodes

To facilitate gas transport to the cathode-electrolyte interface the cathode should be porous. It must be catalytically active towards oxygen reduction and show considerably electronic conductivity under operating conditions. Presence of ionic conductivity also enhances the cathode efficiency.

$\text{La}_{1-x}\text{Sr}_x\text{MnO}_3$ (LSM) has been the SOFC cathode material of choice the last 30 years. It has excellent electro-catalytic properties for oxygen reduction, high electronic conductivity and thermal and mechanical stability when used in combination with the YSZ electrolyte at high temperatures. Unfortunately, LSM has a relatively low ionic conductivity, and when the temperature is decreased into the IT-SOFC temperature region, the electrochemical reactions are restricted to the areas where electrolyte, cathode and gas are in contact, the triple-phase boundaries. A lot of work has been done to increase the TPB so that LSM can be useful at a lower temperature [47, 115]. To increase the triple phase boundary, it is necessary to decrease the cathode grain size and porosity close to the electrolyte layer, while keeping the cathode porous enough for efficient gas transport. Following this idea, Hamedani and co-workers reported a multi-step spray pyrolysis route to produce graded-porosity LSM cathodes on YSZ [116]. By varying the flow rate and

temperature during the deposition process, they fabricated 30 μm thick cathodes consisting of fine first layers at the electrolyte surface (crystallite size below 100 nm), followed by layers with a gradual increase in crystallite and pore size. This type of graded porosity results in a large number of triple phase boundaries close to the electrolyte, while the coarser outer layers facilitate easy gas transport into the cathode. The authors investigated the effect of type of precursor and solvents and reported that cathodes deposited using organo-metallic precursors and organic solvents had a homogenous and crack-free microstructure as opposed to films deposited using aqueous solutions [116]. The cathodes were deposited at $540\text{ }^\circ\text{C} < T < 580\text{ }^\circ\text{C}$ and no post-annealing procedure was claimed necessary. Only small changes in microstructure were found upon annealing the cathodes at the target operation temperature, which means that the graded cathodes with a “nano-layer” at the electrolyte interface are promising for IT-SOFC. The electrochemical performance of the cathodes was however not reported in this study.

To develop materials that are better suited for low temperature operation than LSM is not an easy task. Ideally the material should have high ionic and electronic conductivity at the target operating temperature, while the demands of high electrocatalytic activity towards oxygen activity, good thermomechanical and chemical compatibility with the electrolyte are fulfilled. Good examples of such materials are found in the $\text{La}_{1-x}\text{Sr}_x\text{Co}_y\text{Fe}_{1-y}\text{O}_{3-\delta}$ (LSC/LSCF) material family. These are called mixed ionic-electronic materials (MIECs). In good MIECs, the combination of high electronic and ionic conductivity has the potential to extend the active oxygen reduction sites to the entire exposed cathode surface.

In order to make high performance cathodes for IT-SOFC, it would be highly beneficial to develop low temperature processing routes. At high processing temperatures, solid state diffusion can lead to formation of undesirable insulating phases in the interface between the electrolyte and the cathode. One example is SrZrO_3 and $\text{La}_2\text{Zr}_2\text{O}_7$ that forms between YSZ and LSCF at high temperatures [117–119]. By implementing thin film fabrication routes, and in particular chemical solution deposition, the cathode processing temperature could be lowered. Thin film fabrication routes are therefore considered as promising fabrication alternatives to the high temperature thick film routes for realizing efficient IT-SOFC cathodes. Compared to the high temperature thick film routes, CSD also results in a much finer grain size and porosity ($<100\text{ nm}$), increasing the inner surface volume and thereby the number of reaction sites substantially. Finally, thin film cathodes are investigated in order to realize the small fuel cells, the μ -SOFC.

The cathode performance is typically measured by impedance spectroscopy of symmetric cells (cathode | electrolyte | cathode). The area specific resistance (ASR) is then given by Eq. (25.2):

$$ASR = \frac{R_p}{2} \times A_{\text{cathode}} \quad (25.2)$$

The polarization resistance R_p is the sum of the real parts of the impedance in the middle and low frequency ranges and A_{cathode} the surface area of one cathode.

Several CSD routes, including various forms of spray pyrolysis, sol-gel and metalorganic deposition, have been demonstrated as viable approaches for fabricating thin film cathodes with enhanced performance in the intermediate temperature range. Using pressurized spray pyrolysis deposition (PSD) Beckel and co-workers deposited LSCF thin film cathodes on $\text{Ce}_{0.8}\text{Gd}_{0.2}\text{O}_{1.9}$ dense pellets [120]. The solution consisted of nitrates and/or chlorides dissolved in ethanol/diethylene glycol monobutyl ether. After the deposition, the sprayed films were amorphous and two post-annealing temperatures were tested for crystallization. Four hours at 650 °C resulted in a porous film with 65 nm grains. Increasing the annealing temperature to 800 °C (4 h), resulted in a doubling in the grain size. The microstructure of the film was reported to have a significant influence on the cathode performance as the large-grained film had twice as high ASR as the small-grained one. This was explained by the decrease in the triple-phase boundary on the electrolyte surface of the large grained film. Beckel and co-workers also compared the spray pyrolysis-deposited LSCF to porous LSCF cathodes made by PLD and found that the sprayed cathodes had four times lower ASR. This was explained by a high in-plane resistivity of the PLD films caused by the columnar texture in these films. For reducing the ASR it was found beneficial to introduce carbon black as pore former or to deposit a thin dense LSCF layer (~50 nm) by PLD prior to spray pyrolysis deposition [120]. A similar PSD process has also been used to deposit LSCF cathodes onto proton-conducting $\text{BaCe}_{0.2}\text{Zr}_{0.7}\text{Y}_{0.1}\text{O}_{3-\delta}$ electrolyte [121]. The ASR values were 0.61 $\Omega \text{ cm}^2$ and 0.89 $\Omega \text{ cm}^2$ at 600 °C in dry and humidified air, respectively; these resistances are the lowest reported for LSCF cathodes on $\text{Ba}(\text{Ce},\text{Zr})\text{O}_3$ -based electrolytes. A novel approach to produce thin film composite cathodes containing both LSCF and CGO was recently reported by Angoua and Slamovich [122]. They used PSD of a single solution containing LSCF and CGO precursors. During annealing the LSCF and CGO phases segregated and crystallized from the amorphous deposited film. The composite cathodes exhibited lower ASR than the pure LSCF cathode [122]. Beckel and co-workers also made LSCF-CGO composite cathodes, but by sequential deposition of LSCF and CGO solutions [120].

Also another type of spray pyrolysis, electrostatic spray deposition (ESD), has been used to fabricate LSCF cathodes. Taniguchi [123], Fu [124], Marinha [125] and their co-workers all studied systematically the relation between the ESD deposition conditions and the resulting microstructure. By optimizing the cathode structure Marinha and co-workers obtained an ASR of 0.13 $\Omega \text{ cm}^2$ at 600 °C [126]. The studied cathode consisted of a first layer deposited by ESD (~7 μm) with a screen-printed layer (~45 μm) on top acting as current collector layer. Addition of the screen-printed layer resulted in a decrease of the ASR values of roughly one order of magnitude. The enhancement was attributed to a better distribution of the current along the cathode functional layer (ESD layer), thus activating a larger volume of the cathode and avoiding any current constriction issues [126].

Another promising CSD route was reported by Peters and co-workers [127]. They fabricated 200–300 nm thick $\text{La}_{0.5}\text{Sr}_{0.5}\text{CoO}_{3-\delta}$ (LSC) on YSZ by metalorganic decomposition. Post-annealing was done by rapid thermal annealing for 5 min at

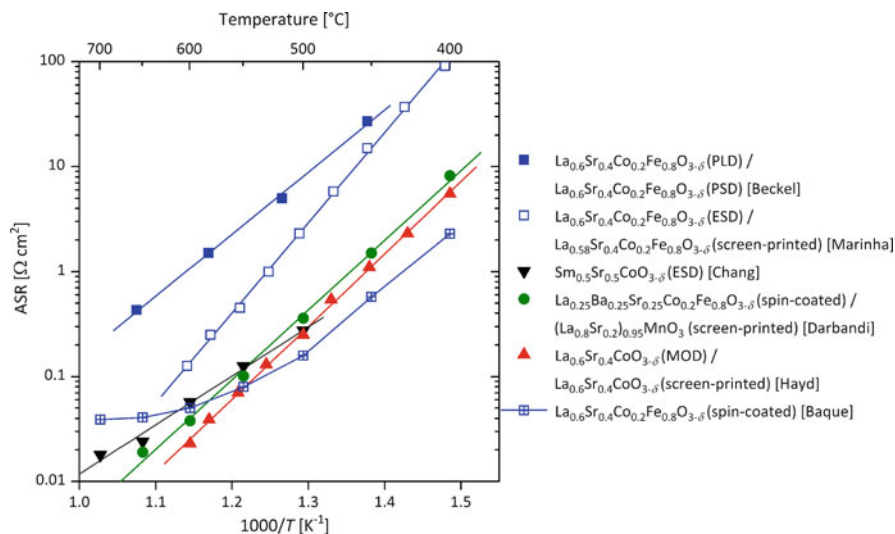


Fig. 25.6 Area specific resistance (ASR) of various thin film cathodes deposited on CGO by Beckel et al. [120], Marinha et al. [126], Chang et al. [129], Darbandi and Hahn [130], Hayd et al. [128], and Baqué et al. [131]. Several of the cathodes had a double-layer structure to improve the current distribution. The spin-coated layers were made from dispersions

170 °C, 700 °C and 900 °C. Under optimized conditions, this route resulted in chemically homogenous, crack-free, large area (25 cm²), well-crystallized LSC thin films. Grain and pore sizes were in the 50 nm range. Although LSC has a high thermal expansion coefficient ($23.7 \times 10^{-6} \text{ K}^{-1}$), when the film is as thin as 200–300 nm the mismatch with the electrolyte becomes much less problematic and the excellent chemical diffusion and oxygen exchange properties can be utilized. A $\sim 30 \mu\text{m}$ thick current collection layer of LSCF was applied on top of the LSC thin film. High electrochemical performance was reported for these cathodes: at 600 °C, the ASR was $0.146 \Omega \text{ cm}^2$ for LSC directly on YSZ and $0.130 \Omega \text{ cm}^2$ for LSC on YSZ with a CGO buffer layer in between to prevent interfacial reactions. Later, Hayd and co-workers improved the processing of the films and improved the ASR values further [128]. Solid precursors of La, Sr, and Co propionates were derived from $\text{La}_2(\text{CO}_3)_3$, Sr metal and $\text{Co}(\text{OH})_2$ by the reaction of with an excess of propionic acid in the presence of propionic acid anhydride. The solid propionates were dissolved in propionic acid with aimed stoichiometry $\text{La}_{0.6}\text{Sr}_{0.4}\text{CoO}_3$. The thin film cathodes were dip-coated onto CGO pellets. Slow heating of the thin films (3 K min^{-1}) during annealing led to a homogeneous microstructure in contrast to rapid thermal annealed films, which were inhomogeneous with cracks and bulges. A screen-printed layer of LSC was used as current collector layer. The lowest ASR value ($0.023 \Omega \text{ cm}^2$ at 600 °C) was obtained by slow heating to 700 °C and immediate cooling without any holding time. This ASR value is the best reported for an SOFC cathode at 600 °C so far. A comparison of the performances of different thin film cathodes is presented in Fig. 25.6.

In addition to the CSD routes described above, a range of sol–gel routes have been used for depositing LSC thin films [132–136], but the electrochemical properties were not studied.

Chang and co-workers recently reported ESD of $\text{Sm}_{0.5}\text{Sr}_{0.5}\text{CoO}_{3-\delta}$ (SSC) cathode films on CGO substrates [129]. The precursor solution was prepared by dissolving nitrates in a solvent mixture of de-ionized water (0.6 vol%), ethanol (1.5 vol%) and 2-(2-butoxyethoxy)-ethanol (butyl carbitol, 97.9 vol%). The best performing film was deposited at 350 °C, was $\sim 7\ \mu\text{m}$ thick and had a highly porous reticular structure, resulting in an ASR at 600 °C of $0.057\ \Omega\ \text{cm}^2$ (Fig. 25.6). The obtained ASR values were one-half to one order of magnitude smaller than that of screen-printed or slurry-painted electrodes [129].

CSD of thin film cathodes is useful to prepare cathodes with nanoscale grains at relatively low temperatures, resulting in large surface area and high porosity. But if the films are very thin the current distribution becomes challenging since the electrons will have to travel long distances laterally in the film. Several studies have shown that a screen-printed layer on top the CSD thin film significantly improves the performance [126–128]. In Fig. 25.6 such cathodes are compared to a few studies with $\sim 7\ \mu\text{m}$ thick SSC made by ESD [129] and $\sim 10\ \mu\text{m}$ thick LSCF made by spin coating a nanoparticle dispersion [131]; it can be seen that the performances are comparable. Thus, a combination of CSD routes and powder processing routes seems to be a good solution for obtaining high-performance cathodes for IT-SOFC.

25.4.3 *Micro-solid Oxide Fuel Cells*

Current battery technology is not expected to satisfy the growing power needs of portable electronic devices. The idea of exchanging the battery with a miniaturized fuel cell that is so powerful it could run a cell phone for a week without recharging is attractive and has generated a lot of research effort the last decade [37, 54, 137–142]. Small prototypes of the low temperature fuel cell technologies have been made: the proton exchange membrane fuel cell (PEMFC) and the direct methanol fuel cells (DMFC). Both of these technologies suffer from quite serious drawbacks. The PEMFC require pure hydrogen as a fuel, involving expensive fuel reforming and critical transport and storage problems. The DMFC requires concentrated toxic methanol to achieve beneficial energy densities and it also has a problem of methanol cross-over. Additionally, methanol is a weak energy source and the DMFC has a hard time producing enough electricity to compete with the batteries. Finally, both the PEMFC and the DMFC operate at such low temperatures that expensive Pt catalyst is needed for efficient operation. The operating temperature of the SOFC has been considered far too high for this type of fuel cell to be useful in its miniaturized version. Using micro-fabrication technology it has been shown that it

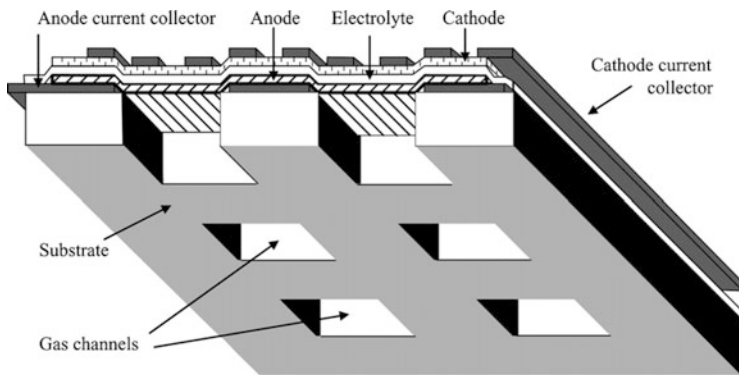


Fig. 25.7 Schematic illustration of a typical μ -SOFC structure made by combining thin film deposition techniques with micro-fabrication technology [54]. The dense substrate is typically Si wafer or Foturan glass-ceramic. Reprinted with permission from Elsevier

is possible to confine the high temperature associated with the SOFCs to a small space so that neighbouring parts will not be affected [141]. The growing competence in complex oxide thin film fabrication has also demonstrated that it is possible to produce SOFCs operating efficiently at much lower temperatures that would be easier to handle. Today, miniaturized SOFC, the so-called μ -SOFCs, operate successfully on a laboratory scale [37].

The μ -SOFC has several advantages compared to PEMFC and DMFC. The most important one is that the μ -SOFC can run on high-energy density hydrocarbon fuels such as propane or butane, resulting in a drastic increase in both the volumetric and the gravimetric energy density compared to the low-temperature fuel cells. With the potential of being made much lighter and much smaller than the PEMFC and DMFC, stacked μ -SOFCs are considered promising power sources for portable electronic devices with power requirements between 1 W and 20 W, such as cell-phones, personal digital assistants, laptops, video camcorders and battery chargers, as well as small medical and industrial devices [142].

In the conventional stationary SOFC, a thick film electrolyte and a cathode are deposited on top of a thick porous cermet anode constituting the mechanical support of the MEA. In most μ -SOFCs, all the layers constituting the MEA (anode, electrolyte and cathode) are deposited as thin films on top of a thicker dense mechanically supporting substrate (Fig. 25.7). The reported MEA thickness in μ -SOFCs ranges from 0.2 μm to 20 μm [37]. After the thin films are deposited, the MEA is released (for gas access) by micro-patterning the substrate. Most often the substrate is a Si wafer, but a patternable glass-ceramic substrate (Foturan) has also been used [141, 143, 144]. The free standing membranes have been made both square and circular with active areas between 0.0004 mm^2 and 20 mm^2 [37].

Chemical solution deposition is considered a good approach for depositing thin films for μ -SOFCs. Electrolytes [78, 143, 145, 146], cathodes [120, 143] and also cermet anodes [147, 148] have been deposited by CSD for the purpose of

integration into μ -SOFCs. Most of the materials and CSD methods for SOFC presented previously in this chapter are highly relevant also for μ -SOFC. See also references in [54]. So far no complete cell has been made entirely from CSD. Muecke and co-workers reported a μ -SOFC in which one of the two YSZ layers in a bi-layered electrolyte was spray-deposited [143]. They first deposited a 550 nm thick YSZ electrolyte by means of PLD and measured OCVs within the range of 400–900 mV in the temperature range of 400–600 °C, regardless of the cathode material used. OCV below the theoretical value indicates gas leakage and it was proposed that the leakage occurred via pinholes in the columnar microstructure resulting from the PLD process. On top of the PLD layer they therefore deposited a second YSZ layer using spray pyrolysis that results in a polycrystalline non-columnar growth. The OCV then increased from 0.8 V to 1.1 V, which is close to the theoretical value. The maximum power output obtained for a μ -SOFC using the bi-layer electrolyte and Pt as electrodes was 152 mW cm⁻² at 550 °C. This maximum power output was quite low, and it was the cathode reaction, in particular, that was found to limit the overall cell performance. A slight improvement was observed when the Pt cathode was exchanged with spray pyrolysis-deposited LSCF [143].

Higher maximum power densities for μ -SOFCs have been obtained by atomic layer deposition (ALD) and by vacuum-based methods. Promising performance has been reached; at the very low temperature of 350 °C and OCV of 1.1 V and a power density of 270 mW cm⁻² was reported by Shim and co-workers [149]. Their YSZ electrolyte was deposited by ALD and was only 60 nm thick. Increasing the temperature to 400 °C, Su and co-workers reached a maximum power density of 677 mW cm⁻² with a cell based on 220 nm YSZ combined with porous Pt electrodes, all deposited by magnetron sputtering [150]. Su and co-workers deposited their layers on a corrugated membrane and obtained therefore a larger exposed electrolyte area per projected area. No long time durability tests have been reported for μ -SOFCs so far. The performance of these cells under long-time operation and also their stability towards complete shut-down and restarts are not known.

A new approach to μ -SOFC fabrication was described by Evans and co-workers [151], using graphite foils as sacrificial substrate for deposition of 3 mol% yttria-stabilised tetragonal ZrO₂ polycrystal (Y-TZP) thin films. A toluene powder suspension of Y-TZP stabilized with sorbitan monooleate was spin-coated onto a flat-pressed graphite foil (5 × 5 cm²). The green film was sintered in air up to 1,350 °C for 2 h during which the graphite foil burned off, forming free-standing Y-TZP foil with 1–10 μ m thickness. The foils were semi-transparent, very flexible, slightly wrinkled and had an increased mechanical stability compared to the thin film electrolytes typically used in μ -SOFC. A μ -SOFC was fabricated by sputtering Pt electrodes onto the Y-TZP foil and placing it between two Foturan pieces with 0.5 cm and 1 cm holes. A measured OCV of 0.98 V and a maximum power density of 12 mW cm⁻² at 500 °C proved the feasibility of this new approach for future μ -SOFC development [151].

References

1. Tagantsev AK, Stolichnov I, Colla EL, Setter N (2001) Polarization fatigue in ferroelectric films: basic experimental findings, phenomenological scenarios, and microscopic features. *J Appl Phys* 90:1387–1402
2. Lou XJ (2009) Polarization fatigue in ferroelectric thin films and related materials. *J Appl Phys* 105:024101
3. Mardare CC, Joanni E, Mardare AI, de Sa CPM, Tavares PB (2005) The performance of Zr as barrier layer for Pt bottom electrodes in Pb(Zr,Ti)O₃ thin film capacitors. *Thin Solid Films* 483:21–26
4. Chen YC, Sun YM, Gan JY (2004) Improved fatigue properties of lead zirconate titanate films made on oxygen-implanted platinum electrodes. *Thin Solid Films* 460:25–29
5. Nakamura T, Nakao Y, Kamisawa A, Takasu H (1994) Preparation of Pb(Zr,Ti)O₃ thin-films on electrodes including IrO₂. *Appl Phys Lett* 65:1522–1524
6. Alshareef HN, Auciello O, Kingon AI (1995) Electrical-properties of ferroelectric thin-film capacitors with hybrid (Pt,RuO₂) electrodes for nonvolatile memory applications. *J Appl Phys* 77:2146–2154
7. Ræder H, Tyholdt F, Booij W, Calame F, Østbø NP, Bredesen R, Prume K, Rijnders G, Muralt P (2007) Taking piezoelectric microsystems from the laboratory to production. *J Electroceram* 19:357–362
8. Ledermann N, Muralt P, Baborowski J, Gentil S, Mukati K, Cantoni M, Seifert A, Setter N (2003) {100}-textured, piezoelectric Pb(Zr_xTi_{1-x})O₃ thin films for MEMS: integration, deposition and properties. *Sensor Actuat A Phys* 105:162–170
9. Yang XY, Cheng JR, Yu SW, Chen F, Meng ZY (2008) Effect of LaNiO₃ sol concentration on the structure and dielectric properties of Pb(Zr_{0.53}Ti_{0.47})O₃ thin films grown on LaNiO₃-coated Si substrates. *J Cryst Growth* 310:3466–3469
10. Chen ST, Wang GS, Zhang YY, Yang LH, Dong XL (2007) Orientation control growth of lanthanum nickelate thin films using chemical solution deposition. *J Am Ceram Soc* 90:3635–3637
11. Meng XJ, Cheng JG, Sun JL, Ye HJ, Guo SL, Chu JH (2000) Growth of (100)-oriented LaNiO₃ thin films directly on Si substrates by a simple metalorganic decomposition technique for the highly oriented PZT thin films. *J Cryst Growth* 220:100–104
12. Wang GS, Zhao Q, Meng XJ, Chu JH, Remiens D (2005) Preparation of highly (100)-oriented LaNiO₃ nanocrystalline films by metalorganic chemical liquid deposition. *J Cryst Growth* 277:450–456
13. Suzuki H, Miwa Y, Naoe T, Miyazaki H, Ota T, Fuji M, Takahashi M (2006) Orientation control and electrical properties of PZT/LNO capacitor through chemical solution deposition. *J Eur Ceram Soc* 26:1953–1956
14. Shturman I, Shter GE, Etin A, Grader GS (2009) Effect of LaNiO₃ electrodes and lead oxide excess on chemical solution deposition derived Pb(Zr_xTi_{1-x})O₃ films. *Thin Solid Films* 517:2767–2774
15. Qiao L, Bi XF (2009) Nanostructure and performance of Pt-LaNiO₃ composite film for ferroelectric film devices. *Acta Mater* 57:4109–4114
16. Li AD, Wu D, Liu ZG, Ge CZ, Liu XY, Chen GX, Ming NB (1998) TEM and AFM study of perovskite conductive LaNiO₃ films prepared by metalorganic decomposition. *Thin Solid Films* 336:386–390
17. Ohno T, Malic B, Fukazawa H, Wakiya N, Suzuki H, Matsuda T, Kosec M (2009) Stress engineering of the alkoxide derived ferroelectric thin film on Si wafer. *J Ceram Soc Jpn* 117:1089–1094
18. Suzuki H, Miwa Y, Miyazaki H, Takahashi M, Ota T (2004) Chemical solution deposition of conductive SrRuO₃ thin film on Si substrate. *Ceram Int* 30:1357–1360

19. Miyazaki H, Miwa Y, Suzuki H (2007) Improvement in fatigue property for a PZT ferroelectric film device with SRO electrode film prepared by chemical solution deposition. *Mat Sci Eng B-Solid* 136:203–206
20. Tsymbal EY, Pettifor DG (2001) Perspectives of giant magnetoresistance. In: Ehrenreich H, Spaepen F (eds) *Solid state physics*, vol 56. Elsevier Academic Press Inc, San Diego
21. Parkin S, Jiang X, Kaiser C, Panchula A, Roche K, Samant M (2003) Magnetically engineered spintronic sensors and memory. *Proc IEEE* 91:661–680
22. Prellier W, Lecoeur P, Mercey B (2001) Colossal-magnetoresistive manganite thin films. *J Phys-Condens Mat* 13:R915–R944
23. Fontcuberta J, Balcells L, Bibes M, Navarro J, Frontera C, Santiso J, Fraxedas J, Martinez B, Nadolski S, Wojcik M, Jedryka E, Casanove MJ (2002) Magnetoresistive oxides: new developments and applications. *J Magn Magn Mater* 242:98–104
24. Haghiri-Gosnet AM, Renard JP (2003) CMR manganites: physics, thin films and devices. *J Phys D-Appl Phys* 36:R127–R150
25. Siwach PK, Singh HK, Srivastava ON (2008) Low field magnetotransport in manganites. *J Phys-Condens Mat* 20:273201
26. Jin S, Tiefel TH, McCormack M, Fastnacht RA, Ramesh R, Chen LH (1994) Thousandfold change in resistivity in magnetoresistive La-Ca-Mn-O films. *Science* 264:413–415
27. Bae SY, Wang SX (1998) Novel sol–gel processing for polycrystalline and epitaxial thin films of $\text{La}_{0.67}\text{Ca}_{0.33}\text{MnO}_3$ with colossal magnetoresistance. *J Mater Res* 13:3234–3240
28. Hasenkox U, Mitze C, Waser R, Arons RR, Pommer J, Guntherodt G (1999) Chemical solution deposition of epitaxial $\text{La}_{1-x}(\text{Ca},\text{Sr})_x\text{MnO}_3$ thin films. *J Electroceram* 3:255–260
29. Fors R, Khartsev S, Grishin A, Pohl A, Westin G (2004) Sol–gel derived versus pulsed laser deposited epitaxial $\text{La}_{0.67}\text{Ca}_{0.33}\text{MnO}_3$ films: structure, transport and effects of post-annealing. *Thin Solid Films* 467:112–116
30. Jain M, Lin Y, Shukla P, Li Y, Wang H, Hundley MF, Burrell AK, McCleskey TM, Foltyn SR, Jia QX (2007) Ferroc metal-oxide films grown by polymer assisted deposition. *Thin Solid Films* 515:6411–6415
31. Jain M, Bauer E, Ronning F, Hundley MF, Civale L, Wang H, Malorov B, Burrell AK, McCleskey TM, Foltyn SR, DePaula RF, Jia QX (2008) Mixed-valence perovskite thin films by polymer-assisted deposition. *J Am Ceram Soc* 91:1858–1863
32. Raju AR, Aiyer HN, Nagaraju BV, Mahendiren R, Raychaudhuri AK, Rao CNR (1997) Epitaxial films of $\text{La}_{1-x}\text{MnO}_3$ exhibiting CMR prepared using nebulized spray pyrolysis. *J Phys D-Appl Phys* 30:L71–L73
33. Singh HK, Khare N, Siwach PK, Srivastava ON (2000) Low-field magneto-resistance of spray pyrolysis deposited $\text{La}_{0.67}\text{Ca}_{0.33}\text{MnO}_3$ thin films. *J Phys D-Appl Phys* 33:921–925
34. Aydogdu GH, Kuru Y, Habermeier HU (2008) Novel electronic and magnetic properties of $\text{La}_{0.5}\text{Ca}_{0.5}\text{MnO}_3$ films deposited on (111) SrTiO_3 substrates. *J Cryst Growth* 310:4521–4524
35. Will J, Mitterdorfer A, Kleinlogel C, Perednis D, Gauckler LJ (2000) Fabrication of thin electrolytes for second-generation solid oxide fuel cells. *Solid State Ion* 131:79–96
36. Perednis D, Gauckler LJ (2004) Solid oxide fuel cells with electrolytes prepared via spray pyrolysis. *Solid State Ion* 166:229–239
37. Evans A, Bieberle-Hütter A, Rupp JLM, Gauckler LJ (2009) Review on microfabricated micro-solid oxide fuel cell membranes. *J Power Sources* 194:119–129
38. Holtappels P, Vogt U, Graule T (2005) Ceramic materials for advanced solid oxide fuel cells. *Adv Eng Mater* 7:292–302
39. Fergus JW (2006) Electrolytes for solid oxide fuel cells. *J Power Sources* 162:30–40
40. Arachi Y, Sakai H, Yamamoto O, Takeda Y, Imanishai N (1999) Electrical conductivity of the $\text{ZrO}_2\text{-Ln}_2\text{O}_3$ (Ln = lanthanides) system. *Solid State Ion* 121:133–139
41. Steele BCH (2000) Appraisal of $\text{Ce}_{1-y}\text{Gd}_y\text{O}_{2-y/2}$ electrolytes for IT-SOFC operation at 500 °C. *Solid State Ion* 129:95–110
42. Ishihara T (2006) Development of new fast oxide ion conductor and application for intermediate temperature solid oxide fuel cells. *Bull Chem Soc Jpn* 79:1155–1166

43. Simner SP, Suarez-Sandoval D, Mackenzie JD, Dunn B (1997) Synthesis, densification, and conductivity characteristics of BICUVOX oxygen-ion-conducting ceramics. *J Am Ceram Soc* 80:2563–2568
44. Wachsman ED, Lee KT (2011) Lowering the temperature of solid oxide fuel cells. *Science* 334:935–939
45. Steele BCH, Heinzel A (2001) Materials for fuel-cell technologies. *Nature* 414:345–352
46. Haile SM (2003) Fuel cell materials and components. *Acta Mater* 51:5981–6000
47. Tsipis EV, Kharton VV (2008) Electrode materials and reaction mechanisms in solid oxide fuel cells: a brief review. I. Performance-determining factors. *J Solid State Electrochem* 12:1039–1060
48. Tsipis EV, Kharton VV (2008) Electrode materials and reaction mechanisms in solid oxide fuel cells: a brief review. II. Electrochemical behavior vs. materials science aspects. *J Solid State Electrochem* 12:1367–1391
49. Tsipis EV, Kharton VV (2011) Electrode materials and reaction mechanisms in solid oxide fuel cells: a brief review. III. Recent trends and selected methodological aspects. *J Solid State Electrochem* 15:1007–1040
50. Jasinski P, Molin S, Gazda M, Petrovsky V, Anderson HU (2009) Applications of spin coating of polymer precursor and slurry suspensions for solid oxide fuel cell fabrication. *J Power Sources* 194:10–15
51. Stoermer AO, Rupp JLM, Gauckler LJ (2006) Spray pyrolysis of electrolyte interlayers for vacuum plasma-sprayed SOFC. *Solid State Ion* 177:2075–2079
52. Mehta K, Xu R, Virkar AV (1998) Two-layer fuel cell electrolyte structure by sol–gel processing. *J Sol-Gel Sci Technol* 11:203–207
53. Oh E-O, Whang C-M, Lee Y-R, Park S-Y, Prasad DH, Yoon KJ, Son J-W, Lee J-H, Lee H-W (2012) Extremely thin bilayer electrolyte for solid oxide fuel cells (SOFCs) fabricated by chemical solution deposition (CSD). *Adv Mater* 24:3373–3377
54. Beckel D, Bieberle-Hütter A, Harvey A, Infortuna A, Muecke UP, Prestat M, Rupp JLM, Gauckler LJ (2007) Thin films for micro solid oxide fuel cells. *J Power Sources* 173:325–345
55. Kosacki I, Suzuki T, Petrovsky V, Anderson HU (2000) Electrical conductivity of nanocrystalline ceria and zirconia thin films. *Solid State Ion* 136:1225–1233
56. Suzuki T, Kosacki I, Anderson HU (2002) Microstructure-electrical conductivity relationships in nanocrystalline ceria thin films. *Solid State Ion* 151:111–121
57. Guo X, Waser R (2006) Electrical properties of the grain boundaries of oxygen ion conductors: Acceptor-doped zirconia and ceria. *Prog Mater Sci* 51:151–210
58. Badwal SPS, Drennan J (1987) Ytria zirconia – effect of microstructure on conductivity. *J Mater Sci* 22:3231–3239
59. Badwal SPS, Drennan J (1989) Grain-boundary resistivity in Y-TZP materials as a function of thermal history. *J Mater Sci* 24:88–96
60. Lee JH (2009) Highly resistive intergranular phases in solid electrolytes: an overview. *Mon Chem* 140:1081–1094
61. Guo X, Maier J (2001) Grain boundary blocking effect in zirconia: a Schottky barrier analysis. *J Electrochem Soc* 148:E121–E126
62. Guo X, Sigle W, Maier J (2003) Blocking grain boundaries in yttria-doped and undoped ceria ceramics of high purity. *J Am Ceram Soc* 86:77–87
63. Guo X, Sigle W, Fleig J, Maier J (2002) Role of space charge in the grain boundary blocking effect in doped zirconia. *Solid State Ion* 154:555–561
64. Guo X, Zhang ZL (2003) Grain size dependent grain boundary defect structure: case of doped zirconia. *Acta Mater* 51:2539–2547
65. Chiang YM, Lavik EB, Blom DA (1997) Defect thermodynamics and electrical properties of nanocrystalline oxides: Pure and doped CeO₂. *Nanostruct Mater* 9:633–642
66. Kosacki I, Rouleau CM, Becher PF, Bentley J, Lowndes DH (2005) Nanoscale effects on the ionic conductivity in highly textured YSZ thin films. *Solid State Ion* 176:1319–1326

67. García-Sánchez MF, Peña J, Ortiz A, Santana G, Fandiño J, Bizarro M, Cruz-Gandarilla F, Alonso JC (2008) Nanostructured YSZ thin films for solid oxide fuel cells deposited by ultrasonic spray pyrolysis. *Solid State Ion* 179:243–249
68. Sillassen M, Eklund P, Sridharan M, Pryds N, Bonanos N, Bøttiger J (2009) Ionic conductivity and thermal stability of magnetron-sputtered nanocrystalline yttria-stabilized zirconia. *J Appl Phys* 105:104907
69. Rupp JLM, Gauckler LJ (2006) Microstructures and electrical conductivity of nanocrystalline ceria-based thin films. *Solid State Ion* 177:2513–2518
70. Joo JH, Choi GM (2006) Electrical conductivity of YSZ film grown by pulsed laser deposition. *Solid State Ion* 177:1053–1057
71. Guo X, Vasco E, Mi SB, Szot K, Wachsman E, Waser R (2005) Ionic conduction in zirconia films of nanometer thickness. *Acta Mater* 53:5161–5166
72. Peters C, Weber A, Butz B, Gerthsen D, Ivers-Tiffée E (2009) Grain-size effects in YSZ thin-film electrolytes. *J Am Ceram Soc* 92:2017–2024
73. Chun SY, Mizutani N (2001) The transport mechanism of YSZ thin films prepared by MOCVD. *Appl Surf Sci* 171:82–88
74. Chen CC, Nasrallah MM, Anderson HU (1994) Synthesis and characterization of YSZ thin-film electrolytes. *Solid State Ion* 70:101–108
75. Perednis D (2003) Thin film deposition by spray pyrolysis and the application in solid oxide fuel cells. PhD Dissertation, ETH Zurich
76. Wang HB, Xia CR, Meng GY, Peng DK (2000) Deposition and characterization of YSZ thin films by aerosol-assisted CVD. *Mater Lett* 44:23–28
77. Chiodelli G, Malavasi L, Massarotti V, Mustarelli P, Quartarone E (2005) Synthesis and characterization of $\text{Ce}_{0.8}\text{Gd}_{0.2}\text{O}_{2-y}$ polycrystalline and thin film materials. *Solid State Ion* 176:1505–1512
78. Rupp JLM, Infortuna A, Gauckler LJ (2007) Thermodynamic stability of gadolinia-doped ceria thin film electrolytes for micro-solid oxide fuel cells. *J Am Ceram Soc* 90:1792–1797
79. Rupp JLM, Scherrer B, Schäuble N, Gauckler LJ (2010) Time-temperature-transformation (TTT) diagrams for crystallization of metal oxide thin films. *Adv Funct Mater* 20:2807–2814
80. Kim S, Anselmi-Tamburini U, Park HJ, Martin M, Munir ZA (2008) Unprecedented room-temperature electrical power generation using nanoscale fluorite-structured oxide electrolytes. *Adv Mater* 20:556–559
81. Avila-Paredes HJ, Chen CT, Wang SZ, De Souza RA, Martin M, Munir Z, Kim S (2010) Grain boundaries in dense nanocrystalline ceria ceramics: exclusive pathways for proton conduction at room temperature. *J Mater Chem* 20:10110–10112
82. Shirpour M, Gregori G, Merkle R, Maier J (2011) On the proton conductivity in pure and gadolinium doped nanocrystalline cerium oxide. *Phys Chem Chem Phys* 13:937–940
83. Avila-Paredes HJ, Barrera-Calva E, Anderson HU, De Souza RA, Martin M, Munir ZA, Kim S (2010) Room-temperature protonic conduction in nanocrystalline films of yttria-stabilized zirconia. *J Mater Chem* 20:6235–6238
84. Bhuiyan MS, Paranthaman M, Salama K (2006) Solution-derived textured oxide thin films – a review. *Supercond Sci Technol* 19:R1–R21
85. Peshev P, Slavova V (1992) Preparation of yttria-stabilized zirconia thin-films by a sol-gel procedure using alkoxide precursors. *Mater Res Bull* 27:1269–1275
86. Kueper TW, Visco SJ, Dejonghe LC (1992) Thin-film ceramic electrolytes deposited on porous and nonporous substrates by sol-gel techniques. *Solid State Ion* 52:251–259
87. Jin M, Han S, Sung T, No K (2000) Biaxial texturing of Cu sheets and fabrication of ZrO_2 buffer layer for YBCO HTS films. *Physica C* 334:243–248
88. Zhang YW, Jin S, Liao CS, Yan CH (2002) Microstructures and optical properties of nanocrystalline rare earth stabilized zirconia thin films deposited by a simple sol-gel method. *Mater Lett* 56:1030–1034
89. Smith RM, Zhou XD, Huebner W, Anderson HU (2004) Novel yttrium-stabilized zirconia polymeric precursor for the fabrication of thin films. *J Mater Res* 19:2708–2713

90. Kim SG, Nam SW, Yoon SP, Hyun SH, Han J, Lim TH, Hong SA (2004) Sol-gel processing of yttria-stabilized zirconia films derived from the zirconium *n*-butoxide-acetic acid-nitric acid-water-isopropanol system. *J Mater Sci* 39:2683–2688
91. Akin Y, Aslanoglu Z, Celik E, Arda L, Sigmund W, Hascicek YS (2003) Textured growth of multi-layered buffer layers on Ni tape by sol-gel process. *IEEE Trans Appl Supercond* 13:2673–2676
92. Celik E, Schwartz J, Avci E, Schneider-Muntau HJ, Hascicek YS (1999) CeO₂ buffer layers for YBCO: growth and processing via sol-gel technique. *IEEE Trans Appl Supercond* 9:2264–2267
93. Akin Y, Celik E, Sigmund W, Hascicek YS (2003) Textured CeO₂ thin films on nickel tape by sol-gel process. *IEEE Trans Appl Supercond* 13:2563–2566
94. Bhuiyan MS, Paranthaman M, Sathyamurthy S, Aytug T, Kang S, Lee DF, Goyal A, Payzant EA, Salama K (2003) MOD approach for the growth of epitaxial CeO₂ buffer layers on biaxially textured Ni-W substrates for YBCO coated conductors. *Supercond Sci Technol* 16:1305–1309
95. Gomilsek JP, Skofic IK, Bukovec N, Kodre A (2004) X-ray absorption study of CeO₂ and Ce/V mixed oxide thin films obtained by sol-gel deposition. *Thin Solid Films* 446:117–123
96. Coll M, Gazquez J, Sandiumenge F, Puig T, Obradors X, Espinos JP, Huhne R (2008) Nanostructural control in solution-derived epitaxial Ce_{1-x}Gd_xO_{2-y} films. *Nanotechnology* 19:395601
97. Joo JH, Choi GM (2008) Electrical conductivity of scandia-stabilized zirconia thin film. *Solid State Ion* 179:1209–1213
98. Kosacki I, Anderson HU, Mizutani Y, Ukai K (2002) Nonstoichiometry and electrical transport in Sc-doped zirconia. *Solid State Ion* 152:431–438
99. Ishihara T, Matsuda H, Takita Y (1994) Doped LaGaO₃ perovskite-type oxide as a new oxide ionic conductor. *J Am Chem Soc* 116:3801–3803
100. Feng M, Goodenough JB (1994) A superior oxide-ion electrolyte. *Eur J Solid State Inorg Chem* 31:663–672
101. Yan JW, Matsumoto H, Enoki M, Ishihara T (2005) High-power SOFC using La_{0.9}Sr_{0.1}Ga_{0.8}Mg_{0.2}O_{3-δ}/Ce_{0.8}Sm_{0.2}O_{2-δ} composite film. *Electrochem Solid State Lett* 8: A389–A391
102. Sasaki K, Muranaka M, Suzuki A, Terai T (2008) Synthesis and characterization of LSGM thin film electrolyte by RF magnetron sputtering for LT-SOFCs. *Solid State Ion* 179:1268–1272
103. Taniguchi I, van Landschoot RC, Schoonman J (2003) Electrostatic spray deposition of Gd_{0.1}Ce_{0.9}O_{1.95} and La_{0.9}Sr_{0.1}Ga_{0.8}Mg_{0.2}O_{2.87} thin films. *Solid State Ion* 160:271–279
104. Norby T, Larring Y (1997) Concentration and transport of protons in oxides. *Curr Opin Solid State Mat Sci* 2:593–599
105. Norby T (1999) Solid-state protonic conductors: principles, properties, progress and prospects. *Solid State Ion* 125:1–11
106. Kreuer KD, Paddison SJ, Spohr E, Schuster M (2004) Transport in proton conductors for fuel-cell applications: simulations, elementary reactions, and phenomenology. *Chem Rev* 104:4637–4678
107. Lefebvre-Joud F, Gauthier G, Mougín J (2009) Current status of proton-conducting solid oxide fuel cells development. *J Appl Electrochem* 39:535–543
108. Fabbri E, Bi L, Pergolesi D, Traversa E (2012) Towards the next generation of solid oxide fuel cells operating below 600 °C with chemically stable proton-conducting electrolytes. *Adv Mater* 24:195–208
109. Agarwal V, Liu ML (1997) Preparation of barium cerate-based thin films using a modified Pechini process. *J Mater Sci* 32:619–625
110. Somroop K, Pornprasertsuk R, Jinawath S (2011) Fabrication of Y₂O₃-doped BaZrO₃ thin films by electrostatic spray deposition. *Thin Solid Films* 519:6408–6412

111. Schneller T, Schober T (2003) Chemical solution deposition prepared dense proton conducting Y-doped BaZrO₃ thin films for SOFC and sensor devices. *Solid State Ion* 164:131–136
112. Kjølsøth C, Fjeld H, Prytz Ø, Dahl PI, Estournès C, Haugrud R, Norby T (2010) Space-charge theory applied to the grain boundary impedance of proton conducting BaZr_{0.9}Y_{0.1}O_{3-δ}. *Solid State Ion* 181:268–275
113. Pergolesi D, Fabbri E, D'Epifanio A, Di Bartolomeo E, Tebano A, Sanna S, Licoccia S, Balestrino G, Traversa E (2010) High proton conduction in grain-boundary-free yttrium-doped barium zirconate films grown by pulsed laser deposition. *Nat Mater* 9:846–852
114. Lenrick F, Griesche D, Kim J-W, Schneller T, Wallenberg LR (2012) Electron microscopy study of single crystal BaZr_{0.9}Y_{0.1}O_{3-x} films prepared by chemical solution deposition. *ECS Trans* 45:121–127
115. Jiang SP (2008) Development of lanthanum strontium manganite perovskite cathode materials of solid oxide fuel cells: a review. *J Mater Sci* 43:6799–6833
116. Hamedani HA, Dahmen KH, Li D, Peydaye-Saheli H, Garmestani H, Khaleel M (2008) Fabrication of gradient porous LSM cathode by optimizing deposition parameters in ultrasonic spray pyrolysis. *Mater Sci Eng B-Adv* 153:1–9
117. Yamamoto O, Takeda Y, Kanno R, Noda M (1987) Perovskite-type oxides as oxygen electrodes for high-temperature oxide fuel-cells. *Solid State Ion* 22:241–246
118. Yokokawa H, Sakai N, Kawada T, Dokiya M (1990) Thermodynamic analysis on interface between perovskite electrode and YSZ electrolyte. *Solid State Ion* 40–41:398–401
119. Kim WH, Song HS, Moon J, Lee HW (2006) Intermediate temperature solid oxide fuel cell using (La,Sr)(Co,Fe)O₃-based cathodes. *Solid State Ion* 177:3211–3216
120. Beckel D, Muecke UP, Gyger T, Florey G, Infortuna A, Gauckler LJ (2007) Electrochemical performance of LSCF based thin film cathodes prepared by spray pyrolysis. *Solid State Ion* 178:407–415
121. Ricote S, Bonanos N, Rørvik PM, Haavik C (2012) Microstructure and performance of La_{0.58}Sr_{0.4}Co_{0.2}Fe_{0.8}O_{3-δ} cathodes deposited on BaCe_{0.2}Zr_{0.7}Y_{0.1}O_{3-δ} by infiltration and spray pyrolysis. *J Power Sources* 209:172–179
122. Angoua BF, Slamovich EB (2012) Single solution spray pyrolysis of La_{0.6}Sr_{0.4}Co_{0.2}Fe_{0.8}O_{3-δ}-Ce_{0.8}Gd_{0.2}O_{1.9} (LSCF-CGO) thin film cathodes. *Solid State Ion* 212:10–17
123. Taniguchi I, van Landschoot RC, Schoonman J (2003) Fabrication of La_{1-x}Sr_xCo_{1-y}Fe_yO₃ thin films by electrostatic spray deposition. *Solid State Ion* 156:1–13
124. Fu CY, Chang CL, Hsu CS, Hwang BH (2005) Electrostatic spray deposition of La_{0.8}Sr_{0.2}Co_{0.2}Fe_{0.8}O₃ films. *Mater Chem Phys* 91:28–35
125. Marinha D, Rossignol C, Djurado E (2009) Influence of electro spraying parameters on the microstructure of La_{0.6}Sr_{0.4}Co_{0.2}Fe_{0.8}O_{3-δ} films for SOFCs. *J Solid State Chem* 182:1742–1748
126. Marinha D, Hayd J, Dessemond L, Ivers-Tiffée E, Djurado E (2011) Performance of (La,Sr)(Co,Fe)O_{3-x} double-layer cathode films for intermediate temperature solid oxide fuel cell. *J Power Sources* 196:5084–5090
127. Peters C, Weber A, Ivers-Tiffée E (2008) Nanoscaled (La_{0.5}Sr_{0.5})CoO_{3-δ} thin film cathodes for SOFC application at 500 °C < T < 700 °C. *J Electrochem Soc* 155:B730–B737
128. Hayd J, Dieterle L, Guntow U, Gerthsen D, Ivers-Tiffée E (2011) Nanoscaled La_{0.6}Sr_{0.4}CoO_{3-δ} as intermediate temperature solid oxide fuel cell cathode: Microstructure and electrochemical performance. *J Power Sources* 196:7263–7270
129. Chang CL, Chu TF, Hsu CS, Hwang BH (2012) Preparation and characterization of reticular SSC cathode films by electrostatic spray deposition. *J Eur Ceram Soc* 32:915–923
130. Darbandi AJ, Hahn H (2009) Nanoparticulate cathode thin films with high electrochemical activity for low temperature SOFC applications. *Solid State Ion* 180:1379–1387
131. Baqué L, Caneiro A, Moreno MS, Serquis A (2008) High performance nanostructured IT-SOFC cathodes prepared by novel chemical method. *Electrochem Commun* 10:1905–1908

132. Kweon HJ, Kuk ST, Park HB, Park DG, Kim K (1996) Synthesis of $\text{La}_{0.8}\text{Sr}_{0.2}\text{CoO}_3$ by sol-gel type reaction modified by poly(vinyl alcohol). *J Mater Sci Lett* 15:428–430
133. Kim BJ, Lee J, Yoo JB (1999) Sol-gel derived $(\text{La,Sr})\text{CO}_3$ thin films on silica glass. *Thin Solid Films* 341:13–17
134. Hwang HJ, Moon J, Awano M, Maeda K (2000) Sol-gel route to porous lanthanum cobaltite (LaCoO_3) thin films. *J Am Ceram Soc* 83:2852–2854
135. Pagnier J, Hardy A, Mondelaers D, Vanhoyland G, D'Haen J, Van Bael MK, Van den Rul H, Mullens J, Van Poucke LC (2005) Preparation of $\text{La}_{0.5}\text{Sr}_{0.5}\text{CoO}_3$ powders and thin film from a new aqueous solution-gel precursor. *Mat Sci Eng B-Solid* 118:79–83
136. Westin G, Ottoson M, Pohl A (2008) Alkoxide route to $\text{La}_{0.5}\text{Sr}_{0.5}\text{CoO}_3$ epitaxial thin films on SrTiO_3 . *Thin Solid Films* 516:4673–4678
137. Bonta PVS, O'Neal CB, Muthusami S (2005) Micro fuel cell technologies, advancements, and challenges. In: Shah RK, Ubong EU, Samuelsen S (eds) *Proceedings of the 3rd international conference on fuel cell science, engineering, and technology*. Amer Soc Mechanical Engineers, New York, NY
138. Morse JD (2007) Micro-fuel cell power sources. *Int J Energy Res* 31:576–602
139. La OGJ, In HJ, Crumlin E, Barbastathis G, Shao-Horn Y (2007) Recent advances in microdevices for electrochemical energy conversion and storage. *Int J Energy Res* 31:548–575
140. Litzelman SJ, Hertz JL, Jung W, Tuller HL (2008) Opportunities and challenges in materials development for thin film solid oxide fuel cells. *Fuel Cells* 8:294–302
141. Bieberle-Hütter A, Beckel D, Infortuna A, Muecke UP, Rupp JLM, Gauckler LJ, Rey-Mermet S, Muralt P, Bieri NR, Hotz N, Stutz MJ, Poulikakos D, Heeb P, Muller P, Bernard A, Gmur R, Hocker T (2008) A micro-solid oxide fuel cell system as battery replacement. *J Power Sources* 177:123–130
142. Evans A, Bieberle-Hütter A, Galinski H, Rupp JLM, Ryll T, Scherrer B, Tölke R, Gauckler LJ (2009) Micro-solid oxide fuel cells: status, challenges, and chances. *Mon Chem* 140:975–983
143. Muecke UP, Beckel D, Bernard A, Bieberle-Hütter A, Graf S, Infortuna A, Müller P, Rupp JLM, Schneider J, Gauckler LJ (2008) Micro solid oxide fuel cells on glass ceramic substrates. *Adv Funct Mater* 18:3158–3168
144. Tölke R, Bieberle-Hütter A, Evans A, Rupp JLM, Gauckler LJ (2012) Processing of Foturan® glass ceramic substrates for micro-solid oxide fuel cells. *J Eur Ceram Soc* 32:3229–3238
145. Rupp JLM, Drobek T, Rossi A, Gauckler LJ (2007) Chemical analysis of spray pyrolysis gadolinia-doped ceria electrolyte thin films for solid oxide fuel cells. *Chem Mater* 19:1134–1142
146. Rupp JLM, Solenthaler C, Gasser P, Muecke UP, Gauckler LJ (2007) Crystallization of amorphous ceria solid solutions. *Acta Mater* 55:3505–3512
147. Muecke UP, Graf S, Rhyner U, Gauckler LJ (2008) Microstructure and electrical conductivity of nanocrystalline nickel- and nickel oxide/gadolinia-doped ceria thin films. *Acta Mater* 56:677–687
148. Muecke UP, Akiba K, Infortuna A, Salkus T, Stus NV, Gauckler LJ (2008) Electrochemical performance of nanocrystalline nickel/gadolinia-doped ceria thin film anodes for solid oxide fuel cells. *Solid State Ion* 178:1762–1768
149. Shim JH, Chao CC, Huang H, Prinz FB (2007) Atomic layer deposition of yttria-stabilized zirconia for solid oxide fuel cells. *Chem Mater* 19:3850–3854
150. Su PC, Chao CC, Shim JH, Fasching R, Prinz FB (2008) Solid oxide fuel cell with corrugated thin film electrolyte. *Nano Lett* 8:2289–2292
151. Evans A, Bieberle-Hütter A, Bonderer LJ, Stucklenholz S, Gauckler LJ (2011) Micro-solid oxide fuel cells using free-standing 3 mol.% yttria-stabilised-tetragonal-zirconia-polycrystal electrolyte foils. *J Power Sources* 196:10069–10073

Chapter 26

Transparent Conducting Oxides

Peer Löbmann

26.1 Introduction and Physical Background

The excellent electric conductivity of metals is based on the presence of electrons with a considerable mobility in the metallic crystal lattice. Under these conditions they allow for good interaction of electromagnetic radiation in a broad spectral range: Therefore metals are non-transparent and reflect light. On the first view it would be plausible to assume that reasonable electric conductivity is not compatible with optical transparency. This certainly is true for metals with a partially filled conduction band: Since there is no minimum “threshold-level” the electrons will absorb light in a broad wavelength region.

The situation is quite different in large-bandgap semiconductors: The fully occupied valance band is energetically well separated from the empty conduction band. No visual adsorption is observed if this gap equals or exceeds 3.1 eV. Although above 0 K at least some electrons do populate the conduction band, the overall concentration of the resulting electron–hole pairs is very low. The material basically remains insulating.

In oxidic semiconductors oxygen lattice sites remain unoccupied. Some of them may not be compensated by cation deficiencies (Schottky defects). In these cases charge neutrality requires two “additional” electrons in the material which partially fill the conduction band. In terms of solid state physics, the oxygen vacancies create donor levels in the bandgap close to the conduction band. These electrons together with thermally promoted electrons become (negative) majority charge carriers (n-type conductivity). This mechanism of conductivity is referred to as intrinsic doping.

Cations with d-shells completely occupied form transparent conducting oxides (TCOs) because otherwise $d \rightarrow d$ transitions would cause absorption of

P. Löbmann (✉)

Fraunhofer Institut für Silicatforschung ISC, Neunerplatz 2, 97082 Würzburg, Germany
e-mail: peer.loebmann@isc.fraunhofer.de

electromagnetic radiation and thus coloration. Therefore, only oxides of Zn, In and Sn are promising candidates since their bandgap additionally exceeds 3.1 eV.

Nevertheless, in 1907 CdO (bandgap 2.28 eV) was the first at least partially transparent conducting oxide found [1]. It was prepared by thermal oxidation of sputtered metallic cadmium films. First technical applications were the de-icing of airplane windshields by resistive heating of respective TCO coatings [2]. Cadmium oxide subsequently was replaced by oxides of Zinc, Tin and Indium. In addition to intrinsic doping by oxygen deficiencies, extrinsic doping can be achieved by introducing cations by the substitution of elements of higher valence into the crystal lattice. For example Al^{3+} replacing Zn^{2+} sites induce donor levels close to the valence band. The electric conductivity of so-called Al-doped zinc oxide (AZO) therefore is increased in comparison to undoped ZnO. Similarly Indium oxide (In_2O_3) is regularly doped by Tin (ITO) and antimony is doped into the lattice of tin oxide (ATO). In the case of SnO_2 , alternatively, oxygen sites may be occupied by fluorine. In the resulting FTO the “additional” electrons also contribute to the partial occupation of the valence band.

While resistive heating of windows was the first application of TCO films, display technology and the transparent contacts of solar cells have successively gained higher importance. The role of TCOs for radiative energy management has recently been reviewed [3]. Other applications range from antistatic coatings, electrodes for light emitting diodes to gas sensors. In all of these cases the function of the material relies on electrons as charge carriers (n-type conductivity).

For the preparation of TCO thin films many different technologies have been developed. In each case, a trade-off between material performance and practical considerations has to be balanced: Excellent films may be prepared by e.g. pulsed laser deposition (PLD), but only small substrates may be coated. This prevents a commercial scale-up. Magnetron sputtering has developed into a mature technology for the production of ITO and AZO films. The related investment costs for commercial production sites are considerable. During the floating process, hot glass surfaces are coated by chemical vapor deposition (CVD) with FTO on large areas [4]. This processing is economically highly effective; nevertheless, some haze may impair the visual appearance due to film roughness [5]. In Table 26.1 electrical and optical performances of some selected TCO thin films prepared by different methods are compiled.

Wet chemical processing routes for ITO, AZO and ATO have extensively been investigated. The film performances reported mostly fall behind results achieved by vacuum-based technologies (Table 26.1). This is mainly due to the polycrystalline film structures of sol-gel films and resulting grain boundary scattering. Any residual porosity additionally will increase film resistivity. In Sect. 26.2 general approaches for sol-gel processing of different TCOs will be reviewed, Sect. 26.3 will deal with specific strategies to overcome the difficulties outlined for sol-gel films. Finally cases where the wet-chemical processing provides striking advantages over alternative routes will be highlighted in Sect. 26.4.

Table 26.1 Electrical and optical properties of some TCO thin films prepared by different deposition techniques

Comp.	Hall mobility [cm ² V ⁻¹ s ⁻¹]	Carrier concentr. [*10 ²⁰ cm ⁻³]	Resistivity [Ω cm]	Av. transm. [%]	Spectral range [μm]	Deposition technique	Refs.
ITO	45.0	12.0	1.1 × 10 ⁻⁰⁴	–	–	DC mag. sputt.	[6]
	40.0	18.0	9.5 × 10 ⁻⁰⁵	>80	0.4–0.9	Spray pyrolysis	[7]
AZO	53.5	13.8	8.5 × 10 ⁻⁰⁵	>84	0.4–0.7	PLD	[8]
	9.5	4.8	2.8 × 10 ⁻⁰³	85	0.55	Sol–gel	[9]
	2.0	4.2	7.6 × 10 ⁻⁰³	–	–	Sol–gel	[10]
	25.0	9.0	2.7 × 10 ⁻⁰⁴	–	–	DC mag. sputt.	[11]
	47.7	15.0	8.5 × 10 ⁻⁰⁵	83	0.4	PLD	[12]
ATO	42.0	0.3	5.0 × 10 ⁻⁰³	88	0.55	Sol–gel	[13]
	16.0	0.4	8.0 × 10 ⁻⁰³	81	0.55	Sol–gel	[14]
	17.0	0.2	1.4 × 10 ⁻⁰²	~80	0.55	Sol–gel	[15]
	23.0	0.7	1.6 × 10 ⁻⁰³	–	–	Sol–gel	[16]
	10	4.2	1.5 × 10 ⁻⁰³	>80	0.5–1.5	AC mag. sputt.	[17]
FTO	13	5.0	8.6 × 10 ⁻⁰³	86	0.4–0.8	RF mag. sputt.	[18]
	12	4.2	1.2 × 10 ⁻⁰³	92	0.55	Sol–gel	[19]
	–	–	2.6 × 10 ⁻⁰³	>80	0.4–0.8	Sol–gel	[20]
	20	7.0	5.0 × 10 ⁻⁰⁴	>90	0.4–0.8	APCVD	[21]
FTO	27	3.9	5.9 × 10 ⁻⁰⁴	>86	0.55	APCVD	[22]
	18	7.2	6.2 × 10 ⁻⁰⁴	77	0.45	Spray pyrolysis	[23]

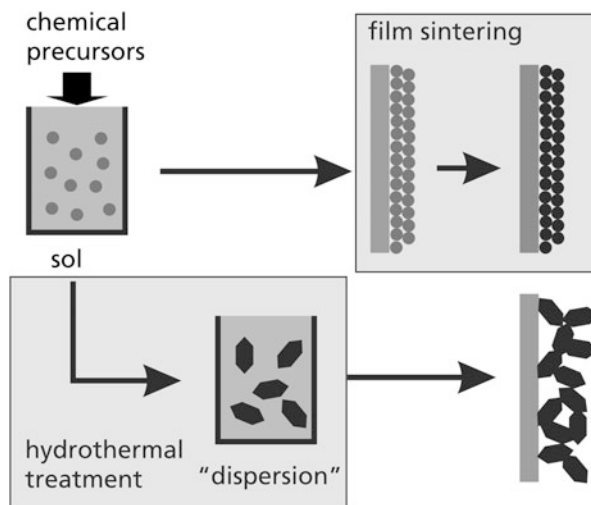
The data refer to the optimum values reported respectively and do not necessarily correspond to identical samples

26.2 Sol–gel Processing of TCO Thin Films: General Approach

Two different strategies are commonly adopted for the deposition of transparent conducting oxides from solutions: In the first case, molecular precursors are dissolved. Amorphous nanoparticles are formed by hydrolysis- and condensation reactions in the liquid state. In this state typical particle sizes range from 2 nm to 10 nm. Further growth and agglomeration continue during the coating procedure as a consequence of solvent evaporation. Non-volatile organic residues such as chelating agents or high-boiling solvent constituents have to be removed by thermal treatment in oxidizing atmosphere. Final densification and crystallization of the respective TCO film takes place at increased temperatures.

For the alternative approach, dispersed crystalline particles of TCOs are employed, their typical grain size exceeding 15 nm. As these building blocks are already conductive, the corresponding films do not necessarily require a thermal crystallization procedure. Dispersions of nanocrystals may be obtained by the hydrothermal treatment of molecular precursor solutions described above. Alternatively, nanoscaled oxide powders from e.g. flame pyrolysis can be

Fig. 26.1 Schematic representation of film preparation from solutions of amorphous precursor particles and dispersions of nanocrystals. The respective thermal crystallization step is highlighted in *grey*



de-agglomerated. The resulting dispersions must be stabilized against sedimentation by chemical surface modification of the particles.

The two general approaches are visualized in Fig. 26.1. Solutions containing (small) amorphous particles will be referred to as “sols” in this chapter. In contrast, precursors with stabilized (larger) crystalline grains will be named “dispersions”.

Coating processes with sols containing amorphous particles are comparably simple and may yield dense films. On the other hand, the film thickness for single coatings seldomly exceeds 200 nm due to tensile stresses during densification. As a thermal pyrolysis and crystallization step is required, thermally labile substrates such as organic polymers cannot be used. Nevertheless the dopant concentrations (e.g. Al or Sn) can easily be varied by adjusting the chemical composition of the precursor mixture. This generally allows a facile optimization of film performance.

In contrast, polymer foils may be coated by dispersions of particles that are already crystalline. The simple arrangement of these inert building blocks during film drying is less likely to build up tensile stresses; thick films are feasible without the formation of cracks. The small contact points between the grains, though, represent a bottle-neck for charge transport in these systems. The electrical current can be enhanced by the formation of sintering necks between particles. Additionally, mechanical stability may be improved by partial reduction of porosity. Unfortunately, these measures are only possible for films on substrates that can withstand the required thermal treatment conditions.

In the following paragraphs some approaches for the preparation of ITO, AZO and ATO thin films by wet chemical processing will be highlighted. It has to be noted, though, that the comparison between performances of films emerging from different studies seems arbitrary or even impossible for several reasons: Even though contamination by Na^+ ions is known to adversely affect film conductivity [24], often the substrate type (“glass” being soda-lime, borosilicate or fused silica

glass?) is not fully disclosed. It is not often clear whether the mass percentage of the dopant refers to the ratio of e.g. In:Sn, $\text{InCl}_3:\text{SnCl}_4$ or $\text{In}_2\text{O}_3:\text{SnO}_2$ in the precursor formulation or in the final product. Even when molar ratios are given, it sometimes remains unclear if the metal ratio In:Sn or the final ratio between the nominal oxides $\text{In}_2\text{O}_3:\text{SnO}_2$ is addressed. Additionally minute variations in processing parameters (air moisture, heating rates etc.) may severely affect the microstructure and subsequently the film performance. Therefore, it is extremely difficult to estimate the origin of surprisingly good/bad results, especially if no thorough characterization of the film morphology is provided. Thus, the discussion has to be limited to some more general aspects; no specific guidelines can be given.

26.2.1 Indium Tin Oxide (ITO)

Even though there are single reports about sol–gel processing of pure indium oxide (IO) [25], commonly ITO with a molar ratio $\text{Sn}/(\text{Sn} + \text{In})$ up to 10 % is synthesized. InCl_3 [10, 26] and $\text{In}(\text{NO}_3)_3$ [27] are the most common indium sources; in the latter case metallic Indium ingots are sometimes dissolved in nitric acid to synthesize the salt as $\text{In}(\text{NO}_3)_3 \cdot 5 \text{H}_2\text{O}$ [28]. Tin is mostly introduced as chloride $\text{SnCl}_2 \cdot 2\text{H}_2\text{O}$ [26], SnCl_4 or $\text{SnCl}_4 \cdot 5\text{H}_2\text{O}$ [28], in some cases tin acetate $\text{Sn}(\text{OOCCH}_3)_4$ is used [29]. Since a variety of solvents (ethanol, 2,4-pentanedione, diethylenetriamine, acetic acid) and mixtures thereof are employed in different mixing and heating sequences, the role of the single components as solvent and/or complexing agent is hard to judge in the respective case.

The compositional flexibility of sol–gel processing can be used to systematically investigate the influence of molar In:Sn ratios up to 30:70 [30]. Any reduction in content of the expensive Indium is highly promising from the commercial point of view if the films do not suffer significant losses in conductivity and transmittance. Precursor solutions with a molar ratio of 50:50 can be prepared using indium tin tert-butoxide ($\text{InSn}(\text{O}^t\text{Bu})_3$, ITBO) as single source precursor; the resulting films exhibit a resistivity of $4.1 \times 10^{-03} \Omega \text{ cm}$ [31].

Some ITO films prepared by sol–gel processing show resistivities as low as $8.0 \times 10^{-04} \Omega \text{ cm}$ [32, 33] and $3.3 \times 10^{-04} \Omega \text{ cm}$ [24], which compete with results obtained by physical vacuum-based technologies. Nevertheless, neither their respective precursor synthesis nor the film preparation techniques seem to be significantly dissimilar to the common state of the art represented in the literature. This fact underlines how important the favorable combination of processing parameters (precursors, synthesis, substrate, conditions during film-preparation and thermal treatment) are. This delicate balance of prerequisites may up to now impede the industrial production of TCO films by sol–gel techniques on a large scale. Therefore future developments should address the stable and cost-efficient processing of these materials as had already been done in the cases of antireflective coatings (see Chap. 28) and TiO_2 thin films for optical applications [34].

Whereas the above routes require thermal treatment of the films above 300 °C for ITO crystallization, alternatively dispersions of crystalline particles may be used (Fig. 26.1). Such dispersions can be synthesized by milling commercially available aggregated powders in the presence of a solvent and different dispersants [35]. The dispersants may either be complexing agents such as β -diketones or functionalized titanium alkoxides as hydrolytically active coupling agents. The size of the resulting secondary particle aggregates ranges from 85 nm to 750 nm depending on the respective additive.

Re-dispersible crystalline ITO powders can be synthesized from aqueous solutions of $\text{InCl}_3/\text{SnCl}_4$ in the presence of NH_3 and β -alanine at 80 °C. After drying, the powders may be treated with ethylene glycol and a carbonic acid and then diluted in alcohols or water. Hydrodynamic particle size determination and TEM imaging indicate that agglomerates are broken down to their primary particle sizes between 8 nm and 20 nm [36]. Dispersions with a nominal primary ITO particle size of 16 nm were commercialized by Nanogate GmbH (Germany).

Coatings manufactured from such dispersions will contain crystalline TCO material even without additional thermal treatment. This generally enables processing of organic polymer substrates and fabrics that would decompose at elevated temperatures [37].

Spin- or dip-coating experiments using such dispersions yield film thicknesses between 400 nm and 1.1 μm in a single coating step without cracking [36, 38]. The resulting films show porosities exceeding 50 %, though [29, 39]. Due to the high thicknesses the sheet resistance of the films may be sufficient for some applications, for samples treated at 500 °C the specific resistivity of 6.3 $\Omega\text{ cm}$ is very high, however. As these films consist of crystalline particles with low sintering activity, even treatment at 800 °C does neither reduce the porosity nor improve conductivity significantly. Interestingly it can be shown by optical spectroscopy that within secondary clusters of well-connected nanoparticles “local” resistivities below $7.0 \times 10^{-04}\ \Omega\text{ cm}$ are measured. It was concluded that fluctuation-induced tunneling between micrometer-size clusters does account for the overall electric performance [39].

26.2.2 Aluminium-Doped Zinc Oxide (AZO)

In contrast to indium oxide there are many reports about the sol–gel processing of undoped zinc oxide [40–43], but more often Al is used as extrinsic dopant to enhance n-type conductivity. When unconventional elements such as e.g. yttrium [44] are employed, losses in transparency mostly compensate the minor improvements of electrical properties.

Zinc acetate dihydrate $\text{Zn}(\text{OAc})_2 \cdot 2\ \text{H}_2\text{O}$ is the common Zn source for most sol synthesis, $\text{Al}(\text{NO}_3)_3 \cdot 9\ \text{H}_2\text{O}$ is mostly applied for doping. There are only a few reports using other compounds such as $\text{AlCl}_3 \cdot 6\ \text{H}_2\text{O}$ [15]. This choice seems justified since it is much more likely to suspect that chloride ions may remain in

the films after thermal treatment whereas nitrate anions will decompose to form volatile products.

Methanol, ethanol, and isopropanol are commonly used as solvents. Additionally, 2-methoxy ethanol, 2-amino ethanol, mono- and di-ethanol amine are employed often. Again their specific functions as solvent and complexing agents is difficult to estimate as there are no systematic comparative studies dealing with their part in AZO thin film formation.

The role of multiple coatings and the influence of single layer thickness for the final film performance was recognized early [36], the resulting “structural zone model” [45] and its implications for sol–gel film optimization are discussed in Sect. 26.3.1.

Most AZO films are subjected to multiple thermal treatment steps after wet chemical deposition. Often multiple coating–firing cycles are performed. Sometimes the final treatment is done in vacuum, inert atmosphere, or even forming gas in order to induce oxygen deficiencies and thus promote intrinsic doping. In Table 26.2 some reported parameters are compiled:

It is difficult to estimate, though, whether the respective experimental parameters in every case result from thoughtful considerations based on pre-test or are sometimes simply due to the equipment available. However, when a temperature range is systematically investigated valuable information is retrieved regarding this particular processing step. A minimum in film resistivity for example is observed at 500 °C for sintering in air [32, 48] atmosphere.

Grain size generally increases with sintering temperature, but for Al-doped samples generally smaller crystallites are observed than for pure ZnO films [46, 48, 49]. Best conductivities are reported for Al-concentrations in the range of 0.8–1.5 mol%, Al-substitution in Zn-sites creates donor levels in the band gap and thus additional electrons in the conduction band. Higher aluminium concentrations may form Al interstitials resulting in greater electron scattering. Aluminium segregation on grain boundaries can additionally increase the resistivity between the individual nanocrystals [32, 46, 47].

Reports of remarkably high conductivities in AZO films prepared by sol–gel processing (e.g. $1.4 \times 10^{-4} \Omega \text{ cm}$ in [32] even without post treatment in H_2/N_2) seem highly encouraging. As already mentioned for ITO films these reports underline the importance of minute control of processing parameters.

26.2.3 Antimony-Doped Tin Oxide (ATO)

Sheet glass is commercially produced by simultaneously cooling and drawing vitreous melts from the flat surface of molten tin baths. When the upper surface of the glass is exposed to organotin compounds such as $^n\text{Bu-SnCl}_3$ at temperatures between 650 °C and 680 °C, their thermal decomposition yields transparent conducting SnO_2 films [4]. This process of so-called *atmospheric pressure chemical vapor deposition* (AP-CVD) is a cost-efficient technique to deposit films with

Table 26.2 Thermal treatment procedures applied to some selected AZO film systems

Drying/pre-bake [°C]	Sintering [°C]	Post-treatment [°C]	Atmosphere	Refs.
30	600	400	N ₂ /H ₂	[13]
260	300–700	–		[32]
350	450–850	–		[46]
70	500–700	500–700	Vacuum	[14]
350	H ₂ /N ₂ 400 + vacuum 700	450	N ₂ /H ₂	[47]
250	550	350–550	Vacuum	[15]
250	400–600	–		[48]
275	Ramp to 550	500–550	N ₂ /H ₂	[49]

sheet resistances of typically 25 Ω sq on glass surfaces moving between 0.8 to 8 m/min. Doping is easily achieved by adding volatile fluorine-containing compounds to the carrier gas stream yielding fluorine-doped tin oxide (FTO). SbCl₃ may correspondingly be used to prepare antimony doped tin oxide (ATO).

Some visual scattering is commonly observed due to sodium chloride crystals formed as by-product on the surface of the hot glass [5]. Regardless of this drawback the market for low-emissive architectural glazing is dominated by this straightforward and low-cost technology. As sol–gel processing is unlikely to provide striking advantages, apparently less focus was put on the coating of glass with tin oxides from solutions.

SnCl₂ and SnCl₄ are mostly used as precursors. Their dissolution in ethanol is likely to produce equilibria of SnCl_{2-x}(OR)_x and SnCl_{4-x}(OR)_x. If these solutions are heated or the solvent is even completely removed [50], any removal of volatile HCl will favor the formation of the alkoxides. In the presence of water introduced by the use of precursor hydrates, initial condensation reactions will lead to amorphous sol particles. The formation of dispersions may further be enforced by the addition of NH₃ and the resulting rise of the pH [51]. Antimony doping is commonly introduced by the addition of SbCl₃, sometimes SbF₃ is used. 4-hydroxy 4-methyl-2-pentanone is applied by some authors as stabilizing agent [52, 53].

Heating the solution of tin- and antimony chloride at 150 °C at 10 bar for three hours in the presence of NH₃ and β -alanine yields dispersions of crystalline ATO particles similar to those reported for ITO [36]. Films prepared from these dispersions retain a granular structure as governed by the primary precursor particles throughout heating at 550 °C.

Even though sol–gel processing turns out to be a very versatile route for ITO, AZO and ATO preparation, the resulting films generally exhibit a small-grained polycrystalline structure mostly including significant shares of porosity. Therefore, the technology seldomly can compete with AP-CVD or physical vapor deposition techniques that often yield dense films sometimes with well-defined columnar microstructures. The following paragraph will outline some strategies to at least partially compensate these shortcomings.

26.3 Optimization Strategies for TCO Thin Films Prepared by Sol–Gel Processing

26.3.1 Dense Films by Multiple Coating Techniques

The assumption that thick films generally will better contribute to the overall conductivity is only true if the film structure is not altered by the single layer thickness of a coating procedure. It was soon recognized for AZO films that both the refractive index and electrical properties improve for multiple coatings compared to thick single layers [13]. Upon closer inspection it turns out that large single layer thicknesses, i.e. thick films prepared by a single sol–gel coating procedure, generally reveal a granular polycrystalline microstructure with significant porosity. If the same overall final thickness is achieved by numerous coating–firing cycles with small single layer thickness, dense and columnar film structures are observed [45, 54]. At intermediate single layer thicknesses a layered structure is observed revealing the number of coating–firing cycles. The respective microstructures are illustrated in Fig. 26.2.

The origin of these different morphologies can be straightforwardly explained by the analysis of film formation on the microscopic scale: Upon thermal treatment of the as-deposited material heterogeneous nucleation and grain growth of crystallites will preferably occur at the substrate surface rather than in the bulk volume of the film (for details see Chap. 17). If the film thickness is high, the increased density of nucleation sites at the substrate will not become apparent in relation to the homogeneous nucleation in the film volume. The microstructure of a fractured edge will appear granular.

When the single layer thickness is reduced, the heterogeneous nucleation on the preceding film surface becomes increasingly dominant. A layered microstructure of the multilayer assembly is observed in cross sectional view.

If the single layer thickness is reduced even further, the film development is mainly governed by epitaxial layer-by-layer growth on the underlying crystalline material. The resulting films exhibit a dense and columnar microstructure comparable to features frequently observed for films deposited by physical vapor deposition. In analogy to classifications used in vacuum-based technologies, a structural zone model has been proposed for the morphology of sol–gel coatings [54].

When sol–gel films are prepared by multiple sol–gel coating procedures, an orientation of the preferred growth direction of crystallites perpendicular to the substrate is often observed [55]. When amorphous substrates are used, this result at first sight seems astonishing since e.g. glass is not expected to favor any specific orientation of nuclei. If one assumes statistical orientation of grains in the layer after first annealing, these crystallites will nevertheless induce homoepitaxial nucleation of the subsequently deposited film material according to their respective alignment (cf. Chap. 16). In the course of subsequent coating–firing cycles, crystallites with their preferential growth direction perpendicular to the substrate

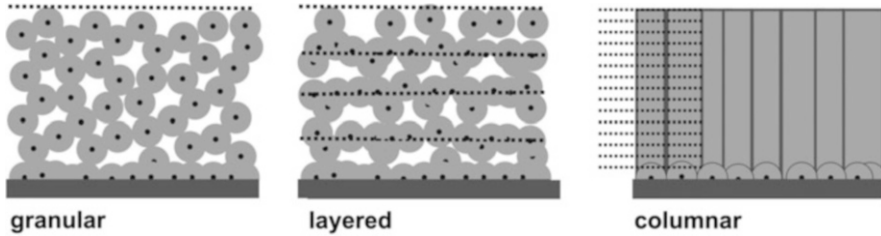


Fig. 26.2 Schematic microstructure of sol-gel derived films with identical final thickness prepared by different numbers of single coatings. The *dotted lines* correspond to the boundaries of the individual layers. The respective nucleation sites for grain growth are marked as *black dots*

will discriminate other grains with alternative orientations. This process is visualized in Fig. 26.3. It should be noted, though, that in contrast to the schematic drawing, in reality, the growth of flat uniform films will take place; in Fig. 26.3 only the processes at the single initial crystallites is shown over time.

The outlined mechanism is indeed supported by experimental results. Nb-doped TiO_2 thin films were prepared by a multiple sol-gel coating process [56] since this system is a promising candidate for novel low-cost TCO films [57, 58].

When films with a final thickness of 100 nm are prepared by a single coating procedure, the typical microstructure of polycrystalline sol-gel films is found. As the single layer thickness is reduced to 20 nm, the region close to the glass substrate appears unaltered. In the upper part of these fivefold coatings, though, columnar grains which obviously emerge from the lower granular part become visible (Fig. 26.4, left).

A further decrease of single layer thickness below 4 nm (30-fold coating) yields fully dense columnar coatings (Fig. 26.4, right). The columnar grains range from substrate to film surface and are single crystals. The vertical features within the grains, though, do not correspond to lattice fringes but to minute fluctuations in film density as a consequence of the multiple coating procedures [56].

Even though fully dense films could be prepared, their specific conductivity falls far behind material deposited by vacuum-based technologies. This fact may be explained by reduced charge-carrier mobility due to a higher lateral density of grain boundaries in the sol-gel derived system. When films with a comparable thickness are prepared by pulsed laser deposition, flat grains with lateral dimensions of several micrometers can be obtained [59].

26.3.2 Infiltration of Porous Films

As already outlined above (Fig. 26.1), coating solutions can also be based on the dispersion of crystalline TCO particles obtained by flame pyrolysis or hydrothermal processing. Films prepared from such dispersions may exhibit considerable porosities due to inter-particle voids and the poor sintering activity of the crystalline

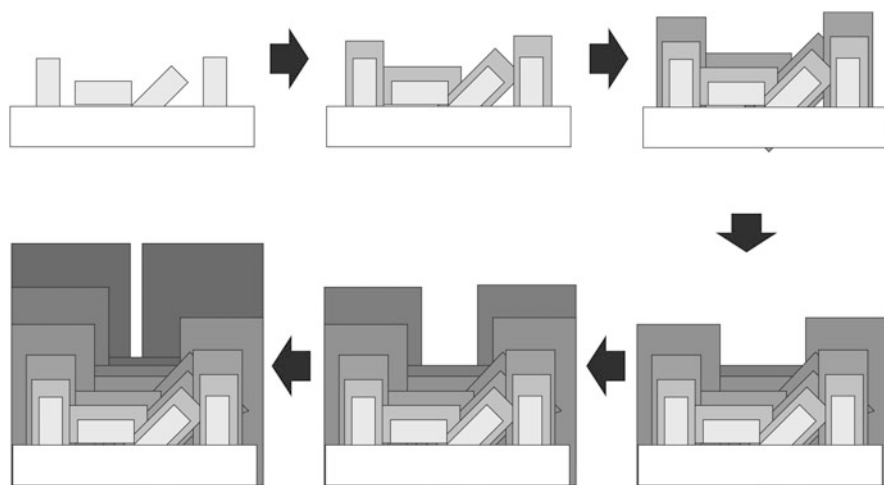


Fig. 26.3 Schematic representation of oriented growth of sol-gel films from randomly oriented initial crystallites during multiple coating experiments

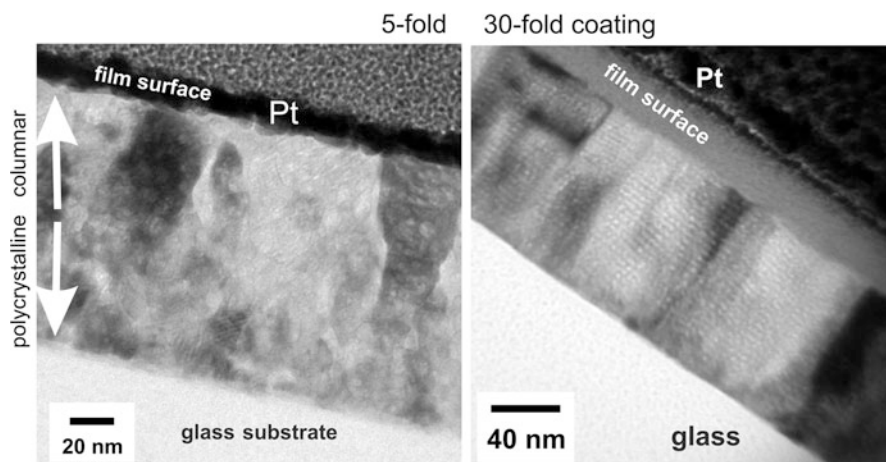


Fig. 26.4 TEM micrographs of Nb-doped TiO₂ thin films prepared by fivefold (*left*) and 30-fold (*right*) sol-gel coating/firing cycles

grains. Since the current pathway is limited by the contact points, the film resistivity may be very high even though the conductivity within the individual grains is excellent [38].

To overcome this drawback, porous films prepared from the dispersion of crystalline material can be infiltrated by coating solutions that contain smaller amorphous particles in a second coating step. For as-annealed films the specific resistivity drops from 0.18 Ω cm to 0.04 Ω cm by a single infiltration. SEM images

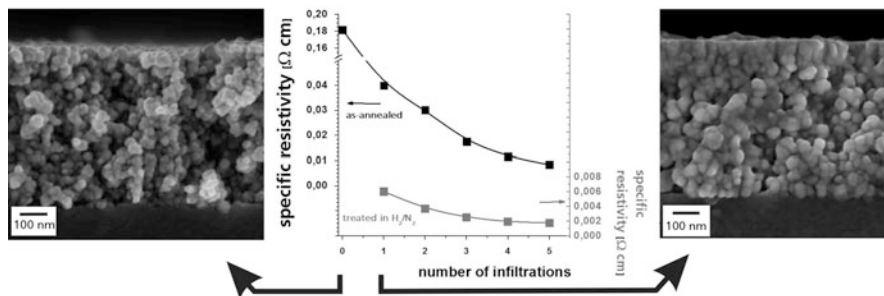


Fig. 26.5 Specific resistivity of films prepared from dispersions of crystalline ITO particles after different numbers of infiltration steps with ITO solutions (*middle*). Data was measured for as-annealed films (*black*) and after treatment in reducing atmosphere (*grey*). Additionally, SEM cross sectional views of a film without (*left*) and after one infiltration step (*right*) are given

indicate that the porous granular film microstructure coarsens due to material deposition in inter-particle necks. The SEM image indicates that the first infiltration process is homogeneous throughout the film profile. Obviously, the capillary attraction is sufficient to distribute the smaller particles from the solution into the depth of the film [60].

Further infiltration steps only increase the conductivity by another factor of 4. Electron microscopy reveals that “true” infiltration does only play a decreasingly important role because the accessibility of the film is reduced by the filling of surface voids. For these films an increase of overall film thickness is observed as the dip-infiltration more and more turns into a dip-coating procedure [60]. When such films are post-treated in 5 % H₂ at 400 °C, oxygen vacancies are created and specific resistivities down to 1.77 E-03 Ω cm are achieved (Fig. 26.5).

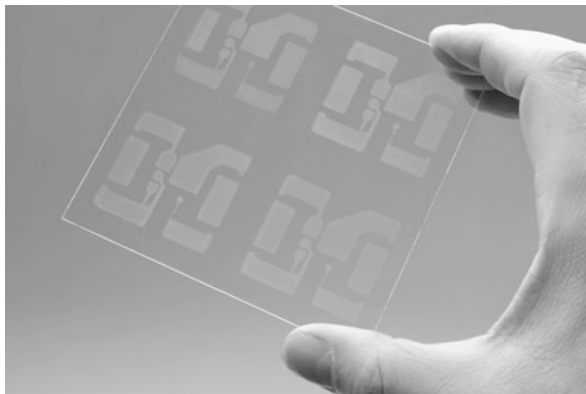
The above examples demonstrate that TCO films with good or at least satisfactory properties can be prepared by the sol–gel route. Up to now their final performance does not justify the elaborate processing technology from the commercial point of view when compared with products from PVD or AP-CVD. However, there are cases where the specific features of wet chemical processing may provide striking advantages. Two such examples will be addressed in the next paragraph.

26.4 Highlights of Sol–Gel Processing of TCO Thin Films

26.4.1 Printing of TCO Films

Innovative lighting technology (e.g. OLEDs) and the emerging field of “Transparent Electronics” [61] frequently require patterned TCO films such as distinct conduction pathways (“transparent wiring”). Unfortunately, neither PVD nor CVD can provide straightforward masking technology suitable for these purposes.

Fig. 26.6 Patterned ITO films on glass substrate deposited by pad-printing. Photo: Fraunhofer ISC



Therefore, laterally structured TCOs have to be prepared by laborious “subtractive” technologies: Large-area films are covered by a photoresist that is microstructured by photolithography, developed, and the exposed TCO surface is subsequently wet-chemically etched. When only low resolutions are required, etching-agents may be selectively distributed by screen-printing.

Direct printing of wet-chemical TCO precursors may provide a superior alternative: No etching procedure is required when the films are deposited on the substrate in the selected pattern. In the case of costly ITO material such a procedure will be specifically attractive from the commercial point of view.

In printing functional materials many parameters concerning the respective printing technology, substrate properties, and required film performance have to be balanced. Concerning sol–gel synthesis especially the solution properties can be tuned with respect to concentration and viscosity: Whereas screen printing may require more pasty compositions, gravure printing and ink-jetting will depend on a higher fluidity of the material.

In Fig. 26.6 patterned ITO films prepared by pad-printing are shown [60]. Both, sols of amorphous particles and dispersions of crystalline particles can be applied [16], but the latter may account for an undesired surface roughness if applications such as OLED lighting are addressed. These pad-printed films have to undergo thermal treatment in order to exhibit a specific conductivity of $16 \times 10^{-03} \Omega \text{ cm}$. Functionalized ITO nanoparticles were used in gravure-printing experiments on polyethylene naphthalate (PEN). Optimum resistivities of $24 \times 10^{-03} \Omega \text{ cm}$ ($400 \Omega \text{ sq}$, 600 nm) were reported after treatment at 180°C under reducing atmosphere [62].

26.4.2 *p-Type Conducting Films*

All TCO materials described in Sect. 26.1 rely on n-type conductivity meaning that electrons from donor levels below the conduction are the (negative) majority charge carriers. In 1997 CuAlO_2 was reported to be the first known p-type conducting TCO

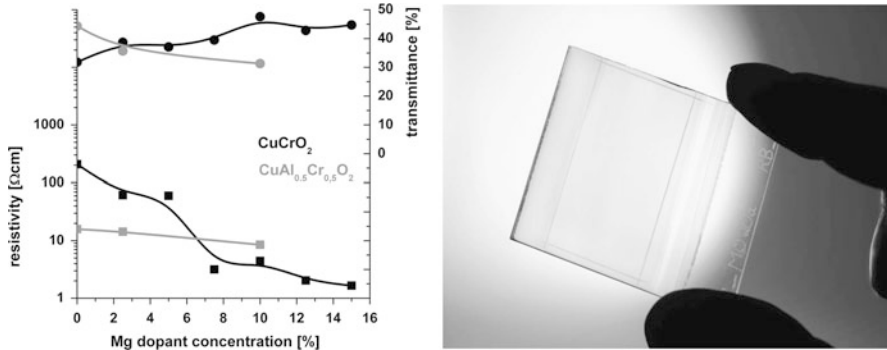


Fig. 26.7 Electrical and optical properties of CuCrO_2 and $\text{CuAl}_{0.5}\text{Cr}_{0.5}\text{O}_2$ as a function of Mg dopant concentration (*left*) and image of $\text{CuAl}_{0.5}\text{Cr}_{0.5}\text{O}_2$ thin film on borosilicate glass (*right*). Photo: Fraunhofer ISC

[63]. Subsequently, some other oxides with the same crystal structure such as CuCrO_2 were investigated. In these so-called delafossites planar arrangement of Al-O (or Cr-O) octahedra are sandwiched by O-Cu-O units in linear coordination. The electrical performance of these materials will never be able to compete with the well-established n-type TCOs due to their intrinsic low carrier mobility [64]. Nevertheless the combination of p-conductivity with transparent n-conductivity may enable the fabrication of transparent electronic and optoelectronic devices [61, 65].

Most early reports on delafossite-type p-TCOs have their focus on film deposition by PLD. Since this method does not provide a perspective on large-area deposition, successively sputtering technologies were applied [16, 66, 67]. As it turns out, up to now the as-deposited films have not shown the delafossite crystal structure [16]. Therefore an ex-situ post-annealing step is necessary similar to the thermal treatment that is required for the pyrolysis and densification of sol-gel films.

CuAlO_2 and CuCrO_2 thin films prepared by sol-gel processing have to undergo a 2-step thermal treatment [68]: At temperatures between 400 °C and 600 °C residual organics are removed in air and first cuprous oxides and spinel phases are detected by XRD measurements. Further annealing in inert gas atmosphere is necessary to obtain CuAlO_2 and CuCrO_2 in the delafossite phase at 920 °C and 700 °C respectively. It turns out that the pyrolysis temperature has a significant influence on the final electric performance of the films [69]: Once an intermediate spinel phase is formed it will obstruct the subsequent transformation into the delafossite phase.

As flexibility of chemical composition is an advantage of sol-gel processing, $\text{CuAl}_x\text{Cr}_{1-x}\text{O}_2$ thin films were prepared in order to optimize electrical performance, optical properties and (low) processing temperature for the formation of the delafossite phase [70]. Pure $\text{CuAl}_{0.5}\text{Cr}_{0.5}\text{O}_2$ exhibits a higher transmittance and lower resistivity than CuCrO_2 , but doping with magnesium has a more marked effect on the latter composition (Fig. 26.7): By addition of 15 % Mg the conductivity of CuCrO_2 can be improved by two orders of magnitude.

Even though the phase development of the delafossite systems is rather complex, this example clearly demonstrates that coatings containing 3–4 metal cations can be handled by an appropriate sol–gel synthesis procedure. Thus it is easy to systematically investigate the influence of compositional changes and the introduction of dopants.

26.5 Concluding Remarks

Compared with vacuum-based technologies TCO thin films may suffer from some shortcomings regarding their polycrystalline structure and residual porosity. It was shown that these weaknesses to a certain extent can be compensated by sophisticated processing. However, it does not seem fruitful to develop elaborate wet-chemical routes just to end up with “me too films” if the related manufacturing technologies cannot compete from the commercial point of view. However, bearing in mind the inherent limitations for certain applications work may be specifically focused on topics as reproducibility and scalability that are widely neglected by academic groups.

Despite the above considerations there are many innovative fields such as printed electronics and transparent p–n junctions where the unique features of sol–gel processing can provide distinct advantages over alternative processing technologies.

References

1. Chopra K, Major S, Padya D (1982) Transparent conductors – A status review. *Thin Solid Films* 102:1
2. Gosh PK, Das S, Kundoo S, Chattopadhyay K (2005) Effect of fluorine doping on semiconductor to metal-like transition and optical properties of cadmium oxide thin films deposited by sol–gel process. *J Sol-Gel Sci Technol* 34:173
3. Granqvist C (2007) Transparent conductors as solar energy materials. A panoramic review. *Sol Energ Mater Sol Cells* 91:1529
4. Henery V. Chemical vapor deposition of tin oxide on float glass in the tin bath. US Patent 4853257
5. Szanyi J (2002) The origin of haze in CVD tin oxide thin films. *Appl Surf Sci* 185:161
6. Szyszka B (2001) Transparente und leitfähige Oxidschichten. *Vakuum in Forschung und Praxis* 1:38
7. Sawada Y, Kobayashi C, Seki S, Funakubo H (2002) Highly-conducting indium–tin-oxide transparent films fabricated by spray CVD using ethanol solution of indium (III) chloride and tin (II) chloride. *Thin Solid Films* 409:46
8. Suzuki A, Matsushita T, Aoki T, Mori A, Okuda M (2002) Highly conducting transparent indium tin oxide films prepared by pulsed laser deposition. *Thin Solid Films* 411:23
9. Biswas P, De A, Ortner K, Korder S (2004) Study of sol–gel-derived high tin content indium tin oxide (ITO) films on silica-coated soda lime silica glass. *Mater Lett* 58:1540

10. Hammad T (2006) ITO Thin films on silicon buffer by sol–gel method. *Mat Sci Forum* 514–516:1155
11. Minami T, Oohashi K, Takata S, Mouri T, Ogawa N (1990) Preparations of ZnO:Al transparent conducting films by D.C. magnetron sputtering. *Thin Solid Films* 193/194:721
12. Agura H, Suzuki A, Matsushita T, Akoi T, Okuda M (2003) Low resistivity transparent conducting Al-doped ZnO films prepared by pulsed laser deposition. *Thin Solid Films* 445:263
13. Schuler T, Aegerter M (1999) Optical, electrical and structural properties of sol–gel ZnO:Al coatings. *Thin Solid Films* 351:125
14. Lin K, Tsai P (2007) Growth mechanism and characterization of ZnO: Al multi-layered thin films by sol–gel technique. *Thin Solid Films* 515:8610
15. Sobajima Y, Kato S, Matsuura T, Toyama T, Okamoto H (2007) Study of the light-trapping effects of textured ZnO:Al/glass structure TCO for improving photocurrent of a-Si:H solar cells. *J Mater Sci Mater Electron* 18:S159
16. Szyszka B, Löbmann P, Georg A, May C, Elsaesser C (2010) Development of new transparent conductors and device applications utilizing a multidisciplinary approach. *Thin Solid Films* 518:3109
17. Jäger S, Szyszka B, Szczyrbowski J, Bräuer G (1998) Comparison of transparent conductive oxide thin films prepared by A.C. and D.C. reactive magnetron sputtering. *Surf Coat Technol* 98:1304
18. Lee S, Hong B, Choi WS (2009) Structural, electrical and optical properties of antimony-doped tin oxide films prepared at room temperature by radio frequency. *J Vac Sci Technol A* 27:996–1000
19. Dua L, De A, Chakraborty S, Biswas P (2008) Study of spin coated high antimony content Sn–Sb oxide films on silica glass. *Mater Charact* 59:578
20. Benrabah B, Bouaza A, Hamzaoui S, Dehbi A (2009) Sol–gel preparation and characterization of antimony doped tin oxide (ATO) powders and thin films. *Eur Phys J Appl Phys* 48:30301
21. Ma H, Zhang D, Win S, Li S, Chen Y (1996) Electrical and optical properties of F-doped textured SnO₂ films deposited by APCVD. *Sol Energ Mater Sol Cells* 40:371
22. Talaty N, Beck K, Citeau H, Kirschbaum K, Giolando D (2009) Characterization of Tin (IV) oxide thin films prepared by atmospheric pressure chemical vapor deposition of cis-[SnCl₄{OC(H)OC₂H₅}₂]. *Z Anorg Allg Chem* 635:53
23. Lin C, Chiang M, Chen Y (2009) Temperature dependence of fluorine-doped tin oxide films produced by ultrasonic spray pyrolysis. *Thin Solid Films* 518:1241
24. Liu J, Rädlein E, Frischat G (1999) Preparation, nanostructure and properties of indium tin oxide (ITO) films on glass substrates. Part 2. Optimisation of properties. *Phys Chem Glasses* 40:282
25. Savarimuthu E, Lalithambika K, Raj A, Nehru LC, Ramamurthy S, Thayumanavan A, Sanjeeviraja C, Jayachandran M (2007) Synthesis and materials properties of transparent conducting In₂O₃ films prepared by sol–gel-spin coating technique. *J Phys Chem Solids* 68:1380
26. Beaurain A, Luxembourg D, Dufour C, Koncar V, Capoen B, Bouazaoui M (2008) Effects of annealing temperature and heat-treatment duration on electrical properties of sol–gel derived indium-tin-oxide thin films. *Thin Solid Films* 516:4102
27. Su C, Sheu T, Chang Y, Wan M, Feng M, Hung W (2005) Preparation of ITO thin films by Sol–gel process and their characterizations. *Synt Met* 153:9
28. Li Z, Ren D (2006) Preparation of ITO transparent conductive film by sol–gel method. *Trans Nonferrous Met Soc China* 16:1358
29. Al-Dahoudi N, Aegerter M (2006) Comparative study of transparent conductive In₂O₃:Sn (ITO) coatings made using a sol and a nanoparticle suspension. *Thin Solid Films* 502:193
30. Biswas P, Dea A, Dua L, Chkoda L (2006) Work function of sol–gel indium tin oxide (ITO) films on glass. *Appl Surf Sci* 253:1953
31. Aksu Y, Driess M (2009) A low-temperature molecular approach to highly conductive tin-rich indium tin oxide thin films with durable electro-optical performance. *Angew Chem* 121:7918

32. Alam M, Cameron D (2001) Characterization of transparent conductive ITO thin films deposited on titanium dioxide film by a sol–gel process. *Surf Coat Technol* 142–144:776
33. Alam M, Cameron D (2002) Investigation of annealing effects on sol–gel deposited indium tin oxide thin films in different atmospheres. *Thin Solid Films* 420–421:76
34. Löbmann P, Röhlen P (2003) Industrial processing of TiO₂ thin films from soluble precursor powders. *J Glass Sci Technol* 76:1
35. Cho Y, Kim H, Hong J, Yi G, Yang S, Yang S (2009) Dispersion stabilization of conductive transparent oxide nanoparticles. *Coll and Surf A* 336:88
36. Goebbert C, Nonninger R, Aegerter M, Schmidt H (1999) Wet chemical deposition of ATO and ITO coatings using crystalline nanoparticles redispersable in solutions. *Thin Solid Films* 351:79
37. Aegerter M, Al-Dahoudi N (2003) Wet-chemical processing of transparent and antiglare conducting ITO coating on plastic substrates. *J Sol-Gel Sci Technol* 27:81
38. Ederth J, Johnson P, Niklasson G, Hoel A, Hultaker A, Heszler P, Granqvist C, van Doorn A, Jongorius M, Burgard D (2003) Electrical and optical properties of thin films consisting of tin-doped indium oxide nanoparticles. *Phys Rev B* 68:155410
39. Ederth J, Heszler P, Hultaker A, Niklasson G, Granqvist C (2003) Indium tin oxide films made from nanoparticles: models for the optical and electrical properties. *Thin Solid Films* 445:199
40. Natsume Y, Sakata H (2002) Electrical and optical properties of zinc oxide films post-annealed in H₂ after fabrication by sol–gel process. *Mat Chem Phys* 78:170
41. Lee J, Ko K, Park B (2003) Electrical and optical properties of ZnO transparent conducting films by the sol–gel method. *J Cryst Growth* 247:119
42. Hammad T (2006) Electrical and optical properties of multilayer sol–gel ZnO coatings. *Int J Modern Phys B* 20:3357
43. Kyaw A, Sun X, Jiang C (2009) Efficient charge collection with sol–gel derived colloidal ZnO thin films in photovoltaic devices. *J Sol-Gel Sci Technol* 52:348
44. Kaur R, Singh A, Mehra R (2006) Sol–gel derived highly transparent and conducting yttrium doped ZnO films. *J Non-Cryst Solids* 352:2335
45. Schuler T, Krajewski T, Grobelsek I, Aegerter M (2006) Influence of structure zone model parameters on the electrical properties of ZnO:Al sol–gel coatings. *Thin Solid Films* 502:67
46. Kuo SY, Chen WC, Lai FI, Cheng CP, Kuo HC, Wang SC, Hsieh WF (2006) Effects of doping concentration and annealing temperature on properties of highly-oriented Al-doped ZnO films. *J Crystal Growth* 287:78
47. Lin J, Wu J (2008) The effect of annealing processes on electronic properties of sol–gel derived Al-doped ZnO films. *Appl Phys Lett* 92:134103
48. Yi SH, Choi SK, Jang JM, Kim JA (2007) Properties of aluminium doped zinc oxide thin film by sol–gel process. *Proc SPIE* 6831:68311A-1-8
49. Copuroglu M, O'Brien S, Crean GM (2009) Sol–gel synthesis, comparative characterization, and reliability analyses of undoped and Al-doped zinc oxide thin films. *Thin Solid Films* 517:6323–6326
50. Boudiar T, Sandu C, Canut B, Blanchin M, Teodorescu V, Roger J (2003) Interest of rapid thermal annealing (RTA) for the elaboration of SnO₂:Sb transparent conducting oxide by the sol–gel technique. *J Sol-Gel Sci Technol* 26:1067
51. Geraldo V, Scalvi L, Morais D, Santilli C, Pulcinelli H (2003) Sb doping effects and oxygen adsorption in SnO₂ thin films deposited *via* sol–gel. *Mat Res* 6:451
52. Puetz J, Chalvet F, Aegerter M (2003) Wet chemical deposition of transparent conducting coatings in glass tubes. *Thin Solid Films* 442:53
53. Guzman G, Dahmani B, Puetz J, Aegerter M (2006) Transparent conducting sol–gel ATO coatings for display applications by an improved dip coating technique. *Thin Solid Films* 502:281
54. Schuler T, Krajewski T, Grobelsek I, Aegerter M (2004) A microstructural zone model for the morphology of sol–gel coatings. *J Sol-Gel Sci Technol* 31:235

55. Alam M, Cameron D (2001) Preparation and properties of transparent conductive aluminum-doped zinc oxide thin films by sol-gel process. *J Vac Sci Tech A* 19:1642
56. Wang C, Meinhardt J, Löbmann P (2010) Growth mechanism of Nb-doped TiO₂ sol-gel multilayer films characterized by SEM and focus/defocus TEM. *J Sol-Gel Sci Technol* 53:148
57. Furubayashi Y, Hitosugi T, Yamamoto Y, Hirose Y, Kinoda G, Inaba K, Shimada T, Hasegawa T (2006) Novel transparent conducting oxide: Anatase. *Thin Solid Films* 496:157
58. Hitosugi T, Ueda A, Furubayashi Y, Hirose Y, Konuma S, Shimada T, Hasegawa T (2007) Fabrication of TiO₂-based transparent conducting oxide films on glass by pulsed laser deposition. *Jpn J Appl Phys* 46:86
59. Yamada N, Hitosugi T, Hoang N, Furubayashi Y, Hirose Y, Shimada T, Hasegawa T (2007) Fabrication of low resistivity Nb-doped TiO₂ transparent conductive polycrystalline films on glass by reactive sputtering. *Jpn J Appl Phys* 46:5275
60. Prodi-Schwab A, Lüthge T, Jahn R, Herbig B, Löbmann P (2008) Modified procedure for the sol-gel processing of indium-tin oxide (ITO) films. *J Sol-Gel Sci Technol* 47:68
61. Facchetti A, Marks T (2010) *Transparent electronics – From synthesis to applications*. Wiley, London
62. Puetz J, Aegerter M (2008) Direct gravure printing of indium tin oxide nanoparticle patterns on polymer foils. *Thin Solid Films* 516:4495
63. Kawazoe H, Yasukawa M, Hyodo H, Kurita M, Yanagi H, Hosono H (1997) P-type electrical conduction in transparent thin films of CuAlO₂. *Nature* 389:939
64. Ingram B, González G, Mason T, Shahriari D, Barnabè A, Ko D, Poeppelmeier K (2004) Transport and defect mechanisms in cuprous delafossites. 1. Comparison of hydrothermal and standard solid-state synthesis in CuAlO₂. *Chem Mater* 16:5616
65. Ohta H, Hosono H (2004) Transparent oxide optoelectronics. *Mater Today* 7:42
66. Tsuboi N, Takahashi Y, Kobayashi S, Shimizu H, Kato K, Kaneko F (2003) Delafossite CuAlO₂ films prepared by reactive sputtering using Cu and Al targets. *J Phys Chem Solids* 64:1671
67. Lu Y, He Y, Yang B, Polity A, Volbers N, Neumann C, Hasselkamp D, Meyer B (2006) RF reactive sputter deposition and characterization of transparent CuAlO₂ thin films. *Phys Stat Sol (C)* 3:2895
68. Götzendörfer S, Polenzky C, Ulrich S, Löbmann P (2009) Preparation of CuAlO₂ and CuCrO₂ thin films by sol-gel processing. *Thin Solid Films* 518:1153
69. Götzendörfer S, Bywalez R, Löbmann P (2009) Preparation of p-typed conducting transparent CuCrO₂ and CuAl_{0.5}Cr_{0.5}O₂ thin films by sol-gel processing. *J Sol-Gel Sci Technol* 52:113
70. Bywalez R, Götzendörfer S, Löbmann P (2010) Structural and physical effects of Mg-doping on p-type CuCrO₂ and CuAl_{0.5}Cr_{0.5}O₂ thin films. *J Mater Chem* 20:6562

Chapter 27

Superconducting Films

Michael Bäcker, Martina Falter, Oliver Brunkahl, and Bernhard Holzapfel

27.1 High Temperature Superconductivity

About 100 years after the discovery of superconductivity by Heike Kamerlingh Onnes [1] the promises of superconductivity for revolutionizing energy applications start to become true. A new generation of superconducting materials and production processes enables new applications such as cables, motors, generators, magnets and fault current limiters. In this chapter the status of high temperature superconducting (HTS) materials and technologies for thin film coating on long length wires will be presented. The main focus will be on basic superconducting properties and critical parameters, chemical solution deposition of thin films and a selection on evolving applications.

Two outstanding properties of high temperature superconductors when cooled under their critical temperature break paradigms in electro technology:

- No ohmic resistance
- Highest energy density (Fig. 27.1)

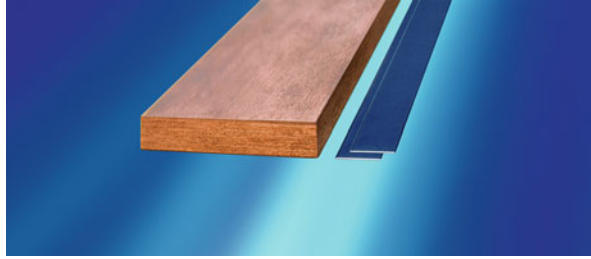
Highlights

- The absence of ohmic resistance allows the construction of HTS-systems with superior energy efficiency e.g. magnetic billet heater saving about 40 % electrical energy compared to conventional systems.
- The high energy density enables the construction of lighter and smaller devices. As an example the diameter of a 6 MW off-shore wind power generator therefore can be reduced from 9 to 2.5 m

M. Bäcker (✉) • M. Falter • O. Brunkahl
Deutsche Nanoschicht GmbH, Rheinbach, Germany
e-mail: baecker@d-nano.com

B. Holzapfel
IFW, Dresden, Germany

Fig. 27.1 Comparison of current density in copper (*left*) and HTS wire (*right*). Both conductors represent a current carrying capacity of 200 A



High temperature superconducting materials were discovered in 1986 by Bednorz and Müller [2, 3]. For all energy applications only HTS are applicable due to their superior operating temperature compared to low temperature superconductors. High temperature superconductivity is defined by a critical temperature above 77 K, the boiling point of liquid nitrogen. In order to be usable in electric devices the ceramic oxide-based HTS materials have to be processed to windable wires or tapes. In contrast to first generation (1G) HTS tapes, where the processing to thin filaments was preferred, second generation (2G) of HTS tapes are based on thin film technology. Thus, these HTS tapes are also called Coated Conductors.

Since the discovery of HTS materials physical vapour deposition techniques were applied for the deposition of HTS films on small areas. Chemical solution deposition was strongly developed starting in 1998 when first promising results were obtained and major drawbacks of the process were overcome by new metal-organic precursors.

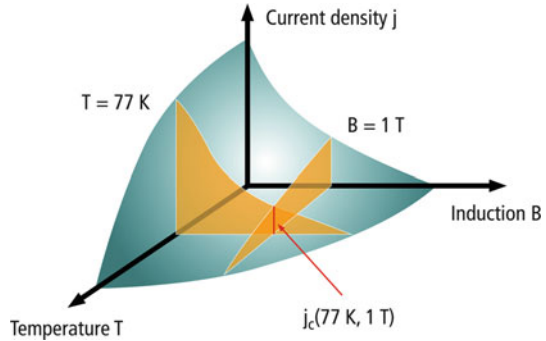
In the last years the successful manufacturing of complete layer architectures of Coated Conductors by CSD methods was demonstrated by several groups worldwide. Nevertheless it is common sense that this technology is the most promising one in terms of economy but also the most challenging one in terms of materials science.

27.1.1 Critical Parameters

27.1.1.1 Critical Temperature

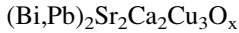
The characteristics of superconducting materials are described by three critical parameters [4]. If these parameters are exceeded, superconductivity will collapse. In particular those characteristics are critical temperature (T_c), critical current density (J_c) and critical magnetic induction (B_{c2}) or the upper critical magnetic field (H_{c2}). The relationship between these parameters is depicted in Fig. 27.2. The foundations of the HTS-wires and tapes are explained using the critical parameters as follows.

Fig. 27.2 Critical temperature (T_c), critical current density (J_c) and critical induction (B_{c2})



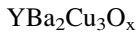
High-Temperature-Superconductivity is generally defined by a transition temperature (critical temperature) above 77 K, the boiling point of liquid nitrogen. So far, two materials have acquired technical relevance for HTS-wires:

Bismuth (Lead-)Strontium-Calcium-Copper-Oxide



$$T_c = 110 \text{ K}$$

Yttrium-Barium-Copper-Oxide



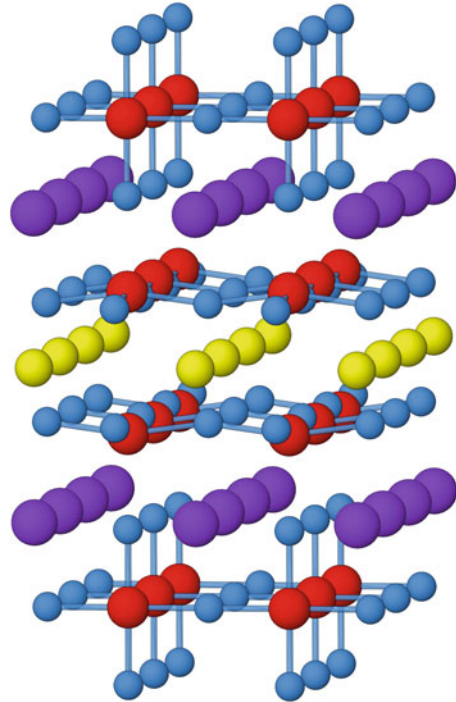
$$T_c = 92 \text{ K}$$

The critical temperature is a material constant and is not influenced by processing. In spite of intensive research and occasional press releases about new superconducting compounds, the materials known so far are the only materials with a commercial potential.

27.1.1.2 Critical Current

In electrical engineering applications, the current carrying capacity of the HTS-wires is the decisive criterion for the technical applicability. All HTSs are ceramic, oxidic materials with copper-oxide layers as a common basis. Their special crystalline structure (Fig. 27.3) causes a strong anisotropy of the critical current density. Thus, the critical current density, parallel to the copper-oxide-layers, is several times higher than vertical to the layers. In the same way, the current carrying capacity through high-angle grain boundaries is strongly restricted. As it is not possible to produce a kilometre-long monocrystal, the industrial manufacturer of HTS-tapes is confronted with the challenge to arrange every superconductor crystal equally within the HTS-wire. This crystalline alignment is called texture. The critical current of a HTS-tape therefore depends on the grade of texture and thus on the manufacturing of the wire.

Fig. 27.3 Crystalline structure of $\text{YBa}_2\text{Cu}_3\text{O}_x$ with copper oxide layers



In this respect, texturing may be carried out either mechanically, like for HTS-tapes of the first generation (1G) on the base of Bismuth-(Lead-)Strontium-Calcium-Copper-Oxide, or by aligned crystal growth, as is used for the HTS-wires of the second generation (2G) on the base of Yttrium-Barium-Copper-Oxide.

Apart from the critical current I_c , the critical current density J_c (I_c related to the cross-section of the superconductor) as well as J_e (I_c related to the total cross-section of the HTS-wire) are parameters that are often used.

27.1.1.3 Critical Magnetic Field and Irreversibility Field

Assuming a certain magnetic field strength (lower critical field, H_{c1}), the magnetic field penetrates by so called vortices all HTS-materials. Above the upper critical magnetic field H_{c2} , superconductivity completely fails. This flux penetration occurs for all so-called type II superconductors under nearly every technically relevant application conditions for HTS-wires. If these HTS-conductors now carry current, the Lorentz force will have an effect on the flux lines moving them perpendicular to the current direction and causing electrical dissipation (Fig. 27.4). This undesired movement may be prevented by flux line pinning of nanoscale regions with normal conductivity. These nano-scale regions may either be crystalline defects, contaminations, precipitates or nano-particles in the HTS-material.

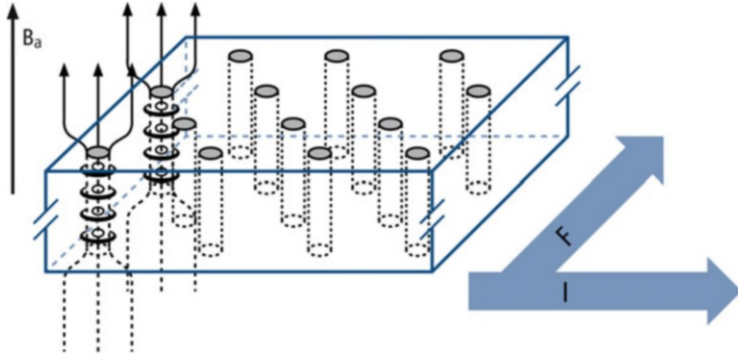


Fig. 27.4 Magnetic flux lines, electrical current (I) and Lorentz-force (F)

Therefore, if required, the aim is to create these pinning centres during manufacturing process, depending on the external magnetic field under specific application conditions of the HTS-wires.

The magnetic field limiting loss-free current transport at a certain temperature by beginning flux line movement is called irreversibility field H_{irr} , representing the decisive parameter for the applicability of the HTS-material in power engineering. Depending on temperature and HTS-crystalline structure, H_{irr} may be below H_{c2} and thus is strongly dependent on material and microstructure.

The main goal of HTS-wire process development therefore is to optimise the critical current and the irreversibility field.

27.2 Coated Conductors: Second Generation (2G) HTS Tapes

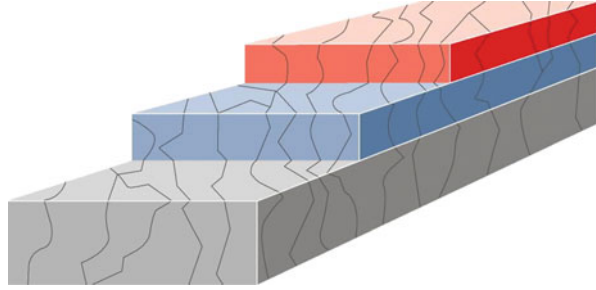
27.2.1 First and Second Generation HTS Tapes

The basic challenge faced during the production of flexible and long conductors of ceramic HTS-materials is their brittleness. The manufacture of thin filaments or thin layers is considered as the solution to this problem. When sufficiently small dimensions are used, the materials are flexible, as for example, is known for glass fibres.

HTS-wires of the first generation (1G) are based on the material Bismuth-(Lead-)Strontium-Calcium-Copper-Oxide (BSCCO) and the filament principle; HTS-wires of the second generation (2G) are based on the material Yttrium-Barium-Copper-Oxide (YBCO) and the layer principle (Fig. 27.5).

HTS-wires of the first generation are manufactured according to the Powder-in-Tube (PiT) procedure. During this process, a malleable metallic cladding tube is filled with fine powder of the oxidic precursor materials, which is shaped afterwards

Fig. 27.5 Layer architecture of 2G HTS tapes with metallic substrate (grey), buffer layers (blue) and HTS layer (red)



by drawing to form a thin wire. These first generation HTS tapes are actually used for prototype HTS systems as described in section "applications". Within the next years, second generation HTS tapes will replace these tapes due to economic reasons – the metal cladding material for first generation tapes is silver, which is prohibitive for reaching price targets for most energy applications.

The basic design of second generation HTS-wires is a multilayer system based on a metal substrate tape coated with ceramic buffer layers deposited first, followed by the actual superconductor layer. The metal substrate contributes stability and flexibility to the HTS tape. The ceramic buffer is required as a barrier in order to prevent the outdiffusion of metal ions from the substrate, particularly of ferromagnetic metals, into the superconducting layer and, vice versa, the indiffusion of oxygen, which would lead to delamination of the layer architecture by forming metal oxides at the interface. The final superconducting layer is responsible for the core properties and may be further covered by mechanical and electrical protective layers.

An impression of the real relation of the individual thicknesses is given in Fig. 27.6.

The metallic substrate has a typical thickness of 80 μm , whereas the complete layer architecture of the superconductor requires a thickness of about 1–2 μm thus being less than 2–3 % of the whole tape thickness.

27.2.2 Challenges and Processes for 2G HTS Tapes

Film deposition is attainable either by physical or by chemical processes. Physical deposition processes, such as sputtering, Pulsed Laser Deposition (PLD) or electron beam evaporation require a high-vacuum, while chemical processes, in particular Chemical Solution Deposition (CSD), may be operated under normal pressure. Metal Organic Chemical Vapour Deposition (MOCVD) occupies an intermediate position, requiring only a moderate vacuum. In general, a much better performance of the superconducting layers is achieved using physical vapour deposition because of the high-vacuum and the low deposition rate minimizing crystalline defects. For high performance HTS-wires for special applications like NMR and MRI magnets

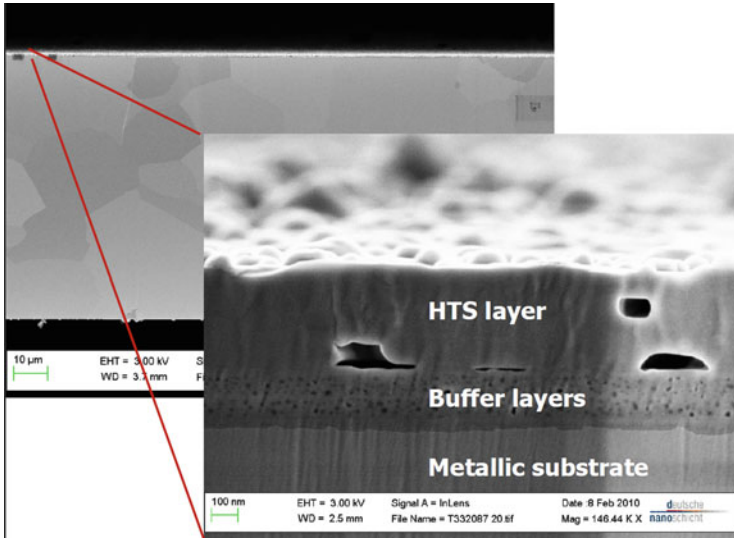


Fig. 27.6 SEM micrograph of a complete layer system of a 2G HTS tape (courtesy of Deutsche Nanoschicht)

the physical deposition methods clearly have their justification and are described elsewhere [5].

From an economic point of view only the chemical solution deposition process will allow reaching the ambitious price targets for HTS tape in the near future. In order to be competitive to copper in energy technology only CSD processes will allow the economic large volume manufacturing due to their general advantages already described before, such as high deposition rate, low investment and low energy and raw material costs. The Holy Grail of HTS wire processing therefore is an HTS-wire only processed via CSD coating technology called an “all-solution Coated Conductor”. Contrary to its economic advantages, chemical solution deposition is considered to be the most challenging process for manufacturing 2G HTS tapes. This is due to the fact described above that all HTS crystals in a tape have to be aligned in order to enable highest current flows.

The crystallization of dried and pyrolysed films deposited by CSD processes normally is not directed and yields untextured polycrystalline films. Therefore this special method requires dedicated strategies to enforce a directed crystallisation towards an orientation of all single superconducting crystals over the whole tape length. This orientated growth in the case of CSD coated HTS tape is enforced by the orientation of the substrate base and the buffer layer. The nucleation energy of the material during the crystallization process is minimized at the interface in the predetermined orientation of the so called template. Following this, the basis of all orientated layers in an HTS tape necessarily must be an orientated substrate.

This substrate consists of special metal alloys, which can be orientated by strong cold deformation and subsequent annealing, notably Nickel-alloys due to their

ability for texturing and their good match of lattice parameters to the subsequently deposited ceramic layers. This given orientation then has to be transferred via the buffer layer into the final HTS layer.

The materials, processes and properties of substrates, buffer layers and HTS layers are described in detail in the following sections.

27.3 CSD HTS Tapes: “All-Solution” Coated Conductor

27.3.1 *Metallic Substrate*

As mentioned before the critical current carrying capacity of polycrystalline HTS materials is strongly dependent on the relative crystalline orientation of neighboring grains. Even a small misalignment of about 10° typically reduces the critical current density by a factor of 10.

As a consequence, the metal substrate tape of a high J_c second generation HTS tape crucially needs such a strong texture over long length. As the grain-to-grain misorientation of the metal substrate is transferred via buffer layers to the superconducting layer, the texture quality of the substrate determines the maximal obtainable critical current density of the whole HTS tape. Besides the high crystalline order the metal substrates for 2G HTS tapes require an extremely smooth surface, they should be mechanically strong and preferable non-magnetic. The low substrate roughness is required for the crystalline orientation transfer to the superconducting layer by epitaxial film growth. Mechanically strong substrates allow the use of thin metal substrates and therefore increase the engineering critical current density, whereas non (ferro)magnetic metal substrates reduce AC losses in applications like cables.

The development of a sharp cube texture in heavily cold rolled face centered cubic metals is a well-known phenomenon and already was studied intensively in the first half of the last century [6, 7]. Most of the work was done based on Cu and Cu alloys. The development of a similar texture, the so called goss-texture, in base centered cubic materials like FeSi is another example and heavily used for low loss electric transformers. In 1996, researchers from Oak Ridge National Laboratory used cube textured pure Ni for the first time as a substrate for epitaxial growth of oxide buffer and superconducting films [8, 9] and achieved high critical current density YBCO films on top of these substrates. With this development the so-called Rolling-Assisted-Biaxially-Textured-Substrates (RABiTS) approach was demonstrated for the first time. In face centered cubic (fcc) metals a sharp cube texture only forms, if heavy cold rolling with deformation degrees larger than 99 % is followed by a recrystallization heat treatment (see Fig. 27.7).

The quality and sharpness of the obtainable texture depends on the type of fcc metal, the cold deformation degree before recrystallization, alloying degree and even the presence of impurities. For pure Ni a sharp cube texture is easily

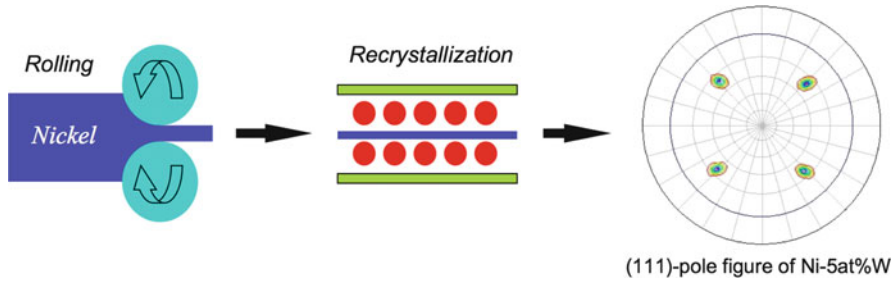
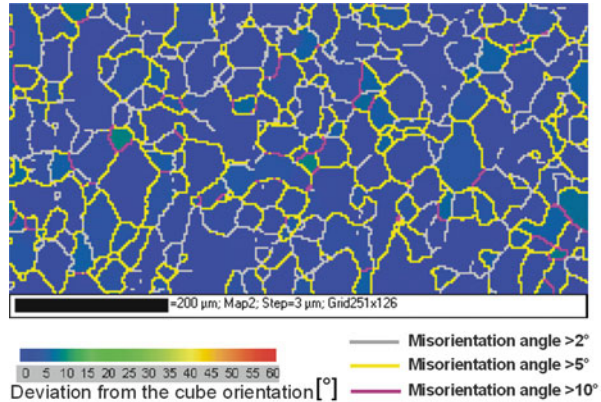


Fig. 27.7 Schematic illustration of the basic texturing process: a fcc metal like Ni is strongly cold deformed by rolling and subsequently recrystallized. This leads to a strong cube texture in this material (courtesy of Evico)

obtainable as illustrated by EBSD (Electron BackScattering Diffraction) analysis in Fig. 27.8. EBSD enables the locally resolved, quantitative measurement of the metal-to-tape surface texture, which is the relevant information for epitaxial film growth of the following buffer and superconducting layers. The EBSD texture maps also contain information about the relative grain-to-grain orientation of neighboring grains, which even allows the quantitative calculation of the superconductor critical current density based on the hypothesis that the superconducting layer copies the metal texture [10]. Pure Ni however is very soft and magnetic and therefore not the ideal substrate material. Alloying Ni by other elements leads to reduced magnetism and solution hardening of the tape, but is in general not favorable for the formation of cube texture. Detailed investigation of possible alloying systems [11, 12] lead to Ni-W as a preferable system, which is now used as a standard coated conductor substrate [13]. Recent research and development even made it possible to realize cube textured non-magnetic Ni-W applicable for high J_c coated conductors [14]. Upscaling of high quality cube-textured substrates for coated conductors is well advanced, kilometers of tape are commercially available (evico GmbH) and Outokumpu VDM GmbH is preparing for supplying tons of cube-textured Ni-W substrates for industrial coated conductor production lines. To further increase the yield strength of cube textured substrates composites were developed where a high strength core is combined with a Ni-W surface layer. A very interesting development is the direct engineering of the geometrical grain boundary network in cube-textured substrates by incorporation of Ag-impurities into Ni. The recrystallization dynamics is changed in a way that elongated grains with a high aspect ratio form. This geometrical arrangement is favorable for high critical currents, if the current flow is parallel to the elongated grain boundaries [15, 16] and multiple times higher critical currents will be achievable.

For perfect epitaxial growth of the following layers not just a substrate roughness of only a few nm is required which has to be realized by the application of highly polished rolls in a clean room rolling environment, but also the substrate surface has to be chemically clean without misoriented Nickel oxide layer. During recrystallization or during an additional annealing step sulphur diffuses to the surface to form

Fig. 27.8 Electron backscattering Diffraction Pattern of a cube textured Ni-alloy sample. The *colour coding* of the sample grains and grain boundaries indicates the deviation from the ideal cube texture and the relative misorientation of neighboring grains (courtesy of Evico)



a cubic (1×1) surface superstructure, which passivating the Nickel surface, thus being essential for a perfect epitaxial buffer layer growth.

27.3.2 Buffer Layers

Ceramic buffer layers in HTS tapes mainly act as a diffusion barrier preventing the diffusion of Nickel into the superconducting layer and avoiding the formation of nickel oxide on the metal substrate surface by diffusion of oxygen resulting in a delamination of the layer architecture. The quality of the diffusion barrier may be determined by different analytical methods such as TOF-SIMS (time-of-flight secondary ion mass spectrometry) for Ni-Diffusion and XRD or ^{18}O -Analysis for O-Diffusion. Dedicated measurements will be discussed for the different buffer layer systems. Based on their major function the buffer layer layers are expected to be dense and chemically inert to the metal substrate and the subsequently deposited HTS layer.

As described above the major issue for high superconducting performance is the orientated growth of the superconducting layer. Therefore the buffer layer has to act as a template for the superconductor. This leads to the second function of the buffer layer, the texture transfer from the metallic substrate surface to the surface of the buffer layer in order to force the crystal growth in the HTS layer in the predetermined direction. Even more the buffer layer acts as a bridge, equalizing the lattice mismatch between the metallic substrate and the HTS material. The analytical methods necessary to determine crystallinity, texture and density of the buffer layers are XRD, EBSD, TEM and RHEED, whereas REM and TEM are useful for the investigation of density.

Beyond diffusion barrier and texture transfer other parameters are essential for an undistorted and homogeneous growth of the subsequent layers. One of these attributes is the roughness or planarity of the surfaces. As nucleation in the

Table 27.1 Possible CSD buffer layer materials

Material	Structure type	a_0 [Å]	Lm^a [Å]	Misfit Ni [%]	Misfit YBCO [%]
$La_2Zr_2O_7$ (LZO)	Pyrochlore	10.8	3.81	7.12	-1.05
CeO_2	Fluorite	5.41	3.83	8.09	-0.52
$SrTiO_3$ (STO)	Perovskite	3.91	3.91	9.97	1.53
Manganate	Perovskite	5.54	3.91	9.97	1.53

^a Lm : Module length or unit length, i.e. length for comparison—e.g. half of the face diagonal in LZO

nm-range is wanted to proceed, a medium surface roughness below 10 nm is required for high performance HTS layers.

In general, buffer layers only act as supporting or enabling layers for the HTS films to carry the desired performance of the HTS tape. Therefore research and development focus on buffer layer systems fulfilling the requirements with an architecture as simple as possible. From the economic point of view this means “as thick as necessary and as thin as possible”.

Many oxide materials fulfill the general requirements described above and were applied successfully as buffer layers for HTS tapes. Nevertheless the suitability of the materials strongly depends on the deposition technique. Whereas physical deposition methods tolerate relatively large lattice mismatches and basic changes in the crystal structure for epitaxial growth, chemical solution deposition is much more sensitive and challenging in the selection of suitable materials. For PVD processes typical buffer layers are MgO, Y_2O_3 , YSZ, Al_2O_3 or GZO [17–19].

Much less materials and structure types were successfully deposited by CSD techniques as shown in Table 27.1 [20].

For the all-solution approach for buffer layers architectures, so far only two-layer-systems have been demonstrated successfully. The first layer system is based on zirconates the second layer consists of titanates. Both buffer layer architectures have different advantages and challenges which will be described in the following.

One obvious difference is the crystal orientation of the buffer layer system relative to the metal substrate already indicated by the lattice parameters listed in Table 27.1. Whereas zirconates grow with an in-plane rotation of 45° , titanates like strontium titanate grow unrotated as illustrated in Fig. 27.9.

27.3.2.1 Lanthanum Zirconate (LZO) and Cerium Oxide (CeO)

The best characterized CSD buffer layer system so far is the combination of lanthanum zirconate and cerium oxide. This system offers various advantages like good lattice mismatch close to both, the parameters of the metallic substrate as well as YBCO (see Table 27.1). In addition both materials are stable and are easily accessible in a wide temperature and atmosphere range. Furthermore in particular cerium oxide is dopable with various elements, enhancing its properties and making it easier to handle. The major drawback of this system is the formation

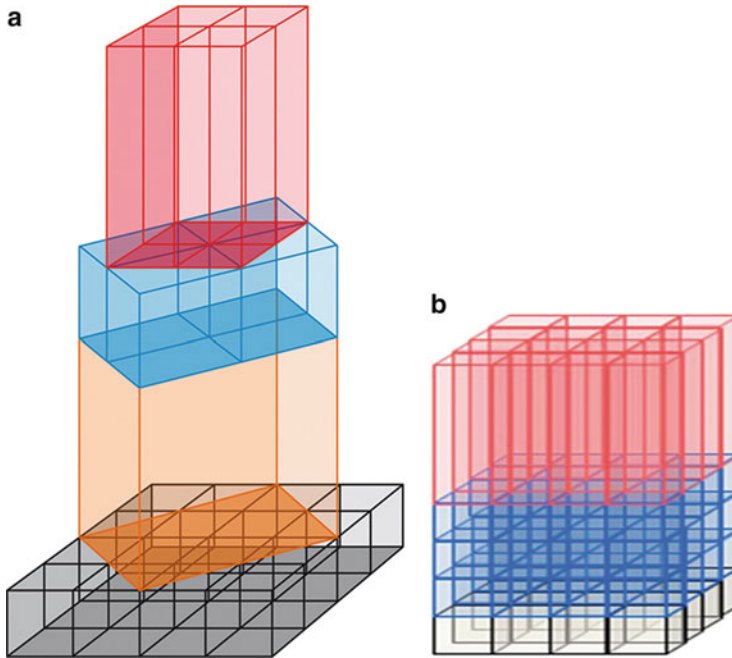


Fig. 27.9 Relative orientation of the layer systems (a) NiW-LZO-CeO₂-YBCO and (b) NiW-STO-YBCO

of barium cerate as a secondary phase at the interface of cerium oxide/YBCO resulting in barium deficit in the HTS layer and subsequently crystalline misorientation and formation of secondary phases. As the cerium oxide layer is indispensable for the epitaxial growth of CSD YBCO layer this reaction has to be suppressed by accurate control of the optimized process parameters.

First approaches for the preparation of lanthanum zirconate coating solutions were carried out by dissolving lanthanum isopropoxide and zirconium n-propoxide in a mixture of n-propanol and 2-methoxyethanol [21]. After partial hydrolysis the solutions then were spin coated on lab-scale samples. Similar approaches were made with tetrabutoxides as organometallic compounds and acetylacetonone as one solvent component [22]. Further development lead to the substitution of toxic 2-methoxyethanol by alternative solvents. A major breakthrough here was the application of propionic acid as a solvent for LZO-coating solutions [23], which allows higher metal concentration, stable solutions and an inherent interface cleaning by slightly etching the substrate surface. Up to now this solvent system is the basis for further developments in this field.

An alternative approach towards LZO coating solutions is the avoiding of all organic solvents using water based solution systems. Remarkable results were obtained with coating solutions based on lanthanum- and zirconium acetates dissolved in a water/acetic acid/triethonamine solvent system [24].

A parallel development regarding metallo-organic salts, solvents and chelating agents was made for cerium oxide coating solutions. From early stage solutions systems based on metal pentanedionates in acetylacetone and methanol [25] more advanced coatings were obtained by using organic acids like glacial acid or propionic acid as solvents [26]. Doping elements like zirconium or other rare-earth elements may be added to the coating solutions. Several approaches are made in qualifying water based solvents systems for cerium oxide coating solutions. Most authors report on nitrates as the initial metal salt [27] dissolved in water with chelating agents such as citric acid [28].

For small sample investigations the coating solutions are applied by conventional spin coating or dip coating on the substrates. Obviously spin coating is not suitable for continuous coating technology and also the simple dip coating is limited for this application due to evaporation of solvents and contamination by the atmosphere due to open coating baths and long term operation. Therefore coating technologies with closed stock reservoirs are preferred like slot die casting or ink-jet printing. Whereas slot die casting is the more robust technology, ink-jet printing offers the opportunity to much more accurate process control [29]. The deposited solution is dried on the substrate at temperatures up to 150 °C within a few minutes. Pyrolysis and crystallization normally is performed in one step between 900 °C and 1,100 °C. If metallic substrates are used as a basis the annealing has to take place in a reducing atmosphere in order to inhibit oxide formation at the metal surface. The addition of humidity in the annealing atmosphere is reported to positively influence the crystal growth and surface roughness of the buffer layers [30].

On textured nickel alloy substrates perfect epitaxial growth of the LZO layers is observed. The texture of the substrate is being adopted by nearly 100 % of the ceramic layer. Among other evidence, this is determined by x-ray pole figure measurements, detecting FWHM values of 5.4° for Ni(111) and 5.5° for LZO (222) (see Fig. 27.10) [31].

Even more impressive than the integral XRD measurements are local analysis by TEM cross section imaging. HRTEM investigations as illustrated in Fig. 27.11 reveal the perfect epitaxial growth of lanthanum zirconate on Ni/W-substrate on an atomic scale.

Nevertheless it has to be pointed out that perfect growth only takes place on single grain surfaces of the substrate. Along grain boundaries, distortions of the epitaxial growth are observable. They have to be minimized in particular by appropriate pretreatment of the substrate. Small-angle grain boundaries and avoiding of grain boundary grooving will be described in section “metallic substrate”.

For the subsequent deposited layers it is essential that the crystalline orientation initiated by the substrate is transferred to the new surface in order to function as an orientation template for the following film. As described above, the perfect orientation of the first atomic layers at the surface are crucial for this transfer. An appropriate analysis method for these atomic layers is RHEED (reflective high energy electron diffraction). Figure 27.12 shows RHEED patterns of a complete buffer layer stack ready to be coated with the HTS layer. The buffer layers were deposited and crystallized one after another. The figure demonstrates the perfect

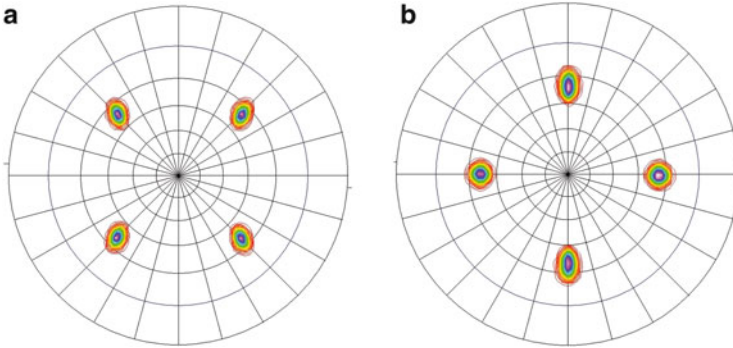


Fig. 27.10 X-ray pole figure ($\text{CuK}\alpha$) of (a) Ni (111) and (b) LZO (111) reflections of an LZO buffer layer annealed at $T = 1,000^\circ\text{C}$ (analysis by IFW Dresden)

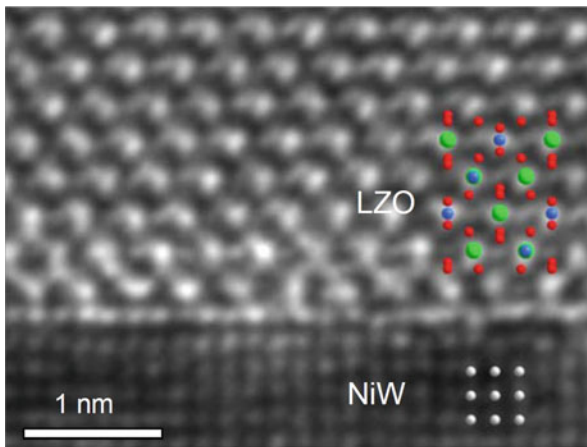


Fig. 27.11 Epitaxial growth of LZO on NiW; *green*: La, *blue*: Zr, *red*: O, *grey*: Ni (HRTEM by University of Bonn, courtesy of Deutsche Nanoschicht)

texture transfer up to the surface of each layer. Even the reflections of the pyrochlore-superstructure of LZO are distinctly observable.

As described above the texture of the buffer layer template is an essential but not a sufficient condition for the growth of high quality HTS layers. The surface roughness of the buffer layer also strongly influences the nucleation of HTS crystals and therefore requires special attention. An analytical approach to conceive this phenomenon is the definition of a surface planarity in percent derived from AFM measurements [32]. Experiments revealed a strong correlation between buffer layer planarity and HTS layer performance defined by the critical current density.

The planarity of buffer layers in particular of cerium oxide layers may be enhanced by doping the layer with other rare-earth elements like gadolinium. According to the favorable trivalent character of rare-earth-ions, doping enables

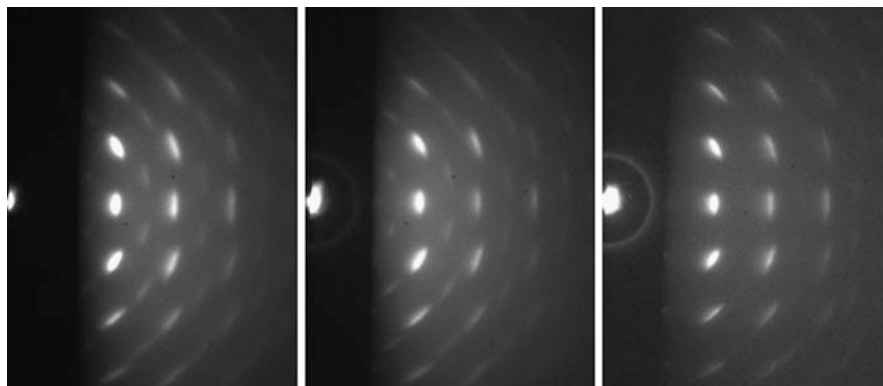


Fig. 27.12 Surface texture of buffer layer stack (RHEED by University of Tübingen, Germany, courtesy of Deutsche Nanoschicht)

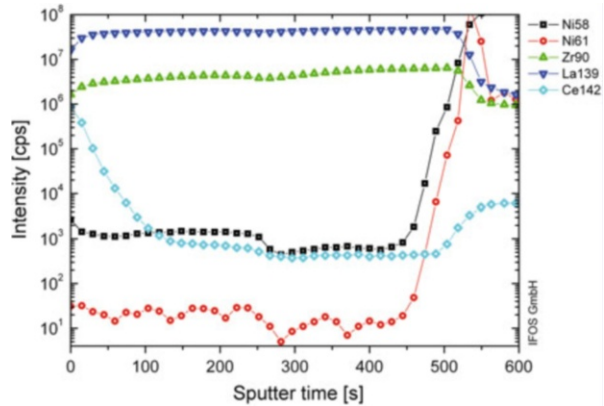
the recovery of lattice imperfections by the implant of voids in the tetravalent cerium oxide. Other groups report on positive effects of other metal dopants like zirconium, copper, silver and manganese. Further, the doping of ceramics with sintering additives is a well known strategy for the enhancement of material properties like avoiding of cracks and internal stress or increasing the density [33]. The field of doping of buffer layers is still a fruitful and evolving research area worldwide.

The effective blocking of nickel-diffusion by the buffer layers may be analyzed by TOF-SIMS. Measurements of a buffer layer stack of LZO and CeO_2 with a total thickness of 250 nm reveal a step of about five orders of magnitude for the nickel-concentration at the interface between buffer layer and metal substrate; whereas there is hardly any Ni detectable in the area of the buffer ceramics (see Fig. 27.13).

27.3.2.2 Titanates

Titanate based layer systems represent an alternative group of buffers applicable for all-solution CSD architectures. The major advantages of these systems are that only one base material is involved and their passivity both, against metal substrates as well as HTS layer. The major drawback of these systems is their relatively large lattice mismatch between buffer material and the substrate of nearly 10 %. This strong mismatch inhibits a crack-free growth of a complete titanate buffer layer on the substrate due to too strong internal stress. The well known work-around for this limitation is the growth of a seed layer not covering the whole surface and the subsequent deposition of thin continuous layers on top of this seed layer. As the seed layer only consists of isolated crystal islands, it is extremely sensitive to processing parameters. Further approaches for “bridging” the lattice mismatch may be the use of doped strontium titanate (STO) or alternatively single ore

Fig. 27.13 TOF-SIMS analysis of buffer layer stack CeO₂ and LZO on nickel-alloy substrate (Analysis by ifos Institute Kaiserslautern, Germany, courtesy of Deutsche Nanoschicht)



mixed alkaline-earth-titanates barium calcium titanate (BCT), or calcium titanate (CTO), respectively.

Coating solutions for titanate layers are well known in the literature [34]. The most commonly used metallo-organic salt for titanium is the isopropoxide [35]. Alkaline-earth metals are usually dissolved as water-free acetates or butyrates, respectively, and combined afterwards with the titanium isopropoxide solution under water-free conditions [36]. Typical solvents are water-free alcohols like methanol or ethanol as well as more complex solvents like 1-methoxy-2-ethanol or preferably as non-toxic 1-methoxy-2-propanol. The stability of the coating solutions mainly depends on the absence of water due to their high sensitivity to hydrolysis for the titanium alcoholates. Other dopants like niobium may easily be added to the stock solutions as water-free metal-organic compound such as butoxides [37].

Due to their sensitivity towards ambient and humid atmosphere the deposition of these coating solutions requires more advanced technologies like slot die casting or ink-jet printing with preferably encapsulated coating solutions. The subsequent drying at temperatures up to 150 °C is followed by a crystallization step at 900–1,050 °C under reducing atmosphere. As the thicknesses of the single titanate layers due to their higher internal stress are far lower than the thicknesses of zirconate based layers, the annealing time may be significantly shortened down to the range of a few minutes.

As mentioned above the seed layer is the key for the epitaxial growth of the complete buffer layer stack. Dependent on the chosen seed layer material, isolated islands are formed.

Figure 27.14 illustrates the various surface structures of the seed layers for STO and CTO, which is also comparable with BCT. The strong texture of the seed is directly visible in the SEM micrograph [38].

After the application of the seed layer it is possible to deposit additional thin layers with reduced internal stress. Nevertheless the lattice mismatch limits the layer thickness to be deposited. Typically several CTO, STO or niobium-doped

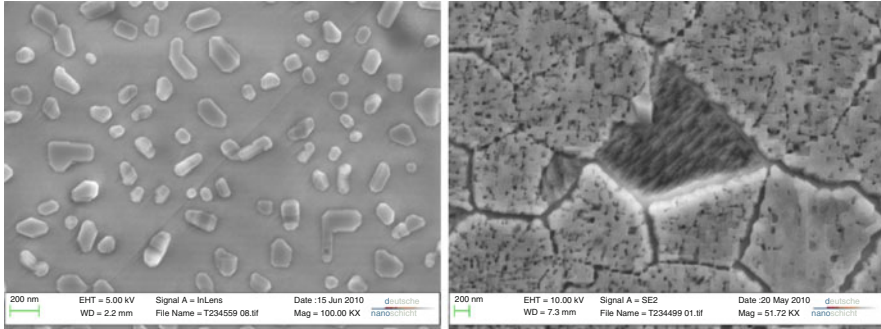


Fig. 27.14 SEM micrograph of titanate seed layers: STO (*left*) and CTO (*right*). The orientation of the ceramics may be deduced by their surface structure (courtesy of Deutsche Nanoschicht)

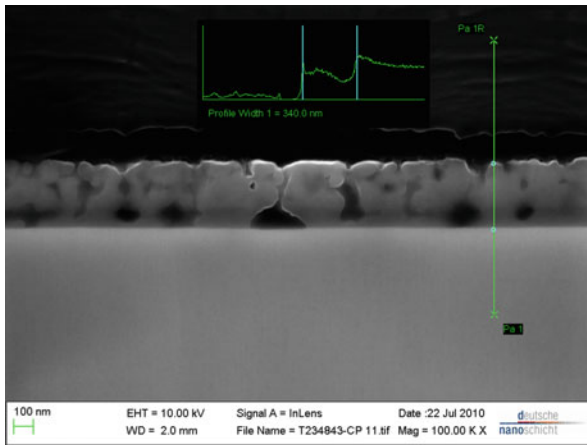


Fig. 27.15 SEM micrograph of a three-layer system indicating the overgrowth of the seed layer islands to a dens ceramic layer is well observable (courtesy of Deutsche Nanoschicht)

STO layers with single thicknesses of 50 nm are deposited on the seed layers (see Fig. 27.15). A total titanate buffer layer stack consists of 4 to 10 layers with a total stack thickness of about 300 nm.

The internal stress and the dislocations lead to a slight broadening of the FWHM in XRD pole figures (see Fig. 27.16). Typically the FWHM is increased by about 1° compared to the metal substrate, but is still sufficient for an epitaxial growth of high quality HTS layers.

As observable in Fig. 27.16 the STO layer orientation is not rotated relative to the substrate orientation in contrast to LZO as shown in Fig. 27.10. Due to their equal orientation, the uniform material and the lower reactivity with the HTS material titanates should be the favorable buffer layer system, but from the processing point of view the multiply repeated production of the extremely thin

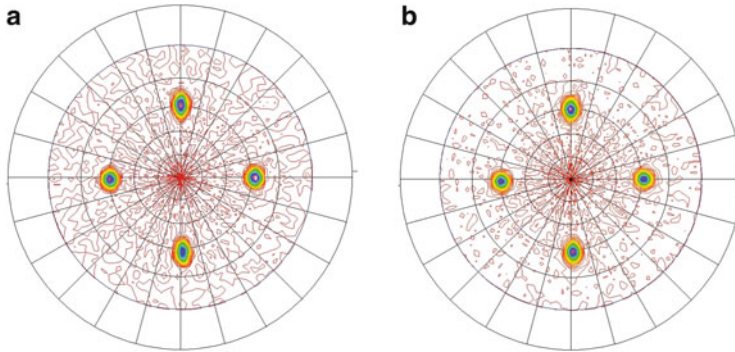


Fig. 27.16 XRD pole figure of (a) Ni (220) and (b) STO (220) (analysis by IFW Dresden)

seed layers and the large internal stress, up to now zirconates are still the standard material. Nevertheless worldwide effort is made to improve the processing and in particular process stability for titanate buffer layer systems.

27.3.3 High Temperature Superconducting (HTS) Layer

This layer consists generally of rare earth barium copper oxide (ReBCO) and yttrium barium copper oxide ($\text{YBa}_2\text{Cu}_3\text{O}_{7-x}$, YBCO) is the most prominent and most produced representative. For the metallo-organic decomposition (MOD) methods liquid precursors are synthesized starting from trifluoroacetates [39], acetyl acetonates [40] or nitrates [41] of Y (or other rare earth elements), Ba and Cu. The three cations are often used in their stoichiometric ratio for YBCO syntheses. Typical YBCO grain sizes in the final coated conductor are 30–100 μm which is much bigger than the individual grain size of a buffer crystal sized about a few 10 nm. The chemical preparation method makes it easy to substitute partially or completely one rare earth metal ion by another, to add doping elements one or to shift the stoichiometric composition of the whole precursor. Superconducting currents are predominately transported within the copper planes of the ReBCO (see Fig. 27.3) which requires a strong biaxial texture with low grain angles and preferably no precipitations of secondary phases within the grain boundaries [42]. As all the precursors consist of organic molecules, ligands or additives it is a further challenge to remove all the carbon. The formation of strongly temperature-stable barium oxide must be either suppressed or a reaction channel to disband this oxide below 800 °C reaction temperature must be found [43], as this remnant can lower the critical current densities by one or two orders of a magnitude.

The well-studied trifluoroacetate (TFA) route [44–46] avoids any barium oxide formation by the intermediate formation of barium fluoride. The corresponding heating schedule consists of three different stages. In the pyrolysis all organic

components of the film are combusted and oxides or oxifluorides of the metal ions remain. This causes enormous film shrinkage and release of aggressive fluorine containing gases that have to be transported away from the film surface.

In the second stage of the heat treatment called annealing or firing barium fluoride decomposes at temperatures around 550–650 °C in ambient pressure at 100 ppm oxygen partial pressure and the formation of the desired YBCO phase starts. During this stage the film shrinks again roughly by the factor of two. The final oxygen load shifts the initially tetragonal grown high temperature phase of $\text{YBa}_2\text{Cu}_3\text{O}_{7-x}$ with $1 > x > \sim 0.5$ to the orthorhombic modification of $\text{YBa}_2\text{Cu}_3\text{O}_{7-\delta}$ with $\delta \ll 1$. This is the modification that can carry current densities exceeding several MA/cm^2 underneath the critical temperature of 90 K.

Figure 27.16 shows the temperature schedule in a lab furnace process dealing with sample dimensions up to a few centimeters. In real industrial production facilities, pyrolyses, annealing, and oxygenation are split into three different independent processes. All-CSD produced coated conductors on 1 cm wide tapes reached critical currents exceeding 100A (resistively measured) for 100 m long pieces measured at 77 K in self field [47]. On single crystals substrates current densities exceeding several MA/cm^2 have been reported [48] (Fig. 27.17).

The best so far reported all-solution coated conductors continuously processed on lengths exceeding 10 m is shown in Fig. 27.18. The coated conductor exhibits up to 2 MA/cm^2 in the HTS layer.

Fluorine-free or fluorine-reduced routes by substituting some of trifluoroacetate precursor salts by other kinds of salts can shorten the pyrolysis time enormously and avoid or at least reduce the release of aggressive fluorine containing gases which makes this approaches more favorable for industrial long length coated conductor production. Polymer assisted deposition approaches (cp. Chapter 6), using polyethylene glycol [49, 50] or polymetacrylic acid [51] resulted in high transport current densities with no or minimal fluorine input.

While the classical TFA-method needs alcoholic or ketone solvents more recent and environment friendly developments start with aqueous solutions of the metal salts stabilized with complexing agents leading e.g. to the formation of metal chelate complexes in the water-based precursor [52]. All types of precursors have in common to be compatible with the addition of suitable polymers, organic macromolecules or ethanolamines which allows the adjustment of the precursor acidity and the viscosity to the coating equipment and the desired final film thickness. Typical thicknesses are around 0.35–1 μm .

High currents in technical superconductors cause undesired energy dissipation by their Lorentz force to the vortices, especially for external magnetic fields parallel to the current flow direction. Figure 27.19 shows the dependence of the normalized critical current on the two-axis orientation for a YBCO sample. The currents are normalized for the magnetic field direction tilted perpendicular (90°) to the superconductor surface and a rotation of the tilted coated of 0° around the magnetic field direction.

This dissipation can be minimized by pinning the vortices inside the lattice. Generally, lattice defects or precipitations in the YBCO grains or at the grain boundaries can act as pinning centers. MOD derived samples already comprise

Fig. 27.17 Typical heating schedule in the TFA-YBCO formation process in a lab scale furnace

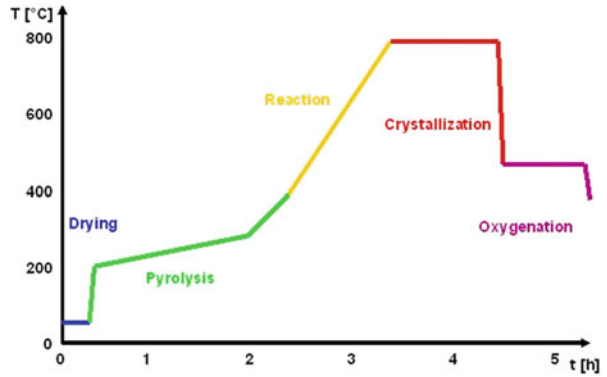


Fig. 27.18 Resistive measurement of the I-U characteristics in a 10 mm wide all-solution coated conductor; self-field at 77 K (courtesy of Deutsche Nanoschicht)

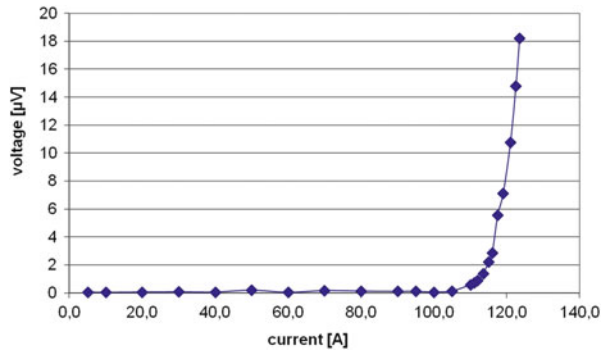
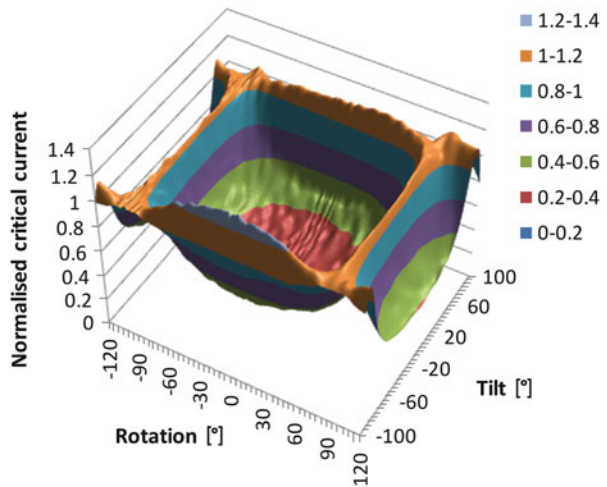


Fig. 27.19 The dependence of the normalized critical current on the two-axis orientation of an inkjet-printed MOD derived conductor sample relative to the external field (0.592 T, liquid nitrogen)



meandering grain boundaries exhibiting a stronger three dimensional pinning [53] compared to pulsed laser deposited superconductor films. The loss of performance in strong magnetic field (0.5–2 T) can even be further suppressed by integrating nanoparticles into the film. This can be done by adding stabilized nanoparticle suspensions (cerium oxide [54]) to the initial YBCO precursor solution resulting in non-superconducting pinning centers in the final film.

For example Zr–Ba-Oxide nanoparticles [55] or Zr acetylacetonate derived nanoparticle suspensions combined with Ba-ion excess concentration in the ReBCO precursor form BaZrO_3 precipitations during the heat treatment of the coated film. Based on this technology strong improvements of critical perpendicular magnetic field in HTS layers up to a factor of 5 compared to un-pinned layers were achieved [56]. Addition of chemical Dy-precursors added to TFA-based YBCO precursors are reported [57] to be converted into $\text{Y}(\text{Dy}_x)\text{Ba}_2\text{Cu}_3\text{O}_y$ with nanoparticle precipitations in the size range 10–50 nm improving the possible current densities for magnetic fields parallel to the superconducting current direction nearly by the factor of two.

27.4 Applications

Two outstanding properties of high temperature superconductors when cooled under their critical temperature break paradigms in electro technology as already described in the introduction:

- No ohmic resistance
- Highest energy density

For a safe, reliable and sustainable energy supply, the efficient generation, transmission, distribution and use of electrical energy are crucial. High-Temperature-Superconductors promise a highly effective and environmental friendly extension of tomorrow's use of energy. Conventional equipment, such as cables, transformers and generators can be designed much more efficiently, compactly and light-weight because High-Temperature-Superconductors offer an unbeatable power density compared to aluminum or copper. Whereas conventional copper-based equipment operates at a current density of 1 to 5 A/mm² high-temperature-superconductors allow current densities of 10,000 to 50,000 A/mm² at operating conditions. Even with support structure and cooling a ten-fold higher power density in a HTS system is possible compared to conventional conductors such as copper and aluminium. Besides highest energy and materials efficiency HTS also enables completely new types of equipment, such as superconducting fault current limiters for effectively and safely limiting short-circuit currents and superconducting magnetic energy storage (SMES) for fast and highly efficient storing of electrical energy [58, 59].

Compared to conventional equipment, the application of HTS components can considerably reduce losses. Some examples have been listed in the following table

Table 27.2 Energy savings by superconductivity

Examples	Loss reduction
Generators	– Some MVA 30–40 % – Over 100 MVA 40–50 %
Transformers	– Stationary 50 % – Mobile 80–90 %
Magnets	– High-field magnets >95 % – HTS-fusion magnets 20 %
HTS-current leads	20–30 %
Induction heating	Up to 50 %
Magnetic separator	>80 %

(Table 27.2). Although conventional equipment is already highly efficient, this can be even further improved by HTS. Thus, especially at high power and over long lifetime there are huge energy saving potentials.

Actually most prototypes and early stage commercial HTS systems are realized with 1G HTS conductors. This first generation HTS tape technology has rapidly enabled the production of larger volumes of 1G HTS-tape conductors. Thus, a number of cable and motor demonstration projects were successfully realised in recent years. However, the use of 1G HTS-tape conductors for commercial products has already been greatly restricted (already) by the high conductor price. 2G conductors, however, offer the perspective of a more economical mass production. Due to the more complex manufacturing technology, however, the production volume of 2G conductors is currently still limited. As the geometric dimensions of 1G and 2G conductors are comparable, 1G conductors can be relatively easily replaced by 2G-conductors in the foreseeable future.

27.4.1 Power Transmission

It is of great importance to generate, transmit and distribute energy efficiently and safely in order to supply our society and economy reliably with energy. In this respect, some of the great challenges are safe integration of increasing regenerative energies, sustainable supply of the increasing energy demand, further reduction of the grid losses and economic modernization of power systems. While doing so, superconducting power equipment, such as generators, cables, transformers, current limiters and magnetic energy storage will play a significant role because they offer a large number of technical and economic advantages compared to conventional solutions [60].

Superconductivity offers a significantly higher current density with lower voltage drops as well as an active short-circuit current limitation. Based on these fundamental characteristics, some clearly defined advantages for network planning and building up of power systems arises as summarized in Table 27.3 [61].

Efficient and safe transmission and distribution of electric energy is the most important task of electrical infrastructure. In the face of the ever growing current

Table 27.3 Consequences of the use of superconductivity for dimensioning and design of power systems

Main HTS characteristic	Consequence for power system dimensioning	Consequence for power systems
Low impedance and low voltage drops	<ul style="list-style-type: none"> – Longer line lengths at HTS voltage level – Longer line lengths at subordinate voltage levels 	<ul style="list-style-type: none"> – Lower total line length – Less switchgear – Fewer substations
High current carrying capacity	<ul style="list-style-type: none"> – Higher power rating per feeder – Reduced number of voltage levels 	<ul style="list-style-type: none"> – Lower total line length – Less switchgear – Omission of one voltage level at generation and transmission level
Short-circuit limitation	<ul style="list-style-type: none"> – Dimensioning to lower shortcircuit currents 	<ul style="list-style-type: none"> – Short-circuit free power systems

consumption and the increasing power supply of regenerative energies, the demands on energy distribution are changing. Both developments place previously unknown demands on power cables. In this context, superconducting cables represent a very interesting alternative to the conventional technology. Superconducting AC cables have already been tested for quite a long time in pilot projects. As for example a 600-m-long 138 kV cable system with a rated power of 574 MVA, which was put into operation in the grid of the Long Island Power Authority (LIPA), USA, in 2008 [62]. Up to now, the cable in the LIPA-grid (Fig. 27.20) has been the longest superconductor cable and the cable with the highest rating operated in a transmission grid. Worldwide there are about 20 HTS cable projects in different voltage levels and lengths in Japan, China, Korea, United States, Netherlands, Denmark and Germany. In 2007 a first project was finalized in Albany, USA (34.5 kV, 800 A, 30 m, 3-ph.) already with a 2G HTS wire section [63].

Furthermore also for power cables the reduction in size (here cross section) is a unique selling proposition in particular in dense urban areas. Figure 27.21 illustrates the dramatic reduction in cross section compared to conventional solutions. The so called retro-fitting, the replacement of a conventional cable in an existing duct in urban areas enabling the transport of up to five times more energy without increasing the cross section, is considered to be one of the most promising value proposition of HTS energy technology.

Apart from load flow and stability of the power system, safe operation of the grids plays a significant role in planning and operating electrical power systems. Ideal fault current limiters are characterized by low impedance in normal operation, fast and effective current limitation in case of the faults and automatic recovery. Conventional measures for short-circuit current limitation either cause a constant impedance increase also in normal operation (for example adaptation of the transformer impedance, short circuit-current limitation choke), or they have to be replaced after each incidence (for example fuses, Is-limiters). Superconducting fault current limiters, however, meet all the demands on an ideal current limiter. The application of this new type of operational equipment in electrical power systems promises numerous technical and economic advantages as they allow the



Fig. 27.20 LIPA HTS cable project (Courtesy of AMSC)

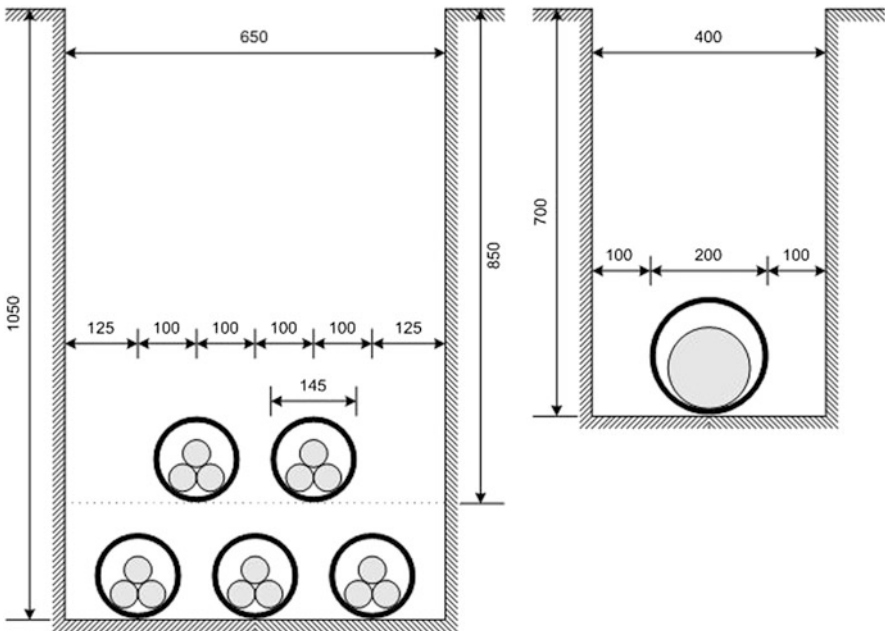
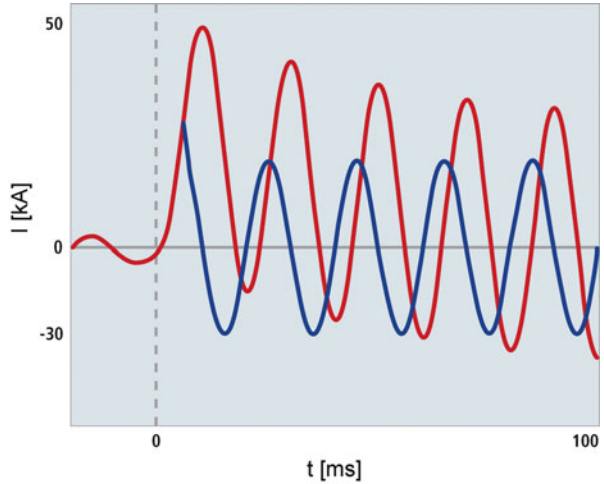


Fig. 27.21 Medium voltage cable cross section and duct size for conventional (left) and HTS (right) cable systems (courtesy of Nexans)

save reduction of the occurring fault already in the first half wave thus efficiently saving the downstream poser equipment (Fig. 27.22).

Presently, superconducting fault current limiters (FCL) are becoming commercially available at least for the medium voltage level from 5 to 50 kV. High voltage FCL are under development and are expected to be available within the next

Fig. 27.22 Principle of superconducting fault current limiter, *red*: unlimited fault, *blue*: fault limitation in first half wave



5 years. The technical feasibility and reliability of this new type of equipment was shown on the medium-voltage level in several demonstrator and field tests [64]. In 2008 and 2009, further prototypes were put in operation on the medium-voltage level. For the first time in HTS systems for electrical grids several projects have been realized without any public funding since 2009 [65]. This underlines the great interest of the utilities in this technology. Up to now more than 20 FCL projects in the medium voltage level worldwide are already finalized or will be finished within the next 2 years. It becomes apparent that the resistive superconducting fault current limiter, which is outstanding due to its simple function and compact design, is developed most frequently. In this type of FCL the HTS material is quenched by exceeding the critical current in the fault state. The complete energy is dissipated in the HTS material thus requiring homogeneous and stable HTS material, high re-cooling power and in the case of high voltage FCL advanced bushings delivering high voltage power into the cryostat.

27.4.2 Industrial Heat Treatment

With a new type of device with superconductive magnets for industrial metal heating, a new dimension of performance in the manufacturing of profiles and pipes from nonferrous metals, such as aluminium, copper and brass, is possible [66]. The system improves the preconditions for extrusion of profiles and pipes. In this process, metal is forced with high pressure through a forming tool so that a metal bar of a clearly defined cross-section is formed. Before reshaping, the raw material, the so-called billet, has to be heated up. The superconductive magnet heater works according to the principle of a normal eddy current brake. In the device there is a superconductive magnetic coil operated with direct current, with

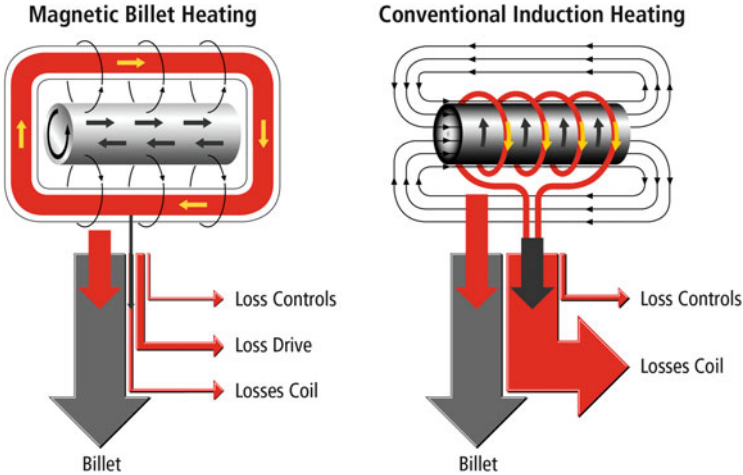


Fig. 27.23 Energy flows for superconductive magnet heaters and conventional induction heaters

the pressing billet being rotated in the generated field by two electro-motors, whereby the braking effect of the magnetic field has to be overcome. This results in the rotating material becoming heated. A magnet heater consumes approx. 40 % less energy than an induction furnace operated with alternating current (Fig. 27.23) and around 60 % less energy than a gas furnace of comparable power. A first commercial HTS system has been (is) operating since 2007 in an industrial production line in Minden, Germany, without any failure.

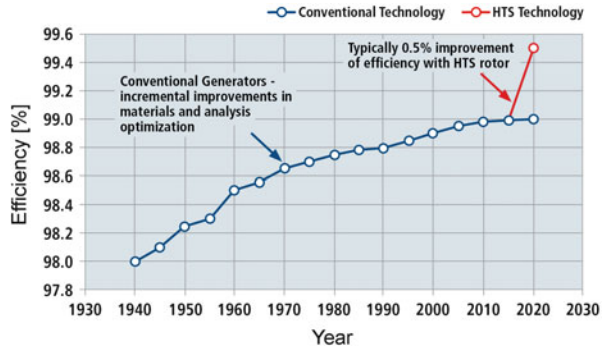
The figure also shows the small losses generated by the required cooling power. For a heating output power of more than 1 MW only a few KW, less than 5 %, cooling power are required.

27.4.3 Rotating Machines

In rotating machines such as motors or generators high-temperature-superconductivity offers the chance of overcoming technical restrictions arising from conventional technology and thus opening up new potential. Consideration is given to machines with an output of more than approx. 2 MW in a large speed range of low-speed drivers for the generation of high torques up to high-speed drivers with outstanding performances.

Less weight, same output—The high current density in the superconducting wires and tapes allow a compacter winding and thus a smaller and lighter design of the machines with, on average, 35 % to 50 % the weight of conventional synchronous motors of equal torque. Figure 27.24 illustrates that the introduction of HTS technology allows an increase of efficiency which is comparable to the increase in motor efficiency within the past 50 years.

Fig. 27.24 Increase in efficiency by introduction of HTS technology for motors (Courtesy of Siemens)



Numerous development programs have been started world-wide in order to test the technical feasibility. Of particular interest in order to realize most advantages offered by HTS technology are island applications such as (like) ship propulsion. New cruise liners today are planned as fully electrical ships in major parts opening up possibilities for ship-builders to significantly increase efficiency and use of the ship by integrating HTS technology. Slow-speed motors for this application were successfully built and tested in Europe (4 MW, 120 rpm, 320 kNm) [67] and in the United States. The ship propulsion motor completed in 2008 had an output power of 36.5 MW at 120 rpm. The weight of less than 75 t for the HTS system has to be compared to a conventional copper motor (21 MH, 150 rpm) [68] of about 183 t showing the enormous potential for weight and size reduction.

Besides motors HTS generators for special applications are considered to even more attractive in terms of reduced size and costs of the whole power generating system. About 95 % of electrical interconnected power systems are supplied by large synchronous generators. In synchronous generators, the rotor or armature, which generates a permanent magnetic field, rotates in the stator. This stator consists of several windings which have been inserted into a magnetic iron yoke. The width of the air gap between rotor and stator is significant to the magnetic design of the generator. The electrical power is taken off the copper windings of the stator. The constant field magnet of the rotor can be advantageously realised with a superconducting field winding. With this design weight and size reductions by one to two thirds compared to a conventional machine of the same capacity are possible. Consequently, either a weight and size reduction or a higher nominal capacity under the given framework conditions (higher power density) can be achieved using a superconducting design.

One example for HTS generators is the equipment of a run-of-river power station in Bavaria, Germany, with a superconducting hydro power generator (Fig. 27.25) [69]. In the course of the modernization of the power station a conventional solution would not have been economical with a turbine renewal and the associated increase of the generator output power under the prevailing constructional restrictions (protection of historic monuments of the building). The higher power density of the superconducting generator makes 1.7 MVA in the size of 1.25 MVA possible. A

Fig. 27.25 HTS rotor for hydro power generator
(Courtesy of Converteam)



total increase of 36 % of the generator output power could be reached by the implemented modernization measures.

Other fields of application for power generation with HTS system are under evaluation worldwide. Wind power generators in particular off-shore installations were identified as one of the most promising applications in the last years resulting in several prototype and demonstrator projects worldwide [70]. Besides the reduction in weight of the nacelle allowing the off-shore mounting of generators for turbines exceeding 5 MW, HTS technology delivers an essential contribution for overcoming rare-earth element shortage in the near future.

This shortage overcome is due to the fact that today direct drive permanent magnet generators appeared to be economically and technically the best solution for power generation in offshore wind parks—demonstrated by many manufacturers introducing this technology. Today the production of permanent magnets consumes the largest proportion of rare earth elements with 40 % of the rare earth-based magnets used for generators and other electrical machines. In 2010 the production of permanent magnets consumed 26,000 tons of rare earth elements (neodymium/praseodymium, dysprosium, terbium) while in 2015 the estimated demand is 48,000 tons; creating a deficit of 15–30 % compared to the expected annual worldwide production [71–72].

Actually China has substantially cut the export of these commodities in 2010, throwing into uncertainty the supply chain logistics of the wind industry—especially concerning offshore wind parks. China controls today 97 % of the rare

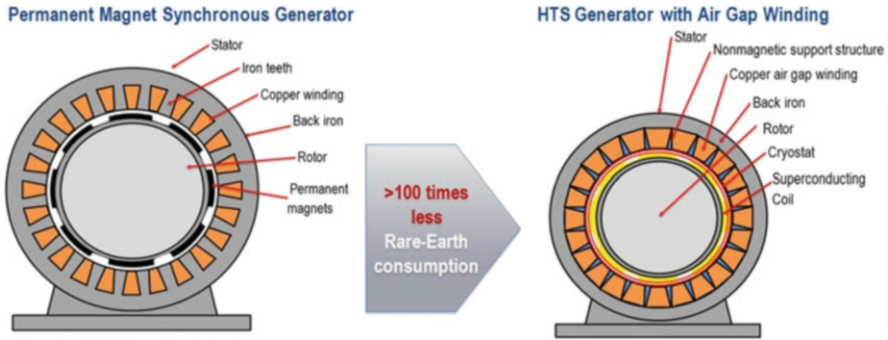


Fig. 27.26 Comparison of size and rare-earth consumption of permanent magnet and HTS generator (Courtesy of Deutsche Nanoschicht)

earth element production needed for the assembly of direct drive permanent magnet generators. Superconductor wind turbine generators are the technical alternative to reduce the requirement of rare earth elements for wind power to a mere fraction of today's level.

Although rare earth elements are required for the production of superconductors, they require only 2 kg of rare earth elements per MW installed generator capacity compared to 250 kg for permanent magnet generators with the same capacity. Moreover the elements needed for superconductors are not as rare as those needed for permanent magnets (Fig. 27.26).

References

1. van Delft D (2007) Freezing physics: Heike Kamerlingh Onnes and the quest for cold (History of science and scholarship in the Netherlands). Edita KNAW, Amsterdam
2. Bednorz J, Müller KA (1990) Earlier and recent aspects of superconductivity. Springer series in solid-state sciences, vol 64. Springer, Berlin, p 189
3. Politis C, Geerk J, Dietrich M, Obst B, Luo HL (1987) Superconductivity above 100 K in Multi-Phase Y-Ba-Cu-O. *Z Phys B: Condens Matter* 66:279–282
4. Buckel W (2004) Superconductivity: fundamentals and applications (Physics). Wiley-VCH, Berlin
5. Bäcker M (2011) 100 years of superconductivity, energy and superconductors – applications of high-temperature-superconductors, Superconductivity. *Z Kristallogr* 226:343–351
6. Wassermann G (1944) *Texturen metallischer Werkstoffe*, vol 1. Edwards Bros, Ann Arbor, MI, p 109
7. Müller HG (1939) Über die Erholung und Rekristallisation von kalt bearbeitetem Nickel. *Z Metallkd* 31:161–167
8. Goyal A (2010) Second-generation HTS conductors. Springer, New York, NY, Softcover reprint of hardcover, vol. 69, 1st edn., 2005, p. 1795
9. Paranthaman MP, Bhattacharya R (2010) High temperature superconductors. Wiley-VCH, Berlin

10. Hänisch J, Sarma VS, Zeimet B, Schindler F, Eickemeyer J, Schultz L, Holzapfel B (2004) Simulation of the critical current density and its dependence on geometrical factors in RABiTS based coated conductors. *Supercond Sci Technol* 17:1003–1008
11. Eickemeyer J, Selbmann D, Opitz R, de Boer B, Holzapfel B, Schultz L, Miller U (2001) Nickel-refractory metal substrate tapes with high cube texture stability. *Supercond Sci Technol* 14:152–157
12. de Boer B, Eickemeyer J, Reger N, Fernandez G-RL, Richter J, Holzapfel B, Schultz L, Prusseit W, Berberich P (2001) Cube textured nickel alloy tapes as substrates for $\text{YBa}_2\text{Cu}_3\text{O}_{7-\delta}$ -coated conductors. *Acta Mater* 49:1421–1428
13. Vannozzi A, Rufoloni A, Celentano G, Augieri A, Ciontea L, Fabbri F, Galluzzi V, Gambardella U, Mancini A, Petrisor T (2006) Cube-textured substrates for YBCO-coated conductors: microstructure evolution and stability. *Supercond Sci Technol* 19:1240
14. Eickemeyer J, Hühne R, Güth A, Rodig C, Klauß H, Holzapfel B (2008) Textured Ni–7.5 at.% W substrate tapes for YBCO-coated conductors. *Supercond Sci Technol* 21:105012
15. Eickemeyer J, Selbmann D, Hühne R, Wendrock H, Hänisch J, Güth A, Schultz L, Holzapfel B (2007) Elongated grains in textured substrate tapes and their effect on transport currents in superconductor layers. *Appl Phys Lett* 90:012510
16. Hammerl G, Herrnberger A, Schmehl A, Weber A, Wiedenmann K, Schneider CW, Mannhart J (2002) Possible solution of the grain-boundary problem for applications of high- T_c superconductors. *Appl Phys Lett* 81:3209–3211
17. Prusseit W, Hoffmann C, Nemetschek R, Sigl G, Handke J (2005) Long length coated conductor fabrication by inclined substrate deposition and evaporation. Presented at EUCAS 2005, Vienna, Austria
18. Samantilleke AP, Rebouta LMF, Garim V, Rubio-Peña L, Lancers-Mendez S, Alpuim P, Carvalho S, Kudrin AV, Danilov YA (2011) Cohesive strength of nanocrystalline ZnO:Ga thin films deposited at room temperature. *Nanoscale Res Lett* 6:309
19. Xiong X, Lenseth KP, Reeves JL, Rar A, Qiao Y, Schmidt RM, Chen Y, Li Y, Xie YY, Selvamanickam V (2007) High throughput processing of long-length IBAD MgO and epi-buffer templates at superpower. *IEEE Trans Appl Supercond* 17:3375–3378
20. Evetts JE, Blamire MG, Mathur ND, Isaac SP, Teo BS, Cohen LF, MacManus-Driscall JL, Littlewood PB, Gehring GA, Venkatesan T, Rzechowski M, Stroud R, Millis AJ (1998) Defect-induced spin disorder and magnetoresistance in single-crystal and polycrystal rare-earth manganite thin films. *Philos Trans: Math Phys Eng Sci* 356:1593
21. Chirayil TG, Paranthaman M, Beach DB, Lee DF, Goyal A, Williams RK, Cui X, Kroeger DM, Feenstra R, Verebelyi DT, Christen DK (2000) Epitaxial growth of $\text{La}_2\text{Zr}_2\text{O}_7$ thin films on rolled Ni-substrates by sol–gel process for high T_c superconducting tapes. *Physica C* 336:63–69
22. Callister WD (2010) *Materials Science and Engineering: International Student Version*. John Wiley & Sons 8:182–190
23. Knoth K, Hühne R, Oswald S, Schultz L, Holzapfel B (2005) Highly textured $\text{La}_2\text{Zr}_2\text{O}_7$ buffer layers for YBCO-coated conductors prepared by chemical solution deposition. *Supercond Sci Technol* 18:334–339
24. Cloet V (2009) Thin $\text{La}_2\text{Zr}_2\text{O}_7$ films made from a water-based solution. *J Solid State Chem* 182:37–42
25. Darhmaoui H, Jung J (2003) Current distribution in $\text{Y}_1\text{Ba}_2\text{Cu}_3\text{O}_{7-\delta}$ disk-shaped thin film by scanning hall probe measurements. *IEEE Trans Appl Supercond* 13:2897–2900
26. Sandiumenge F, Cavallaro A, Gázquez J, Puig T, Obradors X, Arbiol J, Freyhardt HC (2005) Mechanisms of nanostructural and morphological evolution of CeO_2 functional films by chemical solution deposition. *Nanotechnology* 16:1809–1813
27. Fujieda S, Fujita A, Fukamichi K, Hirano N, Nagaya S (2006) Large magnetocaloric effects enhanced by partial substitution of Ce for La in $\text{La}(\text{Fe}_{0.88}\text{Si}_{0.12})_{13}$ compound. *J Alloys Compd* 408–412:1165–1168

28. Van de Velde N, Van de Vyver D, Brunkahl O, Hoste S, Bruneel E, Van Driessche I (2010) CeO₂ buffer layers for HTSC by an aqueous sol-gel method – chemistry and microstructure. *Eur J Inorg Chem* 2:233–241
29. Cloet V, Cordero-Cabrera MC, Mouganie T, Glowacki BA, Falter M, Holzapfel B, Engell J, Bäcker M, Van Driessche I (2006) Sol-gel ink-jet printing technique for synthesis of buffer layers of coated conductors. *Adv Sci Technol* 47:153–158
30. Sathyamurthy S, Kim K, Aytug T, Paranthaman M (2006) Effect of relative humidity on the crystallization of sol-gel lanthanum zirconium oxide films. *Chem Mater* 18:5829–5831
31. Molina L, Knoth K, Engel S, Holzapfel B, Eibl O (2006) Chemically deposited La₂Zr₂O₇ buffer layers for YBCO-coated conductors: film growth and microstructure. *Supercond Sci Technol* 19:1200–1208
32. Coll M, Pomar A, Puig T, Obradors X (2008) Atomically flat surface: the key issue for solution-derived epitaxial multilayers. *Appl Phys Express* 1:121701
33. Mogensen M, Sammes NM, Tompsett GA (2000) Physical, chemical and electrochemical properties of pure and doped ceria. *Solid State Ionics* 129:63–94
34. Schwartz RW, Schneller T, Waser R (2004) Chemical solution deposition of electronic oxide films. *CR Chim* 7:433–461
35. Dawley JT, Ong RJ, Clem PG (2002) Chemical solution deposition of (100)-oriented SrTiO₃ buffer layers on Ni substrates. *J Mater Res* 17:1678
36. Pomar A, Coll M, Cavallaro A, Gàzquez J, González JC, Mestres N, Sandiumenge F, Puig T, Obradors X (2006) All chemical high J_c YBCO multilayers with SrTiO₃ as cap layer. *J Mater Res* 21:1106
37. Siegal MP, Clem PG, Dawley JT, Richardson J, Overmyer DL, Holesinger TG (2005) Optimizing SrTiO₃ films on textured Ni substrates using chemical solution deposition. *J Mater Res* 20:910
38. Kunert J, Bäcker M, Brunkahl O, Wesolowski D, Edney C, Clem P, Thomas N, Liersch A (2011) Advanced titania buffer layer architectures prepared by chemical solution deposition. *Supercond Sci Technol* 24:85018–85023
39. Falter M, Häbler W, Schlobach B, Holzapfel B (2002) Chemical solution deposition of YBa₂Cu₃O_{7-x} film by dip coating. *Physica C* 372–376:46–49
40. Risse G, Schlobach B, Häbler W, Stephan D, Fahr T, Fischer K (1999) Textured YBCO-film formation by sol-gel process and post annealing. *J Eur Ceram Soc* 19:125–130
41. Von Lampe I, Wasche M, Lorkowski HJ (1993) High temperature superconducting ceramics from polymer – metal precursors. *Acta Polym* 44:148–151
42. Dimos D, Chaudhari P, Mannhart J, LeGoues FK (1988) Orientation dependence of grain-boundary critical currents in YBa₂Cu₃O_{7-δ} bicrystals. *Phys Rev Lett* 61:219–222
43. Wesolowski DE, Patta YR, Cima MJ (2009) Conversion behavior comparison of TFA-MOD and non-fluorine solution-deposited YBCO films. *Physica C* 469:766–773
44. Falter M, Demmler K, Häbler W, Schlobach B, Holzapfel B, Schulz L (2003) Chemical solution deposition of YBa₂Cu₃O_{7-x} films and oxide buffer layers by dip coating. *IEEE Trans Appl Supercond* 13:2751–2754
45. Obradors X, Puig T, Pomar A, Sandiumenge F, Mestres N, Coll M, Cavallaro A, Roma N, Gàzquez J, Gonzalez JC, Castano O, Gutierrez J, Palau A, Zalamova K, Morlens S, Hassini A, Gibert M, Ricart S, Moreto JM, Pinol S, Isfort D, Bock J (2006) Progress towards all-chemical superconducting YBCO coated-conductors. *Supercond Sci Technol* 19:13–26
46. Gupta A, Cooper EI, Jagannathan R, Giess EA (1988) Preparation of superconducting oxide films from metal trifluoroacetate solution precursors. In: Nelson DL, George TF (eds) *Chemistry of high-temperature superconductors II*, vol 377. American Chemical Society, New York, NY, pp 265–279
47. Van Driessche I, Feys J, Hopkins SC, Lommens P, Glowacki BA, Granados X, Ricart S, Holzapfel B, Bäcker M (2012) Chemical solution deposition using ink-jet printing for YBCO coated conductors. *Supercond Sci Technol*, 25:65017–65020

48. Puig T, Gutiérrez J, Pomar A, Lloudés A, Gázquez J, Ricart S, Sandiumenge F, Obradors X (2008) Strong isotropic flux pinning in solution-derived $\text{YBa}_2\text{Cu}_3\text{O}_{7-x}$ nanocomposite superconductor films. *Nat Mater* 6:367–373
49. Vilardell M, Granados X, Ricard S, Cobas R, Arjona M, Puig T, Obradors X, Hopkins SC, Glowacki BA, Bennewitz J, Falter M, Bäcker M (2011) Ink jet printing for functional ceramic coatings. *J Imaging Sci Technol* 55:040304-1–040304-7
50. Donglu S, Yongli X, Haibo Y, Han Z, Jie L, Lumin W, Aihua L, Liu HK, Dou SX (2004) The development of $\text{YBa}_2\text{Cu}_3\text{O}_x$ thin films using a fluorine-free sol–gel approach for coated conductors. *Supercond Sci Technol* 17:1420–1425
51. Apetrii C, Schlörb H, Falter M, Von Lampe I, Schulz L, Holzapfel B (2005) YBCO thin films prepared by fluorine-free polymer-based chemical solution deposition. *IEEE Trans Appl Supercond* 15:2642–2644
52. Feys J, Vermeir P, Lommens P, Hopkins SC, Granados X, Glowacki BA, Baecker M, Reich E, Ricard S, Holzapfel B (2012) Ink-jet printing of $\text{YBa}_2\text{Cu}_3\text{O}_7$ superconducting coatings and patterns from aqueous solutions. *J Mater Chem* 22:3717–3726
53. Kim SI, Gurevich A, Song X, Li X, Zhang W, Kodenkandath T, Rupich MW, Holesinger TG, Larbalestier DC (2006) Mechanics of weak thickness dependence of the critical current density in strong pinning ex situ metal-organic-deposition route $\text{YBa}_2\text{Cu}_3\text{O}_{7-x}$ coated conductors. *Supercond Sci Technol* 19:968–979
54. Sathyamurthy S, Leonhard KJ, Paranthaman MP (2005) Chemical synthesis of nanoparticles for artificial pinning centers in YBCO coated conductors. *Mater Res Soc Symp Proc* 868: C7.10.1–C7.10.5
55. Falter M, Bäcker M, Bretos I, Schneller T, Hollmann E, Wördenweber R (2009) Chemical solution deposition derived high-temperature superconducting films with artificial pinning centers. Conference in Dresden, Germany
56. Palau A, Monton C, Rouco V, Obradors X, Puig T (2012) Guided vortex motion in $\text{YBa}_2\text{Cu}_3\text{O}_7$ thin films with collective ratchet pinning potentials. *Phys Rev B* 85:012502
57. Xia JA, Long NJ, Strickland NM, Hoefakker P, Talantsev EF, Li X, Zhang W, Kodenkandath T, Huang Y, Rupich MV (2007) TEM observation of the microstructure of metal-organic deposited $\text{YBa}_2\text{Cu}_3\text{O}_{7-\delta}$ with Dy additions. *Supercond Sci Technol* 20:880–885
58. Tsukamoto O (2008) Overview of superconductivity in Japan – Strategy road map and R&D status. *Physica C: Supercond* 468:1101–1111
59. Malozemoff AP, Maguire J, Gamble B, Kalsi S (2002) Power applications of high-temperature superconductors: status and perspectives. *IEEE Trans Appl Supercond* 12:778
60. Hassenzahl WV, Hazelton DW, Johnson BK, Komarek P, Noe M, Reis CT (2004) Electric power applications of superconductivity. *Proc IEEE* 92:1655
61. Bäcker M (2011) Energy and superconductors – applications of high-temperature-superconductors. *Z Kristallogr* 226:343–351
62. Maguire JF, Schmidt F, Bratt S, Welsh TE, Jie Y (2009) Installation and testing results of long island transmission level HTS cable. *IEEE Trans Appl Supercond* 19:1692
63. Yumura H, Ashibe Y, Itoh H, Ohya M, Watanabe M, Masuda T, Weber CS (2009) Phase II of the Albany HTS cable project. *IEEE Trans Appl Supercond* 19:1698
64. Noe M, Steurer M (2007) High-temperature superconductor fault current limiters: concepts, applications, and development status. *Supercond Sci Technol* 20:R15–R29
65. Dommerque R, Krämer S, Hobl A, Böhm R, Bludau M, Bock J, Klaus D, Piereder H, Wilson A, Krüger T, Pfeiffer G, Pfeiffer K, Elschner S (2010) First commercial medium voltage superconducting fault-current limiters: production, test and installation. *Supercond Sci Technol* 23:034020
66. Kellers J, Bühner C, Hagemann H, Ostermeyer B, Witte W (2009) Magnetic billet heating rivals conventional furnaces. *Heat Process* 7:205–210
67. Nick W, Frank M, Kummeth P, Rabbers JJ, Wilke M, Schleicher K (2010) Development and construction of an HTS rotor for ship propulsion application. *J Phys Conf Ser* 234:032040

68. Kalsi SS (2004) HTS ship propulsion motors. IEEE Trans Power Eng Soc General Meet 2:2047–2048
69. Kellers J (2009) Superconducting generators make big gains for small hydro. Int Water Power Dam Constr 8:28–30
70. Abrahamsen AB, Mijatovic N, Seiler E, Zirngibl T, Træholt C, Nørgård PB, Pedersen NF, Andersen NH, Østergård J (2010) Superconducting wind turbine generators. IEEE Trans Appl Supercond 23:034019
71. Smith MA (2010) Rare earth minerals: the indispensable resource for clean energy technologies. In: Proceedings of technology and rare earth metals conference, Washington, DC
72. Elsner H (2011) Kritische Versorgungslage mit schweren Seltene Erden – Entwicklung. Commod Top News 36:1–8

Chapter 28

Antireflective Coatings and Optical Filters

Peer Löbmann

28.1 Basic Strategies for AR Coatings

When electromagnetic waves pass the border between different optical media, the radiation is at least partially reflected. When the incident medium is air with a refractive index $n_0 = 1$ the reflectivity R is calculated as

$$R = \left[\frac{(1 - n_{\text{substrate}})}{(1 + n_{\text{substrate}})} \right]^2 \quad (28.1)$$

for any given substrate according to the *Fresnel Equations*. For glass ($n = 1.5$) a reflectivity of 4 % is obtained assuming vertical irradiation. For double glazed windows this value adds up to ~16 % since four transitions have to be accounted for.

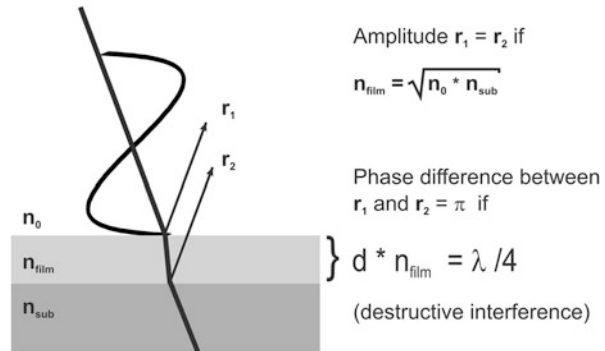
In order to increase light transmission a film with intermediate index of refraction can be applied (Fig. 28.1): Now the light waves are reflected at both interfaces air-film and film-substrate. If the optical film thickness ($d \times n_{\text{film}}$) is $\frac{1}{4}$ of the incident radiation's wavelength the phase difference becomes π and the two reflected waves may cancel out ("phase criterion"). For complete annihilation the amplitude of the interfering radiation also has to be identical. This "amplitude criterion" is fulfilled when the refractive index of the film material is equal to the square root of the refractive index of the substrate. The complete transmission of light with a wavelength of 550 nm thus theoretically requires film material with a refractive index of 1.22 and a layer thickness of 112.7 nm. For radiation with any other frequency a higher reflection will be observed; the so-called bandwidth of the AR coating is limited.

Basic guidelines for antireflective coatings may be derived from the above argumentations. It should be noted, however, that wave angle dependencies, optical

P. Löbmann (✉)

Fraunhofer Institut für Silicatiforschung ISC, Neunerplatz 2, 97082 Würzburg, Germany
e-mail: peer.loebmann@isc.fraunhofer.de

Fig. 28.1 Schematic representation of the transition of electromagnetic radiation through a coated substrate and conditions for destructive interference



dispersion in the different media and adsorption phenomena have to be considered for an exhaustive description of reflection phenomena and more sophisticated product design.

Dense materials with an index of refraction as low as 1.22 are not available in the visible range, some residual reflectance will be observed for such single $\lambda/4$ -layers. Nevertheless if they are applied on top of another $\lambda/4$ -film with a medium refractive index (M-layer), the reflectivity of such double stacks can be reduced to 0 % for a given wavelength. Such assemblies are named *V-type* coatings according to the shape of their optical spectra.

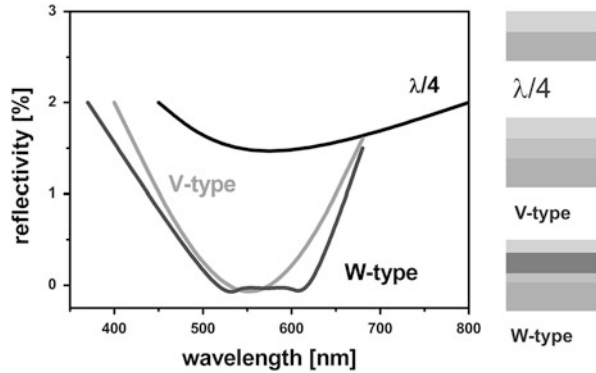
An additional improvement with respect to the bandwidth is obtained by combination of a low-index with a high-index film onto an M-layer (Fig. 28.2). With such a design zero-reflection is approached for two wavelengths. Due to the corresponding spectral response they are often classified as *W-type* coatings.

The spectrum of the reflected radiation from such surfaces is enriched in frequencies set off the respective minimum of reflectance. As a consequence a characteristic color is perceived due to the limited bandwidth of interference-type AR coatings.

Gains in visual neutrality are attainable by increasing the number of films and more complex layouts. The resulting benefits, though, always have to be related to increasing costs of production. Additionally in multilayer assemblies optical losses can arise due to scattering at imperfections at the interfaces between the films.

Besides using interference phenomena, films with a continuous gradient of refractivity may provide antireflective properties: A gradual decrease of n_{film} from $n_{\text{substrate}}$ to unity would optically match the substrate to the ambient atmosphere resulting in optical neutrality. Unfortunately this range cannot be covered by any solid material. The steady increase of porosity of a glass-like film from 0 % (substrate) to 100 % (air) would be ideal, but the mechanical stability of such a system is out of the question. Alternatively e.g. pyramidal surface structures represent a gradual lateral increase in space filling from their top (air with some solid) to the basement (substrate). If such structures are too large, though, scattering will occur. Antireflective properties thus are only expected for sizes well below the incident wavelength which optically are not resolved. Biological examples of such

Fig. 28.2 Design of several interference-type antireflective coatings and related general shape of optical spectra



antireflective surfaces are known from the compound eyes of insects (“moth’s eyes structures”) [1].

All strategies for anti-reflection coatings described above can be realized by sol gel processing. In the following paragraphs the respective techniques will be described. Additionally some practical aspects will be covered and references to commercial products will be given.

28.2 λ/4 Single AR Layers

Sol-gel processing is particularly suitable for the purposeful preparation of films with low refractive indices, because colloidal solutions may well result in porous thin films of e.g. SiO₂. For a long time the lack of suitable precursors has obstructed the wet-chemical processing of dense MgF₂ films as an alternative. Some recent developments described in this paragraph, however, may facilitate this approach.

28.2.1 Porous AR Films

Introducing porosity into a film will decrease its index of refraction n_{film} compared to the dense material n_{solid} according to the *Lorentz-Lorentz equation*:

$$\frac{(n_{\text{film}}^2 - 1)}{(n_{\text{film}}^2 + 2)} = \frac{(1 - P) * (n_{\text{solid}}^2 - 1)}{(n_{\text{solid}}^2 + 2)} \tag{28.2}$$

where P is the porosity i.e. the volume fraction of the pores. For materials such as SiO₂ (n = 1.5), Al₂O₃ (n = 1.7) and TiO₂ (anatase, n = 2.5) commonly used in sol-gel processing porous λ/4 films for a large variety of substrates are conceivable. Considering common glasses (n ~ 1.46–1.65) in most of the cases SiO₂ turns out to

be most suitable because the required porosities around 50 % may provide an at least satisfactory mechanical stability. Additionally good chemical bonding between films and the silica-rich substrate may be anticipated.

The idea of porous SiO₂ antireflective coatings based on colloidal solution deposition dates back to 1949 [2]. Attempts to prepare porous SiO₂ by deposition of dense films from alkali-silicate solutions and subsequent leaching of soluble constituents yielded refractive indices around 1.3, the coatings turned out to be mechanically sensitive, though [3]. The creation of a pore network by assembly of colloidal structures pre-formed in solution has proven to be a far more successful approach.

Monodisperse spherical particles that arrange to a closed packing during film formation would only result in a porosity of 24 %. Broader size distributions, the presence of only partially hydrolyzed precursor in the sol, ripening phenomena and film sintering allow the preparation of dense coatings. On the other side the formation of bulky secondary particle aggregates and incomplete densification generally can lead to significantly higher porosities. In other words sol chemistry, conditions during film formation and annealing are complicated interacting parameters; film porosities therefore definitely cannot be predicted with any certainty. During process development systematic experimental series thus cannot be avoided.

Nevertheless some general guidelines may be applied [4, 5]: The acid-catalyzed hydrolysis of silicon alkoxides favors the formation of linear chain networks of small primary particles. They easily rearrange and consolidate upon drying and thermal treatment. On the contrary larger particles are formed at higher pH levels, the densification of the resulting coarser aggregates is obstructed leading to a generally higher porosity. In practice commercially available products that contain pre-formed colloidal particles (e.g. Ludox[®], Levasil[®], Köstrosol[®]) may be used for the synthesis of coating solutions.

In Fig. 28.3 the optical spectrum of a porous SiO₂ film is given. For a wavelength of 580 nm a residual reflectivity of 0.1 % is achieved corresponding to a film thickness of 145 nm. SiO₂ is the solid backbone of the film ($n_{\text{solid}} = 1.5$); in order to establish an averaged index of refraction of $n_{\text{solid}} = 1.22$ for the whole film, a porosity of 50 % has to be assumed according to the Lorentz-Lorentz equation [Eq. (28.2)]. In order to demonstrate the technical advance the optical data initially reported by Yoldas for porous Al₂O₃ films in 1981 are additionally given in Fig. 28.3 [6, 7].

The calculation porosities based on optical measurements relies on the assessment of the refractive index of the solid phase of the film. Such assessments may be faulty, especially when films are only partially crystalline and contain some amorphous volume fractions. Film porosities can complementarily be determined by Ellipsometric Porosimetry (EP) [8]: When films are measured at varying air moisture, changes of the refractive index can be attributed to the capillary condensation of water. At 100 % relative humidity the complete filling of the pores can be assumed, the refractive index results from the porous solid and water as the second phase with known optical properties. Taking into consideration the measurements

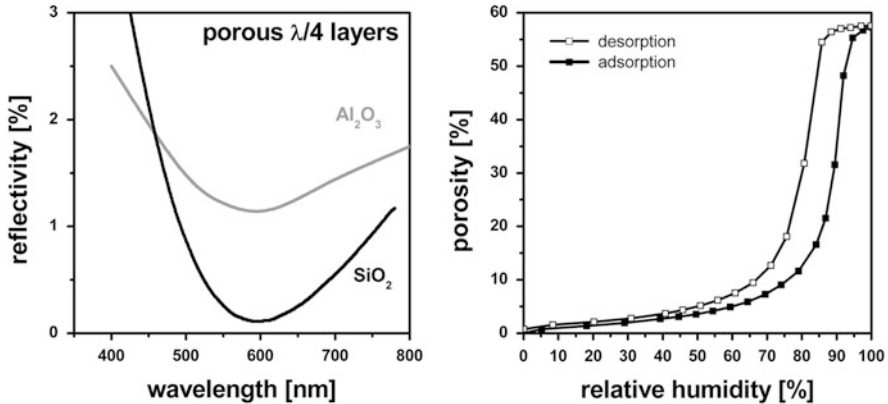


Fig. 28.3 Reflectivity of porous SiO_2 and Al_2O_3 AR-films (*left*) and water adsorption isotherm of SiO_2 coating measured by ellipsometric porosimetry (*right*) (data: SiO_2 : Fraunhofer-Institut für Silicatiforschung, Würzburg, Germany, Al_2O_3 [6] according to [7])

with empty pores (0 % humidity) the total absolute film porosity can be calculated. The adsorption isotherms thus show the porosity filled with water at the corresponding relative humidity. Additionally the analysis of the respective adsorption and desorption branches allows the characterization of pore structures as known from the N_2 -sorption analysis of powders and bulk samples.

The H_2O sorption isotherms of the porous AR film in Fig. 28.3 reveal a porosity of $\sim 58\%$ as anticipated from the reflectance spectrum under the assumption of $n_{\text{solid}} = 1.5$. Additionally pore radius distributions with maxima between 1.5 and 2.0 nm can be calculated (data not shown) [9].

Ellipsometric Porosimetry is a powerful tool for the characterization of thin films; nevertheless faulty results for sol-gel films are possible: The pore system of some TiO_2 coatings has proven to be sealed by an impermeable “sintering skin” that was generated at the air-film interface during thermal curing. In this case the porosity is not accessible to water vapor, EP falsely indicates a dense film. If the top layer is broken up by cracking, the “true” microstructure is exposed [10].

As AR coatings are applied under ambient conditions it has to be considered that their performance to some extent depends on the respective atmosphere: As moisture or other volatile pollutants can readily be adsorbed in the pores, the resulting change in refractive index may decrease the optical transmittance. Film properties such as porosity, pore size distribution and wettability of the inner surface thus may be optimized considering the expected operating conditions.

Another disadvantage caused by the porosity of SiO_2 $\lambda/4$ layers is their limited mechanical stability. Even though such coatings may well resist “normal” handling and weathering, mechanical cleaning that often goes along with the unintentional reaming of abrasive particles (soil, dust) will damage the films. Therefore applications such as displays, architectural or automotive glazings are difficult to address with porous systems.

Fig. 28.4 Solar panel equipped with porous $\lambda/4$ glazing. Image: © Centrosolar Glas GmbH & Co. KG, Germany



Solar panels, though, are mostly positioned somewhat remotely and seldom undergo mechanical cleaning. Porous $\lambda/4$ layers therefore are suitable to enhance the degree of efficiency of solar modules that contain front glazing. In 2008 Centrosolar Glass (Fürth, GERMANY) produced 2,000,000 m² of porous AR films on glass by dip-coating, the thermal hardening can be combined with the tempering required to prepare toughened safety glass. In Fig. 28.4 the photograph of a solar panel equipped with an AR coating is displayed. Respective films exhibit excellent transmittances with a refractive index of 1.22 even after 8 years outdoor exposure.

There are several factors that specifically qualify sol-gel techniques for the industrial processing of AR coatings: When dip-coating is applied both sides of the substrate are equally finished which is essential for best light transmission. Variations of only $\sim 1\%$ with respect to film thickness and index of refraction were reported on 3.75×3.21 m² substrates [11], the related investment costs are significantly lower than for comparable vacuum-based technologies.

It is noteworthy to mention that it took over 50 years from the first patent describing the concept of porous antireflective coatings [2] to the development of coating procedures that meet the requirements of a practical application [12] and successful commercialization [13].

28.2.2 *MgF₂-Films*

With $n = 1.38$ magnesium fluoride has a significant lower index of refraction than SiO₂ ($n = 1.5$), a dense $\lambda/4$ layer does reduce the reflectivity of a glass surface from 4 % to 1.4 %. Compared to SiO₂ generally MgF₂ films with lower porosity and thus higher mechanical stability would allow higher transmissions.

The preparation of dense MgF₂ is possible by vacuum-based evaporation, the maximum substrate size for homogeneous optical coatings, though, is rather limited. Sputtering techniques, which generally allow film preparation on larger areas,

in the case of MgF_2 suffer from fluorine deficiencies in the as-deposited material and consequently deteriorating optical properties.

Up to now inorganic sol-gel science almost exclusively has been engaged in the preparation of oxide materials based on the hydrolysis and polycondensation of metal alkoxides or metal carboxylates. Pure colloidal metal fluorides hardly ever have been addressed; the use of trifluoroacetic acid in the precursor solution generally yields some of the respective oxides or oxofluorides as impurities in the final product after thermal treatment [14].

Colloidal MgF_2 solutions of high purity, though, can be prepared by treatment of Mg alkoxides with anhydrous HF dissolved in e.g. methanol according to



Initially the synthesis route was used for the preparation of metal fluoride powders for catalytic applications [15]. The resulting solutions, however, turned out to be suitable as precursors for the wet chemical deposition of thin films [16]. Since no organic groups are covalently bonded to the MgF_2 particles, in principle thermal annealing is not required to remove such residues as for most oxide systems. Even though systematic investigations on the film formation, resulting microstructures and final film performances are in their early stages, such precursors may be a promising tool for the wet chemical processing of MgF_2 antireflective coatings. In Fig. 28.5 the properties of an initial MgF_2 $\lambda/4$ layer is compared with a state-of-the-art porous SiO_2 film.

28.3 Multilayer AR-Stacks and Optical Filters

Since there are excellent textbooks covering the design and physics of optical multilayer assemblies [17] this paragraph will solely focus on the sol-gel processing of such AR film systems and on related commercial products. Subsequently some topics related to the fabrication of more sophisticated architectures for other optical filters will be highlighted.

28.3.1 *Interference-Type Multiple Layer Stacks for AR Applications*

High-index films which are required for the assembly of interference-type multilayer assemblies were initially used by oneself as reflective coatings for thermal management on architectural glass. To further decrease undesirable transmission of thermal radiation, colloidal noble metal particles can be incorporated. Such modified TiO_2 coatings have been commercialized under the brand name CALOREX by Schott.

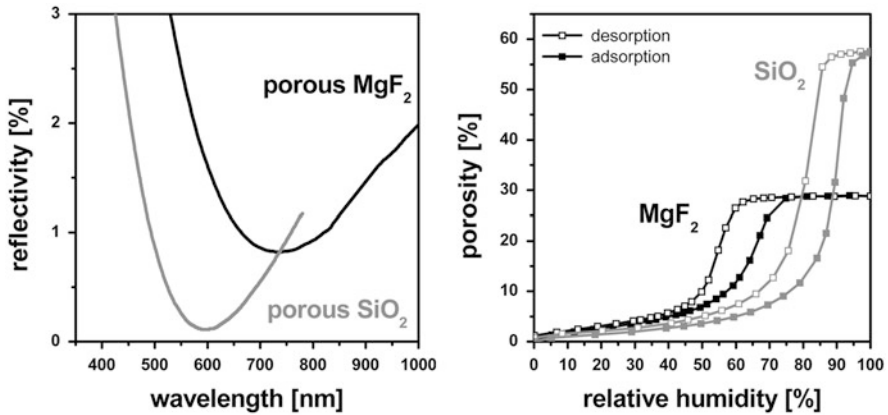


Fig. 28.5 Reflectivity of porous MgF₂ AR-film (*left*) and corresponding water adsorption isotherm measured by ellipsometric porosimetry (*right*). For comparison the data from Fig. 28.3 for porous SiO₂ films are displayed in grey. Data: Fraunhofer-Institut für Silicatforschung, Würzburg, Germany)

In contrast to SiO₂, that generally remains amorphous throughout sol-gel processing, TiO₂ has to be crystallized by thermal annealing in order to attain the desired high index of refraction. It has early been recognized that the substrate type may have a crucial impact on the phase development of the films [3]: On fused silica or borosilicate glass anatase always is the polymorph of TiO₂ initially formed which in some cases may partially be transformed to rutile at higher temperatures. Sodium ions from substrates like soda-lime glass, however, interfere with the crystallization process by either inducing the nucleation of brookite or incorporation of significant amounts of Na into the film. In any case the refractive index of the resulting material is decreased. Especially in multilayer assemblies, where a first TiO₂ film is in contact with the substrate and therefore undergoes multiple firing cycles of the subsequent layers, this unpleasant phenomenon gains importance. Fortunately even thin (<30 nm) SiO₂ barrier layers sufficiently reduce sodium diffusion in cases where the use of expensive substrates is not possible for practical or economic reasons.

There are numerous synthetic pathways for the preparation of TiO₂ coating solutions. Some “historic” precursors were based on the simple alcoholysis of TiCl₄. The resulting coating solutions exhibit low pH-values, often corrosion problems during industrial processing originate from residual HCl. Other routes are mostly based on complexation of titanium alkoxides and subsequent hydrolysis. In order to facilitate reproducible results, “aging phenomena” that change sol properties with time have to be avoided. Particle growth and aggregation for example will affect the film morphology throughout drying and sintering, related variations in sol viscosity require permanent readjustments of processing parameters.

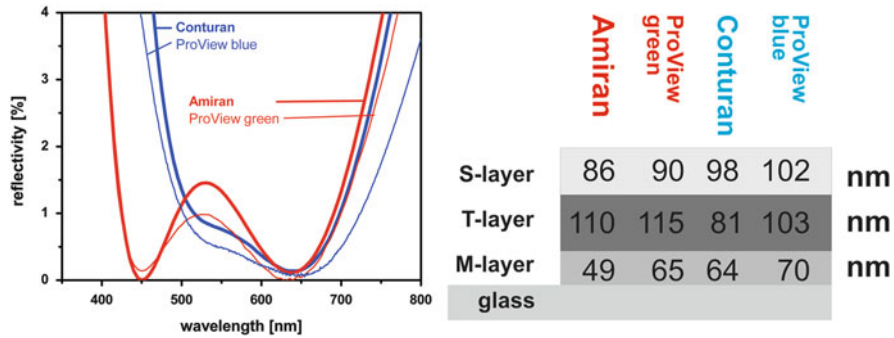


Fig. 28.6 Reflectivity of commercially available triple layer AR coatings (*left*) and associated stack architectures (*right*). Data: Schott AG (Amiran[®] and Conturan[®]) and Berliner Glass Surface Technology (ProView *green* and *blue*), Germany

Recently stable TiO₂ precursor powders have been developed based on complexation of Ti-alkoxides, hydrolysis and subsequent complete removal of volatile components [18]. The powders can be stored under ambient conditions and readily re-dissolve in alcohols, mixtures of alcohols and even water. The resulting coating solutions are non-corrosive and highly stable in an industrial environment [19].

SiO₂ is commonly used as low-index material in interference filter assemblies. In contrast to the preparation of porous λ/layers dense microstructures are desirable for the mechanical stability of the multilayer stacks. Therefore acid-catalyzed hydrolysis and condensation reactions have to be employed in order to ensure optimum densification of the material. Such films easily exhibit optical properties of silica glass. Small amounts (~0.1 %) of carbon may persist even treatment temperatures of 800 °C, the optical absorption below 205 nm, though, is irrelevant for most practical applications [3].

3-layer AR coatings require the deposition of a film with intermediate refractive index (M-layer) on the substrate below the successive T- and S-layers. Such materials may straightforwardly be obtained by the synthesis of coating solutions aiming at a mixed composition of SiO₂ (n = 1.5) and TiO₂ (anatase, n = 2.5) or ZrO₂ (n = 2.15) because the molar proportions add up linearly to the resulting index of refraction.

Figure 28.6 summarizes the optical spectra of some commercially available 3-layer antireflective coatings along with their geometrical layouts as provided by the suppliers. Conturan[®] and AR4 are specifically designed for cover glasses of instrumentations whereas Amiran[®] and AR2 are mostly applied in architectural glazing. Due to their spectral characteristics white light reflected from these surfaces appears tinted slightly bluish and greenish respectively. This coloration could be further reduced by the application of 5- or 7-fold coatings, the higher costs of production, however, are not compatible with most applications addressed.

The higher costs for multilayer assemblies are not only added up by the cumulative expenses of coating/firing cycles. Single defects propagate all the way through every subsequent film. The yield for a projected format may therefore be drastically reduced with increasing film number.

Multilayer interference antireflective films exhibit a higher stability than porous $\lambda/4$ -systems which allows their application on display panels, showcases or architectural glass. Their tolerance to damage, though, is significantly lower: When the outermost S-layer is damaged by e.g. an abrasive particle, the underlying T-layer with is exposed to the ambience. Due to the large difference of refractive index of the adjacent media, more than 20 % of the irradiated light is reflected and the scratch becomes perspicuously visible. If a porous $\lambda/4$ -layer is damaged the reflectance is only increased by 4 % which is far less eye-catching.

28.3.2 *Optical Filters*

Interference assemblies not only can be designed to optimize the transmission of visible light, a large variety of other products such as UV- and IR-filters, cold light mirrors, beam splitters and color conversion filters can be prepared as well. Filters with a lateral gradient of spectral response may be facilitated by a continuous increase of film thicknesses within a stack. Such microstructural features are difficult or even impossible to obtain by other techniques than sol-gel processing: However, raising the withdrawal rate during a dip-coating experiment leads to a continuous increase of film thickness; the resulting multilayers consist of stacked wedge-shaped single films.

If the thickness of 12 alternating T- and S-layers is increased from 50 nm to 80 nm respectively, the transmittance and reflectance of the resulting filter is gradually varied over a broad sector of the visible spectrum from blue to yellow. Such filters are used in lighting industry and for artistic purposes to achieve color effects. They are commercialized by Berliner Glas Surface Technology, Germany, under the brand name VARIOTRANS[®] (Fig. 28.7).

It has to be noted that despite the aforementioned potential accumulation of defects during multilayer deposition it is possible to prepare such elaborate multilayer assemblies on an industrial scale by sol-gel processing. Besides state-of-the-art production facilities and conscious adherence to the established sequence of work steps the role of practical experience cannot be overestimated.

28.4 **Index Gradient Layers**

Other than that mentioned use of constructive and destructive interference of single- and multilayers optical transmission may be optimized by establishing a gradual increase of refractive index from the incident environment to the substrate. Such a “smooth transition” between the adjacent media at least theoretically features maximum bandwidth (“optical neutrality”) and a low angular dependence of reflectivity. The index profile of the interface is only of minor importance to its overall performance [7]. The subsequent paragraphs focus on the implementation of two different related concepts by sol-gel processing of thin films.

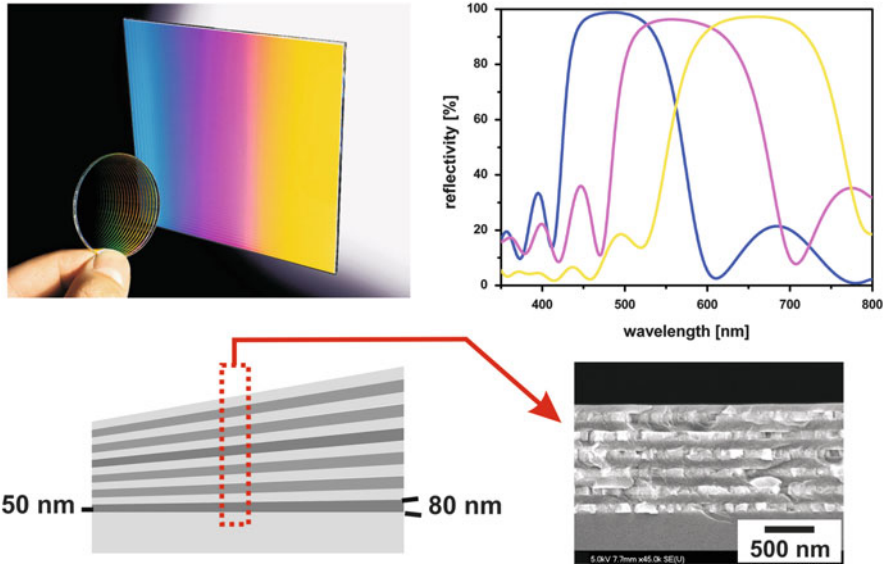


Fig. 28.7 Photograph of color gradient filter VARIOTRANS[®] and reflectivity measured at three different spots of the sample (*top*); schematic drawing of filter layout and cross-sectional SEM image (*bottom*). Sample: Berliner Glas Surface Technology, Germany. Data and images: Fraunhofer-Institut für Silicatforschung, Würzburg, Germany

28.4.1 Films with Graded Porosity

For any dense film material a steady increase of porosity from 0 % to 100 % at the outer film surface could establish a smooth change of its optical properties and thus yield antireflective characteristics. One has to keep in mind, though, that such a perfect gradient has to go along with a dramatic loss of mechanical stability. The use of films with graded porosity therefore will always have to rely on a compromise between optical performance and durability.

As already has been shown for the $\lambda/4$ -layers it is possible to accurately adjust the porosity of sol-gel derived films, therefore the idea to establish graded porosity by subsequent multiple coatings is straightforward.

Coating solutions may undergo aging phenomena which normally is undesirable in terms of stable processing conditions. Debsikdar [20] proposed the use of SiO_2 sols that actually show particle growth for subsequent coating cycles; multilayers with increasing porosities were prepared (Fig. 28.8). Even though this specific synthetic approach yields intriguing results on the laboratory scale, the industrial application of a continuously changing coating precursor seems disadvantageous from the economic point of view. Additionally it has to be noted in general that packing density and thus porosity can not be correlated to the respective particle size of coating solutions.

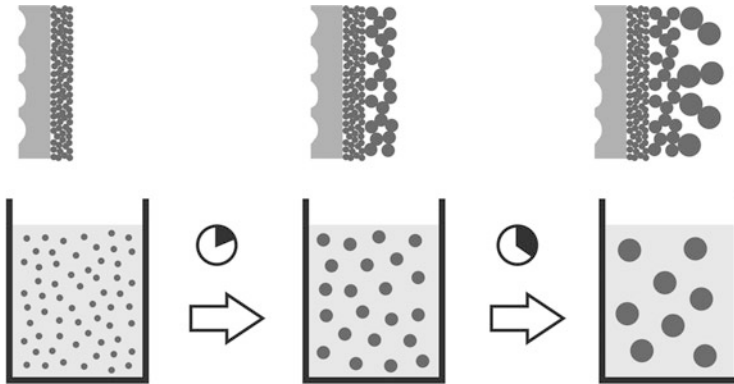


Fig. 28.8 Schematic representation of index-gradient porous multilayer assembly (*top*) prepared by scheduled deposition from coating solution that undergoes particle growth due to aging (*bottom*)

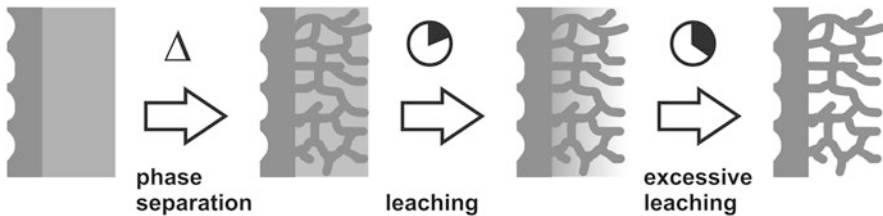


Fig. 28.9 Schematic representation of index-gradient layer prepared by leaching of a phase separated film

Etching of phase-separable glass can result in Si-rich surface regions with graded porosity that exhibit broadband antireflective properties [21]. This approach, however, remains limited to specific glass compositions. Etched surfaces of common glasses are commercialized by Sunarc Technology A/S (Denmark) for solar applications and greenhouses.

Alternatively arbitrary substrates may be coated with dense films that are either leachable or undergo a separation into a persistent and a soluble phase [22] (Fig. 28.9). Glassy coatings with $\text{SiO}_2\text{-B}_2\text{O}_3\text{-Na}_2\text{O}$ composition that are corroded by $\text{NH}_4\text{F}/\text{HNO}_3$ solutions after thermal treatment show residual reflectivity as low as 0.15 % at certain wavelengths [23]. Unintentional excessive leaching, though, should result in films with constant porosity throughout the material or at least a graded film underneath a region with constant porosity. Therefore accurate control of processing parameters is inevitable.

For some laser applications small pore sizes are specifically important for the antireflective materials otherwise scattering may become significant at short wavelengths. The porosity of pure SiO_2 coatings was reduced from 40 % to approximately 23 % by sintering; the resulting pore size was estimated to be

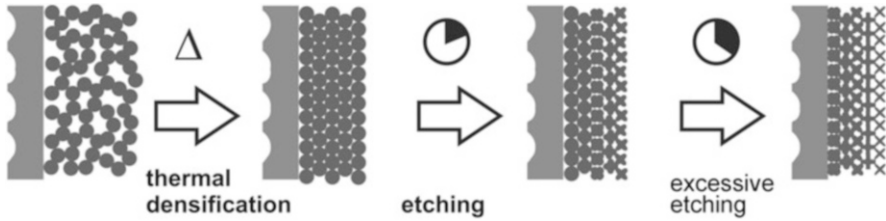


Fig. 28.10 Schematic representation of index-gradient layer prepared by etching of a densified particulate sol-gel film

lower than 1 nm. Etching with dilute hydrofluoric acid creates graded porosity within the upper 100 nm of films with an overall thickness of 425 nm. For such films transmissions exceed 99 % for wavelengths between 300 nm and 850 nm [24]. Optical performance and mechanical surface stability have to be balanced by variation of etching time with respect to the intended application, the latter requirements are less critical for laser systems than for e.g. architectural glazing (Fig. 28.10).

28.4.2 Surface Patterning: “Moth Eye” Structures

Periodic surface patterns on the first view seem completely different from the materials with graded porosity described above. Nevertheless antireflective properties can be provided by such structures based on the same physical principles. In 1967 it was observed that the reflection from the compound eyes of some nocturnal moths is significantly reduced by microscopic surface structures which provide them with reduced visibility to predators [25].

Even though the accurate description of the underlying optical diffraction phenomena requires *rigorous coupled wave analysis* (RCWA) or at least *effective medium theory* (EMT). Figure 28.11 provides a qualitative impression of the related working principle. Any surface structure can be divided into horizontal slices that optically are an average mixture of solid and the enclosed atmosphere. A mean index of refraction may be assigned to each of these segments. If the pattern is a rectangular grating, the effective refractive index is constant in the vertical direction as illustrated in the upper part of Fig. 28.11. If the distance between the neighboring peaks is well below the wavelength of the incident light, no scattering will occur. The respective surface patterns thus may be regarded to work similar to a porous $\lambda/4$ -layer as described in Sect. 28.2.1. In the case of a pyramidal shape the upper slices mainly consist of air with some minor contribution of the solid to its median optical properties, whereas the lower parts approach the refractive index of the substrate (Fig. 28.11 bottom). Again under the precondition of periodicity below the incident wavelength an index gradient analogous to films with graded porosity is established.

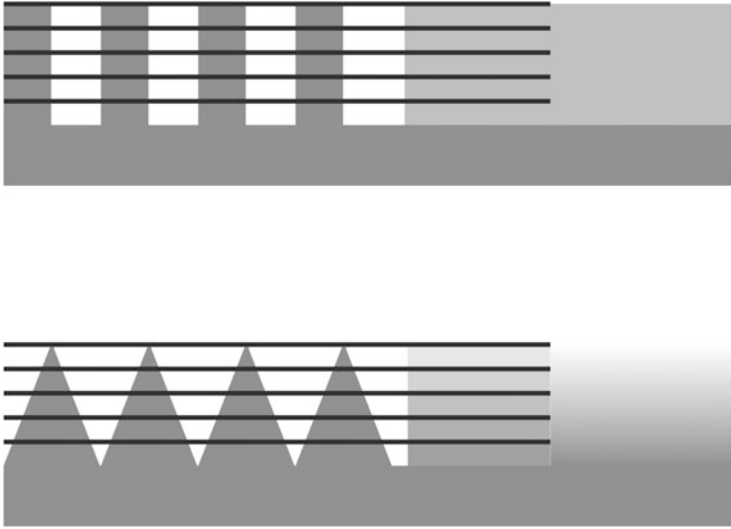


Fig. 28.11 Schematic representation of refractive index from squared (*top*) and pyramidal (*bottom*) surface pattern

Linear gratings can be considered as the simplest cases of periodic surface patterns. Different peak shapes and aspect ratios (depth vs. distance) may be combined with two-dimensional variations such as cross- or hexagonal gratings and even stochastic patterns. Therefore a plethora of surface geometries are feasible. Especially the spectral and angular dependency of transmission and reflection thus can be adapted in a wide range. The related discussion, though, goes far beyond the scope of this chapter. Instead the general sol-gel preparation of surface patterns suitable for AR applications will be addressed. Even though specific sol-gel films may be directly nanostructured by lithography such processes are costly, time consuming and therefore primarily not aimed at antireflective surfaces [26]. Alternatively the embossing of xerogel films prior to thermal curing offers promising perspectives. In this context the origin of indenters and the limitations related to their fabrication becomes important.

Linear structures can be inscribed to photoresists by the interference of the separated parts of a split laser beam, cross- and hexagonal gratings are feasible by repeated exposure of the substrate after rotation of 90° or 60° respectively. Whereas small areas are easy to handle the upscaling becomes increasingly difficult due to the larger experimental setup required, prolonged exposure times and the strict requirement of geometric stability during the experiment. The latter point is especially critical for the processing of gratings in the length scale of some hundred nanometers as necessary for moth-eye structures. Since even after development photoresists are only temporarily stable, a replica of the surface structure is prepared by electrodeposition of Ni. The resulting “master shim” is the basis for secondary reproductions either by repeated galvanic metal deposition or embossing

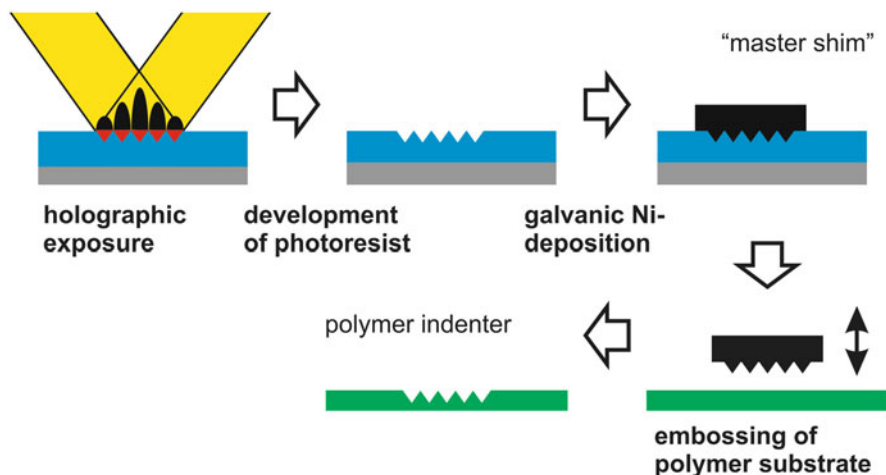


Fig. 28.12 Schematic illustration of processing steps for the fabrication of embossing tools for microstructured surfaces

into polymer surfaces or lacquered surfaces. The sequence of processing steps is summarized in Fig. 28.12.

To obtain sol-gel films suitable for the embossing of surface patterns, their refractive index has to be matched to the glass substrate as close as possible. This is practicable by e.g. the addition of some % Ti precursor to a SiO_2 -based solution. As the transfer of the relief from the indenter to the film requires sufficient ductility of the material, the xerogel film has to be embossed before thermal curing directly after coating. Additionally organic “fluxing agents” of medium or high molecular weight that decompose upon the final thermal treatment may provide additional elastic properties. Master shims and metallic replica are not suitable for this procedure for inorganic sol-gel materials because they generally show a good adhesion to the surface of metals. Therefore reproductions of the initial metal master into polymer-based materials are employed [27].

The embossing process, especially for large areas, requires a considerable level of experience and technical effort. Nevertheless the preparation of greater dimensions without visible junctions is limited by the availability of indenters with the respective sizes as described above.

Another difficulty is the realization of sufficient depths of imprints: Even if the indenter relief was ideally imprinted into the xerogel surface, during the subsequent thermal curing the films undergo shrinkage (Fig. 28.13, top). This effect may escalate due to the presence of sizeable amounts of organic fluxing agents. A straightforward approach to this problem would be the use of indenters with deeper minima between the peaks of the gratings (= higher aspect ratio). Unfortunately such photoresist structures do not exhibit sufficient mechanical stability to sustain the further conversion into master shims.

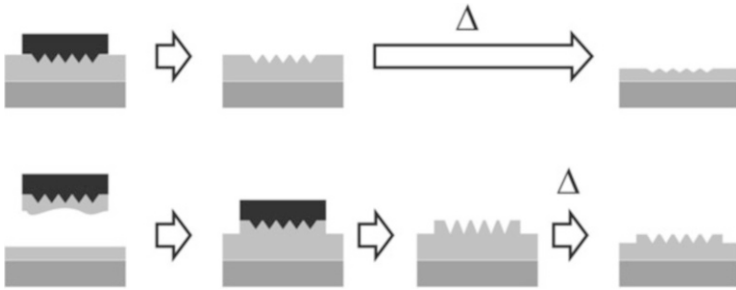


Fig. 28.13 Schematic representation of the embossing of xerogel films (*top*) and the transfer of partially densified material from an indenter to a film surface (*bottom*) prior to thermal annealing

Certain improvements can be achieved by somewhat inventive sample handling (Fig. 28.13, bottom): Polymer indenter foils can be dip-coated alike glass substrates with a sol-gel film that does not require plasticizers. The film is densified structurally conform within its surface patterns during drying. It subsequently may be transferred to a glass freshly coated with the same material and laminated under pressure at temperatures below 120 °C. Needless to say that the related processing requires accurate adjustments between sol synthesis, indenter surface properties, experimental time schedule and transfer parameters. Nevertheless the inherent flexibility of sol-gel processing for the preparation of advanced novel antireflective coatings is clearly demonstrated.

In Fig. 28.14 some examples of surface structures prepared by embossing of sol gel films are given. Even though reflectivities below 1 % are achieved for wavelengths within the maximum sensitivity of the human eye, the optical performance remains below the values of e.g. porous antireflective coatings. This is partially due to still insufficient depths of the structure. This shortcoming may at least be compensated by an improved mechanical stability compared to porous $\lambda/4$ layers. Yet limited bandwidths of such nanostructured coatings are associated with suboptimal patterns shape according to Fig. 28.11.

Besides techniques employing direct lithography of sol-gel films [26], there are additional intriguing approaches: Shear-aligning of colloidal suspensions yields self-assembled antireflection structures in spin-coating experiments [28], leaching of alumina-based sol gel films leads to “flower-like” surface morphologies with graded refractive index [29]. Further research and development in these novel fields will have to demonstrate their scientific and economic sustainability in the future.

28.5 Concluding Remarks

The full width of tactics for the preparation of antireflective coatings reaching from porous $\lambda/4$ films, dense multilayer interference stacks, index gradient systems to nanostructured surface patterns can be accomplished by sol-gel processing. It is

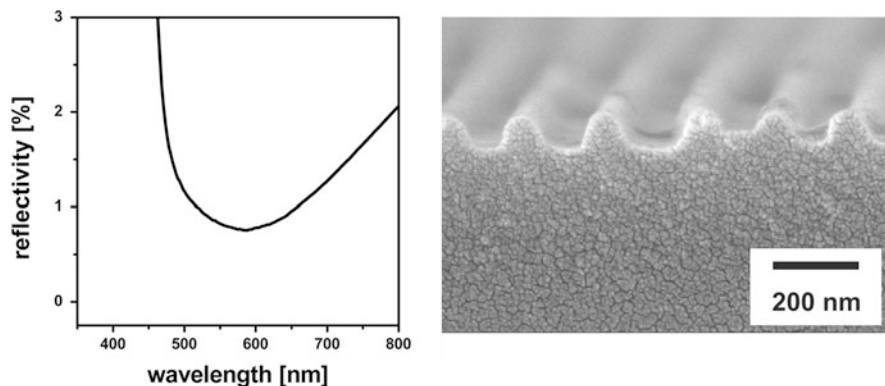


Fig. 28.14 Reflectivity of a cross-grating (*left*) and SEM image of a linear grating (*right*) both prepared by sol-gel processing

remarkable, though, that in the case of e.g. porous AR coatings a time span of half a century lies between first patents and final commercialization. “Boring” and academically ungrateful work regarding solution stability, upscaling of synthesis and coating technology, adhesion, mechanical stability and weathering resistance may not be the only reason for such a tardy economic impact. Since industrial processing of materials and surfaces is often dominated by physical techniques, process engineers sometimes probably are more likely to deprecatingly judge wet chemical processing steps that by mistake are considered excessively unforeseeable and unstable. Therefore successful commercial implementations should serve as good examples and encourage a broader confidence into this promising multidisciplinary technology.

References

1. Wilson SJ, Hutley MC (1982) The optical properties of ‘moth eye’ antireflection surfaces. *Opt Acta* 29:993–1009
2. Moulton H (1949) US Patent 2474061
3. Schroeder H (1969) Oxide layers deposited from organic solutions. In: Hass G, Thun RE (eds) *Physics of thin films: advances in research and development*, vol 5. Academic, New York, NY, pp 87–141
4. Iler RK (1979) *The chemistry of silica*. Wiley, New York, NY
5. Vincent A, Babu S, Brinley E, Karakoti A, Deshpande S, Seal S (2007) Role of catalyst on refractive index tunability of porous antireflective coatings by sol-gel technique. *J Phys Chem C* 111:8291–8298
6. Yoldas B (1981) US Patent 4271210
7. Chen D (2001) Anti-reflection (AR) coatings made by sol-gel process: a review. *Sol Energy Mater* 68:313–336

8. Baklanov MR, Mogilnikov KP (2002) Non-destructive characterization of porous low-k dielectric films. *Microelectron Eng* 64:335–349
9. Rouquerol F, Rouquerol J, Sing K (1999) Adsorption by powders and porous solids: principles, methodology and applications. Academic, London
10. Bockmeyer M, Herbig B, Löbmann P (2009) Microstructure of sol–gel derived TiO₂ thin films characterized by atmospheric ellipsometric porosimetry. *Thin Solid Films* 517:1596–1600
11. Hussmann E (1998) Sol-gel coatings on large glass substrates for multilayer interference systems. *Key Eng Mater* 150:49–66
12. Glaubitt W, Kursawe M, Gombert A, Hofmann T (2002) Novel hybrid sol for producing abrasion-resistant SiO₂ antireflection coatings on glass. PCT/EP 2002/010492
13. Gombert A, Glaubitt W (2000) Antireflective transparent coatings for solar devices. *Sol Energy* 68:357–360
14. Fujihara S, Tada M, Kimura T (1997) Preparation and characterization of MgF₂ thin film by a trifluoroacetic acid method. *Thin Solid Films* 304:252–255
15. Kemnitz E, Gross U, Rudiger S, Shekar C (2003) Amorphous metal fluorides with extraordinary high surface areas. *Angew Chem Int Ed* 42:4251–4254
16. Krüger H, Kemnitz E, Hertwig A, Beck U (2008) Transparent MgF₂-films by sol-gel coating: synthesis and optical properties. *Thin Solid Films* 516:4175–4177
17. Macleod H (2001) *Thin-film optical filters*, 3rd edn. Institute of Physica Publishing, London
18. Löbmann P (2005) Soluble precursor powders as precursors for TiO₂ thin films. *J Sol Gel Sci Technol* 33:275–282
19. Löbmann P, Röhlen P (2003) Industrial processing of TiO₂ thin films from soluble precursor powders. *J Glass Sci Technol* 76:1–7
20. Debsikdar J (1989) US Patent 4830879
21. Lowdermilk W, Milam D (1980) Graded-index antireflection surfaces for high-power laser applications. *Appl Phys Lett* 36:891
22. McCollister H, Boling N (1981) US Patent 4273826
23. Mukherjee S (1981) Gel-derived single-layer antireflection films with a refractive index gradient. *Thin Solid Films* 81:L89–L90
24. Yoldas B, Partlow P (1985) Formation of broad band antireflective coatings on fused silica for high power laser applications. *Thin Solid Films* 129:1–14
25. Bernhard C (1967) Structural and functional adaption in a visual system. *Endeavour* 26:79–84
26. DellaGiustina G, Brusatin G, Guglielmi M, Romanato F (2007) Direct nanopattern of hybrid sol-gel films. *Mater Sci Eng C* 27:1382–1385
27. Heermann J, Löbmann P (2001) Coating and structuring of glass surfaces by sol-gel and embossing techniques. In: 19th International congress on glass, Edinburgh, UK, 1–6 July 2001
28. Linn N, Sun C, Jianga P, Jiang B (2007) Self-assembled biomimetic antireflection coatings. *Appl Phys Lett* 91:101108
29. Yamaguchi N, Tadanaga K, Matsuda A, Minami T, Tatsumisago M (2007) Antireflective properties of flowerlike alumina thin films on soda–lime silica glass substrates prepared by the sol–gel method with hot water treatment. *Thin Solid Films* 515:3914–3917

Chapter 29

Luminescent Thin Films: Fundamental Aspects and Practical Applications

Shinobu Fujihara

29.1 Introduction

Electrons that are excited by any energy sources can possibly emit light when they return to the ground state in many of inorganic and organic materials. This phenomenon is known as luminescence and inorganic materials showing visible luminescence are usually called phosphors. Luminescence as a result of excitation by light (photon), cathode ray, electrical field, heat, and chemical reaction is designated photoluminescence (PL), cathodoluminescence (CL), electroluminescence (EL), thermoluminescence, and chemiluminescence, respectively. Luminescence is particularly sensitive to characteristics of materials such as purity, composition, defects, and phonon frequencies. Luminescence is a radiative process and always competes with non-radiative processes including multi-phonon relaxation and concentration quenching. Basic concepts and applications of phosphors are summarized in the book, “Luminescent Materials,” which is renowned as a comprehensive reference [1].

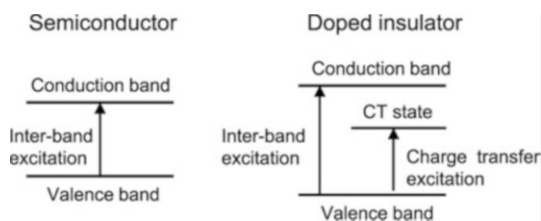
Luminescent metal oxide materials are classified into two basic groups: metal oxide semiconductors that have large band gaps, absorb ultra-violet (UV) light, and emit visible light, and metal oxide insulators (host materials) doped with luminescent transition metal ions (activators).

Figure 29.1 shows a schematic illustration of representative excitation processes in phosphors. Semiconductors are excited exclusively by inter-band electronic transitions, while activators doped in metal oxides can be excited by inter-band transitions in hosts and subsequent energy transfers or direct charge transfers from oxide ions. Emissions from semiconductors usually correspond to band gap energies, but defects or dopants can once trap excited electrons and give lower energy emissions in the visible wavelength region. A well-known example of this

S. Fujihara (✉)

Department of Applied Chemistry, Faculty of Science and Technology, Keio University,
3-14-1 Hiyoshi, Kohoku-ku, Yokohama 223-8522, Japan
e-mail: shinobu@applc.keio.ac.jp

Fig. 29.1 A schematic illustration of excitation processes in two different types of phosphors



type is zinc oxide (ZnO), which emits green light due to the existence of oxygen vacancies generating defect levels within the band gap [2].

Luminescence of rare-earth (RE) ions doped into metal oxide materials is of prime importance and has found numerous practical applications such as fluorescent lamps and cathode-ray tubes so far [3]. RE ions are characterized by their incompletely filled $4f$ electronic orbital, which is a treasure house of electric, magnetic, optical, and optoelectronic functions. Doped RE ions can be excited by any energy sources through intraconfigurational $f-f$ transitions of inner $4f$ electrons, interconfigurational $f-d$ transitions, charge transfers between RE ions and oxide ions, or host lattice absorptions. Luminescence behavior of excited RE ions is subject primary to crystal fields of host lattices as well as lattice imperfection [4]. Lattice phonon also affects quantum efficiencies of emissions from excited RE ions.

The morphology or the shape of phosphors is generally fine powders composed of micrometer-sized, well-developed particles synthesized by conventional solid-state reaction under high-temperature heat treatments. For device applications, phosphor powders are shaped as films (or screens) up to a few hundred micrometer in thickness. Printing techniques are required to obtain films with high uniformity and good adhesion to substrates because they influence greatly optical and luminescent properties of phosphors as an assembly of particles. In fluorescent lamps, phosphor films are coated inside a glass tube, which is filled with mercury gas. By discharge between electrodes at both ends, mercury gas is excited and emit UV lines, which are subsequently utilized for exciting phosphor films. One kind of phosphors emits monochromatic light and therefore phosphor films are composed of two or three kinds of phosphors to emit mixed white light. Fluorescent lamps look white when they are turned off because phosphor films scatter light coming from outside.

Since phosphors are materials of large band gaps, they do not absorb visible light. Therefore, if we could avoid light scattering, phosphors were transparent to the naked eye. "Thin" films of luminescent materials are really transparent and have received considerable attention these days. They are coated on transparent glasses or polymers to give multi-functional optical properties based on high transparency and luminescence. One should know, however, phosphor thin films are usually less bright than powder screens due to the occurrence of multiple internal reflections and light trapping [5], as described later. It is a challenging undertaking to design, synthesize, and utilize luminescent thin films having improved or enhanced emission properties because they can offer new fields of applications as energy-saving

lighting, transparent imaging and displays, and solar energy conversion. This chapter describes preparation of luminescent thin films by various kinds of chemical solution deposition (CSD) methods and their applications. Emphasis is placed on characteristic optical properties of thin films such as transmission, surface Fresnel reflection, total internal reflection, and interference. Applications of luminescent thin films to active waveguides, flat panel displays, X-ray imaging devices, and solar cells are also presented.

29.2 Precursor Chemistry

The sol-gel method is well known as a technology for synthesizing metal oxide thin films [6–8]. In a typical synthesis, raw materials are first dissolved in a certain kind of solvents. Then the resultant solutions are reacted or aged at moderate temperatures and finally coated on a certain kind of substrates by dip-coating or spin-coating. The coated substrates are heat-treated at higher temperatures for removing organic components from films, making good adhesion of films, and/or crystallizing films well. The film thickness is controlled by adjusting the solution viscosity, changing the coating conditions, and/or repeating the coating procedures.

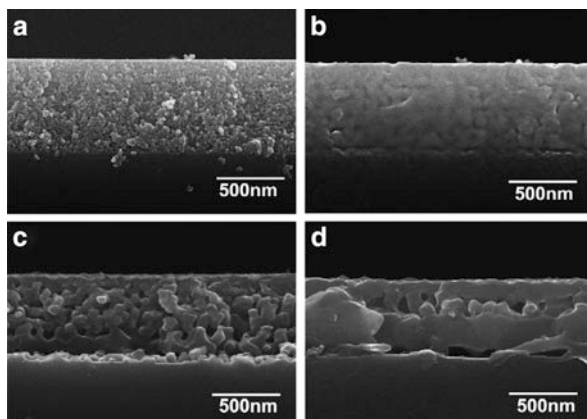
During a sol-gel processing using metal alkoxides, chemical reactions such as hydrolysis and condensation proceed to form viscous sols. Silica (SiO_2) films are one of the most successful examples of sol-gel-derived materials and many kinds of luminescent ions, semiconductor quantum dots, and metal fluoride nanocrystals have been incorporated into silica matrix. For example, Slooff et al. [9] fabricated Er^{3+} -doped sol-gel films and investigated infrared ($1.53 \mu\text{m}$) luminescence properties. Precursor solutions were prepared by mixing tetraethylorthosilicate (TEOS), ethanol, water, and HCl. The solutions were stirred while heated to a temperature of 70°C where they changed from opaque to transparent. Separately, an erbium solution was prepared by dissolving $\text{Er}(\text{NO}_3)_3 \cdot 5\text{H}_2\text{O}$ into ethanol. After mixing and reacting the TEOS and the erbium solution, the resultant precursor solutions were spin-coated onto pre-cleaned Si substrates covered by a 2-nm-thick native oxide. Heat treatments were performed at high temperatures up to 900°C in air or in vacuum. Bullen et al. [10] prepared ZrO_2 - SiO_2 hybrid sol-gel glass films incorporated with a highly luminescent semiconductor quantum dots. Monodisperse core (CdSe) or core-shell (CdSe@CdS or CdSe@ZnS) nanoparticles were prepared by the reaction of organometallic reagents such as dimethylcadmium and diethylzinc in organic surfactants (trioctylphosphine). The nanoparticles were capped with aminoethylaminopropyltrimethoxysilane allowing their dissolution in polar solvents such as propanol or ethanol. A matrix sol-gel solution was synthesized by reacting 3-(trimethoxysilyl)propylmethacrylate, methacrylic acid, and zirconium *n*-propoxide [11]. The capped particles were mixed with the sol-gel solution leading to a final sol that can be used for depositing thin films on substrates by spin- or dip-coating. After deposition the films were dried at low temperatures up to 150°C . Fujihara et al. [12] reported transparent, luminescent sol-gel silica films

on the basis of a $\text{SiO}_2\text{-(Gd,Eu)F}_3$ nanocomposite structure, in which $(\text{Gd,Eu})\text{F}_3$ nanocrystals were dispersed in a silica matrix. RE acetates were dissolved in a mixed solvent of water and trifluoroacetic acid (TFA). TEOS and *N,N*-dimethylformamide were added to ethanol. The former solution was added dropwise to the latter, and the resultant solution was stirred for 1 day at room temperature. The solution was then spin-coated on silica glass substrates and heated at temperatures between 300 and 500 °C for 10 min in a flowing nitrogen atmosphere, followed by quenching. The above examples indicate that the high-temperature treatment is necessary for doping the RE ions directly to the silica matrix, while the incorporation of the luminescent solid particles can be done at the relatively low temperatures.

The formation of metal complexes is also an important step when metal salts such as chlorides, nitrates, sulfates, and acetates are used as starting materials for depositing various kinds of metal oxide thin films. Instead of the formation of sols, chemically stable metal complexes are formed in solutions. The sol-gel processing of ZnO is a good example [13]. Zinc acetate dihydrate was dissolved in 2-methoxyethanol, to which monoethanolamine was added. Aminoethanols act as bidentate ligands to Zn^{2+} , making the solution stable against any precipitates. Both oxygen and nitrogen in $\text{NR}_2\text{CH}_2\text{CH}_2\text{OH}$ ($\text{R} = \text{H}$ or $\text{CH}_2\text{CH}_2\text{OH}$) can make bonds with Zn^{2+} . When the precursor was heated at around 300 °C, the decomposition began by having " $(-\text{N},-\text{O})-\text{Zn}$ " and " $(-\text{COO})-\text{Zn}$ " bonds in the complex broken. Sol-gel-derived Mg-, Cd-, and (Al,Li)-doped ZnO thin films were found to exhibit visible PL which was tunable in a wide range from blue to green and orange [14–16]. For (Zn,Mg)O films, zinc acetylacetonate monohydrate was added to methanol. Magnesium acetate tetrahydrate was added to a mixture of isopropanol and water. A precursor solution was then prepared by mixing the Zn and Mg precursors and deposited on quartz glass substrates by spin-coating. The coated substrates were then heated at 600 or 700 °C for 10 min in air, O_2 , N_2 , or H_2/N_2 atmospheres, followed by quenching. In preparing (Al,Li)-doped ZnO films, $\text{AlCl}_3\cdot\text{H}_2\text{O}$ and LiCl were simultaneously added to the zinc acetylacetonate precursor. The coated substrates were dried at 250 °C before annealing to suppress lithium volatilization.

In the preparation of crystalline RE-doped metal oxides, careful attention should be paid to the homogeneity of precursor solutions. This is because a concentration of RE dopants is usually very low (a few atomic percent) and their aggregation would result in degradation of luminescent properties. $\text{Y}_2\text{O}_3:\text{Eu}^{3+}$ is one of the most popular red-emitting phosphor materials. Many researchers attempted to fabricate $\text{Y}_2\text{O}_3:\text{Eu}^{3+}$ thin films by a variety of CSD methods. Typical examples are introduced below. In the sol-gel process, the main component is an yttrium precursor, which may be yttrium alkoxides or yttrium salts. Rao [5] employed stable yttrium and europium hydroxide gels through the ion exchange process starting from nitrates and chlorides. The gels were mixed and oxalic acid and acetylacetone were added. The film deposition was carried out using the mixtures in a semi-gel state with dip- or spin-coating technique. The films were finally heated at temperatures between 500 and 1,000 °C for 2 h in air. The film thickness was

Fig. 29.2 Cross-sectional SEM images of the $Y_2O_3:Eu^{3+}$ thin-film phosphors after heating at various temperatures: (a) 800; (b) 1,000; (c) 1,200; and (d) 1,400 °C. Reproduced from [18] by permission of Elsevier



increased up to 3.7 μm by repeating the coating for 30 layers. Guo et al. [17] prepared Eu^{3+} - or Er^{3+} -doped Y_2O_3 films starting from metal acetates dissolved in methoxyethanol with the addition of diethylenetriamine. After stirring the mixture for 2 h, proper amount of water was added to the solution. The resultant solution was dip-coated on glass substrates and annealed typically at 600 °C. Cho et al. [18] utilized yttrium nitrate, europium nitrate, and citric acid as precursors in the sol-gel reactions. The nitrates were dissolved in 2-methoxyethanol, to which citric acid were added. A small amount of formaldehyde was also added as a drying control chemical additive. The solution was then spin-coated on (0001) plane-sapphire substrate. The films were finally annealed at temperatures between 700 and 1,400 °C for 2 h in air. Figure 29.2 shows cross-sectional SEM images of the films, after coating ten times, for various heating temperatures. The film thickness decreases slightly with increases in the heating temperature. The increased crystallinity of the films at higher temperatures leads to denser films. The CL and PL properties were found to be superior in these $Y_2O_3:Eu^{3+}$ thin films. Scintillating Eu^{3+} and Tb^{3+} co-doped Gd_2O_3 and Y_2O_3 films were prepared by the sol-gel method by Ramírez et al. [19]. Precursor solutions were prepared using gadolinium acetylacetonate ($Gd(acac)_3$) and yttrium acetylacetonate ($Y(acac)_3$). The gadolinium precursor was dissolved in anhydrous ethanol under vigorous stirring at 40 °C. The yttrium precursor was dissolved in anhydrous isopropanol at 60 °C. In both cases, the gadolinium and yttrium solutions were stirred for 2 h, and acetylacetonate was added as a chelating agent. $Eu(NO_3)_3$ and $Tb(NO_3)_3$ was dissolved in ethanol (for the Gd system) or isopropanol (for the Y system). A definite volume of each dopant was added to both gadolinium and yttrium acetylacetonate solutions. Thin films were prepared on silica glass substrates by the dip-coating technique, which was followed by drying at 100 °C to remove possible water content and the most volatile solvents. The films were then heat-treated at 300 °C to facilitate complete removal of the remaining organic residues and to promote the densification process, and finally at 700 °C for 4 h under a dry oxygen flux.

Luminescent properties are sensitive to impurities such as hydroxyl groups and carbonates which can receive energies from excited electrons as phonons or vibration energies. Therefore, special attention should be paid to heat treatments to remove them from any of the luminescent films when using the CSD technique.

29.3 Materials for Luminescent Thin Films

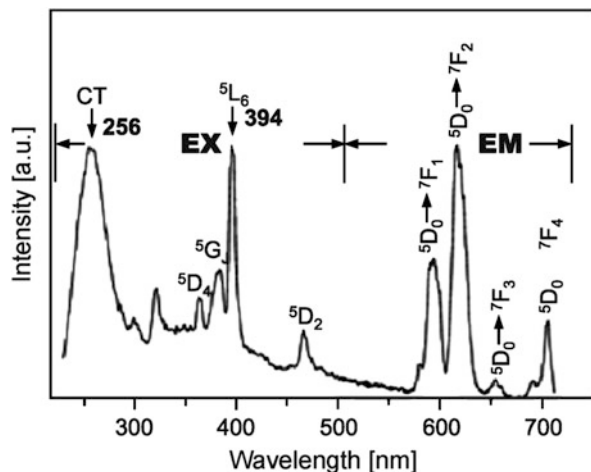
Metal oxide materials containing lanthanum and gadolinium can be good hosts for luminescent RE activators. The $4f$ orbital of La^{3+} is empty, and that of Gd^{3+} is just half-filled. These ions therefore do not impede the RE luminescence due to transitions of $4f$ electrons. Similarly to Y_2O_3 , Gd_2O_3 is a good host material and RE-doped Gd_2O_3 thin films have been prepared by CSD [20–24]. In contrast, La_2O_3 is not suitable for RE-doping because La_2O_3 is highly sensitive to moisture and carbon dioxide under atmospheric environment. Actually, La_2O_3 undergoes hydrolysis to form $\text{La}(\text{OH})_3$ easily, and therefore the surface of La_2O_3 should be coated by other stable materials to be used as the host [25]. CeO_2 is chemically and thermally stable and has also $4f$ -empty Ce^{4+} ions, which can be replaced by luminescent RE ions. However, the substitution of RE^{3+} for Ce^{4+} needs charge compensation by the generation of oxygen defects, which would influence the luminescent properties. Moreover, the crystal structure of CeO_2 is highly symmetric, which lowers probability of electronic transitions in doped Eu^{3+} ions. The CeO_2 -based phosphors are therefore limited to $\text{CeO}_2:\text{Sm}^{3+}$ showing a bright orange luminescence [26].

Table 29.1 summarizes various kinds of phosphor materials, developed as thin films by CSD, together with their precursors, substrates, coating methods, and final heat-treatment temperatures. Amorphous as well as crystalline $\text{CaO-SiO}_2:\text{Eu}^{3+}$ thin films were prepared by Meng et al. [28] because little attention had been paid to the preparation of luminescent silicate (such as Zn_2SiO_4 , CaSiO_3 , and MgSiO_3) films at that time. They showed that the films became thinner and their constituent particles became smaller with increasing the heat-treatment temperature. The crystalline phase was kilchoanite ($\text{Ca}_3\text{Si}_2\text{O}_7$) between 800–900 °C and changed to wollastonite ($\text{Ca}_3\text{Si}_3\text{O}_9$) at 1,100 °C due to reaction with the silica glass substrate. The elimination of OH groups in the films was nearly complete at 700 °C. Figure 29.3 shows PL excitation and emission spectra of the film heated at 800 °C. The broad excitation band centered around 250 nm is attributed to the charge transfer between the Eu^{3+} ions and the surrounding O^{2-} ions, while the narrow lines are due to the $f-f$ transitions in Eu^{3+} . The emissions are originated from the ${}^5\text{D}_0 \rightarrow {}^7\text{F}_J$ ($J = 0, 1, 2, 3, 4$) transitions of Eu^{3+} . The concentration quenching occurred when the Eu^{3+} doping level was above 6 mol% of Ca^{2+} . Partially substituted oxyapatite silicates, $\text{La}_8\text{M}_2(\text{SiO}_4)_6\text{O}_3:\text{Eu}^{3+}$ ($\text{M} = \text{Na}, \text{K}, \text{Mg}, \text{Ca}, \text{Sr}, \text{Y}, \text{and Gd}$), were also prepared as thin films by the sol-gel method [32]. All the oxyapatite films showed red luminescence upon excitation with UV light. Careful examinations of the structure and optical properties revealed that the excitation of Eu^{3+} could be modulated by changing the substituting M ions in the oxyapatites. Because of

Table 29.1 Typical synthetic conditions of various-types of luminescent thin films by CSD, summarized with materials, precursors, substrates, coating methods, and final heat-treatment temperatures

Material	Precursor	Substrate	Coating	Temp. (°C)	Refs.
BaTiO ₃ :Eu ³⁺	Ba(CH ₃ COO) ₂ , Ti(OC ₄ H ₉), EuCl ₃ , acetylacetone, acetic acid, water, i-propanol, polyvinylpyrrolidone	Quartz glass	Dip	700	[27]
CaO–SiO ₂ :Eu ³⁺	Ca(NO ₃) ₂ ·4H ₂ O, Eu(NO ₃) ₃ , TEOS, ethanol, water, HCl	Quartz glass	Dip	500–1,100	[28]
CaBi _{3.75} Nd _{0.25} Ti ₄ O ₁₅ :Eu ³⁺	Bi(NO ₃) ₃ ·5H ₂ O, Eu(NO ₃) ₃ ·5H ₂ O, Ca(NO ₃) ₂ ·4H ₂ O, Nd(NO ₃) ₃ ·6H ₂ O, Ti(OC ₄ H ₉) ₄ , acetic acid, acetylacetone	(111)Pt/Ti/SiO ₂ /Si	Spin	550–750	[29]
GdTaO ₄ :Eu ³⁺	Gd ₂ O ₃ , Eu ₂ O ₃ , 2-methoxyethanol, HNO ₃ , TaCl ₅ , HCl, polyvinylpyrrolidone	Quartz glass	Spin	1,200	[30]
HfO ₂ :RE ³⁺ (RE: Sm, Eu, Tb)	Hf(OC ₄ H ₉) ₄ , RECl ₃ , Hexane	Quartz glass	Dip	800	[31]
La ₁₀ (SiO ₄) ₆ O ₃ :Eu ³⁺	La(CH ₃ COO) ₃ ·1.5H ₂ O, Eu(CH ₃ COO) ₃ ·4H ₂ O, TFA, water, TEOS, ethanol	Quartz glass	Spin	1,000	[32]
LaPO ₄ :Ce ³⁺ , Tb ³⁺	La ₂ O ₃ , Tb ₄ O ₇ , Ce(NO ₃) ₃ ·6H ₂ O, HNO ₃ , water, ethanol, citric acid, (NH ₄) ₂ HPO ₄	Quartz glass	Dip	700–1,100	[33]
LiNbO ₃ :Eu ³⁺	LiOC ₂ H ₅ , Nb(OC ₂ H ₅) ₅ , Eu(ClO ₄) ₃ , polyvinyl alcohol, ethanol, acetic acid, water	z-Cut congruent LiNbO ₃	Dip	700	[34]
Y ₂ Sn ₂ O ₇ :Eu ³⁺	Y(CH ₃ COO) ₃ ·4H ₂ O, Eu(CH ₃ COO) ₃ ·4H ₂ O, SnCl ₄ ·5H ₂ O, ethanol, HNO ₃ , citric acid, polyethylene glycol	Quartz glass	Dip	500–1,000	[35]
YV _x P _{1-x} O ₄ :Eu ³⁺	Y ₂ O ₃ , Eu ₂ O ₃ , NH ₄ VO ₃ , (NH ₄) ₂ HPO ₄ , HNO ₃ , water, ethanol, citric acid, polyethylene glycol	Quartz glass, Si wafer	Dip	700–800	[36]
ZrO ₂ :RE ³⁺ (RE: Sm, Eu, Tb)	Zr(OC ₃ H ₇) ₄ , n-propanol, acetic acid, water, RE(NO ₃) ₃ , 2-methoxyethanol	Quartz glass	Dip	500	[37]

Fig. 29.3 PL excitation ($\lambda_{em} = 616$ nm) and emission ($\lambda_{ex} = 256$ nm) spectra of the $\text{CaO-SiO}_2:0.01\text{Eu}^{3+}$ luminescent film heated at 800°C . Reproduced from [28] by permission of the Royal Society of Chemistry



their high chemical stability and high transparency, the oxyapatite films are potentially used as luminescent thin-film components in optical devices.

A well-known ferroelectric BaTiO_3 was doped with Eu^{3+} and prepared as thin films [27]. The $\text{BaTiO}_3:\text{Eu}^{3+}$ films exhibited a crystalline perovskite phase by heating at 700°C within 2 h and presented good surface morphology. PL was observed due to the electronic transition of the Eu^{3+} ions with the predominant band at 615 nm. The obtained film thickness (approximately 500 nm) should be further optimized to be promising for luminescent applications because the emission intensity was not so strong. Ferroelectric Eu^{3+} -doped $\text{CaBi}_{3.75}\text{Nd}_{0.25}\text{Ti}_4\text{O}_{15}$ thin films were prepared by Wang et al. [29]. Polycrystalline $\text{CaBi}_{3.75-x}\text{Eu}_x\text{Nd}_{0.25}\text{Ti}_4\text{O}_{15}$ films with an Aurivillius phase were obtained up to $x = 0.5$. The films were dense and smooth with uniformly distributed grains at $x < 0.2$. Improved PL and ferroelectric properties were attained for the Eu^{3+} -doped films compared with an undoped film prepared under the same experimental conditions. The PL intensity increased with the heating temperature due to the improved crystallinity of the films. The ferroelectric properties of the films also showed that the $2P_r$ (remnant polarization) reached a maximum value of $30.7 \mu\text{C cm}^{-2}$ when x was 0.2.

Materials for optical coatings or planar waveguides were also doped with RE ions. ZrO_2 having chemical and photochemical stability, high refractive index, and low phonon energy was prepared as thin films and doped with Eu^{3+} , Tb^{3+} , and Sm^{3+} by Reisfeld et al. [37]. PL spectra showed an inhomogeneous broadening unlike the sharp lines in $\text{ZrO}_2:\text{Eu}^{3+}$ crystals, indicating that the films were of amorphous nature. For Eu^{3+} and Tb^{3+} , higher luminescent intensities were observed in the ZrO_2 films, compared with SiO_2 films at comparative concentration of the RE ions per optical path. This is due to the higher refractive index and higher dielectric constant of the ZrO_2 matrix. The $\text{ZrO}_2:\text{RE}^{3+}$ films thus obtained are suitable for active waveguides. The high density of ZrO_2 and HfO_2 makes them also attractive as scintillating materials. RE-doped HfO_2 films were prepared by Lange

et al. [31]. PL of the RE^{3+} ions in HfO_2 could be efficiently excited via the band-to-band excitation of the host. A significant increase in PL efficiency was observed as a result of the heat treatment. The evidence of multiphoton relaxation in the excitation spectra of the RE^{3+} luminescence above 14 eV suggested the possibility of using HfO_2 as a scintillator for the ionizing radiation.

RE orthovanadates (REVO_4) and orthophosphates (REPO_4) are known as important luminescent materials. Actually, $\text{YVO}_4:\text{Eu}^{3+}$ is commercially used as a red phosphor in cathode-ray tubes and high-pressure mercury lamps, and $\text{LaPO}_4:\text{Ce}^{3+}$, Tb^{3+} is used as a green phosphor in tricolor fluorescent lamps. The crystal structure of these compounds depends on the size of the RE ion either with the tetragonal zircon structure (xenotime type) or the monoclinic monazite structure [38]. Yu et al. [36] reported the sol-gel preparation of $\text{YV}_x\text{P}_{1-x}\text{O}_4:\text{Eu}^{3+}$ and $\text{RVO}_4:\text{Eu}^{3+}$ ($0 \leq x \leq 1$; R = Y, La, Gd) nanocrystalline thin films. The films began to crystallize at 400 °C and the crystallinity increased with increasing the heating temperature. Complete solid solutions were formed between YVO_4 and YPO_4 ($0 \leq x \leq 1$) when heated at 800 °C. It was shown that the x values in the $\text{YV}_x\text{P}_{1-x}\text{O}_4:\text{Eu}^{3+}$ films had a great influence on the luminescence properties of Eu^{3+} , such as excitation mechanisms, emission intensity, color, and decay behavior. At $x = 0$, the main excitation band of Eu^{3+} was observed between 200 and 250 nm, which corresponded to the $\text{O}^{2-}-\text{Eu}^{3+}$ charge transfer. At $x = 0.1$, a new broad excitation band from 250 to 330 nm appeared and it became higher and wider with increasing the x values. This band is ascribed to a charge transfer occurring inside the VO_4^{3-} ion from the oxygen ligands to the central vanadium atom. The energy of the excited state is then transferred to the Eu^{3+} ion, resulting in the stronger red emission. The enhancement of the excitation is also known in LaPO_4 codoped with Ce^{3+} and Tb^{3+} . That is, the energy absorbed by the Ce^{3+} ion can be transferred to the Tb^{3+} ion which subsequently shows green emissions. Yu et al. [33] also prepared $\text{LaPO}_4:\text{Ce}^{3+},\text{Tb}^{3+}$ nanocrystalline thin films by the sol-gel method. The films heated below 700 °C were amorphous, while those heated at 700 °C or higher were crystallized and the crystallinity increased with the temperature. The excitation spectrum of the film for the Tb^{3+} emission (543 nm) showed two strong peaks at 256 and 276 nm due to the Ce^{3+} excitation. It was suggested that the energy transfer efficiency from Ce^{3+} to Tb^{3+} depended strongly on their doping concentrations in LaPO_4 .

Eu^{3+} -activated GdTao_4 is also one of the promising candidates for X-ray imaging and flat panel display due to its high density, high luminescence efficiency, stable chemical properties, strong irradiation hardness, and good X-ray absorption. Liu et al. [30] reported the preparation of $\text{GdTao}_4:\text{Eu}^{3+}$ films by the sol-gel method. Transparent, relatively thick $\text{GdTao}_4:\text{Eu}^{3+}$ films were obtained from solutions containing polyvinylpyrrolidone (PVP). The critical thickness of the film (the maximum thickness achievable without crack formation via non-repetitive deposition) was found to be 0.8 μm . The thick $\text{GdTao}_4:\text{Eu}^{3+}$ films exhibited excellent X-ray excited luminescence performances, which would find a potential application in high-resolution X-ray imaging systems.

In preparing luminescent films of complex metal oxides having two or more kinds of cations, a sol–gel technique called a Pechini method is often employed to facilitate homogeneous distribution of cations and viscosity suitable for coating. This method is based on the preparation of solutions from inorganic salts as cation sources, citric acid as a chelating agent, and polyethylene glycol as a cross-linking agent. The above-mentioned $YV_xP_{1-x}O_4:Eu^{3+}$ films were prepared by the Pechini method. Another example is found in $Y_2Sn_2O_7:Eu^{3+}$ thin films [35]. RE acetates and $SnCl_4$ were added to ethanol containing nitric acid. Citric acid and polyethylene glycol were mixed with the solutions for coating. The resultant films showed the occurrence of the multiband orange-red luminescence at a single-wavelength excitation. These spectral features provided the chromaticity of a region between pink and yellowish pink in the Commission Internationale d’Eclairage (CIE) diagram, which would be adequate to use as a new reddish component in reproducing natural light in optical devices.

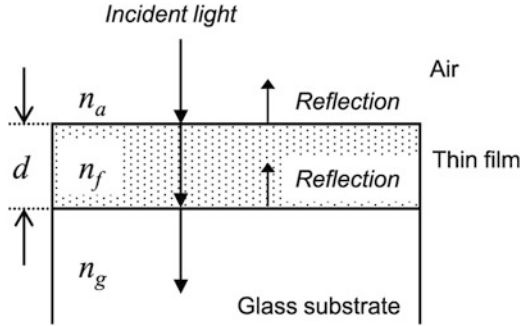
Polymer additives such as PVP [27, 30] and polyvinyl alcohol (PVA) are useful in preparing thin or thick films. Takahashi et al. [34] prepared $LiNbO_3:Eu^{3+}$ thick films on z-cut congruent $LiNbO_3$ wafers by the sol–gel method using PVA. (006)-oriented $LiNbO_3:Eu^{3+}$ epitaxial layers with parallel epitaxial relationships could be grown on the z-cut $LiNbO_3$ wafer. It was found that the refractive index of the $LiNbO_3:Eu^{3+}$ films decreased and the luminescence intensities increased with increases in the Eu^{3+} concentration. The incorporation of the RE ions into $LiNbO_3$ is challenging because of greater difference in the valence states and the ionic radii between Li^+ , Nb^{5+} , and RE^{3+} . Analysis of the $LiNbO_3:Eu^{3+}$ films with Raman spectroscopy indicated that Eu^{3+} might occupy the Nb^{5+} site in the $LiNbO_3$ lattice.

29.4 Optics of Luminescent Thin Films

Transparency is the most important optical property of the luminescent thin films. As shown in Table 29.1, the substrate used in the film fabrication is mostly the quartz (SiO_2) glass. This is because the quartz glass itself is highly transparent in a wide range of wavelengths. In addition, the quartz glass is thermally stable and inert, which is necessary for the high-temperature treatment to crystallize the luminescent thin films sufficiently. Generally, the crystallinity is improved and the luminescent intensity is increased with increasing the heat-treatment temperature. Even when only low-temperature treatments are necessary, the use of other cheaper glasses such as borosilicate or soda-lime glasses is to be avoided because they show weak PL upon irradiation with UV.

Taking account of the interaction between light and solid materials, nothing is completely transparent in air. The speed of light is decreased when travelling inside materials. The ratio of the speed in vacuum (c_0) and that in materials (c) is defined as the refractive index ($n = c_0/c$), when the materials do not absorb light. At the air/glass interface with a step change of the refractive index, a small portion of the

Fig. 29.4 Incidence of light from air into a film coated on a glass substrate



incident light is reflected back, causing a decrease in optical transmittance. This is called Fresnel reflection and reflectance (R) is given by Eq. (29.1),

$$R = (n_a - n_g)^2 / (n_a + n_g)^2 \quad (29.1)$$

for the near-normal incidence of light, where n_a and n_g are the refractive index of air and the glass, respectively. If we take $n_g = 1.47$ for the quartz glass in the visible region, reflectance in air ($n_a = 1$) is 0.0362 for one side of the glass surface. When thin films are coated on glass substrates as depicted in Fig. 29.4, reflectance is changed depending on the refractive index of films (n_f). For $n_f < n_g$ with single-component films, reflectance is reduced and complete anti-reflection (AR) is attained under following conditions [Eqs. (29.2) and (29.3)],

$$n_f^2 = n_a n_g \quad (29.2)$$

$$n_f d = \lambda / 4 \quad (29.3)$$

where d is the film thickness and λ is the wavelength of incident light [39]. For $n_f > n_g$ commonly with luminescent thin films (for example, $n_f = 1.9$ with Y_2O_3 [17]), reflectance is increased and hence transparency is degraded against the environmental light.

When materials absorb light, their refractive index should be expressed as [Eq. (29.4)],

$$N = n + i\kappa \quad (29.4)$$

where N is the complex index of refraction and κ is the extinction coefficient. The reflectance is then influenced by κ with formula [Eq. (29.5)],

$$R = \left\{ (n_a - n)^2 + \kappa^2 \right\} / \left\{ (n_a + n)^2 + \kappa^2 \right\} \quad (29.5)$$

The situation is rather complicated in absorption of luminescent materials. In RE-doped phosphors, for example, absorption related to the RE ions is located at

longer wavelength regions and is relatively small. Large absorption of host lattices occurs at shorter UV wavelength regions. Reflectance of luminescent thin films therefore depends greatly on wavelengths of the incident light.

Two other optical effects are also greatly concerned in luminescent thin films. One is the appearance of interference fringes in thicker films, which can be observed as waving optical transmission spectra. Although increase of the film thickness is often attempted to enhance luminescence, it also results in the interference and sometimes the colorization. The other is the occurrence of total internal reflection of emissions inside luminescent thin films. Total internal reflection takes place when the light is traveling within a more optically dense medium towards a less optically dense medium. In the $\text{Y}_2\text{O}_3:\text{Eu}^{3+}$ film on the quartz glass, for instance, total internal reflection of Eu^{3+} red emissions occurs both at the air/film interface and the film/glass interface. Consequently, the extraction efficiency of emissions in the near-normal direction is not so high in luminescent thin films, which is always the major concern. The requirement of transparency or reflection is subject to how luminescent thin films are practically used in optical or optoelectronic devices, as described next.

29.5 Applications

29.5.1 Active Waveguides

RE-doped planar waveguides have been explored as optical amplifiers and new laser sources for integrated optic devices. In waveguides, light is launched from the edge and travels through films along the direction parallel to the substrate surface based on internal total reflection. High-quality films having high refractive indices are required for efficient luminescence as well as sufficient waveguiding performance in such applications. The sol-gel method has been adopted to prepare $\text{TiO}_2:\text{Er}^{3+}$ films [40], $\text{BaTiO}_3:\text{Er}^{3+}$ films [41], $\text{Al}_2\text{O}_3:\text{Er}^{3+}$ films [42], $\text{SiO}_2\text{-HfO}_2:\text{Er}^{3+}$, Yb^{3+} films [43], $\text{Y}_2\text{O}_3:\text{Tb}^{3+}$ films [44], $\text{Y}_3\text{Al}_5\text{O}_{12}:\text{Tb}^{3+}$ films [45], $\text{Y}_3\text{BO}_6:\text{Eu}^{3+}$ films [46], $\text{ZrO}_2:\text{Eu}^{3+}$ films [47], and $\text{Lu}_2\text{O}_3:\text{Eu}^{3+}$ films [48]. Generally, crystalline films are superior to glass or amorphous films in terms of the dispersion of doped RE ions. The Er^{3+} -doping aims at optical amplification at $1.53\ \mu\text{m}$, following the practically used Er^{3+} -doped fiber amplifier.

The sol-gel method offers advantages for the fabrication of planar waveguides as follow. Amorphous or nanocrystalline thin films can be obtained to suppress light scattering loss. The refractive index can be tuned by changing solution and film compositions. Patterning of films at the gel state is possible for fabricating channel waveguides. The success of the sol-gel-derived films as active waveguides depends on exact control of the thickness up to a micrometer scale without the crack formation [43].

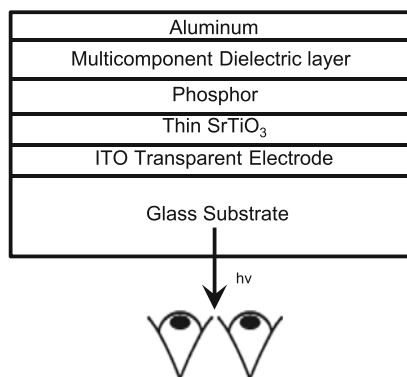
29.5.2 Displays

For display application, luminescent thin films have been believed to exhibit higher contrast and resolution, superior thermal conductivity as well as a high degree of uniformity and better adhesion, since cathodoluminescent $\text{Y}_2\text{SiO}_5:\text{Tb}^{3+}$ films were prepared on fused silica and sapphire substrates using the sol-gel method by Rabinovich et al. [49]. The current state-of-the-art technology for display devices includes plasma display panels (PDP), liquid crystal display (LCD), field emission display (FED), inorganic EL display, and organic EL display (also called organic light-emitting diode; OLED). PDP employs fine powder phosphors which is excited by VUV light from discharged Ne/Xe gas. LCD utilizes light originating from phosphors mounted in fluorescent lamps or white LEDs. Accordingly, luminescent thin films described in this section are intended as those applied in FED and inorganic EL display.

FED is constructed by a planar substrate with an array of field emitters, a conductive extraction grid (gate), and an anode screen mounted parallel to the cathode array [50, 51]. The anode screen is composed of a glass plate coated with a transparent conductive material and a cathodoluminescent phosphor layer. As used in cathode-ray tubes, efficient cathodoluminescent phosphors have been metal sulfides or selenides so far. However, FED phosphors should be stable against the electron beam and hence sulfides are not appropriate because they decompose to generate sulfur which degrades field emitters. In this sense, oxide-based phosphors having excellent chemical and thermal stabilities are quite promising. Pang et al. [20, 52] prepared nanocrystalline $\text{Gd}_2\text{O}_3:\text{RE}^{3+}$ (RE = Eu, Dy, Sm, Er) and $\text{Y}_2\text{O}_3:\text{Eu}^{3+}$ phosphor films by the Pechini sol-gel process. These phosphor films could be patterned into homogeneous and defect-free film stripes with different widths (5–50 μm) by a soft lithography technique (micro-molding in capillaries). In a laboratory scale, thin-film phosphors are not always evaluated with cathodoluminescent properties because of particularity in measurement methods and apparatus. Zhang et al. [53] reported red-green-blue (RGB) full-color displaying $\text{Y}_2\text{SiO}_5:\text{RE}^{3+}$ (RE = Eu, Tb, Ce) thin films prepared from TEOS, $\text{Y}(\text{NO}_3)_3$, and RECl_3 by the sol-gel method. PL of the films were evaluated and discussed with the CIE color coordinate. Recently, Li-doping in phosphors has attracted attention because it can enhance luminescent properties [54]. Cho et al. [55] investigated the cathodoluminescent brightness of sol-gel derived, Li-doped $\text{Y}_2\text{O}_3:\text{RE}^{3+}$ (RE = Eu, Tb, Tm) RGB thin-film phosphors to assess their usefulness in oxide RGB triads for FED.

A conventional inorganic thin-film EL (TFEL) display was constructed with metal sulfide phosphors such as blue-emitting $\text{SrS}:\text{Ce}^{3+}$, green-emitting $\text{ZnS}:\text{Tb}^{3+}$, yellow-emitting $\text{ZnS}:\text{Mn}^{2+}$, red-emitting $\text{CaS}:\text{Eu}^{2+}$, and so on [56]. The problem is that such sulfide phosphors suffer from the lack of primary color emissions and chemical instability, especially against moisture. In recent years, chemically stable metal oxide phosphors have been developed for TFEL devices [57]. $\text{Ga}_2\text{O}_3:\text{Mn}^{2+}$ thin films were prepared by the sol-gel process using gallium acetylacetonate and MnCl_2 [58, 59]. The films had to be post-annealed in an Ar gas atmosphere at

Fig. 29.5 Structure of the TFEL device using three layer dielectrics. Reproduced from [60] by permission of Elsevier



approximately 1,020 °C to improve the luminescent properties. Higher luminance was always obtained in TFEL devices using the sol-gel-derived $\text{Ga}_2\text{O}_3:\text{Mn}^{2+}$ thin films rather than films deposited by magnetron sputtering for comparison. The difference in obtained luminance was explained with the crystallinity and Mn^{2+} content of the thin-film emitting layers. Figure 29.5 shows one of the structures of TFEL devices on glass substrates which require thin-film dielectric layers [60]. The dielectric should have high breakdown strength and high dielectric constant to achieve a high charge transfer through the EL phosphor with low voltage operation. Commercialization of TFEL with oxide phosphors for flat panel displays and lamps on glass substrates depends on the development of phosphors that may be deposited at temperatures of 700 °C or lower.

29.5.3 X-ray Imaging

X-ray phosphors, sometimes referred to as scintillators, are inorganic materials used in medical X-ray imaging applications. X-ray phosphors must be a good absorber of X-rays and actually are high-density compounds containing elements with high atomic numbers such as CaWO_4 , YTaO_4 , $\text{Gd}_2\text{O}_2\text{S}$, and LaOBr [61]. High-resolution X-ray imaging requires thin films of dense materials with high emission yield under X-ray excitation. Murillo et al. [62] prepared polycrystalline $\text{Gd}_2\text{O}_3:\text{Eu}^{3+}$ and $\text{Lu}_2\text{O}_3:\text{Eu}^{3+}$ thin films by the sol-gel method. Scintillation performances of the films revealed a high emission yield with well adapted absorption coefficients for specific X-ray energy ranges. $\text{Gd}_2\text{O}_3:\text{Eu}^{3+}$ was preferable to $\text{Lu}_2\text{O}_3:\text{Eu}^{3+}$ between 53 and 63 keV and for other energies Lu_2O_3 was a better host lattice. A new general scheme based on the use of alkoxide chemistry was proposed for the preparation of various scintillating materials including Ce^{3+} -doped LuBO_3 , GdBO_3 , LuPO_4 , and Lu_2SiO_5 [63].

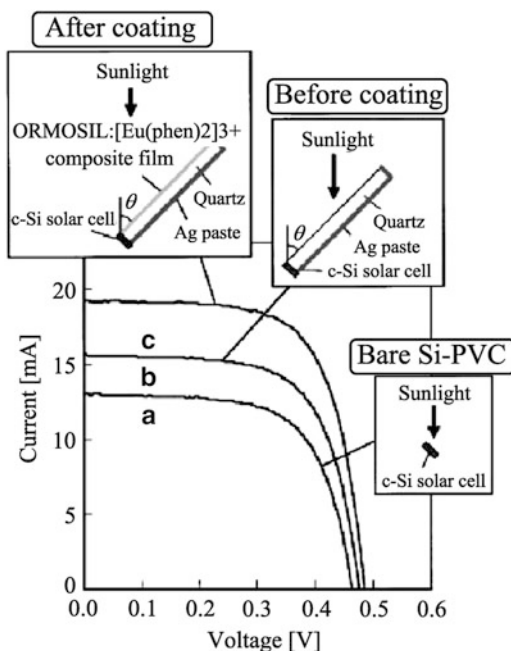
29.5.4 Solar Energy Applications

Applications of luminescent thin films to solar energy conversion technology have been explored for many years. One way of enhancing the performance of solar cells is to concentrate solar irradiance, particularly that part corresponding to high spectral sensitivity of cells. The luminescent solar concentrator (LSC) allows sunlight to be concentrated by way of wavelength conversion. The typical structure of LSC is a transparent glass or plastic plate containing luminescent species such as phosphors and organic dyes [64, 65]. Sunlight enters the upper face of the plate and is partially absorbed by luminescent species. A fraction of emission light is trapped by total internal reflection. Successive reflections transport the emission light to edge-mounted solar cells. Approximately 75–80 % of the emission is trapped by total internal reflection in the plate having the refractive index of nearly 1.5. The concentration factor is proportional to the surface/edge ratio and the optical efficiency of the plate. The advantages of LSC are summarized as follows [66]. LSC can collect both direct and diffuse light. A good heat dissipation of non-utilized energy is attained by the large area of the LSC plate in contact with air. Tracking the sun is unnecessary. The luminescent species can be chosen to allow matching of the concentrated light to the maximum sensitivity of solar cells.

Luminescent thin films deposited on transparent glass plates can also be used as LSC. The advantage of luminescent thin films having optical contact with the transparent plate is that the emission from the thin film is trapped in the plate while parasitic losses due to self-absorption and scattering from impurities can be greatly reduced as compared to luminescent bulk plates [67]. The thin-film LSC has been mostly composed of organic materials or organic–inorganic composites. The former and the latter correspond to polymer films [68] and organically modified sol–gel films [67], respectively, doped with dyes. Machida et al. [69] prepared thin films of organically modified-silicates (ormosil) incorporated with $[\text{Eu}(\text{phen})_2]^{3+}$ complex ions. LSC panels made by the films ($n \approx 1.40$) on quartz plates showed 10–15 % increases in the photovoltaic current of crystalline Si solar cells by the luminescence of Eu^{3+} , as shown in Fig. 29.6.

Another approach for improving the sunlight harvesting efficiency is the effective use of layered thin-film structures found in solar cells. That is, transparent phosphor films are to be inserted in the layered structure. The performance is expected to be enhanced by down-conversion of high energy UV photons to less energetic visible photons which are absorbed by Si solar cells. Chung et al. [70] prepared phosphor coatings consisting of $\text{Y}_2\text{O}_3:\text{Eu}^{3+}$, $\text{Y}_2\text{O}_2\text{S}:\text{Eu}^{3+}$, 3,9–perylene-dicarboxylic acid bis(2–methylpropyl) ester, and tetraphenylporphyrin dispersed in either polyvinyl alcohol or polymethylmethacrylate. Cells coated with $\text{Y}_2\text{O}_3:\text{Eu}^{3+}$ or $\text{Y}_2\text{O}_2\text{S}:\text{Eu}^{3+}$ showed an increased conversion efficiency by up to a factor of 14 under the UV illumination. Fukuda et al. [71] reported polymer coatings containing sol–gel glass encapsulated $\text{Eu}(\text{TTA})_3\text{phen}$. The structure of the cell was cover glass/ethylene vinyl acetate (EVA)/wavelength conversion film

Fig. 29.6 Current–voltage curves of (a) the bare c-Si cell, the LSC-connected c-Si cell; (b) before; and (c) after coating with the ormosil: $[\text{Eu}(\text{phen})_2]^{3+}$ (3 mol%) film. Reproduced from [69] by permission of Elsevier

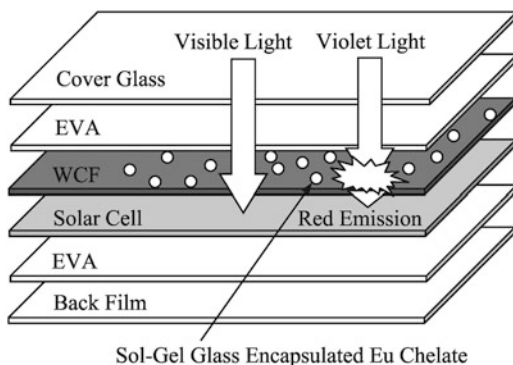


(WCF)/Si cell/EVA/back-film, as shown in Fig. 29.7. The short circuit current was increased by the coatings due to a successful wavelength conversion.

Incorporation of transparent, RE-doped inorganic luminescent thin films, which appear frequently in this chapter, is currently limited by their high crystallization temperatures, lower absorption coefficient against the solar irradiance, and higher refractive indices causing surface reflection. Serious challenges therefore need to be addressed before inorganic phosphor thin films will be applied to solar cells. In this sense, highly transparent metal fluorides with lower refractive indices would be promising. CaF_2 , SrF_2 , BaF_2 , and KMgF_3 were doped with RE ions and their effectiveness were investigated by putting on top of c- and a-Si and CdS/CdTe solar cells by Kawano et al. [72–74]. Increases of conversion efficiencies could be observed by doping Eu^{2+} and Sm^{2+} into the fluoride crystals. $\text{NaYF}_4:\text{Er}^{3+}$ up-conversion phosphors were attached to the rear of a bifacial Si solar cell to enhance its sensitivity in the near-infrared [75]. A close match between spectral features of the external irradiance and the phosphor absorption was consistent with the energy transfer up-conversion process. Detailed discussion on spectral converters based on RE luminescence of both down-conversion and up-conversion has been made recently by Ende et al. [76].

As to metal oxide thin films, PL in $\text{Y}_2\text{O}_3:\text{Yb}^{3+}$ thin films grown on sapphire substrates were investigated by Lu and Chen [77]. Luminescence was enhanced using arrays of gold nanoparticles in the wavelength range from 970 to 1,070 nm. This enhancement was attributed to the resonance of localized surface plasmon resonance modes of the Au nanoparticles with multiple optical transition lines of

Fig. 29.7 A schematic configuration of the solar cell in combination with the wavelength conversion film (WCF). The sol-gel glass encapsulated Eu (TTA)₃phen was mixed with the WCF. Reproduced from [71] by permission of Elsevier



the doped Yb^{3+} ions. Solar cell photon harvesting through efficient frequency shifting was then discussed considering the demonstrated benefits of broad spectral response.

Attempts to suppress surface reflection were made by designing multi-layered anti-reflective (AR) coatings including a $\text{Y}_2\text{O}_3:\text{Eu}^{3+}$, Bi^{3+} luminescent layer [78]. Transparent coatings consisting of a $\text{Y}_2\text{O}_3:\text{Eu}^{3+}$, Bi^{3+} layer (bottom) and a porous SiO_2 layer (top) with the high and the low refractive index, respectively, were fabricated on quartz glass substrates by a sol-gel dip-coating method. Bi-layer structured coatings could reduce Fresnel reflection considerably, showing an excellent AR effect. Moreover, PL intensity from the $\text{Y}_2\text{O}_3:\text{Eu}^{3+}$, Bi^{3+} layer was increased by stacking the porous SiO_2 layer. This phenomenon was explained with increased absorption of excitation light by decreasing Fresnel reflection at the surface and reduced total internal reflection of emission light by easing the difference in the refractive index at the interface.

Another approach is fabricating phosphor thin films with surface nanostructures like the moth-eye structure. Recently, alumina (Al_2O_3) films with pseudo moth-eye structures have been reported by using a sol-gel process and a subsequent hot water treatment [79]. The hot water treatment is very simple and a low cost process with immersing films in hot water. The resultant alumina films had a flower-like structure which worked as AR coatings since the structure exhibited a density gradient from the surface to the substrate. AR phosphor coatings having disordered surface nanostructures have also been fabricated by the sol-gel dip coating method and a subsequent hot water treatment [80]. Thin films of a $\text{Bi}^{3+}, \text{Eu}^{3+}$ -codoped YVO_4 red phosphor were prepared from precursor solutions containing basic aluminum acetate. The hot water treatment of the films resulted in a considerable increase of transmittance and its smaller angular dependence, which could generate the AR effect. The hot water treatment also brought a remarkable change in the surface as well as the cross-section structure in the aluminum-added $\text{YVO}_4:\text{Bi}^{3+}, \text{Eu}^{3+}$ films. The film density and hence the refractive index were gradually changed like a pseudo moth-eye structure, which explained the occurrence of the AR effect. Photoluminescence of the $\text{YVO}_4:\text{Bi}^{3+}, \text{Eu}^{3+}$ films could be enhanced by the AR

effect due to the suppression of surface Fresnel reflection of incident light and total internal reflection of emitted light.

29.6 Concluding Remarks

This chapter gave detailed instructions on how to design and synthesize luminescent thin films by the CSD techniques. Recent advances in applications to active waveguides, displays, X-ray imaging systems, and solar cells were also described to emphasize the importance of luminescent thin films for integrated optical and optoelectronic devices. Particular attention was paid to optical properties characteristic of transparent thin films. We should be concerned about surface Fresnel reflection, total internal reflection, and interference occurring in thin films, in addition to absorption (excitation) and emission related to luminescence. Mostly the substrate used for depositing luminescent thin films is quartz glass because of requirements for high transparency and high chemical and thermal stability. In specific applications, however, the substrates should be other materials such as Si wafers, oxide single crystals, low-cost glass plates, and even plastics. The success of luminescent thin films is therefore dependent on the development of CSD that can realize true “low-temperature” processes (cp. Chap. 18).

References

1. Blasse G, Grabmaier BC (1994) Luminescent materials. Springer, Berlin
2. Vanheusden K, Warren WL, Seager CH, Tallant DR, Voigt JA, Gnade BE (1996) Mechanisms behind green photoluminescence in ZnO phosphor powders. *J Appl Phys* 79:7983
3. Jüstel T, Nikol H, Ronda C (1998) New developments in the field of luminescent materials for lighting and displays. *Angew Chem Int Ed* 37:3084
4. Kenyon AJ (2002) Recent developments in rare-earth doped materials for optoelectronics. *Prog Quant Electron* 26:225
5. Rao PR (1996) Growth and characterization of $Y_2O_3:Eu^{3+}$ phosphor films by sol-gel process. *Solid State Commun* 99:439
6. Brinker CJ, Scherer GW (1990) Sol-gel science. Academic, New York, NY
7. Pierre AC (1998) Introduction to sol-gel processing. Kluwer, Boston
8. Sakka S (ed) (2005) Handbook of sol-gel science and technology; processing, characterization and applications. Kluwer, Boston
9. Slooff LH, de Dood MJA, van Blaaderen A, Polman A (2001) Effects of heat treatment and concentration on the luminescence properties of erbium-doped silica sol-gel films. *J Non-Cryst Solids* 296:158
10. Bullen C, Mulvaney P, Sada C, Ferrari M, Chiasera A, Martucci A (2004) Incorporation of a highly luminescent semiconductor quantum dot in ZrO_2-SiO_2 hybrid sol-gel glass film. *J Mater Chem* 14:1112
11. Nass R, Schmidt H, Arpac E (1990) Synthesis and properties of transparent ZrO_2 containing SiO_2 polymethacrylate polymers. In: Mackenzie JD, Ulrich DR (eds) Proceedings of SPIE: sol-gel optics, vol 1328. The International Society for Optical Engineering, Bellingham, p 258

12. Fujihara S, Koji S, Kimura T (2004) Structure and optical properties of (Gd, Eu)F₃-nanocrystallized sol-gel silica films. *J Mater Chem* 14:1331
13. Fujihara S, Sasaki C, Kimura T (2001) Crystallization behavior and origin of *c*-axis orientation in sol-gel-derived ZnO:Li thin films on glass substrates. *Appl Surf Sci* 180:341
14. Fujihara S, Ogawa Y, Kasai A (2004) Tunable visible photoluminescence from ZnO thin films through Mg-doping and annealing. *Chem Mater* 16:2965
15. Ogawa Y, Fujihara S (2005) Band-gap modification and tunable blue luminescence of wurtzite Mg_xZn_{1-x}O thin films. *Phys Stat Sol (a)* 202:1825
16. Ogawa Y, Fujihara S (2007) Blue luminescence of MgZnO and CdZnO films deposited at low temperatures. *J Electrochem Soc* 154:J283
17. Guo H, Zhang W, Lou L, Brioude A, Mugnier J (2004) Structure and optical properties of rare earth doped Y₂O₃ waveguide films derived by sol-gel process. *Thin Solid Films* 458:274
18. Cho JY, Ko KY, Do YR (2007) Optical properties of sol-gel derived Y₂O₃:Eu³⁺ thin-film phosphors for display applications. *Thin Solid Films* 515:3373
19. Ramírez AJM, Murillo AG, Romo FJC, Salgado JR, Luyer CL, Chadeyron G, Boyer D, Palmerin JM (2009) Preparation and studies of Eu³⁺ and Tb³⁺ co-doped Gd₂O₃ and Y₂O₃ sol-gel scintillating films. *Thin Solid Films* 517:6753
20. Pang ML, Lin J, Fu J, Xing RB, Luo CX, Han YC (2003) Preparation, patterning and luminescent properties of nanocrystalline Gd₂O₃:A (A = Eu³⁺, Dy³⁺, Sm³⁺, Er³⁺) phosphor films via Pechini sol-gel soft lithography. *Opt Mater* 23:547
21. Gu M, Qiu LQ, Liu XL, Zhang R, Xu X (2005) Luminescence properties of Gd₂O₃:Eu³⁺ sol-gel thin films. *Spectrosc Spec Anal* 25:1190
22. Liu XL, Liu BJ, Gu M, Xiao LH, Xu X (2006) Highly enhanced photoluminescence and X-ray excited luminescence of Li doped Gd₂O₃:Eu³⁺ thin films. *Solid State Commun* 137:162
23. Liu XL, Zhou F, Gu M, Huang S, Liu B, Ni C (2008) Fabrication of highly *a*-axis-oriented Gd₂O₃:Eu³⁺ thick film and its luminescence properties. *Opt Mater* 31:126
24. Murillo AG, Ramírez AJM, Romo FJC, Hernández MG, Crespo MAD (2009) Synthesis, structural and optical studies of sol-gel Gd₂O₃:Eu³⁺, Tb³⁺ films. *Mater Lett* 63:1631
25. Hosono E, Fujihara S (2004) Fabrication and photoluminescence of chemically stable La₂O₃:Eu³⁺-La₂Sn₂O₇ core-shell-structured nanoparticles. *Chem Commun* 2062
26. Fujihara S, Oikawa M (2004) Structure and luminescent properties of CeO₂:rare earth (RE = Eu³⁺ and Sm³⁺) thin films. *J Appl Phys* 95:8002
27. Hernández MG, Murillo AG, Romo FJC, Viguera DJ, Chadeyron G, De la Rosa E, Boyer D (2009) Eu-doped BaTiO₃ powder and film from sol-gel process with polyvinylpyrrolidone additive. *Int J Mol Sci* 10:4088
28. Meng QG, Lin J, Fu LS, Zhang HJ, Wang SB, Zhou YB, Zhou YH (2001) Sol-gel deposition of calcium silicate red-emitting luminescent films doped with Eu³⁺. *J Mater Chem* 11:3382
29. Wang WC, Zheng HW, Liu YF, Li ZH, Zhang T, Zhang WF (2009) Photoluminescence and ferroelectric properties of sol-gel-grown Eu-doped CaBi₄Ti₄O₁₅:Nd films. *J Phys D: Appl Phys* 42:105411
30. Liu XL, Han K, Gu M, Huang S, Liu B, Ni C (2009) Optical properties of GdT₂O₇:Eu³⁺ thick films prepared from a PVP-containing solution. *Appl Surf Sci* 255:4680
31. Lange S, Kiisk V, Reedo V, Kirm M, Aarik J, Sildos I (2006) Luminescence of RE-ions in HfO₂ thin films and some possible applications. *Opt Mater* 28:1238
32. Otsuka Y, Fujihara S (2007) Transparent and luminescent thin films of partially substituted La₁₀(SiO₄)₆O₃:Eu³⁺ apatite-type silicates. *J Electrochem Soc* 154:J335
33. Yu M, Lin J, Fu J, Han YC (2003) Sol-gel fabrication, patterning and photoluminescent properties of LaPO₄:Ce³⁺, Tb³⁺ nanocrystalline thin films. *Chem Phys Lett* 371:178
34. Takahashi M, Iyoda K, Maeda Y, Miyauchi T, Ohkido S, Sato S, Wakita K (2008) Preparation and characterization of Eu-doped LiNbO₃ films prepared by the sol-gel method. *J Appl Phys* 103:034101
35. Fujihara S, Tokumo K (2005) Multiband orange-red luminescence of Eu³⁺ ions based on the pyrochlore-structured host crystal. *Chem Mater* 17:5587

36. Yu M, Lin J, Wang SB (2005) Effects of x and R^{3+} on the luminescent properties of Eu^{3+} in nanocrystalline $YV_xP_{1-x}O_4:Eu^{3+}$ and $RVO_4:Eu^{3+}$ thin-film phosphors. *Appl Phys A* 80:353
37. Reisfeld R, Zelner M, Patra A (2000) Fluorescence study of zirconia films doped by Eu^{3+} , Tb^{3+} and Sm^{3+} and their comparison with silica films. *J Alloys Compd* 300–301:147
38. Fidancev EA, Hölsä J, Blaise ML, Porchert P (1991) Simulation of the energy level scheme of Nd^{3+} and Eu^{3+} ions in rare-earth orthovanadates and phosphates. *J Phys Condens Matter* 3:6829
39. Pulker HK (1999) *Coatings on glass*. Elsevier, Amsterdam
40. Bahtat A, Lucas MCM, Jacquier B, Varrel B, Bouazaoui M, Mugnier J (1997) IR luminescence decays and radiative lifetime of the $^4I_{13/2}$ level in Er^{3+} doped sol-gel TiO_2 planar waveguides. *Opt Mater* 7:173
41. Yang XD, Guo H, Chen K, Zhang WP, Lou LR, Yin M (2004) Er^{3+} doped $BaTiO_3$ optical-waveguide thin films elaborated by sol-gel method. *J Rare Earths* 22:36
42. Wang XJ, Lei MK (2005) Preparation and photoluminescence of Er^{3+} -doped Al_2O_3 films by sol-gel method. *Thin Solid Films* 476:41
43. Sigoli FA, Gonçalves RR, Messaddeq Y, Ribeiro SJL (2006) Erbium- and ytterbium-doped sol-gel SiO_2 - HfO_2 crack-free thick films onto silica on silicon substrate. *J Non-Cryst Solids* 352:3463
44. Wu YC, Garapon C, Bazzi R, Pillonnet A, Tillement O, Mugnier J (2007) Optical and fluorescent properties of Y_2O_3 sol-gel planar waveguides containing Tb^{3+} doped nanocrystals. *Appl Phys A* 87:697
45. Potdevin A, Lechevallier S, Chadeyron G, Caperaa N, Boyer D, Mahiou R (2009) Waveguiding terbium-doped yttrium aluminum garnet coatings based on the sol-gel process. *Thin Solid Films* 517:4610
46. Boyer D, Chadeyron GB, Mahiou R, Brioude A, Mugnier J (2003) Synthesis and characterization of sol-gel derived $Y_3BO_6:Eu^{3+}$ powders and films. *Opt Mater* 24:35
47. Ehrhart G, Bouazaoui M, Capoen B, Ferreiro V, Mahiou R, Robbe O, Turrell S (2007) Effects of rare-earth concentration and heat-treatment on the structural and luminescence properties of europium-doped zirconia sol-gel planar waveguides. *Opt Mater* 29:1723
48. Murillo AG, Romo FJC, Luyer CL, Ramírez AJM, Hernández MG, Palmerin JM (2009) Sol-gel elaboration and structural investigations of $Lu_2O_3:Eu^{3+}$ planar waveguides. *J Sol-Gel. Sci Technol* 50:359
49. Rabinovich EM, Shmulovich J, Fratello VJ (1987) Sol-gel deposition of $Tb^{3+}:Y_2SiO_5$ cathodoluminescent layers. *Am Ceram Soc Bull* 66:1505
50. Yoshida Y, Ishizuka A, Makishima H (1995) Present and future of vacuum fluorescent display and field emission display. *Mater Chem Phys* 40:267
51. Yi W, Jeong T, Jin S, Yu SG, Lee J, Heo J, Yoo JB, Kim JM (2001) Characteristic features of new electron-multiplying channels in a field emission display. *J Vac Sci Technol B* 19:2247
52. Pang ML, Lin J, Cheng ZY, Fu J, Xing RB, Wang SB (2003) Patterning and luminescent properties of nanocrystalline $Y_2O_3:Eu^{3+}$ phosphor films by sol-gel soft lithography. *Mater Sci Eng B* 100:124
53. Zhang QY, Pita K, Buddhudu S, Kam CH (2002) Luminescent properties of rare-earth ion doped yttrium silicate thin film phosphors for a full-colour display. *J Phys D: Appl Phys* 35:3085
54. Yi SS, Shim KS, Yang HK, Moon BK, Choi BC, Jeong JH, Kim JH, Bae JS (2007) Improved cathodoluminescent characteristics of $Y_2O_3:Eu^{3+}$ thin films by Li-doping. *Appl Phys A* 87:667
55. Cho JY, Huh YD, Park CR, Do YR (2007) The Effect of annealing temperature on the CL properties of sol-gel derived $Y_2O_3:Re$ ($Re = Eu^{3+}, Tb^{3+}, Tm^{3+}$) phosphors. *J Electrochem Soc* 154:J272
56. Leskelä M, Niinistö L (1992) Applications of rare earths in full-colour EL displays. *Mater Chem Phys* 31:7
57. Minami T (2003) Oxide thin-film electroluminescent devices and materials. *Solid State Electron* 47:2237

58. Minami T, Shirai T, Nakatani T, Miyata T (2000) Electroluminescent devices with $\text{Ga}_2\text{O}_3:\text{Mn}$ thin-film emitting layer prepared by sol-gel process. *Jpn J Appl Phys* 39:L524
59. Miyata T, Nakatani T, Minami T (2000) Manganese-activated gallium oxide electroluminescent phosphor thin films prepared using various deposition methods. *Thin Solid Films* 373:145
60. Kitai AH (2003) Oxide phosphor and dielectric thin films for electroluminescent device. *Thin Solid Films* 445:367
61. Issler SL, Torardi CC (1995) Solid state chemistry and luminescence of X-ray phosphors. *J Alloys Compd* 229:54
62. Murillo AG, Luyer CL, Dujardin C, Martin T, Garapon C, Pédrini C, Mugnier J (2002) Elaboration and scintillation properties of Eu^{3+} -doped Gd_2O_3 and Lu_2O_3 sol-gel films. *Nucl Instrum Methods Phys Res A* 486:181
63. Mansuy C, Nedelec JM, Mahiou R (2004) Molecular design of inorganic scintillators: from alkoxides to scintillating materials. *J Mater Chem* 14:3274
64. Goetzberger A, Wittwera V (1981) Fluorescent planar collector-concentrators: a review. *Solar Cells* 4:3
65. Hermann AM (1982) Luminescent solar concentrators – a review. *Solar Energy* 29:323
66. Reisfeld R (2001) Prospects of sol-gel technology towards luminescent materials. *Opt Mater* 16:1
67. Reisfeld R, Shamrakov D, Jorgensen C (1994) Photostable solar concentrators based on fluorescent glass films. *Sol Energy Mat Sol Cells* 33:417
68. Reisfeld R, Eyal M, Chernyak V, Zusman R (1988) Luminescent solar concentrators based on thin films of polymethylmethacrylate on a polymethylmethacrylate support. *Sol Energy Mat* 17:439
69. Machida K, Li H, Ueda D, Inoue S, Adachi G (2000) Preparation and application of lanthanide complex incorporated ormosil composite phosphor films. *J Lumin* 87–89:1257
70. Chung P, Chung HH, Holloway PH (2007) Phosphor coatings to enhance Si photovoltaic cell performance. *J Vac Sci Technol A* 25:61
71. Fukuda T, Kato S, Kin E, Okaniwa K, Morikawa H, Honda Z, Kamata N (2009) Wavelength conversion film with glass coated Eu chelate for enhanced silicon-photovoltaic cell performance. *Opt Mater* 32:22
72. Nakata R, Hashimoto N, Kawano K (1996) High-conversion-efficiency solar cell using fluorescence of rare-earth ions. *Jpn J Appl Phys* 35:L90
73. Hong BC, Kawano K (2003) PL and PLE studies of $\text{KMgF}_3:\text{Sm}$ crystal and the effect of its wavelength conversion on CdS/CdTe solar cell. *Sol Energy Mat Sol Cells* 80:417
74. Kawano K, Hong BC, Sakamoto K, Tsuboi T, Seo HJ (2009) Improvement of the conversion efficiency of solar cell by rare earth ion. *Opt Mater* 31:1353
75. Shalav A, Richards BS, Trupke K, Krämer KW, Güdel HU (2005) Application of $\text{NaYF}_4:\text{Er}^{3+}$ up-converting phosphors for enhanced near-infrared silicon solar cell response. *Appl Phys Lett* 86:013505
76. van der Ende BM, Aarts L, Meijerink A (2009) Lanthanide ions as spectral converters for solar cells. *Phys Chem Chem Phys* 11:11081
77. Lu YL, Chen XB (2009) Plasmon-enhanced luminescence in $\text{Yb}^{3+}:\text{Y}_2\text{O}_3$ thin film and the potential for solar cell photon harvesting. *Appl Phys Lett* 94:193110
78. Tanaka S, Fujihara S (2011) Design and fabrication of luminescent anti-reflective sol-gel coatings with bi-layer structure. *Int J Appl Ceram Technol* 8:1001
79. Tadanaga K, Yamaguchi N, Uraoka Y, Matsuda A, Minami T, Tatsumisago M (2008) Anti-reflective properties of nano-structured alumina thin films on poly(methyl methacrylate) substrates by the sol-gel process with hot water treatment. *Thin Solid Films* 516:4526
80. Tanaka S, Fujihara S (2011) Luminescent antireflective coatings with disordered surface nanostructures fabricated by liquid processes. *Langmuir* 27:2929

Appendix A: Syntheses

René Thelen and Theodor Schneller

Abstract. In this additional chapter detailed “*cooking recipes*” for a number of standard material systems such as $(\text{Pb}(\text{Zr}_x, \text{Ti}_{1-x})\text{O}_3, (\text{Ba}_x, \text{Sr}_{1-x})\text{TiO}_3, \text{LaNiO}_3, (\text{La}_{0.5}, \text{Sr}_{0.5})\text{CoO}_3$ etc.) are presented in ways, which enable thorough working students to prepare their own coating solutions in a state of the art chemistry laboratory. It may be noted that for some sol-gel type precursor solutions, syntheses under inert atmosphere are required. Moreover well-established procedures to prepare functional crystalline films out of these solutions on platinized silicon wafers by spin coating and subsequent heating processes are depicted. Finally, the preparation of measurable thin film metal-insulator-metal structures from the CSD prepared films is exemplarily described.

A.1 Introduction

The preceding main chapters covered the theoretical principles of solution synthesis and the influences of the different processing steps on the properties of the CSD-derived functional oxide thin films in the style of a research review or textbook. In this appendix, the syntheses of selected well-known CSD material systems are described as instructions to practical work in such detail that they can be easily reproduced by students working carefully.

Certainly the collection of systems presented makes no claim to be complete. The aim is to introduce typical synthesis principles with the example of selected preparation routes which have been optimized at the Institut für Werkstoffe der Elektrotechnik II (IWE II) and reproduced hundreds of times. The material systems are divided into groups according to the components of which they consist. Additionally, some necessary reaction steps such as drying or preparation of educts are explained in more detail.

Basic principles of experimental organic chemistry may be found in [1, 2]. Since moisture-sensitive alkoxides are often used as educts in the described syntheses, some knowledge of working under inert-gas atmosphere is essential. Information about the different techniques (Schlenk technique or glove box) used in the manipulation of air-sensitive compounds can be found in [3, 4].

In the final part (Sect. A.6) of this chapter, standard processing steps for thin film preparation are presented and described in detail.

A.2 Lead-Titanate-Based Material Systems

A large number of routes have been described for the preparation of lead-titanate-based material systems. Depending on the desired characteristics of the deposited thin film, the stoichiometry may be modified by substitution and doping. A large variety of compositions are available, among which Zr-substituted lead titanate ($\text{Pb}(\text{Zr}_x\text{Ti}_{1-x})\text{O}_3$, PZT) plays a prominent role and will be the subject of this section. Other compositions with dopants such as calcium or lanthanum are also easy to create in the same way.

Probably most of the described routes rely on the use of ether-alcohols, such as 2-methoxyethanol (EGMME). In this section, two routes for the synthesis of PZT will be introduced in detail.

The first route is the EGMBE route [5], which is in principle a modified variant of the very well-known route of Budd et al. [6] (cp. Chap. 3) and is based on 2-butoxyethanol (EGMBE) [7, 8], which is regarded as less toxic compared to EGMME. It was modified with a view to simplifying and reducing the synthesis time resulting in a one-pot reaction.

The other route was developed at IWE II and represents a very simple and time-saving synthesis, which avoids ether-alcohols completely. In the following, this route is termed the “IWE route”.

Common to both routes is the use of dried lead (II) acetate, zirconium (IV) - n-propoxide and titanium (IV) isopropoxide. The commercially available lead (II) acetate contains 3 moles of water of crystallization which must be removed to avoid hydrolysis and condensation reactions during the synthesis. Hence, one suitable way of removing the water of crystallization is also described in this section.

To avoid premature hydrolysis and condensation reactions of the alkoxides, all reaction steps must be carried out under a dry argon atmosphere using a glove box and applying the Schlenk technique. The solvents are dried with sodium, then distilled and stored under a dry argon atmosphere.

The molar masses stated below are used for the synthesis of stock solutions with a volume of 25 ml and a final concentration of 1 mol/l. 30 % of zirconia and 70 % of titania corresponding to tetragonal PZT ($\text{PbZr}_{0.3}\text{Ti}_{0.7}\text{O}_3$, PZT30/70), which is chosen as the stoichiometric ratio. To compensate the loss of lead oxide during

Fig. A.1 This figure shows an example of a rotary evaporator with installed round-bottom flask. The dissolution of the lead (II) acetate trihydrate is performed at 60 °C and takes just a few minutes. 320 ml (3.1 moles) of acetic acid anhydride is added to remove the water of constitution and then the mixture is heated again to 70 °C for 2 h. After cooling down, most of the solvent is distilled off under reduced pressure



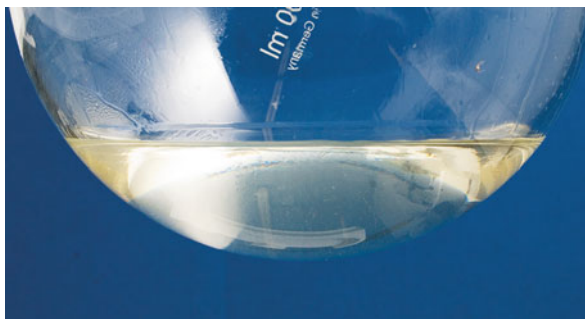
the crystallization of the thin film (volatility of lead (II) oxide at temperatures above ~600 °C) a 15 % excess of lead is applied to the initial weight of lead (II) acetate in both solutions.

A.2.1 Drying of Lead (II) Acetate Trihydrate

The background of this reaction is the chemical removal of the water of crystallization by reacting lead (II) acetate trihydrate with acetic acid anhydride. 379.33 g (1 mol) lead(II) acetate-trihydrate is weighed into a 3-l rotary evaporator with a round-bottom flask and 1–1.5 l glacial acetic acid is added. The mixture is heated to 60 °C in the water bath of the rotary evaporator (Fig. A.1) until the acetate is completely dissolved.

3 moles of acetic acid anhydride are theoretically necessary to remove the water of crystallization, but in order to be sure it is recommended to use a slight excess of anhydride (e.g. ~ 3% excess; 3.1 mol). After installing the round-bottom flask, the mixture is heated at 70 °C for 1.5 h and then cooled down to room temperature. Most of the solvent is removed by distillation at 40–50 °C under reduced pressure in

Fig. A.2 Photograph showing a clear, colorless and gel-like liquid as the result of the distillation



the rotary evaporator, until approx. 200 ml of a gel-like, clear, and colorless liquid remains (Fig. A.2).

This residue is digested in 1.5 l acetone and stored in a fridge to crystallize overnight. To separate the re-crystallized lead (II) acetate the mixture is filled into a glass frit. This special type of Schlenk tube is equipped with a frit and a side-arm through which the glass frit can be evacuated or purged with inert gas (Fig. A.3). Depending on the resulting precipitate, frits with different pore sizes are available. In this case, a frit with a pore size of 16–40 μm is sufficient for medium-fine precipitations.

The filtration can be speeded up by closing the glass frit with blind plugs and applying a slight overpressure with inert gas. Another effect of this overpressure is the simultaneous drying of the filter cake when most of the solvent is filtrated.

In the first step, an argon tube is installed on the hose connection of the glass frit. The mixture is completely filled into the glass frit, filtrated and dried by using the argon pressure. To remove residues of acetic acid and acetic acid anhydride, 200 ml acetone is added twice and filtrated as described above. Finally, the filter cake is washed with 200 ml diethyl ether.

The filter cake is then dried under reduced pressure for some days. It is useful to store the closed frit in a drying oven at 60 °C overnight.

A.2.2 PZT30/70 According to the EGMBE Route

9.349 g (28.75 mmol) dried lead (II) acetate, 2.454 g (7.50 mmol) zirconium (IV) n-propoxide and 4.968 g (17.50 mmol) titanium (IV) isopropoxide are weighed into a two-necked round-bottom flask in a glove box. In this route, 5 ml of ethylene glycol monobutyl ether (2-butoxyethanol; EGMBE) are added using a volumetric pipette. The neck with the small ground joint is closed by an adapter with a hose connection and a one-way tape stopcock whereas the large ground joint is closed with a plug. After weighing, the flask is installed in a fume-hood equipped with Schlenk apparatus, where in the first step the argon tube is connected to the adapter on the small ground joint (Fig. A.4).

Fig. A.3 Picture showing the re-crystallized lead (II) acetate in the glass frit after filtering and drying under argon pressure. The filter cake is subsequently washed with acetone and diethyl ether and dried for few days under reduced pressure



After opening the stopcock it is possible to open the flask. The reflux condenser is either directly installed on the large ground joint or connected by means of an additional adapter between the two components. To avoid impurities of the precursor solution it is recommended to use PTFE bushings instead of grease for the ground joint connections.

To control the argon flow during the process it is necessary to install an adapter with a hose connection and a PVC hose on the cooler, which is connected to a T-piece and a bubble counter. The bubble counter is filled with silicone oil and serves as an argon flow monitor. It also helps to prevent the back diffusion of

Fig. A.4 The complete set-up for the synthesis of a PZT solution. A two-necked round-bottom flask is installed above a magnetic stirrer with hot plate and oil bath. The small ground joint is closed by an adapter with a hose connection. On the large ground joint, the reflux condenser is installed; the ground joint of the condenser is closed by an adapter with a hose connection. The adapter is connected to a T-piece and bubble counter by a PVC hose



ambient air. After assembling the flask in the hood, the solution is refluxed at 130 °C for 2 h. When the final reaction temperature is reached, it is possible to close the side stopcock and connect the argon tube with the T-piece. It is necessary to monitor the argon flow during the whole synthesis, especially during the steps in which the flask is opened, for example to add solvents. If equilibrated temperature is maintained in the flask during refluxing, the inert gas flow can be kept to a minimum. After 1.5–2 h, the initial suspension is converted to a clear, yellow

Fig. A.5 A PZT solution directly after refluxing and cooling down. Typically these solutions are clear and are of a *yellow* color



solution, which indicates successful conversion. To continue processing the precursor is cooled down to room temperature, at which it has to be ascertained that the argon flow is sufficient (Fig. A.5). Otherwise ambient air will be sucked into the flask possibly leading to undesirable sol-gel reactions.

The next step is the removal of the reaction by-products by distillation under reduced pressure at max. 40 °C. After 20 min of distillation a brown-viscous gel is obtained, which must be re-dissolved in 5 ml 2-butoxyethanol. This step takes some time because of the gel viscosity. However, by continuously actuating the stirring bar it is possible to mix both phases thus obtaining a homogeneous solution.

The re-dissolution step is followed by partial hydrolysis [8] and condensation initiated by adding small amounts of nitric acid in 2-butoxyethanol and deionized (DI) water in 2-butoxyethanol:

- Hydrolysis solution 1 (2.3 ml): 2 ml 70 % HNO_3 in 50 ml 2-butoxyethanol (anhydr.);
- Hydrolysis solution 2 (3.1 ml): 1 ml DI water in 50 ml 2-butoxyethanol (anhydr.);

Both solutions are added through a dropping funnel while stirring the precursor solution for 1 h after the solutions have been added.

To complete the synthesis, the solution must be decanted quantitatively into a 25 ml volumetric flask and the final concentration is adjusted by adding 2-butoxyethanol.

A.2.3 PZT30/70 According to the IWE Route

9.349 g (28.75 mmol) dried lead(II) acetate, 2.454 g (7.50 mmol) zirconium(IV) - n-propoxide and 4.968 g (17.50 mmol) titanium(IV) isopropoxide are weighed into a two-necked round-bottom flask without any additional solvent. The next step includes refluxing of the suspension at 130 °C for 2 h under argon. After conversion to a clear yellow solution, the precursor is cooled down to room temperature.

The reaction by-products are removed by distillation under reduced pressure at max. 40 °C. After the distillation step, a yellow, foamy viscous gel is obtained, which is re-dissolved in 5 ml n-butanol. It is recommended that the gel should be dissolved at a slightly raised temperature of max. 50 °C to accelerate the process.

1.8 ml (27.8 mmol) acetyl acetone (Hacac) as a stabilization agent is added by means of a dropping funnel while stirring the precursor solution for 1 h. The amount of acetyl acetone depends on the titanium compound. For each mol of titanium 1 mol of acetyl acetone is added to the solution.

The last step includes adjusting the final concentration by decanting the precursor solution quantitatively into a 25 ml volumetric flask and adding n-butanol up to the mark.

A.3 Material Systems Based on Alkaline Earth Titanates

In this section, the synthesis of precursor solutions for systems based on alkaline earth titanates is described. The most frequently used systems are $(\text{Ba}_x, \text{Sr}_{1-x})\text{TiO}_3$ (BST), SrTiO_3 (STO) and BaTiO_3 (BTO). It should be noted that the synthesis routes described here may also be used in an analogous manner for related material systems such as $\text{Ba}(\text{Zr}_x, \text{Ti}_{1-x})\text{O}_3$. Moreover, dopants such as manganese, niobium etc. can easily be added if necessary.

Most synthesis schemes for suitable precursor solutions are typical hybrid routes, what means that they consist of alkaline earth carboxylates and a metal alkoxide of the transition metal. Often alkaline earth acetates and propionates are used as educts for the synthesis and the corresponding carboxylic acid is used as one part of the solvent mixture. Accordingly, these routes may be called the “acetate” and “propionate” routes.

In particular, in the case of the propionate route two pathways for the preparation of the necessary metal propionates have been established at IWE II, depending on the requirements of the thin films to be derived later from them [9].

The first route is based on the conversion of the corresponding alkaline earth compounds such as hydroxides or carbonates into the metal propionate which can be isolated, stored and used for the synthesis. The reaction is quick and large amounts of the metal propionate can easily be prepared. Syntheses based on the use of these metal propionates are presented in Sect. A.3.2. The second way to

prepare the metal propionates is by reacting the educts (alkaline earth metal carbonates) in situ with the carboxylic acid during the synthesis of the stock solution. An example of such a synthesis is presented in Sect. A.3.3.

However, for all these pathways it is very important that the educts are of high purity, because excessive amounts of secondary metals such as sodium will deteriorate the leakage current properties of the final thin film. In this context, it has to be noted that typically the purity of commercially available alkaline earth metal hydroxides is not as high as that of the carbonates.

All reactions pathways for the synthesis of alkaline earth titanate solutions have in common the need for stabilization of the alkoxide compound with acetyl acetone. Calculations for the initial weight of the stabilization agent are presented in the following Sect. A.3.1.

Typical concentrations of those solutions are 0.1 mol/l or 0.3 mol/l, depending on the desired thickness and microstructure (see Chap. 17). The calculations given in these instructions are based on the synthesis of 25 ml stock solutions with a concentration of 0.3 mol/l. As an example of the different material systems, in this section the synthesis of a $(\text{Ba}_{0.7}\text{Sr}_{0.3})\text{TiO}_3$ (BST70/30) precursor solution is described in detail. The syntheses of BTO and STO precursor solutions can be performed accordingly.

A.3.1 Calculations for the Initial Weight of the Stabilization Agent

As the titanium component is an alkoxide (e.g. titanium (IV) n-butoxide; $\text{Ti}(\text{O}^n\text{Bu})_4$) and is sensitive to water/moisture, it is necessary to stabilize it with acetyl acetone. Two moles of Hacac are added per mole of titanium. The following equations describe the calculation of the amount of Hacac [Eq. (A.1)] and the corresponding volume of solvent [Eq. (A.2)], with the implicit understanding that no mixing effects occur, i.e. ideal behavior:

$$V_{\text{Hacac}} = \left(\frac{M \times c \times V_{\text{total}}}{\delta} \right) \times 2 \quad (\text{A.1})$$

- V_{Hacac} : volume of Hacac [ml]
- M : molecular weight of Hacac [100.12 g/mol]
- c : concentration of the stock solution [mol/l]
- V_{total} : total volume of the stock solution
- δ : density of Hacac [0.97 g/ml]

The outcome of Eq. (A.2) is the volume of the solvent or solvent mixture, which depends on the Hacac volume. In the case of a stock solution with a concentration of 0.3 mol/l, 1.55 ml Hacac is needed to stabilize the butoxide:

$$V_{\text{solvent}} = V_{\text{total}} - V_{\text{Hacac}} = 25 \text{ ml} - 1.55 \text{ ml} = 23.45 \text{ ml} \quad (\text{A.2})$$

In order to obtain optimal coating behavior for these hybrid routes, a solvent mixture is used to prepare the alkaline earth titanate solutions. In the case of the propionate route, the mixture consists of one part n-butanol and 1.5 parts propionic acid (overall 2.5 parts). For the acetate route, three parts acetic acid and one part 2-methoxyethanol are used, i.e. in total four parts of solvent. The volume of the different solvents can be calculated according to the result of Eq. (A.2). As an example, Eq. (A.3) shows the calculation for the solvent parts necessary for the acetate route.

$$V_{\text{part}} = \frac{V_{\text{solvent}}}{\text{total parts}} = \frac{23.45 \text{ ml}}{4} = 5.86 \text{ ml} \quad (\text{A.3})$$

Thus, taking the solvent composition into account (three parts acetic acid, one part 2-methoxyethanol) the outcome of Eq. (A.3) is that 5.86 ml 2-methoxyethanol and 17.58 ml acetic acid are used for the acetate route. These are, of course, theoretical calculations and in practice the composition may vary slightly (volume of the alkoxide and potentially slight mixing effects), which is, however, of no significance since the results are ultimately highly reproducible. The composition of the solvent for the propionate route can be calculated in the same manner.

A.3.2 Synthesis According to the Propionate Route

As mentioned above, there are two pathways for the preparation of solutions according to the propionate route. Thus, Sect. A.3.2.1 is divided into subsections in which first the conversion of the alkaline earth compounds is described and then, resulting from the prepared metal propionates, the synthesis of a BST70/30 precursor solution is described. Section A.3.2.2 deals with the synthesis of a BST70/30 precursor solution with the in situ conversion of the alkaline earth compounds. Taking into account the calculations for the stabilization agent (Eqs. A.1 and A.2) and the ratio of propionic acid and n-butanol (1:1.5) in the solvent mixture, the total volume of the two solvents can be calculated (Eq. A.3).

A.3.2.1 BST70/30 Precursor Solutions Based on the Use of Metal Propionates

Preparation of Alkaline Earth Metal Propionates

The synthesis of barium and strontium propionate is similar to the drying of lead (II) acetate, described in Sect. A.2.1. In the following, the conversion of barium

hydroxide to barium propionate is described. Strontium hydroxide can be converted according to the same steps.

1 l of deionized (DI) water is filled into a 3 l rotary evaporator with a round-bottom flask. Barium hydroxide is weighed into a beaker and then added to the DI water. Subsequently, the threefold amount of propionic acid is added to the suspension and then heated to 60 °C in the water bath of the rotary evaporator. Then most of solvent is removed under reduced pressure until a clear, colorless and gel-like residue remains in the flask. To crystallize the propionate, at least 1 l of acetone is added to the gel and then the flask is stored overnight in a fridge.

The suspension is filled into a glass frit, filtrated under argon pressure and washed twice with acetone. After closing the frit with a blind plug, the precipitate is first dried by using argon pressure and then completely dried out under reduced pressure for some days. It is recommended to store the glass frit in a drying oven overnight to speed up drying.

These propionates can be used directly for the synthesis of material systems based on alkaline earth metals. The synthesis is straightforward and the metal propionates obtained are good educts as long as demands on purity are not too high. They are soluble in the most frequently used solvents such as carboxylic acids (acetic acid, propionic acid), alcohols (n-butanol) and ether alcohols (e.g. 2-methoxyethanol).

Synthesis of BST70/30 Based on the Use of Metal Propionates

1.487 g (5.25 mmol) barium propionate and 0.526 g (2.25 mmol) strontium propionate are weighed into a 50 ml round-bottom flask. After adding 9.4 ml of propionic acid with a volumetric pipette, the propionates can be easily dissolved on a magnetic stirrer at room temperature. Dissolution takes just a few minutes. Separately, 2.550 g (7.50 mmol) titanium n-butoxide is weighed into a 25 ml volumetric flask in a glove box, diluted with a small amount of n-butanol and stabilized with 1.55 ml (15 mmol) acetyl acetone. The two solutions are combined by adding the propionate solution quantitatively to the alkoxide solution. The final concentration is adjusted by adding solvent up to the mark.

A.3.2.2 BST70/30 Precursor Solutions Based on In Situ Conversion of Alkaline Earth Carbonates

As mentioned in the introduction to Sect. A.3, another way of preparing alkaline earth titanate solutions is the in situ conversion of the alkaline earth metal carbonates with the corresponding carboxylic acid during solution synthesis. Notes in Sect. A.3.2 for the solvent composition also apply to this description.

1.036 g (5.25 mmol) barium carbonate and 0.332 g (2.25 mmol) strontium carbonate are weighed into a round-bottom flask and 9 ml propionic acid are added with a volumetric pipette. The round-bottom flask is installed on a magnetic stirrer with a hot plate and an oil bath and closed with a reflux condenser. The suspension is refluxed for at least 12 h at a temperature of 140 °C. During this time the suspension is converted into a clear, colorless solution.

The preparation of the stabilized titanium (IV) n-butoxide component has already been described in Sect. A.3.2.1.1. The synthesis is completed by decanting the propionate solution into the volumetric flask and adding solvent to adjust the concentration.

A.3.3 Synthesis of BST70/30 Precursor Solutions According to the Acetate Route

In the same way as for the propionate route, a solvent mixture is also used for the acetate route. However, the latter solution consists of acetic acid and 2-methoxyethanol with a volumetric ratio of three parts acetic acid and one part 2-methoxyethanol. By taking the amount of chelating agent into account (Sect. A.3.1), it is again possible to calculate the total volume of acetic acid and 2-methoxyethanol (see Sect. A.3.1) in the solvent mixture.

1.340 g (5.25 mmol) barium acetate and 0.463 g (2.25 mmol) strontium acetate are weighed into a round-bottom flask and 10 ml acetic acid are added with a volumetric pipette. The neck of the round-bottom flask is closed with a plug. The conversion is carried out at room temperature on a magnetic stirrer and after at most 30 min the acetate is completely dissolved.

During this dissolution step, 2.550 g (7.50 mmol) titanium (IV) n-butoxide is weighed into a 25 ml volumetric flask and diluted with some milliliters of the calculated amount of 2-methoxyethanol and stabilized with 1.55 ml (15 mmol) acetyl acetone. The colorless solution is converted into a transparent yellow solution indicating that the reaction has taken place. The residual volume of 2-methoxyethanol can then be added to the alkoxide solution. This step is carried out in an inert atmosphere, e.g. in a glove box.

To complete the synthesis, the acetate solution is decanted quantitatively into the volumetric flask and the final concentration is adjusted by adding acetic acid up to the mark.

A.4 Conductive, Oxidic Material Systems

The syntheses of conductive oxide precursor solutions are based on the so-called all-propionate in propionic acid route (APP route) [10,11], which represents a simple and flexible route to obtain a series of conductive oxide thin films. The

starting materials are mostly acetates or carbonates of the respective metal, dissolved in propionic acid and converted into the corresponding metal propionates.

In this section, the syntheses of lanthanum nickel oxide (LaNiO_3 —LNO), lanthanum strontium cobalt oxide ($(\text{La}_x, \text{Sr}_{1-x})\text{CoO}_3$ —LSCO) and lanthanum strontium calcium manganese oxide ($(\text{La}_x, (\text{Sr}_y, \text{Ca}_{1-y})_{1-x})\text{MnO}_3$ —LSCMO) are described.

The following descriptions are based on the synthesis of a precursor stock solution with a volume of 25 ml and a concentration of 0.3 mol/l. All conductive, oxidic precursor solutions have a MOD (metallo-organic decomposition) character, i.e. they are relatively insensitive to humidity so that they can be handled at ambient atmosphere. In order to adjust the thickness per coating step, these stock solutions may be diluted with propionic acid.

A.4.1 LNO According to the APP Route

2.580 g (7.50 mmol) lanthanum acetate sesquihydrate ($1.5 \text{ H}_2\text{O}$) and 1.865 g (7.50 mmol) nickel acetate tetrahydrate are weighed into a 100 ml round-bottom flask. The values for the initial weights depend on the content of water of constitution of the starting materials.

25 ml propionic acid and 5 ml propionic acid anhydride are added with a volumetric pipette and the suspension is heated in an oil bath to a temperature of 90°C until it is converted into a clear, green solution. In the next step, the liberated acetic acid and most of the propionic acid is distilled off under reduced pressure (vacuum pump or a water-jet vacuum pump). The resulting green gel is re-dissolved in 10 ml propionic acid by gently heating the reaction mixture.

To complete the synthesis, the solution must be decanted quantitatively into a 25 ml volumetric flask and the final concentration is adjusted by adding propionic acid (Fig. A.6).

A.4.2 LSCO According to the APP Route

The following description deals with the synthesis of an LSCO solution with a composition of $(\text{La}_{0.5}, \text{Sr}_{0.5})\text{CoO}_3$. In this route, the acetates of lanthanum and cobalt are used as educts, whereas the carbonate is used for the strontium compound. It should be noted that the dissolution of the carbonate is quite time-consuming, so that it is recommended that this part of the synthesis should be performed separately overnight.

0.554 g (3.75 mmol) of strontium carbonate is weighed into a 50 ml round-bottomed flask and 15 ml propionic acid are added with a volumetric pipette. The suspension is refluxed overnight at a temperature of 140 – 150°C and is completed when the suspension is converted to a clear, colorless solution.

Fig. A.6 Picture showing stock solutions (from left to right) of lanthanum nickel oxide (LNO), lanthanum strontium cobalt oxide (LSCO) and lanthanum strontium manganese oxide (LSMO) in volumetric flasks after adjusting the final concentration. Lanthanum calcium manganese oxide has the same color as LSMO and is not shown in this figure



1.286 g (3.75 mmol) lanthanum acetate sesquihydrate and 1.868 g (7.50 mmol) cobalt acetate tetrahydrate are weighed separately into a round-bottom flask and then added quantitatively to the propionate solution.

Additionally, 10 ml propionic acid and propionic acid anhydride are added to remove the water of constitution. The amount of the anhydride depends on the content of crystal water in the educts. To guarantee complete removal of the crystal water, it is possible to use a slight excess of the anhydride (e.g. 1 % excess).

The suspension is heated in an oil bath to a temperature of 90 °C for 30 min. The resulting solution is dark purple. The excess of anhydride, propionic acid and the liberated acetic acid is removed by distillation under reduced pressure (vacuum pump or water-jet vacuum pump). Subsequently, the resulting gel is re-dissolved in 10 ml propionic acid by gently heating the reaction mixture.

To complete the synthesis, the solution must be decanted quantitatively into a 25 ml volumetric flask and the final concentration is adjusted by adding propionic acid up to the mark (Fig. A.6).

A.4.3 LSCMO According to the APP Route

This material system is derived from lanthanum manganese oxide by partial replacement of the lanthanum by Sr, Ca or mixtures of the two and has the general composition $\text{La}_x(\text{Sr}_y\text{Ca}_{1-y})_{1-x}\text{MnO}_3$. As an example, the syntheses of solutions with the most typical compositions $\text{La}_{0.7}\text{Ca}_{0.3}\text{MnO}_3$ ($y = 0, x = 0.7$; LCMO70/30) and $\text{La}_{0.7}\text{Sr}_{0.3}\text{MnO}_3$ ($x = 0.7, y = 1$; LSMO70/30) are described. Other compositions of this material system can be prepared in the same way.

Generally, there are two different ways of preparing LSCMO solutions. Since carbonates of calcium and strontium are used, the problem arises from the low solubility of the carbonates in propionic acid. To circumvent this problem, it is

possible to convert the carbonates to propionates and isolate them in a separate step or to convert all the components in one refluxing step by adding a few drops of DI water to the reaction mixture with a pipette.

The first method has already been specified above in Sect. A.3.2.1.1 and will not be further described here. In the case of calcium carbonate, the conversion and isolation can be performed in the same manner as in the strontium propionate synthesis.

The problem of the second route is the low solubility of the carbonates in pure propionic acid, so that the reaction can be very time-consuming. The reaction can be speeded up by adding small amounts of water, as mentioned above.

A.4.3.1 LCMO70/30 According to the APP Route

The educts for this material system consist of lanthanum acetate sesquihydrate, calcium carbonate and manganese acetate dihydrate.

All educts are weighed into a 50 ml round-bottom flask; 10 ml propionic acid and 1 ml DI water are added with a volumetric pipette. The suspension is refluxed at a temperature of 140 °C for 3 h. The endpoint of the reaction is reached when a clear and slightly orange solution is obtained. The reaction mixture is cooled down to 50 °C for the following step, which includes distillation under reduced pressure to remove the water and most of the propionic acid. As a result of this distillation, an orange, gel-like residue remains in the flask, which can be dissolved in 5 ml propionic acid. To complete the solution, the reaction mixture is decanted quantitatively into a 25 ml volumetric flask and the concentration is adjusted by adding propionic acid.

A.4.3.2 LSMO70/30 According to the APP Route

Basically, the synthesis of LSMO70/30 follows the same reaction pathway as the synthesis of LCMO70/30. The acetates of lanthanum and manganese are used as educts, whereas for the strontium component the carbonate is used.

All components are weighed into a 50 ml round-bottom flask and after adding 10 ml of propionic acid and 1 ml of DI water, the suspension is refluxed at 140 °C for 3 h. The result of the refluxing step is a clear, slightly orange solution. To remove the water and the main part of the acid, distillation under reduced pressure is performed at a maximum temperature of 50 °C. The orange, gel-like residue obtained is dissolved in 5 ml of propionic acid. Finally, the solution is decanted into a volumetric flask and the concentration is adjusted by adding propionic acid (Fig. A.6).

A.5 Other Material Systems

Aluminium-oxide-based thin films are interesting for a number of applications such as buffer, isolation or adhesion layers. Ultrathin aluminium oxide films, for example, have been used instead of TiO_2 to improve the adhesion between SiO_2/Si and Pt for CSD processes at high temperatures (800–1,000 °C) [12]. In the following, two sol-gel-based synthesis routes for pure aluminium oxide (Al_2O_3 — AlO_x) and lanthanum aluminium oxide (LaAlO_3 —LAO) precursor solutions are presented.

A.5.1 Synthesis of Aluminium Oxide

In the following, the synthesis of an AlO_x precursor solution with a concentration of 0.5 mol/l and a volume of 25 ml is described.

3.079 g (12.50 mmol) aluminium (III) sec-butoxide is weighed into a 25 ml round-bottom flask in a glove box. It is recommended to lower the high viscosity by adding a small amount of 2-propanol (anhydrous) before adding the stabilizer. The alkoxide is stabilized with 1.29 ml (12.5 mmol) acetyl acetone and the solution is then stirred on a magnetic stirrer for half an hour. The clear, yellowish solution is decanted quantitatively into a 25 ml volumetric flask and the concentration is adjusted by adding 2-propanol.

A.5.2 Synthesis of Lanthanum Aluminium Oxide (LAO) According to the 2-Ethylhexanoic Acid Route

This synthesis is based on the conversion of the lanthanum acetate sesquihydrate with 2-ethylhexanoic acid¹ and mixing the obtained solution with an AlO_x precursor solution prepared according to Sect. A.5.1. The concentration is adjusted by adding toluene to the combined solutions. The values of the initial weights of the educts correspond to the synthesis of a stock solution with a concentration of 0.3 mol/l and a volume of 25 ml.

2.580 g (7.50 mmol) lanthanum acetate sesquihydrate is weighed into a round-bottom flask and 10 ml 2-ethylhexanoic acid are added with a volumetric pipette. The reaction mixture is heated to 100 °C in an oil bath. After about 1 h the suspension is converted into a clear, colorless solution. Most of the 2-ethylhexanoic

¹ It should be noted that if stronger carboxylic acids such as acetic acid or propionic acid are used, an esterification reaction occurs in the final hybrid-type precursor solution. The released water thus reacts with the aluminium alkoxide forming a useless gel.

acid and the liberated acetic acid are removed by distillation under reduced pressure at a temperature between 100 and 120 °C. Subsequently the gel-like residue is dissolved in 5 ml toluene.

While this gel is dissolving, the alkoxide solution can be prepared in a glove box. Therefore 1.847 g (7.50 mmol) of aluminium sec-butoxide is weighed into a 25 ml volumetric flask. As already described in Sect. A.5.1, the alkoxide is diluted with 1 ml 2-propanol (anhydrous) to lower the viscosity. The mixture is homogenized by shaking the flask slightly and stabilization is accomplished by adding 774 μl (7.50 mmol) acetyl acetone.

In the last step, the lanthanum precursor solution is quantitatively decanted into the volumetric flask containing the AlO_x precursor and the final concentration is adjusted by the addition of toluene.

A.6 Thin Film Fabrication

Although thin film processing of the various precursor solutions can be basically performed in a number of ways, in this section information is first given about some general processing steps. These aspects concern substrate cleaning, coating solution preparation and finally the deposition of the films with the example of PZT and BST. With respect to the film deposition process, it must be noted that contamination of the thin films with particles from the environment must be prevented in order to avoid inhomogeneities of the layers which would negatively influence the microstructure and the electrical properties (e.g. short circuits) of the final film. Thus thin film preparations including substrate and coating solution preparation are typically done in a clean room environment, but as a minimum requirement flow boxes are recommended. The clean room has the additional advantage of air conditioning with a controlled temperature of ~ 21 °C and relative humidity around 45–50 %. The latter is of particular importance for moisture-sensitive material systems such as sol-gel PZT, where undesired chemical reactions can otherwise occur in the as-deposited film directly after the coating step.

In the last section, wet chemical etching procedures are discussed as simple ways of patterning and an example is also presented in detail.

A.6.1 Substrate Preparation

The cleaning procedure is of particular importance for preparations before deposition. Kern [13] investigated different cleaning procedures and give an overview of different wet chemical cleaning methods. In recent years, cleaning techniques have been subjected to essential changes resulting in new cleaning techniques (e.g. gas-phase cleaning, plasma stripping) because of the more stringent requirements for Si-based devices. Reinhardt et al. [14] give an overview of the current status on this topic.

In this section, a well-established wet chemical cleaning procedure (for lab use) will be presented briefly. It is suitable for smaller pieces of wafers with dimensions such as $1 \times 1 \text{ cm}^2$ or $1 \times 1 \text{ in.}^2$, which are typically used in labs and which are prepared from larger wafers (4 or 6 in. in diameter) by cutting or dicing after protecting the surface with a photoresist. A typical cleaning procedure consists of cleaning in different solvents for some minutes in an ultrasonic bath. The solvents used for the cleaning procedure must be of clean room quality (CMOS quality or better) otherwise contaminations with particles may occur.

The wafers are first flushed with acetone (wash bottle) to remove a good portion of the resist and then they are directly (without interim drying!) placed into a beaker filled with acetone and subsequently into a beaker filled with 2-propanol to remove the contaminated acetone. Rinsing for 5 min in an ultrasonic bath has been shown to be sufficient for both solvents. Finally, the wafer is rinsed in DI water (clean room quality) to remove 2-propanol. This can be done either automatically with a quick dump rinser or if this is not available in the same way as described above. After drying, the wafer can be used for deposition.

Typically, thin films are deposited on oxidized silicon wafers coated with Ti or TiO_2 as an adhesion layer and Pt as the bottom electrode. Pt has a number of characteristics which make it a suitable material for the use as an electrode. It can be used for integration processes of ferroelectric thin films because of its thermal stability, high conductivity, and resistance to oxidation [15]. However, problems may also occur in using the bi-layer Pt/Ti stack due to the formation of Pt hillocks, which influence the quality of the thin films, e.g. by causing short circuits [15–17]. To improve the interface conditions it has proved appropriate to include a pre-annealing step in which the substrate is heat-treated at a temperature of $700 \text{ }^\circ\text{C}$ or at least at the temperature used for the later crystallization of the thin film in an oxygen atmosphere. This preannealing step is normally performed in either a rapid thermal annealing furnace or a diffusion furnace.

A.6.2 Coating Solution Preparation

Due to the fact that the precursor stock solutions are typically prepared in a conventional laboratory environment with normal ambient atmosphere (in the case of PZT, in an inert gas but probably not particle-free atmosphere), it is necessary to remove particles from the solutions. This can be done with syringe membrane filters. A wide range of filter materials with different pore sizes are commercially available. The best results have been obtained with Teflon® (polytetrafluoroethylene—PTFE) filters with a pore size of $0.2 \text{ }\mu\text{m}$. Depending on the material system and the desired properties of the final film, “coating solutions” are often first prepared from the usually more highly concentrated stock solutions by dilution with the corresponding solvent. These coating and stock solutions are then filtered through the syringe filter with a 5 ml disposable syringe into a bottle

Fig. A.7 The stock solution is filtered through a syringe membrane filter with a pore size of $0.2\ \mu\text{m}$ and PTFE as filter material, which is inert to most of the solvents. This step is done directly before spin coating and after optionally diluting the stock solution



immediately prior to use (Fig. A.7). Needless to say, the bottle must be clean, and this can be done either by flushing with particle-free DI water or acetone. The filtered solution can be directly used for the deposition experiments.

A.6.3 Coating and Crystallization

As already pointed out in the introductory part of this chapter the theoretical background of the transformation from the initial precursor solution to the crystalline film has been presented in detail in various chapters of this book (see e.g. - Chaps. 11 and 15). Thus in this section, some practical remarks for the successful deposition and crystallization of the thin film systems chosen as examples are presented briefly.

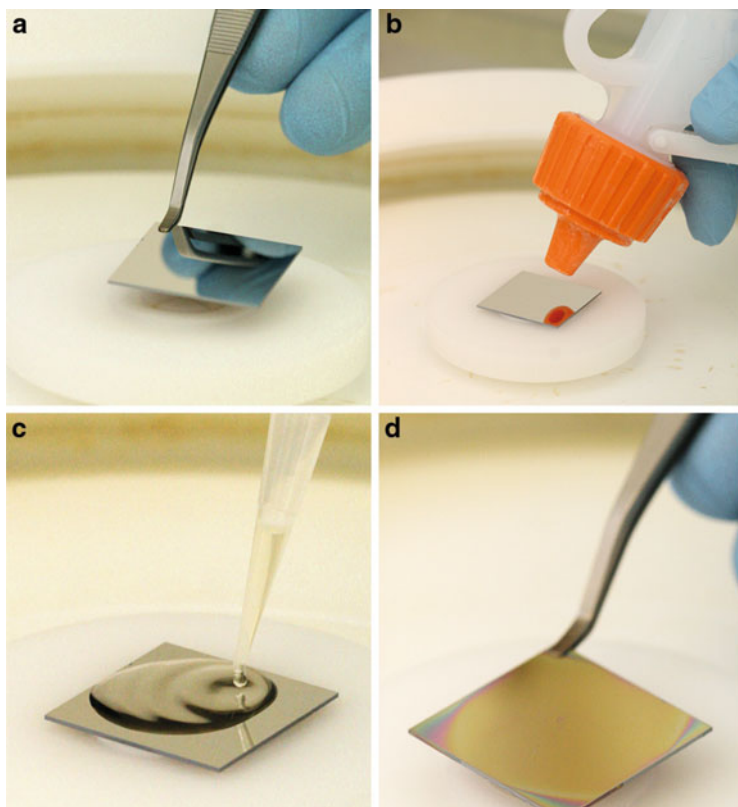


Fig. A.8 Series of pictures showing the whole spin coating process starting by placing the substrate on the spin coater (a), removing particles with a N_2 -spray gun (b) applying the solution with a pipette (c). Picture (d) shows the as-deposited film before heat treatment

The following descriptions refer to deposition by spin coating in which the substrate is placed on a spin coater and after applying the solution the wafer is accelerated to several thousand revolutions per minute ($\sim 1,000$ – $4,000$ rpm) according to the desired film thickness. Before applying the solution it is useful to clean the substrate with nitrogen (N_2 -spray gun) to remove any adherent particles from the wafer (Fig. A.8).

Spin coating is followed by heat treatment for the removal of the organic species and crystallization into the desired oxide phase. This heat treatment can be applied in two ways: a two-step process and a one-step process. Briefly, in the two-step process, removal of the organic species (pyrolysis) and crystallization are carried out in separate steps at two different temperatures, whereas in the one-step process pyrolysis and crystallization are performed in the same step at a sufficiently high temperature for crystallization of the oxide phase [18].

In Sect. A.6.3.1, deposition of PZT (IWE route) is presented as a typical example of a two-step process. The deposition of BST is described as an example of a

Table A.1 Details of the deposition of PZT30/70 according to the IWE route

Step	Parameters
Concentration	0.33 mol/l
Speed	500 rpm/5 s 3,000 rpm/30 s
Heat treatment	
Step 1 (heating/pyrolysis)	Drying/pyrolysis: hot plate 350 °C/2 min/ambient atmosphere
Step 2 (crystallization)	Crystallization: rapid thermal annealing (RTA), 700 °C/5 min/O ₂
Number of repetitions	3

one-step process (Sect. A.6.3.2). Films produced from precursor solutions based on the APP route can be also prepared according to the one-step process if different or higher crystallization temperatures are applied. Details of these materials may be found in the literature [10, 11].

A.6.3.1 PZT30/70 According to the IWE Route

The deposition of PZT is a typical example of a two-step process in which pyrolysis and crystallization are carried out in separate steps. The following description is based on the preparation of PZT30/70 thin films with a thickness of about 130–150 nm. Table A.1 summarizes the most important parameters.

The substrate is placed on the vacuum chuck and purged with N₂ to remove any contaminations (particles). After applying 250 µl of the filtrated solution with a pipette, the substrate is accelerated by the spin coater process to a speed of 500 rpm for 5 s and then directly to 3,000 rpm for 30 s. Immediately after spin coating, the substrate is placed on the hot plate at a temperature of 350 °C at ambient atmosphere for 2 min. This cycle is repeated three times to obtain the desired film thickness. Finally, the substrate is crystallized in a rapid thermal annealing furnace (RTA) at 700 °C for 5 min in oxygen atmosphere.

A.6.3.2 Processing of BST70/30

In this section, the processing of a barium strontium titanate (Ba/Sr ratio of 70 %/30 %) solution is described as an example of a one-step process. Some general information is first given about the deposition of BST solutions. Typical film thicknesses of BST thin films are about 120 nm and the final film thickness is obtained by repeated coatings as already described in Sect. A.6.3.1. The number of coatings depends on the concentration of the solution. One coating step with a 0.1 mol/l solution results in a layer approximately 10 nm in thickness, whereas a coating step with a 0.3 mol/l solution results in a layer of 30 nm. The choice of concentration depends on the desired microstructure of the final BST thin film (see Chap. 17). The present process flow is based on the use of a solution with a

Table A.2 Details of the deposition of $(\text{Ba}_{0.7}\text{Sr}_{0.3})\text{TiO}_3$ according to the one-step process

Step	Parameters
Concentration	0.3 mol/l (\rightarrow fine-grained microstructure)
Speed	500 rpm/5 s 4000 rpm/30 s
Heat treatment: step 1	Pyrolysis and crystallization: diffusion furnace, 700 °C/10 min/O ₂
Number of repetitions	4

concentration of 0.3 mol/l. However, the procedure is basically the same for processing the 0.1 molar solutions. Moreover, the processing of other Ba/Sr ratios and acetate-based solutions follows the same principles. However, it should be noted that, due to the slightly higher decomposition temperatures in the acetate route, 750 °C is sometimes applied for crystallization in order to ensure complete removal of residual carbonates, although the films are already fully crystalline after 700 °C treatment. Table A.2 shows the parameters for the deposition of BST solutions based on the propionate route.

The substrate is placed on the vacuum chuck of the spin coater and purged with N₂ (spray gun) to clean it of any contamination with particles. Using a pipette, 250 µl of the solution is applied to the wafer and the spinning process is started immediately. Hence, for the first 5 s, the wafer is accelerated to 500 rpm and then directly to 4,000 rpm for 30 s. Each layer is immediately crystallized before the next deposition step. In the case of BST deposition, the heat treatment (pyrolysis and crystallization) is carried out in a diffusion furnace (oxygen atmosphere). The final film thickness is obtained by subsequent deposition and crystallization steps.

A.6.4 Chemical Etching

This final section deals with the etching of oxidic thin films which is a necessary step, for example, to uncover the bottom electrode for electrical characterization and to measure the film thickness by profilometry. A brief overview of suitable etching solutions for a selection of different material systems is given in Table A.3. The etching step is performed immediately after lithography and will not be presented in this section because that would be beyond the scope of this chapter. The focus is laid on wet etching, which is a simple, cost-saving method and easy to implement in a standard laboratory. On the other hand, there are certain safety risks because of the use of inorganic acids such as hydrochloric acid or the most frequently used hydrofluoric acid. The precision is also not as high as in the case of dry etching methods due to possible underetching. However, the latter methods require special technical equipment and are therefore cost-intensive and not easy to implement. The most commonly used dry etching method is reactive ion etching (RIE), in which the thin film is etched by a combination of reactive gases and an argon plasma.

Table A.3 Overview of materials and etching solutions

Material systems	Composition of the etching solution
Lead-based material systems (e.g. PZT)	40 % HF, 65 % HNO ₃ , D -water (1:1:2)
Alkaline-earth-titanate-based material systems (e.g. BST, BTO, STO)	40 % HF, 65 % HNO ₃ , DI water (1:1:2)
Conductive material systems	20–30 % HCl
AlO _x (non-crystalline)	40 % HF, 65 % HNO ₃ , DI water (1:1:2)
LAO	30 % H ₂ O ₂ , 96 % H ₂ SO ₄ (1:1) (permonosulfuric acid, Caro's acid)

Wet chemical etching processes are based on a chemical transformation of the material and a subsequent dissolution of the etching products in the etching solution. The solutions typically consist of diluted inorganic acids or mixtures of different inorganic acids (enhanced selectivity). In certain cases, such as anisotropic etching of silicon, inorganic bases or alkaline aqueous solutions are used. Seidel et al. [19, 20] give an overview of the topic of anisotropic etching of silicon in which the best-known etchants are presented and investigated.

At IWE, a wet-chemical etching solution consisting of hydrofluoric acid (40 %), nitric acid (65 %) and DI water (ratio 1:1:2) has been created, which is suitable for etching material systems based on lead and alkaline earth titanates. In order to control the etching rate it is possible to increase the amount of DI water. This etchant is also suitable for etching aluminium oxide (if is not crystalline).

A suitable etching solution for conductive, oxidic material systems is hydrochloric acid. The acid should be diluted to concentrations between 20 and 30 %.

Lanthanum aluminium oxide thin films can be etched with permonosulfuric acid (also known as Caro's acid), a mixture of one part hydrogen peroxide (30 %) and one part sulfuric acid (96 %).

A.6.4.1 Procedures of Wet Chemical Etching

There are many ways to perform wet chemical etching. The effort involved in the procedure depends on the requirements of the etched thin film ultimately produced, i.e. whether it is necessary to determine the thickness via profilometry and to make electrical measurements, or if only a quick electrical characterization is required.

A well-established method for the first case is to etch a corner of the thin film to obtain a proper edge and to uncover the bottom electrode. In this method, the substrate is dipped into the etching solution for a few seconds after the major part of the film has been protected by photoresist. In the following, the procedure is described in detail and the results of the different steps are shown in the series of photographs in Fig. A.9.

The sample (Fig. A.9a) and the areas of the thin film which are not be etched are first masked with a photoresist which can be applied to the substrate with a cotton

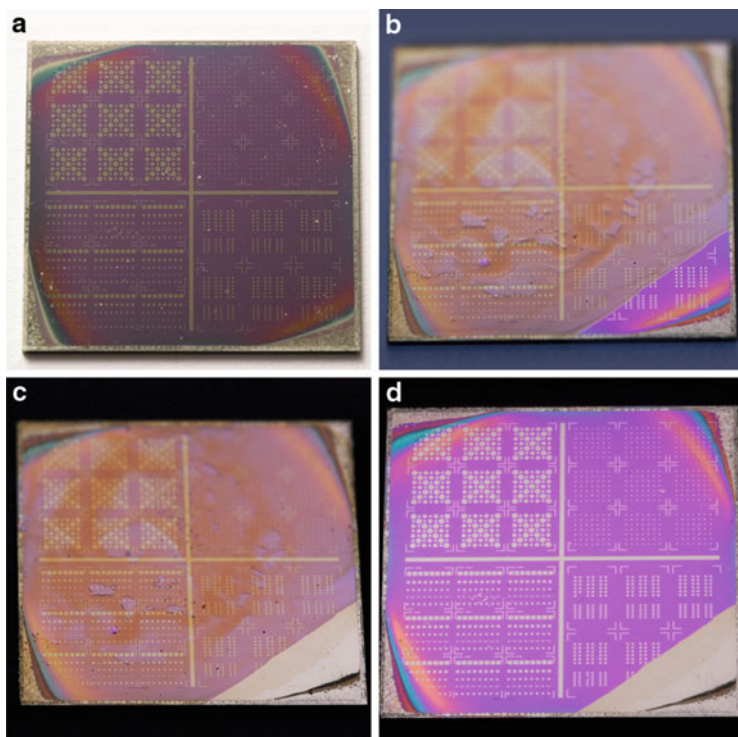


Fig. A.9 Series of pictures showing a PZT30/70 thin film on a Pt/TiO₂/SiO₂/Si-substrate. (a) The thin film is electroded Pt top electrodes of different dimensions. Here the top electrodes were deposited by a sputtering process and structured by lithography with lift-off. (b) Sample after application of photoresist on the thin film with the etching corner at the bottom right. (c) The thin film after dipping into the etching solution and rinsing with DI water. The shining silver bottom electrode at the bottom right corner indicates the successful etching step. (d) The final thin film after stripping off the photoresist

swab. A small area in the corner of the substrate is not covered (Fig. A.9b). With the thin film being thus protected it is possible to perform etching by dipping the uncovered corner into the etching solution. Typical PZT thin films with a thickness ~150 nm are etched within 10 s. To control the etching rate it is possible to dilute the solution with DI water. Immediately after the etching step the substrate is rinsed with DI water and dried with nitrogen or compressed air. The result of this procedure can be seen in Fig. A.9c. When etching is complete, the photoresist is stripped by dipping the sample into acetone and DI water and the sample is dried again with nitrogen or compressed air. The resulting sharp edge can be seen in Fig. A.9d. The samples treated by this method are appropriate for electrical characterization and profilometer measurements.

If only a quick electrical characterization of the prepared film is planned, a different “*quick&dirty*” method for etching may be used. In this case, a small droplet of the etching solution is applied with a microsyringe to an edge of the

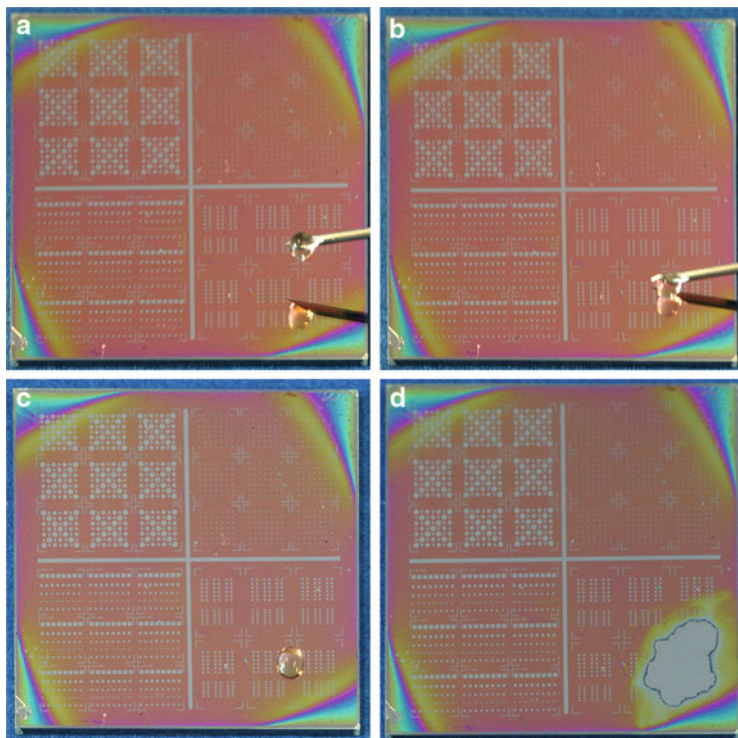


Fig. A.10 Series of pictures showing point etching with a microsyringe. (a) and (b) showing a droplet of the etching solution on the tip of the syringe. (c) The droplet is applied to the bottom right corner of the thin film. (d) The thin film after removal of the droplet and rinsing with DI water. As mentioned above the shining silver Pt bottom electrode indicates the successful etching step

sample (Fig. A.10). Depending on the etching rate, the substrate is then cleaned with DI water and dried as already described above. The result is a small dot where the bottom electrode is revealed, which is sufficient for electrical measurements. This method is very fast because there is no need to protect the whole thin film with photoresist since just a small area comes in contact with the etching solution. However, it should be noted that vapors of the etching solutions may deteriorate the surface of the non-protected ceramic thin film.

References

1. Harwood LM, Moody CJ, Percy JM (1998) Experimental organic chemistry: preparative and microscale, 2nd edn. Blackwell
2. Schwetlick K (1993) Organikum; Organisch-chemisches Praktikum. 19., bearbeitete und erweiterte Auflage, Barth Verlagsgesellschaft mbH, Leipzig

3. Shriver DF, Drezdron MA (1986) *The manipulation of air-sensitive compounds*, 2nd edn. Wiley, Chichester
4. Hünig S, Kreitmeier P, Märkl G, Sauer J (2006) *Arbeitsmethoden in der organischen Chemie (Wire-O-Bindung)*, Verlag Lehmanns, Berlin
5. Schneller T, Waser R (2007) Chemical modifications of $\text{Pb}(\text{Zr}_{0.3}\text{Ti}_{0.7})\text{O}_3$ precursor solutions and their influence on the morphological and electrical properties of the resulting thin films. *J Sol-Gel Sci Technol* 42:337–352
6. Budd KD, Dey SK, Payne DA (1985) Sol-gel processing of PbTiO_3 , PbZrO_3 , PZT, and PLZT thin films. *Br Ceram Proc* 36:107–121
7. Nouwen R, Mullens J, Franco D, Yperman J, Van Poucke LC (1996) Use of thermogravimetric analysis-Fourier transform infrared spectroscopy in the study of the reaction mechanism of the preparation of $\text{Pb}(\text{Zr,Ti})\text{O}_3$ by the sol-gel method. *Vib Spectrosc* 10:291–299
8. Wouters D, Norga G, Maes H, Nouwen R, Mullens J, Franco D, Yperman J, Van Poucke LC (1991) US Patent 6300144
9. Hasenkox U, Hoffmann S, Waser R (1998) Influence of precursor chemistry on the formation of MTiO_3 (M = Ba, Sr) ceramic thin films. *J Sol-Gel Sci Technol* 12:67–79
10. Hasenkox U, Mitze C, Waser R (1997) Metal propionate synthesis of magnetoresistive $\text{La}_{1-x}(\text{Ca,Sr})_x\text{MnO}_3$ thin films. *J Am Ceram Soc* 80:2709–2713
11. Reichmann R, Schneller T, Hoffmann-Eifert S, Hasenkox U, Waser R (2001) Morphology and electrical properties of SrTiO_3 -films on conductive oxide films. *J Eur Ceram Soc* 21:1597–1600
12. Halder S, Schneller T, Waser R (2007) Enhanced stability of platinized silicon substrates using an unconventional adhesion layer deposited by CSD for high temperature dielectric thin film deposition. *Appl Phys A* 87:705–708
13. Kern W (1990) The evolution of silicon wafer cleaning technology. *J Electrochem Soc* 137:1887–1892
14. Reinhardt KA, Kern W (2008) *Handbook of silicon wafer cleaning technology*, 2nd edn. William Andrew, Burlington, MA
15. Cao JL, Solbach A, Klemradt U, Weirich U, Mayer J, Böttger U, Schorn P, Schneller T, Waser R (2006) Structural investigations of Pt/TiO_x electrode stacks for ferroelectric thin film devices. *J Appl Phys* 99:114107
16. Hren PD, Rou SH, Al-Shareef HN, Ameen MS, Auciello O, Kingon AI (1992) Bottom electrodes for integrated $\text{Pb}(\text{Zr,Ti})\text{O}_3$ films. *Integr Ferroelectr* 2:311–325
17. Kneer EA, Birmie DP, Schrimpf RD, Podlesny JC, Teowee G (1995) Investigation of surface roughness and hillock formation on platinized substrates used for Pt/PZT/Pt capacitor fabrication. *Integr Ferroelectr* 7:61–73
18. Schwartz RW, Schneller T, Waser R (2004) Chemical solution deposition of electronic oxide films. *CR Chimie* 7:433–461
19. Seidel H, Csepregi L, Heuberger A, Baumgärtel H (1990) Anisotropic etching of crystalline silicon in alkaline solutions. I. Orientation dependence and behavior of passivation layers. *J Electrochem Soc* 137:3612–3626
20. Seidel H, Csepregi L, Heuberger A, Baumgärtel H (1990) Anisotropic etching of crystalline silicon in alkaline solutions. II. Influence of dopants. *J Electrochem Soc* 137:3626–3632

Index

A

- A-B diblock copolymers, 526
- ADDC. *See* Angle-dependent dip coating (ADDC)
- Aerosol deposition
 - applications
 - LSMCD and MOCVD technique, 300
 - spray pyrolysis, 299–300
 - generation and particle size distributions
 - atomization, liquid solution, 279
 - atomizer flow rate data, 278, 279
 - bipolar, 282
 - corona charging, 283
 - CSD precursor solutions, 277
 - diameter, 281
 - discrete histogram data, 280
 - histogram data measure, 281–282
 - input gas pressures, 282
 - liquid, 280
 - lognormal, 280, 281
 - LSMCD process, 278, 283
 - mass and volume, 280, 281
 - pneumatic atomization, 278, 279
 - Rayleigh limit and Boltzmann average, 282–283
 - statistical methods, 278–279
 - techniques, 278
 - topographical features, 278
 - MOCVD, 275–277
 - relationships, structure-processing-property
 - crystallization, CSD deposited films, 298–299
 - differentiation, 298
 - fabrication process, 297–298
 - SZM, 298, 299
 - thermal processing, 298
 - spin coating (*see* Spin coating, aerosol deposition)
 - techniques, 296–297
 - transport (*see* Transport, aerosol particle deposition)
- AFM. *See* Atomic force microscope (AFM)
- Al-doped ZnO (AZO), 310, 656, 657
- Alkali-metals-based perovskites
 - description, 55
 - $K_{0.5}Na_{0.5}NbO_3$, 58–59
 - $K(Ta,Nb)O_3$, 57, 58
 - $LiNbO_3$ and $LiTaO_3$
 - description, 55
 - Hirano's ethoxides-based synthesis, 56
 - peroxide-based synthesis route, 57–58
 - texture, grain size, porosity and roughness, 55–56
 - water-based sol preparation route, 56, 57
 - $Na_{0.5}Bi_{0.5}TiO_3$, 60–61
- Alkaline earth titanates
 - BST70/30 precursor (*see* BST70/30 precursor solutions)
 - educts, metal propionates, 754–755
 - initial weight calculations, stabilization agent, 755–756
 - material, 754
 - stabilization, alkoxide compound, 755
 - synthesis schemes, precursor solutions, 754
- Alkoxide-derived precursors
 - coordination modes, 220, 221
 - FTIR spectra, 220–222
 - hydrolysis and condensation reactions, 220
 - infrared spectra, 220
 - modification, titanium tetraisopropoxide, 220–221

- (Alk)oxolation, 13–14
- All-propionate in propionic acid route (APP route), 758
- LNO, 759
- LSCMO (*see* Lanthanum strontium calcium manganese oxide (LSCMO) material system)
- LSCO solution, 759–760
- All-propionate-routine (APP), 40
- “All-solution” coated conductors, 679
- buffer layers
 - CSD materials, 683
 - LZO and CeO, 683–688
 - relative orientation, 683, 684
 - titanates (*see* Titanates)
 - HTS layer (*see* High temperature superconductivity (HTS))
 - metallic substrate
 - cube textured Ni-alloy sample, 681, 682
 - texturing process, 680, 681
- Aluminium-doped zinc oxide (AZO)
- acetate dihydrate, 660
 - definition, 656
 - grain size, 661
 - thermal treatment procedures, 661
- Aluminium oxide synthesis
- description, 762
 - LAO, 2-ethylhexanoic acid route, 762–763
 - precursor solution, 762
- Amorphous functional-oxide films, 441
- Angle-dependent dip coating (ADDC), 248–249
- Annealing/firing barium fluoride, 691
- Antimony-doped tin oxide (ATO), 249, 661–662
- Anti-reflection (AR) coatings
- bandwidth, M-layer, 708, 709
 - index gradient layers (*see* Index gradient layers)
 - interference phenomena, 708
 - multilayer AR-stacks and optical filters, 713–716
 - $\lambda/4$ single layers
 - MgF₂-films, 712–714
 - porous AR films, 709–712
 - sol-gel processing, 709
- AP-CVD. *See* Atmospheric pressure chemical vapor deposition (AP-CVD)
- APP. *See* All-propionate-routine/All-propionate in propionic acid route (APP)
- Aqueous precursor systems
- film deposition and properties control (*see* Film deposition and properties control)
 - gel decomposition (*see* Gel decomposition) gel formation mechanism, 103–112
 - metal ions, water (*see* Metal ions, water)
 - multimetal oxide films, 93
 - water deposition methods, 93–94
 - water soluble precursors, 94
- AR coatings. *See* Anti-reflection (AR) coatings
- Atmosphere effects, pyrolysis and crystallization
- global
 - endo/exothermic reactions, 351
 - heat treatment, 351
 - TGA/DTA analyses, 350–351
 - thermolysis, 351
 - impacts, 349
 - local/in-situ
 - BST films, 352
 - decomposition reactions, 351
 - ferroelectric film, 351, 352
 - hydroxyl, 352
 - kinetic-based approach, 352
 - materials, 351
 - organic content, 351
 - oxidizing, 350–352
 - “processing window”, 352
 - PZT films and Pt electrodes, 351
 - wet vs. dry O₂, 352
- Atmospheric pressure chemical vapor deposition (AP-CVD), 661–662, 666
- ATO. *See* Antimony-doped tin oxide (ATO)
- Atomic force microscope (AFM)
- heated cantilever, 532
 - line scans, inter-particle distances, 526, 527
 - PTO grains, 530, 531
- Attenuated total reflectance (ATR), 217–218
- AZO. *See* Aluminium-doped zinc oxide (AZO)
- B**
- Barium strontium titanate (BST)
- alkaline earth acetates and propionates, 62
 - capacitance, 567
 - “chelate process”, 62
 - chemical routes, 61
 - CSD-derived, 556
 - CSD growth, 62, 63
 - either acetates/alkoxides, 64
 - ethoxide route, 63

- inkjet-printed, 561
 - Barium titanate (BTO)
 - BaTiO₃ films, 554–555
 - ceramic/mesoscopic layers, 558
 - deposition, 559, 560
 - homogeneous nucleation, 558
 - microemulsion mediated synthesis, 559
 - permittivity, Pt/BaTiO₃/Pt capacitors, 423, 424
 - Base metal bottom electrodes
 - CSD, functional oxide films (*see* Chemical solution deposition (CSD))
 - equilibrium approaches (*see* Equilibrium approaches, oxide-base metal integration)
 - integration, electroceramic thin films, 571–572
 - Binary systems, CSD
 - coordination shells, zirconium atoms, 193–194
 - crystallization process, 201
 - curve fitting procedures, 199, 201
 - EXAFS analysis, 198, 199
 - FTIR measurements, 195, 196
 - lead(II)acetate trihydrate, 197, 198
 - lead compound, 197, 198
 - materials properties, 192
 - monomeric Zr(acac)₄ complex, 195, 196
 - oxide and methoxy-PT, 201
 - oxygen coordination numbers and zirconium, 193, 195
 - Pb L_{III} EXAFS spectra, PT, 202
 - PbTi-p and PbTi-b, 198
 - precursor material, 196
 - spectra evaluation, EXAFS, 193, 195
 - TiO₂ anatase and rutile, 199–200
 - titanium alkoxides, 195
 - trigonal bipyramidal oxygen environment, 196–197
 - zirconium alkoxides, 193, 194
 - zirconium-*n*-butoxid, 192–193
 - Zr K-edge EXAFS spectra, 199, 200
 - Zr-O distances, crystals, 193, 194
 - BST. *See* Barium strontium titanate (BST)
 - BST70/30 precursor solutions
 - acetate route, 758
 - alkaline earth metal propionates
 - preparation, 756–757
 - in situ conversion, carbonates, 757–758
 - synthesis, 757
 - coating and crystallization, 767–768
 - BST thin film systems
 - control, CSD processing, 417
 - dielectric permittivity, 417, 418
 - heating procedure and solution concentration
 - categorization, thin film structures, 423
 - columnar microstructure, 423–425
 - control, 423
 - crystallization behavior, 422
 - CSD solutions, 422, 423
 - growth mechanism, 422–423
 - homogeneous and heterogeneous nucleation events, 421
 - perovskite phase, 421
 - processing, CSD, 422
 - high-*k* material, 417
 - multilayer ceramic capacitors (MLCC), 417
 - precursor chemistry
 - alkaline earth carboxylates, 418
 - decomposition and phase formation behavior, 418
 - decomposition regimes, 418–419
 - effects, 418, 419
 - FTIR and XRD analysis, 419
 - metal-Ti-oxo-carbonate phase, 421
 - nucleation, 420
 - perovskite phase formation, 420
 - synthesis, 418
 - type I and II, 419
 - thermodynamics and heating processes, 417
 - BTO. *See* Barium titanate (BTO)
 - Buried layer, 599
- ## C
- Carboxylate based precursor systems
 - acidity effect, 29–30
 - acid strength, 30, 31
 - long vs. short chain carboxylates, 39–44
 - metal carboxylates, 29–31
 - MOD-processes, 32–39
 - synthesis aspects
 - CSD precursor solutions, 32
 - description, 30
 - metal carboxylate, 30–31
 - water of constitution, 31, 32
 - CBD. *See* Chemical bath deposition (CBD)
 - CeO. *See* Cerium oxide (CeO)
 - Ceramic coating technology, 551
 - Cerium oxide (CeO)
 - and LZO
 - CSD buffer layer materials, 683
 - epitaxial growth, NiW, 685, 686
 - metallo-organic salts, 685

- Cerium oxide (CeO) (*cont.*)
 preparation, 684
 surface planarity, 686
 surface texture, buffer layer stack,
 685, 687
 x-ray pole measurements, 685, 686
 textured layers, CeO₂, 126
 un-doped CeO₂, 635
- Cetyltrimethylammonium bromide
 (CTAB), 251, 252
- Chemical bath deposition (CBD)
 applications, 336
 as-deposited films, 336
 coatings, 319
 control
 film thicknesses, aqueous liquid
 deposition, 333
 LFD, 334–335
 maintaining, “pH-stats”, 334
 nucleation and growth, 333
 SAMs, 335
 solid and inducing film formation, 335
 solid-solid interactions, 333
 description, 143
 early 1980s, 319
 functional properties, 319
 interactions, organic molecules, 336
 limitations, 335
 LPD, 143–144
 non-aqueous approaches, 336
 SILAR, 143
 sol-gel synthesis, 335–336
 solution chemistry (*see* Solution chemistry)
 substrate effects (*see* Substrate
 effects, CBD)
 synthesis, oxide powers, 320
 techniques, 319
 thin nonmetallic inorganic films, 320
- Chemical deposition technique, 673, 678, 679
- Chemical etching, thin film fabrication
 LAO, 769
 material, 768, 769
 oxidic thin films, 768, 769
 procedures, wet
 microsyringe, 770–771
 Pt/TiO₂/SiO₂/Si-substrate, 769–770
 requirements, 769
 processes, 769
 solution, 769
- Chemical reactivity
 condensation, 13–15
 Lewis acid properties, 11
 modifications
 alcohol exchange, 16
 alkanolamines, 18
 β-diketones, 16–17
 carboxylic acids, 18–19
 metal alkoxides, 15–16
 Sol-Gel transition, 11–13
- Chemical solution deposition (CSD)
 advantages, 567
 “all-solution” coated conductor (*see*
 “All-solution” coated conductors)
 CSD-derived BST thin films, 556
 dielectric layers, 552
 kinetic route, functional oxide films
 “composite-gel architecture” process
 flow strategy, 586, 587
 film processing, 585
 polarization hysteresis loops, CSD PZT
 film, 588, 589
 preparation, CSD PZT films, 583–584
 process space, CSD PZT films
 synthesis, 586, 587
 properties, chelating ligands, 585, 586
 relative fraction, copper oxide
 detection, 586, 588
 thermodynamic equilibrium processing
 environment, 583
 two-pronged strategy, 585
- lead processing, ferroelectric thin films
 condensation, PbTiO₃, 603, 604
 crystalline phase nucleation, 604
 gradient and gradient free films,
 601, 602
 PbTiO₃, TiO₂ leads, 603
 perovskite growth and
 densification, 605
 perovskites, 602
 PZT, 601
- processing films, fabrication, 557
 textured layers, 126
- thin ceramic/mesoscopic BTO layers, 558
- thin film cathodes
 ASR, 642, 644
 LSM, 641
 performance, IT-SOFC, 642
 spray pyrolysis, 643
- thin film electrolytes
 bulk-type materials, 636
 chemical and thermo-mechanical
 stability, YSZ, 639
 deposition techniques, 637
 grain boundary region, 634
 impurities, 639
 IT-SOFCs, 640

- $\text{La}_{0.8}\text{Sr}_{0.2}\text{Ga}_{0.8}\text{Mg}_{0.2}\text{O}_{3-\delta}$ (LSGM), 640
microstructure and electrical properties,
YSZ and CGO, 637, 638
performance, MEAs, 633–634
polycrystalline material, 635, 636
polymeric precursors, 635
propionate-based precursors, 641
slurry-based, 633
substrates, TECs, 637
two-stage spin coating procedure,
632, 633
- Citrato-ligands, 105
- Citric acid, 101
- Classical dip coating
ADDC, 248, 249
control, microstructure, 246–247
draining, 248
drying stress and cracking, 244–245
effect, condensed phases
drying stages, 242–243
rheology, 243–244
solids concentration and time
scale, 241–242
equipment, 249
film thickness and stream line position
Landau-Levich based model, 237, 238
measures, 238–239
Newtonian liquids, 237
parameters, 239
vs. withdrawal speed curve, 237–238
flow patterns, streamlines, 235, 236
glue removal, thermal processing, 248–249
optimization optical ATO, 249
pure and binary fluids
consequences, sol-gel film
deposition, 241
differences, 240
ellipsometry and fluorescence
imaging, 239
Marangoni effect, 240–241
sol-gel, 239
thickness profiles, 239–240
steady-state, 235, 236
substrates, 248
tube and cylindrical cavities, 249, 250
withdrawal process, 249
- CMR. *See* Colossal magnetoresistance (CMR)
- Coated conductors
“all-solution” (*see* “All-solution”
coated conductors)
definition, 674
HTS tapes
first and second generation, 677–679
processes, 2G, 678–680
- Coating solutions
butoxides complexes, 20–21
complex oxide film processing, 21
CSD, 19–20
hydrolysis and condensation, 21
metal alkoxides, 20
preparation, 20
- Coincident site lattice (CSL), 398–399
- Colossal magnetoresistance (CMR)
definition, 625
effects, 626
oxides, 627
- Commercial off the shelf (COTS) systems, 314
- Complex alkoxide precursors
aluminate spinel precursor, 86–87
molecular structure design concept, 85–86
oxygen atoms, 85, 86
- Complex metal-oxide films
 $\text{Ba}_{1-x}\text{Sr}_x\text{TiO}_3$, 152, 153
description, 152
 $\text{La}_{1-x}(\text{Sr},\text{Ca})_x\text{MnO}_3$, 152, 154
 $\text{YBa}_2\text{Cu}_3\text{O}_{7-x}$, 155–156
- Composite film processing, particles larger
than 100 nm
description, 478
economic production, 477
failure mechanism
mitigation measures, 447
reduction, temperature, 447
thermal, 446
thermo-chemical, 446–447
thermo-chemo-mechanical, 447
sintering temperature reduction
aid, 447–448
mixed powder sizes, 448–449
small powder sizes, 448
sol infiltration, 449
sol-gel (*see* Sol-gel films)
thick films
ceramic materials, 446
description, 445
different techniques, 445
electrophoresis and spray coating, 445
materials, 445
powder based deposition routes, 445
screen printing, 445–446
- “Composite gel architecture” approach,
586–588
- Condensation
(Alk)oxolation, 13–14

- Condensation (*cont.*)
 description, 13
 olation, 14–15
 reactions, 99–100
- Conductive oxide precursor solutions
 APP route
 LNO, 759
 LSCMO (*see* Lanthanum strontium calcium manganese oxide (LSCMO) material system)
 LSCO solution, 759–760
 description, 758–759
 lanthanum, 759
 transparent conducting oxides
 ATO, 661, 662
 AZO, 660
 ITO, 659
- Copolymer micelle lithography, gold
 nanoparticle hard masks
 diblock-copolymer, 528
 dimensions and inter-micelle spacing, 528
 line scans, preparation process, 526, 527
 template-based preparation, PbTiO_3
 nanograins, 526, 527
- COTS. *See* Commercial off the shelf (COTS) systems
- Crystallization and phase evolution behavior
 “amorphous”, 358
 analysis, 358
 chemical effects hydroxyl content, 367–368
 organic content, 368–369
 control
 coherent/semi-coherent interface, 376
 free energy variation, 375–376
 temperature, PLZT deposited films, 374–375
- CSD based films, 358
 film properties, 358
 intermediate
 carboxylate, 363
 fluorite/pyrochlore phase, 361
 formation, pyrochlore, 361
 free energy material
 materials, 362
 microstructures, PZT and BST thin films, 363, 364
 nature and distribution, 363
 non- ABO_3 stoichiometry, 361–362
 perspectives, 360–361
 pO₂ effects, 363
 preparation, BT and ST thin film, 363
 pyrochlore matrix and perovskite
 growth, TEM, 362
 mapping, free energy
 chemical, physical and structural factors, 358–359
 free energy vs. composition, PbO-TiO_2 material system, 359–360
 free energy vs. temperature, 358, 359
 kinetic constraints, 360
 nucleation and growth
 curves, 366
 densities, 366
 description, 363
 functions, nuclei radius, 364, 366
 Gibbs free energy, 363–364
 homogeneous and heterogeneous, 364–365
 Johnson-Mehl-Avrami model, 366
 magnitude effects, 373–375
 process, 366–367
 relationship, 366
 physical characteristics
 heat treatment, 371
 impacts, 370
 properties, 370, 371
 surface energies, 370–371
 structural factors
 calculation, free volume, 372
 changes, pyrolysis, 372
 differences, 372–373
 EXAFS analysis, 372
- CSD precursors
 evolution
 acetate precursors, 226–227, 420
 crystals, 224
 formation, M-O-M bonds, 224, 356
 FTIR (*see* Fourier transform infrared (FTIR) spectroscopy)
 gel film, 224
 group frequencies, 224, 225
 lanthanum zirconate, 224–225
 lead zirconium titanate (PZT), 171, 172, 224
 niobium silicate formation, 226
 thermal treatment, 227
 vitreous materials, 224
 identification, 218
 inorganic (*see* Inorganic (water-based) precursors)
 organics
 alkoxides (*see* Alkoxide-derived precursors)

- group frequencies, 218, 219
 - CSD. *See* Chemical solution deposition (CSD)
 - CSD technology
 - binary systems (*see* Binary systems, CSD)
 - CBD, 143
 - citrate gel/pechini process, 142–143
 - complex-oxide, 51
 - ferroelectric, 532
 - microstructural instability, ultrathin perovskite films, 519, 520
 - PAD, 141–142
 - processing routes, 518
 - PTO islands, 523
 - Sol-Gel, 142
 - ternary systems (*see* Ternary systems, CSD)
 - CSL. *See* Coincident site lattice (CSL)
- D**
- Decomposition behavior and temperature, crystallization film
 - additional effects, 347
 - alkoxide derived (organic)
 - acetone, 171
 - DTA curve and XRD patterns, 174, 175
 - FTIR reflection spectra, volatile species, 171–172
 - isopropoxide precursors, 172–173
 - material system influences, 173
 - $\text{Na}_{0.5}\text{Bi}_{0.5}\text{TiO}_3$ acetate-butoxide, 174–175
 - temperature ranges, 174
 - TG/DTG/EGA-MS/DTA analysis, air, 169, 170
 - total mass loss, 169
 - solution precursor effects
 - BST system, 346
 - FTIR, 346–347
 - impacts, 346
 - precursor chemistry and thermal treatment, 346
 - PZT material system, 346
 - shorter chain organic species and lower boiling point solvents, 347
 - variations, precursor selection, 347
 - XRD analysis, 346
 - water-based, 175
 - Decomposition behavior, MOD processes
 - deposited layer, 35
 - long chain metal carboxylates, 38–39
 - metal acetates and propionates, 36–38
 - organic radicals, 36
 - thermogravimetric analysis, 35–36
 - Densification processes
 - capillary contraction
 - definition, 353
 - driving forces, 354–355
 - relationship, processing conditions and film properties, 355–356
 - consolidation behaviour, solution derived ZrO_2 thin films, 353–354
 - continued condensation reactions, 353
 - contributions, 353
 - crystalline ferroelectric materials, 353
 - skeletal and structural relaxation, 353
 - structural evolution, pyrolysis, 356–357
 - viscous flow, 353
 - volatilization, 354
 - Dielectric film processing
 - BTO film, 559, 560
 - cationic surfactant, 559
 - CSD processes, 557, 558
 - micro structure, 557
 - PZT/PLZT, 557, 558
 - Differential scanning calorimetry (DSC)
 - and DTA, 168
 - operating principle, 168
 - sensitivity, 168
 - temperature range, 168
 - Differential thermal analysis (DTA)
 - DSC sensitivity, 168
 - and DTG temperatures, 171
 - PZT precursors, 172–173
 - and TA, 164
 - Dip-coating technique
 - applications, 233
 - classical (*see* Classical dip coating)
 - composite sol-gel films, 455
 - EISA process (*see* Evaporation induced self-assembly (EISA))
 - microstructures, 257
 - precursor solution chemistry, 234–235
 - process, 233, 234
 - structure and properties, 257
 - technical stages, 233
 - thin film formation, 233–234
 - wet chemical thin film deposition, 233
 - Direct methanol fuel cells (DMFC), 645, 646
 - Dispersive spectrometers
 - double fascicules and prism, 216
 - schematic, 216, 217
 - single-beam, 216
 - DMFC. *See* Direct methanol fuel cells (DMFC)
 - DTA. *See* Differential thermal analysis (DTA)

E

E-beam lithography. *See* Electron beam lithography

ED. *See* Electroless deposition (ED)

EGA. *See* Evolved gas analysis (EGA)

EISA. *See* Evaporation induced self-assembly (EISA)

Electrode materials

multilayer capacitors, BaTiO₃ and LaNiO₃ layers, 556, 557

oxidation resistant, 554

reducing atmosphere, 555–556

Electroless deposition (ED), 323–326

Electron beam lithography

advantages, 490, 491

damage

exposure, 498

knock-on displacement and radiolysis, 498–499

Knotek-Feibelman mechanism, 499–500

SCRIBE process and different mechanisms, 498

electron gun, 490

exposure, 490–491

inorganic materials

FEG-SEM, 491

metal halides, 491–494

metal oxides, 494–498

VG-STEM, 491

limitation, 490, 491

physical-chemical solution deposition

metal naphthenates, 508–510

paradigm shift, 500

spin-coatable metal alkoxides

(*see* Spin-coatable metal alkoxide electron beam resistance)

positive resists, 490

process, 490

structure, 490

Electrophoresis, 552

Electrostatic spray deposition (ESD), 633, 640–641, 643, 645

Ellipsometric porosimetry (EP), 710, 711

EP. *See* Ellipsometric porosimetry (EP)

Epitaxial films

CBD method, 383

crystallization

critical nucleus formation, 388–389

differences, 389

free energy function, 389

kinetic limited, 389–390

metastable phases, 390–391

CSD and MOD, 383

grain growth (*see* Grain growth, epitaxial films)

heating, 384

limitation, CSD film thickness, 401

mechanical instability, 386–388

MOCVD, 401–402

patterning, 400–401

photoresist coatings, 383

precursor chemistries, 385–386

review, 384

soft lithographic and

photolithographic, 384

spin-coating, 383–384

synthesis, single crystal thin films, 383

ZnO, 401

Equilibrium approaches, oxide-base metal integration

microstructural and electronic properties as-fired and reoxidized and BaTiO₃ film, 579, 580

BaTiO₃ film, 581, 582

dielectric properties, films, 581

film morphologies, 577

grain and coherent crystal size, 581, 582

nickel-based electrodes, 579

permittivity and loss tangent vs. field measurements, 579, 580

preparation, BaTiO₃ film, 577, 579

solution chemistry and processing

chelate-based chemistry, 574–575

phase evolution, BaTiO₃ films, 576–578

rapid drying, hotplate, 575

X-ray diffraction patterns, PZT

xerogels, 575, 576

thermodynamics, oxidation

equations, metal, 572

Gibb's free energy, formation, 573

oxygen partial pressures, 573, 574

Richardson-Ellingham

diagram, 573, 574

ESD. *See* Electrostatic spray deposition (ESD)

Evaporation induced self-assembly (EISA)

advantages, 252

amphiphilic molecules, 249

critical micelle concentration (CMC), 250

definition, 250

film formation, 249

gelation, sol-gel species, 250

hexagonal silica-surfactant

mesophases, 251

inorganic polymerization, 253

liquid-crystalline nature, 253–254

- macroscopically inhomogeneous
 - films, 251–252
 - nanocrystal (*see* Nanocrystal)
 - organic-inorganic
 - nanocomposites, 254–255
 - schematic phase CTAB, 251, 252
 - silica-surfactant micelles, 252–253
 - sol-gel, 252
 - stages, 250, 251
 - steady-state film thinning profile, 252, 253
 - surfactants and concentration, 250–251
 - Evolved gas analysis (EGA)
 - acetone amount, 171
 - TA, 169
 - EXAFS. *See* Extended X-ray absorption fine structure spectroscopy (EXAFS)
 - Extended X-ray absorption fine structure spectroscopy (EXAFS), 54
 - theory, 181–184
- F**
- FEG-SEM. *See* Field Emission Gun-equipped Scanning Electron Microscope (FEG-SEM)
 - Ferroelectric nanograins, templated growth
 - CSD technique, 519, 520
 - embedding technique, 521
 - self-assembly technique, 520
 - Ferroelectric nanotubes, soft-template infiltration, 524–525
 - Ferroelectric thin films
 - optimal functionality, film and device, 600
 - principle, flexural heteromorph structure, 599, 600
 - PZT, 600
 - Field effect transistor (FET), 504–505
 - Field Emission Gun-equipped Scanning Electron Microscope (FEG-SEM), 491
 - Film deposition and properties control
 - carboxylate, aqueous CSD, 120–121
 - layer thickness, 122
 - metal ion concentration, 121
 - morphology control, process conditions
 - AR-FTIR, 125
 - crystallization temperature, 124
 - lanthanum, 124
 - ZnO film, 122, 124
 - superconducting layers, 126
 - textured layers, 126
 - thicker layers, 122
 - ultrathin film deposition, 127–132
 - ultrathin layers, 127
 - wetting
 - aqueous chemical solution deposition
 - methods, 117–118
 - CSD method, 117
 - LSMCD technique, 117
 - Pb(II) citrate and acetate, 119–120
 - polyvinyl alcohol, 118
 - PZT water based precursor, 119
 - SPM/piranha, 118–119
 - UV/ozone technique, 118
- Fourier transform infrared (FTIR) spectroscopy
 - advantages, 217
 - alkoxide-derived precursors, 220–222
 - barium strontium titanate thin film systems, 419, 420
 - crystallization, strontium niobate films, 225, 226
 - doped lanthanum chromites, 226, 227
 - electron beam resists, 503
 - GATR-FTIR, 225, 226
 - group frequencies, 225
 - impurity traces and compound formation, 227
 - measurement, 216
 - metal carboxylates, coordination modes, 221
 - performance, 217
 - polystyrene absorbance and transmittance, 215
 - preparation, PZT film and powder, 224, 225
 - schematic, 217
 - SnO₂ formation, 227, 228
- Fresnel reflection and reflectance, 735
- G**
- Gas phase techniques, 552, 556
 - Gel decomposition
 - cation distribution, 115
 - homogeneity, 115–116
 - homogeneous precursor solution, 114
 - mechanism
 - citratoperoxo metal ion gels, 113–114
 - homogeneous gel/gel film, 113
 - thermal decomposition, 114
 - powders *vs.* films, 116–117

- Gel formation mechanism
- alkoxide ligands, 109–110
 - aqueous carboxylate, 103–104
 - carboxylate salts/complexes, 109
 - carboxylates, complexation and gel formation
 - ammonium bridges, 107
 - citrate-ligands, 105
 - EXAFS, 106
 - oxo-peroxo-citrate metal complexes, 106
 - tetranuclear ammonium citratoperoxotitanate complex, 107
 - tetranuclear anion, 108
 - citrate complex, 111
 - concept
 - aqueous carboxylate, 104
 - network formation mechanism, 104–105
 - water evaporation, 104
 - hydrogen peroxide, 110
 - metal ions, 109
 - polymer complex methods, 111–112
 - precursor solution, 108
- Giant magnetoresistive (GMR) effect, 625
- Gold nanoparticle hard masks. *See* copolymer micelle lithography, gold nanoparticle hard masks
- Grain growth, epitaxial films
- amorphous material, 391
 - compositions, 392
 - conversion, polycrystalline $Zr(Y)O_2$ film, 392, 393
 - dark field TEM, 392
 - description, 391
 - dislocation network forms, 392
 - dissimilar structures
 - CSL and NCSL, 398–399
 - lattice spacing, 398
 - rules, 399–400
 - elimination, 392
 - heat treatment, 391
 - interface, 392
 - $LiNbO_3$, 393
 - mechanisms, 393
 - multilayered
 - CeO_2 , 395
 - LTO seed, 395
 - metal substrates, 394
 - Ni-W substrate, 394–395
 - PZT/LSMO/ $SrTiO_3$ specimens, 395–396
 - superconducting wires, 395
 - YBCO synthesis, 395
 - non-oxide, 394
 - solid-solution compositions, 393
 - $SrZrO_3/SrTiO_3$ interface, 393
 - strain energy, 392
 - thermodynamics, morphological instabilities, 396–398
 - vapor grown films, 392
- H**
- High temperature superconductivity (HTS)
- annealing/firing barium fluoride, 691
 - dependence, normalized critical current, 691
 - energy density, 673, 674
 - first and second generation, tapes
 - “all-solution coated conductor”, 679
 - film deposition, 678
 - nickel-alloys, 679–680
 - heating schedule, TFA-YBCO, 691, 692
 - MOD, 690
 - parameters
 - current, 675–676
 - magnetic and irreversibility fields, 676–677
 - materials, 675
 - relationship, parameters, 674, 675
 - processes, 2G tapes, 678–680
 - resistive measurement, I-U characteristics, 691, 692
 - Zr–Ba-Oxide nanoparticles, 693
- Homogeneity, solution, 115–116, 203, 432, 433
- Homogeneity, (micro) structural, 454, 562
- HSQ. *See* Hydrogen silsesquioxane (HSQ)
- HTS. *See* High temperature superconductivity (HTS)
- Hydrogen silsesquioxane (HSQ), 533, 536
- Hydrolysis, 11
- Hydrolysis, organic media
- metal oxide sol-gel process, 72–73
 - molecular mechanisms, 73–76
 - sol-gel transformations, 72
 - supramolecular sol-gel mechanisms and colloid particles, 76–79
- I**
- Index gradient layers
- films, graded porosity etching, phase-separable glass, 718

- porous multilayer assembly,
 - preparation, 717, 718
 - preparation, etching, 719
 - preparation, phase separated film
 - leaching, 718
 - “moth eye” structures
 - linear gratings, 720
 - processing, embossing tools
 - fabrication, 720–721
 - realization, depths of imprints, 721, 722
 - reflectivity, cross and linear gratings, 722, 723
 - refractive index, 719, 720
 - sol-gel processing, thin films, 716
 - Indium tin oxide (ITO)
 - compositional flexibility, 659
 - preparation, 659
 - Re-dispersible crystalline powders, 660
 - spin/dip-coating experiments, 660
 - Infrared (IR) spectroscopy
 - advantages and disadvantages, 215–216
 - analysis, 213
 - characteristics, 229
 - complex molecules, 215
 - crystallization, 229
 - CSD precursors (*see* CSD precursors)
 - description, 213, 214
 - frequencies, 214
 - FTIR, 216–217
 - gaseous, liquid and solid samples
 - preparation, 218
 - investigation, precursors, 213
 - spectrometers (*see* Spectrometers)
 - transmission, spectrum, 214
 - vibrational modes, CH₂ groups, 215, 216
 - visible and microwave, electromagnetic field, 213, 214
 - Inkjet printing and direct writing methods
 - application (*see* Printed strain gages and load-frame testing)
 - conductive samples, 317
 - development, 316–317
 - integration, solution precursors, 316
 - low process temperature metal ink (*see* Low process temperature metal ink)
 - LTCC, 303
 - materials, 303
 - oxides and metals
 - applications, 311
 - AZO, 310
 - chemistries and processing, 309
 - copper traces, 311, 312
 - gravure printing, 310
 - high quality buffer and superconducting YBCO layers, 309
 - materials, 309
 - nano-lithography, 310
 - PDMS, 310–311
 - piezoelectric, pneumatic, or thermal methods, 309
 - precursors, 309–310
 - stamp relief structure, 311
 - TFTs, 310
 - volume fraction inks, 310
 - X-ray diffraction and optical imaging, 311, 313
 - yttrium, barium acetate and copper, 310
 - techniques, 303
 - transparent conductors and dielectrics, 318
 - Inkjet technology, 561
 - Inorganic (water-based) precursors
 - chelating agents, 222
 - FTIR spectra
 - La-Co-CA system, 222, 223
 - pyro-P and tripoly-P solutions, 222–223
 - group frequencies, 218, 219
 - nitrates, 222
 - Institut für Werkstoffe der Elektrotechnik II (IWE II), 748
 - Intermediate temperature solid oxide fuel cell (IT-SOFCs)
 - definition, 631
 - electrolytes, 640
 - performance cathodes, 642
 - temperature region, 641
 - IR spectroscopy. *See* Infrared (IR) spectroscopy
 - Isomeric zirconium butoxides, 8
 - ITO. *See* Indium tin oxide (ITO)
 - IT-SOFCs. *See* Intermediate temperature solid oxide fuel cell (IT-SOFCs)
 - IWE II. *See* Institut für Werkstoffe der Elektrotechnik II (IWE II)
- L**
- Lanthanum aluminium oxide (LAO), 762, 769
 - Lanthanum nickel oxide (LNO), 759
 - Lanthanum strontium calcium manganese oxide (LSCMO) material system
 - solution preparation, 760–761
 - synthesis
 - LCMO70/30, 761
 - LSMO70/30, 761

- Lanthanum strontium cobalt oxide (LSCO), 759–760
- Lanthanum zirconate (LZO)
and CeO (*see* Cerium oxide (CeO))
'seeds', growth, 397
- LAO. *See* Lanthanum aluminium oxide (LAO)
- Laser-assisted low temperature crystallization
absorption, ferroelectric materials, 439–440
advantages, 439
amorphous films, 440
annealing, 440
ArF and KrF gases, excimer, 440
experimental setup, 440
preparation, $\text{Bi}_{1.5}\text{Zn}_{0.5}\text{Nb}_{1.5}\text{O}_{6.5}$, 440
semiconductor industry, 439
size-and cost, 440
- La_3TaO_7 (LTO), 395
- Lead-titanate-based material systems
characteristics, 748
drying, lead (II) acetate trihydrate, 749–750
EGMME route, 748
ether-alcohols, 748
flow chart, 53
preparation, 748
PZT30/70
EGMME route, 750–753
IWE route, 754
removing water, crystallization, 748–749
- Lead zirconate titanate (PZT)
control, microstructure and orientation, 409–417, 557
deformation modes, 613, 614
dielectric constant, 610
elements/pMUT, 607, 608
ferroelectric, 609
MEMS, 599
perovskite materials, 563
solid solution system, 600
- LED. *See* Light emitting diode (LED)
- Lewis acid properties, 11
- LFMR. *See* Low field magnetoresistance (LFMR)
- Light emitting diode (LED), 401, 402
- LIPA. *See* Long Island Power Authority (LIPA)
- Liquid phase deposition (LPD), 143–144, 323, 325–326
- Liquid source misted chemical deposition (LSMCD), 117, 278, 283, 285–287
- Lithium rechargeable batteries
capacity, 477
charging and discharging, 476–477
cyclic voltammograms, 476
electrochemical
measurements, 476
properties, 475–476
formation, 477
precursor solution preparation, 475
synthesis, 478
X-ray diffraction, 476
- Long Island Power Authority (LIPA), 695, 696
- Long vs. short chain carboxylates
advantages, 40
alkoxides, 39
APP, 40
carbon, 40
copper and chromium dodecanoate, 39
lead neodecanoate, 42
long-chain lead carboxylates, 39
metal carboxylates, 41, 42
trifluoroacetates, 43–44
- Low field magnetoresistance (LFMR), 626, 628
- Low process temperature metal ink
chemistry and formulation, 303–304
compositions, 304
functional materials, 303
nanoparticle synthesis (*see* Nanoparticle synthesis)
- Low temperature co-fired ceramics (LTCC), 303, 304, 460
- Low-temperature processing,
functional-oxide films
activation, 441
amorphous, 441
application requirements, 432
chemical solution deposition process, 432
description, 431
design, heterometallic precursor, 431
invisible electronic circuits, 432
laser-assisted heating, 439–440
lead titanate, 441
photochemical activation, 438–439
properties, BST films, 432
seeding layers and crystallization (*see* Seeding layers and crystallization seeds)
sol-gel (*see* Sol-gel hydrothermal processing)
solution chemistry
BaTiO₃ and SrTiO₃, 433
PbZrO₃–PbTiO₃, 433, 434

- perovskite phase, 433
 - preparation, LiNbO₃ thin films, 432–433
 - Zr/Ti ratio, PZT-based thin films, 433, 434
 - stability, 432
 - LPD. *See* Liquid phase deposition (LPD)
 - LSC. *See* Luminescent solar concentrator (LSC)
 - LSMCD. *See* Liquid source misted chemical deposition (LSMCD)
 - LTCC. *See* Low temperature co-fired ceramics (LTCC)
 - LTCC technology, 303, 304
 - LTO. *See* La₃TaO₇ (LTO)
 - Luminescent solar concentrator (LSC), 739, 740
 - Luminescent thin films
 - active waveguides, 736
 - device applications, 726
 - displays, 737
 - electrons, 725
 - excitation processes, phosphors types, 725, 726
 - materials, 730–734
 - optics (*see* Optics, luminescent thin films)
 - precursor chemistry, 727–730
 - RE ions, 726
 - solar energy applications (*see* Solar energy applications)
 - X-ray imaging, 738
 - LZO. *See* Lanthanum zirconate (LZO)
- M**
- Magnesium fluoride (MgF₂)-films
 - colloidal, 713
 - preparation, 712–713
 - properties, $\lambda/4$ layer, 713
 - Magnetoresistance (MR) materials
 - avoidance, organic solvents, 627
 - CMR, 625–626
 - definition, 625
 - doped perovskite type manganite, 626
 - epitaxial manganite films, 626
 - GMR effect, 625
 - metal ions concentration, precursor solutions, 627
 - spray pyrolysis, 628
 - Materials, luminescent thin films
 - lanthanum and gadolinium, 730
 - optical coatings/planar waveguides, 732
 - PL excitation and emission spectra, 730, 732
 - polymer additives, 734
 - preparation, 734
 - RE orthovanadates (REVO₄) and RE orthophosphates (REPO₄), 733
 - synthetic conditions, CSD, 730, 731
 - MEA. *See* Membrane-electrode assembly (MEA)
 - Mechanical instability, epitaxial films
 - crack extension, 387–388
 - critical thickness, 386–387
 - differentiation, free energy function, 387–388
 - elastomer, 388
 - evaporation causes, 386
 - formation, ‘mud’ cracks, 386
 - storage, strain energy, 387
 - tensile stresses, 387
 - waxy films, 386
 - Membrane-electrode assembly (MEA)
 - anode-supported conventional SOFC, plate design, 629, 630
 - components, 632
 - performance, 633
 - MEMS. *See* Micro-electro mechanical systems (MEMS)
 - Metal acetates and propionates
 - classification, 36–37
 - cobalt and silver acetate, 37
 - decomposition behavior, 37
 - description, 36
 - nickel oxide, nitrogen, 38
 - temperatures, 38–39
 - Metal alkoxides
 - central atom electronegativity and radius, 9
 - chemical reactivity (*see* Chemical reactivity)
 - chemical structure, 6
 - coating solutions, 19–21
 - CSD processing, 3
 - electronic and sterical factors, 6
 - indication, 9
 - isomeric zirconium butoxides, 8
 - organic solvents, 8
 - properties
 - HCl, 4
 - polar metal-oxygen bond, 4, 6
 - silicon, 4
 - structural elements and nomenclature, 4, 5
 - water, 4
 - sol-gel reaction, 3–4
 - spectroscopic methods, 10
 - structures selection, 6, 7
 - synthesis concepts, 4

- Metal ions, water
 aqua ligand protons, 96, 97
 atoms electronegativities, 98
 cation and hydrolysis reaction, 95, 96
 complexation, ligands
 anions/molecules, 100
 citric acid, 101
 hydrolyzing and precipitating, 102
 metal ion-ligand systems, 103
 Pb^{2+} -citrate complexation, 101–102
 polydentate molecules, 100
 Ringbom's side reaction coefficient
 $\alpha_{\text{M(X)}}$, 101
 condensation reactions, 99–100
 deprotonation reaction, 99
 partial charges model, 98
 pH diagram, 97
 precipitation, water evaporation, 103
 small size and charge cations, 96
 sol-gel synthesis, 95
 solvating water molecules, 95
 tetravalent, 97
 valency, 96
- Metallic oxide base electrodes
 BTO on LNO, 556, 567
 control, stoichiometry, 624
 CSD, LNO, 623
 PZT on LNO, 622–623
 solution synthesis, LNO, 759
 SrRuO_3 (SRO), 624–625
- Metallo-organic-decomposition (MOD)
 processes
 carboxylates, 33
 decomposition behavior, 35–39
 description, 32
 M-carboxylates, 32–33
 thin-film-deposition and thermal
 treatment, 33–35
- Metal-organic chemical vapor deposition
 (MOCVD)
 metallo-organic precursors, 276, 300
 processing
 aerosol, 297, 299
 conditions, 277
 control parameters, 277
- Metallo-organic decomposition/metal organic
 deposition (MOD), 32, 144
- Methyl silsesquioxane (MSQ), 533–535
- MgF_2 -films. *See* Magnesium fluoride
 (MGF_2)-films
- Micelles templated by self-assembly of
 ligands (MTSAL)
 complex precursors, 87–88
 surface ligand, 84–85
 transformation, 77–78
- Micro-electro mechanical systems (MEMS),
 594–595
- Micro-solid oxide fuel cells
 PEMFC and the DMFC, 645, 646
 μ -SOFC structure, 646–647
- Mixed metallo-organic precursor systems
 alkali-metals-based perovskites, 55–61
 alkalis, 52
 barium/strontium titanate films, 52
 BST, 61–64
 CSD, 51
 environment awareness, 51–52
 EXAFS, 54
 PLZT gels and films, 52–53
 PZT sol, 54
 spectroscopic and chromatographic
 methods, 53
 transalcoholysis reaction, 53
 zirconium EXAFS spectra, 54
- MLCC. *See* Multilayer ceramic capacitors
 (MLCC)
- MOCVD. *See* Metal-organic chemical vapor
 deposition (MOCVD)
- MOD. *See* Metallo-organic decomposition/
 metal organic deposition (MOD)
- Molecular mechanisms, hydrolysis and
 condensation
 heteroligands, 75
 metal alkoxide complexes, 73
 metal-oxygen cores, 74, 75
 thermodynamically driven
 transformation, 76
 zirconium hydroxo-alkoxides, 73–74
 $\text{Zr}_4(\text{O}^{\text{n}} \text{Pr})_{16}$, 73, 74
- MR materials. *See* Magnetoresistance (MR)
 materials
- MSQ. *See* Methyl silsesquioxane (MSQ)
- MTSAL. *See* Micelles templated by
 self-assembly of ligands (MTSAL)
- Multilayer AR-stacks and optical filters
 color gradient filter VARIOTRANS[®]
 and reflectivity, 716, 717
 interference assemblies, 716
 interference-type, applications
 outermost S-layer, damage, 716
 reflectivity, triple layer coatings
 and architectures, 715
 TiO_2 , 714
- Multilayer ceramic capacitors (MLCC)
 design parameters, 553, 554
 estimation, capacitance, 550

- miniaturization
 - characteristics, thin film deposition
 - methods, 552, 553
 - electrophoresis, 552
 - gas phase techniques, 552
 - surface area, chip, 551
 - thin films, preparation, 552
 - thin film technologies, 551
 - Pt inner electrodes, 550
- N**
- Nano-composite electro-ceramic thin films
 - characteristics, multilayered oxide, 459–460
 - electrochromism characteristics, 459
 - heterogeneity, 463–464, 478
 - micro-emulsion mediated synthesis
 - BTO particles, 460
 - dielectric properties, 461–462
 - formation, nano-crystalline core-shell structures, 462–464
 - LTCC, MEMS and MLCC, 460
 - multiferroicity, 459
 - oxide thin films, 459
 - self-assembling (*see* Self-assembling/self-organized organic systems)
 - super-lattice ordering (*see* Super-lattice ordering, nano-composite thin films)
 - synthesis, 459
 - Nanocrystal
 - artificial solids, 257
 - coupling interactions, 257
 - DNA hybridization, 256
 - 3D NC arrays, 257
 - gel formation, 257
 - micelles, 255–256
 - polymer/silica, 255, 256
 - synthesis procedures, 255
 - Nanoparticle synthesis
 - Debye model with Lindemann law, 304
 - LTCC technology, 304
 - microemulsion mediated synthesis, 559
 - reactivity, 304
 - silver (*see* Silver (Ag) nanoparticle synthesis)
 - sintering reaction, melting
 - temperatures, 304
 - NCSL. *See* Near coincident site lattice (NCSL)
 - Near coincident site lattice (NCSL), 399
 - Nucleation site, e-beam lithography
 - separated PTO nanoislands deposit, 523, 524
 - TiO₂ dot structures, 523, 524
 - TiO₂ patterning, 522, 523
 - topographic AFM scan, PTO
 - crystals, 524, 525
 - two-layer resist process, PMMA
 - polymer, 522, 523
- O**
- Olation, 14–15
 - Optical filters
 - color gradient filter VARIOTRANS® and reflectivity, 716, 717
 - interference assemblies, 715–716
 - Optics, luminescent thin films
 - incidence, light, 735
 - materials, light absorption, 735
 - RE-doped phosphors, 735–736
 - transparency, 726, 734
 - Optimization strategies, TCO thin films
 - dense films, multiple coating techniques
 - microstructures, 663, 664
 - oriented growth of sol-gel films, 664, 665
 - preparation, Nb-doped TiO₂ thin films, 664, 665
 - infiltration, porous films, 664–666
 - Orientation and microstructure design, crystallization film
 - amorphous films
 - columnar growth, 408
 - competition, 408
 - control, compositional
 - homogeneity, 408
 - evolution, 410
 - materials and compositions, lattice
 - constants, 409, 410
 - phase formation, 408
 - (Ba_{1-x}Sr_x)TiO₃ Films (*see* BST thin film systems)
 - differences, 425
 - 'dissolution principle', 426
 - formation, 407
 - intermediate phases, 407
 - metal-Ti-oxo carbonate phase, 426
 - microstructure, 425
 - Pb(Zr_xTi_{1-x})O₃ films (*see* Pb(Zr_xTi_{1-x})O₃ films)
 - processing, 407

- Orientation and microstructure design (*cont.*)
 thermolysis and structural relaxation
 reactions, 407
- Oxide thin films, electronic and ionic
 conductivities
 metallic oxide base electrodes, 622–625
 MR materials (*see* Magnetoresistance (MR)
 materials)
 SOFCs (*see* Solid oxide fuel cells (SOFCs))
 utilization, 621
- P**
- PAD. *See* Polymer-assisted deposition (PAD)
- Patterning methods
 alignment system, 561, 562
 BST films, 561
 inkjet technology, 561
 processing, TMC, 559, 560
 thin film printing methods, 562
 TMC, dielectric and electrode layers,
 560, 561
- Pb(Zr_xTi_{1-x})O₃ films
 alloy formation, 414
 compositions, 409
 control, texture orientation, 410
 description, 409
 epitaxial system, 412
 exothermic reaction, 412
 heterogeneous nucleation, 411
 impact, film thickness and precursor
 chemistry, 416–417
 intermetallic phase model, 411–412
 memory applications, 409, 410
 microstructure evolution process, 410–411
 nanocrystalline fluorite/pyrochlore
 phases, 411
 pyrolysis, 412
 PZT/Pt interface, 414
 substrate, 415
 tetragonal distortion, 409, 410
 texture and microstructure development,
 414–415
 transmission electron microscopic
 and XRD, 413–414
- Pechini method/process/route, 112, 142, 734
- PEMFC. *See* Proton exchange membrane
 fuel cell (PEMFC)
- PFM. *See* Piezoelectric force microscopy
 (PFM)
- Phosphors, 725
- Photoluminescence (PL)
 excitation, 730, 732
 and ferroelectric properties, 732
 intensity, Y₂O₃:Eu³⁺, Bi³⁺, 741
- Physical deposition technique, 674,
 678–679, 683
- Physical vacuum-based technologies, 659
- Piezoelectric force microscopy (PFM)
 ferroelectric switching, islands, 524
 in-plane images, piezoelectric active
 surface fraction gain, 533, 534
 and micro-Raman spectroscopy, 525
 MSQ embedded PTO grain array, 534, 535
 setup, 529
- Piezoelectricity
 advantages, 598
 coefficients
 in-plane stress, 606
 transverse, 606, 607
 variation, electrodes, 606
 deformation, 597
 electrostatic devices, 598
- MEMS devices
 advantage, 614
 deformation modes, PZT thin film,
 613, 614
 energy harvesting, 610
 measurements, 610, 611
 one array element, ink-jet printing
 head, 613, 614
 optical scanner, imaging, 612, 613
 poLight tunable lens, autofocus camera
 systems, 611, 612
 PZT ceramics, 609
 resonant vibration harvester, 611, 612
 TFBAR, 609
 thin film vibration energy harvester,
 610, 611
- micromachining and thin film structures,
 607–608
- momentum, ferroelectric films, 599
- PZT, 597
- Piezoelectric micromachined ultrasonic
 transducers (pMUT), 607–608
- PL. *See* Photoluminescence (PL)
- PMMA. *See* Polymethyl methacrylate
 (PMMA)
- pMUT. *See* Piezoelectric micromachined
 ultrasonic transducers (pMUT)
- Polar oxide thin films, MEMS applications
 conversions and signal generations, 594

- integration, ferroelectric thin films
 - (*see* Ferroelectric thin films)
 - miniaturized systems, 594
 - piezoelectricity (*see* Piezoelectricity)
 - pyroelectricity (*see* Pyroelectricity)
 - sensors and actuators, 593
 - silicon technology, 595
 - Polydimethylsiloxane (PDMS), 310–311
 - Polymer-assisted deposition (PAD)
 - chemical solution deposition method, 144
 - complex metal-oxide films, 152–156
 - CSDs, 141–142
 - metal-oxides, 141
 - metal polymer solutions, 145–146
 - MOD, 144
 - process, prepare film coatings, 144–145
 - simple metal-oxide films, 147–151
 - thermal depolymerization, 146–147
 - Polymer complex methods
 - acrylic acid, 112
 - carboxylate sol-gel route, 111
 - organic polymerization methods, 112
 - Pechini route, 112
 - Polymer precursor spin coat technique, 635, 640
 - Polymethyl methacrylate (PMMA), 522, 523
 - Porous AR films
 - acid-catalyzed hydrolysis, silicon alkoxides, 710
 - factors, sol-gel techniques, 712
 - film porosities determination, EP, 710–711
 - Lorentz-Lorentz equation, 709
 - mechanical stability, 711
 - optical spectrum, SiO₂ film, 710, 711
 - solar panel, $\lambda/4$ glazing, 712
 - Porous films, 664–666
 - Precursor chemistry
 - formation, metal complexes, 728
 - preparation, crystalline RE-doped metal oxides, 728
 - properties, 730
 - sol-gel method, 727
 - Y₂O₃, 729
 - Pressurized spray deposition (PSD), 633, 643
 - Printed strain gages and load-frame testing
 - coating, fiberglass-epoxy composite, 313
 - commercial, 313
 - COTS, 314
 - design resistance, 313, 314
 - EH-Link™ 8 strain gage system, 316, 317
 - energy-harvesting, 315–316
 - green energy, 312–313
 - hysteresis, 314
 - measures, 314
 - Microstrain SG-Link devices, 315, 316
 - monitors, self-powered wireless, 314
 - Optomec Aerosol Jet M³D print system, 313
 - sensor optimization, 313
 - silver inks, 313, 314
 - transmissions, 317
 - transverse and longitudinal strain measure, 314, 315
 - Printing techniques, 726
 - Proton exchange membrane fuel cell (PEMFC), 645, 646
 - PSD. *See* Pressurized spray deposition (PSD)
 - Pyroelectricity
 - coefficient, 595, 596
 - first and second order phase transition, 596
 - thermal energy harvesting, 597
 - PZT films
 - polarization hysteresis loops, CSD, 589
 - synthesis, device-quality thin films, 586
 - X-ray diffraction patterns, 575, 576
- Q**
- Quaternary systems
 - Fourier transforms, 208
 - PLZT films, 205
 - Ti K-edge XANES spectra, 206, 207
 - TiO₂ modifications anatase, 206–207
- R**
- RABiTS. *See* Rolling-assisted-biaxially-textured-substrates (RABiTS)
 - Rare-earth (RE) ions
 - acetates, 734
 - concentration, 732
 - luminescence, 726
 - RE-doped phosphors, 735–736
 - RE-doped planar waveguides, 736
 - Refined machining techniques, 594
 - RE ions. *See* Rare-earth (RE) ions
 - Ringbom's side reaction coefficient $\alpha_{M(X)}$, 101
 - Rolling-assisted-biaxially-textured-substrates (RABiTS), 680
- S**
- SAMs. *See* Self-assembled monolayers (SAMs)
 - Scanning probe microscopy (SPM) techniques

- Scanning probe microscopy (SPM) techniques (*cont.*)
- converse piezoelectric effect, ferroelectric perovskites, 530
 - detectable phase shift, ferroelectric crystals, 530, 531
 - heated AFM cantilever, 532
 - optical lever arm, cantilever bending detection, 529
 - PFM setup, 529
 - principle, 528–529
 - PTO grains, 530, 531
- SCRIBE. *See* Sub-nanometer Cutting and Ruling by an Intense Beam of Electrons (SCRIBE)
- Seeding layers and crystallization seeds
- deposition/heating steps, 436
 - nucleation rate, 434
 - Pt-Pb intermetallic phase, 435
 - SEM micrographs, PZT 53/47 thin films, 434–435
 - thermal decomposition/oxidation, 435
 - XRD patterns, amorphous PZT 30/70 thin films, 435, 436
- Self-assembled monolayers (SAMs), 329–330, 336
- Self-assembling/self-organized oxide systems
- characteristics
 - electrical, 467–471
 - magnetic and magnetoelectric, 471–472
 - optical, 472–474
 - structural and micro-structural, 466–467
 - controls, 464
 - growth mechanism, 465
 - guideline, 465
 - multiferroic films, 465–466
 - nanostructures, 464
 - organic, 464
 - oxide, 464
 - physical vapor deposition, 465
 - polystyrene and polymethyl methacrylate, 464
 - synthesis, 464
 - types, oxide systems, 465
 - VHN, 464
- Self-assembly technique, 520
- SILAR. *See* Successive ion layer adsorption and reaction (SILAR)
- Silicon technology, 595
- Silver (Ag) nanoparticle synthesis
- agglomeration, 305
 - chemical reduction, 304
 - coated and stabilized, 306
 - DC resistivity, direct written traces, 306, 307
 - “green” chemistries, 308
 - metallo-organic precursor routes, 308–309
 - metal resistivities *vs.* thermal treatment, 306, 307
 - precursors, 306
 - print method properties, 306, 307
 - redox reaction, 305
 - size-sintering relationship, 305
 - starch and glucose, 307–308
 - strong reducing agents, 306
 - suspensions, 305–306
 - thermal analysis, 306
- Simple metal-oxide films
- epitaxial Eu_2O_3 films, 147–149
 - UO_2 and U_3O_8
 - epitaxial growth, 149
 - polymorphic hexagonal and orthorhombic, 150
 - X-ray diffraction pattern, 149, 150
- Single source precursors (SSP)
- application, 72
 - complex alkoxide precursors, 85–87
 - construction, 71
 - hydrolysis, organic media (*see* Hydrolysis, organic media)
 - materials preparation
 - dispersions deposition, 80–82
 - porous substrates, 84–85
 - principal groups, 79–80
 - metal oxide sol-gel, 71
- Size effects, 517, 520, 551, 563
- SOFCs. *See* Solid oxide fuel cells (SOFCs)
- Solar energy applications
- configuration of solar cell and WCF, 739–741
 - conversion technology, 739
 - LSC panels, 739, 740
 - multi-layered AR coatings, 741
 - phosphor thin films, surface nanostructures, 741
 - sunlight harvesting efficiency, 739
- Sol-gel films, composite
- advantages, 450
 - coating
 - dip, 455
 - spin (*see* Spin coating, composite sol-gel films)
 - spray, 456
 - conventional ceramic film technologies, 450

- electrophoretic deposition, 455–456
- film deposition
 - crystallisation, 451
 - drying, 451
 - pyrolysis stage, 451
 - substrate, 451
 - volume changes, 451
- infiltration process, 457–458
- inks production, 450
- interfacial polymerisation, 457
- pressure, 458–459
- screen printing, 454–455
- sedimentation, 456
- sintering aids, 458
- Sol-gel hydrothermal processing
 - advantages, 436–437
 - amorphous, 437
 - conventional and hybrid, 437
 - low temperature, 436
 - low-temperature water-based synthesis, ZnO film, 437–438
 - perovskite formation, 437
- Sol-gel processing, TCO thin films
 - deposition, 657
 - dispersed crystalline particles, 657
 - ITO (*see* Indium tin oxide (ITO))
 - minute variations, processing parameters, 659
 - optimization strategies (*see* Optimization strategies, TCO thin films)
 - preparation, 658
 - printing, 666–667
 - p-type conducting, 667–669
- Sol-gel transition
 - description, 11
 - factors, 12
 - hydrolysis, 11
 - nucleophilic substitution, 11–12
 - silicon alkoxides, 12
 - tetravalent metal cations, 12–13
- Solid oxide fuel cells (SOFCs)
 - CSD (*see* Chemical solution depositions (CSDs))
 - electrical conductivity, oxygen ion-conducting electrolytes, 631
 - IT-SOFC, 631
 - MEA, 629, 630
 - micro-solid (*see* Micro-solid oxide fuel cells)
 - preventions, wide-spread market uptake, 630
 - requirements, electrolyte, 629
 - working principle, 629, 630
 - YSZ, 631–632
- Solution chemistry, CBD
 - ED, 323–324
 - framework
 - complexing agent, 321
 - controlling, 321–322
 - “forced hydrolysis”, 321
 - liquid phase deposition, 320
 - metals products, 320
 - non-oxide films, 321
 - oxide products, 321
 - parameters, 323
 - salts, 320
 - supersaturation, 322–323
 - LPD, 323
 - organic additives, 324, 326
 - oxide materials, 324–326
 - SILAR, 323
 - variations, 324
- Spectrometers
 - ATR, 217–218
 - dispersive, 216–217
 - FTIR spectroscopy (*see* Fourier transform infrared (FTIR) spectroscopy)
- Spin-coatable metal alkoxide electron beam resist
 - alkoxide-based multicomponent materials, 505
 - Al₂O₃ resist, 502, 503
 - aluminium *tert*-butoxide with ethyl acetoacetate, 502, 503
 - condensed titanium isopropoxide films, 502
 - exposure process
 - curves, 501–502
 - energy electrons, 504
 - fraction, aluminium *tert*-butoxide, 504
 - FTIR spectra, 503
 - SEM images, 504
 - sensitivity, 503
 - stability, 502–503
 - tentative exposure mechanism, Al₂O₃ resist, 503, 506
 - FET, 504–505
 - FTIR spectra, Al₂O₃ resist, 505
 - hydrolysis reaction, 500–501
 - I_d-V_{ds} characteristics, 505, 507
 - La_{0.7}Sr_{0.3}MnO₃, 502
 - periodic arrays, ferroelectric cells, 505, 508
 - polymerization, 500
 - stabilized metal alkoxides, 504
 - stabilizing, 501–502

- Spin-coatable metal alkoxide electron
 - beam resist (*cont.*)
 - titanium isopropoxide films, 502
 - UV-patterning, 501
- Spin coating
 - composite sol-gel films
 - cracked PZT thick film, high powder loading, 452, 453
 - description, 451
 - fabrication technique, 454
 - homogeneity, 454
 - powder loading, 451–452
 - properties, 452, 453
 - surface quality, 452–453
 - thickness variation and cracking, 454
 - uniformity, 452
 - conformality-related film defect, 276
 - evolution, fluid thickness, 264
 - fluid flow and evaporation
 - advantages, 266
 - contributions, 267
 - ethanol rotating, 267
 - Meyerhofer treatments, 267
 - RHS, 266
 - rotational forces, 265
 - velocity vs. depth profile, 265–266
 - volatile solvents, 266
 - process and topographical features, 275–276
 - solution precursors, 273
 - spinning speed, 263–264
 - stable solution, 265
 - stages, 263
 - thickness, 265
 - trenched structure, 276
 - uniformity and defect diagnosis
 - chuck marks, 270–271
 - comets, 268
 - striations, 268–270
 - variation, gradual radial thickness, 271–273
- SPM techniques. *See* Scanning probe microscopy (SPM) techniques
- Spray coating, 445, 456
- Spray pyrolysis methods
 - and aqueous nitrate precursors, 628
 - ESD and PSD, 633
 - sol-gel and metalorganic deposition, 643
- Sputtering techniques, 668, 712–713
- SSP. *See* Single source precursors (SSP)
- Structure zone model (SZM), 298–299
- Sub-nanometer Cutting and Ruling by an Intense Beam of Electrons (SCRIBE), 493, 496, 498, 499
- Substrate effects, CBD
 - ceria film, 331–332
 - complex topographies, 332
 - film formation mechanisms
 - aqueous inorganic solutions, 326, 327
 - chemical nature, 326
 - deposition conditions, 328
 - description, 326
 - electrostatic interactions, 328–329
 - hydrolysis and condensation reactions, colloidal particles, 327
 - hydroxyapatite coatings, 328
 - ion-by-ion growth, 326
 - orthopedic implant applications, 327, 328
 - transparency, 327
 - functionalization, 329–330
 - laminated composites, 332–333
 - LPD technique, 332
 - organic layers, 332
 - patterning, 330–331
 - polymer spheres, 332
 - porous nickel oxide, 331
 - synthesis materials, 332
 - TiO₂-V₂O₅ mesoporous powders, 332
- Successive ion layer adsorption and reaction (SILAR), 143, 323, 325–326
- Superconducting films
 - coated conductors (*see* Coated conductors)
 - conventional equipment, 693
 - HTS (*see* High temperature superconductivity (HTS))
 - industrial heat treatment, 697–698
 - power transmission
 - advantages, network planning, 694, 695
 - LIPA HTS cable project, 695, 696
 - principle, fault current limiter, 695–697
 - voltage cable, 695, 696
 - rotating machines
 - efficiency increment, HTS technology, 698, 699
 - HTS rotor, hydro power generator, 699, 700
 - size and RE consumption, permanent magnet and HTS, 701
 - savings, 693–694
- Super-lattice ordering, nano-composite thin films

- batteries
 - lithium rechargeable (*see* Lithium rechargeable batteries)
 - micro, 474
 - conventional layered oxides, 474
 - electronic devices, 474
 - transmission electron micrographs, 474–475
- Supramolecular sol-gel mechanisms and colloid particles
 - alkoxide, 77
 - heterometallic species, 79
 - microhydrolysis, 76
 - MTSAL concept, 77, 78
 - perovskites, microhydrolysis, 78–79
 - polyoxometallate type, 77
- Synthesis, CSD-derived functional oxide thin films
 - alkaline earth titanates (*see* Alkaline earth titanates)
 - aluminium oxide (*see* Aluminium oxide synthesis)
 - conductive oxide precursor solutions
 - APP route, 758
 - lanthanum, 759
 - lead-titanate (*see* Lead-titanate-based material systems)
 - principles, 747–748
 - thin film fabrication (*see* Thin film fabrication)
- SZM. *See* Structure zone model (SZM)

- T**
- TCOs. *See* Transparent conducting oxides (TCOs)
- TEM. *See* Transmission electron microscopy (TEM)
- Template controlled growth
 - bottom-up growth technique, 518
 - copolymer micelle lithography, gold nanoparticle hard masks, 526–528
 - crystalline thin films, 517
 - embedding
 - frequency dependent I-V curves measurements, 535, 536
 - gain, piezoelectric activity, 533, 534
 - HSQ/MSQ, 533
 - I-V plots recording, displacement current peaks, 534, 536
 - MSQ, PTO grain array, 534, 535
 - PTO islands, platinumized silicon substrate, 533
 - ferroelectric
 - characterization, SPM techniques (*see* Scanning probe microscopy (SPM) techniques)
 - nanograins, 519–521
 - nanotubes, soft-template infiltration, 524–525
 - nucleation process, 517, 518
 - nucleation site, e-beam lithography (*see* Nucleation site, e-beam lithography)
 - processing, ferroelectric nanostructures fabrication, 521, 522
 - seed layers and seeds, orientation selection, 518–519
- Ternary systems, CSD
 - amorphous film, 204
 - EXAFS measurement, 203
 - homogeneous distribution, metal components, 203–204
 - lead zirconate titanate precursors, 204
 - pyrolysis, 205
 - PZT materials, 202
 - thermal treatment and homogeneity, 203
 - zirconium local environment, 205
 - Zr-O-Zr bonds, 203
- TFBAR. *See* Thin film bulk acoustic wave resonator (TFBAR)
- TFTs. *See* Thin film transistors (TFTs)
- Thermal analysis (TA)
 - CSD precursors, 169–176
 - EGA, 168–169
 - equipment, 164
 - liquid precursors, 163
 - methods, 164–166
 - TG and scanning calorimetry, 163
 - thin films, 176
- Thermal depolymerization, 146–147
- Thermochemical nanolithography, 532
- Thermodynamics and heating processes
 - atmosphere effects, pyrolysis behavior
 - global, 349–350
 - impacts, 349
 - local/in-situ, 350–352
 - conversion, crystalline state vs. amorphous state, 343
 - description, 343
 - impact, temperature regime, 343–344
 - solution synthesis and thin film processing, 343
 - transformation, 343
 - crystallization and phase evolution
 - behavior (*see* Crystallization and phase evolution behavior)
 - decomposition behavior and pathway

- Thermodynamics and heating processes (*cont.*)
- additional effects, 347
 - solution precursor effects, 346–347
 - kinetic competition, 376–377
 - reactions and byproducts
 - acid vs. base catalysis, 347
 - alcohol, ester, ether and water, 349
 - DTA/TGA and DMSA data, 347–349
 - evolution, gaseous species, 349
 - FTIR, 349
 - gel decomposition, 349
 - lead acetate tri-hydrate precursor, 348
 - methoxyethanol gel-derived PZT
 - powers, 347
 - nature, 347
 - spectral ranges, 349
 - thermolysis and pyrolysis
 - characteristics, 344–345
 - definitions, 344
- Thermogravimetry (TG)
- and DTA, 167–168
 - and DTG, 167
 - and scanning calorimetry, 163
- Thin film bulk acoustic wave resonator (TFBAR), 609
- Thin-film-deposition and thermal treatment
- events comparison, 34–35
 - MOD/hybrid solution, 33–34
 - pyrolysis, 34
 - temperatures, 35
- Thin film fabrication
- chemical etching (*see* Chemical etching, thin film fabrication)
 - coating and crystallization
 - BST70/30 processing, 767–768
 - description, 765–766
 - PZT30/70 deposition, IWE Route, 767
 - spin coating, 766
 - preparation
 - coating solution, 764–765
 - substrate, 763–764
 - processing, 763
- Thin film multilayer capacitors (TMC)
- ceramic layer material and manufacturing technologies, 547–549
 - core-shell structures, 553, 555
 - dielectric film processing, 556–559
 - electrical properties
 - capacitance, CSD-derived multilayer, 564–566
 - capacitance density and resistivity, PLZT film thickness, 563
 - dielectric constant, 564
 - stable dielectric characteristics, 563
 - top-down patterning methods, 564, 565
 - “transferring method”, 566
 - electrode materials, 554–556
 - ferroelectrics and dielectrics, 548
 - miniaturization, 549
 - MLCC (*see* Multilayer ceramic capacitors (MLCC))
 - patterning (*see* Patterning methods)
- Thin film printing methods, 561, 562
- Thin film transistors (TFTs), 310
- Titanates
- FWHM and XRD pole, 689, 690
 - layer systems, 687
 - seed layers, 688, 689
 - sensitivity, 688
 - three-layer system, seed layer overgrowth, 688–689
- TMC. *See* Thin film multilayer capacitors (TMC)
- Transmission electron microscopy (TEM), 392
- Transparent conducting oxides (TCOs)
- ATO, 661–662
 - AZO (*see* Aluminium-doped zinc oxide (AZO))
 - electrical and optical properties, 656, 657
 - optimization strategies (*see* Optimization strategies, TCO thin films)
 - oxidic semiconductors, 655
 - resistive heating, windows, 656
 - sol–gel processing (*see* Sol-gel processing, TCO thin films)
- Transport, aerosol particle deposition
- aggregation and film growth
 - critical thickness, 294–295
 - deposition, 292–293
 - liquid droplets, 293–294
 - nucleation, 292, 293
 - surface energy, 293
 - thermal processing, 295
 - carrier gas trajectories, 288
 - collection efficiency
 - calculation, 291
 - electric field, 290–291
 - description, 283
 - electrical, gravitational and stokes force, 285, 286
 - electric field, 289, 290
 - film thickness, 292
 - gas flow, 284
 - impaction, particle size distribution, 288

- internal and external forces, 284
 - linearity, 292
 - LSMCD
 - deposition chamber, 287
 - processes, 285–286
 - polarities charges, 289–290
 - precursor utilization, 291–292
 - small particles, 289
 - spray and misted deposition, 288–289
 - stokes force, 284
 - thermophoretic forces, 284–285
 - variation, 287–288
- Trifluoroacetates
- CSD technology, 43
 - epitaxial films, 43
 - and hydrogen peroxide, 43
 - pyrolysis, 44
 - transition temperature, 44
- Trigonal bipyramidal oxygen environment, 196–197
- U**
- Ultrathin film deposition
- aqueous chemical solution deposition, 132
 - crystallization, 130
 - CSD film thickness, 129–130
 - DRAM, 128
 - drying kinetics, 131
 - microstructural instability
 - phenomenon, 132
 - silicate formation, 131
 - SiO₂/Si substrate deposit, 127–128
 - thermal processing, 131
 - thickness uniformity and continuity, 130
- UV patterning, photosensitive precursor film applications
- double exposures, 488–489
 - “moth eye effect”, 489
 - SEM photograph, 488, 489
 - surface-relief gratings, 488
 - two-beam-interference method, 488
- approaches, 483
- binary and multi-component systems
- Al₂O₃-SiO₂ preparation, 488
 - ferroelectric materials, 487
 - oxides, 487
 - PZT preparation, 487–488
- fine-patterning process, 483, 484
- limitation, 489–490
- metal-alkoxide with β -diketones compounds, 485
- description, 484
 - gel films, 485
 - optical absorption spectra, ZrO₂ films, 485–486
 - precursors, 484–487
 - reaction model, 485
 - UV-irradiation, 486
- metal complexes, carboxylic acids, 487
- micropatterns, oxide thin films, 483, 484
- positive-type, 488
- techniques, 483
- V**
- Vacuum Generators 501HB Scanning Transmission Electron Microscope (VG-STEM), 491
- Vertical hetero-epitaxial nano-composite (VHN), 464
- X**
- X-Ray absorption spectroscopy (EXAFS)
- absorption coefficient, 182
 - applications, innovative materials
 - Cu-O pair contribution, 209
 - HTS, 209
 - Yttrium barium copper oxide, 210
 - CSD (*see* CSD technology)
 - data analysis and interpretation
 - function, Mn-O, 188, 189
 - manganese compounds, oxidation states, 190, 192
 - Mn-Br distance, 190
 - oxygen signal, 190
 - photoelectron, 190–191
 - structural parameters, 190
 - XANES analysis, 192
 - data reduction and evaluation
 - absorption edge step, 185–186
 - amplitude, 188, 189
 - “elemental” absorption coefficient, 186–187
 - Fourier transformed spectrum, 187–188
 - oscillatory part, absorption coefficient, 186, 187
 - description, 181
 - equation, 182–183
 - experimental design

X-Ray absorption spectroscopy (EXAFS)
(*cont.*)
absorption coefficient, 184
transmission and fluorescence mode
measurements, 184–185
principles, 181
X-ray diffraction (XRD) analysis, 313,
346, 413, 416, 419, 436, 682,
685, 689, 690
X-ray imaging, 738
X-ray phosphors, 738
X7R materials, 553

Y

YBCO. *See* Yttrium barium copper
oxide (YBCO)
YSZ. *See* Yttria-stabilized zirconia (YSZ)
Yttria-stabilized zirconia (YSZ)
definition, 629
gas-tight, 634
and Gd-doped CeO₂ (CGO), 637, 638
grain boundary conductivity, 636
IT-SOFC, 631
Yttrium barium copper oxide (YBCO), 210,
395, 690–693